1.1 Fundamentals of Corrosion

Gerald S. Frankel
The Ohio State University, Columbus, Ohio

Dieter Landolt
Ecole Polytechnique Federale Lausanne
Lausanne, Switzerland

1.1.1 Introduction

Corrosion can be defined as an irreversible reaction of a material with the environment, which usually (but not always) results in a degradation of the material or its properties. So there are several aspects of corrosion: the material, the environment, and the material properties. Considerable information is available in textbooks [1–5] and other reference sources [6–9].

This general definition of corrosion includes reactions of widely varying material classes, such as the degradation of polymers by ultraviolet radiation, and the attack of refractory bricks during steelmaking. However, the focus of much of the field of corrosion is on the degradation of metals, which will be the focus of this volume. The corrosion of metals can take many forms, which are important to understand since the best methods of corrosion prevention depend upon the form of corrosion.

Many forms of corrosion will be discussed in detail in various chapters of this volume. The most basic form of corrosion is *uniform corrosion* during which a metallic object is more or less uniformly consumed and converted to ionic species. Much of our fundamental understanding of corrosion, such as thermodynamics and kinetics, is based on uniform corrosion, and the first few chapters of this volume will assume that corrosion is uniform in nature. Corrosion is often not uniform in nature, and various aspects of nonuniform, or localized corrosion will be addressed later in this volume. *Passivity* is the state of a metal that is protected by a thin surface oxide film called passive film. This subject will be the focus of Sect. 3.2 in this volume. *Pitting* is a form of localized corrosion that occurs when the thin passive film that protects most corrosion-resistant engineering alloys is compromised. The rate of attack at pits can be extremely high so pitting can lead to perforation of a structure or initiation of a crack. Localized corrosion often initiates at an occluded region where the environment has limited access. This form of corrosion, called *crevice corrosion*, is extremely important in fastened structures, which often contain many crevices. Localized corrosion is sometimes observed at grain boundaries when the composition of the grain boundary or region near the grain

boundary is different than that in the metal grain. This type of corrosion, called *intergranular corrosion* is a severe problem with stainless steels and aluminum alloys. Corrosive attack can be localized at one component of a structure made from different metals that are electrically connected as a result of *galvanic corrosion*. The corrosion of metal alloys often results in preferential reaction of one or more of the alloying elements, called *dealloying*. A common by-product of the corrosion process is hydrogen. Hydrogen can interact with metals in various ways to result in degradation of properties, primarily mechanical properties. A generic name for such degradation is *hydrogen damage*. The mechanical properties of metals can be severely degraded by the combined effects of the environment and an applied stress. *Stress corrosion cracking* is the premature failure of metal structures as a result of these effects. *Corrosion fatigue* occurs when the applied stress is fluctuating rather than constant.

Metals are generally produced by reduction of ores that are found in nature. Primary metal processing is costly and energy-intensive. Considerable effort and expense is put into fabricating metal alloys, such as steel, aluminum alloys, brasses, and so on, with the proper combination of properties such as shape, strength, conductivity, and so on. Subsequent exposure of these metal alloys to aggressive environments results in degradative changes in these properties. In general, the product of corrosion, rust for example, tends to be similar in nature to the ores from which the metal was originally derived.

This reversion of metal back to the state whence it came during the corrosion process can be considered extractive metallurgy in reverse. However, the energy expended during the metal-refining process is lost during corrosion. This degradation is also similar to the shorting of the two terminals of a battery. The energy stored in the battery, or in the metal, is simply lost. This loss of energy results in a financial loss. The cost of corrosion has been calculated by various means. A study completed in 2002 found that the total annual direct cost of corrosion in the United States is $279 billion or 3.1% of the gross domestic product [10]. The cost is borne, for instance, by the rebuilding of roads and bridges by funds that might be spent for new schools and hospitals. Companies suffer the costs of corrosion of processing equipment by expensive and nonproductive downtime in addition to the replacement cost.

Beyond the costs of corrosion are the safety concerns. Human lives depend upon the safe operation of a range of metallic structures that are prone to the ravages of corrosion. Obvious examples are airplanes made from high-strength aluminum alloys and pressure vessels that could endanger many lives if ruptured.

Corrosion considerations are critical in many applications. For instance, the chemical industry uses very aggressive environments for synthesis, and purity is usually extremely important. Therefore, the reactors and vessels must be essentially inert and resist the aggressive attack of the process environment. Corrosion resistant alloys have wide usage in this industry. Microelectronics is another area in which corrosion is important even though the environment is typically not very aggressive. In this case, the size of the structures is such that the smallest amount of corrosion could cause a failure, for example, a short in a submicron-sized conductor line. Other corrosive environments and industries in which corrosion is critical include oil and gas recovery and processing, marine and seawater applications, underground

pipelines, power plants, and Al alloys in aerospace applications. As a final example, the corrosion of reinforcing steel bars in concrete structures results in the degradation and expensive repair of structures such as bridges and parking decks.

The rate of corrosion will depend on a number of factors, including thermodynamic, kinetic, and mass-transport-related aspects. The first few sections of this volume will describe these influences on corrosion.

1.1.2 Fundamentals of Corrosion Electrochemistry

Corrosion is an electrochemical process. Therefore, some understanding of the fundamentals of electrochemistry is necessary [11–13]. Electrochemistry is the study of reactions that occur at the interface of an electrode, which is a metallic or semiconducting solid or liquid, and an electrolyte, which is a liquid or solid ionic conductor. These reactions typically involve the transfer of charge across the interface. There are two types of charge transfer reactions. Ion transfer reactions involve the transfer of ions from the electrode to the electrolyte, or vice versa. Electron transfer reactions involve the transfer of charge between ions in the electrolyte (or adsorbed on the surface), and typically occur heterogeneously at an electrode surface. Redox reactions are pure electron transfer reactions that occur at inert electrode surfaces. A more detailed discussion of electrochemical concepts can be found in the other volumes of this encyclopedia. A simplified view of certain aspects relevant to corrosion will be presented in this section.

1.1.2.1 Corrosion Reactions

Corrosion often involves oxidation of metal atoms to form ionic species with higher oxidation state and the liberation of electrons. For a generic metal M:

$$M \longrightarrow M^{z+} + ze^- \qquad (1)$$

Examples of real metals:

$$Fe \longrightarrow Fe^{2+} + 2e^- \qquad (2)$$

$$Zn \longrightarrow Zn^{2+} + 2e^- \qquad (3)$$

$$Al \longrightarrow Al^{3+} + 3e^- \qquad (4)$$

These are called half-cell reactions because the electrons liberated by the oxidation reaction must be consumed by a reduction reaction occurring on the same electrode. A reduction reaction that is common in acids is hydrogen evolution:

$$2H^+ + 2e^- \longrightarrow H_2 \qquad (5)$$

The complete corrosion reaction for Zn in an acid would be the sum of the oxidation and reduction reactions:

$$Zn + 2H^+ \longrightarrow Zn^{2+} + H_2 \qquad (6)$$

The sites for the oxidation reactions are called anodes, and the sites for the reduction reactions are called cathodes. Anodes and cathodes can be spatially separated at fixed locations associated with heterogeneities on the electrode surface. Alternatively, the locations of the anodic and cathodic reactions can fluctuate randomly across the sample surface. The former case results in a localized form of corrosion, such as pitting, crevice corrosion, intergranular corrosion, or galvanic corrosion, and the latter case results in nominally uniform corrosion.

1.1.2.2 Electrolytes

The corrosion of metals usually occurs in an environment that can be considered to be an electrolyte. Electrolytes encountered in corrosion are usually liquids containing

dissolved ionic species. The most common solvent in nature is water, a polar molecule that facilitates dissolution of ions.

Electrolytes must have sufficient conductivity to allow the passage of corrosion currents from the anodes to the cathodes, which occurs as a result of ion transport. Electrolytes contain both positively charged ions, cations, and negatively charged ions, anions. The sum of the positive charge must equal the sum of the negative charge since the electrolyte itself is electrically neutral. Electrolytes can also contain dissolved neutral species such as organic molecules and gases. Dissolved gases, oxygen in particular, can play a critical role in the corrosion process, as described in the following section.

The structure of the solvent water changes when ions are introduced. Because of the charge dipole of the water molecules, a sheath of oriented water forms around ions. The negatively charged sides of the water dipoles, where the oxygen atoms reside, are attracted to cations, whereas the positively charged sides of the water dipoles, where the hydrogen atoms reside, are attracted to anions. The water sheaths around cations are more stable than those around anions because of steric effects; water molecules can pack more easily in a radial fashion when the oxygen atom is pointed inward.

As described above, corrosion involves at least one anodic oxidation reaction that liberates electrons, and at least one cathodic reduction reaction that consumes the electrons. The anodic and cathodic sites must be electrically connected, and an electronic current flows between these sites through the metal. The circuit is completed by a current that flows in the electrolyte between the anodic and cathodic sites. Current flows in electrolytes by ion transport. Faraday's law relates current density at the electrode to flux of the reacting species:

$$i = nFJ \tag{7}$$

where i is current density (A cm^{-2}), n is the charge number (dimensionless), F is Faraday's constant (96 487 C mol^{-1}), and J is the flux of the reacting species (mol cm^{-2} s^{-1}). Transport processes will be discussed in more detail in Sect. 1.4 in this volume.

1.1.2.3 Electrode Potential and Structure of the Interface

At equilibrium, the charges in an electrolyte are randomly oriented. However, corrosion occurs at the interface of a metal and an electrolyte. The introduction of the discontinuity associated with an electrode changes the situation (much like the introduction of an ion), leading to a redistribution of charges at the interface. The interface as a whole remains electrically neutral, but there is a local loss of electroneutrality. At the electrode surface there is an excess of charge of one sign and in the solution there is an excess of charge of the opposite sign. As a consequence, a potential drop develops at the metal–solution interface.

Consider a Cu electrode in $CuSO_4$ at equilibrium. There is no potential gradient or concentration gradient in the solution. However, there is charge separation at the interface resulting in a potential drop. At equilibrium, this potential drop is representative of the reversible potential. Note that it is impossible to measure the absolute value of a single electrode potential; only the potential difference between two electrodes can be measured. To characterize electrode potentials in practice one uses a reference electrode, which is an electrode that has a fixed

potential drop. Electrode potentials are always reported versus a specific reference electrode, such as the standard hydrogen electrode (SHE) or the saturated calomel electrode (SCE).

The separation of charge at an electrode–electrolyte interface may be viewed as a capacitor, as first suggested by Helmholtz. One plate of the capacitor is thought to be the excess (or depletion of) electrons at the metal surface and the other is a plane of excess positively (or negatively) charged ions in solution adjacent to the surface. The distance between the two planes is on the order of only one- or two-tenths of a nanometer. The electric field between the planes is extremely large, on the order of 10^7 V cm^{-1}. This is the reason why charged species can easily cross the interface during electrochemical reactions.

There are two possible structures for the Helmholtz double layer, which are related to the waters of solvation associated with ions in solution. Because anions often do not carry a solvent sheath, they adsorb directly on the surface. The literature sometimes distinguishes the outer Helmholtz plane, corresponding to the distance of closest approach of hydrated cations, from the inner Helmholtz plane corresponding to the distance of closest approach of nonhydrated species. Ions situated in the inner Helmholtz plane are referred to as specifically adsorbed or contact adsorbed ions. Note that cations are attracted to surfaces with negative charge and anions to surfaces with positive charge. Adsorbed solvent dipoles tend to be oriented similar to those in an ion solvation sheath. The simplified Helmholtz double layer model is very useful for understanding charge transfer reactions but it is unable to explain all experimental observations.

Gouy and Chapman later suggested that the thermal energy of the ions would result in a diffuse layer on the solution side of the interface with the concentration of excess charges at a maximum close to the electrode surface and gradually decreasing with distance into the electrolyte (on the order of nanometers). However, the Gouy–Chapman diffuse layer model also does not match well with all experimental data.

Stern then synthesized the Helmholtz and Gouy–Chapman models into a concept in which two regions of charge separation exist: a region corresponding to the Helmholtz layer where the potential varies linearly, and a region corresponding to the Gouy–Chapman layer where the potential varies exponentially with distance from the interface. In concentrated solutions, most of the charge is in the Helmholtz double layer, and the diffuse region can be neglected. Conversely, in dilute solutions (having ionic concentration less than about 10^{-3} mol L^{-1}), the diffuse region dominates.

The electrochemical interface can also be viewed using a different framework [11, 13–18]. The electrical potential of the interior of an electrode with respect to a point at infinity in a charge-free vacuum is referred to as φ, the Galvani or inner potential. An energy of $e\varphi$ is required to transport an electron from infinity to the interior of the electrode. This potential can be considered to be composed of the sum two other potentials, $\varphi = \psi + \chi$, where ψ is the outer potential and χ is the surface potential. The outer potential arises from excess charge on the surface, and $e\psi$ is the energy required to bring a charge close enough to the surface to avoid image charges in the electrode. The surface potential results from adsorbed ions or oriented dipoles on the surface.

The difference in the inner potentials of the two phases at an electrochemical interface, the inner potential difference or Galvani potential difference, cannot be measured directly. The difference between the outer potentials of the two phases is called the Volta potential difference, and is measured by the Kelvin Probe technique, as described in Sect. 7.8 in this volume.

References

1. M. Fontana, N. Greene, *Corrosion Engineering*, McGraw-Hill, New York, 1978.
2. H. H. Uhlig, *Corrosion and Corrosion Control*, John Wiley & Sons, New York, 1971.
3. H. Kaesche, *Metallic Corrosion*, NACE International, Houston, Tex., 1985.
4. D. A. Jones, *Principles and Prevention of Corrosion*, 2nd ed., Prentice Hall, Englewood Cliffs, N. J., 1996.
5. D. Landolt, *Corrosion et chimie de surfaces des métaux*, Presses polytechniques et universitaires romandes, Lausanne, 1993.
6. L. L. Shreir, R. A. Jarman, G. T. Burstein, (Eds.), *Corrosion*, Butterworth-Heinemann, Oxford, 1994.
7. J. R. Davis, (Ed.), Corrosion in *Metals Handbook*, 9th ed., ASM International, Metals Park, Ohio, 1987, 1–1415, Vol. 13.
8. H. H. Uhlig, *Corrosion Handbook*, John Wiley & Sons, New York, 1940.
9. M. Pourbaix, *Atlas of Electrochemical Equilibria in Aqueous Solutions*, NACE International, Houston, Tex., 1984.
10. Corrosion Costs and Preventive Strategies in the United States, Tech Brief FHWA-RD-01-157, US Dept. of Transportation.
11. J. O'M. Bockris, A. K. N. Reddy, *Modern Electrochemistry*, Plenum Press, New York, 1970.
12. A. Bard, L. Faulkner, *Electrochemical Methods*, John Wiley & Sons, New York, 1980.
13. K. J. Vetter, *Electrochemical Kinetics*, Academic Press, New York, 1967.
14. S. Trasatti, *Electrochim. Acta* **1983**, *24*, 1083.
15. M. Stratmann, H. Streckel, *Corros. Sci.* **1990**, *30*, 681.
16. F. T. Wagner in *Structure of Electrified Interfaces* (Eds.: J. Lipkowski, P. N. Ross), VCH Publishers, New York, 1993.
17. S. Trasatti, *Electrochim. Acta* **1987**, *32*, 843.
18. S. Trasatti, *Electrochim. Acta* **1991**, *36*, 1659.

1.2 Thermodynamics of Electrolytic Corrosion

Gerald S. Frankel
The Ohio State University, Columbus, Ohio

Dieter Landolt
Ecole Polytechnique Federale Lausanne
Lausanne, Switzerland

1.2.1 Introduction

Thermodynamic calculations are extremely important in the field of corrosion because they can be used to predict the tendency for a metal to corrode in a given environment. Details of thermodynamic principles can be found in a number of textbooks [1–3]. The *Atlas of Electrochemical Equilibria in Aqueous Solutions* by Marcel Pourbaix provides a comprehensive summary of the application of thermodynamics to corrosion as well as a compendium of stability diagrams for all elements in water [4].

1.2.2 Fundamentals of Thermodynamics

The free energy for any species, G, is related to the standard free energy, G^0, which is the free energy for the species in its standard state, and the activity of the species, a:

$$G = G^0 + RT \ln a \tag{1}$$

where R is the gas constant and T is the temperature. Consider the generic chemical reaction:

$$a\mathrm{A} + b\mathrm{B} = c\mathrm{C} + d\mathrm{D} \tag{2}$$

where the capital letters represent species and the small letters represent stoichiometric numbers for which the reaction balances. The free energy change, ΔG, is a measure of driving force for the reaction to proceed. The free energy change is given by the difference of the free energy of the products and reactants:

$$\begin{aligned}\Delta G &= G_{\mathrm{prod}} - G_{\mathrm{reac}} \\ &= (cG_{\mathrm{C}} + dG_{\mathrm{D}}) - (aG_{\mathrm{A}} + bG_{\mathrm{B}}) \\ &= (cG^0_{\mathrm{C}} + cRT \ln a_{\mathrm{C}} + dG^0_{\mathrm{D}} \\ &\quad + dRT \ln a_{\mathrm{D}}) - (aG^0_{\mathrm{A}} + aRT \ln a_{\mathrm{A}} \\ &\quad + bG^0_{\mathrm{B}} + bRT \ln a_{\mathrm{B}}) = \Delta G^0 \\ &\quad + RT \ln \left(\frac{a^c_{\mathrm{C}} a^d_{\mathrm{D}}}{a^a_{\mathrm{A}} a^b_{\mathrm{B}}} \right)\end{aligned} \tag{3}$$

where $\Delta G^0 = (cG^0_{\mathrm{C}} + dG^0_{\mathrm{D}}) - (aG^0_{\mathrm{A}} + bG^0_{\mathrm{B}})$.

In generalized form:

$$\Delta G = \Delta G^0 + RT \ln \left\{ \frac{\Pi (a_{\mathrm{prod}})^j}{\Pi (a_{\mathrm{reac}})^k} \right\} \tag{4}$$

If $\Delta G < 0$ for a given reaction, it will tend to proceed spontaneously in the direction written because the free energy of the products on the right-hand side of the equation is less than that of the reactants on the left-hand side. At equilibrium, $\Delta G = 0$.

1.2.3 Thermodynamics of Electrochemical Reactions

Many chemical oxidation–reduction reactions can be performed in an electrochemical cell in which electrons liberated by oxidation of a species at one electrode (anode) flow through an external conductor to a second electrode (cathode) where they are consumed by a reduction reaction. A corresponding ionic current flows through the electrolyte that separates the electrodes in the electrochemical cell. In such a device,

the chemical energy change resulting from the Gibbs free energy change, ΔG, can be harvested as electric energy according to

$$\Delta G = -nFE^{\text{rev}} \tag{5}$$

In this expression, n is the charge number (dimensionless), F is the Faraday constant (96 485 C mol^{-1}) and E^{rev} is the reversible potential of the cell reaction.

An electrochemical cell reaction (overall reaction) includes at least two half-cell reactions or *electrode reactions* that either liberate or consume electrons. For the overall reaction (2), for example, the half-cell reactions might be expressed as:

$$a\text{A} = cC + n\text{e}^-$$

(anodic half-cell reaction) (6)

$$b\text{B} + n\text{e}^- = d\text{D}$$

(cathodic half-cell reaction) (7)

A potential can be assigned to each of these half-cell reactions provided a suitable reference is chosen, since it may be recalled that only the potential between two electrodes can be measured. It is customary to use the standard hydrogen electrode (SHE) as a universal reference when listing the potential of a half-cell. The SHE corresponds to the half-cell reaction:

$$2\text{H}^+ + 2\text{e}^- = \text{H}_2 \tag{8}$$

under conditions in which the activity of the protons is unity, $a_{\text{H}^+} = 1$, and the partial pressure of hydrogen gas is one bar, $P_{\text{H}_2} = 1$ bar (1 bar = 0.987 atm). The potential of the SHE is arbitrarily set at zero, $E^{\text{o}}_{\text{SHE}} \equiv 0$. Correspondingly, the free energy of protons in solution at unit activity is arbitrarily set to 0 as a reference.

On the basis of this convention, the reversible potential of any electrode reaction can be computed from thermodynamic data using Eq. (5). For example, the reversible potentials of the half-cell reactions (6) and (7) can be computed from the free energy changes of the following overall reactions:

$$a\text{A} + n\text{H}^+ = c\text{C} + \left(\frac{n}{2}\right)\text{H}_2 \tag{9}$$

$$b\text{B} + \left(\frac{n}{2}\right)\text{H}_2 = d\text{D} + n\text{H}^+ \tag{10}$$

for conditions in which $a_{\text{H}^+} = 1$ and $P_{\text{H}_2} = 1$ bar. If all species appearing in the stoichiometric equations of a half-cell reaction (in the above example the species A, B, C, and D) are in their standard state with free energy G^0, the calculated potential is the standard potential of the half-cell reaction:

$$E^0 = \frac{-\Delta G^0}{nF} \tag{11}$$

Equation (5) or (11) can be applied directly to half-cell reactions such as (6) and (7) and the resulting potentials obtained will be identical to those obtained from the overall reactions (9) and (10) because of the definition of the SHE as the universal standard. A selection of standard potentials of half-cell reactions is shown in Table 1 [5]. By international convention, electrode reactions in thermodynamic tables are always written as reduction reactions, so the more noble metals have a positive standard potential. Lists such as that in Table 1 are also called electromotive force series or tables of standard reduction potentials.

Compilations of thermodynamic data and standard potentials in electrochemistry references, such as the Pourbaix atlas [4], often use a convention that assigns zero to the free energy or chemical

Tab. 1 Electromotive force series [5]

Electrode reaction	*Standard potential (V)*
$Au^{3+} + 3e^- \longrightarrow Au$	1.50
$Pd^{2+} + 2e^- \longrightarrow Pd$	0.987
$Hg^{2+} + 2e^- \longrightarrow Hg$	0.854
$Ag^{+} + e^- \longrightarrow Ag$	0.800
$Cu^{+} + e^- \longrightarrow Cu$	0.521
$Cu^{2+} + 2e^- \longrightarrow Cu$	0.337
$2H^{+} + 2e^- \longrightarrow H_2$	0.00
$Pb^{2+} + 2e^- \longrightarrow Pb$	−0.126
$Sn^{2+} + 2e^- \longrightarrow Sn$	−0.136
$Ni^{2+} + 2e^- \longrightarrow Ni$	−0.250
$Co^{2+} + 2e^- \longrightarrow Co$	−0.277
$In^{3+} + 3e^- \longrightarrow In$	−0.342
$Cd^{2+} + 2e^- \longrightarrow Cd$	−0.403
$Fe^{2+} + 2e^- \longrightarrow Fe$	−0.440
$Ga^{3+} + 3e^- \longrightarrow Ga$	−0.530
$Cr^{3+} + 3e^- \longrightarrow Cr$	−0.740
$Zn^{2+} + 2e^- \longrightarrow Zn$	−0.763
$Mn^{2+} + 2e^- \longrightarrow Mn$	−1.18
$Zr^{4+} + 4e^- \longrightarrow Zr$	−1.53
$Al^{3+} + 3e^- \longrightarrow Al$	−1.66
$Mg^{2+} + 2e^- \longrightarrow Mg$	−2.37
$Na^{2+} + 2e^- \longrightarrow Na$	−2.71
$Ca^{2+} + 2e^- \longrightarrow Ca$	−2.87
$K^{2+} + 2e^- \longrightarrow K$	−2.93
$Li^{2+} + 2e^- \longrightarrow Li$	−3.05

potential of a pure element at 298 K in its stable state. This convention is different than the classical physiochemical scale derived from the third law of thermodynamics in which $S = 0$ for all solids at 0 K (assuming they are well ordered, homogeneous, and in internal equilibrium) and $H = 0$ for all elements in their stable states at 298 K. The electrochemical thermodynamic data are perhaps better viewed as standard free energies of formation, since the standard free energy of formation of a compound is the free energy change for the formation of the compound from its elements in their stable states at 1 atm pressure.

Another way of looking at the energetics of electrode reactions is to say that the charge transfer at the interface involves both a change in the chemical state of the reacting species and work to move the charged species across the potential drop at the interface. Thus, one can define an electrochemical free energy change for a half-cell reaction as:

$$\Delta\overline{G} = \Delta G + nF\Delta\Phi \qquad (12)$$

where $\Delta\Phi$ is the potential drop across the interface. The electrochemical free energy change is the sum of a chemical and an electrical component. For the following discussion, it is convenient to refer the potential drop at the interface (its absolute value cannot be measured) to the SHE, by setting $\Delta\Phi = E$. When an electrochemical half-cell reaction is at equilibrium, it is reversible (it proceeds equally fast in both directions) and $\Delta\overline{G} = 0$. Furthermore, at equilibrium, $E = E^{\text{rev}}$. Therefore, Eq. (12) simplifies to Eq. (5). This equation indicates that there is a reversible potential that balances the chemical free energy change of any electrochemical half reaction to keep the reaction at equilibrium, regardless of the concentrations of the species.

As mentioned above, the reaction is in equilibrium at the reversible potential, and will proceed in both directions at the same rate. At a potential above the reversible potential, the reaction will proceed predominantly in the oxidizing direction and the reaction will proceed predominantly in the reducing direction below the reversible potential.

1.2.3.1 Example 1

The standard potential for a reaction can be calculated from the standard free energy change using Eq. (11). Consider the half reaction representing the rusting of iron:

$$3Fe + 4H_2O = Fe_3O_4 + 8H^+ + 8e^- \tag{13}$$

In order to get the standard reduction potential, the half reaction should be written as a reduction reaction:

$$Fe_3O_4 + 8H^+ + 8e^- = 3Fe + 4H_2O \tag{14}$$

The standard reduction potential can thus be calculated:

$$E^0 = \frac{-(3G^0_{Fe} + 4G^0_{H_2O} - G^0_{Fe_3O_4} - 8G^0_{H^+} - 8G^0_{e^-})}{nF} \tag{15}$$

The values for the various standard free energies can be found in references, such as the Pourbaix atlas [4]:

$$\begin{aligned} E^0 &= \frac{-[3(0) + 4(-56\,690) - (-242\,400) - 8(0) - 8(0)]\text{cal C}^{-1}}{[8(96\,487)]} \\ &= -0.020 \text{ cal C}^{-1}(4.19 \text{ J cal}^{-1}) \\ &= -0.085 \text{ V} \end{aligned} \tag{16}$$

Note that $G^0_{Fe} = 0$ is a statement of the convention described above (the use of standard energies of formation), $G^0_{H^+} = 0$ is a result of using the SHE reference scale, and $G^0_{e^-} = 0$ is a statement of the assumption that electrons in the metal are in their standard state.

1.2.3.2 Example 2

Thermodynamics can be used to predict the spontaneous direction of an electrochemical reaction (tendency for reaction to occur), but not the rate of reaction. Consider the electrochemical cell in Fig. 1, which shows a two-compartment cell separated by a semipermeable membrane. One side contains a Zn electrode in a solution containing Zn^{2+} ions at a concentration of 1 M, and the other side contains a Cu electrode in a solution containing Cu^{2+} ions at a concentration of 1 M. Every species is in its standard state. The cell is represented by the following cell reaction:

$$Zn + Cu^{2+} = Zn^{2+} + Cu \tag{17}$$

This cell reaction consists of two half-cell reactions, each of which has an accompanying standard potential. Subtraction of

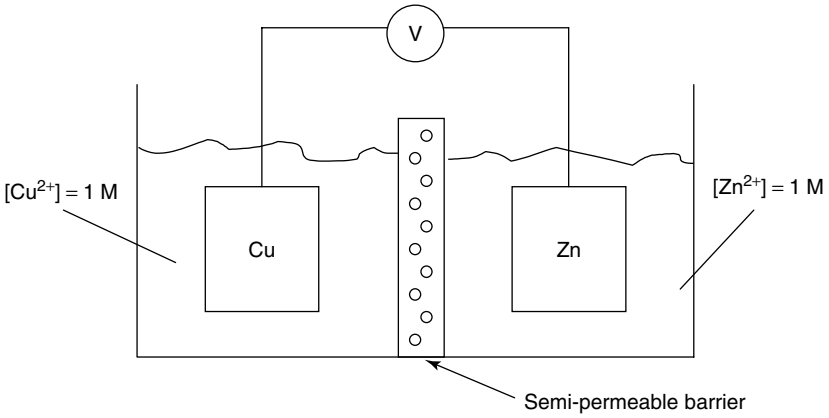


Fig. 1 Schematic representation of a corrosion cell consisting of Cu and Zn electrodes in solutions of unit cation activity.

one half-cell reaction from the other yields the cell reaction, Eq. (17). Subtraction of the standard potentials yields the standard cell potential.

$$\begin{aligned} &Cu^{2+} + 2e^- = Cu \quad E^0_{(Cu^{2+}/Cu)} = 0.337\,V \\ &-\left(\begin{matrix} Zn^{2+} + 2e^- = Zn \\ E^0_{(Zn^{2+}/Zn)} = -0.763\,V \end{matrix}\right) \\ &\overline{Zn + Cu^{2+} = Zn^{2+} + Cu \quad E^0_{cell} = 1.10\,V} \end{aligned} \tag{18}$$

Since $E^0_{cell} > 0$, $\Delta G^0_{cell} = -nFE^0_{cell} < 0$, and the reaction will proceed as written. Reactions with $E^0_{cell} < 0$ will proceed in the reverse direction. This calculation assumes that all species are in their standard states. If this is not the case, the Nernst equation must be used, as described below.

The half-cell reaction with the more active (negative) half-cell potential will proceed as an oxidation reaction, and the one with the more noble (positive) half-cell potential will proceed as a reduction reaction. In other words, noble metals tend to plate out, and active metals tend to dissolve. As a result, the direction of a cell reaction with all species in their standard states can be determined by inspection.

1.2.3.3 Example 3

The electrochemical cell in Fig. 2 shows a two-compartment cell with a Pb electrode in a Pb^{2+} solution on one side and a Pt electrode cell on the other side in a pH 0 acid saturated with H_2 gas at 1 bar. This approximates the case of a lead electrode in an acid solution. The Pt electrode acts as a catalyst for the hydrogen reaction:

$$\begin{aligned} &Pb^{2+} + 2e^- = Pb \\ &\qquad\qquad E^0_{(Pb^{2+}/Pb)} = -0.126\,V \\ &-\left(2H^+ + 2e^- = H_2 \; E^0_{(H^+/H_2)} = 0.0\,V\right) \\ &\overline{Pb^{2+} + H_2 = Pb + 2H^+ \; E^0_{cell} = -0.126\,V} \end{aligned} \tag{19}$$

Since $E^0_{cell} < 0$, the reaction proceeds in the reverse direction. Pb tends to spontaneously corrode in pH 0 acid, not plate out. However, the rate of corrosion is

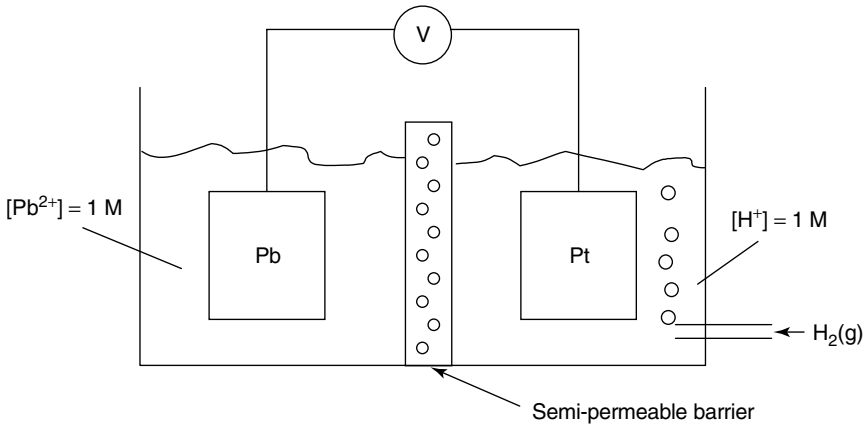


Fig. 2 Schematic representation of a corrosion cell consisting of a Pb electrode in a unit activity solution of lead ion and a Pt electrode in a solution of unit H^+ ion and hydrogen gas partial pressure of 1 atm. This is representative of Pb dissolution in an acidic solution, but allowing for separation of the anodic and cathodic reactions.

extremely slow because of kinetic factors, as will be described in more detail in chapter 1.3.

1.2.4 Nernst Equation

Reactants and products are not typically in their standard states. The Nernst equation accounts for the effects of activity on reversible potential. Equation (4) presents the free energy change for a generalized reaction in which the reactants and products are not in their standard states. If the reaction is a reduction reaction (the reactants and products are the oxidized and reduced form of a species, respectively), we can consider that $\Delta G = -nFE^{\text{rev}}$ and $\Delta G^0 = -nFE^0$. Substituting into Eq. (4):

$$E^{\text{rev}} = E^0 + \frac{RT}{nF} \ln \left\{ \frac{\Pi (a_{\text{ox}})^j}{\Pi (a_{\text{red}})^k} \right\} \qquad (20)$$

This equation, called the Nernst equation, describes the reversible potential of an electrochemical half reaction in which the oxidized and reduced species are not necessarily in their standard states. For dilute solutions, the activity coefficient is approximately equal to one so:

$$a_{\text{A}} = \gamma_{\text{A}} c_{\text{A}} \approx c_{\text{A}} = [\text{A}] \qquad (21)$$

where γ_{A} is the activity coefficient of species A, and c_{A} and [A] represent the concentration of species A in moles per liter. It should be noted that equating activity to concentration for dilute concentrations is a statement of Henry's Law, which utilizes a hypothetical standard state of 1 mol L^{-1}. The Henrian activity is different than that obtained from Raoult's Law, which states that activity equals mole fraction (activity coefficient equals one) when mole fraction is close to unity. Raoultian activity is used commonly in electrochemistry for gases and solvents. Thus, for the general half reaction:

$$a\text{A} + b\text{B} + n\text{e}^- = c\text{C} + d\text{D} \qquad (22)$$

the Nernst equation is:

$$E^{\text{rev}} = E^0 + \left(\frac{RT}{nF}\right) \ln \left(\frac{[\text{A}]^a [\text{B}]^b}{[\text{C}]^c [\text{D}]^d} \right) = E^0 + \left(\frac{0.059}{n}\right) \log \left(\frac{[\text{A}]^a [\text{B}]^b}{[\text{C}]^c [\text{D}]^d} \right) \quad \text{at room temperature} \qquad (23)$$

1.2.4.1 Example 3

Consider the electrochemical cell shown in Fig. 3, which has Co in a solution with $[\text{Co}^{2+}] = 10^{-6}$ M and Fe in a solution with $[\text{Fe}^{2+}] = 1$ M. The cell reaction is:

$$\text{Co} + \text{Fe}^{2+} = \text{Co}^{2+} + \text{Fe} \qquad (24)$$

First consider the situation for this cell at standard state:

$$\begin{array}{l} \text{Fe}^{2+} + 2\text{e}^- = \text{Fe} \quad E^0_{(\text{Fe}^{2+}/\text{Fe})} = -0.44\,\text{V} \\ -\left(\begin{array}{l} \text{Co}^{2+} + 2\text{e}^- = \text{Co} \\ \qquad\qquad E^0_{(\text{Co}^{2+}/\text{Co})} = -0.277 \end{array} \right) \\ \hline \text{Co} + \text{Fe}^{2+} = \text{Co}^{2+} + \text{Fe} \\ \qquad\qquad E^0_{\text{cell}} = -0.163\,\text{V} < 0 \end{array} \qquad (25)$$

Since $E^0_{\text{cell}} < 0$, the reaction proceeds in the reverse direction if all reactants and products are in their standard states. However, for the concentrations given, the Nernst equation must be used:

$$E^{\text{rev}}_{(\text{Co}^{2+}/\text{Co})} = -0.277 - \left(\frac{0.059}{2}\right) \log \left(\frac{1}{10^{-6}} \right) = -0.454\,\text{V}$$

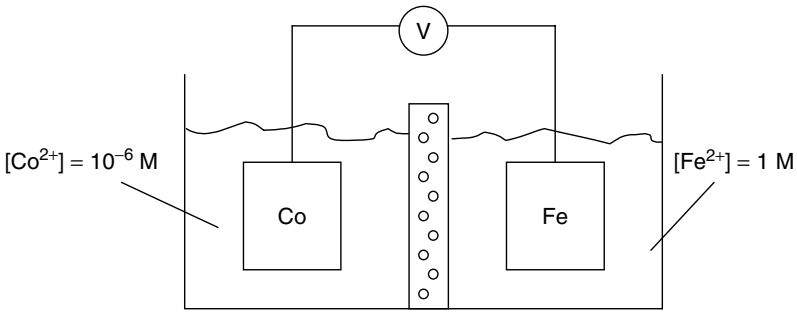


Fig. 3 Schematic representation of a corrosion cell consisting of Co and Fe electrodes, but where the Co ion solution is not unit activity.

$$E^{\text{rev}}_{\left(\text{Fe}^{2+}/\text{Fe}\right)} = E^{0}_{\left(\text{Fe}^{2+}/\text{Fe}\right)} = -0.44\ \text{V}$$

$$E^{\text{rev}}_{\text{cell}} = E^{\text{rev}}_{\left(\text{Fe}^{2+}/\text{Fe}\right)} - E^{\text{rev}}_{\left(\text{Co}^{2+}/\text{Co}\right)} = 0.014\ \text{V} > 0 \quad (26)$$

Since $E^{\text{rev}}_{\text{cell}} > 0$, the reaction proceeds in the forward direction when $[\text{Co}^{2+}] = 10^{-6}$ M, which is opposite of the tendency when $[\text{Co}^{2+}] = 1$ M. The low cobalt ion concentration reverses the tendency of the reaction by promoting Co dissolution.

1.2.5 Cathodic Reactions in Corrosion

In most environments of interest to corrosion, there is not a large concentration of metal ions acting as cathodic reactants. The important cathodic reactions in corrosion mechanisms involve water. There are two primary cathodic reactions, each of which takes a different form in acids or bases. The first is the hydrogen evolution reaction (HER), in which hydrogen gas is evolved.

$$2\text{H}^+ + 2\text{e}^- \longrightarrow \text{H}_2(\text{g}) \quad \text{acids} \quad (27)$$

$$2\text{H}_2\text{O} + 2\text{e}^- \longrightarrow \text{H}_2(\text{g}) + 2\text{OH}^- \quad \text{bases} \quad (28)$$

The Nernst equation for the HER given in Eq. (27) is:

$$E^{\text{rev}}_{(\text{H}^+/\text{H}_2)} = E^{0}_{(\text{H}^+/\text{H}_2)} + \left(\frac{0.059}{2}\right)\log[\text{H}^+]^2 = 0.059\log[\text{H}^+] = -0.059\ \text{pH} \quad (29)$$

It can be easily shown that the Nernst equation for the base form of the HER given in reaction (28) is also $E^{\text{rev}} = -0.059$ pH.

When dissolved oxygen gas is present in the aqueous solution, the following oxygen reduction reactions are possible:

$$\text{O}_2 + 4\text{H}^+ + 4\text{e}^- \longrightarrow 2\text{H}_2\text{O} \quad \text{acids} \quad (30)$$

$$\text{O}_2 + 2\text{H}_2\text{O} + 4\text{e}^- \longrightarrow 4\text{OH}^- \quad \text{bases} \quad (31)$$

The Nernst equation for the acid form of the oxygen reduction reaction is:

$$E^{\text{rev}}_{(\text{O}_2/\text{H}_2\text{O})} = E^{0}_{(\text{O}_2/\text{H}_2\text{O})} - \left(\frac{0.059}{4}\right)\log[\text{H}^+]^{-4} = 1.229 - 0.059\ \text{pH} \quad (32)$$

As for the case of the hydrogen evolution reaction, the Nernst equation for the base

form of the oxygen reduction reaction is the same as that for the acid form. The base form of either the hydrogen evolution reaction or the oxygen reduction reaction is obtained from the acid form by adding a multiple of the water dissociation reaction:

$$H_2O \longrightarrow H^+ + OH^- \qquad (33)$$

1.2.6 Pourbaix Diagrams

It is possible to use the Nernst equation, which relates reversible potential to pH and cation concentration, to generate phase stability plots in potential/pH space. Such diagrams are called Pourbaix diagrams, after Marcel Pourbaix who pioneered their development. Pourbaix diagrams are visual representations of the equilibrium conditions in potential/pH space. They are based on thermodynamics, and indicate the stable phase for given conditions, but say nothing about rates of reactions from one phase to another.

1.2.6.1 Pourbaix Diagram for Water

The Nernst equation for the HER was given in Eq. (29) as $E^{\text{rev}}_{(H^+/H_2)} = -0.059$ pH. This is a line in E/pH space that intersects (0,0) and has a slope of -0.059 V pH^{-1}. The HER is in equilibrium along this line. At potentials above this line in E/pH space, the reactions proceed in the oxidizing direction; water (H^+) is the stable phase and any dissolved H_2 gas that might be present in solution is oxidized. Below this line, H_2 gas is the stable phase, and water (or H^+) is reduced.

The Nernst equation for the oxygen reduction reactions, $E^{\text{rev}}_{(O_2/H_2O)} = 1.229 - 0.059$ pH, can also be plotted in E/pH space. This line is parallel to the hydrogen line, but is offset by 1.23 V. Above the oxygen line, O_2 is the stable phase, and water (or OH^-) is oxidized. Below the oxygen line, water is stable, and O_2 is reduced.

By plotting both the oxygen and hydrogen lines together on one plot, Fig. 4, the region for water stability is determined. Water is stable between the oxygen and hydrogen lines; it is oxidized to O_2 above the oxygen line and reduced to H_2 below the hydrogen line. A voltage of at least 1.23 V needs to be applied between two electrodes to hydrolyze or decompose water.

1.2.6.2 Pourbaix Diagram for Metals

Pourbaix diagrams for metals in aqueous solutions can be generated in order to visualize the stability regions for the metal and its various corrosion products. In order to construct a metal Pourbaix diagram, the possible reaction products in an aqueous solution must be known. In general, a metal will oxidize to form a soluble cation, a soluble anion, or a metal oxide or hydroxide. For a generic metallic element M, the electrochemical half reactions that form these various products are:

$$M \longrightarrow M^{n+} + ne^- \qquad (34)$$

$$M + nH_2O \longrightarrow MO_n^{m-} + 2nH^+ + (2n - m)e^- \qquad (35)$$

$$M + nH_2O \longrightarrow MO_n + 2nH^+ + 2ne^- \qquad (36)$$

$$M + nH_2O \longrightarrow M(OH)_n + nH^+ + ne^- \qquad (37)$$

Pourbaix diagrams must also consider chemical reactions in which a species containing a metallic element at a given

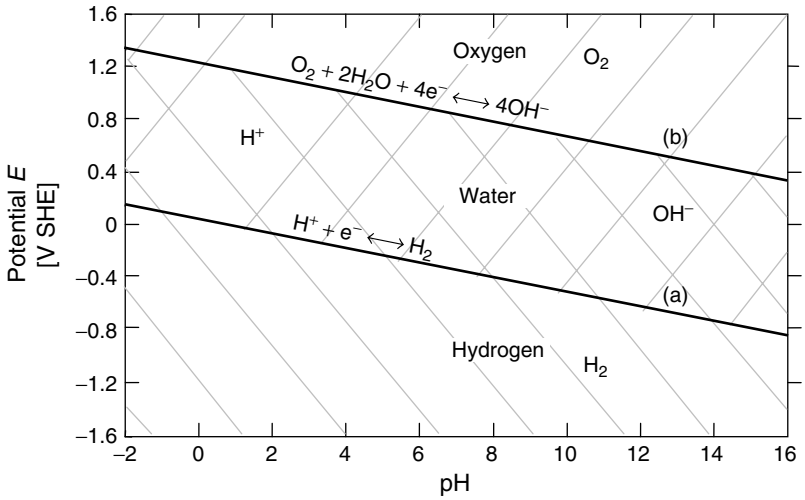


Fig. 4 Pourbaix diagram for water.

oxidation state changes into another species containing the metallic element in the same oxidation state. For example, a soluble cation or oxy-anion can precipitate to form an oxide or hydroxide:

$$m\mathrm{M}^{(2n/m)+} + n\mathrm{H_2O} = \mathrm{M}_m\mathrm{O}_n + 2n\mathrm{H}^+ \tag{38}$$

$$m\mathrm{M}^{(n/m)+} + n\mathrm{H_2O} = \mathrm{M}_m(\mathrm{OH})_n + n\mathrm{H}^+ \tag{39}$$

$$m\mathrm{MO}_{n+1}^{(2/m)-} + 2\mathrm{H}^+ = \mathrm{M}_m\mathrm{O}_n + \mathrm{H_2O} \tag{40}$$

$$\mathrm{MO}_{n-1}^{(n-2)-} + \mathrm{H_2O} + (n-2)\mathrm{H}^+ = \mathrm{M(OH)}_n \tag{41}$$

$$\mathrm{HMO_2}^- + \mathrm{H}^+ = \mathrm{MO} + \mathrm{H_2O} \tag{42}$$

Depending on the metal system being studied, it might also be necessary to consider reactions involving two dissolved species that occur homogeneously in solution. The two dissolved species might have the same or different oxidation states. An example of a reaction involving a change in oxidation state is the oxidation of a dissolved cation to a higher oxidation state reaction (43) and an example of a chemical reaction between two dissolved species with the same oxidation state is the equilibrium between a cation and an oxy-anion reaction (44).

$$\mathrm{M}^{n+} \longrightarrow \mathrm{M}^{n+1} + \mathrm{e}^- \tag{43}$$

$$\mathrm{M}^{n+} + n\mathrm{H_2O} = \mathrm{HMO}_n{}^{n-1} + (2n-1)\mathrm{H}^+ \tag{44}$$

1.2.6.3 Example: Pourbaix Diagram for Fe

In order to illustrate how the Nernst equations for the various reactions involving a metal in an aqueous solution can be combined to create a Pourbaix diagram for that metal, it is instructive to create a real diagram. A portion of the Pourbaix diagram for Fe will be developed in this section.

Fe can dissolve to form a ferrous cation, Fe^{2+}:

$$\mathrm{Fe} \longrightarrow \mathrm{Fe}^{2+} + 2\mathrm{e}^- \tag{45}$$

The Nernst equation for reaction (36) is:

$$E^{\text{rev}}_{\left(\text{Fe/Fe}^{2+}\right)} = E^{0}_{\left(\text{Fe/Fe}^{2+}\right)} + \left(\frac{0.059}{2}\right)\log([\text{Fe}^{2+}]) = -0.44 + 0.0295\log[\text{Fe}^{2+}] \quad (46)$$

This line is dependent on the Fe^{2+} activity or concentration, and independent of pH. It can be represented by a family of horizontal lines in E/pH space, depending on the value of $[Fe^{2+}]$. For the case in which metal is dissolving into a solution that nominally does not contain any of the ionic species (the typical case in corrosion), an interesting situation exists. The reversible potential for dissolution of a metal into a solution that has a metal ion concentration of 0 is $\log(0) = -\infty$. However, a very small amount of dissolution will result in a finite ion concentration in solution. For metal corrosion in a solution that contains no metallic ions, a concentration of 10^{-6} M is usually assumed for determination of reversible potential. This is a reasonable value for the influence of corrosion in a typical situation. At Fe^{2+} activities of 1 and 10^{-6}, the reversible potential is -0.44 and -0.617 V, respectively. These lines, which are plotted in Fig. 5, represent equilibrium for reaction (45). Above these lines the reaction will proceed as oxidation, and Fe^{2+} is the stable species; below these lines Fe is stable.

Consider now the reaction of Fe to form ferrous hydroxide:

$$\text{Fe} + 2\text{H}_2\text{O} \longrightarrow \text{Fe(OH)}_2 + 2\text{H}^+ + 2\text{e}^- \quad (47)$$

$$E^{\text{rev}} = E^{0} + \left(\frac{0.059}{2}\right)\log([\text{H}^+]^2) = -0.047 - 0.059\ \text{pH} \quad (48)$$

This line is parallel to the hydrogen and oxygen reaction lines with a slope of -0.059 V pH^{-1}. Along the line, reaction (47) is in equilibrium, below the line Fe is stable, and above the line $Fe(OH)_2$ is stable.

Fe^{2+} reacts to form $Fe(OH)_2$ by a chemical reaction (a precipitation reaction with no charge transfer):

$$\text{Fe}^{2+} + 2\text{H}_2\text{O} = \text{Fe(OH)}_2 + 2\text{H}^+ \quad (49)$$

The equilibrium constant for this reaction describes the combinations of Fe^{2+} concentration and pH for which this reaction is at equilibrium:

$$K = \frac{[\text{H}^+]^2}{[\text{Fe}^{2+}]} = 10^{-13.29} \quad (50)$$

$$\text{pH} = 6.645 - \left(\tfrac{1}{2}\right)\log[\text{Fe}^{2+}]$$

This relationship is independent of potential, and is displayed in the Pourbaix diagram as a vertical line at a given pH that depends on $[Fe^{2+}]$, and separates the Fe^{2+} and $Fe(OH)_2$ phases. For

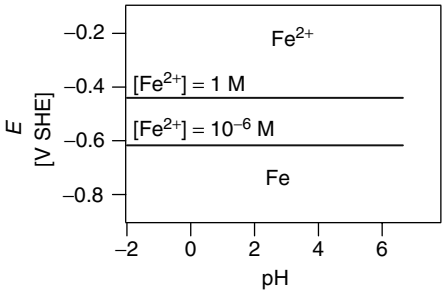


Fig. 5 Partial Pourbaix diagram for Fe showing the lines for the Nernst equation for the equilibrium between Fe and Fe^{2+}.

$[Fe^{2+}] = 10^{-6}$ and 1, the line is pH = 9.65 and 6.65, respectively. These lines connect to with the lines separating the Fe/Fe^{2+} and $Fe/Fe(OH)_2$ phases to form a clear separation of the three phases, Fig. 6.

Fe can react to form an oxy-anion, dihypoferrite, or $HFeO_2^-$, according to:

$$Fe + 2H_2O \longrightarrow HFeO_2^- + 3H^+ + 2e^- \quad (51)$$

$$\begin{aligned} E^{rev} &= E^0 + \frac{0.059}{2}\log([H^+]^3[HFeO_2^-]) \quad (52)\\ &= E^0 + \frac{0.059}{2}\log[HFeO_2^-] - \left(\frac{3}{2}\right)(0.059)\ pH\\ &= 0.493 + 0.0295\log[HFeO_2^-] - 0.0886\ pH \end{aligned}$$

This line depends on both pH and ion concentration. So it has a finite slope in E/pH space and varies with $[HFeO_2^-]$. It is plotted in Fig. 7 for $[HFeO_2^-] = 10^{-6}$. When $[HFeO_2^-] = 1$, the equilibrium is at pH values higher than 16.

$Fe(OH)_2$ dissolves chemically to form $HFeO_2^-$ according to:

$$Fe(OH)_2 = HFeO_2^- + H^+ \quad (53)$$

$$K = [H^+][HFeO_2^-] = 10^{-18.3} \quad (54)$$

$$pH = 18.3 + \log[HFeO_2^-]$$

For $[HFeO_2^-] = 10^{-6}$, the equilibrium line is pH = 12.3, Fig. 7. When $[HFeO_2^-] = 1$, the equilibrium line is off of the diagram. To finish the Pourbaix diagram for Fe, it is necessary to consider other substances, including $Fe(OH)_3$, and Fe^{3+}. The reactions must be written, and the Nernst equations or solubility equations must be developed and plotted. The full Fe Pourbaix diagram is given in Fig. 8.

1.2.6.4 Comments on Pourbaix Diagrams

Pourbaix diagrams are very useful tools for predicting corrosion behavior. The

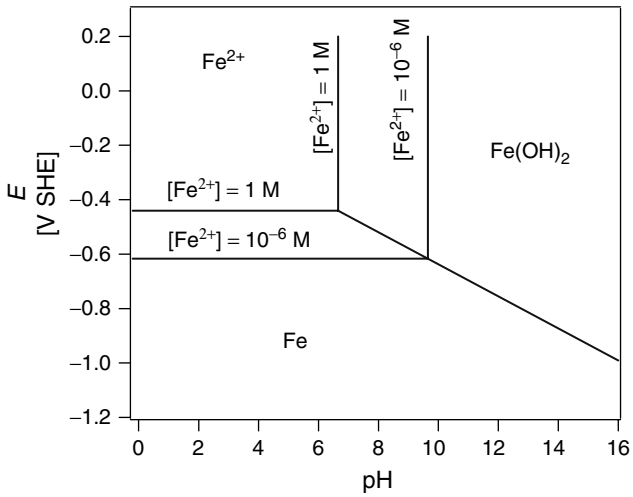


Fig. 6 Partial Pourbaix diagram for Fe showing the lines separating the Fe, Fe^{2+}, and $Fe(OH)_2$ phase fields.

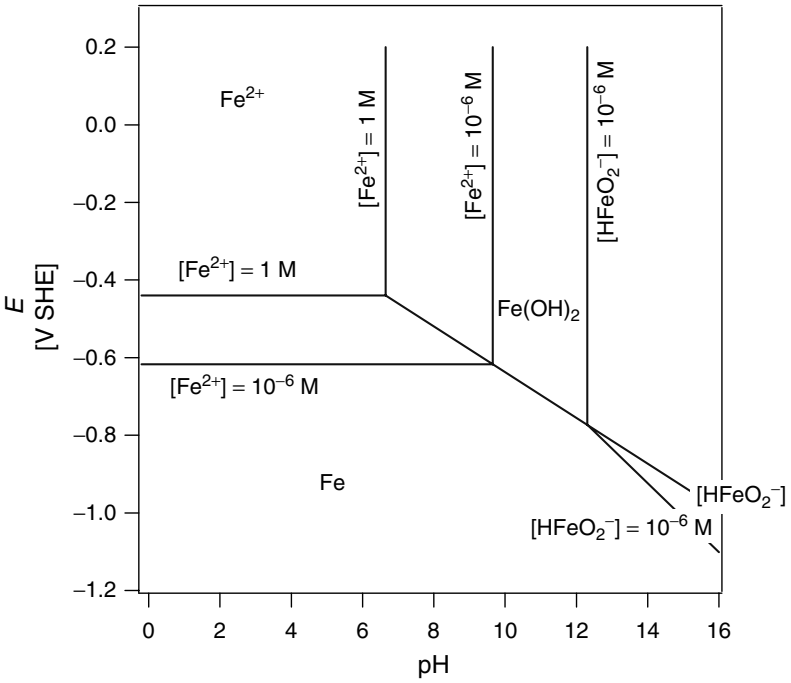


Fig. 7 Partial Pourbaix diagram for Fe showing the lines separating the Fe, Fe^{2+}, and $Fe(OH)_2$ and $HFeO_2^-$ phase fields.

diagrams for many elements are complied in the Pourbaix atlas [4]. However, it is critical to understand both the limitations of Pourbaix diagrams, and their proper interpretations. In general, there are three types of phase fields in Pourbaix diagrams: immunity, corrosion, and passivity. The region where the metal M is the stable phase, which is typically at low potentials, is considered to be a region of immunity. In this region, corrosion is thermodynamically unfavored; the tendency would be for any metal ions in solution to plate out. Phase fields in which a dissolved cation or oxy-anion is stable are considered to be regions of corrosion where the tendency would be for corrosion to occur. For most metals, the corrosion regions are at the acid and base ends of the diagram. Some metals, such as Cr, dissolve transpassively as a result of a stable ionic phase at high potentials even in the mid-pH range. Some metals, such as Sn, will form a gaseous metal hydride phase at low potentials. This phase is also a region where the metal will react, and should be considered a region of corrosion. Phase fields in which the stable substance is a solid oxide or hydroxide are considered to be regions of passivity. The assumption is that the oxide or hydroxide will form on the metal surface and decrease the rate of corrosion to a very low value. Most metals (W is a notable exception) have a passivity field in the mid-pH range.

All Pourbaix diagrams for metal–water systems include the lines for the cathodic reactions in water (the oxygen and hydrogen reactions). The relative position of these lines to the stable phases indicates

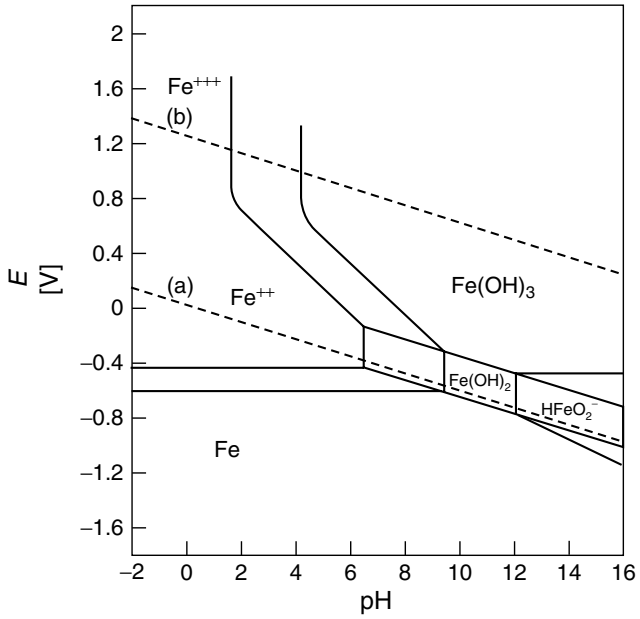


Fig. 8 Full Pourbaix diagram for Fe showing the lines for ion concentrations of 1 and 10^{-6}.

the availability of the cathodic reactions for corrosion. In order for either the oxygen reduction or hydrogen evolution reaction to act as a cathodic reaction for a corrosion process, the E/pH conditions must be below the respective lines where the tendency for the reactions would be towards reduction. In order for a corrosion reaction to proceed, the potential must be above $E^{\mathrm{rev}}_{(\mathrm{M/M^+})}$. So the phase space between $E^{\mathrm{rev}}_{(\mathrm{M/M^+})}$ and the oxygen or hydrogen line is where corrosion is possible. For noble metals such as Cu, E^{rev} is above the hydrogen line. This means that open circuit corrosion of Cu will not occur in association with hydrogen evolution; Cu is immune in a deaerated environment (ignoring other effects such as complexation). Cu will corrode in an aerated solution (one containing dissolved oxygen gas) because $E^{\mathrm{rev}}_{(\mathrm{Cu/Cu^{2+}})}$ is well below the oxygen line.

It is possible that different oxides or hydroxides may form, each of which has a different free energy. As a result, the Pourbaix diagram will change, depending upon the exact phases that are considered. For instance, the Pourbaix diagram considering Fe_3O_4 and Fe_2O_3 will be different than that shown in Fig. 8.

Passivity and alloy dissolution are covered in detail in other chapters of this volume. However, Pourbaix diagrams can be used to suggest the influence of alloying on passivation or oxide film formation. It is possible for one element in an alloy to enrich in a surface oxide layer if the oxide of that metal is stable in an E/pH region where the other elements are not stable. This results in an effective extension of the passivity region for the base metal of the alloy. An example of this is stainless steel. The

Pourbaix diagram for Fe shows that the corrosion region extends into mid-pH values at moderate potentials. The phase field for Cr_2O_3 overlays much of this territory, allowing for an enhancement in the passivity of Fe alloys by the addition of Cr.

The primary limitation for Pourbaix diagrams is that they are constructed purely from thermodynamic data. They are simply visual representations of the thermodynamic data. As such, they provide no information about corrosion rates. It is possible for substances that are thermodynamically unstable to be metastable, and exert a strong influence on the corrosion kinetics. For instance, Ni is quite resistant to acids, even though thermodynamics predicts that Ni^{2+} should be the stable phase at potentials above the Ni/Ni^{2+} reversible potential because of the metastability of NiO. On the other hand, some thermodynamically stable phases provide little protection.

Metal ion concentration has a strong influence on the equilibria; as mentioned above, $E^{rev}_{(M/M^+)} = -\infty$ if $[M^+] = 0$. The exact composition of an environment is often not known, especially given the possibility for local variations. The boundaries for ion concentrations of 10^{-6} are only guidelines.

Both oxidation and reduction reactions that occur as corrosion proceeds can result in pH changes. The O_2 reduction and hydrogen evolution reactions both either consume protons or produce hydroxyls. Therefore, under conditions in which there is a spatial separation of cathodic and anodic reactions, the pH at the cathodic sites will increase. Hydrolysis of metal cations will result in a decrease in pH at anodic sites. Even for uniform corrosion, with distributed and changing anodic and cathodic sites, the pH will tend to increase with time as the alkalinity generated by the cathodic reactions will only balance the acidity produced by hydrolysis if the hydrolysis reactions proceed completely to uncharged hydroxides. Using appropriate consideration of the local pH, Pourbaix diagrams can still be used to predict the reactions for these corrosion situations that experience changes in pH with time.

Finally, the Pourbaix diagrams given in the Pourbaix atlas are only for simple binary systems $M-H_2O$. However, it is possible to extend the Pourbaix diagram concept to more complicated systems if the free energies of every species are known. For instance, the system $Cu-Cl-H_2O$ has been studied [6]. The addition of chloride to the system necessitates consideration of a number of new solid substances (CuCl, $CuCl_2$, $3Cu(OH)_2 \cdot CuCl_2$) and new dissolved species (Cl^-, $CuCl_2^-$, $CuCl_2^{2-}$, $CuCl^+$, $CuCl_3^-$, and $CuCl_4^{2-}$). The copper-chloro complexes that can form in an aqueous chloride environment are less noble than the cupric ion. In fact, there is a range of stability for $CuCl_2^-$ below the hydrogen line in solutions containing sufficient chloride. This means that copper will spontaneously corrode in deaerated chloride solutions because of the complexation by chloride.

There is a need to develop the concept of stability diagrams to complex systems such as real alloys in concentrated acids or organic solvents. In such systems, it is critical to accurately represent the standard state properties as well as the activity coefficients. Recently, approaches have been developed and applied to a range of problems such as the formation of iron sulfide scales [7].

1.2.7 Thermodynamics of High Temperature Corrosion

High temperature corrosion and oxidation will be covered in a separate chapter. However, some basics of the thermodynamics will be addressed here. Consider a metal M reacting at high temperature with O_2:

$$\left(\frac{2x}{y}\right)\mathrm{M} + \mathrm{O_2} \longrightarrow \left(\frac{2}{y}\right)\mathrm{M}_x\mathrm{O}_y \quad (55)$$

The free energy change differs from the standard free energy change ΔG^0 if the reactants and products are not in their standard states:

$$\Delta G = \Delta G^0 + RT \ln\left\{\frac{a_{\mathrm{M}_x\mathrm{O}_y}^{2/y}}{(a_{\mathrm{M}}^{2x/y})(a_{\mathrm{O_2}})}\right\}$$

$$= \Delta G^0 + RT \ln\left(\frac{1}{p_{\mathrm{O_2}}}\right) \quad (56)$$

At equilibrium, $\Delta G = 0$:

$$\Delta G^0 = -RT \ln\left(\frac{1}{p_{\mathrm{O_2/MO}}}\right)$$

$$= RT \ln(p_{\mathrm{O_2/MO}}) \quad (57)$$

where $p_{\mathrm{O_2/MO}}$ is the O_2 pressure at which the system is in equilibrium. According to Eq. (57) equilibrium at a given temperature is possible at only one O_2 pressure.

The thermodynamic data describing equilibrium can be plotted in an Ellingham diagram, Fig. 9 [1]. This diagram is a compilation of lines for standard free energy for oxidation of different elements. It can be used to determine the equilibrium temperature for a given reaction and given value of oxygen partial pressure, CO/CO_2 ratio, or H_2/H_2O ratio. Conversely, the equilibrium values for the gas pressures or ratios can be determined for a given temperature.

In order to determine the equilibrium temperature for a given reaction and oxygen partial pressure, a line is drawn starting from the point at the very top of the free energy scale to the left of the plot. This point is $\Delta G^0 = 0$ and $T = 0$ K. The line is extended from that point to the appropriate point on the $p_{\mathrm{O_2}}$ scale on the bottom and to the right of the figure. The value of temperature at the point of intersection of that line and the $\Delta G^0 - T$ line for the given reaction is the equilibrium temperature. The reaction will tend to go in the oxidizing direction at temperatures below this equilibrium temperature, and in the reducing direction at higher temperature. The CO/CO_2 ratio and H_2/H_2O ratio scales are used with the points marked H and C, respectively, on the line to the left.

The Ellingham diagram assumes 1 bar total pressure ($p_{\mathrm{ref}} = 1$), pure metal reacting ($a_{\mathrm{m}} = 1$), and pure metal oxide forming ($a_{\mathrm{ox}} = 1$). All equations are written for 1 mole O_2. The slopes of the lines are a result of the entropy change for the reaction:

$$\left.\frac{\partial \Delta G}{\partial T}\right|_P = -\Delta S \quad (58)$$

For most of the reactions, 1 mole of gas is consumed to make a solid product, resulting in a decrease in entropy and a positive slope. The slope changes at temperatures above the boiling point of the metal. The line for the oxidation of C to CO has a negative slope because 1 mole of gas is reacting to create 2 moles of product, which involves an increase in entropy. Similarly, the line for oxidation of C to CO_2 is horizontal.

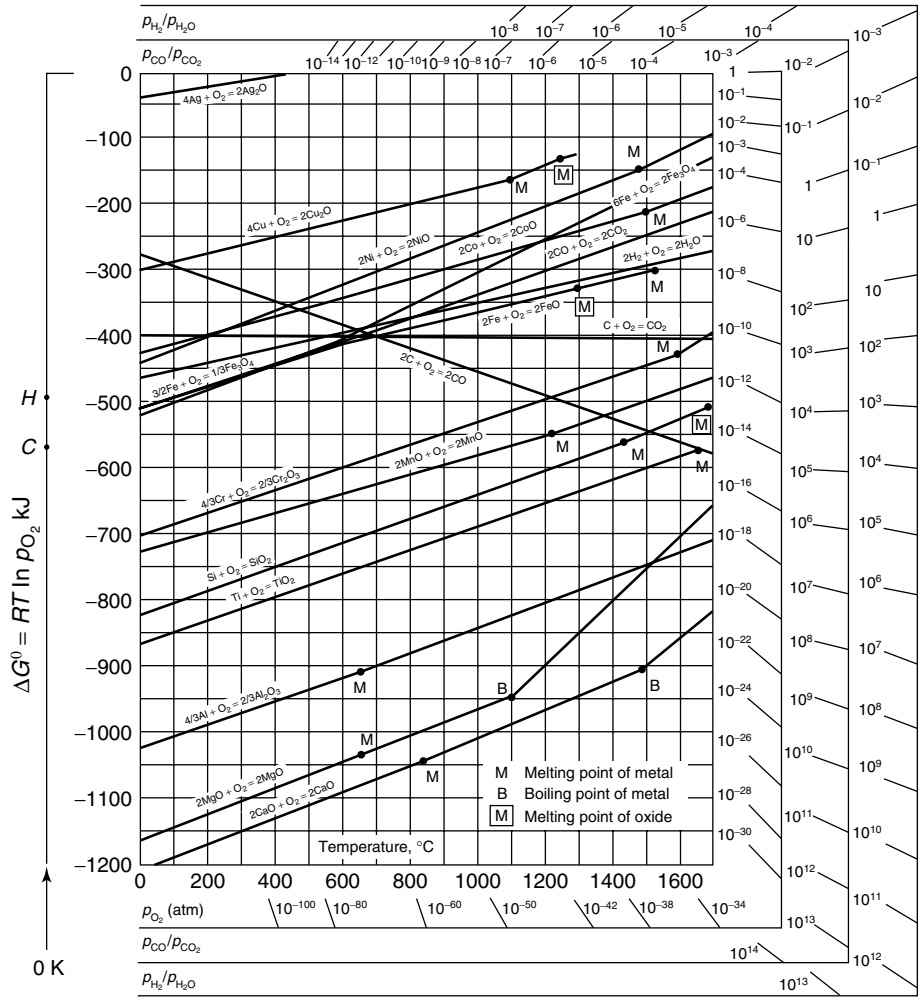


Fig. 9 Ellingham diagram [1].

References

1. D. R. Gaskell, *Introduction to Metallurgical Thermodynamics*, 3rd ed., Taylor & Francis, Washington, DC, 1995.
2. R. T. DeHoff, *Thermodynamics in Materials Science*, McGraw-Hill, New York, 1993.
3. C. H. P. Lupis, *Chemical Thermodynamics of Materials*, North Holland, New York, 1983.
4. M. Pourbaix, *Atlas of Electrochemical Equilibria in Aqueous Solutions*, NACE International, Houston, Tex., 1974.
5. J. R. Davis, (Ed.), Corrosion in *Metals Handbook*, 9th ed., ASM International, Metals Park, Ohio, 1987, 1–1415, Vol. 13.
6. M. Pourbaix, *Lectures on Electrochemical Corrosion*, 3rd ed., NACE International, Houston, Tex., 1995.
7. A. Anderko, S. J. Sanders, R. D. Young, *Corrosion* **1997**, *53*, 43–53.

1.3 Kinetics of Electrolytic Corrosion Reactions

Gerald S. Frankel
The Ohio State University, Columbus, Ohio

Dieter Landolt
Ecole Polytechnique Federale Lausanne
Lausanne, Switzerland

1.3.1 Introduction

The information about the tendency for corrosion to occur that can be obtained from thermodynamic calculations is important and useful. However, most of the science and engineering aspects in the field of corrosion focus on knowing and reducing the *rate* of corrosion. The rate of corrosion is not addressed by thermodynamics; it falls instead within the purview of kinetics. So the kinetics of electrochemical reactions in general, and corrosion reactions specifically, are at the heart of the subject of corrosion. This chapter will introduce electrochemical kinetics at a simple level, with sufficient detail to develop the concept of mixed potential theory. The interested reader is referred to other volumes of this encyclopedia and to textbooks in corrosion [1–9] for a more detailed description. The kinetic underpinnings of some of the electrochemical techniques for determination of corrosion rate will also be presented. The influence of transport on the rates of electrochemical reactions will be discussed in the next chapter (see Chapter 1.4).

1.3.2 Measures of Corrosion Rate

Corrosion rates can be given in a number of different units using different measures of material loss. The easiest way to determine a corrosion rate is by immersing a sample into a corrosive environment for a period of time and measuring the weight loss during that time. The weight loss must be normalized by the sample area in order to determine a corrosion rate, so one set of proper units for corrosion rate is weight loss per unit area per unit time; for instance, mg cm^{-2} s^{-1}. It is very common to divide this measure of weight loss corrosion rate by the density of the corroding material to get a corrosion rate in units of thickness lost per unit time; for instance, mils per year (mpy, which is thousandths of an inch per year) or mm yr^{-1}.

Electrochemical techniques for determination of corrosion rate generate a value in units of A cm^{-2}, which is current density. The rate of material loss, r (mm yr^{-1}), is related to the corrosion current density, i_{corr} (A cm^{-2}), by:

$$r = \frac{CMi_{corr}}{\rho nF} \qquad (1)$$

where M is the molecular weight of the corroding metal (g mol^{-1}), ρ is the density of metal (g cm^{-2}), and C is a constant to alter units of thickness and time.

1.3.3 Exchange Current Density; Kinetics at Equilibrium

Consider an electrochemical half-reaction at equilibrium:

$$M^{z+} + ze^- \longleftrightarrow M \qquad (2)$$

The fact that a reaction is at equilibrium does not mean that the system is at rest and inactive. Rather, for a system at equilibrium, the rate of the reaction in the forward direction is equal to the rate in the reverse direction. Indeed, it is

possible that the rate of the reaction in both directions is extremely rapid. This equal rate of the forward and reverse reactions at equilibrium is defined as the exchange current density, i_0.

The hydrogen reaction in acid solutions was presented in the last chapter (Chapter 1.2):

$$2H^+ + 2e^- \longleftrightarrow H_2(g) \qquad (3)$$

The exchange current density for the hydrogen reaction is strongly dependent on the catalytic properties of the metal surface on which the reaction occurs. For instance, it varies from 10^{-12} A cm^{-2} for Pb to 10^{-3} A cm^{-2} for Pd at 25 °C in 1 M H_2SO_4 [7]. Since hydrogen evolution is the primary cathodic reaction when a metal corrodes in an acid environment, this variability can have large implications on the corrosion rate. In fact, the rate of the corrosion reaction can be limited by the rate of the cathodic reaction, which is strongly dependent on the exchange current density of the reaction. An example is corrosion of lead in acid. The thermodynamic tendency is for Pb to corrode with simultaneous hydrogen evolution. However, the exchange current density for the hydrogen reaction on Pb is extremely small. As a result, the rate of Pb dissolution in acids is negligible and Pb can, for example, be used to contain sulfuric acid. Recall that there is a reversible potential associated with the equilibrium of any electrode reaction. Therefore, it is possible to represent the situation of equilibrium for an electrochemical reaction as a point in potential versus log current density space, (E^{rev}, i_0), Fig. 1. The reason for plotting the current density on a logarithmic axis will become clear shortly.

Exchange current density is dependent on the concentrations of reactants and products:

$$i_0 \propto c_R^{\delta} c_P^{\gamma} \qquad (4)$$

where c_R and c_P are the surface concentrations of the reactants and products, respectively, and δ and γ are typically fractional and positive. This expression, which will be derived in the next chapter, shows that i_0 tends to increase with concentration. Note that E^{rev} is also affected by concentration through the Nernst equation. So the location of the point representing equilibrium in Fig. 1 will vary with solution concentration. These issues will also be addressed in further detail in the next chapter.

1.3.4 Overvoltage

The point representing equilibrium on Fig. 1 indicates a finite exchange current density. Since this current density is the

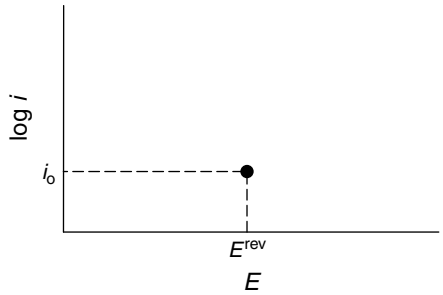


Fig. 1 Representation of equilibrium in E–log i space.

rate in both the forward and reverse directions, the net current density is zero. However, at a potential different than E^{rev}, the half-cell reaction will proceed preferentially in one direction and a net current will be measured.

Overvoltage, $\eta = E - E^{rev}$, is defined as a change in potential from the reversible potential of a given electrode reaction. Associated with this potential change is a change in the net reaction rate so that the reaction proceeds predominantly in one direction. The current is anodic (oxidizing, positive) for anodic polarization (a potential change to a value higher than the reversible potential), and cathodic (reducing, negative) for cathodic polarization (a potential change to a value lower than the reversible potential), Fig. 2.

In electrochemistry, potential and current are interdependent. It is possible to control either one and measure the other.

1.3.5 Activation Overvoltage

If the concentrations of the reactants and products at the electrode surface are the same as in the bulk solution, the overvoltage resulting from a potential change is called activation overvoltage or charge transfer overvoltage. It stems from the fact that the rate of charge transfer at the electrode–electrolyte interface is not infinitely fast. Note that the concentration at the electrode surface equals the bulk concentration when the rate of mass transport is fast compared to the rate of charge transfer. This aspect will be discussed in more detail in Chapter 1.4.

For a system in which the rate of reaction is limited by activation overvoltage, the relationship between the rate of reaction, or current density i, and the driving force for the reaction, or potential E, is given by the Butler–Volmer equation:

$$i = i_0 \exp\left[\frac{\alpha n F (E - E_{rev})}{RT}\right] - i_0 \exp\left[\frac{-(1-\alpha) n F (E - E_{rev})}{RT}\right]$$

$$i = i_0 \exp\left[\frac{\alpha n F \eta}{RT}\right] - i_0 \exp\left[\frac{-(1-\alpha) n F \eta}{RT}\right] \quad (5)$$

where α is the charge transfer coefficient. The value of α is usually close to 0.5, but must be between 0 and 1. The Butler–Volmer equation will be derived in the next section.

1.3.6 Development of Butler–Volmer Equation

The very large field that exists across an electrode/electrolyte interface precludes

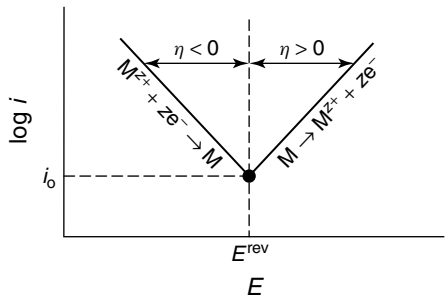


Fig. 2 Schematic representation of the relationship between current and potential for a simple electrochemical reaction under activation control.

the use of Ohm's law to describe the relationship between the potential drop and the current that passes. Instead, it is necessary to use activated state theory, which considers that a system must surmount an activation energy barrier before proceeding along a reaction coordinate.

Figure 3 shows the free enthalpy as a function of reaction coordinate going from a position in the metal to a position in the solution. The free enthalpy in solution is assumed to be lower than that in the metal, so the tendency for the reaction is to proceed in the oxidizing direction. Between those two locations, however, is a peak in the free energy curve. In order for the reaction to proceed to the right, the system must overcome an activation energy barrier equal to ΔG_a^*. The activation energy for the reverse direction (cathodic or reducing direction), ΔG_c^*, is higher than that in the forward direction because the free enthalpy of the oxidized state is lower than that of the reduced state.

For an electrochemical half-cell reaction, such as the generic one given in Eq. (2), the activation energies for the anodic and cathodic reactions are given by:

$$\Delta G_a^* = \Delta G_{a,ch}^* - \alpha n F \Delta\Phi \quad (6)$$

$$\Delta G_c^* = \Delta G_{c,ch}^* + (1-\alpha) n F \Delta\Phi \quad (7)$$

The factor α is the charge transfer coefficient described above. The charge transfer coefficient characterizes the symmetry of the activation energy barrier and therefore is also sometimes called symmetry coefficient. This is made clear in Fig. 3, where α is seen to be the fractional length along the reaction coordinate from the metallic state at which the activated state is located. The value of α is typically close to 0.5; when $\alpha = 0.5$, the activated state is exactly midway between the two end

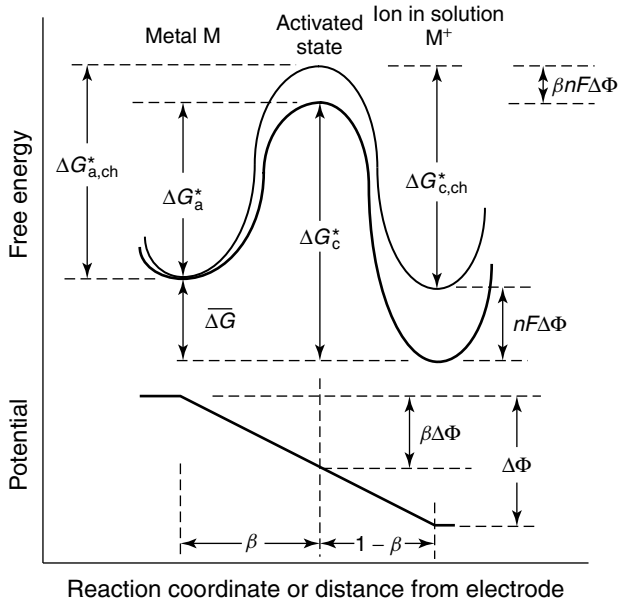


Fig. 3 Variation of free energy and potential with reaction coordinate, which relates to distance from an electrode across an electrode–electrolyte interface.

states, and the free energy curve is symmetrical. The activation energy is seen in Eqs. (6 and 7) to be composed of two parts, a chemical and an electrical component. The chemical portion, $\Delta G^*_{a,ch}$ or $(\Delta G^*_{c,ch})$ ignores the contribution of the potential drop across the interface, which is shown schematically in the lower half of Fig. 3. The potential drop along the reaction coordinate is assumed to be linear, as is the assumption for the potential drop across the Helmholtz double layer. The work associated with moving a mol of charged species through that potential drop is $nF\Delta\Phi$. This work must be added to the chemical portion of the free enthalpy change. The free enthalpy change in going from the reduced to the oxidized state is equal to the chemical free enthalpy change of the two states plus the work associated with the electric potential difference:

$$\overline{\Delta G} = (G_{\text{ion,ch}} - G_{\text{metal,ch}}) + nF\Delta\Phi = \Delta G_{\text{ch}} + nF\Delta\Phi \quad (8)$$

However, only a portion of the work associated with moving the charged species through the electric field is added to the activation energy. That is the source of the α and $(1-\alpha)$ factors in Eqs. (6 and 7). This addition is shown graphically in Fig. 3.

According to the Arrhenius law, the rate of a reaction is exponentially dependent on the negative of the activation energy. So the rates of the forward (anodic) and reverse (cathodic) reactions are:

$$r_a = K_a \exp\left(\frac{-\Delta G^*_a}{RT}\right) \quad (9)$$

$$r_c = K_c \exp\left(\frac{-\Delta G^*_c}{RT}\right) \quad (10)$$

where K_a and K_c are the reaction rate constants. For a first-order oxidation reaction of a species A, $K_a = k_a c_A$, and for a first-order reduction reaction of a species B, $K_c = k_b c_B$, where c_A and c_B are the respective concentrations and k_a and k_b are constants. For a metal dissolution reaction, the concentration of reacting species is constant.

Equations (6 and 7) can be substituted into Eqs. (9 and 10). The absolute value of the potential drop across the interface, $\Delta\Phi$, is not measurable, but it is related to the electrode potential measured against a reference electrode, E, according to:

$$E = \Delta\Phi + C \quad (11)$$

where C is a constant. Furthermore, the rate of reaction can be expressed as current density using Faraday's law.

$$i = \frac{\rho n F r}{M} \quad (12)$$

Combining the equations, one gets for the anodic and cathodic reaction rates:

$$i_a = K'_a \exp\left[\frac{\alpha n F E}{RT}\right] \quad (13)$$

$$i_c = K'_c \exp\left[\frac{-(1-\alpha) n F E}{RT}\right] \quad (14)$$

where the terms in the pre-exponentials are combined into K'_a and K'_c. At equilibrium, $E = E^{\text{rev}}$, and $i_a = i_c \equiv i_0$:

$$i_0 = i_a = i_c = K'_a \exp\left[\frac{\alpha n F E^{\text{rev}}}{RT}\right] = K'_c \exp\left[\frac{-(1-a) n F E^{\text{rev}}}{RT}\right] \quad (15)$$

At some potential E greater than E^{rev}, a net anodic current will flow:

$$i_{\text{net}} = i_a - i_c = K'_a \exp\left[\frac{\alpha n F E}{RT}\right] - K'_c \exp\left[\frac{-(1-\alpha) n F E}{RT}\right] \quad (16)$$

From the definition of overvoltage presented above, $E = E^{\text{rev}} + \eta$. For anodic polarization, where $E > E^{\text{rev}}$, $\eta = \eta_a > 0$. Substituting:

$$i_{\text{net}} = K'_a \exp\left[\frac{\alpha n F (E^{\text{rev}} + \eta)}{RT}\right] - K'_c \exp\left[\frac{-(1-\alpha) n F (E^{\text{rev}} + \eta)}{RT}\right] \quad (17)$$

but K'_a and K'_c can be related to i_0 and E^{rev} via Eq. (15). Substituting back into Eq. (17), one gets the Butler–Volmer equation:

$$i_{\text{net}} = i_0 \exp\left[\frac{\alpha n F \eta_a}{RT}\right] - i_0 \exp\left[\frac{-(1-\alpha) n F \eta_a}{RT}\right] \quad (18)$$

In Eq. (18), the first term represents the anodic partial current density i_a (taken as positive) and the second term is the cathodic partial current density i_c (taken as negative). The net current is the sum of the two terms. It is positive when the electrode is polarized anodically and negative when the electrode is polarized cathodically.

$$i_{\text{net}} = i_a + i_c$$
$$i_a = i_0 \exp\left[\frac{\alpha n F \eta_a}{RT}\right]$$
$$i_c = -i_0 \exp\left[\frac{-(1-\alpha) n F \eta_a}{RT}\right] \quad (19)$$

The Butler–Volmer equation describes the kinetics for electrochemical reactions that are controlled by the transfer of charge across the interface. It has been derived here in a simplified way. For a more complete discussion of charge transfer reactions and of electron tunneling, the reader is referred to the volume of this series dealing with electrode kinetics.

The Butler–Volmer equation is plotted in Fig. 4. The symmetry of the curve will depend on the symmetry factor, α. When $\alpha = 0.5$, the curve is symmetrical, as is shown in Fig. 4(a). For $\alpha \neq 0.5$, the curve is asymmetrical, as in Fig. 4(b). When plotted on i versus E axes, the curve crosses the x-axis at the reversible potential.

These equations are straight lines in a plot of E versus $\log i$, such as that in Fig. 2. This plot of E versus $\log i$ is called an Evans diagram. Actually, the Butler–Volmer equation is described better by the curve in Fig. 5. The net current at the reversible potential is zero because the forward and reverse current, each equal to the exchange current density, balance each other. The log of the current density approaches negative infinity at the reversible potential at which the net current density goes to zero, and the polarization curve points down at the reversible potential when plotted on semilogarithmic axes.

1.3.7 Tafel Equation

For a sufficiently large value of anodic polarization from the reversible potential (overpotential $\eta_a > \sim 50$ mV), the first term on the right side of Eq. (18) dominates the second term. Therefore, at large overpotentials, the Butler–Volmer equation simplifies to:

$$i_{\text{net}} = i_0 \exp\left[\frac{\alpha n F \eta_a}{RT}\right] \quad (20)$$

Rearranging, one gets the Tafel equation:

$$\eta_a = b_a \log\left(\frac{i}{i_0}\right) \quad (21)$$

where $b_a = 2.3RT/\beta nF$ is the anodic Tafel slope. For $\alpha = 0.5$ and $n = 1$, $b_a = 0.12$ V (or V decade^{-1}). A similar equation is

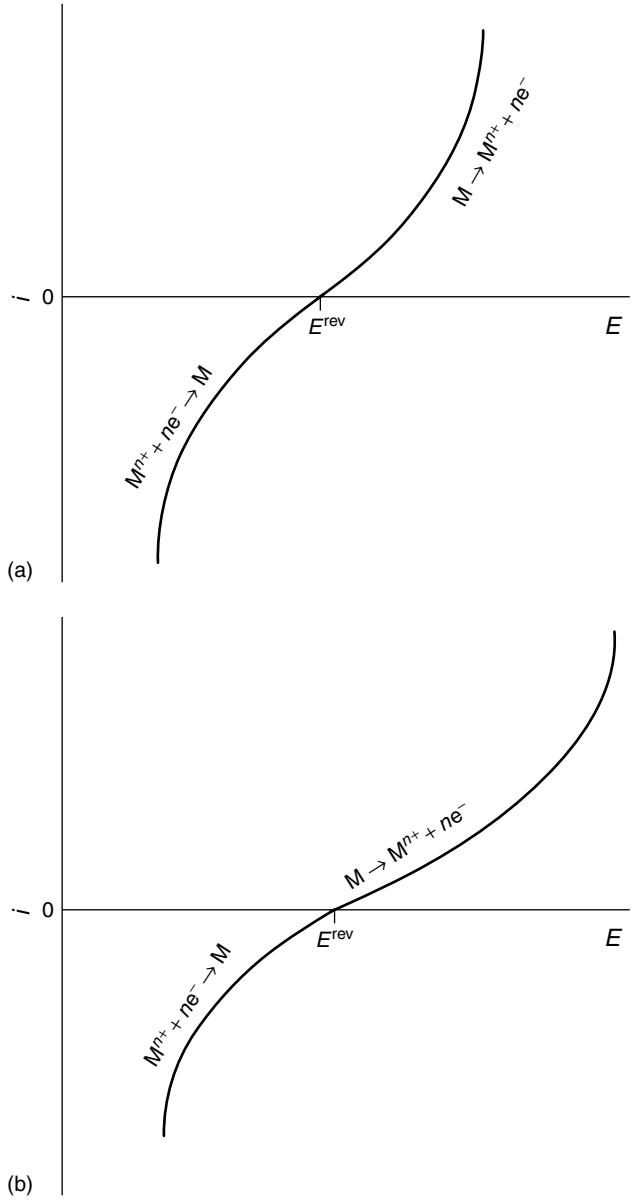


Fig. 4 Electrode kinetics as expressed by the Butler–Volmer equation: (a) symmetrical curve when $\alpha = 0.5$ and (b) symmetrical curve when $\alpha \neq 0.5$.

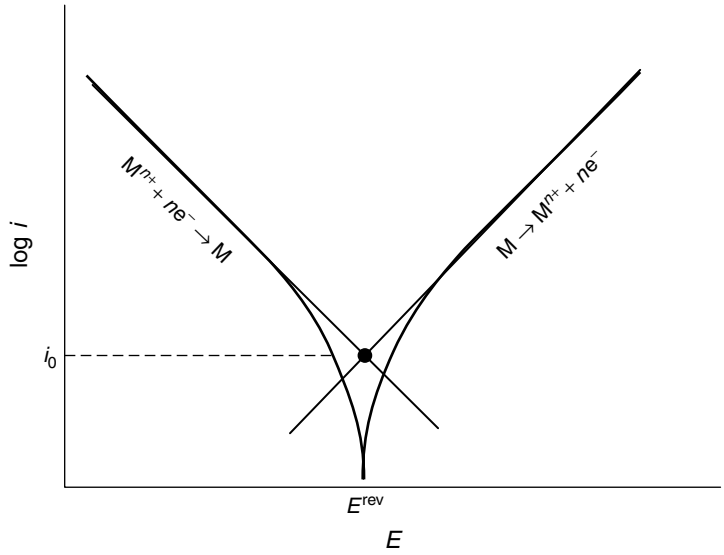


Fig. 5 Electrode kinetics as expressed by the Butler–Volmer equation, plotted in semilogarithmic space.

found for cathodic activation polarization

$$\eta_c = -b_c \log\left(\frac{|i|}{i_0}\right) \tag{22}$$

Corrosion conditions typically are far removed from the reversible potentials for any of the reactions. Therefore, Tafel kinetics is usually an accurate description of corrosion kinetics in which mass transfer is not important.

1.3.8 Low-field Approximation

For low values of overpotential, η, the Butler–Volmer equation can be linearized. For values of $x < 1$, $\exp x \approx 1 + x$. So Eq. (18) can be simplified to:

$$i_{net} = i_0\left(\frac{\alpha n F \eta_a}{RT}\right) - i_0\left(\frac{-(1-\alpha) n F \eta_a}{RT}\right) = \frac{i_0 n F \eta}{RT} \tag{23}$$

Near the reversible potential, the current density is seen to be linearly dependent on overpotential with a slope that scales with exchange current density. This linearity of current to potential is similar to Ohm's law, and the proportionality is called polarization resistance, $i = \eta / R_p$, where $R_p = RT / i_0 n F$.

Note that, in contrast to the low-field approximation, the Tafel equation is sometimes referred to as the high-field approximation since it is only valid for large values of overpotential.

1.3.9 Multistep Reactions

The Butler–Volmer equation given in Eq. (18) is only strictly valid for single step reactions. Reactions involving more than one electron transfer often proceed in several consecutive steps. Multistep reactions typically have one significantly slower step that may be considered to be

rate-determining, while the others would be fast and in equilibrium. Under these conditions, the electrochemical kinetics can conveniently be described by another form of the Butler–Volmer equation:

$$i_{\text{net}} = i_0 \exp\left[\frac{\overleftarrow{\alpha} F \eta_a}{RT}\right] - i_0 \exp\left[\frac{\overrightarrow{\alpha} F \eta_a}{RT}\right] \quad (24)$$

where $\overleftarrow{\alpha}$ and $\overrightarrow{\alpha}$ are the overall transfer coefficients for the anodic and cathodic reactions, respectively. The values of $\overleftarrow{\alpha}$ and $\overrightarrow{\alpha}$ do not necessarily sum to unity as in the case of α and $(1-\alpha)$, but they are related by:

$$\overleftarrow{\alpha} + \overrightarrow{\alpha} = \frac{n}{\upsilon} \quad (25)$$

where n is the total number of electrons in the overall reaction and υ is the stoichiometric number, or the number of times that the rate-determining step (RDS) must occur for the overall reaction to occur once. The overall transfer coefficient is an experimental parameter related to the measured Tafel slope since at large anodic overpotential, η_a, Eq. (25) is simplified to:

$$i_a = i_0 \exp\left[\frac{\overleftarrow{\alpha} F \eta_a}{RT}\right] \quad (26)$$

The Tafel slope can then be defined as:

$$b_a = \frac{2.3RT}{\overleftarrow{\alpha} F} \quad (27)$$

1.3.10 The Hydrogen Evolution Reaction

The hydrogen evolution reaction (HER) is an interesting multistep reaction to discuss because it is relatively simple and very important in corrosion. In acids, the electrode reaction for hydrogen evolution is:

$$2H^+ + 2e^- = H_2 \quad (28)$$

Reaction (28) is actually a two-step reaction that can occur in a number of ways, depending upon the metal electrode and the environment. Electrochemical reduction of a proton yields adsorbed atomic hydrogen:

$$H^+ + e^- = H_{ad} \text{ (Volmer reaction)} \quad (29)$$

This reaction can be followed by either chemical desorption and recombination of two adsorbed hydrogen atoms:

$$2H_{ad} = H_2 \text{ (Tafel reaction)} \quad (30)$$

or electrochemical desorption, which involves the simultaneous reduction of a proton:

$$H^+ + H_{ad} + e^- = H_2 \quad \text{(Heyrovsky reaction)} \quad (31)$$

Either the discharge or one of the desorption reactions can be the RDS. The other reactions in the process are then considered to be fast and in equilibrium. An example is slow discharge followed by fast chemical desorption:

$$H^+ + e^- \longrightarrow H_{ad} \text{ RDS} \quad (32)$$
$$2H_{ad} \longleftrightarrow H_2$$

For this mechanism, $\upsilon = 2$ since the RDS must happen twice for the full reaction to proceed once. Fast discharge followed by slow chemical desorption is given by:

$$H^+ + e^- \longleftrightarrow H_{ad} \quad (33)$$
$$2H_{ad} \longrightarrow H_2 \text{ RDS}$$

For this mechanism, $\upsilon = 1$. From electrochemical measurements, it is possible to determine the probable mechanism for the HER. More about the HER can be found in the volume on kinetics and in a Chapter 2.2.

1.3.11 Mixed Potential Theory

Under conditions of importance in corrosion, the predominant cathodic reaction is typically one of the hydrogen or oxygen reactions described above. Furthermore, the electrode potential is usually far from the reversible potentials for the any of the reactions occurring on the surface.

The principle of charge conservation dictates that, to avoid the accumulation of charge on a freely immersed electrode, the sum of all of the oxidation currents must equal the sum of all of the reduction currents. Any electrode immersed in an environment will naturally have a potential, called the corrosion potential, which fulfills this requirement. Therefore, at the corrosion potential:

$$\Sigma I_a + \Sigma I_c = 0 \qquad (34)$$

Note that reduction currents (I_c) are negative. The corrosion potential is also called the open-circuit potential, free potential, or rest potential. The corrosion potential is a mixed potential indicating that its value depends on the rate of the anodic as well as the cathodic reactions.

The situation can best be visualized using an Evans diagram, Fig. 6. In this figure, the Tafel lines for the anodic and cathodic branches of the hydrogen reaction are shown together with the Tafel lines for the dissolution and plating of a metal with reversible potential below that for the hydrogen reaction. These are the possible electrochemical reactions for an active metal in acid containing little dissolved metal ion, where the primary cathodic reaction is hydrogen evolution. In this figure, E^{rev}_{M/M^+} and E^{rev}_{H/H^+} represent the reversible potentials for the metal dissolution and hydrogen evolution reactions, respectively; $i_{0,M/M^+}$ and $i_{0,H_2/H^+}$ represent the exchange current densities for metal dissolution and hydrogen evolution on M, respectively. The principle of charge conservation, Eq. (34) can be applied. Since the reactions are all occurring on a single electrode of given area,

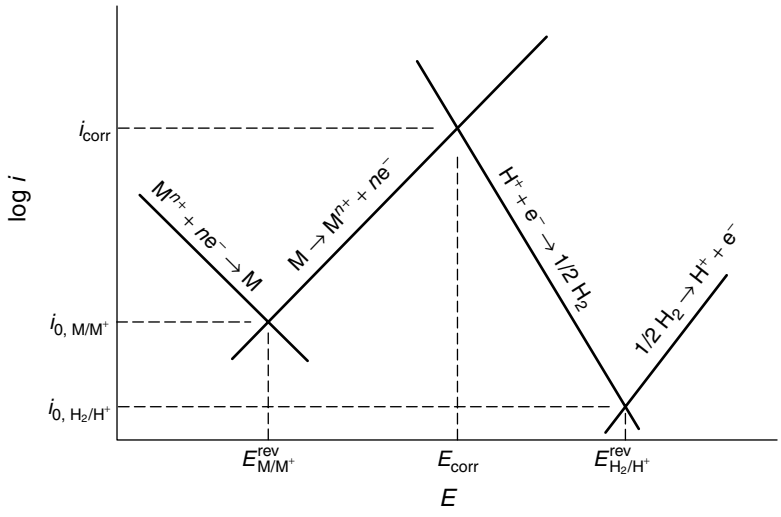


Fig. 6 Schematic Evans diagram for corroding active metal in an acid.

Eq. (34) can be written in terms of current density, $i = I/A$:

$$\Sigma i_a + \Sigma i_c = 0 \qquad (35)$$

The total oxidation and reduction current densities will be equal at the point at which the anodic line for the metal dissolution reaction intersects the cathodic line for hydrogen evolution. The potential at which these lines intersect is the corrosion potential. The rate of the anodic reaction at the corrosion potential is the corrosion rate (corrosion current density). The corrosion potential always takes a value between the reversible potentials for the two partial reactions.

The corrosion potential and current density can shift with time if the surface or solution changes and the Tafel lines representing the reactions change. Note that the electrode is *not in equilibrium* at the corrosion potential since net changes are occurring: metal is being oxidized and water or other oxidants are being reduced.

The corrosion potential and current density are influenced by both thermodynamics, through the reversible potentials of the various reactions, and kinetics, through the exchange current densities and the Tafel slopes of the reactions.

The concept of the corrosion potential can also be illustrated in a linear $i-E$ plot. Figure 7 shows two curves representing the Butler–Volmer equation for the metal and hydrogen reactions. The point at which the rate of metal dissolution equals the rate of hydrogen evolution is the potential at which the metal curve is as high above the potential axis as the hydrogen curve is below the axis. That distance is the corrosion rate.

Polarization curves of metals in solution can be determined by potentiodynamic polarization, as will be described in detail in a Chapter 7.3.1. Using a potentiostat,

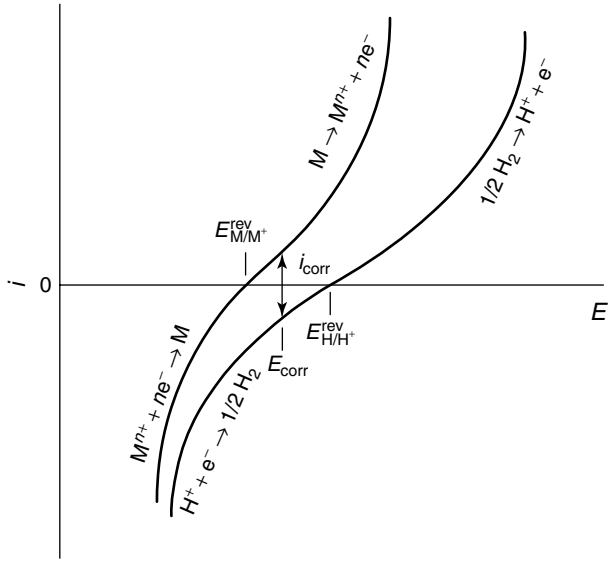


Fig. 7 Kinetics of a corroding active metal in an acid, plotted on linear axes.

a counterelectrode (CE), and a reference electrode (RE), the potential of a sample is scanned or stepped over a range from about 250 mV below the corrosion potential to well above the corrosion potential. The current density is determined as a function of the potential and plotted on a semilog plot such as that shown in Fig. 5. The net measured current for the case of a metal corroding at a mixed potential in a solution containing an oxidizing agent will look like the curve presented in Fig. 5. However, the current will go to zero at the corrosion potential, and extrapolation to the corrosion potential of the linear regions of the semilogarithmic plot, or Tafel regions, gives the corrosion rate, Fig. 8.

The curve in Fig. 8, which is the net current as a function of potential for a metal corroding in an acid accompanied by hydrogen evolution, looks like the one in Fig. 5, which represents the forward and reverse directions of a single reaction. Similarly, an equation similar in form to the Butler–Volmer equation can be derived to describe the curve in Fig. 8.

One form of the Tafel equation is:

$$i = i_0 \exp\left(\frac{\eta}{b'}\right) \tag{36}$$

where $\eta = E - E_{\text{rev}}$ and $b' = b/2.3$. Consider the case of metal M dissolving in acid. The Tafel equations for the anodic dissolution of M and hydrogen evolution on are given by:

$$i_a = i_{0,a} \exp\left(\frac{E - E_a^{\text{rev}}}{b'_a}\right) \tag{37}$$

$$|i_c| = i_{0,c} \exp\left(\frac{E_c^{\text{rev}} - E}{|b'_c|}\right) \tag{38}$$

The net current is then given by:

$$i_{\text{net}} = i_a - |i_c| = i_{0,a} \exp\left(\frac{E - E_a^{\text{rev}}}{b'_a}\right) - i_{0,c} \exp\left(\frac{E_c^{\text{rev}} - E}{|b'_c|}\right) \tag{39}$$

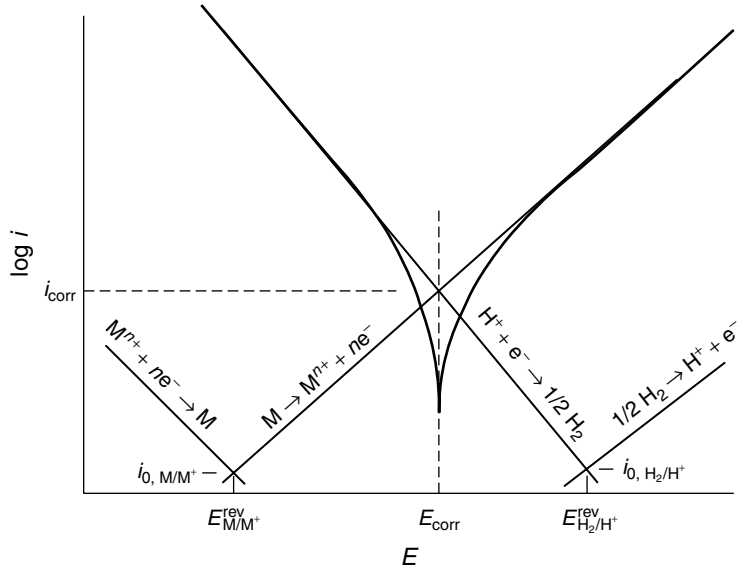


Fig. 8 Relationship of measured polarization curve to the Evans diagram for a corroding active metal in an acid.

But, at $E = E_{corr}$, $i_a = |i_c| = i_{corr}$:

$$i_{corr} = i_{0,a} \exp\left(\frac{E_{corr} - E_a^{rev}}{b'_a}\right) = i_{0,c} \exp\left(\frac{E_c^{rev} - E_{corr}}{|b'_c|}\right) \quad (40)$$

Solving for $i_{0,a}$ and $i_{0,c}$, and substituting into Eq. (39):

$$i = i_{corr}\left[\exp\left(\frac{E - E_{corr}}{b'_a}\right) - \exp\left(-\frac{E - E_{corr}}{|b'_c|}\right)\right] = i_{corr}\left[\exp\left(\frac{2.3(E - E_{corr})}{b_a}\right) - \exp\left(-\frac{2.3(E - E_{corr})}{|b_c|}\right)\right] \quad (41)$$

Equation (41) is identical in form to Eqs. (18 and 24). The curve is centered around E_{corr} rather than E^{rev}, and the current density at zero "overpotential" is i_{corr} instead of i_0. This expression, along with the theory for mixed potentials, was derived by Wagner and Traud, and therefore will be referred to as the Wagner–Traud equation. As described in the Chapter 7.3.1.2 on experimental techniques, the Wagner–Traud equation is used in software analysis packages that accompany modern computer-controlled potentiostats. A nonlinear least squares fit of this equation to the experimental data provides values of E_{corr}, i_{corr}, b_a, and b_c with the assumption that perfect Tafel behavior is observed for both the anodic and cathodic reactions, and that the extrapolations of the Tafel portions of the curves both intersect at the corrosion potential.

1.3.12 Effect of Multiple Oxidizing Agents

Environments can contain a range of oxidizing agents with stronger oxidizing power than the hydrogen ion. Many environments such as natural waters, or the thin adsorbed water layers that exist in atmospheric conditions, are enriched in dissolved molecular oxygen. As described in Chapter 1.2, the standard potential for the oxygen reduction reaction is 1.23 V higher than that for the hydrogen evolution reaction. The rate of oxygen reduction is often diffusion limited. The kinetics of such reactions will be discussed in the next chapter. In aerated neutral solutions, the oxygen reduction reaction usually dominates the HER because the rate of the latter is low. In acids, however, the reverse is true. The dominant reaction is the one that has the highest current density at a given potential, as is discussed below.

Besides oxygen, solutions can contain other oxidizing species, such as peroxide, persulfate, nitrate, and ferric ions. The reversible potential associated with the reduction of these species will depend on their concentration.

An Evans diagram can also be used to understand the situation when metal corrodes in a solution containing more than one oxidizing agent, or reducible species. Figure 9 shows the case for metal dissolving in an acid solution containing ferric ions, which can reduce to ferrous ions. Equation (34) still holds; charge neutrality must be observed. In order to determine the corrosion potential in this case, it is necessary to determine the curves representing the total oxidation and reduction rates. The rates of all reactions at any given potential must be summed.

Starting from high potentials, there would be no available reduction reaction until the potential decreased below the reversible potential for the Fe^{3+}/Fe^{2+} reaction. The ferric/ferrous reaction is the only

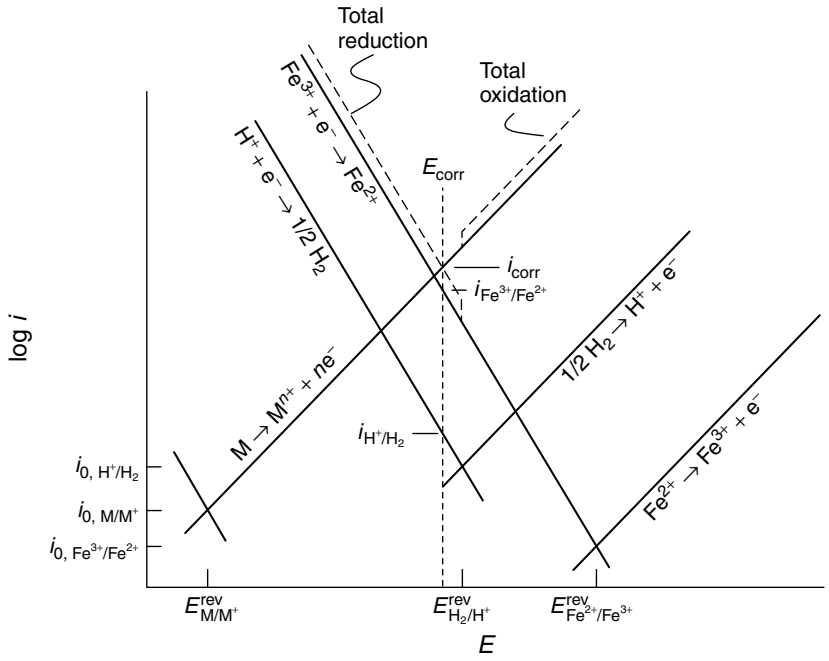


Fig. 9 Schematic Evans diagram for corroding active metal in an acid containing ferric ions, which act as an added oxidizing agent.

reduction reaction possible until the potential decreases below the H^+/H_2 reversible potential. So between the two reversible potentials, the curve for total reduction is identical to the curve for the ferric/ferrous reduction. Below the reversible potential for the hydrogen reaction, the total reduction rate is determined by adding the rates of the two reactions, and is shown schematically by the dashed line in Fig. 9. The current density is plotted on a log scale so the separation of the dashed line from the ferric/ferrous line is exaggerated in the figure.

The total rate of oxidation is determined similarly. Below the reversible potential for metal dissolution, no oxidation reactions are possible. Above that potential, metal oxidation is the only anodic reaction until the potential increases above the reversible potential for the hydrogen reaction. Above that potential, any dissolved hydrogen gas would be oxidized to H^+. Above the reversible potential for the ferric/ferrous reaction, ferrous ions can be oxidized.

The intersection of the curves representing the total oxidation and reduction currents, respectively, is the corrosion potential. This potential is higher than the value one would measure if only the hydrogen reaction was present. The addition of ferric ions not only increases the corrosion potential but also the corrosion rate. The rate of the ferric reduction and hydrogen evolution reactions can be determined by the rate of each reaction at the corrosion potential. These rates are marked on Fig. 9 as $i_{Fe^{3+}/Fe^{2+}}$ and i_{H^+/H_2}.

1.3.13 Galvanic Corrosion

Many engineering structures are fabricated from a variety of materials that are each selected because of a range of properties, such as cost, strength, weight, electronic, magnetic, optical, and so on. The latest magnetic recording heads used in high-density disk drives are an example of a structure composed of many different materials. These devices have numerous thin films stacked on top of each other and a cross-section of the thin film stack is exposed by lapping. Such a structure has severe galvanic corrosion susceptibility where the corrosion of one of the components is greatly accelerated.

In order for galvanic corrosion to occur, the following conditions are necessary: (1) dissimilar metals must be (2) in electrical contact, and (3) in ionic contact (exposed to the same electrolyte). Dissimilar metals immersed in an electrolyte but isolated from each other will not suffer from galvanic corrosion. They will each corrode, but they will not interact galvanically. Similarly, two shorted metals immersed in isolated electrolytes will not galvanically corrode. If the two electrodes are in a single solution, but the solution resistance between them is extremely high, they will act as if they were in different electrolytes, and will not interact galvanically. The role of solution resistance in determining the extent of galvanic interaction will be discussed below.

In Chapter 1.2 on thermodynamics, the electromotive series was shown to be a ranking of the reactivity of various pure metals under the specific conditions of standard state of all species. Furthermore, the Nernst equation was used to show that dissimilar metals generate a cell potential. Differences in reversible potential can thus cause galvanic corrosion. However, metals and alloys used in corrosive environments are usually not at their reversible potential, but at their corrosion potential. As we have seen above, the corrosion potential is determined by kinetic as well as thermodynamic factors. Therefore, its value for a given metal depends on the environment. It is this potential that is the driving force for galvanic corrosion. The galvanic series is a listing of metals and alloys according to the value of their corrosion potential in a given environment. Like the electromotive series, a material that is lower in the galvanic series is relatively active and will corrode preferentially when galvanically coupled to a material that is higher in the series. The more noble metal supports the cathodic reaction, and corrodes to a lesser extent.

The galvanic series for seawater is widely reported and widely used for relative comparison of the galvanic nature of materials. However, it is necessary to develop a galvanic series for every environment of interest as the order of nobility can change from one environment to another.

Evans diagrams can be used to understand the rate of galvanic corrosion. Figure 10 shows the case of two corroding metals in galvanic contact. The Evans diagrams for metals M and N are overlaid in the figure. Metal N is more noble than metal M, with a higher reversible potential. Both corrode with the evolution of hydrogen gas. The exchange current density for hydrogen evolution is assumed to be different for the two different surfaces. The intersections of the respective anodic dissolution curves and hydrogen evolution curves give the corrosion potentials and corrosion rates of M and N, $i_{\mathrm{corr,M}}$, and $i_{\mathrm{corr,N}}$, in the uncoupled condition.

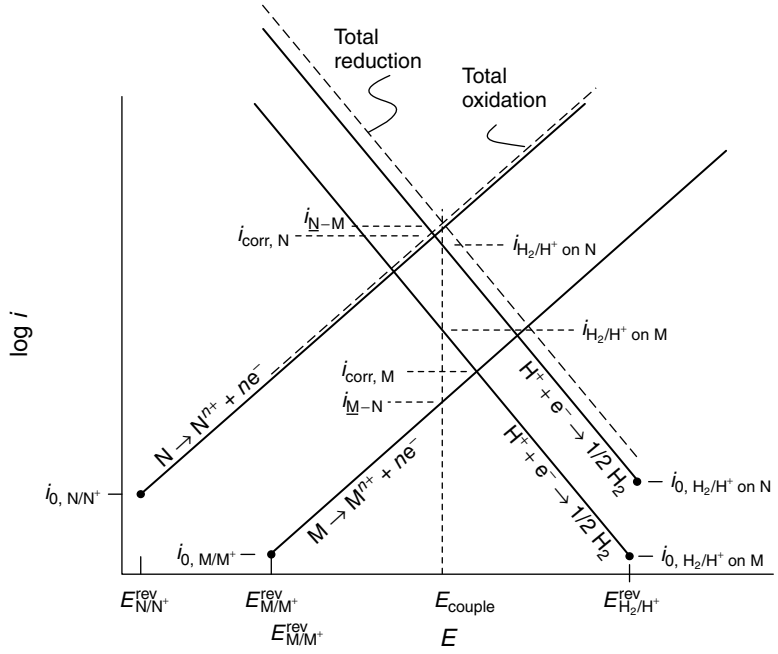


Fig. 10 Evans diagram describing the galvanic coupling of two corroding metals.

As for the mixed potential on a single electrode surface, the principle of charge conservation is upheld in galvanic corrosion. To determine the situation that exists upon electrical shorting of the metals M and N in Fig. 10, it is necessary to consider the total oxidation and reduction rates (note that the position of the total rate lines are schematic in the figure). Charge conservation requires that the total oxidation and reduction currents, not current densities, must be equal. However, assuming for now that equal areas of the two metals are in contact allows the plots to be in terms of current density. Ignoring the influence of ohmic potential drop between the two electrodes, they will both have the same potential that corresponds to the intersection of the total oxidation and reduction lines. This potential that we shall call couple potential, is 'mixed' in the sense that it falls between the two corrosion potentials in the same solution. The galvanic coupling increases the potential of the more active metal N and decreases the potential of the more noble metal M. The rate of any reaction can be determined from the intersection of the couple potential coordinate and the given Tafel line. It is seen that $i_{\underline{N}-M}$, the corrosion rate of the more active metal N when contacted to the more noble metal M, is higher than the corrosion rate of N in the uncoupled state, $i_{corr,N}$. Conversely, the corrosion rate of M is lower when coupled to N ($i_{\underline{M}-N}$) than in the uncoupled state. The rate of the cathodic reaction, hydrogen evolution, increases on M (from $i_{corr,M}$ to $i_{H_2/H^+\,on\,M}$) and decreases on N (from $i_{corr,N}$ to $i_{H_2/H^+\,on\,N}$) when coupled, compared to the uncoupled state, which follows from the respective changes in potential from the corrosion potentials to the couple potential.

In galvanic corrosion, the areas of the coupled electrodes are typically unequal. In that case, the Evans diagram must be drawn in terms of I (current) instead of i (current density). The principle of charge conservation states that the anodic current must equal the cathodic current:

$$I_a + I_c = 0 \tag{42}$$

$$i_a A_a + i_c A_c = 0 \tag{43}$$

For reactions taking place uniformly on a single electrode, $A_a = A_c$, so that $i_a = i_c$. However, for galvanic corrosion where $A_a \neq A_c$,

$$i_a = -i_c \left(\frac{A_c}{A_a} \right) \tag{44}$$

Corrosion rate is given by current density, not current. Therefore, the corrosion rate of the anodic metal in a galvanic couple will depend upon the ratio of the cathodic area to the anodic area. The galvanic interaction of a metal-coated metal structure that is scratched down to the substrate metal will depend upon the relative nobility of the two metals. For the case of a steel structure plated with a layer of Ni, which is more noble than the steel, the cathode-to-anode ratio would be large and corrosion of the steel in the scratch would be greatly accelerated. In the case of galvanized steel sheet, the Zn coating is anodic so that the cathode-to-anode ratio is small. The corrosion rate of the Zn is not greatly affected by the galvanic coupling to the steel in a scratch. On the other hand, the corrosion rate of the steel would be greatly reduced.

Figure 11 shows the influence of Pt area on the galvanic corrosion of metal M. The galvanic coupling of an equal area of Pt with M results in an increase in the potential of M and an increase in the

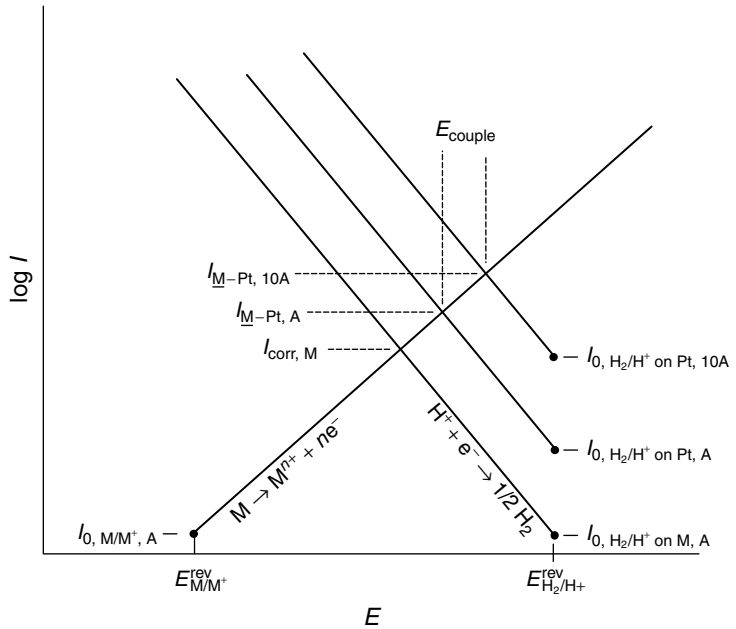


Fig. 11 Influence of area ratio on galvanic corrosion for an active metal/noble metal couple.

corrosion rate (from $I_{corr,M}$ to $I_{\underline{M}-Pt,A}$). This is a result of increased surface area available for the cathodic reaction and the higher exchange current density for hydrogen evolution on Pt relative to M. Consider the case of a sample of M connected to an area of Pt that is 10 times larger. The exchange current (not current density) for the hydrogen evolution reaction on Pt increases by a factor of 10 because of the larger area. This is represented in Fig. 11 by the subscripts A and 10A. The new couple potential and dissolution current of M therefore increase relative to the couple of equal areas, from $I_{\underline{M}-Pt,A}$ to $I_{\underline{M}-Pt,2A}$. Since the area of M did not change in this example, the increase in dissolution current means an increase in corrosion current density and corrosion rate.

It is possible to use experimental polarization curves for two metals to predict the extent of galvanic coupling when they are connected. Figure 12 shows polarization curves for two metals, N and M. Ignoring the contributions from the other reactions and the effects of ohmic potential drops and assuming equal areas of M and N, the couple potential can be assumed to be at the intersection of the hydrogen evolution curve on M with the N dissolution curve. This point also provides the dissolution rate of N when coupled to M, $i_{\underline{N}-M}$. The dissolution rate of M in the coupled state, $i_{\underline{M}-N}$, is determined by extrapolation of the linear Tafel part of the anodic polarization curve for M to the couple potential.

The effect of area ratio is handled with experimental polarization curves in a similar fashion to that shown for schematic Evans diagrams in Fig. 11. Figure 13 shows experimental polarization curves for metals

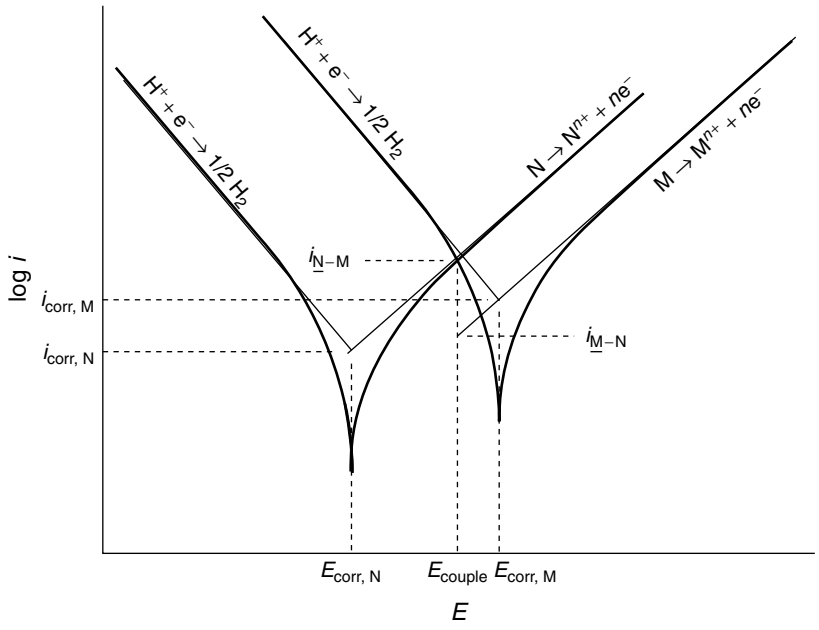


Fig. 12 Prediction of galvanic corrosion interaction from measured polarization curves.

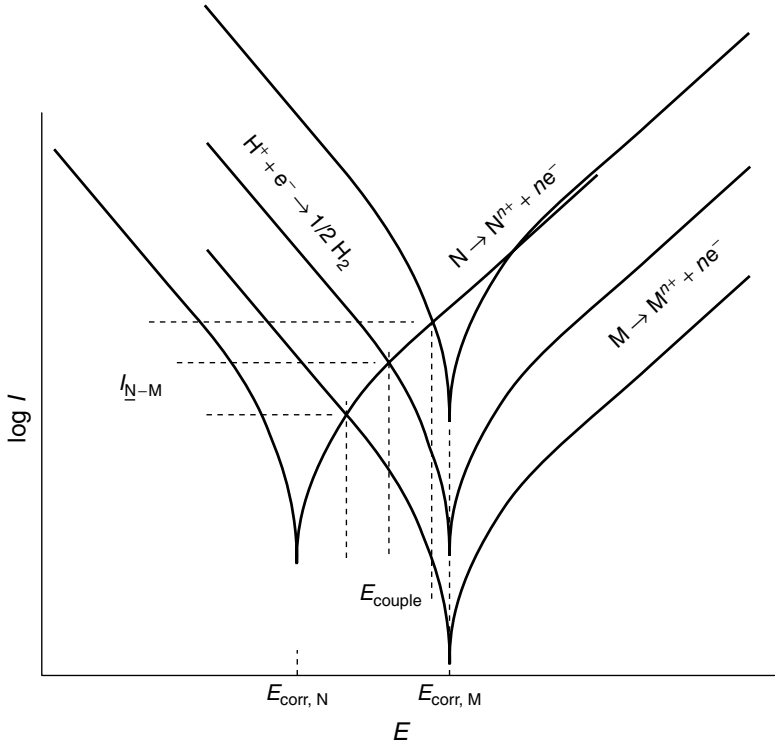


Fig. 13 Prediction of influence of area ratio on galvanic corrosion using measured polarization curves.

M and N drawn in terms of current. The curve for M is offset along the current axis showing the situation for M electrodes with three different areas. As the area of M increases, the couple potential (ignoring effects of ohmic potential drops) approaches the uncoupled corrosion potential for M in the given solution, which is the highest possible couple potential. Similarly, the lowest possible couple potential, found when the N : M area ratio is very low, is the uncoupled corrosion potential for N in the environment. The corrosion current is given by the intersection of the two potential-current polarization curves, and the current densities are determined by dividing the current by the electrode areas.

1.3.14 Ohmic Potential Drops

The passage of current through an ionic electrolyte of finite resistivity results in an ohmic potential drop along the current path according to Ohm's law. There are two aspects of corrosion that are influenced by ohmic potential drops: measured polarization curves and any form of corrosion in which the anodic and cathodic reactions are separated spatially, such as in galvanic corrosion.

In an electrochemical experiment involving current flow from an anode to a cathode, the potential sensed by the reference electrode will have an ohmic potential drop component, since the RE is usually

immersed in the potential field associated with the current flow between the working electrode (WE) and the counter electrode (CE). This can lead to an error in the measured potential equal to the ohmic potential drop between WE and RE.

The use of a Luggin capillary allows an RE to intersect the potential field generated between a WE and a CE at a position close to the WE so as to avoid much of the ohmic potential drop. The Luggin capillary should not be closer to the surface than a distance about equal to its diameter in order to prevent shielding of the surface. Therefore, there will always be some amount of ohmic potential drop in a controlled potential measurement. Generally, the ohmic potential drop will be smaller, the lower the current density and the better the conductivity of the electrolyte.

The existence of an ohmic potential drop during a potential measurement can alter the shape of the measured polarization curve. The current measured at a given potential is less than expected because the potential at the interface is less than what is intended. On a semilog plot, the ohmic potential drop causes the polarization curve to bend away from the linear Tafel region toward lower currents.

A number of techniques exist to compensate for the ohmic potential drop. It is possible to measure the solution resistance between the RE and WE either before or after the experiment, and then perform a postmeasurement calculation of the ohmic potential drop for the current measured at every potential. This value can be subtracted from the expected potential in order to compensate for the ohmic drop. Modern potentiostats allow for real-time feedback and control. The feedback can be performed assuming a constant resistance, which can be measured before the experiment. It is also possible to continuously determine the ohmic potential drop using a current interrupt method. The applied potential and thus current are periodically interrupted for a very short period (on the order of 10 μs). When the current is interrupted, the ohmic potential drop immediately vanishes, while the activation and concentration overpotentials take some time to decay. Extrapolation of the potential transient back to the time of interruption provides a real-time measure of the ohmic potential drop. The instrument or controlling computer can compensate for this ohmic potential drop during the next period when the potential is reapplied with the assumption that the resistance does not change.

Ohmic potential drops also play a role in galvanic corrosion and other forms of localized corrosion, in which the anodes and cathodes are spatially separated. Ionic current must then flow some distance through the electrolyte. Two galvanically coupled electrodes will not reach the exact same potential as a result of the ohmic potential drop that will occur along the current path through the electrolyte.

Consider first the case of two metals that are different in nobility, for instance Fe and Pt. Figure 14 shows the situation for uncoupled Fe and Pt electrodes immersed in some electrolyte. Since they are not connected, there is no current flowing through the electrolyte, and no potential drop in the electrolyte. However, there is a potential drop at each electrode–electrolyte interface. A potential drop exists also at the interface between the reference electrode and the electrolyte. It is indicated in the figure by the vertical arrow. The corrosion potential of each metal is given by the distance (and direction) from the metal potential to the point at the back of the arrow for the reference electrode.

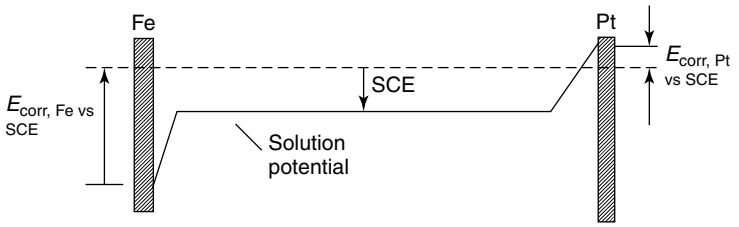


Fig. 14 Potential distribution between uncoupled Fe and Pt electrodes.

This is because the corrosion potential is measured by a voltmeter connected to the back of the metal electrode and the back of the reference electrode. The corrosion potential of the Pt is higher than that of the Fe, but the measured potentials do not depend on the position of the reference electrode within the solution because the solution potential is constant.

Figure 15 shows the situation when the Fe and Pt electrodes are shorted so that the metal are equal for the two electrodes. The potential drops across the interfaces change and electrons flow through the wire connecting them and an ionic current flows through the electrolyte. As a result of the ionic current, there is a potential drop in the solution. The couple potential of the Fe and Pt measured by a voltmeter using a reference electrode will now depend on the position of the reference electrode, but will not depend on whether the other voltmeter lead is connected to the Fe or Pt electrode because the metals potentials are identical. Again considering that the measured potential is given by the difference between the metal potential and the potential at the back of the reference electrode, it is clear that the potential measured when the reference electrode is close to the Fe electrode will be lower than that measured when the reference electrode is close to the Pt electrode.

Figure 16 shows schematically how the potentials measured at two galvanically connected electrodes will not meet at the intersection of the polarization curves if there is significant ohmic potential drop, but be separated by an amount equal to the ohmic potential drop, $I \times R$. The current

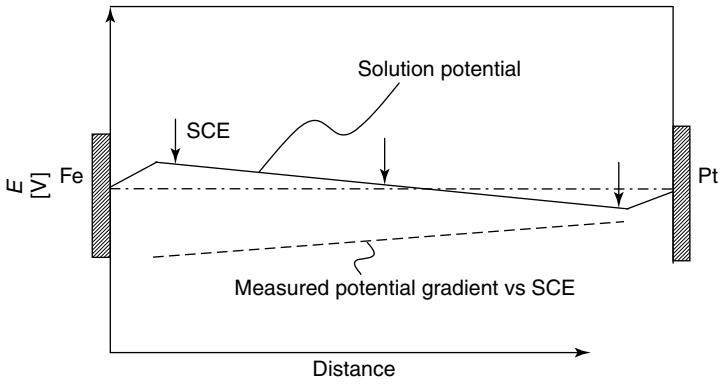


Fig. 15 Potential distribution between coupled Fe and Pt electrodes.

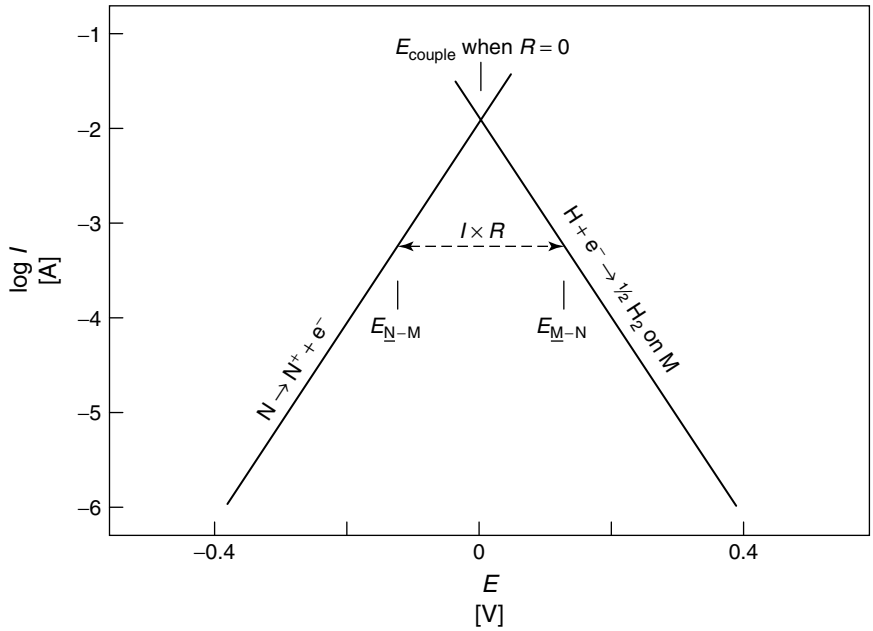


Fig. 16 Influence of ohmic potential drop on galvanic couple.

at the coupled potentials is the galvanic current, and is less than for the case in which $R = 0$. The existence of an ohmic potential drop in the solution decreases the effect of galvanic corrosion. In the limiting case, when the ohmic resistance becomes sufficiently high, the system behaves as if the electrodes were not coupled at all.

Figure 17 shows how the system determines what the galvanic current, ohmic potential drop, and electrode potentials will be. In Fig. 17(a), the anodic Tafel line for an active metal N and the hydrogen evolution Tafel line on metal M are given with the assumption that the Tafel slopes are equal. Also shown are curves representing $I \times R$ for three different values of R, the solution resistance between the electrodes. The line $I \times R$ has the shape of an exponential curve in the semilogarithmic space. The position at which the $I \times R$ curve for a given resistance intersects the Tafel lines determines the galvanic current, ohmic potential drops, and the potentials of the electrodes.

The situation is more complicated for the case in which the Tafel slopes are unequal, Fig. 17(b). The $I \times R$ curves must intersect the two Tafel plots at the same current since the galvanic current flowing through the electrodes must be the same. In order for this to occur, the $I \times R$ curves must be centered along a line that bisects the two Tafel lines. This is reasonable since there is no reference of the ohmic potential drop to a RE scale. It is just a potential consumed in the solution as a result of the current flow.

It should be noted that a resistance in the external connection of the metals can result in an ohmic potential drop in that path. Such an ohmic potential drop will have a similar effect on the electrode potentials.

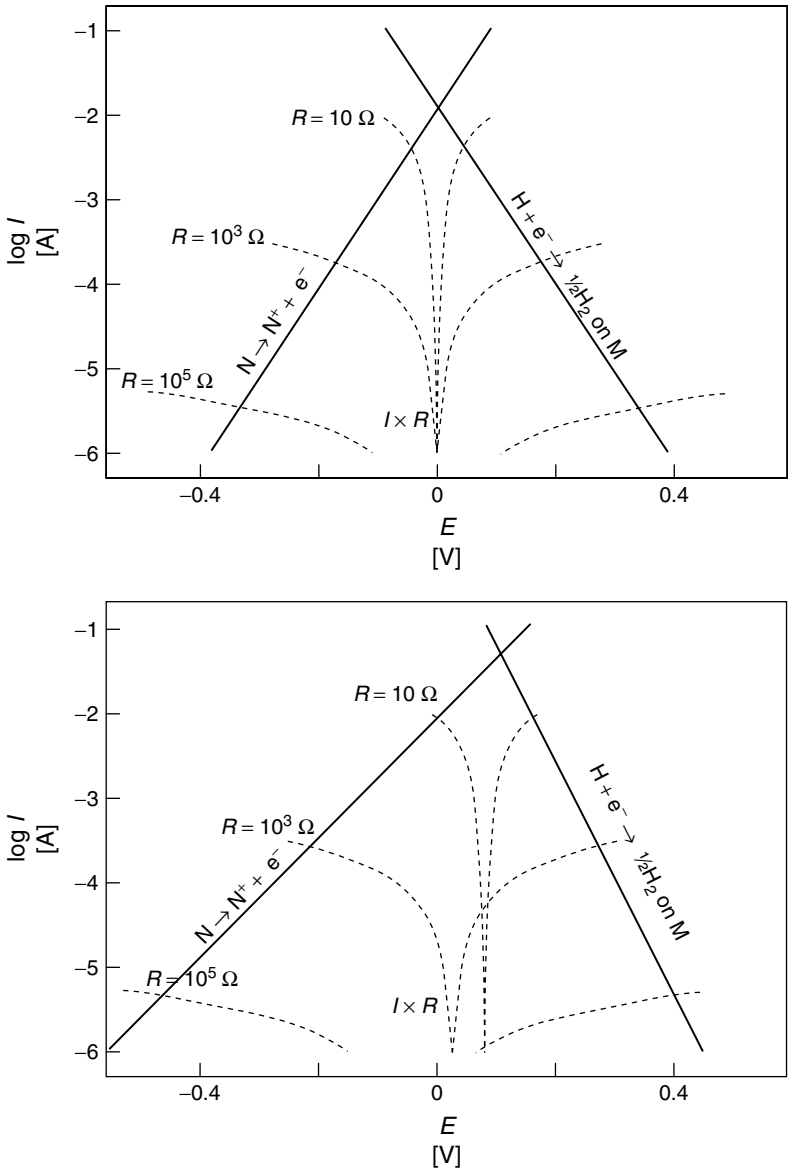


Fig. 17 Schematic representation of how the *IR* drop affects galvanic couple potentials: (a) equal anodic and cathodic Tafel slopes and (b) unequal anodic and cathodic Tafel slopes.

1.3.15 Polarization Resistance and Linear Polarization

It was shown above that the corrosion rate can be determined experimentally from the extrapolation of the linear portions of the polarization curves plotted in semilogarithmic space back to the corrosion potential. In order to perform Tafel extrapolation, it is necessary to polarize the electrode to large potentials on either side of the corrosion potential. It is also possible to determine corrosion rate experimentally using much smaller polarization from the corrosion potential, as is shown in this section.

Equation (41) represents the measured or net current as a function of applied potential. For small $E - E_{corr} = dE$:

$$\exp\left(\frac{E - E_{corr}}{b'}\right) \cong 1 + \frac{dE}{b'} \qquad (45)$$

For small differences in potential from E_{corr}, dE, the measured net currents will be small, di. Substituting into Eq. (41):

$$di = i_{corr}\, dE \left(\frac{1}{b'_a} + \frac{1}{b'_c}\right) \qquad (46)$$

Polarization resistance, R_P, can be defined as the slope of the linear polarization curve at the corrosion potential:

$$R_P \equiv \left.\frac{dE}{di}\right|_{E=E_{corr}} \qquad (47)$$

Note that the units of R_P are $\Omega\ cm^{-2}$. Rearranging Eq. (46), and knowing that $b = 2.3b'$:

$$i_{corr} = \frac{b_a b_c}{(b_a + b_c)2.3R_P} \qquad (48)$$

This is the Stern–Geary equation, which shows that the corrosion rate can be determined by a small polarization from the corrosion potential, unlike Tafel extrapolation, which requires large potential changes from the corrosion potential. The Tafel slopes b_a and b_c must be known to get i_{corr} from R_P. In order to get the Tafel slopes, it is necessary to apply large potential changes from E_{corr}, which defeats the purpose of the linear polarization technique. However, it is possible to make assumptions about the Tafel slopes with little error. Assuming that $b_M = b_H = 0.1$ V,

$$i_{corr} \approx \frac{0.022}{R_P} \qquad (49)$$

This expression will provide corrosion rate values that are typically not more than a factor of 2 from those determined using the real Tafel slopes.

The Stern–Geary equation is valid for finite values of b_a and b_c. For neutral aerated solutions, the cathodic reaction is often oxygen reduction, and it is typically diffusion limited so that $b_c \to \infty$. In that case, the Stern–Geary equation reduces to:

$$i_{corr} = \frac{b_a}{2.3R_P} \qquad (50)$$

Just as the Butler–Volmer equation was shown to be linear near E^{rev} with a slope inversely proportional to i_0 (low-field approximation, Sect. 1.3.8), the net current in a mixed potential system, represented by Eq. (41), is linear near E_{corr}, with a slope inversely proportional to i_{corr}.

Since polarization resistance measurements are made near the corrosion potential, the net currents are often low. Therefore, errors associated with ohmic potential drop are usually small. However, there are cases for which ohmic potential drop creates significant error in the R_P measurement. The measured R_P^m is the sum of the true polarization resistance,

R_P^0, and the ohmic resistance, R_Ω:

$$R_P^m = R_P^0 + R_\Omega \qquad (51)$$

The relative experimental error, ε, is:

$$\varepsilon = \frac{R_P^m - R_P^0}{R_P^0} = \frac{R_\Omega}{R_P^0} \qquad (52)$$

Even if R_Ω is low, the error can be large if R_P^0 is also low, as is the case for systems with high corrosion rates. Similarly, large errors can occur in low conductivity media in which R_Ω is high. The ohmic resistance can be estimated using the methods described above.

References

1. D. Landolt, *Corrosion et chimie de surfaces des métaux*, Presses polytechniques et universitaires romandes, Lausanne, 1993.
2. M. Fontana, N. Greene, *Corrosion Engineering*, McGraw-Hill, New York, 1978.
3. H. H. Uhlig, *Corrosion and Corrosion Control*, John Wiley & Sons, New York, 1971.
4. H. Kaesche, *Metallic Corrosion*, NACE International, Houston, Tex., 1985.
5. A. Bard, L. Faulkner, *Electrochemical Methods*, John Wiley & Sons, New York, 1980.
6. D. A. Jones, *Principles and Prevention of Corrosion*, 2nd ed., Prentice Hall, Englewood Cliffs, N.J., 1996.
7. J. O'M. Bockris, A. K. N. Reddy, *Modern Electrochemistry*, Plenum Press, New York, 1970.
8. L. L. Shreir, R. A. Jarman, G. T. Burstein, (Eds.), *Corrosion*, Butterworth-Heinemann, Oxford, 1994.
9. Corrosion, in *Metals Handbook*, 9th ed., ASM International, Metals Park, Ohio, 1987, 1–1415, Vol. 13.

1.4 Transport Phenomena in Electrolytic Corrosion

Dieter Landolt
Ecole Polytechnique Federale Lausanne
Lausanne, Switzerland

Gerald S. Frankel
The Ohio State University, Columbus, Ohio

1.4.1 Introduction

The kinetics of electrochemical reactions described in the last chapter are only strictly applicable to the situation in which the surface concentrations of all species are identical to the bulk solution concentrations. Mass transport considerations often play an important role in both cathodic and anodic corrosion reactions. More details in the area of mass transport can be found in several textbooks[1–3].

1.4.2 Ion Transport in Electrolytes

Current flow in electrolytes results from the movement of ions. There are three mechanisms of ion transport in electrolytes: convection, diffusion, and migration.

Convection is hydrodynamic flow resulting from a pressure, density, or temperature gradient. The flux of a species i resulting from hydrodynamic flow, $J_{\mathrm{conv},i}$ (mol cm^{-2} s^{-1}), is the product of the concentration of that species, c_i, and solution velocity, v_{sol}:

$$J_{\mathrm{conv},i} = c_i v_{\mathrm{sol}} \tag{1}$$

Diffusion is the net flux of matter resulting from the random motion of a species in a concentration gradient. The flux of a dissolved species i due to diffusion, $J_{\mathrm{diff},i}$ (mol cm^{-2} s^{-1}), is given by Fick's first law:

$$J_{\mathrm{diff},i} = -D_i \left(\frac{\partial c_i}{\partial x} \right) \tag{2}$$

The diffusion coefficient of dissolved ions or neutral species such as oxygen in aqueous solution is on the order of 1×10^{-5} cm^2 s^{-1}. Under nonsteady state conditions diffusion is described by Fick's second law, which states that the change of concentration with time is equal to the difference of the diffusive fluxes in and out of a given volume element.

$$\frac{\partial c_i}{\partial t} = D_i \left(\frac{\partial^2 c_i}{\partial x^2} \right) \tag{3}$$

Sometimes a dissolved species may react chemically, for example, a metal ion produced by anodic dissolution may undergo hydrolysis. In that case, the above equation must be modified by including a term that takes into account the chemical reaction. For example, for a species being consumed by an irreversible first-order chemical reaction having a rate constant k_{ch}, one gets

$$\frac{\partial c_i}{\partial t} = D_i \left(\frac{\partial^2 c_i}{\partial x^2} \right) - k_{\mathrm{ch}} c_i \tag{4}$$

Migration is the preferential drift of ions in a potential gradient toward the electrode of the opposite sign. Ions will move in a field with a net drift velocity, v_{d} (cm s^{-1}), that is proportional to the potential gradient, $\partial\Phi/\partial x$ (V cm^{-1}):

$$v_{\mathrm{d}} = -u_{\mathrm{e}} \left(\frac{\partial \Phi}{\partial x} \right) \tag{5}$$

The quantity u_{e} (cm^2 V^{-1} s^{-1}) is the electric mobility and indicates the velocity the ion would acquire in an electric field of 1 V cm^{-1}. When discussing transport processes in solution, it is more convenient to define a mobility u_i (mol cm^2 J^{-1} s^{-1}),

which is the velocity that one mole of ionic species i would acquire under the effect of a force of 1 N, independent of the nature of that force. The flux due to migration is then

$$J_{\mathrm{migr},i} = z_i F u_i c_i \left(\frac{\mathrm{d}\Phi}{\mathrm{d}x}\right) (\mathrm{mol\ cm^{-2}\ s^{-1}}) \tag{6}$$

It can be shown that the mobility defined in this way is related to the diffusion coefficient by

$$D_i = u_i RT \tag{7}$$

where R is the universal gas constant (J mol^{-1} K^{-1}) and T the absolute temperature. This equation is known as Nernst–Einstein relation.

The total flux of a given species, J_i (mol cm^{-2} s^{-1}), is the sum of the contributions of diffusion, migration, and convection.

$$J_i = J_{\mathrm{diff},i} + J_{\mathrm{migr},i} + J_{\mathrm{conv},i} \tag{8}$$

The movement of charged ionic species results in an ionic current flow in the solution. The charge per mole of any given ionic species is $z_i F$ (C mol^{-1}). Taking the sum over all cationic and anionic species present in the electrolyte yields for the current density:

$$i = \sum z_i F J_i \tag{9}$$

In this equation $z_i > 0$ for cations and $z_i < 0$ for anions. In reality, only diffusion and migration contribute directly to the current flow because convection moves anions and cations in the same way and its contribution to the net current is zero. This can be shown mathematically as follows. Remember that electrolytes outside the double layer are electrically neutral, which means that the sum of the positive charges is equal to the sum of the negative charges of dissolved species. The electroneutrality condition thus gives

$$\sum z_i c_i = 0 \tag{10}$$

With the convective flux Eq. (1), this yields

$$\begin{aligned} i &= \sum z_i F J_{\mathrm{conv},i} = \sum z_i F c_i v_{\mathrm{sol}} \\ &= F v_{\mathrm{sol}} \left(\sum z_i c_i\right) = 0 \end{aligned} \tag{11}$$

showing that the contribution of convection to current flow is indeed zero. The current density in the electrolyte therefore is the sum of the contributions of diffusion and migration:

$$\begin{aligned} i &= \sum (J_{\mathrm{diff},i} + J_{\mathrm{migr},i}) \\ &= -F \sum z_i D_i \left(\frac{\partial c_i}{\partial x}\right) \\ &\quad - F^2 \sum z_i^2 u_i c_i \left(\frac{\mathrm{d}\Phi}{\mathrm{d}x}\right) \end{aligned} \tag{12}$$

In the absence of concentration gradients in the electrolyte, the ionic current obeys Ohm's law,

$$i = -\kappa \left(\frac{\mathrm{d}\Phi}{\mathrm{d}x}\right) \tag{13}$$

where κ is the electrolyte conductivity (Ω^{-1} cm^{-1}). This equation can be compared to the more general Eq. (12). In the absence of concentration gradients $(\partial c_i/\partial x) = 0$, and the first term of Eq. (12) is therefore zero. Under these conditions, the current density is given by the second term and comparison with Eq. (13) yields an expression for the conductivity:

$$\kappa = F^2 \sum z_i^2 u_i c_i \tag{14}$$

The equation indicates that conductivity is proportional to the concentration of the ionic species present and on their mobility. For example, for a NaCl solution

$z_{Na^+} = 1, z_{Cl^-} = -1, c_{Na^+} = c_{Cl^-} = c_{NaCl}$, we obtain

$$\kappa = F^2(u_{Na^+} + u_{Cl^-})c_{NaCl} \qquad (15)$$

The conductivity of NaCl solution is simply proportional to its concentration. In reality, there will be a slight deviation from the predicted linear relationship, especially at higher concentrations. The reason is that the transport theory exposed here strictly applies only to dilute solutions in which ion–ion interactions can be neglected.

The deviation from linearity is even more pronounced for so-called weak electrolytes, which are acids and bases (often organic) that are not completely dissociated into ions. Aqueous solutions of acetic acid are a classical example. The degree of dissociation of acetic acid depends on concentration; the higher the concentration, the larger is the proportion of neutral molecules. The conductivity of acetic acid solutions, therefore, increases much less with concentration than that of so-called strong electrolytes like potassium chloride, which are completely dissociated in water. Another way of expressing this behavior is to say that the molar conductivity (conductivity divided by concentration) of weak electrolytes decreases strongly with increasing concentration. For dilute acetic acid solutions, it varies approximately with the inverse of the square root of concentration.

For certain discussions, it is convenient to define a new transport property, the transport number t_i. The transport number of an ionic species i, also called transference number, indicates the fraction of current transported by that ion in solutions without concentration gradient.

$$t_i = \frac{i_i}{i} \qquad (16)$$

Using the equation for current density (12) in the absence of concentration gradients, it can be easily shown that the transport number for a given ionic species depends on its relative concentration in the solution and on its mobility:

$$t_i = \frac{z_i^2 u_i c_i}{\sum z_i^2 u_i c_i} \qquad (17)$$

Suppose that a 0.5 M sulfuric acid electrolyte contains a small concentration, say 10^{-3} mol L^{-1}, of copper sulfate. In this multicomponent solution, different cationic and anionic species are present such as cupric ions, protons, bisulfate, and sulfate ions. Equation (17) indicates that, because of its small concentration, the transport number of cupric ion will be extremely small, somewhere around 0.001. So, only a very small fraction of the current in the solution will be carried by cupric ion. Consider now the electrodeposition of copper on a cathode from such a solution. Assuming copper deposits with 100% current efficiency, the cathodic current passing the interface (faradaic current) will be entirely due to cupric ion discharge:

$$Cu^{2+} + 2e^- \longrightarrow Cu \qquad (18)$$

In other words, at the interface the charge transfer reaction of cupric ion accounts for the entire current flow, but outside the double layer the cupric ions contribute in a negligible manner to current flow. This immediately raises the question of how copper ion will get to the electrode surface in sufficient quantity to account for the faradic current. Obviously, additional transport mechanisms are needed for this, namely, diffusion and convection. From hydrodynamic theory, it is known that the fluid velocity is zero at a solid surface. The convective flux therefore is zero also at the surface and diffusion alone must account

for the flux of cupric ion in the immediate vicinity of the electrode surface:

$$J_i = -D_i \left(\frac{\mathrm{d}c_i}{\mathrm{d}x}\right)_{x=0} \tag{19}$$

In our example, the subscript i stands for Cu^{2+}. The current density for copper deposition is then

$$i = nF J_i = -nF D_i \left(\frac{\mathrm{d}c_i}{\mathrm{d}x}\right)_{x=0} \tag{20}$$

where the charge number n is equal to the valence of the discharging cupric ion, $n = z_i = 2$. The described situation is special in that we could neglect migration due to the small concentration of cupric ions. A more general expression can be derived taking into account the contribution of migration:

$$i = nF J_i = -\left[\frac{nF D_i}{(1 - t_i)}\right]\left(\frac{\mathrm{d}c_i}{\mathrm{d}x}\right)_{x=0} \tag{21}$$

Equation (21) relates the faradic current density due to the electrochemical reaction of a species i in a multicomponent solution to the concentration gradient at the surface. For small values of the transport number, Eq. (21) reduces to Eq. (20). In the example given above, sulfuric acid plays the role of a supporting electrolyte. A supporting electrolyte does not participate directly in the electrode reaction, but its presence reduces the electric field in the electrolyte by increasing the conductivity. Supporting electrolytes are extensively used in laboratory experiments because they reduce errors in measured potentials resulting from ohmic drops between reference and working electrodes (see Chapter 1.3.14) and in their presence, mass transport at electrodes can be treated in terms of simple diffusion theory, neglecting migration. This concept will be used extensively in the next section.

1.4.3 Generalized Butler–Volmer Equation

In this section, the effect of concentration variations at the electrode surface on overvoltage is explored. For this purpose, we shall first reconsider the Butler–Volmer equation that was introduced in Chapter 1.3.6.

Consider an electrochemical reaction in equilibrium:

$$\mathrm{O} + n\mathrm{e}^- = \mathrm{R} \tag{22}$$

where O and R are the oxidized and reduced species, respectively, for example, Fe^{3+} and Fe^{2+} .

At equilibrium, the Nernst equation applies:

$$E^{\mathrm{rev}} = E^0 - \left(\frac{RT}{nF}\right)\ln\left(\frac{c_{\mathrm{R,b}}}{c_{\mathrm{O,b}}}\right) \tag{23}$$

where $c_{\mathrm{O,b}}$ and $c_{\mathrm{R,b}}$ are the bulk concentrations of O and R. Assuming first-order kinetics, the rate of the forward (reduction or cathodic) reaction for Eq. (22), v_{c}, is given by the product of the rate constant, k_{c}, and the concentration of the oxidized species at the surface where $x = 0$, $c_{\mathrm{O,s}}$:

$$v_{\mathrm{c}} = k_{\mathrm{c}}\, c_{\mathrm{O,s}} = \frac{-i_{\mathrm{c}}}{nF} \tag{24}$$

where i_{c} is cathodic current density. Similarly, for the backwards or anodic reaction:

$$v_{\mathrm{a}} = k_{\mathrm{a}}\, c_{\mathrm{R,s}} = \frac{i_{\mathrm{a}}}{nF} \tag{25}$$

The net current is the difference of the anodic and cathodic currents:

$$i_{\mathrm{net}} = i_{\mathrm{a}} + i_{\mathrm{c}} = nF(k_{\mathrm{a}}\, c_{\mathrm{R,s}} - k_{\mathrm{c}}\, c_{\mathrm{O,s}}) \tag{26}$$

An expression can be given for the reaction rate constants based on activated complex theory, and assuming that the potential drop at the interface adds to the activation

energy linearly with reaction coordinate. This was discussed in detail in Chapter 1.3.6. The reaction rate constants are:

$$k_c = k_c^0 \exp\left\{\left[-\frac{(1-\alpha)nF}{RT}\right]E\right\} \quad (27)$$

$$k_a = k_a^0 \exp\left\{\left[\frac{\alpha nF}{RT}\right]E\right\} \quad (28)$$

Insertion of these into Eq. (26):

$$i_{net} = nFk_a^0 c_{R,s} \exp\left\{\left[\frac{\alpha nF}{RT}\right]E\right\} - nFk_c^0 c_{O,s} \exp\left\{\left[-\frac{(1-\alpha)nF}{RT}\right]E\right\} \quad (29)$$

At equilibrium, $i_a = -i_c = i_0$, $c_s = c_b$, and $E = E^{rev}$. Substituting into Eqs. (24) and (25):

$$i_0 = nFk_a^0 c_{R,b} \exp\left\{\left[\frac{\alpha nF}{RT}\right]E^{rev}\right\} \quad (30)$$

$$i_0 = nFk_c^0 c_{O,b} \exp\left\{\left[-\frac{(1-\alpha)nF}{RT}\right]E^{rev}\right\} \quad (31)$$

Setting Eqs. (30) and (31) equal:

$$k_a^0 c_{R,b} \exp\left\{\left[\frac{\alpha nF}{RT}\right]E^{rev}\right\} = k_c^0 c_{O,b} \exp\left\{\left[-\frac{(1-\alpha)nF}{RT}\right]E^{rev}\right\} \quad (32)$$

Rearranging:

$$\exp\left\{\left[\frac{nF}{RT}\right]E^{rev}\right\} = \left(\frac{c_{O,b}}{c_{R,b}}\right)\left(\frac{k_c^0}{k_a^0}\right) \quad (33)$$

which is just the Nernst equation, where $(RT/2.3nF)\log(k_c^0/k_a^0) = E^0$. Substituting Eq. (33) into Eq. (30):

$$i_0 = nFk_a^0 \left(\frac{k_c^0}{k_a^0}\right)^{\alpha} c_{R,b}^{(1-\alpha)} c_{O,b}^{\alpha} \quad (34)$$

The exchange current increases as the concentration of either oxidized or reduced species increases, as mentioned in Chapter 1.3.3.

A simplified plot of the kinetics near E^{rev} is given in Fig. 1. Equation (30) can be rearranged to give:

$$\log i_0 = \log(nFk_a^0) + \log c_{R,b} + \left(\frac{\alpha nF}{2.3RT}\right)E^{rev} \quad (35)$$

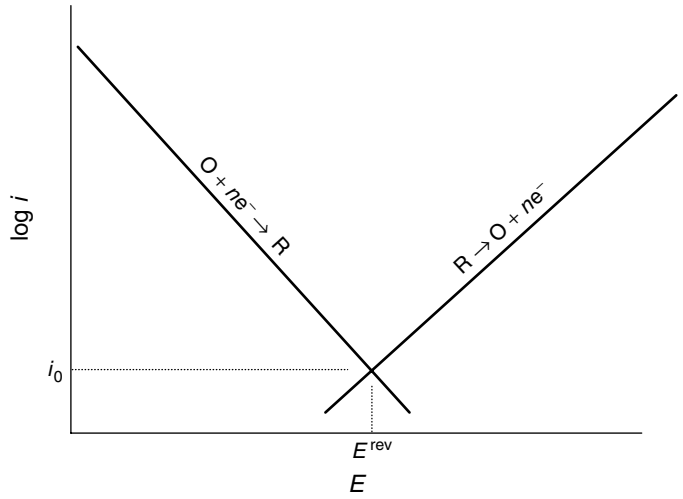


Fig. 1 Evans diagram showing kinetics near the reversible potential.

So a plot of log i_0 versus E^{rev} for constant $c_{R,b}$ (but varying $c_{O,b}$) would be a straight line of slope $\alpha nF/2.3RT$. In other words, the point (i_0, E^{rev}) follows along the anodic Tafel line because of an offset of the cathodic Tafel line, Fig. 2. So, changing the concentration of the oxidized species affects the cathodic kinetics, but not the anodic kinetics. Similarly, the anodic Tafel line is offset for constant $c_{O,b}$ and varying

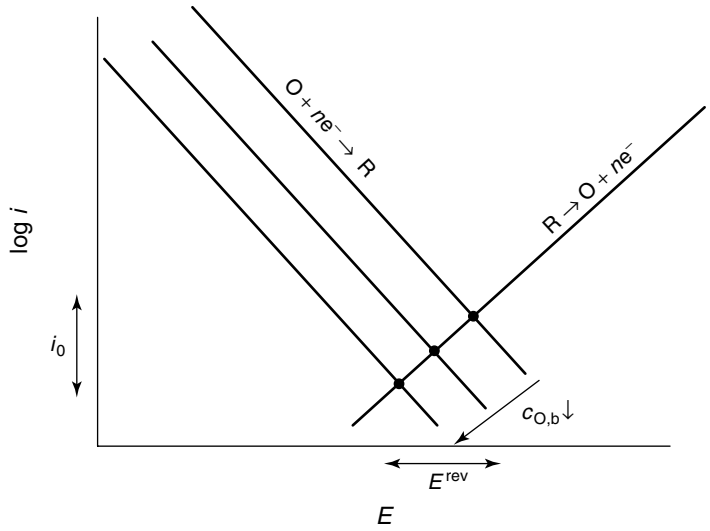


Fig. 2 Influence of the bulk solution concentration of the oxidized species on electrode kinetics.

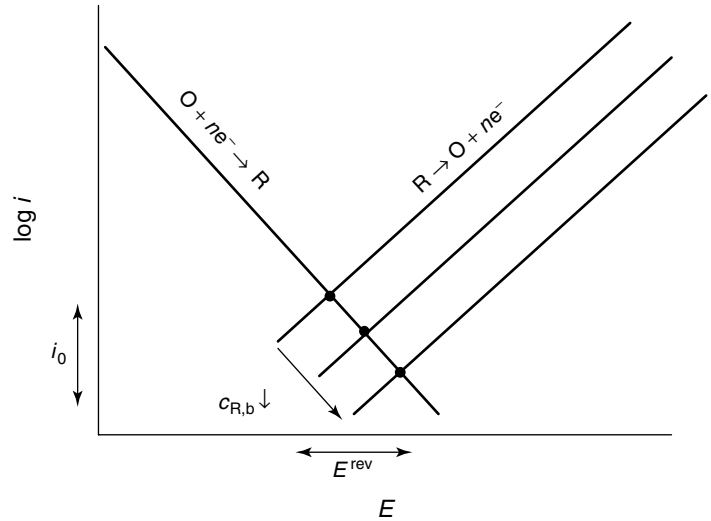


Fig. 3 Influence of the bulk solution concentration of the reduced species on electrode kinetics.

$c_{R,b}$, and changing the concentration of the reduced species affects the anodic kinetics, but not the cathodic kinetics, Fig. 3.

Substituting Eqs. (30) and (31) into Eq. (29), one gets the generalized Butler–Volmer equation:

$$i = i_0 \left(\frac{c_{R,s}}{c_{R,b}}\right) \exp\left[\left(\frac{\alpha n F}{RT}\right)(E - E^{rev})\right] - i_0 \left(\frac{c_{O,s}}{c_{O,b}}\right) \exp\left[-\left(\frac{(1-\alpha)nF}{RT}\right) \times (E - E^{rev})\right] \quad (36)$$

Mass transport limitations, as expressed by the preexponential factors, cause the current to level off at high overvoltage, Fig. 4. This equation reduces to the Butler–Volmer equation for $c_s = c_b$.

For $E < E^{rev}$, the cathodic term dominates:

$$i = -i_0 \left(\frac{c_{O,s}}{c_{O,b}}\right) \times \exp\left[-\left(\frac{(1-\alpha)nF}{RT}\right)(E - E^{rev})\right] \quad (37)$$

The discussion so far shows that the rate of the charge transfer reaction at the interface depends not only on the applied potential but also on the concentration of reacting species prevailing at the electrode surface. Or, this concentration can deviate from the bulk concentration.

1.4.4 Concentration Overvoltage

Consider now a metal sample being corroded by an oxidizing agent, B, which is being transported from the bulk and consumed at the surface. For neutral species such as oxygen, or charged species present in small amounts in the presence of a supporting electrolyte, the contribution of migration to transport is small (Sect. 1.4.2). The flux at the electrode–electrolyte interface is then given by Eq. (19). For the subsequent discussion, we shall assume that near the electrode surface there is a stagnant layer of electrolyte of thickness δ, which is called the Nernst diffusion layer or, somewhat loosely, the diffusion layer, Fig. 5. The assumption of a stagnant layer

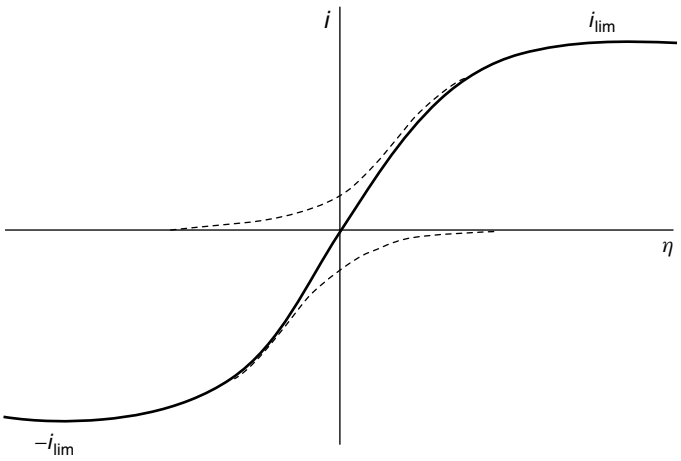


Fig. 4 Schematic representation of the influence of mass transport limitations on electrode kinetics.

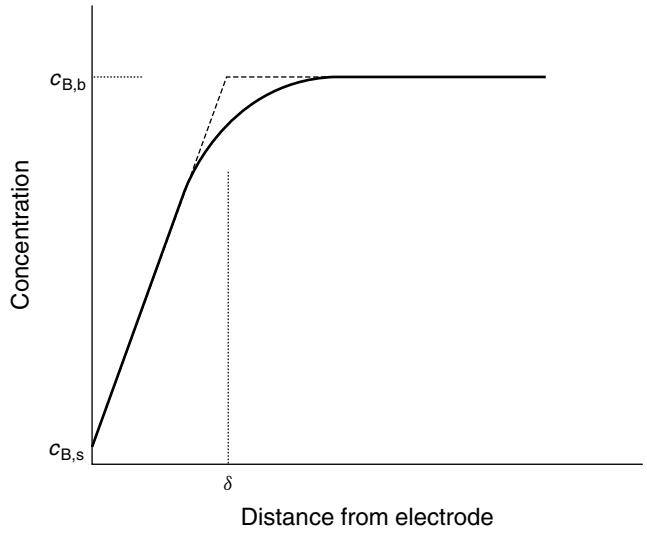


Fig. 5 Schematic representation of concentration in diffusion layer.

of liquid of finite thickness near the electrode is a gross simplification of the real situation. In fact, the solution velocity v_{sol} decreases gradually as one approaches the electrode surface and it vanishes only at zero distance. However, the concept of a stagnant diffusion layer is extremely useful for treating convective mass transport at electrodes. It allows one to easily separate the respective contributions of convection and diffusion. Within the stagnant diffusion layer, only diffusion contributes to the flux of the reacting species; outside the diffusion layer, no concentration gradients exist and convection is the only transport mechanism for the reacting species. The role convection plays for the rate of the electrode reaction can be understood by considering that convection determines the thickness of the stagnant diffusion layer; the higher the prevailing convection rate, the smaller the thickness of the Nernst diffusion layer and the higher, therefore, the flux of the reacting species at the electrode surface. Convective transport rates have been evaluated for many flow systems with different geometry and flow rates, using analytical computation or experimental determination [3]. A particularly well-characterized system is the rotating disk electrode frequently used for controlling mass transport in laboratory experiments. The flux of the reacting species at a rotating disk is proportional to the square root of rotation rate.

Assume that a species B is reduced cathodically. Integration of Eq. (19) over the Nernst diffusion layer yields for the current density:

$$i = \frac{-nFD_B(c_{B,b} - c_{B,s})}{\delta} \tag{38}$$

Solving this equation for surface concentration of B gives

$$c_{B,s} = c_{B,b} + \frac{i\delta}{nFD_B} \tag{39}$$

Note that in this expression i is a negative quantity. In absolute values, one would write:

$$c_{B,s} = c_{B,b} - \frac{|i|\delta}{nFD_B} \tag{40}$$

The surface concentration of the reacting species decreases with increasing current density. For a given current density, it is lower the larger the thickness of the diffusion layer, or in other words, the lower the convection rate.

Suppose now that one increases the cathodic current density ever more and the surface concentration of the reacting species, $c_{B,s}$, decreases correspondingly. Eventually, one reaches a value of $c_{B,s} = 0$ and this is the maximum possible rate since the surface concentration cannot become negative. The current density corresponding to this condition is the limiting current density i_{lim}.

$$i_{lim} = \frac{-nFD_B c_{B,b}}{\delta} \tag{41}$$

Dividing Eq. (38) by Eq. (41) yields Eq. (42)

$$\frac{i}{i_{lim}} = 1 - \frac{c_{B,s}}{c_{B,b}} \tag{42}$$

which can be rearranged to give Eq. (43).

$$\frac{c_{B,s}}{c_{B,b}} = 1 - \frac{i}{i_{lim}} \tag{43}$$

Substituting into Eq. (37):

$$i = i_0 \left(1 - \frac{i}{i_{lim}}\right) \times \exp\left[\frac{-(1-\alpha)nF}{RT}(E - E^{rev})\right] \tag{44}$$

This can be rearranged to yield Eq. (45), which describes the current–potential relationship for a cathodic reaction controlled by charge transfer kinetics and mass transport.

$$i = \frac{i_0 \exp\left[\frac{-(1-\alpha)nF}{RT}(E - E^{rev})\right]}{1 - \frac{i_0}{i_{lim}} \exp\left[\frac{-(1-\alpha)nF}{RT}(E - E^{rev})\right]} \tag{45}$$

If $i_{lim} > i_0 \exp\{[-(1-\alpha)nF/RT]\ (E - E^{rev})\}$, then the denominator of Eq. (45) goes to 1 and this equation becomes the Tafel equation. However, if $i_{lim} < i_0 \exp\{[-(1-\alpha)nF/RT](E - E^{rev})\}$, this equation becomes $i = i_{lim}$ and the reaction rate is independent of potential.

Another way to look at the situation of combined influences of charge transfer overvoltage and mass transport is to rearrange Eq. (44):

$$E - E^{rev} = \eta = -\frac{RT}{(1-\alpha)nF} \ln \frac{i}{i_0} - \frac{RT}{(1-\alpha)nF} \ln\left(1 - \frac{i}{i_{lim}}\right) \tag{46}$$

The total overvoltage is seen to be a sum of the charge transfer overvoltage (first term on the right-hand side) and the concentration overvoltage (second term on the left-hand side).

The concentration overvoltage goes to negative infinity as the current approaches the limiting current, Fig. 6. The limiting current increases with increasing solution velocity, temperature, and bulk concentration of reacting species, which affect the parameters in Eq. (45). The charge transfer (activation) and concentration overvoltages combine as shown in Fig. 7. This is the typical polarization behavior observed for a system under mixed charge transfer and transport control.

1.4.5 Effect of Mass Transport on Corrosion Reactions

Mass transport is of primary importance for the rate of corrosion in environments with limited cathodic reactant, for example, in a neutral solution containing dissolved oxygen as reacting species. The

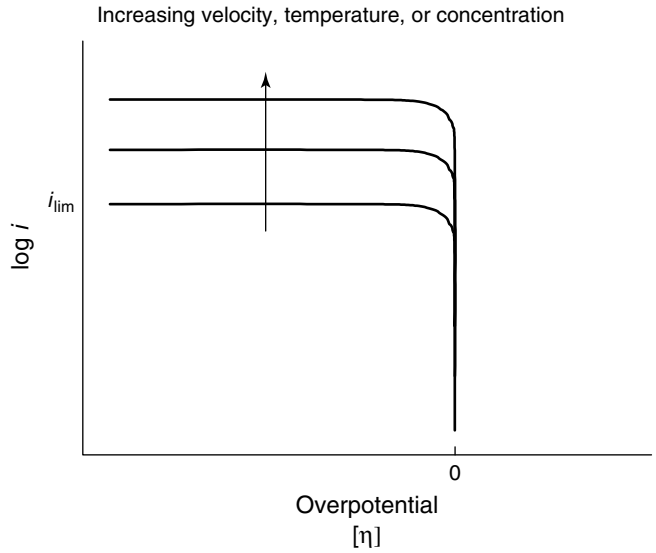


Fig. 6 Effect of various parameters on concentration overpotential.

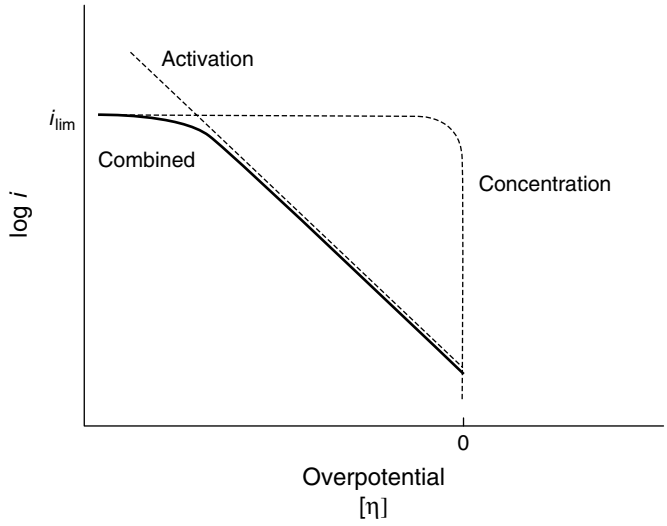


Fig. 7 Combination of activation and concentration overpotential.

maximum corrosion rate in such a situation is given by the limiting current density of the cathodic reactant to the surface,

$$i_{corr} = i_{lim} \tag{47}$$

An example is corrosion of steel in an aerated neutral solution in which the rate of oxygen reduction reaction is largely controlled by mass transport. An Evans diagram for this situation is given in Fig. 8.

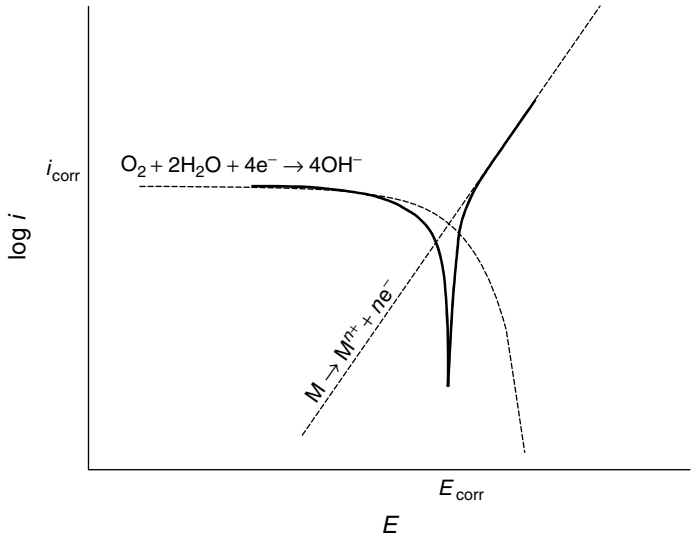


Fig. 8 Evans diagram representing the corrosion of a metal at a rate controlled by oxygen diffusion to the surface.

Similarly, the rate of corrosion of iron in dilute hydrochloric acid is limited by the rate of the mass transport of the proton to the iron surface.

Corrosion of metals usually leads to formation of dissolved metal ions at the corroding surface. These ions will diffuse towards the bulk solution and as a consequence a concentration gradient exists in the diffusion layer adjacent to the electrode. Similarly, as we have seen before for the case of transport of reactants in presence of an excess of supporting electrolyte the dissolution current can be expressed as

$$i = \frac{nFD_{\mathrm{M}}(c_{\mathrm{M,s}} - c_{\mathrm{M,b}})}{\delta} \qquad (48)$$

where we used the subscript M to designate the dissolving metal ion. Rearranging yields

$$c_{\mathrm{M,s}} = \frac{c_{\mathrm{M,b}} + i\delta}{nFD_{\mathrm{M}}} \qquad (49)$$

where this time i is a positive quantity (anodic current density). With increasing dissolution rate, the surface concentration of the dissolving species increases. However, contrary to the case of reactant mass transport, the change in surface concentration of a reaction product does not affect the overvoltage provided the reaction proceeds far from equilibrium so that the reverse reaction can be neglected. This is usually the case in corrosion. Eventually, as the surface concentration increases further at higher current densities, it may reach the saturation concentration resulting in the precipitation of a salt formed between the metal cation and an electrolyte anion. This precipitation occurs at the electrode surface and results in the formation of a solid film through which ions must migrate before dissolving into the solution. Under steady state conditions, the thickness of the salt film does not change and its rate of formation by metal oxidation at the film-metal interface equals its rate

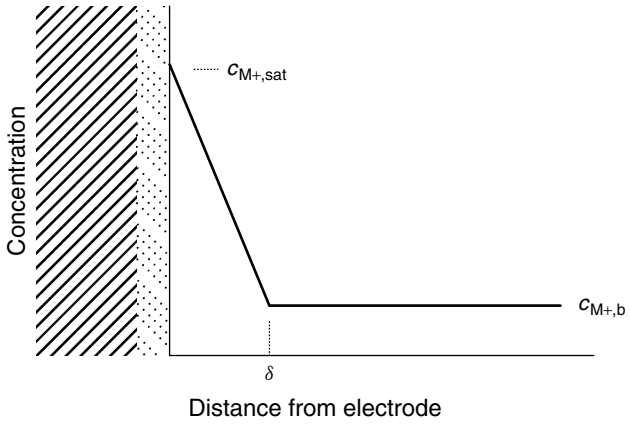


Fig. 9 Concentration profile near an electrode covered by a salt film and dissolving under mass transport control.

of dissolution at the film-solution interface. Since dissolution is mass transport controlled, a limiting current is observed given by

$$i_{\mathrm{lim}} = \frac{nFD_{\mathrm{M}}(c_{\mathrm{M,sat}} - c_{\mathrm{M,b}})}{\delta} \qquad (50)$$

where $c_{\mathrm{M,sat}}$ is the saturation concentration of the transport limiting metal cation. Usually, in corroding systems the metal ion concentration in the bulk solution is zero, $c_{\mathrm{M,b}} = 0$. The described situation is schematically presented in Fig. 9. Salt films and mass transport controlled dissolution processes play an important role in several phenomena, including pitting corrosion and electropolishing of metals.

References

1. D. Landolt, *Corrosion et chimie de surfaces des métaux*, Presses polytechniques et universitaires romandes, Lausanne, 1993.
2. A. Bard, L. Faulkner, *Electrochemical Methods*, John Wiley & Sons, New York, 1980.
3. J. Newman, *Electrochemical Systems*, 2nd ed., Prentice Hall, Englewood Cliffs, N. J., 1991.

2.1
Uniform Corrosion of Metals in Acid, Neutral and Alkaline Electrolytes

Ralf Feser
University of Applied Sciences, Iserlohn, Germany

2.1.1
Fundamental Aspects of Uniform Corrosion

2.1.1.1 Introduction to Uniform Corrosion

It is of importance to predict the lifetime of a metallic component in a specific corrosive system. For uniform corrosion (also called *homogeneous corrosion*), the lifetime can be calculated if the kinetics of the reactions are known and if no localized attack or corrosion cracks could appear. In this chapter, the kinetic aspects of the homogenous corrosion process will be considered. Only electrochemical corrosion mechanisms are regarded, not chemical and physical ones.

Uniform corrosion is defined as a corrosion process with a uniform metal dissolution rate over the entire metal surface exposed to the corrosive environment. The result is a uniform loss of the metal, which leads to a smooth reduction of thickness. However, the uniformity of the corrosion attack depends on the observation technique. For instance, an electron microscope can reveal inhomogeneities not visible to the naked eye.

For polycrystalline metals, the dissolution rate of the various crystallographic orientations is different. Grain boundaries or precipitations will also show a different corrosion rate. There is no accepted definition for what constitutes uniform corrosion. A possible definition could be that the variation of thickness loss all over the surface should not be greater than ±5%.

2.1.1.2 Homogenous Mixed Electrode

During homogenous corrosion, several nonreversible reactions take place at one electrode at the same time, which leads to a uniform reduction of the component thickness. Homogenous corrosion is often found in solutions in which no corrosion products could be formed at the metal surface. Corrosion is composed of at least two partial reactions (see Fig. 1):

(a) Dissolution of the metal:

$$\mathrm{M} \longrightarrow \mathrm{M}^{z+} + ze^{-} \qquad (1)$$

(b) Reduction of the oxidizing agent:

$$\mathrm{Ox} + ze^{-} \longrightarrow \mathrm{Red} \qquad (2)$$

From a thermodynamic point of view, it is necessary that the equilibrium potential of the oxidizing agent is more positive than

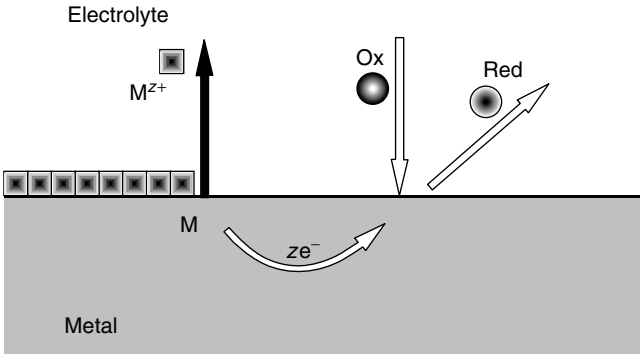


Fig. 1 Corrosion process at the metal–electrolyte interface.

the one of the metal in the same solution. For the charge transport in the solution, the electrolyte has to have a certain conductivity, this means ions have to be present in the solution. If not, the corrosion rate will be negligibly small, as is often the case in nonaerated, distilled, or deionized water. Electrons can easily be transported in metals owing to their conductivity. Therefore, the electrical circuit is closed in a conductive electrolyte and corrosion reactions can take place at the metal electrode surface.

The dissolution and reduction reactions are evenly distributed during uniform corrosion as demonstrated in Fig. 2. The arrows symbolize the reaction rate. Arrows pointing away from the surface represent metal dissolution, whereas arrows pointing toward the metal surface represent reduction of the oxidizing agent. For homogenous corrosion, the rate of the dissolution reaction, or the anodic current density should be equal at all places on the surface. This results in a uniform loss of metal. The distance between the two half reactions will be infinitesimally small, and the locations of the reactions will continuously shift across the surface in a random fashion [1].

The sum or net current i_s is given by the kinetics of four single reactions:

$$i_s = i_M{}^+ + i_M{}^- + i_{Ox}{}^+ + i_{Ox}{}^- \qquad (3)$$

where $i_M{}^+$ represents metal dissolution, $i_M{}^-$ the redeposition of the metal, $i_{Ox}{}^+$ the oxidation of the reduced species

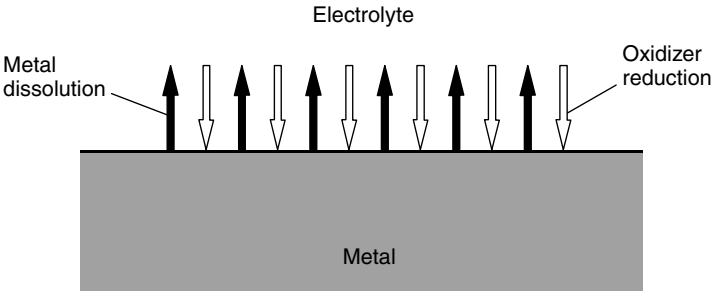


Fig. 2 Uniform corrosion of metals.

of the oxidizing agent, and i_{Ox}^- its reduction. Since the redeposition of the metal ions and the oxidation of the reduced species of the oxidizing agent are usually slow, they can be neglected. In Fig. 3, a schematic polarization curve is shown, representing the oxidation of the metal and the reduction of the oxidizing agent.

The free corrosion potential, E_{corr}, lies in between the standard potentials of the two electrochemical systems.

$$E_M < E_{corr} < E_{Ox} \tag{4}$$

The corrosion potential has, ideally, the same value over the entire metal surface. The current potential dependence can be described by the modified Butler–Volmer equation for the corrosion reaction:

$$i = i_{corr}\left[\exp\left(\frac{E - E_{corr}}{b_a'}\right) - \exp\left(-\frac{E - E_{corr}}{|b_c'|}\right)\right]$$

$$= i_{corr}\left[\exp\left(\frac{2.3(E - E_{corr})}{b_a}\right) - \exp\left(-\frac{2.3(E - E_{corr})}{|b_c|}\right)\right] \tag{5}$$

The polarization π is the deviation from the free corrosion potential:

$$\pi = E - E_{corr} \tag{6}$$

The corrosion rate can be estimated from a semilogarithmic plot of the polarization curve.

If more than one oxidizing agent is present in the solution, both could be reduced. The currents are added and the corrosion rate is higher compared to the presence of only one of the oxidizing agents. For example, in slightly acidic, oxygen-containing solutions, the reduction of both O_2 and H^+ is possible.

The corrosion current can be influenced by the formation of a layer of corrosion products at the surface and change with time. In most cases, the corrosion rate

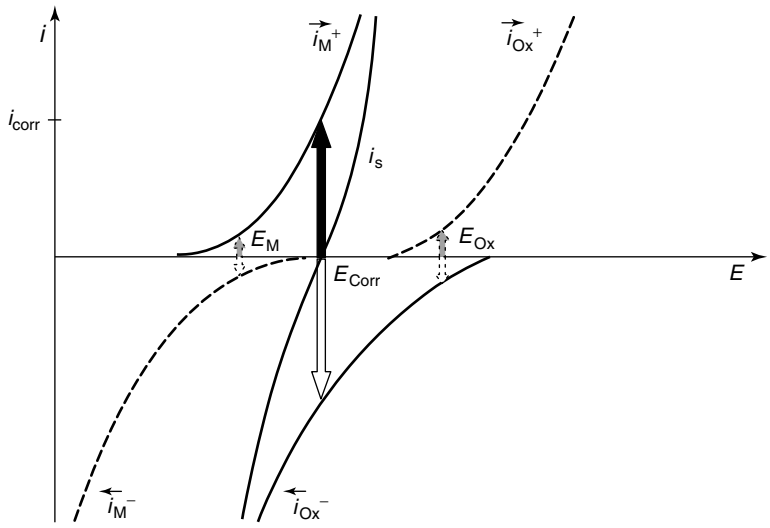


Fig. 3 Schematic polarization curve of a corroding metal.

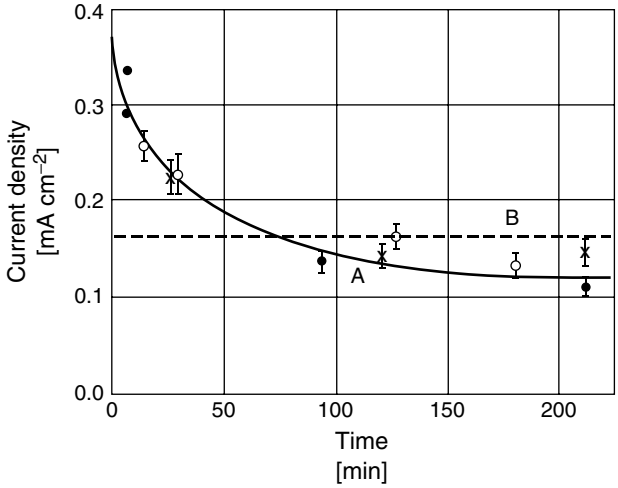


Fig. 4 Change of corrosion rate, determined by polarization measurements, of electrodes made from Siemens Martin steel in O_2-saturated artificial seawater (——— A) and analytically determined mean corrosion rate (- - - - B) (after Engell) [2].

decreases until a steady state is reached, see Fig. 4.

If corrosion products are formed at the metal surface, the corrosion process can easily become nonuniform and shallow pit formation can take place, for example.

It should be pointed out that corrosion is a system property. Small changes of the electrolyte, for example, pH, temperature, content of the oxidizing agent, or the addition of halide ions or metal ions of higher valence can change corrosion behavior drastically. Further factors influencing the rate of uniform corrosion are

- welding, heat treatment, and mechanical surface treatment;
- distribution of any alloying elements;
- rate of flow of the electrolyte.

It is therefore often necessary to test the corrosion behavior of metals by experiments, to be sure whether the corrosion rate is low enough for the conditions under which the metal should be used.

2.1.1.3 Determination of the Homogenous Corrosion Rate

If the corrosion current is determined from polarization curves, the metal loss can be calculated from Faraday's law, according to

$$Q = \frac{\Delta m}{M} nF = I_{\mathrm{corr}} t \qquad (7)$$

where Δm is the mass loss, M is the atomic weight, n is the charge number, F is the Faraday constant, I_{corr} is the corrosion current, and t is the time. The corrosion rate w can be expressed as

$$w = \frac{d}{t} = \frac{I}{A} \frac{M}{\rho} \frac{1}{nF} \qquad (8)$$

where d is the depth of corrosion, A is the exposed area, and ρ is the density of the metal.

The corrosion current density i_{corr} can be expressed as $i_{corr} = I_{corr}/A$ and therefore,

$$w = i_{corr}\left(\frac{M}{\rho}\right)\left(\frac{1}{nF}\right) \qquad (9)$$

It should be pointed out that the sum current, which can be measured in electrochemical experiments as the current between the counter and the working electrode, is not the corrosion current. The corrosion current I_{corr} cannot be measured directly, and has to be determined by extrapolation from semilogarithmic plots of the polarization curve or from the slope of the polarization curve at E_{corr} using the Stern–Geary equation.

The most common method for the determination of the corrosion rate of homogeneous corrosion is the measurement of weight loss. The mass change is measured after exposure of the metal to the corrosive media for a defined time and conditions. The material consumption rate v is calculated by the weight loss Δm per time t and area A

$$v = \frac{\Delta m}{At} \qquad (10)$$

The unit is usually g m^{-2} h^{-1}.

The corrosion rate, w, can be calculated if the density is known:

$$w = \frac{v}{\rho} \qquad (11)$$

The unit is usually mm yr^{-1} (The unit of mils per year or thousandths of an inch per year is commonly used in the US). In most cases, it is convenient to define a metal as a corrosion resistant material if the corrosion rate is <0.1 mm yr^{-1}. A limited resistance is given for values between 0.1 and 1.0 mm yr^{-1}. Above 1.0 mm yr^{-1}, the corrosion rate is too high for most applications. In the case of homogenous corrosion, thickening of the wall will increase the lifetime of a component. However, this is not true for all systems. For example, in electronic devices, low corrosion rates could lead to a loss of function and therefore to failure. Another example is the pharmaceutical industry, in which corrosion rates must often be much below 0.1 mm yr^{-1} to prevent contamination.

For the determination of weight loss, the corrosion products have to be removed. Inhibited acids are normally used for this purpose, but it is important to be sure that such acids remove only the corrosion products and do not attack the base metal. For example, the following acids could be used: inhibited hydrochloric acid for iron, sulfuric acid for copper, and chromium trioxide solutions for zinc. The chemical cleaning procedures for the removal of corrosion products are further described in ISO 8407 [3]. The removal of corrosion products is also necessary to confirm homogenous corrosion and exclude possible local corrosion attack.

If the corrosion rate is very low, the determination of the dissolved metal ions by chemical techniques, for example, atomic absorbance spectroscopy (AAS) is recommended. The amount of corrosion products has to be considered for the calculation of the corrosion rate.

2.1.1.4 Cathodic Corrosion Reactions in Acids

After Brønstedt, an acid is defined as a proton donor.

The equilibrium for an acid, HA, in water can be written as

$$HA + H_2O \longleftrightarrow H_3O^+ + A^- \qquad (12)$$

or simply as

$$HA \longleftrightarrow H_{(aq)}{}^+ + A_{(aq)}{}^- \qquad (13)$$

For the corrosion process it is of interest whether an acid dissociates totally or not. The strength of an acid is indicated by the equilibrium constant K_s, which can be expressed as a pK_s value.

$$pK_s = pH + \log\left(\frac{c_{HA}}{c_{A^-}}\right) \qquad (14)$$

Strong acids, like HCl and H_2SO_4, are practically completely dissociated in water. A weak acid, such as acetic acid, with the same pH is more corrosive than a strong acid at the same pH value because of its buffering capacity. In weak acids, the H^+ ions consumed by the reduction reaction accompanying dissolution will be replaced by H^+ ions, produced from the previously undissociated acid molecules. Therefore, the total amount of H^+ ions, which could be reduced, is higher in comparison to strong acids at the same pH. In principle, the corrosion reactions in acids are given by the following equation:

$$M + zH^+ \longrightarrow M^{z+} + \left(\frac{z}{2}\right) H_2 \qquad (15)$$

This reaction consists of the two partial reactions:

anodic oxidation:

$$M \longrightarrow M^{z+} + ze^- \qquad (16)$$

cathodic reduction:

$$zH^+ + ze^- \longrightarrow \left(\frac{z}{2}\right) H_2 \qquad (17)$$

Simultaneous reduction of oxygen and hydrogen is of interest in slightly acidic solutions.

2.1.1.5 Kinetic of Cathodic Reactions and Influence of Transport Processes

2.1.1.5.1 Transport-controlled Hydrogen Reduction Transport processes to and from the metal surface influence the corrosion rate, as described in detail in a previous Chapter. If the rate-determining step of the reaction is the transport of the oxidizing agent, for example, H^+ ions, to the metal surface, the cathodic reaction kinetics cannot be described by the Butler–Volmer equation.

The current density for the transport of H^+ ions to the metal surface i_H could be described by the following transport equation:

$$i_H = \frac{F D_{H^+}[(c_{H^+})^* - (c_{H^+})_O]}{\delta} \qquad (18)$$

where D_{H^+} is the diffusion coefficient, $(c_{H^+})^*$ is the concentration of H^+ ions at the surface, $(c_{H^+})_O$ is the concentration of H^+ ions in the electrolyte, and δ is the thickness of the diffusion layer. Under the assumption that all H^+ ions reaching the metal surface are instantaneously reduced, $(c_{H^+})^*$ tends to zero and therefore, the limiting current density $i_{H,diff}$ is given by

$$i_{H,diff} = -F D_{H^+} \frac{(c_{H^+})_O}{\delta} \qquad (19)$$

This equation shows the dependence of the diffusion-limited current density on the diffusion layer thickness. Typical values are 10^{-4} cm^2 s^{-1} for D_{H^+} and 5×10^{-3} cm for δ. The current increases with decreasing diffusion layer thickness, for example, by raising the flow rate of the electrolyte, as long as the flow is laminar.

Figure 5 shows the cathodic polarization curve for iron in solutions with different pH values. The diffusion current, indicated by the horizontal lines of the curve, increases with decreasing pH value.

The corrosion rate cannot exceed the diffusion-limited cathodic current. This fact can be used for an estimation of the probable maximum value of the corrosion rate.

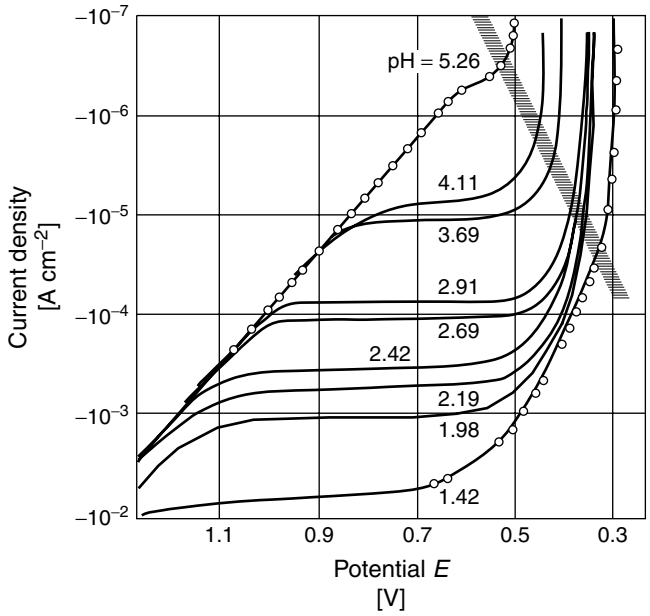


Fig. 5 Cathodic polarization curve of iron (below shaded line identical to the polarization curve of cathodic hydrogen evolution) in HCl/NaCl solution, O_2-free, of various pH values [2].

2.1.1.5.2 **Oxygen Reduction** Oxygen reduction often plays a major role in corrosion, in particular in neutral and alkaline electrolytes. The oxygen-reduction mechanism is called either direct or indirect, depending on the details of the reaction. The indirect reduction mechanism includes the formation of intermediate products [4].

Direct reduction in acidic solutions:

$$O_2 + 4H^+ + 4e^- \longrightarrow 2H_2O \qquad (20)$$

Indirect reduction in acidic solutions:

$$O_2 + 2H^+ + 2e^- \longrightarrow H_2O_2 \qquad (21)$$

$$H_2O_2 + 2H^+ + 2e^- \longrightarrow 2H_2O \qquad (22)$$

Direct reduction in neutral and alkaline solutions:

$$O_2 + 2H_2O + 4e^- \longrightarrow 4OH^- \qquad (23)$$

Indirect reduction in neutral and alkaline solutions:

$$O_2 + H_2O + 2e^- \longrightarrow HO_2^- + OH^- \qquad (24)$$

$$HO_2^- + H_2O + 2e^- \longrightarrow 3OH^- \qquad (25)$$

Oxygen reduction is kinetically hindered and large overpotentials are necessary for higher current densities.

Oxygen in the gas phase, usually from air, is in equilibrium with the aqueous electrolyte. The amount of oxygen that is dissolved in the electrolyte depends on the partial pressure of oxygen in the gas phase. The oxygen concentration decreases with increasing salt concentration of the electrolyte, and increasing temperature. The concentration of dissolved oxygen also depends on the nature of the electrolyte, which is demonstrated in Fig. 6.

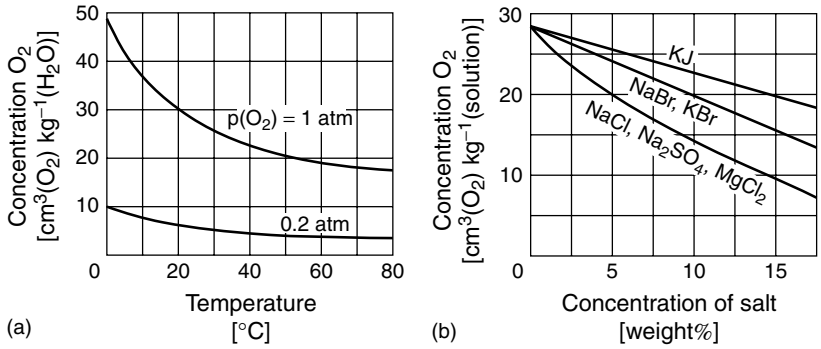


Fig. 6 Solubility of oxygen: (a) in water at an oxygen pressure of 1 and 0.2 atm; (b) in salt solutions at 25 °C and 1 atm oxygen pressure [2].

The rate-determining step of the oxygen reduction during corrosion of most metals is the transport of dissolved oxygen to the metal surface. Therefore, the diffusion-limited current can be calculated with the transport equations in the case of a fully transport-controlled reaction.

The current density for the oxygen diffusion-limited $i_{O_2,\text{diff}}$ current is given by the following equation:

$$i_{O_2,\text{diff}} = -4FD_{O_2}\frac{(c_{O_2})_O}{\delta} \qquad (26)$$

The oxygen diffusion-limited current is characterized by the horizontal parts of the polarization curves in Fig. 7. Typical values of the parameters for a neutral salt solution open to air are 10^{-5} cm^2 s^{-1} for D_{O_2}, 2×10^{-7} mol cm^{-3} for c_{O_2}, and 5×10^{-3} cm for δ.

2.1.1.6 Corrosion in Mineral Acids

Corrosion in mineral acids is usually uniform if no inhomogenities in the metal are present. A practical use for uniform corrosion is cleaning of metals by pickling, for example, in HCl or H_2SO_4. Combustion of sulfur-containing fossil fuels can produce sulfuric acid; chlorine-containing plastics can produce hydrochloric acid on burning. These compounds attack engines, boilers, and heat exchangers. Mineral acids are normally strong acids. Some acids form passive, metal oxide layers by corrosion. In concentrated nitric acid, passive layers can be formed on steels; chromate layers are formed in chromic acids on a great variety of materials, for example, zinc and aluminum; in phosphoric acid, phosphate layers can be formed, for instance, on steels. These conversion and passive layers reduce the uniform corrosion rate.

Mineral acids could be subdivided into reducing or oxidizing acids. The primary cathodic reaction is reduction of H^+ ions in reducing acids and reduction of the acid anions in oxidizing acids. In the case of nitric acid, the following reactions can take place:

$$HNO_3 \rightleftharpoons H^+ + NO_3^- \qquad (27)$$

$$NO_3^- + H_2O + 2e^- \rightleftharpoons NO_2^- + 2OH^- \qquad (28)$$

Oxidizing acids can be defined by whether the redox potential is more positive than the potential of the hydrogen electrode at the same pH.

2.1.1.7 Corrosion in Organic Solutions

It was found that the corrosion rate in a mixture of alcohol and sulfuric acid was

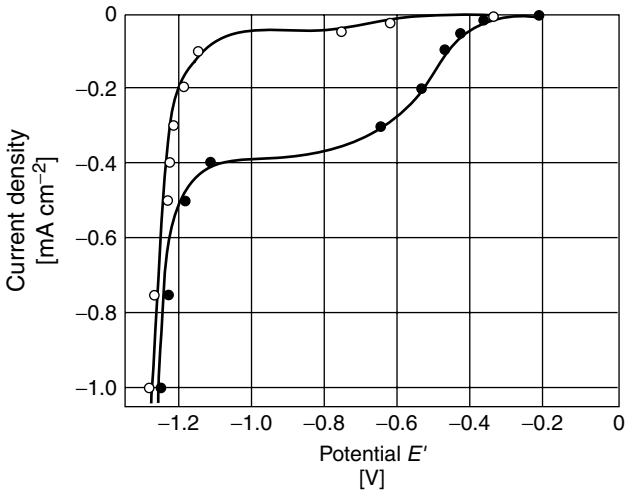


Fig. 7 Polarization curve of cathodic oxygen reduction with superimposed cathodic water dissociation at 18-8-CrNi steel in air-saturated, stirred NaOH/0.5 M NaCl solution, pH 11, 25 °C (●) as well as in practically O_2-free solution (○); potential E' referred to saturated calomel electrode [2].

higher than that in water and sulfuric acid, whereas in a mixture of acetone and sulfuric acid, the corrosion rate was low [5]. The character of the solvent influences greatly the corrosion process, which is demonstrated in Fig. 8. One could subdivide solvents into

- protic solvents (alcohol, carboxylic acids, amines, water, etc.);
- dipolar aprotic (dimethyl, formamide, propylene carbonate, acetonitrile, ketones, aldehydes, esters, asymmetric halogenated hydrocarbons, etc.);
- nonpolar aprotic (aromatic and aliphatic hydrocarbons, symmetric halogenated hydrocarbons, etc.).

The protic or aprotic character of a solvent is determined by the ability of the solvent to provide protons. Protic media contain some quantity of acidic hydrogen atoms and aprotic media do not. The nature of the solvent influences the solubility of all species involved in the corrosion process [5].

2.1.1.7.1 **Single or Multicomponent Media**

It is possible to subdivide corrosive media into pure solutions and mixed solutions. The latter could consist of one or more phases and one or more components. A medium must contain an oxidizing agent and be conducting in order to be corrosive. Corrosive, one-component systems have an oxidizing group in their molecular structure, which is responsible for the metal attack. The corrosion-inducing groups are mostly hydroxyl or carboxyl groups from carboxylic acids, which can donate hydrogen atoms. In multicomponent systems, the oxidizing species are dissolved. In these systems, species that are familiar from aqueous solutions are often responsible for corrosion, such as oxygen, solvated protons, or metal ions of higher valence.

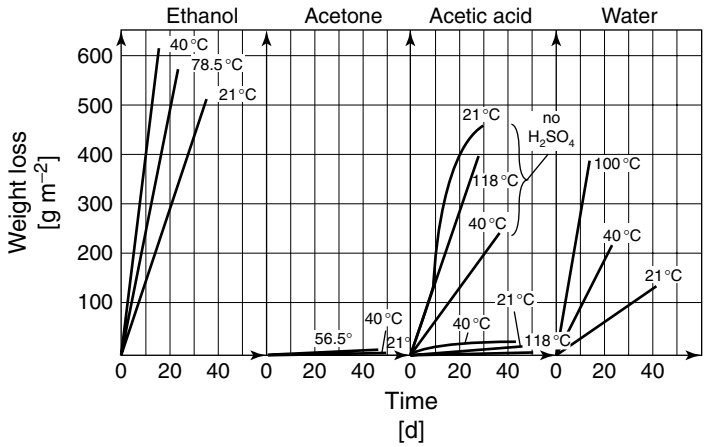


Fig. 8 Corrosion of nickel in different solvents with 0.05 wt% H_2SO_4 at various temperatures [5].

The corrosion reaction is, in principle, comparable to aqueous corrosion.

The anodic partial reaction is

$$M \longrightarrow M^{z+} + ze^- \qquad (29)$$

or

$$M + zX^- \longrightarrow MX_z + ze^- \qquad (30)$$

(X = halogen ion, organic acid anion, etc.)

whereby the metal dissolves as a charged or uncharged complex or reacts to a solid component.

The cathodic partial reaction can be represented as the reduction of a solvated proton to hydrogen:

$$H_{solv}{}^+ + e^- \longrightarrow \tfrac{1}{2}H_2 \qquad (31)$$

or as the reduction of acidic hydrogen of a proton donor.

$$AH + e^- \longrightarrow \tfrac{1}{2}H_2 + A^- \qquad (32)$$

The transport processes influence the corrosion reaction too. In Fig. 9, the corrosion rate of zinc, iron, and nickel in different alcohols is shown. With increasing chain length of the solvent, the corrosion rate decreases. This can be explained by the increase of the viscosity, which leads to a decrease of the diffusion coefficient [6].

In organic solvents, the solubility of oxygen is in many cases higher by a factor 5–8 than that in water [7].

The addition of water influences the corrosion rate in various ways. Figure 10 shows the influence of water on the corrosion rate of iron in various acids. In formic acid, only a slight dependence of the corrosion rate with increasing water content was observed. The other acids show an increase of the corrosion rate with the water content. The effect of water on the anodic reaction is explained either by activation of the metal dissolution by H_2O and OH^- [8–10] or by an increase of the solubility of anodic products connected with a decrease of the passivity of the metal.

In acidified organic solvents, a decrease of the corrosion rate with increasing water content can be found, which is demonstrated in Fig. 11. Stainless steels and nickel-base alloys show a large reduction of the corrosion rate if the water

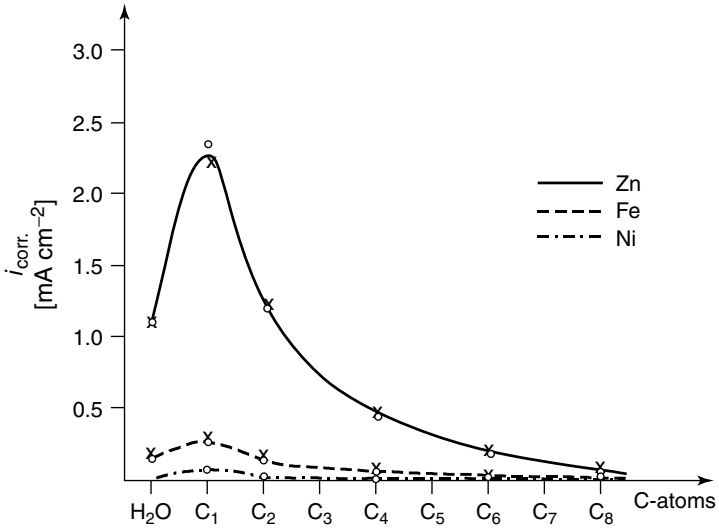


Fig. 9 Corrosion rate (mA cm^{-2}) of zinc, iron, and nickel in primary alcohols of different chain length with added 0.01 N HCl + 1 N LiCl at 25 °C (hydrogen bubbling) [5].

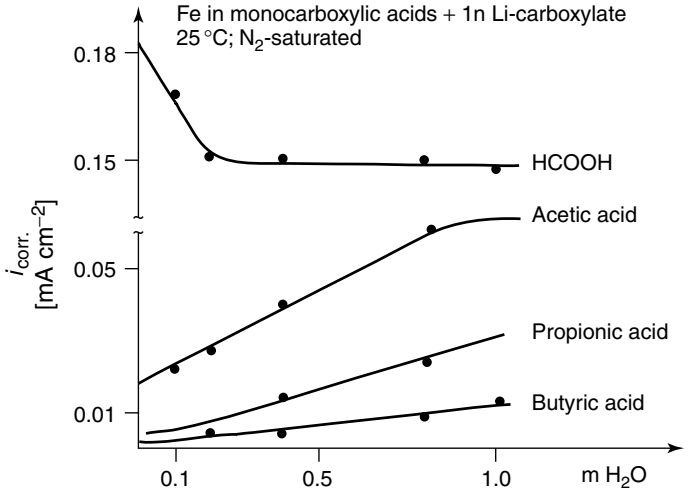


Fig. 10 Corrosion rate (mA cm^{-2}) of iron in different monocarboxylic acids with addition of 1 N lithium carboxylate and water content (up to 1 M) at 25 °C [5].

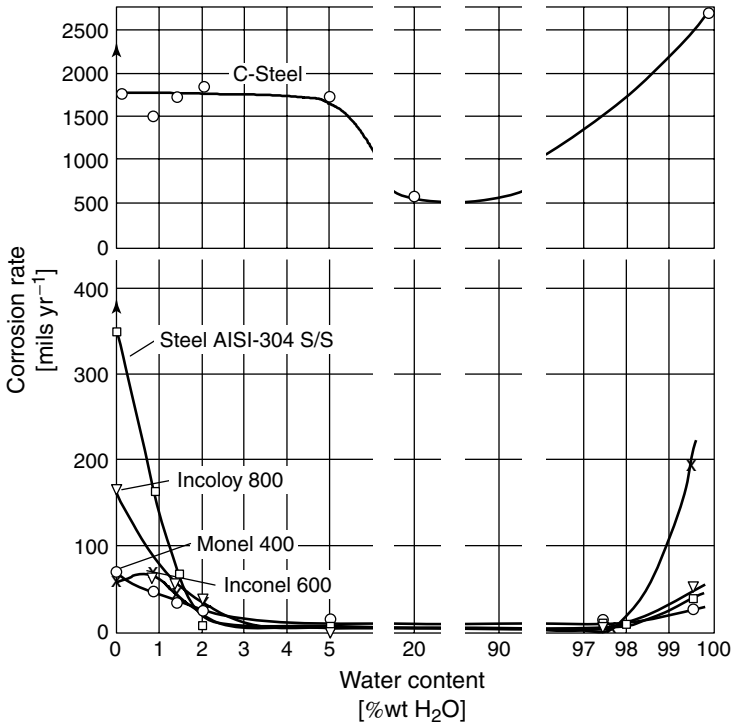


Fig. 11 Corrosion rate of different alloys in dimethyl formamide +0.5 wt% HCl with varying water content at 242–100 °C [5].

content exceeds about 1 wt%. The reason for this behavior is the formation of a passive layer.

2.1.2 Corrosion of Various Metals

In the following section, examples for homogenous corrosion are given. It is impossible to discuss all possible corrosion systems, but the main principles of the corrosion process in acids or neutral and alkaline solutions will be demonstrated.

2.1.2.1 Iron

2.1.2.1.1 Potential–pH Diagram of Iron A potential–pH diagram is shown in Fig. 12 showing that iron is thermodynamically stable at low potentials. Dissolution of iron takes place to Fe^{2+} ions and, at higher potentials, to Fe^{3+} ions. Two type of oxides can be formed, Fe_3O_4 and Fe_2O_3. At high pH values (>14) dissolution to $HFeO_2^-$ ions is possible. The oxides, usually called *rust*, can appear in several forms. In water systems, the formation of FeOOH instead of Fe_2O_3 can be assumed, which can appear as α-, β-, γ- or δ-FeOOH.

2.1.2.1.2 Corrosion of Iron in Acids The corrosion of iron in various electrolytes was investigated in detail by Heusler [12], Lorenz and Heusler [13], and Bockris and coworkers [14]. They especially studied the reaction mechanism of the dissolution process.

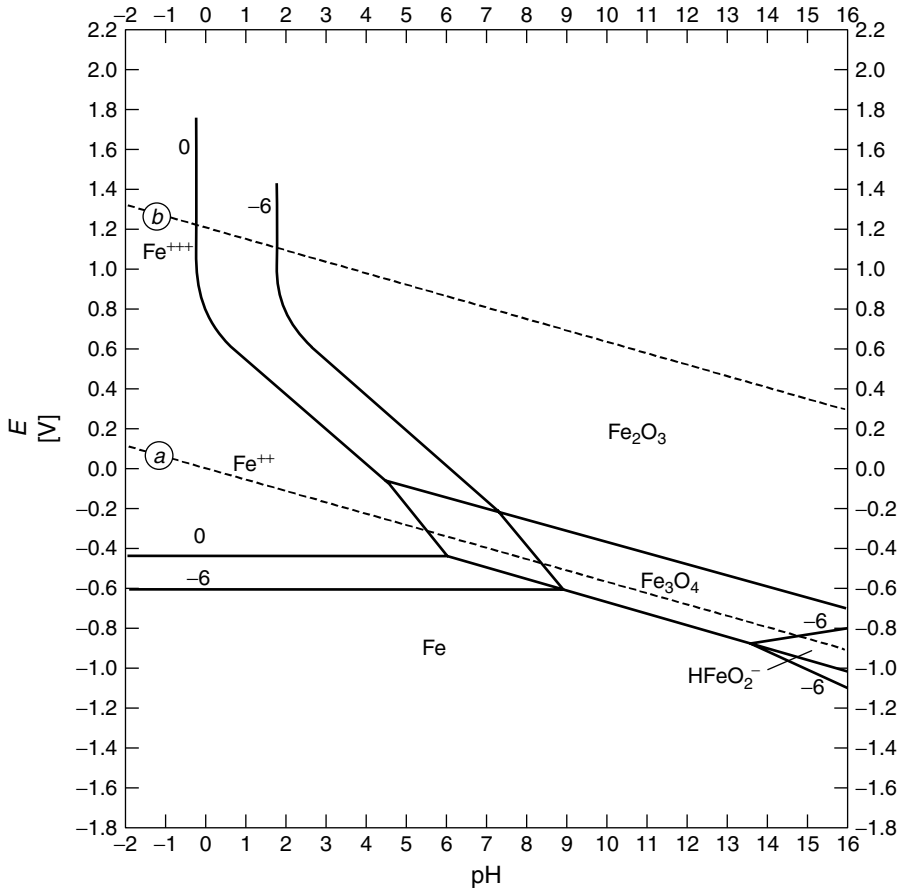


Fig. 12 Potential–pH diagram of iron [11].

Iron dissolution is catalyzed by OH^- ions. At the surface of the iron electrode, even in acidic solutions, OH^- ions could be present according to the following equation:

$$H_2O \longrightarrow (OH^-)_{ad} + H^+ \qquad (33)$$

Iron dissolves according to the following reaction steps:

Iron reacts with OH^- ions and forms a $FeOH_{ad}$ complex

$$Fe + OH_{ad}{}^- \longrightarrow FeOH_{ad} + e^- \qquad (34)$$

The $FeOH_{ad}$ complex catalyzes the charge-transfer reaction:

$$Fe + OH_{ad}{}^- + FeOH_{ad} \longrightarrow Fe(OH)^+ + Fe(OH)_{ad} + 2e^- \qquad (35)$$

In acid solution, the $Fe(OH)^+$ ion is unstable

$$Fe(OH)^+ + H^+ \longrightarrow Fe^{2+} + H_2O \qquad (36)$$

Assuming that Reaction (34) is at equilibrium and Reaction (35) is the rate-determining step, a Tafel slope of 29 mV

can be calculated, which fits experimental results.

Other experimental results show Tafel slopes of 40 mV. Bockris explains these results with an alternative reaction mechanism. It is assumed that FeOH is an intermediate product, but not a catalyst.

$$Fe + OH^- \longrightarrow FeOH + e^- \quad (37)$$

$$FeOH \longrightarrow FeOH^+ + e^- \quad (38)$$

$$FeOH^+ \longrightarrow Fe^{2+} + OH^- \quad (39)$$

The Tafel slope for this reaction can be calculated as 40 mV if Reaction (38) is assumed to be the rate-determining step.

The addition of silicon to cast iron has a positive effect. SiO_2 layers are formed at the surface and protect the iron from further attack. With increasing Si content, the corrosion resistance in sulfuric acid increases. With >14.5% Si, the corrosion rate is very low [15].

A negative influence on corrosion resistance in sulfuric acid is observed with increasing carbon content. The corrosion rate of iron in sulfuric acid is too high for the successful application of unalloyed steels [15].

The corrosion rate of iron in acids is quite high and decreases with time, as a result of the formation of layers of product at the surface. These layers are not well defined and they consist of impurities from the steel, such as copper.

In sulfuric acid, iron could be passivated by anodic polarization, which leads to low metal dissolution rates; without the polarization, active iron corrosion appears. Alloying elements influence the corrosion rate. Copper has a positive effect and normally reduces the corrosion rate, whereas sulfur and phosphorus increase the corrosion rate. In low-sulfur-containing iron, copper can also increase the corrosion rate [16].

2.1.2.1.3 **Corrosion of Iron in Neutral and Alkaline Solutions** Noticeable oxidation and dissolution of iron in neutral electrolytes only occur if an oxidizing agent is present. The cathodic partial reaction in neutral salt solutions is usually the reduction of dissolved oxygen. The diffusion of the oxidizing agent, O_2, toward the surface governs the reaction rate. A proportionality, therefore, exists between

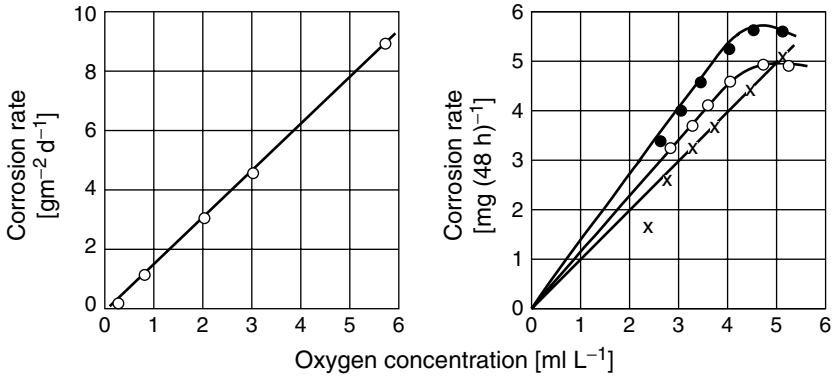


Fig. 13 Influence of oxygen concentration on the corrosion rate of unalloyed steel in salt solution at 25 °C (free convection): (a) 1.5×10^{-3} M $CaCl_2$; (b) solution with KCl (●), Na_2SO_4 (○), NaCl (×) [17].

the corrosion rate of iron and the oxygen concentration. Figure 13 shows the increase of the corrosion rate with increasing oxygen content [17]. In neutral solutions, for example, Na_2SO_4 and NaCl at room temperature without complexing agents, the corrosion rate in equilibrium with air is roughly 0.1–1 mm yr^{-1} [18, 19].

The addition of Cu to steel increases the corrosion resistance against atmospheric corrosion due to the reduced oxygen reduction inside the rust layers that are formed on these alloys [20].

In strong alkaline solutions, the dissolution of iron is accompanied by the formation of $HFeO_2^-$ ions. The following reaction mechanism is assumed [21, 22]:

Anodic reaction:

$$Fe + OH^- \rightleftharpoons FeOH_{ads} + e^- \quad (40)$$

$$FeOH_{ads} + OH^- \rightleftharpoons Fe(OH)_{2ads} + e^- \quad (41)$$

$$Fe(OH)_{2ads} + OH^- \rightleftharpoons HFeO_2^- + H_2O \quad (42)$$

Cathodic reaction:

$$H_2O + e^- \rightleftharpoons H_{ads} + OH^- \quad (43)$$

$$H_{ads} + H_{ads} \rightleftharpoons H_2 \quad (44)$$

The corrosion rate increases with the temperature of NaOH and with concentration, which is demonstrated in Figs. 14 and 15.

2.1.2.2 Stainless Steel

2.1.2.2.1 Corrosion of Stainless Steels in Acids Stainless steels are iron-based alloys with chromium as the main alloying element. The most interesting alloys for technical applications are ferritic stainless steels, austentic stainless steels, and duplex stainless steels. The distinction between the stainless steels comes from their different crystallographic structures. Ferritic–martensitic stainless steels and martensitic stainless steels have less nickel and a higher carbon content and can be hardened by heat treatment. The corrosion behavior of these steels is mainly influenced by the formation of carbides, which generally increase the corrosion rate.

For the formation of passive layers, at least 10.5% Cr is necessary. The activation potential of iron–chromium alloys in sulfuric acid changes, depending on the chromium content. Alloys with chromium

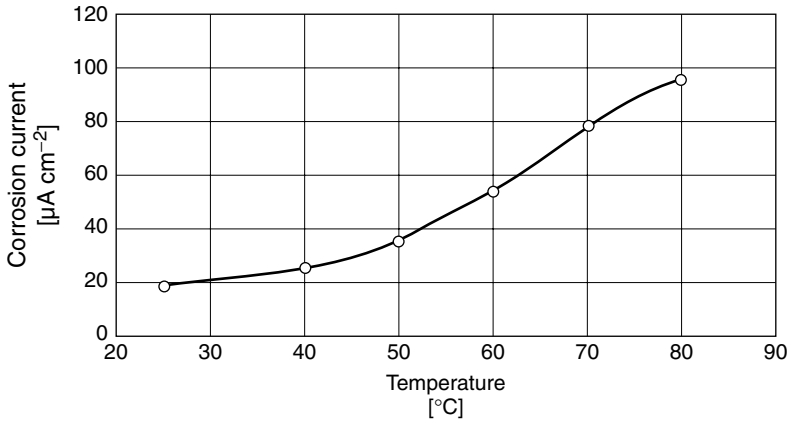


Fig. 14 Corrosion current of steel in 10 N NaOH at various temperatures [22].

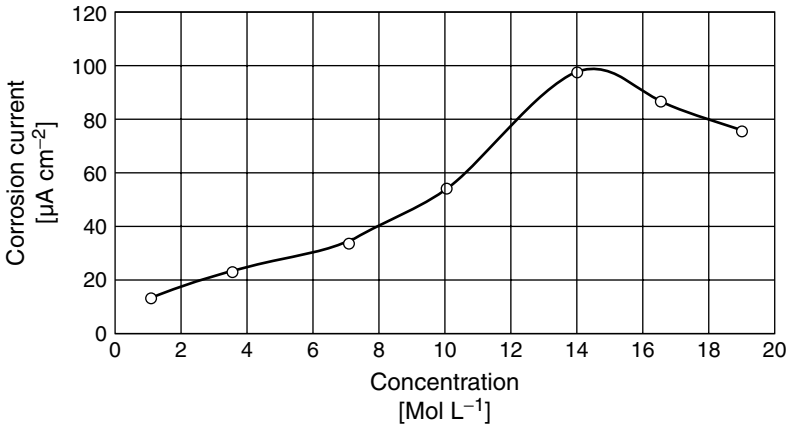


Fig. 15 Corrosion rate of steel in NaOH solutions of various concentrations [22].

contents below 10% behave comparably with iron, whereas alloys above 15% Cr show a behavior similar to chromium. This is demonstrated in Fig. 16. Most technical alloys, therefore, contain more than 13% Cr. The influence of alloying elements on the electrochemical behavior in solution, in which the alloy is able to passivate, is schematically shown in Fig. 17 [23].

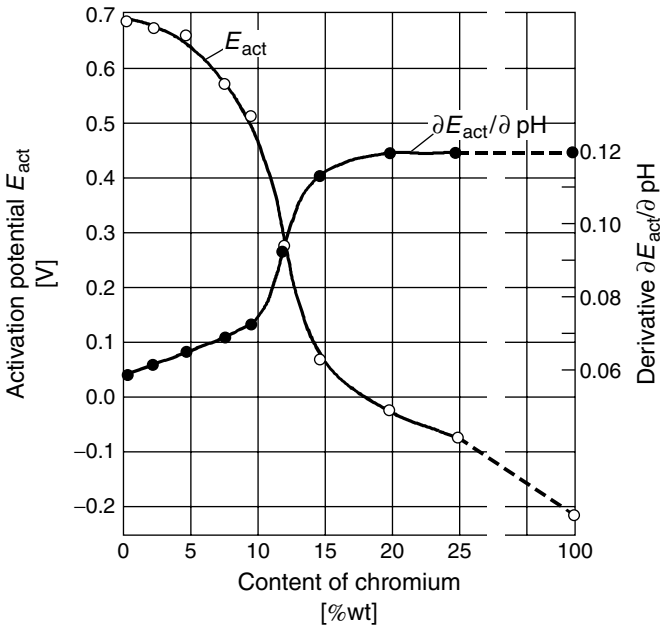


Fig. 16 The activation potential and its derivative $\partial E_{act}/\partial$ pH for Cr–Fe alloys in H_2SO_4 solution [2].

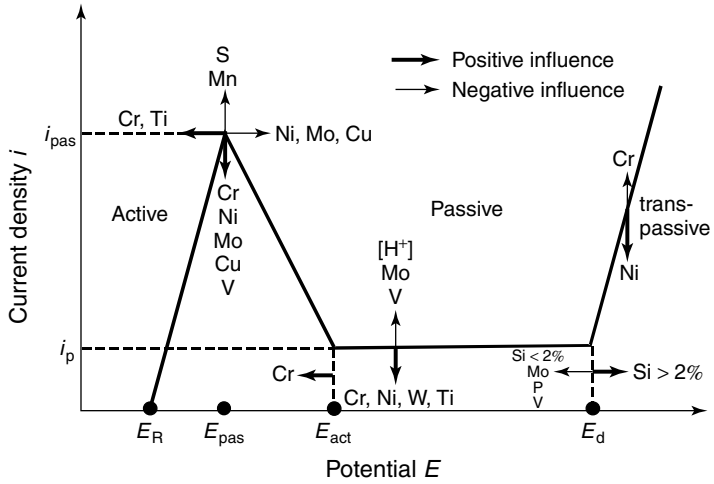


Fig. 17 Characteristic values of polarization curves of steels and alloys that can be passivated. Influence of alloying elements: (⟶) positive influence; (→) negative influence; i_{pas}, passivating current density; i_p, passive current density; E_R, rest potential; E_{pas}, passivating potential; E_{act}, activation potential; and E_d, breakthrough potential [23].

Austenitic stainless steels are susceptible to pitting corrosion. In concentrated hydrochloric acid, the pits are very close to one another; therefore it can be defined as uniform corrosion. The corrosion rate in HCl for stainless steels with 18% Cr and 10% Ni is too high to be acceptable for use. In very diluted solution, in which the homogeneous corrosion rate is low enough, they could be used, but stress–corrosion cracking could appear. The resistance against pitting corrosion, and therefore the field of use for the steels, increases with the content of chromium, molybdenum, and nitrogen in the steel. The corrosion resistance can be expressed by the pitting corrosion resistance equivalent. The solubility of molybdenum increases with the nickel content, as nickel stabilizes the austenitic structure. The transition from stainless steel to nickel-base alloys is continuous [24–26].

The corrosion behavior of stainless steels in sulfuric acid depends mainly on the reducing and oxidizing capabilities of the sulfuric acid itself. H_2SO_4 changes from a reducing agent at concentrations of roughly 0–65% for all temperatures and up to 85% at low temperatures, to oxidizing at higher concentrations. Isocorrosion charts in Fig. 18 show corrosion rates below 0.1 mm yr^{-1} at very low and very high concentrations. The influence of typical alloying elements is also demonstrated.

Stainless steel with 18% Cr and 8% Ni is not very resistant to sulfuric acid. Addition of alloying elements can lead to a limited increase of the corrosion resistance. Increase of the nickel content has a beneficial effect and leads to an expansion of the corrosion resistance of the steel as can be seen in Fig. 18.

Small amounts of noble metals such as Pt, Pd, and Cu increase the corrosion resistance of 18-8 CrNi steels in sulfuric acid, which is demonstrated in Fig. 19. It is assumed that the noble metals become

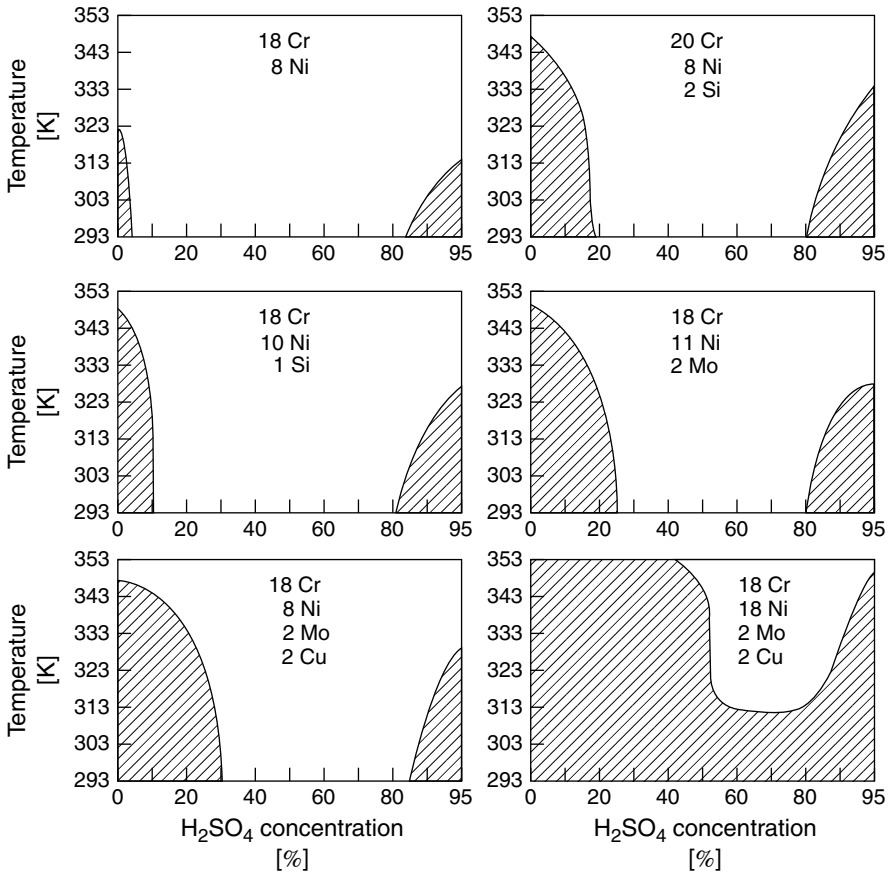


Fig. 18 Influence of various alloying elements to corrosion behavior of Cr–Ni alloys in sulfuric acid. Shaded area (⁄⁄⁄): corrosion rate <0.1 mm yr^{-1} [15].

enriched at the surface by selective corrosion. The overpotential of the cathodic reaction is reduced and therefore the passivation is facilitated. For practical purposes, the addition of Cu is of high interest because of the low costs of this alloying element compared to Pt and Pd. In highly corrosion resistant stainless steels, for example, 1.4529 (main components: ~20% Cr, ~6.5% Mo, ~2.5% Ni, ~1% Cu), copper is used as an alloying element.

In phosphoric acid, common ferritic Cr steels have very limited resistance and only show acceptable corrosion rates at low concentration. In comparison to this behavior, austenitic stainless steels do show a high corrosion resistance over the full concentration range up to 65 °C and in boiling H_3PO_4 solutions, up to 40% [27].

High chromium contents increase the corrosion resistance of ferritic stainless steels in highly concentrated sulfuric acid. For example, the ferritic steel 1.4575 (main components: ~28% Cr, ~4% Ni, ~2% Mo) is successfully used for applications in this field. At temperatures above 120 °C, the alloy can be used at concentrations between

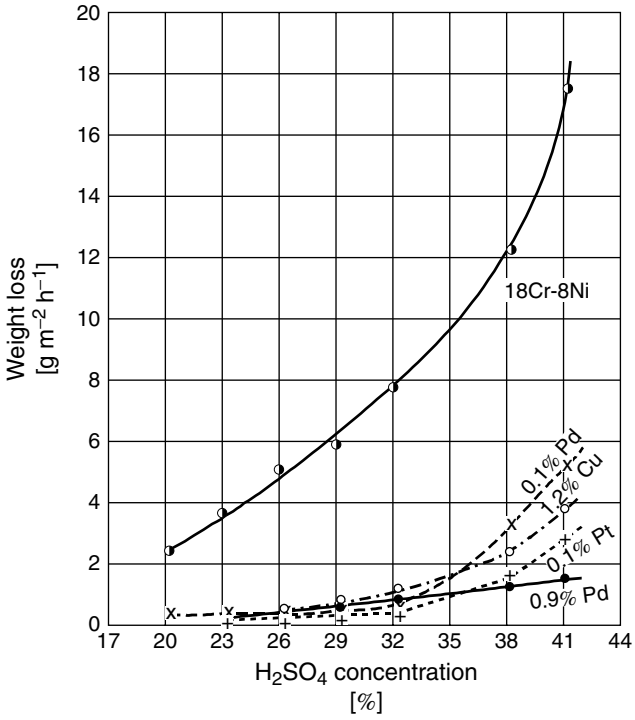


Fig. 19 Influence of small amounts of Cu, Pd, and Pt on the corrosion rate of 18-8 CrNi steel in H_2SO_4 at 20 °C as a function of acid concentration [2].

95 and 100% H_2SO_4 with corrosion rates <0.1 mm r^{-1}.

Manufacturing and welding of ferritic stainless steels has to be done carefully to avoid the precipitation of carbides and other phases, which increase the susceptibility to localized forms of corrosion.

2.1.2.2.2 **Stainless Steels in Neutral and Alkaline Solutions** In neutral solutions, stainless steels are generally very resistant against corrosion, except when they are exposed to solutions containing halide ions, such as chloride, iodide, bromide, and fluoride. In these solutions, pitting corrosion could appear because of the localized destruction of the passive layer. In alkaline solutions, the resistance of stainless steels is, in general, quite high. In NaOH solutions of all concentrations up to temperatures of 65 °C, stainless steels are not attacked. Type 304 (~18% Cr, ~10% Ni) and 316 alloys (~17% Cr, ~11% Ni, ~2% Mo) resist boiling NaOH up to concentrations of nearly 20%.

Stainless steels are also used in drinking water systems, as their corrosion rate is negligible in drinking water. The amount of dissolved metal ions in drinking water is regulated. A study of stainless steel tubes (18% Cr, 10% Ni) that were in service for 10 years showed that the material consumption rate was below 10^{-5} mm yr^{-1}. In new tubes, the rate could be slightly higher [28].

2.1.2.3 Nickel

2.1.2.3.1 Potential–pH Diagram of Nickel

The potential–pH diagram of nickel is shown in Fig. 20. In acidic solutions, dissolution to Ni^{2+} can appear at potentials above the equilibrium potential. In alkaline solutions, $HNiO_2^-$ ions can be formed. Various oxides and hydroxides can be formed on nickel, for example, $Ni(OH)_2$, Ni_3O_4, Ni_2O_3, and NiO_2. In contradiction to the thermodynamic expectations, nickel is very stable in alkaline solutions (see below). The corrosion rate in acidic solutions is also low, which can be attributed to the high overpotential of hydrogen evolution.

2.1.2.3.2 Corrosion of Nickel in Acids

Nickel and nickel-based alloys play a major role in the chemical process industry because of their excellent corrosion resistance and their low susceptibility to stress corrosion cracking.

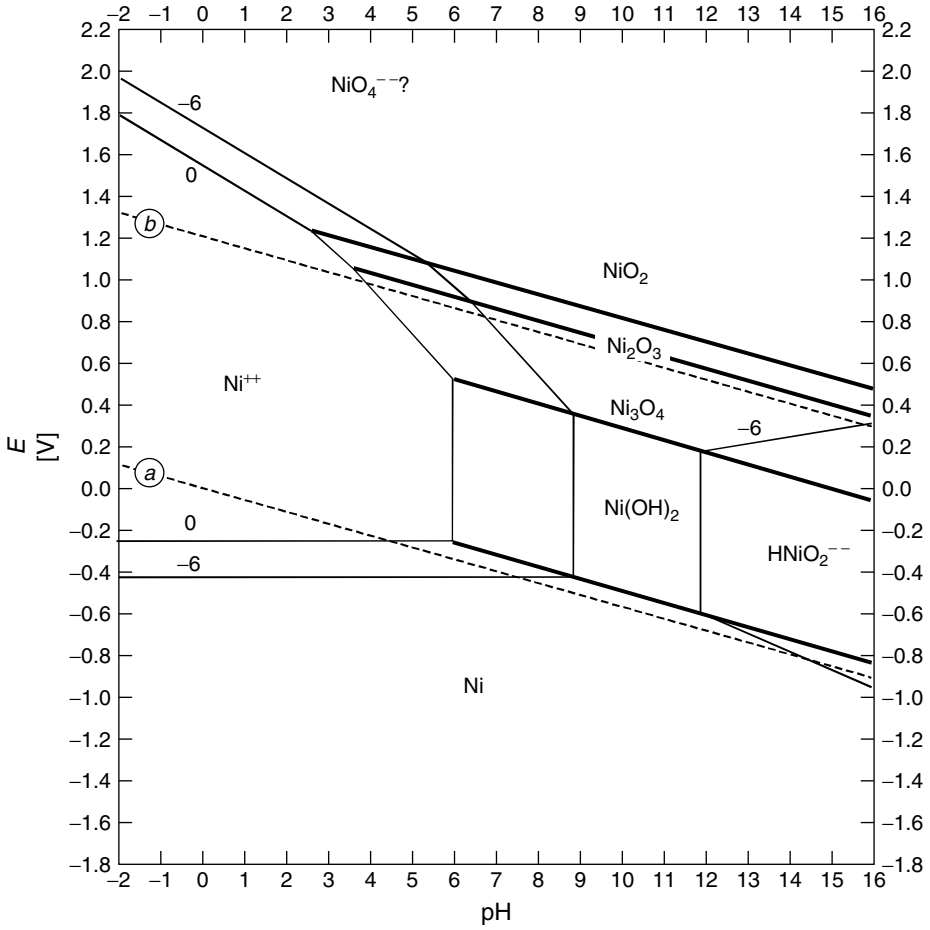


Fig. 20 Potential–pH diagram of nickel [11].

In electrochemical experiments of nickel in sulfuric acid, passive behavior can be seen, but the passive range is relatively small and transpassive dissolution is found at high potentials (Fig. 21). The passive behavior is the result of a NiO or $Ni(OH)_2$ film. At higher temperatures, active dissolution of nickel appears [29].

Oxidizing acids, such as nitric acid or chromic acid attack pure nickel severely, as do solutions containing oxidizing salts, such as iron, copper, or mercury sulfates or chlorides. In these solutions, nickel is obviously already in the transpassive region.

In reducing acids, like HCl, the corrosion resistance of nickel is low, so its use is limited to low concentrations and temperatures in the absence of oxygen. If these acids contain oxygen, the corrosion rate increases.

Nonaerated organic acids do not normally attack nickel. In boiling organic acids or those with a high degree of aeration, high corrosion rates could appear. In fatty acids, nickel is stable up to 210 °C [30].

Nickel alloys can be subdivided into the following groups:

- nickel–copper alloys;
- nickel–molybdenum alloys;
- nickel–chrome–iron alloys;
- nickel–chrome–molybdenum alloys;
- nickel–chrome–iron–molybdenum–copper alloys.

Nickel–copper alloys show good corrosion resistance in nonaerated hydrofluoric acid over the entire concentration range. The highest corrosion rates can be observed between 35 and 75% with values of $<0.5\ mm\ yr^{-1}$. In aerated solutions, nickel alloy 400 (composition ~30% Cu,

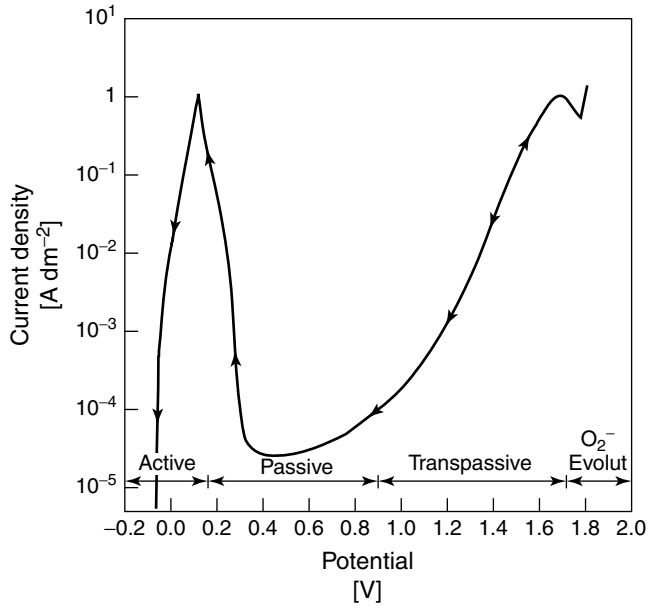


Fig. 21 Polarization curve of pure nickel in deaerated 1 N H_2SO_4 at 25 °C [29].

~1.5% Fe, Ni ≥ 63%) could be used in boiling hydrofluoric acid up to 20%. Stress corrosion cracking has been observed at nickel copper alloys in hydrofluoric acid when the samples are in contact with the vapor phase.

Figure 22 shows the influence of aeration and temperature of nickel alloy 400 in flowing sulfuric acid. In nonaerated solutions, the alloy could be used up to concentrations of 85% H_2SO_4 at 30 and 60 °C. In aerated solutions, the corrosion rate is higher.

In hydrochloric acid, nickel–copper alloys show insufficient corrosion resistance. Copper shifts the passivation potential of nickel in hydrochloric acid to more positive values and increases the critical passivation current density. With increasing copper content, passivation disappears and corrosion rate increases, which can be seen in Fig. 23. Alloy 400 (~30% Cu) is compared with nickel 200 (99.2% Ni). Aeration increases the corrosion rate.

Chromium improves the corrosion behavior of nickel in oxidizing acids by facilitating the formation of a passive layer. It reduces the critical passivating current and increases the passive range.

Alloys with ~30% molybdenum can be used under reducing conditions, for example, in nonaerated hydrochloric acid. The iso-corrosion diagram is shown in Fig. 24 and reflects the good corrosion resistance over the whole temperature and concentration range of the acid.

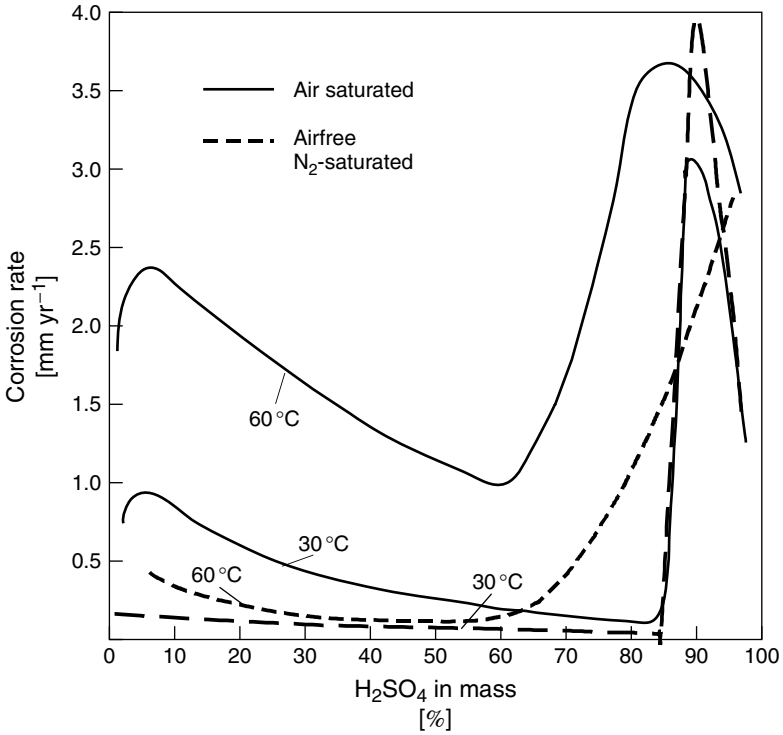


Fig. 22 Corrosion of NiCu30Fe (alloy 400) in H_2SO_4 at 30 and 60 °C; flow velocity, 5.2 m min^{-1} [29].

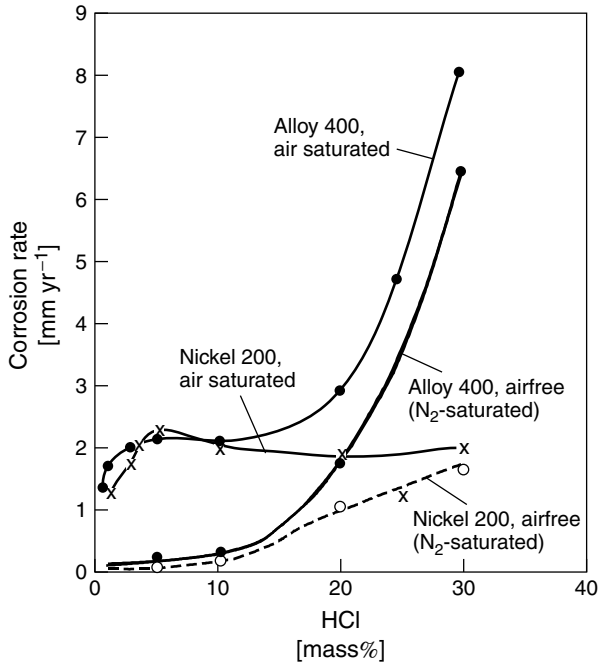


Fig. 23 Corrosion of nickel 200 (99.2% Ni) and NiCu30Fe (alloy 400) in HCl of various concentrations at 30 °C [29].

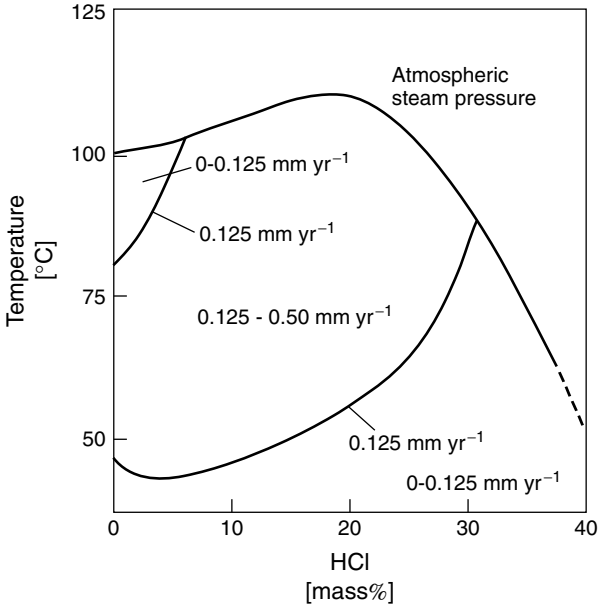


Fig. 24 Iso-corrosion diagram of alloy B-2 in HCl [29].

Nickel–chromium–iron alloys are mainly used for high-temperature applications in gases.

Nickel–chrome–molybdenum alloys combine the good resistance of nickel–molybdenum alloys under reducing conditions with the performance of nickel–chrome alloys under oxidizing conditions. Nickel–chrome–iron–molybdenum–copper alloys also show good corrosion resistance under oxidizing and reducing conditions. Both types of alloys also show good performance even when oxidizing salts, such as Fe^{3+}, are present [31].

2.1.2.3.3 **Corrosion of Nickel in Neutral and Alkaline Solutions** Nickel is corrosion resistant with corrosion rates below 0.13 mm yr^{-1} in neutral or alkaline salt solutions, for example, chlorides, alkali carbonates, bicarbonates, silicates, phosphates, sulfates, and nitrates. High corrosion rates can appear in acidic and oxidizing waters with high content of Fe(III) or copper salts.

In seawater, nickel shows a corrosion rate below 0.13 mm yr^{-1} and could be classified as corrosion resistant. In stagnant seawater, formation of a biofilm on the surface is possible and this could lead to microbiological-induced corrosion. In order to prevent this, nickel–copper alloys with ~30% Cu are used, because copper has an antibacterial effect.

Nickel is one of the most resistant metallic materials in sodium and potassium alkaline hydroxide solutions. Nickel can also be used for temperatures above the boiling point. If the temperatures exceed 300 °C, LC-nickel (low carbon), with a reduced carbon content, should be used. In the temperature region between 315 and 650 °C, graphite could precipitate at the grain boundaries, this leads to sensitization of the metal and intergranular corrosion.

2.1.2.4 **Aluminum**

2.1.2.4.1 **Potential–pH Diagram of Aluminum** Aluminum is an amphoteric metal; it can be used in the presence of water only because of its ability to form a protective layer of aluminum oxides. The potential–pH diagram in Fig. 25 shows that aluminum is stable only at low potentials. For Al^{3+} concentration of 10^{-6} mol L^{-1}, the stability region of the aluminum oxide ranges between pH 4 and 8.5. In this range, aluminum can be successfully used for technical applications. When using potential–pH diagrams, it is important to bear in mind that metal ion concentrations rarely reach more than 10^{-6} mol L^{-1}.

2.1.2.4.2 **Corrosion of Aluminum in Acids** The passive layer can consist of different modifications of the oxide Al_2O_3, hydroxide $Al(OH)_3$, or the oxyhydroxide AlOOH (→ passivity).

The pH limits for the successful use of aluminum depend on various factors, for example, temperature, the specific oxide modification at the surface, and whether substances are present, which could form complexes, or insoluble salts with aluminum.

In acids, aluminum dissolves to Al^{3+} ions according to the following reaction:

$$Al \longrightarrow Al^{3+} + 3e^- \qquad (45)$$

The oxide layer dissolves and Al^{3+} ions are formed.

$$Al(OH)_{3(aq.)} + 3H^+ \longrightarrow Al_{(aq.)}{}^{3+} + 3H_2O \qquad (46)$$

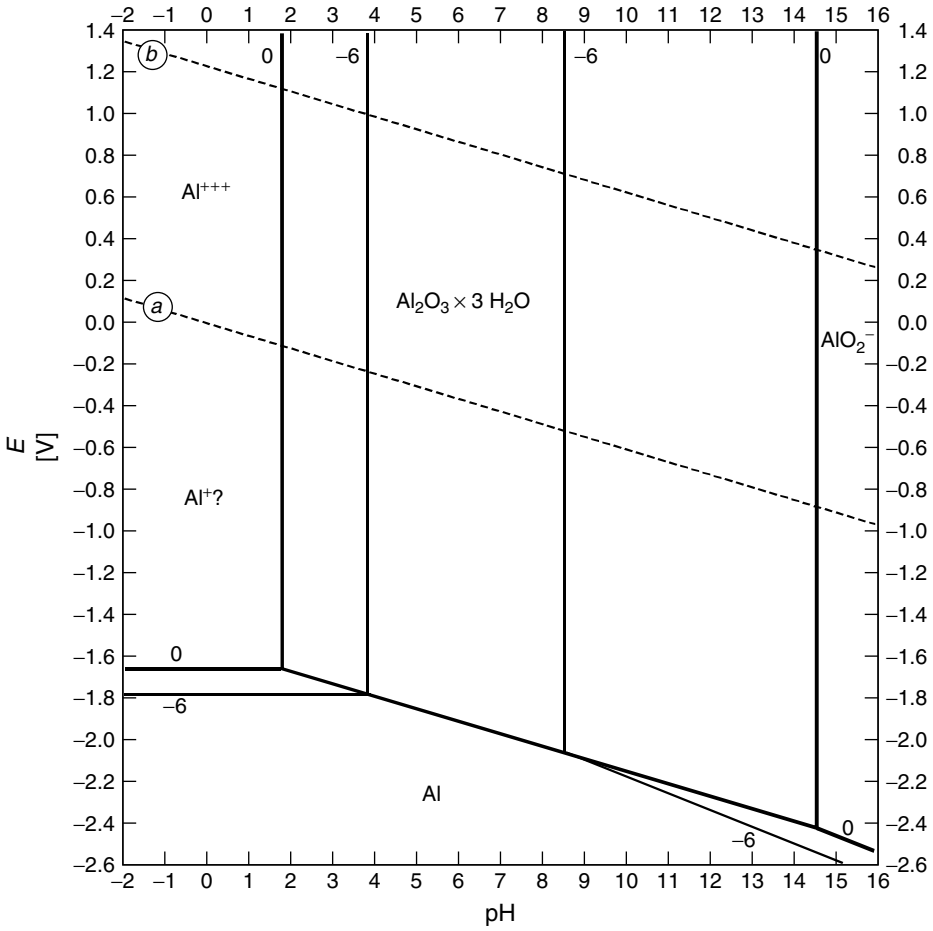


Fig. 25 Potential–pH diagram of aluminum.

The use of aluminum in acids is very limited. Pure aluminum shows the highest corrosion resistance and could be used at room temperature in up to 25% sulfuric acid, in which the dissolution rate is between 0.18 and 0.3 mm yr^{-1}. With increasing content of alloying components, the corrosion resistance decreases as can be seen in Fig. 26.

Nearly all acids attack aluminum, but concentrated nitric acid does not. In Fig. 27, the corrosion rate of aluminum in nitric acid of different concentrations and temperatures in the region of 0–30 °C is shown. The corrosion rate increases with decreasing acid concentration. Increasing flow velocity of the medium increases the corrosion rate, especially if it is two-phase flow [32].

In sulfuric acid, chromic acid, or mixtures of the two, the thickness of the oxide layer can be increased by anodic polarization. Homogeneous dissolution of aluminum is promoted and oxides are formed at the surface. The rate of dissolution of the oxides is lower than

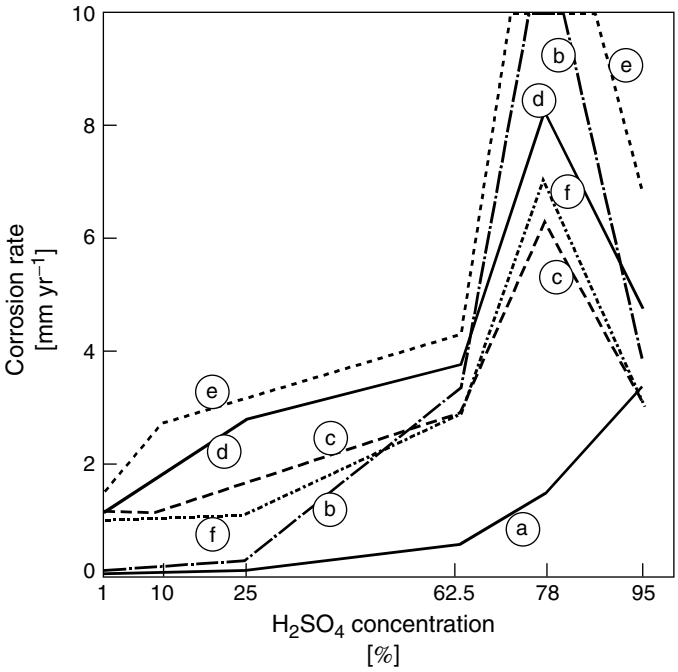


Fig. 26 Corrosion of aluminum and aluminum alloys in sulfuric acid at 293 K [15]: (a) Al99.98 R; (b) Al 99.5; (c) AlMn alloy; (d) AlMg 3; (e) AlMg 7; and (f) AlSi 12.

the formation of fresh oxide, the layers that are formed are very homogenous. This anodizing process produces protective layers, which increase the corrosion resistance. A further improvement of the corrosion resistance against atmospheric corrosion could be realized by water vapor oxidation.

2.1.2.4.3 **Corrosion of Aluminum in Neutral and Alkaline Solutions** In neutral noncomplexing solutions, aluminum is resistant against corrosion. In Na_2SO_4 – solutions, the dissolution current is very low and in the order of 0.1 μA cm^{-2}. The resistance is attributed to the formation of the thin passive layer, which has a low conductivity (see above) [33, 34], therefore the cathodic partial reaction of the corrosion is hindered (→ passivity). The best corrosion resistance is shown by aluminum of high purity (Al 99.98). In Cl^--containing solutions, pitting corrosion could appear (→ pitting corrosion).

The corrosion resistance of anodized aluminum is more or less comparable with the untreated aluminum in an acidic and alkaline environment. The formation of pits is decreased under atmospheric corrosion conditions (→ pitting corrosion).

In alkaline solutions, the dissolution of aluminum proceeds as

$$Al + 4OH^- \longrightarrow Al(OH)_4{}^- + 3e^- \quad (47)$$

and the oxide layer dissolves as

$$Al(OH)_3 + OH^- \longrightarrow Al(OH)_4{}^- \quad (48)$$

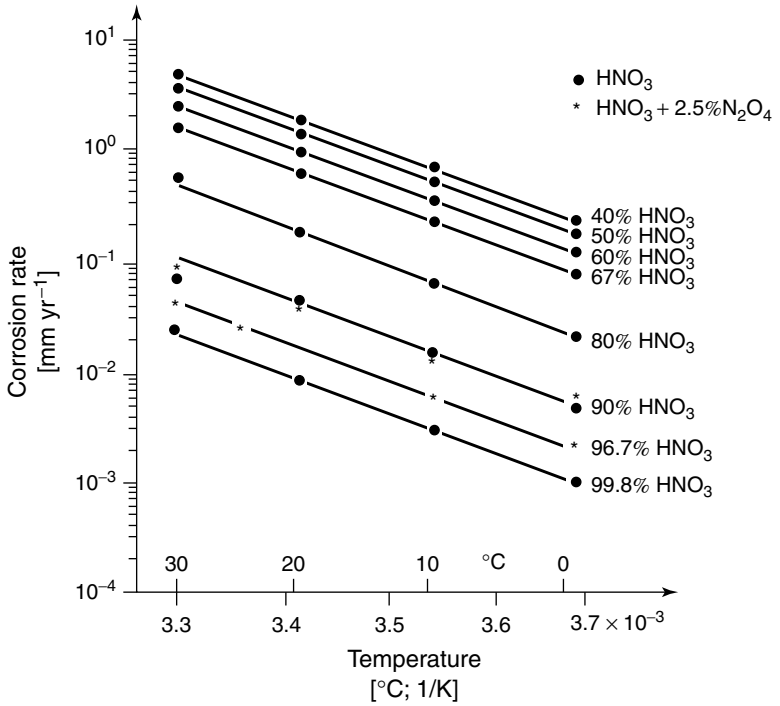


Fig. 27 Corrosion of Al 99.5 in static nitric acid; Arrhenius diagram [32].

Cathodic protection needs careful potential control to avoid cathodic corrosion. With increasing cathodic polarization, the rate of aluminum dissolution increases, as is shown in Fig. 28. This effect is called *cathodic corrosion of aluminum* and is attributed to the formation of OH^- ions at the metal surface during the reduction of oxygen or water.

2.1.2.5 Magnesium

2.1.2.5.1 Potential–pH Diagram of Magnesium

Magnesium is a metal with a very negative standard potential of −2.37 V.

The potential pH–diagram of magnesium is shown in Fig. 29. The region of stability of magnesium is below the stability line of water (a). Therefore, magnesium reacts very easily with water with formation of H_2. In alkaline solution, magnesium forms $Mg(OH)_2$, which passivates the metal. $Mg(OH)_2$ is thermodynamically more stable in water than MgO.

2.1.2.5.2 Corrosion of Magnesium in Acids

Magnesium and its alloys are heavily attacked in all acids, except hydrofluoric acid (HF) and chromic acid (H_2CrO_4). In HF, an insoluble layer of MgF_2 is formed, which protects the magnesium from further attack. In dilute solutions of HF (concentration 6–60%), the corrosion rate at 20 °C is around 1 mm yr^{-1}.

In pure H_2CrO_4, the magnesium is attacked at a very low rate. Boiling 20% H_2CrO_4 solution can be used to remove corrosion products from magnesium.

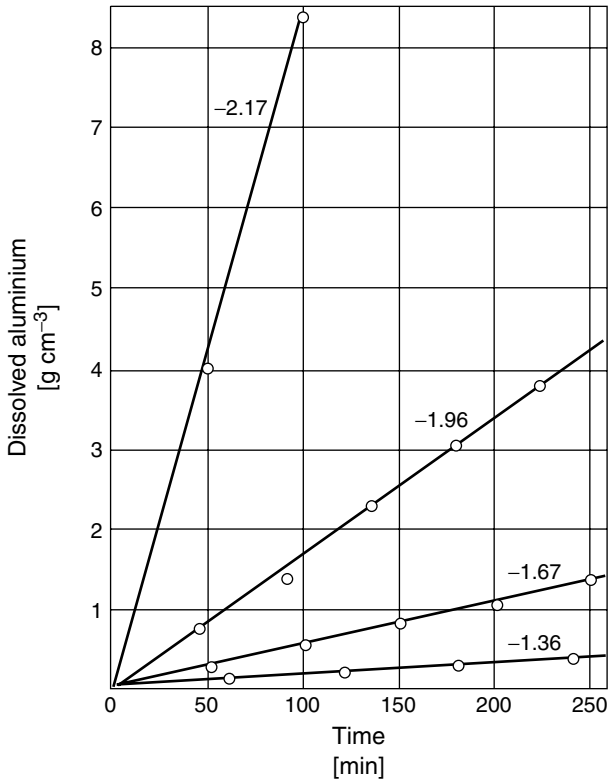


Fig. 28 Cathodic corrosion of aluminum: mass loss for cathodic, potentiostatic polarization in 1 M Na_2SO_4/NaOH solution, pH 11, 25 °C, in the regions of hydrogen evolution for various potentials [2].

2.1.2.5.3 **Corrosion of Magnesium in Neutral and Alkaline Solutions** Magnesium is highly susceptible to galvanic corrosion. Small amounts of impurities in the alloy can have a tremendous influence on the corrosion susceptibility. In Fig. 30, the influence of various elements is demonstrated. Small additions of copper, iron, nickel, and cobalt have an extremely negative effect on the corrosion resistance. The tolerance limit for iron is 0.015%, for nickel 0.0005%, and for copper 0.1% [35]. Because of the low solid solubility of these elements, they precipitate as inclusions. These act as active cathodic sites for the reduction of water and therefore, the corrosion rate of magnesium is increased.

The corrosion reaction of magnesium in aqueous environments can be formulated as

$$Mg \longrightarrow Mg^{2+} + 2e^- \quad (49)$$

$$2H_2O + 2e^- \longrightarrow H_2 + 2OH^- \quad (50)$$

$$Mg^{2+} + 2OH^- \longrightarrow Mg(OH)_2 \quad (51)$$

Hydrogen evolution at the electrode is a consequence of the reduction of water. Oxygen reduction does not play a major role in the corrosion process.

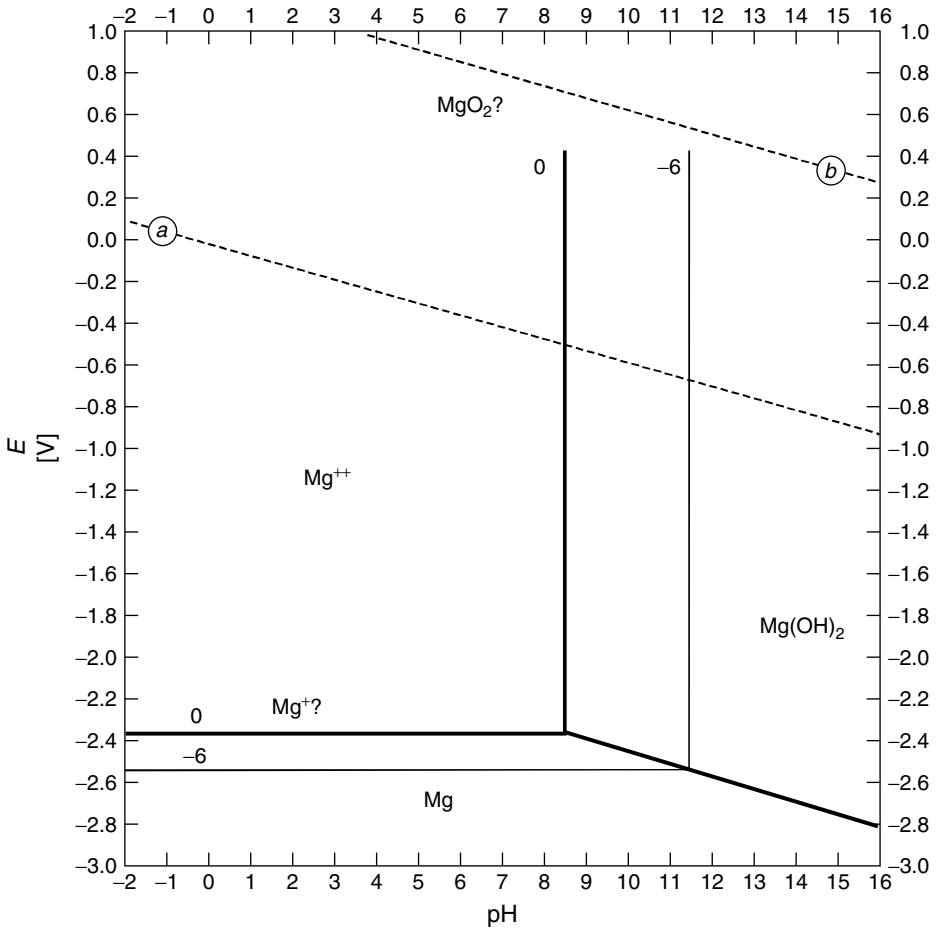


Fig. 29 Potential–pH diagram for magnesium.

The corrosion resistance of magnesium in the atmosphere is attributed to the formation of a surface film of $Mg(OH)_2$, which keeps the surface pH at about 11 or higher. This keeps the magnesium in its region of passivity.

Pure magnesium is seldom used for technical applications. In industry, the following magnesium alloy groups are applied:

- magnesium with the addition of aluminum, zinc, and manganese;
- magnesium with the addition of rare earth, zinc, thorium, silver, and so forth.

2.1.2.6 Zinc

2.1.2.6.1 Potential–pH Diagram of Zinc

The stability of zinc is shown in Fig. 31 for the system zinc–water for two different concentrations of dissolved species (10^{-1} and 10^{-6} mol L^{-1}). As can be seen from the diagram, zinc is an amphoteric metal, which dissolves to Zn^{2+} ions in the acidic

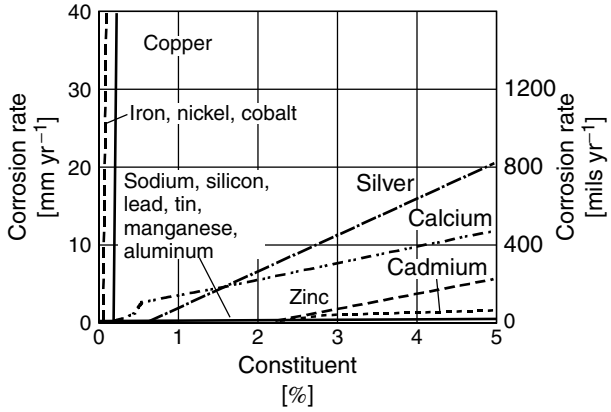


Fig. 30 Effect of alloying and contaminant metals on the corrosion rate of magnesium, determined by alternate immersion in 3% NaCl solution [35].

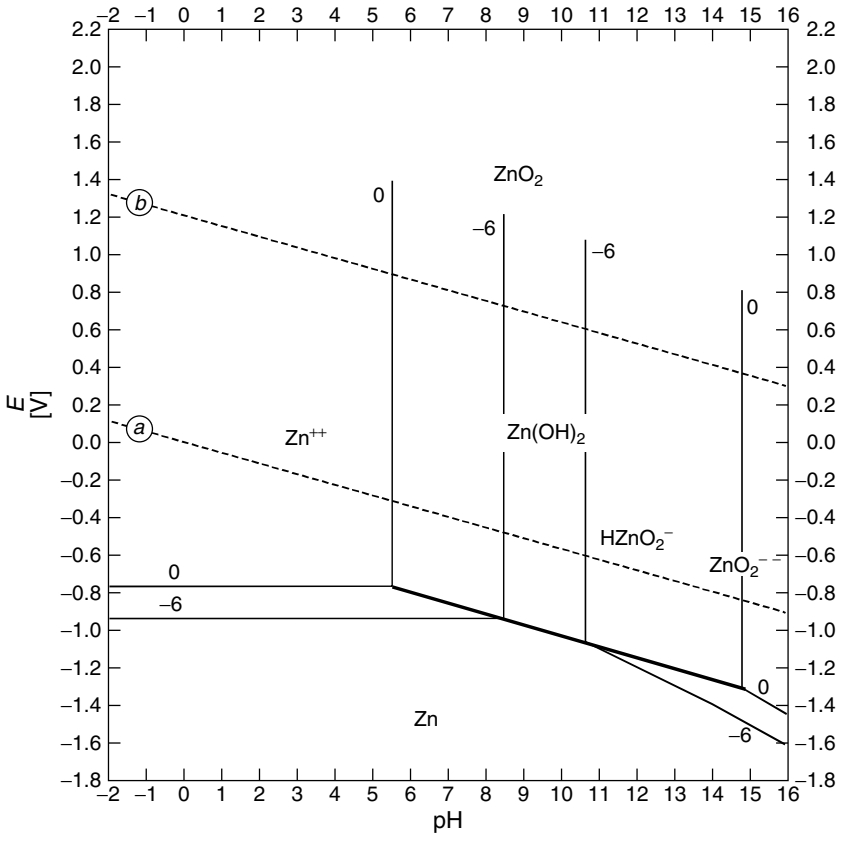


Fig. 31 Potential–pH diagram for zinc.

pH region and to $HZnO^{2-}$ ions in alkaline solutions. In between these two areas, $Zn(OH)_2$ is stable. The concentration of dissolved species influences the stability regions. At negative potentials, zinc is stable. As for all amphoteric metals, strong cathodic polarization leads to the formation of OH^- ions at the electrode surface, which raises the pH value until the metal is not stable.

2.1.2.6.2 **Corrosion of Zinc in Acids** Zinc is heavily attacked in acids with H_2 gas formation. In solutions with pH values below 3, the corrosion rate is in the region of ~40 mm yr^{-1}.

In sulfuric acid, the dissolved zinc hinders the kinetics of the hydrogen reduction [28], which can be seen in Fig. 32.

2.1.2.6.3 **Corrosion of Zinc in Neutral and Alkaline Solutions** The dissolution of zinc in neutral and noncomplexing solutions is a consecutive process of two steps of a charge-transfer process with the formation of adsorbed single charged species [37].

$$Zn \longrightarrow Zn_{ad}{}^{+} + e^- \quad (52)$$

$$Zn_{ad}^{+} \longrightarrow Zn_{ad}{}^{2+} + e^- \quad (53)$$

Zinc corrodes significantly in oxygen-free – distilled water, as shown in Table 1. With increasing oxygen content, carbon dioxide concentration, and temperature, the corrosion rate increases and reaches a maximum at around 65 °C.

The cathodic reaction in distilled water is determined by the reduction of water.

$$2H_2O + 2e^- \longrightarrow H_2 + 2OH^- \quad (54)$$

In oxygen-containing solutions, the cathodic reaction is oxygen reduction.

$$O_2 + 2H_2O + 4e^- \longrightarrow 4OH^- \quad (55)$$

In distilled water, local corrosion attack often occurs. With increasing carbon dioxide concentration, uniform corrosion attack becomes more likely.

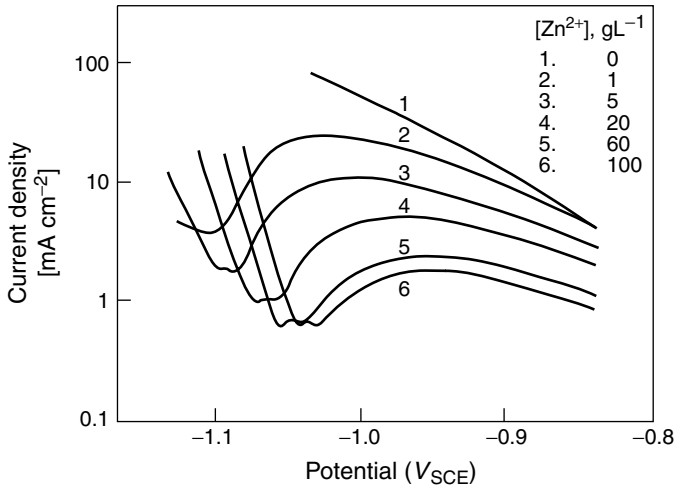


Fig. 32 Effect of Zn^{2+} concentration on voltammograms in 200 g L^{-1} H_2SO_4 solutions. After Wang and coworkers [36].

Tab. 1 Corrosion rate of zinc in distilled water at various temperatures with and without oxygen bubbling [38]

Test condition	*Temperature (°C)*	*Corrosion rate (mm yr^{-1})*
Boiled distilled water;	Room	25.4
specimens immersed in	40	48.3
sealed flasks	65	83.8
Oxygen bubbled slowly	Room	218.4
through the water	40	348.0
	65	315.0

The corrosion rate is influenced by the hardness of the water. At high temperatures, in hard water, the corrosion rate is low. For example, in 75 °C, carbon dioxide–free water, the corrosion rate is below 1 μm yr^{-1} (see Fig. 33) [38].

Zinc alloys with addition of >0.03% aluminum are susceptible to intergranular corrosion attack [2, 39].

The corrosion rate of zinc in neutral salt solution varies with the type of anions. Factors influencing the solubility of zinc in the solution affect the corrosion rate. The solubility of zinc in the solution is increased by Cl^- or SO_4^{2-} anions, which enhance the corrosion rate. Anions such as carbonates and phosphates increase the formation of solid-salts and have an inhibitive effect. The reaction of chromate with the zinc surface produces passive layers, which reduce the corrosion rate strongly.

2.1.2.7 Copper

2.1.2.7.1 Potential–pH Diagram of Copper

The potential–pH diagram of copper is shown in Fig. 34. Copper is stable

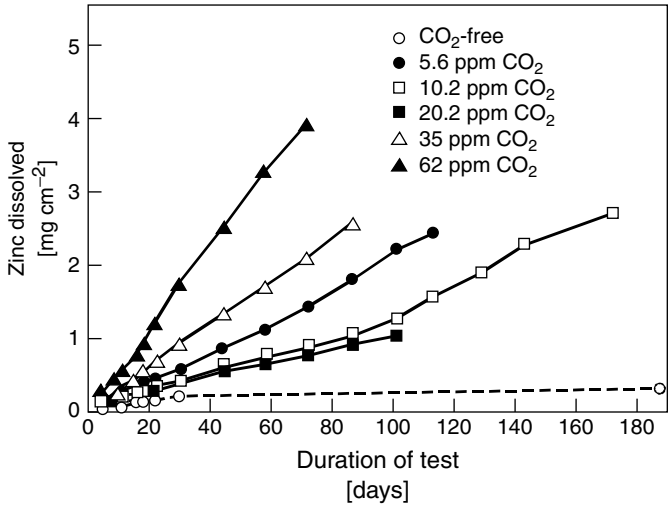


Fig. 33 Effect of free carbon dioxide on the dissolution of zinc in hot hard supply water. After Kenworthy and Smith [38].

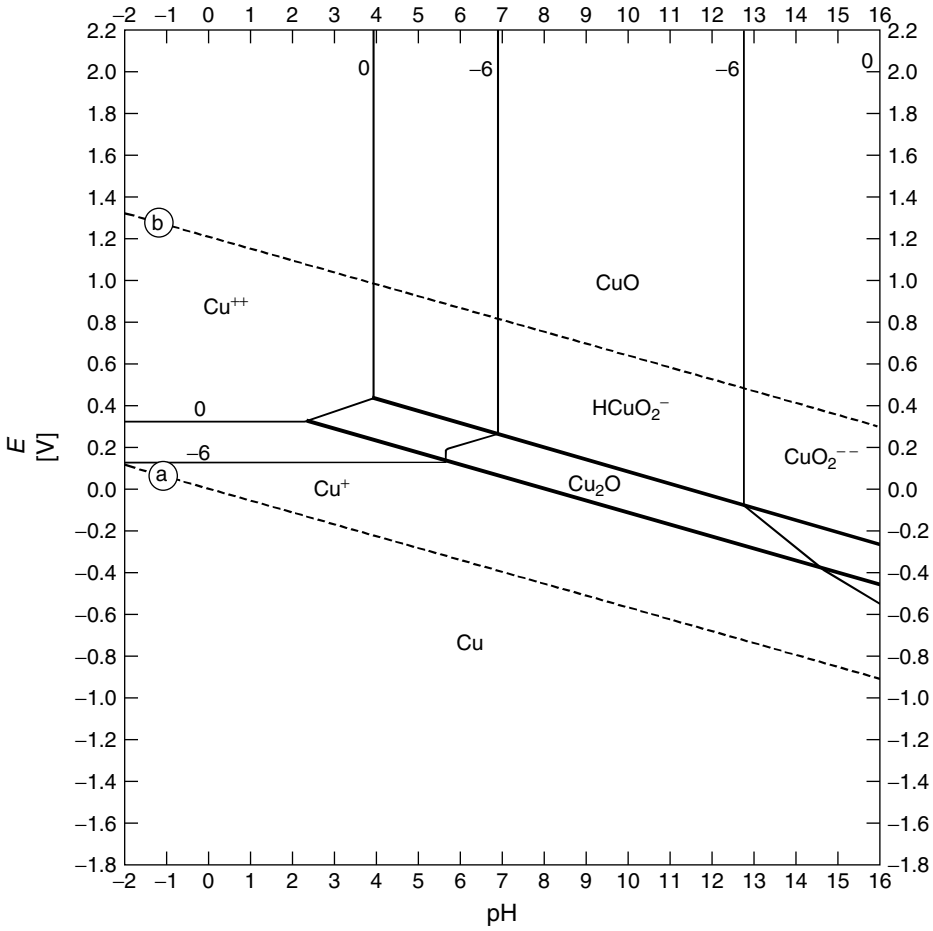


Fig. 34 Potential–pH diagram of copper [11].

in a wide pH and potential range. At high and low pH values, dissolution to Cu^{2+} and $HCuO_2^-$ can take place. Two types of copper oxides can be formed, copper(I)oxide, Cu_2O and copper (II)oxide, CuO. In case of atmospheric corrosion, the formation of carbonates and sulfates has to be considered.

2.1.2.7.2 **Corrosion of Copper in Acids**
The homogenous corrosion rate of copper in nonoxidizing deaerated acids is small, therefore copper could be used in, for example, CH_3COOH, H_2SO_4, and HCl. The oxygen content of the acid has a large influence on the corrosivity of the medium. With increasing oxygen content, the corrosion rate increases. This behavior is demonstrated in Fig. 35.

The dissolution of copper is described by the following reaction:

$$Cu \longrightarrow Cu^+ + e^- \qquad (56)$$

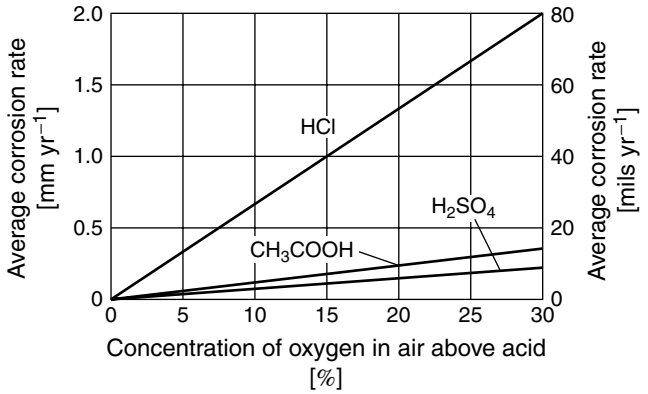


Fig. 35 Effect of oxygen on corrosion rates of copper in 1.2 N solutions of nonoxidizing acids. Specimens are immersed for 24 h at 24 °C. Oxygen content of the solutions varied from test to test, depending on the concentration of oxygen in the atmosphere above the solution [40].

Cu^+ is further oxidized:

$$Cu^+ \longrightarrow Cu^{2+} + e^- \qquad (57)$$

Dissolution of copper to Cu^{2+} ions takes place over Cu^+ intermediates. If oxygen is present, nonelectrochemical oxidation of Cu^+ to Cu^{2+} is possible.

$$2Cu^+ + O_2 + H^+ \longrightarrow 2Cu^{2+} + H_2O \qquad (58)$$

This means that reaction of Cu to Cu^+ becomes the rate-determining step. As this is faster than

$$Cu^+ \longrightarrow Cu^{2+} + e^- \qquad (59)$$

the corrosion rate increases [2]. This reaction mechanism explains the varying corrosion behavior, depending on the oxygen concentration.

Silicon increases the corrosion resistance of copper in sulfuric acid. Silicon bronze (C65500, Si ~3%) could be successfully used in H_2SO_4 in a wide range of concentrations, which is demonstrated in Fig. 36.

The addition of oxidizing salts of iron or copper to the sulfuric acid increases the corrosion rate significantly [40], see Fig. 37.

It has been found that copper–aluminum–iron alloys and copper–nickel alloys show quite good corrosion behavior in H_3PO_4.

In aerated hydrochloric acid, copper is heavily attacked, especially at higher temperatures and concentrations, which is demonstrated in Fig. 38.

Copper alloys, especially alloy C71500 (copper 70%, nickel 30%), could be used for applications in hydrofluoric acid, because the corrosion rate at 16–27 °C is low (180 μm yr^{-1}) [40].

Oxidizing acids, like HNO_3, do attack copper severely.

2.1.2.7.3 **Corrosion of Copper in Neutral and Alkaline Solutions** Copper and its alloys are widely used in water transportation systems. The corrosion rate is mainly determined by the formation of oxide layers at the surface [41]. First, copper dissolves to Cu^+ ions:

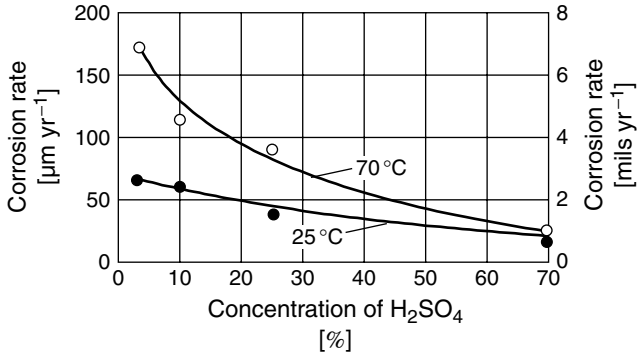


Fig. 36 Corrosion of C65500 in H_2SO_4 solutions. Specimens were immersed for 48 h at the indicated temperatures. The solution was not agitated or intentionally aerated [40].

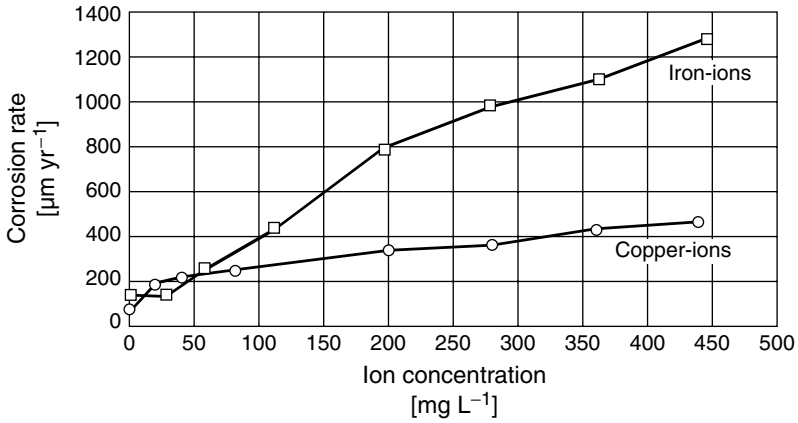


Fig. 37 Corrosion of copper in boiling 30% H_2SO_4, containing copper and iron salts [40].

$$Cu \longrightarrow Cu^+ + e^- \qquad (60)$$

The formation of the red brown cuprite, Cu_2O, results from the reaction with water.

$$2Cu^+ + H_2O \longrightarrow Cu_2O + 2H^+ \qquad (61)$$

Cuprite can be further oxidized to Cu (II), which can precipitate as tenorite, CuO, with a black color.

$$\tfrac{1}{2}Cu_2O + \tfrac{1}{2}H_2O \longrightarrow CuO + OH^- + e^- \qquad (62)$$

$$Cu^{2+} + H_2O \longrightarrow CuO + 2H^+ \qquad (63)$$

In drinking water with dissolved carbonic acid, the formation of malachite $CuCO_3 \cdot Cu(OH)_2$ with a blue to green color is often observed [41].

The corrosion rate of copper in water is very low. In drinking water systems, the copper release to the water has to be controlled for hygienic and health reasons. The use of copper in drinking water systems is specified in DIN 50930,

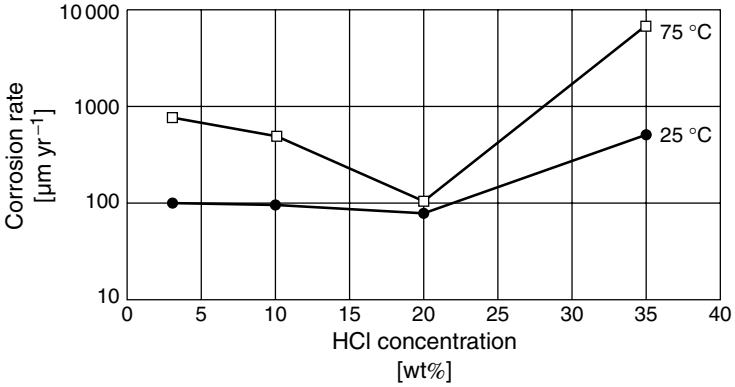


Fig. 38 Corrosion of C65800 totally submerged in HCl, nonaerated, 48 h test duration [40].

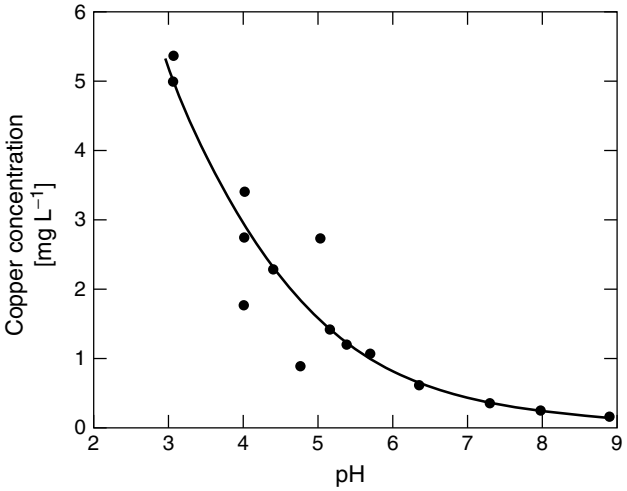


Fig. 39 Effect of pH on the release of copper into solution [41].

wherein the water parameters are defined. In Fig. 39, the copper release in a system, in which the water consumption of households was simulated, is shown.

Copper dissolution is mainly determined by the anions in the water, for example, SO_4^{2-}, Cl^-, HCO_3^-, and PO_3^{2-}. Sulfates strongly catalyze the corrosion of copper, especially pitting corrosion, chlorides are much less aggressive. Bicarbonates seem to increase copper solubility and copper release in stagnant water. Phosphates inhibit the solubility of copper.

In salt solutions, as long as they are nearly neutral, the corrosion rate of copper is normally low [42]. The corrosion rate

increases in NaCN solutions, because of the formation of soluble copper–cyanide complexes. Salts that hydrolyze in water and produce an acidic pH, attack copper and copper alloys.

Copper and its alloys are resistant to alkali solutions at room temperature, except those containing NH_4OH or compounds that hydrolyze to NH_4OH, or cyanides. Both anions NH_4^+ and CN^- form complexes with high solubility. Increasing the temperature increases the corrosion rate. In anhydrous NH_3, the corrosion rates are low, at room temperature $\sim$2.5 μm yr^{-1}. Brass is susceptible to stress corrosion cracking in solutions containing ammonia ions [42].

2.1.2.8 Titanium

2.1.2.8.1 Potential–pH Diagram of Titanium The potential–pH diagram of titanium is shown in Fig. 40. Titanium is not a noble metal. The thermodynamic stability of titanium is much below the stability line

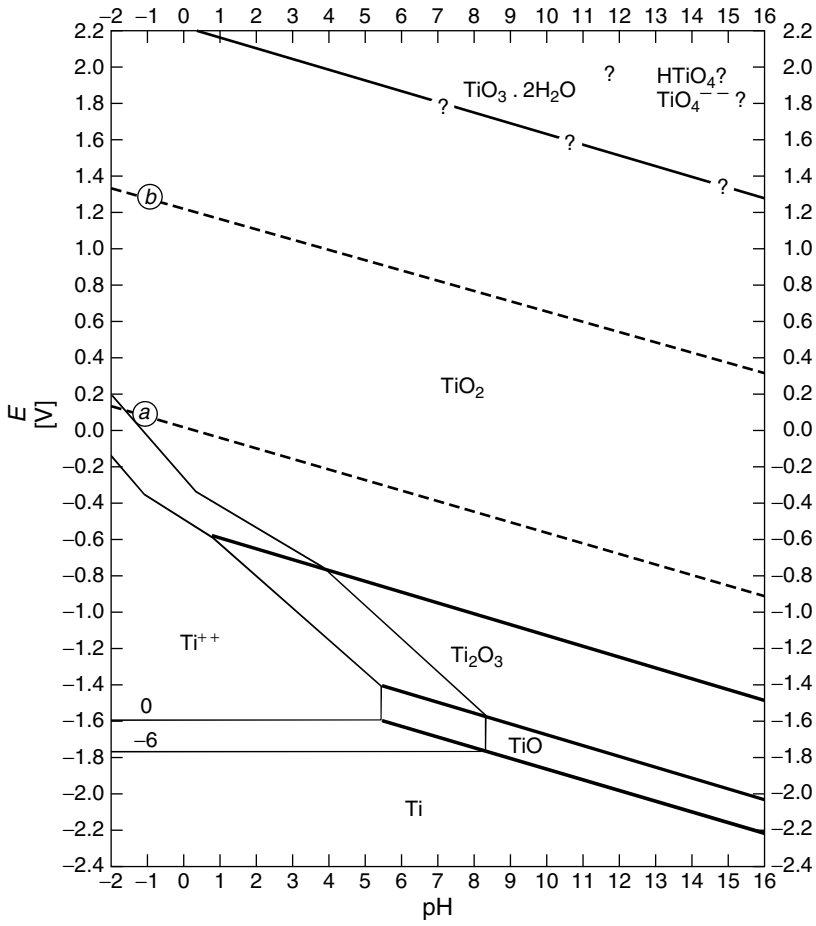


Fig. 40 Potential–pH diagram of titanium.

of water (a). But, because of the formation of oxides and hydroxides (not shown in this diagram) especially TiO_2, titanium is resistant in a wide pH and potential region. Only in acidic solutions can Ti^{2+} and Ti^{3+} ions be formed. The complexing acid HF is especially effective at corroding titanium.

2.1.2.8.2 **Corrosion of Titanium in Acids**

Titanium shows an excellent corrosion resistance in acids, due to the formation of the protective TiO_2 passive layers. The presence of oxygen or water is necessary, for the formation of TiO_2 oxide layer, even small amounts of water and oxygen are sufficient. TiO_2 is an *n*-type semiconductor, which can heal itself if it is damaged. In the absence of a source of oxygen, titanium will corrode because no oxide film will be established.

The addition of Pd has a particularly beneficial effect on the corrosion resistance. The addition of Pd reduces the overpotential of H_2 formation and therefore passivation of the alloy is facilitated [2]. The addition of molybdenum and vanadium increases the corrosion resistance of titanium in acids. The good corrosion resistance of titanium in acids results from the high stability of the oxide film, which is attacked only by hot concentrated HCl, H_2SO_4, and HF.

In oxidizing media and acids, titanium alloys are, in general, corrosion resistant, for example, in chromic, nitric, perchloric, and hypochlorus acids and their salts.

In nitric acid, titanium is corrosion resistant over the entire concentration range, as long as the temperature is below 80 °C. At higher temperatures, corrosion becomes significant. In boiling HNO_3 in the middle concentration range, the highest corrosion rates could be found, which is shown in Fig. 41. The addition of certain metal ions, for example, Si^{4+}, Cr^{6+}, Fe^{3+}, and Ti^{4+} to boiling nitric acid reduces the corrosion rate very effectively,

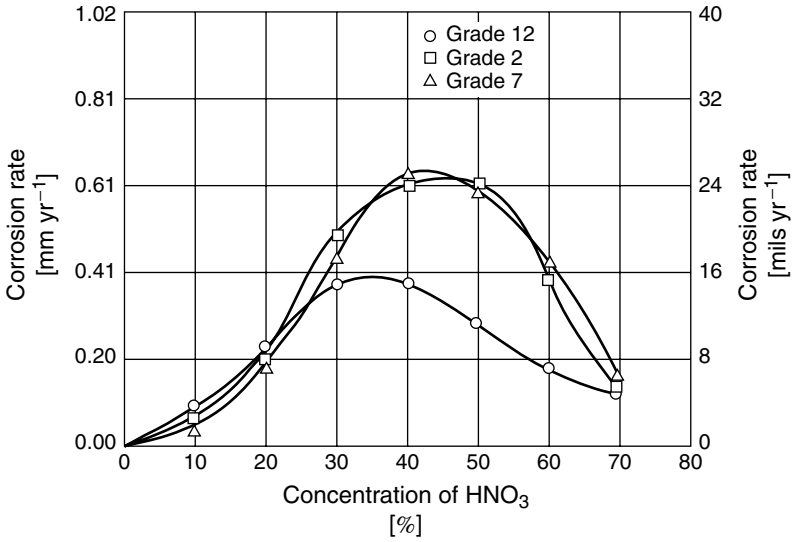


Fig. 41 Corrosion of titanium alloys in boiling, uninhibited HNO_3 solutions. Acid solutions were refreshed every 24 h [43].

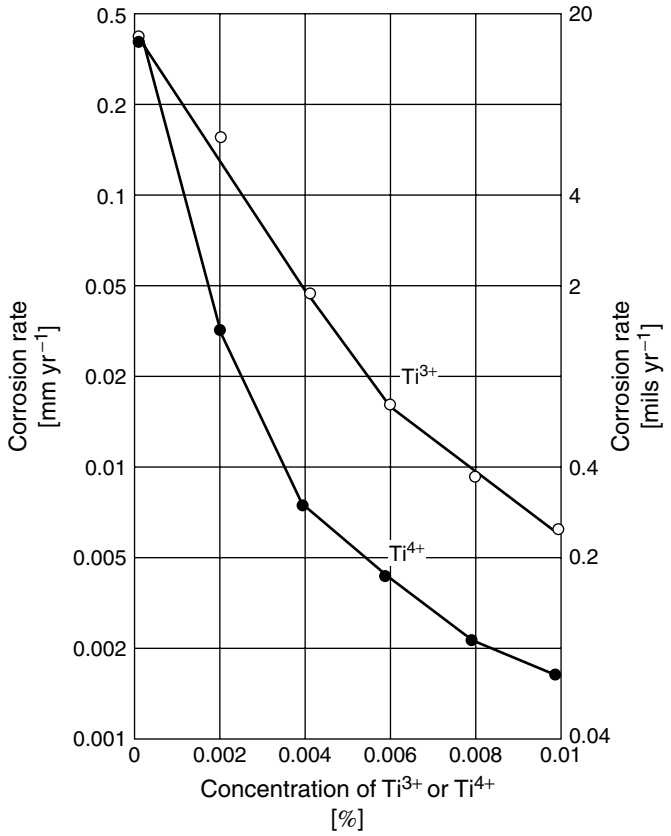


Fig. 42 Inhibitive effect of dissolved Ti^{3+} and Ti^{4+} ions on the corrosion of titanium after 65 h in boiling 6 N HNO_3 solutions [43].

as depicted in Fig. 42. Titanium alloys, which form α- β- or β-phases, show reduced corrosion resistance in nitric acid [40].

Solutions of hydrofluoric acid lead to high corrosion rates over the entire concentration and temperature ranges, because fluoride ions form stable and soluble complexes with titanium.

Sulfurous acid, aqueous hydrogen sulfide solutions, boric, and/or carbonic acid do not attack titanium even if the temperature is above the boiling point.

Titanium alloys are normally very resistant to aerated organic acids. In nonaerated strong acids at high concentrations and temperatures, the corrosion rate is significant. In most cases, alloyed titanium (grades 7 and 12) shows a better corrosion resistance than unalloyed titanium [42].

2.1.2.8.3 **Corrosion of Titanium in Neutral and Alkaline Solutions** In water, steam, and seawater, titanium is resistant even at high temperatures [44]. In water with high chloride levels, crevice corrosion could appear if tight crevices are present. Titanium shows very low corrosion rates even in seawater [43].

In peroxide solutions, corrosion of titanium occurs. The protective oxide film can be destroyed, depending on concentration, temperature, and pH.

Under alkaline conditions, soluble titanium peroxyl complexes can be formed; which increase the corrosion rate [45, 46]. In high concentrated H_2O_2, significant corrosive attack can occur.

Titanium alloys are resistant to alkaline media [43]. In most cases, the corrosion rate is low even in boiling solutions, except in boiling potassium hydroxide. In concentrated NaOH and KOH solutions, the corrosion rate increases at temperatures above the boiling point.

Hot, concentrated NaOH attacks the oxide film. At temperatures of 80 °C NaOH (pH > 12) hydrogen embrittlement can occur. Brittle TiH precipitations are formed in the alloy.

Titanium is resistant to most organic liquids, for example, alcohols, ketones, ethers, aldehydes, and hydrocarbons. Normally, these liquids contain traces of water, which are sufficient for the formation and rehealing of the passive layer. In anhydrous liquids, passive film formation is hindered, and this leads to stress corrosion cracking in methanol.

In chlorinated hydrocarbons, hydrolysis is possible, whereby HCl could be formed. The corrosion rate will then depend on the specific conditions such as temperature and HCl concentration.

References

1. C. Wagner, W. Traud, *Z. Elektrochem.* **1938**, *44*, 391.
2. H. Kaesche, *Die Korrosion der Metalle*, Springer-Verlag, Berlin, Germany, 1990.
3. International Standard, ISO 8407, 1989.
4. C. H. Hamann, W. Vielstich, *Elektrochemie*, 3. Aufl., Wiley-VCH, Weinheim, Germany, 1997.
5. E. Heitz in *Advances in Corrosion Science and Technology* (Eds.: M. G. Fontana, R. W. Staehle), Plenum Press, New York, 1974, Vol. 4, pp. 149–243.
6. E. Heitz, M. Kukovic, K. H. Maier, *Werkst. Korros.* **1970**, *21*, 457–462.
7. E. Heitz, *Werkst. Korros.* **1979**, *21*, 360–367.
8. K. E. Heusler, *Z. Elektrochem.* **1962**, *66*, 177–184.
9. W. J. Lorenz, *Corros. Sci.* **1965**, *5*, 121–131.
10. A. Bukowiecki, *Werkst. Korros.* **1959**, *10*, 91–105.
11. M. Pourbaix, *Atlas of Electrochemical Equilibria in Aqueous Solutions*, Pergamon Press, Oxford, 1966.
12. K. E. Heusler, Iron in *Encyclopedia of Electrochemistry of the Elements* (Ed.: A. J. Bard), Part A, Marcel Dekker, New York, Basel, 1982, Vol. IX, pp. 229–387.
13. W. J. Lorenz, K. E. Heusler, Anodic dissolution of iron group elements in *Corrosion Mechanisms* (Ed.: F. Mansfeld), Marcel Dekker, New York, Basel, 1987.
14. J. O'M. Bockris, D. Drazic, A. R. Despic, *Electrochim. Acta* **1961**, *4*, 325.
15. Dechema Werkstofftabelle "Schwefelsäure", Burkholt, H., Dechema Frankfurt (1971).
16. I. Albrecht, H.-E. Bühler, S. Baumgartl, *Arch. Eisenhüttenwesen* **1974**, *45*, 561.
17. A. Rahmel, W. Schwenk, Korrosion und Korrosionsschutz von Stählen, Verlag Chemie, Weinheim, 1977, p. 91.
18. Dechema Werkstofftabelle "Natriumsulfat", J. Küpper-Feser, Dechema Frankfurt (1997).
19. Dechema Werkstofftabelle, "Natriumchlorid", E. Rabald, H. Bretschneider, Dechema Frankfurt (1962).
20. M. Stratmann, J. Müller, *Corros. Sci.* **1994**, *36*, 327.
21. M. Pourbaix, *Atlas of Electrochemical Equilibria in Aqueous Solutions*, Pergamon Press, Oxford, 1966, p. 310.
22. J.-Y. Zou, D.-T. Chin, *J. Electrochem. Acta* **1987**, *32*(12), 1751–1756.
23. E. Wendler-Kalsch, *Korrosionskunde*, Springer-Verlag, Berlin, Germany, 1998.
24. U. Heubner, Nickelwerkstoffe und hochlegierte Sonderedelstähle, Expert Verlag, Ehningen, 1993, p. 24.
25. W. Betteridge, *Nickel and its Alloys*, MacDonald and Evans, Estover, Plymouth, 1977.
26. O. Kubaschewski, *Iron – Binary Phase Diagrams*, Springer-Verlag, Berlin, Germany, 1982.

27. Dechema Werkstofftabelle, "Phosphorsäure", L. Hasenberg, Dechema Frankfurt (1992).
28. W. Schwenk, G. W. F. Wasser, *Abwasser* **1992**, *133*(6), 281–286.
29. U. Brill, Korrosion von Nickel, Cobalt und Nickel- und Cobalt-Basislegierungen, Krupp VDM GmbH, Werdohl, 1992.
30. W. Z. Friend, *Corrosion of Nickel and Nickel-Base Alloys*, John Wiley & Sons, New York, 1980, pp. 32–94.
31. U. Heubner, Nickelwerkstoffe und hochlegierte Sonderedelstähle, Expert Verlag, Ehningen, 1993, p. 42.
32. E.-M. Horn, *Werkst. Korros.* **1996**, *47*, 323–332.
33. H. Kaesche, *Z. Phys. Chem. N. F.* **1962**, *34*, 87.
34. H. Kaesche, *Werkst. Korros.* **1963**, *14*, 557.
35. G. L. Makar, J. Kruger, *Int. Mater. Rev.* **1993**, *38*(3), 138–153.
36. Y. Wang, T. J. O'Kneefe, W. J. James, *J. Electrochem. Soc.* **1980**, *127*, 2589–2593.
37. L. Gaiser, K. E. Heusler, *Electrochim. Acta* **1970**, *15*, 161.
38. X. G. Zhang, *Corrosion and Electrochemistry of Zinc*, Plenum Press, New York, 1996.
39. L. P. Devillers, P. Niessen, *Corros. Sci* **1976**, *16*, 243–252.
40. ASM Handbook, Corrosion, ASM International USA, 1992, p. 628, Vol. 13.
41. J. F. Gerguson, Ov. Franqué, *Internal Corrosion of Water Distribution Systems*, American Water Works Associations, Denver, Colo., 1996, pp. 231–268.
42. *ASM Handbook, Corrosion*, ASM International, USA, 1992, p. 630, Vol. 13.
43. *ASM Handbook, Corrosion*, ASM International, USA, 1992, p. 669, Vol. 13.
44. P. C. Hughes, I. R. Lamborn, *J. Inst. Met.* **1960–1961**, *89*, 165.
45. T. M. Sigulovskaya et al., UDC 620.193.01, *Zashch. Met.* **1976**, *12*(4), 363–367.
46. L. Clerbois, L. Plumet, U.S. Patent 4,372,813, 1983.

2.2 Hydrogen Ingress during Corrosion

Bruce Pound
Exponent, Menlo Park, California

2.2.1 Introduction

The behavior of hydrogen in metals has attracted considerable interest in various areas, particularly corrosion. Hydrogen has long been known to have an adverse effect on the mechanical properties of steels and other alloys. Concern about its effect has prompted numerous studies of hydrogen in metals and alloys aimed at understanding the processes that lead to hydrogen degradation. A range of processes are involved: interfacial charge transfer, adsorption, absorption, transport, trapping, and finally degradation itself. These processes are discussed in this chapter, primarily from the viewpoint of aqueous corrosion.

2.2.2 Hydrogen Evolution

2.2.2.1 General Mechanisms

Hydrogen can be evolved during the corrosion of metals in aqueous solutions. The hydrogen evolution reaction (HER) involves the cathodic reduction of hydrogen ions in acid solutions (Reaction 1) or of water in alkaline or neutral solutions (Reaction 2):

$$2H_3O^+ + 2e^- \longrightarrow H_2 + 2H_2O \quad (1)$$

$$2H_2O + 2e^- \longrightarrow H_2 + 2OH^- \quad (2)$$

Reaction (1) as well as Reaction (2) can occur in natural environments, because a corroding metal can develop quite acidic solutions within actively growing cracks and pits (typically with a pH of 1–3.5 [1, 2]), even when the bulk solution has a high pH.

Two basic mechanisms have been identified for the HER, each one consisting of two steps. The first step in both cases is the discharge of H^+ (or more strictly, H_3O^+) or H_2O to form an adsorbed hydrogen atom (H_{ads}) on the metal surface [3, 4]. In an acidic solution, for example,

$$H_3O^+ + e^- \longrightarrow H_{ads} + H_2O \quad (3)$$

The subsequent desorption step depends on the metal and the cathodic current density. It can occur by either chemical desorption, which is also referred to as recombination,

$$H_{ads} + H_{ads} \longrightarrow H_2 \quad (4)$$

or electrochemical desorption

$$H_{ads} + H_3O^+ + e^- \longrightarrow H_2 + H_2O \quad (5)$$

More discussions of the HER are provided in an earlier chapter.

2.2.2.2 Reaction Kinetics

The kinetics of the HER (Reactions 1 and 2) in different environments are generally characterized in terms of the exchange current density (i_o) and other parameters such as the transfer coefficient. The values of i_o for the HER can differ by orders of magnitude between metals. Table 1 lists values for various metals in sulfuric acid [5]. The noble metals such as palladium and platinum exhibit high values, whereas metals such as cadmium, lead, and mercury are distinguished by very low values.

Theoretical values of the transfer coefficient have been determined from current–potential relationships for the two HER mechanisms (Reactions 3–5) [6]. The form of the relationship depends on

Tab. 1 Exchange current densities for hydrogen evolution in ~1 M H_2SO_4

Metal	i_o *(A cm^{-2})*
Pd	1×10^{-3}
Pt	7.9×10^{-4}
Rh	2.5×10^{-4}
Ir	2.0×10^{-4}
Ni	6.3×10^{-6}
Au	4.0×10^{-6}
W	1.3×10^{-6}
Nb	1.6×10^{-7}
Ti	6.3×10^{-9}
Cd	1.6×10^{-11}
Mn	1.3×10^{-11}
Tl	1.0×10^{-11}
Pb	1.0×10^{-12}
Hg	5×10^{-13}

the mechanism, the rate-determining step, and the adsorption isotherm assumed for H_{ads}. The coverage of adsorbed hydrogen has been considered in terms of Langmuir adsorption and Temkin adsorption. The Langmuir isotherm is applicable to non-interacting species and can be assumed for low coverages of H_{ads}. It predicts that the coverage will increase as the potential becomes more negative. The Temkin isotherm should be used when the coverage of hydrogen is high enough that the interaction between the adsorbed atoms becomes appreciable.

The rate of Reaction (3) is given in terms of the current density (i) by

$$i = 2F\left[k_1 a_{H_3O^+}(1-\theta)e^{-\beta\eta F/RT} - k_{-1}\theta e^{(1-\beta)\eta F/RT}\right] \quad (6)$$

where $a_{H_3O^+}$ is the activity of hydrogen ions, θ is the coverage, β is the symmetry factor, η is the overpotential, F is the Faraday constant, R is the gas constant, T is the absolute temperature, and k_1 and k_{-1} are the rate constants for the forward and reverse reactions, respectively. In the case of a mechanism involving, for example, slow discharge followed by fast recombination, the reverse reaction is assumed to be negligible and Reaction (4) is assumed to be in equilibrium. For this mechanism with Langmuir adsorption, the rate can be expressed in two forms, depending on whether the surface coverage is assumed to approach 0 or 1:

$$i = 2Fk_1 a_{H_3O^+} e^{-\beta\eta F/RT} \quad (\theta \longrightarrow 0) \quad (7)$$

$$i = 2Fk_1 a_{H_3O^+} k' \frac{k_2^{1/2}}{k_{-2}^{1/2} p_{H_2}^{1/2}} e^{-\beta\eta F/RT} \quad (\theta \longrightarrow 1) \quad (8)$$

where k_2 and k_{-2} are the forward and reverse rate constants for recombination, k' is a constant associated with the coverage, and p_{H_2} is the partial pressure of hydrogen. In both cases, the transfer coefficient is equal to the symmetry factor, which is generally taken as 0.5. Table 2 shows the transfer coefficients obtained for the HER mechanisms under conditions of Langmuir adsorption and Temkin adsorption.

Comparison of theoretical values of the transfer coefficients with measured values may allow the HER mechanism to be identified. The dependence of coverage on the overpotential can also be useful for this purpose. Table 3 shows the values of $\partial \ln\theta/\partial\eta$ for several mechanisms, in which the coverage was assumed to be much less than one [5].

The probable mechanism for hydrogen evolution has been determined for relatively few metals and, even then, mainly in acid solutions (Table 4) [5]. For metals such as mercury with low exchange current densities, proton discharge is the

Tab. 2 Transfer coefficients for HER mechanisms[a]

Mechanism	*Langmuir*	*Temkin*	
		Nonactivated	*Activated*
Slow discharge–fast chemical	0.5	0.5	0.5
Slow discharge–fast electrochemical	0.5	1.0	1.0
Fast discharge–slow chemical	2.0	2.0	1.0
Fast discharge–slow electrochemical	1.5	1.5	1.0
Coupled discharge–chemical	0.5	0.4	0.3
Coupled discharge–electrochemical	0.5	0.5	0.5

[a]The symmetry factor (β) is assumed to have a value of 0.5.

Tab. 3 Dependence of hydrogen coverage on overpotential for HER mechanisms[a]

Mechanism	$\partial \ln \theta / \partial \eta$
Slow discharge–fast chemical	$-F/4RT$
Fast discharge–slow chemical	$-F/RT$
Slow discharge–fast electrochemical	0
Fast discharge–slow electrochemical	$-F/RT$

[a]The coverage is assumed to be $\ll 1$.

Tab. 4 Probable mechanisms for the HER on various metals in acid solutions

Mechanism	*Metals*
Slow discharge–fast electrochemical	Hg, Pb, Cd
Fast discharge–slow electrochemical	Ni, W, Au
Fast discharge–slow chemical	Pt, Rh

rate-determining step and is followed by electrochemical desorption. The rate-determining step switches to electrochemical desorption for metals such as nickel that exhibit higher exchange current densities. For metals such as platinum and rhodium with even higher exchange current densities, the desorption step is still rate determining but occurs by chemical recombination. In the case of iron, hydrogen evolution proceeds by a coupled discharge-chemical desorption mechanism in sulfuric acid [7]. The type of desorption on iron depends strongly on the solution composition and cathodic current density, such that electrochemical desorption can predominate in alkaline solutions [8].

When surface films are present on the metal, the discharge kinetics are likely to be quite different from those for the bare metal. If protons are involved in the hydrogen evolution mechanism, they may in principle be reduced either at the film–electrolyte interface or the metal–film interface, depending on the discharge kinetics and whether the film is electronically conducting [9]. In general, hydrogen reduction at the electrolyte interface will be favored for oxides that are electronically conducting or have a low solubility for hydrogen.

2.2.3 Hydrogen Absorption

2.2.3.1 Mechanisms

The cathodic reduction of H_3O^+ or H_2O on a metal surface can lead to

the absorption of atomic hydrogen by the metal. Two mechanisms have been proposed for hydrogen absorption. In the first mechanism, the adsorbed hydrogen atom, instead of desorbing from the metal surface, enters the metal [7]:

$$H_{ads} \longrightarrow H_{abs} \qquad (9)$$

The absorbed hydrogen atom, H_{abs}, occupies interstitial sites within the lattice of transition metals and loses its electron to the electronic bands of the metal, thus existing as a screened proton [10]. In the adsorption–absorption mechanism, hydrogen entering the metal goes through the same adsorbed intermediate as that leading to hydrogen evolution. An alternative mechanism involves entry of hydrogen in the same step as that in which it is discharged [11]:

$$H_3O^+ + e^- \longrightarrow H_{abs} + H_2O \qquad (10)$$

In this case, the intermediate states for hydrogen entry and hydrogen evolution are different. In other words, hydrogen evolution and hydrogen absorption are treated as independent of each other. This mechanism has not been demonstrated experimentally, and it is generally accepted on the basis of permeation data that the adsorbed intermediate, H_{ads}, is involved in hydrogen absorption [6, 12].

The effect of hydrogen entry on the kinetics of the HER have been taken into account in a mechanistic model developed for steady state conditions [13–15]. It was assumed that (1) the only reactions are hydrogen discharge, recombination, and absorption, (2) the reverse discharge reaction (hydrogen oxidation) can be neglected, and (3) the adsorption–absorption step is in local equilibrium. Data from hydrogen permeation experiments (see Sect. 2.2.5.1) can be analyzed using this model to calculate the transfer coefficient, exchange current density, and surface coverage as well as the rate constants for hydrogen discharge, recombination, adsorption, and absorption.

Another approach, which has been applied to iron and steel, is to obtain the steady state coverage by means of a galvanostatic pulse technique (see Sect. 2.2.5.2.2) and then to use this value in conjunction with permeation measurements to determine the rate constant for hydrogen entry [16]. In the case of iron, the coverage ranged from 0.05 to 0.12 in alkaline solutions [16] and from 0.01 to 0.1 in acidic solutions [17] for overpotentials from −0.3 to −0.4 V.

2.2.3.2 Promoters of Hydrogen Entry

The entry of hydrogen into metals is promoted by various compounds, especially those involving elements from Groups VB (P, As, and Sb) and VIB (S, Se, and Te) of the periodic table. Some anions such as CN^-, CNS^-, and I^- and certain carbon compounds such as CS_2, CO, and CSN_2H_4 also promote hydrogen entry. The effectiveness of promoters can differ considerably, even within specific groups. However, the order of effectiveness varies between different studies [18]. The experimental evidence indicates that the hydride of the promoter is the species that primarily affects hydrogen entry and that the amount of hydrogen adsorbed is related to the bond strength of the hydride [18, 19].

The effect of promoters has been attributed to poisoning of the hydrogen atom recombination, which is thought to increase the coverage of H_{ads} [20] or to decrease the $M–H_{ads}$ bond energy [18]. Because the volatile hydrides of elements from Groups VB and VIB are strongly chemisorbed by clean metal surfaces, their action has also been linked to dissociative

chemisorption of their molecules [12, 21]. Poisoning of the recombination step by H_2S in acidic solutions has been demonstrated by a sharp decrease in the recombination rate constant with small additions of H_2S [15]. This decrease is accompanied by an increase in the hydrogen coverage at a given overpotential. The results for H_2S in acidic solutions have been explained on the basis of a mechanism in which H_2S provides a bridge for hydrogen discharge, resulting in the formation of an intermediate ($H...H_2S$) that acts as the poisoning species [15, 22].

The effect of chemisorbed sulfur on the HER has been studied using a sulfur radiotracer method in combination with polarization measurements [23]. In the case of single-crystal (110) platinum in acid, the chemisorbed sulfur causes a large decrease in the HER rate, apparently due to a blocking effect of sulfur on the sites of adsorption of the weakly bonded hydrogen. The HER, however, is not completely poisoned by sulfur, even at the sulfur-saturation coverage ($\theta = 0.8$).

Both the potential and the pH at the electrolyte–cathode interface are key factors in promoting hydrogen entry. A marked increase in hydrogen entry occurs when the hydrides of reducible compounds of P, As, Sb, S, Se, or Te are produced at sufficiently negative potentials. An increase is also obtained by the addition of phosphine, hydrogen sulfide, or arsine directly to the solution. The promoters from Groups VB and VIB are effective only in the range of pH in which the molecular hydrides are stable. A feature of the Group VB elements is that their hydrides are relatively stable in acidic and alkaline solutions and can therefore function in both solutions. The molecular form of the Group VIB hydrides, in contrast, is favored only in acidic solutions, so the capacity of these hydrides to act as promoters is limited to these solutions.

The effect of a promoter varies with its concentration. Figure 1 shows the rate of hydrogen permeation through a steel membrane under cathodic polarization in the presence of Group VB and VIB elements [12]. In most cases, the promoters achieve their maximum effect at relatively low concentrations. Because of hydrolysis and other secondary reactions, higher concentrations often lead to the deposition of insoluble products that can inhibit hydrogen entry.

2.2.3.3 Inhibitors of Hydrogen Entry

The entry of hydrogen into metals can be impeded by some species, particularly polar organic compounds containing nitrogen, sulfur, or oxygen. One of the most effective inhibitors of hydrogen entry is dibenzyl sulfoxide [24]. Several sulfoxides, hydroxlamine acids, and silanes have been found to inhibit hydrogen absorption by steel in dilute sulfuric acid during corrosion or cathodic polarization [25]. Hydrogen entry into steel is also inhibited by various nitrile and triazole compounds.

Corrosion inhibitors have been used to decrease hydrogen absorption [26–28]. Diamines with long carbon chains are particularly effective in reducing the corrosion rate and hydrogen absorption in hydrogen sulfide environments [29]. Some compounds inhibit metal dissolution but increase the proportion of hydrogen entering the metal. This problem is caused by decomposition of the corrosion inhibitor to form a promoting hydride. An example of such an inhibitor is thiourea, which is thought to react with adsorbed hydrogen to release hydrogen sulfide [30]. Higher thiourea derivatives and many other sulfur-containing organic

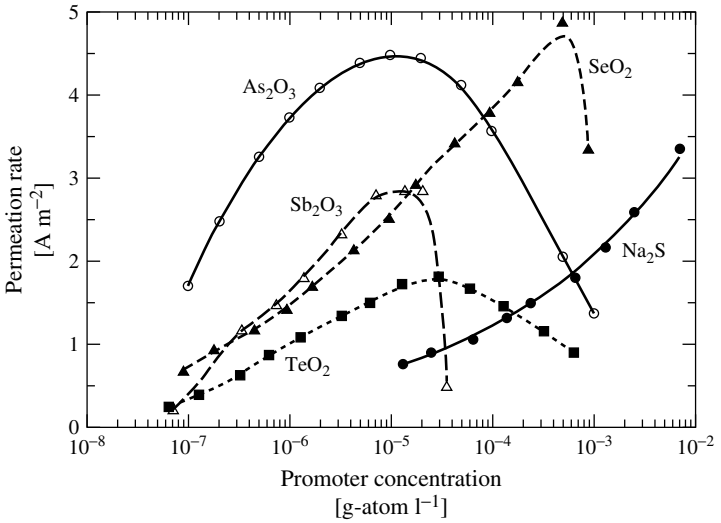


Fig. 1 Effect of promoter concentration on hydrogen permeation through steel cathodically charged at 22.5 A m^{-2} in a Na_2SO_4/H_2SO_4 solution (pH 2.6) [12]. (Reprinted with permission of William Andrew Publishing/Noyes Publications.)

compounds such as the sulfoxides inhibit hydrogen entry as well as corrosion. However, the inhibition of metal dissolution does not correlate directly with inhibition of hydrogen absorption.

Hydrogen absorption can also be reduced by the deposition of certain metals. In cases such as tin and cadmium, the metal layer acts as a barrier to hydrogen ingress because diffusion is very slow through these metals [31]. In other cases such as zinc, lead, and bismuth, hydrogen absorption is decreased by inhibiting the hydrogen discharge reaction or reducing the rate of hydrogen entry such that most of the hydrogen atoms adsorbed on the surface form molecular hydrogen. Monolayers of lead and zinc produced by underpotential deposition have been found to inhibit both the HER and the absorption of hydrogen into steels [32, 33]. Similar effects have been reported for multiple layers of zinc on iron [34] and of bismuth on AISI 4340 steel and alloy 718 [35].

Surface films such as oxides can also inhibit hydrogen absorption by a metal, since hydrogen must first enter the film and then move through it before entering the actual metal. Either of these steps may severely limit the rate of hydrogen absorption. The effect of oxides on hydrogen absorption is discussed further in Sect. 2.2.5.5.

2.2.3.4 Solubility of Hydrogen

The steady state concentration of hydrogen dissolved in the subsurface layer (that is, below the first atomic plane) of a metal can be related to the fugacity (f_{H_2}) of gaseous hydrogen with which the subsurface layer of hydrogen would be in equilibrium [36]. This fugacity is considered to be the effective fugacity of the hydrogen-producing phase. If the adsorbed hydrogen and dissolved hydrogen are assumed to be in equilibrium with gaseous hydrogen, f_{H_2} can be expressed

as a function of coverage through their respective chemical potentials [37]. In the electrochemical situation, the coverage at the reversible potential for the HER (θ_r) is equivalent to the equilibrium coverage at 1 atm of H_2. Accordingly, f_{H_2} can be expressed by

$$f_{H_2} = \frac{\theta}{1-\theta}\frac{1-\theta_r}{\theta_r} \tag{11}$$

The ratio, $\theta/(1-\theta)$, and hence the fugacity of H_2 can be calculated as a function of the potential of the HER. The fugacity depends on the mechanism of the HER. In the case of a fast discharge–slow recombination mechanism, the fugacity is given by

$$f_{H_2} = \exp\left(\frac{-2\eta F}{RT}\right) \tag{12}$$

Because the overpotential is negative for hydrogen evolution, increases in η can markedly increase the effective fugacity and hence the concentration of dissolved hydrogen. Fugacities of the order of 10^6 atm can be achieved with cathodic charging [36]. For some mechanisms (e.g. slow discharge–fast electrochemical desorption), however, f_{H_2} will be less than 1 atm when an overpotential is applied.

Most of the data for the solubility of hydrogen in metals are based on equilibrium with hydrogen gas. At moderate pressures, the lattice concentration of dissolved hydrogen obeys Sievert's law; that is, the hydrogen concentration is proportional to the square root of the pressure. For iron and other low solubility elements, the concentration increases exponentially with temperature. The heat of solution is positive for endothermic absorbers, with a value of 27.2 to 28.6 kJ mol^{-1} in the case of iron [38–40]. For iron, the lattice solubility, C_s, of hydrogen in equilibrium with hydrogen gas can be expressed as [39]

$$C_s = 1.57 \times 10^{20} P^{1/2} \times \exp\left(-\frac{28\,600 \pm 2800 \text{ J mol}^{-1}}{RT}\right) \tag{13}$$

where C_s is in atom H cm^{-3} and P is the pressure of hydrogen gas in atm. The intrinsic lattice solubility for ferritic iron and steels is in fact very small, and the total hydrogen concentration at ambient temperature greatly exceeds the lattice concentration. Nearly all of the dissolved hydrogen results from attractive interactions with microstructural features in the iron and steel.

The solubility of hydrogen in iron alloys varies with composition (see also Sects. 2.2.4.2 and 2.2.4.3). Electrochemical data for Fe-Cr alloys containing up to 30 at% Cr show that the solubility increases sharply with chromium content up to about 10 at% but then exhibits relatively little change (Fig. 2) [41]. Data for Fe-Ni alloys at 70 °C show similar behavior, with little change occurring after 40 wt% Ni [42].

The partial molal volume (V_H) of dissolved hydrogen is about 0.30 nm^3 $atom^{-1}$ for all metals in which it has been measured [43]. A number of measurements have been made on α-iron, and the overall results indicate a value of 0.33 nm^3 $atom^{-1}$, or 2.0 cm^3 mol^{-1} [38, 44, 45].

The solubility of hydrogen in the lattice increases with tensile stress but decreases with compressive stress. In the presence of a uniform stress (σ), the chemical potential of dissolved hydrogen is lowered by an amount σV_H. At constant chemical potential, the solubility (C_σ) in the presence of stress is given by [46]

$$C_\sigma = C_{\sigma=0} \exp\left(\frac{-\sigma V_H}{RT}\right) \tag{14}$$

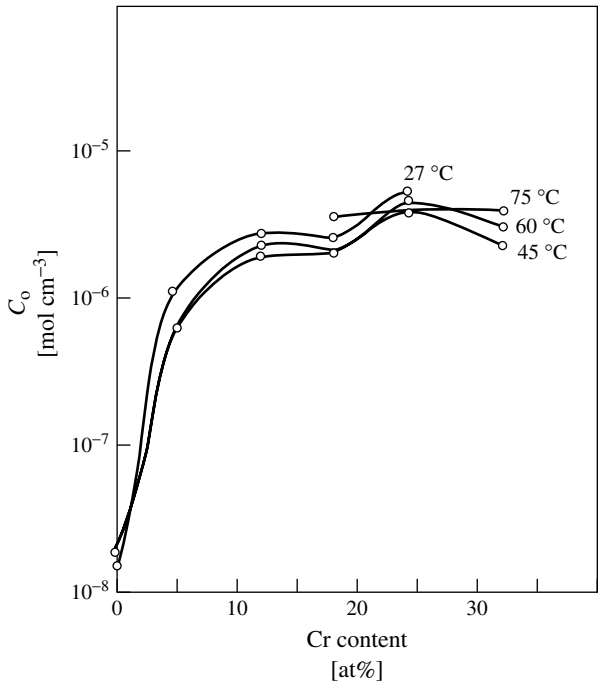


Fig. 2 Dependence of hydrogen solubility on chromium content in Fe-Cr alloys. The solubility was obtained from electrochemical permeation measurements on an Fe-Cr membrane (thickness of 0.13 mm) with a cathodic charging current of 20 mA cm^{-2} [41]. (Reprinted from Electrochim. Acta, Copyright 1970, with permission from Elsevier Science.)

The validity of this equation has been demonstrated experimentally for externally applied uniaxial tensile and compressive stresses [47].

2.2.4 Hydrogen Diffusion

Hydrogen transport in a metal can occur by lattice diffusion, dislocation motion, or short-circuit diffusion along grain boundaries. Hydrogen can diffuse rapidly through the lattice in many metals, particularly those with a body-centered cubic (bcc) structure such as α-iron, ferritic steels, and β-titanium alloys. However, grain boundary diffusion and dislocation transport can also contribute to the movement of hydrogen.

2.2.4.1 Diffusion Kinetics

Hydrogen absorbed in the subsurface layer of a metal subsequently diffuses into the bulk metal and attains a concentration, $C(x,t)$, at a distance x after time t. In the absence of any interaction with microstructural heterogeneities, the lattice diffusion of hydrogen can be represented by the classical form of Fick's second law:

$$\frac{\partial C(x,t)}{\partial t} = D\left(\frac{\partial^2 C(x,t)}{\partial x^2}\right) \qquad (15)$$

The diffusivity (D) of hydrogen in the metal lattice is usually assumed to be

independent of concentration in analyses of hydrogen diffusion, although this assumption is not strictly correct. The diffusivity can exhibit a concentration dependence for several reasons such as hydrogen-induced changes in the lattice constant or electronic density, or trapping of hydrogen on crystal imperfections and formation of immobile dimers and clusters [48]. Blocking of interstitial sites can also cause the diffusivity to become concentration-dependent. At high concentrations, the limited number of empty sites (those not filled with foreign atoms) available for the diffusing hydrogen can lead to a considerable decrease in the diffusivity.

A large quantity of experimental data has been obtained for the diffusivity of hydrogen in various metals, particularly palladium, iron, and nickel [49]. The dependence of diffusivity on temperature generally follows an Arrhenius relationship over a wide temperature range, although marked breaks occur for some metals. Palladium is characterized by remarkably consistent data over a broad range of temperatures. The data for nickel are as consistent as those for palladium at temperatures above 100 °C but show greater scatter at lower temperatures. In contrast, the data for iron show a large amount of scatter, ranging up to four orders of magnitude around ambient temperature. This scatter is attributed to surface effects and hydrogen trapping (see Sect. 2.2.4.2).

Table 5 compares values of the preexponential factor (D_o) and activation energy (E_a) from the dependence of diffusivity on temperature for α-iron [48]. The data were compiled for specimens on which surface effects were reduced by use of a palladium coating on one side. At higher temperatures, the activation energy falls in a narrow range from 6.7 to 7.1 kJ mol^{-1}, but at temperatures of 70 °C and lower, the activation energy varies between 4.2 and 7.1 kJ mol^{-1}. This range is consistent with other values of 6.9 kJ mol^{-1} [38] and 8.0 kJ mol^{-1} [50]. The diffusivity for

Tab. 5 Activation energies and preexponential factors for the diffusion of hydrogen in α-iron

Iron purity	*Technique*	*T range (K)*	E_a *(kJ mol^{-1})*	D_o *(m^2 s^{-1})*
Four pass zone refined Ferrovac E	High vacuum	322–779	7.08	1.6×10^{-7}
Three pass zone refined	High vacuum	300–870	6.7	2.3×10^{-7}
>99.9%	High vacuum	342–619	6.7	1.01×10^{-7}
Zone refined >99.996%	Gas-phase charge, electrochemical	283–333	7.05	1.23×10^{-7}
High-purity >99.99%	Electrochemical	223–323	5.6[a]	7.6×10^{-8}
Single crystals	Electrochemical	230–300	6.7	1.10×10^{-7}
Armco	Electrochemical	283–340	5.57	6.0×10^{-8}
Single crystals >99.9%	Electrochemical	283–343	4.86	6.20×10^{-8}
>99.99%	Electrochemical	223–323	4.2	4.90×10^{-8}

[a] At room temperature. The Arrhenius plot exhibited curvature at lower temperatures.

iron at ambient temperature is 6.0 to 8.3×10^{-9} m^2 s^{-1} [48], which compares with typical values of 1.9 to 4.5×10^{-9} m^2 s^{-1} for palladium [51–53] and 4 to 9×10^{-14} m^2 s^{-1} for nickel [54, 55].

The diffusivity of hydrogen decreases with increasing mass of its isotope. The classical isotope effect reflects the square root of the mass ratio; that is, D_H/D_D would be expected to have a value of 1.41. However, hydrogen and deuterium exhibit nonclassical isotope effects in iron. The isotope effect in iron is a function of temperature, with D_H/D_D decreasing from 1.8 at room temperature to 1.1 to 1.2 at temperatures around 700 °C [39, 48].

The effect of deformation on hydrogen transport has been the subject of numerous studies. The underlying premise was that transport could be enhanced as a result of hydrogen entrainment by mobile dislocations [56, 57]. Experimental support for this premise was provided by studies showing that plastic deformation accelerated the release of tritium from a range of metals [58] and increased the depth of tritium penetration into type 304L stainless steel [59]. Of particular note was the fact that the release rate of tritium for type 304L stainless steel could be correlated with the mobile dislocation density. Some electrochemical permeation studies appeared to provide further evidence of enhanced hydrogen transport by dislocations, but the data were found to have been affected by Joule heating [60, 61]. In contrast to these studies, a subsequent permeation study involving iron, nickel, and an austenitic stainless steel showed no evidence of enhanced transport [62]. Other permeation measurements likewise did not show any indication of dislocation transport in polycrystalline nickel, but they did do so in the case of single-crystal nickel at sufficiently high strain rates [63]. Thus, the overall evidence indicates that dislocation transport does occur but is observable only under certain conditions.

2.2.4.2 Hydrogen Trapping

Hydrogen diffusing through a metal may be delayed or trapped at microstructural features such as dislocations, grain boundaries, and internal interfaces [64, 65]. These traps can be regarded as sites in the metal with potential energy wells that are greater than those associated with normal interstitial sites in the lattice. A trap is characterized in terms of its depth or binding energy, which is the difference between the minimum of the trap energy well and the minimum of the lattice energy well [40, 50, 66]. The strength of a trap can also be represented by the trapping or interaction energy, which is composed of the binding energy, the activation energy for diffusion, and an additional energy to escape from the trap [65, 67, 68]. The additional energy component is usually assumed to be negligible [50, 68].

The hydrogen atoms are partitioned between the traps and normal lattice sites depending on the binding energy of the hydrogen atom to the trapping site, and it is usual to classify traps as reversible or irreversible. A trap is considered reversible if it releases hydrogen at a significant rate. Often, the rate constants for trapping and release by a reversible trap are large enough to permit equilibrium between the trapped and lattice hydrogen. An irreversible trap site is characterized by a sufficiently deep potential energy well that the hydrogen does not have enough thermal energy to overcome the energy barrier.

Traps can also be classified as an attractive type or a physical type [65]. In the case of attractive traps, the forces acting on hydrogen in the metal lattice can be

electronic or be due to stress fields or temperature gradients:

- Attractive electronic forces are associated with solute elements that lie to the left of the metal in the periodic table [69]. Titanium, for example, lies to the left of iron and has been shown to trap hydrogen reversibly in an iron lattice [68].
- Stress fields result in a distortion of the lattice. In a tensile stressed region, hydrogen migrates toward and is trapped by centers of dilation. The stress field around a crack, for example, creates a high triaxial stress that dilates the metal lattice, with the result that hydrogen is attracted towards the crack. Traps associated with stress fields also tend to have a physical character.
- The solubility of hydrogen increases with temperature. As a result, hydrogen is attracted to hotter regions of the metal.

Physical traps are generally associated with discontinuities in the lattice, such as voids, particle–matrix interfaces, and grain boundaries. A hydrogen atom near a purely physical trap is not specifically attracted but, once trapped, has difficulty escaping. Most traps can probably be considered to have both attractive and physical characteristics. An edge dislocation is a good example of a mixed trap with both sets of characteristics; the tensile stress field provides some attractive character, while the core region provides some physical character.

The decreased rate of hydrogen transport caused by trapping results from the finite probability that the hydrogen atoms will jump into trap sites coupled with the longer residence time at a trap site compared with that at a lattice site. Because the traps act as sinks or sources of hydrogen, the classical diffusion equation (Fick's second law) is no longer valid and is generally modified so that the effect of trapping on the diffusion rate can be taken into account.

If the number of trap sites is not fixed, as at a void, the trap is referred to as unsaturable from the viewpoint that the trapped hydrogen concentration can increase without limit as the lattice concentration increases [40]. For many traps such as dislocations and grain boundaries, the number of trap sites is fixed, so the capacity of the trap for hydrogen is finite, and the trap is described as saturable.

The total hydrogen concentration in a metal is the sum of the concentration of hydrogen at normal lattice sites and the concentration of hydrogen at irreversible and reversible trap sites. The concentration of hydrogen at trap sites, at which near saturation occurs at low temperatures, is expressed in terms of Fermi–Dirac statistics [38]. For a single trap site X, the trapping can be represented by $\mathrm{H} + X = \mathrm{H_X}$, with a corresponding equilibrium distribution given by

$$\frac{C_\mathrm{x}}{(1 - C_\mathrm{x})} = \frac{c}{(1 - c)} \exp\left(\frac{H_\mathrm{B}}{kT}\right) \qquad (16)$$

where C_x is the concentration of trapped hydrogen, c is the atom fraction of hydrogen in equilibrium with hydrogen gas, H_B is the binding enthalpy for the trap, and k is Boltzmann's constant. For iron, c is small, so the $(1 - c)$ term can be neglected.

The occurrence of trapping is well established for iron and steels [65, 70], but there is a considerable amount of evidence that it also occurs in other metals and alloys [54, 66, 71–73]. Table 6 shows reversible and irreversible hydrogen traps in steels [64, 65, 67, 74]. The boundary between reversible

Tab. 6 Classification of hydrogen traps in steels

Type	*Trap*	E_T *(kJ mol^{-1})*[a]
Atomic	Ni	(8.0)
	Mn	(8.7)
	Cr	(9.6)
	V	(15.4)
	Ce	(15.4)
	Nb	(15.4)
	Ti	26.1
	O	(68.5)
	Ta	(94.6)
	La	(94.6)
	Nd	(129.3)
Linear	Dislocation	24–30
Planar or two-dimensional	AlN interface	65
	TiC interface	77.2–94.6
	Fe_3C interface	83.9
	MnS interface	77.2
	Grain boundary	26; 53–59 (high angle)
	Internal free surface	70–95
Volume	Microvoid	52
	Void	29

[a]Trapping or interaction energy. Values in parentheses are calculated.

and irreversible trapping is considered to be 60 kJ mol^{-1} for the trapping or interaction energy [67]. In general, solute atoms, dislocations, and low-angle grain boundaries tend to be reversible traps, whereas interfaces between the matrix and particles such as TiC are usually irreversible traps. The interaction of hydrogen with grain boundaries is actually very weak in pure iron but is increased when carbon or carbides are present at these locations [75].

The hydrogen diffusivity measured in the presence of traps is lower than that for the trap-free metal (see Sect. 2.2.5.1.4). The effect of solutes on the diffusivity for ferrite is shown in Fig. 3 [68]. Even small amounts of chromium and titanium produce a significant decrease in the diffusivity. These elements are considered to act as traps in iron, whereas the role of nickel is uncertain [65]. Nickel has a relatively small effect at levels up to 5 wt%, but when its level is increased from 5 to 40 wt%, the diffusivity is decreased by almost six orders of magnitude at ambient temperature [42]. This decrease, however, is associated with a phase transformation (α to γ) rather than with trapping by solute atoms. In contrast to the diffusivity, the solubility of hydrogen is increased by the addition of traps [65], as shown for elements such as chromium, manganese, titanium, and vanadium in iron [76, 77].

The relative importance of traps can differ greatly between metals, as seen by comparing the activation energies for diffusion with the binding energies of potential traps. This comparison depends on the type of crystal structure. In a face-centered cubic (fcc) lattice, the energy for binding hydrogen to defects such as vacancies or edge dislocations is considerably smaller than the activation energy for diffusion [78]. For example, the binding energy for an edge dislocation in nickel is 7.5 to 13.4 kJ mol^{-1} [66, 79], whereas the activation energy for diffusion is about 40 kJ mol^{-1} [66, 80]. In the case of copper, dislocations have almost no effect as traps [81]. Austenitic stainless steels also exhibit activation energies for diffusion (typically about 53 to 54 kJ mol^{-1} [82, 83]) that are significantly higher than the binding energies for defects such as vacancies (29 kJ mol^{-1} [84]). Therefore, these defects cause little hindrance to hydrogen diffusion in fcc metals. However, in the case of iron with its bcc lattice, the activation energy for diffusion is low enough (4.2 to 7.1 kJ mol^{-1}, see Sect. 2.2.4.1) so that such defects can cause a sizable decrease in the diffusivity.

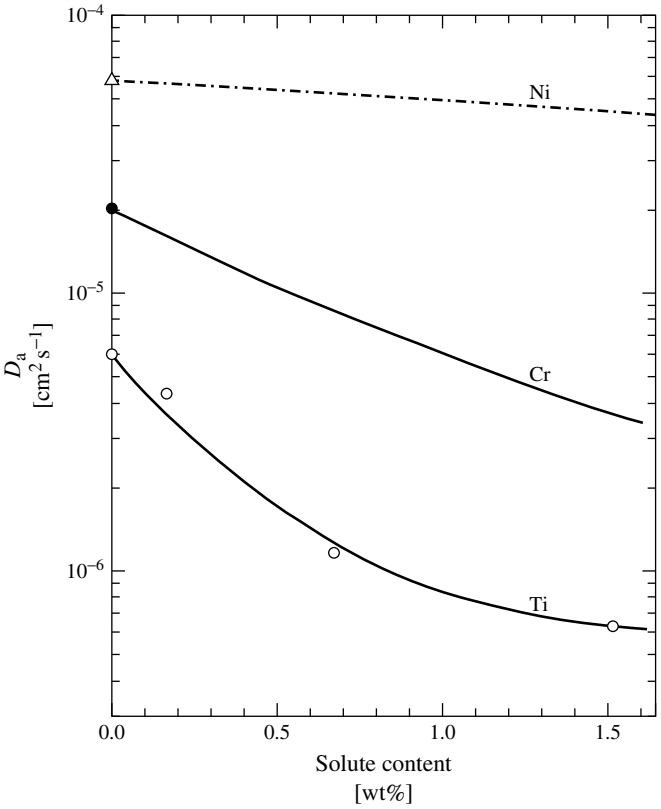


Fig. 3 Effect of solutes on the diffusivity of hydrogen in ferrite [68]. (Reprinted with permission from The Minerals, Metals & Materials Society.)

2.2.4.3 Hydrogen Antitrapping

Antitraps can also be present in metals. They fall into two groups – repellers and obstacles [65]. A repeller has one or more of the following characteristics: it is a solute atom that lies to the right of the matrix metal in the periodic table [69]; it produces a compressive stress field in the lattice; or it causes a reduction in the local hydrogen solubility. An obstacle is a physical discontinuity of the lattice through which hydrogen does not have significant mobility. An example would be an incoherent precipitate that does not dissolve hydrogen and does not induce a local stress field. In general, antitraps have both a repeller and an obstacle character. Moreover, some defects such as edge dislocations may have both a trapping and antitrapping character.

When diffusing hydrogen encounters an antitrap, the hydrogen is forced to go around it and the diffusion path is therefore lengthened. Consequently, the presence of antitraps, as with traps, lowers the apparent diffusivity [65]. The addition of a repeller element has been shown, in the case of cobalt, to decrease the diffusivity of hydrogen in iron [85] and, in the case of palladium, to reduce

the susceptibility of AISI 4130 steel to hydrogen-assisted cracking [86]. Unlike traps, antitraps decrease the solubility of hydrogen [65], as observed when elements such as copper, cobalt, tin, aluminum, and carbon are added to liquid iron [76].

2.2.4.4 Methods to Study Trapping

A range of methods including electrochemical techniques, autoradiography, and thermal desorption have been used to study hydrogen trapping. Mechanical relaxation methods have also found wide use and are described in several reviews [87, 88].

Electrochemical techniques allow the binding energies and densities of traps to be determined (see Sect. 2.2.5). For example, the binding energy and density of traps in iron with different amounts of cold work have been evaluated using electrochemical measurements in conjunction with gas-phase charging [89]. The trap density was shown to increase from about 10^{21} m^{-3} in the annealed condition to 10^{23} m^{-3} in the heavily (80%) cold-worked condition. The binding energy, however, was independent of the amount of cold work, suggesting that a single type of trap was operative. More complex cases of trapping involving iron-titanium-carbon alloys have also been examined using electrochemical techniques [68]. Rate constants were determined for trapping and release at reversible traps and for trapping at irreversible traps in these alloys. Electrochemical data have likewise been obtained for a martensitic stainless steel to determine the rate constants for trapping and release as well as the trap densities and binding energy [90].

In autoradiography, the metal is typically charged with tritium-enriched hydrogen [91, 92]. The diffusible hydrogen is then removed by outgasing, and the metal is exposed to a photographic emulsion to provide an image of the tritium retained at strong traps. Correlation of the image with microstructural features observed using scanning or transmission electron microscopy provides information about the location of hydrogen. Autoradiography has been applied to different metals including iron, maraging steel, and nickel [75, 91–93], and it has provided direct evidence that hydrogen can be trapped at dislocations, grain boundaries, and carbide and carbonitride interfaces.

Thermal desorption involves monitoring the evolution, or outgassing, of hydrogen from a metal as the temperature is increased at a given rate [94]. Peaks are observed in the evolution rate at various temperatures, and they correspond to traps with different binding energies. The area under a peak is equivalent to the amount of hydrogen in traps with the same binding energy. The results can be used to estimate the activation energies for detrapping, from which the binding energies can be obtained. Thermal desorption has been used to investigate trapping at, for example, dislocations and MnS interfaces in AISI 4340 steel [94], TiC interfaces in steel [95], and grain boundaries in nickel [66].

2.2.5 Electrochemical Techniques

Electrochemical techniques provide a highly sensitive, convenient approach for investigating hydrogen ingress in metals. The application and analyses for the different techniques have been described in several reviews [96, 97].

2.2.5.1 Permeation Techniques

The permeation technique has been widely used in studies of hydrogen ingress to

determine the hydrogen diffusivity and subsurface hydrogen concentration. It is based on the cell originally described by Devanathan and Stachurski [98]. The metal of interest is formed into a membrane that separates the cell into two sections (Fig. 4). One side of the metallic membrane is made cathodic either potentiostatically or galvanostatically, so that hydrogen is formed on the surface. Some fraction of the adsorbed hydrogen enters the metal and diffuses to the other side, where it exits and is anodically oxidized, usually under potentiostatic conditions.

The concentration gradient and therefore the hydrogen flux, $J(x,t)$, vary through the membrane with time and distance. The anodic current transient represents the variation in the flux at the output side, $i = FJ(L,t)$, where L is the thickness of the membrane and F is the Faraday constant. The current eventually reaches a steady state value (i_∞) as the concentration gradient in the membrane becomes linear, with i_∞ being a direct measure of the resulting flux, J_∞, given by

$$J_\infty = \frac{D(C_\infty - C_L)}{L} \qquad (17)$$

where $C_\infty = C(0,t)$ at steady state. The concentration at the output surface (C_L) is assumed to be approximately zero when a sufficiently high anodic potential is applied to that side. Measurement of the steady state flux for a given membrane thickness therefore allows C_∞ to be determined if D is known.

The permeation techniques have some disadvantages [96]. A principal one is that long charging times (of the order of days) may be required for hydrogen to diffuse through many metals, especially those with a fcc lattice. Aside from

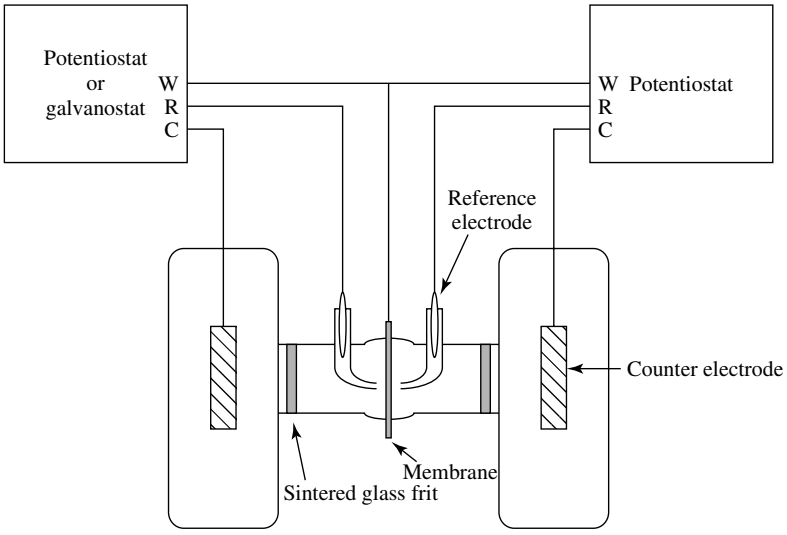


Fig. 4 A typical permeation cell to study the diffusion of hydrogen through a metal membrane [96, 98]. Although not shown, provision is usually made for deaerating the electrolyte. (Reprinted with permission from Kluwer Academic/Plenum Publishers.)

practicality, longer charging times increase the likelihood of changes in the surface condition, due to, for example, deposition of impurities on the cathode surface.

Gas-phase charging has also been used to study hydrogen permeation through metals. The surface coverage and the rate of hydrogen entry in gas-phase charging depend on the fugacity of H_2. The relationship between coverage and fugacity is discussed in Sect. 2.2.3.4. If equilibrium is assumed at the input surface of the membrane, the subsurface concentration of hydrogen can be obtained using Sievert's law (see Sect. 2.2.3.4).

2.2.5.1.1 **Potentiostatic Charging** The original mathematical treatments for the electrochemical methods were developed for potentiostatic charging and did not consider trapping. The kinetics of hydrogen permeation were first analyzed for the case of diffusion control without any rate limitation at the input surface [98, 99]. When the rate of hydrogen entry is not limited, cathodic charging produces a step function in the subsurface concentration of hydrogen, and hydrogen ingress is controlled solely by diffusion in the bulk metal. The kinetics of hydrogen entry are assumed to be fast enough to maintain equilibrium at the input surface, thereby resulting in a constant subsurface concentration. A further assumption is that hydrogen arriving at the exit surface is immediately oxidized, such that the subsurface concentration on this side is maintained at zero.

Since the flux is related to the concentration through Fick's first law, the anodic current is given by

$$i = -FD\left(\frac{\partial C}{\partial x}\right)_{x=L} \tag{18}$$

For pure diffusion control, the current can be expressed in the form

$$\frac{i}{i_\infty} = \frac{2}{(\pi\tau)^{1/2}}\sum_{n=0}^{\infty}(-1)^n \times \exp\left[-\frac{(2n+1)^2}{4\tau}\right] \tag{19}$$

where $\tau = Dt/L^2$. The concentration profile and a typical anodic current transient are shown schematically in Fig. 5. The transients are typically characterized by four parameters: half-rise time ($t_{1/2}$), time lag (t_L), inflection-point time (t_i), and breakthrough time (t_b). The diffusivity can be obtained from any of these time characteristics, as shown in Table 7. Under diffusion-controlled conditions, these time characteristics should be proportional to the square of the thickness. This dependence provides a straightforward test to verify that the permeation rate is controlled by diffusion rather than surface kinetics. Multiple values of the diffusivity can be obtained from successive transients at different charging currents to determine also whether the diffusivity is independent of hydrogen concentration.

When charging is stopped, the flux at the output side decays according to conditions at the input side [99, 100]. Two limiting cases have been considered. In the first case, the input side becomes impermeable to hydrogen at the end of charging, and so hydrogen is removed from the membrane at the slowest possible rate. The second case assumes that hydrogen egress occurs very rapidly at the input side, allowing hydrogen to be removed at the fastest possible rate.

When the rate of hydrogen entry is restricted at the input surface, the permeation rate is still assumed to be controlled by diffusion, but the finite surface kinetics

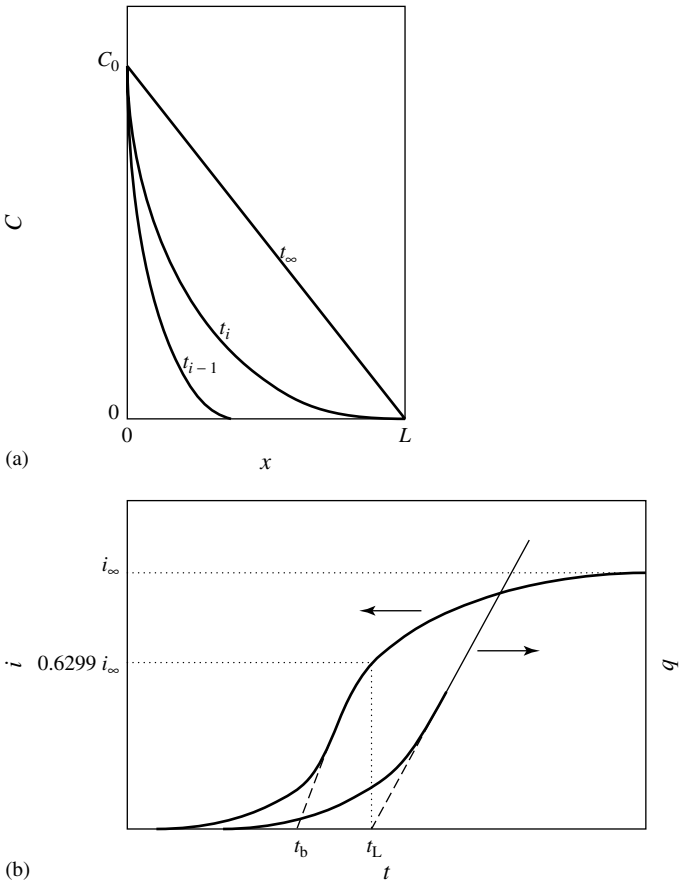


Fig. 5 Variation in (a) concentration gradient and (b) anodic current with time for a membrane with a constant concentration at the input side [97]. (Reprinted from J. Less-Common Met., Copyright 1976, with permission from Elsevier Science.)

Tab. 7 Time characteristics from anodic permeation transients

Characteristic	*Corresponding current*	*Potentiostatic*[a]	*Galvanostatic*
$t_{1/2}$	$0.5i_\infty$	$0.14L^2/D$; $0.38L^2/D$ (finite entry)	
t_L	$0.63i_\infty$	$L^2/6D$	$L^2/2D$
t_i	Inflection point	$0.924L^2/\pi^2D$	$1.65L^2/\pi^2D$
t_b	Tangent at inflection point extrapolated to initial level	$0.5L^2/\pi^2D$	$0.76L^2/\pi^2D$

[a] For pure diffusion control, except where indicated.

result in a step function in flux rather than concentration [53, 101]. The subsurface concentration at the entry side increases with time until it reaches a steady state. In this case, the ratio of i/i_∞ is given by

$$\frac{i}{i_\infty} = 1 - \frac{4}{\pi}\sum_{n=0}^{\infty}\frac{(-1)^n}{2n+1} \times \exp\left[-\frac{\pi^2(2n+1)^2 Dt}{4L^2}\right] \quad (20)$$

The concentration profile and a typical anodic transient are shown in Fig. 6. As can be seen in Table 7, the functional dependence of $t_{1/2}$ on L is the same whether or not the entry kinetics are restricted, but the proportionality constant differs.

2.2.5.1.2 **Galvanostatic Charging** Galvanostatic charging tends to be used more often than potentiostatic charging in

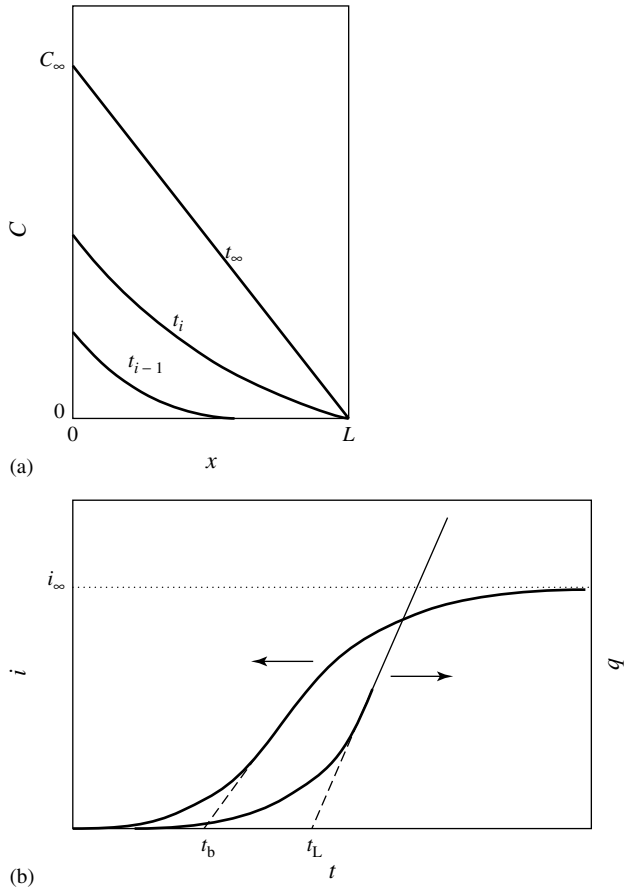


Fig. 6 Variation in (a) concentration gradient and (b) anodic current with time for a membrane with a constant flux at the input side [97]. The anodic current in this case typically increases at a slower rate than that for a constant concentration. (Reprinted from J. Less-Common Met., Copyright 1976, with permission from Elsevier Science.)

membrane permeation studies. The entry side condition in many galvanostatic studies is implicitly assumed to be a constant concentration, but mathematical treatments have been derived on the basis of the assumption that a constant cathodic current creates a constant-flux boundary condition at the entry surface [51, 97], as in the entry-limited case under potentiostatic conditions.

The permeation of hydrogen through a metal membrane under galvanostatic charging has been treated using a one-dimensional model for diffusion without trapping. If the flux is independent of time, as assumed for a constant charging current, the anodic current–time relationship is identical to that derived for potentiostatic charging with rate-limited hydrogen entry. As with potentiostatic charging, multiple values of the diffusivity can be determined from successive transients. Diffusion control of the permeation rate can be verified also for galvanostatic charging by using the time characteristics, since they should be proportional to the square of the thickness in this case too (Table 7).

2.2.5.1.3 **Time-dependent Entry Kinetics**
Neither the constant-flux nor the constant concentration models are strictly correct because the inward and outward fluxes at the input surface have finite rate constants.

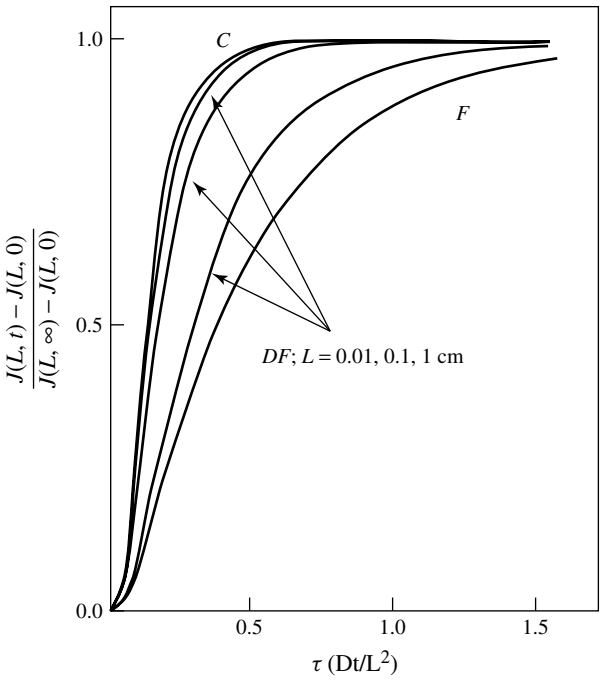


Fig. 7 Theoretical permeation transients showing the increase in flux, $J(L, t) - J(L, 0)$, as a fraction of the overall increase, $J(L, \infty) - J(L, 0)$, with τ [102]. Input conditions assumed for the transients: (*C*) constant concentration; (*F*) constant flux; and (*DF*) flux decreasing with time. (Reprinted from Scr. Metall., Copyright 1980, with permission from Elsevier Science.)

If the new surface coverage is achieved instantaneously when charging begins, the overall flux of hydrogen into the metal should in fact decrease with time as the surface concentration rises from the initial value to C_∞ [102]. The permeation curves approach those for constant flux and constant concentration at the extremes of membrane thickness, as shown in Fig. 7. The constant concentration curve, for example, is a good approximation to that for decreasing flux only for $L \geq 1$ cm, which is significantly higher than the 0.03 to 0.2 cm range commonly used in permeation experiments.

In the early potentiostatic experiments by Devanathan and Stachurski [98], the time required for the subsurface concentration to become constant, as assumed, was treated simply as a shift in the timescale at the beginning of a permeation curve. However, the permeation behavior for the constant concentration case and that in which the overall entry flux decreases as the concentration increases differ in a manner more complicated than just a shift in timescale [102].

2.2.5.1.4 **Effect of Trapping** Multiple charging/discharging is often used in permeation studies, and the first transient is normally slower than subsequent ones, as shown in Fig. 8. The generally accepted interpretation is that, during the first transient, irreversible traps are effective but gradually become filled as the hydrogen flux rises to a steady state. Successive transients are considered to involve only reversible traps.

The effect of trapping on the diffusion of hydrogen is treated mathematically by modifying Fick's second law. The usual approach is to include trapping terms in which the rate of trapping is assumed to be proportional to the concentration of diffusing hydrogen. However, most, if not all, diffusion/trapping models for

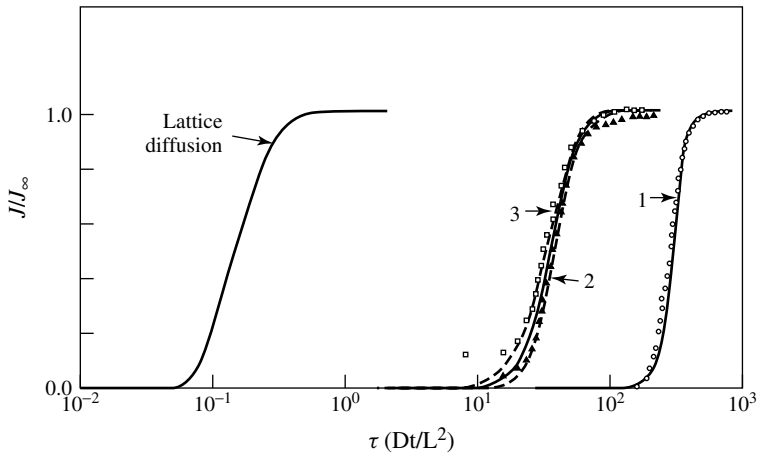


Fig. 8 Permeation transients for a type 410 stainless steel membrane (thickness of 0.5 mm) in acidified NaCl at 23 °C [90]. The steel was discharged after each transient, which is numbered according to its position in the sequence. ——— Theory; ----- Range of uncertainty in fit to experimental data, which are shown as points. (Reprinted from Acta Metall., Copyright 1989, with permission from Elsevier Science.)

the permeation techniques use a constant concentration on the input side.

A general model for hydrogen diffusion with reversible trapping was formulated by McNabb and Foster [103]. The general diffusion equation can be written as

$$\frac{\partial C}{\partial t} + N_r\left(\frac{\partial n_r}{\partial t}\right) = D\nabla^2 C \qquad (21)$$

where $\partial n_r/\partial t = k_r C(1-n_r) - pn_r$, k_r is the rate constant for reversible trapping, p is the rate constant for hydrogen release from the trap, n_r is the fraction of traps occupied, and N_r is the number of traps per unit volume. McNabb and Foster analyzed several cases involving diffusion through a membrane with a constant hydrogen concentration (C_0) on the input side. As n_r increases, the rate of trapping ($\partial n_r/\partial t$) decreases and eventually has no effect on diffusion, provided that no damage is induced in the metal. At steady state, the flux of hydrogen should be independent of trapping and therefore be given by $C_0 D/L$. However, this independence is strictly true only for dilute trap concentrations, since the diffusion cross-sectional area becomes limited if a large number of traps are present [48].

The time lag for membrane permeation with reversible trapping is given by

$$t_L = \frac{L^2}{6D}\left[1 + \frac{3\alpha}{\omega} + \frac{6\alpha}{\omega^2} - \frac{6\alpha}{\omega^3}(1+\omega)\ln(1+\omega)\right] \qquad (22)$$

where $\alpha = N_r k_r/p$ and $\omega = C_0 k_r/p$. In the case of thick specimens in which $D/L^2 \ll p$ and $C_0 k_r$, local changes in the lattice concentration are considered to occur so slowly that the trapped and lattice hydrogen have time to reach equilibrium. Using this condition, McNabb and Foster showed that, for low hydrogen concentrations, the differential equation for diffusion simplifies to the classical expression except that the apparent diffusivity (D_a) measured in the presence of trapping is a factor of $1/(1+\alpha)$ lower than that for the trap-free metal; that is,

$$D_a = \frac{D}{1 + N_r k_r/p} \qquad (23)$$

Thus, the standard solutions of the diffusion equations can be used for the analysis of experimental results. Clearly, in the absence of traps ($N_r = 0$) or with negligible trapping ($k_r \approx 0$), $N_r k_r/p \ll 1$ and $D \approx D_a$. When the traps near saturation ($n_r \to 1$), the apparent diffusivity increases with lattice concentration and approaches the lattice diffusivity at high concentrations according to Eq. (24) [50, 89]:

$$D_a = \frac{D}{1 + 3N_r/C_0} \qquad (24)$$

The effect of both irreversible and reversible traps can be represented by [104]

$$\frac{\partial C}{\partial t} = D\left(\frac{\partial^2 C}{\partial x^2}\right) - N_r\left(\frac{\partial n_r}{\partial t}\right) - N_i\left(\frac{\partial n_i}{\partial t}\right) \qquad (25)$$

where $\partial n_i/\partial t = k_i C(1-n_i)$, and k_i, n_i, and N_i are as defined for reversible traps but i refers to irreversible. For low fractional occupancies ($n \ll 1$), the diffusivity can again be obtained from the time lag:

$$t_L = \left(\frac{L^2}{6D}\right)\left(1 + \frac{N_r k_r}{p}\right) f(\kappa) \qquad (26)$$

where $f(\kappa)$ is a function of κ, which itself is given by $N_i k_i L^2/D$. Hence, the influence

of reversible and irreversible traps on the apparent diffusivity is multiplicative:

$$D_a = D\left[\left(1 + \frac{N_r k_r}{p}\right) f(\kappa)\right]^{-1} \quad (27)$$

The combined effects of reversible and irreversible trapping have been analyzed in detail, although solutions were obtained only for low fractional occupancy of reversible traps [105]. A generalized model was later developed for hydrogen transport that incorporates the combined effects of reversible and irreversible traps with varying degrees of occupancy [90]. Analytical solutions are not possible for the generalized case, so the equations must be solved using numerical analysis.

2.2.5.2 Pulse Techniques

2.2.5.2.1 Potentiostatic Pulse Most applications of the potentiostatic pulse technique have involved just one surface of a metal specimen. The technique is therefore suitable for bulk specimens since only a single surface need be exposed to the electrolyte. The principle of the technique is shown schematically in Fig. 9. The metal is charged with hydrogen at a constant potential E_c for a time t_c, after which the potential is stepped anodically to a value E_a. The anodic step results in a current transient due to hydrogen diffusing back to the entry surface and being reoxidized.

The analytical model originally developed for the potentiostatic pulse technique applied only to pure diffusion control and did not take trapping into account [41].

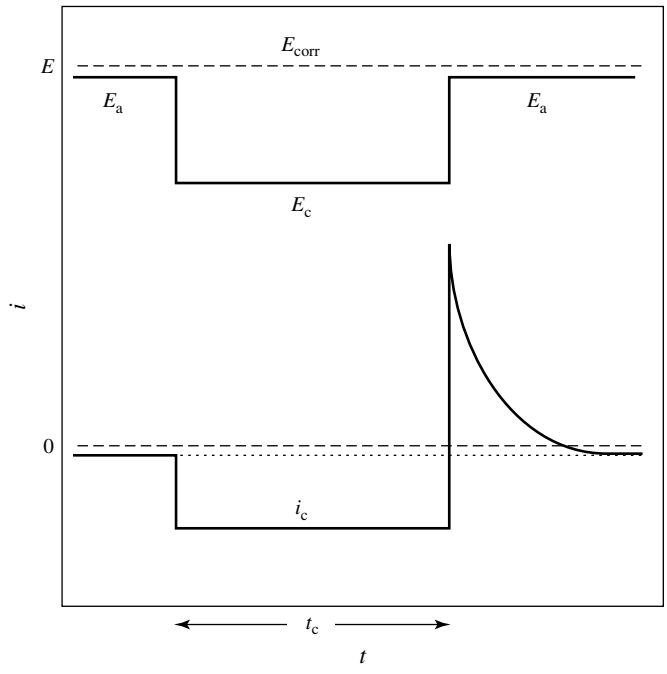


Fig. 9 Potential profile and current response for the potentiostatic pulse technique [106]. (Reprinted from Acta Metall., Copyright 1987, with permission from Elsevier Science.)

Under these conditions, the anodic current is given by

$$i = FD^{1/2}C_0\pi^{-1/2}[t^{-1/2} - (t + t_c)^{-1/2}] \quad (28)$$

A more general model was later developed to allow for the effect of trapping on diffusion without or with surface constraints; that is, for cases involving either constant concentration or constant flux at the input surface [106, 107]. For pure diffusion control, the anodic current or the anodic charge can be analyzed as a function of charging time to determine $C_0 D_a^{1/2}$ and an apparent trapping constant (k_a), which is a rate constant for irreversible trapping measured in the presence of reversible traps. k_a is given by $k/(1+\alpha)$, where $k = k_i N_i$. As k_a increases, progressively more hydrogen is trapped and the total outflow is reduced, as shown in Fig. 10. In the case of diffusion control with a limited rate of entry, an analytical expression can be obtained only for the anodic charge, but it allows both the ingress flux and k_a to be evaluated.

The irreversible trapping constant, k, can be expressed by $k_a D/D_a$ and can therefore be calculated from k_a by using diffusivity data to correct for the effect of reversible traps. The magnitude of k depends on the density of particles or defects providing irreversible traps, the radius of the trap defects, the diameter of the metal atom, and D [108].

2.2.5.2.2 **Galvanostatic Pulse** The galvanostatic pulse technique has been used in combination with conventional permeation measurements to measure the steady state coverage of adsorbed hydrogen and the rate constant for hydrogen entry,

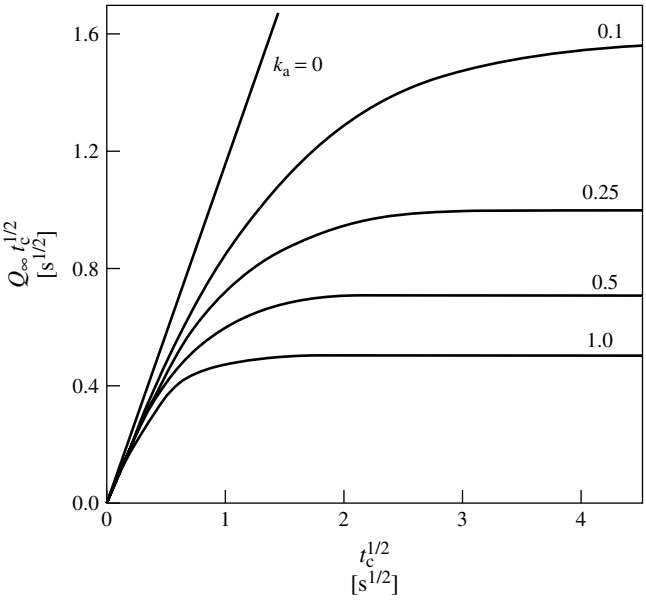


Fig. 10 Variation in the nondimensional anodic charge (Q_∞) with charging time (t_c) for the case of pure diffusion control under potentiostatic pulse conditions [106]. (Reprinted from Acta Metall., Copyright 1987, with permission from Elsevier Science.)

since these two parameters determine the entry flux of hydrogen [16]. A constant cathodic current is used to maintain a steady state coverage of hydrogen, which is then rapidly oxidized by applying an anodic current pulse. Potential transients are obtained with and without hydrogen present on the surface, allowing the coverage to be determined. Steady state permeation data are then used together with the coverage to evaluate the entry rate constant.

2.2.5.2.3 **Triangular Pulse** With the triangular pulse method, each side of a membrane is initially held at a constant potential so that permeation occurs in a normal manner [109]. After a steady state is achieved, an anodic or cathodic triangular pulse is applied to the entry side and the change in the oxidation current is measured at the output side. The duration of the pulse is typically 0.01 to 0.03 s. Analytical solutions for the current have been obtained for pure diffusion control and for entry-limited diffusion control. An anodic current peak is obtained in response to the triangular pulse, and the time corresponding to the half-peak width is characteristic of the type of kinetic control.

2.2.5.3 Potentiometric Techniques

This group of methods relies on potentiometric measurement at the detection side to determine the hydrogen concentration. Three basic variations of this approach have been described: the step, pulse, and sinusoidal methods [97]. In the step method, the hydrogen concentration is initially homogeneous throughout the membrane. The concentration is then increased at the input side and kept constant under potentiostatic control. The change in concentration at the detection side is followed by monitoring the potential. The inflection-point time and breakthrough time are related to the diffusivity through the same equations as those for galvanostatic charging.

The pulse method involves subjecting the membrane to a short cathodic current pulse. The concentration gradient created at the input side during this pulse decreases as hydrogen diffuses to the other side. As with the step method, the change in concentration at the detection side is monitored through the potential. The diffusivity can be calculated from the breakthrough time by the same equation as that for potentiostatic charging with pure diffusion control.

In the sinusoidal method, the concentration of hydrogen at the input side of a membrane is varied periodically. After a few periods, the concentration at the detection side begins to oscillate also, but the amplitude is damped and the phase is shifted with respect to the oscillation at the entry side. Comparison of the concentration waves at the two sides allows the diffusivity to be calculated from either the phase shift or the ratio of the amplitudes.

2.2.5.4 Alternating Current Technique

The alternating current technique is essentially a variant of the permeation method [48]. The current measured at the output side varies sinusoidally in response to the alternating cathodic current. The diffusivity can be determined from both the phase difference of the alternating current between the two sides and the amplitude of the alternating current at the output side.

2.2.5.5 Surface Effects of the Metal and Films

The anodic current at the output surface of a metal specimen is analyzed on the basis that it results from the oxidation

of hydrogen alone, with no contribution from the metal itself. In practice, any contribution from metal oxidation can be avoided by using a palladium coating on the output surface. This procedure is normally adopted in permeation experiments and could also be applied in the case of pulse methods. However, use of a coating means that potential information concerning the entry flux for the metal of interest would not be available. An alternative approach is to correct the measured anodic current for other contributions.

Any film present on the input surface must be stable, regardless of the charging method used. In the simplest case, reduction of the film causes a time delay such that the measured diffusivity differs from the true diffusivity for the metal [110]. At sufficiently high current densities, this difference becomes small. Hydrogen will permeate through stable surface oxides on metals [111, 112], but it can be slowed enough that the breakthrough time and lag time measured in permeation experiments will yield incorrect values of the diffusivity [97].

The diffusion of hydrogen into a metal covered by a film has been examined for the case of a semi-infinite solid [110, 113]. In other work, hydrogen transport through a metal with a surface oxide has been analyzed in terms of diffusion through laminated layers [114]. A model was later proposed for coupled transport involving diffusion through a metal membrane followed by an activated jump across the passive film on the output surface [55]. Oxidation of the permeating hydrogen was assumed to occur at the interface between the metal and the passive film, so that the hydrogen moved through the film as an ion. An alternative model involves entry of hydrogen into the passive film as a proton and electron that each move independently, with oxidation occurring at or near the film–electrolyte interface [55, 115].

2.2.5.6 Diffusion Control

The membrane in permeation experiments is frequently coated with palladium on both sides to minimize kinetic limitations on the transfer of hydrogen between the adsorbed and absorbed states. The coating on the output side, as noted above, also prevents oxidation of the metal. Although the coatings are intended to facilitate surface reactions, the membrane itself must be thick enough to ensure that the rate of permeation is controlled by diffusion. The diffusivity should therefore be determined for membranes of varying thickness to verify that diffusion is rate-controlling (Sect. 2.2.5.1).

When permeation is controlled solely by the rate of diffusion through the membrane, the subsurface and adsorbed hydrogen on the entry side are considered to be in equilibrium (see Sect. 2.2.5.1.1), characterized by a constant (K), and the steady state flux of hydrogen is given by [6, 7]

$$J_\infty = \frac{DK\theta}{L} \tag{29}$$

provided that the surface coverage and the fraction of subsurface interstitial sites occupied are low. The steady state flux can be related to the cathodic charging current through the coverage, with the form of the relationship depending on the mechanism of hydrogen evolution. In the case of iron with its coupled discharge-recombination mechanism, the cathodic current is given by [6]

$$i_c = k_1 a_{H_3O^+}(1-\theta) \times \exp\left(\frac{-\beta\eta F}{RT}\right) = k_2\theta^2 \tag{30}$$

The steady state flux can therefore be written as

$$J_\infty = \frac{DK}{L}\left(\frac{i_c}{k_2}\right)^{1/2} \qquad (31)$$

Hence, the steady state flux through an iron membrane under pure diffusion control should be proportional to the square root of the cathodic current density. Deviations from the square root dependence have been observed [116, 117], particularly at extreme current densities, but this relationship seems to hold generally [7, 118]. The relationship between J_∞ and η can also be derived, and values of $\partial\eta/\partial \ln J_\infty$ for coupled discharge-recombination and other mechanisms are shown in Table 8 [6].

2.2.5.7 Experimental Issues

Regardless of the technique used, the metal surface and its immediate environment should remain unchanged during hydrogen ingress. Hence, the use of buffered electrolytes may be desirable to minimize pH changes near the surface. Various buffers have been used to provide charging and oxidation solutions with pH values from 2 to 10 [18, 119]. However, sulfuric acid (typically pH 1.2) or sodium hydroxide (typically pH 13) is generally used as the charging solution in permeation experiments. Sodium hydroxide (pH 13) is normally used also on the oxidation side, where the output surface of the permeation membrane is protected by a palladium coating in most cases. The coating itself is usually electroplated, but electroless deposition has occasionally been used.

Preelectrolysis of the solutions can be important if charging times are long enough so that significant amounts of impurities could be deposited on the cathode surface. However, such precautions will not prevent changes at the surface if impurities are introduced at a later stage. In permeation experiments with nickel and some of its alloys, silicate dissolution from the cell glassware has been found to result in the deposition of silicon-based compounds during tests lasting several days [120].

Another consideration is the magnitude of the charging current or potential. Charging under highly cathodic conditions by any technique can cause undesirable effects in the metal under study. As

Tab. 8 Relationships between the kinetics of hydrogen evolution and hydrogen permeation

Mechanism	$-\partial\eta/\partial \ln J_\infty$		$J = f(i_c)$	
	Langmuir	***Temkin***[a]	***Langmuir***	***Temkin***[a]
Slow discharge–fast chemical	0	0	–	–
Slow discharge–fast electrochemical	RT/F	RT/F	i_c^{-2}	i_c
Fast discharge–slow chemical	RT/F	RT/F	i_c	$i_c^{1/2}$
Fast discharge–slow electrochemical	RT/F	RT/F	$i_c^{2/3}$	$i_c^{2/3}$
Coupled discharge–chemical	$4RT/F$	$5RT/2F$	$i_c^{1/2}$	i_c
Coupled discharge–electrochemical	0	0	–	–

[a] Nonactivated adsorption.

the charging current or potential is increased, the subsurface concentration of hydrogen can increase and may eventually exceed a critical value, above which changes occur in the microstructure. Such changes are thought to be the reason for the anomalous behavior observed in permeation transients for iron at high current densities [121].

2.2.5.8 Selected Metals

2.2.5.8.1 **Palladium** The high solubility of hydrogen coupled with rapid kinetics for hydrogen entry have made palladium the focus of numerous studies. It has widely been assumed in these studies that the subsurface concentration in palladium and palladium coatings instantaneously increases to a constant value at the start of charging. However, the more appropriate input condition for potentiostatic charging appears to be a step function in flux, as shown in Fig. 11 [53].

Hydrogen evolution on palladium involves fast discharge followed by slow recombination [6], so J_∞ can be proportional to i_c or $i_c^{1/2}$, depending on whether adsorption occurs under Langmuir or Temkin conditions (Table 8). Experimental data for palladium in fact show a linear dependence on i_c at low charging currents (Fig. 12) [51, 122] and an approximately square root dependence at high charging currents [123]. The linear dependence, however, is also consistent with a constant-flux model [51]. After the linear region, J_∞ becomes virtually independent of charging current but then varies with $i_c^{1/2}$ at higher charging currents as the surface coverage and therefore recombination rate of adsorbed hydrogen increase.

2.2.5.8.2 **Iron and Steel** Hydrogen permeation through iron and steel membranes has been investigated extensively. The assumption has usually been made that, as with palladium, a constant

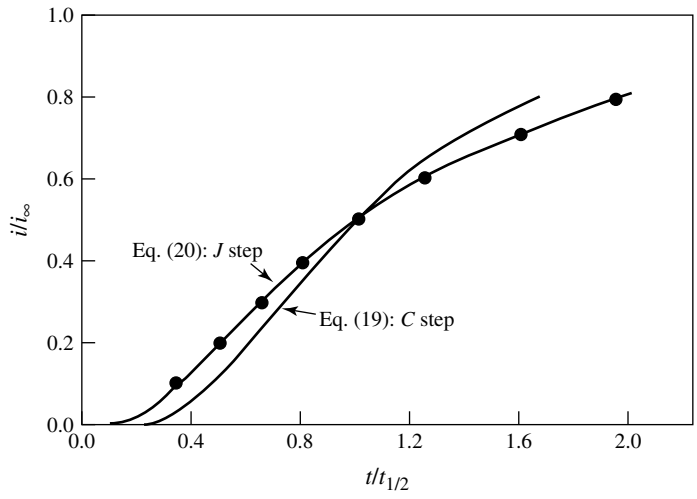


Fig. 11 Fractional attainment of steady state current as a function of time normalized about $t_{1/2}$ [53]. Points indicate experimental data for palladium. (Reproduced by permission of The Electrochemical Society, Inc.)

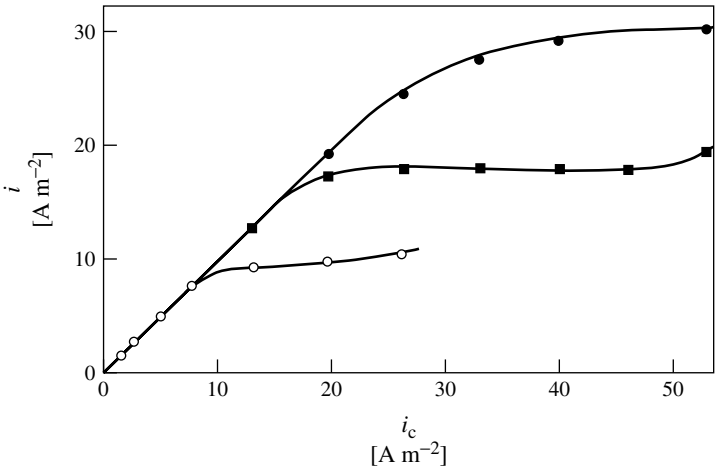


Fig. 12 Dependence of steady state anodic current density on charging current density for a palladium membrane [122]. Data for all curves are coincident for $i_c < 8$ A m^{-2}. Membrane thickness (mm): ● 0.15; ■ 0.25; ○ 0.50. (Reprinted with permission from The Minerals, Metals & Materials Society.)

subsurface concentration is instantly achieved at the input surface, whether potentiostatic or galvanostatic charging was used. Theoretical curves for permeation in the absence of trapping have been fitted to experimental data for iron and mild steel in H_2SO_4 and NaOH with and without promoters present [102]. For both potentiostatic and galvanostatic charging, the experimental data appear to be fitted better by the constant concentration curve than by the constant-flux curve, as shown in Fig. 13. However, the data still differ significantly from the constant concentration curve and differ even more from a decreasing flux curve. These deviations were attributed to trapping, which has been theoretically shown to affect the shape of the permeation curve [124].

2.2.5.8.3 **Nickel** Nickel is representative of the fcc group of metals, with their markedly different hydrogen ingress characteristics than those for iron and palladium. Hence, various studies have been directed towards the transport of hydrogen in nickel, despite the difficulty in accurately determining the low diffusivity at ambient temperature [41, 54, 80]. As with palladium and iron, it has been generally assumed that a constant concentration is immediately achieved upon charging, irrespective of the method used.

Although the binding energy for dislocations in nickel is much lower than the activation energy for diffusion (see Sect. 2.2.4.2), some studies suggest that dislocations can cause a small decrease in the diffusivity for heavily cold-worked nickel [54, 93]; it was found, for example, that 80% cold work reduces the diffusivity for Ni 270 (99.97% Ni) by a factor of about two, which is reflected by a shift in the hydrogen permeation curve (Fig. 14). Grain boundaries, on the other hand, provide paths for short-circuit diffusion in nickel [93, 125], although there is evidence from thermal analysis data

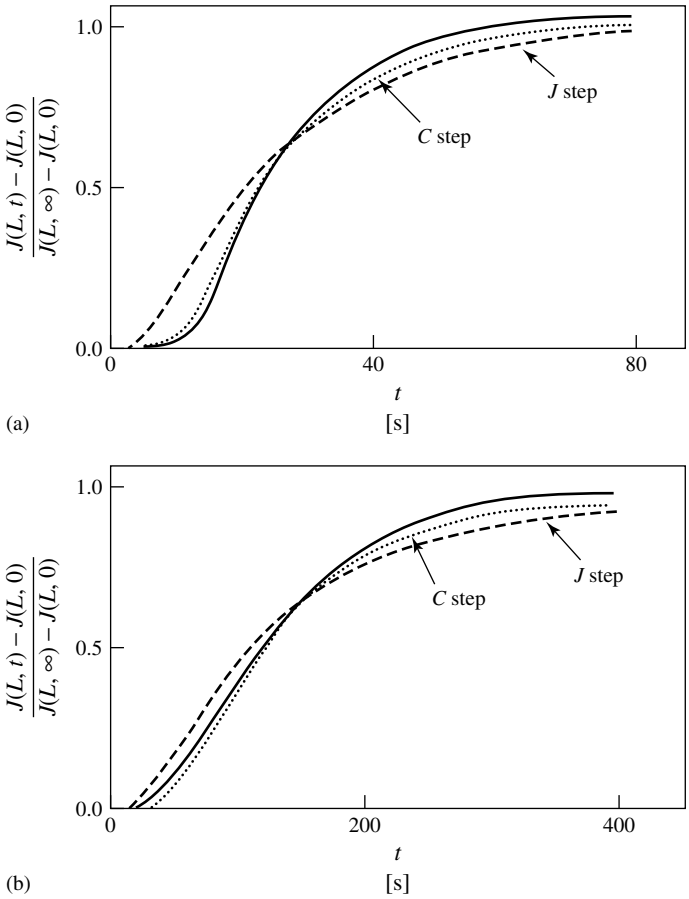


Fig. 13 Comparison of experimental (solid curve) and theoretical permeation transients for Armco iron [102]. Experimental data: (a) potentiostatic charging in 0.5 M H_2SO_4; (b) galvanostatic charging at 2 mA cm^{-2} in 0.1 M NaOH. (Reprinted from Scr. Metall., Copyright 1980, with permission from Elsevier Science.)

that trapping can also occur at these locations [66].

2.2.6 Hydrogen Degradation

2.2.6.1 Classification

The ingress of hydrogen can lead to degradation of the metal. The degradation can take various forms, which have been classified phenomenologically into nine different categories: hydrogen-environment embrittlement (HEE), hydrogen stress cracking (HSC), loss in tensile ductility, hydrogen attack, blistering, shatter cracks/flakes/fisheyes, microperforation, degradation in flow properties, and metal hydride formation [126]. The first three of these categories are related and are collectively referred to as hydrogen embrittlement (Table 9). HEE is distinguished from HSC by the mode of hydrogen entry,

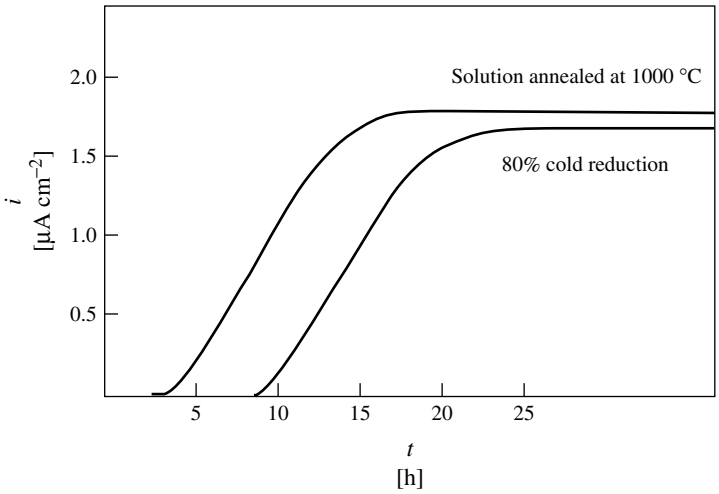


Fig. 14 Effect of cold work on hydrogen permeation through Ni 270 charged at 2 mA cm^{-2} in 0.05 M H_2SO_4 containing 3 mg l^{-1} $NaAsO_2$ [54]. (Reprinted with permission from the copyright holder, NACE International.)

Tab. 9 Forms of degradation classified under hydrogen embrittlement

	Hydrogen-environment embrittlement (HEE)	***Hydrogen stress cracking (HSC)***	***Loss in tensile ductility***
Typical materials	Steels, Ni-base alloys, metastable stainless steel, titanium alloys	Carbon and low-alloy steels	Steels, Ni-base alloys, Be-Cu bronze
Usual source of hydrogen (not exclusive)	Gaseous H_2	Thermal processing, electrolysis, corrosion	Gaseous H_2, internal hydrogen from electrochemical charging
Typical conditions	10^{-6} to 10^{8} Pa gas pressure	0.1 to 10 ppm total hydrogen content	0.1 to 10 ppm total hydrogen content, range of gas pressure exposure
	Observed −100 to 700 °C. Most severe near 20 °C	Observed −100 to 100 °C. Most severe near 20 °C	Observed −100 to 700 °C
	Strain rate important; embrittlement more severe at low strain rates; generally more severe in notched or precracked specimens	Strain rate important; embrittlement more severe at low strain rates; always more severe in notched or precracked specimens	Occurs in absence of effect on yield stress; strain rate important

while HSC is distinguished from loss in tensile ductility by the mechanical property (tensile strength vs. ductility) that is degraded.

HSC involves the brittle fracture of a nominally ductile alloy under a sustained load at tensile stresses below the yield strength. For HSC to occur, hydrogen must be absorbed into the alloy and then transported through it, along either a concentration gradient or a stress gradient. Some time is therefore required for cracks to nucleate. HSC is normally associated with steels but has been observed to a limited extent in other materials when hydrogen is concentrated near the surface.

HEE is the degradation observed in mechanical properties during the plastic deformation of alloys exposed to, usually, gaseous hydrogen. Similar behavior sometimes occurs when the hydrogen is provided by a gas such as H_2S, by electrolytic charging, or by corrosion. HEE has been exhibited by ferritic steels, nickel-base alloys, and metastable austenitic steels.

Loss in tensile ductility is characterized by a decrease in elongation and reduction in area in an ordinary tensile test. It has been observed in steels (ferritic, martensitic, and austenitic), nickel-base alloys, aluminum alloys, and titanium alloys. The percentage loss in ductility depends on the hydrogen content of the alloy.

Two other types of hydrogen degradation can result from corrosion: hydride formation and blistering. The degradation in tantalum, niobium, vanadium, titanium, zirconium, and their alloys results from the precipitation of metal hydride phases, which are relatively brittle (see Sect. 2.2.6.3.5). Blistering occurs when hydrogen diffuses to nonmetallic inclusions or other internal defects, where molecular hydrogen is formed by recombination. The pressure of molecular hydrogen can become high enough to cause localized plastic deformation of the alloy. Blistering generally occurs in more ductile steels under conditions in which hydrogen embrittlement does not occur.

The pressure caused by the accumulation of molecular hydrogen can result in not only blisters near the surface of the steel but also internal cracks that may propagate in a straight or stepwise manner (Fig. 15) [127, 128]. This type of damage is referred to as hydrogen-induced cracking (HIC) and is generally associated with low-strength steels (typically <550 MPa) in aqueous hydrogen sulfide environments. It is considered to include blister cracks near the surface as well as internal cracks [127–129]. The cracks can develop in the absence of an applied or residual tensile stress and are oriented parallel to the rolling direction of the steel.

A special form of HIC that occurs in low-strength steels in the presence of a stress is stress-oriented hydrogen-induced cracking (SOHIC) [127, 130, 131]. It is characterized by the formation of a stacked array of hydrogen-induced cracks, as shown in Figs. 16 and 17. These small cracks are oriented parallel to the rolling direction, but the stack itself is perpendicular to the stress. The cracks become linked by transgranular cracks to produce an overall crack perpendicular to the stress.

HIC differs from sulfide stress cracking (SSC), which also results from the absorption of hydrogen during corrosion in aqueous H_2S environments [127, 128]. Whereas HIC does not require an applied stress and occurs in low-strength steels, SSC does require an external tensile stress and occurs in high-strength steels or in hard areas associated with the heat-affected zones adjacent to welds. However, SSC cracks in the heat-affected zone can lead to SOHIC in the adjacent base metal.

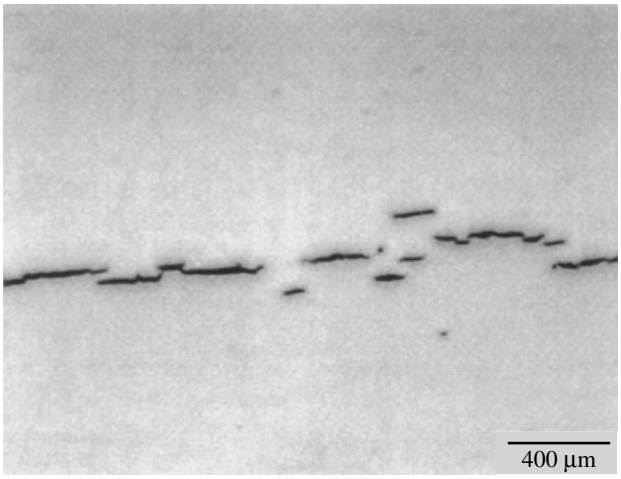


Fig. 15 Stepwise cracking in type A516-70 pressure vessel steel exposed to NACE TM0284-96 Solution A for 96 h at 25 °C [128]. (Reprinted with permission from the copyright holder, NACE International.)

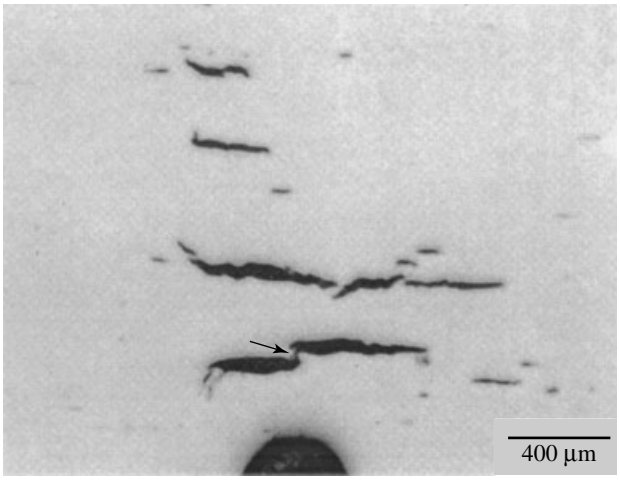


Fig. 16 Stacking of SOHIC cracks at the root of a notch in type A516-70 pressure vessel steel tested at 60% yield strength in NACE TM0284-96 Solution A for 168 h at 25 °C [128]. The arrow indicates linking of stacked cracks. (Reprinted with permission from the copyright holder, NACE International.)

2.2.6.2 **Hydrogen Trapping**

Hydrogen traps can have a marked effect on the susceptibility of an alloy to hydrogen embrittlement. The effect can be beneficial or detrimental, depending on the nature of the trap [67]. Fine, homogeneously distributed traps (reversible or irreversible) are considered beneficial. Examples of

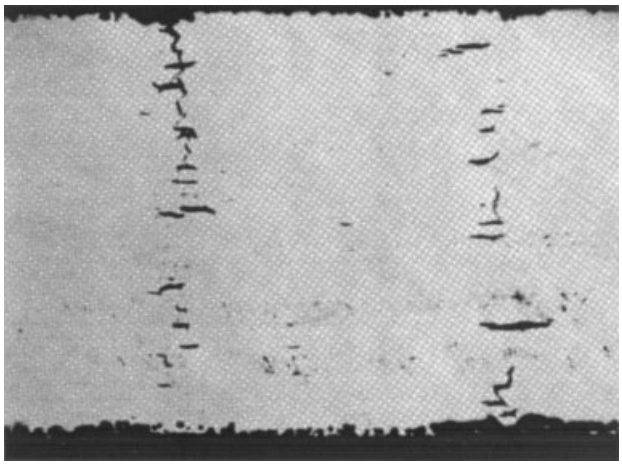


Fig. 17 SOHIC produced across the thickness of a steel sample at 50% yield strength in a NACE TM0177-86 test [127]. (Reprinted with permission from the copyright holder, NACE International.)

such traps in α-iron are solute atoms, low-angle grain boundaries, or small ($\ll 1$ µm) particles. The irreversible traps can delay the onset of cracking but are not expected to affect its extent, whereas reversible traps can both delay the onset of cracking and decrease its extent. Reversible traps, however, can release their hydrogen under certain conditions and accelerate crack initiation [67, 132, 133]. Unlike fine, homogeneously distributed traps, irreversible traps that are heterogeneously distributed and have a high saturability are considered detrimental, because they can increase the extent of cracking. These traps promote hydrogen concentration centers, making the alloy more susceptible to hydrogen-induced damage. Such traps in α-iron include large (>1 µm) particles and high-angle grain boundaries.

The role of microstructure has been treated in terms of the trap theory of hydrogen embrittlement [65, 133]. The theory assumes that, regardless of the mechanism of embrittlement (see Sect. 2.2.6.3), the concentration of trapped hydrogen must reach some critical value at a potential crack site for cracking to occur. The critical concentration is determined by many factors, such as the type of trap, its shape and location in the lattice, and the state of stress at the site. Whether or not a crack will be initiated depends not only on the magnitude of the critical concentration but also on the capacity of the trap and on the quantity of hydrogen that reaches the trap during the time of exposure. The quantity of hydrogen reaching the trap itself depends on various factors such as the entry kinetics, exposure time, and diffusion characteristics.

The trap theory is supported by experimental results for iron-titanium alloys in which the density of reversible and irreversible traps was varied [67]. Increasing the density of reversible traps, for example, was found to decrease the susceptibility to intergranular cracking, as described above. Reversible traps in the form of PdAl precipitates likewise appear to play an important role in suppressing intergranular cracking of a palladium-modified

martensitic stainless steel [134]. Traps can also have a beneficial effect in other alloys. For example, the absence of intergranular fracture in dispersion-strengthened alloys such as Ni-2ThO_2 and Ni-20Cr-2ThO_2 has been attributed to trapping at the interface between the matrix and the fine oxide particles (see Sect. 2.2.6.4.3) [135].

Changes in the type of traps have been shown to affect the crack path in precharged 4340 steel [74]. At low strengths, the steel contains a relatively high density of reversible traps but too few large irreversible traps to promote much interfacially aligned cracking. The high-strength steel, on the other hand, contains a relatively high density of irreversible interfacial traps and tends to exhibit primary and secondary crack paths along these traps. It has been shown in fact from trapping measurements that the irreversible trapping constant, k (see Sect. 2.2.5.2.1), for 4340 steel increases with yield strength over the range 1000 to 1400 MPa [136].

Trapping can also play an important role in the hydrogen embrittlement of more complex alloys. In the precipitation-strengthened, Fe-based superalloy, 903, microvoid formation and subsequent slip band fracture result from the trapping of hydrogen at slip band intersections and dislocations within the slip bands [137]. Atomistic simulations for nickel have shown that, of the two trap sites, trapping at slip band intersections is the controlling step in the fracture process, with binding energies within the intersection being close to 39 kJ mol^{-1} compared with 12 kJ mol^{-1} for individual dislocation cores. Fracture is thought to occur when hydrogen reaches a critical concentration at the slip band intersections, with the rate of crack growth being controlled by the diffusion of hydrogen through the lattice. Trapping studies of 18Ni maraging steel have indicated that strong trapping, especially at prior austenite grain boundaries, plays a role in its susceptibility to hydrogen embrittlement [91, 138, 139]. In the case of a martensitic stainless steel, the predominant factor determining the relative time-to-failure appears to be the fractional occupancy of the reversible trap sites [140].

A model has been developed to quantitatively account for the role of hydrogen–microstructure interactions in the growth of cracks [141]. The model indicates that the rate of crack growth is essentially determined by two basic factors: the rate of hydrogen supply to the fracture process zone, which is controlled by one of the processes (e.g. diffusion) for hydrogen supply, and the partitioning of hydrogen among the different microstructural features or traps, which is controlled by the hydrogen–trap interactions and determines the contribution by each trap to the overall crack growth rate.

2.2.6.3 Theories

Various theories have been proposed to account for the degradation caused by hydrogen. None of them, however, provides a general model for the different forms of hydrogen degradation.

2.2.6.3.1 **Internal Pressure** This theory considers hydrogen embrittlement to be caused by the formation of molecular hydrogen and the resulting buildup of pressure at internal voids or other internal surfaces [142, 143]. It provides an explanation for blistering in low-strength steels but does not adequately account for other forms of degradation such as HSC.

2.2.6.3.2 **Surface Energy** The adsorption of hydrogen atoms was postulated to decrease the surface energy of the free surfaces resulting from crack propagation [144, 145]. This decrease reduces the work of fracture and hence promotes cracking. There are several arguments against the surface energy theory [38]. It considerably underestimates the work of fracture and does not account for discontinuous cracking. Moreover, it is not specific for hydrogen and does not explain why oxygen, which adsorbs more strongly than hydrogen, does not promote cracking but rather inhibits the effect of hydrogen.

2.2.6.3.3 **Decohesion** The fundamental concept of this theory is that atomic hydrogen at high local concentrations reduces the maximum cohesive force against separation of the metal atoms [36, 146–148]. The hydrogen can be in the lattice, grain boundaries, or interphase boundaries. Fracture occurs when the local tensile stress exceeds the hydrogen-decreased maximum cohesive force. The theory does not attempt to explain why the cohesive force is lowered by hydrogen.

2.2.6.3.4 **Slip Softening** The basis of a cracking theory proposed by Beachem was that the role of hydrogen is to increase dislocation motion [149]. Enhancement of dislocation motion and dislocation injection at surfaces, with localized softening, has been reported. However, hardening effects have also been observed. In addition, the point has been made that enhanced dislocation motion is a factor in hydrogen degradation but is not a model in itself [38].

2.2.6.3.5 **Hydrogen-related Phase Changes** Hydrogen degradation of some metals is attributed to stress-induced precipitation of brittle metal hydrides [150–152]. These metals typically form stable hydrides in the absence of stress, and the hydrides are thermodynamically more stable under the stress field and hydrogen concentration at the crack tip. In some cases, hydrides that are unstable in the absence of stress can be stabilized by the stress field. Local stress fields and dislocations are generated when hydrides are formed, and they can contribute to failure, which occurs by cleavage of the brittle hydride phase. Hydrogen degradation by stress-induced hydride precipitation occurs under conditions in which the hydrides can form fast enough to preclude other forms of failure.

Metals such as Nb, Ta, V, Ti, Zr, and their alloys are capable of forming hydrides, but other metals can form pseudohydrides under high fugacity conditions, such as cathodic charging [152]. These pseudohydrides are actually high-concentration solid solutions formed in the presence of a miscibility gap. Pseudohydride formers include Ni, Pd, and their alloys.

Another case of hydrogen-related second-phase embrittlement has been postulated to occur in metastable austenitic stainless steels, such as types 304 and 316 [152–154]. The premise is that hydrogen enhances transformation of the austenitic phase to martensitic phases. Although there is evidence that martensites are present at the fracture surfaces of hydrogen embrittled metastable stainless steels, it has not been shown whether these phases are required for fracture or whether they result from the enhanced deformation caused by hydrogen.

2.2.6.4 **Alloys**

Hydrogen embrittlement can involve different fracture modes, depending on the

alloy and its strength. It is usually associated with brittle fracture in the form of intergranular cracking or cleavage, but many alloys exhibit ductile fracture with losses in ductility. These alloys are generally less subject to mechanical degradation than those that have a propensity to cracking. The hydrogen embrittlement susceptibility of alloys that undergo cracking is often characterized in terms of a threshold stress intensity required for crack growth.

2.2.6.4.1 **Steels** In general, the susceptibility of steels to hydrogen embrittlement increases with their strength. Tests on steels of varying strength, however, have shown that the susceptibility is much more sensitive to the specific nature of the microstructure than to the strength; in other words, the susceptibility is more directly an effect of microstructure than of strength [65, 155].

The effect of a particular alloying element on the susceptibility to hydrogen embrittlement depends on the microstructure and strength. The concentration of the element is also a factor. The effects of solutes on the hydrogen embrittlement susceptibility of steel are summarized in Table 10 [155]. Chromium, particularly at low concentrations, and manganese increase the susceptibility to embrittlement, whereas silicon produces a decrease, especially in higher-strength steels. Titanium promotes hydrogen embrittlement in maraging steels but is usually very beneficial in ferritic and other martensitic steels.

Microstructure can have a considerable effect on the susceptibility of steels to hydrogen embrittlement [155]. Untempered martensite promotes environmental embrittlement, apparently due in large part to the brittle nature of the martensite plates [156, 157]. Grain refinement generally increases the resistance to cracking under a wide range of polarization and environmental conditions [158, 159]. This effect has been observed for iron and various iron alloys, including 4340 steel, maraging steel, and Fe-Ti alloys [155].

Hydrogen degradation of low-strength steels (yield strength below 700 MPa) occurs principally in the form of reduced ductility or blistering. Hydrogen tends to degrade the properties without changing the microstructural mode of fracture [149, 160]. It has been reported to enhance

Tab. 10 Effect of solutes on susceptibility of steel to hydrogen embrittlement

Element	*General susceptibility*	K^{a}_{Ienv}	*Crack growth rate*
Manganese	Increases	Reduces	Not known
Sulfur and phosphorus	Appears to increase	Little effect	Should increase
Carbon (in carbon martensites)	Appears to increase	Reduces	Not known
Chromium	Increases	Little effect	Should increase
Titanium (in general)	Reduces	Not known	Not known
Titanium (in maraging steels)	Increases	Not known	Not known
Silicon	Reduces	Reduces	Reduces
Molybdenum	No consistent behavior	Little effect	Not known
Nickel	Not known	Little effect	Not known

[a] Threshold stress intensity for crack growth in environmental tests.

void nucleation, void growth, and void coalescence [155]. The hydrogen effects become more pronounced with increasing hydrogen content or charging rate and with increasing strength [36, 161].

Fracture of high-strength steels in hydrogen environments occurs by intergranular cracking or quasi-cleavage [162–164]. Figure 18 shows intergranular cracking in a high-purity 4340-type steel exposed to hydrogen. Intergranular cracking is promoted by the presence of impurity elements at grain boundaries. Phosphorus and sulfur, in particular, enhance cracking [156, 162, 165, 166]. Manganese and silicon are also detrimental when segregated to grain boundaries, whereas titanium and aluminum have a beneficial effect, as do fine grains and fine carbides [38, 155, 167]. The threshold stress intensities for crack growth in high-strength steels exposed to hydrogen-containing environments are considerably lower than those measured in air, as shown in Fig. 19 [168]. The hydrogen-environment threshold values, which are commonly denoted by K_{ISCC} in the case of aqueous environments, generally undergo a marked decrease with increasing yield strength.

Ultrahigh-strength steels (yield strength above 1400 MPa) are highly susceptible to cracking in hydrogen environments. These steels have been found to exhibit low values of K_{ISCC} in aqueous solutions containing NaCl (Fig. 20) [169], and although chlorides are the principal cause of stress corrosion cracking (SCC) in many alloys, there is little doubt that hydrogen plays the dominant role in most SCC failures of martensitic steels [136, 155]. Under appropriate conditions, the rate of crack growth in martensitic steels is determined by diffusion of hydrogen to the embrittlement sites ahead of the crack tip [141].

2.2.6.4.2 **Stainless Steels** Ferritic stainless steels exhibit high ductility and low strength, and consequently, they have little susceptibility to hydrogen

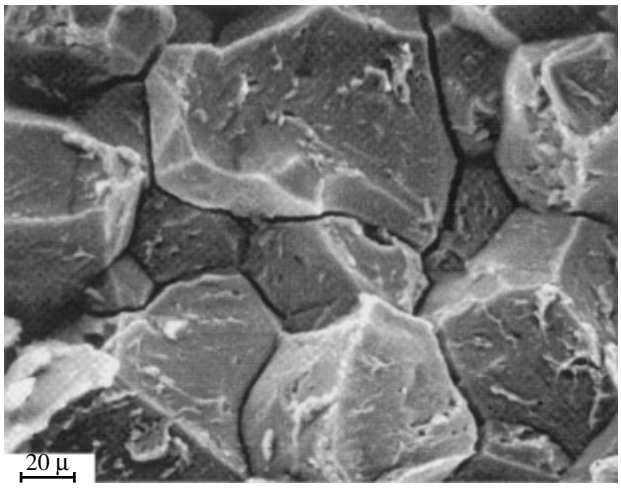


Fig. 18 Intergranular cracking in a high-purity 4340-type steel exposed to hydrogen [162]. (Reprinted with permission from The Minerals, Metals & Materials Society.)

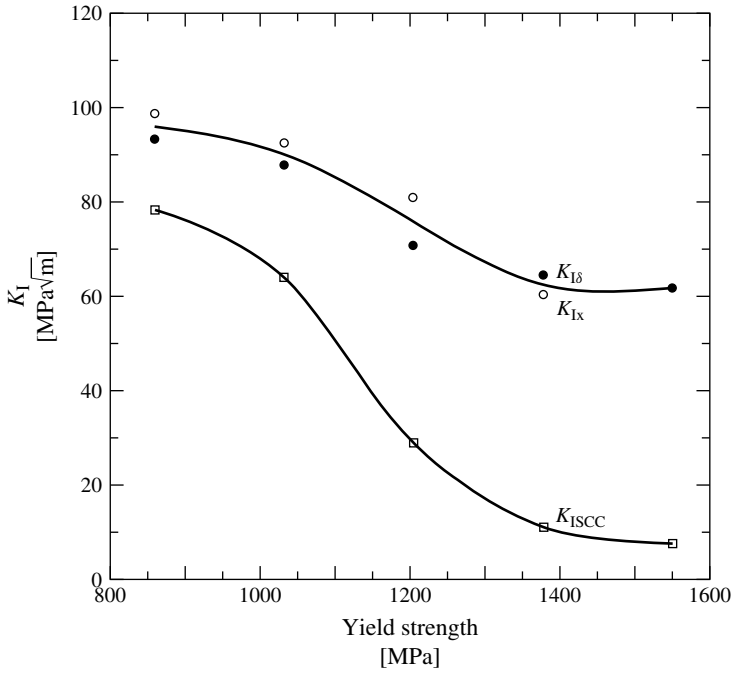


Fig. 19 Fracture toughness indices (K_{Ix} and $K_{I\delta}$) and K_{ISCC} for AISI 4340 steel as a function of yield strength [168]. K_{Ix} was measured in air and K_{ISCC} was measured in flowing seawater. $K_{I\delta}$ was calculated from measurements of the fracture surface after SCC. (Reprinted with permission from the copyright holder, NACE International.)

embrittlement. However, cold work may render these steels susceptible to cracking in hydrogen environments. The effect of hydrogen on the fracture mode of a ferritic (type 430) stainless steel is shown in Fig. 21 [170]. Whereas an uncharged specimen exhibits ductile fracture involving microvoid coalescence, specimens charged with hydrogen undergo brittle fracture, mainly in the form of transgranular cracking but with a small fraction of intergranular cracking.

Austenitic stainless steels, as with their ferritic counterparts, are relatively resistant to hydrogen embrittlement but can be made more susceptible by cold work. This increased susceptibility is ascribed to the deformation-induced formation of martensite in metastable stainless steels. In the case of stable austenitic stainless steels with high yield strengths, the susceptibility is generally considered to be governed by yield strength. The base composition of the stainless steels influences their resistance to hydrogen embrittlement, with nickel having a beneficial effect, as does chromium at levels higher or lower than 18% [171, 172].

Metastable austenitic stainless steels that are cathodically charged with hydrogen can exhibit cleavage-like transgranular fractures, which resemble those observed in SCC. However, hydrogen embrittlement is unlikely to be the cause of SCC in austenitic stainless steels

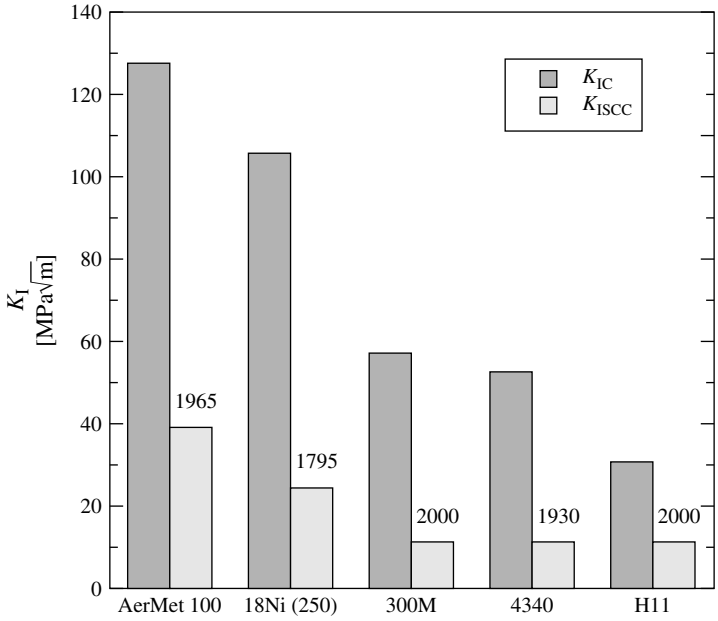


Fig. 20 Comparison of fracture toughness (K_{IC}) and K_{ISCC} for ultrahigh-strength steels [169]. K_{ISCC} was measured in 3.5% NaCl. The numbers by the bars are the tensile strengths (MPa) of the steels as tested. (Reprinted with permission from ASM International.)

for several reasons [173]. One reason is that stable austenitic steels undergo SCC but show only superficial cleavage-like cracking under cathodic polarization. Another reason is that the effects of alloy composition and temperature on SCC are inconsistent with a hydrogen model.

The martensitic and precipitation-hardening stainless steels are more susceptible to hydrogen embrittlement than are the austenitic alloys. The susceptibility of these stainless steels is sensitive to microstructure and strength level. Figure 22 shows the resistance to cracking for a martensitic (type 410) stainless steel and some precipitation-hardening stainless steels in an H_2S-saturated solution [174]. The low resistance of type 410 stainless steel is typical for most martensitic stainless steels, which are especially prone to hydrogen-assisted cracking [175].

Intergranular hydrogen cracking in a precipitation-hardening martensitic stainless steel has been suppressed by the addition of palladium. Heat treatment of the alloy produces submicrometer-sized PdAl precipitates that act as reversible traps and are thought to reduce the amount of hydrogen at prior austenite grain boundaries [134].

2.2.6.4.3 **Nickel Alloys** Nickel and its alloys can undergo hydrogen degradation in aqueous environments but are generally less susceptible than ferritic and martensitic steels. Degradation can occur by intergranular, transgranular, or quasi-cleavage cracking. Hydrogen segregates at

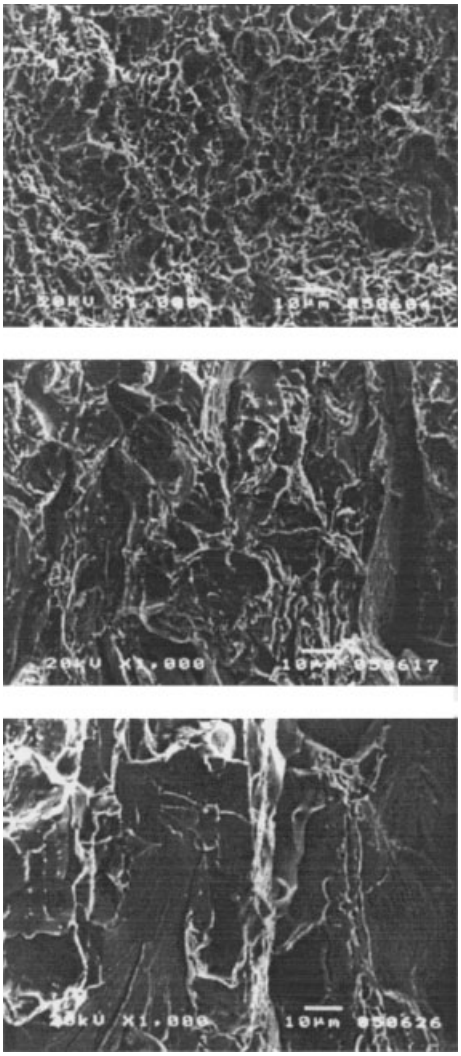


Fig. 21 Fracture surfaces of type 430 stainless steel tensile tested at a strain rate of 1.4×10^{-6} s^{-1}: (a) in air; (b) with hydrogen charging at 50 A m^{-2}; and (c) with hydrogen charging at 500 A m^{-2} [170]. (Reproduced by permission of The Electrochemical Society, Inc.)

grain boundaries in nickel, and as the level of segregation increases, the amount of intergranular fracture increases until the fracture becomes completely intergranular at a critical concentration of grain boundary hydrogen [152]. Synergistic effects of sulfur and hydrogen segregation at grain boundaries have been observed under cathodic charging conditions [176]. The segregation of sulfur greatly decreases the amount of hydrogen required to achieve the critical grain boundary concentration for intergranular fracture [177].

Alloying chromium with nickel increases the resistance to oxidation and general corrosion, particularly for about 20% Cr. However, Ni-20Cr undergoes a transition from ductile rupture to intergranular fracture in the presence of hydrogen [178], and it loses a considerable degree of ductility [178, 179]. Binary Ni-Fe alloys show a decreasing susceptibility to hydrogen-induced loss in ductility as the Fe content is increased, particularly between 20 and 50% Fe [179, 180].

Dispersion-strengthened alloys such as Ni-2ThO_2 and Ni-20Cr-2ThO_2, when charged with hydrogen, undergo only moderate losses in ductility, rather than brittle intergranular fracture as occurs in nickel [135]. Hydrogen is thought to be trapped at the oxide particle–matrix interface and therefore unable to build up at grain boundaries. These traps, however, could be expected to saturate eventually, if enough hydrogen were present [181].

The susceptibility of Ni-Cr-Fe alloys (intermediate- and high-Ni) to hydrogen degradation depends on the type of thermomechanical treatment [155]. Cold-worked alloys are generally rendered more susceptible to HSC if they are aged. The age-hardening alloys tend to be most susceptible in their peak-aged condition. Cathodic charging of aged nickel-base alloys such as 718 produces

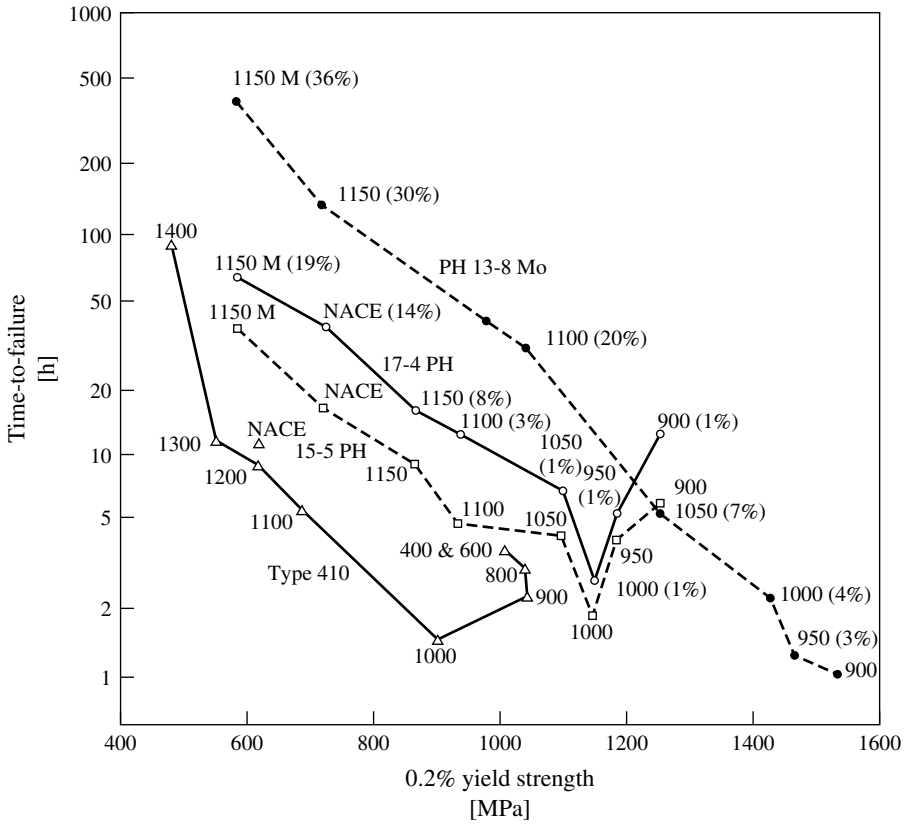


Fig. 22 Cracking resistance (represented by time-to-failure) of various stainless steels as a function of yield strength [174]. The tests were performed under an applied stress of 345 MPa and in a 5% NaCl–0.5% acetic acid solution saturated with H_2S. The numbers in parentheses indicate approximate amounts of austenite. (Reprinted with permission from the copyright holder, NACE International.)

little loss in ductility [182] but does result in cracking [183].

The nickel-base alloys, C-4, C-276, and 625, are resistant to HSC in the heavily cold-worked condition (48% and higher) [184]. Aging these alloys, however, markedly decreases their resistance to HSC. The decrease in some cases may be related to grain boundary segregation of phosphorus [185]. Tests on two nickel-base alloys (600 and 690) together with two iron-base alloys (321 and 800) that contain nickel have shown that the strain-to-failure of cathodically charged specimens decreases with increasing nickel content and that this decrease corresponds to an increase in the hydrogen diffusivity [186].

Nickel-copper alloys are susceptible to hydrogen embrittlement. The presence of copper at a level of 30% or higher has little effect on the loss in ductility and the intergranular fracture induced by hydrogen in nickel [180]. Thus, 70Ni-30Cu alloys also undergo intergranular fracture. The precipitation-hardening 70Ni-30Cu alloy,

K-500, exhibits considerable degradation under cathodic charging [187, 188]. The extent of embrittlement depends on the heat treatment and microstructure, and it may be related to the grain boundary segregation of sulfur [155]. Some heat treatments of Ni-Co alloys can also cause a grain boundary segregation of sulfur, thereby enhancing hydrogen embrittlement [189].

2.2.6.4.4 **Titanium Alloys** Hydrogen degradation of titanium and its α and $\alpha - \beta$ alloys results principally from the precipitation of titanium hydride in the α phase. The susceptibility to hydride-induced embrittlement typically decreases with increasing temperature as a result of an increase in hydrogen solubility. β titanium alloys have a high solubility for hydrogen, so embrittlement of these alloys is generally not associated with hydride precipitation [190]. Even when aged to cause α precipitation, alloys such as Beta-21S and Beta-C show no evidence of bulk hydrides in the α phase, except on the surface in some cases [191–193].

There is strong electrochemical evidence that hydrogen is at least partly responsible for SCC of α and near-α titanium alloys in aqueous solutions [194–196]. Figure 23 shows the resistance of a near-α titanium alloy to SCC in 3.5% NaCl with and without arsenic present [196]. As to be expected for a hydrogen-dependent process, the presence of the hydrogen entry promoter has a marked effect on the SCC resistance of the alloy under the appropriate type of mechanical loading (Mode I).

Pure α titanium suffers little damage by hydrogen at low concentrations (<200 ppm), but impurities can greatly increase its sensitivity to hydrogen. Thus, commercially pure titanium exhibits a

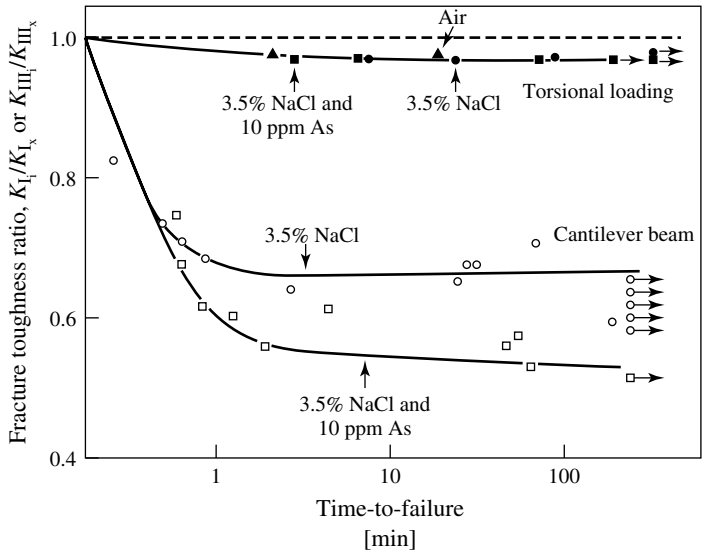


Fig. 23 Resistance to SCC of Ti-8Al-1Mo-1V in 3.5% NaCl solution with and without arsenic present and at a potential of −500 mV (SCE) [196]. (Reprinted with permission from the copyright holder, The Minerals, Metals & Materials Society.)

transition from ductile to brittle fracture at significantly lower concentrations than those required in pure titanium.

In the $\alpha-\beta$ alloys, hydrogen segregates to $\alpha-\beta$ interfaces and forms hydride phases that tend to grow preferentially into the α phase [197]. Cracking has been found to occur at the $\alpha-\beta$ interface, both in SCC [198] and in hydrogen [199].

High-strength, aged β titanium alloys are susceptible to environmentally assisted cracking in aqueous halide solutions under certain conditions [200–202]. This cracking has been attributed to hydrogen embrittlement [201], because $\alpha-\beta$ titanium alloys are susceptible to hydrogen embrittlement and because both gaseous hydrogen and cathodically precharged hydrogen embrittle β titanium alloys [203, 204]. A further reason is that high-strength bcc steels are very susceptible to hydrogen embrittlement. Environmentally assisted cracking in modern alloys such as Beta-C and Beta-21S is almost entirely intergranular. In older alloys, it can also involve transgranular cleavage or quasi-cleavage. Unaged, solution-treated β titanium alloys are resistant to environmentally assisted cracking in chloride solutions and undergo fracture by transgranular microvoid formation.

References

1. B. F. Brown, C. T. Fujii, E. P. Dahlberg, *J. Electrochem. Soc.* **1969**, *116*, 218, 219.
2. A. J. Sedriks, J. A. S. Green, D. L. Novak, *Corrosion* **1971**, *27*, 198–202.
3. J. O'M. Bockris in *Modern Aspects of Electrochemistry* (Eds.: J. O'M. Bockris, B. E. Conway), Academic Press, New York, 1954, pp. 180–276, Vol. 1.
4. E. Gileadi, B. E. Conway in *Modern Aspects of Electrochemistry* (Eds.: J. O'M. Bockris, B. E. Conway), Butterworths, Washington, D.C., 1964, pp. 347–442, Vol. 3.
5. J. O'M. Bockris, A. K. N. Reddy, *Modern Electrochemistry*, Plenum Press, New York, 1970.
6. J. McBreen, M. A. Genshaw in *Fundamental Aspects of Stress Corrosion Cracking* (Eds.: R. W. Staehle, A. J. Forty, D. van Rooyen), NACE, Houston, Tex., 1969, pp. 51–63.
7. J. O'M. Bockris, J. McBreen, L. Nanis, *J. Electrochem. Soc.* **1965**, *112*, 1025–1031.
8. E. G. Dafft, K. Bohnenkamp, H. J. Engell, *Corros. Sci.* **1979**, *19*, 591–612.
9. J. S. L. Leach in *Stress Corrosion Cracking and Hydrogen Embrittlement of Iron Base Alloys* (Eds.: R. W. Staehle, J. Hochmann, R. D. McCright et al.), NACE, Houston, Tex., 1977, pp. 16–20.
10. R. A. Oriani in *Fundamental Aspects of Stress Corrosion Cracking* (Eds.: R. W. Staehle, A. J. Forty, D. van Rooyen), NACE, Houston, Tex., 1969, pp. 32–49.
11. A. N. Frumkin in *Advances in Electrochemistry and Electrochemical Engineering* (Ed.: P. Delahay), Interscience Publishers, New York, 1963, pp. 287–391, Vol. 3.
12. T. Zakroczymski in *Hydrogen Degradation of Ferrous Alloys* (Eds.: R. A. Oriani, J. P. Hirth, M. Smialowski), Noyes Publications, Park Ridge, N. J., 1985, pp. 215–250.
13. R. N. Iyer, H. W. Pickering, M. Zamanzadeh, *Scr. Metall.* **1988**, *22*, 911–916.
14. R. N. Iyer, H. W. Pickering, M. Zamanzadeh, *J. Electrochem. Soc.* **1989**, *136*, 2463–2470.
15. R. N. Iyer, I. Takeuchi, M. Zamanzadeh et al., *Corrosion* **1990**, *46*, 460–468.
16. C. D. Kim, B. E. Wilde, *J. Electrochem. Soc.* **1971**, *118*, 202–206.
17. H. Flitt, J. O'M. Bockris, *Int. J. Hydrogen Energy* **1982**, *7*, 411.
18. J. F. Newman, L. L. Shreir, *Corros. Sci.* **1969**, *9*, 631–641.
19. T. Zakroczymski, Z. Szklarska-Smialowska, M. Smialowski, *Werkst. Korros.* **1976**, *27*, 625.
20. W. Beck, A. L. Glass, E. Taylor, *J. Electrochem. Soc.* **1965**, *112*, 53–59.
21. H. Inai, C. Kemball, *Proc. R. Soc.* **1968**, *A302*, 399–407.
22. A. Kawashima, K. Hashimoto, S. Shimodaira, *Corrosion* **1976**, *32*, 321–331.
23. E. Protopopoff, P. Marcus, *J. Electrochem. Soc.* **1988**, *135*, 3073–3075.
24. G. Trabanelli, F. Zucchi, G. Gullini et al., *Br. Corros. J.* **1969**, *4*, 212–215, 267–270.

25. I. L. Rozenfeld, D. M. Kramarenko, E. N. Lantseva, *Zashch. Metal.* **1967**, *3*, 172; cited in ref. [12].
26. R. L. Martin, *Mater. Performance* **1980**, *19*(6), 20–23.
27. K. van Gelder, M. J. Simon Thomas, C. J. Kroese, *Corrosion* **1986**, *42*, 36–43.
28. R. L. Martin, *Mater. Performance* **1983**, *22*(9), 33–36.
29. S. M. Wilhelm, D. Abayarathna, *Corrosion* **1994**, *50*, 152–159.
30. E. Jackson, M. J. Wilkinson, *Br. Corros. J.* **1976**, *11*, 208–211.
31. M. Zamanzadeh, A. Allam, C. Kato et al., *J. Electrochem. Soc.* **1982**, *129*, 284–289.
32. G. Zheng, B. N. Popov, R. E. White, *J. Electrochem. Soc.* **1993**, *140*, 3153–3158.
33. B. N. Popov, G. Zheng, R. E. White, *Corros. Sci.* **1994**, *36*, 2139–2153.
34. D. H. Coleman, G. Zheng, B. N. Popov et al., *J. Electrochem. Soc.* **1996**, *143*, 1871–1874.
35. B. N. Popov, G. Zheng, R. E. White, *Corrosion* **1995**, *51*, 429–435.
36. R. A. Oriani, *Ann. Rev. Mater. Sci.* **1978**, *8*, 327–357.
37. P. K. Subramanyan in *Comprehensive Treatise of Electrochemistry* (Eds.: J. O'M. Bockris, B. E. Conway, E. Yeager et al.), Plenum Press, New York, 1981, pp. 411–462, Vol. 4.
38. J. P. Hirth, *Metall. Trans.* **1980**, *11A*, 861–890.
39. N. R. Quick, H. H. Johnson, *Acta Metall.* **1978**, *26*, 903–907.
40. H. H. Johnson, *Metall. Trans.* **1988**, *19A*, 2371–2387.
41. J. O'M. Bockris, M. A. Genshaw, M. Fullenwider, *Electrochim. Acta* **1970**, *15*, 47–60.
42. W. Beck, J. O'M. Bockris, M. A. Genshaw et al., *Metall. Trans.* **1971**, *2*, 883–888.
43. H. Peisl in *Hydrogen in Metals, Topics in Applied Physics* (Eds.: G. Alefeld, J. Völkl), Springer-Verlag, New York, 1978, pp. 53–74, Vol. 28.
44. R. Oriani, *Trans. Metall. Soc. AIME* **1966**, *236*, 1368, 1369.
45. J. O'M. Bockris, W. Beck, M. A. Genshaw et al., *Acta Metall.* **1971**, *19*, 1209–1218.
46. J. C. M. Li, R. A. Oriani, L. S. Darken, *Z. Phys. Chem. Frankfurt* **1966**, *49*, 271–290.
47. H. A. Wriedt, R. A. Oriani, *Acta Metall.* **1970**, *18*, 753–760.
48. P. Kedzierzawski, in *Hydrogen Degradation of Ferrous Alloys* (Eds.: R. A. Oriani, J. P. Hirth, M. Smialowski), Noyes Publications, Park Ridge, New Jersey, 1985, pp. 251–270.
49. J. Völkl, G. Alefeld in *Hydrogen in Metals, Topics in Applied Physics* (Eds.: G. Alefeld, J. Völkl), Springer-Verlag, New York, 1978, pp. 321–348, Vol. 28.
50. R. A. Oriani, *Acta Metall.* **1970**, *18*, 147–157.
51. J. G. Early, *Acta Metall.* **1978**, *26*, 1215–1223.
52. V. Breger, E. Gileadi, *Electrochim. Acta* **1971**, *16*, 177–190.
53. M. Fullenwider, *J. Electrochem. Soc.* **1975**, *122*, 648–650.
54. R. M. Latanision, M. Kurkela, *Corrosion* **1983**, *39*, 174–181.
55. Su-Il Pyun, R. A. Oriani, *Corros. Sci.* **1989**, *29*, 485–496.
56. P. Bastien, P. Azou, *C. R. Acad. Sci. Paris* **1951**, *232*, 1845–1848.
57. J. K. Tien, A. W. Thompson, I. M. Bernstein et al., *Metall. Trans.* **1976**, *7A*, 821–829.
58. J. A. Donovan, *Metall. Trans.* **1976**, *7A*, 1677–1683.
59. M. R. Louthan Jr., G. R. Caskey Jr., J. A. Donovan et al., *Mater. Sci. Eng.* **1972**, *10*, 357–368.
60. M. Kurkela, R. M. Latanision, *Scr. Metall.* **1979**, *13*, 927–932.
61. R. Otsuka, M. Isaji, *Scr. Metall.* **1981**, *15*, 1153–1156.
62. T. Zakroczymski, *Corrosion* **1985**, *41*, 485–489.
63. G. S. Frankel, R. M. Latanision, *Metall. Trans.* **1986**, *17A*, 861–867, 869–875.
64. G. M. Pressouyre, *Metall. Trans.* **1979**, *10A*, 1571–1573.
65. I. M. Bernstein, G. M. Pressouyre in *Hydrogen Degradation of Ferrous Alloys* (Eds.: R. A. Oriani, J. P. Hirth et al.), Noyes Publications, Park Ridge, N. J., 1985, pp. 641–685.
66. S.-M. Lee, J.-Y. Lee, *Metall. Trans.* **1986**, *17A*, 181–187.
67. G. M. Pressouyre, I. M. Bernstein, *Acta Metall.* **1979**, *27*, 89–100.
68. G. M. Pressouyre, I. M. Bernstein, *Metall. Trans.* **1978**, *9A*, 1571–1580.
69. J. Friedel, *Ber. Bunsen-Ges.* **1972**, *76*, 828–831.
70. P. Kedzierzawski in *Hydrogen Degradation of Ferrous Alloys* (Eds.: R. A. Oriani, J. P. Hirth, M. Smialowski), Noyes Publications, Park Ridge, N. J., 1985, pp. 271–288.

71. B. G. Pound, *Acta Metall.* **1990**, *38*, 2373–2381.
72. B. G. Pound, *Corrosion* **1991**, *47*, 99–104.
73. D. A. Mezzanotte, J. A. Kargol, N. F. Fiore, *Metall. Trans.* **1982**, *13A*, 1181–1186.
74. R. Gibala, D. S. DeMiglio in *Hydrogen Effects in Metals* (Eds.: I. M. Bernstein, A. W. Thompson), TMS, Warrendale, Pa., 1981, pp. 113–122.
75. T. Asaoka, G. Lapasset, M. Aucouturier et al., *Corrosion* **1978**, *34*, 39–47.
76. M. Weinstein, J. F. Elliott, *Trans. AIME* **1963**, *227*, 382–393.
77. B. T. Lee, J. Y. Lee, S. H. Hwang, *Arch. Eisenhuttenwes.* **1982**, *53*, 71–76.
78. W. D. Wilson, S. C. Keeton in *Advanced Techniques for Characterizing Hydrogen in Metals* (Eds.: N. F. Fiore, B. J. Berkowitz), TMS AIME, Warrendale, Pa., 1981, pp. 3–22.
79. G. J. Thomas in *Hydrogen Effects in Metals* (Eds.: I. M. Bernstein, A. W. Thompson), TMS, Warrendale, Pa., 1981, p. 77–85.
80. A. Atrens, D. Mezzanotte, N. F. Fiore et al., *Corros. Sci.* **1980**, *20*, 673–684.
81. K.-T. Kim, S.-S. Kim, S.-I. Pyun, *J. Korean Inst. Metals* **1988**, *26*, 568–572.
82. T.-P. Perng, C. J. Altstetter, *Acta Metall.* **1986**, *34*, 1771–1781.
83. M. R. Louthan Jr., R. G. Derrick, *Corros. Sci.* **1975**, *15*, 565–577.
84. K. L. Wilson, M. I. Baskes, *J. Nucl. Mater.* **1978**, *76/77*, 291–297.
85. K. W. Lange, H. J. Koning, *Proceedings of the Second International Conference on Hydrogen in Metals* (Ed.: P. Azou), 1973, Paper 1A5.
86. B. E. Wilde, C. D. Kim, J. C. Turn, *Corrosion* **1982**, *38*, 515–524.
87. E. Lunarska, A. Zielinski in *Hydrogen Degradation of Ferrous Alloys* (Eds.: R. A. Oriani, J. P. Hirth, M. Smialowski), Noyes Publications, Park Ridge, N. J., 1985, pp. 289–320.
88. Ch. A. Wert in *Hydrogen in Metals, Topics in Applied Physics* (Eds.: G. Alefeld, J. Völkl), Springer-Verlag, New York, 1978, pp. 305–330, Vol. 28.
89. A. J. Kumnick, H. H. Johnson, *Acta Metall.* **1980**, *28*, 33–39.
90. A. Turnbull, M. W. Carroll, D. H. Ferriss, *Acta Metall.* **1989**, *37*, 2039–2046.
91. M. Aucouturier, G. Lapasset, T. Asaoka, *Metallography* **1978**, *11*, 5–21.
92. P. Lacombe, M. Aucouturier, J. P. Laurent et al. in *Stress Corrosion Cracking and Hydrogen Embrittlement of Iron Base Alloys* (Eds.: R. W. Staehle, J. Hochmann, R. D. McCright et al.), NACE, Houston, Tex., 1977, pp. 423–431.
93. A. M. Brass, A. Chanfreau, J. Chêne in *Hydrogen Effects on Material Behavior* (Eds.: N. R. Moody, A. W. Thompson), The Minerals, Metals, and Materials Society, Warrendale, Pa., 1990, pp. 19–31.
94. J. Y. Lee, J. L. Lee, W. Y. Choo in *Current Solutions to Hydrogen Problems in Steels* (Eds.: C. G. Interrante, G. M. Pressouyre), ASM, Materials Park, Ohio, 1982, pp. 423–427.
95. S. M. Lee, J. Y. Lee, *Acta Metall.* **1987**, *35*, 2695–2700.
96. B. G. Pound in *Modern Aspects of Electrochemistry* (Eds.: J. O'M. Bockris, B. E. Conway, R. E. White), Plenum Press, New York, 1993, No. 25, pp. 63–133.
97. N. Boes, H. Züchner, *J. Less-Common Met.* **1976**, *49*, 223–240.
98. M. A. V. Devanathan, Z. Stachurski, *Proc. R. Soc. London, Ser. A* **1962**, *270*, 90–102.
99. J. McBreen, L. Nanis, W. Beck, *J. Electrochem. Soc.* **1966**, *113*, 1218–1222.
100. L. Nanis, T. K. G. Namboodhiri, *J. Electrochem. Soc.* **1972**, *119*, 691–694.
101. E. Schmidt, H. Siegenthaler, *Helv. Chim. Acta* **1970**, *53*, 321–330.
102. P. H. Pumphrey, *Scr. Metall.* **1980**, *14*, 695–701.
103. A. McNabb, P. K. Foster, *Trans. Metall. Soc. AIME* **1963**, *227*, 618–627.
104. M. Iino, *Acta Metall.* **1982**, *30*, 367–375.
105. J. B. Leblond, D. Dubois, *Acta Metall.* **1983**, *31*, 1459–1469, 1471–1478.
106. R. McKibbin, R. M. Sharp, D. A. Harrington et al., *Acta Metall.* **1987**, *35*, 253–262.
107. B. G. Pound, *Corrosion* **1989**, *45*, 18–25.
108. B. G. Pound, R. M. Sharp, G. A. Wright, *Acta Metall.* **1987**, *35*, 263–270.
109. P. Kedzierzawski, Z. Szklarska-Smialowska, M. Smialowski, *J. Electrochem. Soc.* **1980**, *127*, 2550–2555.
110. M. A. Fullenwider, *Hydrogen Entry and Action in Metals*, Pergamon Press, New York, 1983.
111. T. S. Elleman, K. Verghese, *J. Nucl. Mater.* **1974**, *53*, 299–306.
112. K. Zhao, J. Xiao, M. Hu, *Werkst. Korros.* **1985**, *36*, 117–119.
113. R. C. Miller, F. M. Smits, *Phys. Rev.* **1957**, *107*, 65–70.

114. R. Ash, R. M. Barrer, D. G. Palmer, *Br. J. Appl. Phys.* **1965**, *16*, 873–884.
115. R. M. Torresi, O. R. Camara, C. P. De Pauli, *Electrochim. Acta* **1987**, *32*, 1357–1363.
116. W. Raczynski, *Arch. Hutn.* **1958**, *3*, 59.
117. A. F. Jevsieyev, *Electrokhimiya* **1970**, *6*, 841.
118. G. M. Pressouyre, I. M. Bernstein, *Corros. Sci.* **1978**, *18*, 819–833.
119. B. G. Pound, *Corrosion* **1990**, *46*, 50–56.
120. A. Turnbull, R. G. Ballinger, I. S. Hwang et al. in *Hydrogen Effects on Material Behavior* (Eds.: N. R. Moody, A. W. Thompson), The Minerals, Metals, and Materials Society, Warrendale, Pa., 1990, pp. 121–130.
121. W. Beck, J. O'M. Bockris, J. McBreen et al., *Proc. R. Soc. London, Ser. A* **1966**, *290*, 220–235.
122. J. Bowker, G. R. Piercy, *Metall. Trans.* **1985**, *16A*, 715–719.
123. S. Schuldinger, J. P. Hoare, *J. Electrochem. Soc.* **1956**, *103*, 178–181.
124. G. R. Caskey, W. L. Pillinger, *Metall. Trans.* **1975**, *6A*, 467–476.
125. T. Tsuru, R. M. Latanision, *Scr. Metall.* **1982**, *16*, 575–578.
126. J. P. Hirth, H. H. Johnson, *Corrosion* **1976**, *32*, 3–26.
127. R. D. Merrick, *Mater. Performance* **1989**, *28*(2), 53–55.
128. M. A. Al-Anezi, G. S. Frankel, A. K. Agrawal, *Corrosion* **1999**, *55*, 1101–1109.
129. M. Elboujdaini in *Uhlig's Corrosion Handbook* (Ed.: R. W. Revie), 2nd ed., John Wiley & Sons, New York, 2000, pp. 205–220.
130. W. Bruckhoff, O. Geier, K. Hofbauer, Rupture of a sour gas line due to stress oriented hydrogen induced cracking; failure analyses, experimental results and corrosion prevention, *CORROSION/85*, Paper No. 389, NACE, Houston, Tex., 1985.
131. J.-L. Crolet, *Mater. Performance* **2000**, *39*(3), 86–90.
132. G. M. Pressouyre, I. M. Bernstein, *Metall. Trans.* **1981**, *12A*, 835–844.
133. G. M. Pressouyre, *Acta Metall.* **1980**, *28*, 895–911.
134. J. R. Scully, J. A. Van Den Avyle, M. J. Cieslak et al., *Metall. Trans.* **1991**, *22A*, 2429–2444.
135. A. W. Thompson, B. A. Wilcox, *Scr. Metall.* **1972**, *6*, 689–696.
136. B. G. Pound, *Acta Mater.* **1998**, *46*, 5733–5743.
137. N. R. Moody, S. L. Robinson, J. E. Angelo et al. in *Hydrogen Effects on Material Behavior* (Eds.: A. W. Thompson, N. R. Moody), The Minerals, Metals, and Materials Society, Warrendale, Pa., 1996, pp. 967–977.
138. B. G. Pound, *Corros. Sci.* **2000**, *42*, 1269–1281, 1941–1956.
139. D. P. Dautovich, S. Floreen in *Stress Corrosion Cracking and Hydrogen Embrittlement of Iron Base Alloys* (Eds.: R. W. Staehle, J. Hochman, R. D. McCright et al.), NACE, Houston, Tex., 1977, pp. 798–815.
140. A. Turnbull, R. B. Hutchings, A. T. May in *Hydrogen Effects on Material Behavior* (Eds.: N. R. Moody, A. W. Thompson), The Minerals, Metals, and Materials Society, Warrendale, Pa., 1990, pp. 223–230.
141. R. P. Wei, M. Gao in *Hydrogen Degradation of Ferrous Alloys* (Eds.: R. A. Oriani, J. P. Hirth, M. Smialowski), Noyes Publications, Park Ridge, N. J., 1985, pp. 579–607.
142. C. Zapffe, C. Sims, *Trans. AIME* **1941**, *145*, 225–261.
143. A. S. Tetelman, W. D. Robertson, *Trans. TMS-AIME* **1962**, *224*, 775–783.
144. N. J. Petch, *Philos. Mag.* **1956**, *1*, 331–337.
145. N. J. Petch, P. Stables, *Nature* **1952**, *169*, 842, 843.
146. A. R. Troiano, *Trans. ASM* **1960**, *52*, 54–80.
147. R. A. Oriani in *Stress Corrosion Cracking and Hydrogen Embrittlement of Iron Base Alloys* (Eds.: R. W. Staehle, J. Hochmann, R. D. McCright et al.), NACE, Houston, Tex., 1977, pp. 351–358.
148. R. A. Oriani in *Environment-Induced Cracking of Metals* (Eds.: R. P. Gangloff, M. B. Ives), NACE 10, NACE, Houston, Tex., 1988, pp. 439–448.
149. C. D. Beachem, *Metall. Trans.* **1972**, *3*, 437–451.
150. D. G. Westlake, *Trans. ASM* **1969**, *62*, 1000–1006.
151. S. Gahr, M. L. Grossbeck, H. K. Birnbaum, *Acta Metall.* **1977**, *25*, 125–133.
152. H. K. Birnbaum in *Environment-Induced Cracking of Metals* (Eds.: R. P. Gangloff, M. B. Ives), NACE 10, NACE, Houston, Tex., 1988, pp. 21–29.
153. R. B. Benson, R. K. Dann, L. W. Roberts, *Trans. Metall. Soc. AIME* **1968**, *242*, 2199–2205.
154. N. Narita, H. K. Birnbaum, *Scr. Metall.* **1980**, *14*, 1355–1358.

155. A. W. Thompson, I. M. Bernstein, *Advances in Corrosion Science and Technology* (Eds.: R. W. Staehle, M. G. Fontana), Plenum Press, New York, 1979, pp. 53–175, Vol. 7.
156. E. Snape, *Corrosion* **1968**, *24*, 261–282.
157. J. W. Kennedy, J. A. Whittaker, *Corros. Sci.* **1968**, *8*, 359–375.
158. A. S. Tetelman in *Fundamental Aspects of Stress Corrosion Cracking* (Eds.: R. W. Staehle, A. J. Forty, D. Van Rooyen), NACE, Houston, Tex., 1969, pp. 446–460.
159. B. B. Rath, I. M. Bernstein, *Metall. Trans.* **1971**, *2*, 2845–2851.
160. A. W. Thompson, I. M. Bernstein, *Proceedings of the 2nd International Conference on Hydrogen in Metals*, Pergamon Press, Oxford, 1978, Paper 3A-6, Vol. 10.
161. A. R. Troiano in *Hydrogen in Metals* (Eds.: I. M. Bernstein, A. W. Thompson), ASM, Materials Park, Ohio, 1974, pp. 3–16.
162. S. K. Banerji, C. J. McMahon, H. C. Feng, *Metall. Trans.* **1978**, *9A*, 237–247.
163. R. P. Wei, G. W. Simmons, *Scr. Metall.* **1976**, *10*, 153–157.
164. R. Viswanathan, S. J. Hudak Jr., *Metall. Trans.* **1977**, *8A*, 1633–1637.
165. G. Sandoz, *Metall. Trans.* **1971**, *2*, 1055–1063.
166. G. Sandoz, *Metall. Trans.* **1972**, *3*, 1169–1176.
167. T. Fujita, Y. Yamada in *Stress Corrosion Cracking and Hydrogen Embrittlement of Iron Base Alloys* (Eds.: R. W. Staehle, J. Hochmann, R. D. McCright et al.), NACE, Houston, Tex., 1977, pp. 736–746.
168. M. H. Peterson, B. F. Brown, R. L. Newbegin et al., *Corrosion* **1967**, *23*, 142–148.
169. T. J. McCaffrey, *Adv. Mater. Processes* **1992**, *9*, 47–50.
170. S. K. Yen, Y. C. Tsai, *J. Electrochem. Soc.* **1996**, *143*, 2736–2741.
171. A. W. Thompson in *Hydrogen in Metals* (Eds.: I. M. Bernstein, A. W. Thompson), ASM, Materials Park, Ohio, 1974, pp. 91–101.
172. A. W. Thompson, I. M. Bernstein, *Rev. Coatings Corros.* **1975**, *2*, 3–44.
173. R. C. Newman, A. Mehta in *Environment-Induced Cracking of Metals* (Eds.: R. P. Gangloff, M. B. Ives), NACE 10, NACE, Houston, Tex., 1988, pp. 489–509.
174. R. R. Gaugh, Sulfide stress cracking of precipitation-hardening stainless steels, CORROSION/77, Paper No. 109, NACE, Houston, Tex., 1977.
175. H. Spaehn in *Environment-Induced Cracking of Metals* (Eds.: R. P. Gangloff, M. B. Ives), NACE 10, NACE, Houston, Tex., 1988, pp. 449–487.
176. R. H. Jones, S. M. Bruemmer, M. T. Thomas et al., *Metall. Trans.* **1983**, *14A*, 223–232, 1729–1736.
177. D. Lassila, H. K. Birnbaum, *Acta Metall.* **1987**, *35*, 1815–1822.
178. A. W. Thompson, *Metall. Trans.* **1974**, *5*, 1855–1861.
179. P. Blanchard, A. R. Troiano, *Mem. Sci. Rev. Metall.* **1960**, *57*, 409–414.
180. G. C. Smith in *Hydrogen in Metals* (Eds.: I. M. Bernstein, A. W. Thompson), ASM, Materials Park, Ohio, 1974, pp. 485–511.
181. J. D. Frandsen, N. E. Paton, H. L. Marcus, *Scr. Metall.* **1973**, *7*, 409–414.
182. R. J. Walter, R. P. Jewett, W. T. Chandler, *Mater. Sci. Eng.* **1969-1970**, *5*, 98–110.
183. D. L. Dull, L. Raymond, *Metall. Trans.* **1973**, *4*, 1635–1637.
184. R. D. Kane, M. Watkins, D. F. Jacobs et al., *Corrosion* **1977**, *33*, 309–320.
185. B. J. Berkowitz, R. D. Kane, *Corrosion* **1980**, *36*, 24–29.
186. K. Mummert, H. J. Engelmann, S. Schwarz et al. in *Hydrogen Effects on Material Behavior* (Eds.: A. W. Thompson, N. R. Moody), The Minerals, Metals, and Materials Society, Warrendale, Pa., 1996, pp. 679–688.
187. J. L. Mihelich, A. R. Troiano, *Nature* **1963**, *197*, 996, 997.
188. J. A. Harris, R. C. Scarberry, C. D. Stephens, *Corrosion* **1972**, *28*, 57–62.
189. J. D. Fransen, H. L. Marcus, A. S. Tetelman in *Effect of Hydrogen on Behavior of Materials* (Eds.: A. W. Thompson, I. M. Bernstein), AIME, New York, 1976, pp. 299–306.
190. N. E. Paton, J. C. Williams in *Titanium and Titanium Alloys – Source Book*, ASM, Materials Park, Ohio, 1982, pp. 185–207.
191. G. A. Young, J. R. Scully, *Scr. Metall. Mater.* **1993**, *28*, 507–512.
192. M. A. Gaudett, J. R. Scully, Environmentally Assisted Cracking of High Strength Beta Titanium Alloys, Report to the Office of Naval Research, Grant No. N000014-91-J-4164, 1994.
193. G. A. Young, J. R. Scully in *Beta Titanium Alloys in the 1990's* (Eds.: D. Eylon,

R. R. Boyer, D. A. Koss), TMS, Warrendale, Pa., 1993, pp. 147–158.
194. J. A. S. Green, A. J. Sedriks, *Corrosion* **1972**, *28*, 226–230.
195. J. C. Scully in *Effect of Hydrogen on Behavior of Materials* (Eds.: A. W. Thompson, I. M. Bernstein), TMS-AIME, New York, 1976, pp. 129–147.
196. J. A. S. Green, H. W. Hayden, W. G. Montague in *Effect of Hydrogen on Behavior of Materials* (Eds.: A. W. Thompson, I. M. Bernstein), TMS-AIME, New York, 1976, pp. 200–215.
197. J. D. Boyd, *Trans. ASM* **1969**, *62*, 977–988.
198. M. J. Blackburn, J. A. Feeney, T. R. Beck in *Advances in Corrosion Science and Technology* (Eds.: R. W. Staehle, M. G. Fontana), Plenum Press, New York, 1973, pp. 67–292, Vol. 3.
199. H. G. Nelson in *Hydrogen in Metals* (Eds.: I. M. Bernstein, A. W. Thompson), ASM, Materials Park, Ohio, 1974, pp. 445–464.
200. J. A. Feeney, M. J. Blackburn, *Metall. Trans.* **1970**, *1*, 3309–3323.
201. L. M. Young, R. P. Gangloff in *Titanium '92, Science and Technology* (Eds.: F. H. Froes, I. L. Caplan), TMS-AIME, Warrendale, Pa., 1993, pp. 2209–2216, Vol. 3.
202. B. P. Somerday, J. A. Grandle, R. P. Gangloff, *Proceeding of the Tri-Service Conference on Corrosion*, The Army Materials Technology Laboratory, United States Army, 1994, pp. 375–392.
203. N. E. Paton, R. A. Spurling, C. G. Rhodes in *Hydrogen Effects in Metals* (Eds.: I. M. Bernstein, A. W. Thompson), TMS-AIME, Warrendale, Pa., 1981, pp. 269–279.
204. W. W. Gerberich, N. R. Moody, C. L. Jensen in *Hydrogen Effects in Metals* (Eds.: I. M. Bernstein, A. W. Thompson), TMS-AIME, Warrendale, Pa., 1981, pp. 731–745.

2.3 Corrosion of Alloys

Hermann Kaiser and Gerald A. Eckstein
Universität Erlangen-Nürnberg, Erlangen
Germany

2.3.1 Introduction

Metallic engineering materials are usually alloys that were designed to meet high demands with respect to mechanical strength, corrosion resistance, and other properties. Unfortunately, however, the corrosion of alloys is more complex and far less understood than that of pure metals. Apart from the occurrence of microgalvanic elements in multiphase alloys this results from differences in the dissolution rates of the alloy components that induce compositional and structural modifications in the alloy surface. The present section concentrates on the fundamental problem of the anodic dissolution of single-phase, binary alloys in the active state. This process proceeds either in a simultaneous or in a selective mode. In the former, a steady state is established in which the components dissolve at a rate proportional to their concentration in the alloy. In the latter, preferential dissolution of the less noble component (dealloying) persists. Rate control of the electrodissolution of individual alloy components may originate from reaction steps that are absent or irrelevant for the anodic dissolution of pure metals, and the debate about the correct "mechanism" of alloy dissolution continues. Following some basic thermodynamic considerations, the discussion of alloy dissolution therefore starts with the academic, but straightforward behavior of liquid alloys in aqueous solutions. Low melting point solid alloys are considered next since they are best suited to perform fundamental studies concerning the role of solid-state diffusion processes in dealloying at ambient temperature. Dealloying of certain low-melting alloys is also of technical relevance. For higher-melting engineering materials and binary noble metal alloys of predominant scientific interest, the simultaneous and selective dissolution modes are discussed in greater detail. Particular attention is paid to the formation of mechanically weak, porous microstructures that result from the dealloying of these materials and appear to be associated with the phenomenon of stress corrosion cracking (see Chapter 4.4). In addition to this, a survey of various proposals with respect to the dealloying mechanism is given. In the end, recent experimental attempts to clarify this mechanism by high-resolution microscopic methods such as scanning tunneling microscopy (STM) are presented.

2.3.2 Basic Thermodynamics

For a single-phase binary alloy A–B, the two anodic partial reactions of metal dissolution are

$$A_{alloy} \longrightarrow A^{n_{A^+}} + n_A e^- \qquad (1a)$$

$$B_{alloy} \longrightarrow B^{n_{B^+}} + n_B e^- \qquad (1b)$$

Complete equilibrium of the alloy electrode will only be established if the equilibrium potentials of both reactions, as given by the Nernst equations (see Chapter 1.2)

$$E_A = E_A^0 + \frac{RT}{n_A F} \ln \frac{a_{A^{nA^+}}}{f_A X_A} \qquad (2a)$$

and

$$E_B = E_B^0 + \frac{RT}{n_B F} \ln \frac{a_{B^{nB^+}}}{f_B X_B} \qquad (2b)$$

are equal, that is, $E_A = E_B$. Rewriting this condition, where $E^0_{A,B}$ are the standard electrode potentials of the alloy components, $a_{A^{nA+}}$ and $a_{B^{nB+}}$ are the activities of the ions in the solution, $X_{A,B}$ and $f_{A,B}$ denote their atom fraction and activity coefficient in the alloy phase, respectively, and all other quantities have their usual meaning, the equilibrium condition may be expressed in the form

$$\frac{(a_{A^{nA+}})^{1/n_A}}{(a_{B^{nB+}})^{1/n_B}} = \exp\left[(E^0_B - E^0_A)\frac{F}{RT}\right] \times \frac{(f_A X_A)^{1/n_A}}{(f_B X_B)^{1/n_B}} \quad (3)$$

From this equation, it becomes obvious that the ratio of the equilibrium ion activities in the solution is linked with the alloy composition as expressed by the bulk atom fractions of the components, X_A and $X_B = 1 - X_A$. In general, therefore, the establishment of complete equilibrium for an alloy electrode requires a change of composition both of the alloy phase and of the electrolyte solution [1]. For solid alloys at ambient temperature, compositional changes (due to the preferential dissolution of one alloy component) will be restricted to the uppermost atomic layers. Further equilibration between the surface and the bulk of the alloy is prevented by solid-state diffusion limitations. Complete thermodynamic equilibrium for both components is therefore expected to evolve only with liquid alloys in which the diffusivity at ambient temperature is extremely high (for dilute Zn-amalgams, e.g., interdiffusion coefficients $\tilde{D}_{Zn}$ of the order of 10^{-5} cm^2 s^{-1} have been reported under these conditions [2]).

In the case of a large difference of the standard potentials of the components, $\Delta E^0 = E^0_B - E^0_A$, the equilibrium potential of the alloy electrode, E_{AB}, with A being the less noble component, is virtually equal to the equilibrium potential of A. As an example, the equilibrium potential, E, of a dilute liquid zinc amalgam electrode in a solution containing Zn ions is given by

$$E \cong E^0_{Zn/Zn^{2+}} + \frac{RT}{2F}\ln\frac{a_{Zn^{2+}}}{a_{Zn(\text{in Hg})}} \quad (4)$$

[3]. There is evidence that the open circuit potential (OCP) of solid alloy electrodes with large ΔE^0 in deaerated solutions may also be determined by the less noble component, A. However, since there is no equilibration between the surface and the bulk, such OCP reflect the surface activity of the less noble component rather than that of the bulk [4]. A more detailed discussion of the thermodynamics of alloy electrodes with due consideration of the Gibbs energy of mixing of the alloy phase has been given by Heusler [5].

2.3.3 Anodic Dissolution of Liquid Alloy Electrodes

Some basic aspects of alloy dissolution are best illustrated by the behavior of a liquid binary alloy A–B. This is due (1) to the absence of crystallization overvoltage and dissolution induced structural surface modifications [6] as well as (2) to the high diffusivity in the alloy phase that provides for the reactant supply at the alloy/electrolyte interface if one alloy component dissolves preferentially (at a higher rate than the other) [7]. Provided that the standard electrode potential difference of the components, $\Delta E^0 = E^0_B - E^0_A$, is large ($\Delta E^0 > RT/F$) and their charge transfer reactions are fast, one expects a schematic polarization curve as shown by Fig. 1(a). For $E_A < E < E_B$, only the less noble component, A, dissolves (“selective dissolution” or “dealloying”), the partial anodic

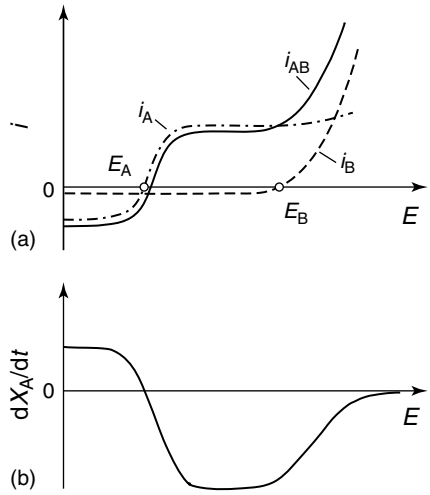


Fig. 1 (a) Schematic polarization curve of a liquid alloy A–B (total current j_{AB}) and partial polarization curves of the alloy components (partial currents j_A and j_B) at constant atom fraction, X_A. The electrolyte solution is considered to contain ions of both components that are cathodically deposited at $E < E_A$ and $E < E_B$, respectively. Transport limitations for the cathodic deposition as well as for the anodic dissolution of A are indicated. (b) Variation of X_A with time in dependence on the electrode potential. Note that $dX_A/dt > 0$ results from cathodic deposition of A; whereas, $dX_A/dt < 0$ indicates preferential dissolution of that component. (From Ref. [1].)

polarization curve of A being characterized by a region of kinetic control at low, and by an anodic limiting current due to mass transfer (diffusion) in the alloy phase at high overpotentials, respectively. At $E > E_B$, there is increasing codissolution of the more noble component, B, and throughout the total current of metal dissolution, j_{AB}, is thought to be given by the superposition of the partial anodic currents of the alloy components, that is,

$$j_{AB} = j_A + j_B \tag{5}$$

Because of the high diffusivity of liquid alloys, the selective dissolution of component A results in a continuous variation of the average alloy composition, dX_A/dt, which is given by

$$\frac{dX_A}{dt} = -\frac{1}{m_A + m_B} \times \left[(1 - X_A)\frac{j_A}{n_A F} - X_A \frac{j_B}{n_B F} \right] \tag{6}$$

where m_A and m_B are the numbers of moles of the alloy components [1]. As schematically illustrated by Fig. 1(b), selective dissolution of A at $E > E_A$ is indicated by negative values of dX_A/dt. For $E > E_B$, however, dX_A/dt gradually approaches zero. This corresponds to a transition from selective dissolution to a stationary state of simultaneous (nonpreferential) dissolution of the components. From Eq. (6), it may be derived that simultaneous dissolution only occurs if

$$Z_A \equiv \frac{j_A n_B X_B}{j_B n_A X_A} = 1 \tag{7}$$

where Z_A is called the selectivity coefficient of A. Therefore, selective dissolution of A requires that $Z_A > 1$. This criterion is also applicable to solid electrodes.

A more complicated situation will arise, however, if $\Delta E^0 = E_B^0 - E_A^0$ is small. In this case, the kinetics of the charge transfer reactions of both components may dominate and selective dissolution becomes generally less important [1].

2.3.4 Anodic Dissolution of Low-Melting Solid Alloys

The interdiffusion coefficient $\widetilde{D}$ of solid electrodes at ambient temperature is by

many orders of magnitude lower than the diffusivity in liquid electrodes. However, alloy systems in which the ambient temperature corresponds to a large fraction of the melting temperature, T_M, still exhibit a relatively high diffusivity under these conditions. This is due to the proportionality between the activation energy of diffusion and T_M [8]. Moreover, the lability of surface atoms is increased in comparison to higher-melting alloys. This makes low-melting alloys particularly interesting for fundamental research in the field of alloy dissolution in aqueous electrolytes [9]. Also, their behavior may be considered to model the corrosion behavior of higher-melting alloys at elevated temperatures as encountered, for example, in molten-salt corrosion [10, 11].

2.3.4.1 Sn–In Alloys

Various investigations in the field of dealloying of low-melting alloys have concentrated on the selective dissolution of In from $Sn_{0.95}In_{0.05}$ alloys (that is, from the tin-rich terminal solid solution of In in Sn with β-Sn structure and incipient melting point, $T_M \approx 220\,^{\circ}C$). The kinetics of this process was shown to be largely governed by the solid-state diffusion of the electronegative component, In, in the alloy phase [12]. Potentiostatic anodic polarization under conditions in which the electropositive component, Sn, is stable, is therefore expected to induce a depletion of the electrode surface with In. Disregarding the concentration gradient of the ions simultaneously set up in solution [7] and the problem of a moving alloy/solution interface, the resulting concentration profile in the alloy phase may be calculated by the well-known solution of the diffusion equation for a semi-infinite medium with the initial (bulk) concentration, c_{In}^{b}, and fixed surface concentration, c_{In}^{s}, as follows

$$c_{In}(x,t) = c_{In}^{s} + (c_{In}^{b} - c_{In}^{s})\mathrm{erf}\left(\frac{x}{2\sqrt{\widetilde{D}t}}\right) \tag{8}$$

Here, x is the distance from the (original) alloy/electrolyte interface, $\widetilde{D}$ is the interdiffusion coefficient in the alloy, t is the polarization time, and c_{In}^{s} may be thought to represent a value of local equilibrium that may be derived from the Nernst equation (that is, $c_{In}^{s} \approx 0$ for overvoltages $\eta \gg RT/F$). As shown by Fig. 2, such profiles have been measured by electron beam microanalysis and the experimental values can be fitted by using Eq. (8) and a value of $\widetilde{D} = 5 \times 10^{-12}\ cm^2\ s^{-1}$ at $T = 298$ K [13]. The current density of In dissolution, i_{In}, can then be obtained by differentiating Eq. (8) with respect to x at $x = 0$ and inserting into Fick's first law, which yields

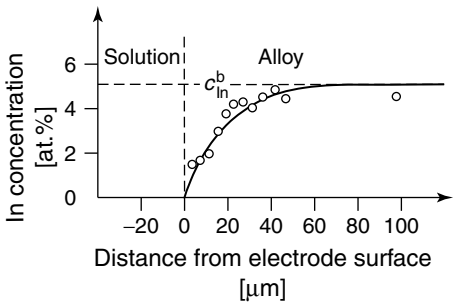


Fig. 2 Concentration profile of In in the near surface region of a $Sn_{95}In_5$ electrode due to the selective anodic dissolution of In in 3 N NaCl + 0, 01 N HCl at 25 °C and $E_H = -0.47$ V. Open circles from microprobe measurements, solid line calculated from Eq. (8) for $c_{In}^{s} = 0$ and $\widetilde{D} = 5 \times 10^{-12}\ cm^2\ s^{-1}$. (From Ref. [13].)

an expression of the form

$$i_{\mathrm{In}}(t) = zF\, c^{\mathrm{b}}_{\mathrm{In}} \sqrt{\frac{\widetilde{D}}{\pi t}} \qquad (9)$$

which is, in general electrochemistry, referred to as Cottrell equation (see, for example, Ref. [14]). In the present case, the validity of Eq. (9) was confirmed by chronoamperometry, yielding values of the interdiffusion coefficient, $\widetilde{D}$, that vary between $\approx 10^{-11}$ and about 10^{-12} cm^2 s^{-1}, depending on both electrode potential and temperature [12, 13, 15]. Reference is also made to constant current chronopotentiometry measurements. Assuming that the electrode potential of $Sn_{0.95}In_{0.05}$ is defined by the reversible reaction $In_{(Sn-In)} \rightleftharpoons In^{3+} + 3e^-$, its variation with time, as given by the Nernst equation

$$E_{\mathrm{In(Sn-In)}/\mathrm{In}^{3+}}(t) = E^0_{\mathrm{In}/\mathrm{In}^{3+}} + \frac{RT}{3F} \times \ln \frac{a^{\mathrm{s}}_{\mathrm{In}^{3+}}(t)}{a^{\mathrm{s}}_{\mathrm{In}}(t)} \qquad (10)$$

reflects an increase of the ion activity at the alloy/electrolyte interface, $a^{\mathrm{s}}_{\mathrm{In}^{3+}}$, and a decrease of the In activity in the alloy surface, $a^{\mathrm{s}}_{\mathrm{In}}$, due to the selective dissolution of In. However, upon reaching a characteristic transition time, τ, at which $a^{\mathrm{s}}_{\mathrm{In}}$ drops to zero, a change in the potential variation is observed, and by inserting τ into the Sand equation (see, for example, Ref. [14]) $\widetilde{D}$ may be determined. Making additional allowance for the steady state diffusion of In^{3+} ions in the electrolyte, this method yields values of $\widetilde{D}$ that agree well with those from chronoamperometry and other methods [15]. It should be noted, however, that all the values of $\widetilde{D}$ that have been determined with anodically polarized Sn–In electrodes appear to exceed the interdiffusion coefficient estimated by the extrapolation of high-temperature diffusivity data of the Sn–In system [16, 17] by orders of magnitude. A possible explanation for this discrepancy is given by the volume diffusion mechanism of the selective dissolution of higher-melting alloys (see below).

Similar to the dealloying behavior of other intermediate phases such as ε-Ag–Cd [18], the selective dissolution of In from a γ-Sn–In electrode with composition $Sn_{80}In_{20}$ was shown to result in a phase transformation with the Sn-rich terminal solid solution (β-Sn) as a product phase. Because of the close structural relationship of the parent and product phases this γ-Sn–In $\rightarrow$ β-Sn phase transformation is expected to produce negligible volume constraints [19]. Therefore, it should fulfill Wagner's criteria of diffusion driven phase transformations [20, 21], that is, (1) a plane (stable) interface between the product and parent phase develops, (2) the interface advances into the parent phase with a parabolic rate law, and (3) the composition of both phases at this interface is given by the equilibrium phase diagram (see Fig. 3). These expectations have been confirmed both by metallography and by electron beam microanalysis [13].

2.3.4.2 Zn–Cu Alloys

According to X-ray diffraction and light optical investigations, the anodic dissolution of ε-brass results in a $\varepsilon \rightarrow \gamma \rightarrow \alpha$ phase transformation with porous product phases [22, 23]. As revealed by a more detailed investigation of the corrosion morphology, the extent of this transformation depends on the overpotential of the zinc dissolution reaction [24]. At a low overpotential of $E_{\mathrm{H}} = -0.75$ V, the only product phase is γ. Similar to the scheme of

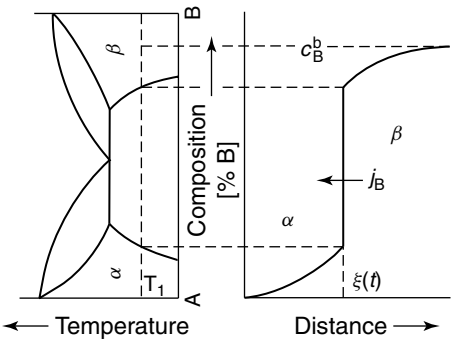


Fig. 3 Composition profile for the growth of a single-phase α layer from the B-rich β phase of a simple eutectic system A–B due to the diffusion limited dissolution of B. ξ denotes the instantaneous position of the moving α/β interface, the compositions at both sides of the interface represent the equilibrium values as given by the phase diagram at the temperature under consideration, T_1 (schematic).

diffusion driven phase transformations depicted in Fig. 3, the γ-Zn–Cu phase grows with stable $\varepsilon \rightarrow \gamma$ interface and parabolic rate law. In contrast to the Sn–In case, however, the ε-brass $\rightarrow$ γ-brass transformation is accompanied by a significant volume change due to a higher density of γ [25]. Since the product phase, γ, remains coherent with the parent phase of lower density, ε, the phase transformation induces tensile stresses and cracks within the brittle γ layer. Thus, electrolyte may penetrate by these cracks and form new centers of attack plus secondary cracks beneath the γ layer. In total, there is a rapid deterioration of ε-brass by this combination of chemical attack and mechanical destruction (see Fig. 4). At high overpotentials such as $E_H = -0.25$ V, the surface concentration of Zn, c_{Zn}^s, may be expected to drop to values below the stability limits of the γ- or β'-phases [26]. In accordance with this, the product phase formed under these conditions was shown to consist of pure, or nearly pure, porous Cu that grows with a fissured micromorphology [24].

2.3.4.3 δ-Zn–Fe and γ-Zn–Ni Alloys

Frequent constituents of protective zinc coatings on steel, Zn–Fe intermetallics such as the ζ-, δ-, Γ_1- and Γ-phases, represent alloys of relatively low melting point, high ΔE^0, and considerable technical importance. A detailed electrochemical study has been performed, so far, only with the δ phase of this alloy system. Even though the selective dissolution of Zn prevails at low overpotentials of the Zn dissolution reaction (e.g. at $E_H = -0.70$ V), a formation of intermediate product phases (such as the more Fe-rich Γ_1- and Γ- phases) was not observed. However, dezincification of

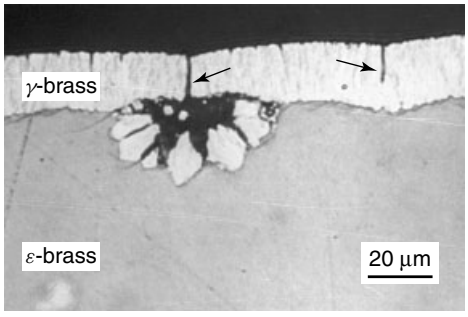


Fig. 4 Growth of a coherent γ-brass product layer by the diffusion limited dezincification of ε-brass. 42 h anodic polarization in acidified 1 N Na_2SO_4 at room temperature and $E_H = -0.75$ V. Dezincification of ε-brass is locally enhanced by the formation of cracks in the brittle product layer (see arrows). Light optical micrograph of metallographic cross section. (Reprinted from Ref. [24], with permission from Elsevier Science.)

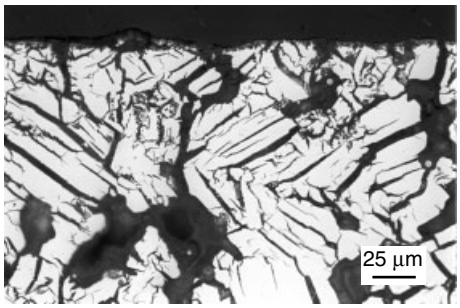


Fig. 5 Formation of cracks in the surface of brittle δ-Zn−Fe ($Zn_{93}Fe_7$) due to the selective anodic dissolution of Zn (dezincification); 236 h anodic polarization in 1 N Na_2SO_4/0.01 N H_2SO_4 at room temperature and $E_H = -0.7$ V. Large pores at the bottom of the image result from the metallurgical preparation of the alloy. Light optical micrograph of metallographic cross section. (From Ref. [27].)

the δ phase per se induces a lattice contraction next to the alloy/electrolyte interface that produces tensile stresses and cracks in the surface of the corroding electrode [27]. These cracks provide quick access of the electrolyte solution, and by the creation of secondary cracks, this leads to a rapid deterioration of the alloy (see Fig. 5).

Similar cracking phenomena have been reported to be associated with the corrosion of electro-deposited γ-phase Zn−Ni coatings that are of considerable interest as corrosion protective coatings for automotive applications [28–30]. However, the cause of this cracking may be more complex than in the case of δ-Zn−Fe since the γ-Zn−Ni phase is quoted rather ductile. Nevertheless, cracking is clearly linked with dealloying and appears to be important for the lifetime of the deposit.

2.3.5 Corrosion of Higher-Melting Alloys

For most engineering alloys, the ambient temperature only corresponds to a small fraction of the melting temperature, T_M. As outlined above, this implies a very low solid-state diffusivity under these conditions that impedes the establishment of complete equilibrium of the alloy electrode according to Eq. (3). At anodic polarization of a binary alloy A–B, the enrichment of a more noble component, B, will therefore be restricted to the uppermost atomic layers of the electrode surface, and the selective dissolution of less noble components may be expected to become very slow as long as there is no restructuring of the B atoms in the form of a B-rich porous reacted layer (see below). In accordance with the general principles that have been described for the dissolution of liquid alloys, the dissolution mode of higher-melting alloys may be simultaneous or selective.

2.3.5.1 Simultaneous Dissolution

In the case of simultaneous dissolution of a binary alloy A–B with $\Delta E^0 \gg RT/F$ and $E \geq E_B$, the overpotential of the dissolution of the less noble (fast dissolving) component, A, clearly exceeds that of the more noble (slow dissolving) component, B. Thus, the condition for simultaneous dissolution, Eq. (7), will only be satisfied if the dissolution rate of A is suppressed by an enrichment of B in the electrode surface. It appears, therefore, that the simultaneous (steady state) dissolution mode is always preceded by a transient period of selective dissolution. This transition from the selective to the simultaneous dissolution mode was illustrated, for example, by a γ-spectroscopic analysis of

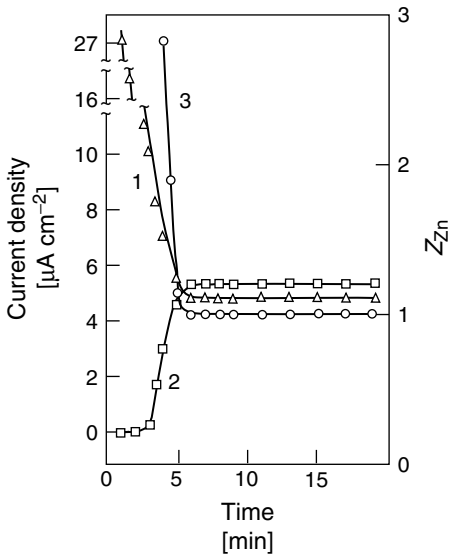


Fig. 6 (1) Transients of the partial currents of Zn dissolution; (2) Cu dissolution; and (3) of the dezincification coefficient, Z_{Zn} during galvanostatic anodic polarization of α brass ($Cu_{70}Zn_{30}$) in 1 N NaCl + 0, 01 N HCl at $i = 1 \times 10^{-5}$ A cm^{-2}. (Reprinted from Ref. [32], Copyright 1981, with permission from Elsevier Science.)

the time dependence of the dissolution of α-brass ($Cu_{0.7}Zn_{0.3}$) in 0.01 N HCl at a constant current density of 10^{-5} A cm^{-2}: As shown by Fig. 6, the partial dissolution rate of Zn decreases, whereas that of Cu dissolution increases until a steady state is achieved after some 6 min. Simultaneously, the dezincification coefficient, Z_{Zn}, drops from rather high values to 1 [31, 32].

The enrichment of the slow dissolving component, B, in an alloy surface under simultaneous dissolution conditions may be rationalized by a model of alloy dissolution that is based on the simplifying assumptions (1) that a homogeneous solid solution may be described as a heterogeneous dispersion of atomic dimensions with area fraction (surface mole fraction) X_j^s for component j, and (2) that the alloy components dissolve independently. The partial current density i_j of an alloy component j will then be given by $i_j = i_j^* \cdot X_j^s$, where i_j^* is the current density of the pure metal, j, and for a binary alloy A–B, the total current density of alloy dissolution, i_{AB}, becomes

$$i_{AB} = i_A^* \cdot X_A^s + i_B^* \cdot X_B^s \tag{11}$$

Eq. (7) then reads [33]

$$\frac{n_B i_A^* X_A^s}{n_A i_B^* X_B^s} = \frac{X_A^b}{X_B^b} \tag{12}$$

where X_j^b is the bulk mole fraction of component j. From Eq. (12), it becomes obvious that X_A^s and X_B^s will be different from the bulk mole fractions, X_A^b and X_B^b, as long as the current densities of the pure metals are not equal. A more detailed "phenomenological theory" of the simultaneous (steady state) dissolution of alloys, based on the introduction of formal rate constants has been given by Seo and Sato [34] and, more recently, by Heusler [35]. Accordingly, the surface mole fraction X_B^s of the slow-dissolving component B of a binary alloy A–B is given by

$$X_B^s = \frac{X_B^b}{X_B^b + \alpha(1 - X_B^b)} \tag{13}$$

where α is the ratio of the phenomenological dissolution rate constants k_B/k_A of components A and B, which are assumed to be independent on the alloy composition. Figure 7 shows X_B^s as a function of the bulk mole fraction, X_B^b, at different values of α as calculated from Eq. (13). Experimental evidence of the excess of the slow-dissolving alloy component in the electrode surface was obtained from the soft X-ray spectroscopy of the surface of α-brass electrodes that were polarized to the potential region of steady state, simultaneous dissolution in acidic sulfate solution. Here, the thickness of the resulting excess Cu in the electrode surface was shown to be of the order of 10 nm [36]. In addition to this, differential reflectometry may be a promising method for the in situ detection of dissolution-induced surface composition changes [37]. Rambert and Landolt determined the surface excess of Pd for the simultaneous dissolution of Ag–Pd and other noble metal alloys in 12 M LiCl solutions by Auger electron spectroscopy (AES) and in situ coulometry. For Ag–Pd alloys, they found by both methods the surface enrichment in Pd to decrease with increasing Pd concentration in the bulk alloy (see Fig. 8) and to be confined to a few, typically 4–8 atomic layers [38, 39].

Other research in the field of simultaneous dissolution has focused on the active dissolution of Fe–Cr alloys, which was shown to proceed in the simultaneous mode at quasi–steady state conditions [40]. Applying γ-spectroscopic methods, Kolotyrkin [41] measured the partial anodic polarization curves of the components Fe and Cr and was able to show that the dissolution rate of Cr from the alloy is more decreased than would have been expected on the basis of its bulk mole fraction (that is, Cr becomes the slow-dissolving component), and the contrary is true for the dissolution of Fe. This implies an enrichment of the Cr in the corroding alloy surface that may promote its subsequent passivation [34]. Also, with increasing Cr concentration of the alloy, the Tafel slope of the partial polarization curves of the components was shown to change from values that are typical for pure Fe to values that are typical for pure Cr [40, 41]. It appears, therefore, that for Fe–Cr alloys, the dissolution of the alloy components occurs in an interdependent

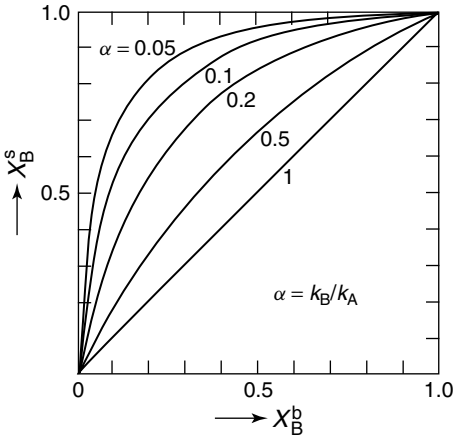


Fig. 7 Relation between the surface atomic fraction, X_B^s, of a slow-dissolving component, B, and the bulk atomic fraction of B, X_B^b, as calculated from Eq. (13) for the steady state (simultaneous) dissolution of a binary alloy A–B at different values of α. (From Ref. [34], Copyright 1987, American Chemical Society, with permission.)

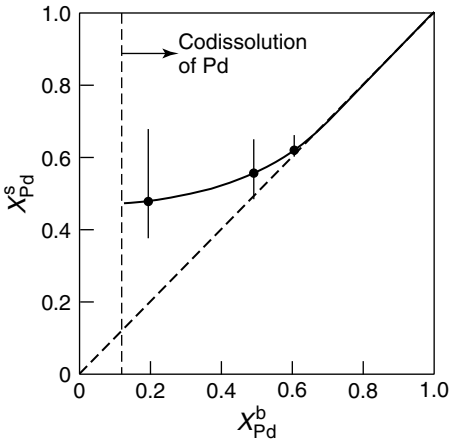


Fig. 8 Experimental surface atomic fraction of Pd, X^s_{Pd}, derived from Auger data, as a function of the bulk atomic fraction, X^b_{Pd}, for Ag–Pd alloys dissolved anodically in 12 M LiCl solutions at 10^{-4} A cm^{-2} (10 mC cm^{-2}). The simultaneous dissolution mode is only achieved for X^b_{Pd} > ca. 0.1. (Reprinted from Ref. [38], Copyright 1986, with permission from Elsevier Science.)

way rather than independently. On the basis of electrode impedance spectroscopy (EIS) investigations of the dissolution of Fe–Cr alloys, the coupling of the partial anodic currents was associated with the interaction of adsorbed surface species of the components [42, 43].

A regime of simultaneous dissolution has also been found for Cu–Ni alloys in acidic chloride solutions. Rotating ring-disk electrode studies revealed an apparent Tafel region of the alloy and component polarization curves with mixed mass transfer and kinetic rate control [44, 45]. For a $Cu_{90}Ni_{10}$ alloy, the kinetic parameters again indicate a coupling of the copper and nickel partial currents under steady state conditions [44].

Analyzing the dissolution kinetics of alloys in a more general way, Heusler attributed deviations from the "ideal behavior" in simultaneous alloy dissolution (that is, a composition dependence of the phenomenological rate constants of individual alloy components) to a dissolution mechanism that proceeds from kinks in the steps of low-index planes, the concentration of these kinks depending on the alloy composition [35].

2.3.5.2 Selective Dissolution (Dealloying)

For dealloying to occur, it appears to be a necessary prerequisite that the bulk concentration of the fast-dissolving component exceeds a sharp limit ("parting limit"). As originally introduced by Tammann [46], the parting limits depended on the nature of the environment (that is, on its redox-potential), and their physical significance was therefore questioned by Gerischer [1]. However, it was shown by Sieradzki and coworkers that, even when the electrode potential is as high as the equilibrium potential of the more noble component, Cu, rapid dealloying of Cu–Zn and Cu–Al alloys only occurs if a critical concentration of the less noble components Zn and Al is exceeded [47]. This observation led to the concept of an "absolute" parting limit that is defined as a critical concentration of the fast-dissolving component that is required to allow dealloying at an arbitrarily high anodic potential. This absolute dealloying threshold is of great interest for the design of alloys that do not suffer from dealloying.

Moreover, it represents an important issue with respect to the theory of selective alloy dissolution (see in following text).

2.3.5.2.1 **Phenomenology of Dealloying**
According to the overall reaction

$$AB_{(cryst)} \longrightarrow A^{n+} + ne^- + B^*_{(cryst)} \quad (14)$$

gross dealloying of a higher-melting alloy, A–B, is associated with the formation of a crystalline product phase, $B^*_{(cryst)}$. The latter is typically a sponge structure, composed of a system of interconnected pores or tunnels that allow electrolyte ingress, and a skeleton of the pure, or almost pure noble component, B. As depicted schematically in Fig. 9, dealloying often occurs uniformly, that is, with a plane reaction front. Little is known about the propagation kinetics of this front, but in the case of caustic leaching of Al–Cu–Zn alloys, a parabolic rate law has been reported [48]. In other cases, dealloying was promoted by grain boundaries, slip lines and martensite phases due to the presence of lattice defects such as dislocations and stacking faults [49, 50].

More detailed information with respect to the nature of $B^*_{(cryst)}$ has been elaborated from various ex situ and in situ techniques such as transmission and high-resolution scanning electron microscopy [51–55], electrode capacity measurements [56], electrochemical and quartz crystal impedance spectroscopy [57, 58], gas adsorption [59], X-ray line broadening [60, 61] and small-angle-X-ray scattering [60, 62] as well as in situ small-angle neutron scattering [63, 64]. From these measurements it was concluded that, depending on the alloy/electrolyte system, the pore and ligament size are typically of the order of $\approx$ 5–50 nm at ambient temperature (see Fig. 10). It should be noted, however, that upon aging, the pores of the dealloyed layer coarsen [59, 64] and this coarsening was shown to depend on the electrode potential [57, 64]. In any case, dealloying produces structures of very high surface area ($\approx 20\ m^2\ g^{-1}$ [59]). This is exploited, for example, to prepare catalysts by caustic leaching of alloys such as Ni–Al and Al–Cu– Zn.

Moreover, it is evident that the intrinsic mechanical strength and fracture toughness of such nanoporous structures is low [55, 65]. Insofar, gross dealloying represents a serious form of corrosive deterioration. In addition to this, there is little doubt with respect to an association between dealloying and the stress corrosion cracking of certain alloys.

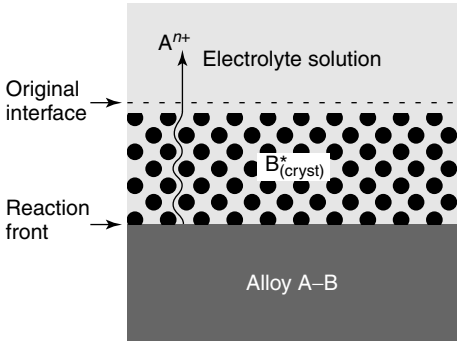


Fig. 9 Formation of a uniform, porous reacted layer, $B^*_{(cryst)}$, for the selective dissolution of a less noble component, A, from a higher-melting alloy A–B (schematic).

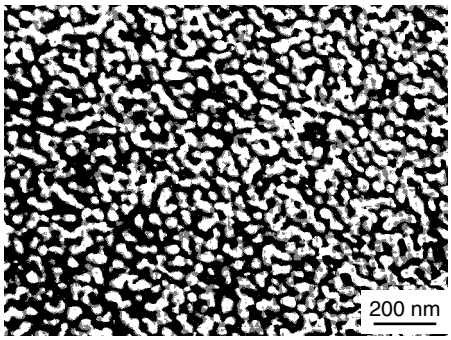


Fig. 10 Transmission electron micrograph of the microstructure resulting from selective anodic dissolution of Cu from a Cu_3Au electrode (50 s anodic polarization at $i = 1$ mA cm^{-2} in 1 M H_2SO_4). Black network is Au-rich $Au^*_{(cryst)}$, white spots are pores. (From Ref. [52], with permission.)

2.3.5.2.2 Dealloying of Engineering Materials

***α* and *α*–*β* brass** Even though dezincification of brass is a rare problem nowadays, it remains a potential cause of the failure of components such as condenser tubes or fittings for water services. For α-brass, dezincification may occur either uniformly ("layer-type" dezincification, see Fig. 11) or localized ("plug-type" dezincification). Layer-type dezincification appears to be favored by an acid environment and a high zinc content of the alloy, whereas the plug type has been reported to prevail in virtually neutral solutions and with alloys of relatively low zinc content [66]. The β phase constituent in duplex $\alpha-\beta$ brass is more rapidly dezincified than the α phase. From a comparison of the corrosion behavior of α and partially ordered $\beta + \beta_1$ brasses of similar composition (Cu−38 wt.% Zn and Cu−41 wt.% Zn, respectively), it has been concluded that this is not simply due to an increased Zn concentration in the β phase, but is likely to reflect the structural differences of both phases [67]. Other factors that stimulate the dezincification of both α- and $\alpha-\beta$ brasses are the presence of chlorides, high concentrations of $CuCl_2^-$ ions, stagnant environments, differential aeration cells and elevated temperatures. In chloride solutions, such conditions are typically encountered at a later stage of corrosion when mass transport restrictions by a deposit, corrosion product, or crevice have been established and create a local environment, in which the copper in the brass is nearly in equilibrium with Cu_2O, CuCl, and accumulated $CuCl_2^-$ anions [68, 69]. Experimentally, the necessity

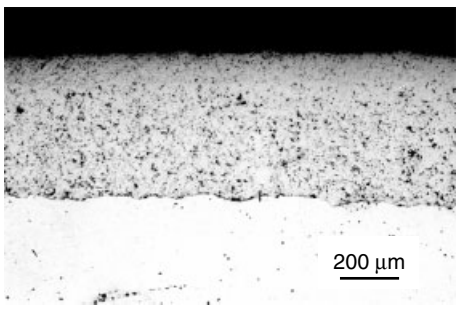


Fig. 11 Uniform dezincification of α brass (Cu−30 wt.% Zn) resulting from 96-h anodic polarization in acidified 0.5 M NaCl at 65 °C and $E_H = 0$ mV. (a) Porous dezincified zone and (b) unattacked alloy. (Reprinted from Ref. [71], by courtesy of Marcel Dekker, Inc.)

of Cu-ion accumulation in the electrolyte in order to induce dezincification was demonstrated by measurements of the dezincification coefficient, Z_{Zn}: Following an intermediate period of simultaneous dissolution of Cu and Zn (see Fig. 6), there is a reincrease of Z_{Zn}, which may be delayed or accelerated by a renewal of the electrolyte or by the addition of $CuCl_2$, respectively. This effect has been called ''pseudopreferential dissolution'' [32, 70].

The stimulating effect of the above factors on dezincification is largely reflected by test procedures such as ISO 6509, that rely on an exposure of brass to $CuCl_2$-solutions at a temperature of about 75 °C [72]. On the other hand, dezincification of α brass is prevented by small alloying additions of Sn, Al and, more effectively, by ~ 0.02–0.04% As. In domestic waters, there is, in addition, a beneficial role of bicarbonate that competes with the detrimental role of chlorides [73]. The inhibition of dezincification by As fails, however, if α-brass contains traces of elements such as Mg [74]. Upper limits of the magnesium content are therefore standardized. Moreover, there is no inhibition by As of the dezincification of the β phase in duplex brass. This problem may be largely overcome by a heat treatment in the α field of the Cu–Zn phase diagram to produce a virtually β-free structure. The mechanisms that have been proposed to explain the effectiveness of As in inhibiting the dezincification of α brass [75–80] are closely associated with the mechanism of dezincification per se (see in the following text).

Al-bronzes Commercial Al-bronzes (Cu–Al alloys containing up to ~13.5 wt.% Al) combine high strength and high corrosion resistance, for example, in saline waters including impingement attack. Binary alloys with up to ~9.4 wt.% Al exhibit a single-phase face centered cubic (fcc) structure if cooled under equilibrium conditions, and do not appear to suffer from selective dissolution (dealuminization). Under nonequilibrium situations, however, a second phase may appear for Al contents exceeding ~ 8.4 wt.% [81]. Depending on Al contents and heat treatment (cooling rate), this second phase will consist of hypo- and hypereutectoid martensites or eutectoid γ_2 phase. In 1 N sulfuric acid solutions, all these second phases may dealuminize [82], whereas in neutral chloride solutions this has only been observed for the hypereutectoid martensites and γ_2 [83]. In any case, however, the γ_2 phase proves most detrimental for the corrosion resistance. Nickel additions, on the other hand, are beneficial in this respect since they suppress the formation of a continuous network of γ_2 and instead favor the formation the κ phase that has been reported to passivate in chloride solutions [83].

Other Cu-based alloys Dealloying phenomena have also been discussed for Cu alloys from the Cu–Ni, Cu–Mn, and Cu–Sn systems [45, 84, 85]. In the case of long-term corrosion of Sn-bronze (α-Cu–Sn) in natural environments, which is obscured by complex patina formation, it has been shown that the relevant dealloying process is decuprification rather than destannification (as formerly assumed).

Noble metal alloys Alloys based on the pseudoternary phase diagram (Au, Pt, Pd)–Ag–Cu are used in jewelry, for electric contacts, and for dental restorations. They must meet very high demands with respect to tarnish resistance and to a release of ions that may affect biocompatibility. In the case of

dental alloys, these requirements are usually fulfilled with high nobility, predominantly single-phase alloys containing Au plus Pt-group metals at concentrations of at least 75 wt.% [86, 87]. Because of the high gold price, however, low nobility alloys have received increasing attention. For such alloys, it has become obvious that the occurrence of second or multiple phases, in addition to alloy composition, exerts a great influence on tarnish and corrosion resistance [88, 89].

Austenitic stainless steels In the vicinity of stress corrosion cracks of austenitic stainless steels (that is, under conditions of localized active dissolution in hot, acid chloride solutions), the formation of a corrosion sponge enriched both in chromium and oxygen has been detected [90, 91]. Simulating the electrochemical conditions within such cracks by immersing austenitic stainless steels in hot, acidified 15 M LiCl solutions, and subsequently analyzing the resulting surface layers by AES depth profiling, revealed evidence that the sponge results from dealloying and is a nickel-enriched metallic layer with chromium oxide precipitated within its pores [92]. An accumulation of Ni (and Mo) in the surface of a commercial austenitic stainless steel has also been found by an electron spectroscopy for chemical analysis study of its active dissolution in hydrochloric acid [93].

2.3.5.2.3 Electrochemical Aspects of Dealloying

Quasi–steady state polarization curves Partial anodic polarization curves of fast-dissolving alloy components under quasi–steady state conditions are of considerable interest for both practical and theoretical reasons. Experimental methods for their evaluation have been reviewed in the literature [71]. The most thoroughly investigated alloy/electrolyte system appears to be the anodic dissolution of Cu from binary Cu–Au alloys in acidic solutions. This is due to (1) a large difference of the standard potentials of the alloy components, (2) a complete miscibility of the alloy components at $T > 410\,^{\circ}C$, and (3) the availability of i_{Cu} from ammeter readings in a potentiostatic circuit using deaerated solutions [94, 95]. Typical examples of quasi-stationary partial anodic polarization curves of copper dissolution from various Cu-Au alloys in 1 N $Na_2SO_4 + 0.01$ N H_2SO_4 are shown in Fig. 12. Similar polarization curves have been reported for

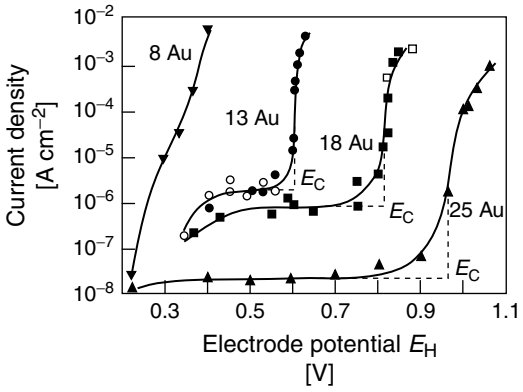


Fig. 12 Quasi-stationary anodic polarization curves and critical potentials, E_C, for the dissolution of Cu from Cu–Au alloys with increasing Au concentration (in atomic%) in deaerated 0.1 N $Na_2SO_4 + 0.01$ N H_2SO_4 at room temperature, open symbols from chemical analysis, closed symbols from ammeter readings. (Data for Cu–13 Au and Cu–18 Au from Ref. [94], reproduced by permission of The Electrochemical Society, Inc., data for Cu–8 Au and Cu–25 Au from Ref. [95].)

the Cu−Pd [96, 97], Ag−Au [98], and other alloy systems. Accordingly, these curves consist of two potential regions that are separated by a critical potential, E_C. At subcritical potentials ($E < E_C$), the current density of copper dissolution is very low (comparable to the dissolution rates of passive alloys), decreasing with increasing Au content of the alloy and virtually independent of the electrode potential. Gross dealloying, terminating the protective effect of the noble component, Au, is only observed at $E > E_C$. As also indicated by Fig. 12, E_C is shifted into the anodic direction by increasing the Au concentration of the alloy. Other variables that affect E_C are

- The nature of the electrolyte solution. (For Ag−Au alloys, E_C depends on the concentration of Ag^+ ions in the solution [99], for Cu_3Au alloys, E_C decreases with increasing chloride concentration, but increases upon derivatization with an alky-thiol [100–103]).
- The state of order of the alloy phase. (The critical potential of ordered Cu_3Au alloys in acid sulphate solutions is about 250 mV more noble than that of the same alloy in the disordered state [104, 105]).
- Mechanical strain and/or martensitic transformations. (The critical potential of $Cu_{87}Au_{13}$ alloys is slightly decreased by cold work [94], that of $Co_{80}Ni_{10}Pd_{10}$ alloys decreases as a result of a strain-induced martensitic $\gamma \rightarrow \varepsilon'$ transformation [106]).

Chronoamperograms and chronopotentiograms More information with respect to the processes that are responsible for the low-current potential regime of the partial anodic polarization curves may be derived from current-time transients. As shown by Fig. 13, there is a continuous decay of the dissolution rate of Cu from a Cu−20 at.% Pd alloy in acidified 1 N Na_2SO_4 ($E_C \approx 0.72$ V) as long as $E < E_C$. Similar transients have been reported in the literature for other alloy/electrolyte systems. Usually, they follow a power law of the form $i(t) \propto t^{-m}$ where m varies from ≈ 0.5 to ≈ 1, depending on the alloy/electrolyte system, the electrode potential, the time regime, and on other parameters [97, 99, 102, 103, 107–109]. It is generally accepted that the above decay of the dissolution current of a fast-dissolving component is due to the accumulation of

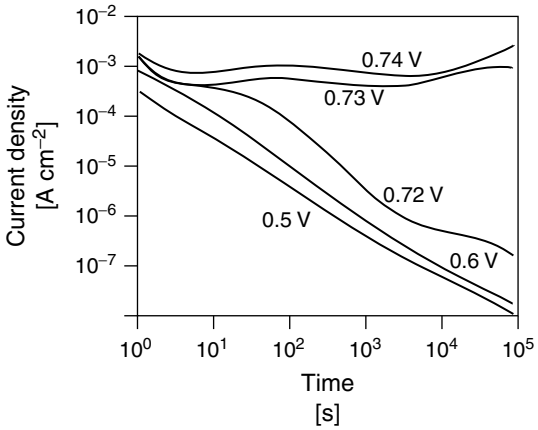


Fig. 13 Current transients for the dissolution of Cu from $Cu_{0.8}Pd_{0.2}$ in acidified 1 N Na_2SO_4 (pH 2) at various electrode potentials. (From Ref. [97].)

the slow-dissolving component in a protective overlayer. This indicates that the low-current region of the quasi-stationary polarization curve at $E < E_C$ reflects compositional and microstructural changes in the electrode surface rather than a bulk property of the alloy. For a $Cu_{87}Au_{13}$ electrode, the extent of the accumulation of Au was estimated from the charge that is consumed to dissolve Cu during 1 h and was found to vary between ≈ 10 and ≈ 100 atom layers at low and at high electrode potential, respectively [94]. As illustrated by Fig. 14, this result was confirmed by the application of AES to various Cu−Pd and Cu−(Ag)−Au electrodes after anodic polarization in different solutions [96, 102, 110]. From a thermodynamic point of view, the modified composition surface layer represents a nonequilibrium state that tends to reorganize upon termination of the anodic polarization [111]. This follows, in particular, from the observation that the charge that is consumed to dissolve Ag from various Ag-Au alloys in nitrate solutions during three subsequent potential pulses of duration τ_0, $q = q_1 + q_2 + q_3$, exceeds the charge q_4 of a single pulse of the same height but with duration $\tau = 3\tau_0$ (see Fig. 15) [112].

Similar conclusions with respect to the nature of the protective overlayer have been drawn from chronopotentiometric experiments with Ag−Au and disordered Cu_3Au electrodes in solutions containing the ions of the less noble components.

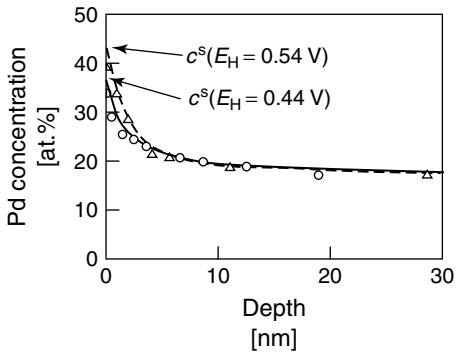


Fig. 14 Composition–depth profile and surface concentrations of Pd, c^s, for a $Cu_{0.85}Pd_{0.15}$ electrode after anodic polarization in 0.5 M Na_2SO_4 + 0.005 M H_2SO_4 at different electrode potentials $E < E_C$. The electrode was removed from the solution when the net current had decreased to zero. (From Ref. [96], reproduced by permission of The Electrochemical Society, Inc.)

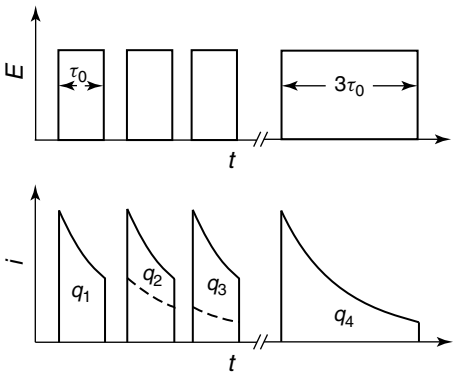


Fig. 15 Confirmation of the reorganization of the protective Au overlayer on Ag−Au electrodes upon interruption of the anodic polarization. The sum of the charges q_1, q_2, and q_3, transferred during three identical anodic impulses exceeds the charge q_4 associated with of a single impulse of equal height but triple duration (schematic). Dashed lines represent current transients in the absence of reorganization. (Reprinted from Ref. [112]. Copyright 1991, with permission from Elsevier Science.)

Both alloy electrodes were reported to be quasi-reversible with respect to the dissolution of the surface atoms of the less noble components, that is, they establish partial equilibrium between the solution and the surface atoms (rather than with the bulk atoms) of the less noble components, Cu and Ag, respectively. Thus, by application of the Nernst equation, the normalized surface activities of these components that result from galvanostatic anodic pulses could be determined from the chronopotentiograms and were shown to be lower than the initial activities prior to anodic current flow. In addition to this, it could be shown that upon an interruption of the applied current the initial potential, and hence the initial activity of the less noble alloy component, is reestablished, in the course of time, due to relaxation processes that induce a reorganization of the atoms in the electrode surface [4, 112].

Potentiodynamic anodic polarization curves

Potentiodynamic anodic polarization curves of binary noble metal alloys exhibit current density maxima at $E < E_C$ rather than potential-independent low-current regions (see, e.g. Fig. 16). By analogy with the theory of linear sweep voltammetry of simple redox reactions [113], these maxima may be considered to result from an intersection of the three-dimensional (3D) current–time–potential surface of the alloy electrode with a plane generated by the function $E = E_i + \nu \cdot t$, where E_i and ν are the initial electrode potential and the linear potential sweep rate, respectively. By consequence, their height is expected to increase with increasing values of ν. This effect has been intuitively exploited to evaluate the dealloying resistance of noble metal dental alloys [114], since quasi-stationary current densities of such materials, by virtue of their high noble metal content, are typically at a level of the order of noise [115]. In detail, it has been suggested to rely on the charge $q = \int_{t_1}^{t_2} i \, dt \propto \int_{E_1}^{E_2} i \, dE$ that is consumed within a relevant interval of the electrode potential, $\Delta E = E_2 - E_1$, as a criterion for the corrosion resistance of

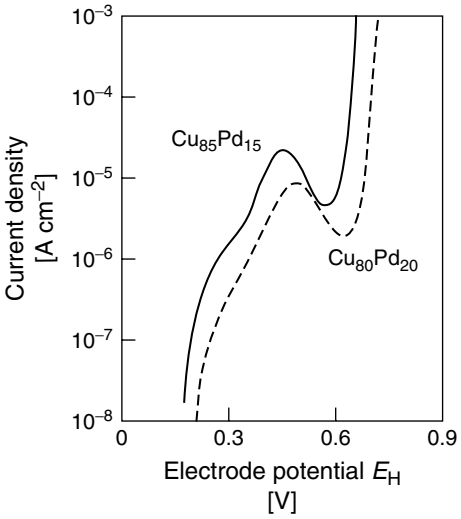


Fig. 16 Potentiodynamic anodic polarization curves of Cu dissolution from binary Cu–Pd alloys in 0.1 N Na_2SO_4 acidified with H_2SO_4 to pH 2 at a polarization rate $\nu = 3$ mV min^{-1}. (From Ref. [97].)

a dental alloy [116, 117]. The advantage of this electrochemical method over chemical analysis of the solution lies in its capability to detect the formation of insoluble corrosion products such as AgCl or Ag_2S.

Scratching techniques Dealloying rates at the earliest stages of preferential dissolution ($t \approx 1$ ms) may be determined from freshly generated surfaces, using the potentiostatically controlled scratched rotating disk electrode. Early measurements of this kind were undertaken to check an electrochemically controlled stress corrosion cracking mechanism of α-brass, yielding initial current densities of preferential zinc dissolution >5 A cm^{-2} [118]. A more recent study of the earliest stages of brass dezincification demonstrated the usefulness of this technique by revealing two consecutive kinetic regimes, the first of which involving a coupling of preferential zinc dissolution with the formation of an adsorbed monolayer of CuOH [119].

2.3.5.2.4 **Theoretical Aspects** Every model of selective alloy dissolution must involve a transport mechanism by virtue of which the atoms of the less noble component reach the alloy/electrolyte interface and the atoms of the more noble component aggregate. For a binary alloy, the basic transport mechanisms are as follows: (1) both metals ionize but the more noble component is subsequently redeposited, (2) only the less noble component ionizes while residual atoms of the more noble component aggregate via surface migration and thus expose fresh alloy to the electrolyte solution, and (3) only the less noble component dissolves and both metals are mobile in the solid via volume diffusion [120].

Ionization–redeposition mechanism Dealloying of a binary alloy A–B with a less noble component A via the ionization–redeposition mechanism would be described by the anodic reactions

$$A_{(A-B)} \rightleftharpoons A^{n+}_{(aq)} + ne^- \quad (15a)$$

$$B_{(A-B)} \rightleftharpoons B^{n+}_{(aq)} + ne^- \quad (15b)$$

and the consecutive cathodic reaction

$$B^{n+}_{(aq)} + ne^- \rightleftharpoons B^{*}_{(cryst)} \quad (16)$$

Assuming that reactions (15a), (15b), and (16) are independent of each other, and considering that the activity of component B in the alloy is less than unity, the equilibrium potential of reaction (15b) will be more noble than the equilibrium electrode potential of reaction (16). Hence, from the viewpoint of equilibrium thermodynamics, the ionization–redeposition mechanism is impossible. However, if in accordance with the principles of irreversible thermodynamics coupling between the anodic reactions (15a) and (15b) occurs, reaction (15b) may take place at potentials less noble than the equilibrium potential of reaction (16). The redeposition of intermediate ions $B^{n+}_{(aq)}$ at the same electrode potential becomes then possible [120]. Using a rotating ring-disk electrode that might detect intermediate Au^{3+} ions (see Chapter 2.4 in Volume 3), no indication for the ionization–redeposition mechanism was found for the anodic polarization of a $Cu_{90}Au_{10}$ alloy [120]. For brass, however, the situation is more complex. Electromotive force (EMF) measurements in the cell Zn–Cu|Cu^+|Cu yield surface activities of Cu for the alloy electrode that significantly exceed unity. This has been taken as evidence for a coupling of the anodic reactions [111, 121]. Also, the delayed reincrease of the dezincification coefficient

of α-brass ($Z_{Zn} > 1$) that results from the accumulation of Cu ions in the solution as described above, must be associated with the redeposition of the more noble component, Cu [32, 70]. Moreover, there is direct metallographic evidence for the redeposition of Cu in the form of twinned crystals during the dezincification of brass in solutions such as contaminated tap water [122].

Surface-diffusion mechanism In the field of dealloying, surface-diffusion processes have been discussed by various authors. Assuming (1) a blocking of the dissolution from kinks by ad-atoms of the more noble component at $E < E_C$ and (2) the formation of surface vacancies by the alternate dissolution of the slow-dissolving component from terrace sites at $E \geq E_C$, Gerischer first associated E_C with the depassivating effect of a ''recrystallization'' of more noble ad-atoms (that is, with the formation of the porous product phase B^*_{cryst}) under the assistance of the surface diffusion of both ad-vacancies and ad-atoms [1, 123].

These ideas were later substantiated by transmission electron micrographs of corroded Ag–Au foils, showing an island and channel structure similar to the micromorphology observed in vapor deposition and electrodeposition on crystalline substrates, that is, similar to cases with definite contribution of the surface diffusion of ad-atoms. Discarding a significant role of surface vacancies, it was concluded therefore, that during the selective dissolution of Ag from Ag–Au alloys, the depassivating surface recrystallization of Au (that is, the reordering of the surface by the nucleation and growth of Au-rich islands) proceeds via the surface diffusion of Au ad-atoms [124]. As a secondary effect, the formation of pits by the growth and coalescence of the gold islands was observed. A detailed analysis of the kinetics of this ''surface disordering–reordering model'' yielded criteria for the transformation of pits to stable tunnels and the above power law for the current transient of the less noble component, that is, $i(t) \propto t^{-m}$, with m depending on the alloy composition [125].

Nucleation and growth concepts Gerischer's model of alloy dissolution, in addition, associated the critical potential, E_C, with nucleation constraints for (1) the formation of the product phase B^*_{cryst} or (2) the formation of dissolution nuclei (that is, the coalescence of dissolution-induced surface vacancies in the terraces). Applying classical nucleation theory, the overvoltage η for the formation of critical 3D dissolution nuclei with radius r_c in the terraces of a pure metal will be given by

$$\eta = \frac{2\gamma V_m}{nF\, r_c} \tag{17}$$

where γ is the liquid/solid interfacial free energy and V_m is the molar volume, and a similar expression may be derived for the formation of critical 2D nuclei [6, 126]. In the latter case, the steady state current density, i_N, resulting, for example, from a multinuclear multilayer dissolution process, is given by an expression of the form

$$i_N = A \exp\left(B\frac{nF}{RT}\eta\right) \exp\left(-\frac{C}{\eta}\right) \tag{18}$$

where A, B, and C are constants that follow from the literature [6, 127]. Since the second exponential term in Eq. (18), which reflects the 2D nucleation rate, with increasing η varies between the limits of 0 and 1, i_N increases abruptly when a critical potential threshold is exceeded. This threshold has been associated with the critical potential, E_C, of selective alloy

dissolution [106, 128]. However, a quantitative treatment of this concept is missing. Other aspects of nucleation theory were considered in the context with the surface disorder that develops during the initial stages of selective dissolution [129] and within the framework of percolation concepts (see in the following text).

Volume diffusion mechanism On the basis of diffusivities extrapolated from high-temperature data, volume diffusion is considered inoperable in higher-melting alloys at room temperature. However, if the formation of excess surface vacancies (monovacancies or vacancy aggregates such as divacancies) by the dissolution of less noble atoms from terrace sites is taken into account, a new situation arises: Provided that the annihilation of these vacancies at sinks is outperformed by their production, the excess surface vacancies may diffuse into the interior of the alloy. The interdiffusion coefficient of the alloy components in the vicinity of the surface, $\widetilde{D}$, may then approximately be expressed as

$$\widetilde{D} \approx D_V X_V^s \tag{19}$$

where D_V is the diffusivity of the vacancies and X_V^s their surface mole fraction. Since X_V^s will be much higher than the equilibrium value, X_V^{eq}, the diffusivity in the vicinity of the electrode surface will be enhanced [120]. Assuming that $\widetilde{D}$ is independent on composition and on location, the current density of Cu dissolution from Cu−Au alloys, for example, under pure rate control by solid-state diffusion will be given by

$$i_{Cu} = X_{Cu}^b \frac{2F}{V_m} \left[\frac{\widetilde{D}}{2(1 - X_{Cu}^b)t} \right]^{1/2} \tag{20}$$

where X_{Cu}^b is the bulk mole fraction of Cu, F is Faraday's constant, and V_m is the molar volume. Considering further that in pure Cu the diffusivity of divacancies, D_{Cu}, is much higher than that of monovacancies, and assuming a surface mole fraction of divacancies of $X_{Cu}^s = 10^{-2}$, it was shown by Pickering and Wagner that for $X_{Cu}^b = 0.9$ and $t = 1000$ s the effective thickness of the interdiffusion zone is of the order of 10 nm, and the current density, i_{Cu}, as calculated from Eq. 20, is reasonably high ($i_{Cu} \approx 2 \times 10^{-4}$ A cm^{-2}) [120]. Moreover, enhanced diffusion in alloy electrodes may be promoted by the highly defective nature of the noble metal rich layer that is formed in the surface of an alloy electrode at $E < E_C$ [109]. As an extreme case, the formation of high-diffusivity paths due to local amorphization caused by an excess of nonequilibrium vacancies has been discussed in the literature [130].

Attempts to verify the above volume diffusion mechanism experimentally included X-ray and electron diffraction experiments with electrodes that were corroded at $E > E_C$, as well as investigations by positron annihilation spectroscopy (PAS). In the former case, the occurrence of broadened diffraction lines at Bragg angles between those of the bulk alloy and the pure, noble component was taken as a confirmation of the volume diffusion mechanism [54, 120, 131]. More direct evidence was obtained from the PAS experiments with dezincified brass, where experimental positron lifetimes correlated well with calculated values in vacancies or vacancy aggregates [78–80]. On the other hand, it has been objected that Eq. (20) predicts a $t^{-1/2}$ dependence of the current density, which is in contradiction to many experimental results. It has been shown, however, that this particular problem may

be overcome by due consideration of the role of vacancy sinks within the interdiffusion zone [132].

Refinements of the above volume diffusion concept have been made by a model that includes a contribution of surface-diffusion processes to the dissolution reaction of the more active component at subcritical potentials. By adjustment of different parameters, this model allows for the calculation of current-time transients and concentration–depth profiles of the alloy components [102]. In addition to this, mixed control of the dissolution rate of the more active component by both charge transfer and volume diffusion has been discussed. This case is particularly interesting for short polarization times. The analysis yields, for example, the concentration–depth profile and the surface concentration of the more noble component, c_B^s, in dependency on the product $k\sqrt{(t/\widetilde{D})}$, where k is a kinetic factor, t is the polarization time, and $\widetilde{D}$ is the interdiffusion coefficient. Moreover, it predicts the occurrence of different time domains in the dissolution current transients [109].

Percolation concepts Percolation concepts of dealloying are based on the association of sharp parting limits with the abrupt occurrence of connected paths of the fast-dissolving component, when in a random solid solution the concentration of that component is being increased. Early approaches of this idea made use of probability calculus to determine the fraction of chains of the less noble component in dependence on the alloy composition. For infinite chain lengths, the results were sharp composition thresholds that varied with the chain multiplicity and were associated with Tammann's parting limits for environments with different oxidative power. Moreover, a decisive role of surface diffusion was postulated.

More recently, percolation theory and computer simulation of the dissolution process was applied. This latter approach resulted in 2D and 3D percolation thresholds (that is, composition thresholds at which infinite connected paths of the fast dissolving component were formed) as well as in images of the atomic scale disorder induced by dealloying. 3D site percolation thresholds ($\approx$ 20 at.% in a fcc lattice), leading to an infinite connected cluster of nearest neighbors of less noble atoms, were considered to correlate with the absolute parting limits of alloys with high $\Delta E^0 = E_B^0 - E_A^0$ such as α-brass. This implies that the overpotential will be high enough to dissolve the less noble component from highly coordinated terrace sites. Higher absolute parting limits were associated with alloys of low ΔE^0, which were considered to dissolve only from sites with lower coordination such as kink sites (that is, via a surface-diffusion modified layer-by-layer process). Correspondingly, higher parting limits were correlated with 2D percolation thresholds [68, 133]. In the case of fcc Ag–Au alloys, it has been alternatively argued that the selective dissolution of Ag at alloy compositions between the site percolation threshold ($\approx$20 at.% Ag) and the experimental dealloying threshold ($\approx$ 60 at.% Ag) is suppressed by the simultaneous formation of Au-oxide or Au-hydroxide within the dissolution channels [134].

In addition to this, the critical potential, E_C, and the current transients have been addressed within the framework of percolation theory. E_C has been associated in essence with (1) the overvoltage required to create a curved perturbation

in a flat surface at multiple, highest-density percolation clusters of A (that is, to create dissolution nuclei at preexisting nucleation centers) and (2) the competition between the roughening effect of selective dissolution and the smoothing action of surface diffusion. Referring E_C to the reversible potential of pure, fast-dissolving component, the following expression for E_C has been derived [99, 135]

$$E_C = \frac{\gamma V_m}{nF\xi} + \frac{2RT}{nF}\sinh^{-1}\left[\frac{2\pi^2 N_S D_S}{J_0}\frac{1}{\xi^2}\right] \quad (21)$$

In this equation, γ is the free energy of the solid/electrolyte interface, V_m is the molar volume and $\xi = 1 + X_A/1-X_A$ is the average size of the percolating A cluster in units of the nearest neighbor spacing for an alloy A–B with a mole fraction, X_A, of the fast-dissolving component, A. Associating ξ with the radius of a critical nucleus, the first term on the right side of Eq. (21) may be considered a nucleation overvoltage that increases with decreasing X_A (see Eq. 17). The second term accounts for the smoothing effect of surface diffusion. Here, N_S is the surface density of ad-atoms, D_S is the surface diffusivity, J_0 is the mass flux corresponding to the exchange current density and all other quantities have their usual meaning. As shown by Fig. 17, there is good match between the experimental E_C values of Ag–Au alloys in $HClO_4$ solutions containing various concentrations of Ag^+ ions and values calculated from a variant of Eq. (21) while making reasonable assumptions with respect to γ and $D_S J_0^{-1}$ [134].

2.3.5.2.5 **Nanoscopic Investigations of Dealloyed Surfaces** From the background of competitive models of selective alloy dissolution as described above, a closer microscopic examination of this process with the ultimate objective of atomic resolution and chemical information on an atomic scale appears mandatory. Ex situ transmission electron microscopy (TEM) of thin, corroded alloy films provides lateral resolution at the nanometer scale, but suffers from poor depth resolution and from structural relaxation processes that may occur after termination of the anodic polarization and transferring the samples into high vacuum. Classical TEM investigations in this field were performed under open circuit conditions in oxidizing environments (that is, at $E \geq E_C$) [51, 53, 124], more recent potentiostatic

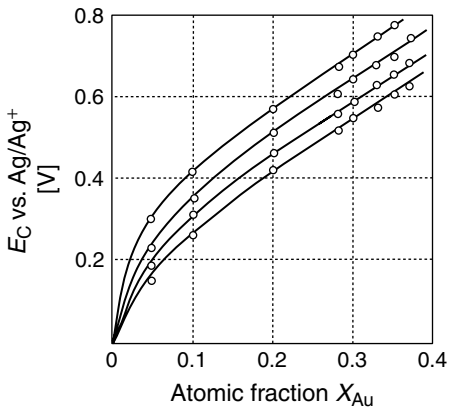


Fig. 17 Experimental and calculated values (open circles and solid lines, respectively) of the critical potential, E_C, of Ag–Au alloys in 0.1 M $HClO_4 + AgClO_4$ solutions as a function of the atomic fraction of Au. Curves in ascending order correspond to Ag^+ concentrations of the solution of 10^{-1}, 10^{-2}, 10^{-3}, and 10^{-4} M. E_C is measured with respect to the Ag/Ag^+ electrode in the same solution. See original reference for the fitting parameters. (From Ref. [134], with permission.)

polarization experiments also permitted high-resolution TEM studies of the corrosion micromorphology at $E < E_C$. In a study of Cu dissolution from $Cu_{90}Pd_{10}$ and $Cu_{85}Pd_{15}$ alloys, for example, bright field TEM micrographs revealed the formation of isolated pits and pit clusters that grow into the interior of the electrode in the form of tunnels. Chemical information was provided by a dark field technique, which showed that virtually pure Pd accumulates on the surface in the form of islands and, in particular, near the pits and at the pits walls. For $E > E_C$, the formation rate of these pits was considerably increased [97, 136]. This latter observation was considered to support the nucleation and growth model of selective alloy dissolution. Similar pits and pit clusters with noble metal accumulation in the vicinity of the pit were observed by with $Cu_{82}Au_{18}$ alloys after anodic polarization in 1 N Na_2S_4 + 0.01 N H_2SO_4 solutions at $E < E_C$, and with $Cu_{95}Au_5$ alloys, that do not show a discernible critical potential. Here, the formation of the pits was associated with a local breakdown of the protective overlayer that may be assisted by the surface stress that results from the lattice mismatch between the Cu-rich bulk alloy and the Au (or Au-rich) overlayer and is evident from Moiré patterns [54, 137].

By STM, most limitations of the TEM method may be overcome. This holds, in particular, for the electrochemical STM (EC-STM) technique that allows a real-time in situ study of electrodissolution processes at a lateral resolution at the nanometer scale or better, with the substrate and the tip controlled potentiostatically or galvanostatically during imaging (see Chapter 3.1 in Volume 3). Moreover, atomic height steps and topographic changes in the subnanometer range can be resolved [138]. On the other hand, chemical information is difficult to derive from STM and there is limited access of this method to the investigation of 3D porous structures as observed at $E > E_C$ [139]. Moreover, the quality of the surface preparation turns out to be a crucial point for STM studies of dealloying.

With mechanically polished β-brass, Alkeperov and coworkers investigated the initial (selective) stage of open circuit dissolution in acidified 1 N NaCl by ex situ STM and observed considerable faceting of the surface as well as the formation of 3D Cu nuclei. These morphological changes were attributed to both surface and volume diffusion processes. Pseudopreferential dissolution at a later stage of corrosion was assumed to proceed via the redeposition of Cu ions on the previously formed Cu nuclei [140]. In neutral chloride solutions, Morales and coworkers observed the development of a characteristic ''island'' and void structure, the ''islands'' consisting of faceted plateaus. Increasing the electrode potential enhanced the faceting, but smoothened the individual terraces on a fine scale. This observation was associated with enhanced Cu ad-atom mobility caused by an increased coverage with Cl^- ions, and from a detailed topographic analysis of the corroded surfaces, it was concluded that the kinetics of β-brass dealloying is controlled by surface-diffusion processes rather than by volume diffusion of Zn [141]. Moffat and coworkers [103] examined mechanically polished, polycrystalline Cu_3Au surfaces in 0.01 M H_2SO_4 + 0.99 M Na_2SO_4 by EC-STM and were able to differentiate three distinctive regimes of dealloying. At low overpotentials, the growth and dissipation of hill-like clusters (ca. 1 nm in height) was observed and was associated with the surface diffusion of Au ad-atoms. At higher potentials within the passive domain ($E < E_C$), localized regions of greater roughness were

detected. By analogy with the TEM results of Kabius and coworkers [136], these features were correlated with gold clusters that are formed in the vicinity of dissolution nuclei. At $E > E_C$, the surface coverage with hill-like Au clusters was increased, and upon reversal of the potential to $E < E_C$, these clusters dissipated as a result of the high surface mobility of Au. E_C was therefore explained as a roughening transition that occurs by nucleation and growth and depends on the exposure of fresh sites by the migration of passivating Au atoms on the surface. Taking into account that the surface migration of Au is increased by the adsorption of Cl^- [142], this view explains the depression of E_C in chloride solutions.

Significant progress in the STM investigation of dealloying was achieved by sample preparation via vapor deposition [143–145] or magnetron sputtering [99, 134, 146] of the alloy components. This technique does not require mechanical polishing and results in polycrystalline material with a sharp {111} texture and low defect, atomically smooth surfaces consisting of large terraces separated by steps. Alternatively, high-quality surfaces may be prepared from melt-grown single crystals by combined sputtering and annealing in ultrahigh vacuum (UHV) at elevated temperature [147–149]. Following one of these preparations, various ex situ and in situ STM observations were made with corroded Ag–Au and Cu–Au surfaces.

Au–Ag alloys Oppenheim and coworkers monitored corrosion of Ag–Au {111} surfaces in 0.1 M $HClO_4$ by EC-STM with monolayer depth resolution. By choosing low-Ag content alloys with compositions well below the parting limit, the preferential dissolution of Ag was confined to the first few atomic layers. Under these conditions, the authors demonstrated the dissolution of Ag atoms from terrace sites by the occurrence of surface roughening that evolved in the formation of monolayer deep pits or vacancy clusters on the terraces (see Fig. 18). When the accessible Ag atoms were exhausted, the roughened surface rearranged by vacancy cluster annihilation at the steps. By increasing the Ag concentration of the bulk alloy to value of 15 at.%, the terraces broke up into smaller ones. This result was associated with 2D percolation effects [143]. With a low-Ag content alloy of similar composition, Corcoran detected an interconnected island and channel structure that develops over several atomic planes. The average size scale of this structure was decreased by adding Ag^+ ions to the 0.1 M $HClO_4$ solution [146].

In addition to this, Wagner and collaborators reported on EC-STM results with $Ag_{0.8}$–$Au_{0.2}$ alloy thin films in 1 M $HClO_4 + 10^{-3}$ M $AgClO_4$ electrolyte (that is, with an alloy composition above the parting limit). At a subcritical potential of $E_{Ag/Ag^+} = 80$ mV, the STM images revealed the growth and coalescence of 1–3 monolayer deep vacancy clusters at step edges and on the terraces, as well as the formation of faceted Au-island structures. As E_{Ag/Ag^+} was increased to 120 mV, the coverage of the surface by the Au-islands was significantly increased. These surface morphology alterations were taken as a basis of modeling the transient electrochemical behavior at $E < E_C$ within the framework of the percolation concept and under particular consideration of vacancy cluster motion [99].

Cu–Au alloys Chen and coworkers studied Cu dissolution from gold-rich, disordered Au_3Cu films with {111} surfaces in 0.6 M NaCl + 0.01 M HCl by EC-STM. In

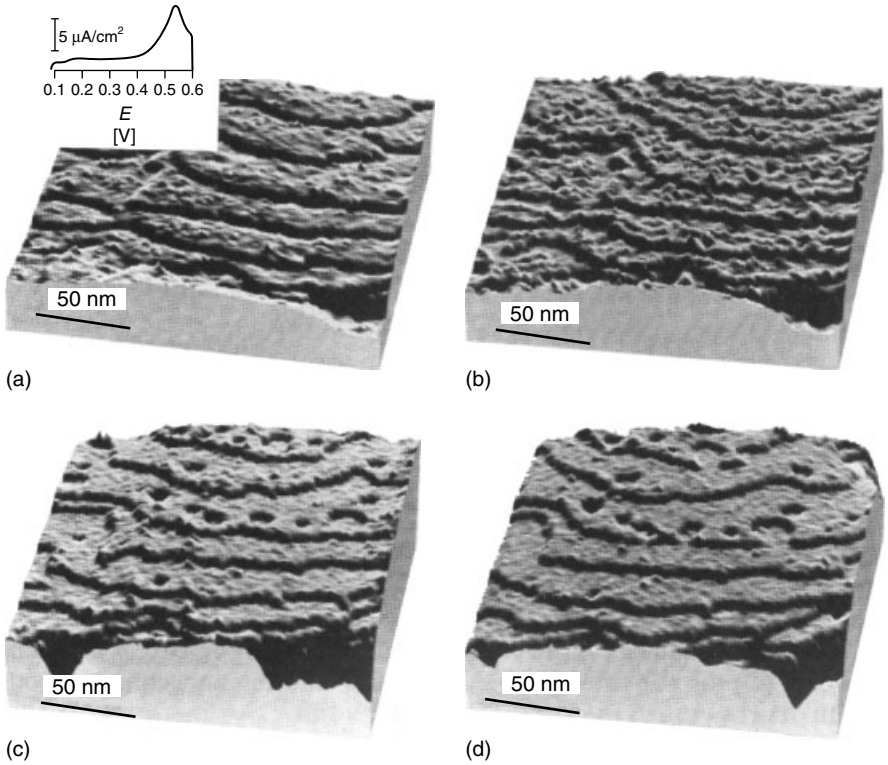


Fig. 18 In situ STM images of a $Au_{0.93}Ag_{0.07}$ alloy surface in 0.1 M $HClO_4$ (a) immediately; (b) 10 min; (c) 51 min; and (d) 86 min after scanning the electrode potential from the open circuit value to 0.6 V with respect to a Ag/1 mM Ag^+ reference electrode (vertical scale is extended ×10; the inset shows the current density during the potential scan). The initial roughening of the terraces (a) and (b) evolves in monolayer deep pits (c). Pits near the steps fused with them and left the steps highly curved (d). (Reprinted with permission from Ref. [143]. Copyright 1991, American Association for the Advancement of Science.)

the subcritical potential region of Au_3Cu, the dissolution of Cu also initiated the formation of monolayer deep pits (''voids'') in the terraces and near the steps. By the growth and coalescence of these pits, areas of the second atomic layer were exposed. However, the second layer remained smooth until the whole first layer of atoms disappears. This result was considered to be due to Au atoms of the first layer filling the holes in the second layer via surface diffusion, and indicates a 2D layer-by-layer dissolution process. At $E > E_C$, 2D layer-by-layer dissolution was replaced by the 3D growth of voids and it was hypothesized that this is related to the formation of highly mobile $Au(Cl^-)_n$ complexes [144, 145].

Eckstein revealed a dependence of the dealloying behavior of Au_3Cu on the orientation of the crystal surface [149]. Prior to electrochemical experiments, deviations from the bulk structure and composition in the topmost layers of low-index surfaces were detected by UHV structural characterization methods such as

low-energy electron diffraction (LEED), surface X-ray diffraction (SXRD) and STM. The $Au_3Cu(111)$ surface was found completely terminated by Au, whereas the (001) and (110) surfaces were only enriched in that component. The $Au_3Cu(001)$ surface, in particular, contained small clusters of Cu atoms in the topmost 2 atomic layers [148, 149]. These peculiarities of the low-index surfaces were reflected by their anodic dissolution behavior as monitored by EC-STM at increasing potential. In 0.1 M H_2SO_4, anodic dissolution from $Au_3Cu(111)$ was observed to begin at $E_H \approx 900$ mV, whereas $Au_3Cu(001)$ is already attacked at $E_H \approx 330$ mV. In the former case, dissolution required the formation and coalescence of monolayer deep vacancy clusters on the terraces of the topmost Au layer. Contrary to this, dissolution from $Au_3Cu(001)$ was facilitated by the embedded clusters of Cu atoms that serve as preexisting nucleation centers for 1–2 atom deep vacancy clusters that evolve in an island and channel structure. In 0.1 M H_2SO_4 + 0.1 mM HCl solutions, similar observation were made at significantly lower potentials, emphasizing the distinctive role of Cl^- adsorption on the dissolution process.

Dealloying of copper-rich, ordered Cu_3Au at subcritical potentials was

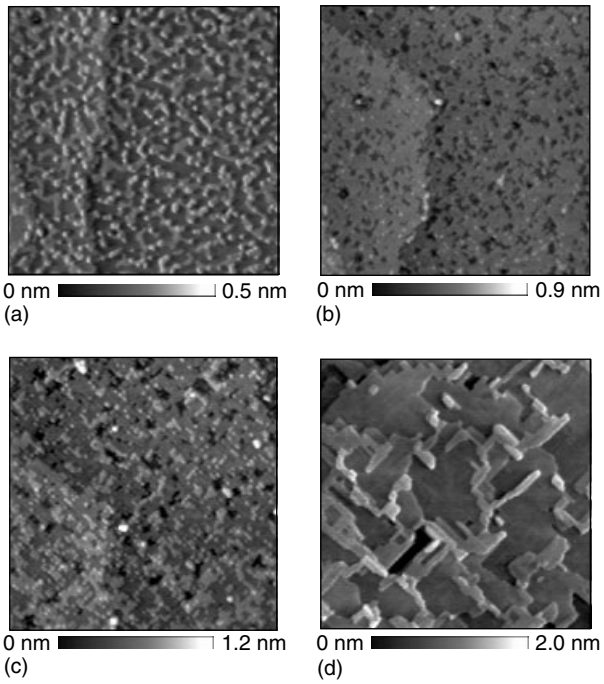


Fig. 19 In situ STM images of ordered $Cu_3Au(001)$ in 0.1 M H_2SO_4. (a) 44 min after scanning the electrode potential from an initial value of $E_H = 0.1$ V to $E_H = 0.25$ V; (b) 95 min after extending scan (a) to $E_H = 0.31$ V; (c) 240 min after extending scans (a + b) to $E_H = 0.35$ V; and (d) 254 min after extending scans (a − c) to $E_H = 0.49$ V. Image size is 200 nm × 200 nm (a − c) and 350 nm × 350 nm (d). (See text; from Ref. [149].)

investigated in a similar way. Prior to anodic dissolution the uppermost layers of (111) surfaces were of stoichiometric composition, whereas the Au atom fractions of the first and second layers of both $Cu_3Au(001)$ and $Cu_3Au(110)$ were ≈ 0.5 and ≈ 0 in accordance with the layer composition of the ordered bulk alloy [147, 150]. EC-STM investigations of these low-index Cu_3Au surfaces at increasing, subcritical potentials permitted deeper insight in the dealloying mechanism of this alloy: Dissolution of Cu from $Cu_3Au(001)$ in 0.1 M H_2SO_4, in particular, was initialized by a periodic layer-by-layer process. At electrode potentials up to $E_H = 0.25$ V, vacancy clusters (evolving in channels) and Au-rich islands were formed on the terraces, whereas dissolution at steps was largely inhibited at this stage (Fig. 19a). In the course of additional anodic polarization up to $E_H = 0.31$ V, dissipation of the Au-rich islands was observed (Fig. 19b). This indicates an intermixing of Au atoms from the islands and Cu atoms from the Cu_3Au substrate (surface alloying) that may be assisted by the relief of surface stress that results from the misfit between an Au (or Au-rich) lattice and Cu_3Au. Simultaneously, crystallographically oriented vacancy clusters were nucleated on the atomic plane beneath and at steps, thus initiating the next period of the layer-by-layer process that is visible at $E_H = 0.35$ V (Fig. 19c). Further increasing the electrode

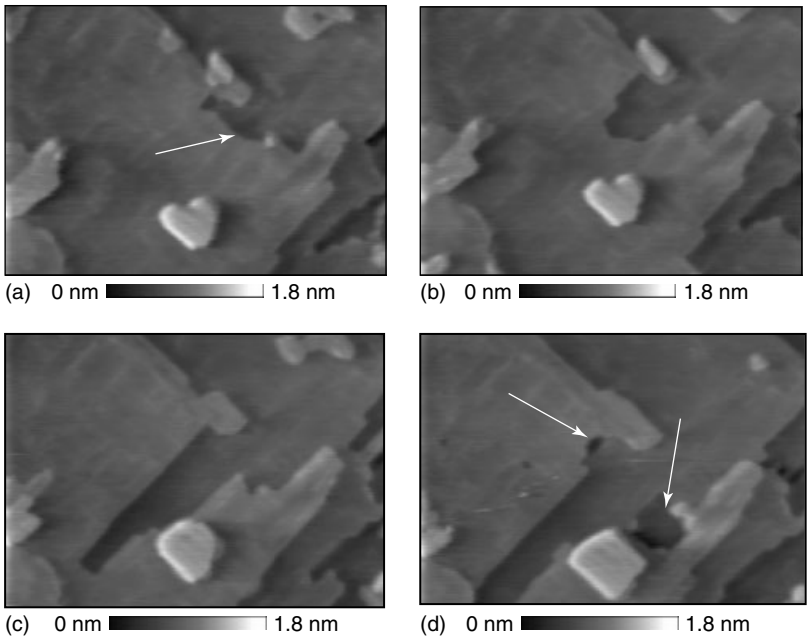


Fig. 20 In situ STM images of tunnel growth on faceted, $Cu_3Au(001)$ subsequent to the anodic polarization procedure of Fig. 19. (a) Nucleation of a 2D tunnel at a step (256 min at $E_H = 0.55$ V); (b) and (c) anisotropic growth of the 2D tunnel (261 min at $E_H = 0.57$ V and 274 min at $E_H = 0.59$ V, respectively); and (d) additional formation of 3D tunnels (287 min at $E_H = 0.63$ V). Image size is 150 nm × 200 nm throughout. (From Ref. [149].)

potential to $E_H = 0.49$ V, however, caused a considerable reordering of the (001) surface and ultimately resulted in the formation of numerous microfacets separated by steps (Fig. 19d). At this state, dissolution proceeds by 2D tunnels that nucleate at the steps and propagate on the terraces (Fig. 20a–c). Finally, with E approaching E_C, 3D tunnel growth was observed on $Cu_3Au(001)$ (Fig. 20d). $Cu_3Au(111)$, as the most reactive surface, dissolved by a similar layer-by-layer mechanism whereas dissolution from $Cu_3Au(110)$ was partly obscured by intense roughening [149].

Résumé EC-STM is a promising method for the in situ study of dealloying on a nanoscopic scale. Even though atomic resolution with alloy electrodes in solution has not been achieved so far, previous suggestions with respect to the inhibition of steps and the formation of vacancy clusters (''dissolution nuclei'') on the terraces at subcritical potentials have been elegantly confirmed. Moreover, evidence for a complex interplay of processes such as surface diffusion, surface alloying, and possible relaxation of stress at the island/alloy substrate interface has been elaborated. For a complete understanding of the dealloying mechanism, however, atomic resolution and chemical information on an atomic scale appear indispensable. As long as this objective is not achieved, the additional use of integral surface sensitive techniques such as in situ SXRD may be helpful.

References

1. H. Gerischer, *Werkst. Korros.* **1961**, *12*, 608–613.
2. H. W. Schadler, R. W. Grace, *Trans. AIME* **1959**, *215*, 559–566.
3. C. Wagner, W. Traud, *Z. Elektrochem.* **1938**, *44*, 391–454.
4. A. R. Pawlowych, D. L. Pile, H. W. Pickering et al., *Z. Phys. Chem.* **1998**, *207*, 113–126.
5. K. E. Heusler, *Electrochim. Acta* **1996**, *41*, 411–418.
6. K. J. Vetter, *Electrochemical Kinetics: Theoretical and Experimental Aspects*, Academic Press, New York, 1967.
7. D. D. MacDonald, *Transient Techniques in Electrochemistry*, Plenum Press, New York, 1977, pp. 85–92.
8. H. Bakker in *Diffusion in Crystalline Solids* (Eds.: G. E. Murch, A. S. Nowick), Academic Press, New York, 1984, pp. 189–256.
9. J. I. Gardiazábal, J. R. Galvele, *J. Electrochem. Soc.* **1980**, *127*, 255–258.
10. J. W. Koger, S. L. Pohlmann, Corrosion, *Metals Handbook*, 9th ed., ASM International, Metals Park, Ohio, 1987, pp. 88–91, Vol. 13.
11. F. Lantelme, S. Belaidouni, *Electrochim. Acta* **1980**, *26*, 1225–1236.
12. A. I. Marshakov, A. P. Pchel'nikov, V. V. Losev et al., *Élektrokhimiya* **1981**, *17*, 732–772.
13. H. Kaiser, *Werkst. Korros.* **1989**, *40*, 1–6.
14. A. J. Bard, L. Faulkner, *Electrochemical Methods*, John Wiley & Sons, New York, 1980.
15. A. G. Berezhnaya, V. V. Ékilik, *Élektrokhimiya* **1993**, *29*, 910–912.
16. W. K. Warburton, D. Turnbull in *Diffusion in Solids, Recent Developments* (Eds.: A. S. Nowick, J. J. Burton), Academic Press, New York, 1975, pp. 171–229.
17. A. Sawatzky, *J. Appl. Phys.* **1958**, *29*, 1303–1305.
18. G. Schwitzgebel, Y. Zohdi, P. Michael, *Acta Met.* **1975**, *23*, 1551–1555.
19. G. V. Raynor, J. A. Lee, *Acta Met.* **1954**, *2*, 616–620.
20. W. Jost, *Diffusion in Solids, Liquids and Gases*, Academic Press, New York, 1973, pp. 69–75.
21. G. H. Geiger, D. R. Poirier, *Transport Phenomena in Metallurgy*, Addison-Wesley, Reading, Mass., 1973, pp. 451–496.
22. H. W. Pickering, P. J. Byrne, *J. Electrochem. Soc.* **1969**, *116*, 1492–1496.
23. H. W. Pickering, *J. Electrochem. Soc.* **1970**, *117*, 8–15.
24. H. Gladen, H. Kaiser, H. Kaesche, *Corros. Sci.* **1990**, *30*, 737–741.

25. E. A. Owen, G. D. Preston, *Proc. Phys. Soc.* **1924**, *36*, 49–66.
26. G. Schwitzgebel, *Z. Phys. Chem. N.F.* **1975**, *95*, 15–24.
27. H. Kaiser, *Mater. Corros.* **1996**, *47*, 34–41.
28. M. Stein, S. P. Owens, H. W. Pickering et al., *Electrochim. Acta* **1998**, *43*, 223–226.
29. A. M. Alfantazi, U. Erb, *Corros. NACE* **1996**, *52*, 880–888.
30. T. C. Simpson, H. E. Townsend in *Corrosion Tests and Standards: Application and Interpretation*, ASTM Manual Series, MNL 20 (Ed.: R. Baboian), ASTM, Philadelphia, Pa., 1995, pp. 513–524.
31. A. D. Sitnikov, A. P. Pchel'nikov, I. K. Marshakov et al., *Zashchita Metallov.* **1978**, *14*, 258–265.
32. A. P. Pchelnikov, A. D. Sitnikov, I. K. Marshakov et al., *Electrochim. Acta* **1981**, *26*, 591–600.
33. R. F. Steigerwald, N. D. Greene, *J. Electrochem. Soc.* **1962**, *109*, 1026–1034.
34. M. Seo, N. Sato, *Langmuir* **1987**, *3*, 917–921.
35. K. E. Heusler, *Corros. Sci.* **1997**, *39*, 1177–1191.
36. J. E. Holliday, H. W. Pickering, *J. Electrochem. Soc.* **1973**, *120*, 470–475.
37. R. E. Hummel in *Electrochemical and Optical Techniques for the Study and Monitoring of Metallic Corrosion*, NATO ASI Series, Series E: Applied Sciences (Eds.: M. G. S. Ferreira, C. A. Melendres), Kluwer Academic Publishers, Dordrecht, 1991, pp. 241–283, Vol. 203.
38. S. Rambert, D. Landolt, *Electrochim. Acta* **1986**, *31*, 1421–1431.
39. S. Rambert, D. Landolt, *Electrochim. Acta* **1986**, *31*, 1433–1441.
40. T. Tsuru, *Mater. Sci. Eng.* **1991**, *A146*, 1–14.
41. Y. M. Kolotyrkin, *Electrochim. Acta* **1980**, *25*, 89–96.
42. M. Keddam, O. R. Mattos, H. Takenouti, *Electrochim. Acta* **1986**, *31*, 1159–1165.
43. M. Keddam in *Corrosion Mechanisms in Theory and Practice* (Eds.: P. Marcus, J. Oudar), Marcel Dekker, New York, 1995, pp. 55–122.
44. F. K. Grundwell, *Electrochim. Acta* **1991**, *36*, 2135–2141.
45. H. P. Lee, K. Nobe, *J. Electrochem. Soc.* **1993**, *140*, 2483–2489.
46. G. Tammann, *Z. Anorg. Allg. Chem.* **1919**, *107*, 1.
47. K. Sieradzki, J. S. Kim, A. T. Cole et al., *J. Electrochem. Soc.* **1987**, *134*, 1635–1639.
48. J. B. Friedrich, D. J. Young, M. S. Wainwright, *J. Electrochem. Soc.* **1981**, *128*, 1845–1850.
49. R. Bakish, W. D. Robertson, *Acta Metals* **1956**, *4*, 342–351.
50. H. Kaiser, H. Kaesche, *Z. Metallkd.* **1979**, *70*, 582–588.
51. H. W. Pickering, P. R. Swann, *Corrosion* **1963**, *19*, 373t–389t.
52. H. W. Pickering in *Fundamental Aspects of Stress Corrosion Cracking* (Eds.: R. W. Staehle, A. J. Forty, D. van Rooyen), NACE International, Houston, Tex., 1969, pp. 159–177.
53. P. R. Swann, W. R. Duff, *Met. Trans.* **1970**, *1*, 69–73.
54. B. G. Ateya, J. D. Fritz, H. W. Pickering, *J. Electrochem. Soc.* **1997**, *144*, 2606–2613.
55. R. Li, K. Sieradzki, *Phys. Rev. Lett.* **1992**, *68*, 1168–1171.
56. H. W. Pickering, *J. Electrochem. Soc.* **1968**, *115*, 690–694.
57. R. G. Kelly, A. J. Young, R. C. Newman in *Electrochemical Impedance: Analysis and Interpretation* (Eds.: J. R. Scully, D. C. Silverman, M. W. Kendig), ASTM International, San Diego, Calif., 1991, pp. 94–112.
58. U. Pittermann, R. Reining, K. G. Weil, *J. Electrochem. Soc.* **1994**, *141*, 3416–3422.
59. D. J. Young in *Advances in Phase Transitions* (Eds.: J. D. Embury, G. R. Purdy), Pergamon Press, Oxford, 1987, pp. 116–130.
60. H. Kaiser, Ph.D. Thesis, University of Erlangen-Nürnberg, Erlangen, 1976.
61. J. B. Friedrich, M. S. Wainwright, D. J. Young, *J. Electrochem. Soc.* **1981**, *128*, 1840–1844.
62. A. Craievich, A. Guinier, *Acta Met.* **1973**, *21*, 1327–1333.
63. S. G. Corcoran, D. G. Wiesler, J. Barker et al., *Mater. Res. Soc. Symp. Proc.* **1995**, *376*, 377–382.
64. S. G. Corcoran, D. G. Wiesler, K. Sieradzki, *Mater. Res. Soc. Symp. Proc.* **1997**, *451*, 93–98.
65. J. S. Chen, A. Kadic-Galeb, M. Ferrari et al., *Mech. Res. Commun.* **1992**, *19*, 555.
66. L. L. Shreir in *Corrosion* (Eds.: L. L. Shreir, R. A. Jarmann, G. T. Burstein), Butterworth-Heinemann, Oxford, 1994, pp. 1:151–1:190.

67. R. Zwicker, Ph.D. Thesis, University of Erlangen-Nürnberg, Erlangen, 1994.
68. K. Sieradzki, R. C. Newman, T. Shahrabi in *Advances in Localized Corrosion* (Eds.: H. S. Isaacs, U. Bertocci, J. Kruger et al.), NACE, Houston, Tex., 1987, pp. 161–164.
69. R. C. Newman, T. Shahrabi, K. Sieradzki, *Corros. Sci.* **1988**, *28*, 873–886.
70. A. D. Sitnikov, A. P. Pchel'nikov, I. K. Marshakov et al., *Zashchita Metallov.* **1979**, *17*, 34–38.
71. H. Kaiser in *Corrosion Mechanisms* (Ed.: F. Mansfeld), Marcel Dekker, New York, Basel, 1987, pp. 85–118.
72. International Standard ISO 6509 (1981–07), *Corrosion of metals and alloys – Determination of dezincification resistance of brass.*
73. M. E. D. Turner, *Proc. Soc. Water Treat. Exam.* **1961**, *10*, 162–179.
74. C. Breckon, P. T. Gilbert, *Chem. Ind.* **1964**, (January), 35–36.
75. V. F. Lucey, *Br. Corros. J.* **1965**, *1*, 9.
76. V. F. Lucey, *Br. Corros. J.* **1965**, *1*, 53.
77. M. J. Pryor, K.-K. Giam, *J. Electrochem. Soc.* **1982**, *129*, 2157–2162.
78. J.-P. Hirvonen, R. O. Toivanen, V. K. Lindroos, *Mater. Res. Soc. Symp. Proc.* **1988**, *125*, 87–93.
79. W. Qiu, F. Gan, L. Yao et al., *Mater. Sci. Forum* **1992**, *105–110*, 1189–1192.
80. J.-Y. Zou, D.-H. Wang, W.-Ch. Qiu, *Electrochim. Acta* **1997**, *42*, 1733–1737.
81. R. Heidersbach, *Corrosion* **1968**, *24*, 38–43.
82. R. Langer, H. Kaiser, H. Kaesche, *Werkst. Korros.* **1978**, *29*, 409–414.
83. P. Süry, H. R. Oswald, *Corros. Sci.* **1972**, *12*, 77–90.
84. D. S. Keir, M. J. Pryor, *J. Electrochem. Soc.* **1980**, *127*, 2138–2144.
85. L. Robbiola, J.-M. Blengino, C. Fiaud, *Corros. Sci.* **1998**, *40*, 2083–2111.
86. International Standard ISO 1562 (1993–12), *Dental casting gold alloys.*
87. Revised ANSI/ADA Specification No. 5-1981, cited in *J. Am. Dent. Assoc.* **1982**, *104*, 70.
88. H. J. Mueller, *Metals Handbook*, ASM International, Metals Park, Ohio, 1987, pp. 1336–1366.
89. D. W. Jones in *Medical and Dental Materials* (Ed.: D. F. Williams), VCH Publishers, New York, 1992, pp. 430–455.
90. J. M. Silcock, P. R. Swann in *Mechanisms of Environment Sensitive Cracking of Materials* (Eds.: P. R. Swann, F. P. Ford, A. R. C. Westwood), The Metals Society, London, 1977, pp. 66–82.
91. G. M. Scamans, P. R. Swann, *Corros. Sci.* **1978**, *18*, 983–995.
92. R. C. Newman, R. R. Corderman, K. Sieradzki, *Br. Corros. J.* **1989**, *24*, 143–147.
93. I. Olefjord, B. Brox, U. Jelvestam, *J. Electrochem. Soc.* **1985**, *132*, 2854–2861.
94. H. W. Pickering, P. J. Byrne, *J. Electrochem. Soc.* **1971**, *118*, 209–215.
95. W. Popp, Diploma Thesis, University of Erlangen-Nürnberg, Erlangen, 1980.
96. J. Gniewek, J. Pezy, B. G. Baker et al., *J. Electrochem. Soc.* **1978**, *125*, 17–23.
97. B. Kabius, Ph.D. Thesis, University of Erlangen-Nürnberg, Erlangen, 1987.
98. N. V. Vyazovikina, I. K. Marshakov, *Zashchita Metallov.* **1979**, *15*, 656–600.
99. K. Wagner, S. R. Brankovic, N. Dimitrov et al., *J. Electrochem. Soc.* **1997**, *144*, 3545–3555.
100. K. Hashimoto, T. Goto, W. Suetaka et al., *Trans. JIM* **1965**, *6*, 107–113.
101. B. D. Lichter, W. F. Flanagan, J. B. Lee et al. in *Environment-Induced Cracking of Metals, NACE 10* (Eds.: R. P. Gangloff, M. B. Ives), NACE International, Houston, Tex., 1990, pp. 251–259.
102. J. Laurent, D. Landolt, *Electrochim. Acta* **1991**, *36*, 49–58.
103. T. P. Moffat, F. F. Fan, A. J. Bard, *J. Electrochem. Soc.* **1991**, *138*, 3224–3235.
104. B. W. Parks, J. D. Fritz, H. W. Pickering, *Scr. Met.* **1989**, *23*, 951–956.
105. R. Reining, K. G. Weil, *J. Electrochem. Soc.* **1992**, *139*, L93–L95.
106. H. Kaiser, *Corros. Sci.* **1993**, *34*, 683–699.
107. J. D. Fritz, Ph.D. Thesis, The Pennsylvania State University, University Park, Pa., 1988.
108. J. Laurent, D. Landolt, *Mater. Sci. Forum* **1989**, *44/45*, 213–222.
109. B. G. Ateya, H. W. Pickering, *Corros. Sci.* **1996**, *38*, 1245.
110. G. Hultquist, H. Herø, *Corros. Sci.* **1984**, *24*, 789–805.
111. I. D. Zartsyn, A. V. Vvedenskii, I. K. Marshakov, *Elektrokhimiya* **1994**, *30*, 544–565.
112. A. V. Vvedenskii, I. K. Marshakov, *Electrochim. Acta* **1991**, *36*, 905–910.
113. W. Reimuth, *Anal. Chem.* **1960**, *32*, 1509–1512.

114. N. K. Sarkar, R. A. Fuys, J. W. Stanford, *J. Dent. Res.* **1979**, *58*, 1572–1577.
115. W. Popp, H. Kaiser, H. Kaesche et al., Metallic corrosion, *Proceedings – 8th ICMC*, Dechema, Mainz, 1981, pp. 76–81.
116. P. P. Corso, R. M. German, H. D. Simmons Jr., *J. Dent. Res.* **1985**, *64*, 854.
117. L. Reclaru, J.-M. Meyer, *J. Dent. Res.* **1995**, *22*, 301–311.
118. R. C. Newman, G. T. Burstein, *Corros. Sci.* **1981**, *21*, 119–128.
119. G. T. Burstein, G. Gao, *J. Electrochem. Soc.* **1994**, *141*, 912–921.
120. H. W. Pickering, C. Wagner, *J. Electrochem. Soc.* **1967**, *114*, 698–706.
121. I. K. Marshakov, A. V. Vvedenskii, V. Y. Kondrashin et al., *Anodnoe Rastvorenie i Selektivnaya Korroziya Splavov (Anodic Dissolution and Selective Corrosion of Alloys)*, Voronezh Gos. University, Voronezh, 1988.
122. R. M. Horton, *Corros. NACE* **1970**, *26*, 160–163.
123. H. Gerischer, H. Rickert, *Z. Metallkd.* **1955**, *46*, 681–689.
124. A. J. Forty, P. Durkin, *Philos. Mag. A* **1980**, *42*, 295–318.
125. A. J. Forty, G. Rowlands, *Philos. Mag. A* **1981**, *43*, 171–188.
126. D. A. Vermilyea, *J. Chem. Phys.* **1956**, *25*, 1254–1263.
127. E. B. Budevski in *Comprehensive Treatise of Electrochemistry* (Eds.: B. E. Conway, J. O'M. Bockris, E. Yaeger et al.), Plenum Press, New York, 1983, pp. 399–450, Vol. 7.
128. H. Kaesche in *Advances in Localized Corrosion* (Eds.: H. S. Isaacs, U. Bertocci, J. Kruger et al.), NACE International, Houston, Tex., 1987, pp. 153–159.
129. A. V. Vvedenskii, *Zashchita Metallov.* **1996**, *32*, 592–597.
130. Y. A. Popov, Y. V. Alekseev, *Zashchita Metallov.* **1991**, *27*, 575–580.
131. H. W. Pickering, *J. Electrochem. Soc.* **1968**, *115*, 143–147.
132. A. V. Vvedenskii, I. K. Marshakov, V. N. Storozhenko, *Elektrokhimiya* **1994**, *30*, 459–472.
133. K. Sieradzki, R. R. Corderman, K. Shukla et al., *Philos. Mag. A* **1989**, *59*, 713.
134. R. C. Newman, S. G. Corcoran, J. Erlebacher et al., *MRS Bull.* **1999**, *24*(7), 24–28.
135. K. Sieradzki, *J. Electrochem. Soc.* **1993**, *140*, 2868–2872.
136. B. Kabius, H. Kaiser, H. Kaesche in *Surfaces, Inhibition and Passivation* (Eds.: E. McCafferty, R. J. Brodd), The Electrochemical Society, Pennington, 1986, pp. 562–573, Proceedings Vol. 86-7.
137. J. D. Fritz, H. W. Pickering, *J. Electrochem. Soc.* **1991**, *138*, 3209–3218.
138. A. J. Bard, F.-R. F. Fan in *Scanning Tunneling Microscopy and Spectroscopy. Theory, Techniques and Applications* (Ed.: D. A. Bonnell), VCH Publishers, New York, 1993, pp. 287–324.
139. H. W. Pickering, Y. C. Wu, D. S. Gregory et al., *J. Vac. Sci. Technol., B* **1991**, *9*, 976–983.
140. S. D. Alekperov, A. B. Pchel'nikov, V. N. Chervyakov et al., *Protect. Metals* **1989**, *25*, 709–712.
141. J. Morales, P. Esparza, S. Gonzalez et al., *Langmuir* **1996**, *12*, 500–507.
142. R. J. Nichols, M. Magnussen, J. Hotlos et al., *J. Electroanal. Chem.* **1990**, *290*, 21–31.
143. I. C. Oppenheim, D. J. Trevor, Ch. E. D. Chidsey et al., *Science* **1991**, *254*, 687–689.
144. S. J. Chen, F. Sanz, D. F. Ogletree et al. in *10th European Congress on Corrosion – Progress in the Understanding and Prevention of Corrosion* (Eds.: J. M. Costa, A. D. Mercer), The Institute of Metals, London, 1993, pp. 1664–1673.
145. S. J. Chen, F. Sanz, D. F. Ogletree et al., *Surf. Sci.* **1993**, *292*, 289–297.
146. S. G. Corcoran, *Symposium on Critical Factors in Localized Corrosion III*, The Electrochemical Society, Pennington, 1999, pp. 500–507.
147. H. Niehus, C. Achete, *Surf. Sci.* **1993**, *289*, 19–29.
148. O. Bunk, J. H. Zeysing, R. L. Johnson et al., *Phys. Rev.* **1999**, *B62*, 8436–8440.
149. G. A. Eckstein, Ph.D. Thesis, University of Erlangen-Nürnberg, Erlangen, 2001.
150. E. G. McRae, T. M. Buck, *Surf. Sci.* **1990**, *227*, 67–72.

3.1 Atmospheric Corrosion

Christofer Leygraf
Royal Institute of Technology, Stockholm, Sweden

3.1.1 Introduction

Atmospheric corrosion involves various forms of corrosion effects at ambient temperature in which the Earth's atmosphere is the corrosive environment. Atmospheric corrosion has been recognized for several thousand years and the atmosphere is the most abundant environment to which solid materials are exposed. Hence, its implications in our society are enormous and range from bridges, elevated highways, railway and subway systems, aircraft, automobiles, and buildings, to industrial processes, electronic components and systems, to artistic or historic objects, such as statues and monuments. In the United States, for example, the total costs for all forms of corrosion have been estimated to be around 1000 US$ per capita per year. A substantial part of that amount is due to consequences of atmospheric corrosion.

Atmospheric corrosion is very complex and involves chemical, electrochemical, and physical processes in an interfacial regime that extends from the atmosphere (the gas phase) over a thin water layer (the liquid phase) to the corroding metal (the solid phase), see Fig. 1. The water layer is of crucial importance with a thickness that ranges from nanometers to millimeters, depending on humidity, precipitation, and sheltering conditions. Dry atmospheric corrosion, or dry oxidation, occurs virtually without any water layer present. A common example is the tarnishing of silver or copper, which can proceed through reaction with reduced sulfur compounds at low relative humidity (<50%). Damp atmospheric corrosion is triggered by elevated relative humidity and traces of atmospheric pollutants and results in a thin, mostly invisible water layer. Wet atmospheric corrosion, finally, occurs in rain or other forms of bulk water and results in a relatively thick water layer, often clearly visible to the eye.

Although atmospheric corrosion degrades most materials, such as calcareous stones, glasses, polymers, or metals, our understanding originates mostly from investigations of metallic objects. Hence, in order to illustrate the most important processes and concepts involved in atmospheric corrosion, this chapter is primarily based on our knowledge of

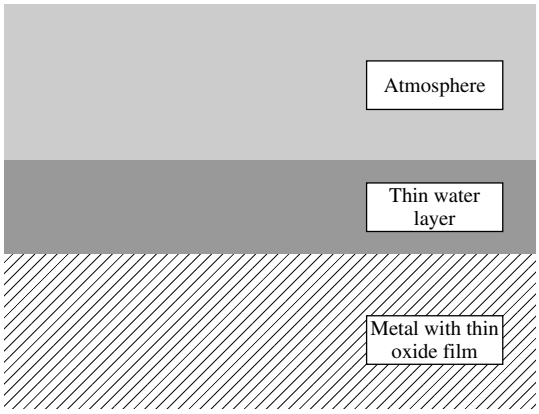


Fig. 1 The interfacial regime that extends from the atmosphere (the gas phase) over a thin water layer (the liquid phase) to the oxide-covered metal (the solid phase).

oxide-covered metals [1]. The description ranges from the very first stages of atmospheric corrosion (occurring within far less than a second of exposure), to intermediate stages, to the final stages (occurring after years of exposure).

3.1.2 The Different Stages of Atmospheric Corrosion

3.1.2.1 Initial Stages

3.1.2.1.1 **Surface Hydroxylation** When the metal is exposed to the atmosphere, there is an instant reaction of water vapor with the metal oxide surface. In most cases, the water molecule dissociates upon reaction and forms metal–oxygen or metal–hydroxyl bonds. The probability for the water molecule to dissociate, rather than to bond to the substrate in molecular form, increases with the number of lattice defects in the metal oxide. As a result, surface hydroxyl groups are formed, which act as adsorption sites for other water molecules. Surface hydroxylation is a rapid process that occurs on a timescale far shorter than a second.

3.1.2.1.2 **Adsorption and Absorption of Water** With surface hydroxyl groups present, the substrate is less conducive to rapid combination with water, which from now on bonds in molecular form. The first layer of adsorbed water molecules has a very high degree of ordering relative to the substrate. Subsequent adsorbed or absorbed layers contain water molecules that are less influenced by the substrate and possess a higher degree of random orientation. Aqueous films exhibit properties close to bulk water when their average thickness exceeds two or three equivalent monolayers [2]. This term refers to the amount of water when uniformly distributed on the surface. The water molecules commonly bond to the substrate as clusters or small droplets during early stages of interaction. One main reason is the similarity in bond strength between neighboring hydrogen-bonded water molecules on one hand and the bond strength between water molecules and the hydroxylated substrate on the other hand [3]. Another main reason is substrate heterogeneity caused by lattice defects such as grain boundaries, steps, kinks, and terraces. Interaction between water molecules and

the substrate may proceed – reversible or irreversible. In the former case, water is said to physisorb, whereas it chemisorbs in the latter case and forms a surface species.

Most real surfaces that are exposed to outdoor or indoor environments are far from clean and contain adsorbed particles with properties that are more or less hygroscopic and attract water. Porosity and roughness are other surface properties that may have a substantial influence on water adsorption characteristics. Figure 2 illustrates how humidity typically interacts with a metal surface during an outdoor exposure that lasts over several days or weeks [4]. The figure displays how the mass of gold changes during exposure to the outdoor environment. The mass response consists of periodic mass variation that is superimposed on a monotonous mass increase. The periodic variation coincides with variation in relative humidity, characteristic of any 24-h cycle. During nighttime, the relative humidity increases, which causes water to physisorb. The opposite situation occurs during daytime. Hence, each 24-h cycle results in a typical dry-wet-dry cycle. The monotonous mass increase, on the other hand, is due to irreversible processes, such as deposition of aerosol particles, and chemisorption of water or other reactants to form reaction products. The amount of reversibly adsorbed water is a measure of the mass of the aqueous adlayer. It depends on many factors, including the mass of hygroscopic particles, and reaches values typically in the range from 10^{-2} to 10^{-1} g m^{-2} ($10^{0} - 10^{1}$ μg cm^{-2}). The corresponding masses of water on metal surfaces covered by dew or rain is 10^{1} g m^{-2} and 10^{2} g m^{-2} ($10^{3} - 10^{4}$ μg cm^{-2}), respectively.

3.1.2.1.3 **Electrochemical Reactions** The aqueous adlayer is a crucial prerequisite for atmospheric corrosion. It acts as medium for electrochemical reactions and as solvent for atmospheric pollutants that deposit and dissolve in the aqueous

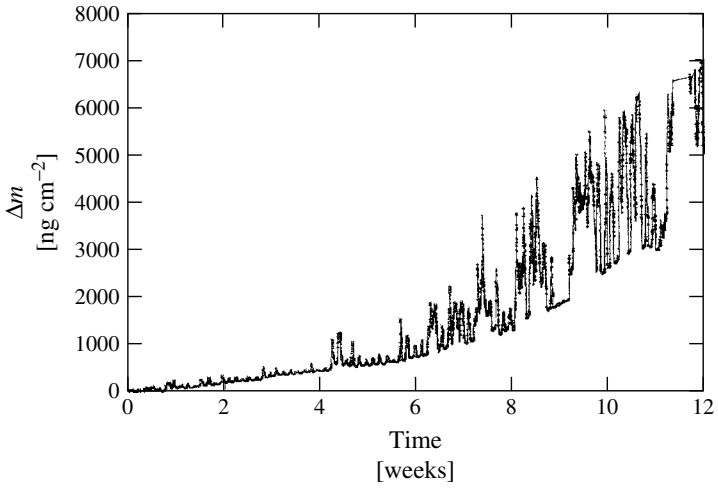


Fig. 2 Mass changes of gold as a function of time during an outdoor exposure. The data are based on experimental in situ data obtained by the quartz crystal microbalance. (Reproduced with permission from Ref. [4].)

phase. The electrochemical reactions occur at the interface between the metal and the aqueous layer. Surface heterogeneity results in surface sites conducive to predominantly anode reactions (see Chapter 1, Volume 4) and other surface sites conducive to predominantly cathode reactions (see Chapter 1, Volume 4). The dominant anode reaction in atmospheric corrosion is the metal dissolution process (see Chapter 1, Volume 4), normally written as

$$Me \longrightarrow Me^{n+} + ne^{-} \qquad (1)$$

Because of the ready access of atmospheric oxygen to a metal surface exposed to a thin liquid layer, the most common cathode reaction (see Chapter 1, Volume 4) for metals exposed to a thin aqueous phase is the oxygen-reduction process (see Chapter 1, Volume 4):

$$\tfrac{1}{2}O_2 + H^+ + 2e^- \longrightarrow OH^- \qquad (2)$$

When the aqueous layer is thin enough (less than 10 µm or so, see below) to permit ample access of oxygen to the metal surface, the anode reaction rather than the cathode reaction is rate limiting. This is the most common situation in atmospheric corrosion [5]. However, the surface and exposure conditions alter over a dry-wet-dry cycle or with extended exposure time and may eventually reach a situation in which the cathode reaction becomes the rate-limiting part (Sect. 3.1.2.3).

To illustrate the dependence of oxygen-reduction rate on liquid layer thickness, Fig. 3 displays a plot of the limiting current density for oxygen reduction (i_{lim}) as a function of inverse thickness of the liquid layer (X_f) [6]. In the thickness range above a few tenths of µm, the limiting current density is proportional to the inverse of the liquid layer thickness, which implies that oxygen diffusion through the liquid layer to the cathode reaction site is the rate-limiting step. In the thickness range below a few tenths of µm, the oxygen-reduction rate is

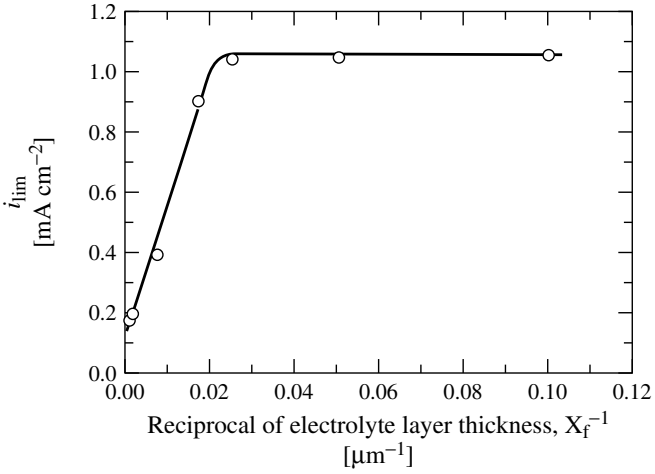


Fig. 3 Plot of the limiting current density for oxygen reduction (i_{lim}) as a function of the inverse of the liquid layer thickness (X_f). The data were obtained for platinum in a phosphate-buffered solution. (Reproduced with permission from Ref. [6].)

independent of the liquid layer thickness and, hence oxygen diffusion is no longer a rate-limiting step. In this thickness range, the solvation of oxygen is believed to be the rate-determining step for oxygen reduction. A thickness of a few tenths of μm is equivalent to a liquid layer mass of a few mg cm^{-2}. This relatively large amount of water is likely to be observed during dew or rain, but less likely during drier exposure conditions, see Sect. 3.1.2.1.

3.1.2.2 Intermediate Stages

3.1.2.2.1 Gas Deposition When the aqueous phase has formed, atmospheric constituents can deposit and dissolve into the liquid layer. Important atmospheric constituents known to influence atmospheric corrosion rates include gases, such as sulfur dioxide (SO_2), carbon dioxide (CO_2), nitrogen dioxide (NO_2), ozone (O_3) or hydrogen sulfide (H_2S), and aerosol particles, such as sodium chloride (NaCl) and ammonium sulfates ($(NH_4)_2SO_4$, $(NH_4)HSO_4$). The transfer of these species from the atmosphere to the aqueous phase may occur through dry deposition as a consequence of diffusion or gravitational settling, in which case there are no condensed water particles involved, or through wet deposition, in which case the transfer of species occurs through condensed water particles from rain, dew, fog, or snow.

According to Henry's law, the chemical activity, [X], of any dissolved gaseous constituent, X, in the liquid phase is directly proportional to the partial pressure, $p(X)$, of the same constituent in the gas phase:

$$[X] = H(X) \times p(X) \qquad (3)$$

$H(X)$ is Henry's law constant for species X.

For Henry's law to be valid, the aqueous layer and the atmosphere need to be in equilibrium. In most atmospheric corrosion applications, however, the equilibrium conditions are violated as a result of variations in atmospheric conditions and as a result of kinetic constraints. A major constraint is the relatively slow deposition rate of most atmospheric constituents, that is, the rate at which a gas or a particle in the atmosphere is transferred from the atmosphere into the aqueous phase. The deposition rate is controlled by aerodynamic factors, such as wind speed and type of wind flow, and surface specific factors, such as chemical makeup and thickness of the liquid layer. The deposition rate outdoors for important gaseous corrosion stimulators is typically in the range from 10^{-3} to 10^{-2} ng cm^{-2} s^{-1} [7]. Indoors, the corresponding deposition rates are one or two orders of magnitude lower.

3.1.2.2.2 Change in Liquid Layer Chemistry When dissolved into the aqueous phase, the atmospheric constituents alter the chemistry of the aqueous layer through various chemical or electrochemical reactions. One important chemical process is the deposition of sulfur dioxide into the aqueous layer to form bisulfite (HSO_3^-) ions:

$$SO_2(aq) \longrightarrow H^+ + HSO_3^- \qquad (4)$$

Reaction (4) is of vital importance since the ions produced may enhance the metal dissolution process (Sect. 3.1.2.2.3). When oxidants, such as nitrogen dioxide or ozone, dissolve into the aqueous phase, the bisulfite ion oxidizes to bisulfate (HSO_4^-), for example,

$$HSO_3^- + O_3 \longrightarrow HSO_4^- + O_2 \qquad (5)$$

Reaction (5) results in a more acid aqueous layer that triggers the metal

dissolution process further. Besides sulfur dioxide, many other atmospheric constituents may acidify the aqueous layer. They include carbon dioxide, nitrogen dioxide, and carbonyl compounds (HCHO and CH_3CHO) when forming their associated acids (H_2CO_3, HNO_3, HCOOH, and CH_3COOH). When the corroding surface undergoes dry-wet-dry cycles, changes in activity of chemical constituents may occur over several orders of magnitude. The pH of the aqueous layer also changes as a result of cycling humidity conditions. Hence, during wetting of the surface (for example, at nighttime when the temperature decreases), the aqueous phase dilutes and the activity of chemical constituents decreases. The reverse holds true during the drying of the surface, which may result in highly acidified conditions and enhanced momentary metal dissolution rates.

3.1.2.2.3 **Proton- and Ligand-induced Metal Dissolution** As described in Sect. 3.1.2.1.2, surface hydroxyl groups spontaneously form on the metal oxide surface in contact with the aqueous phase. These groups possess ion exchange properties and may easily be replaced by protons (H^+) and ligands such as bisulfite (HSO_3^-) or bisulfate (HSO_4^-) from the aqueous phase. Detailed studies of minerals in aquatic systems have provided insight into their dissolution mechanisms [8]. When the ligand exchange takes place, it weakens the bond between the surface metal center and its neighbor atoms, whereby the dissolution of the metal atom is promoted. An analogous mechanism may operate during atmospheric corrosion, with proton- or ligand-induced metal dissolution as an important step, at least in the initial stages. In particular, protons play a vital role during that process. They are mobile and readily form bonds between adjacent surface metal sites. If two or more proton-bonded neighbors surround a surface metal center, the bonds of the metal oxide lattice may weaken through bond polarization and the surface metal detaches from the lattice. When entering into the liquid layer, the metal ion forms a hydrated aquo-metal ion or anion-complex. The broken bond at the surface of the metal oxide is spontaneously hydroxylated. New protons are released that can participate in the detachment of another surface metal atom. The result is a dissolution process of the metal oxide that is highly acid-dependent with a dissolution rate, R_{diss} which can be written as

$$R_{diss} = C[a_{H^+}]^n \tag{6}$$

where n and C are constants and $[a_{H^+}]$ is the activity of protons. The process is schematically depicted in Fig. 4 for ligand-induced metal dissolution during initial stages of SO_2-induced atmospheric corrosion.

3.1.2.2.4 **Ion Pairing** Upon dissolution, the metal ion can coordinate with a variety of counterions in the aqueous layer. This ion-pairing process can be rationalized by means of the Lewis acid-base concept. When the metal ion (the Lewis acid, that is, a species that accepts an electron pair) and the counterion (the Lewis base, that is, a species that donates an electron pair) interact, the electrons involved form a covalent bond. Lewis acids and bases are more likely to coordinate if their electrons possess similar properties. So-called soft acids or bases have valence

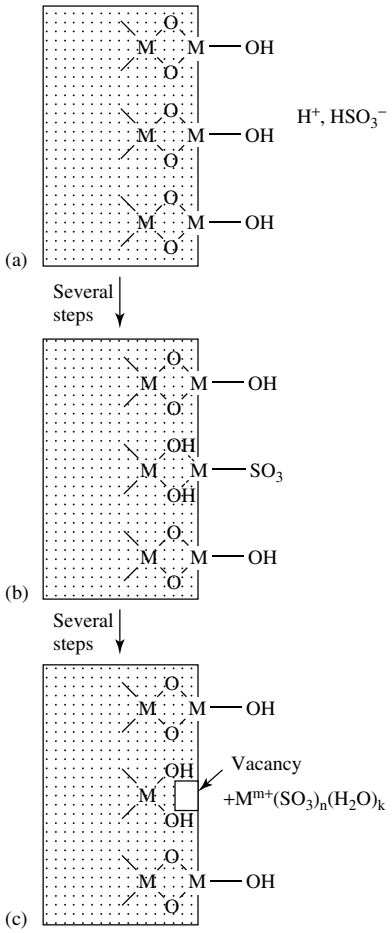


Fig. 4 Important steps during initial stages of SO_2-induced atmospheric corrosion: formation of protons and bisulfite ions in the aqueous layer (a), ligand exchange between a surface hydroxyl group and a bisulfite ion and subsequent weakening of adjacent bonds through proton-bonded neighbors (b), detachment of metal surface center that enters the aqueous phase as a hydrated metal anion-complex (c). (Reproduced with permission from Ref. [7].)

electrons that can more easily be removed or polarized. Hard acids or bases, on the other hand, have valence electrons that are more tightly held and are not so easily polarized. Hard acids preferentially coordinate with hard bases and soft acids with soft bases.

A selection of important metal ions and counterions, all of importance in atmospheric corrosion, have elsewhere been classified into hard, intermediate, and soft Lewis acids and bases [9]. The Lewis acid-base concept explains why hard acids, such as Al^{3+} and Ti^{4+} commonly form oxides or sulfates as corrosion products, whereas soft acids, such as Cu^{+} and Ag^{+}, commonly form sulfides. The concept also explains why intermediate acids, such as Zn^{2+}, Cu^{2+}, and Ni^{2+}, possess the ability to form corrosion products with a broader range of counterions [7].

3.1.2.2.5 **Photosensitivity** Many corrosion products possess semiconducting properties. When interacting with photons (see Chapter 1, Volume 6) of higher energy than the band gap of the semiconductor, electron-hole pairs are generated, which change the conditions for chemical reactions in different ways. Yet, there is not ample evidence of photosensitivity in atmospheric corrosion processes. One example is the exposure of copper to H_2S gas. In simulated sunlight, the corrosion rate was accelerated by a factor of between 1.5 and 2 [10]. Another example is the atmospheric corrosion of iron, which also is enhanced by solar photons. Iron forms hydroxide complexes, which are sensitive to solar photons. Upon absorption, the [Fe(OH)] complex undergoes charge transfer to the metal ion, OH radicals are liberated and a complex series of aqueous chemical reactions are triggered, including the sequential corrosion of iron.

3.1.2.2.6 **Nucleation of Corrosion Products** With prolonged exposure, the concentration of ion pairs in the aqueous phase gradually increases. If supersaturation is reached, the ion pairs precipitate into a solid phase. This transformation is complex and the ion pairs may pass through the colloidal state before they reach the solid state. Nucleation of precipitated species is facilitated by the heterogeneous nature of the substrate surface and the overall formation rate of the precipitate seems more often to be limited by its growth rate rather than by its nucleation rate. Evidence of this lies in the frequent observation of many small precipitated nuclei rather than a few larger ones, see Fig. 5 [11].

3.1.2.3 Final Stages

3.1.2.3.1 **Coalescence of Corrosion Products** The number of precipitated nuclei, and also their size, increases with exposure to the atmosphere. The nuclei will soon coalesce and will completely cover the metal surface. These precipitates are frequently referred to as corrosion products and play a crucial role for the metal in any given atmospheric environment. The corrosion products increase in thickness until they become visible to the eye (the rust layer on steel and the patina layer on copper are common examples) or remain invisible (the passive film on stainless steel being the most important example).

Further growth of the corrosion product layer requires that reactants from the aqueous phase, such as protons, chloride, or sulfate ions, must be transported inwards through the layer. Alternatively, metal ions must be transported outwards, or both inwards and outwards transport processes occur simultaneously. Hence, transport processes of anions or cations through the corrosion products are important parameters that may govern the atmospheric corrosion rate. Transport of electrons through the corrosion products may also be important. Electron transport is crucial so that electrons released in the anodic reaction can be transported to and consumed in the cathodic reaction. When the corrosion products possess poor electron conduction properties, the electron transport may become rate limiting. This situation cannot be fully comprehended

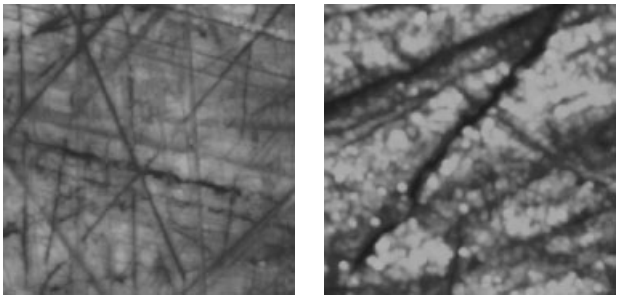


Fig. 5 AFM-images of a diamond polished copper surface before exposure (left) and after 24-h exposure to humidified air at 80% relative humidity (right). The formation of many small and equally sized islands (of cuprous oxide) form evidence that the growth rate, rather than the nucleation rate, in this case is the limiting step in the formation process of reaction products. (Reproduced with permission from Ref [11].)

without considering the availability of oxygen for the cathodic reaction. Oxygen enters from the atmosphere through the aqueous phase to the cathodic site. Hence, as long as the aqueous phase is thin enough (less than a few tenths of μm, Sect. 3.1.2.1), the access to oxygen is normally not rate limiting.

In all, the question of which process is rate limiting in atmospheric corrosion depends on many factors, including metal ion and cation transport properties through the corrosion products, and the access of oxygen through the aqueous phase.

3.1.2.3.2 **Dry-wet-dry Cycling** A key feature during atmospheric corrosion is the cyclic exposure condition during which atmospheric corrosion normally proceeds, at least outdoors. As demonstrated in previous sections, this results in an aqueous phase with altering thickness and, consequently, also in a strongly varying chemistry. The result is a gradual evolution of corrosion products characterized by a sequential growth that is triggered by cyclic environmental conditions. The sequential growth is common for all metals and proceeds through a sequence of consecutive steps, each one involving dissolution of species from the corrosion products followed by ion pairing, and subsequent reprecipitation. The dissolution process is accelerated by protons or other ions, including sulfate and chloride, during the wet part of the cycle. Once dissolved, the metal ions coordinate with counterions to form ion pairs according to their classification as hard or soft Lewis acids and bases. When approaching dry conditions, the ion pairs reach supersaturation and precipitate into a solid phase. Repeated dry-wet-dry cycles results in a sequential growth of corrosion products that become less soluble and, hence, more corrosion resistant.

The altering exposure conditions also causes other changes in properties of the corrosion products, such as the kinetics of the anodic and cathodic reactions involved. This has been clearly demonstrated on iron and steel, where redox-reactions (see Volume 2) are coupled with electron-transfer reactions (see Volume 2) [12]. The changes that occur during dry-wet-dry cycling can be demonstrated by assuming a rust layer consisting of lepidocrocite (γ-FeOOH) with a neutral aqueous phase, in which the anodic and cathodic reactions are

$$Fe \longrightarrow Fe^{2+} + 2e^- \quad (7)$$

$$\tfrac{1}{2}O_2 + H^+ + 2e^- \longrightarrow OH^- \quad (8)$$

When going from dry-to-wet conditions, the rust layer is partly changed in that some of the Fe^{3+} ions are reduced to Fe^{2+} through an additional cathodic reaction in the rust layer:

$$Fe^{3+} + e^- \longrightarrow Fe^{2+} \quad (9)$$

When the concentration of Fe^{2+} ions in the rust layer increases, the electronic properties of the layer change, which facilitates charge-transfer reactions, such as oxygen reduction. Further reduction of the lepidocrocite layer partly transforms it into magnetite (Fe_3O_4). Magnetite has electron conductivity properties close to those of metals, whereby the electron-transfer rate of electrons from the anodic to the cathodic site is increased. Overall, the change from dry-to-wet conditions results in reduction of the rust layer and enhanced rates of oxygen reduction. In the beginning of this change, the anodic reaction (metal dissolution) is balanced by the rate of reduction of Fe^{3+} to Fe^{2+}. During later stages, the metal dissolution

rate is balanced by the oxygen-reduction rate. Thus, the corrosion rate increases during this part of the cycle. When the rust layer is covered by a thick aqueous phase, the diffusion of oxygen from the gas phase through the aqueous phase and pores in the rust layer to the cathodic reaction site now becomes rate determining.

When going from wet-to-dry conditions, the thickness of the liquid layer decreases, which increases the oxygen-transfer rate to the cathodic sites. Hence, during the first part of the drying cycle the corrosion rate increases further. But the drying also results in a reoxidation of Fe^{2+} to Fe^{3+}, which reduces the electronic conductivity of the rust layer. Consequently, the oxygen-reduction rate is reduced, as is the corrosion rate. The results on iron demonstrate that considerable changes occur in the rust layer during dry-wet-dry cycles [12]. Changes in corrosion product properties are anticipated to be of importance during cyclic exposure conditions of other metals as well.

3.1.2.3.3 **Aging and Thickening of Corrosion Products** As demonstrated in the previous section, repeated events of dissolution-coordination – precipitation during dry-wet-dry cycling continuously causes the layer of corrosion products to age by changing its chemical composition, structure, crystallinity, thickness, electron conductivity, anodic and cathodic reaction rates, and corrosion rates. The evolution of corrosion products starts with the nucleation of an initial phase, continues by renewed dissolution of part or all of the initial phase. This is followed by ion pairing of metal ions and counterions of the aqueous layer, reprecipitation and rearrangement of new compounds in which the previous compounds act as seed crystals, renewed dissolution, ion pairing, and so forth. From this follows a gradual evolution of compounds in the corrosion products resulting in a continuously less soluble corrosion product layer. Evidence of this lies in the sequence of the formation of compounds found in corrosion products on copper, nickel, and zinc, see Fig. 6 [1]. The compounds may either undergo changes from an initial amorphous structure to a crystalline structure, or from one crystalline structure to another, structurally related, structure. The former situation is commonly seen on nickel and the latter on copper and zinc.

After long enough exposure time, the formation of corrosion products acquires stationary conditions characterized by nearly constant thickness and corrosion

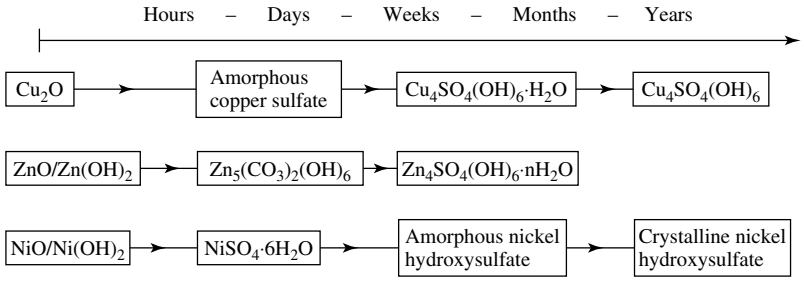


Fig. 6 Sequence of formation of compounds found in corrosion products formed on copper, zinc, and nickel in outdoor rain-sheltered exposure conditions a function of exposure time. (Reproduced with permission from Ref. [1].)

rate. During this final evolution stage, the runoff rate of metal from the corrosion products equals the corrosion rate. The time required to reach stationary atmospheric corrosion conditions is usually from several years to several decades. The gradual transformation to more resistant corrosion products supports the common observation that corrosion products formed after very long atmospheric exposure resemble, or are identical to, minerals formed as the result of natural processes in soil and rock.

3.1.3 Atmospheric Corrodents

3.1.3.1 Introduction

The atmospheric region closest to Earth, the troposphere, comprises more than two thousand chemical species – either as gases or as parts of atmospheric particles. More than 99.99% by weight of all gases consist of N_2, O_2 and rare gases (Ne, Kr, He, and Xe). Among these, only O_2 is of importance in atmospheric corrosion because of its role as an electron acceptor in cathodic reactions and its involvement in chemical transformations of the atmosphere. Other constituents of importance in atmospheric corrosion, but of lower concentration, include H_2O and CO_2. The important role of H_2O is evident from previous sections. Its concentration varies from around 100 ppmv (parts per million per volume) to around 10 000 ppmv. CO_2 is soluble in water and contributes to the acidification of the aqueous phase by forming the carbonate ion (CO_3^{2-}).

Atmospheric corrodents, that is, constituents capable of corroding a metal when exposed to the atmosphere, have a total concentration of less than 10 ppmv. These corrodents originate either from atmospheric gases or atmospheric particles and will be briefly discussed below. A more comprehensive description of atmospheric corrodents is given elsewhere [1].

3.1.3.2 Gases

3.1.3.2.1 **Ozone** Most chemical species in the atmosphere are oxidized, a process that is triggered mostly by the hydroxyl radical (OH·) and the ozone molecule (O_3). Both oxidants are produced by atmospheric photochemistry, with the dominant source reaction being the photolysis of nitrogen dioxide (NO_2), followed by combination with molecular oxygen:

$$NO_2 + h\nu \longrightarrow NO + O \qquad (10)$$

$$O + O_2 \longrightarrow O_3 \qquad (11)$$

The hydroxyl radical is produced when O_3 is photodissociated by ultraviolet radiation, generating an energetic oxygen atom that combines with a water molecule.

3.1.3.2.2 **Nitrogen Dioxide** Nitrogen dioxide (NO_2) is produced by rapid oxidation of nitric oxide (NO), which is formed during high-temperature combustion processes in vehicles, power plants, and so forth. NO_2 is also formed further away from the emission source through oxidation of NO by ambient O_3:

$$NO + O_3 \longrightarrow NO_2 + O_2 \qquad (12)$$

Nitrogen dioxide is quite insoluble in water, but may form nitric acid (HNO_3), which is most soluble, through reaction of NO_2 in the gas phase with the hydroxyl radical:

$$NO_2 + OH\cdot \longrightarrow HNO_3 \qquad (13)$$

This reaction requires a third body that carries away excess energy.

3.1.3.2.3 **Ammonia** Ammonia (NH_3) is produced both in natural ecosystems and by anthropogenic sources, such as agricultural industries, synthetic fertilizers, and burning of biomass. It is the only common atmospheric gas that is a base and is highly soluble in water.

3.1.3.2.4 **Hydrogen Sulfide** Hydrogen sulfide (H_2S) is produced mainly through anaerobic (see Chapter 6.6, Volume 4) degradation of organic sulfur compounds, largely a natural process. Most atmospheric corrosion induced by H_2S occurs near pulp mills or in oil fields. H_2S is slightly soluble in water and dissociates according to

$$H_2S(g) \longrightarrow H_2S(aq) \longrightarrow H^+ + HS^- \quad (14)$$

where the HS^- ion acts as the corrosive species.

3.1.3.2.5 **Sulfur Dioxide** Sulfur dioxide (SO_2) has many anthropogenic sources including the combustion of coal and oil containing sulfur. It is also emitted during metal-smelting processes, petrochemical, pulp, and paper industries.

In the gas phase, SO_2 can react with the hydroxyl radical ($OH\cdot$) to produce sulfuric acid (H_2SO_4) as an end product:

$$SO_2(g) + OH\cdot \longrightarrow HSO_3\cdot \longrightarrow \text{several steps} \longrightarrow H_2SO_4 \quad (15)$$

Sulfuric acid dissolves rapidly in any available water and dissociates. SO_2 is moderately soluble in water, where it is oxidized into the sulfate ion according to

$$SO_2(g) \longrightarrow SO_2(aq) \longrightarrow \text{several steps} \longrightarrow SO_4{}^{2-} \quad (16)$$

3.1.3.2.6 **Hydrogen Chloride** Most gaseous hydrogen chloride (HCl) enters the atmosphere mainly through dechlorination of airborne sea salt particles, which occurs when strong acids, such as nitric or sulfuric acid, deposit on them. HCl is highly soluble in water and dissociates readily to form the chloride ion (Cl^-), a highly corrosive species:

$$HCl(g) \longrightarrow HCl(aq) \longrightarrow H^+ + Cl^- \quad (17)$$

3.1.3.2.7 **Organic Acids** Formic acid (HCOOH) and acetic acid (CH_3COOH) are the most common of the organic acids known to be corrosive. They are emitted in many industrial processes and also through incomplete combustion of wood or other vegetation. It is one of the corrosive gases that can reach higher concentrations indoors rather than outdoors, mainly caused by the use of organic adhesives and plastics, tobacco smoke, and freshly cut wood. The organic acids are highly soluble in water.

3.1.3.2.8 **Summary** Table 1 summarizes typical concentration ranges of the gaseous corrosion stimulators described above. Data are given for both outdoor and indoor atmospheric environments. A comparison reveals, in general, lower levels indoors rather than outdoors. The reason is the enhanced indoor absorption of gases on walls, ceilings, and through ventilating systems and air filtration. Solubilities of the gases are given through Henry's law constant, which gives the relation between the activity of a species in the aqueous phase and the partial pressure of the same species in the atmosphere (Sect. 3.1.2.2).

Tab. 1 Outdoor and indoor concentration ranges (in ppbv, parts per billion per volume) of selected gaseous air constituents of importance in atmospheric corrosion together with their solubilities in aqueous systems, expressed as Henry's law constant (H, M atm^{-1})

Species	*Outdoor (ppbv)*	*Indoor (ppbv)*	*H (M atm^{-1})*
O_3	4–40	3–30	0,012
NO_2	10–80	1–30	0,007
NH_3	5–15	10–250	58
H_2S	0,5–25	0,1–0,7	0,1
SO_2	1–70	0,3–15	1,2
HCl	0,2–3	0,05–0,2	1,1

3.1.3.3 Particles

In addition to gases, aerosol particles turn out to be of utmost importance in atmospheric corrosion. Aerosols (that is, an ensemble of small liquid and/or solid particles suspended in the air) are generated with two characteristic size distributions. Smaller particles (termed *the accumulation mode*), with a diameter of less than around 1 μm, are formed through condensation of low-volatility gases. A common and important aerosol particle is ammonium sulfate ($(NH_4)_2SO_4$), which forms when ammonia is absorbed in, for example, cloud droplets and there combines with oxidized sulfur dioxide (Sect. 3.1.3.2). Larger particles (termed *the coarse mode*), with diameter of more than around 1 μm, are produced through different mechanical processes that result in windblown soil dust, sea spray, volcanic dust, and plant particles. The aerosol particles are deposited and dissolved into the aqueous layer on metal surfaces with deposition rates that vary with particle size. In dry deposition, smaller particles behave like gases and diffuse towards surfaces. Larger particles, on the other hand, follow motions of the air to the surface, while still larger particles have more momentum and impact on the surfaces independent of air movement. During wet deposition, the particles are captured by raindrops before reaching the surface on which they deposit.

Aerosol particles are chemical mixtures of a number of ionic species, including ammonium, sulfate, chloride, nitrate, and hydrogen. The actual chemical mixture of each particle reflects the chemical conditions in which the particle was formed. Once adsorbed on a metal surface, the water-soluble part of each particle acquires water from the atmosphere and deliquesces, whereby it transforms into a concentrated aqueous solution. The ionic constituents that are liberated into the aqueous film may have a significant influence on the atmospheric corrosion processes. Moreover, many particles possess hygroscopic properties and retain water. Hence, a typical particle may triple its volume when the relative humidity increases from dry to 90%.

3.1.3.4 Corrodent-metal Susceptibilities

Experience has shown that each metal behaves in a unique way with respect to atmospheric corrosion behavior. A particular corrodent does not necessarily corrode all metals and a particular metal is not necessarily susceptible to all corrodents. Table 2

Tab. 2 Metal sensitivities to atmospheric corrodents. H = high sensitivity, M = moderate sensitivity, L = low sensitivity, N = no sensitivity. Unfilled location implies that experimental data are missing

	Ag	*Al*	*Cu*	*Fe*	*Ni*	*Pb*	*Sn*	*Zn*
CO_2/CO_3^{2-}	L			M	L	M		M
NH_3/NH_4^+	M	L	M	L	L	L	L	L
NO_2/NO_3^-	N	L	M	M	M	M	L	M
H_2S	H	L	H	L	L	L	L	L
SO_2/SO_4^{2-}	L	M	H	H	H	M	L	H
HCl/Cl^-	M	H	M	H	M	M	M	M
$RCOOH/COOH^-$	L	L	M	M	M	H	L	M
O_3	M	N	M	M	M	M	L	M

is a summary of selected corrodent-metal susceptibilities and includes eight corrodents or corrodent pairs and eight metals [1]. Data from the literature are not always conclusive and therefore pairs of corrodents have been included in certain cases, indicating that the gaseous form or the ionic form or both may be the most active corrodent. It should be emphasized that the data in the table are not quantitative, meaning that identical sensitivity designations for different metals do not imply identical corrosion rates.

3.1.4 Laboratory Tests

3.1.4.1 Introduction

From previous sections, it is evident that many parameters can influence the atmospheric corrosion of a given metal. In order to perform more systematic studies of their influence, laboratory tests are frequently used in which only a few selected parameters are varied. By applying laboratory tests, individual parameters can be studied and varied under controlled conditions. Comparisons can also be made of the corrosion resistance in a given atmospheric environment of different metals under well-defined conditions. This section discusses general design considerations and describes important laboratory tests and how well they are able to mimic the atmospheric corrosion in ambient environments.

3.1.4.2 Design Considerations

A laboratory test must be designed and performed so that the most important parameters from an atmospheric corrosion perspective are controlled. Reproducibility and the ability to mimic the atmospheric corrosion in different ambient environments are other important criteria of a laboratory test. Parameters to consider in accelerated tests are sample preparations prior to exposure, relative humidity, temperature, exposure time, corrodents, and corrodent delivery rate [1].

3.1.4.2.1 **Exposure Chamber** Laboratory tests are commonly performed in an exposure chamber, see Fig. 7, in which the freshly prepared sample is exposed to a flowing atmosphere of filtered air to which corrodents are added. The volume should be of several dm^3 (litres) and the sample area of a few cm^2. All internal walls in contact with the atmosphere should be made of an inert material, for example, glass or polytetrafluoroethylene.

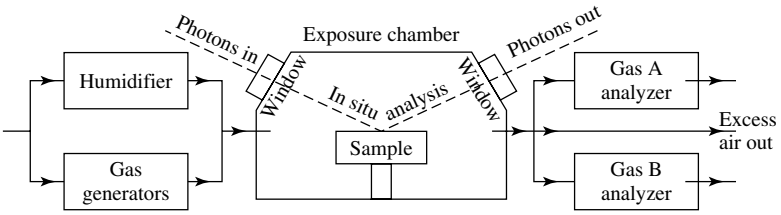


Fig. 7 Schematic diagram of an exposure chamber for controlled laboratory tests. (Reproduced with permission from Ref. [1].)

Condensation should be avoided. The air is filtered and purified from particles and gases by, for example, oil traps, particle filters, and activated charcoal, before it is humidified and corrodents added.

3.1.4.2.2 **Sample Preparation** For reproducibility reasons, it is important to consider a proper sample preparation, otherwise the resulting corrosion effect may be different from one exposure to the next. The test sample, usually a flat-shaped pure metal, is commonly prepared before exposure through some mechanical or chemical treatment, such as abrasion with SiC paper, diamond polishing, or immersion in a mild acid, followed by rinsing with demineralized water and alcohol. Immediately after surface preparation, the metal forms an oxide or oxyhydroxide upon exposure to the ambient environment that usually possesses some corrosion protective properties. The properties of the oxide or oxyhydroxide film may age with time, which may alter its corrosion protective ability. Hence, it is important also to consider the storage time prior to exposure.

3.1.4.2.3 **Relative Humidity, Temperature, and Exposure Time** The air is typically humidified at a constant relative humidity within the range from 50 to 95% and the variation in relative humidity should be kept within ±3% of the desired value. In order to avoid water droplets or aerosols, the air should never pass through water during the humidification step, but only above the water surface.

The temperature is usually kept constant in the range from 20 to 30 °C and within ±1 °C of the desired value. Within this range, the temperature dependence on the atmospheric corrosion rate is not so emphasized and the selected temperature value not so critical. If performing laboratory tests that are based on cyclic variations of relative humidity and temperature, it should be remembered that cyclic tests are difficult to reproduce between different experimental setups.

The exposure time depends on the aim of the test, test severity, and the corrosion resistance of the actual metal. It is usually selected in the range of a few days to a few weeks. Data on corrosion effects can be interpolated or extrapolated by applying an empirical relationship between corrosion effect (M) as a function of time (t):

$$M = At^n \tag{18}$$

with n usually in the range between 0.5 and 1.0 and A a constant of proportionality.

3.1.4.2.4 **Corrodents and Their Delivery** The choice of corrodents, their concentrations, and delivery rates are other important parameters to consider in laboratory tests. Despite the importance of aerosol particles, most tests so far reported have

been based on gases. Comparison with exposures in natural atmospheres suggest that gas concentrations in the range of a few tens to a few hundreds of ppbv (volume parts per billion) give reasonable agreement with field data. Higher levels may introduce physical or chemical processes during atmospheric corrosion that are not representative of field exposures, whereas lower levels may increase the exposure time too much.

Table 3 is a summary of commonly used corrodents in laboratory exposures [1]. Methods to generate and monitor the corrodents are also displayed in the table. For several important constituents, no suitable continuous monitoring technique is available. Gaseous chlorine is often used as a substitute for hydrogen chloride, for which there is no simple way of generation. However, the use of gaseous chlorine is debated because of its absence in many important atmospheric environments. It may introduce a corrosion chemistry into the experiments regarded as unrealistic.

An often overlooked but important parameter in laboratory tests is the delivery rate of corrodents through the gas phase to the corroding surface. This rate is determined by flow conditions near the surface and the local air velocity. The most common and realistic flow condition is turbulent flow, in which convection is the dominant delivery mechanism of corrodents to the surface. In laminar flow, diffusion is the dominant transport mechanism, especially at low air speeds. Because of reactions between the metal surface and the airborne corrodent, there is a boundary region in the gaseous regime next to the surface, characterized by a depletion in corrodent characterization, see Fig. 8 [1].

The atmospheric corrosion rate is usually said to be under mixed control, with the rate determined both by the delivery rate of corrodents to the surface and by the reaction rate of reactants with the surface. Two extreme situations can be identified. Under highly turbulent and well-stirred airflow conditions, there is no limitation in transport rate and the corrosion rate is only determined by surface reaction rates. On the other hand, when the corroding surface acts as an ideal absorber for corrodents, there is no limitation in surface reaction rate and the corrosion rate will be limited by transport processes to the surface.

Tab. 3 Commonly studied air constituents in laboratory tests, and techniques for their generation and continuous analysis

Air constituent	*Generating technique*	*Analytical technique*
SO_2	Permeation tube	Fluorescence
NO_2	Permeation tube	Chemiluminescence
NH_3	Permeation tube	Chemiluminescence
O_3	UV radiation	UV photometry
H_2S	Permeation tube	Lead acetate densitometry or conversion to SO_2 and fluorescence measurements
Cl_2	Permeation tube	No suitable technique for continuous measurements
$(NH_4)_2SO_4$	Solution atomizer, spraying	No suitable technique for continuous measurements
NaCl	Spraying	No suitable technique for continuous measurements

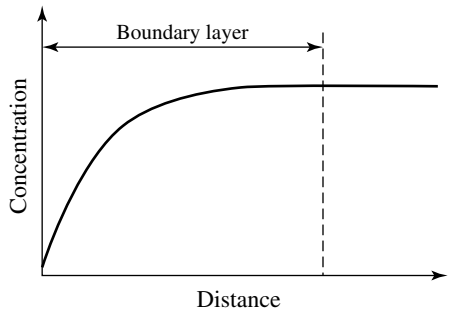


Fig. 8 Boundary region in the gas phase next to the surface, characterized by a depletion in corrodent concentration.

3.1.4.3 Simulation Considerations

One primary aim of laboratory tests is to mimic specific field exposures under accelerated conditions. This requires that the exposure conditions of the laboratory test trigger the same corrosion processes as the actual field exposure does. In view of the multitude of different air constituents and climatic factors that may influence the corrosion behavior during exposure in any natural environment, one may ask whether the laboratory test really can be represented by only a few parameters present. To explore this question, a comprehensive study has been performed in which the corrosion effects of nickel have been compared in the field and laboratory, respectively [13].

The natural exposure situation of a large number of sheltered test sites was analyzed with respect to relative humidity and airflow rate. By using a set of representative and constant values of relative humidity, temperature, and airflow rate, and with sulfur dioxide and nitrogen dioxide as the only gaseous corrodents, it turned out that the laboratory test generated not only similar corrosion rates but also a similar composition of corrosion products in the laboratory and field investigations, respectively. Hence, by applying these exposure parameters, the same processes appear to be operating during the atmospheric corrosion of nickel under field and laboratory conditions, respectively.

Each metal behaves in a unique way with respect to atmospheric corrosion properties, and the conclusions drawn from the nickel study cannot necessarily be drawn for other metals. However, if the same or similar corrosion products are formed on a given metal when exposed to a laboratory and a natural atmospheric environment, respectively, the results suggest that the same corrosion processes are operating in both exposures. Table 4 displays examples of reported laboratory tests that have generated corrosion products similar to those seen in natural field exposures [13–18]. It appears that certain combinations of two or three corrodents at concentrations below 1 ppmv, together with a proper choice of relative humidity and airflow rate, can generate the corrosion products that are formed in natural field environments.

3.1.4.4 Standardized Accelerated Tests

Standardized laboratory exposures for accelerated corrosion tests have been developed for various industrial products and applications. Previous tests usually used only one gaseous corrodent, mainly sulfur dioxide or hydrogen sulfide, at very high concentrations (>10 000 ppbv). More recently developed laboratory tests for evaluating, for example, electronic devices

Tab. 4 Characteristics of laboratory tests with corrosion products similar to those in certain field environments

Corrodent	*Metal*	*Main phase (s)*	*Type of simulated field environment*	*Ref.*
SO_2, NO_2	Nickel	$NiSO_4 \cdot 6H_2O$	Rural, urban	13
SO_2, NO_2	Copper	Cu_2O, $Cu_4(SO_4)(OH)_6$, $Cu_4(SO_4)(OH)_6 \cdot H_2O$	Urban	14
$(NH_4)_2SO_4$	Copper	Cu_2O, $Cu_4(SO_4)(OH)_6$, $Cu_4(SO_4)(OH)_6 \cdot H_2O$	Rural Office	15
NaCl, SO_2	Zinc	$Zn_5(OH)_8Cl_2 \cdot H_2O$	Marine	16
Cl_2, NO_2, H_2S	Copper	Cu_2O, $Cu_2Cl(OH)_3$ $Cu_4(SO_4)(OH)_6 \cdot H_2O$	Indoor industry (pulp and paper)	17
SO_2, NO_2	Nickel Copper Gold-plating	Ni(II)-sulfates and hydroxysulfates	Traffic Telephone exchange	18

consist of flowing gas and multicorrodent mixtures of mainly sulfur dioxide, hydrogen sulfide, nitrogen dioxide, or chlorine gas at much lower concentrations (<1000 ppbv). These accelerated tests all operate at constant temperature and relative humidity. Frequently used tests are those adopted by the International Electrotechnical Commission (IEC) [19] and by the Battelle Institute in USA [20], respectively. Their aim is to mimic indoor exposure situations.

An accelerated corrosion that aims to mimic outdoor exposures has been adopted by the International Organization for Standardization (ISO). It is based on cyclic deposition of sodium chloride (NaCl) aerosols, and to cyclic changes in dry and wet conditions [21].

3.1.4.5 Important Laboratory Test

Whereas the standardized accelerated tests emphasize robustness and reproducibility in performance, a number of important accelerated tests have been developed for scientific purposes that emphasize versatility, scientific understanding and ability to extract in situ information during ongoing atmospheric corrosion. Advanced laboratory tests allow exposures of metals in the presence of several gaseous corrodents at very low concentrations (<100 ppbv), in situ analysis of the deposition rate of each investigated corrodent and in situ analysis of the chemical composition of initially formed corrosion products, both as a function of exposure time. The schematics of an exposure chamber is illustrated in Fig. 7. The deposition rate is obtained by comparing the concentration of gaseous corrodents at the inlet and outlet of gas to the exposure chamber from which the consumption of gas in the chemical reactions can be deduced. The continuous growth of corrosion products on the metal surface can be obtained from several techniques that can provide in situ information during exposure of the metal surface to the atmosphere. Such techniques include infrared reflection absorption spectroscopy (IRAS, identification of chemical species), quartz

crystal microbalance (QCM, changes in mass, see Chapter 7, Volume 4), atomic force microscopy (AFM, changes in surface topography, see Chapter 7, Volume 4) and the Kelvin probe (variation in corrosion potential along the corroding surface, see Chapter 7, Volume 4). The use of such techniques have generated a better molecular insight into the corrosion mechanisms that govern the role of gaseous or particulate corrodents.

One excellent example of a multianalytical laboratory study is the influence of submicron sized particles of ammonium sulfate ($(NH_4)_2SO_4$) on the atmospheric corrosion of selected metals [22]. These particles were aerosolized and deposited under dry conditions on the metal surface, whereby the deposited amounts corresponded to up to 10 years of exposure in indoor locations of USA. By introducing humidity into the exposure chamber, the particle-induced corrosion process could be followed by a multitude of analytical techniques, including infrared spectroscopy and the Kelvin probe. As an example, Fig. 9 displays the variation of corrosion potential in the vicinity of a deposited particle, as obtained by the Kelvin probe. Such results help in interpreting the corrosion behavior observed during indoor or outdoor exposures, which largely is influenced by deposited aerosol particles.

3.1.5 Field Tests

3.1.5.1 Introduction

Corrosion in natural outdoor or indoor environments is complex because of the influence of many different parameters. Yet, it is possible to grasp, at least qualitatively, the behavior of atmospheric corrosion through consideration of concepts and

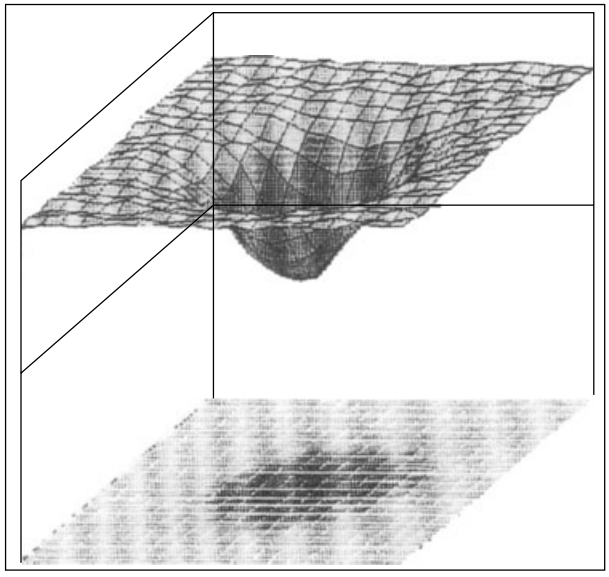


Fig. 9 The variation in corrosion potential (vertical axis) over a surface area sized 2000 × 2000 μm 18 hours after depositing an $(NH_4)_2SO_4$ particle. The results were obtained by a Kelvin probe during exposure at 300 K and 93% relative humidity. (Ref. [22].)

parameters, as they were described in Sect. 3.1.2. The most crucial parameter is surface water, deposited under conditions of high relative humidity or rainfall and given up by evaporation under less humid conditions. Triggered by cyclic or strongly varying humidity conditions, atmospheric corrosion normally proceeds through a sequence of consecutive steps, each one corresponding to a dry-wet-dry cycle and consisting of dissolution of species, followed by ion pairing and subsequent reprecipitation. The dissolution process is accelerated by protons or other ions, including sulfate and chloride. Once dissolved in the aqueous adlayer, the metal ions tend to coordinate with counterions. The composition of counterions is highly dependent on the chemical and flow conditions of the atmospheric environment. When the ion pairs reach supersaturation, they will precipitate into a solid phase. With this conceptual framework in mind, it is easier to understand some specific differences between outdoor and indoor atmospheric corrosion.

3.1.5.2 Outdoor Exposures

3.1.5.2.1 **Time-of-wetness** From what has been said previously, it is evident that important atmospheric parameters to influence outdoor atmospheric corrosion are relative humidity, temperature, concentration of aerosol and gaseous corrodents, flow conditions, and degree of sheltering. The combined action of relative humidity, temperature, and deposited aerosol particles (which may retain the aqueous adlayer on the surface) largely determines the degree of surface wetting. An important concept for characterizing a wetted surface, and established from an atmospheric corrosion perspective, is the so-called *time-of-wetness*. It is commonly defined as the time during which, simultaneously, the temperature is $>0\,^{\circ}C$ and the relative humidity $\geq 80\%$. However, actual conditions that determine if a surface is wet are far more complicated to define than through this relatively simple definition. In fact, detailed surface studies have shown that the time during which the surface is wet enough for atmospheric corrosion to occur commonly exceeds the time-of-wetness as defined above (see Fig. 10). One main reason are all deposited aerosol particles that retain surface water even when the relative humidity is significantly below 80%. Another reason is the freezing point for the aqueous adlayer, that often is found to be in the range between -5 and $-10\,^{\circ}C$. From this follows that the actual time for the surface to be ''wet'' is extended as compared to the definition of time-of-wetness from above [4].

Atmospheric corrosion rates are commonly related to a ''critical relative humidity'', above which the corrosion rate increases significantly and below which the rate is insignificant for many practical purposes. Depending on metal and exposure conditions, critical relative humidities have been reported in the range from 50 to 90%. The critical relative humidity is associated with the point of deliquescence of deposited aerosol particles, above which the aerosols rapidly absorb water until a saturated solution is obtained. For a single-phase aerosol, there is a well-defined critical relative humidity, whereas for a mixture of phases (the common situation in natural outdoor environments) the critical relative humidity is lower than those of the single phases.

3.1.5.2.2 **The ISO Classification System** On the basis of a worldwide atmospheric exposure program, known as

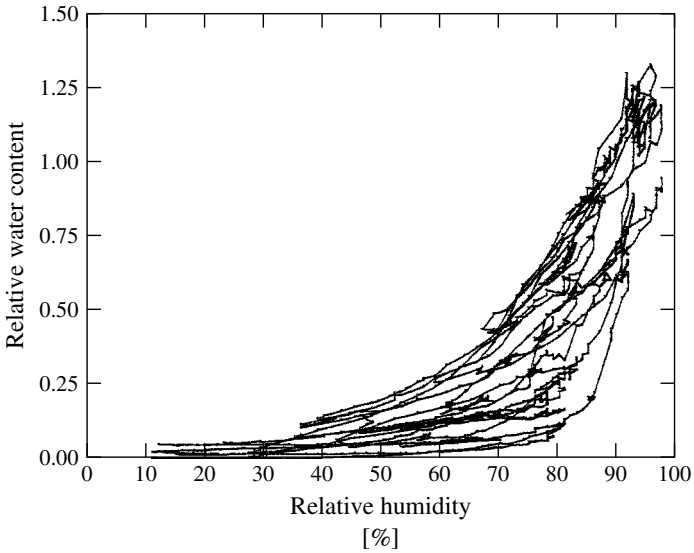


Fig. 10 The relative mass of water, defined as the total mass of water divided by the total mass of deposited particles, retained on a gold surface and plotted as a function of relative humidity during a large number of consecutive 24-h cycles. Each cycle is represented by one increase (during nighttime) and one decrease (during daytime) in relative mass of water and relative humidity, respectively. The figure clearly shows that significant amounts of water are present at a relative humidity far below 80%. The data have been obtained through outdoor use of the quartz crystal microbalance. (Adapted with permission from Ref [4].)

ISO CORRAG [23], the International Organization for Standardization (ISO) has implemented a classification system for evaluating atmospheric corrosivity and on the basis of variables that are fairly easy to obtain [24, 25]. This ISO classification has found several applications, for example, to predict the long-term corrosion behavior in different environments and to evaluate the effect of protective coatings. It contains two principally different approaches of assessing the corrosivity of any outdoor atmospheric environment. The first is based on exposure of standard specimens of steel, copper, zinc, and aluminum for one year whereby the corrosion effect is measured through mass loss measurements. One of five measured corrosivity classes is assigned for each metal. The second approach is based on the measurement of the deposition rate of sulfur dioxide, deposition rate of chloride ions, and time-of-wetness at the site, the combination of which results in an estimated corrosivity class. On the basis of the measured or the estimated corrosivity class, a prediction of the extent of long-term corrosion damage of steel, copper, zinc, and aluminum can be made.

3.1.5.2.3 **Corrosion Rates** The most precise way of defining the corrosion effect is through the measurement of the difference in mass of the metal before exposure and after exposure and subsequent dissolution of corrosion products. Hence, the

corrosion effect upon atmospheric exposure is commonly determined as a mass loss of metal.

In Sect. 3.1.4.2, an empirical relationship between corrosion effect (M) and exposure time (t) was introduced:

$$M = At^n \tag{18}$$

It turns out to be a fairly good approximation in most outdoor exposures – provided the exposure period is long enough – and for a variety of metals and alloys, including carbon and low alloy steels, galvanized steel, and zinc, copper, and copper alloys. The A factor in the relationship gives the initial corrosion rate and the exponent n is a measure of the protective ability of the corrosion products formed. In benign environments, the generated corrosion product films possess protective properties, resulting in n-values of 0.6 or lower. In highly aggressive environments, on the other hand, n-values close to 1 are often observed. This corresponds to a situation in which the corrosion product films possess little protective properties, if any. The corrosion rate in this case is mainly governed by the supply.

3.1.5.2.4 **Effect of Rain Sheltering** Rain-sheltered outdoor exposures differ from unsheltered exposures in several ways. During sheltering, the surface is shielded from direct precipitation and solar radiation. Sheltering may also prevent coarse aerosol particles, such as windblown sea salt or soil dust, from reaching the exposed metal surface. On the other hand, it does not hinder smaller aerosol particles and gases from reaching the surface and interacting. There is no easy way of predicting if rain sheltering has an accelerating or retarding effect. Direct precipitation, for instance, may increase the corrosion rate by wetting the surface and depositing atmospheric constituents. On the other hand, it may decrease the corrosion rate by washing off deposited corrodents from the metal surface.

3.1.5.2.5 **Acid Deposition** Sulfur dioxide and nitrogen dioxide are two important acidifying pollutants that contribute to acid deposition effects of materials. Sulfur dioxide concentrations increase in countries characterized by rapid industrialization with a lack of emission controls and decrease in countries with emission controls combined with the use of coal and oil with low sulfur content. The concentration of nitrogen dioxide in the same environments are characterized by more constant values or increasing trends. Hence, the molar ratio between nitrogen dioxide and sulfur dioxide has increased with time, thus changing the mechanism for the oxidation of S(IV) to S(VI) (Sect. 3.1.2.2). While accelerated corrosion tests with different concentrations of sulfur dioxide and nitrogen dioxide have unambiguously proven that nitrogen dioxide increases the atmospheric corrosion rates of several metals, the corresponding effect of nitrogen dioxide in field exposures has so far been unsuccessful. This experimental contradiction is most likely related to the inherent difference between accelerated tests performed in the laboratory, in which each gaseous constituent can be controlled separately, and field exposures, characterized by an uncontrolled multipollutant exposure situation. Since nitrogen dioxide and ozone are intertwined (Sect. 3.1.3.2), the oxidizing role of nitrogen seen in laboratory exposures is hidden in field exposures because of the presence of ozone and other oxidants.

3.1.5.3 Indoor Exposures

Although the same fundamental corrosion related processes and concepts operate in both indoor and outdoor atmospheric corrosion, corrosion rates indoors are generally found to be lower than outdoors. The main reasons are the variations in relative humidity, that are far less dramatic indoors than out, and the deposition rates and concentrations of gas or particle corrodents, generally also lower indoors than out. The same physicochemical processes operate, however, including the adsorption of water, deposition of gases and particles into the liquid layer, proton and ligand-induced dissolution, ion pairing, and precipitation and growth of corrosion products. Dry-wet-dry cycles are less common indoors and only expected in locations with relatively high outdoor-indoor exchange rates. As a result, mean indoor corrosion rate values of most metals, including iron, copper, nickel, cobalt, and zinc are typically between two and three orders of magnitude lower than outdoors (Fig. 11) [26]. Silver is an exception, which exhibits similar indoor and outdoor corrosion rates (Fig. 12) [26].

The difference between indoors and outdoors also results in differences in chemical composition of the corrosion products. They contain metal-carboxylates as important constituents indoors, but not outdoors [27].

3.1.5.4 Standardized Field Tests

Considering the large number of environmental parameters that can influence the exposure of a metal in a natural environment, there is a need to standardize the exposure situation so that comparisons can be made between the corrosion results from different outdoor exposures [28]. The outdoor exposure site should represent a general macroclimate, that is, uniform conditions of a specific rural, urban, marine, or industrial environment, and the site location should be selected accordingly. The test site should be located so that point sources of emission can be avoided and samples be exposed facing south in

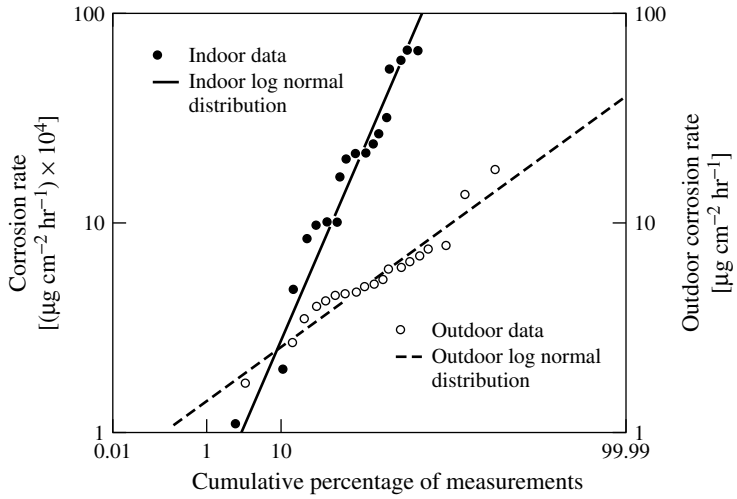


Fig. 11 Mean indoor and outdoor corrosion rates of iron as a function of the cumulative percentage of measurements. (Reproduced with permission from Ref [26].)

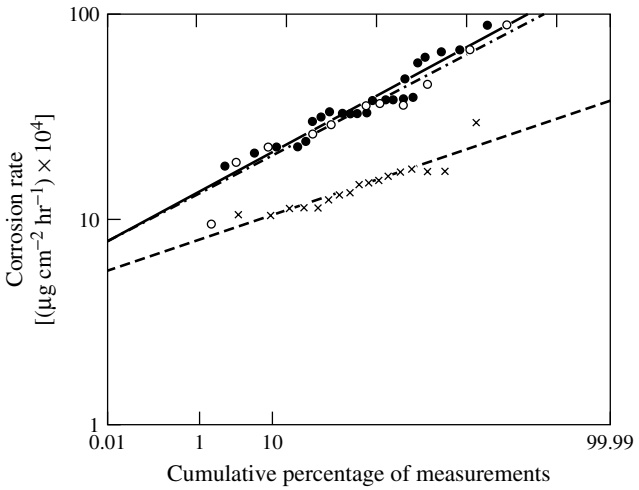


Fig. 12 Mean indoor and outdoor corrosion rates of silver as a function of the cumulative percentage of measurements. Filled and unfilled circles are indoor corrosion data, whereas crosses are outdoor corrosion data. (Reproduced with permission from Ref [26].)

the northern hemisphere and north in the southern hemisphere. It should furthermore be located at or near ongoing measurements of gaseous and/or particle measurements. Recommended instrumentation includes a thermograph and hygrograph for ambient temperature and relative humidity monitoring, equipment for measuring wind velocity and wind direction, frequency, duration, and amount of precipitation (rain gauges), time-of-wetness (either through relative humidity and temperature data or through so-called *time of wetness-sensors*), chloride ion deposition (through the wet candle method), and determination of sulfur dioxide concentration (through sulfation plates or the peroxide candle method) [28].

3.1.6 Important Applications

As pointed out in the introduction, outdoor and indoor atmospheric corrosion effects have important implications in a large variety of applications. It is beyond the scope of this chapter to describe these applications in detail and the reader is referred to more comprehensive chapters on, for example, architectural and structural applications, cultural artifacts, and electronic devices [1].

References

1. C. Leygraf, T. Graedel, *Atmospheric Corrosion*, John Wiley & Sons, New York, 2000.
2. E. Mc Cafferty, V. Pravdic, A. C. Zettlemoyer, *Trans. Faraday. Soc.* **1970**, *66*, 1720–1731.
3. P. A. Thiel, T. M. Madey, *Surf. Sci. Rep.* **1987**, *7*, 211–385.
4. M. Forslund, C. Leygraf, *J. Electrochem. Soc.* **1997**, *144*, 105–113.
5. K. Barton, *Protection Against Atmospheric Corrosion*, John Wiley & Sons, London, 1976, p. 29.
6. A. Nishikata, Y. Ichihara, Y. Hayashi et al., *J. Electrochem. Soc.* **1997**, *144*, 1244–1252.

7. C. Leygraf in *Corrosion Mechanisms in Theory and Practice* (Eds.: P. Marcus, J. Oudar), Marcel Dekker, New York, 1995, pp. 421–455.
8. W. Stumm, G. Furrer, *Aquatic Surface Chemistry* (Ed.: W. Stumm), John Wiley & Sons, New York, 1987, 197–219.
9. R. G. J. Pearsson, *J. Am. Chem. Soc.* **1963**, *85*, 3533–3539.
10. T. E. Graedel, J. P. Franey, G. W. Kammlott, *Science* **1984**, *224*, 599–601.
11. T. Aastrup, M. Wadsak, M. Schreiner et al., *Corros. Sci.* **2000**, *42*, 957–967.
12. M. Stratmann, *Ber. Bunsen-Ges. Phys. Chem.* **1990**, *94*, 626–639.
13. S. Zakipour, J. Tidblad, C. Leygraf, *J. Electrochem. Soc.* **1997**, *144*, 3513–3517.
14. J. Tidblad, C. Leygraf, *J. Electrochem. Soc.* **1995**, *142*, 749–756.
15. R. E. Lobnig, D. J. Siconolfi, R. P. Frankenthal et al., *Proc. 3rd Int. Symp. Corrosion and Reliability of Electronic Materials and Devices* (Eds.: R. B. Commizzoli, R. P. Frankenthal, J. D. Sinclair), The Electrochemical Society, Pennington, N.J., 1994, pp. 63–78.
16. T. Falk, J.-E. Svensson, L.-G. Johansson, *J. Electrochem. Soc.* **1998**, *145*, 2993–2999.
17. M. Lenglet, J. Lopitaux, C. Leygraf et al., *J. Electrochem. Soc.* **1995**, *142*, 3690–3696.
18. S. Zakipour, C. Leygraf, *J. Electrochem. Soc.* **1986**, *133*, 21–30.
19. IEC 68-2-60 (Second edition), Environmental testing-part 2: Tests-Ke: flowing mixed gas corrosion tests, *Draft International Standard*, International Electrotechnical Commission, 1995.
20. W. H. Abbott, *Br. Corros. J.* **1989**, *24*, 153–158.
21. ISO TC 156 WG7/N137, Accelerated corrosion testing involving cyclic exposure to salt mist, ''dry'' and ''wet'' conditions, *Draft International Standard*, International Organization for Standardization, 1998.
22. R. Lobnig, D. J. Siconolfi, J. Maisano et al., *J. Electrochem. Soc.* **1996**, *143*, 1175–1182.
23. D. Knotkova, L. Vrobel, *Proc. 11th Int. Corros. Congress*, Florence, Italy, 1990, p. 5.581.
24. ISO 9223, *Corrosion of Metals and Alloys, Classification of Corrosivity Atmospheres*, International Organization for Standardization, Geneva, Switzerland, 1991.
25. ISO 9224, *Corrosion of Metals and Alloys, Guiding Values for the Corrosivity Categories of Atmospheres*, International Organization for Standardization, Geneva, Switzerland, 1991.
26. D. W. Rice, R. J. Cappell, W. Kinsolving et al., *J. Electrochem. Soc.* **1980**, *127*, 891–901.
27. D. Persson, C. Leygraf, *J. Electrochem. Soc.* **1995**, *142*, 1468–1477.
28. H. H. Lawson, *Atmospheric Corrosion Test Methods*, NACE International, Houston, Tex., 1995.

3.2 Passivity of Metals, Alloys, and Semiconductors

Joachim Walter Schultze
AGEFeV-Institut an der Heinrich-Heine-Universität Düsseldorf, Universitätsstr. 1, D-40225 Düsseldorf/Germany

Achim Walter Hassel
Max-Planck-Institut für Eisenforschung, Düsseldorf Max-Planck-Str. 1, D-40237 Düsseldorf/Germany

3.2.1 Introduction

3.2.1.1 Definition of Passivity

Unstable metals dissolve by active corrosion in many solutions:

$$\mathrm{M} \longrightarrow \mathrm{M}^{z+}(\mathrm{aq}) + ze^- \qquad (1)$$

They become "passive" if they substantially resist corrosion under conditions in which the bare metal would react significantly. This behavior is due to the inhibition of active dissolution by the more or less spontaneous formation of a dense passive film of limited ionic conductivity, which is formed by an anodic reaction of the type

$$\mathrm{M} + \frac{z}{2}\mathrm{H_2O} \longrightarrow \mathrm{MO}_{z/2} + z\mathrm{H}^+ + ze^- \qquad (2)$$

Figure 1 gives a schematic diagram for a metal electrode. Various ion-transfer reactions (ITRs) and electron-transfer reactions (ETRs) can occur, which stabilize or dissolve the passive film [1, 2]. They will be explained in Sect. 3.2.2.6.

The phenomenon of passivity was discovered by Schönbein for Fe [3]. In the following 200 years, passivity research has been widely extended to many systems. For a historical review, see Ref. [4]. The International Symposia on Passivity of Metals documented highlights of the scientific progress. For references, see [1]. Moreover, the classical books by Young [5] and Kaesche [6], and a number of reviews [7–16] and fundamental articles should be mentioned.

At first, the term passivity was extended to other metal/electrolyte systems of the type *M/ox/electrolyte*. Later, it was found that passivity is a general phenomenon, which can be also observed for other systems. In 1983, the aforementioned symposium series was renamed to include semiconductors: *5th International Symposium on Passivity of Metals and Semiconductors* [12]. Similarly, passivation in nonaqueous electrolytes can be included too, for example, molten salts in which passivating films of nitrides or other compounds are formed.

Thus, we can apply a general definition:

> *A passive system consists of a thermodynamically unstable material, which is covered by a passive film separating the material from a corroding liquid (or gaseous) phase. This film prohibits the active attack of the bare metal. It is formed from the metal itself and components of the environment (oxygen, water or other liquids). Formation is typically an electroless process in water or in air, or is an anodic process in water. The anodic current density may be supplied from an exterior circuit or compensated by cathodic currents, for example, hydrogen evolution or oxygen reduction at open circuit conditions.*

This definition excludes inhibitor films or other corrosion-protecting layers such as paint and so on, which have the same function as passive films but a different origin. Such films are formed from components in the electrolyte (inhibitors) or are deposited in a technical process (e.g. cathodic deposition of paint).

In electronics and other fields "passivation" includes all protective films against corrosion, even if they are deposited by any other technique rather than anodization,

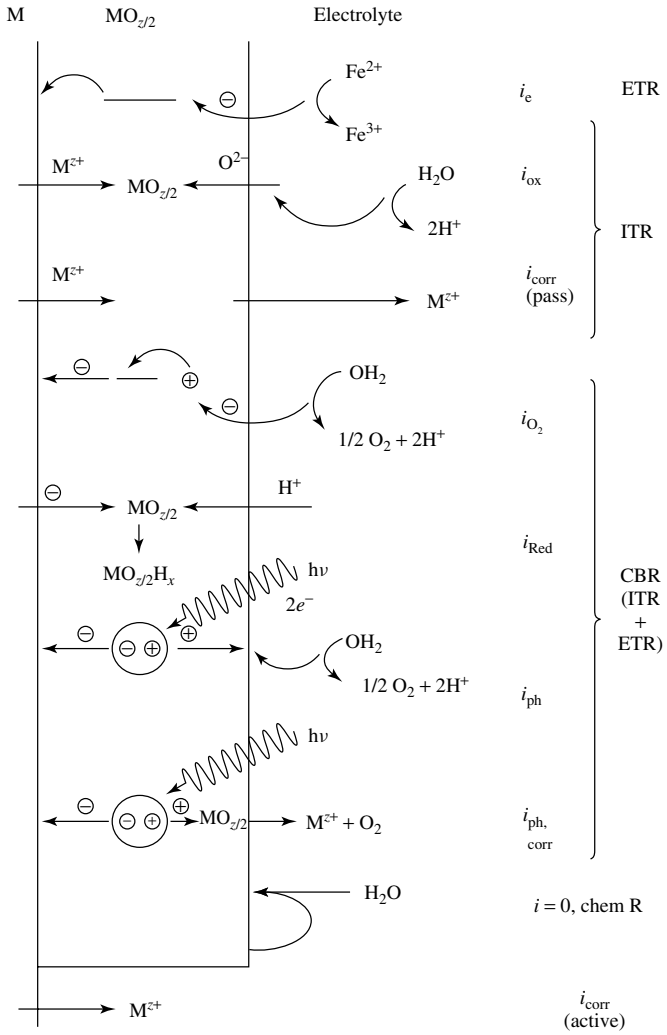


Fig. 1 Schematic diagram of passivated Ti. For explanation of possible ion-transfer reactions, ITRs, electron-transfer reactions, ETRs, and reactions with break or formation of chemical bonds, CBR, see Sect. 3.2.2.6 [1].

for example, Physical vapor deposition (PVD), or oxidation by oxygen or steam. In this chapter, however, we will focus on anodic films formed in liquid electrolytes.

3.2.1.2 Survey of Systems

Because of the variety of chemical systems, passive films and passive systems vary over a wide range. To characterize the systems, we can distinguish them by properties of the following:

1. The film:
 - *thickness of the film*: monomolecular or thick films,

- homogeneity (on pure metals, one oxide), or heterogeneity (vertical, e.g. sandwich oxides, lateral, e.g. at grain boundaries, porous films),
- *electronic properties of the film*: metallic conduction, semiconductors, insulators,
- redox processes (lower or higher oxides of the metal)
- *origin*: natural, (air, water), technical (anodic, modified), fresh/aged
- *crystallinity*: epitaxial, amorphous morphology.

2. The substrate:
 - *chemistry of the substrate*: type of metal or semiconductor, purity, alloys. Figure 2 gives a survey of passivating elements with a simple characterization of passivating, corroding, and redox processes. This characterization, of course, is qualitative only because of various competing influences.
 - *metallurgy of the substrate*: single crystals with defined orientation, thin films, polycrystalline materials, surface properties (roughness), and modified substrates.
3. The electrolyte:
 - chemistry (film forming or aggressive ions), concentration, temperature, flow rates, and so on have to be considered, since they influence the stability or destruction of the passive film.

3.2.2 General Principles of Passivity

In this chapter, the general principles, experiments and values for passive films are discussed. In Sect. 3.2.3.2, details for Al are given as a simple example for the high field growth of oxide films. Many systems behave similarly, but some others differ strongly. Table 1 gives representative data for many systems: thermodynamic data (U_{ox}), ionic data (growth constants) and electronic data (E_g, etc.). The data will be explained in the following sections. In the conclusions, a short summary is given for Fe, Pt, Al and Si.

3.2.2.1 Thermodynamics and Bond Polarity

In the middle of the last century, thermodynamic arguments for oxide film formation were favored by Pourbaix [17]. In many systems, the oxidation state of oxides increases with increasing potential. Pourbaix diagrams show the stability of the metal and special oxides as a function of pH and potential. One diagram refers to one or more special oxides. For hydroxides other values have to be taken, but the difference between oxides and hydroxides is often very small. In Sect. 3.2.3.2, an example is given for Al. For other examples, namely, Ti, see Refs. [1, 2].

In Table 1, U_{ox} refers to the potential for the given oxide formed by Eq. (2). It decreases with decreasing electronegativity of the metal, that is, with increasing ionicity of the bond. Correspondingly, the band gap energy E_g increases [18–20].

The review of thermodynamic data gives, of course, only a first insight into the range of stability of passive films. On the other hand, fundamental kinetic phenomena, for example, growth, the formation of duplex films with different oxidation state or the stability of passive metals in acid solution cannot be explained by thermodynamics, but require kinetic arguments [16].

Electronic properties, such as the flat-band potential U_{FB} and the positions of the conduction and valence band, U_{CB} and U_{VB}, can be included. Figure 1 in Ref. [1] shows an advanced diagram for

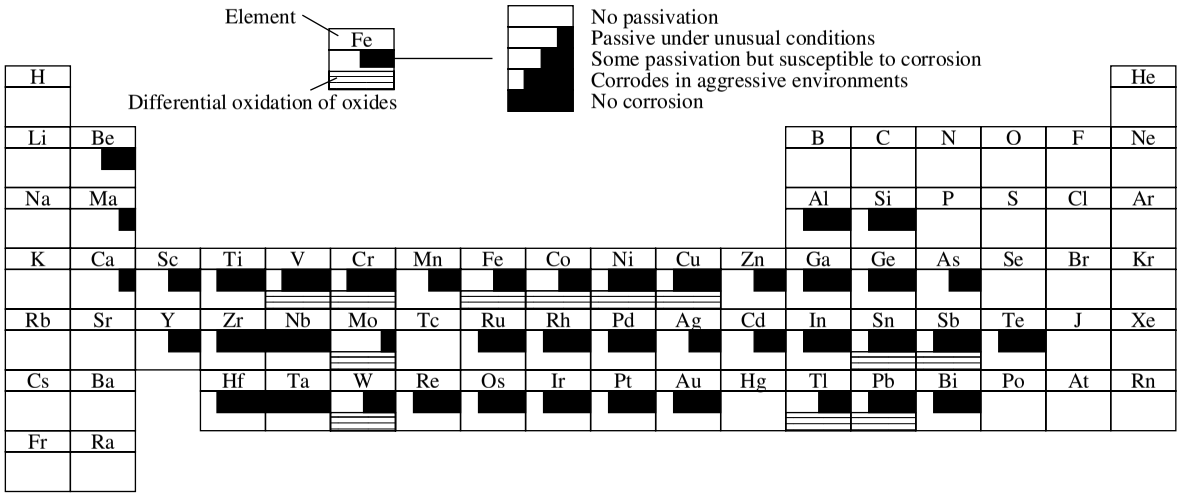


Fig. 2 Periodic system with elements qualitatively marked for passivation or corrosion in aqueous solution. Differential oxidation of oxides indicates possible application, for example, in batteries.

Tab. 1 Typical data for passive films taken from Ref. [1], density ρ, dielectric permittivity ε, band gap energy E_g, flat band potential U_{FB}, equilibrium potential of oxide electrode U_{ox} (Reaction 2 [16]), donor concentration N, difference of electronegativity $\Delta\chi$, transference number of cations t_+, formation factor dd/dU, and initial oxide thickness d_0. Because of the strong dependence of properties on the preparation technique, the microstructure and the sensitivity of thin films, the reliability of these data is less than for bulk, crystalline solids

Metal	*Oxide*	ρ [g cm^{-3}]	ε	E_g [eV]	U_{FB} [V]	U_{ox} [V]	N [cm^{-3}]	$\Delta\chi$	t_+	dd/dU [nm V^{-1}]	d_0 [nm]
Al	Al_2O_3	3–3.4	7.5–15	7–9.5		−1.35		1.5	0.4–0.5	0.75–2	2–4.3
Au	$Au_2O_3/Au(OH)_3$	12.7	16–120		1.3	1.45		2.4		0.7–1	
Be	BeO	3	6.8			−1.76		1.5	0.75	0.76	0.65
Bi	Bi_2O_3	7–9	18–40	2.7		0.38		1.9			25
Cr	Cr_2O_3			3.5		−0.6		1.6			
Cu	Cu_2O		7–12	1.8	−0.28	0.42		1.9			
	CuO	6	18	0.6–1.7	0			2			
Fe	Fe_2O_3/Fe_3O_4	5.2		1.9	0.4	−0.08	10^{20}	1.9		0.6	
Hf	HfO_2	10	14–34	5.1	0	−1.57	10^{18}	1.3	0	1.8–2.4	4.1–5.1
Ir	IrO_2					0.93		2.2			
Mo	MoO_3	4.5				−0.04				3.5	3.1
Nb	Nb_2O_5	4.4–5	41–46	3.4–5.3	−0.08	−0.65	10^{18}–10^{19}	1.6	0.33	2.1–3.7	1.5–3.6
Ni	NiO/NiOOH			3.5		0.08		1.8			
Pb	PbO_2							1.8			
Pt	PtO			1.3	0.9	0.98		2.2		0.6	
Sb	Sb_2O_5	5.2	20	3	−0.22	0.15	10^{17}	1.9			
Si	SiO_2	2.1	3.8	9		−0.86		1.8	0	0.4–0.7	
Sn	SnO_2	6.7		3.5	0.5	−0.11	10^{19}–10^{20}	1.8		1	
Ta	Ta_2O_5	8–8.7	12–27	4–4.6	−0.8	−0.81		1.5	0.3–0.5	1.3–2.4	1–2
Te	TeO_2	5						2.1			
Ti	TiO_2	3.4–4.2	7–114	3.2–3.8	0–0.3	−0.86	10^{20}	1.6	0.4	1.3–3.3	1.3–5.4
V	V_2O_5	3.4–4.3				−1.02		1.6	0.28	6.5	5
W	WO_3	6.5	23–57	2.7–3.1	0.6		10^{17}–10^{18}	1.7	0.37	1.8	1.5
Zn	ZnO			3.2		−0.42		1.6			
Zr	ZrO_2	5.5–5.8	12–31	4.6–8	−0.82	−1.43		1.4	0	1.7–3	1.7–5.3

Ti, which combines thermodynamic data of Pourbaix with electronic properties of TiO_2. For the application of such electronic data for redox processes, see Sect. 3.2.4.3.

3.2.2.2 Experimental Techniques for Characterization of Passive Films

A large number of experimental techniques were used to prove the existence of films and to find out their properties. We have to distinguish various groups of methods:

- nondestructive in situ methods (e.g. ellipsometry, EIS)
- destructive in situ measurements (e.g. cathodic reduction)
- ex situ measurements that involve the problems of redox reactions, aging, recrystallization, etc. (e.g. X-ray photoelectron spectroscopy (XPS) spectra as nondestructive, sputter profiles as destructive analysis).

According to the applied method, the following investigations can be grouped:

- Electrochemical DC-investigations yield potentials U, current densities i, and charge densities q. They analyze the films by destructive dissolution or controlled formation and take kinetic data from i, or stoichiometric information from coulometry.
- Electrochemical small signal AC-analysis that yields capacities C, resistances R or conductivities, detection of space charges, and other electronic properties. Large signal analysis by DC pulses yields kinetic information under instationary conditions.
- Mechanical investigations, for example, gravimetric measurements with the electrochemical quartz microbalance. Measurements of elasticity and deformation, for example, by indentation or by the film deflection method.
- Measurements of topography from optical microscopy, scanning electron microscopy (SEM), scanning tunnelling microscopy (STM), atomic force microscopy (AFM), Laser profilometry, Kelvin- and electrochemical probes.
- Spatially resolved electrochemistry by scanning probes or microcells, for example, Kelvin probe, Electrochemical Microscope, investigation of single grains of polycrystalline materials.
- Chemical analysis, for example, locally resolved concentration.
- Spectroscopic measurements (intensity, phase of incident, and emitted photons), which yield chemical, electronic, structural, and thickness information, for example, by photon/photon effects (e.g. ellipsometry) or photon absorption (e.g. reflectometry) or structural information (e.g. from Extended X-ray absorption fine structure (EXAFS) or Electron Back Scatter Diffraction EBSD).
- Various combined measurements, often combinations of spectroscopy and electrochemistry, yield information on special processes, for example, in photoelectrochemistry or electroluminescence.

The evaluation of film properties from such techniques depends on the validity of many assumptions and of applied models. Therefore, various different methods have to be simultaneously applied to get a reliable picture of the system.

3.2.2.3 Thickness and Stoichiometry of Passive Films

The thickness d of passive films ranges from monomolecular films in case of Pt and Au to thick films in the micrometer range in case of Al. The initial or native oxide thickness d_0 is often in the nm range (Table 1). It decreases with increasing U_{ox}.

Depending on the experimental conditions, however, thick films may be formed on many metals. Chemical, electrochemical and spectroscopic techniques allow a determination of the thickness of homogeneous films. On the basis of Eq. (2), the interpretation of coulometric data, that is, the charge density q, according to Faraday's law gives an approximation of film thickness:

$$d = \frac{qM}{zrF\rho} \tag{3}$$

where M = molecular weight, r = roughness factor, and ρ = density of a presumed homogeneous oxide. The assumption of a constant thickness, stoichiometry, and density of a crystalline film is a first, rough approximation only. Figure 3 shows a schematic survey in a logd/logU plot.

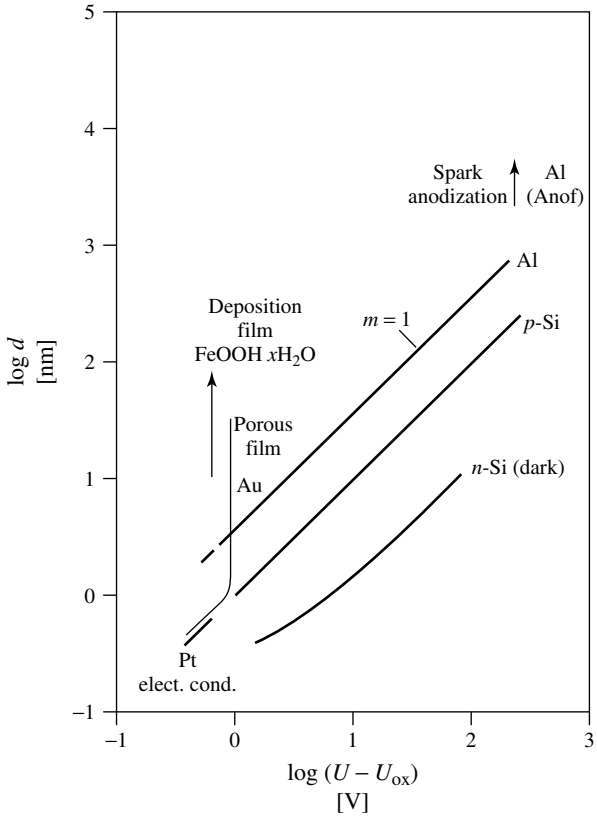


Fig. 3 Schematic diagram of oxide thickness versus formation potential in a double logarithmic plot: Al [21] and *p*-Si are taken as examples of oxides growing according to the high field law till 100 V. Thicker Al_2O_3-films by sparking ("Anof" [22]). *n*-Si as example of influence of a potential drop in the semiconductor. Pt: high field growth limited by the onset of oxygen evolution. Au: initial high field growth, then formation of a porous hydrated oxide film during oxygen evolution. FeOOH: deposition of a conducting layer from solution [23].

Many insulating (Al, Si) or semiconducting (Fe, Pt) films grow according to the high field model. Then, the formation potential U_f mainly determines the film thickness d:

$$d = d_0 + k(U_f - U_{ox}) \qquad (4)$$

with d_0 = initial (air) passivity, $k = dd/dU$ = film-formation constant given in Table 1. $k = 2\ \text{nm V}^{-1}$ is a typical value. It corresponds to a field strength of $5 \times 10^6\ \text{V cm}^{-1}$. Equation (4) corresponds to a straight line in Fig. 3, with a slope = 1. The smaller influence of polarization time t is given on a logarithmic scale [1]. Typically, the extension of t by one order of magnitude yields a thickness increase of 10% only. For details, see Sect. 3.2.3.2. Electronic conduction or increasing passive corrosion limit the film thickness in some cases, for example, for Pt due to oxygen evolution at above 2 V [23] or in case of passive iron due to transpassive dissolution [24].

Electronically conducting films deposited from solution can grow continuously with time. Sometimes, they appear together with real passive films and cannot be distinguished (see passive iron as example). The thickness is homogeneous all over the surface only in case of films formed by the high field model [25]. With many real films, lateral (y-direction) gradients of thickness dd/dy from 10^{-6} to 10^3 have to be taken into account [26]. For advanced techniques in Electrochemical Micro- and Nano Technology [27], the role of thickness gradients and concentration gradients is important.

The density of amorphous passive films usually is less than that of crystalline modifications and is not exactly known.

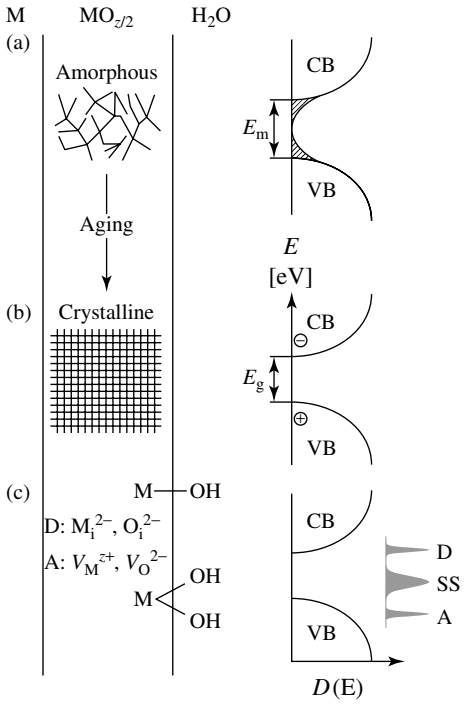


Fig. 4 Schematic representation of crystal structure (left side) and band structure of passive films. (a) amorphous film, (b) crystalline oxide, (c) doped oxide. CB and VB = conduction and valence band, E_g = band gap energy, D,A = donor and acceptor states, SS = surface states [1].

Moreover, gradients of stoichiometry limit the accuracy of thickness determinations that often only refer to parts of the passive film. Many oxide films show an increase of oxidation state from metal to the electrolyte, for example, on Cu [13]. In case of passive iron, many traditional techniques only evaluate the thickness of the outer Fe_2O_3-film, but not that of the inner Fe_3O_4-layer. While Vetter [28] described the film by a duplex model, Wagner [14] presented a model with continuous change of stoichiometry.

3.2.2.4 Chemistry, Crystal Structure and Aging

3.2.2.4.1 Chemistry and Crystal Structure

Passive films of some nanometer thickness are too thin for traditional chemical analysis. Ultrahigh vacuum (UHV) surface-sensitive analysis like Auger and XPS, however, give film compositions with an accuracy of about 10%. Uncertainties arise from undefined contact with air, surface contamination without sputtering, and from preferential sputtering after cleaning the surface. In case of pure metals and films without concentration gradients, the crystal structure of the oxide gives evidence for stoichiometry.

Various sophisticated methods were applied to determine the crystal structure of passive films. A long discussion was devoted to the role of ex situ measurements that were carried out first. After removal from the electrolyte, crystallization, oxidation by air and oxide growth may take place. For example, it is well known that the amorphous passive films crystallize under irradiation with electrons [29]. Therefore, electron diffraction measurements yield crystalline Al_2O_3-, Ta_2O_5-, or Fe_2O_3-films, which differ from the in situ structure. EXAFS measurements [30–32], on the other hand, can be carried out in situ, but they require smooth surfaces, complex equipment and are very time-consuming. Therefore, they are only available for a few systems, and the relevance for technical materials is limited.

Many passive films are amorphous or nanocrystalline [33, 34], with broad distribution functions of distances and coordination numbers instead of sharp, well-defined values of crystals [35]. Spectroscopic evidence can be obtained in situ or ex situ for special crystal forms, for example, by Raman and IR [36] or Anisotropy Microellipsometry AME [37]. This allows the observation of the crystallization processes, but it does not exclude the existence of surrounding different phases.

For an example of a careful analysis of crystal growth of TiO_2, see Ref. [38]. Another type of microstructure refers to films the structure of which depends on the orientation of the metal grains, for example, in case of Ti [37, 38], Zr [39, 40], Ta [40] and Al [41]. Amorphous films do not have a structure and are nonepitaxial. In case of Zr, epitaxial growth of oxide was observed by AME [39].

3.2.2.4.2 Aging

So-called "aging" of passive films is not well defined. It involves various transformations such as stoichiometric changes, swelling or dehydration, recrystallization, further growth, corrosion, or depletion of defects. Many film properties such as ionic and electronic conductivity and potential distribution change with time. As a consequence of aging, film stability or corrosion resistance will usually be improved, at least changed during long-term application of the material. Aging often hinders a straightforward model interpretation. A typical example is given by potentiostatic pulse measurements over 6 to 10 orders of magnitude, from μs to

ks. At first an amorphous film is formed, which slowly transforms into a crystalline one. The crystal structure, band structure, and electronic conductivity develop slowly. A simple calculation may explain that. Within the first μs, the current density is about 1 A cm^{-2}, which means an average lifetime of 10^{-3} s for an ion on a lattice-like position. This short time will be much less than the expected relaxation time of a crystal lattice of 10^2 s or more. Therefore, during fast formation, amorphous oxides will be preferred, which can slowly (or never?) crystallize.

An example will be shown below (Fig. 23) with oxygen evolution at a growing TiO_2-film. In contrast to the expected decrease of oxygen evolution, this increases after a lifetime of 100 s because of an improvement of electronic conductivity. For this and other reasons, film aging is of great practical relevance and is an important object of future research. Another example was observed with the passive film of Cu. Within the first ms, a homogeneous, nonstoichiometric film $Cu(OH)_x$ is formed, which separates slowly into the Cu_2O/CuO-sandwich [42]. For monomolecular films on Au, aging was observed with pulse measurements [43].

3.2.2.5 Potential Distribution at the Interface

The rate and equilibria of reactions are given by the local electrochemical potential μ* of an ion and the energetic position of electrons in the bands.

$$\mu_i^* = \mu_{i,0} + RT \ln a_i + z_i F \varphi(x) \quad (5)$$

$$E_C = E_C(\text{bulk}) - F\varphi(x) \quad (6)$$

They depend on the local Galvani potential $\varphi(x)$, the chemical activity (concentration), which is a function of the electronic and ionic conductivity, of the thickness d, and of the pH value. Because of the excess charges q at the interfaces or space charges ρ within the oxide, $\varphi(x)$ changes resulting in a field strength $E_S = d\varphi/dx$. As shown by Güntherschulze and Betz [44–46], Verwey [47], or Mott [48] this is important for the migration of charge carriers, ions, and electrons as well. An exact evaluation of the total potential drop has been given by Vetter [28]

$$\Delta\varphi = \varphi_m - \varphi_e = \Delta\varphi_{m/ox} + \Delta\varphi_{ox} + \Delta\varphi_H \quad (7)$$

with the consequences for ion-transfer reactions. $\Delta\varphi_{ox}$ equals the band bending (see Sect. 3.2.2.8). It determines the rate of ionic migration in the oxide, while $\Delta\varphi_H$ determines that of ITR at the oxide surface.

Figure 5 shows a schematic diagram. In equilibrium, the proton-transfer reaction (14) ($H_2O \rightarrow OH^-(ox) + H^+$ (aq)) determines $\Delta\varphi_H$ at the interface:

$$\Delta\varphi_H = \Delta\varphi_H^0 - 2.3\frac{RT}{F}\text{pH} \quad (8)$$

Since this potential drop is very important for oxides, its pH-dependence is often eliminated using U(hess), the potential of the hydrogen electrode in the same solution, as reference. For some oxides, $\Delta\varphi_H$ can depend on U (Fig. 5b). Above the valence band potential, U_{VB}, $\Delta\varphi_H$ increases, if electronic equilibrium is maintained (e.g. for Fe). Then, the equilibrium of Eq. (8) will be left, and oxygen evolution starts. On the other hand, $\Delta\varphi_H$ remains constant, for example, for Ta_2O_5 or Al_2O_3, since electron exchange with the metal is impossible. Ti represents an intermediate case, as can be seen from a time-dependent oxygen evolution (see Fig. 23).

The potential distribution given by Eq. (7) is reflected in the equivalent circuit diagram shown in Fig. 6. The resistances of the Helmholtz layer and

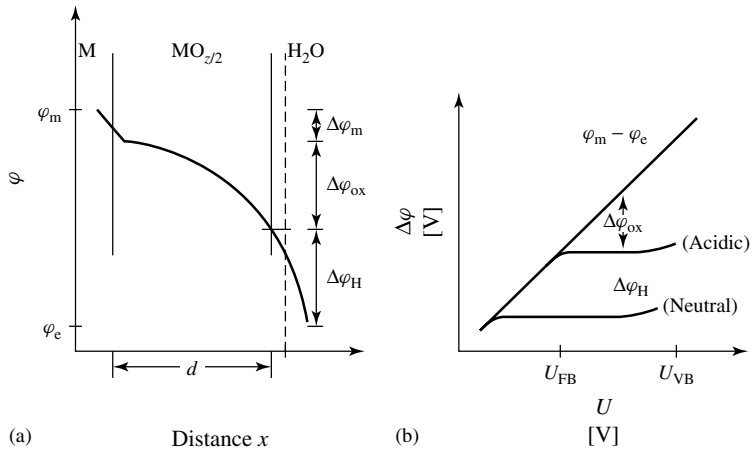


Fig. 5 Schematic shape (a) of the potential drop across an *n*-type semiconducting oxide film and (b) its changes with potential. In (b) the drop $\Delta\Phi_{m/ox}$ is neglected. Near U_{VB} the influence of the VB may become important and $\Delta\Phi_H$ increases, if electronic equilibrium between metal and the VB is maintained [2].

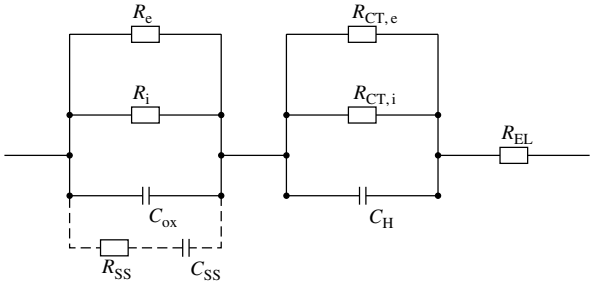


Fig. 6 Equivalent circuit diagram for an oxide film with ionic and electronic conductivity. R_e = electronic resistance, R_i = ionic resistance, R_{SS} = resistance of surface states. (For detailed discussion, see Sect. 3.2.2.10.)

the oxide are in series with parallel capacitances. Since ITR and ETR have to be distinguished, a detailed analysis will be given after discussion of these reactions in Sect. 3.2.2.10. Corresponding to Eq. (7) for the potential differences, we obtain an equation for the reciprocal capacities:

$$\frac{1}{C} = \frac{1}{C_{ox}} + \frac{1}{C_H} + \frac{1}{C_m} \approx \frac{1}{C_{ox}} + \frac{1}{C_H} \quad (9)$$

If $C_H \gg C_{ox}$ and $C_m \gg C_{ox}$, the approximation

$$\frac{1}{C} \approx \frac{1}{C_{ox}} = \frac{d}{\varepsilon\varepsilon_0} \quad (10)$$

(C_{ox} = oxide capacity, d = film thickness, ε = relative permittivity number of the oxide, ε = permittivity of vacuum) can be used, for example, for insulating oxide films with negligible space charge. For thick semiconducting films with thin space

charge layers, d_{SC} the Schottky–Mott analysis has to be applied [49], which starts from the Poisson Eq. (11)

$$\left(\frac{d^2\varphi}{dx^2}\right) = -\frac{\rho(x)}{\varepsilon\varepsilon_0} \tag{11}$$

$$d_{SC} = \frac{\varepsilon\varepsilon_0}{C_{SC}} \tag{12}$$

and

$$C_{SC}^{-2} = \frac{(U - U_{FB} - kT/e)}{(\varepsilon\varepsilon_0 zeN)} \tag{13}$$

At high potentials, the calculated $d_{SC} > d$, then C is given by given by Eq. (10) again which gives a lower value for C. A frequency-dependence of a Schottky–Mott diagram indicates a mobility of donors. A nonlinearity, on the other hand, can be used for evaluation of space charge profiles within the oxide [49].

A survey of typical relationships between C and d is given in the double logarithmic plot log C versus log d in Fig. 7. If Eq. (10) is valid, straight lines with a slope of -1 should be obtained. Such a behavior is observed for Al in a wide range, since the formed oxide is a true insulator. A similar behavior is observed for passive iron at constant potential, for example, at 0.7 V in a limited range of thickness. At higher potentials the slope is also near to -1, but the lines are shifted to larger thickness values. This is connected with the extension of the space charge layer. For gold oxide, the decrease of C with increasing d is observed for thin films only, at $d > 3$ nm, C becomes independent as a

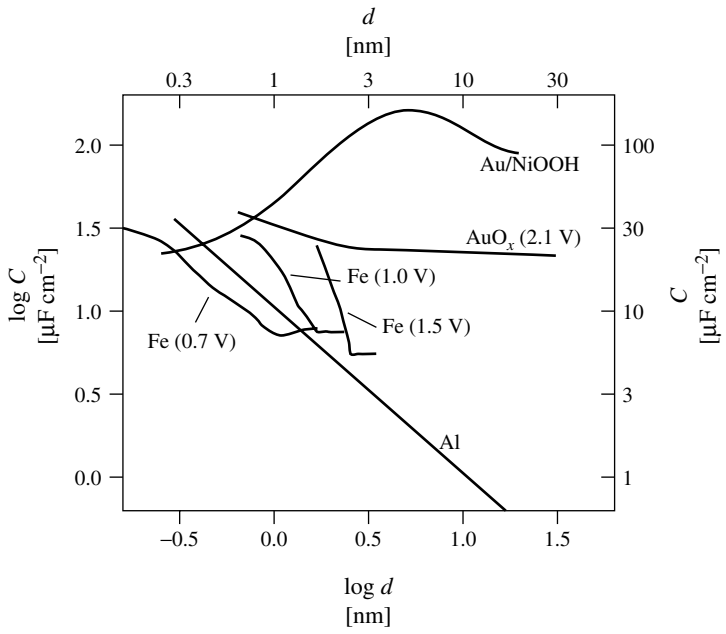


Fig. 7 Double logarithmic plot of film capacity C versus film thickness d. Al as example of an insulating, homogeneous film [21]. Fe as example of a semiconducting film with capacities depending on d and U (Schottky–Mott). Au as example of an insulating thin film with a porous hydrated film outside. NiOOH on Au as example of a conducting deposition film [23].

result of the ionic conductivity of the outer layer. Finally, in case of deposition layers of NiOOH on Au, the capacity increases, since NiOOH is a good conductor at high potentials with a high adsorption capacity at the surface.

3.2.2.6 Electrochemical and Chemical Reactions in Passive Systems

3.2.2.6.1 **Reactions** Equation (2) is a simplified description of the passivation reaction. In fact, however, the phenomenon of passivity depends on various reactions of the substrate, the oxide film and side reactions. Oxide growth, corrosion, redox processes of the oxide, and redox reactions of species in the electrolyte have to be distinguished.

The reactions will be explained for a pure metal in water forming a passive film. Figure 1 gives a schematic diagram. The active corrosion (1) and the passivation reaction (2) have been described already. The overall Reaction (2) consists of the partial ITR (14 and 15)

$$H_2O \longrightarrow OH^-(ox) + H^+ \qquad (14)$$

At the oxide/electrolyte interface and the Reaction (15) at the inner metal/oxide interface.

$$M \longrightarrow M^{z+}(ox) + ze^- \qquad (15)$$

The migration of cations and/or anions from plane x_i to plane x_{i+1} within the oxide follows (see Fig. 18):

$$M^{z+}(x_i) \longrightarrow M^{z+}(x_{i+1}) \qquad (16)$$

and

$$O^{2-}(x_j) \longrightarrow O^{2-}(x_{j-1}) \qquad (17)$$

For reactions given above and in the following, it is important to distinguish

- steady state reactions at constant film thickness, and
- instationary processes with film growth, corrosion, reduction or modification. For example, the anodic ion-transfer reaction (18)

$$M^{z+}(ox) \longrightarrow M^{z+}(aq) \qquad (18)$$

is part of an anodic corrosion reaction or a chemical dissolution. In the presence of complexing ions Y^-, the kinetics may change, if a different complex is transferred:

$$M^{z+}(ox) + yY^- \longrightarrow [MY_y]^{z-y}(aq) \qquad (19)$$

If only Reactions (15, 16 and 18) take place at constant thickness ($i_{14} = 0$), the net reaction corresponds to the active corrosion (1). But because of the intermediate stage of ions within the passive film with an anodic current at constant film thickness, it is called ''passive corrosion''. On the other hand, redox or hydration processes of the oxide film, for example,

$$MO_{y/2} + \left(\frac{(z-y)}{2}\right) H_2O \longrightarrow MO_{z/2} + (z-y)H^+ + (z-y)e^- \qquad (20)$$

$$MO_{z/2} + \frac{z}{2}H_2O \longrightarrow M(OH)_z \qquad (21)$$

belong to the group of instationary processes. Reaction (20) requires a simultaneous electron-transfer reaction (ETR) from the oxide to the metal

$$e^-(ox) \longrightarrow e^-(m) \qquad (22)$$

Besides the electrochemical reduction to the metal, (i.e. the inverse of Reaction (2)),

$$MO_{z/2} + zH^+ + ze^- \longrightarrow M + \frac{z}{2}H_2O \qquad (23)$$

the cathodic reduction to a soluble product, may take place.

$$MO_{z/2} + zH^+ + (z-y)e^- \longrightarrow M^{y+} + \frac{z}{2}H_2O \quad (24)$$

This reaction occurs, for example, with passive iron. The inverse reaction is also well known as an additional mechanism of passivation of iron in solutions containing Fe^{2+}-ions [50]. If the solubility product is not reached, chemical dissolution takes place

$$MO_{z/2} + zH^+ \longrightarrow M^{z+} + \frac{z}{2}H_2O \quad (25)$$

In Reactions (2, 14 to 25), only water molecules and protons are considered, but in alkaline solutions equivalent reactions with OH^- may be valid.

ITR may be joined by simultaneous ETR, without direct participation of the substrate and the oxide. For example, the anodic current density of Reaction (2) may be supplied from an outer circuit, but alternatively it may be compensated by cathodic currents such as hydrogen evolution or oxygen reduction at open-circuit conditions:

$$2H^+ + 2e^- \longrightarrow H_2 \quad (26)$$

or

$$O_2 + 4H^+ + 4e^- \longrightarrow 2H_2O \quad (27)$$

On the other hand, oxygen evolution (inverse of Reaction (27)) may take place at high potentials. Other redox reactions may be discussed too. For detailed discussions, outer-sphere and inner-sphere reactions have to be distinguished [51, 52], see Sect. 3.2.2.8).

3.2.2.6.2 **Current Densities *i*** The relation between reaction rates v [mol cm^{-2}] and current densities i is given by the following equation:

$$i_i = v_i z F = k_i c^v z F \quad (28)$$

with $k = k_{max} \exp(E_a/RT)$ = rate constant and v = electrochemical reaction order [16]. Under electrochemical conditions, only a total current density i can be measured, which consists of the partial anodic or cathodic current densities of all processes of oxide formation (ITR), corrosion (ITR), ETR and capacitive charging:

$$i = i_{ox} + i_{redox} + i_{corr} + i_C \quad (29)$$

Any discussion of the processes presumes the evaluation of all partial reactions. Under instationary conditions, the capacitive current i_C has to be taken into account. Table 2 gives a summary of processes and their partial current densities.

3.2.2.7 **Ionic Properties, Migration and Ion-Transfer Reactions**

For the formation and stability of passive films, bulk and surface reactions are important. Ionic reactions in the bulk are called migration, while reactions at the surface are called ion-transfer reactions (ITRs). Both are driven by an electric field $d\varphi/dx$, while chemical diffusion plays a role if gradients of the chemical potential exist. The general transport equation is

$$f_c v = -K = -\left(\frac{1}{N_A}\right)\frac{d\mu^*}{dx} = -\left(\frac{1}{N_A}\right)\frac{d\mu}{dx} + ze^-\frac{d\varphi}{dx} \quad (30)$$

with f_c = friction constant, v = velocity, N_A = Avogadro's number. The so-called constant f_c, however, will exponentially decrease with increasing electric field.

Tab. 2 Data for net reactions (spaces) and partial reactions (lines) described in the text. ne^- = number of involved electrons; mH^+ = number of involved protons. The total cathodic reduction is described for an island mechanism differing from anodic formation. Partial current densities give the local current dependent on the coordinate x. Transference numbers t have to be considered within the oxide, for example, in case of oxide formation $i = i_{15} = i_{16} + i_{17} = (t_+ + t_-)i = i_{14}$. In case of partial oxidation/reduction of an oxide by a combined ITR/ETR the local current densities of O^{2-} and e^- have to be added: $i(x) = i_{15} = i_{17}(x) + i_{22}(x) = (t_e(x) + t_-(x))i = i_{14}$. Cathodic intercalation of protons takes place by a process analogue to anodic partial oxidation, differing only by the sign of I and the migration of protons instead of O^{2-} -ions

Eq. of partial react.	*Type part. react.*	*Ions involv.*	*Rate det. $\Delta\varphi$*	*Descript. of next spaces→*	*Anodic oxide format.*	*Cathodic total reduction*	*Diff. an. oxid./diff. cath. reduction*	*Passive corr. (stead. state)*	*Chem. diss.*
				Net reaction	2	Inv. 2 = 23	20 inv. 20	1	24
				i_{total}	$i > 0$	$i < 0$	$i > 0 / i < 0$	$i > 0$	$i = 0$
				dd/dt	>0, Eq. (2)	<0	>0	0	<0
				ne^-/mH^+-	ze/zH^+	ze/zH^+	$(z-y)e^-/zH^+$	ze^-/OH^+	$0e^-/zH^+$
14	ITR	H^+/OH^-	$\Delta\varphi_H$		$i = i_{14} > 0$	$i = i_{14} < 0$	$i = i_{14}$	0	$i_{14} = -i_{18} < 0$
15	ITR	M^{z+}	$\Delta\varphi_m$		$i = i_{15}$	$i = i_{15} < 0$	0	$i = i_{15} > 0$	0
16	ITR	M^{z+}	$\Delta\varphi_{ox}$		$t_+ i = i_{16}$	0(island reduct.)	0	$i = i_{16} > 0$	0
17	ITR	O^{2-}	$\Delta\varphi_{ox}$		$t_- i = i_{17}$	0	$t_-(x)i = i_{17} > 0 /$ $t_-(x)i = i_{17} < 0$	0	0
18	ITR	M^{z+}	$\Delta\varphi_H$		0	$i = i_{18} < 0$		$i = i_{18} > 0$	$i_{18} = -i_{14} > 0$
22	ETR	e^- only	$\Delta\varphi_{ox}$ W_t		0	0	$t_e(x)i = i_{22} > 0$ $t_e(x)i = i_{22} < 0$	0	0

The rate of migration is given by ionic conductivities κ_{ion} of the compound, transference numbers t of migrating ions (M^{z+} and O^{2-}), and defect concentrations (intrinsic or impurities and grain boundaries). Ideal, stable insulators, and semiconductors are characterized by $\kappa_{ion} = 0$. The migration rate of passive films, however, increases with increasing field corresponding to the friction constant f_c. In case of a high field, the back reaction can be neglected, and the current density is given by

$$i_{ox} \approx i_{0,ox} \exp\left(\frac{\alpha_{ox} a z F \Delta\varphi_{ox}}{RTd}\right) \qquad (31)$$

with a = jump distance, α_{ox} = transfer coefficient, and $i_{0,ox}$ = exchange current density of ion migration. It follows that there is no definite value but a range of ionic conductivity for electrochemical conditions.

In Fig. 8, the ionic and the electronic conductivities are given in a double logarithmic plot. We discuss the vertical axis of Fig. 8 at first. The ranges of stable systems ($\log \kappa_{ion} < -15$) layer formation ($\log \kappa_{ion} < -7$) and breakdown ($\log \kappa_{ion} > -6$) are separated by orders of magnitude.

Real oxide films usually are nonstoichiometric because of an excess of metal ions or a deficiency of oxygen ions. Moreover, foreign ions like protons or impurities can contribute to the donors, acceptors or traps in the band gap. Defect concentrations N of passive films are very high, usually in the range from 10^{19} to 10^{21} cm^{-3} (Table 1). The value of N obtained from capacity

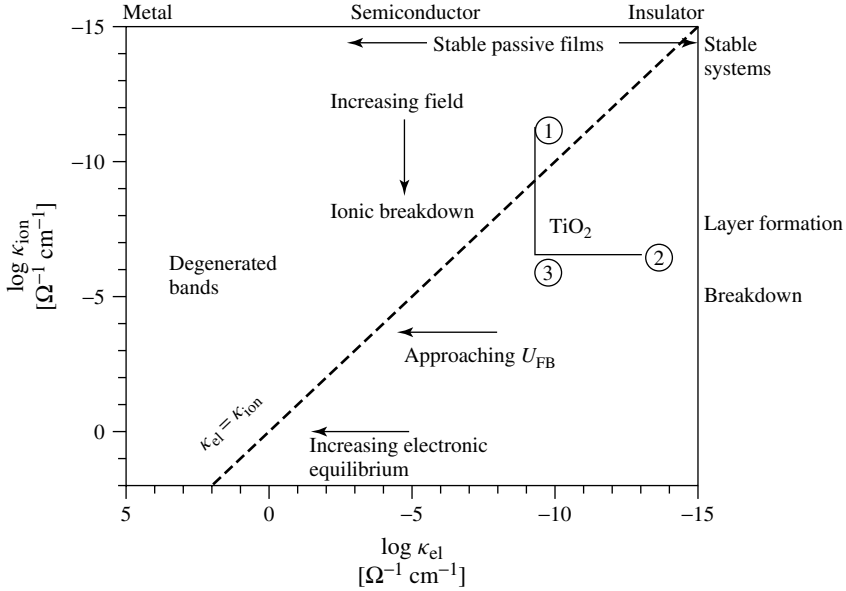


Fig. 8 Double logarithmic plot of ionic and electronic conductivity, κ_{ion} and κ_{el}, of oxide films. Dotted line: ionic conductivity equals the electronic one. Arrows indicate changes due to increasing field, approaching U_{FB} and increasing electronic equilibrium. Passive Ti as example: 1: stable passive film of TiO_2 near the flat band potential; 2: insulating film of TiO_2 on anisotropic metal plane (xxx0); 3: as 2, but for the isotropic, close packed metal plane (0001).

measurements, however, gives information on electronic defects, which may differ from intrinsic or extrinsic ionic defects. That was shown for ion implanted TiO_2 as example [35].

Qualitative information on ion mobility is obtained from oxide growth or current densities, since the transport of ions in oxide films takes place by migration and/or diffusion of defects (grain boundaries, linear dislocations, vacancies or interstitials and channels in the amorphous structure). The concentration of interstitials and ion vacancies varies with the distance from the substrate and the field strength. Advanced models take that into account [14, 25]. For artificial concentration gradients, see Sect. 3.2.3.5. Marker experiments yield transference numbers t given in Table 1. They show a mobility of anions and cations as well. This corresponds to a heteropolar crystal. Most oxides are in fact heteropolar compounds and consist of metal and oxygen ions in a first approximation. In fact, however, the covalent character of the oxide becomes important with decreasing difference of electronegativity $\Delta\chi$. For heteropolar oxides, $\Delta\chi > 2$. Gold oxide, on the other hand, is a mostly covalent compound ($\Delta\chi = 1.1$).

ITR take place at the oxide/electrolyte interface. They can be described by the Butler–Volmer equation using the potential drop at the interface $\Delta\varphi_H$ or the overvoltage η_H

$$i_H \approx i_0 \left\{ \exp\left(\frac{\alpha z F \Delta\varphi_H}{RT}\right) - \exp\left(-\frac{(1-\alpha) z F \Delta\varphi_H}{RT}\right)\right\} \quad (32)$$

$$= i_0' \left\{ \exp\left(\frac{\alpha z F \eta_H}{RT}\right) - \exp\left(-\frac{(1-\alpha) z F \eta_H}{RT}\right)\right\} \quad (33)$$

With $\eta_H = \Delta\varphi_H - \Delta\varphi_H^0$, $\Delta\varphi_H^0$ given by Eq. (8), α = transfer coefficient. Concentrations of reacting ions are included in the exchange current density i_0. Near the equilibrium potential, the transfer resistance of a surface reaction is given by

$$R_D = \frac{RT}{zFi_0} \quad (34)$$

with the i_0 for the correspondent ITR.

At high anodic overpotentials, $RT/\alpha zF < \eta_H$, the modified Tafel-Equation is obtained with η_H instead of η:

$$\log\frac{i}{i_0} = \frac{\eta_H}{\left(\frac{\alpha zF}{2.3RT}\right)} \quad (35)$$

Note that η_H will be in the range of mV, while the total overpotential $\eta \approx U$ can reach 100 V and more. Figure 9 gives a very good example of various ITR at the oxide surface of passive Fe. Here, the experimental parameter U(hess) is chosen to eliminate the pH-dependence [24]. These experimental results were used to explain the difference between η_H and U [16, 28]. For example, the independence of the passive corrosion (15, 16, 18) = (1) of U means that $\eta_H = 0$ or $\Delta\varphi_H$ = const. The transpassive corrosion, on the other hand, indicates an increase of $\Delta\varphi_H$ and $\eta_H > 0$ [24]. Note that the anodic dissolution of Fe^{2+} decreases with increasing U near U_{FB}, which is due to the enrichment of electrons or Fe^{2+} respectively at the oxide surface. The pH-dependence can be explained by Eq. (8) [16, 24].

3.2.2.8 Electronic Behavior and ETR

3.2.2.8.1 Band Structure of Oxide Films

Independent of ionic conductivity, we have to discuss the electronic conductivity κ_{el} of passive films, which is considered along

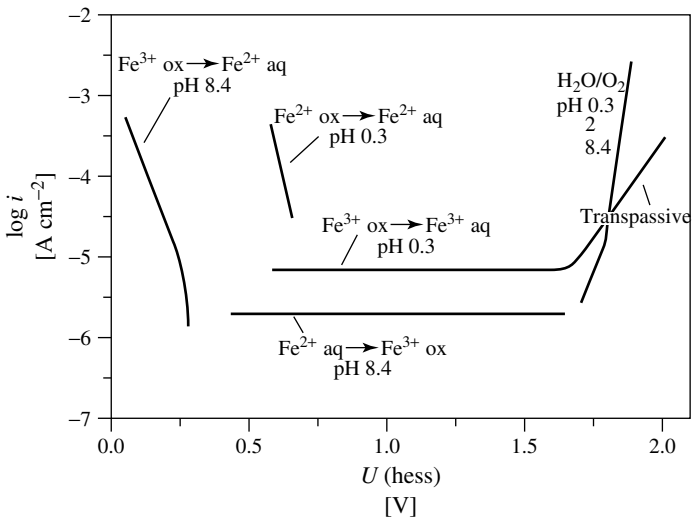


Fig. 9 Tafel plots of reactions on passive iron: ETR, H_2O/O_2 at pH 0.3, pH 2, pH 8.4; ITR, passive corrosion; ETR + ITR, $Fe^{2+}ox \rightarrow Fe^{2+}aq$ at pH 0.3, layer reduction at pH 8.4, formation of deposition layer.

the horizontal axis of Fig. 8. κ_{el} of passive films ranges from those of insulators (e.g. Si, Al) to those of semiconductors (Fe, Ti, Ni) and conductors (Ir, Pb). The conductivity depends on the band gap energy E_g and the position of the Fermi level E_F within the conduction band or in the band gap, which changes, with U.

In general, the valence band VB originates from the 2p orbitals of oxygen, while the outer orbitals of the metal ions form the conduction band CB. Because of the electronic contact with the metal, most passive films are *n*-type semiconductors. *p*-type oxides are formed on Cu and Ni.

Figure 10 shows band structure data for passive films of various metals relative to the solid-state energy scale E ($E_{vac} = 0$) and versus the potential of the hydrogen electrode. Data are taken from Refs. [1, 53, 54].

The detailed band structure can be derived from electrochemical measurements:

1. $C(U)$ (potential dependent capacity) yields donor concentration N, U_{FB}, and surface states [37].
2. The photocurrent $i_{ph}(h\nu, U)$ yields U_{FB}, and E_g, and position of bands [51, 52].
3. $i_{ox}(U)$ yields information on U_{FB} and the band bending $\Delta\varphi_{ox}$.
4. ETR-measurements yield information on tunnel probabilities, position of bands E_C and E_V and resonance states (e.g. donors).

Table 1 gives typical values for macroscopically averaged films. Exact data may vary because of different preparation and microstructure [37–39]. In Refs. [1, 2] the band structure data of Ti are included into an advanced Pourbaix diagram for estimations of electronic processes. Figure 11 shows the band positions at the flat band potential. At different potentials, a positive or negative band bending

$$U - U_{FB} = \Delta\varphi_{ox} \qquad (36)$$

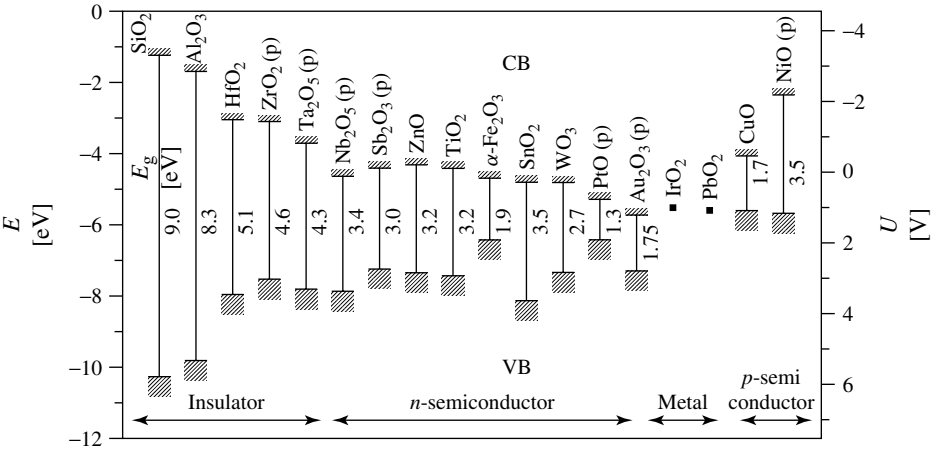


Fig. 10 Data and position of conduction and valence band for oxide films. (Data taken from Refs. [1, 53, 54].)

occurs. For *n*-type oxide films, we have 5 different cases (see Fe Refs. [24] or Ta [55, 56] and Refs. [38, 39] for further examples):

1. an enrichment layer at $U - U_{FB} < 0$
2. the flat band situation at $U - U_{FB} = 0$
3. the formation of a space charge layer at $d_{SC} < d$ and for $U - U_{FB} < U_{VB} - U_{FB}$
4. an approximation of the condensor formula for $d_{SC} \gg d$ and absence of electronic equilibrium
5. and a limited potential drop in the oxide $U_{VB} - U_{FB} = \Delta\varphi_{ox}$ in case of electronic equilibrium at $U > U_{VB}$.

An example is shown in Fig. 11 for passive iron [24]. For the insulating Ta,

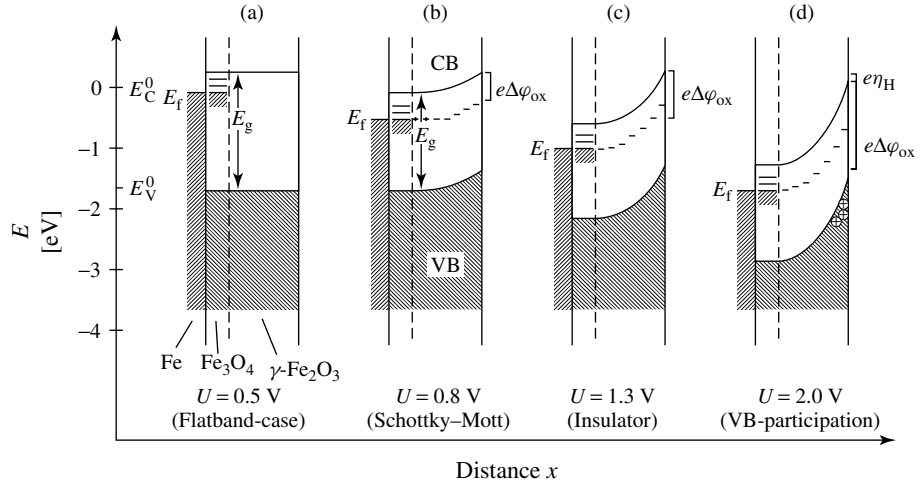


Fig. 11 Band structure model for the passive film on Fe at four characteristic potentials.

a quantitative calculation of the band bending is described in Refs. [55, 56].

3.2.2.8.2 **Electron-Transfer Reactions ETR at Oxide Films** For the rate of ETR, electron conduction within the oxide is necessary. The term ''electronic conduction'' must be specified. Faraday [57] interpreted his elegant experiment on Fe with electronic conductivity. Vetter [58] formulated it more precisely: redox equilibria should be established. But it was shown later that the electronic exchange between the electrolyte and Fe takes place by electron tunnelling, but not by conduction within the bands [24, 59]. In case of Ti and other valve metals, the electronic equilibrium between the metal and the valence band at the oxide surface is hindered (Ti) or blocked (Al, Ta). Hence, ETR are impossible at valve metals even at $U > U_{VB}$.

ETR are important for the formation (indirect), reduction, and modification of oxide films (see Sect. 3.2.4.3). They can be treated on the basis of various theoretical models like the Marcus–Gerischer theory [51, 52, 60] or the perturbation theory of Dogonadze [51]. For semiconducting oxide films, the first one is most appropriate [52]. ETR are considered as elastic (iso energetic) exchange of electrons between occupied and empty energy states in the oxide and electrolyte, respectively. The probability of electron exchange is given by the tunnel probability W for elastic exchange processes, in the first approximation according to the Gamov-formula. For the distribution functions in the electrolyte the Marcus model is used, while the electron states in the oxide are described by the band model.

$$i_+ = e^- \int W D_{vac}(\mathrm{ox}) D_{red}(El)\, dE \quad (37)$$

with $D_{vac}(\mathrm{ox})$ = empty states in the oxide, and $D_{red}(\mathrm{El})$ = occupied states in the electrolyte.

In contrast to metals, the relevant ETR do not take place at the Fermi level, but at higher or lower energy states. Figure 12 gives a schematic diagram of different possibilities for the case of anodic polarization. An ETR can take place [52]

1. *via the conduction band CB:*
 (a) at the oxide surface via the edge of the conduction band, usually

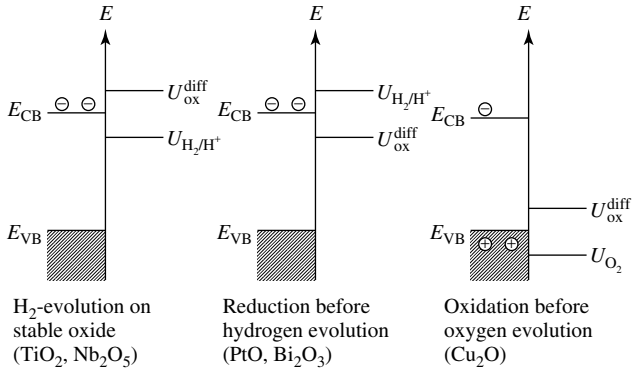


Fig. 12 Schematic diagram of different mechanisms of electron exchange between the redox system, the oxide and the metal [1].

an adiabatic ETR, it is observed for n-type oxides at low potentials, especially at $U < U_{FB}$.

(b) via direct [61] or resonance [37, 51, 62] tunnel processes (nonadiabatic) to the conduction band of the oxide. It takes place at n-type semiconductors at intermediate potentials $U > U_{FB}$. Then, log i can be correlated with the space charge layer d_{SC} or its capacity C_{SC} [37, 61].

(c) the same process to the lower band edge in the bulk [61]. Resonance tunnelling increases with donor concentration. For examples, see Refs. [37, 51]

2. *between electrolyte and the metal*

(d) by resonance tunnelling [63]

(e) by direct tunnelling. This process happens at thin films of noble metals, for example, Pt or Au. [63, 64]

3. *via the valence band VB [24]*

(f) at the oxide surface via the edge of the VB, usually an adiabatic ETR),

- via the VB at the surface with following tunnel process to the metal [54]. This process is favored by n-type oxides at high potentials or at p-type oxides [24, 51, 52]. Oxygen evolution takes place via the VB and can be correlated with the VB-position [52]
- via hole diffusion in the VB. this could be observed at p-type oxides.

The dominating process depends on the band structure of the oxide, the film thickness, and the electrode potential. Cathodic reactions usually take place via the CB, while anodic processes at high potentials (e.g. oxygen evolution) obey the VB-mechanism. Figure 13 shows some Tafel diagrams for ETR at passive iron for which CB- and VB-mechanisms were observed. The lower part gives the obtained transfer coefficients. $\alpha_{cath} \rightarrow 1$ indicates a CB-mechanism, while $\alpha_{anod} \rightarrow 1$ indicates a VB-mechanism. In the following, we will give some general rules

Using these considerations, the exchange current density of ETR was explained in a first approximation by the energetic difference between the redox potential U_{redox} and the next band edge $U_B = E_B/e$. Figure 14 shows the data for three different redox systems referred to the exchange current density on Pt. The expected relation from the model [52]

$$\frac{d \log \left(\frac{i_{0,sc}}{i_{0,Pt}} \right)}{d E_B/e} = -1/120 \text{ mV} \qquad (38)$$

is indicated by the straight line. In spite of various reasons for deviations, the general tendency is quite well pronounced.

Combined reactions (CBR) The description given above is correct for outer-sphere ETR, where the hydration shell is not changed, but only compressed or expanded. For inner sphere ETR, where hydration molecules are exchanged or ETR coupled with ITR or reactions with formation or breaking of chemical bonds CBR, the theory is more difficult [51, 52]. In general, CBR are complex reactions involving electrons, surface states, and ions in solution as well. The oxygen evolution is a good example. i can depend on various values, $i = f\ (c_{SS}, N_D, \Delta\varphi_{ox}, \Delta\varphi_H, \text{pH} \ldots)$.

In special cases, inelastic processes contribute too, for example, by the Poole–Frenkel effect [61]. In photoelectrochemistry, finally, the photocurrent is initiated by vertical electron/hole pair generation with following charge separation.

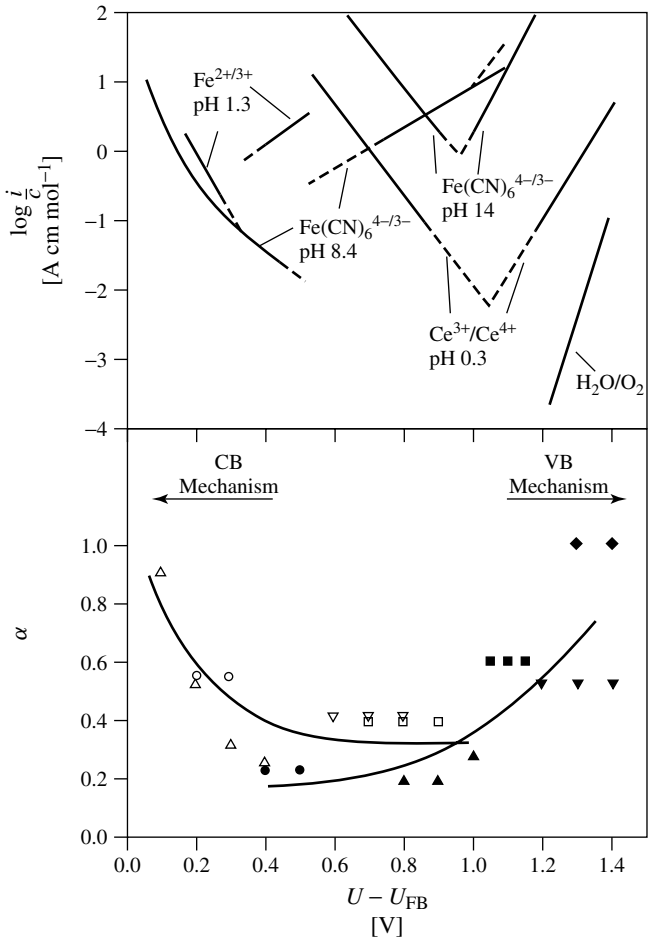


Fig. 13 Upper part: Tafel curves for ETR on passive iron [24]. The *i*-values of different authors were normalized taking the ratio i/c. Lower part: transfer coefficients taken from the Tafel plot in dependence on the band bending $U - U_{FB}$.

3.2.2.9 Mixed Ionic/Electronic Conductivity

Combining the results of Sects. 3.2.2.7 and 3.2.2.8, it becomes clear that ions and electrons move in passive films dependent on the electrode potential and electric field strength respectively, and the history of the film. Therefore, neither the vertical nor the horizontal axis of Fig. 8 can describe the conductivity of all oxides. Many oxides are distributed around the diagonal for which $\kappa_{el} = \kappa_{ion}$. Moreover, they have to be represented not by a point but by a region in Fig. 8.

In the eighties, there was a long discussion about an appropriate description of passive films by the properties of a semiconductor or chemiconductor [65]. This problem is, in fact, a problem of definition, the appropriate timescale and the

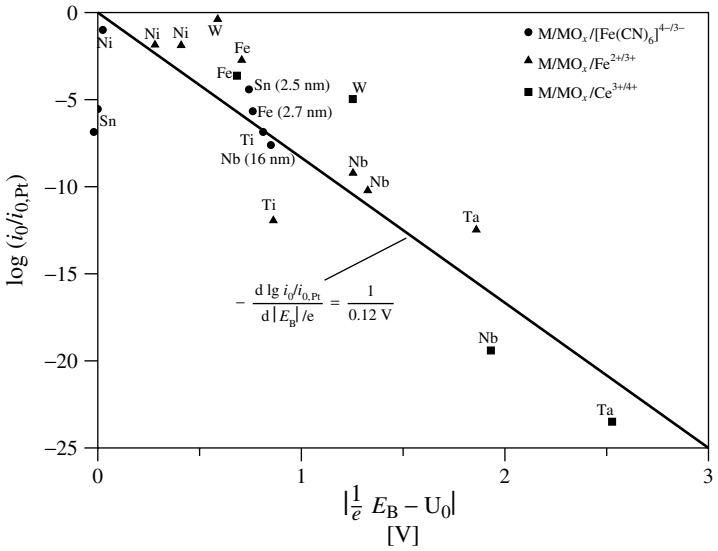


Fig. 14 Next-band approach of various outer-sphere ITR at passive metals [52].

aim of the description. By definition, a semiconductor is not changed by a flux of current, that is, the transference numbers of all ions are zero by definition, that is, $\kappa_{ion} = 0$. As was shown in the Sect. 3.2.2.7, however, ions can move at high fields. Therefore, oxide films with movable ions are by definition not ideal semiconductors. The timescale of electronic processes, however, is shorter by orders of magnitude. Their electronic behavior can easily be understood with the model of semiconductors, which may be applicable for at least short periods as long as the concentrations of donors and acceptors can be approximated as constant [49]. For example, the Schottky–Mott analysis and a derived band structure can be used and are valid as long as no major changes occur. It is well known, on the other hand, that by intercalation of ions at low potentials or by exhaustion of donors at high field strengths the properties and therefore also the band model change continuously. A frequency dependence of C indicates the beginning of ion migration.

3.2.2.10 Equivalent Circuit Diagrams

At steady state and for small signal AC-polarization, semiconductors and oxide films can be represented by a resistance and a capacitor in parallel, and the electrolyte resistance in series. This is experimentally correct, but it does not help understand the system and different experiments. For a general description of oxide films, however, we must introduce four corrections:

1. The resistances are usually not ohmic, but exponential resistances dependent on the electrode potential.
2. According to Fig. 8 and the discussion given above, electronic and ionic resistances have to be separated and specified for the special reaction.
3. Oxide films behave as diodes. In special cases, a diode must be added to simulate

the U/i-behavior, as it was shown for passive Cu as example [66].
4. Surface states must be added as shown in Fig. 6

3.2.3 Growth of Oxide Films and Ionic Migration

3.2.3.1 Survey on the Growth of Oxide Films

Because of different chemical, ionic and electronic properties, the oxide growth on metals, alloys and semiconductors follows different mechanisms and different laws. The most important contribution comes from the migration of ions in electric fields exceeding 5×10^6 V cm^{-1}.

The nature of the mobile ionic species was questionable for a long period of time. For passive Al, Verwey [47] assumed in 1935 that exclusive transport of Al-cations occurs in a fixed oxygen matrix. The idea of mobile cations dominated the oxide formation theories for the next 30 years. It seemed to be reasonable, as the volumes of cations are much smaller than O^{2-}-anions (e.g. by a factor of 20 for Al^{3+}), even if the experimental results indicated a combined transport. Marker experiments in the sixties proved cation-transference numbers in the range from 0.3 to 0.7 for many systems (Al, Be, Nb, Ta, Ti, V, W) coming closer to 0.5 with increasing current density, that is, cations and anions move in fact simultaneously (Table 1). This indicates that effects of charge distribution become more important than individual ion properties like size or polarizability [25]. Exceptions are the crystalline oxides on Hf and Zr, which are pure oxygen conductors.

In addition to migration, diffusion in the oxide or precipitation from the electrolyte can contribute. Following an inspection of Fig. 3 and other data, we can distinguish seven groups

1. Valve metals form homogeneous insulating oxide films by the high field law. This will be explained with Al as example. In Fig. 3, the slope is $m = 1$.
2. Under corroding conditions, the same metal can form porous films, which is well known for Al (see Sect. 3.2.3.2.7).
3. Semiconducting oxides grow at first according to the high field mechanism, but at higher potentials, oxygen evolution and corrosion limit the growth (Pt, Au, Fe).
4. If oxides with different metal valency exist, duplex films may be formed (e.g. Cu, Fe, Au, see Sect. 3.2.3.3.3).
5. If metal ions are in the electrolyte, anodic or electroless deposition can take place (e.g. FeOOH, see Sect. 3.2.3.3.4).
6. On alloys, the metal ions may have different transference numbers and corrosion rates. In dependence on potential, concentration gradients will be generated in the passive film (see Sect. 3.2.3.5).
7. Within semiconductors, large potential drops can exist. Then, oxide formation is hindered (e.g. *n*-Si). For compound semiconductors, the same problems arise as for alloys (e.g. InP, see Sect. 3.2.3.4).

3.2.3.2 Insulating Passive Films on Metals: Growth, and Corrosion of Al as Example

Oxide growth and passivity are discussed in this chapter for aluminum as a clear, simple example of high field growth and corrosion for the following reasons:

1. Aluminum forms an insulating, homogeneous oxide of the barrier type in acetate solution.
2. The space charge within the oxide is negligible.

3. To neglect passive corrosion, a solution of acetate is chosen.
4. ETR do not occur under usual conditions.
5. There is no influence of the grain structure of the substrate.
6. Detailed investigations by potentiodynamic and potentiostatic conditions were carried out in a wide range of U and T.
7. A porous oxide can be formed depending on the formation conditions.

3.2.3.2.1 **Thermodynamic Aspects** The common way to describe the thermodynamic equilibrium of a metal in contact with water is the so-called Pourbaix diagram [17]. This potential-pH diagram is shown in Fig. 15 for the system aluminum/hydrargillite/water at 25 °C. Among all solid modifications of hydrated Al_2O_3 that is, hydrargillite, bayerite, böhmite, corundum, aluminum hydroxide only hydrargillite was considered as the most stable form, beside the metallic aluminum itself.

Only the aluminic ion Al^{3+} and the aluminate ion are taken into consideration that is, neglecting the cations $Al(OH)^{2+}$ and $Al(OH)_2{}^{+}$ related to chloride complexes.

The reactions of main interest are the oxide formation (39) and the corrosion reactions in acidic and alkaline solutions (41) and (43), respectively:

$$2Al + 3H_2O \longleftrightarrow Al_2O_3 + 6H^+ + 6e^- \quad (39)$$

$$E = -1.550 - 0.0591\text{pH} \quad (40)$$

$$Al \longleftrightarrow Al^{3+} + 3e^- \quad (41)$$

$$E_0 = 1.663 + 0.0197 \log(Al^{3+}) \quad (42)$$

$$Al + 2H_2O \longleftrightarrow AlO_2{}^- + 4H^+ + 3e^- \quad (43)$$

$$E_0 = 1.262 - 0.0788\text{pH} + 0.0197 \log(AlO_2{}^-) \quad (44)$$

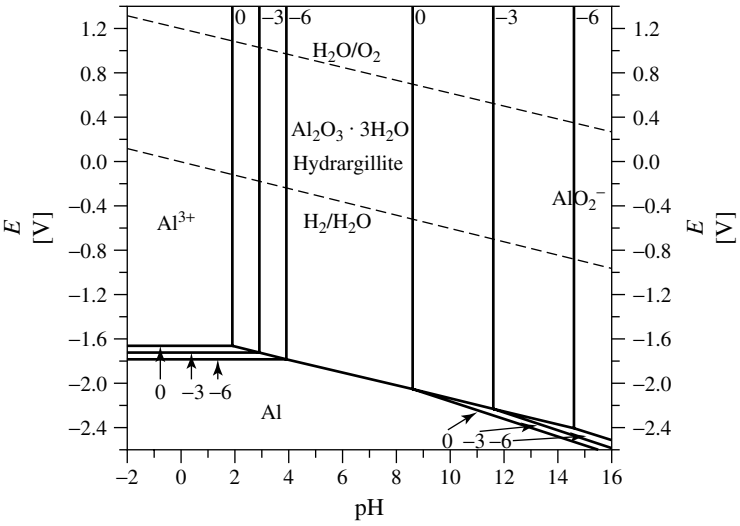


Fig. 15 Potential-pH diagram, the so-called Pourbaix diagram of aluminum in water at 25 °C for hydrargillite as the most stable form of hydrated aluminum oxides.

From the thermodynamic data, the relative stability of Al^{3+} and AlO_2^- with respect to

$$Al^{3+} + 2H_2O \longleftrightarrow AlO_2^- + 4H^+ \quad (45)$$

is

$$\log \frac{AlO_2^-}{Al^{3+}} \longleftrightarrow -20.30 + 4pH \quad (46)$$

This yields a limit of the domains of relative predominance of Al^{3+} and AlO_2^- of $pH = 5.07$.

For the solubility of aluminum and its oxide, the following 4 equations are used

$$2Al^{3+} + 3H_2O \longleftrightarrow Al_2O_3 + 6H^+ \quad (47)$$

$$\log(Al^{3+}) = 5.70 - 3pH \quad (48)$$

$$Al_2O_3 + H_2O \longleftrightarrow 2AlO_2^- + 2H^+ \quad (49)$$

$$\log(AlO_2^-) = -14.6 + pH \quad (50)$$

For plotting the potential-pH diagram, characteristic limits of the domains are calculated from eqns. 39, 41, 43, 47, 49. For this purpose, concentrations of 10^0, 10^{-3} and 10^{-6} mol l^{-1} are taken into consideration. Additionally, the stability domain of water is plotted in the same diagram by dotted lines. Aluminum is seen to be a very base metal as it has no domain of stability in common with water. Consequently it dissolves under hydrogen evolution (26) in all solutions. In acids, the trivalent aluminum cation is formed, whereas aluminate ions are formed in alkaline solutions. In neutral solutions, however, the solubility of the oxide film formed is small enough to passivate the metal.

It must be emphasized that Fig. 15 does not prove a thermodynamic stability of Al but a metastable state due to a kinetic hindrance caused by the passivity of aluminum.

3.2.3.2.2 **A Survey on Oxide Formation from CVs** Potentiodynamic measurements of oxide formation are useful to get a survey on the influence of potential U on i_{ox}, irreversibility of oxide formation, electrode or oxide capacity C, and thickness d from the oxide formation charge q_{ox}.

In the lower part of Fig. 16, the potentiodynamic oxide formation according to Eq. (39) is shown on a pure aluminum (99.99%) sample in an acetate buffer of $pH = 6.0$. The sweep rate in these experiments was $dU/dt = 100$ mV s^{-1}. Simultaneously the electrode capacity C was recorded with a lock-in amplifier at 1013 Hz and is shown in the upper part of the figure. The $U(t)$ diagram used is shown as an insertion. The initial film thickness d_0 in this experiment was 1.0 nm.

In the first and following scans, i increases rapidly to a maximum value and than reaches a plateau value

$$i = i_{ox} = \left(\frac{(kzFr\rho)}{M}\right)\frac{dU}{dt} \quad (51)$$

(k = film formation factor) After reaching the upper oxide formation potential U_f, i rapidly decreases down to zero during the cathodic cycle. In a subsequent anodic sweep, i remains negligibly small until the former U_f is reached. Usually, the half wave potential (the potential where the current reaches 50% of the plateau current) is seen as the beginning of new oxide formation.

The lower part of the figure can be summarized as follows:

1. The oxide formation is irreversible
2. The current density $i = i_{ox}$ is the same for each cycle (except for the first one) and reaches values of (316 ± 6) μ A cm^{-2} at the highest potential.

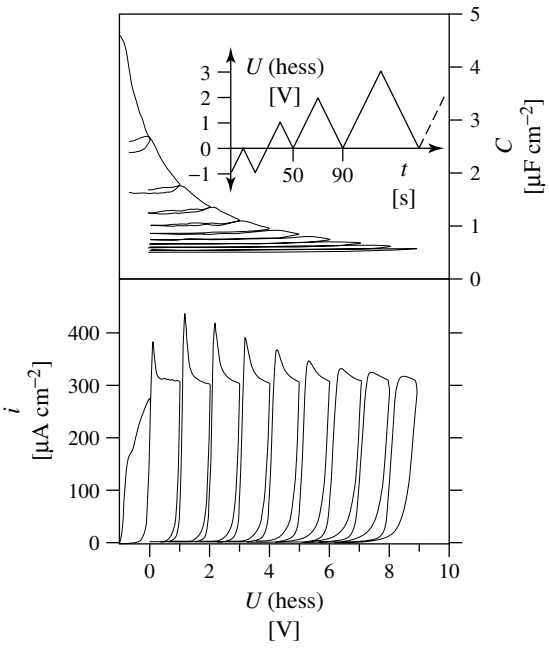


Fig. 16 Successive cyclovoltammograms of oxide formation on aluminum in an acetate buffer (pH = 6.0) $dU/dt = 100\ mVs^{-1}$; the upper part shows the capacity that was recorded simultaneously. The potential time program that was used is given as an insert.

This corresponds to $k = 1.6\ nm\ V^{-1}$ (with $\rho = 3.5\ g\ cm^{-3}$)

3. A sharp current overshoot is observed for the first cycles, which broadens more and more from cycle to cycle
4. The distance between falling current in the cathodic cycle and rising current of the subsequent anodic cycle increases more and more. This potential difference corresponds directly to a delay of oxide formation indicating a kinetic hindrance, in spite of the constant potential sweep rate.

The simultaneously recorded capacity (upper part of Fig. 16) starts at a value of nearly $5\ \mu F\ cm^{-2}$ and decreases with increasing potential in the anodic sweep. But in the cathodic run, that is, with decreasing U, C remains constant demonstrating

1. the irreversible oxide formation, and
2. the absence of any space charge, that is, the film behaves as an ideal insulator and Eq. (9, 10) can be applied.
3. results are shown in Fig. 7.

In the subsequent anodic cycle, the capacity remains constant until the former oxide formation is exceeded. Simultaneously with the increasing current C decreases further. This behavior is discussed in more detail in Sect. 3.2.3.2.5.

3.2.3.2.3 The Film Formation Factor *k*

A central point in the investigation of passive films and their formation kinetics is the determination of film thickness d and film formation factor k given by Eq. (51) (see Table 1). Usually, only i, q and C are accessible from electrochemical experiments. The variation of the physical properties of the oxide like ρ, D, U_0 show a large spread in the literature [25]. The error

in the determination of d is accordingly large (up to 30%) in spite of its importance.

From electrochemical measurements, we obtain coulometric data, if $i = i_{ox}$ can be presumed.

Then we obtain

$$q = q_{Ox} = \int_{t=0}^{t} i_{ox}\,dt \qquad (52)$$

Under potentiostatic conditions $i(t)$ has to be integrated:

$$q = \sum_{n=1}^{N-1} (t_{n+1} - t_n)\frac{i_{n+1} + i_n}{2} \qquad (53)$$

For details, see Ref. [53].

These equations, however, give only values of Δd. The total film thickness $d = \Delta d + d_0$ can be determined only if the initial film thickness d_0 is known. The slope of a d vs. U plot yields the film formation factor k. A value of 1,6 nm V^{-1} is found for Al in acetate or borate buffers by different authors.

The film thickness can be determined by Transmission-Electron-Microscopy (TEM) of thin slides that had been prepared by ultramicrotomy [67]. Takahashi et al. [68] applied this technique to Al formed galvanostatically at $i = 1$ mA cm^{-2} in borate or acetate buffer. In both cases $k = 1{,}6$ nm V^{-1} was obtained. Combining with coulometric data a density of ρ_{ox} $(Al_2O_3) = 3.5$ g cm^{-3} and a molar mass of M $(Al_2O_3) = 102$ g mol^{-1} are determined.

The determination of d by optical methods is also possible but causes some problems. Because of the high transparency of the aluminum oxide, methods based on UV-VIS spectra are useless. For infrared light, aluminum oxide shows some absorption lines, which are very sensitive to the amount of water included or adsorbed. The absorption bands belong to the crystalline oxide, which requires a separation of water content, degree of crystallinity and film thickness. Nevertheless, infrared spectroscopy can be useful to determine the degree of crystallinity or the number of surface states [69].

Ellipsometry is a useful method if a consistent set of optical parameters (k, n) can be determined. Then a measurement of the complex refraction index allows the determination of d and k.

UHV analysis can also be applied. Angle resolved x-ray photoelectron spectroscopy (ARXPS) also allows the determination of the film thickness. The method uses the fact that the ratio between the aluminum oxide peak and the peak of the metallic aluminum changes with angle of incidence since the length of path in the oxide increases for a grazing incidence [70, 71].

The film thickness can be also determined from sputter profiles [72]. Typical methods are ToF-Secondary Ion Mass Spectroscopy (ToF-SIMS), Ar-ion sputtering in combination with Auger or XPS, SNMS (secondary neutral mass spectroscopy), GDOES (glow discharge optical emmission spectroscopy). The thickness range that can be investigated ranges from a few nanometers to tenths of micrometer. The difficulty with all sputter methods is the same: a calibration with a standard is necessary to convert sputter time into thickness.

In summary, we assume $k = 1.6 \pm 0.2$ nm V^{-1} (at 100 mV s^{-1}) for Al.

3.2.3.2.4 **Electrochemical Impedance Spectra EIS and Equivalent Circuit Diagram** A simple but meaningful characterization method is given by the determination of C with a lock-in amplifier. A small ac voltage perturbation of, for example, 10 mV is superimposed to U and the resulting

AC-current is measured. A reasonable frequency is 1 kHz. This measurement was already shown in Fig. 16. In Fig. 7, log C is plotted as a function of the log d. The straight line that is obtained proves the validity of Eq. (6) over the whole range of thickness and independent of U. The relative permittivity of the oxide has a value of 12 (pH = 6.0 acetate or borate) [53].

In fact, the behavior of an aluminum electrode in aqueous solution is more complex and thus the equivalent circuit shown in Fig. 6 is used to describe it. It consists of an RC combination where $C = C_{ox}$ is the above discussed capacitance of the oxide and $R = R_{ox}$ results from the remaining ionic conductivity of the oxide. The oxide/electrolyte interface is represented by an RC combination in series to the first one where $C = C_H$ is the capacitance of the Helmholtz layer and $R = R_{CT}$ is the charge-transfer resistance of the interface. Finally a serial resistance R_{EL} for the (uncompensated) electrolyte resistance is introduced. In case of Al, the electronic elements (R_e and $R_{CT,e}$) and surface states (R_{SS} and C_{SS}) can be neglected.

To determine numerical values for the different elements of the equivalent circuit they have to be separated, for example, by electrochemical impedance spectroscopy (EIS). Similar to the above-described lock-in measurement a small ac signal of a few mV is superimposed to the electrode potential. The resulting current and its phase shift are then measured as a function of the frequency. Typical impedance spectra of thin oxide films on aluminum are shown in Fig. 17. At high frequencies ($10^5 - 10^6$ Hz) the capacitors act as shorts and only the electrolyte resistor determines the impedance, which is typically 10 Ohm for concentrated electrolytes and independent of the electrode. At the lowest frequencies, for example, 10^{-2} Hz or below, current flow through the capacitors is impossible and the impedance of the system is given by the sum of the 3 resistors in the current path. The

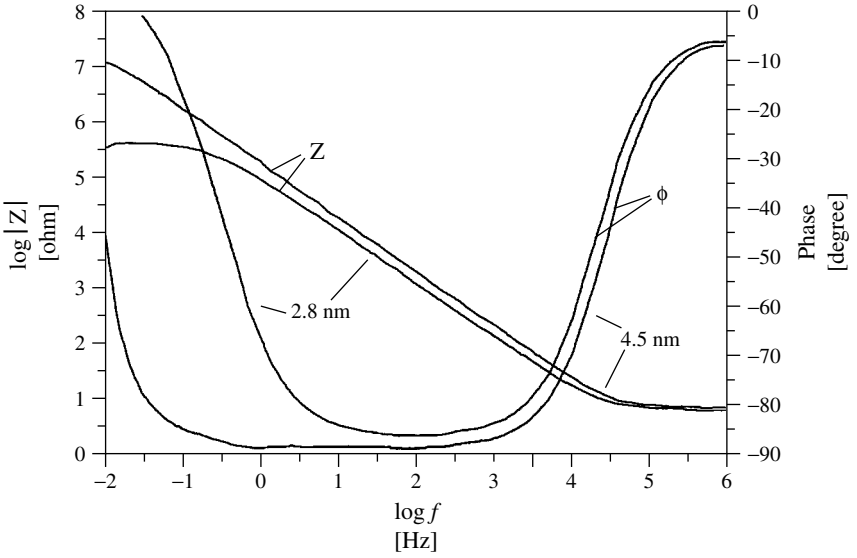


Fig. 17 Electrochemical impedance spectra of aluminum in an acetate buffer of pH 6.0.

resistance is mainly determined by R_{ox} since it is much larger than R_{CT} and R_{EL}. For intermediate frequencies, for example, 1 kHz, the impedance is determined by the capacitance for insulating oxide films like those formed on aluminum. For a precise analysis, the impedance data must be determined in a nonlinear least square fit (NLLS-fit) [73].

3.2.3.2.5 **Kinetics of Film Growth** The film of Al_2O_3 protects the metal from an environmental attack. Film growth requires a transport of anions or cations or both through the existing film. The conditions are shown in Fig. 18 schematically. Since there is no major activity gradient, the driving force for an ionic migration in the passive layer is given by the electrical field strength [25, 74].

$$E_s = \frac{d\varphi}{dx} = \frac{\Delta\varphi_{ox}}{d} = \frac{(U - U_{FB})}{d} \quad (54)$$

In a first approximation, the Reaction (14) H_2O/OH^- at the interface oxide electrolyte was considered to be fast. Verwey [47] proposed a model that explains the experimental results of Güntherschulze and Betz [46] by a rate determining migration within the oxide given by Eq. (31):

$$i_{ox} \approx i_{o,ox} \exp\left(\frac{\alpha_{ox} a z F \Delta\varphi_{ox}}{RTd}\right) \quad (31)$$

The exchange current density $i_{o,ox}$ of ion migration in the oxide and the experimental field constant β summarize several constants:

$$i_0 = \nu\rho a \exp\left(\frac{-E_A}{RT}\right) \quad (55)$$

$$\beta = \frac{\alpha a z R F}{RT} \quad (56)$$

with ν = jump frequency of the ions, ρ = charge carrier concentration, E_A = activation energy for the ion jump. α transmission factor, a = jump distance, z = valence of the respective ion.

In contrast, Mott [75, 76] and Cabrera [15, 48] considered the ITR of metal ions at the interface M/ox, that is, Reaction (15) as rate determining step. Since both models yield the same Eq. (31), a decision is still open.

A good insight into the anodic oxide formation is gained from potentiostatic pulse measurements. Figure 19 shows current transients $i(t)$ of anodic oxide formation on aluminum at pH = 6.0. Various potential steps from 0 V (hess) were chosen to an oxide formation potential between 3.3 and 5.9 V [77]. This corresponds to an increase in field strength from 6.6 to 10.1 $MVcm^{-1}$. The initial film thickness of 7.4 nm is given by a prepolarization to 3 V (hess). Each experiment must be performed on a different sample with respect to the irreversible

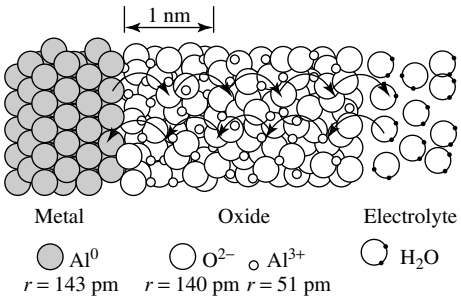


Fig. 18 Schematic of the conditions during oxide growth. The proportions are true to scale with respect to the Goldschmidt radii. Ions need several jumps to cross the entire film [53].

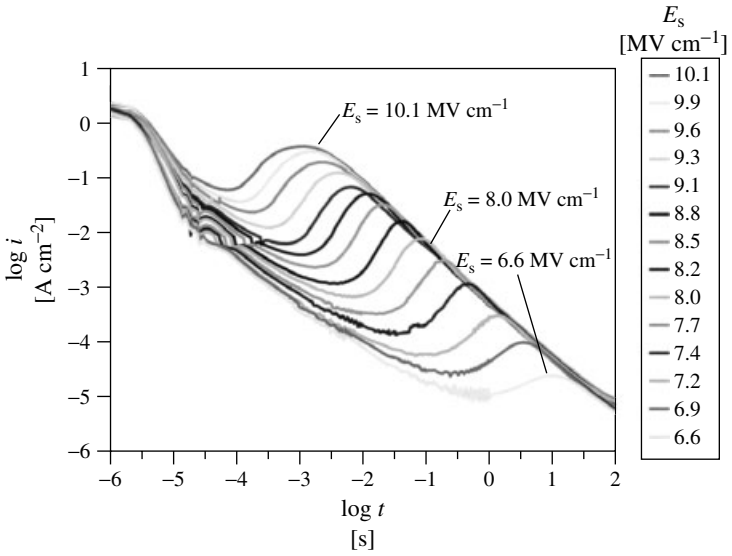


Fig. 19 Current transients of potentiostatic pulse experiments on aluminum at pH = 6.0 covered by an initial film thickness of 7.4 nm. The influence of the applied field strength on the time to current maximum is clearly seen. The field strengths ranges from 10.1 MVcm^{-1} down to 6.6 MVcm^{-1}. The current density in the overshoot decreases monotonically with decreasing field strength.

oxide formation. A double logarithmic presentation is chosen with respect to the extreme dynamics in current and time. The resulting transients can be separated in several domains in which different processes dominate. Immediately after the potential step the capacity of the oxide layer and the double layer capacity are charged. In a well conducting electrolyte, this so-called Debye charging dominates for only a few µs: $i \approx i_C \gg i_{ox}$. Later a further decrease of the current is observed that was explained by the so-called dielectric relaxation [78–82]. The same current distribution is however also observed for a depletion of defects within the oxide by electronic tunnelling [21].

A further oxide growth requires a migration of ions. In the case of aluminum, both anions and cations are emitted from the interfaces [25] into the oxide and migrate through the oxide as shown in Fig. 18 [53].

The injection of ions into the oxide forms a space charge that lowers the local field strength and thus inhibits further injection. As a result, the transport numbers come closer to 0.5 at high field strengths. Ions move through the oxide by a field-assisted thermally activated jump mechanism [47] at field strengths of several MVcm^{-1} over defects in the oxide [25]. The current reaches its maximum when the space charges reach the opposite interface. The time difference t_{max} and current density are described with respect to the high field law by [25]:

$$t_{max} = \frac{d\rho}{i_0 \exp(\beta E)} \tag{57}$$

$$i_{max} = i_0 \exp(\beta E) \tag{58}$$

with t_{max} = time to current maximum, i_{max} = current density of the maximum (Overshoot). Ions that have passed through the film combine with their counterions to form new oxide. As a result, $d\varphi/dx$ as driving force decreases. Thus, i decreases as well Eq. (58). Finally a stationary situation is reached, when $i = i_{corr}$, that is, when passive corrosion is reached (see Sect. 3.2.4.1). As a result, the current stabilizes on that level [16, 53]. For other corrosion phenomena, see Sect. 3.2.3.2.6.

The high field law predicts an infinite growth of d. In an approximation, it can be described by the reciprocal law

$$\frac{1}{d} = \frac{1}{d_o} - A\log(t - t_o) \approx \frac{1}{d_o} + A'\log t \tag{59}$$

In reality, however, this growth is limited by the dissolution of the oxide at the oxide electrolyte interface. For details, see Sects. 3.2.3.2.6 and 3.2.4.1.

Because of Eq. (31) film thickness differences will be immediately equalized. The resulting film thickness differences in noncorrosive electrolytes are extremely small. ($\ll$1 nm) [83].

Experimental results depend very much on the thickness, temperature, and potential. For example, measurements of E_a gave only reasonable results using high field oxide growth experiments in the temperature range between 210 and 353 K. An activation energy of 1.8 eV was obtained [82] which is similar to the values of other authors [84–86].

3.2.3.2.6 **Corrosion and Breakdown** Corrosion of Al and its alloys is a topic of high technological relevance due to the widespread application of Al as cheap and light material, in surface technologies, optics, as condensors, and in microelectronics. The corrosion depends on aggressive ions in solution, impurities in the metal, and local defects. Homogeneous (Sect. 3.2.4) and localized corrosion (Sect. 3.2.5) have to be distinguished.

In neutral solutions, i_{corr} is in the range of a few μA cm^{-2} on Al. Stationary conditions will be reached when the oxide formation is commensurate with the corrosion. d remains constant while the metal underneath the passive film slowly dissolves [87]. This can be studied in the steady state. The ITR (15) called ''passive corrosion'' takes place as long as the solubility product is not yet reached [16]. Because of the increase of solubility in acid and alkaline solutions, corrosion is enhanced in acid and alkaline solutions. This will be explained by Eq. (60) in Sect. 3.2.4.1.

Dielectric breakdown is important for condensor production. This is based on localized ionic and electronic collisions and will be explained in Sect. 3.2.5.2.

3.2.3.2.7 **Porous Aluminum Oxide** So far the aluminum oxide films discussed were of the barrier type. A different type of oxide is formed in solutions that dissolve aluminum oxide. These are for example acidic solutions like sulfuric or phosphoric acid or solutions with complexing agents like oxalic acid. Phosphorus acid is simultaneously acidic and complexing [88].

In a first step, a thin film of oxide from the barrier type may be formed. This will be partly dissolved at some locations. These thinner flaws are more reactive than their surrounding and new oxide is formed. The bottom of the flaw dissolves faster while new oxide is formed on the whole surface underneath the existing layer. As a result, small pores are

formed which are regularly distributed on the surface. Since oxide formation rate, dissolution rate and the migration at the bottom of the pores depend on the type and concentration of the electrolyte the diameter of the pores and the thickness of the walls can be influenced in a wide range, for example, $r_{pore} = 10 - 100$ nm [89]. The depth of the pores can reach several tens of micrometers [90]. The impressive aspect ratio of $A > 100$ [91] yields a promising base material in the upcoming nanotechnology [92].

With respect to their appearance these patterns are called honeycomb structures. These films are widely used in industry in the so-called ELOXAL procedure (electrolytic oxidized aluminum). The final step of this film formation is a sealing of the pores that can be performed anodically in a nondissolving electrolyte or more commonly in boiling water [93]. These films show a significant corrosion resistance, a sufficient mechanical stability and can be easily colored or coated. A lot of effort has been spent on the investigation of the mechanisms, on mathematical modelling and especially on EIS characterization of various porous oxide films. If small impacts are introduced prior to the anodizing, absolutely regular films are formed. Released from the base metal, these membranes show Knudsen perm selectivity and hence, are of interest, for example, as ultrafilters even for the separation of isotopes of the same gas H_2, HD, D_2.

3.2.3.2.8 **Other Types of Passive Aluminum Oxide Films, Anof, Modified Aluminum, Alloys** If aluminum is polarized to higher potentials, breakdown of the film can occur. Optical observation shows small sparks on the surface indicating local breakdown. This behavior can be systematically used for the preparation of a different type of aluminum oxide, the so-called ANOF oxides [94]. At high anodizing voltages, an oxidation in plasmalike conditions is achieved where parts of the aluminum surface will melt and react with the electrolyte to form a very stable, corrosion and wear resistant passive film.

This surface melting and oxide heating takes place especially in the direct vicinity of the spark. As a result, new oxide is formed locally leading to a local reinforcement of the surface. The next spark will occur in a neighboring region, which finally leads to several micrometer thick films that can be either homogeneous [94] or systematically structured [90]. This structure is the reason that these films were soon of interest as a human bone substitute [95] or as a base material for deposition of catalysts [22].

It is also possible to form a film ex situ by either

1. Gas phase oxidation = GPO (reaction of Al with oxygen) [96]
2. Physical vapor deposition = PVD (electron beam assisted evaporation of aluminum oxide onto a metal) [96]
3. Chemical vapor deposition CVD [97]

GPO films are dense and homogeneous but a variation of the film thickness is almost impossible. PVD on the other hand allows a variation of the film thickness but the films are porous and inhomogeneous in thickness [96].

Once a passive film is formed, it can be modified. A chemical etching technique [98] forms polishing films in the outermost region, which are of different composition and reactivity. A significant amount of Cl, Cr, or W can be incorporated and allows the oxygen evolution, a

reaction that usually does not take place on aluminum.

Aluminum oxide films can be modified by

1. implantation with ions [99–102]
2. irradiation [103]
3. local ablation [104]
4. heat treatment [105] and
5. sealing [93].

From the viewpoint of corrosion resistance, chromate conversion coatings still play an important role [106] even though a replacement of the toxic chromate is desirable. Rare earth metals are promising superseders for the chromium. They can be incorporated in the layers and enhance the corrosion resistance.

3.2.3.3 Other Systems

3.2.3.3.1 Other Metals Forming Insulating Oxide Films In Sect. 3.2.3.2, Al was selected as example because of the simplicity of the oxide growth: a homogeneous film is formed, there is no influence of grain structure, and there are no side reactions, but only field dependent ITR. The absence of side reactions such as evolution of hydrogen or oxygen is due to the large band gap of 8.3 eV. There are a number of other metal oxides with a similar large band gap. The corresponding metals show the same phenomenon of field dependent oxide growth and passivity. However, similarities and differences have to be taken into account:

1. Ta and Nb are very similar. Like Al, they can be used in the production of electrolyte condensors for voltages up to 150 V. This is due to the absence of side reactions and corrosion.
2. Zr, Hf, Ta, Nb, Bi, W, follow the high field mechanism and form insulating oxides. But the grain orientation has a small (Nb, Ta) or large (Zr, Hf) influence, as can be seen from grain dependent interference colors [107]. Hf and Zr form crystalline or amorphous films. The transport number of cations is near to 1 due to grain boundary migration.
3. Oxide formation on Si follows the high field law, but because of the influence of the potential drop in the substrate it will be discussed in Sect. 3.2.3.3.3.

3.2.3.3.2 Semiconducting and Metallic Oxide Films on Metals In case of Al, ETRs could be neglected because of the large band gap of Al_2O_3 and the lack of a space charge. For some other metals, the band structure of the oxide, an appreciable space charge, the occurrence of redox reactions, and intercalation of protons change the picture. The band structure models of passive iron are shown in Fig. 11 and the schematic representation of ETR in Fig. 12.

- Ti, Fe, Pt and Au obey the high field law, but side reactions, for example, O_2–evolution cause limitations of the accessible potential region (Au, Pt, Fe) to $U < 2$ V. In case of Ti a polarization up to 100 V is possible, but oxygen evolution starts at $U > 3$ V and causes a limitation of anodic coulometry. Moreover, d and N depend on the orientation of Ti-grains [37].
- Fe, Cu, Au and others form duplex layers, that is, layers with different valency (Fe, Cu) or different hydration (Au) (see Sect. 3.2.3.3.3).
- Fe_3O_4 and PbO_2 are metallic conducting oxides. Therefore, no potential drop can exist within the oxide. Fe_3O_4 is fast dissolving and not passivating, but PbO_2 is stable in various electrolytes.

- Pt, Au, Cu and Fe form oxide layers that can be reduced to the metal (Pt, Au, Cu) or to a soluble ion (Fe) (see Sect. 3.2.4.3).
- Ni and Pb form oxides that can reversibly be oxidized and reduced. Therefore, they are used in batteries.
- alloys form oxides according to the high field law, but because of different mobilities and corrosion resistances of cations, sandwich oxides can be formed with potential dependent composition (see Sect. 3.2.3.4).

3.2.3.3.3 **Duplex Films** Various passive films are not homogeneous, but show a duplex structure or a continuous gradient of composition. We can distinguish duplex oxides with a sharp step of metal valency (Cu), stepwise or continuous change of valency (Fe), change of hydration (Au) and foreign oxides on an oxide of the substrate ($Au/Au_2O_3/FeOOH$ or Cu/CuOx/FeOOH, see Sect. 3.2.3.3.4).

1. Cu gives the clearest example [13, 42]. During the reduction of the passive film, two peaks are observed which can be attributed to the reduction of CuO to Cu_2O and that of Cu_2O to Cu. Figure 20 shows results of potentiodynamic measurements after potentiostatic polarization at $U = 1.5$ V

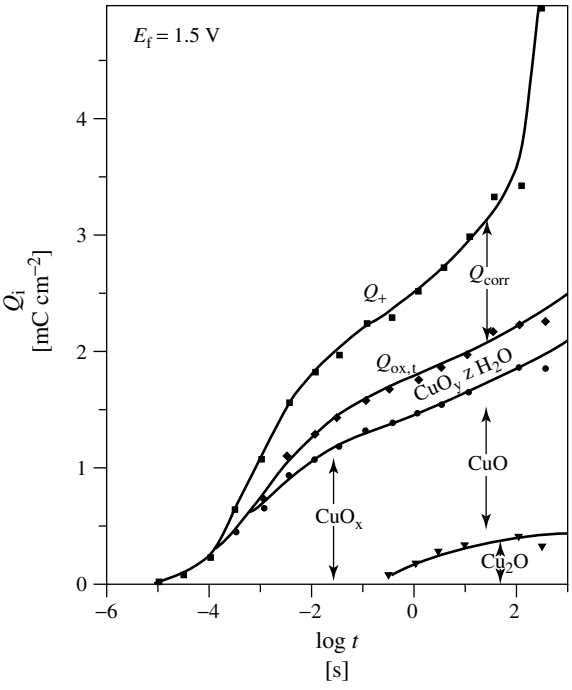


Fig. 20 Oxide formation on Cu and corrosion during a potentiostatic transient in dependence of log t. $U = 1.5$ V, pH 9. The total anodic charge q_+ is obtained by integration of i over t. Coulometric measurements of oxide reduction after the formation at t_f yield the charges q of different oxides. The corrosion charge q_{corr} is obtained from q_+ by subtraction of q_{ox} [13].

as a function of the polarization time t. After $t = 1$ sec, the oxide peaks clearly separate. The physical reason is given by the band structure. At U(hess) > 0.7 V, the valence band of Cu_2O reaches the Fermi level. Holes accumulate and cause the formation of CuO. At U(hess) > 1.2 V, a third peak indicates the formation of another (or higher) oxide. In the equivalent circuit, diodes can simulate the potential dependence [66].

2. The oxide film on iron consists of an inner Fe_3O_4 layer with a metallic conductivity and an outer Fe_2O_3-film (see Fig. 11). Vetter used a stepwise model [16], while Wagner [14] developed a continuous model based on an increasing number of vacancies. The controversy is not yet finally solved, since reduction measurements determine the outer film only without a clear result for the boundary. Electron diffraction yields an outer γ-Fe_2O_3-layer, but this result suffers from a possible recrystallization in vacuum.
3. At gold oxide, an insulating oxide is formed up to $U = 2.0$ V. Then, the valence band reaches the Fermi level, and oxygen evolution and corrosion starts. A conducting hydrous layer is formed at a constant rate [108]. The electrode capacity remains constant, since the potential drop across the inner oxide is electronically limited, and the outer hydrous layer is ionically conducting. ETR can take place at the inner $Au_2O_3/Au(OH)_3$-interface.

3.2.3.3.4 **Passivation with Participation of the Electrolyte** The high field model of oxide growth excludes a contribution from metal ions in the electrolyte. In some cases, however, a precipitation of oxide from the electrolyte can contribute to passivation.

Cohen [50] showed that Fe^{2+}-ions dissolved in the electrolyte can be deposited as FeOOH on top of the usual passive film. Another example is given by Ti in alkaline solution of H_2O_2. Ti-ions corrode very fast and become redeposited as a substoichiometric TiO_{2-x}. The oxide film is conducting and thicker than a usual TiO_2-passive film. Such substrates are used in microtechnology, for example, in the LiGA-process for Ni-deposition which is much faster than on a usual passive film.

The observations can be generalized. Besides the homogeneous oxide growth by Reaction (2), a dissolution/precipitation mechanism may contribute to the passivation. If it takes place by corrosion of an ion with lower valency (e.g. Fe^{2+}), the following reaction (inverse of Reaction 17) includes oxidation and the necessary ETR (15). Then, the supporting passive film has to be electronically conducting. On the other hand, if it consists of passive corrosion (11) and following chemical precipitation (inverse of 18) without a redox process, electronic conduction is not necessary.

Duplex films of different metals are formed, if the substrate is passivated by its own ions, and foreign ions deposit from the electrolyte. For example, FeOOH layers are deposited on other metals, for example, Cu or Au. The FeOOH-layer on Cu improves the corrosion stability of Cu.

3.2.3.3.5 **Semiconductors**

Passivity of elemental semiconductors Si forms an insulating oxide obeying the high field law [109, 110], but during oxide formation, oxygen evolution is possible by electron tunnelling [54]. The reaction requires holes from the valence band. Therefore, p-Si behaves as a metal due to the formation of an enrichment layer

of the valence band. From a formal point of view, *p*-Si behaves as a valve metal. *n*-Si, on the other hand, blocks on the anodic side. Holes are not available. At an increasing potential drop within Si, the valence band can approach or even exceed the Fermi level. Because of large tunnel distances and a lack of thermal generation of holes, there is no electronic equilibrium in the space charge layer. A large potential drop up to 100 V can be generated in *n*-Si, and oxide formation is almost impossible. This simple fact explains the difference between the oxide formation lines in Fig. 3 for *n*- and *p*-Si.

Under illumination, holes will be generated. Then, the oxide formation proceeds fast, and *n*-Si behaves as *p*-Si [54].

Passivity of compound semiconductors

Although Si is by far the most important semiconductor, it has some disadvantages, for example, an indirect band gap. Compound semiconductors are more expensive, more difficult in production and processing. But they have lot of advantages for special applications like optoelectronics, high-speed transistors, for example, in the Terahertz range or for water-splitting photoelectrodes. II–VI semiconductors, for example, CdSe or ZnO, are rarely used compared with the III–V semiconductors like GaAs and InP. Their advantages are direct band gap and a high-charge carrier mobility for quick charge separation. Their passivity plays an important technical role, for example, during production of large, very large, ultralarge scale-integration (LSI, VLSI, ULSI) devices. Here, a thin passive film should be used for insulation of different transistors but thermal oxides are usually to conductive.

During oxidation of GaAs and InP, both components of the composition semiconductor will be oxidized. On (100) InP, a homogeneous mixture of In_2O_3 and PO_x is formed under UV-ozone oxidation conditions [111]. The thickness increases logarithmically with exposure time [112]. Because of the different oxidation states of As, the conditions are more complex in the case of GaAs oxidation. A mixture of As_2O_3, As_2O_5 and Ga_2O_3 is formed on a (100) surface. ARXPS and TEM measurements confirm that a layered structure of (100)GaAs//As_2O_3,Ga_2O_3//As_2O_5,Ga_2O_3 is formed. The kinetics are more difficult in this case, a linear growth is observed for the Ga_2O_3 and the As_2O_5 while As_2O_5 shows a logarithmic growth [111].

The disadvantage of the passive films formed by UV-ozone or thermal oxidation is due to the comparatively high conductivity that prevents use as a gate insulator. Oxide films can also formed anodically in aqueous solutions of tungstates [113], phosphates [114], in alcohol-water mixtures and in alcoholic solutions [115]. The resistivity of the anodic films is usually higher and also the photo-transfer can be blocked at the oxidized InP. Surface analytical investigations revealed that a two-layer structure is formed. It consists of an indium rich outer layer of In_2O_3 and an inner layer with complex composition consisting of In_2O_3, P_2O_5, $InPO_4$, $In(PO_3)_3$, and $In(PO_y)_3$ with $y = 3 - 5$ [112] [116].

Similar to the formation of porous aluminum oxide a passivation – dissolution mechanism can be used to form nanoporous structures on InP. If (001)*n*-InP is polarized anodically under illumination in HCl solutions, nanoscaled pores are formed [117]. For potentials up to 1.2 V vs. SCE the main reaction is uniform anodic dissolution. Above this potential porous InP with a surface oxide is formed. The overpotential and anodizing time influence pore diameter (110–250 nm), wall thickness (16–50 nm) and pore length

(17–80 μm). These materials show photoluminescence with strong red shift, which is assigned to the formation of surface states on the anodized wall surfaces.

3.2.3.4 Passivation of Alloys

Passivity of alloys is a complex topic and the exact behavior of an alloy is hard to predict. Some mechanisms, however, are known and the principle function of some alloying elements is understood. In a first approach, they can be divided into ''oxide former,'' for example, Cr, and ''dissolution moderator,'' for example, Mo.

Mechanistic studies are often performed on binary alloys. Hf-Zr-binary alloys are excellent examples [118]. Because of the lanthanoid contraction, both elements show an extraordinary chemical similarity. The atom radii are identical and hence both can substitute for each other easily. Both elements form stable passive films and so do all their alloys. The physical parameters of the oxides such as density, permittivity, and crystallinity show a continuous changeover with variation of the atomic ratio.

Things become more difficult if the passivation behavior of both components significantly differs. One element may dissolve while the second remains is enriched in the surface and finally determines the passivation behavior of the alloy. Among all alloys, steel is the most important and hence numerous investigations have been performed on Fe-Cr alloys. For decades, it has been known that a critical value of chromium in iron-chromium binary alloys exists that changes the passivation behavior dramatically [119]. An electron configuration theory explaining this effect by a filling of the vacant d-orbitals with donor electrons from metallic iron as well as from adsorbed oxygen lacks from neglecting the passive film [120].

The percolation model was reactivated by Sieradzki and Newman [121] who proposed a bridging of Cr atoms by O to form a network of −Cr−O−Cr. The critical concentration of Cr is thus calculated where the number of connections falls below the value necessary for forming a connected chromium oxide surface. The enrichment of chromium at the surface was demonstrated by many authors [122–125]. One example is the work of Oblonsky et al. [126] who used in situ XANES (X-ray absorption near edge spectroscopy) to determine how various atomic concentrations of chromium in the alloy influence the chromium content in the oxide film. Very roughly enrichment by a factor of 2 is observed. Virtanen et al. used the same technique and studied stability and reaction mechanisms in the systems Fe, Fe−Cr and Cr [127]. A direct proof of the enrichment of chromium on Fe-Cr alloys is possible from combining electrochemical methods with inductively coupled plasma optical emission spectroscopy (ICP-OES) [128]. In this experiment, the total current following a potential step is recorded while the electrolyte from the surface is continuously exchanged and analyzed by an ICP-OES. Thus, it is possible to distinguish the different contributions of the elements to the current. The difference between total current and dissolution current gives an idea of the passivation current. Hamm et al. [129] demonstrated the benefit of this method. Polarization in the active region dissolves both elements in their bulk ratio. At the beginning of the transpassive region, however the preferential dissolution of Fe is observed. These results are in agreement with the experiments of Bojinov et al. [130] on 12% and 25% Cr alloys.

The same effect of preferential dissolution of iron and subsequent passivation of the alloy mainly from the alloying

element is found for intermetallics of iron and aluminum [131]. The formation of stoichiometric phases such as β-FeAl or Fe3Al causes an inhomogeneous behavior if grains of different composition are adjacent on the surface [124]. Duplex films are formed under these conditions. The strong enrichment of aluminum reflects in the formation of an aluminum rich inner layer, which is responsible for the passivity. In addition, an outer precipitated mixed aluminum -iron oxy hydroxide is formed [132].

On the basis of the results of preferential dissolution and starting from the percolation model, McCafferty [133, 134] developed a graph theory for the formation of oxide networks on binary alloys that is in agreement with the experimental findings on alloys such Fe-Cr, Co-Cr, Al-Cr, Ni-Cr, Fe-Si and Cu-Ni.

A second important group of alloying elements beside the passivity promoters are the dissolution moderators or blockers. These elements slow down the anodic dissolution rate. A prominent example is Mo in iron. Molybdenum does not form stable passive films but increases the stability of alloys significantly. Indirect conclusions that Mo hinders the surface mobility of Fe were confirmed during the last years with scanning probe techniques. Marcus and also Strehblow [135, 136] confirmed in their surface science approach that the mobility of Fe is slowed down significantly. This increases the activation energy for the ion-transfer into the electrolyte and thus stabilizes the alloy.

3.2.4 ITR at the Homogeneous Oxide/Electrolyte Interface: Corrosion and Modification

Until now, passivation has been described under the aspects of film formation and the ionic migration within the film. For the stability of passive films a steady state, however, reactions at the interface oxide/electrolyte have to be discussed. According to the experimental observations, we will treat 4 different processes:

1. passive corrosion (steady state),
2. instationary corrosion during oxide growth,
3. oxide reduction and oxidation, and
4. oxide modification by intercalation.

From a molecular point, on the other hand, we have to distinguish 5 types of pure ITR and CBR (see Fig. 1 and Table 2):

1. the anodic ITR of OH^--ions necessary for film formation
2. the anodic ITR of cations, the passive corrosion
3. the cathodic ITR of OH^--ions necessary for film reduction
4. the cathodic ITR or migration of cations necessary for film reduction which can be a reductive dissolution or a reduction to the metal,
5. ITR of other ions, for example, protons, during intercalation or modification
6. combined ETR necessary for film oxidation or reduction

3.2.4.1 Passive Corrosion in the Steady State

In the steady state, a passive substrate can corrode at constant film thickness. For this case, the following ITR at the interface oxide/electrolyte are considered:

$$H_2O \longrightarrow OH^-(ox) + H^+ \quad (14)$$

and

$$M^{z+}(ox) \longrightarrow M^{z+}(aq) \quad (18)$$

Reaction (14) is in equilibrium, that is, $\Delta\phi_H = \Delta\phi_{H,0}$. Then, $\eta_H = 0$ and $i_{14} = 0$.

This is not the case, however, for the ITR of metal ions. Equation (18) is not in equilibrium, and the current density $i = i_M{}^{z+}$ is that of Reaction (18).

The pH-dependence of i_{corr} of Al is a good example. $\Delta\phi_H$ is given by pH according to Eq. (5). In acidic solutions, we can expect a decrease of i with increasing pH. But in alkaline solution Al can dissolve as aluminate, the reaction of which is catalyzed by OH^-. (Eq. 43). Then, i_{corr} should increase again. Careful experiments have verified these expectations [87, 137]. Results are shown in Fig. 21. The expected minimum occurs in the neutral region.

In case of passive iron, the situation is more complex. As Fig. 9 shows, five observations have to be explained:

1. In the passive region at constant pH, the dissolution of Fe^{3+} -ions $i_{corr} = \text{const.}$
2. At constant U, i_{corr} decreases with increasing pH.
3. In acid solution, at constant pH, the corrosion depends on the nature of the anion.
4. In the transpassive region, i_{corr} increases exponentially with potential.
5. At low potentials, near U_{FB}, the dissolution of Fe^{2+} increases with decreasing U.

In extension of the treatment given by Ref. [139], Eq. (25)) must be specified:

$$i = i_0 f(c_x) g(a_y) \exp\left(\frac{\alpha z F \Delta\varphi_H}{RT}\right) \quad (60)$$

with $f(c_x) =$ any function of a complexing agent, and $g(a_y) =$ any function of the activity of the transferred ion in the oxide surface. Together with $\Delta\phi_H$ we have three parameters determining the rate of the reaction. The equilibrium (14) and the dependence of $\Delta\phi_H$ on pH Eq. (8) explain the observation (1) and (2). The influence of U on $\Delta\phi_H$ (see Fig. 5) explains (4).

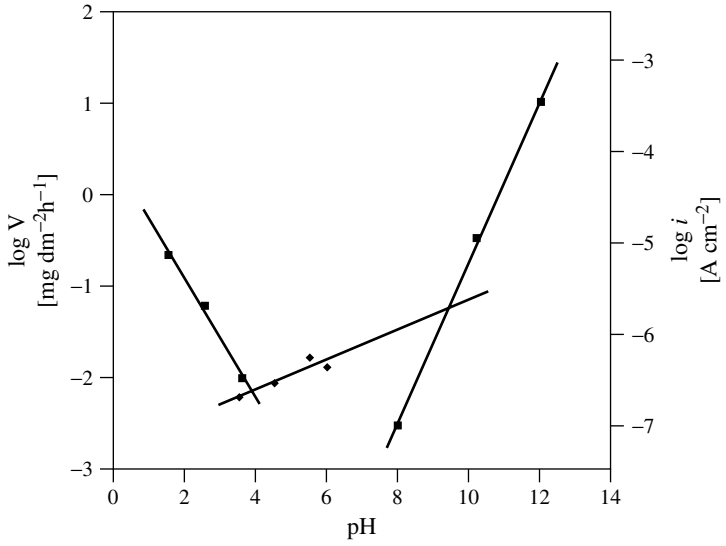


Fig. 21 pH-dependence of the corrosion on aluminum: the left axis shows the logarithm of mass loss and the right axis the corresponding corrosion current density (data in acidic and alkaline regions are taken from Ref. [138] neutral region is taken from Ref. [87]).

The influence of anions (3) is due to the adsorption of SO_4^{2-}-ions (c_x) that catalyze a different reaction, that is, the transfer of $FeSO_4^{+}$-ion. The function $g(a_y)$ finally represents an electronic function, that is, the increasing activity of Fe^{2+} in the surface.

3.2.4.2 Corrosion during Oxide Growth

Instationary passive corrosion occurs for example at changing pH or changing potential. Here we refer to the work of Vetter and Gorn [139]. Figure 22 shows their classical diagram for passivation of Fe. It was obtained from slow, instationary measurements of $U(i)$ with analytical detection of i_{corr}. In pure acid solution, the solubility product of Fe_2O_3 is not reached. Hence, the oxide dissolves slowly, but in the steady state, due to anodic polarization, it is formed with the same rate, that is, the layer formation current $i_l = 0$. For example, in 1N H_2SO_4, a passive corrosion $i = i_{corr}$ is observed in the steady state with about 6 μA cm^{-2}, but $i_l = 0$. The exchange current density of layer formation by Reaction (14) is about 0.3 μA cm^{-2}. Switching to a higher current density $i > i_{corr}$, the potential increases, i_{corr} increases fast, but i_l increases, too. At a lower, still positive current density, the potential decreases, and the passive film dissolves slowly. Under these conditions, $i_l < 0$, while $i_{corr} > 0$, that is, it is still positive. The fundamental result is given by the difference between the equilibrium potentials of Reactions (14) and (18), as long as the solubility product of the oxide is not maintained.

Potentiostatic pulse experiments yield a different, good example. Starting from

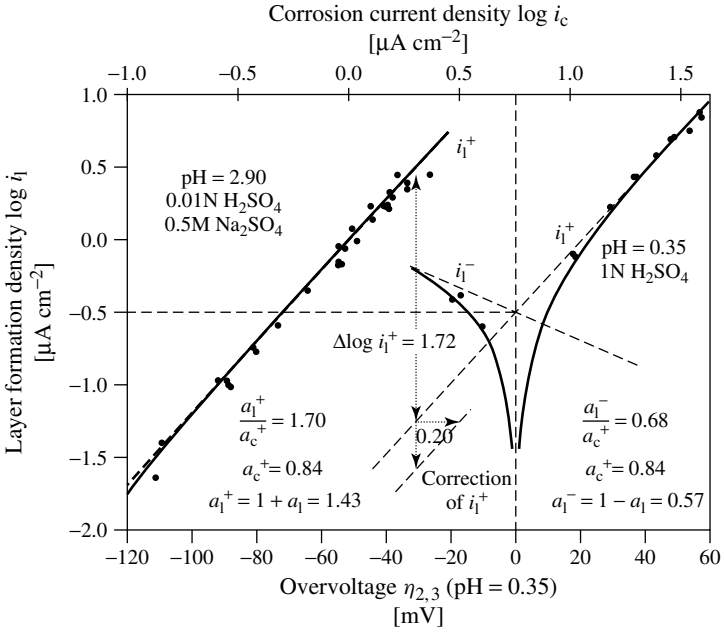


Fig. 22 A classical diagram for the competition between layer formation (i_l) and corrosion ($i_{corr} = i_C$). The upper scale gives the overpotential at the oxide/electrolyte interface η_H. Measurements were carried out at various pH values at constant sulfate concentration [139].

a bare surface, oxide is formed which requires an anodic current $i_{14} > 0$. In contrast to the conditions of steady state, Reaction (14) is not in equilibrium, that is, $\Delta\phi_H > \Delta\phi_{H,0}$, and $\eta > 0$. The increasing overpotential of the Helmholtz layer, however, causes an increasing corrosion of metal ions, too.

Experiments were carried out with electropolished Ti in sulfuric acid solution [2]. The current transients yield the overall current density i and the total charge flux at the electrode interface. Analytic determination of the corroded Ti by atomic absorbance spectroscopy (AAS) measurements yielded i_{corr}. As long as i_{O_2} can be neglected,

$$i_{ox} = i - i_{corr} \tag{61}$$

can be evaluated exactly. Results are shown in Fig. 23. Both current densities i_{ox} and i_{corr} decrease continuously with time. The oxygen evolution i_{O_2} shows an opposite behavior that is correlated to the aging of the film and the formation of a band structure, that is, electronic effects. This is not considered here. (See Sect. 3.2.2–3.2.4 for aging effects).

The quantitative evaluation follows the analysis given in Ref. [139]. Both i_{ox} and i_{corr} follow the experimental Eq. (62).

$$\log i = k - \log t \tag{62}$$

The field strength $\Delta\varphi_{ox}/d$ as well as $\Delta\varphi_H$ and η_H decrease with t. Then, the ratio i_{corr}/i_{ox} is given by Eqs. (63 and 64), respectively [139]:

$$\log \frac{i_{corr}}{i_{ox}} = f(\Delta\varphi_H, \Delta\varphi_{ox}) \tag{63}$$

and

$$i_{ox} = i_{ox,0}\left[\left(\frac{i_{corr}}{i_{corr,0}}\right)^{\frac{\alpha_{ox}^{+}}{\alpha_{corr}^{+}}} - \left(\frac{i_{corr}}{i_{corr,0}}\right)^{-\frac{\alpha_{ox}^{-}}{\alpha_{corr}^{+}}}\right] \tag{64}$$

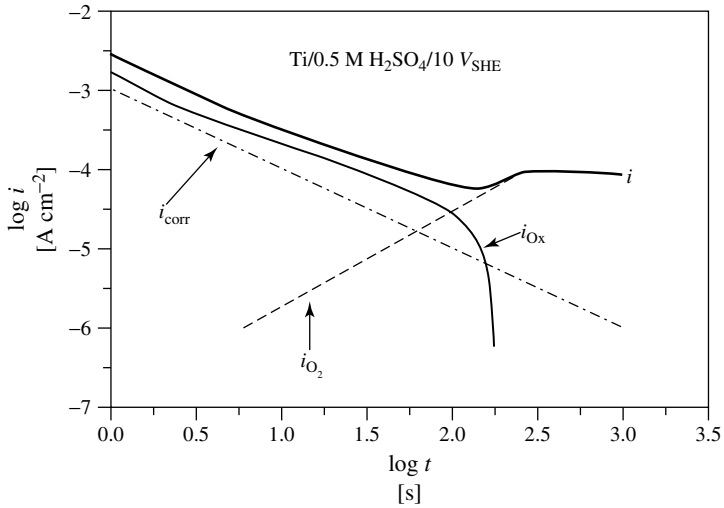


Fig. 23 Potentiostatic current density transients i(t) for Ti/0.5 M H_2SO_4. i_{corr} was determined by analytical measurements (AAS). $i_{ox} = i - i_{corr}$ was obtained by subtraction. The rate of O_2-evolution (CBR with involved ETR) depends on the formation of a band structure and becomes dominant after 100 s.

This equation was verified by correspondent experiments for other oxide films on copper [13].

3.2.4.3 Oxide Reduction and Oxidation

Passive films of most valve metals are formed by a single stoichiometric oxide only, for example, in case of Al, Ta, and Hf. For other oxides, especially those marked in Fig. 2, redox reactions may take place.

At first, we discuss oxide reduction. This can take place by various processes according to the reverse Reaction (2) = (24), that is, reduction to the metal, (24), that is, reductive dissolution, or (20) differential reduction to a lower oxide.

The back Reaction (2) is a field-dependent ITR. The transport through the film would be possible under extreme conditions at very negative potentials only. At dislocations and at the edge of oxide islands, the local field strength is much higher than within the homogeneous film. Hence, the reverse Reaction (2) takes preferentially place via the so-called ''island mechanism of oxide reduction''. This was verified for Pt, Au, and Cu.

Reductive dissolution is well known from Cohen's work on passive iron [50]. Fe_2O_3 is reduced to Fe_3O_4 that dissolves fast. The overall process is

$$Fe_2O_3 + 6H^+ + 2e^- \longrightarrow 2Fe^{2+} + 3H_2O \qquad (65)$$

This is to explain by Eq. (60). The oxide is too thick for a cathodic ion migration, and an island reduction is impossible, since there is no free metal surface. But because of the electronic conductivity, the activity of Fe^{2+} in the surface increases, and an anodic ITR of Fe^{2+} takes place. It is combined, however, with the threefold cathodic reaction of OH^--ions, which must dissolve simultaneously. Thus, the total current is cathodic, but it corresponds to 1 e per Fe^{3+}-ion only.

Reduction to a lower oxide takes place if the ETR (15) through the oxide is possible, and if the reduction potential of the oxide exceeds the potential of the hydrogen evolution. A typical example is given by the reduction of CuO to Cu_2O [13, 42], or of NiOOH to NiO [23]:

$$2CuO + H_2O + 2e^- \longrightarrow Cu_2O + 2OH^- \qquad (66)$$

This reaction consists of a cathodic ITR of OH^- at the interface, and an equal electron transport through the interfaces Cu/Cu_2O and Cu_2O/CuO. Thus, in case of Reactions (65 and 66), ETR in the bulk oxide and ITR at the oxide surface are involved.

Now we can generalize the conclusions. For the oxidation or reduction of an oxide, some of the following conditions must be fulfilled:

1. The reaction should be possible because of thermodynamics (e.g. $U > U_{ox}$ for anodic processes)
2. Redox reactions should not limit the potential (e.g. $U < U_{redox}$ for an anodic process)
3. If the process involves ETR, the electron-transfer via the CB or VB should be possible.

Figure 24 shows some examples in an energetic diagram. It shows the case in which an oxide can be oxidized before anodic oxygen evolution (Cu_2O to CuO), since the conditions (1) and (3) are full filled. In case of $Ni(OH)_2$, $U_{ox} > U_{O_2}$, but the oxygen evolution is strongly hindered, while the oxidation is fast. Hence, the oxide oxidation takes place in spite of the fact that rule (2) is not fulfilled.

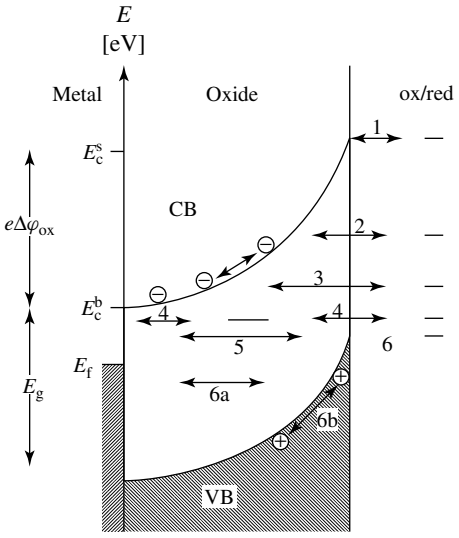


Fig. 24 Energetic diagram for competition between different redox processes of the oxide and other redox reactions, for example, evolution of hydrogen or oxygen.

On the other hand, the reduction of PtO requires only condition (1) and (2), but not (3), since it is a pure ITR. In contrast to that, oxides of valve metals are stable even at low potentials because hydrogen evolution proceeds faster than the oxide reduction. They can be only dissolved, for example, in case of Al, by a local pH shift due to hydrogen evolution.

Redox reactions of the oxide film depend on the band position. The *p*-type oxides of Cu and Ni can be oxidized and reduced via the valence band. The reduction of Fe_2O_3, on the other hand, requires an ETR by tunnelling from the conduction band to the surface with the consequence of dissolution of Fe^{2+}. The valve metals could be reduced by electrons from the conduction band at very negative potentials, but then hydrogen evolution takes place first.

Figure 25 shows relevant data for various oxides. Squares refer to the total oxidation process, while the open circles give data for the differential process. On the left side of the line for hydrogen evolution, the latter one is preferred, while on the right side of the line for O_2-evolution, this reaction should take place. In both cases, however, slow kinetics can change the thermodynamic preference.

3.2.4.4 **Modification of Oxide Films by ITR of Other Ions** In the preceding section, more or less stoichiometric redox processes were discussed. Foreign ions may change the electronic and other oxide properties by intercalation of small amounts. The theoretical description can be started from Eq. (60) for ITR. At first, foreign ions have to be adsorbed and incorporated into the oxide surface. Then, they can migrate or diffuse into the film. Intended and nonintended modifications have to be distinguished.

The induction of pitting corrosion by penetration of Cl^--ions into the oxide is a well-known example of nonintended processes (see Sect. 3.2.5.3). The anions can migrate at positive potentials, that is, at positive band bending, towards the metal surface and dissolve the oxide. Another example is given by passive Ti. At low potentials, near U_{FB}, a small amount of protons penetrates into the oxide causing an increase of donor concentrations enhancing ETR. The process depends on diffusion and migration conditions. It starts already at low anodic band bending. Then, diffusion must overcompensate the opposite migration. At large band bending, however, migration wins, and protons leave the film again [49].

Various possibilities of intended modification of oxide films were reported in the literature [140]. The term modification is used in different connections:

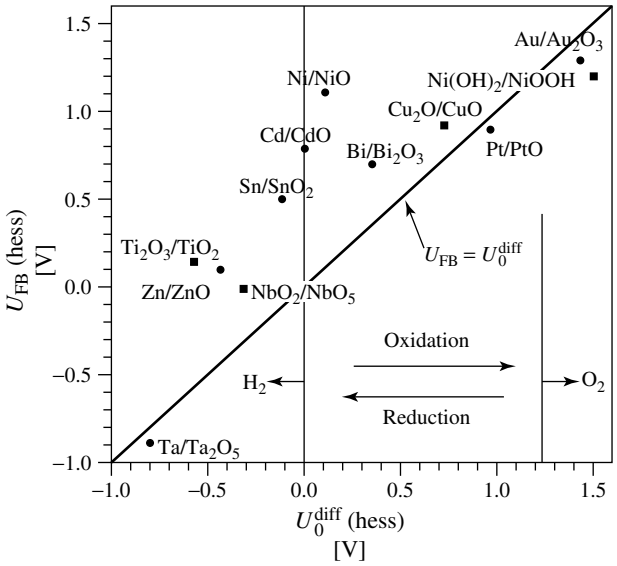


Fig. 25 Flat band potential U_{FB}, versus potentials of different (squares) or total (circles) oxidation.

1. passive films modified after or during formation,
2. modification during technical usage, for example, by inhibitors,
3. by usage of a special substrate, for example, an alloy,
4. Chemical and/or topographic modification.

Chemical modification causes concentration gradients [26]. This causes changes of local electronic properties. It can be obtained by macroscopic deposition or mixing or by molecular processes like intercalation, diffusion or ion implantation [141].

For the application of valve metals in electrocatalysis, the strategy is changed. In that case, a high reactivity of the surface and a good electronic conductivity must be established. The application of Ti-0.2Pd improves the stability of the passive film at negative potentials. For real electrocatalysis, for example, with DSA, the formation of passive films has to be avoided. Instead, mixed TiO_2/RuO_2 or IrO_2 is deposited by a thermal process. The formation of an insulating TiO_2-film during technical usage passivates the electrode that must be renewed. Examples are schematically shown in Fig. 26 [141]. Three types of modification are represented:

1. a homogeneous, molecular or atomic doping, for example, by ion implantation,
2. a heterogeneous microscopic modification, for example, by Pd incorporated into TiO_2,
3. a surface modification, for example, by cathodic deposition of Pd on a passive film.

Modification can occur during the technical usage, for example, in solutions of inhibitors. At first, they are enriched at the oxide surface, but sometimes they are

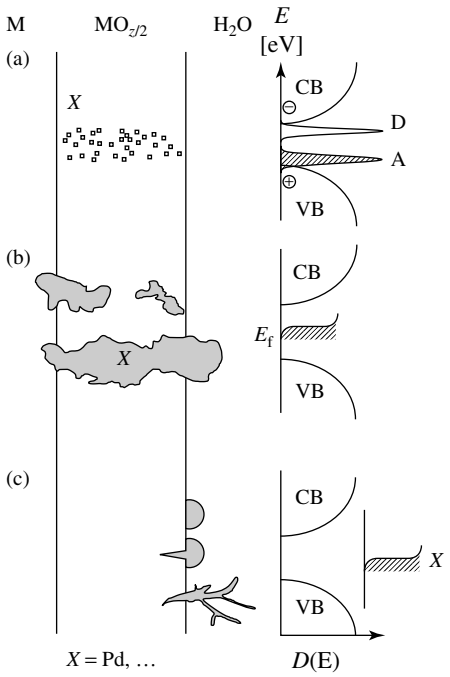


Fig. 26 Schematic diagram of structure and electronic states of modified passive films.

diffusing into the film or corroding metal ions form together with the inhibitor more stable, mixed films, usually with a vertical concentration gradient [142].

Besides this chemical modification, topographic modifications are applied, for example, with porosification of Al_2O_3 with following sealing (Sect. 3.2.3.2.7) or by local laser irradiation (Sect. 3.2.5.5).

3.2.5 Corrosion at Inhomogeneous Films: Breakdown, Pitting and Localized Attack

Homogeneous corrosion or corrosion at homogeneous surfaces is a minor problem that can be solved, for example, by anodization. Larger problems arise with inhomogeneous films or localized attack. Here again we have to distinguish between microscopic and molecular reasons on the one hand, and macroscopic phenomena such as dielectric breakdown, pitting corrosion, localized corrosion induced by focused signals, filiform corrosion etc., on the other hand. Both aspects are connected, but in different ways. At first, we will mention the microscopic and molecular reasons. Then the macroscopic effects will be interpreted.

3.2.5.1 Microscopic and Molecular Reasons for Local Corrosion

The following reasons have to be distinguished:

1. Inhomogeneous passivation of pure metals due to local differences of substrate structure, for example, grains and twins [2, 38].
2. Chemical inhomogeneities originating from local inclusions of foreign substances [143, 144].
3. Mechanical effects [145], for example, stress in the oxide film causing local cracks of the film
4. Changes of local conductivity, for example, by avalanches
5. Local enrichment of charge carriers, for example, by focused signals like a localized field or localized radiation [2].

3.2.5.2 Dielectric Breakdown

The passive films on valve metals are almost perfect insulators. Those dielectric films are used in condensors [146], in tunnel junctions [147] and for insulation of semiconductors [148]. The basic requirement is the ability to withstand an electric field of $0.1–1\ GVm^{-1}$ without electric breakdown. The breakdown of passive films means a spontaneous local

increase of conductivity, usually by many decades. It may be indicated by different effects [149, 150]:

- irregular current peaks
- visible sparks
- potential fluctuations, increasing noise
- audible noise (cracking).

Experimentally the process of local breakdown ranges from an inconspicuous repassivation to an explosion-like dissolution or vaporization of large parts of the sample. This depends on the electrical and chemical energy stored in the system. The passive film represents the dielectric medium of a capacitor, which is short-circuited by the local breakdown. The electric energy stored on the capacitor heats the breakdown channel, eventually up to temperatures where metal vaporization or plasma formation occurs. At these increased temperatures a very fast reaction of the less noble metals with water or the adjoining metal leads to a destruction of the sample.

Because of the enormous industrial importance there is a tremendous number of investigations dealing with the break down of these films. A number of reviews by Agarwal [151], Solomon [152], Klein [153], DiStefano and Schatzkes [154], Ikonopisov [149] and Parkhutik, Albella and Martinez–Duart [155] lead to an overview over this wide field. The stability of the film and the mechanism of the breakdown process can depend on

- type of base metal
- purity, crystallographic structure and roughness of the base material
- process of oxide formation
- anodizing conditions and oxide thickness
- electric field strength
- the oxide band gap
- temperature
- type and composition of the adjoining phase
- the composition and concentration of electrolyte.

There are a lot of investigations of the breakdown of anodic valve metal oxide films in the electrolyte or in a metal-oxide-metal contact. Because of the enormous differences in all of these parameters, there is no general model that can explain all the experimental findings. In fact, each model has only a limited range of validity and should not be stressed beyond this range.

Collision ionization model The common collision ionization model of the electric breakdown as summarized by O'Dwyer [156] requires a sufficiently high probability for the ionization process. Later this model was extended by Ikonopisov [150]. If the ionization cross section, film thickness and energy dissipation are large enough, an ionic avalanching will finally destroy the passive film.

Tunnel model for thin films In some cases, the validity of the collision ionization model is limited. For ultrathin films with $d < 10$ nm the number of ions is too small for an establishment of the avalanche and a different model was proposed. In Fig. 27, the breakdown voltage U_{BD} was determined as a function of d or the film formation potential U_{Form}. A straight line with a slope of $E_{BD} = 6,25$ MV cm^{-1} is obtained. This value is just the reciprocal of the film formation factor k (Chapter 3.2.3.2.3). This identity of E_{Form} and E_{BD} in Fig. 28 demonstrates the common origin of the responsible process for Al, Hf, Nb, Ta, Ti, Zr [157] and probably other metals.

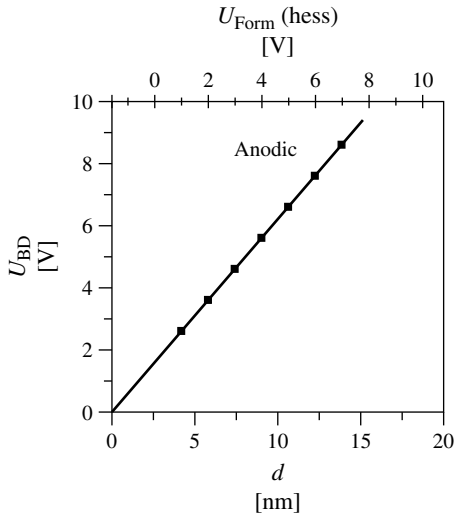


Fig. 27 Breakdown potential U_{BD} at $T = 298$ K for the anodic polarization of anodic metal-insulator-metal (MIM) systems (Al/AlOx/Ag) as a function of the film thickness d. The formation potential for anodically formed oxides is given in the upper abscissa for comparison [21].

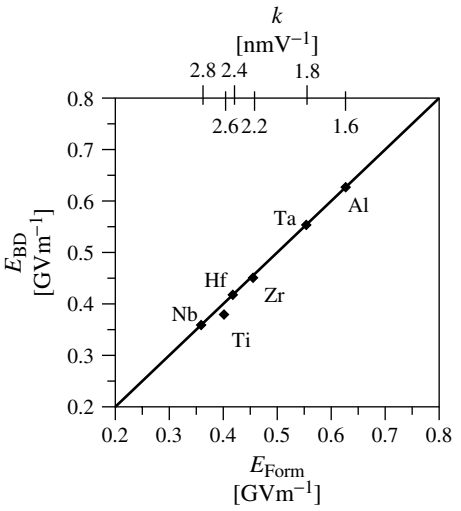


Fig. 28 Breakdown fieldstrength E_{BD} at $T = 298$ K for different valve metals as a function of the respective formation fieldstrength E_{Form}. The corresponding film formation factor is given in the upper abscissa for comparison. The full line shows where breakdown fieldstrength and formation fieldstrength are equal [21].

If E_S in a MIM contact with anodic oxide film exceeds E_{Form}, some defects with the critical activation energy become mobile. The movement of these defects will then initiate the breakdown by means of enhanced electronic tunnelling. A distortion of tunnel barriers due to ionic defects in the insulator was discussed by Schmidlin et al. [158]. In their calculations, they derived significant increases of the tunnel current i_{tunnel} due to the barrier deformation caused by ionic defects. Finally local conducting paths will be formed initiating the breakdown. Recently, a quantitative calculation was demonstrated by means of thin valve metal oxide films [157].

For these very thin oxide films ($d <$ 10 nm), single electron tunnel processes

are significantly more probable than interaction processes such as collision ionization. A defect that is only slightly shifted within the oxide can modify the tunnel path of the electrons and serve as a centre for resonance tunnelling. Because of the shortening of the effective tunnel length, i will increase significantly. This i may locally heat the sample adjacent to the tunnelling path. This heating at a given E_S on the other hand will activate further defects. An additional barrier deformation will result, which cause a further increase of i_{tunnel}. Within this positive feedback loop various processes like sample heating, increasing current flow, and mobilization of ionic defects contribute to the final breakdown. In fact, this activation of defects is more complex. The process does not only depend on U but also on T and the time for which the sample is polarized. Current transients of potentiostatic pulse steps with voltages above U_{BD} show a significant transient behavior. The destructive processes occur after a minimum time. For short times ($t < 1$ ms), a sample can survive above E_{BD}.

3.2.5.3 Pitting Corrosion

Oxide films may be destroyed by aggressive ions. Different mechanisms have been discussed:

The penetration/dissolution mechanism: Cl^- migrates or diffuses into the oxide, destabilizes it and finally causes active dissolution.

The breakdown/adsorption mechanism: At first, the oxide film breaks down owing to mechanical stress. Then, Cl^- is adsorbed at the bare metal and enhances active dissolution. The Sato model [11] focuses on pitting and transpassive dissolution. It assigns the breakdown to the electrostriction pressure resulting from the high field strength E_S. E_S produces a compressive stress that can exceed the breakdown stress of the oxide. It explains the differences in breakdown stability of thinner and thicker oxide films. The surface tension decreases with d and stabilizes oxide. The lowering of breakdown stability after anion adsorption is assigned to a lowering of the surface tension.

The detailed mechanisms for different systems have been discussed at all passivity meetings (see Ref. [1]) and cannot be discussed here in detail.

3.2.5.4 Cathodic Breakdown

At potentials U(hess) < 0 V hydrogen evolution becomes thermodynamically possible (see Fig. 25). On base metals, however, oxide films are stable under these conditions. At the surface of homogeneous films, hydrogen evolution is kinetically hindered by the large electronic resistance of the film. Moreover, hydrogen evolution requires the adsorption of H-atoms, for example, on Pt. But most oxides are not catalytically active.

Two exceptions of this general statement are known [159–161].

1. Protons can be discharged at the interface oxide/electrolyte by tunnelling of electrons (thin films of few nm) or by an enlarged conductivity at weak spots of inhomogeneous films. Then, solved hydrogen weakens the oxide structure, reduces it to the metal, changes it partially to a hydride, or diffuses to the electrolyte. With increasing local current density the pH value close to the oxide surface increases and, hence, corrosion starts. This process is autocatalytic, the cathodic current density increases up to values of hydrogen evolution at the bare metal.
2. Protons enter the film and diffuse to the metal surface and are discharged

there. Tiny bubbles are formed and oxide locally flakes off, and crevices are formed. The increasing current density locally increases the pH value. This is also an autocatalytic process. In case of Ti, protons migrate into the oxide that is partially reduced. The electronic conductivity increases, and the lower oxide dissolves slowly. This is observed in reducing electrolytes. To protect the passive film, Ti 0.2Pd is used. Pd accumulates at the oxide surface, allows hydrogen evolution at a more positive potential and, thus, stabilizes the oxide film of Ti.

For Al, these models correspond to the experimental findings that the films are metastable for some time until a cathodic breakdown occurs, ms to s for thin Al_2O_3-films or some 10 s for thicker ones. In a first step about 0,5 % of the surface are thinned. Depending on the potential either lateral growth of the pores is observed a flaking off of the oxide [161].

3.2.5.5 Laser Induced Breakdown or Oxide Growth

The interaction of photons with oxide films depends mainly on three parameters:

the wavelength of the incident light ($h\nu >$ or $< E_g$),
the electrode potential and the correspondent band bending,
the thickness of the passive film or that of the space charge layer, respectively.

With respect to localized corrosion, various experiments with focused laser light were carried out. They show that the passive film may be destroyed by a laser pulse. The mechanism of destruction depends on the band gap of the oxide and the photon energy. In case of $h\nu < E_g$, photons generate a thermoelastic effect at the inner metal/oxide interface. It results in a mechanical ejection of the passive film and cavitation in the electrolyte [104]. This effect can be used for measurement of pit growth.

In the opposite case, $h\nu > E_g$, photons produce electron-hole pairs. Accumulation of holes at the oxide surface increases the local potential drop which may cause a fast photocorrosion. Ion migration is enhanced in the thin film, corrosion is enhanced, and altogether a fast dissolution of metal takes place by a photoelectrochemical process in the passive film. An example is given for Ti [160]. This technique can be used for microstructuring of Ti- or Al surfaces [104]. On the other hand, anodic metal ion dissolution competes with the opposite anodic film forming ITR of oxygen ions. Therefore, in dependence on the special conditions, laser induced oxide growth may overcome pit formation [160].

3.2.6 Applications

Traditionally, passive films are applied for corrosion protection. This requires a stable film with negligible ionic conductivity (see Fig. 8) and without mechanical stress. The transfer resistance R should be high. Therefore, most investigations refer to mechanisms for hindrance of ionic processes, for example, by modification by inhibitors, ion implantation etc.

Passivation techniques have to compete with other techniques of surface protection, like phosphating, electrodeposition of paint and others. In high-tech systems, especially in micro and nanotechnology [27], passivation has to compete with other microstructuring techniques, like PVD, CVD or PACVD (plasma assisted chemical vapour deposition). Here, the advantages

and disadvantages of electrochemical techniques become obvious: passivation can be carried out in micro and nanostructures, for example, in porous silicon [162, 163]. While PVD techniques are confined to smooth surfaces, the electric double layer follows all topographical changes even in systems with high aspect ratio as long as the electrolyte gets in contact with the surface of the substrate.

Application of passivation in nanotechnology causes some problems. The advantage of passivation consists in the formation of a homogeneous film in solutions of good conductivity. This is due to the poor conductivity of passive films: the film spreads over the whole surface even in case of a localized counterelectrode. This property is a strong disadvantage for nanotechnology. The localization of the electric signal is difficult. By analogy to the Wagner-number, the problem was rationalized by the EMT-number, given by the ratio [163]

$$[\mathrm{EMT}] = \frac{R_{\mathrm{pol}}}{R_{\mathrm{EL}}} \qquad (67)$$

A 3D structuration can be achieved, if $[\mathrm{EMT}] \ll 1$, that is, at high R_{EL}. If the structure resistance $R_{\mathrm{pol}} > R_{\mathrm{EL}}$, the field delocalizes, and 2D-structures are obtained only. Highest R_{EL}-values can be realized in monomolecular condensation films. For example, localized passivation of silicon or Ti may be important in nanotechnology. This can be done applying Scanning X Microscopy (SXM) techniques in moist gas atmosphere [164, 165]. This allows the production of oxide patterns of some nm height and width of 20 to 100 nm.

Other techniques may be applied. Future high-tech applications can use the advantages of localized passivation and localized breakdown. Electrochemical passivation can be localized by mask techniques, for example, photoresist or protective ion implantation. For example, microstructures of titanium dioxide can be realized protecting the surrounding surface by nitrogen implantation [167]. The application of localized breakdown is another technique. Laser induced breakdown can be used to dissolve the passive film and to corrode the underlying metal. The process is similar to electrochemical machining, but it differs by the higher resolution without application of masks.

Two applications of oxide films will be mentioned but not discussed in detail, since corrosion protection is not the aim of them. For electrolyte condensors, the stabilization of oxide films is very important. Their applicability is limited by dielectric or cathodic breakdown. Therefore, the stabilization follows similar procedures as for passive films.

In electrocatalysis, on the other hand, a high reactivity of Ti electrodes is required. This is realized by the deposition of conductive oxides that are not typical passive films [166]. Their lifetime, however, will be limited by passivation of the inner surface Ti/catalytic layer. Therefore, the passivation is avoided as far as possible.

3.2.7 Conclusions

1. Starting from experimental application of passivity, simple metals were investigated at first. Improved techniques yielded a better understanding of ionic and electronic properties at the interface, at first for single crystals. Now an even better understanding is achieved using microscopic techniques of electrochemistry, which reveal the microstructure of passive films. Advanced techniques of surface preparation allow

the application in high-tech areas, such as microelectronics etc.

2. Each system differs from the others. Many aspects of solid-state physics, electrochemistry and materials science have to be considered.:
 - ITR locally different (grain boundaries)
 - ITR in the oxide (migration) and at the surface (corrosion)
 - Electronic equilibrium: /yes/no?
 - Potential distribution: constant field (Insulator, no space charge), band bending (space charge, Schottky–Mott)

3. New materials and new applications require new investigations. Special requirements in μ- and nanotechnology.

Therefore, passive films and their stabilization will be hot topics in future as they were in the past.

Acknowledgments

The financial support of PC-Institut der Heinrich–Heine-Universität Düsseldorf, Fonds der Chemischen Industrie, and Ministerium für Schule, Wissenschaft und Forschung des Landes Nordrhein–Westfalen as well as the Max–Planck–Institut für Eisenforschung, The Japan Society for the Promotion of Science and the Alexander von Humboldt–Stiftung is gratefully acknowledged.

References

1. J. W. Schultze, M. M. Lohrengel, *Electrochim. Acta* **2000**, *45*, 2499.
2. J. W. Schultze, B. Davepon, in *Passivity of Metals and Semiconductors* (Ed.: M. B. Ives) The Electrochemical Society, Pennington, NJ, Proc. Vol. 99-42, 1999, p. 485.
3. C. Schönbein, *Pogg. Ann.* **1836**, *37*, 390.
4. H. Uhlig in *Passivity of Metals* (Eds.: R. P. Frankenthal, J. Kruger), The Corrosion Monograph Series, The Electrochemical Society, Princeton, NJ, 1978, p. 1.
5. L. Young, *Anodic Oxide Films*, Academic Press, London, 1961.
6. H. Kaesche, *Metallic Corrosion*, NACE, Houston, Tex., 1985.
7. M. J. Dignam in *Oxides and Oxide Films* (Ed.: J. W. Diggle), Marcel Dekker, New York, 1973, p. 92, Vol. 1.
8. S. R. Morrison, *Electrochemistry at Semiconductor and Oxidized Metal Electrodes*, Plenum Press, New York, 1980.
9. M. J. Dignam in *Comprehensive Treatise of Electrochemistry* (Ed.: J. O'M. Bockris), Plenum Press, New York, 1981, p. 247, Vol. 4.
10. N. Sato, G. Okamoto in *Comprehensive Treatise of Electrochemistry* (Ed.: J. O'M. Bockris), Plenum Press, New York, 1981, p. 193, Vol. 4.
11. N. Sato, *Electrochemistry at Metal and Semiconductor Electrodes*, Elsevier, Amsterdam, 1998.
12. M. Froment, (Ed.), *Passivity of Metals and Semiconductors*, Elsevier, Amsterdam, 1983; The Fifth International Symposium on Passivity, Bombannes, France, 1983.
13. M. M. Lohrengel, J. W. Schultze, H. D. Speckmann et al., *Electrochim. Acta* **1987**, *32*, 733.
14. C. Wagner, *Ber. Bunsenges. Phys. Chem.* **1973**, *77*, 1090.
15. N. Cabrera, *Philos. Mag. A* **1949**, *40*, 175.
16. K. J. Vetter, *Electrochemical Kinetics*, Springer-Verlag, Berlin, Germany, 1967.
17. M. Pourbaix, *Atlas d'Equilibres Electrochimiques a 25 °C*, Gauthier Villars, Paris, 1963.
18. F. Di Quarto, C. Sunseri, S. Piazza et al., *J. Phys. Chem. B* **1997**, *101*, 2519.
19. A. K. Vijh, *J. Electrochem. Soc.* **1969**, *116*, 353.
20. A. K. Vijh, *J. Electrochem. Soc.* **1969**, *116*, 972.
21. A. W. Hassel, D. Diesing, *Thin Solid Films* **2002**, *414*, 296.
22. F. Patcas, W. Krysmann, D. Hönicke et al., *Catal. Today* **2001**, *69*, 379.
23. J. W. Schultze, M. M. Lohrengel, D. Roß, *Electrochim. Acta* **1983**, *28*, 973.

24. U. Stimming, J. W. Schultze, *Electrochim. Acta* **1979**, *24*, 859.
25. M. M. Lohrengel, *Mater. Sci. Engin.* R **1993**, *11*, 243.
26. J. W. Schultze, *Mater. Sci. Forum* **1995**, *185–188*, 377.
27. J. W. Schultze, (Ed.), *Special Issue of Electrochim. Acta* **2001**, *47*, 1.
28. K. J. Vetter, *Electrochim. Acta* **1971**, *16*, 1923.
29. J. Kruger, *Mater. Sci. Forum* **1995**, *185–188*, 367.
30. W. Walkenhorst, *Naturwissenschaften* **1947**, *34*, 373.
31. A. Aladjem, D. G. Brandon, J. Yahalom, *Electrochim. Acta* **1970**, *15*, 663.
32. K. Shimizu, G. E. Thompson, G. C. Wood, *Thin Solid Films* **1981**, *77*, 313.
33. J.-L. Delplancke, R. Winand, *Electrochim. Acta* **1988**, *33*, 1539.
34. J.-L. Delplancke, R. Winand, *Electrochim. Acta* **1988**, *33*, 1551.
35. J. W. Schultze, L. Elfenthal, K. Leitner et al., *Electrochim. Acta* **1988**, *33*, 911.
36. L. Arsov, C. Kormann, W. Plieth, *J. Electrochem. Soc.* **1991**, *138*, 2964.
37. S. Kudelka, A. Michaelis, J. W. Schultze, *Electrochim. Acta* **1996**, *41*, 863.
38. U. König, B. Davepon, *Electrochim. Acta* **2001**, *47*, 149.
39. M. Schweinsberg, S. Kudelka, A. Michaelis et al., *Mater. Corros.* **1998**, *49*, 161.
40. J. W. Schultze, M. Pilaski, M. M. Lohrengel et al., *Farad. Disc.* **2002**, *121*, 211.
41. A. Moehring, M. M. Lohrengel, *GDCh Monogr.* **1998**, *14*, 424.
42. H.-D. Speckmann, M. M. Lohrengel, H.-H. Strehblow, *Ber. Bunsenges. Phys. Chem.* **1985**, *89*, 392.
43. J. W. Schultze, M. M. Lohrengel, *Ber. Bunsenges. Phys. Chem.* **1976**, *80*, 552.
44. A. Güntherschulze, H. Betz, *Z. Phys.* **1931**, *68*, 145.
45. A. Güntherschulze, H. Betz, *Z. Elektrochem.* **1931**, *37*, 726.
46. A. Güntherschulze, H. Betz, *Z. Phys.* **1934**, *92*, 367.
47. E. J. W. Verwey, *Physica* **1935**, *2*, 1059.
48. N. Cabrera, N. F. Mott, *Rep. Prog. Phys.* **1949**, *12*, 163.
49. U. König, J. W.Schultze in *Interfacial Electrochemistry* (Ed.: A. Wieckowski), Marcel Dekker, New York, 1999, p. 650.
50. M. Cohen in *The Passivity of Metals* (Eds.: R. P. Frankenthal, J. Kruger), Corrosion Monograph Series, The Electrochemical Society, Princeton, NJ, 1978, p. 521.
51. W. Schmickler, J. W. Schultze in *Modern Aspects of Electrochemistry* (Eds.: J. O'M. Bockris, B. E. Conway, R. E. White), Plenum Publ. Corp., 17(1986) p. 357.
52. J. W. Schultze, L. Elfenthal, *J. Electroanal. Chem.***1986**, *204*, 153.
53. A. W. Hassel, Ph.D. thesis, Heinrich-Heine-Universität Düsseldorf, Verlag Shaker, Aachen, 1997.
54. H. Bloeß, G. Staikov, J. W. Schultze, *Electrochim. Acta* **2001**, *47*, 335.
55. V. Macagno, J. W. Schultze, *J. Electroanal. Chem.* **1984**, *180*, 157.
56. J. W. Schultze, V. A. Macagno, *Electrochim. Acta* **1986**, *31*, 355.
57. M. Faraday, *Experimental Researches in Electricity*, reprinted 1965, Dover Publications, New York, 1965, p. 234 (s. Ref.(1)), Vol. 2.
58. K. J. Vetter, *Z. Phys. Chem. NF* **1955**, *4*, 165.
59. J. W. Schultze, U. Stimming, *Z. Phys. Chem. NF* **1975**, *98*, 285.
60. H. Gerischer, *Physical Chemistry, an Advanced Treatise, IXa* Academic Press, New York, 1970, p. 463.
61. P. Meisterjahn, J. W. Schultze, B. Siemensmeyer et al., *Chem. Phys.* **1990**, *141*, 131.
62. K. E. Heusler, K. S. Yun, *Electrochim. Acta* **1977**, *22*, 977.
63. W. Schmickler, J. W. Schultze, *Z. Phys. Chem. NF* **1978**, *110*, 277.
64. J. W. Schultze, K. J. Vetter, *Electrochim. Acta* **1973**, *18*, 889.
65. B. D. Cahan, C.-T. Chen, *J. Electrochem. Soc.* **1982**, *129*, 921.
66. M. M. Lohrengel, J. W. Schultze, H. D. Speckmann, *Electrochim. Acta* **1986**, *31*, 123.
67. K. Shimizu, G. E. Thompson, G. C. Wood et al., *Philos. Mag. A* **1989**, *60*, 591.
68. H. Takahashi, K. Fujimoto, H. Konno et al., *J. Electrochem. Soc.* **1984**, *131*, 1856.
69. S. Desset, O. Spalla, P. Lixon et al., *Colloids Surf. A* **2002**, *196*, 1.
70. J. Finster, D. Schulze, *Phys. Stat. Sol. A* **1981**, *68*, 505.
71. D. F. Mitchell, K. B. Clark, J. A. Bardwell et al., *Surf. Interface Anal.* **1994**, *21*, 44.
72. A. Zangwill, *Physics at Surfaces*, Cambridge University Press, New York, 1988.
73. C. Gabrielli, *Identification of Electrochemical Processes by Frequency Response Analysis*, Solartron Electronic Group Ltd., 1980.

74. A. J. Davenport, G. T. Burstein, *J. Electrochem. Soc.* **1990**, *137*, 1496.
75. N. F. Mott, *J. Chem. Phys.* **1947**, *44*, 172.
76. N. F. Mott, *Trans. Faraday Soc.* **1947**, *43*, 429.
77. T. Ismer, Diploma Thesis, Heinrich-Heine-Universität Düsseldorf 1994.
78. E. von Schweidler, *Ann. Phys. Leipzig* **1907**, *24*, 711.
79. A. K. Jonscher, *Nature* **1977**, *267*, 673.
80. A. K. Jonscher, *Phys. Status Sol. B* **1977**, *83*, 585.
81. H. Kliem, B. Schumacher, *IEEE Trans. Electr. Insul.* **1987**, *22*, 219.
82. S. Rüße, Ph.D. thesis, Heinrich-Heine-Universität Düsseldorf, Dusseldorf, Germany, 1994.
83. A. W. Hassel, M. M. Lohrengel, S. Rüße et al., *Bull. Chem. Technol. Maced.* **1994**, *13*, 49.
84. J. F. Dewald, *J. Electrochem. Soc.* **1955**, *102*, 1.
85. P. Winkel, C. A. Pistorius, W. Ch. van Geel, *Philips Res. Repts.* **1958**, *13*, 277.
86. A. C. Harkness, L. Young, *Can. J. Chem.* **1966**, *44*, 2409.
87. A. W. Hassel, M. M. Lohrengel, *Mater. Sci. Forum.* **1995**, *185–188*, 581.
88. A. Mozalev, A. Poznyak, I. Mozaleva et al., *Electrochem. Commun.* **2001**, *3*, 299.
89. E. Palibroda, T. Farcas, A. Lupsan, *Mater. Sci. Engin.* **1995**, *B32*, 1.
90. N. Itoh, K. Kato, T. Tsuji et al., *J. Membrane Sci.* **1996**, *117*, 189.
91. J. W. Schultze, K. G. Jung, *Electrochim. Acta* **1995**, *40*, 1369.
92. D. Ebling, Ph.D. thesis, Heinrich-Heine-Universität Düsseldorf, Dusseldorf, Germany, 1991.
93. S. Ahmaniemi, P. Vuoristo, T. Mäntylä, *Surf. Coat. Technol.* **2002**, *151–152*, 412.
94. P. Kurze, W. Drysmann, W. Knöfler, *Stomatologie Der DDR* **1986**, *36*, 549.
95. W. Knöfler, P. Kurze, *Zahn-, Mund-, Und Kieferheilkunde Mit Zentralblatt* **1986**, *74*, 706.
96. D. Diesing, A. W. Hassel, M. M. Lohrengel, *Thin Solid Films* **1999**, *26*, 282.
97. H. Nakai, O. Harasaki, J. Shinohara, *Mater. Chem. Phys.* **1998**, *1–3*, 131.
98. K. Shimizu, G. M. Brown, K. Kobayashi et al., *Corros. Sci.* **1999**, *41*, 1835.
99. J. W. Schultze, B. Danzfuss, O. Meyer et al., *Mat. Sci. Eng.* **1985**, *69*, 273.
100. S. M. Duvanov, A. G. Balogh, *Nucl. Instrum. Meth. Phys. Res. B* **2000**, *171*, 475.
101. A. L. Stepanov, V. A. Zhikharev, D. E. Hole et al., *Nucl. Instrum. Meth. Phys. Res. B* **2000**, *166–167*, 26.
102. Z. He, P. Jung, *Nucl. Instrum. Meth. Phys. Res. B* **2000**, *166–167*, 165.
103. T. Yano, K. Ichikawa, M. Akiyoshi et al., *J. Nucl. Mater.* **2000**, *283–287*, 947.
104. T. Kikuchi, S. Z. Chu, S. Jonishi et al., *Electrochim. Acta* **2001**, *47*, 225.
105. M. García-Méndez, N. Valles-Villarreal, G. A. Hirata-Flores et al., *Appl. Surf. Sci.* **1999**, *151*, 139.
106. G. S. Frankel, R. L. McCreery, *Interface*, Winter, **2002**, 34.
107. A. Michaelis, M. Schweinsberg, *Thin Solid Films* **1998**, *313–314*, 756.
108. M. M. Lohrengel, J. W. Schultze, *Electrochim. Acta* **1976**, *21*, 957.
109. H. J. Lewerenz, J. Stumper, C. Pettenkofer et al., *Electrochim. Acta* **1989**, *34*, 1729.
110. G. Mende, J. Finster, D. Flamm et al., *Surf. Sci.* **1983**, *128*, 169.
111. Z. H. Lu, B. Bryskiewicz, J. McCaffrey et al., *J. Vac. Sci. Technol B* **1993**, *11*, 2033.
112. M. J. Graham, *Corros. Sci.* **1995**, *37*, 1377.
113. A. Pakes, P. Skeldon, G. E. Thompson et al., *Corros. Sci.* **2002**, *44*, 2161.
114. T. Djenizian, G. I. Sproule, S. Moisa et al., *Electrochim. Acta* **2002**, *47*, 2733.
115. D. L. Lile, D. A. Collins, *Appl. Phys. Lett.* **1976**, *28*, 554.
116. N. Simon, I. Gerard, C. Mathieu et al., *Electrochim. Acta* **2002**, *47*, 2625.
117. A. Hamamatsu, C. Kaneshiro, H. Fujikura et al., *J. Electroanal. Chem.* **1999**, *473*, 223.
118. K. Kluger, Dissertation Universität Düsseldorf, Düsseldorf, Germany, (1993).
119. C.-O. A. Olsson, D. Landolt, *Electrochim. Acta*; in press.
120. H. H. Uhlig, *Z. Elektrochem.* **1958**, *62*, 700.
121. K. Sieradzki, R. C. Newman, *J. Electrochem. Soc.* **1986**, *133*, 1979.
122. S. Quian, R. C. Newman, R. A. Cottis et al., *J. Electrochem. Soc.* **1990**, *137*, 435.
123. C. Calinski, H.-H. Strehblow, *J. Electrochem. Soc.* **1989**, *136*, 1328.
124. R. Kirchheim, B. Hein, S. Hofmann et al., *Corros. Sci.* **1990**, *31*, 573.
125. T. Kamimura, M. Stratmann, *Corros. Sci.* **2001**, *43*, 429.
126. L. J. Oblonsky, M. P. Ryan, H. S. Isaacs, *J. Electrochem. Soc.* **1998**, *145*, 1922.

127. S. Virtanen, P. Schmuki, H. S. Isaacs, *Electrochim. Acta* **2002**, *47*, 3117.
128. K. Ogle, S. Weber, *J. Electrochem. Soc.* **2000**, *147*, 1770.
129. D. Hamm, K. Ogle, C.-O. A. Olsson et al., *Corros. Sci.* **2002**, *44*, 1443.
130. M. Bojinov, I. Betova, G. Fabricius et al., *Corros. Sci.* **1999**, *41*, 1557.
131. C. Queitsch, J. Engelmann, H. Worch, *Korrosion Dresden* **1989**, *20*, 257.
132. S. Frangini, N. B. de Christofaro, A. Mignone et al., *Corros. Sci.* **1997**, *39*, 1431.
133. E. McCafferty, *Corros. Sci.* **2000**, *42*, 1993.
134. E. McCafferty, *Corros. Sci.* **2002**, *44*, 1393.
135. P. Marcus, *Electrochim. Acta* **1998**, *43*, 109.
136. S. Haupt, H.-H. Strehblow, *Corros. Sci.* **1995**, *37*, 43.
137. A. W. Hassel, D. Diesing.
138. A. Y. Chatalov, *Dokl. Akad. Naouk S.S.S.R.* **1952**, *86*, 775.
139. K. J. Vetter, F. Gorn, *Electrochim. Acta* **1973**, *18*, 321.
140. P. Marcus, B. Baroux, M. Keddam, (Eds.), *Modification of Passive Films*, European Federation of Corrosion Publication # 12, The Institute of Materials, London, UK, 1994.
141. J. W. Schultze, *Mater. Chem. Phys.* **1989**, *22*, 417.
142. M. Goledzinowski, S. Haupt, J. W. Schultze, *Electrochim. Acta* **1984**, *29*, 493.
143. H.-H. Strehblow, C. J. Doherty, *J. Electrochem. Soc.* **1978**, *125*, 30.
144. H.-H. Strehblow, C. M. Melliar-Smith, W. M. Augustyniak, *J. Electrochem. Soc.* **1976**, *125*, 916.
145. D. H. Bradhurst, J. S. L. Leach, *J. Electrochem. Soc.* **1966**, *113*, 1245.
146. C. J. Kaiser, *Capacitor Handbook*, C. J. Publishing, 1995.
147. J. Drucker, K. Hansma, *Phys. Rev. B* **1986**, *30*, 4348.
148. G. Mende, F. Fenske, H. Flietner et al., *Electrochim. Acta* **1994**, *39*, 1259.
149. S. Ikonopisov. *Electrochim. Acta* **1977**, *22*, 1077.
150. S. Ikonopisov, A. Girginov, M. Machkova, *Electrochim. Acta* **1979**, *24*, 451.
151. V. K. Agarwal, *Thin Solid Films* **1974**, *24*, 55.
152. P. Solomon, *J. Vac. Sci. Technol.* **1977**, *14*, 1122.
153. N. Klein in *Advances in Electronics and Electron Physics* (Ed.: L. Marton), Academic Press, New York, 1969, Vol. 26.
154. T. H. DiStefano, M. Schatzkes, *J. Vac. Sci. Technol.* **1976**, *13*, 50.
155. V. Parkhutik, J. M. Albella, J. M. Martinez Duart in *Modern Aspects of Electrochemistry* (Ed.: B. E. Conway), Plenum Press, New York, 1992, p. 315, Vol. 23.
156. J. J. O'Dwyer, *The Theory of Electrical Conduction and Breakdown in Solid Dielectrics*, Clarendon Press, Oxford, 1973.
157. A. W. Hassel, D. Diesing, *Thin Solid Films* **2002**, *414*, 296.
158. F. W. Schmidlin, *J. Appl. Phys.* **1966**, *37*, 2823.
159. R. Oltra, M. Indrianjafy, R. Roberge, *J. Electrochem. Soc.* **1993**, *140*, 343.
160. J. W. Schultze, S. Kudelka, B. Davepon et al., *Electrochemical Society Proceedings* 97-26, The Electrochem. Society, Pennington, NJ, 1997, pp. 725–739.
161. A. W. Hassel, M. M. Lohrengel, *Electrochim. Acta* **1995**, *40*, 433.
162. M. Jeske, K. G. Jung, J. W. Schultze et al., *Surf. Interf. Analysis* **1994**, *22*, 363.
163. J. W. Schultze, A. Bressel, *Electrochim. Acta* **2001**, *47*, 3.
164. H. Sugimura, N. Kitamura, H. Masuhara, *Jpn. J. Appl. Phys.* **1992**, *31*, L1506.
165. H. Sugimura, T. Uchida, N. Kitamura et al., *Appl. Phys. Lett.* **1996**, *69*, 1288.
166. S. Trasatti, (Ed.), *Electrodes of Conductive Metallic Oxides*, Elsevier, New York, 1981, Vol. A, B.
167. O. Voigt, B. Davepon, G. Staikov et al., *Electrochim. Acta* **1999**, *44*, 3731.

4.1
Crevice Corrosion

Robert G. Kelly
University of Virginia, Charlottesville, Virginia

4.1.1
Definition of Crevice Corrosion

4.1.1.1 Characteristics

Crevice corrosion occurs when a wetted metallic surface is in close proximity to another surface as shown schematically in Fig. 1. Typically, the average separation (called the gap, g) between the two surfaces is between 0.1 and 100 μm. For some material/environment combinations, this geometric arrangement can lead to accelerated attack of the metal surface as shown in Fig. 2. There are numerous practical cases of geometries that lead to crevice corrosion; in almost any engineered structure there are many instances in which two or more materials are, by design, in close proximity. From overlapping fuselage skins on aircraft to flanges on pipes to multiple layers in integrated circuit interconnects, crevices are ubiquitous. If electrolytes can be rigorously excluded from these regions, crevice corrosion is not possible, as one of the requirements for corrosion has been removed. Unfortunately, achieving and maintaining such complete exclusion of electrolytes is often impossible, so an appreciation of crevice corrosion becomes important.

A generic geometry for crevice corrosion can be seen in Fig. 1 in cross section. The *substrate* is the metallic material of interest. It is separated from the *crevice former* by a gap, g, which, for an ideal crevice, is constant over the length of the crevice, l. The *fully exposed surface* is that area of the substrate outside the crevice former, which is fully immersed in the electrolyte. Its properties can strongly influence the rate of crevice corrosion [2, 3].

4.1.1.2 Relation to Other Forms of Localized Corrosion

Crevice corrosion shares many characteristics and phenomenology with other forms of localized corrosion such as pitting (Chapter 4.2), intergranular attack (Chapter 4.3), environment-assisted cracking (Chapter 4.4), and dealloying (Chapter 2.3). In all of these cases, the electrochemical and chemical conditions within an occluded region become altered with respect to the conditions on fully exposed surfaces. These variations can lead to rates of attack within the occluded region that are many orders of magnitude higher than those observed on the fully exposed surfaces. Generally, a material/environment combination that leads to pitting can also lead to crevice corrosion. Because of the

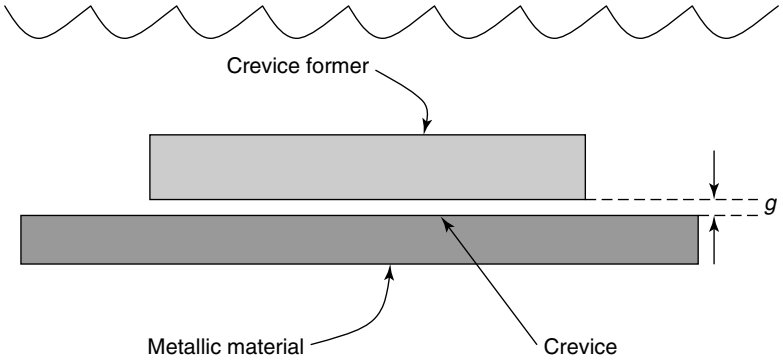


Fig. 1 Crevice corrosion occurs when a wetted metallic surface is in close proximity to another surface as shown schematically here.

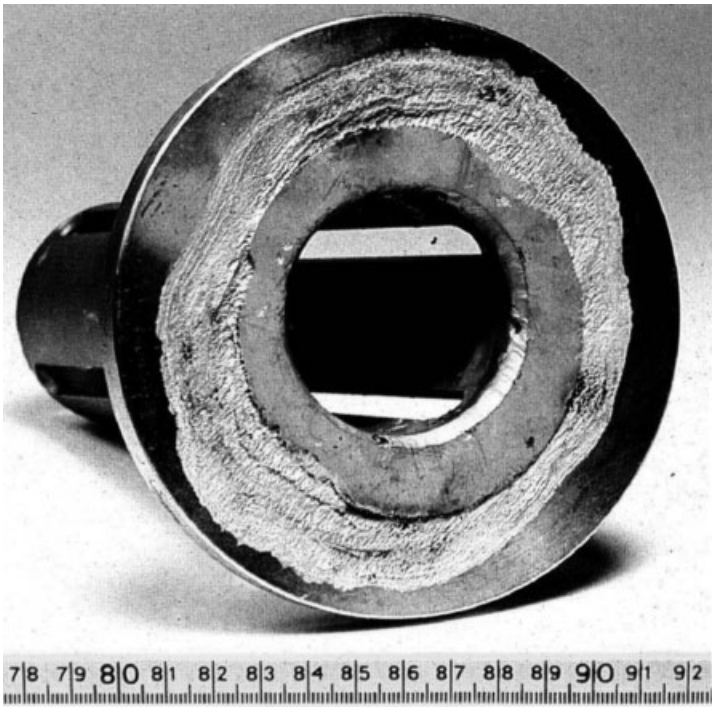


Fig. 2 Crevice corrosion under seal in Type SS316 sieve from steam condenser cooling water system exposed to flowing seawater for 2 years at less than 40 °C [1].

many commonalities among the various types of localized corrosion, understanding crevice corrosion allows insights to be gained into the factors that influence the other forms of localized corrosion.

4.1.1.3 Examples

Several examples of the results of crevice corrosion are shown in Figs. 3 to 6. The similarities in topography amongst the examples include the accelerated attack of the substrate under the crevice former and the virtual absence of attack on the fully exposed surface. The accelerated attack within the crevice usually appears as uniform corrosion or pitting. In some cases, it is thought that the attack starts as metastable pits that coalesce into a more uniform attack.

The remainder of this chapter will describe the mechanisms that control such behavior, approaches to mitigating it, as well as some illustrative examples in which it is of critical importance to safe operation of engineered structures.

4.1.2 Fundamental Phenomena of Crevice Corrosion

Crevice corrosion relies primarily on three fundamental types of processes: electrochemical reactions, homogeneous chemical reactions, and mass transport. The electrochemical reactions include both dissolution and reduction reactions. The spatial variation of the rates of these reactions determines the development of the attack topography. The important types of homogeneous chemical reactions include hydrolysis, precipitation reactions, and homogeneous oxidation/reduction reactions of dissolved species. These reactions can have substantial effects on the corrosivity of the occluded environment, in particular with regard to the local pH. Mass transport by diffusion and convection tend to minimize differences between the occluded region conditions and those on the fully exposed surface. However, the tight geometry inherent in crevices leads to severe restriction of mass transport, allowing large differences in concentration and electrochemical potential to develop and be maintained between the fully exposed surface and the occluded crevice region.

4.1.2.1 Electrochemical Reactions

As with all corrosion, crevice corrosion involves concomitant anodic and cathodic reactions. The location and intensity of these reactions determines the development of the morphology both inside and outside the crevice that characterize crevice corrosion. In general, crevice corrosion occurs with a large-scale (0.1–10 mm) separation of the anodic and cathodic reactions. The scale of the separation of anodic and

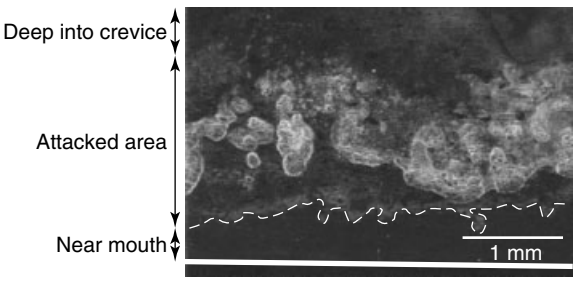


Fig. 3 Crevice corrosion of Type 304 SS after polarization at +0.05 V (SCE) in 0.017 M NaCl. The mouth of the crevice is indicated by the solid white line.

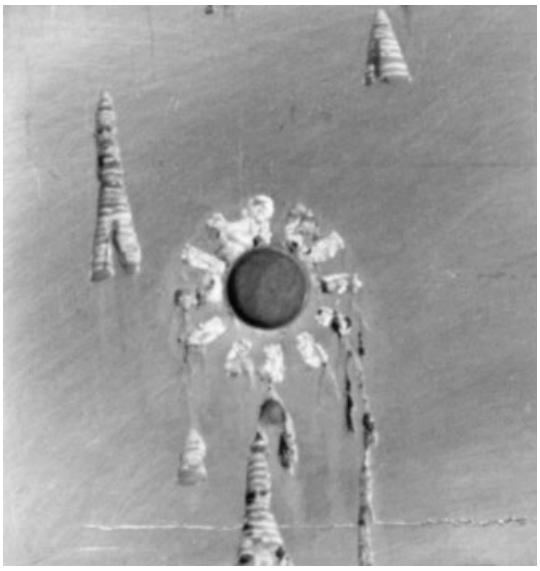


Fig. 4 Example of the results of crevice corrosion. Type 304 SS exposed to 6 wt.% ferric chloride for 48 h at room temperature with castellated crevice washer applied around center hole. Pitting also occurred at several sites outside the crevice. The draining of the occluded solution from the crevice sites (and pits) led to the river pattern of attack outside the initial localized corrosion sites.

cathodic reactions for crevice corrosion contrasts with that of uniform corrosion in which the separation of the anodic and cathodic reactions is thought to be submicron, with the locations of the reactions varying with time producing a uniform dissolution of surface.

In crevice corrosion, a net cathodic reaction occurs on surfaces outside the crevice, whereas a net anodic reaction occurs on the surfaces inside the crevice. The metal provides the electron path and the electrolyte within the occluded region and in the bulk provides the ionic path to complete the circuit. The types of electrochemical reactions are no different from those that occur in other forms of corrosion.

4.1.2.1.1 **Dissolution Reactions** The spatial distribution of the metal dissolution within an occluded region defines crevice corrosion. The metal dissolution reactions are those described in Chapter 1.3. The intensity of these reactions varies, but propagation rates for active crevice corrosion are often on the order of 0.1 to 50 mA cm^{-2}, or approximately 40 to 20 000 mpy. As crevice corrosion occurs primarily on materials selected for their corrosion resistance, such penetration rates are unanticipated. The fact that the attack is hidden makes it difficult to detect, increasing the danger associated with it.

In general, one finds that the material outside the occluded region is virtually unattacked. Most often, the fully exposed material dissolves under passive conditions, with penetration rates of less than 1 μA cm^{-2} (ca. 0.5 mpy). In some cases, evidence of cathodic protection of the fully exposed surface can be observed (e.g. formation of calcareous deposits). Just inside the occluded region, there is also usually minimal attack. The amount of attack increases as one moves deeper into the crevice, with a maximum in the attack depth often occurring between 0.1 and 3 mm from the mouth. At points further into the crevice, the amount of attack is

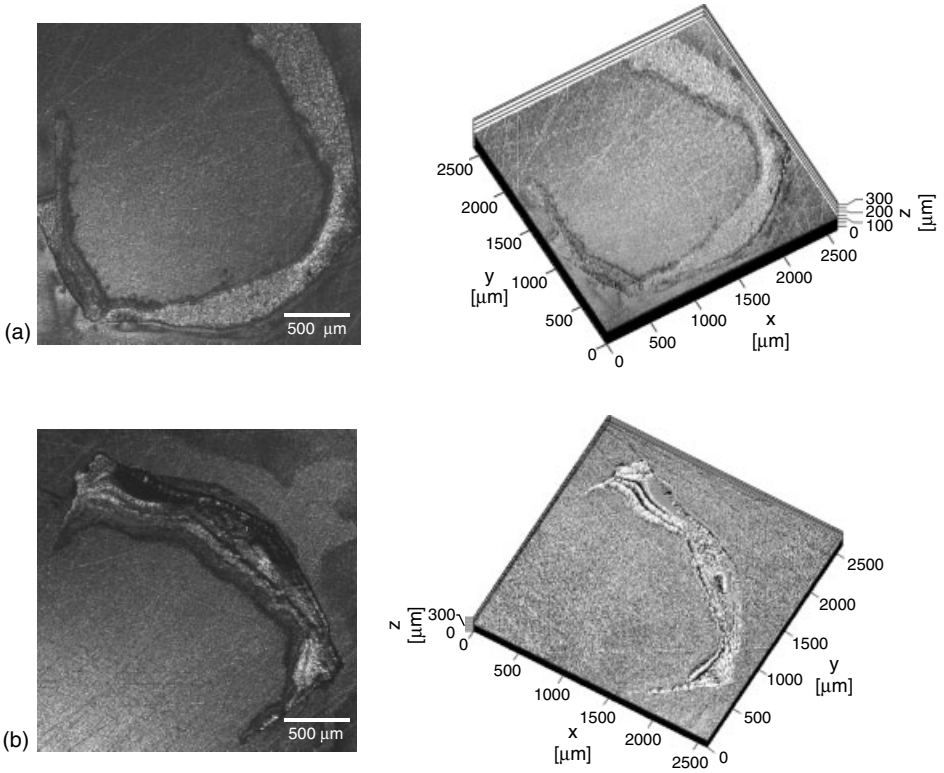


Fig. 5 Confocal laser scanning micrographs of air aged (a) 625 and (b) C22 after cyclic potentiodynamic polarization (CPP) testing at 95 °C in pH 7.75 (100 : 1) electrolyte. Both two-dimensional reflected light intensity images and three-dimensional representations are shown. The accumulated anodic charge for each alloy was approximately 2.5 C [4].

minimal. This *intermediate attack* is a characteristic of crevice corrosion, although exceptions can be observed in which the extent of attack increases with increasing depth. Examples of crevice corrosion attack are shown in Figs. 3 to 6.

One of the most important characteristics defining the susceptibility of a material to crevice corrosion is the dependence of its dissolution behavior (e.g. passive current density, active–passive transition) on pH and aggressive ion concentration. Materials that depassivate more easily (i.e. at a higher pH or lower chloride concentration) are more susceptible to crevice corrosion. Conversely, alloying elements, surface engineering, or thermomechanical treatments that inhibit the dissolution rate of a material in aggressive solutions lead to better resistance to crevice corrosion. Finally, passivity of the material in the bulk solution is a requirement for crevice corrosion, as with pitting.

4.1.2.1.2 **Cathodic Reactions** For materials at their open circuit potential (OCP), the overall rate of the cathodic reaction(s) must balance the anodic dissolution reactions. In crevice corrosion, the cathodic reactions occur predominantly outside the

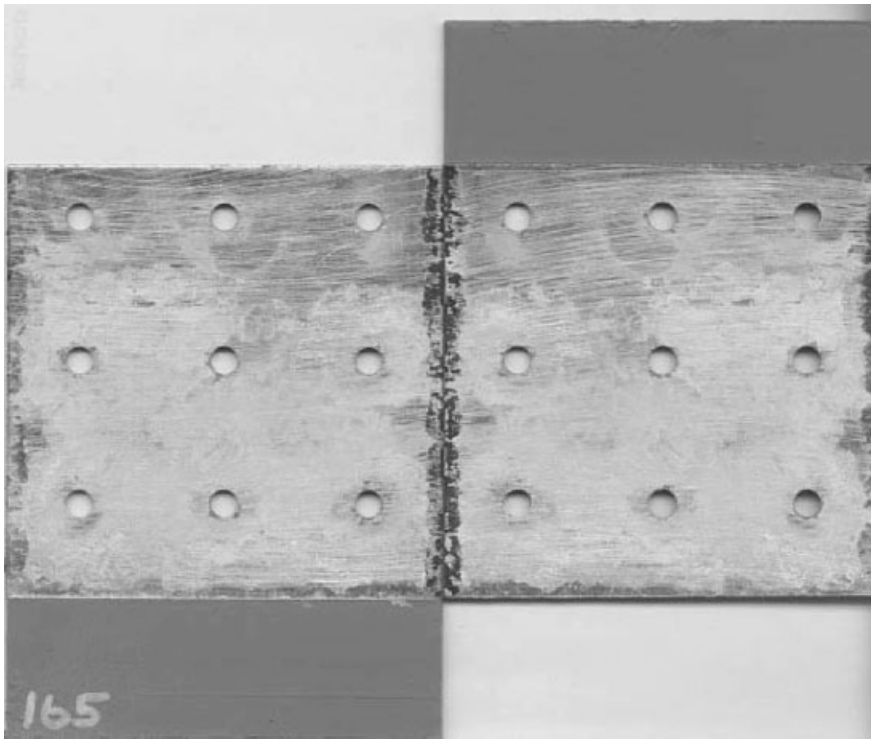


Fig. 6 Crevice corrosion of AA2024-T3 faying surfaces after 3-month exposure to simulated lap joint solution. Exterior surfaces were painted [5].

crevice. A cathodic reaction can serve several functions in the initiation and stabilization of crevice corrosion:

1. Raise the potential above some critical potential (e.g. to generate metastable pits within the crevice).
2. Maintain the crevice actively corroding by consuming the electrons generated from the dissolution reactions inside the crevice.
3. Protect the fully exposed surface from other forms of localized corrosion such as pitting, which would tend to destabilize the crevice by acting as drains for cathodic reactions.

In most cases of corrosion in aqueous solution, the oxygen reduction reaction is the primary reaction outside the crevice. More on the oxygen reduction reaction can be found elsewhere in the Encyclopedia (Chapter 1.3). For the present discussion, its importance lies in its high reversible potential, its sluggish kinetics, and its production of hydroxide ions. The high reversible potential provides the possibility of very large polarizations of passive metals and alloys; materials can obtain high OCP in oxygen-bearing solutions. These high potentials increase the likelihood that the interface exceeds some critical potential for localized corrosion (Chapter 4.2). In the case of crevice corrosion, this critical potential may be due to the formation of metastable pits within the crevice that produce a critical crevice solution (CCS) (see Sect. 4.1.2.5.1).

Once initiated, the active crevice can be maintained if and only if the external cathodic reaction can consume the electrons generated by the dissolution rate within the occluded region at a rate that allows the maintenance of the CCS. If the cathodic reaction kinetics is too sluggish, the mass transport of aggressive solution from within the crevice will exceed the ability of the dissolution reactions within the crevice to maintain it, and the crevice would repassivate. Somewhat sluggish cathodic kinetics prevent the rapid penetration of structures by crevice corrosion that is characteristic of pitting, in which transient rates on the order of 10 to 100 A cm^{-2} are observed (Chapter 4.2). Stable crevice corrosion rates tend to be several orders of magnitude slower than initial pitting rates (although crevice corrosion can occur under more mild conditions of chloride concentration, temperature, and potential). Finally, the production of hydroxide ions on the fully exposed surface tends to increase the surface pH, decreasing its susceptibility to other forms of localized corrosion (such as pitting). This phenomenon allows virtually all of the cathodic reaction on the fully exposed surface to be used to consume electrons freed by dissolution reactions within the crevice (except for the small passive current of the external surface).

4.1.2.1.3 **Separation of Anodic and Cathodic Reactions** In the absence of a physical separation of anodic and cathodic reactions, classical crevice corrosion does not occur. The separation of anodic and cathodic reactions allows the formation and maintenance of a pH differential cell and a potential gradient between the fully exposed surface and the material in the occluded region. Figure 7 shows a schematic of a crevice with varying degrees of separation of anodic and cathodic reactions. Case 1 represents an early stage of crevice corrosion in which there is no discernible difference between inside and outside the occluded regions. The electrons generated by the dissolution reaction are consumed by cathodic reactions locally. Case 2 represents the propagation stage of crevice corrosion in which the separation of anode and cathode has occurred. This separation can occur because of the depletion of a cathodic reactant (e.g. dissolved oxygen) within the occluded region. Under such a circumstance, the interior of the occluded region becomes a net anode, whereas the fully exposed surface becomes a net cathode.

Note that some reduction reaction can occur within the occluded region and some dissolution occurs on the fully exposed surface. It has been estimated that as much as 15–20% of the electrons can be consumed by cathodic reactions within occluded regions on some materials [6–8]. On the fully exposed surface, passive dissolution continues to occur. The electrons liberated during the passive dissolution are consumed by cathodic reactions locally. The majority of the cathodic reaction is used to consume electrons generated by dissolution in the occluded region once crevice corrosion has initiated.

4.1.2.1.4 **Area Effects** As could be surmised from mixed potential theory (Chapter 1.3), the amount of fully exposed surface that can interact with the material in the occluded region will have a strong effect on crevice corrosion rates. Because of the strong coupling between these two regions on the metal surface, increasing the area of the cathodic reaction (the fully exposed surface) relative to the area of the anodic reaction (the occluded region) will

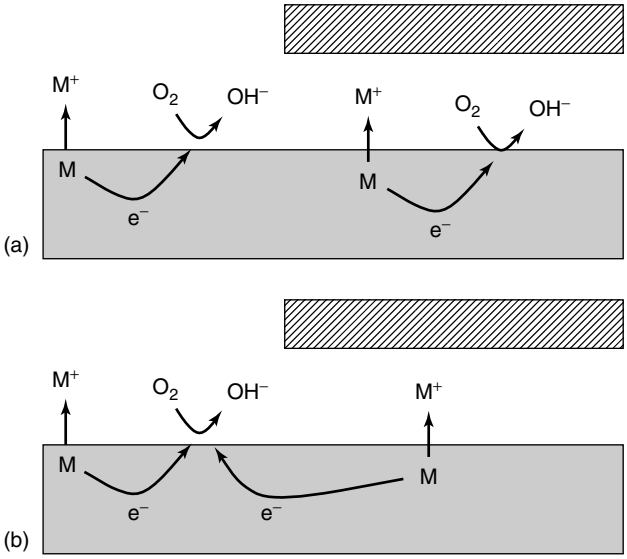


Fig. 7 Schematic of a crevice showing extremes of separation of anodic and cathodic reactions. (a) Case 1: electrons generated by the dissolution reaction are consumed by cathodic reaction locally both inside and outside the crevice. (b) Case 2: complete separation of anode and cathode. Interior of the occluded region becomes a net anode, whereas the fully exposed surface becomes a net cathode.

increase the dissolution rate of the crevice, just as in galvanic corrosion (Chapter 1.3). This effect is shown in Fig. 8.

In general, the area of crevice attack is the more fixed quantity, whereas the area of fully exposed surface that participates can become very large, such as in an internal tank surface on which a crevice forms due to sludge deposition on the bottom of the tank. As discussed

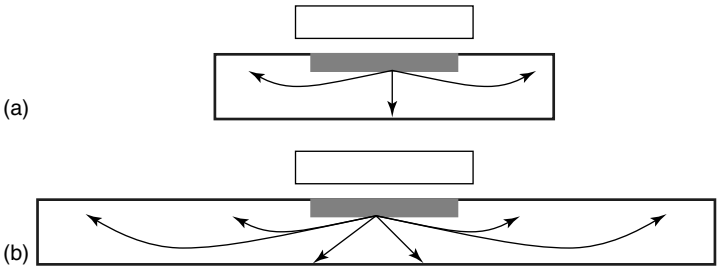


Fig. 8 Effect of the area of the cathodic reaction (the fully exposed surface) relative to the area of the anodic reaction (the occluded region). An increase in the dissolution rate of the crevice will occur (just as in galvanic corrosion) owing to need to satisfy the summation of the anodic reaction rates equaling the sum of the cathodic reaction rates.

in Sect. 4.2, next to alloying, the most successful inhibition strategies for crevice corrosion involve reducing the rate of the cathodic reaction outside the crevice.

4.1.2.2 **Homogeneous Chemical Reactions** Chemical reactions that occur within the crevice are extremely important to the initiation and stabilization of crevice corrosion, as well as in the determination of its penetration rate. The three major types of chemical reactions that influence the chemical environment within an occluded region are hydrolysis, precipitation, and chemical dissolution.

4.1.2.2.1 **Hydrolysis** The chemical reactions of metal cations with water (hydrolysis) produce oxides and hydroxides that can change the local pH by overwhelming any buffering capacity of the solution. Metal hydroxides have equilibrium pH values that are generally far from neutral pH. Equilibrium pH values for metal hydrolysis reactions are shown in Table 1 for the primary metal ions emanating from stainless steels [9].

Measurements of pH inside active occluded regions have been in general agreement with the values shown in Table 1 [10–12]. Even more acidic values have been measured in some cases [13, 14]. This effect is thought to be due to the increase in the activity coefficient for hydrogen ion as a result of high chloride concentrations [15]:

$$\mathrm{pH} = -\log(\gamma_{H^+}[H^+]) \qquad (1)$$

This increase in the acidity of the crevice environment generally increases the dissolution rate of the alloy. During the early stages of crevice corrosion development, the falling pH leads to depassivation of the material in the crevice via dissolution of the passive oxide. This increase in dissolution rate leads to the production of more metal cations, leading to more hydrolysis, and subsequently to a further drop in pH. As discussed below, this drop in pH is accompanied by an increase in the concentration of anions from the bulk environment. In chloride-containing solutions, this further stabilizes the active crevice by making reformation of the passive oxide more difficult. The autocatalytic nature of crevice corrosion (i.e. dissolution leading to a decrease in pH, leading to increased dissolution, etc.) does not continue without end; the chemical conditions inside the crevice region eventually reach a steady state determined in large part by the chemical equilibria of the occluded solution.

Note that the values of pH in Table 1 were determined for the equilibrium of metal salts dissolved in water. They can be expected to occur within occluded regions as long as *all* of the cathodic reaction occurs outside the occluded region. To the extent that the cathodic reaction occurs within the occluded region, the pH will move towards

Tab. 1 Equilibria of some hydrolysis reactions [9]

Reaction	*Equilibrium pH of reaction*
$Fe^{2+} + H_2O \longrightarrow FeOH^+ + H^+$	$pH = 4.75 - \frac{1}{2}\frac{1}{2}\log[Fe^{2+}]$
$Ni^{2+} + 2H_2O \longrightarrow Ni(OH)_2 + 2H^+$	$pH = 6.09 - \frac{1}{2}\frac{1}{2}\log[Ni^{2+}]$
$Cr^{3+} + 3H_2O \longrightarrow Cr(OH)_3 + 3H^+$	$pH = 1.6 - \frac{1}{3}\log[Cr^{3+}]$

the equilibrium pH of the alloy. The equilibrium pH of an alloy is the pH that would be expected to be obtained when, for example, an alloy dissolves under open circuit conditions in a small volume of solution. Such alloy equilibrium pH values are generally higher than those of the metal salts because the production of metal ions by oxidation must be accompanied by cathodic reactions, which in aqueous solutions, tend to produce hydroxyl ions. For example, the equilibrium pH of Type 304 SS is 10.6 [16]. The low pH values observed in crevice corrosion of many materials are due to the fact that in practice the majority of the cathodic reaction occurs *outside the crevice*. For crevices polarized in laboratory experiments, the vast majority of the cathodic current is supported at the counter electrode.

Other homogeneous reactions that may occur within occluded regions include redox reactions and other chemical reactions. For example, it has been proposed [17] that nitrate acts as an inhibitor within occluded regions such as pits or crevices via the reduction of nitrate to ammonium:

$$NO_3^- + 4H^+ + 3e^- \longrightarrow NH_4^+ \quad (2)$$

This reaction would tend to limit the pH of the local solution and thereby slow dissolution. Conversely, thiosulfate has been proposed to disproportionate to sulfur and sulfite within the crevice, leading to accelerated dissolution in the crevice.

4.1.2.2.2 **Precipitation** Precipitation of corrosion products occurs when the solubility of the least soluble species is reached. These precipitates tend to occur within the crevice between the area of lowest pH within the occluded region and the bulk electrolyte. In some cases, these precipitates will additionally isolate the occluded solution.

4.1.2.2.3 **Chemical Dissolution of Alloy Constituents** Certain alloy constituents can be dissolved chemically and thereby make important changes in the local environment either directly (e.g. by adsorption of the product species) or indirectly (e.g. by catalyzing electrochemical reactions or via hydrolysis effects). One primary example of this phenomenon is the dissolution of MnS inclusions in austenitic stainless steels, which produces sulfur species such as bisulfide (HS^-), which accelerates the dissolution of the material in acidic solutions [18].

Many theories have proposed changes in the occluded chemistry and are key owing to effects of the dissolution products of the MnS inclusions. Because most dissolved sulfur species have been observed to enhance metal dissolution, many sulfur species have been predicted to result from MnS inclusion dissolution in the occluded region [19–27]. Virtually all of the oxidation states of sulfur have been implicated, from a valence of -2 (HS^-) to $+6$ (SO_4^{2-}).

Recently, Brossia and Kelly [28] studied the influence of alloy sulfur on the crevice solution chemistry and nature of the surface in the crevice at initiation. Through the use of occluded solution analysis, high-resolution transmission electron microscopy/energy dispersive spectroscopy (TEM/EDS), small-spot X-ray photoelectron spectroscopy (XPS), and electrochemical measurements, the dominance of the aqueous sulfide species on the occluded solution chemistry evolution the initiation of crevice corrosion was shown. MnS inclusions were shown to dissolve chemically to form sulfide. No other sulfur species

were produced as shown in Fig. 9. Thus, results from the use of a MnS powder electrode to simulate these inclusions need to be interpreted carefully, in that the powder electrode, in addition to having MnS present, also had Mn_2O_3 and more importantly S^0, which are not present in the inclusions in the alloys. The elemental sulfur was shown to catalyze the formation of thiosulfate upon polarization of the MnS powder, a process that does not occur for inclusions in the alloy.

The production of aqueous sulfide via the chemical dissolution of MnS inclusions was shown to increase the aggressiveness of the low pH, high $[Cl^-]$ occluded solution as shown in Fig. 10 such that crevice corrosion can occur at rates on the order of 30 to 50 mA cm^{-2}. As the alloy sulfur content decreases, the difficulty in obtaining the aqueous sulfide content increases, lengthening the initiation time. Nonetheless, even at the lowest alloy sulfur contents studied (17 ppmw), crevice corrosion initiation due to aqueous sulfide accumulation still occurred.

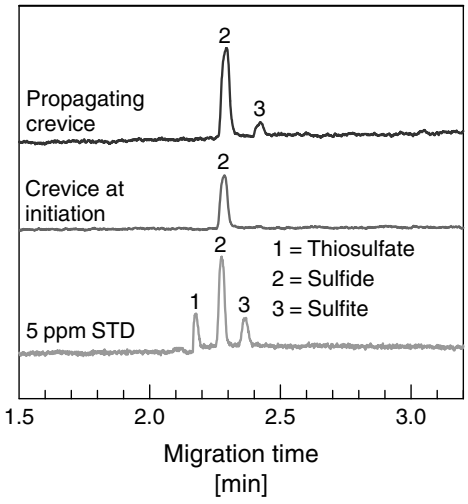


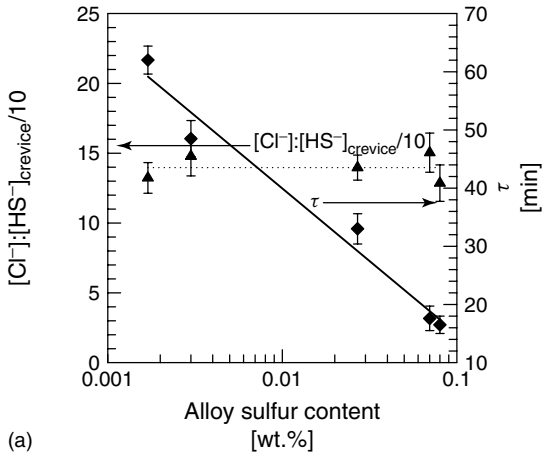
Fig. 9 Occluded solution analyses showing dissolved sulfur species in (a) solution taken from a crevice during steady state propagation; (b) solution taken from a crevice at initiation; and (c) a 5 ppm standard solution ($1 = S_2O_3^{2-}$, $2 = HS^-$, $3 = SO_3^{2-}$). At initiation, the only dissolved sulfur species observed was sulfide. In no crevice was thiosulfate observed. Note the vertical scales for each electropherogram are different so that they could all be shown on the same plot.

4.1.2.3 Mass Transport of Species

Taken together, the processes described above tend to lead to a concentrated, acidic solution of metal salts within the crevice. Metallic materials tend to dissolve rapidly upon polarization in these solutions. Thus, maintenance of the occluded solution composition is critical to stability of crevice corrosion. As mentioned above, diffusion acts to destabilize crevices by dispersing the concentrated solution, whereas migration effects tend to concentrate aggressive anionic species into the crevice.

This section describes the balance of these opposing mass transport forces for the geometry of crevice corrosion. Mass transport of species in aqueous solution can occur by three processes: migration, diffusion, or convection. In most cases of crevice corrosion, convection can be ignored owing to the restricted geometry involved.

4.1.2.3.1 **Migration** Migration is the movement of ions in the presence of an electric field. The electric field can be externally applied (such as via a



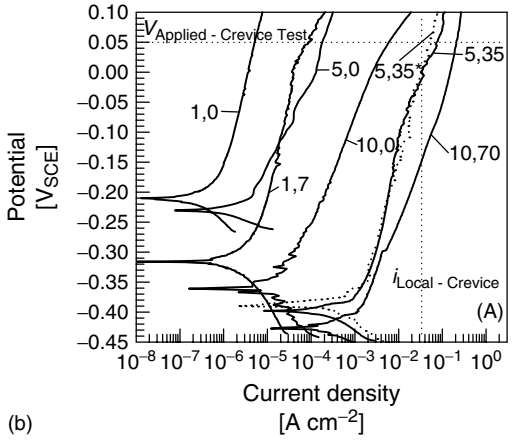


Fig. 10 (a) Influence of alloy sulfur content on the initiation time, τ, and the crevice solution at τ as characterized by the $[Cl^-]:[HS^-]$ (R). Note that although the crevice solution composition is independent of the alloy sulfur level ($R = 141 \pm 11$), the time to develop the critical chemistry needed to initiation attack is strongly dependent upon the sulfur levels. (b) Polarization behavior of Type 304 SS in deaerated pH 2.75 solution of differing $[Cl^-]$ (M): $[H_2S]$ (mM). Note that the addition of thiosulfate (5,35*) did not substantially influence the polarization behavior [28].

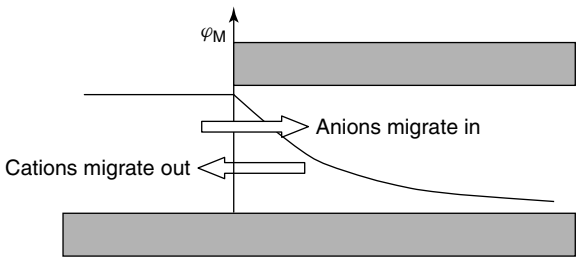


Fig. 11 The potential gradient that develops in crevice corrosion is such that cations are driven out of the crevice whereas anions are driven into the crevice.

potentiostat) or occur naturally such as the development of distinct anodes and cathodes during localized corrosion. Mobility differences among ions have important effects on the establishment of aggressive conditions within a crevice. The potential gradient that develops in crevice corrosion is such that cations are driven out of the crevice whereas anions are driven into the crevice as shown in Fig. 11. The extent of accumulation or depletion of ions within the crevice depends on their relative ionic mobility.

Chloride has a very high mobility relative to most other commonly encountered ions (Table 2). As it is also often present at a high concentration relative to other ions, chloride often carries the majority of the current in crevice corrosion. As shown in Fig. 12, it is by this mechanism that chloride accumulates in the crevice

Tab. 2 Equivalent conductance for several common ions at infinite dilution and 25 °C. Equivalent conductance is defined as $\lambda_i^o = |z_i|F^2 u_i$ where u_i is the mobility and $|z_i|$ is the charge [29]

Ion	*Equivalent conductance (mho cm^2 equiv^{-1})*
Cl^-	76.34
HSO_4^-	50
HCO_3^-	41.5
Cu^{2+}	54

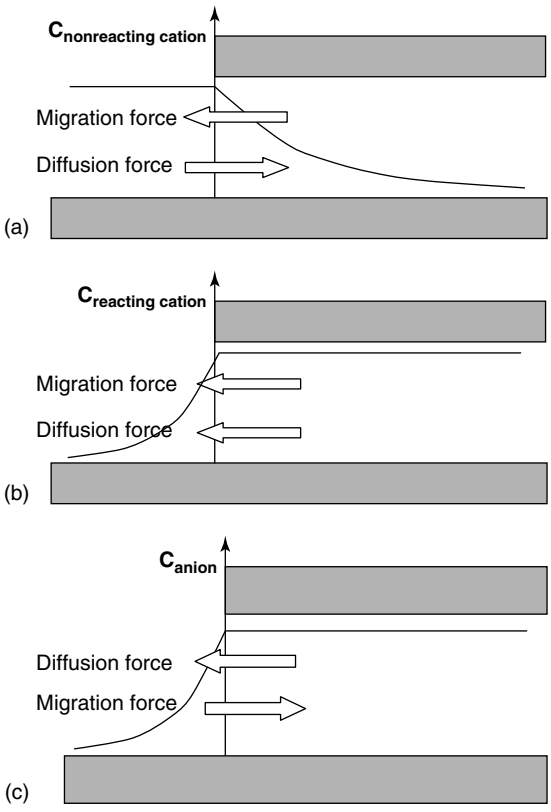


Fig. 12 (a) In the case of nonreacting cations (i.e. those not produced or consumed in the crevice, such as Na^+), the migration and the diffusion effects act in opposite directions. (b) In the case of reacting cations (e.g. cations from metal dissolution), both the migration and the diffusion effects act to lower the concentration within the occluded region. (c) In the case of anions, the migration and the diffusion effects act in opposite directions.

as corrosion occurs. Simultaneously, the nonreacting cations in solution are driven out of the crevice. For the counterions to the chloride and other anions (such as Na^+ in NaCl solutions), these effects lead to a severe depletion of their concentration within the crevice. This depletion occurs because there is no source for these ions within the crevice. The dissolution products of the alloy (which tend to be metallic cations) are also driven out of the crevice by the potential field. In contrast to the electrolyte counterions, the dissolution of the metal within the crevice acts as a source for cations. To the extent that metal dissolution can meet the mass transport forces driving cations out, the metal cation concentration within the crevice will remain constant or increase.

4.1.2.3.2 **Diffusion** Diffusion is the movement of species in the presence of a chemical potential gradient. The process tends to eliminate concentration gradients. As mentioned above, the dissolution of metal within occluded regions combined with the restricted mass transport inherent in crevices leads to a concentrated metal salt solution within the crevice. As most bulk solutions have low concentrations of metal ions, there exists a very strong driving force for diffusion in the form of a concentration gradient on the order of several mol L^{-1} mm^{-1}. Such gradients exist for not only the primary metal ion (e.g. Fe^{2+} for stainless steels), but also for the primary anion species (e.g. chloride in seawater). As mentioned above, the chloride ion concentration within the occluded region is increased as a result of migration effects that are initially stronger than the diffusive effects. In the case of the metal ions, both the migration and the diffusion effects act to lower the concentration within the occluded region. At steady state, the production rate of metal ions by dissolution is equal to the combined migration and diffusion removing metal ions from the crevice. Of course, there is no source of anions such as chloride within the occluded region, so that at steady state, the removal of chloride ions by diffusion is equally balanced by its ingress due to migration as shown in Fig. 12.

4.1.2.3.3 **Convection** As mentioned above, convection is usually not considered important in crevice corrosion because of the restricted geometry. There are some cases in which this assumption is not valid. Alkire [19] has investigated the effects of flow past the mouths of localized corrosion sites (pits). They found that a recirculation motion could develop within a localized corrosion site. Although this flow can mix the occluded solution, there was little mixing between the occluded region solution and the bulk solution. Flow-*through* crevices can inhibit the initiation of crevice corrosion by making the development of the aggressive environment in the occluded region more difficult. There are a variety of ''flow-through'' crevices, including support plates in heat exchangers in nuclear reactors [20].

4.1.2.4 Range of Rates and Limitations by Each Process

The propagation of crevice corrosion, cannot be sustained at rates on the order of A cm^{-2} for long periods of time. Like all corrosion, the anodic reaction, cathodic reaction, or solution properties can control the rate. For example, if the dissolution kinetics in the occluded solution are sluggish, the polarization by the cathodic reaction has a more limited effect. On the other hand, diffusion

limitations (or sluggish kinetics) at the cathode will limit the degree to which it can support high rate anodic reactions in the crevice. Finally, dilute bulk solutions lead to large ohmic drop between the external cathode and the internal anode. The voltage lost in this ohmic drop is not available to drive the interfacial reactions, again limiting the rate. In practice, all of these processes occur.

4.1.2.5 Proposed Mechanisms

4.1.2.5.1 **Critical Crevice Solution** The CCS framework has its origins in the qualitative description of the initiation of stainless steel crevice corrosion proposed by Fontana and Greene [22]. The general description of the evolution of aggressive occluded environments has its basis in the acid-hydrolysis theory of Hoar [23]. It has served the corrosion community for several decades. It has provided the foundation for the education of generations of students in localized corrosion. Its extension to cracks, coating disbondment, and other occluded regions has allowed many important insights to be gained. In essence, it uses the concept of an occluded cell to describe the process by which extremely concentrated and aggressive solutions can develop inside occluded regions.

After deoxygenation of the solution within the crevice [deoxygenation is a rapid process due to the low equilibrium concentration of dissolved oxygen gas (0.25 mM at room temperature in pure water) and the restricted mass transport. Reduction of dissolved oxygen gas effectively deoxygenates the crevice on the time scale of minutes to less than an hour], the material inside the crevice becomes the net anode, and the boldly exposed material outside the crevice becomes the net cathode. The accelerated oxidation and subsequent hydrolysis of the metal cations leads to acidification of the crevice, with strongly hydrolyzed cations such as chromium leading to occluded cell pH values of zero or even less [9–14]. The presence of such a solution can depassivate even corrosion-resistant materials, leading to accelerated attack inside the crevice. The initiation and propagation of crevice corrosion is determined by the ability of the metal inside the crevice to produce sufficient cations (and their subsequent hydrolysis) to create and maintain an aggressive occluded solution against the destabilizing force of diffusion.

Success of the CCS model has been demonstrated by a large number of experimental measurements of low crevice pH values in a variety of alloys [9–14], including a rationalization of the effects of alloying elements in stainless steels by Oldfield and Sutton via the effect of these alloying elements on the pH needed to achieve a critical current density for passivation of 10 $\mu A\ cm^{-2}$ [39].

4.1.2.5.2 **Ohmic Drop** The IR^* framework proposed by Pickering [26] focuses attention on the role of ohmic drop in occluded regions in providing the stabilizing force for crevice corrosion to occur in materials that are spontaneously active, but exhibit an active–passive transition. Polarization of the material outside the crevice to its passive region leads to accelerated corrosion within the crevice. This seeming paradox can be understood by analysis of the potential drop that occurs in solution and the effect of the restricted geometry of the crevice.

As shown in Fig. 13, although the potential of the fully exposed surface will be at the applied potential (assuming minimal IR drop between the reference electrode and the fully exposed surface), and thus

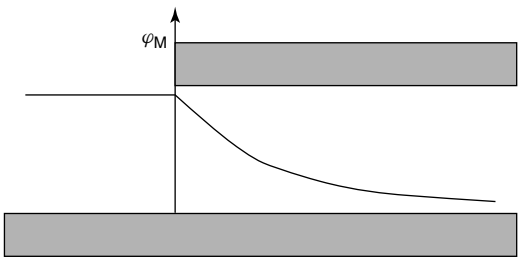


Fig. 13 Although the potential of the fully exposed surface will be at the applied potential (assuming minimal *IR* drop between the reference electrode and the fully exposed surface), and thus passive, the current that passes down the crevice will lead to potential drop because of the finite resistivity of the solution and restricted geometry of the crevice.

passive, the current that passes down the crevice will lead to potential drop because of the finite resistivity of the solution and restricted geometry of the crevice. If the combination of crevice length, gap, and solution resistivity is sufficient to lead to a potential drop of at least IR^* (using the terminology of Pickering [31]), then there will be a location in the crevice (x_{crit}) at which the potential falls into the active region of the polarization curve. At this site, rapid dissolution of the metal will occur.

Ignored by most implementations of the CCS framework, ohmic drop can not only lead to passive-to-active transitions, but also can, in the context of environmental cracking, make hydrogen evolution, and therefore embrittlement, more viable at the crack tip. The IR^* framework has been successfully demonstrated in several model metal/environment systems [34, 35], and has been invoked to rationalize the practically important case of the crevice corrosion of Alloy 625 in chlorinated seawater [32, 33].

The success of the IR^* framework includes its ability to predict the presence of the intermediate attack often observed in crevice corrosion; that is, the most severe attack takes place not at the deepest portion of the crevice, but at some point between it and the crevice mouth. Although it is successful in such predictions, it inherently assumes the existence of an active-passive transition in the electrochemical behavior of the material in the crevice environment. Although some crevice corrosion systems do show such behavior, there are many that do not. However, extensive studies of such behavior are lacking, in large part due to uncertainties in the composition of such environments.

4.1.2.5.3 **Combining Effects** The Evans diagram in Fig. 14 shows schematically the electrochemistry of active crevice corrosion under open circuit conditions. The fully exposed surface provides the vast majority of the cathodic current. Its relatively large surface area is a key in this regard. The occluded region, although made of the same material, exhibits substantially different electrochemical kinetics due to the aggressive solution at its interface. Two cases are shown; in the first, the material corrodes actively, whereas in the second the material undergoes an active–passive transition. The first represents the expected behavior according to the CCS theory, whereas the second case describes the stabilization of crevice corrosion described by the IR^* theory.

One of the limitations in much of the computational modeling of crevice corrosion has been the absence of approaches that consider both migration and diffusion processes within the occluded region. Modeling using CCS theory relies strictly

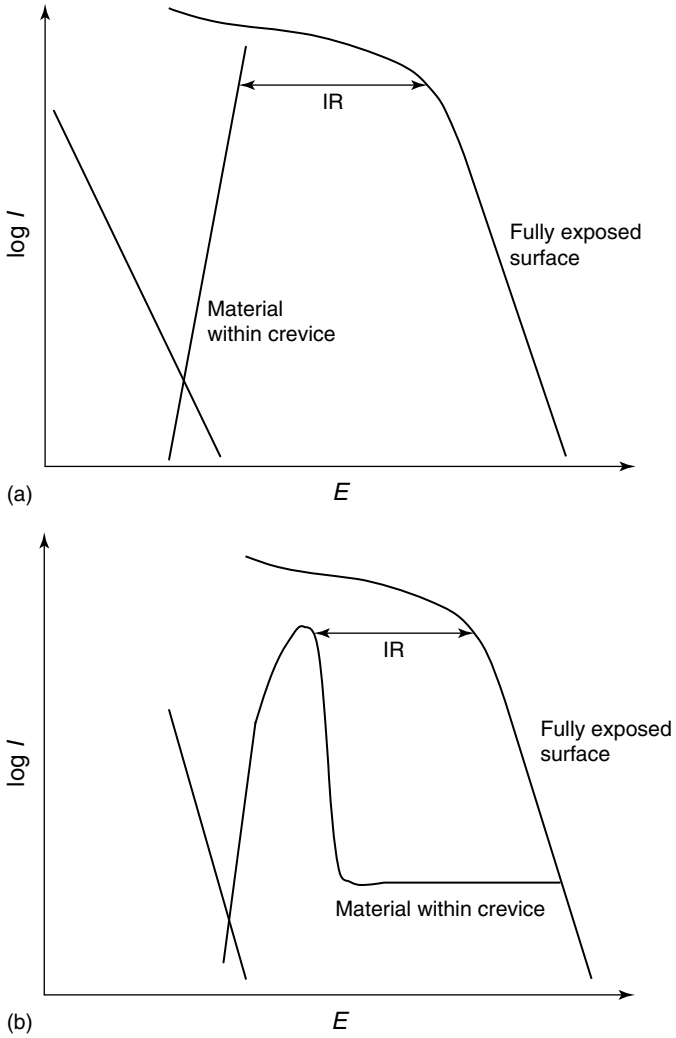


Fig. 14 Electrochemistry of propagating crevice corrosion. Two cases are shown: (a) the material in the crevice corrodes actively and (b) the material in the crevice undergoes an active–passive transition.

on diffusion, whereas IR^* modeling considers only ohmic drop effects.

Recently, Kelly and Stewart [30] and Stewart [16] have developed a computational framework that allows such considerations. The initial application of the framework was to understand the existence of intermediate attack in crevice corrosion for austenitic stainless steels in chloride solutions, as shown previously in Fig. 3.

The sample shown in Fig. 3 was held several hundred millivolts below its pitting potential [28]. After an incubation period, crevice corrosion initiated. The area immediately inside the crevice was

unattacked (as was that portion of the sample that was boldly exposed outside the crevice). Deeper into the crevice the attack became increasingly severe for approximately a millimeter before decreasing in severity with further depth. This intermediate attack (IA) is often observed in crevice corrosion of many alloys. Any complete description of crevice corrosion must therefore be able to rationalize such behavior.

Pickering and coworkers [31, 34, 35] have demonstrated both experimentally and computationally that for systems that meet the criteria of the IR^* theory, IA is predicted. The amount of potential drop increases as one moves into the crevice because of the current leaving the crevice. If the geometry, solution conductivity, and passive current density of the material in the environment conspire to create sufficient ohmic drop, then the potential of some portion of the material within the crevice falls to the primary passive potential. Under these circumstances, the passive film is not stable and active dissolution occurs. The potential difference between the applied potential and the primary passivation potential is referred to as IR^*. Deeper still into the crevice the ohmic drop leads to decreased dissolution as the overpotential for the anodic reaction decreases. Thus, ohmic drop is responsible for the initiation and stabilization of crevice corrosion according to this model.

Note that the IR^* model applies strictly only to materials that undergo an active–passive transition in the crevice solution, which is maintained at the same composition as the bulk solution. In systems in which the occluded solution has been shown to differ from the bulk, the theory must be modified to quantitatively predict the position of the IA, but as long as the material undergoes an active–passive transition, the basic description remains intact. In many systems, the occluded solution leads to active behavior only or unstable passivation [36, 37]. For these systems, ohmic drop still occurs due to the current emanating from the crevice, but it acts to destabilize, not stabilize crevice corrosion. For example, Type 304 stainless steel is spontaneously passive in the dilute bulk solution, but does not passivate in stimulants of occluded crevice solutions [28].

The CCS theory of crevice corrosion cannot predict IA. The CCS theory bases its predictions on the predominance of occluded chemistry changes in determining crevice corrosion susceptibility. As shown by Watson and Postelwaite [38], the CCS theory predicts that the most severe attack will occur at the deepest part of the crevice, that is, the most occluded portion. At this most occluded point, the chemistry will be the most altered, and thus the attack will be expected to be most severe there.

A paradox thus exists in crevice corrosion. The theory that can explain one of the most commonly observed phenomena (IA) is of restricted applicability, whereas the theory that cannot rationalize IA is thought to occur more widely. Kelly and Stewart sought to resolve this paradox by considering both ohmic drop and chemical changes. A set of boundary conditions was selected for which neither the CCS model nor the IR^* model alone would predict IA. The electrochemical boundary conditions were based upon measurements for stainless steel in solutions simulating occluded conditions.

Details of the work can be found elsewhere [30]. Briefly, the geometry used was that of a one-dimensional crevice (i.e. a slot) with a constant 4-μm gap and a 1-cm

depth (L : g = 2500). The initial solution in the crevice was neutral 0.3 M NaCl. The polarization behavior of the material was allowed to vary with the local pH as has been shown to be the case for stainless steel [28]. This dependence was modeled by use of the electrochemical behavior shown in Fig. 15.

Figure 16 shows the evolution of the pH profile within the crevice. Owing to the lack of buffering, within 2 s of the start of the simulation, the pH has dropped to 6 throughout the crevice. As the simulation continues, the pH continues to fall owing to the Cr^{3+} hydrolysis. The decrease in pH is more marked at positions just in

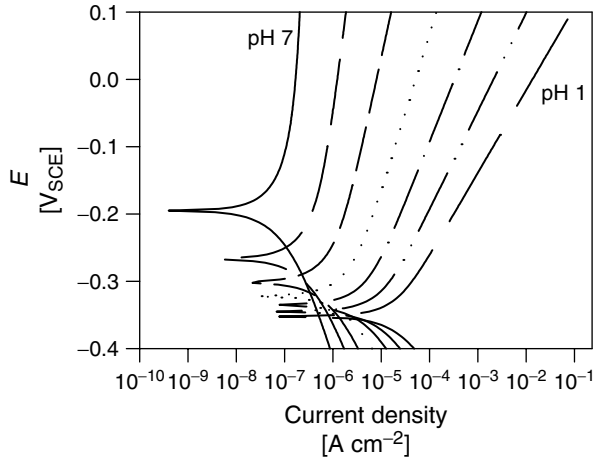


Fig. 15 Assumed polarization behavior for the material within the crevice as a function of pH. The cathodic reactions are assumed to produce charge, but no pH-altering species [30].

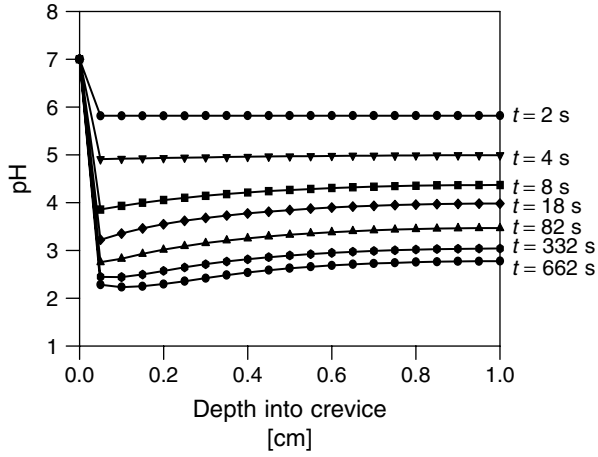


Fig. 16 pH as a function of depth inside the crevice and time. Although the pH falls throughout the crevice, it does so essentially uniformly for the boundary conditions selected [30].

from the mouth. The position of minimum pH continues to move deeper into the crevice with time, but the differences in pH between the mouth, the minimum point and the base of the crevice are small (<0.5 pH units).

Figure 17 shows the evolution of the potential profile within the crevice. Initially, the profile is flat. All points within the crevice are polarized to the value at the mouth. Within a short time, the currents increase due to the pH changes and larger ohmic drop occurs. After 82 s, the potential at the base of the crevice is more than 300 mV below that at the mouth. Over the next 480 s the potential profile flattens somewhat, and the maximum potential difference is slightly more than 250 mV. In addition to this decrease in potential drop, an inflection point can be observed in the profile at a distance of approximately 0.15 cm from the mouth.

Figure 18 shows the evolution of the current density distribution within the crevice. If these curves were integrated with respect to time, then the amount of metal dissolved could be calculated. The peak in the dissolution current density at an intermediate point within the crevice can be clearly observed. This intermediate attack develops very quickly (<8 s). The point of maximum attack moves slowly deeper into the crevice until it stabilizes at 0.07 cm for these boundary conditions.

The *IR** model *requires* that the material of interest exhibit active–passive behavior in the occluded solution. Many engineering materials do not meet this requirement of the model [28, 36, 37]. In such cases, the ohmic drop would act to limit the extent of crevice corrosion according to mixed potential theory by reducing the overpotential for the dissolution reaction. Thus, although the *IR** model can predict IA in some systems, its applicability is somewhat limited. It should be noted that owing to the general lack of information concerning occluded chemistries, the relative proportions of systems exhibiting active–passive versus active behavior has not been determined.

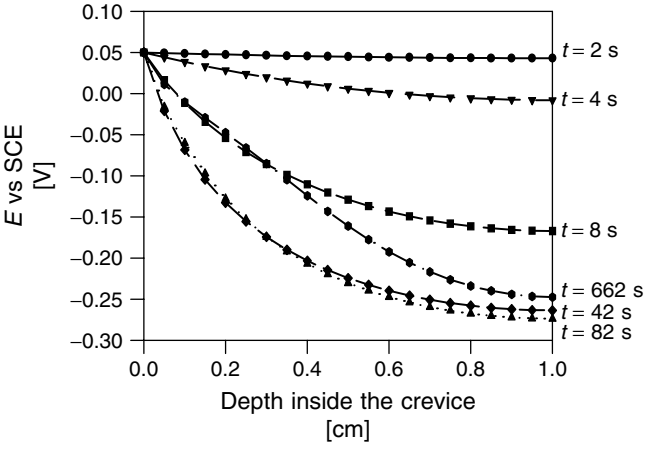


Fig. 17 Potential of the material as a function of depth into the crevice and time. Note the increase in the potential (decrease in the ohmic drop) between 82 and 662 s that results from increased solution conductivity within the crevice [30].

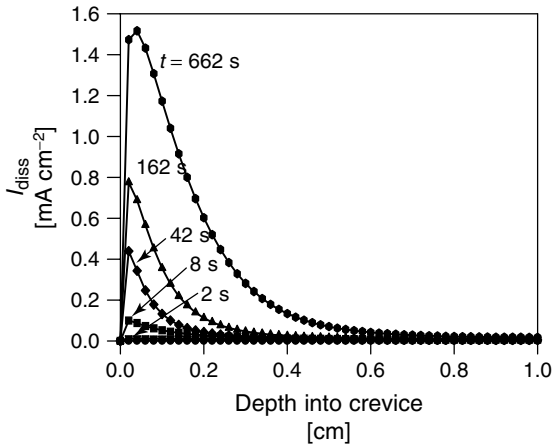


Fig. 18 Anodic dissolution current as a function of depth into crevice and time. Note the development of a peak in the profile indicating the position of maximum attack [30].

In engineering systems, it is likely that CCS and *IR* interact to focus attack at intermediate positions within the crevice. The modeling work shown above demonstrates the close interaction between the two aspects of crevice corrosion. Neither can predict IA alone with the boundary conditions selected. The *IR** model would predict a maximum of attack at the mouth, and the attack would be minimal due to the absence of any change in chemistry. The CCS model would predict maximum attack at the base of the crevice where the solution is most occluded [39, 40]. The approach presented here demonstrates that for reasonable boundary conditions (similar to those measured for Type 304 SS in solutions based on occluded solution analyses) IA can be predicted if and only if both chemical changes and ohmic potential drop are considered. These two phenomena are closely linked. The chemical changes lead to increased currents in some areas that lead to increased potential drop. The increased potential drop mitigates the attack deeper in the crevice. This mitigation of the attack deep in the crevice leads to a slightly less aggressive environment because mass transport out of that portion overwhelms the production of Cr^{3+}. The attack is also mitigated at positions very close to the mouth because of the ability of mass transport to prevent the change in the chemistry. The result of these two opposing forces is IA.

4.1.2.6 Scaling Relations in Crevice Corrosion

A scaling factor (sometimes called a scaling "law") describes the effect of crevice geometry on the corrosion behavior (concentration, potential, and attack gradients) of an occluded region. For corrosion conditions to remain constant as crevice geometry is changed, the potential and chemical distributions must remain constant on a normalized length scale. A scaling law is a factor of two geometric measures of a crevice that must be maintained as the scale of a crevice is altered. The two most common scaling factors are L/G and L^2/G where $L =$ either the length of the crevice or the distance between the crevice mouth and the site of greatest attack (x_{crit}), and $G =$ the crevice gap as shown in Fig. 1. A detailed review of scaling factors can be found in Ref. [41]. One practical application of a quantitative understanding of

crevice corrosion is the use of a scaling factor to determine under what conditions crevice corrosion can occur.

A major barrier to the quantitative understanding of crevice corrosion has been the difficulty in producing crevices experimentally that can be modeled computationally. Pickering and coworkers [42–44] have overcome this barrier at the millimeter scale in their studies of Ni in sulfuric acid.

For crevices in which there are negligible currents generated at the tip, and one or both of the crevice flanks have a constant active current density over the entire surface area, the scaling factor L_c^2/G, where L_c is the crevice length and G is the crevice gap, has been shown to apply by Turnbull [45] and Psaila-Dombrowski [46]. Modeling by Gartland [47] and Watson and Postlethwaite [38] showed that the scaling factor X_p^2/G also held when the crevice wall was passive until the distance into the crevice X_p was reached where active corrosion took over. This finding was important because no longer was the entire crevice length considered, but only the region that remained passive.

In work performed by Xu and Pickering [43], X_p^2/G was also shown to be the correct scaling factor for *IR*-controlled crevice corrosion. However, their work also suggested that if the passive current is negligible when compared to the current in the active region, the scaling factor is reduced to X_p/G. Their experimental results (at gaps of 0.3 mm or greater for Ni in sulfuric acid) were consistent with this scaling factor.

In more recent modeling by DeJong [41, 44], it was shown that the correct scaling factor for active corrosion controlled by the *IR** mechanism was x_{crit}^2/G. The system of interest was nickel in 0.5 M H_2SO_4, a system that exhibits active–passive behavior. As with the work by Xu and Pickering, only initial potential distributions were considered, and no chemistry changes were allowed within the crevice. Six electrochemical boundary conditions described mathematically, were examined by DeJong as to their effect on the position of the active region on the crevice wall. All six of the boundary conditions had the same peak current of 10 mA cm^{-2}. However, the basic shape, potential at which the peak current was reached, E_{crit}, and the passive current density were varied. Using each of the six boundary conditions, one-dimensional models were performed for a crevice length of 0.7 cm with crevice gaps ranging from 10 to 150 μm.

From the resulting potential distributions, the value of x_{crit} was determined on the basis of the value of E_{crit} of the boundary condition used. Both x_{crit}^2/G and x_{crit}/G were plotted. It was concluded that the scaling factor x_{crit}^2/G was the correct one based on the linearity exhibited at gaps $<$100 μm on the quadratic axes, which is the scale on which practical crevices exist, whereas the x_{crit}/G plots exhibited no such linearity. DeJong suggested that the reason for loss of linearity of the x_{crit}^2/G plots at larger gaps was due to the active region nearing the crevice tip, which altered the current produced by the crevice, thereby changing the value of x_{crit}.

Lee and coworkers [49] explored crevice gaps on the size scale of practical crevices ($<$100 μm) both experimentally and computationally. In that work, microfabrication methods were used to produce crevice formers of rigorously controlled dimensions. These formers were then utilized in crevice corrosion experiments on Ni200 in 0.5 M H_2SO_4 in order to study the effect of crevice gap on the position of the critical distance for crevice corrosion (known as x_{crit} or x_{pass}). These results were

then compared to results of computational modeling to better understand the geometric scaling factors that apply to crevice corrosion. Details can be found in Ref. [49].

Crevice corrosion initiated immediately upon application of +0.4 V (SCE), as expected for *IR**-controlled crevice corrosion. An example of the attack observed afterwards is shown in Fig. 19 for a gap of 93 μm. Three regions of attack were observed; passive dissolution was observed from the mouth to some distance inside the crevice (termed x_{crit}), a region of accelerated attack was then observed at intermediate distances, and finally a region of variable attack was observed at the greatest distances from the mouth.

The potential and current distribution results from the computational modeling are shown in Fig. 20. The calculated x_{crit} values (determined by locating the position at which the potential falls into the active region) are also shown. A comparison of the data from the crevice corrosion experiments and those predicted by the model is shown in Fig. 21. Figure 22 plots the same data, but with the ordinate axis is now in terms of x_{crit}^2.

This work also allowed experimental confirmation of the conclusions of DeJong regarding the applicability of quadratic scaling factors for *IR*-controlled crevice corrosion at small gaps (<100 μm for the Ni/H_2SO_4 system studied here). The interpretation of Xu and Pickering of a linear scaling factor for this system is understandable in light of the flatness of the x_{crit} versus G plots, especially at larger gaps.

4.1.3 Prevention

4.1.3.1 By Geometry

The primary means of the prevention of crevice corrosion is via careful design. To the extent possible, passive materials should not be placed in crevice arrangements. Unfortunately, in most engineering structures complete avoidance of crevices is not practical; pipe sections must be connected via flanges, vessels are not made from a single sheet of materials, and so on. In these cases, careful design would dictate maximizing the gap and minimizing the length (depth) of any

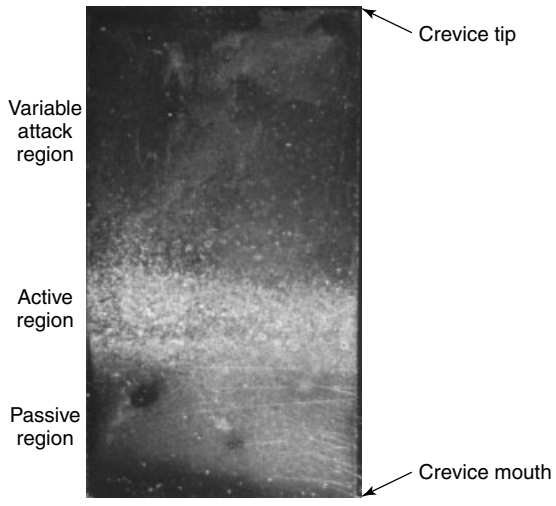
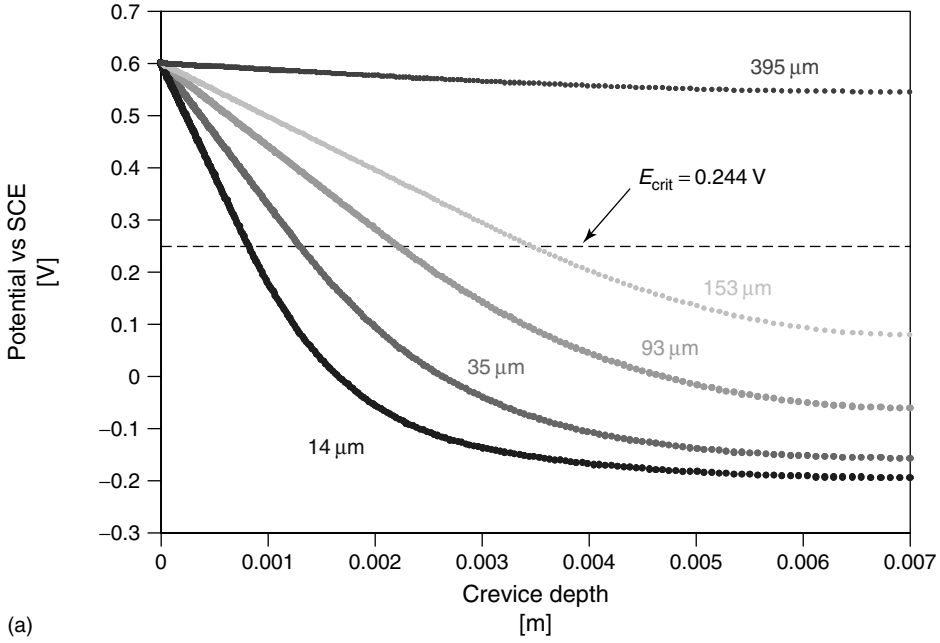
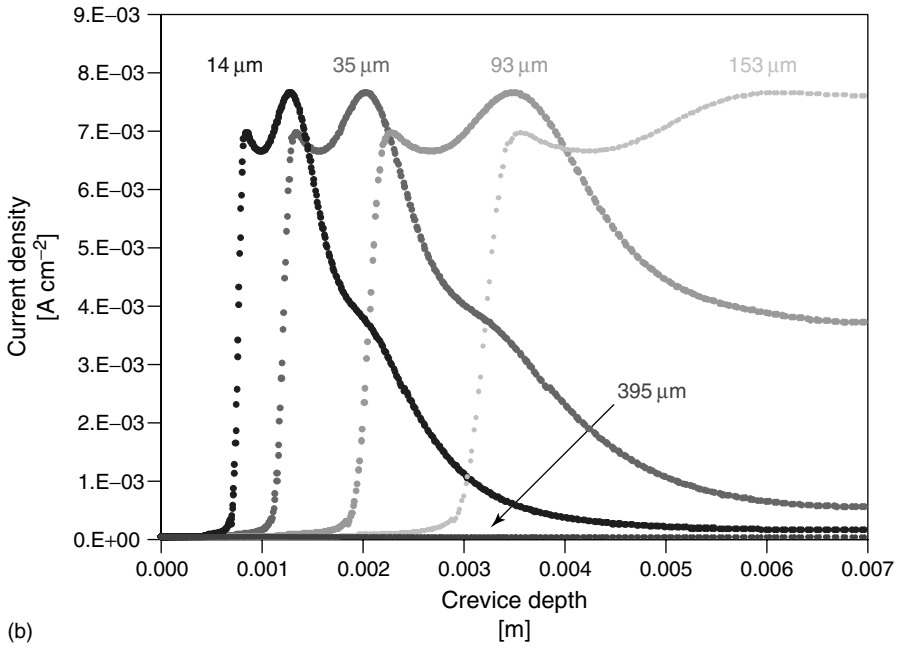


Fig. 19 Photomicrograph of crevice attack of Ni after 1 min with the mouth held at −0.4 V (SCE) in 0.5 M H_2SO_4 showing the three regions of attack observed. Area is 4 mm × 7 mm [49].



(a)



(b)

Fig. 20 (a) Potential distributions from computational work for gaps ranging from 14 to 395 µm. The potential of the metal in the 395-µm gap never reaches E_{crit} and is passivated at the onset. (b) Corresponding current distributions for each gap size; notice that the 395-µm gap exhibits very low current indicating passive corrosion only [49].

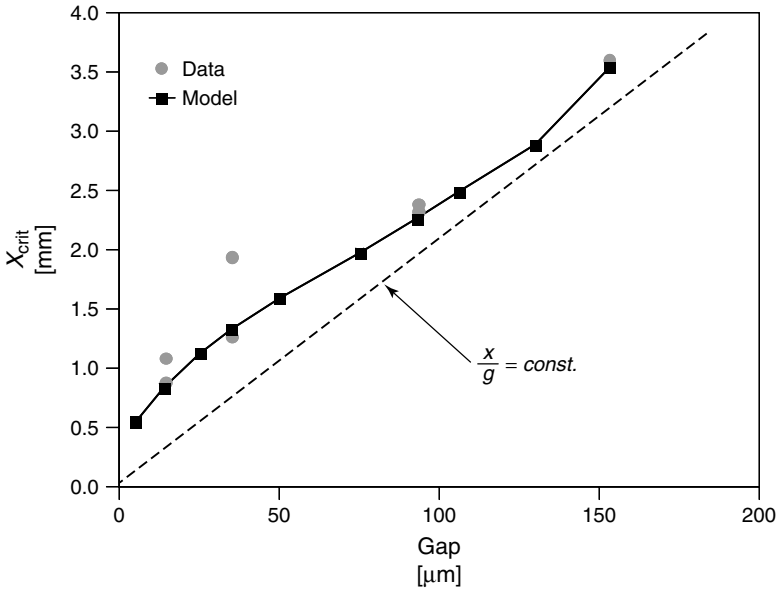


Fig. 21 Comparison of experimental (red circles) and computational (black squares) data of x_{crit} for Ni200 in 0.5 M H_2SO_4 as a function of gap plotted on linear scales for both x_{crit} and gap [49].

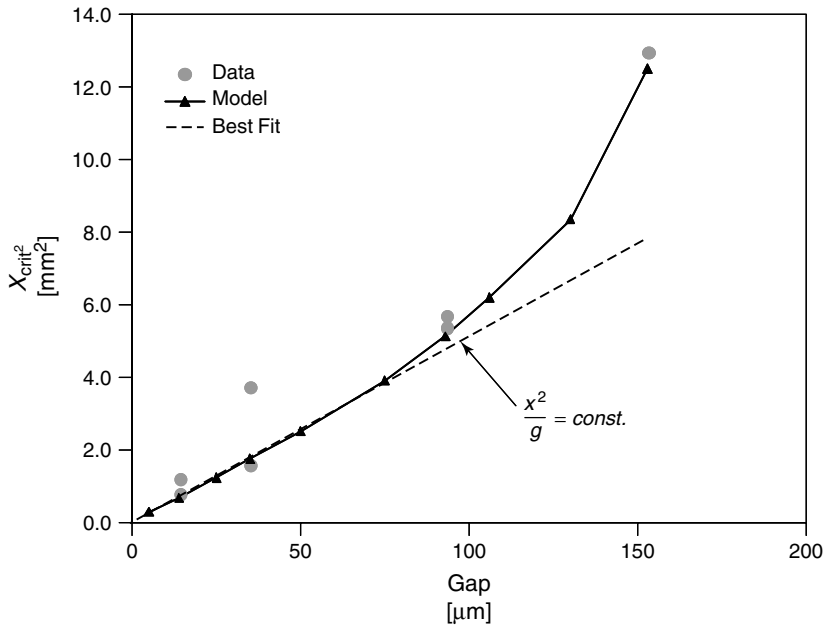


Fig. 22 Comparison of experimental (red circles) and computational (black squares) data of x_{crit} for Ni200 in 0.5 M H_2SO_4 as a function of gap plotted on a quadratic scale for x_{crit} and a linear scale for gap [49].

crevices created. By making the geometry less restricted, the development of an aggressive chemistry is more difficult, and the potential drop within the crevice will also be smaller.

Making a crevice so tight as to preclude electrolyte uptake is usually not practical in the long term. Extremely tight crevices that are *not* watertight exhibit tremendous capillary action, drawing in solution over long distances just as a large tree draws moisture from the soil to the top of its canopy. The extremely restricted geometry is perfect for the development of severe crevice corrosion. Even crevices that are initially ''too tight for water uptake'' will probably loosen with time, leading to electrolyte ingress.

4.1.3.2 By Flow

Alkire and his coworkers [50] have demonstrated the effects of flow on the inhibition of pitting. Similar ideas can be applied to crevice corrosion. In both instances, flow would act to inhibit *initiation* of attack to the extent that the flow lines enter the occluded region. For pit initiation, as described in Chapter 4.2, flow at the surface is very successful at delaying or preventing aggressive solution development. In a crevice, the large length-to-gap ratio makes initiation control much less effective than for pits.

Ironically, once a crevice has initiated, the flow of solution across the fully exposed surface generally acts to increase the propagation rate. This effect results from the effect of increased flow on cathodic reactions on the fully exposed surface that are mass transport controlled, such as oxygen reduction. As the cathodic reaction rate increases, the polarization of the internal, crevice anode increases as well, leading to increased dissolution rates. This effect is mitigated to the extent that the crevice is under ohmic control due to the restricted geometry.

4.1.3.3 By Material Selection

Material selection for crevice corrosion resistance normally follows that used for resistance of pitting resistance (Chapter 4.2). Ratings based on composition have been published for ferrous materials, using the critical crevice temperature (CCT) as the figure of merit. There is a strong correlation between the CCT and the pitting resistance equivalence number (PREN, see Chapter 4.2) for stainless steels as might be expected. In both cases, the more Cr, Mo, and N in the alloy, the higher the resistance. In all cases, the CCT is lower than the critical pitting temperature (CPT).

In general, the lower the passive current density of the material, the smaller its active–passive transition, and the more stable its oxide, the more resistant it is to crevice corrosion. Of particular importance is the dependence of these parameters on the pH and chloride content.

4.1.3.4 By Inhibition

In addition to alloying, solution phase inhibition has been shown to reduce the occurrence of crevice corrosion. Again, similarities to inhibitors for pitting (see also Chapter 4.2) have been observed, as expected. Inhibitors tend to be less effective for crevice corrosion than pitting because of the much longer transport lengths required for the inhibitor to move close to the active region. In order to arrive there in sufficient concentration to be effective, the bulk concentration generally needs to exceed the bulk chloride concentration by a factor of five or more (on a molar basis).

Many nonaggressive anions have been investigated as localized corrosion

inhibitors in Cl^- solutions, including SO_4^{2-}, ClO_4^-, and NO_3^- [51]. Anions that are not electroactive (e.g. SO_4^{2-} and ClO_4^-) have been suggested to function as inhibitors via a supporting electrolyte effect [52–54]. A supporting electrolyte effect occurs when a species, for example, sulfate, competitively migrates and adsorbs on the metal surface with Cl^-, thereby slowing or preventing the increase in the Cl^- concentration in the occluded region. Thus, the relative concentration and mobility of the other anion compared to Cl^- is critically important. The presence of SO_4^{2-} would delay the accumulation of Cl^- in the occluded site, but the same occluded site chemistry would be necessary for initiation to occur. Newman and Ajjawi [55], proposed that some inhibiting anions form a salt film during the early stages of localized corrosion initiation, under which passivation can occur via inward water diffusion. In the case of NO_3^-, an electroactive anion, Newman and coworkers [55, 56] proposed that inhibition occurs via one of three possible mechanisms: (1) electroreduction of NO_3^- to NH_4^+, which consumes H^+ and produces water; (2) electroreduction of NO_3^- to elemental nitrogen, which in turn blocks some proportion of the active kink sites on the surface at which dissolution occurs; or (3) formation of a redox couple between Fe^{2+} and NO_3^- that consumes H^+ at low pH and assists in the formation of an Fe–OH barrier film at high pH.

Brossia and Kelly [26] studied the effect of bulk solution composition on crevice corrosion initiation and the occluded solution composition. As shown in Fig. 23,

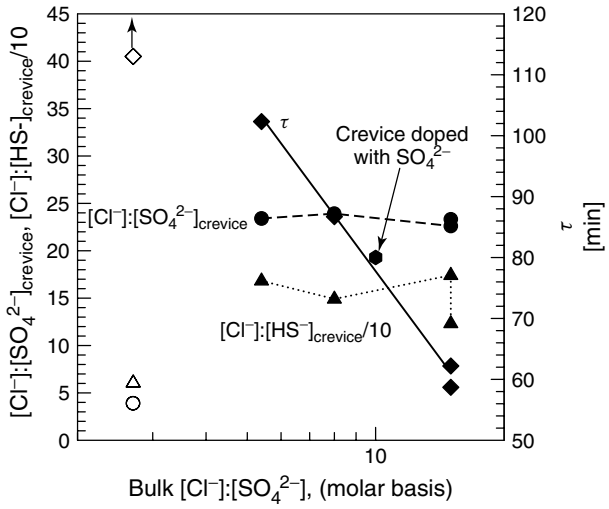


Fig. 23 Effect of bulk $[Cl^-]:[SO_4^{2-}]$ on the initiation time and the crevice solution at τ as characterized by the $[Cl^-]:[SO_4^{2-}]$ and $[Cl^-]:[HS^-]$ (R) in the crevice. In cases in which initiation occurred (filled symbols), the crevice solution was independent ($R = 154 \pm 23$) of the initial bulk $[Cl^-]:[SO_4^{2-}]$, and was within the experimental error of that observed in Cl^- only solutions ($R = 141 \pm 11$). In the solutions containing only 17 mM NaCl, the initiation time was 32 min [26].

the initiation time decreased as the bulk $[Cl^-]:[SO_4^{2-}]$ ratio increased. For samples that suffered crevice corrosion, the crevice solution composition, as characterized by the $[Cl^-]:[SO_4^{2-}]$ ratio in the crevice (23.3 ± 0.5) and $[Cl^-]:[HS^-]$ ratio "R" $= 154 \pm 23$ in the crevice, was independent of the bulk electrolyte composition. The $[Cl^-]:[HS^-]$ ratio was the same, within experimental error, as that observed in the absence of sulfate for those samples that initiated crevice corrosion. At higher bulk sulfate concentrations tested (i.e. 6 mM, which corresponds to a $[Cl^-]:[SO_4^{2-}]$ ratio of 2.8), samples did not initiate crevice corrosion within 180 min. Also shown is the initiation time observed for a test in which the bulk solution was 17 mM NaCl and the initial crevice solution contained 17 mM NaCl + 1.7 mM Na_2SO_4, indicating that changing the initial crevice solution is similar to changing the bulk solution composition.

The results of crevice tests performed in which different amounts of nitrate were added to the bulk solution of 17 mM NaCl are shown in Fig. 24. In all experiments, the $[Cl^-]$ in the bulk was the same while the nitrate concentration was varied to give different ratios of $[Cl^-]:[NO_3^-]$. With increases in the bulk $[Cl^-]:[NO_3^-]$ ratio, the initiation time decreased, with additions to the bulk solution of as little as 1.7 μM NO_3^- resulting in a delay in initiation (46 min in 17 mM NaCl + 1.7 μM $NaNO_3$

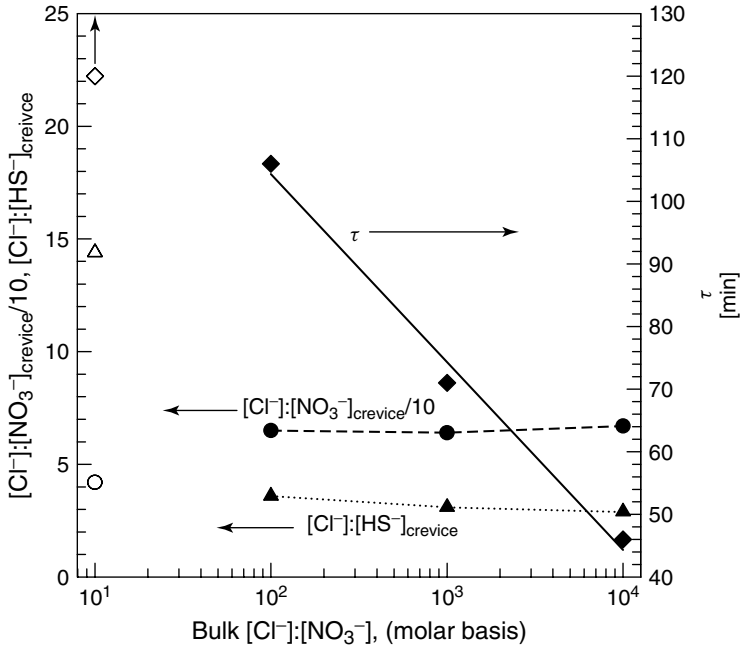


Fig. 24 Effect of bulk $[Cl^-]:[NO_3^-]$ on the initiation time and the crevice solution at τ as characterized by the $[Cl^-]:[NO_3^-]$ and $[Cl^-]:[HS^-]$ (R) in the crevice. In cases in which initiation occurred (filled symbols), the crevice solution was independent ($R = 3.2 \pm 0.4$) of the initial bulk $[Cl^-]:[NO_3^-]$. In solutions containing only 17 mM NaCl, the initiation time was 32 min [26].

compared to 32 min in 17 mM NaCl). For samples that suffered crevice corrosion, the crevice solution, as characterized by the $[Cl^-]:[NO_3^-]$ ratio (65.3 ± 1.5) and the $[Cl^-]:[HS^-]$ ratio "R" $= 3.2 \pm 0.4$, was independent of initial bulk solution composition. The relative concentrations of Cl^-, NO_3^- and HS^- in the crevice were substantially different than the relative concentrations observed in experiments in which the bulk solution contained sulfate rather than nitrate. At higher bulk nitrate concentrations tested (i.e. 1.7 mM, which corresponds to a $[Cl^-]:[NO_3^-]$ ratio of 10), the sample did not initiate crevice attack in 180 min.

The lack of any effect of sulfate on R indicates that the mechanism by which sulfate is inhibiting crevice corrosion is through a supporting electrolyte effect [51–54]. Thus, the increases in initiation time are due to the competitive migration of SO_4^{2-} and Cl^-, with accumulation of the critical concentration of Cl^- needed being delayed. Initially doping the crevice with a 17 mM NaCl + 1.7 mM Na_2SO_4 solution led to an initiation time in line with experiments in which SO_4^{2-} was added to the bulk, indicating that changing the initial crevice chemistry has the same effect as changing the initial bulk solution chemistry.

The addition of nitrate to the bulk solution led to more significant delays in initiation of crevice corrosion (Fig. 7) of 304 SS compared to sulfate. For example, to produce an initiation time of 75 min required 1.5 mM SO_4^{2-}, but only 23 μM NO_3^-. At low bulk $[Cl^-]:[NO_3^-]$ ratios ($[NO_3^-] = 1.7$ mM), no initiation of crevice corrosion was observed within 180 min, whereas in solutions in which crevice corrosion did occur the composition of the crevice solution was essentially independent of the initial concentration of nitrate in the bulk solution. However, the relative concentration of Cl^- compared to NO_3^- in the crevice was nearly three times

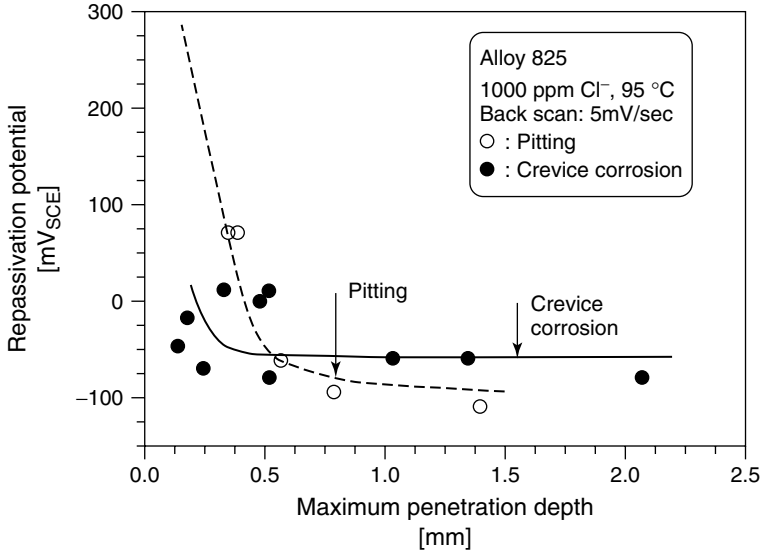


Fig. 25 The repassivation potential as a function of prior crevice corrosion and pit depth showing a bounding value independent of penetration depth [58].

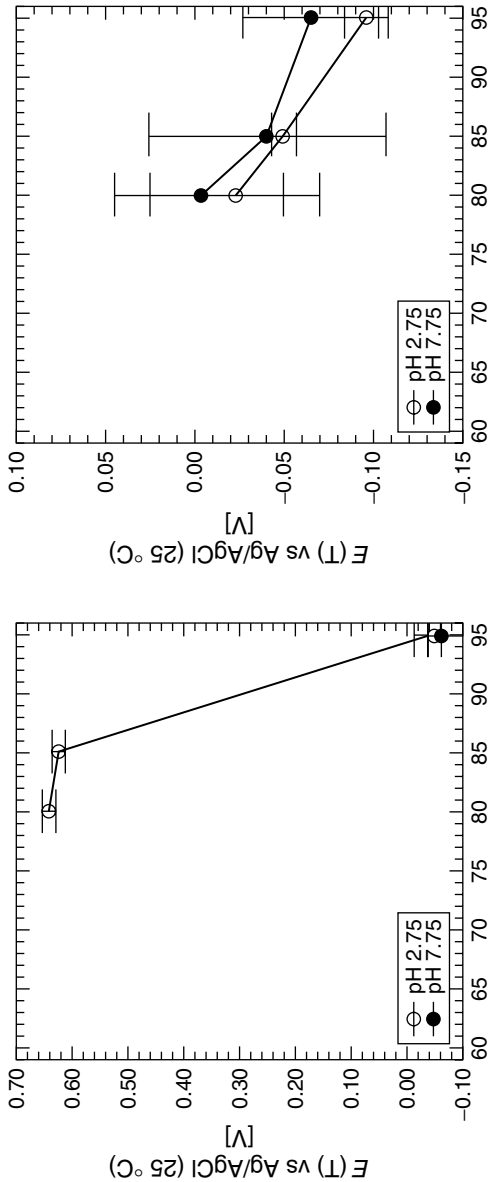


Fig. 26 Effect of temperature and bulk pH on the repassivation potential, ($E_{r,crev}$), for crevice corrosion for Alloy 22 in: (a) 10 : 1 and (b) 100 : 1 electrolytes. All electrolytes contained 5 M LiCl and then, either 0.24 M $NaNO_3$ + 0.26 M Na_2SO_4 (for the 10 : 1), or 0.024 M $NaNO_3$ + 0.026 M Na_2SO_4 (for the 100 : 1) [59].

greater than the relative concentration of Cl^- compared to SO_4^{2-}. One might expect this difference to arise from differences in the mobility of these ions, however their mobilities are quite similar (76.3, 80.0, and 71.4 mho $cm^2/equiv^{-1}$ for Cl^-, SO_4^{2-} and NO_3^-, respectively) [29]. Furthermore, the $[Cl^-]:[HS^-]$ ratios in these experiments (3.2 ± 0.4) were much lower than those observed in experiments conducted in the baseline 17 mM NaCl solutions (141 ± 11). Thus, nitrate must have inhibiting effects in addition to any supporting electrolyte effect.

In the case of crevice corrosion, Ives [57] has shown that cerium treatments of fully exposed surface can inhibit crevice corrosion of stainless steels. This effect is presumably a poisoning of the rate of oxygen reduction (cerium oxides are poor oxygen reduction surfaces), which leads to an inability of the external surface to support the dissolution rate of the occluded region to the extent necessary to produce and maintain an aggressive occluded solution. Insulating coatings (e.g. paints) on the fully exposed surface can also mitigate crevice corrosion in a similar manner by reducing the ability of that surface to consume the electrons generated by the anodic dissolution within the crevice. This decrease in cathode area limits the rates of anodic dissolution possible within the crevice and thereby can limit crevice corrosion. It should be noted that many corrosion-resistant alloys are notoriously difficult to paint owing to poor adherence between the passive film and the organic coating. Loss of adhesion can lead to additional crevice sites.

4.1.3.5 By Potential Control

Potential control can be effective in suppressing the initiation and propagation of crevice corrosion. The electrochemical potential of an interface can be controlled by either an external device (e.g. a power supply) or a sacrificial anode attached to the structure.

Maintaining the potential of the alloy–solution interface at sufficiently low potential has been shown to prevent crevice corrosion stabilization [58]. As shown in Fig. 25, the repassivation potential for crevice corrosion becomes independent of the amount of charge passed. Kehler and coworkers [59] have demonstrated the same for Alloy 625 and Alloy 22, including the deleterious effects of increased temperature and concentration ratio of $[Cl^-]$: [other anions]. Data for Alloy 22 are shown in Fig. 26.

Cathodic protection can be used to combat crevice corrosion [60, 61], in some cases, with sufficiently low potentials preventing it altogether. It should be noted that *anodic protection* is generally not effective in preventing crevice corrosion. In fact, anodic polarization generally *increases* the rate of the crevice attack. The only situation for which anodic polarization would be useful in preventing crevice corrosion is for systems that can be completely described by the ohmic drop model and for which no changes occur in either the occluded solution composition or the electrochemical behavior of the material in the occluded region.

References

1. E. D. D. During, *Corrosion Atlas*, Elsevier, New York, 1988.
2. G. Salamat, G. A. Juhl, R. G. Kelly, *Corrosion* **1995**, *51*, 826–836.
3. J. R. Kearns, M. J. Johnson, J. F. Grubb, *Corrosion/86*, Paper No. 228, NACE International, Houston, Tex., 1986.
4. B. A. Kehler, G. O. Ilevbare, J. R. Scully, Localized corrosion in *Proceedings of Corrosion/2001 Research Topical Symposium* (Eds.:

G. S. Frankel, J. R. Scully), NACE International, Houston, Tex., 2001, pp. 30–64.
5. L. B. Simon, G. Skennerton, J. L. Elster et al., *Aging Aircraft 2000*, NASA, St. Louis, Mo., 2000.
6. T. R. Beck, *Electrochim. Acta* **1984**, *29*, 485.
7. G. S. Frankel, *Corros. Sci.* **1990**, *30*, 1203.
8. B. M. Ikeda, M. G. Bailey, M. J. Quinn et al. in *Application of Accelerated Corrosion Testing to Service Life Prediction of Materials* (Eds.: G. Cragnolino, N. Sridhar), American Society for Testing and Materials, Philadelphia, Pa., 1995, Vol. ASTM STP 1194.
9. A. Turnbull in *Advances in Localized Corrosion* (Eds.: H. Isaacs, U. Bertocci, J. Kruger et al.), NACE International, Houston, Tex., 1990, p. 359.
10. W. Wang, A. Pourbaix, *Cebelcor, RA 12/R17*, **1980**.
11. B. F. Brown, C. T. Fujii, E. P. Dahlberg, *J. Electrochem. Soc.* **1969**, *116*, 218.
12. J. Mankowski, S. Smialowska, *Corros. Sci.* **1975**, *15*, 925.
13. T. Suzuki, M. Yamabe, Y. Kitamura, *Corrosion* **1978**, *29*, 18.
14. J. Mankowski, Z. Szklarska-Smialowska, *Corrs. Sci.* **1975**, *15*, 493.
15. Y. Hisamatsu in *Passivity and Its Breakdown on Iron and Iron-Based Alloys* (Eds.: R. Staehle, H. Okada), NACE International, Houston, Tex., 1976, p. 99.
16. K. C. Stewart, Ph. D. Dissertation, University of Virginia, Charlottesville, Va., 1999.
17. K. Osozawa, N. Okato in *Passivity and Its Breakdown on Iron and Iron-Based Alloys* (Eds.: R. Staehle, H. Okada), NACE International, Houston, Tex., 1976, p. 135.
18. G. Wranglen, *Corros. Sci.* **1974**, *14*, 331.
19. G. S. Eklund, *J. Electrochem. Soc.* **1974**, *121*, 467.
20. S. E. Lott, R. C. Alkire, *J. Electrochem. Soc.* **1989**, *136*, 973.
21. T. Suter, T. Peter, H. Böhni, *Mater. Sci. Forum* **1995**, *192–194*, 25.
22. M. G. Fontana, N. D. Greene, *Corrosion Engineering*, McGraw-Hill, New York, 1967, p. 41.
23. T. P. Hoar, *Faraday Soc. Discuss.* **1947**, *1*, 299.
24. Z. Szklarska-Smialowska in *Sulfide Inclusions in Steel* (Eds.: J. J. deBarbadillo, E. Snape), American Society for Metals, Metals Park, Ohio, 1975, p. 380.
25. C. S. Brossia, R. G. Kelly in *Critical Factors in Localized Corrosion II* (Eds.: P. M. Natishan, R. G. Kelly, G. S. Frankel et al.), The Electrochemical Society, Pennington, N. J., 1996, p. 210.
26. C. S. Brossia, R. G. Kelly, *Corrosion* **1998**, *54*, 145.
27. R. C. Newman, H. S. Isaacs, B. Alman, *Corrosion* **1982**, *38*, 261.
28. C. S. Brossia, R. G. Kelly, *Corros. Sci.* **1982**, *40*, 1851.
29. R. C. Weast, (Ed.), *Handbook of Chemistry and Physics*, 68th ed., CRC Press, Boca Raton, Fla., 1987, p. D–168.
30. R. G. Kelly, K. C. Stewart in *Passivity of Metals and Semiconductors VIII* (Eds.: M. B. Ives, B. R. MacDougall, J. A. Bardwell), The Electrochemical Society, Princeton, N. J., 1999, p. 546–554, Vol. PV 99-42.
31. H. W. Pickering, *Mater. Sci. Eng. A* **1995**, *198*, 213.
32. R. S. Lillard, M. P. Jurinski, J. R. Scully, *Corrosion* **1994**, *50*, 251.
33. B. A. Shaw, P. J. Moran, P. O. Gartland, *Corros. Sci.* **1991**, *32*, 707.
34. H. W. Pickering, K. Cho, E. Nystrom, *Corros. Sci.* **1993**, *35*, 775.
35. Y. Xu, M. Wang, H. W. Pickering, *J. Electrochem. Soc.* **1993**, *140*, 3448.
36. G. Salamat, G. A. Juhl, R. G. Kelly, *Corrosion* **1995**, *51*, 826.
37. T. Hakkarainen in *Corrosion Chemistry Within Pits, Crevices and Cracks* (Ed.: A. Turnbull), Her Majesty's Stationery Office, London, 1984, p. 17.
38. M. Watson, J. Postelwaite, *Corrosion* **1990**, *46*, 522.
39. J. W. Oldfield, W. H. Sutton, *Br. Corros. J.* **1978**, *13*, 104.
40. R. A. H. Edwards in *Advances in Localized Corrosion* (Ed.: H. S. Isaacs), NACE International, Houston, Tex., 1990, p. 381.
41. L. A. DeJong, M. S. Thesis, University of Virginia, Charlottesville, Va., 1999.
42. H. W. Pickering, *Corros. Sci.* **1989**, *29*, 325.
43. Y. Xu, H. W. Pickering, *J. Electrochem. Soc.* **1993**, *140*, 658.
44. M. Wang, H. W. Pickering, Y. Xu, *J. Electrochem. Soc.* **1995**, *142*, 2986.
45. A. Turnbull, J. G. N. Thomas, *J. Electrochem. Soc.* **1982**, *129*, 1412.
46. M. J. Psaila-Dombrowski, Ph.D. Dissertation, Massachusetts Institute of Technology, Boston, Mass., 1990.

47. P. O. Gartland, *Corrosion 96*, Paper 311, National Association of Corrosion Engineers, Houston, Tex., 1996.
48. L. A. DeJong, R. G. Kelly in *Critical Factors in Localized Corrosion III* (Eds.: R. G. Kelly, P. M. Natishan, G. S. Frankel et al.), The Electrochemical Society, Pennington, N. J., 1998, p. 678, Vol. PV 98-17.
49. J. S. Lee, M. L. Reed, R. G. Kelly in *Corrosion and Corrosion Protection* (Eds.: J. D. Sinclair, E. Kalman, M. W. Kendig et al.), The Electrochemical Society, Princeton, N. J., 2001, pp. 279–290, Vol. PV 2001-22.
50. R. C. Alkire, D. B. Reiser, R. L. Sari, *J. Electrochem. Soc.* **1984**, *131*, 2795.
51. Z. Szklarska-Smialowska, *Pitting Corrosion of Metals*, NACE International, Houston, Tex., 1986.
52. I. L Rosenfeld, V. P. Maksimchuk, *Dokl. Akad. Nauk. SSSR* **1960**, *131*, 354.
53. M. Prazak, J. Tousek, W. Spanily, *Zashchita Metallov*. **1969**, *5*, 371.
54. H. P. Leckie, H. H. Uhlig, *J. Electrochem. Soc.* **1966**, *113*, 1261.
55. R. C. Newman, M. A. A. Ajjawi, *Corros. Sci.* **1986**, *26*, 1057.
56. R. C. Newman, T. Shahrabi, *Corros. Sci.* **1987**, *27*, 827.
57. Y. C. Lu, M. B. Ives, *Corros. Sci.* **1995**, *37*, 145.
58. N. Sridhar, D. S. Dunn, C. S. Brossia et al. in *Research Topical Symposium on Localized Corrosion* (Eds.: G. S. Frankel, J. R. Scully), NACE International, Houston, Tex., 2001, p. 1.
59. B. A. Kehler, G. O. Ilevbare, J. R. Scully, *Corrosion* **2001**, *57*, 1042.
60. R. S. Lillard, M. J. Jurinski, J. R. Scully, *Corros. J.* **1994**, *50*, 251.
61. T. S. Lee, A. H. Tuthill, *Corrosion/82*, Paper 63, NACE International, Houston, Tex., 1982.

4.2 Pitting Corrosion

Hans-Henning Strehblow
Institut Für Physikalische Chemie, Heinrich-Heine-Universität, D-40225 Düsseldorf, Germany

4.2.1 Introduction

Localized corrosion of metals is closely related to the passivation of their surface. The presence of passivating layers protects reactive metals against their rapid environmental degradation, as does oxidation and dissolution in electrolytes. However, the presence of aggressive anions leads to local break down of passivity and the formation of corrosion pits by so-called pitting corrosion or pitting. All halides act as aggressive anions although other anions, such as the pseudohalide thiocyanate (SCN^-), sulfates, and perchlorate may cause pitting in special conditions. Fluoride is extremely aggressive causing localized corrosion in alkaline and weakly acidic electrolytes but general breakdown of passivity and general dissolution of the surface of iron, nickel, steel, and stainless steel in strongly acidic solutions. Chloride is the most important anion because of its presence in most technical environments such as seawater or salt on the roads in winter. Thus, the allover presence of chloride leads to the localized corrosion of cars, ships, buildings, road constructions, and also of metal tools and housewares, down to small-size metal components of integrated electronic circuits. Almost all metals and alloys are susceptible to pitting with only very few exceptions, for example, pure chromium.

The technical importance of this kind of corrosion has attracted many research groups for many decades, and various metals and alloys have been studied with a variety of methods. Many papers have been published, and there exists a large literature on this technologically important subject. The following reviews are recommended for further reading [1–4]. Nevertheless, the discussion about the leading mechanisms of pitting corrosion still remain rather controversial, which is in part a consequence of the complexity of the systems. This chapter intends to sort out the leading factors that determine the mechanism of break down of passivity and the growth of corrosion pits.

4.2.2 Phenomenological Aspects of Pitting

4.2.2.1 Critical Potentials and Polarization Curves

Pitting corrosion causes a decisive change of the polarization curve of metals. Figure 1 depicts the characteristic features of a metal with the potential range of active dissolution, passivity, and transpassive behavior. If the metal forms electronically insulating passivating oxide films, the passive range will extend to very positive potentials of more than 100 V, as in the case of the valve metals – aluminum, tantalum, and others. The presence of aggressive anions like chloride causes pitting and results in an increase of the current density for a potential above a critical value, $E_{p,n}$, well within the passive range that goes along with pitting (Fig. 1). Pit growth will stop if the potential is decreased below the repassivation potential $E_{p,r}$. Usually $E_{p,r}$ is more negative than the nucleation potential $E_{p,n}$. The experimental results require a distinction between these two values for the pitting potential E_p because of the following reasons. Nucleation of corrosion pits takes time and a potentiodynamic polarization

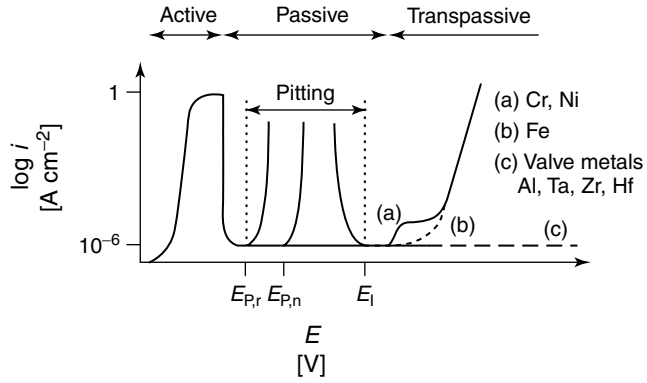


Fig. 1 Schematic current density potential curve of metals with active, passive, and transpassive potential range and the critical potentials E_P and E_I restricting the pitting range. Valve metals with insulating passive layers showing neither transpassive metal dissolution nor oxygen evolution.

curve may easily overrun E_p before pits are detected by a current increase. The accumulation of corrosion products within the pit electrolyte leads to an increase of the concentration of aggressive anions. Because of the concentration dependence of E_p, this will cause a negative shift of $E_{p,r}$ relative to $E_{p,n}$. Besides these two reasons for the hysteresis of E_p, metastable pitting is observed at low potentials with current oscillations caused by the birth and death of corrosion pits. A continuous growth is obtained at sufficiently positive potentials only. The hysteresis of pit nucleation and repassivation may, however, disappear in many systems. Usually the pitting potential depends on the concentration of the aggressive anions, A, in a semilogarithmic relation according to Eq. (1) [5–7].

$$E_P = a + b \log[A] \quad (1)$$

$$E_I = a + b \log\left(\frac{[A]}{[I]}\right) \quad (2)$$

There also exists, however, an upper potential limit E_I for pit growth in the presence of inhibiting anions, I. This has been found for stainless steel in chloride solutions with nitrate as an inhibitor [8] and for Fe and Ni in mixtures of halides with nitrate or perchlorate [6, 7]. If the potential is shifted above E_I, pits will stop growing, whereas new pits are formed when E becomes negative to E_I (Fig. 1). These inhibition potentials E_I change with the concentration of both ions again in a semilogarithmic relation. Figure 2 gives an example for the dependence of the critical potentials E_p and E_I on the concentration [A] and the concentration ratio [A]/[I]. The strong dependence of the inhibition potential on this ratio leads to a decrease of the potential range in which pitting may occur, that is, the potential gap between the two lines of Fig. 2. For sufficiently small ratios, pitting may be suppressed completely.

It seems reasonable that these critical potentials may be explained on a thermodynamical basis. E_P has been interpreted by electrosorption of the aggressive anions at the bare metal surface of a pit to a minimum surface concentration, in order to inhibit its repassivation [3, 7, 9]. Similarly,

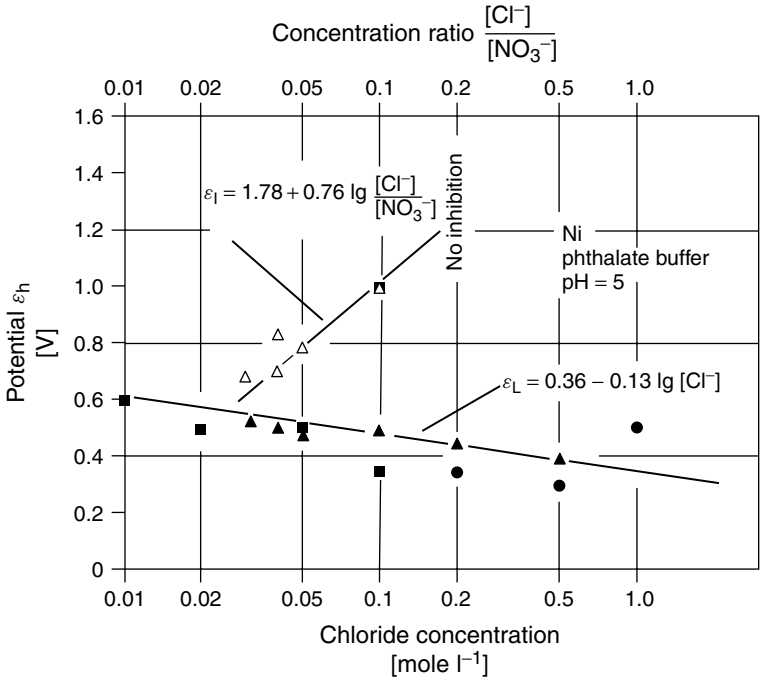


Fig. 2 Pitting potential E_P solid symbols and inhibition potential E_I open symbols as a function of the concentration of aggressive anions A (Cl^-) and its ratio to the inhibiting anion I (NO_3^-) [7].

the inhibition potential may be explained by competitive adsorption of the aggressive and inhibiting anions. This interpretation may also explain the relatively large prelogarithmic factors that have been found experimentally.

4.2.2.2 Pitting and Cathodic Counterreactions

Corrosion is an electrochemical process that consists of at least two reactions that compensate each other electronically in open circuit conditions. The anodic metal dissolution is counterbalanced by the cathodic reduction of a redox system within the electrolyte. Various processes may serve as cathodic counterreactions. The most common are oxygen reduction and hydrogen evolution in acidic electrolytes. Others are the reduction of Fe^{3+} and $[Fe(CN)_6]^{3-}$ in solution. These systems are often used for chemical corrosion tests. Pitted metals expose a small area of a few intensively dissolving corrosion pits that are not protected by a passive layer and a large cathode of the passive metal surface. Because of the large size of the cathode, a much smaller cathodic current density is required for the compensating reduction of the redox system in comparison to the active metal dissolution within the pits. However, electronic conduction is still required across the passive layer. Figure 3 depicts the existing sections of a pitted metal surface with the related electrode reactions, the very small metal dissolution i_{pass}, and the redox reaction $i_{ca,pass}$ via the protecting oxide film and

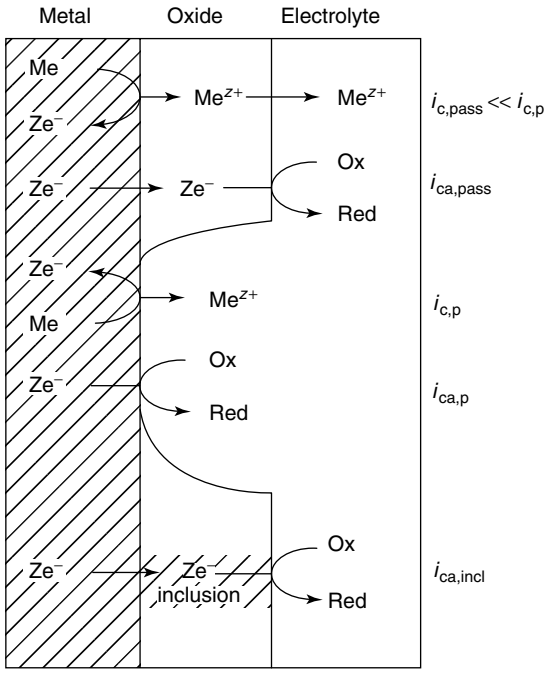


Fig. 3 Schematic diagram of a passivated metal showing the corrosion current densities of metal dissolution and redox reactions at the surface of the passive layer, a pit, and an electron conducting inclusion.

the related reactions at the pit surface $i_{c,p}$ and $i_{ca,p}$, respectively. These passivating oxide or hydroxide films on many metals, such as copper, iron, nickel, steels, and alloys of various compositions have semiconducting properties. There are others with insulating oxide films such as Al, Ta, and so on, which cannot mediate the electron transfer. In these cases, inclusions play an important role by acting as local electronically conducting cathodes with a contribution $i_{ca,incl}$ to the total cathodic current density. Cu-inclusions in commercial aluminum alloys are an example. Last but not least, the actively dissolving pit surface itself permits a balancing cathodic process $i_{ca,p}$. Even on a perfectly passivated valve metal surface, a nucleated pit may grow, however, with a reduced current density. All partial current densities compensate each other for open circuit conditions according to the equation

$$i = 0 = i_{pass} + i_{c,p} + i_{ca,pass} + i_{ca,p} + i_{ca,incl} \quad (3)$$

Whether the total corrosion process is determined by the kinetics of anodic metal dissolution or the cathodic process depends on the size of the cathode and the kinetics of the partial electrode processes. The slowest reaction is the rate-determining step, as is usual in kinetics. In the case of a well-passivated valve metal, this is most probably the cathodic reaction, whereas for metals with semiconducting oxides, the rate-determining step will be anodic metal dissolution. In order to study the partial reactions of pitting corrosion separately, potentiostatic experiments are preferred. The cathodic process is replaced by the electronic circuit of the potentiostat to investigate the anodic metal

dissolution separately. Similarly, the kinetics of redox processes on passivated metal surfaces have been examined separately.

4.2.2.3 Test Procedures and Ranking of Metals

Various test procedures have been proposed to predict the lifetime of alloys in aggressive environments. This also includes a ranking of alloys to aid in materials selection. Most tests refer to the critical potentials of nucleation and a stable growth of corrosion pits, E_{np}, or their repassivation, E_{rp}. Some tests are electrochemical and thus use potentiostats or galvanostats, whereas others are chemical and use oxidizing agents as $FeCl_3$ or the $Fe(CN)_6^{3-}/Fe(CN)_6^{4-}$ redox couple besides the presence of aggressive anions such as Cl^-. A review of test procedures is presented in Ref. [10].

Potentiodynamic polarization determines E_{np} for positive scans, whereas negative scans yield E_{rp}. If they are different, the polarization curve shows a hysteresis. In many cases, this difference gets smaller with decreasing scan rates, indicating that the critical potentials are influenced by the composition of the pit electrolyte as well as kinetic factors like pit nucleation and pit growth. The ASTM standard G61 applies 10 mV min^{-1} [11]. Potentiostatic tests depend less on the experimental conditions and thus are more reliable but time consuming. Usually a potential is applied and the current density is followed for some time. If the current decreases continuously, $E < E_{np}$ will hold, whereas it increases when E exceeds E_{np}. If pits are formed at $E > E_{np}$ and then the potential is stepped to less positive values, the current density will drop continuously when $E < E_{rp}$ is reached. For some systems, both critical potentials are very close to each other. A stepwise approach of nucleation and repassivation conditions with decreasing difference of the applied potentials yields the critical value. Some authors facilitate the nucleation of pits by mechanical scratching of the passivated metal surface or reduction of preexisting oxide films at negative potentials [6]. Similarly, very nonstationary conditions of the passive layer caused by rapid potential changes increases the nucleation rate [6]. In conclusion, the critical potentials are a reasonable measure for the resistance of a metal to pitting for given environmental conditions and they might be used for a ranking. Many authors accept E_{rp} as the more important value. For a sufficiently long time, a pit will nucleate finally and it is a matter of the experimental conditions, that is, of $E > E_{np}$ whether it will grow and cause damage or not. Unfortunately, for many metals, the critical values are accurate to several 10 mV only so that a ranking of metals with similar composition may cause problems. Only in some very special cases the critical potential may be determined with an accuracy of a few mV only (Fe in ClO_4^-) [6, 12].

Galvanostatic tests apply a constant current to the specimen. The related electrode potential increases because of the progress in passive film formation to a maximum that will be close to E_{np}. Because of the formation and growth of corrosion pits, E decreases finally to a constant value that is close to E_{rp}. Potential oscillation during the approach of stationary conditions is related to the repassivation of some of the still-growing pits, which decreases the total area of growing pits and thus leads to an intermediate potential increase. The current density must be large enough to overcome the maximum of the anodic current density of the polarization curve

so that the electrode may be passivated, a necessary condition for localized corrosion versus the general active metal dissolution. Galvanokinetic experiments have been proposed for the determination of critical potentials. In these cases, the current is changed continuously or stepwise [10].

Localized corrosion in aggressive environments requires a cathodic counterreaction to compensate electronically the anodic metal dissolution. To get close to the conditions of actual corroding systems, chemical corrosion tests are applied. The ASTM standard G48 [13] exposes a metal specimen to a 6% $FeCl_3$ solution for one or more days, others use a 10% solution [10]. The weight loss of the specimen is taken as a measure of the extent of localized corrosion because of the high solubility of the corrosion products in the acidic solution. Some laboratories use the temperature as an additional variable with ASTM G 150 as a test. The critical pitting temperature is the value that causes pitting. The chemical $FeCl_3$ test has a serious problem if E_{np} is below $E = 0.90$ V, the redox potential of the 10% test solution, which consequently causes pitting for all these metals. Addition of Fe^{2+} lowers the electrode potential of the $FeCl_3$ solution, which thus permits a modification to get a ranking for metals with lower critical potentials. Mixtures of $Fe(CN)_6^{3-}/Fe(CN)_6^{4-}$ can also be used to influence the redox potential that is independent of the chloride content and pH.

The complexity of chemical tests causes less reliable results. Therefore, the critical potentials determined by potentiostatic measurements are usually accepted as the most reliable results, which may be used as a criterion for the ranking of the corrosion properties of metals. Inhibition potentials are usually of less importance due to the relatively negative rest potentials of the metals in their technical environment. Despite its relatively positive standard potential of $E^0 = 1.23$ V, dissolved oxygen leads to a negative rest potential due to the large overpotential required for its reduction.

4.2.2.4 Potentiostatic Current–time Curves

Potentiostatic pitting experiments have a characteristic current–time curve. During the early stage of pit growth, the nominal current density increases with the second or third order of time [8, 14, 15], whereas in later stages a square root time law may be observed. These time laws are a direct consequence of a local pit current density i_{pit} that is constant or decreases with time and a constant number of corrosion pits or a constant nucleation rate. A constant i_{pit} corresponds to a linear growth of the pit radius dr/dt. The surface of a hemispherical pit increases with r^2. If all pits start at the beginning of a potentiostatic experiment, one obtains a second-order law, $i = a\,t^2$. A constant nucleation rate ($dN/dt = k$) with the pit number growing linearly with time yields a third-order law, $i = a\,k\,t^3$. The constant a contains stoichiometric factors and $i_{c,p}$, which often are potential dependent. As a consequence of ohmic drops and a limitation of diffusion of corrosion products out of the pits, $i_{c,p}$ may decrease in later stages of pit growth with $t^{-1/2}$. A detailed discussion yields a $t^{1/2}$-dependence of the nominal current density, that is, $i = \text{const}\,t^{1/2}$, if the number of pits remains constant [2, 3] and an appropriately higher exponent for a still nonvanishingly small nucleation rate. As a consequence, $a\,i = \text{const}\,t^{1/2}$ to $i = \text{const}\,t$ behavior is often found for long-time pitting tests.

Log i /log t plots have been used to determine the order of t and the nucleation rate in early stages of pit growth. As an example, Fig. 4 depicts the current increase of 1 h prepassivated iron electrodes in 0.1 M phthalate buffer pH 5.0 with 0.01 M KCl and 0.01 M K_2SO_4 [6]. Passivation for 1 h at 0.78 V and subsequent addition of chloride yields a slope of 2, which indicates a pit nucleation immediately at the beginning of the experiment only and a constant pit number during its further course. If, however, the electrode has been passivated for 1 h at 1.18 V and if the potential has been decreased to 0.78 V immediately before the addition of chloride, the current increases much faster with a constant nucleation rate of pits and a slope of 3. An increased pit nucleation is also detected by visual inspection of the electrode surface. Longer

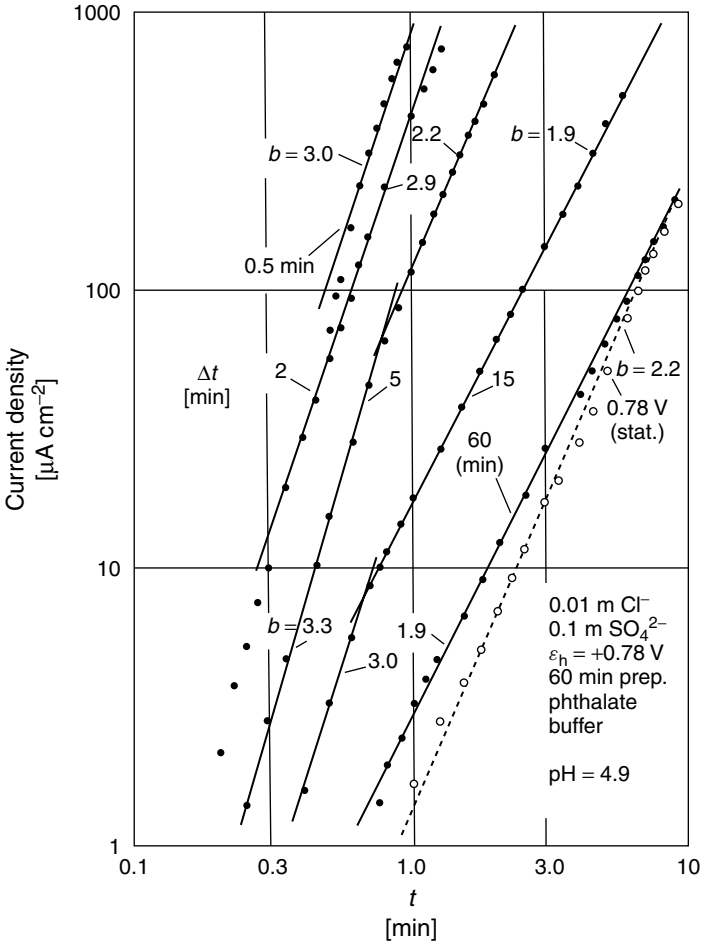


Fig. 4 Current increase with time during pitting of iron in 0.05 M phthalate buffer pH 4.9 + 0.1 M K_2SO_4. Addition of 0.1 M KCl after 1 h prepassivation at $E = 1.18$ V and potential drop to $E = 0.78$ V. Δt = waiting time at 0.78 V till chloride addition [6].

waiting times at 0.78 V decrease the pit nucleation again with a slower current increase and a change of the slope from 3 to 2 at decreasing times of exposure to chloride. Apparently, the nonstationary situation of the passive layer due to potential changes increases the nucleation rate. This is interesting in so far as a passivation at more positive potentials leads to a larger thickness of the passive layer and a subsequent potential decrease a smaller electrical field strength within the layer. Oxide thinning requires time, which then causes an increase of the field strength again. Apparently the nucleation is not related to the thickness of the oxide and its electrical field strength, but to the nonstationary situation of the passive layer. These findings support the idea that the film-breaking is enhanced by potential changes that might induce stresses to the film because of the electrostriction and chemical changes, which have been examined in detail with X-ray photoelectron spectroscopy (XPS) for iron [16].

4.2.3 Pit Growth

4.2.3.1 Local Current Densities

The local current density within corrosion pits may be extremely large. If the precipitation of corrosion products does not occur, the metal dissolution is controlled by charge transfer and ohmic effects, and hence the corrosion process is potential dependent. This situation requires a sufficiently acidic solution to avoid the precipitation of insoluble oxides or a still not saturated or supersaturated pit electrolyte with no formation of a salt layer. Pitting at potentials close to the critical value E_p occurs usually with moderately small local current densities $i_{c,p}$ that, however, may increase with potential to extremely large values. Very high $i_{c,p}$ values may be observed only for short times because of the accumulation of corrosion products and their limited transport from the pit electrolyte to the bulk solution. During intense metal dissolution, one obtains finally a saturation of the pit electrolyte and the precipitation of a salt film. This salt layer reduces the metal dissolution to much smaller values, which now becomes transport-controlled. Visually, this development goes along with the change from a polygonal to a hemispherical shape of the pit. The precipitation of a salt film and the electropolishing starts at the bottom of the pit and metal dissolution continues independently of the crystallographic orientation of the crystallite [6, 17]. The local current density has been determined by direct microscopic observation of the growth of individual pits. This involves potentiostatic transients including high potentials with extremely high local current densities and thus very short experiments in the millisecond range. For this purpose, a special electrochemical cell was attached to a microscope and the pit growth was registered with a movie camera [9, 18]. Furthermore, potentiostatic pulse experiments in the millisecond range provide a large number of corrosion pits in an early stage of their development with a size distribution. Short passivation times below the critical potential in the chloride-containing electrolyte of only a few seconds lead to a poor performance of the passive layer with a related large nucleation rate [19]. A potential step below the critical potential stops the growth of corrosion pits immediately. Figure 5 gives an example for a potentiostatic transient for Ni in phthalate buffer pH 5.0 with 0.1 M KCl and a passivation at 0.5 V for only 1 s [19]. The high current density for $E = 1.30$ V and its decay within 1 ms refers to the thickening of the

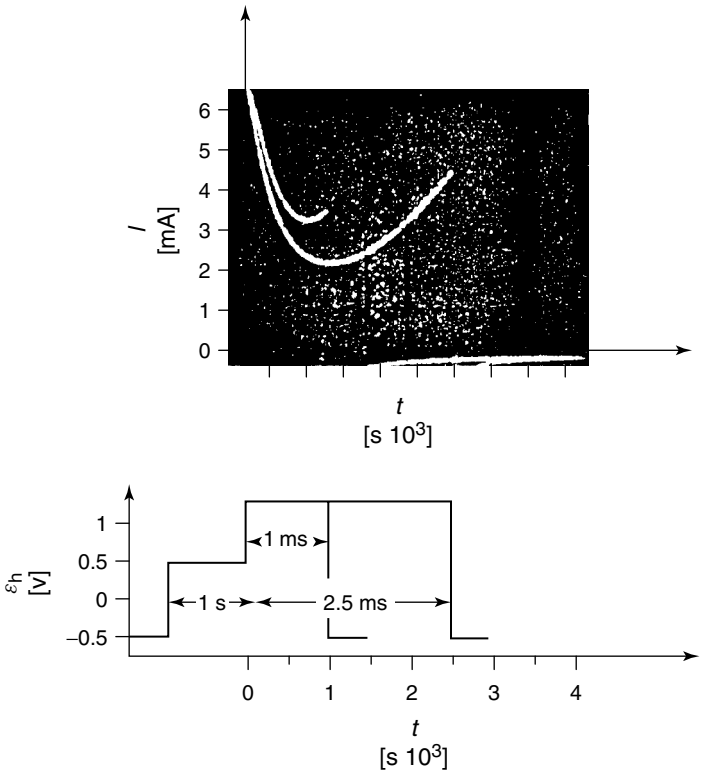
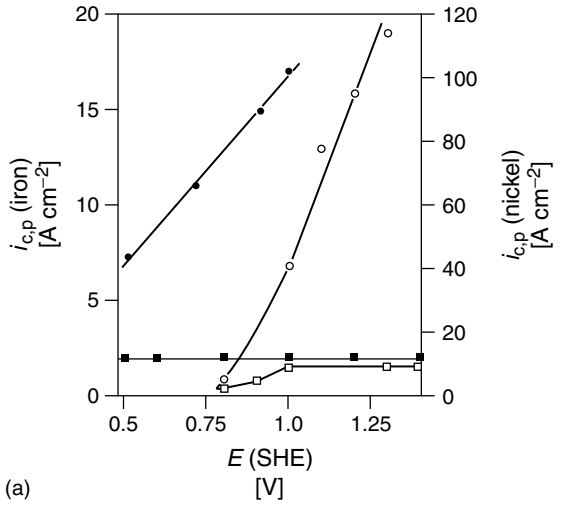


Fig. 5 Potentiostatic transients for pit nucleation at $E = 1.30$ V on Ni ($A = 0.02$ cm^2) in phthalate buffer pH 5.0 + 0.1 M Cl^- after 1 s prepassivation at $E = 0.5$ V [19].

oxide layer; the increase for t >1 ms is a consequence of the formation of a large number of pits with a fast growth and a related high local current density. With the assumption that the largest pits have been formed at the beginning of the transient and have grown during the whole time of the experiment, one obtains the local current density for a hemispherical corrosion pit from its radius by applying Faraday's law.

Figure 6 depicts the current density of Fe and Ni specimens that have been submitted to this type of potentiostatic transients in chloride solutions [9]. The diameter of the electrodes was less than 1 mm in order to maintain a homogeneous potential across the specimen surface and to avoid large ohmic drops in front of the electrodes with a large density of small growing pits. The experiments of Fig. 6 refer to pits with µm dimensions. For these conditions, the potential drop within the pit electrolyte is still negligible, if $i_{c,p}$ does not exceed about 10 A cm^{-2}. As a consequence, a constant growth of the pit radius with time was found, which will slow down however for later stages. Pit current densities of several 10 A cm^{-2} are effected by an ohmic drop that cannot be avoided in principle. The $i_{c,p}/E$-curves directly match the measured polarization curves of small metal surfaces



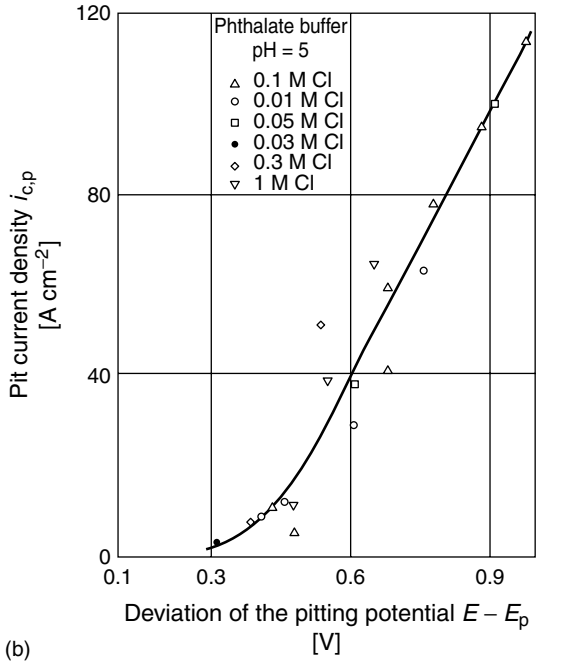


Fig. 6 (a) Local pit current density $i_{c,p}$ as a function of the potential in phthalate buffer pH 5.0. Ni: ○ 0.1 M KCl; □ 0.1 M KCl + 0.1 M K_2SO_4; Fe: ● 0.01 M KCl, ■ 0.01 M KCl + 0.1 M K_2SO_4 [18]. (b) Local pit current density $i_{c,p}$ of Ni as a function of the deviation of the potential E from the critical value E_P in phthalate buffer pH 5.0 with various additions of chloride [9].

in solutions of high chloride content when passivation is avoided completely as will be discussed in Sect. 4.2.3.3 and Fig. 7. For those microelectrodes, the current–density–potential–curves have been corrected for the ohmic drop. Once a pit has nucleated, its local current density refers to the applied electrode potential. For very positive potentials, well within the passive range, extremely high dissolution current densities of several 10 A cm^{-2} up to more than 100 A cm^{-2} have been

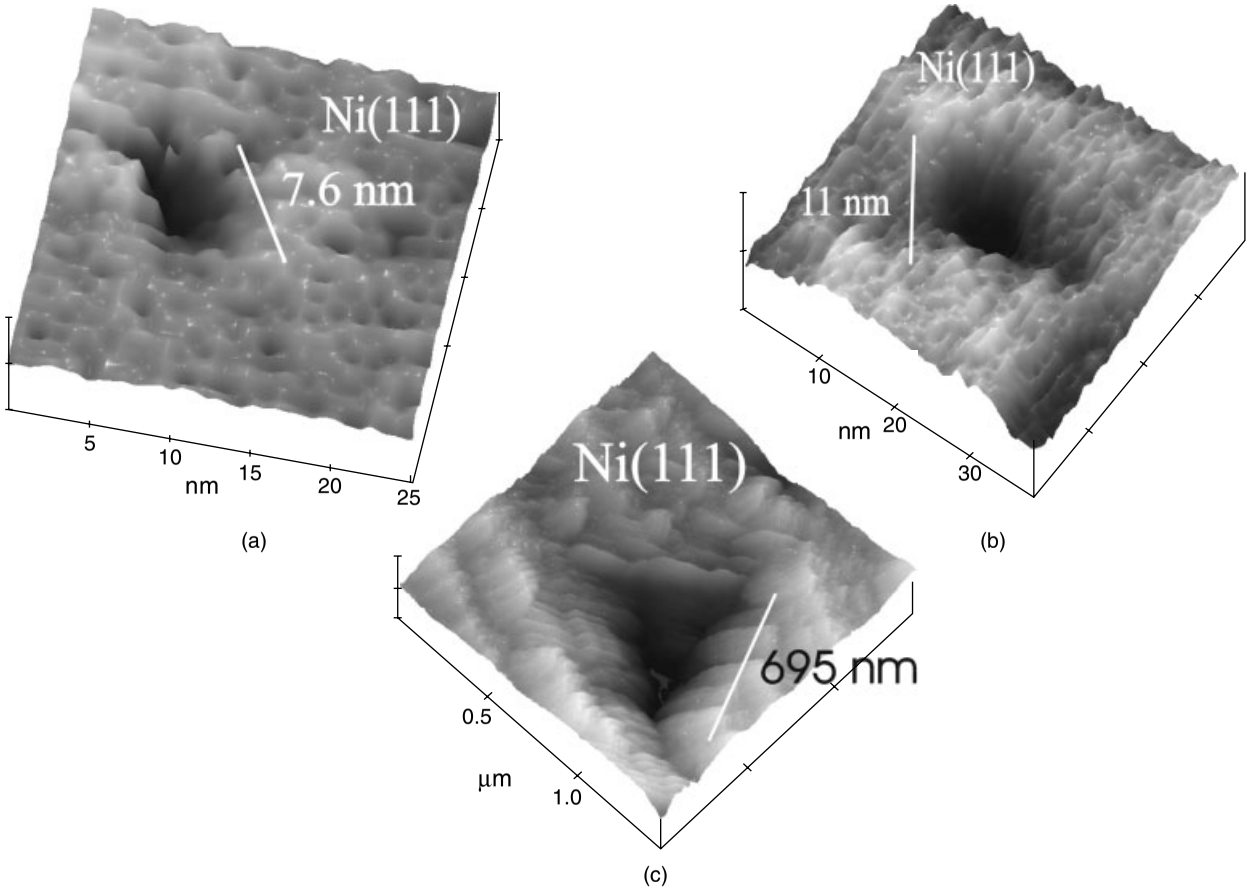


Fig. 7 Sequence of in situ topographic STM images of pits grown on an Ni (111)-oriented single crystal in 0.2 M NaCl pH 5.6 within 5 ms after 10 s prepassivation and stop of growth at $E = -0.5$ V [27].

deduced [17, 18, 20]. Extrapolating the dissolution kinetics of free metal corrosion to potentials in the passive range of the polarization curve leads to extremely high local current densities of 10^3 to 10^6 A cm^{-2} [21]. These large current densities would cause precipitation of a salt film within 10^{-4} to 10^{-8} s. Current densities of more than 10^3 A cm^{-2} are possible in principle according to the oscillation frequency of the metal atoms at the surface if no activation energy slows down the ion transfer. However, current densities up to only 120 A cm^{-2} have been observed for a free corroding Ni-surface (Fig. 6a) [17, 18] and 1000 A cm^{-2} for a few μs on Al-surfaces freshly formed within the electrolyte by a breaking technique [22].

The local pit current density $i_{c,p}$ increases with the chloride concentration, whereas the critical pitting potential E_p decreases with increasing chloride concentration. If, however, $i_{c,p}$ is presented relative to E_p, the data fit one single curve (Fig. 6b). Apparently the effects of chloride concentration and potential compensate each other [9]. The addition of nonaggressive anions such as sulfate or nitrate shift the exponential current increase to positive potentials with a large plateau at low potentials [9]. These plateau values are in the range of some few A cm^{-2}, that is, 5 A cm^{-2} for Ni in 0.1 M KCl + 0.1 M K_2SO_4 and 2 A cm^{-2} for Fe in 0.01 M KCl + 0.1 M KSO_4 (Fig. 6a) [18]. Apparently the potential-independent plateau values of $i_{c,p}$ are related to the formation of a salt layer, which provides electropolishing conditions at the pit surface. If, however, the current gets still smaller, that is, for Ni below 1.0 V, the growth of the pit gets instable and irregular pit shapes are observed. Similarly, high current densities have been found by so-called two-dimensional pitting on thin vapor-deposited Ni-20% Fe and Al-films on a glass substrate [23–25]. In any case, these extremely high current densities are effective only up to the time when precipitation of a salt film slows down $i_{c,p}$. These diffusion-limited current densities are still high in the range of about 1 A cm^{-2}. At potentials just above the critical value E_p, $i_{c,p}$ is smaller in any case, although it is charge transfer controlled on a pit surface free of any precipitates. For these conditions, the growth of pits may be unstable and their shape becomes irregular.

4.2.3.2 Pit Size and Pit Shape

The size and form of corrosion pits depend on the experimental or environmental conditions. Relatively uncontrolled pit growth in open-circuit conditions with a possible precipitation of oxides and hydroxides in alkaline and neutral electrolytes causes irregular localized corrosion structures, whereas very regular pits are usually formed during short time potentiostatic experiments in acidic electrolytes. In order to understand the mechanisms of localized corrosion, experiments with well-controlled potentiostatic conditions are preferred. Any complicating factors related to the corrosion conditions in practice may be studied separately on the basis of the understanding of the processes under well-controlled electrochemical conditions. The visual investigation of corrosion pits has made progress with the availability of appropriate analytical methods. Microscopic in situ and ex situ investigations of pitting on metal electrodes had their limits at a level of the resolution of the light microscope of 1 μm. This improved about 35 years ago with the invention of the Secondary Electron Microscope (SEM) and more recently with the Scanning Tunneling Microscope (STM) and the Scanning Force Microscope (SFM). The last two

methods permit even in situ investigations of metal surfaces. Besides the general technical information, there exists a strong interest in the mechanism of local break down of passivity and pit nucleation as well as the growth of corrosion pits in the various stages of their development. For this reason, well-characterized potentiostatic pitting experiments are preferred. The main mechanisms of pit nucleation postulate a penetration of aggressive anions, the localized dissolution of the passive film or a film breaking corresponding to the penetration, adsorption, or film-breaking mechanism respectively (see Sect. 4.2.4). As will be discussed in the section on the mechanisms, film breaking is favored for the nonstationary situation of the passive layer and the adsorption mechanism for its stationary state. In any case, it is of interest to learn about the shape of a pit at its very early state of development and how it changes as it grows further. These observations will provide arguments for the distinction of possible mechanistic steps. Furthermore, the nucleation of pits at inclusions, which are of decisive importance for alloys for technical application, should be mentioned.

Two main lines have been followed for the investigation of early stages of pitting. Maurice, Inard, and Marcus used STM to investigate the nucleation of corrosion pits on Ni (111) surfaces prepassivated for 30 min in 0.1 M sulfate solutions pH 3.0 at 0.85 V with a subsequent addition of 0.05 M NaCl (Pitting potential 0.75 V) [26]. Numerous triangular pits 20 nm wide and 2 nm deep are found oriented parallel to the steps of the terraces. Ca 20% grow further to ca 70 nm still keeping their form and orientation and only 0.1% reach a size of some 100 nm with a longish irregular shape. These pits should be seen as repassivated metastable pits, as they grow only to a small size within more than 30 min. A completely different procedure was followed by Kunze and Strehblow [27]. They formed pits on Ni (111) by potentiostatic transients as described in Fig. 5. The poor prepassivation of the surface at 0.39 V for some seconds after preactivation at −0.1 V and a step to potentials in the range of 1.0 to 1.5 V in 0.2 M NaCl solution pH 5.6 causes the nucleation of an immense number of corrosion pits for this nonstationary situation of the passivating film. Their growth was stopped after some ms only with a final step to $E = -0.1$ V below the pitting potential. With these conditions, the growth of pits has been frozen in the initial stage of their development. Figure 7 depicts a representative sequence of in situ STM images that demonstrate the development

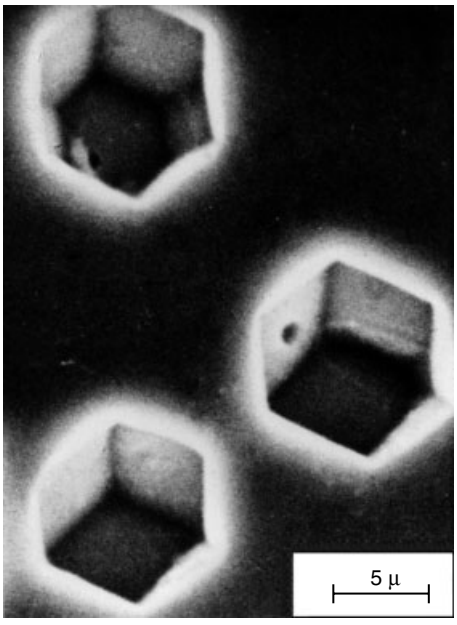


Fig. 8 SEM image of polygonal pits grown on iron in phthalate pH 5.0 + 0.01 M Cl^- at $E = 1.18$ V within 3 s showing densely packed (110) crystal planes on a (111)-oriented surface [6].

of a small longish crack in the passive layer to a triangular pit that supports the film-breaking mechanism for these conditions [27]. Larger triangular pits are found at later stages. If the pits are grown on differently oriented Ni crystallites, other shapes of polygonal pits are found, like octahedrons with square openings on a 100 surface. The pit surface is apparently formed by the most densely packed (111) surface. The form of the orifice is a consequence of the special orientation of the crystal surface. On bcc Fe, a combination of (110) and (100) surfaces is found, which leads to hexagons for the pit orifice for the (111) surface of crystallites [6] (Fig. 8). The accumulation of corrosion products causes their final precipitation and the formation of a salt layer due to the intense dissolution within the pit. This situation changes the pit from a polygon to a hemisphere with electropolishing of its surface. These pits grow without any relation to the crystallographic orientation of the metal and cross the interface of crystallites. This is found especially in the presence of sulfate within the electrolyte additionally to chloride (Fig. 9) [6]. Very irregular closed pits are found in the vicinity of the critical potential. They grow underneath a remaining metal layer with several breakthroughs (Fig. 10) [9]. Apparently the partially closed pit stabilizes the accumulation of corrosion pits that otherwise would repassivate much easier for the localized corrosion in the vicinity of the critical potential.

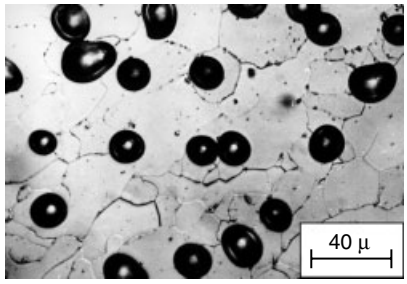


Fig. 9 Hemispherical pits grown on iron in phthalate buffer pH 5.0 + 0.01 M Cl^- + 0.1 M SO_4^{2-} at $E = 1.18$ V within 30 s [6].

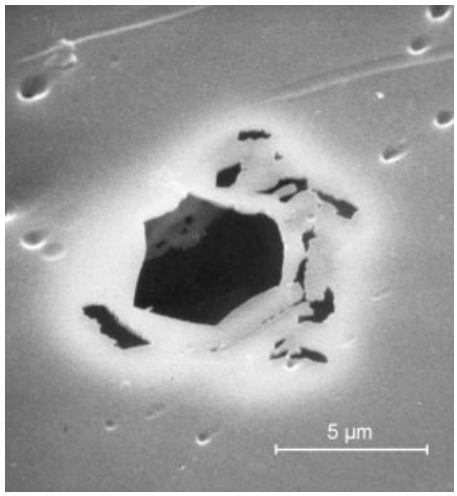


Fig. 10 Metal covered irregular pit on nickel grown in phthalate buffer pH 5.0 + 0.1 M KCl + 0.1 M K_2SO_4 at $E = 0.90$ V within 10 s [9].

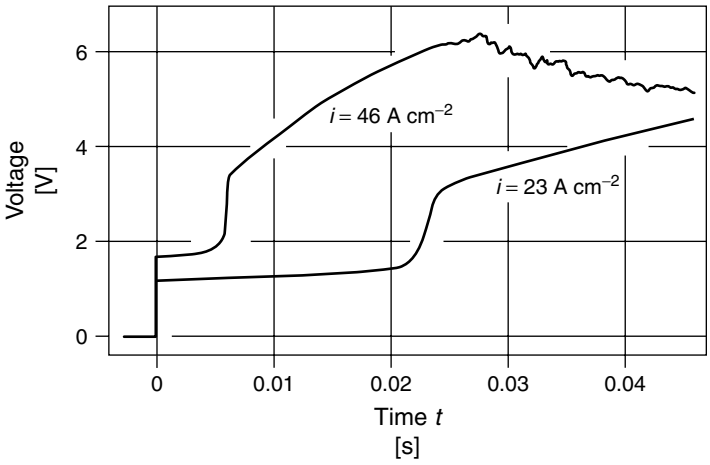


Fig. 11 Galvanostatic transient of a nickel microelectrode in 4 M HCl with $i = 23$ and 46 A cm^{-2} [20].

4.2.3.3 Pit Models, Microelectrodes, and Calculations

The very high local dissolution current densities within pits may also be measured directly when the whole metal surface is acting as a pit. This may be achieved for small electrodes in solutions with a high content of aggressive anions ($\geq$1 M), a condition that avoids passivation. The small size ensures a homogeneous potential distribution all over the metal surface and a sufficiently small ohmic drop in front despite the high current densities. This situation is well known for the conditions of electrochemical machining. There again, a high chloride concentration avoids passivation although the potential is well within the passive range. These electrodes have been studied with galvanostatic transients. Figure 11 depicts an example for the related change of the potential with time for Ni in 4 M HCl solution with $i = 23$ and 46 A cm^{-2} [20]. The same shape has been observed for smaller chloride concentrations and for Fe specimens. The potential is constant up to a transition time τ with a following step and a subsequent slower increase. The experimental data follow Sand's equation (Eq. 4) with the diffusion constant D of the metal ions, their charge z_M, and their concentrations at the metal surface c_M and within the bulk $c_{M,b}$ [20].

$$i\sqrt{t} = \tfrac{1}{2} z_M F[(\pi D)(c_M - c_{M,b})]^{1/2} \quad (4)$$

In the absence of the supporting electrolyte, that is, a solution containing the salt of the dissolving metal only, one has to use the effective diffusion constant $D_{eff} = D\,(1 + z_M/z_A)/t_A$ with the transfer number t_A and the charge z_M and z_A for the metal ion and the aggressive anions, respectively. At $t = \tau$, the concentration c_M gets to its saturation value and a precipitation of a salt film occurs. This film blocks the metal dissolution and causes a potential step with a subsequent further increase due to the thickening of the salt layer. $i\sqrt{\tau}$ is independent of the applied current density, decreases linearly with the bulk concentration of the metal ions, and is described quantitatively by Eq. (4). The superposition of the galvanostatic transient by short additional transients permits the determination of the ohmic drop in front

of the electrode [20]. These investigations lead to the model of a bilayer structure of the salt film with an inner thin poreless part that takes over most of the increase of the electrode potential up to several volts and an outer porous part that takes over up to 1 V as an ohmic drop within the electrolyte of the pores [20].

A completely different behavior is observed for Fe and Ni specimens in solutions without aggressive anions like sulfuric-, nitric-, and perchloric acid. For similar galvanostatic transients, a rapid passivation is observed with a fast potential increase and much smaller and current dependent values for $i\sqrt{\tau}$ [3, 9]. In the absence of aggressive anions, there is no dissolution and precipitation of corrosion products, but the formation of a passive layer occurs at the metal surface with a final oxygen evolution. Similarly, potentiostatic transients have been examined in the presence of high chloride concentrations that show a drop of the current density when a salt film is formed. On iron, these conditions cause a regular roughness of the surface. In comparison to Ni, its salt layer apparently has less electropolishing properties [9]. An interruption of the current for $t < 1$ s is sufficient to dissolve the salt layer and to recover the state of the metal surface with good reproducibility for a subsequent transient. These results lead to the conclusion that no passivating film has formed during potentiostatic transients in solutions of high chloride content, which would require a much longer time for its dissolution.

Similar results have been obtained by other groups on metal specimens with different geometry. Pitting has also been studied using the so-called lead-in-pencil geometry, which may be treated as a one-dimensional pit because of their small width and larger depth. In these cases, it is a consequence of the experimental conditions and the pit geometry whether the precipitation of a salt film occurs or major ohmic drops cause a stable metal corrosion [2, 3]. Similar ideas have been published more recently by N. J. Laycock and R. C. Newman [28].

An interesting alternative is pitting on thin vapor-deposited metal films such as Al or Ni-20 Fe [23–25]. In this case, pitting leads to a rapid perforation of the film and a further circular growth. These two-dimensional pits lead to simpler relations for the accumulation of corrosion products in comparison to the hemispherical situation. $i\sqrt{\tau}$ is radius independent and proportional to $i_{c,p}$ instead of to $i_{c,p}r$. Also in these cases, local current densities of up to $i_{c,p} = 100$ A cm^{-2} have been measured.

4.2.3.4 Precipitation of Salt Films Within Pits

In the case of a hemispherical pit, the accumulation of corrosion products at the pit surface relative to the bulk $\Delta c = c_M - c_{M,b}$ follows Eq. (6), which is similar to the linear transport described by Eq. (4). The same symbols are used as for Eq. (4). V_M is the molar volume of the metal. The geometric factor a is introduced as a modification to Fick's diffusion law in combination with Faraday's law, if the hemispherical electrode does not have a convex ($a = 1$) but a concave geometry ($a = 3$) (Eq. 5). This factor has been estimated [6, 29] and later confirmed by computer simulation [30, 31].

$$i_{c,p} = z_M F D_{eff} \frac{\Delta c}{ar} \tag{5}$$

$$i_{c,p}\sqrt{t} = z_M F \sqrt{\frac{\Delta c D_{eff}}{V_M a}} \tag{6}$$

$$\Delta c = c_M - c_{M,b}$$

An equivalent relation has been deduced for nonstationary transport conditions with corrections that are negligible for values $i\sqrt{t} < 12\ \mathrm{A\,cm^{-2}\,s^{1/2}}$ [29]. If saturation is achieved at the pit surface for $t = \tau$ with $c_M = c_{M,s}$, the precipitation of a salt film will occur. The related calculation has been confirmed by direct observation of the pits that change their shape from a polygon to a hemisphere when the salt film precipitates [17]. Similarly the growth of the pit radius r slows down for $t > \tau$ [9].

4.2.3.5 Ohmic Drops

The potential drop within the electrolyte for an open hemispherical pit can be estimated by the simple equation

$$\Delta U = \frac{a i_{c,p} r}{\kappa} \qquad (7)$$

with specific conductivity κ, local current density $i_{c,p}$, radius r, and geometric factor $a = 3$ [6]. It depends on the specific situation whether ΔU is large enough to shift the potential below the Flade potential, that is, in the active range of the polarization curve (Fig. 1), which is often used to explain the stable pit growth. For 0.5 M H_2SO_4 with $\kappa = 0.22\ \mathrm{cm^{-1}\,\Omega^{-1}}$ and $i_{c,p} = 0.3\ \mathrm{A\,cm^{-2}}$, which is a reasonable value for moderately high pit current densities for Fe, one obtains $\Delta U > 1$ V for a pit radius $r > 2.4$ mm, but only $\Delta U = 0.41$ mV for $r = 1\ \mu$m. This short calculation demonstrates that it is absolutely necessary to define well which state of the growth of a pit is discussed. Potential drops may stabilize localized corrosion for large pits but never for small ones, that is, at the initial stages. The conductivity of the electrolyte is of course another factor that has to be taken into account. The accumulation of ions within a corroding pit may increase κ and thereby reduce ΔU compared to the value obtained with the bulk conductivity. Evidence for potential control of pit growth is given for studies on Al by Hunkeler and Böhni [32]. They found a linear dependence of the product $i_{c,p}r$ on the voltage drop ΔU as given by Eq. (7). There exists a large literature on the measurements of potential drops in corrosion pits and their influence on their stable growth during many years. Herbsleb [33] and Pickering and Frankenthal [34] measured the potential drop within actively corroding pits in chloride-containing sulfuric acid. These studies refer to pits in the mm range and thus show appropriate ohmic drops that shift the applied potential in the active range of the polarization curve, which is in agreement with the above-mentioned estimate. Hydrogen evolution in an acidified pit electrolyte may lead at these negative potentials even to gas bubbles that cause a crevicelike situation with a further stabilization of the potential shift. In a recent experimental study, the close relation between pitting and crevice corrosion was pointed out [35]. In deep and narrow artificial crevices, a potential drop of up to $U = -0.6$ V was measured. It should be pointed out that these large shifts refer to pits and crevices with mm dimensions especially for narrow openings and not to initial stages of pitting with open pits in the μm-range. Usually a pit starts with a small size and thus needs other factors stabilizing its growth. Ohmic drops may also play a major role for covered pits as shown in Fig. 11.

4.2.3.6 Composition of the Pit Electrolyte

The accumulation of electrochemically nonactive electrolyte components is closely related to the concentration polarization ΔU within the electrolyte, similar to a Boltzmann dependence of the

concentration c_j of these species on the electrical energy ΔUzF [6, 29]. Together with the electroneutrality equation, one obtains a dependence of the concentration of the corroding metal ions c_M at the metal surface on ΔU with $\Delta c = c_M - c_{M,b} = c_M$, for vanishingly small bulk concentrations $c_{M,b}$ [6, 29]. $c_{j,b}$ and $c_{M,b}$ are the corresponding bulk values.

$$c_j = c_{j,b} \exp\left(\frac{-\Delta U z_j F}{RT}\right) \tag{8}$$

$$\Delta c = c_M - c_{M,b} = c_M = -\left(\frac{1}{z_M}\right) \times \sum c_{j,b} z_j \exp\left(\frac{-\Delta U z_j F}{RT}\right) \tag{9}$$

Equation (8) requires that only one electrochemical process occurs with no subsequent reactions within the bulk electrolyte. The concentration of the metal cations c_M may be also calculated from Eq. (5). For vanishingly small bulk concentration of the cations, Δc equals the surface concentration c_M. The accumulation of cations is proportional to the local pit current density and the pit radius (Eq. 5). One may therefore take $i_{c,p}r$ as a measure of the cation concentration at the pit surface, which depends on the age of the pit. Therefore this scale is included in Fig. 12.

$$\Delta c = c_M = \frac{a i_{c,p} r}{z_M F D_{eff}} \tag{5a}$$

The concentrations c_j at the pit surface of species that are not involved in the electrode process and the metal ion concentration have been calculated according to Eq. (8) for some bulk electrolytes frequently used for pitting studies (Fig. 12).

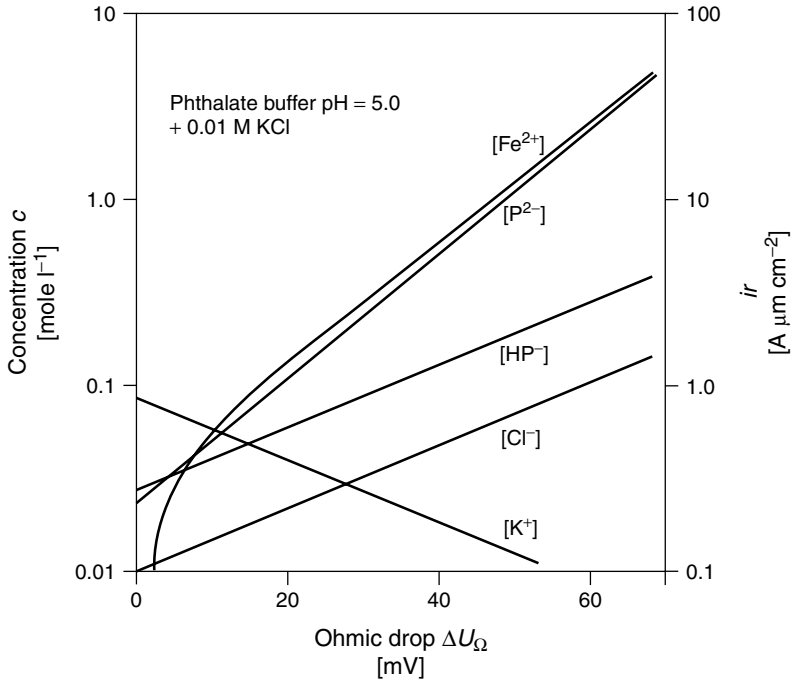


Fig. 12 Concentration of cations and anions at a dissolving pit surface as a function of the potential drop ΔU_Ω within the electrolyte and the related product $i_{c,p}r$ [26].

Metal ion concentrations c_M go up to saturation of a few moles per liter when the potential drop increases to several tens of millivolts, which is usually the case for a pit radius of several micrometers. Equation (9) was applied for the calculation of the concentrations c_M at the pit surface.

pH shifts have often served to explain the stability of a corroding pit. Equation (8) permits the calculation for buffered solutions when the pH is not affected by hydrolysis of the corrosion products [29]. Buffer ions change in concentration in agreement with the pH shift as given for the phthalate buffer in Fig. 12. An accumulation of dissolving metal ions leads to a depletion of the other cations and consequently to a positive pH shift according to Eq. (10).

$$\mathrm{pH} - \mathrm{pH_b} = \frac{\Delta U}{0.059} \qquad (10)$$

In nonbuffered solutions, the usual hydrolysis equilibrium of the metal ions leads to acidification according to

$$\mathrm{Me^{z+} + H_2O \longleftrightarrow MeOH^{(z-1)+} + H^+} \qquad (11)$$

With $[\mathrm{MeOH}^{(z-1)+}] = [\mathrm{H}^+]$ for nonbuffered electrolytes, one obtains

$$[\mathrm{H}^+] = \sqrt{K_h[\mathrm{M}^{z+}]} \qquad (12)$$

With hydrolysis constants of $K_h = 10^{-10}$ and 10^{-7}, one obtains for the saturation concentrations 4.8 and 4.2 M, pH values of 4.3 and 2.4 for saturated $NiCl_2$ and $FeCl_2$ solutions, respectively. These calculations show that the precipitation of hydroxide within a corrosion pit may be prevented for these metals by acidification. However, as discussed before, passivation should nevertheless be possible for many technically important metals. For Fe, Ni, and other metals, especially in acidic media, passivity cannot be explained on the basis of thermodynamic equilibria and Pourbaix diagrams. In these cases, passivity is a kinetic phenomenon. This detail will be discussed again together with the mechanism of a stable pit growth.

4.2.3.7 Minimum Chloride Concentration for Pitting

An attempt has been made to explain the requirement for a minimum concentration of aggressive anions to maintain stable pit growth [29]. With the assumption that a salt film of thickness δ has to be maintained at the growing pit surface, one obtains

$$c_{min} = aV_m i_{c,p} \frac{\delta}{DFV_s} = 0.5 i_{c,p} \delta \qquad (13)$$

With this assumption the experimentally found value of $c_{min} = 3 \times 10^4$ M has been confirmed with a local current density $i_{c,p} = 1\ \mathrm{A\ cm^{-2}}$, a salt layer thickness $\delta = 5$ nm, geometric factor $a = 3$, molar volume $V_m = 3.55\ \mathrm{cm^3\ val^{-1}}$ for the equivalent volume for Fe metal and $V_s = 21.25\ \mathrm{cm^3\ val^{-1}}$ for $FeCl_2$, and diffusion constant $D = 10^{-5}\ \mathrm{cm^2\ s^{-1}}$ for Cl ions.

4.2.3.8 Accumulation of Aggressive Anions

The accumulation of aggressive anions has been found at the surface of even small polygonal pits of a few μm diameters when they had not yet changed to a hemisphere by the precipitation of a salt film. A special preparation technique of pulling the electrode with actively corroding pits into a benzene layer above the electrolyte preserved the special situation at the corroding pit surface even after rinsing with acetone and dry storage in air [36]. These pits remained active and continued their growth immediately when reintroduced into the electrolyte at the same potential. However, they became inactive when rinsed

with water or on stepping the potential to below the critical value. With electron microprobe analysis, a chloride could be found (Fig. 13) that corresponds to a layer of ca 5 nm $FeCl_2$ when the pit remained active but which was lost completely by rinsing with water or repassivation [36]. These studies show clearly that the formation of a thin layer of aggressive anions, even in pits of a few μm, is responsible for a stable pit growth. The later precipitation of much thicker salt films in larger pits of

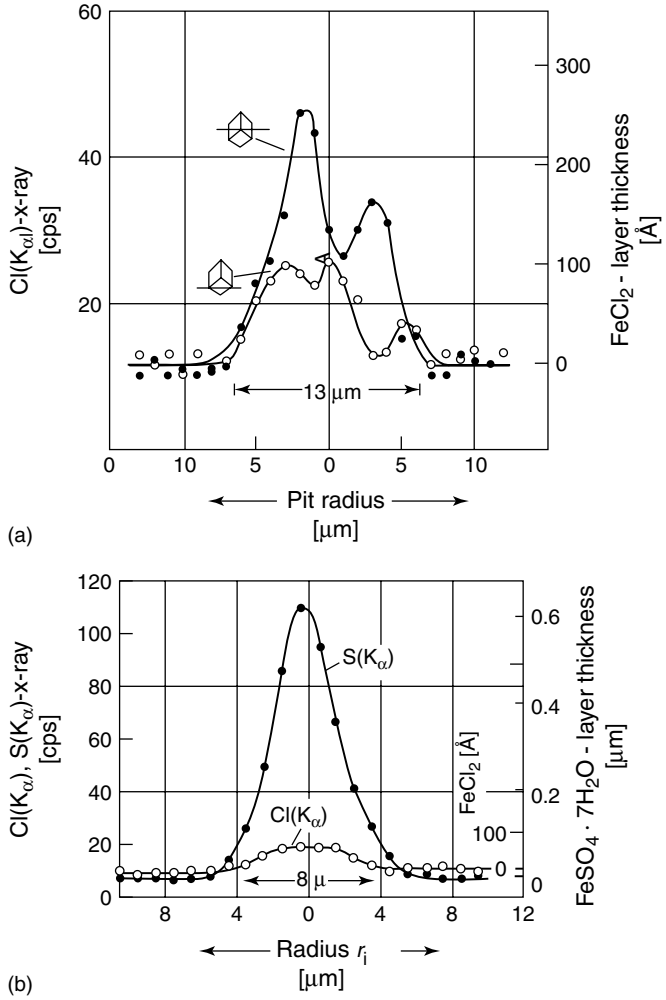


Fig. 13 (a) Electron microprobe cross section of a 13-μm wide hexagonal pit on iron formed on phthalate buffer pH 5.0 + 0.01 M Cl^- at $E = 1.11$ V within 5 s showing the accumulation of chloride within the pit [6]. (b) As Fig. 13(a), hemispherical electropolished pit, 8-μm wide grown in phthalate buffer pH 5.0 + 0.01 M Cl^- + 0.1 M SO_4^{2-} at $E = 1.14$ V within 10 s showing Cl^- and SO_4^{2-} accumulation within the pit [6].

several 10 µm provide further stabilization but they are not a necessary condition for the stability of localized corrosion. The presence of nonaggressive anions in the bulk electrolyte also caused their accumulation but did not suppress the additional presence of aggressive anions that are absolutely necessary for a stable pit growth. The electropolishing conditions in sulfate-containing solutions cause large amounts of these anions to correspond to several 100 nm of $FeSO_4$ within the hemispherical pits but did not avoid the additional and necessary accumulation of ca 5 nm $FeCl_2$ [36].

4.2.3.9 Repassivation of Corrosion Pits

The accumulation of corrosion products within the pits suggest that a high concentration of chloride is a necessary condition for a stable growth in their early stage of development. As a consequence, the kinetics of repassivation of small pits may be related to the transport of accumulated aggressive anions from the pit to the bulk electrolyte [19, 29]. If this transport is the rate-determining step, one expects the repassivation time to increase with the depth of a corrosion pit and thus to the distance the chloride has to travel by diffusion. If we simply apply the relation of Einstein–Smoluchowski for the transport time t_r out of a pit of radius r (Eq. 14), and if the radius r is given by the local current density $i_{c,p}$ and the lifetime t_p of the pit by Eq. (15), we obtain Eq. (16) for the repassivation time t_r.

$$t_r = \frac{r^2}{2D} \tag{14}$$

$$r = \frac{i_{c,p} t_p V_m}{z_m F} \tag{15}$$

$$t_r = \frac{i_{c,p}^2 t_p^2 V_m^2}{2D z_m^2 F^2} = k t_p^2 \tag{16}$$

t_r increases with the square of the lifetime t_p of a pit. The constants k_i have been estimated from $D = 5 * 10^{-6}$ cm^2 s^{-1}, $zF/V_m = 2.72 * 10^4$ A s cm^{-3} for Fe and $2.93 * 10^4$ A s cm^{-3} for Ni to $k_{Fe} = 1.35 * 10^{-4} i_{c,p}^2$ and $k_{Ni} = 1.16 * 10^{-4} i_{c,p}^2$ for Fe and Ni, respectively. To check the $i_{c,p}^2$ and t_p^2 dependence of t_r, potentiostatic pulse measurements have been performed [19] (Fig. 14). The potential was pulsed for about 10 ms up to 1 s, to values above the pitting potential E_p and back to $E < E_p$ for increasing time Δt_r. When the potential was finally pulsed back to the potential within the pitting range, the current density started to increase to the same level that had been reached at the end of the previous pitting period, if Δt_r was short enough. When Δt_r was too long, at least some of the pits repassivated and the subsequent pitting period had to start again with the nucleation of new pits at a smaller value of the average current density of the electrode. The interval Δt of a first deviation from a continuous increase of the current density for a set of pulse experiments is taken as the repassivation time t_r. A double logarithmic plot of t_r and t_p shows a slope of approximately 2 as required by Eq. (16). t_r also changes proportionally with $i_{c,p}^2$. The estimated values agree sufficiently well with the experimental data.

One may therefore conclude that the rate-determining step for the repassivation is the transport of accumulated aggressive anions out of small pits. This result coincides well with the explanation that localized corrosion is stabilized at its initial stage by the accumulation of aggressive anions, which prevent the formation of a passive layer at the active pit surface.

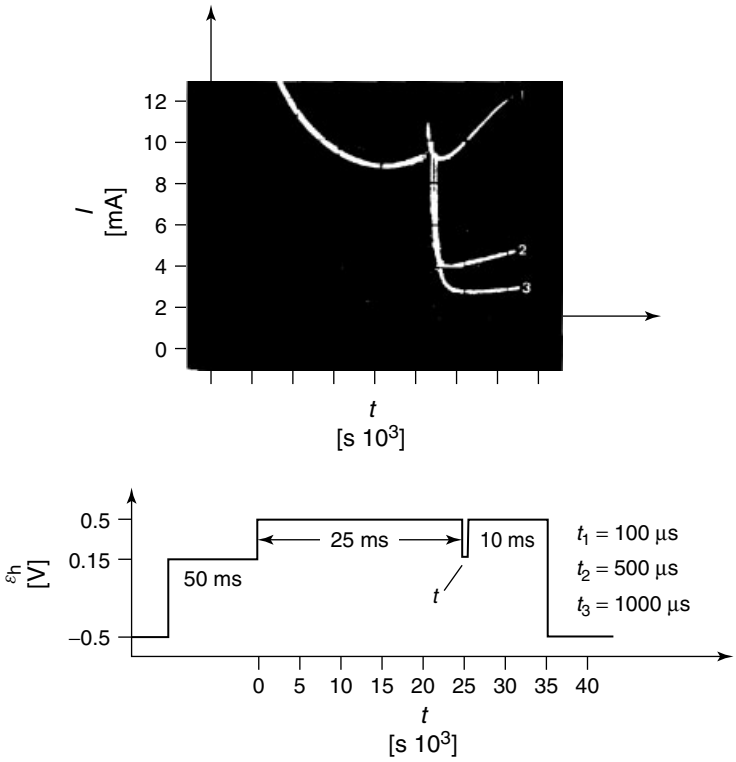


Fig. 14 Repassivation of small corrosion pits on an iron electrode ($A = 0.13\ cm^2$) during potentiostatic steps to $E < E_P$ for $t > 0.1$ s after pit growth at 0.5 V for 25 ms seen by the decrease of the anodic current and following increase due to new nucleation of pits in phthalate buffer pH 5.0 + 0.03 M Cl^- [19].

4.2.3.10 **Alloying Metals and Inclusions**

Alloying metals are very important factors to stabilize an alloy against general and localized corrosion. Among these, Cr plays a very important role for iron and nickel base metals. It accumulates in the passive layer because of its extremely small dissolution currents even in strongly acidic electrolytes [37, 38]. Pure Cr is not attacked by any halides. The critical pitting potential is increasing with the Cr content of the alloy. Iron-chromium thin film alloys show a critical concentration of 16% Cr, above which pitting is suppressed at any potential. This behavior has been explained by a percolation mechanism with sufficiently large iron clusters, to start a pit that will propagate under a passive layer only if there is a sufficiently continuously connected amount of iron [39].

The effect of Cr is beneficial not only for stainless steels but also for Ni base alloys like Alloy 22 and Hastelloy C4 with ca. 20% Cr. These alloys are resistant to general corrosion and pitting, even in highly chloride-containing solutions like Q brine (>8 M Cl^-). Pitting is obtained at elevated temperatures at sufficiently positive potentials only [40]. This is again a consequence of the presence of Cr, which

forms an almost pure Cr_2O_3-containing passive layer due to preferential Ni dissolution [41]. The addition of high amounts of silicon to iron (>20%) apparently protect against pitting [42]. For these alloys or silicides, an almost pure SiO_2-film is formed in acidic electrolytes [43]. SiO_2 is resistant to the attack of chlorides and thus protects against general dissolution and pitting in the presence of chlorides.

A different influence is observed by additions of molybdenum to technical alloys. Similar to the influence of Cr, Mo shifts the pitting potential to more positive values. It apparently stops pitting as a result of the formation of insoluble compounds. All halides MoX_2 and MoX_3 are insoluble in water [44]. Accumulations of halides may therefore be bound to insoluble corrosion products, thus preventing pit growth in a very early stage of development. Although still under discussion, many authors do not find Mo enrichment within the passive layer in that it presumably does not prevent pitting by stabilization of the passivating oxide. Pure Mo does not passivate in sulfuric acid and thus should dissolve preferentially. Thus Mo is thought even to destabilize passive layers on Ni base alloys [45]. In conclusion, the mechanistic details of the influence of Mo to pitting are still unsolved and under discussion.

The addition of nitrogen to steel also has a beneficial effect on the resistance to pitting. In this case, negatively charged nitrogen accumulates at the metal–oxide interface besides some dissolution of NH_3. The formation of Cr- and Mo-nitrides at the surface of stainless steel could be excluded by XPS investigations. It has been proposed that the presence of N^{3-} at the metals surface repels the aggressive Cl^- anions, thus avoiding the nucleation of pits and their growth [46]. By this mechanism, nitrogen facilitates an effective repassivation of a metal surface and of defects in the passive layer, thus preventing the development and growth of pits [46].

Besides the major alloying elements, nonmetallic precipitates and inclusions are preferential sites for pitting. A major role is found for MnS inclusions that are common in steels. It is interesting that the attack occurs at the inclusion–metal phase boundary. The formation of a pit does not require the complete dissolution of the inclusion. It has been proposed that the special chemistry within the pit electrolyte with the formation of sulfur-containing compounds such as sulfides, sulfur, sulfites, and even sulfates has a strong influence on localized corrosion [47]. This is supported by a pronounced increase of the pitting potential by 100 mV of steel in the presence of MnS inclusions when the pH is increased from 4 to 5. Most of these explanations do not include the special role of chloride although a strong decrease of the pitting potential by almost 200 mV with the increase of its concentration from 0.02 M to 0.5 M is reported [47]. MnS inclusions provoke pitting of steels at more negative potentials in comparison to their absence. Ti_2S inclusions may also initiate pitting, however, they are less effective and thus less harmful. The presence of Ti may even reduce the influence of MnS owing to its competition for sulfur. Addition of Ti to steels shift the pitting potential by more than 100 mV to more positive values [47].

Not all MnS-inclusions are the site of pit nucleation. There exist different MnS precipitates. Some form at oxide inclusions like Al_2O_3 or Cr_2O_3 particles and at Nb-carbonitrides or simply at no nucleation site. MnS precipitates at hard oxide inclusions are dangerous because they form microcrevices during cold rolling of steels. The decohesion of MnS at these oxide

particles thus causes preferential sites for localized corrosion. The close relation of pitting and crevice corrosion has been mentioned already in Sect. 4.2.3.5. It is the task of steel making to avoid the formation of oxide inclusions and other nucleation sites for MnS to reduce pitting at these precipitates. An interesting method to study the influence of inclusions is the application of microelectrochemical techniques [48]. The decrease of the area of the investigated steel surface by the use of a capillary of the microelectrochemical cell shows that MnS inclusions are dissolved with and without the presence of chloride, whereas chloride is needed to grow a pit at these sites. Active and nonactive inclusions may be distinguished and the measured pitting potential may be increased remarkably by a decrease in the size of the MnS inclusions below 1 μm. Furthermore, the measured current noise increases with the size of the surface area, which is closely related to the number of inclusions that are accepted for these measurements by the size of the capillary.

Another danger is the formation of Cr-carbides at grain boundaries. They cause the depletion of the adjacent metal in Cr and thus reduce locally the protection of the alloy. As a consequence, pits may form at these sites at more negative potentials. They may merge together and cause intergranular corrosion.

4.2.4 Breakdown of Passivity and Pit Nucleation

Three main mechanisms are being discussed for the processes leading to the breakdown of passivity and the nucleation of corrosion pits [19] (Fig. 15). The penetration mechanism involves the migration of aggressive anions from the electrolyte through the passive layer to the oxide–metal interface under the influence of the high electrical field strength of most passivating films. The film-breaking mechanism starts with cracks in the passive layer, exposing small areas of bare metal surface to the electrolyte and the related very intense metal dissolution that leads to the formation of a pit. The adsorption mechanism refers to the increase in the transfer of cations from the passive film to the electrolyte due to the complexing properties of the aggressive anions. This process causes a thinning of the passive layer and a final removal, thus exposing the bare metal surface to the electrolyte.

4.2.4.1 Penetration Mechanism

The penetration mechanism requires the transfer of the aggressive anions from the electrolyte to the metal–oxide interface. The application of surface analytical methods such as X-Ray Photoelectron Spectroscopy (XPS), Auger Electron Spectroscopy (AES), and Secondary Ion Mass Spectroscopy (SIMS) do not clearly support this mechanism. Careful measurements begin with a specimen prepassivated in a solution without any aggressive anions and with their being added later to avoid incorporation during film growth to study their penetration. For these conditions, Cl has been found in the outer parts of a film only. Usually, passive films have at least a bilayer structure. Usually the outer part is a hydroxide film. This hydroxide part on passive Ni incorporates chloride. Chloride has been found in the inner layer only when the passive layer has been formed in a solution containing chloride. Similar results were obtained for prepassivated FeCr alloys [49, 50]. Another possibility is its incorporation after long waiting periods in chloride-containing solutions with continuous breakdown and repair events of the passive layer, which

correspond to an incorporation into a partially growing new film. Passive layers often act as ion exchangers, at least in their less densely packed outer part. The inner barrier type oxide is not penetrated by aggressive anions.

Other serious objections to the penetration mechanism refer to the kinetics of pit formation. A poorly prepassivated specimen is submitted to pitting within only a few ms as presented for the potentiostatic transient of Fig. 5. Even for well-prepassivated specimens, pit nucleation takes less than 1 s [19] if the conditions are in favor for breakdown of passivity with a high electrode potential and high chloride concentration. A penetration of halides is expected with a similar transfer rate as the outward migration for cations during corrosion in the passive state, which occurs

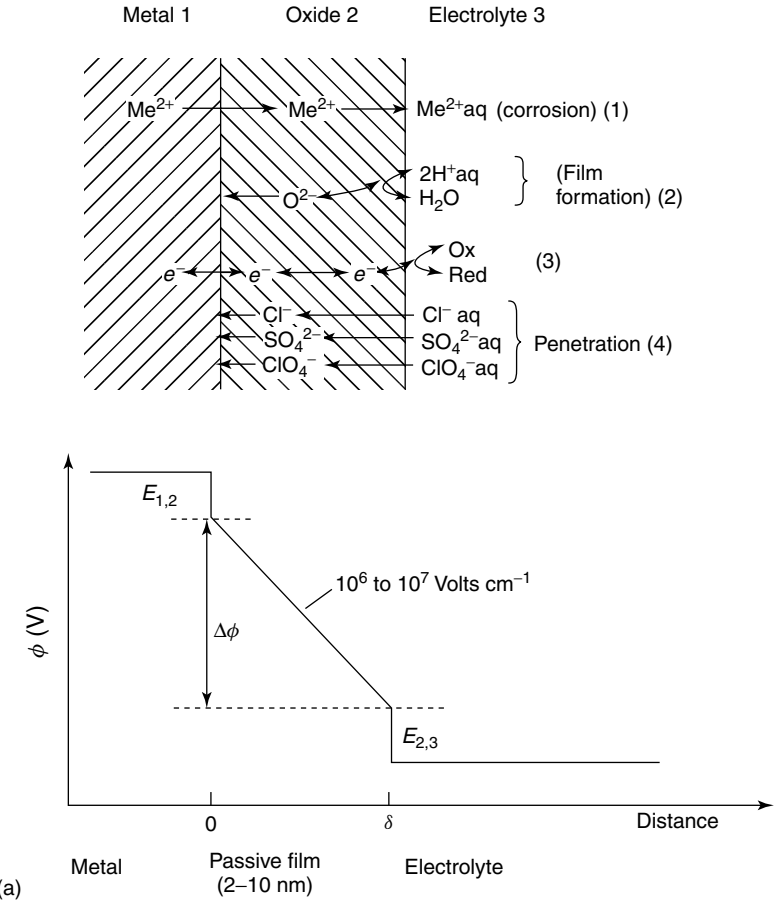


Fig. 15 Schematic diagram demonstrating the three mechanisms leading to the breakdown of passivity and pit nucleation [19], (a) penetration mechanism with migration of aggressive anions in the high electrical field of the passive layer; (b) film-breaking mechanism with the competing processes at defects; and (c) adsorption mechanism with complexing and enhanced transfer of cations to the electrolyte.

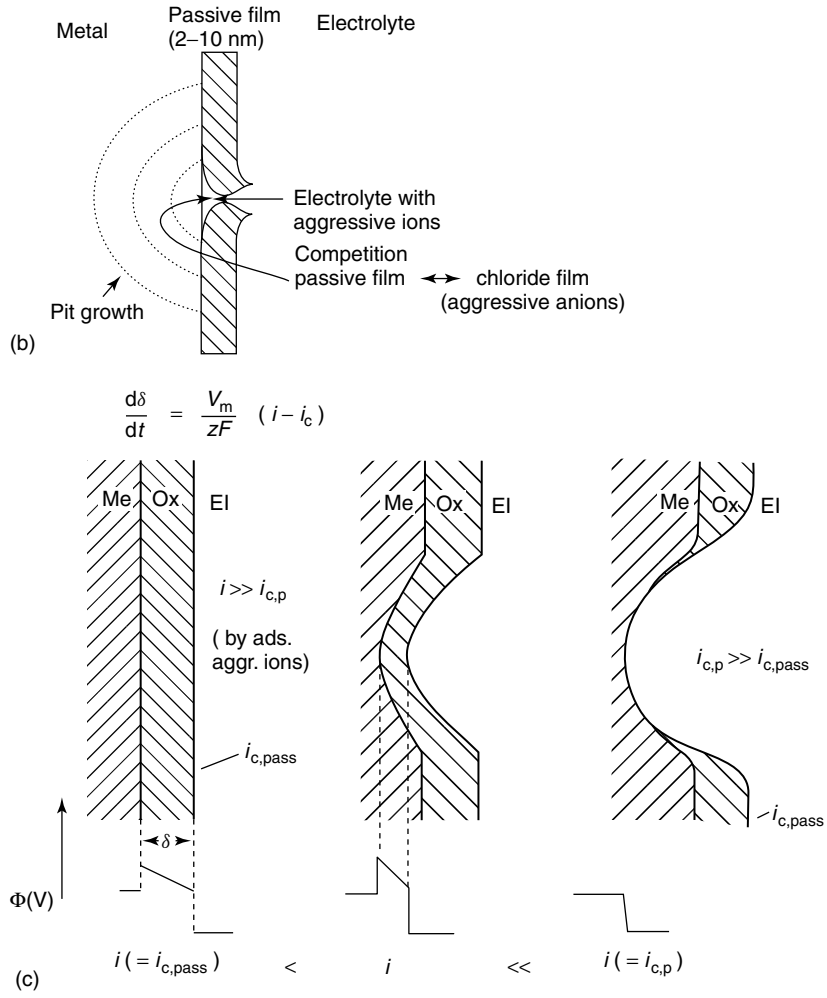


Fig. 15 (*Continued*)

in the range of μA cm^{-2}. This, however, contradicts a nucleation time of <1 s or even in the ms range. Similarly, the results of Fig. 4 in Sect. 4.2.2.4 contradict the penetration as the leading mechanism. A sudden decrease of the potential reduces the electrical field strength within the layer, which increases again during its thinning with time. The electrical field, however, is the driving force for the migration of anions into and through the layer. For this reason, film breaking has been postulated as the effective mechanism for pit nucleation for a nonstationary state of the layer.

The point defect model of passivity and its breakdown is a variant of the penetration mechanism [51]. The transport of cations from the metal surface to the oxide–electrolyte interface corresponds to an inward movement of cation vacancies V_{M^+}. This inward transport of V_{M^+} is supported by their high concentration at

the oxide surface. This in turn is favored by a small concentration of anion vacancies $V_{O^{2-}}$ at the oxide surface because both vacancy concentrations are inverse to each other corresponding to the equilibrium of a Schottky pair formation. The concentration of anion vacancies decreases by incorporation of Cl^- from the electrolyte. If the transfer of cation vacancies into the metal is slower than their transport to the oxide–metal interface so that they accumulate at the metal surface, the related voids may lead to a local breakdown of the passive layer. This situation has been discussed quantitatively; and with a sufficiently large number of parameters, one can describe the dependence of the critical potentials on the concentration of aggressive anions. There are, however, criticisms on the details of the point defect model in literature. In many cases, the growth of passive layers follows the high-field mechanism with exponential and not linear transport equations as assumed in the original paper because of the very high field strength of several 10^6 V cm^{-1}.

Several observations discussed in the following sections support either the film breaking or the adsorption mechanism for the nonstationary or stationary conditions of the passive film.

4.2.4.2 Film-breaking Mechanism

As mentioned already for the discussion of the penetration mechanism, pit nucleation is an extremely fast process of a few ms only for nonstationary conditions of the passive layer. Stepping of the potential in either direction, positive or negative, causes excessive formation of corrosion pits, especially for potentials well above the critical value and in the presence of a high concentration of aggressive anions. Even for stationary conditions, a fast nucleation of many pits is observed for sufficiently positive potentials and high chloride contents. The sequence of STM images of Fig. 8 demonstrates clearly that pits for nonstationary passive layers start with small cracks in the nm range, that is, of the thickness of the passive film, which develop to a polygonal shape during their further growth. These observations support the film-breaking mechanism.

If these defects in the film are cracks that occur during potential changes, they should be detected by their intense metal dissolution even in the absence of aggressive anions. The defects should be numerous and the local current density should be large so that dissolving cations may be detected with a Rotating Ring Disc Electrode (RRDE). Iron is a suitable metal for these studies as it dissolves as Fe^{2+} within the pits, whereas Fe^{3+} is formed at the surface of the passive layer. Therefore, these cations may be detected at a Pt-ring by their oxidation to Fe^{3+}. A step to negative potentials clearly shows a transient of Fe^{2+} formation as shown for a transient of an Fe-disc in 0.5 M H_2SO_4 from $E = 1.30$ to 0.70 V [52]. This is a consequence of the formation of many defects within the passive layer and the related Fe-dissolution at their surface. The absence of aggressive anions leads to a rapid repassivation. Therefore, only an intermediate dissolution could be found. In the presence of halides, these defects would develop to visible pits. These studies give further proof that potential changes cause multiple cracking of the passive layer. The related defects are the sites of pit nucleation. Electrostriction or chemical changes within the passive layer may serve as a reasonable explanation for the development of stress within the film, which initiates the observed defects.

Measurement of the electrochemical current noise is aimed at correlating the observed current fluctuations with breakdown and repair events that might lead to the formation of stable growing pits [53, 54]. In view of this mechanistic interpretation, the application of statistical methods to the occurrence of current spikes and the observed probability of pit formation lead to a stochastic model for pit nucleation. The evaluation of current spikes in the time and frequency domain yields parameters such as the intensity of the stochastic process λ and the repassivation rate τ [53]. They depend on parameters such as the potential, state of the passive layer, and concentration of aggressive anions.

4.2.4.3 Adsorption Mechanism

Several experimental results support the adsorption mechanism for stationary conditions of the passive layer. Even the stationary passive current density depends on the composition of the electrolyte. For iron in 0.5 M H_2SO_4, the passive current density is 7 $\mu A\,cm^{-2}$, whereas less than 1 $\mu A\,cm^{-2}$ is detected in 1 M $HClO_4$. From these observations, a catalysis for the transfer of Fe^{3+} from the passive layer to the electrolyte by SO_4^{2-} ions was concluded [55, 56]. Similarly, the dissolution Ni^{2+} from passive nickel and nickel base alloys is accelerated by organic acids like formic acid and leads to a removal of NiO from the passive layer [57]. Additions of citrate to the electrolyte cause the thinning of passive layers on stainless steel and increase its Cr content [58]. Apparently Fe and Ni ions are complexed at the surface of the passive film, which causes an enhancement of their dissolution into the electrolyte. It should be mentioned that the dissolution of Cr^{3+} apparently is not catalyzed by these anions and remains within the passive layer. This is a reason for its protecting properties, which will be discussed in detail later.

Similar mechanisms are effective in the presence of halides. These details have been studied for the passivity and its breakdown of iron in solutions containing chloride and fluoride [59–62] and of nickel in the presence of fluoride [61–63]. Fluoride is a well-suited model system because it has a very strong effect on the enhanced dissolution of the passive layer and its final general breakdown in acidic electrolytes. Breakdown of passivity of iron by fluoride has been followed with the RRD-electrode and XPS-studies (Fig. 16) [59]. In acidic electrolytes, the steps of passivity breakdown are well separated and affect the total surface. The addition of fluoride increases the dissolution rate to an intermediate value, which changes with the first order of the HF concentration. After one to two hours, Fe shows current oscillations that finally lead to a complete breakdown of passivity. These oscillations are closely related to Fe^{2+}-formation, which is detected at the analytical half ring R_1. Similarly, the complete breakdown results in intense Fe^{2+}-production. The intermediate increase of the passive current density refers to Fe^{3+}-formation, which unfortunately cannot be detected at the analytical half ring R_2. The strong complex $[FeF_5H_2O]^{2-}$ in solution cannot be reduced at reasonable ring potentials. A similar dependence is found for the increase of the passive current density on Ni in HF solution [63] and the locally increased dissolution in the passive state of Fe in chloride solution [60]. The enhancement of the passive current density suggests a thinning of the passive layer according to the adsorption mechanism. This has been found for Fe and Ni in fluoride-containing solutions [63, 64], but

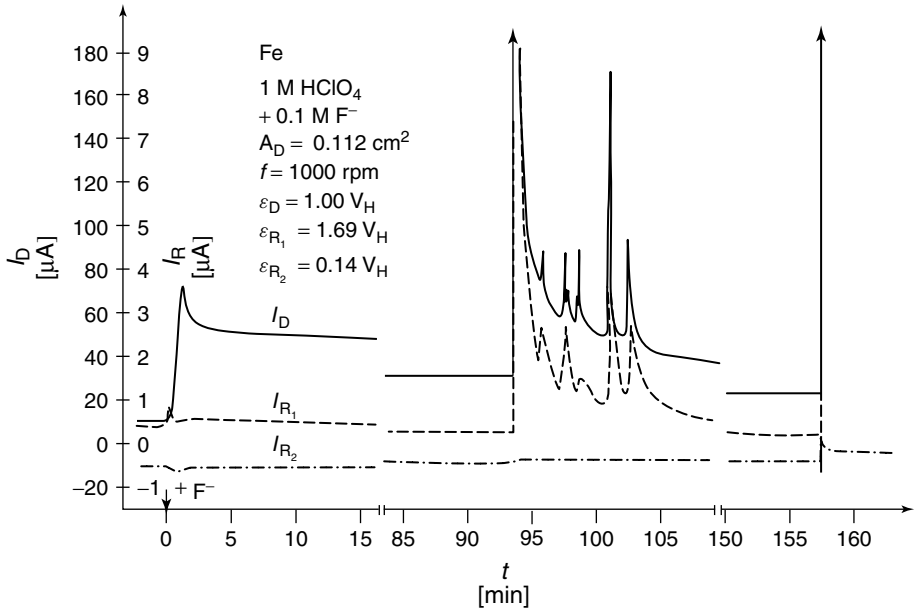


Fig. 16 The stages of breakdown of passivity of iron in 1 M $HClO_4$ after addition of 0.1 M HF at $t = 0$ min examined with a RRD electrode with a Pt split-ring and an Fe-disc of A = 0.112 cm^2, 2 h prepassivation of Fe-disc at $E = 0.1$ V in 1 M $HClO_4$, Fe^{2+} detection at ring 1 (I_{R1}) parallel to current transients and final increase of I_D at the Fe disc [59].

also for Fe in solutions of the other halides such as Br^-, Cl^-, and I^- with XPS [64].

These findings suggest that the strong complexing properties of the halides cause the formation of strong surface complexes with the cations at the oxide surface. The transfer of these complexes is apparently very much enhanced, which causes a thinning of the passive layer and the establishment of a new stationary situation with a higher electrical field strength within the film and an increased dissolution rate. Fluctuations of this dissolution process lead to a temporary and finally to a complete breakdown of passivity. The mentioned electrochemical reaction order of one suggests the fast formation of a surface complex with one halide, which is described for the case of Fe in HF solution by the equilibrium of Eq. (17). After its transfer into the electrolyte according to the rate-determining step of Eq. (18), it is further complexed in a solution according to the fast reaction of Eq. (19).

$$Fe^{3+}(ox) + HF(aq) \longleftrightarrow FeF^{2+}(ad) + H^+(aq) \quad (17)$$

$$FeF^{2+}(ad) \longrightarrow FeF^{2+}(aq) \quad (18)$$

$$4HF + H_2O + FeF^{2+}(aq) \longrightarrow FeF_5{}^{2-}H_2O(aq) + 4H^+(aq) \quad (19)$$

The analysis of this mechanism leads to a first-order reaction with respect to the halides. The general breakdown of passivity by fluoride in comparison to the local effect by the other halides should be seen by their strong complexing properties. The intermediate enhanced dissolution in the passive state with a

higher dissolution rate and a thinner passive layer will be followed by statistical breakdown and repair events with a final and permanent breakdown. These stages can be followed in detail for Fe in acidic fluoride solution due to the general attack of the passive layer but should be similar for the other halides. Once the passive film has been removed completely or locally, the intense dissolution of the unprotected metal surface is a consequence. This high local or general corrosion rate will stabilize the situation as is discussed for a stable pit growth.

The influence of anions can also be seen more quantitatively by the stability constants K of their complexes with the cations of the passive layer as presented in Table 1. They refer to the reaction described by Eq. (20). The constants K^* refer to the equilibrium with HF that is the species in acidic electrolytes owing to the weakness of this acid.

$$\mathrm{Me}^{z+} + X^- \longleftrightarrow \mathrm{Me}X^{(z-1)+}$$
$$K_1 = \left\{ \frac{[\mathrm{Me}X^{(z-1)+}]}{[Me^{z+}][X^-]} \right\} \qquad (20)$$

The electrochemical reaction order of one leads to the formation of the cation complex with one anion. This complex has less positive charge and thus requires less activation energy for its transfer from its potential well within the matrix of negatively charged O^{2-} ions at the oxide surface to the electrolyte. The stability constants for fluorides are very large, especially in the case of Fe^{3+}, which causes an attack all over the passive layer. The smaller constants for the other anions yield a preferential attack at special surface sites, which are more prone to complexing than others. In alkaline solutions, there exists a competition of halides and OH^- for surface cations with smaller nucleation rates and a transition of general breakdown to localized corrosion in the case of fluoride.

Discussions on the mechanism of pitting should include the special role of chromium. Pure Cr is not susceptible to pitting and resists the attack of all halides. Similarly, it stabilizes the surface of Fe–Cr alloys and stainless steel. The pitting potential increases with the Cr content of the metal. For most halides, the stability constants for Cr^{3+}-complexes are relatively small with the exception of fluoride. Furthermore, the situation of Cr^{3+} is very special because of the very slow exchange rate of its ligands in the first coordination shell. This is a consequence of the large ligand field stabilization of Cr^{3+} complexes with octahedral coordination with 3 electrons in the lower t_{2g} and none in the higher e_g level. This situation causes an extremely slow exchange rate to form a

Tab. 1 pK-values of stability constants of metal ion complexes with halides for the reaction: $\mathrm{Me}^{z+} + X^- \longrightarrow \mathrm{Me}X^{(z-1)+}$ including constants referring to HF (*) in acidic solutions [65]

Anion	Fe^{3+}	Ni^{2+}	Cr^{3+}
F^-/HF (*)	5.17/2.26 (*)	0.66	4.36/1.42 (*)
Cl^-	0.62	−0.25	−0.65
Br^-	−0.21	−0.12	−2.65
I^-	1.30	–	−5.0

surface complex $CrCl^{2+}$ and the dissolution via surface complexes gets negligibly small. Cr_2O_3 and $CrCl_3$ are described as insoluble in cold water. It is however a slow dissolution rate rather than the insolubility of these compounds, as they dissolve readily when heated in water. As a consequence, Cr has an extremely small dissolution current density in the passive state and is resistant to localized corrosion by halides. For these reasons, Cr is a well-protecting alloying element in stainless steel and other Cr-containing alloys.

4.2.4.4 Current Noise and Metastable Pitting

Many authors try to analyze current oscillations that are closely related to pitting events. These current transients in the range of 10 nA to some μA decrease with the prepassivation time of a specimen, the potential, and the chloride concentration. Their shape with a parabolic increase in time and an abrupt decrease or the reverse behavior has also been related to the presence or absence of MnS, respectively. It is proposed that these current oscillations are related to breakdown and repassivation events at inclusions or at the passivated metal surface [47]. Related studies have been performed close to the pitting potential in which the nucleation and growth of pits is probabilistic [66]. Some pits enter the stage of stable growth after some time with a related continuous but shaky increase of the current density. However, the birth and the initial growth of a pit is a complex interaction of several factors like the potential, the composition of the electrolyte, like its chloride concentration and pH, the composition of the metal surface including the role of inclusions, and the composition and structure of the passive layer. Therefore related questions on the mechanism are still under discussion and not solved. The situation is better defined at more positive potentials well above the pitting potential in which, however, the special role of inclusions is no longer separated from an intense influence of the other mechanisms of pit nucleation as discussed in Sects. 4.2.4.1 to 4.2.4.3. In any case, the accumulation of aggressive anions seems to be essential for the stage of metastable pitting and especially the further growth of a pit. Inside the pit, a sufficient concentration of aggressive anions is required to prevent repassivation so that the pit may grow and finally will enter the stage of stable growth.

An interesting discussion of current measurements on microdimensional electrodes of stainless steel wires is given by Mattin and Burstein [67]. Their analysis of current transients at a very low level in chloride-containing 0.075 M $HClO_4$ leads to the distinction of metastable and stable pits. According to their discussion, the remaining passive layer protects the pit analyte from being diluted from the bulk solution. Only when the film breaks off too will small pits repassivate, whereas a few larger ones are deep enough to keep their local environment undiluted so that they survive. A similar discussion by Newman's group, for pitting close to the critical potential of stainless steel, assumes covered pits for an early stage, which keep the accumulated corrosion products inside the pit with even a precipitation of a salt film as discussed previously in Refs. [68, 69]. The more effective transport at the pit edge causes a preferential passivation at the orifice and an undercutting during continued dissolution with a remaining passivated metal layer forming a cap. This layer is perforated from inside leading to a complicated structure as shown in Fig. 10. All these discussions are in agreement to the concept of the accumulation of aggressive

anions as a necessary condition to avoid the formation of a passive layer and to maintain pit growth. If the local dissolution current density $i_{c,p}$ close to the pitting potential is small, a covered pit is required to maintain the corrosive environment. At more positive potentials, $i_{c,p}$ is large enough to stabilize the pit electrolyte for an open pit. This simpler geometry permits a better quantitative description as given in Sect. 4.2.3.6 by Eqs. 5a, 8, and 9. However the main mechanisms for pit growth with prevented repassivation due to accumulated aggressive anions are the same.

4.2.4.5 Mechanistic Consequences for Breakdown of Passivity

In the light of these experimental results and arguments, pit nucleation can be explained by the film-breaking or the adsorption mechanism. For nonstationary conditions of the passive layer, the observation of Fe^{2+} dissolution transients are a good argument for frequent breakdown and repair events even in absence of halides. In their presence, repair of defects will not occur with the related formation of pits. Pit nucleation is very much increased after potentiostatic potential pulses caused by more frequent film breakdown. Pits may form in much less than one second and many more pits are observed even when the potential of a prepassivated specimen is pulsed to more negative values before the addition of chloride to the solution. This contradicts the penetration mechanism caused by the reduced electrical field strength within the film.

For stationary conditions, the passive layer is more effectively attacked via the adsorption mechanism. Strong support is provided by the increased dissolution in the passive state and the observed breakdown of passivity of iron by fluoride running through three stages. XPS studies prove the thinning of the passive layer by complexing anions.

In the vicinity of the pitting potential and for open-circuit conditions, inclusions play a decisive role for the nucleation of pits including the occurrence of microcrevices and the stabilization of the pit electrolyte at these sites.

In any case, the presence of aggressive anions seems to play a decisive role. The adsorption mechanism and the influence of complexing properties of halides include the chemical aspects for the mechanism, which is ignored in most papers. Besides, for the nucleation of pits, halides are also important for their further growth, which will be discussed in the next section.

4.2.4.6 Factors Stabilizing Pit Growth

The stabilization of the growth of corrosion pits may be influenced by several complicating factors depending on the state of their development. However, the presence of halides within the electrolyte is a necessary condition. Pit growth will stop when halide-containing electrolytes are replaced by halide-free solutions [70]. One needs a bulk concentration of at least 0.0003 M to cause stable pit growth [6, 14, 29]. Furthermore, the repassivation kinetics of pits are closely related to the transport of locally accumulated halides to the bulk electrolyte [19, 29]. These details are explained best by the complexing properties of the halides. The accumulation of corrosion products and consequently of halides prevents film repair and the repassivation of corrosion pits. Any oxide formation will stop immediately because of the large local concentration of complexing halides.

Potential drops are frequently used to explain a shift of the local potential from its potentiostatically fixed value

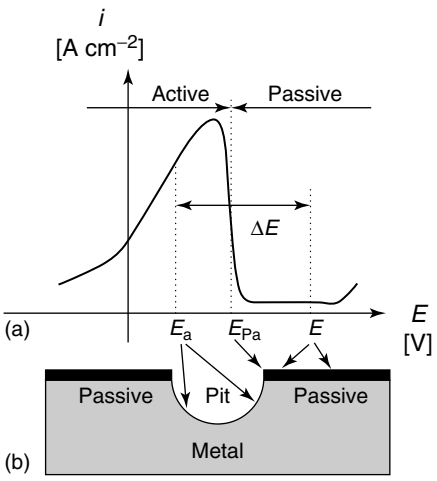


Fig. 17 (a) Polarization curve of a metal with active and passive potential range and passivation potential E_{pa}, (b) passivated metal with actively corroding pit, potential drop $\Delta E = E - E_a$ shifting the local potential from the potentiostatically fixed value E to E_a below E_{pa} in the active range of the polarization curve for large or covered pits and narrow deep crevices only.

to the range of active metal dissolution [34, 35, 71] (Fig. 17). Although a shift of about 1 V is reasonable for deep crevices, large pits, and especially covered pits, this explanation will not be sufficient for open pits with μm dimensions, a stage through which all pits have to pass. Large potential shifts have been measured within pits of mm dimensions [33–35] especially in solutions of low conductivity but they cannot occur within pits of μm and sub μm size. Similar problems are encountered with pH shifts. Even though local acidification may lead easily to a pH of 4 to 3, this is not a sufficient condition to prevent repassivation. Passivity is found for metals like Fe, Ni, and stainless steel even in strongly acidic electrolytes. The usual −60 mV/pH shift cannot change the potentiostatically fixed potential locally to the active range of the polarization curve even for large acidifications. There is a difference for metals like Cu, Al, and others, which follow the Poubaix diagram and, which cannot be passivated in strongly acidic electrolytes. Local acidification due to hydrolysis of corrosion products may be essential for these metals and may serve at least for a further stabilization of pitting. However, even in these cases, one cannot ignore that the presence of halides is required. Their chemistry seems to be the main basis for the nucleation of corrosion pits and the stabilization of pit growth on most metals and alloys.

In later stages, the precipitation of a salt film is a secondary stabilizing factor. This salt layer may serve as a reservoir for locally high halide concentrations and a barrier to take over a large portion of the potential drop stabilizing pitting at lower levels of the local current density. This precipitation is ruled by the product $i\sqrt{t}$ of Sand's equation (Eqs. 4 and 6). For $i\sqrt{t} < i\sqrt{\tau}$, open pits are stabilized by accumulated halides, whereas for $i\sqrt{t} > i\sqrt{\tau}$, a salt layer stabilizes additionally.

4.2.5 Conclusion

The aim of this chapter is to describe some basic experimental results and calculations that support the leading mechanisms of localized corrosion. There are two main mechanisms that cause breakdown

of passivity and pitting corrosion. The film-breaking mechanism is most effective for nonstationary situations of the passive layer, whereas the adsorption mechanism is more effective for its stationary state. The special complexing properties of halides are responsible not only for breakdown of passivity but also for the further pit growth at a high level of current density. This is the main chemical issue that gives a logical answer to why the halides are so special for pitting. Besides these chemical properties as the primary stabilizing factor, several secondary effects stabilize a corrosion pit at a later stage of its growth as salt film formation, potential drops, and acidification. The chemistry of the metal and metal components of alloys gives further explanations with respect to the observations to pitting corrosion. Cr stabilizes the passive layer due to the extremely slow dissolution kinetics of its compounds. As a consequence, it will automatically accumulate within the passive layer of alloys and gives an extremely good protection against general and localized dissolution. The effect of some metals like Mo is discussed, but is still very controversial. It however seems reasonable that the precipitation of insoluble halides like $MoCl_3$ or $MoCl_2$ is a good explanation for its protecting properties against localized corrosion in many technically applied alloys.

References

1. S. Szklarska-Smialowska, *Pitting Corrosion of Metals*, NACE International, Houston, Tex., 1986.
2. H. Böhni in *Corrosion Mechanisms* (Ed.: F. Mansfeld), Marcel Dekker, New York, 1987, p. 285.
3. H.-H. Strehblow in *Corrosion Mechanisms in Theory and Praxis* (Eds.: P. Marcus, J. Oudar), Marcel Dekker, New York, 1995, pp. 201–237; 2002, pp. 243–285 (2nd edition).
4. H.-H. Strehblow in *Corrosion and Environmental Degradation* (Ed.: M. Schütze), Wiley-VCH, Weinheim, New York, 2000, pp. 52–61.
5. Ya. Kolotyrkin, V. A. Gilman, G. M. Florianovich, *Dokl. Akad. Nauk* **1963**, *148*, 113.
6. K. J. Vetter, H.-H. Strehblow, *Ber. Bunsen-Ges. Phys. Chem.* **1970**, *74*, 449, 1024.
7. H.-H. Strehblow, B. Titze, *Corros. Sci.* **1977**, *17*, 461.
8. W. Schwenk, *Corrosion* **1964**, *20*, 129t.
9. H.-H. Strehblow, *Habilitationsschrift*, Freie Universität Berlin, Berlin, 1977, pp. 148–154.
10. J. W. Oldfield, *Int. Mater. Rev.* **1987**, *32*(3), pp. 1–18.
11. ASTM G61-78, *Standard Practice for Conducting Cyclic Potentiodynamic Polarization Measurements for Localized* Corrosion, American Society for Testing and Materials, Philadelphia, Pa.
12. H. Prinz, H.-H. Strehblow, *Corros. Sci.* **1998**, *40*, 1671.
13. ASTM G48-76, *Standard Methods for Pitting and Crevice* Corrosion, *Resistance of stainless steel and Related Alloys by Use of Ferric Chloride Solution*, American Society for Testing and Materials, Philadelphia, Pa.
14. H. J. Engell, N. D. Stolica, *Z. Phys. Chem. N.F.* **1959**, *20*, 113.
15. H. Kaesche, *Z. Phys. Chem. N.F.* **1962**, *34*, 87.
16. S. Haupt, H.-H. Strehblow, *Langmuir* **1987**, *3*, 873.
17. H.-H. Strehblow, M. B. Ives, *Corros. Sci.* **1976**, *16*, 317.
18. H.-H. Strehblow, J. Wenners, *Z. Phys. Chem N.F.* **1975**, *98*, 199.
19. H.-H. Strehblow, *Werkst. Korros.* **1976**, *27*, 792.
20. H.-H. Strehblow, J. Wenners, *Electrochim. Acta* **1977**, *22*, 421.
21. Th. R. Beck, R. C. Alkire, *J. Electrochem. Soc.* **1979**, *126*, 1662.
22. G. S. Frankel, B. M. Rush, C. V. Jahnes et al., *J. Electrochem. Soc.* **1991**, *138*, 643.
23. A. Seghal, D. Lu, G. S. Frankel, *J. Electrochem. Soc.* **1998**, *145*, 2834.
24. G. S. Frankel, *Corros. Sci.* **1990**, *30*, 1203.
25. G. S. Frankel, J. R. Scully, C. V. Jahnes, *J. Electrochem. Soc.* **1996**, *143*, 1834.
26. V. Maurice, V. Inard, P. Marcus, Proceedings of the symposium critical factors in localized corrosion III in *194th Meeting*

of the Electrochemical Society, November 2–6, 1998 (Eds.: R. G. Kelly, P. M. Natishan, G. S. Frankel et al.), The Electrochemical Society Proceedings Series, PV 98-17, The Electrochemical Society, Boston, Pennington, N.J., 1998, pp. 552–562.
27. H.-H. Strehblow in *Corrosion Mechanisms in Theory and Practise* (Ed.: P. Marcus), Marcel Dekker, New York, 2002, pp. 243–285.
28. N. J. Laycock, R. C. Newman, *Corros. Sci.* **1997**, *39*, 1771.
29. H.-H. Strehblow, *Werkst. Korros.* **1984**, *35*, 437.
30. J. Newman, D. N. Hansen, K. J. Vetter, *Electrochim. Acta* **1974**, *22*, 829.
31. G. Engelhardt, H.-H. Strehblow, *J. Electroanal. Chem.* **1994**, *365*, 7.
32. F. H. Hunkeler, H. Böhni, *Werkst. Korros.* **1983**, *34*, 593.
33. G. Herbsleb, *Dissertation*, Bonn, Germany, 1962.
34. H. W. Pickering, R. P. Frankenthal, *J. Electrochem. Soc.* **1972**, *119*, 1297, 1304.
35. K. Cho, H. W. Pickering, *J. Electrochem. Soc.* **1990**, *137*, 3313.
36. H.-H. Strehblow, K. J. Vetter, A. Willgallis, *Ber. Bunsen-Ges. Phys. Chem.* **1971**, *75*, 823.
37. H. Fischmeister, U. Roll, *Z. Fresenius Anal. Chem.* **1984**, *319*, 639.
38. S. Haupt, H.-H. Strehblow, *Corros. Sci.* **1995**, *37*, 43.
39. M. P. Ryan, N. J. Laycock, R. C. Newman et al., *J. Electrochem. Soc.* **1998**, *145*, 1566.
40. A. Thies, J. W. Schultze, *Mater. Corros.* **1996**, *47*, 146.
41. T. Jabs, P. Borthen, H.-H. Strehblow, *J. Electrochem. Soc.* **1997**, *144*, 1231.
42. U. Wolff, Bildung und Stabilität von anodischen Deckschichten auf Eisen-Silizium-Leyierungen, *Dissertation*, Technische Universität Dresden, Germany.
43. C. Schmidt, H.-H. Strehblow, *Surf. Interface Anal.* **1999**, *27*, 984.
44. Chemical Rubber Co, *Handbook of Chemistry and Physics*, 58th ed., CRC Press, Cleveland, Ohio, 1977, p. B133.
45. R. Newman, *International Workshop on Long-term Extrapolation of Passive Behavior*, Washington, D.C., 2001.
46. H. J. Grabke, *Iron Steel Inst. Jpn* **1996**, *36*, 777.
47. B. Baroux in *Corrosion Mechanisms in Theory and Practice* (Eds.: P. Marcus, J. Oudar), Marcel Dekker, New York, 1995, p. 274–278.
48. T. Suter, H. Böhni, *Electrochim. Acta* **1997**, *42*, 3275.
49. W. P. Yang, D. Costa, P. Marcus, *Oxide Films on Metals and Alloys* (Eds.: B. MacDougall, R. S. Alwitt, T. A. Ramanarayanan), PV 92-22, The Electrochemical Society, Princeton, N.J., 1992, p. 516.
50. S. Mischler, A. Vogel, H. J. Mathieu et al., *Corros. Sci.* **1991**, *32*, 925.
51. C. Y. Chao, L. F. Lin, D. D. Macdonald, *J. Electrochem. Soc.* **1981**, *128*, 1191, 1194.
52. B. P. Löchel, H.-H. Strehblow, *Werkst. Korros.* **1980**, *31*, 353.
53. U. Bertocci, Advances in localized corrosion in *NACE Proceedings of 2nd International Conference on Localized Corrosion* (Eds.: H. S. Isaacs, U. Bertocci, J. Kruger et al.), NACE, Orlando, Fla., Houston, 1987, p. 127.
54. J. Steward, D. E. Williams, *J. Electrochem. Soc.* **1981**, *128*, 131.
55. H.-H. Strehblow, *Dissertation*, Freie Universität Berlin, Berlin, Germany, 1971.
56. K. J. Vetter, F. Gorn, *Electrochim. Acta* **1973**, *18*, 321.
57. S. Benamar, Effets des Acides Organiques sur la Corrosion et la Passivation du Nickel et d'Alliages a Base de Nickel, Thesis, Université Pierre et Marie Curie, Paris, 1998.
58. I. Milosev, H.-H. Strehblow, *Biomed. Mater. Res.* **2000**, *52*, 404.
59. B. P. Löchel, H.-H. Strehblow, *Electrochim. Acta* **1983**, *28*, 565.
60. K. E. Heusler, L. Fischer, *Werkst. Korros.* **1976**, *27*, 551.
61. H.-H. Strehblow, B. Titze, B. P. Löchel, *Corros. Sci.* **1979**, *19*, 1047.
62. H.-H. Strehblow, B. P. Löchel in *Passivity of Metals and Semiconductors* (Ed.: M. Froment), Elsevier Science Publishers, New York, 1983, p. 379–386.
63. B. P. Löchel, H.-H. Strehblow, *J. Electrochem. Soc.* **1984**, *131*, 713, 522.
64. W. Khalil, S. Haupt, H.-H. Strehblow, *Werkst. Korros.* **1985**, *36*, 16.
65. L. G. Sillén, *Stability Constants of Metal Ion Complexes*, Suppl. 1, Special Publ. 25, The Chemical Society, Burlington House, London, 1971, p. 167, 171, 217.
66. U. Bertocci, Y. Yang-Xiang, *J. Electrochem. Soc.* **1984**, *131*, 1011.
67. S. P. Mattin, G. T. Burstein in *Progress in the Understanding and Prevention of Corrosion* (Eds.: J. M. Costa, A. D. Mercer), Institute of Materials, London, 1993, pp. 1109–1114.

68. P. Ernst, N. J. Laycock, M. H. Moayed et al., *Corros. Sci.* **1997**, *39*, 1133.
69. N. J. Laycock, S. P. White, J. S. Noh et al., *J. Electrochem. Soc.* **1998**, *145*, 1101.
70. H. J. Engell, N. D. Stolica, *Arch. Eisenhüttenwesen* **1959**, *30*, 239.
71. G. Herbsleb, H. J. Engell, *Z. Elektrochem.* **1961**, *65*, 881.

4.3 Intergranular Corrosion

John R. Scully
Professor of Materials Science and Engineering, Department of Materials Science and Engineering, University of Virginia, Charlottes Ville, VA, 22904

4.3.1 Introductory Comments and Definition of Intergranular Corrosion

4.3.1.1 Conceptual Descriptions of Intergranular Corrosion

Intergranular corrosion (IGC) in polycrystalline materials involves preferential corrosion at or in regions adjacent to grain boundaries [1]. The surfaces created in this manner expose individual grain facets on either side of the original boundary. Figure 1 illustrates a cross-sectional slice through a polycrystalline material that has undergone intergranular attack (IGA). (IGC is referred to as preferential corrosion at or adjacent to grain boundaries of a metal or alloy. Intercrystalline corrosion has the same meaning. IGA is often used to describes damage at grain boundaries caused by IGC.) Figure 2 illustrates a plan view of an intergranular surface. This mode of corrosion occurs when either the kinetic rate and/or thermodynamic driving force for corrosion is greater at, or adjacent to grain boundaries compared to the grain interiors. The exposure of specific crystalline materials to certain environments can promote IGC. The requirements are a susceptible metallurgical condition (discussed below in the context of physical metallurgy concepts) and a specific chemical environment and set of electrochemical conditions that, in conjunction, promote the differences in corrosion dissolution behavior required to obtain such localized corrosive attack. Theoretically, IGC is driven by microstructural factors at the nanometer or micrometer scale, a specific environment, and electrochemical driving forces. Many electrochemical frameworks exist that do not involve a role for stress. However, in practice, mechanical driving forces are often not entirely absent. Therefore, IGC differs from intergranular stress corrosion cracking (IGSCC) (see Chapter 4.4 in Volume 4) because of lack of, or low levels of external applied stress or residual stress. Despite these differences in driving forces, many alloys that exhibit IGC are also found to be susceptible to IGSCC. However, this is not always the case.

4.3.1.1.1 Preexisting Active Dissolution Paths Based on Compositional and/or Structural Heterogeneity

A grain boundary itself or an adjacent region may corrode at a higher rate than the grain interior as a result of an enhanced thermodynamic and/or kinetic tendency for corrosion relative to the grain matrix. IGC could occur in a material with a grain boundary composition or structure that produces differences in the thermodynamic and/or kinetic properties governing corrosion (see Chapter 1.2 in Volume 4). In the preexisting active path IGC mechanism, the exposed grain boundary or adjacent material actively dissolves in the electrolyte while grain interiors are passive. The most prevalent and technologically significant forms of IGC occur when either a segregant is enriched at the grain boundary, an actively corroding precipitate phase forms at the boundary, or a beneficial element normally in solid solution is depleted from the boundary region. The vast majority of IGC examples involve one of these cases. Thus compositional, structural, or compositional and structural heterogeneity can promote IGC. The electrochemical frameworks for IGC

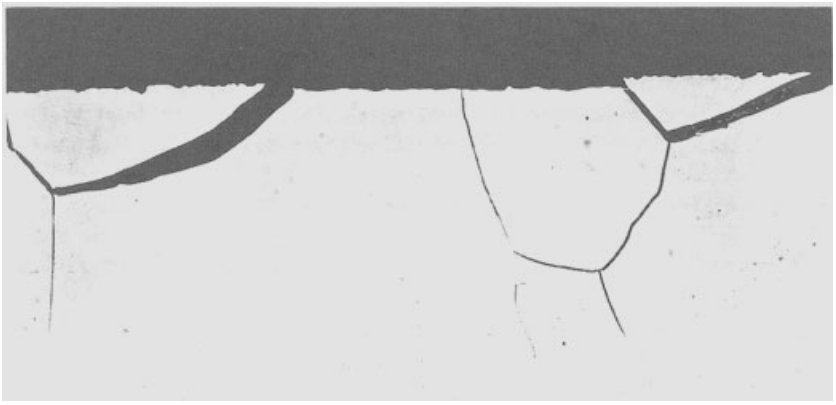


Fig. 1 Cross-sectional view of intergranular corrosion in a ''sensitized'' austenitic stainless steel alloy exposed to boiling $H_2SO_4 + FeCl_3$. Note that corrosion preferentially occurs along the grain boundaries. (From Corrosion of Stainless Steels A. John Sedriks, copyright © John Wiley & Sons. Reprinted by permission of John Wiley & Sons, Inc.)

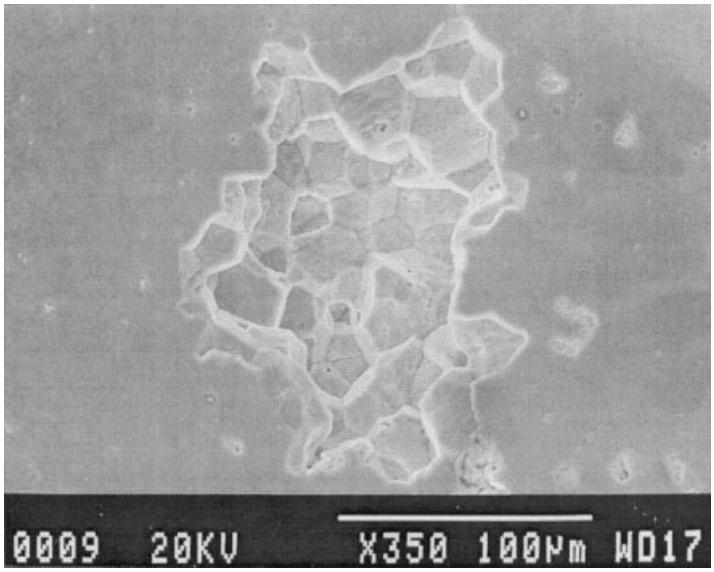


Fig. 2 Plan view of intergranular corrosion in a peak-aged Al-5.4% Cu-0.5% Mg-0.5% Ag (wt. %) alloy. Note that corrosion has occurred preferentially along the grain boundaries. (Micrograph provided by D. A. Little, University of Virginia.)

based on these situations are depicted in Figs. 3 and 4. In the scenario depicted by Fig. 3, the grain boundary and the grain interiors both dissolve at a sufficiently high potential; but since the grain boundary zone dissolves at a higher rate, some IGA would be observed arising from the difference in dissolution rate. A variation of this electrochemical framework involves the case in which the cathodic half-cell

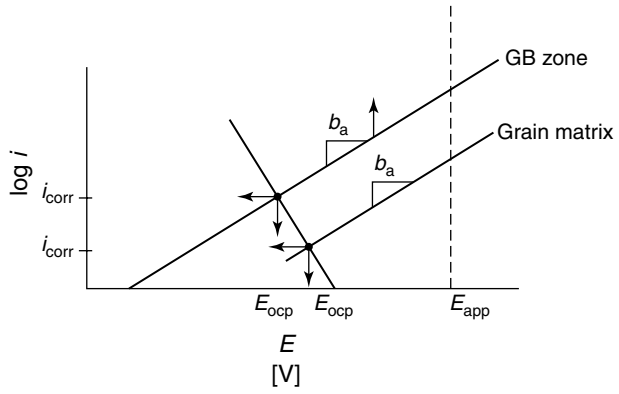


Fig. 3 Electrochemical framework for intergranular corrosion described by an Evans diagram depicting the anodic half-cell reaction kinetics for the grain boundary zone and the grain matrix. In this case, enhanced active dissolution occurs in both the grain boundary region and in the matrix. At a fixed potential, given by E_{app}, the anodic dissolution rate is accelerated along the grain boundary compared to the matrix.

reaction is also enhanced at the grain boundary either intrinsically or due to segregated impurities. In this case, open circuit corrosion can be enhanced along the grain boundary even if the anodic half-cell reaction rates on the grain boundary material are identical to those of the matrix. The situations described by Fig. 4(a, b) are given below.

4.3.1.1.2 **Dissolution Path Defined by Differences in Depassivation/Repassivation Properties of Metals with Protective Oxide**
Another form of IGC occurs when a material containing a passivating surface oxide film is depassivated (i.e. reactivated) or has a difficult time repassivating locally at grain boundaries such as when exposed in either oxidizing or reducing acids. Examples of solid solution alloys exhibiting this type of behavior include Fe-Cr and Fe-Cr-Ni alloys with grain boundary Cr depletion [2–4]. Both the primary passive and Flade potential of Fe-Cr alloys are a strong function of Cr content and solution pH (see Chapter 3.2 in Volume 4) [2, 5]. Greater than 10 to 13% Cr is typically required to lower the Flade or primary passive potential sufficiently and reduce the critical current density for passivity such that spontaneous passivity is observed in practice (although, the classic austenitic stainless steel popular for over 70 years is based upon the classic composition 18% Cr-8% Ni). (The exact Cr content in solid solution required for passivity depends on the specific environment.) Therefore, chemically induced depassivation and subsequent corrosion may occur preferentially at grain boundaries depleted in the average solid solution Cr content when exposed to certain oxidizing or reducing acids. Sometimes, IGA can occur in a reducing acid such as H_2SO_4 containing an oxidizing species that acts as a ''chemical potentiostat.'' The oxidizing agent accelerates the cathodic reaction rate and raises the global open circuit potential of the stainless steel. In these cases, the grain matrix containing a high Cr level

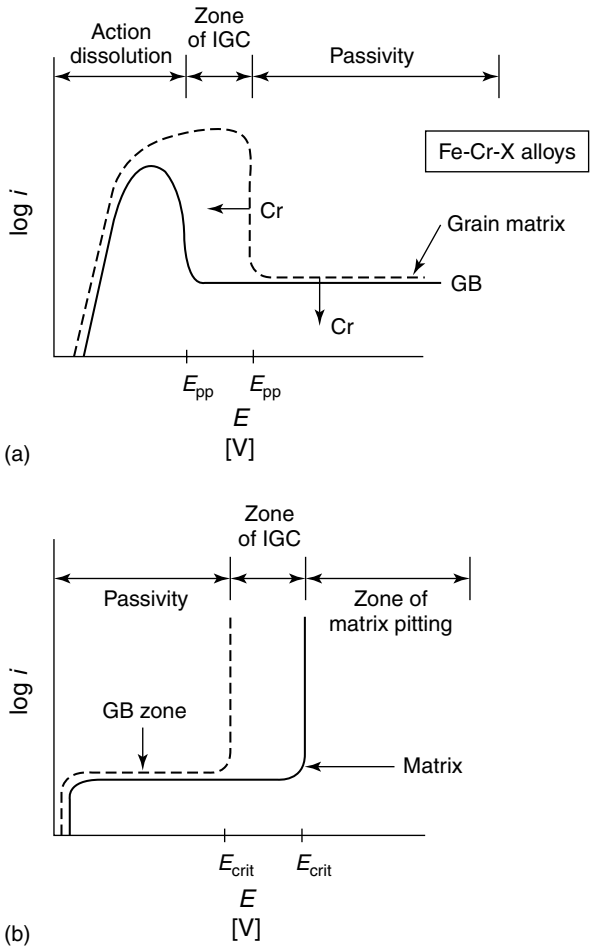


Fig. 4 Electrochemical frameworks for the intergranular corrosion of alloys that exhibit uniform passivity prior to sensitization in the environment given. Case (a) different primary passive potentials and active dissolution regions for the grain boundary and grain matrix such as is observed for Fe-Cr and Fe-Ni-Cr alloys. IGC occurs over the potential range at which the matrix is passive while the grain boundary is active. Case (b) different critical potential for grain boundary and matrix. The critical potentials have been shown to be associated with pitting, repassivation, and/or transpassive dissolution.

may remain passive while the Cr-depleted grain boundary reactivates and corrodes in the reducing acid. Hence, the potential range at which IGC is possible resides between the high potential associated with the passivation of the Fe-rich gb and the lower passivation potential of the Fe-Cr alloy matrix. The Fe-rich grain boundary

corrodes under active dissolution while the grain interior is passive. The electrochemical framework describing this type of IGC is shown in Fig. 4(a). Clearly, absence of a Cr compositional gradient at the boundary eliminates a zone that is susceptible to IGC. Such phenomena may occur in sensitized stainless steels when exposed in reducing acids possibly containing an oxidizer or in environments in which an occluded cell enables formation of a reducing acid at a local site as discussed below. Moreover, mechanically induced depassivation in less aggressive solutions, even high purity water, can lead to IGC and IGSCC along Cr-depleted grain boundaries. In this case, the region along the boundary that is depleted in Cr exhibits higher bare surface dissolution rates and slower repassivation rates compared to Fe-Ni-Cr alloys containing a greater amount of Cr in solid solution [6]. Note, however, that this scenario is not always the case. Extremely oxidizing environments such as concentrated nitric acid and oxalic acid tests at 1 A cm^{-2} detect carbide, sigma, and nitride phases instead of Cr depletion. This issue will be discussed below.

The last electrochemical framework for IGC also involves passive materials. IGC can occur when grain boundaries develop lower critical potentials associated with pitting or transpassivity. Pitting or transpassive dissolution then occurs preferentially along grain boundaries in solutions in which oxidizing conditions exist. This situation is shown in Fig. 4(b).

4.3.2 Critical Factors in Intergranular Corrosion

4.3.2.1 Metallurgical Factors

Grain boundaries in single-phase materials, defined as homophase interfaces, are regions separating grains of different crystallographic orientation but possessing the same crystal structure and composition. Homophase interfaces can have lower surface energies than other surfaces, as well as different local nanostructure and nanochemistry, compared to grain interiors. Such differences can establish a preferred IGC path. IGC is usually attributed to the following causes related to such homophase interfaces [7]:

1. Solute enrichment due to equilibrium segregation.
2. Solute enrichment or depletion due to nonequilibrium segregation effects.
3. Solute depletion due to slow volume diffusion coupled with fast grain boundary diffusion and heterogeneous precipitation of phases.
4. Preferential precipitation of detrimental phases at homophase interfaces by heterogeneous nucleation.

Note that the strain energy alone associated with homophase interfaces (i.e., grain boundaries) in high-purity metals does not appear to contribute greatly to the corrosion susceptibility of boundaries beyond some grain boundary grooving [8]. Hence, the most technologically significant causes of IGC are listed above. However, other mechanisms can exist. Single-phase alloys consisting of substitutional solid solutions may experience enhanced IGC susceptibility in certain environments, usually associated with dealloying of one of the elements in solid solution. Strain energy associated with substitutional solid solutions may explain this form of susceptibility.

4.3.2.1.1 Role of Grain Boundary Structure and Interface Energy at Homophase and Heterophase Interfaces

Differences in structure and energy result from the creation of a solid-state interface

even in high-purity metals. Homophase interface energy was first described by nearest-neighbor broken bond models [9], later by dislocations [10], and recently by atomic simulation [11]. Given the five macroscopic and three microscopic degrees of freedom of homophase boundaries, their structure and energy can vary greatly [9]. The variation of grain boundary misorientation, interface energy, and structure have long been known to be significant factors affecting grain boundary segregation [12], fracture [13], boundary creep-cavitation [14] and sliding [15], liquid metal embrittlement [16], intergranular corrosion [17–19], and stress corrosion [20]. Several studies indicate that coincident site lattice (CSL) boundaries are extremely resistant to these phenomena [19, 20] and that a material could be rendered more resistant by creating a network of these special resistant boundaries [21–23]. Kronberg and Wilson demonstrated that certain grain boundaries could be formed in which atoms in each grain were coincident with a certain fraction of atom positions in the adjacent grain [24]. For instance, in Fig. 5, 1/5 of the atoms in grain A are coincident with grain B. The boundary illustrated is a tilt boundary in a simple cubic type Bravais lattice with a 36.9° rotation of crystal A with respect to crystal B about a ⟨100⟩ type direction. A *coincident site lattice* is defined as the reciprocal of the density of coincident sites that would be common to both lattices after the rotation. For example, $\Sigma = 5$ in Fig. 5. One explanation for reduced IGC of certain boundaries is that dissolution of atoms shared by both lattices on either side of the boundary is more difficult than those atoms "dangling" with fewer nearest neighbors that can participate in bonding.

One proposal for IGC is related to crystallographic etch pit formation at grain boundaries. According to this theory, grain boundary susceptibility is related to the crystallographic facet exposed on the boundary and the different rates of dissolution of such facets. Bicrystal studies as

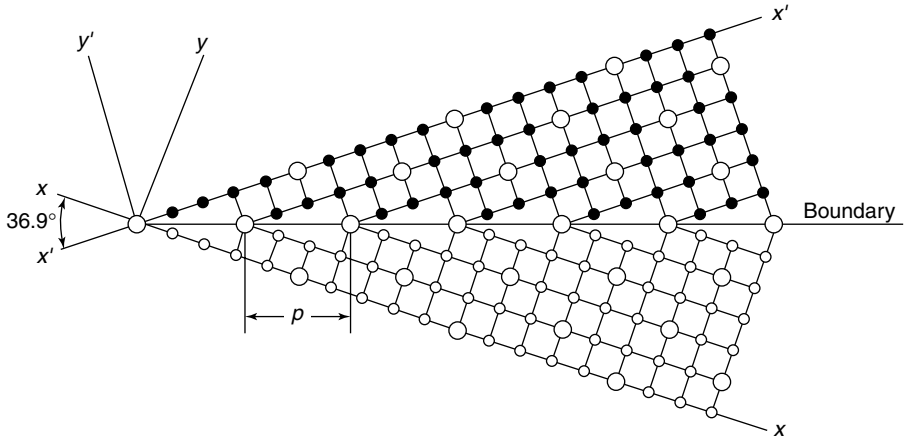


Fig. 5 A coincident site boundary based on a 36.9° tilt about ⟨100⟩ in a simple cubic lattice. One of every five lattice sites is coincident to both boundaries, $\Sigma^{-1} = 1/5$ or $\Sigma = 5$. (Ref. [25], from Physical Metallurgy Principles, 3rd edition by Reed-Hill/Abbaschian, © 1992. Reprinted with permission of Brooks/Cole, a division of Thomson Learning: www.thomsonrights.com, Fax 800 730-2215.)

a function of tilt and twist angle of cross-boundary misorientation consistently indicate a strong relationship between IGC as well as IGSCC susceptibility and misorientation angle with deep minima in susceptibility at certain "special" angles that have a high degree of coincidence including very low tilt angles below 15 to 20 degrees [17, 19, 20] as shown in Fig. 6. Some studies find a correlation between grain boundary energy, intergranular corrosion [19], as well as IGSCC [20] properties. However, such relationships are not always observed and, consequently, variation in grain boundary energy with a misorientation angle cannot be used alone to forecast all the grain boundary properties necessary to predict IGC or IGSCC. Unfortunately, there is currently no quantitative model that can predict precisely how segregation, IGC or IGSCC, varies with boundary structure.

Certain homogeneous single-phase, solid solution alloys are found to undergo IGC through a mechanism related to the grain boundary structure. In the case of homogeneous solid solutions that are not aged, a fundamental weakening of grain boundaries can occur through alloying to form substitutional solid solutions. Systems such as Cu-Au, Ni-Pd, and Ag-Au are homogeneous solid solutions that exhibit IGC in certain solutions [26–29]. Here, the Au or Pd solute are thermodynamically stable against oxidation in the aggressive oxidizing solutions (e.g. $FeCl_3$). The alloyed Cu or Ni actively dissolves preferentially (i.e. by dealloying) (see Chapter 2.3 in Volume 4). This type of IGC can be interpreted to occur by dealloying that occurs at higher rates along grain boundaries. One theory is that incorporation of a substitutional alloying element of different atomic size than the solvent element introduces strain energy. This strain energy is more easily accommodated along boundaries by the

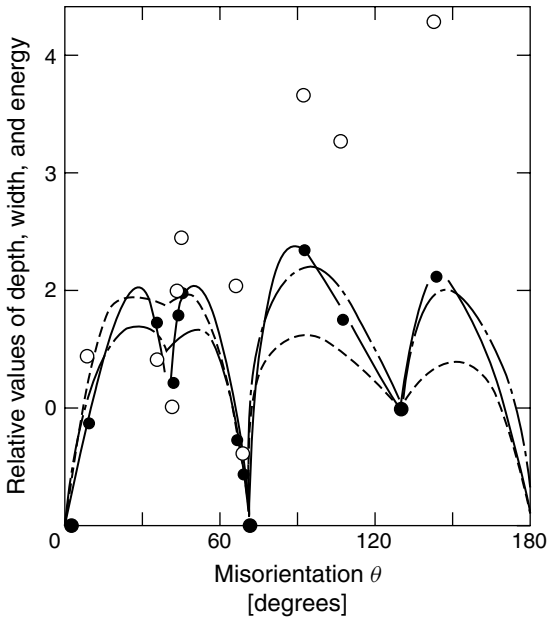


Fig. 6 Relationship between intergranular corrosion depth (●), width (○), and grain boundary energy (– – –) and misorientation angle for symmetric [110] tilt boundary in a Cu-9 at. % Al alloy. Deep minima are observed at specific angles such as 38.9° $\Sigma = 9$ (221) associated with certain CSL relations [19].

incorporation of dislocations. Elastic strain energy associated with dislocations or preferential dissolution of grain facets with certain crystallographic orientations drives preferential corrosion at grain boundaries. Moreover, alloying additions can have a secondary role of altering stacking fault energy (A lower stacking fault energy can create larger regions between partial dislocations that have the effect of hindering cross slip. In turn, coplanar slip prevails because dislocations cannot cross slip.) to enhance coplanar slip, which enlarges slip step size at boundaries. Consequently, dissolution can be enhanced at grain boundaries despite a substitutional solid solution alloy that is globally homogeneous in composition.

4.3.2.1.2 **Role of Local Composition Changes and Impurity Segregation** The chemical character of IGC-susceptible grain boundaries often differs as a result of segregation of detrimental impurities to boundaries or depletion of beneficial elements during precipitation and growth of a second phase. Such segregation often further lowers the energy of the interface [9]. Alternatively, segregation of foreign impurity atoms may change the corrosion properties of grain boundaries (e.g. sulfur, phosphorus, etc.). Detrimental impurities atoms (e.g. S, P in Fe, Pb, Sn in Fe, Bi in Cu, S in Ni, Mg in Al, etc.) are often dissolved in dilute solid solution within many engineering alloys [30]. The impurity atom may become enriched at grain boundaries (i.e. segregated and/or "trapped") with enrichment factors $>10\,000$, subject to the equilibrium or nonequilibrium thermodynamic processes governing the concentration of solute at such an interface [30].

It is instructive at this point to review the equilibrium or nonequilibrium thermodynamics governing interface segregation. Recall that grain boundaries are sinks in which impurities or solute might become concentrated. The thermodynamic description of equilibrium segregation involves redistribution of alloyed solute such that the total free energy of the system is minimized. For a two-component system such as a binary alloy, if one considers a dilute solution of component B dissolved as solute in solvent A, the surface excess of B at surfaces per unit area, Γ_B, is given by [7, 9]

$$\Gamma_B = -\left(\frac{1}{RT}\right)\frac{\partial\gamma}{\partial \ln X_B} \qquad (1)$$

Where γ is the boundary energy per unit area, X_B is the mole fraction of the solute component B, R is the universal gas constant, and T is temperature. (The formal definition of the Gibbs Adsorption Isotherm is $d\gamma = -\Sigma_i \Gamma_i d\mu_i$, where μ_i is the chemical potential of the component, i, in the solid solution. The expression listed in Eq. (2) is a simplification for a dilute, 2 component, ideal solid solution at constant temperature and pressure.) The significance of this equation is that segregation of B occurs on boundaries in A when such solute accumulation decreases the surface energy of the boundary. Stated another way, when surface energy decreases with increasing X_B, then the boundary excess, Γ_B, is positive. Conversely Γ_B is negative when surface energy increases with increasing solute enrichment. Consequently, grain boundary segregation would not be expected in the latter case. A number of different surface energy isotherms have been measured experimentally. It has been suggested that if $\partial\gamma/(\partial \ln X_B)$ is plotted as a function of the logarithm of the solid solubility limit of the solute for different binary alloys, a view of whether solute B promotes equilibrium surface and/or boundary segregation can be obtained as

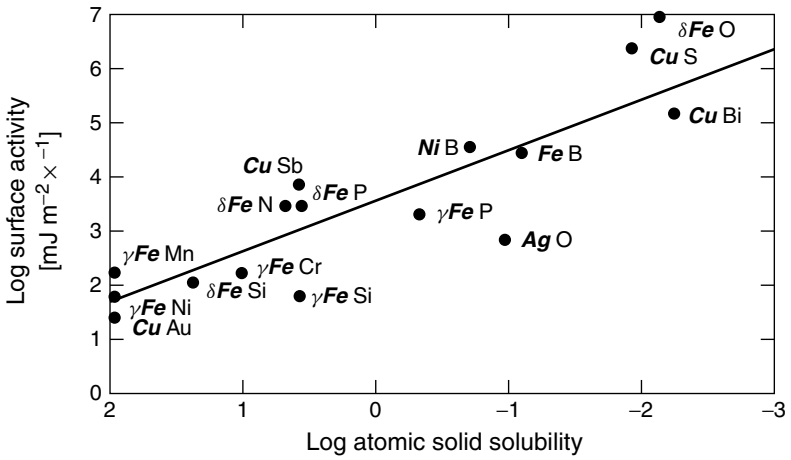


Fig. 7 Variation in surface activity for binary alloys versus log of atomic solubility. The solvent element is bold and italicized for each alloy. (Ref. [31], reprinted with permission from TMS The Minerals, Metals and Materials Society.)

shown in Fig. 7 [31]. This plot indicates that a characteristic of high surface activity is low solid solubility regardless of the exact alloy [9]. However, knowledge of $\partial\gamma/(\partial \ln X_B)$ is often not available.

For dilute binary alloys involving a dilute solid solution of solute B in solvent A, surface segregation X_S is given in terms of X_B and the free energy of segregation per mole of solute, ΔG_S in a Langmuir–McClean type expression [32].

$$\frac{X_S}{1 - X_S} = \frac{X_B}{1 - X_B} \exp\left[\frac{-\Delta G_S}{RT}\right] \quad (2)$$

Surface enrichment occurs when ΔG_S is less than zero. This expression indicates that X_S increases as ΔG_S becomes increasingly negative, increases with X_B, and decreases as temperature is increased. It is common to report enrichment ratios expressed as $\beta_S = X_S/X_B$.

Seah [33] and Miedema [34] have both reported means to estimate ΔG_S. A major factor determining ΔG_S in the case of a dilute solid solution is the difference in the heats of sublimation of the solvent and solute because this parameter provides a rough estimation of the difference in surface energies. Segregation is favored if enrichment of the solute lowers the surface energy, that is, if the solute has a lower molar surface energy than the solvent. Another aspect of these estimations is related to the relief of elastic strain energy brought about by segregation. The source of the strain originates from the atomic size difference between solute and solvent. In summary, solute with large positive lattice misfits that do not prefer to mix with the solvent (e.g., high heat of mixing) and that have weak bond strengths segregate more readily to surfaces.

The equilibrium segregation tendencies of grain boundaries, expressed in terms of X_{gb}, are very similar and contain the same basic features discussed above. A similar equation predicts segregation in terms of the bulk solid solubility of solute component B and a term representing the free energy difference between a solute in solution versus solute that is segregated to

a boundary [32, 35].

$$\frac{X_{gb}}{1 - X_{gb}} = \frac{X_B}{X_B^{sat}} \exp\left[\frac{-\Delta G'}{RT}\right] \qquad (3)$$

Here X_B^{sat} is the maximum solubility of solute B. It is interesting to note that as the equilibrium solubility of B decreases, grain boundary enrichment often increases leading to grain boundary concentrations that are 1000 to 10 000 times X_B. Hence, small overall concentrations of impurities that promote IGC may be considerably enriched at boundaries. The relation between enrichment ratio, $\beta_b = X_{gb}/X_B$, and solid solubility, X_B^{sat}, is depicted in Fig. 8.

True equilibrium segregation would not be expected to extend beyond the effective thickness of the grain boundary itself. In

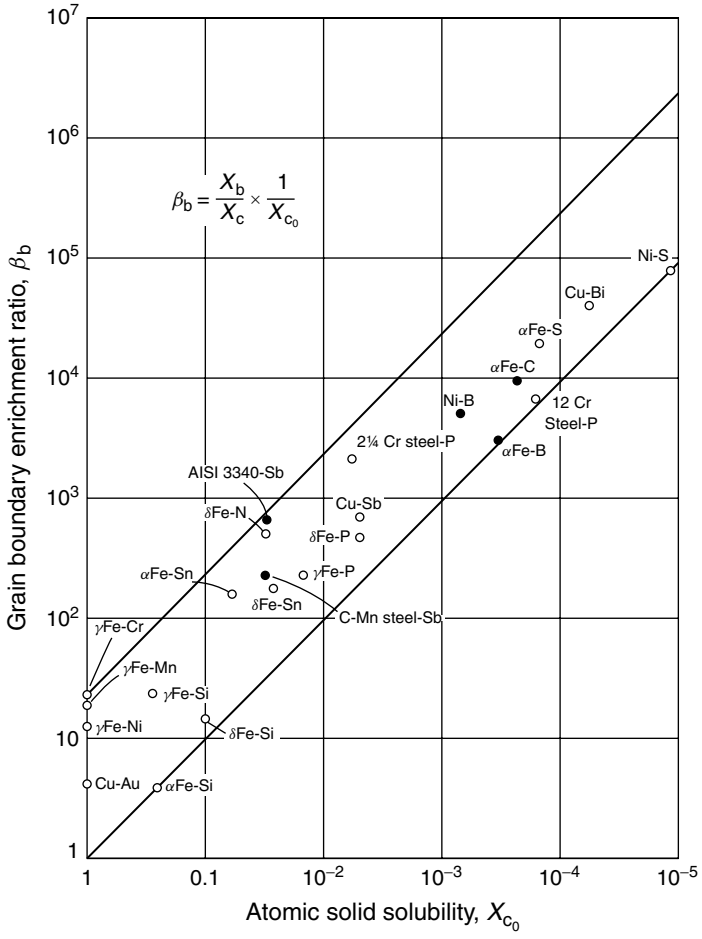


Fig. 8 Correlation between measured grain boundary enrichment ratio, $\beta_b = X_{gb}/X_B^{sat}$, with maximum solute solubility, X_B^{sat}, of solute B. The first element listed is the solvent in each alloy. (Ref. [30], reprinted with permission from The American Society for Metals – ASM International.)

fact, the original thermodynamic derivation of the Gibbs Adsorption Isotherm involves a boundary phase of zero volume. However, segregation often exists over a longer distance from the grain boundary. Nonequilibrium segregation results from flow of excess vacancies to or from boundaries. Such boundaries serve as vacancy sinks that can accommodate nonequilibrium vacancy concentrations [36]. This flow, resulting from nonequilibrium concentrations of vacancies, can produce either solute enrichment or depletion at boundaries [7]. Such segregation or depletion could occur during cooling, heating, mechanical deformation, irradiation, and so on [7]. The basis for such segregation is vacancy–solute coupled transport by two means [37, 38]:

1. Reverse atom flow in response to vacancy flow (for substitutional impurities).
2. The dragging of solute atoms by vacancies (applicable for interstitial or substitutional impurities).

In the former case, the steady state solute gradient is related to the steady state vacancy gradient modified by a term that is based on the differences in volume diffusivities of solute B, D_B, and solvent A, D_A.

$$\frac{\partial \ln C_B}{\partial x} = \frac{\partial \ln C_V}{\partial x}\left[\frac{D_B - D_A}{D_B}\right] \quad (4)$$

Here, C_B is the solute concentration, C_V is the vacancy concentration, and x is a perpendicular distance to a boundary. The vacancy concentration gradient at the grain boundary, as shown in Fig. 9, will depend upon both the solutionizing temperature responsible for high-vacancy concentrations and the severity of quench, which acts to freeze in the nonequilibrium vacancy concentration. As the quench rate decreases, the vacancy concentration gradient will decrease as well, as shown in Fig. 9. Note that when $D_B > D_A$, the gradient in solute B will be in the same direction as the vacancy gradient. However, when $D_A > D_B$ segregation of B will occur at the vacancy sink such as a grain boundary [7].

The second type of nonequilibrium segregation occurs when solute is bound to

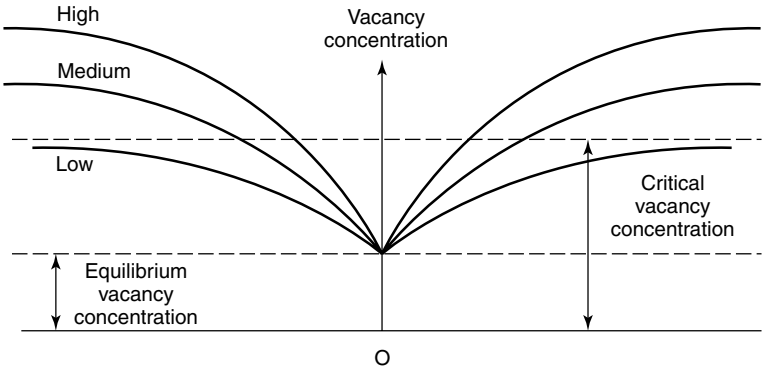


Fig. 9 Schematic view of high, medium, and low excess vacancy concentrations as a function of distance from a grain boundary serving as a vacancy sink. The equilibrium vacancy concentration at the given temperature is given by the dotted line. (Ref. [25], from Physical Metallurgy Principles, 3rd edition by Reed-Hill/Abbaschian, © 1992. Reprinted with permission of Brooks/Cole, a division of Thomson Learning: www.thomsonrights.com, Fax 800 730-2215.)

vacancies with a binding energy greater than kT and excess vacancies exist. Diffusion and annihilation of vacancies at boundaries will result in drag transport of the solute to the same vacancy sink [38]. In dilute solid solutions in which the concentrations of solute and vacancies are equal, the two types of gradients are equal.

$$\nabla C_B = \nabla C_V \tag{5}$$

Both of these segregation phenomena can contribute to solute segregation that occurs over a longer distance from the boundary than expected from pure equilibrium considerations. Indeed, many measured segregation solute profiles near boundaries extend into grains at a greater distance than expected from equilibrium vacancy consideration. If such segregation affects corrosion tendencies, then IGC can occur.

Segregation tendencies also depend in a complex manner on boundary structure and energy. Since segregation is site-specific, it follows that segregation will depend on orientation, although expressions are lacking [9]. The impact of interfacial segregation on materials properties is significant; it influences grain boundary diffusion, grain growth, creep by interface cavitation, and precipitate ripening kinetics as well as IGC and cracking.

In the case of IGA by electrochemical dissolution, the segregant may depassivate the grain boundary region by disrupting the formation of protective oxide films. Two critical aspects of the IGC phenomena are (1) the monolayer coverage of the segregant at the planar boundary in question, and (2) the degree to which a given segregant monolayer coverage alters resistance to corrosion (i.e. its potency). For instance, sulfur locally depassivates nickel (i.e. disrupts the protective oxide film) and raises the *active* dissolution rate in acids depending on its coverage [39]. High levels of sulfur and other elements at the grain boundaries of nickel will have a significant effect on grain boundary dissolution since sulfur poisons surface sites, reduces metal–metal bond strengths such that the activation energy barrier for cation release is reduced, and prevents oxygen adsorption, limiting passivity [39]. The result is that grain interiors remain passive while the grain boundary can exhibit active–passive behavior on E-log i diagrams. Consequently, intergranular dissolution can occur when sulfur is segregated to nickel boundaries. The extent of dissolution is related to the S coverage (anodic segregation during corrosion is another means by which sulfur may be concentrated at metal surfaces); a longer segregating heat treatment will produce more grain boundaries that corrode. Since adsorbed sulfur is highly stable, it remains adsorbed during dissolution and a fraction of a monolayer of sulfur can contribute to considerable dissolution occurring over micrometers [40]. Other corrosion processes have been proposed for P, S, and C segregation in Fe, as well as for Mg segregation on grain boundaries in Al. These are discussed in the following text.

4.3.2.1.3 **Role(s) of Boundary Precipitate Formation and Solute Depletion** Many examples of depletion of beneficial elements from the matrix adjacent to grain boundaries exist as well. Here, the large, rapidly grown precipitate formed at grain boundaries depletes the region adjacent to the grain boundary of alloying elements that can be beneficial to corrosion. Numerous phenomena result from elemental depletion near grain boundaries including precipitate free zone (PFZ) development, IGC, and IGSCC. Precipitation of a grain boundary phase that is prone to corrosion

is another process that can render a grain boundary prone to IGC.

Let us review the metallurgical processes controlling this phenomenon. Common features include heterogeneous precipitation at grain boundaries and redistribution of the solute participating in the precipitation reaction. Two important factors are the alloying concentration of the solute forming the detrimental precipitate, and the conditions that promote heterogeneous nucleation on boundaries. A simple example that conveys the notion of such a phenomenon involves solute depletion next to a growing precipitate in the case of one-dimensional transport. The metallurgical basis for solute depletion around a precipitate phase can be described as follows [25, 41]. Consider a binary alloy of overall composition, C_B^o, with a terminal solid solution representing finite solubility of component B in the A-rich α phase as indicated by the solvus composition, C_s. Consider that this room-temperature two-phase alloy can exist as an α solid solution at high temperature but forms β phase precipitates in an α matrix as temperature is lowered. Figure 10(a)

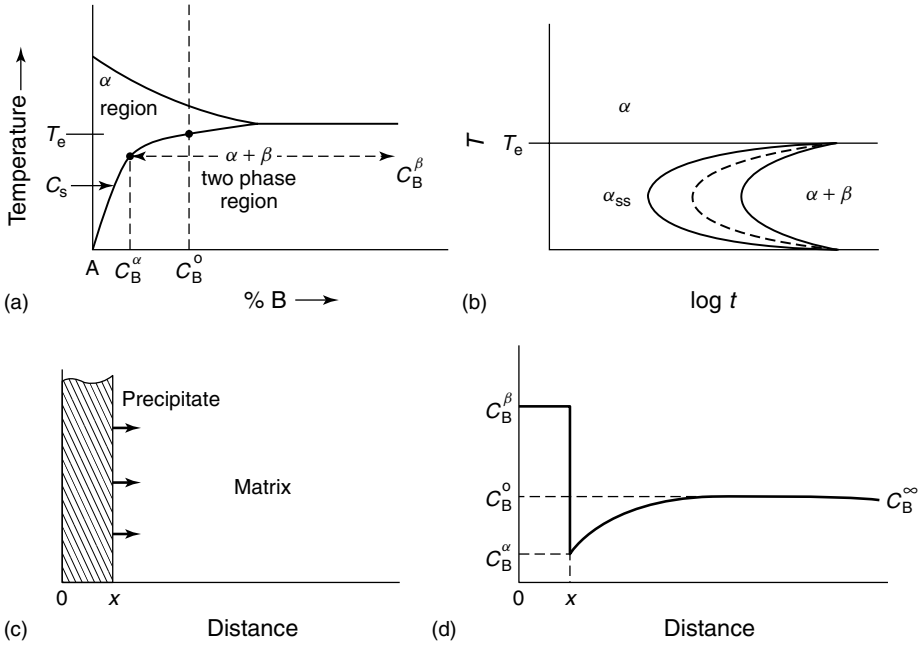


Fig. 10 Thermodynamic and kinetic basis for solute depletion in the case of a binary alloy consisting of solvent A and solute B. (a) Binary equilibrium phase diagram with complete miscibility in the liquid state, partial miscibility in the solid state given by existence of a terminal solid solution. C_s is the composition along the solvus line. C_B^o is the overall composition of the alloy. (b) Time–temperature-transformation diagram for precipitation of β in an α matrix for the alloy shown in (a) with overall composition, C_B^o. (c) Schematic of precipitate location relative to concentration profile. (d) Concentration profile for solute B in the α matrix in the case of diffusion-controlled growth of the β phase precipitate. The situation shown is observed when local equilibrium is attained in the matrix at the surface of the β precipitate. C_B^∞ is the nonequilibrium α phase composition far from the precipitate. It is equal to the overall composition C_B^o. C_B^α is the alloy composition in equilibrium with the β phase precipitate.

illustrates the applicable region of the binary equilibrium phase diagram that describes this situation. Figure 10(b) illustrates the applicable time–temperature-transformation (TTT) diagram. Suppose that a solution heat-treated alloy of overall composition C_B^o is rapidly cooled below T_e to T_1. The concentration of B in the newly formed β phase precipitates is C_B^β, which is assumed to be higher than that in the matrix. If the time for B atoms to cross the interface from the α to the β phase is short compared to the time required for B atoms to diffuse to the interface, then the concentration of B in the α matrix will be lowered until it equals the equilibrium concentration defined by the phase diagram, C_B^α, in the α phase adjacent to the β phase precipitate [41]. However, moving away from the boundary, the concentration of B in the α matrix equals C_B^o or C_B^∞, especially for finite heat-treatment times. This is assumed to be the matrix concentration before precipitation in the case in which the alloy was just solution heat-treated. Hence, formation of the β phase precipitate produces a local depletion of alloying element B from the α solid solution near the β phase precipitate as shown in Fig. 10(c, d). The concentration profile shown in Fig. 10(d) will exist under circumstances in which the β phase is precipitated from α under diffusion control and final equilibrium is not attained. Solutionizing above T_e, heat treatment for a short time at T_1 followed by rapid cooling to room temperature effectively freezes in the concentration C_B^∞ far from precipitates (i.e., the equilibrium concentration C_B^α is not attained uniformly across the matrix).

IGC susceptibility is created when such solute depletion adjacent to a β phase, formed along α grain boundaries, occurs more or less continuously adjacent to α grain boundaries as depicted in Fig. 10(d). This situation requires heterogeneous nucleation of the β phase on α grain boundaries. Preferred locations of heterogeneous precipitation include grain boundaries, impurity particles, and dislocations [25]. The standard metallurgical factors that normally promote heterogeneous precipitation (e.g. high heat-treatment temperatures, slow continuous cooling, lack of nucleation promoters or other heterogeneous nucleation sites besides the boundaries themselves) will promote grain boundary precipitation. If the surface energy and lattice strain between the precipitated phase and the heterogeneous nucleation site are lower than between the new phase and the homogeneous matrix of the parent phase, then the critical free energy of heterogeneous nucleation and the critical nucleus will be small in comparison to that for homogeneous nucleation. Stated another way, at temperatures just below the solvus associated with precipitation of the second phase, the rate of homogeneous nucleation is very small because the critical free energy of homogeneous nucleation is very large. Not only is the critical free energy of heterogeneous nucleation smaller at such high temperatures but also the rate of the heterogeneous precipitation process is greater because diffusion of solute B to form the precipitate is faster at high temperature. Consider precipitation of the β phase from a α solid solution that exists above a certain equilibrium temperature, T_e. The TTT diagram for such a heterogeneous nucleation process will differ from that for homogeneous nucleation depicted in Fig. 10(b). Figure 11 illustrates the important TTT aspects of this process in case of homogeneous versus heterogeneous nucleation. Figure 12 depicts resulting microstructures during various cooling sequences.

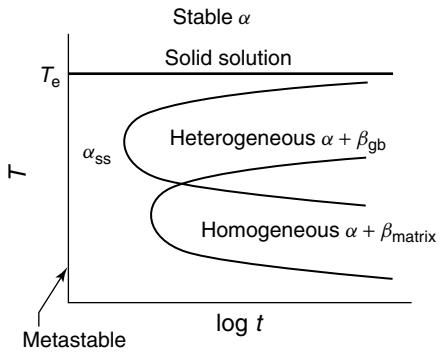


Fig. 11 Schematic of time–temperature-transformation diagram for alloy indicated in Fig. 10 indicating regions of both heterogeneous and homogeneous precipitation of the β phase in a α matrix.

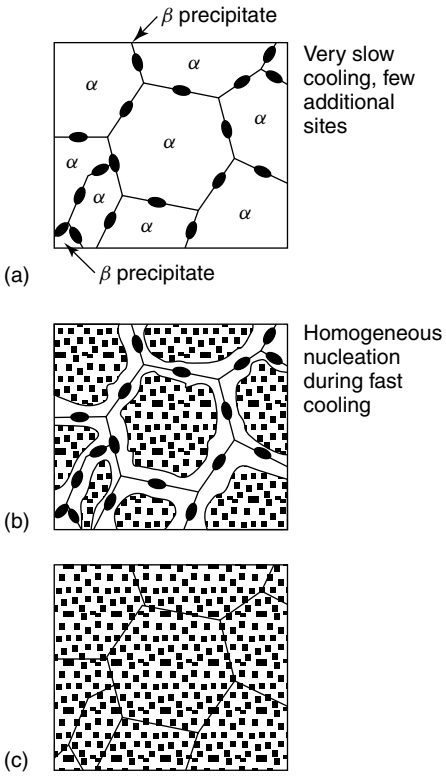


Fig. 12 Schematic microstructures in the case of (a) completely heterogeneous nucleation; (b) mixed heterogeneous-homogeneous nucleation with a precipitate free zone (PFZ); and (c) homogeneous nucleation. β phase precipitates in α matrix are indicated.

Heterogeneous nucleation is promoted by small undercoolings below T_e, known as the solvus temperature in the case of a α solid solution decomposing to α and β precipitates. Figure 12(a) depicts completely heterogeneous nucleation. Heterogeneous nucleation can be suppressed by a large drop in temperature below the equilibrium temperature achieved with a rapid cooling rate or quench. Heterogeneous nucleation and growth of precipitates at boundaries normally occur at higher rates, lead to larger precipitates, and thus, greater solute-depleted zones adjacent to boundaries for slow diffusing elements (Fig. 12b). Therefore, heterogeneous nucleation and growth of grain boundary precipitates must be avoided if IGA by grain boundary precipitation and solute depletion is to be minimized. Ideal homogeneous precipitation is shown in Fig. 12(c).

The TTT behavior governing precipitation of the second phase precipitate in the supersaturated solid solution is an approximate indicator of the time–temperature-corrosion diagram. Such a diagram is illustrated by Fig. 13 for an Al-Cu-Mg alloy [42], Plastic deformation prior to precipitation, low aging temperatures, and nucleation promoters that promote nucleation but retard growth

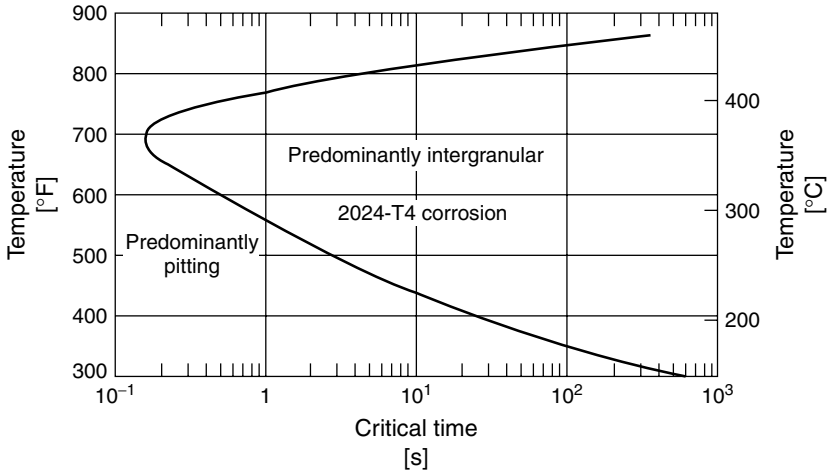


Fig. 13 Time–temperature-sensitization curve for Al-3.8 to 4.9% Cu-1.2 to 1.8% Mg alloy (AA 2024-T3) illustrating regions of pitting and IGC corrosion in terms of isothermal heat-treatment time and temperature. (Ref. [43], reprinted with permission from ASM International.)

are all measures that can be taken to minimize heterogeneous nucleation on grain boundaries.

A more sophisticated and appropriate description of the depletion of a beneficial alloying element when precipitates are formed on grain boundaries is described by the ''collector-plate'' mechanism and other more advanced treatments. This mechanism describes heterogeneous precipitation of a second-phase precipitate at grain boundaries and considers grain boundary transport as well as bulk diffusion [44]. Once again solute in the matrix diffuses to the solute rich precipitate. The key advancement over the solute-depletion mechanism described by Zener is the recognition that solute transport is faster along the grain boundary than in the grain matrix. If precipitate formation is diffusion controlled and precipitates are heterogeneously nucleated on

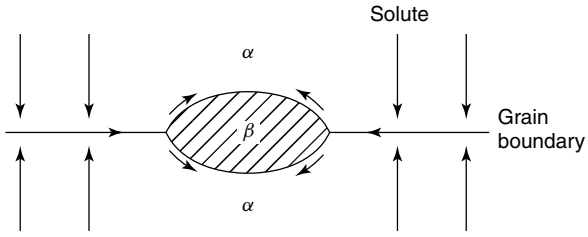


Fig. 14 Grain boundary precipitate growth showing solute transport path during precipitate growth according to the collector-plate mechanism. Solute B is transported to the α–α grain boundary and then along the boundary to form the β precipitate. Diffusion-controlled precipitate growth results in solute depletion from the α phase along the homophase boundary due to fast boundary transport [44].

boundaries as shown in Fig. 14, then the solute concentration along the boundary can rapidly drop from the overall composition C_B^o to C_B^α along the boundary even for widely spaced β precipitates.

During many commercial procedures, a concern exists for heterogeneous nucleation and precipitation during continuous cooling. Quench factor analysis has been developed to use the entire time–temperature-sensitization curve [43]. The quench factor, τ, is given by

$$\tau = \int \frac{dt}{C_t} \tag{6}$$

where t is time and C_t is the critical time as a function of temperature (Fig. 15). When τ equals 1, the fraction transformed during continuous cooling equals the fraction transformed given by the loci of critical times on the time–temperature-transformation or time–temperature-sensitization curve. The fraction transformed or the corresponding extent of IGC is indicated by ξ:

$$\xi = 1 - \exp(k\tau) \tag{7}$$

Quench factor analysis has successfully predicted the IGC characteristics of AA 2024-T4 [43].

An example of elemental depletion that promotes IGC and stress corrosion is grain boundary Cu depletion in Al-Cu, Al-Cu-Mg, and Al-Cu-Li alloys (see below). Beneficial Cu is depleted from the Al-rich matrix near the grain boundaries and collected at θ-Al_2Cu, S-Al_2CuMg, and T_1-Al_2CuLi precipitate phases, respectively. This is discussed further below under the sections referring to Al-base alloys.

Another example involves grain boundary Cr depletion (commonly referred to as sensitization) in Fe-Ni-Cr alloys containing interstitially dissolved carbon [45, 46]. Here, Cr depletion occurs upon the formation of $Cr_{23}C_6$ and other carbides [47]. Carbide formation occurs profusely on boundaries as a result of C segregation, heterogeneous carbide nucleation, and fast

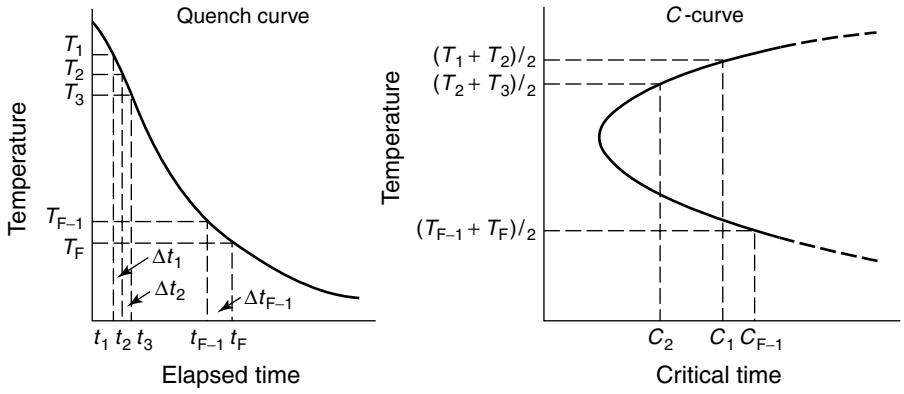


Fig. 15 Graphical illustration of method for determination of τ in quench factor analysis. C_n is the critical time to achieve a fraction transformed at a certain temperature indicated by the time–temperature-transformation curve. (Ref. [43], reprinted with permission from ASM International.)

transport of carbon along boundaries to support carbide growth. A common feature in all of these systems is the depletion of an alloying element that is beneficial for corrosion resistance when retained in solid solution (e.g. Cr in Fe-base alloys, or Cu in Al-base alloys).

A third example of grain boundary precipitation that may trigger IGC involves formation of a grain boundary precipitate phase, which itself corrodes more readily than the solid solution matrix. Some carbides are preferentially attacked in sensitized stainless steels. Al-Mg alloys serve as an excellent example of this type of intergranular corrosion-prone alloy. Here precipitation of the Al_8Mg_5 phase along grain boundaries can render the alloy prone to IGC. A final example is T_1-Al_2CuLi precipitate phases precipitation along subgrain boundaries in Al-Li-Cu alloys. The most severe IGC is observed when a continuous connected path of these precipitates is formed along a large number of grain boundaries.

4.3.2.1.4 **Role(s) of Precipitate Free Zones**

PFZs may form adjacent to grain boundaries in many materials. PFZs are caused by the role of grain boundaries as a sink for annihilation of supersaturated concentrations of vacancies (Fig. 9), or by segregation or precipitation of the supersaturated solute that depletes the zone near the grain boundary of solute [48]. Vacancy-depletion profiles can exist even if the solute concentration profile remains constant. Vacancy-depletion profiles occur in the region adjacent to boundaries as supersaturated vacancies migrate to grain boundaries where such excess vacancies are annihilated. Depletion of excess vacancies affects the transport of substitutional solute atoms that participate in precipitation and can lead to PFZ formation. Depletion of excess solute can also occur in the zone near a grain boundary. Solute depletion occurs near a boundary as a result of heterogeneous nucleation of a new phase incorporating the solute on boundaries and associated solute depletion. When the solute concentration drops substantially in this zone, homogeneous precipitation becomes impossible as indicated in Figure 16. PFZs are an important factor affecting the IGC susceptibility of homophase interfaces because the resultant changes in alloy composition and precipitate density within the PFZ can affect microgalvanic coupling, local anode-cathode ratios, and thus the corrosion behavior of these regions. Concomitant solute redistribution, precipitate identity, density, and the relative distribution of solute atoms in the PFZ can change corrosion properties. A more complicated effect may be related to differences between the character of the plastic deformation in the PFZ compared to grain interiors.

4.3.2.2 **Environmental Factors**

4.3.2.2.1 **Bulk Chemistry and Solution Composition**

The bulk chemical composition, oxidizing power, reducing acid strength as well as temperature of the test solution are important factors that determine whether IGC occurs. Aggressive test environments have been devised so that a metallurgical condition that leads to IGC susceptibility can be elucidated by direct evidence of boundary attack in a short-term lab test. These environments promote differences in the electrochemical behavior of the boundary region compared to the grain interiors as shown in the electrochemical frameworks depicted in Figs. 3 and 4. In the case of stainless steels, a range of industry IGC

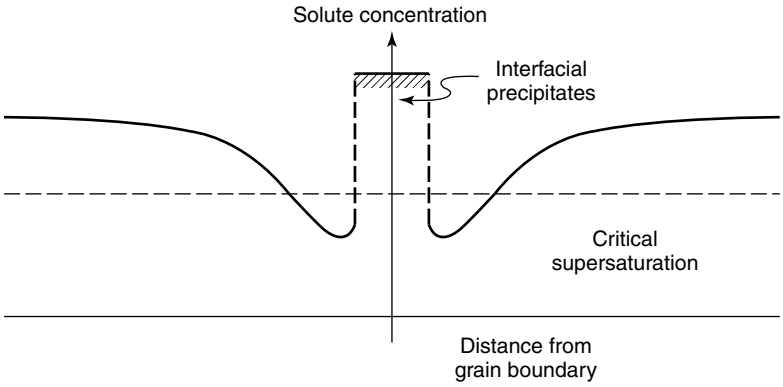


Fig. 16 Solute-depletion profile across a grain boundary indicating the solute-depletion mechanism of PFZ formation. Solute concentrations below the dotted line associated with the critical supersaturation needed for precipitation prohibit precipitate formation. (Ref. [41], from Physical Metallurgy Principles, 3rd edition by Reed-Hill/Abbaschian, © 1992. Reprinted with permission of Brooks/Cole, a division of Thomson Learning: www.thomsonrights.com, Fax 800 730-2215.)

test environments have been developed (see Table 1) and methods to detect IGC susceptibility have been standardized [49, 50]. Streicher has extensively reviewed IGC test environments and techniques for stainless steels [51]. These can detect metallurgical conditions leading to IGC susceptibility by etch classification (oxalic acid), mass loss (nitric acid, ferric and copper sulfate with sulfuric acid), and by observation of fissures in bends (copper sulfate in sulfuric acid with metallic Cu) [51]. Some of these test environments promote IGC when Cr depletion exists, while others are so oxidizing (e.g., in the nitric acid test, the stainless steel specimen is polarized to $+1\ V_{SCE}$ by oxidizing nitric acid; in the ferric sulfate-sulfuric acid test, the specimen is polarized to $0.6\ V_{SCE}$ through the oxidizing power of the ferric ions) that they attack grain boundary Cr carbides, nitrides, or other intermetallic phases such as sigma. In fact, the 10% oxalic acid test, often used as a rapid initial screening test for IGA, involves an overetch at $1\ A\ cm^{-2}$ for 1.5 min. The test specimen develops an anodic potential near $1.7\ V_{SCE}$, which attacks carbides to produce a ditch or dual structure. Grain-to-grain variations in the etch rate resulting from the variation of crystallographic orientation can produce a step structure without grain boundary susceptibility. Caution is warranted in the interpretation of such data since grain boundary carbides may still exist in the presence of "healed" grain boundaries at which Cr-depletion profiles have been eliminated.

In the case of other alloys, such as Al-base precipitation age-hardened materials, a range of environments have also been proposed (see Table 2) and test methods standardized [52, 53]. The NaCl-H_2O_2 environment probably induces widespread pitting. In this case, the local chemistry and electrochemical conditions that develop in the pit environment then induce IGC of exposed grain boundaries within the pit.

Tab. 1 Standard intergranular corrosion tests for austenitic stainless steels (after Ref. [50, 51])

ASTM standard [ISO standard] (common name)	*Environment*	*Exposure time*	*Evaluation*	*Phase or region attacked*
A 393/A763 ISO 3651 (Strauss)	15.7% H_2SO_4 5.7% $CuSO_4$ boiling	Several 72-h periods with fresh solution for each	Appearance after bending	Cr-depleted areas at carbides
A 262 practice A (oxalic acid)	10% H_2SO_4, anodic at 1 A cm^{-2}, ambient temp.	One 1.5-min period	Type of attack	Cr-depleted areas at carbides
A 262 practice B	50% H_2SO_4 + 2.5% $Fe_2(SO_4)_3$	One 120-h period	Wt. loss per unit area	Cr-depleted areas at carbides and sigma phase
A 262 practice C (Huey)	65% HNO_3 boiling	Five 48-h periods with fresh solution for each	Average wt. loss per unit area	Cr-depleted areas at carbides and sigma phase
A 262 practice D	10% HNO_3 + 3% HF, 70 °C	Two 2-h periods with fresh solution for each	Wt. loss per unit area	Cr-depleted areas at carbides and in Mo-bearings steels
A 262 practice *E* (copper accelerated Strauss)	15.7% H_2SO_4 5.7% $CuSO_4$ boiling, specimen not in contact with Cu	One 24-h period	Appearance after bending	Cr-depleted areas at carbides
A 262 practice *E*/A 763 (Streicher)	50% H_2SO_4 + $CuSO_4$ boiling, solid Cu in solution, specimen not in contact with Cu	One 120-h period	Wt. loss per unit area	Cr-depleted areas at carbides

Note: ISO standard 3651 covers other variations on the tests listed above.

4.3.2.2.2 **Local Chemistry and Solution Composition** In certain cases, pitting induces IGC. IGC susceptibility occurs because of the creation of specific local environments and associated electrochemical conditions within and near pit sites as well as the need for a specific metallurgical condition that causes susceptibility. Figure 17(a) illustrates inter-subgranular corrosion inside a pit formed on an Al-Li-Cu-Ag alloy [54]. In the case of many Al-Cu-X alloys, corrosion from a planar electrode surface commences at constituent particles that induce microgalvanic coupling. Galvanic corrosion can take the form of cathodic trenching due to enhanced cathodic activity or halide-induced acid pitting adjacent to Cu-rich particles. Note that this initial corrosion process occurs regardless of temper and IGC susceptibility because constituent particles are not altered by artificial aging.

Tab. 2 Summary of the laboratory test method for detecting IGC susceptibility in a variety of alloys

Test	*Standard*	*Materials*	*Type of susceptibility detected*
Strauss	ASTM A262, Practice *E*	Austenitic stainless steels	Intergranular attack associated with Cr carbides or nitrides
	ASTM A763, Practice Z	Ferritic stainless steels	Intergranular attack associated with Cr carbides or nitrides
Huey	ASTM A262, Practice C	Austenitic stainless steels	Intergranular attack associated with Cr carbides and σ-phase
Streicher	ASTM A262, Practice B	Austenitic stainless steels	Intergranular attack associated with Cr carbides
	ASTM A763, Practice X	Ferritic stainless steels	Intergranular attack associated with Cr carbides, Cr nitrides, and intermetallic phases such as σ-phase
Copper–copper sulfate-sulfuric acid	ASTM A262, Practice F	Mo-containing cast austenitic stainless steels	Intergranular attack associated with Cr carbides or nitrides
	ASTM A763, Practice Y	Ferritic stainless steels	Intergranular attack associated with Cr carbides or nitrides
Oxalic acid etch	ASTM A262, Practice A	Austenitic stainless steels	Intergranular attack associated with Cr carbides
	ASTM A763, Practice W	Ferritic stainless steels	Intergranular attack associated with Cr carbides
Hydrochloric acid	None	Austenitic stainless steels	Preferential weld metal corrosion due to δ-ferrite
Electrochemical potentiokinetic polarization	ASTM G108	304 and 304L austenitic stainless steels	Intergranular attack associated with Cr carbides
Galvanostatic	None	Carbon steels	Preferential corrosion of weld metal and of HAZ
Exfoliation	ASTM G34	2XXX (Al-Cu-X) and 7XXX (Al-Zn-X) series Al alloys	Exfoliation corrosion
	ASTM G66	5XXX (Al-Mg-X) series Al alloys	Exfoliation corrosion
NaCl + hydrogen peroxide immersion test	ASTM G110		Intergranular corrosion of heat-treatable Al alloys

Note: HAZ: Heat-affected zone.

However, such corrosion transitions to IGC and IsubGC when the corrosion damage reaches a critical depth is presumably associated with formation of a solution chemistry that promotes IGA (Fig. 17b, 17c) [55]. However, such a transition only occurs in specific tempers susceptible to IGC. Corrosion sites also serve to expose many grain and/or subgrain boundaries, but this role is purely secondary since any two-dimensional slice through a 3-D volume of polycrystalline material will

already expose many grain boundaries. A third role of pits is to produce a geometry that promotes stress concentration. However, this is more important in the context of IGSCC. Therefore, the primary role of initial pitting or cathodic trenching in the context of IGA is to produce the local environment necessary to develop differences in the corrosion behavior of grain interiors compared to grain boundary regions. (Presumably, IGC rates must exceed cathodic corrosion rates or pit growth rates in order for IGA to develop.) In the chemistry change model of localized corrosion (see Chapters 4.1 and 4.2 in Volume 4), dissolution produces cations that in turn hydrolyze in aqueous solutions to produce protons. Anions, including halides

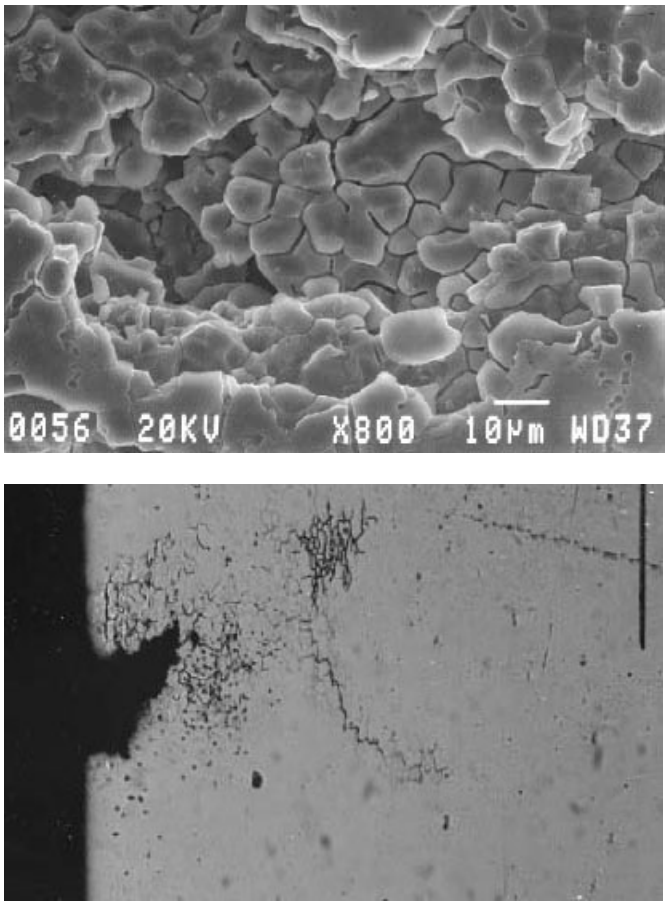


Fig. 17 Example of IGC at the base of a pit in an underaged Al-2.8% Cu-1.7% Li-0.5% Mg-0.5% Zr-0.36% Ag (wt. %) alloy. (a) plan view inside pit. (b) cross-sectional view. Note absence of IGC from the machined surface at left side in the cross-sectional view in (b). IGC is observed inside the pit. (Ref. [54] reprinted with permission from NACE International.) (c) Focused ion beam cross section through a pit reveals IGC inside the pit. (Ref. [55] reprinted with permission from NACE International.)

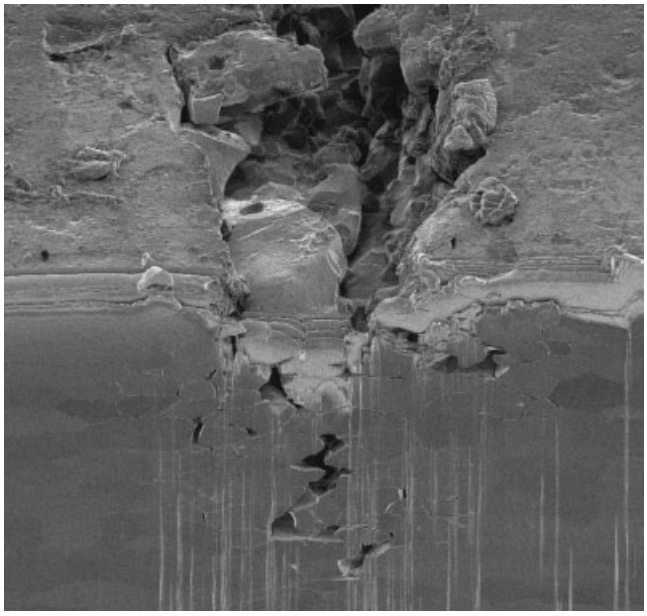
(c) 

Fig. 17 (*Continued*)

such as Cl^-, migrate into pits in order to maintain electroneutrality. Hence, the pit environment is often acidified and high in anion concentration. Moreover, chemical concentration, pH and potential gradients often exist within such pit sites. At certain locations along such gradients, IGC susceptibility may be promoted in a material possessing a susceptible metallurgical condition. Hence, local solution compositions and electrochemical conditions within pits can induce IGC and IGSCC.

4.3.2.3 Mechanical Factors

4.3.2.3.1 Role(s) of Residual and Applied Stress IGC and IGSCC are closely related phenomena. It is often observed that rates of IGC are accelerated by tensile stress at the surface of the material [56]. In some cases, tensile stress is required in order for IGC to even be seen. In other cases, IGC is not eliminated by the removal of stress but is more extensive and exhibits a faster growth rate when stress is applied. Often regions of significant compressive and tensile residual stress exist in a welded component. The total resolved stress state remains zero when there is no externally applied stress. IGC is accelerated and IGSCC is rendered possible when fabrication that involves machining exposes regions containing high tensile residual stresses. Exact quantification of the stress levels necessary for IGC and IGSCC can be difficult because of the presence of unaccounted-for residual stresses in many material product forms as well as additional stressing induced by welding and corrosion product wedging. Therefore, precise determination of the effects of tensile stress on IGC can be thwarted in laboratory coupon testing. The propensity for IGC and IGSCC in solution treated and quenched, as well as welded materials is often minimized

by stress-relieving practices, but this does not eliminate metallurgical susceptibility. Quench stresses are often relieved by mechanical prestretching conducted prior to artificial aging. Drawing stresses are often relieved by thermal treatment.

4.3.2.3.2 **Role of Corrosion Product Wedging** Corrosion product wedging can increase applied stress during corrosion. The corrosion products often occupy a greater volume than the original material itself. It was proposed that oxides formed in cracks in 18% Cr to 8% Ni stainless steel caused stress corrosion cracking (SCC) and such stresses have been measured [57]. The effect is particularly important during exfoliation type IGC in which corrosion occurs preferentially along the boundaries of elongated grains typical of unrecrystallized rolled or extruded plate or sheet product [58]. Thus, the corrosion product serves to wedge open and load the longitudinal IGA such that the intergranular attack proceeds as if under the short-transverse – longitudinal (SL) crack growth configuration [59]. As mentioned above, IGC is enhanced by stress.

4.3.3 Example Alloy-environment Systems

4.3.3.1 Intergranular Corrosion in Fe-Ni-Cr and Fe-Cr-Ni-Mo Alloys

The Cr-depletion theory has been accepted as the mechanism by which a sensitized stainless steel becomes susceptible to intergranular corrosion [60]. Recall that a minimum of 10 to 13 wt. % Cr in solid solution is required to form protective passive films on Fe-Ni-Cr alloys

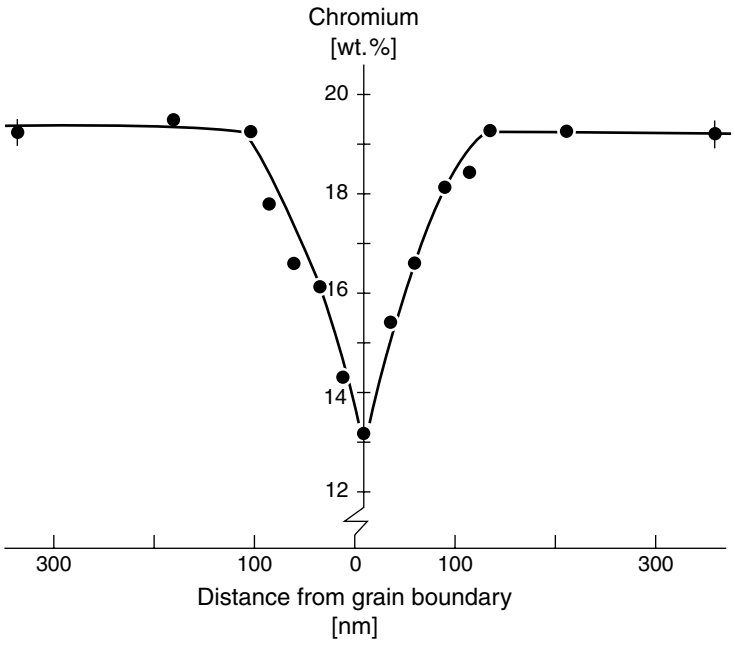


Fig. 18 Cr-depletion profile across a grain boundary in a sensitized stainless steel. (Ref. [61], from Corrosion of Stainless Steels A. John Sedriks, copyright © John Wiley & Sons. Reprinted by permission of John Wiley & Sons, Inc.)

in corrosive solutions. The matrix of the stainless steel remains passive while the Cr-depleted grain boundary (Fig. 18) exhibits an active-passive transition on an E-log(i) diagram (Fig. 4a). Hence, depletion of Cr at grain boundaries in austenitic stainless steels by formation of insoluble carbides $(Fe,Cr)_{23}C_6$ between 425 and about 815 °C creates zones along grain boundaries that are iron-rich and highly susceptible to active corrosion in specific environments [61, 62]. At equilibrium, the following solid-state reaction applies and the Cr content in equilibrium with the carbides can be defined.

$$23Cr + 6C = Cr_{23}C_6 \qquad (8)$$

The equilibrium level of Cr adjacent to a carbide particle depends critically on carbon activity, alloying content, and temperature. Equilibrium grain boundary Cr concentrations as low as 6.6, 8.4, and 10.8 wt. % have been measured adjacent to carbides in AISI 316LN stainless steel (containing 18 wt. % Cr) after sensitization at 600, 650, and 700 °C, respectively [63]. Hence, the Cr content of grain interiors can remain at 18% while the grain boundary zone is depleted to the equilibrium levels cited above as illustrated by Fig. 18. Sensitization also depends critically on carbon content as shown in Fig. 19. Cr diffusion is slow in austenitic Fe-base alloys, carbide precipitation initially does not deplete carbon contents in the alloy, and Cr-depletion profiles in Fe-base alloys can persist after long times in the temperature range from 425 and 815 °C. Above this temperature range, thermally activated Cr diffusion is faster, which can lead to leveling of Cr concentration in depleted zones [62]. Other metallurgical factors controlling IGC susceptibility in stainless steels include molybdenum and chromium depletion caused by the formation of other intermetallic precipitates such as chi and sigma phases [61].

There are important differences between the thermal conditions that produce IGC susceptibility in ferritic, austenitic, and duplex stainless steels [61, 62]. Cr diffusion is slow in austenitic stainless steels and this minimizes the risk of sensitization below about 425 °C for short heating periods.

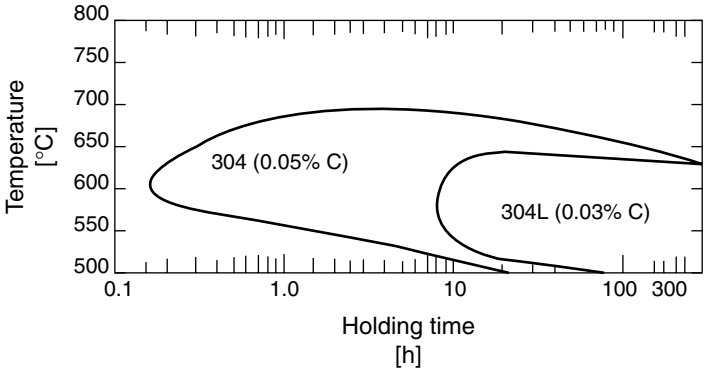


Fig. 19 Time–temperature-sensitization curves for AISI 304 (0.05 wt. %) and 304L (0.03 wt. %) stainless steel obtained using the Strauss test. (Ref. [61], from Corrosion of Stainless Steels A. John Sedriks, copyright © John Wiley & Sons. Reprinted by permission of John Wiley & Sons, Inc.)

In ferritic stainless steels, Cr diffusion is faster leading to more rapid sensitization over a lower temperature range as shown in Fig. 20. This is because of rapid carbide and nitride formation [64]. At higher temperatures, Cr diffusion occurring in body-centered cubic ferrous-based materials is considerably more rapid than in face center cubic (f.c.c.) materials. This tends to level concentration profiles and mitigate IGC susceptibility even for diffusion-controlled precipitation. However, sensitization can occur even in rapidly cooled ferritic material due to more rapid carbide formation kinetics. There are other important differences between austenitic and ferritic stainless steels. Chromium nitride precipitation can promote IGC in ferritic materials owing to the lower solubility of nitrogen in ferritic (b.c.c) compared to austenitic (f.c.c.) stainless steels. Sensitization in duplex stainless steels is complex and has been attributed to several mechanisms [61].

Sensitization diagrams (Figs. 19 and 20) for austenitic and ferritic stainless steels of varying carbon contents roughly follow the TTT behavior of carbide precipitation [65]. Increasing carbon content facilitates more extensive carbide precipitation at shorter

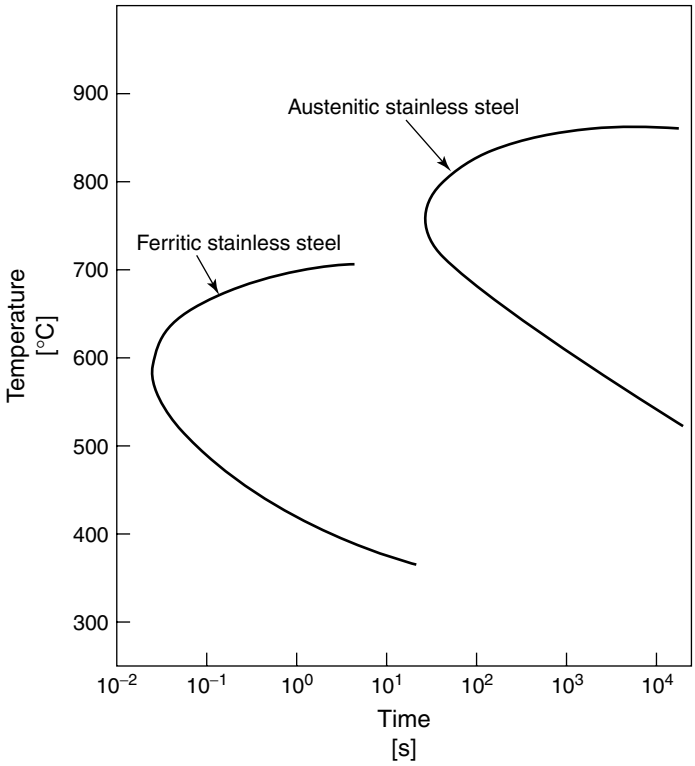


Fig. 20 Time–temperature-sensitization behavior diagrams for austenitic and ferritic stainless steels illustrating different time–temperature regimes for sensitization. (Ref. [61], from Corrosion of Stainless Steels A. John Sedriks, copyright © John Wiley & Sons. Reprinted by permission of John Wiley & Sons, Inc.)

times as TTT diagrams indicate. Thus, the use of low carbon austenite alloys containing less than 0.03% C (e.g. AISI 304L, 316L) can help minimize carbide formation and associated Cr depletion. However, the exact Ni and Cr content of the stainless steel govern the critical carbon content required to avoid IGA by sensitization [66]. Thus, the critical carbon content depends on the exact alloy composition. Boundary Cr depletion usually occur during processing (e.g. slow quenching of thick sections, isothermal age hardening) or subsequent fabrication practices (e.g. weld heat-affected zones). Sensitization in heat-affected zones (HAZs) of welded stainless steels leads to IGC susceptibility [67]. The HAZ is the region of metal exposed to the temperature range associated with rapid carbide precipitation for sufficient time to achieve sensitization. Since the temperature range for carbide formation in austenitic stainless steels differs from that for carbide precipitation (and Cr depletion) in ferritics, the exact position of IGC in the HAZ differs in the case of ferritic versus austenitic stainless steels.

The phenomenon of knife-line attack within weld HAZs describes susceptibility to IGC and IGSCC in stabilized grades of austenitic stainless steels [61, 68]. Stabilization is a term used to describe depletion of solid solution carbon due to niobium and titanium alloying. These elements produce carbides in the temperature range from 870 to 1150 °C in austenitic stainless steels such as AISI 347 [61]. Little carbon remains in solid solution to be precipitated as $(Fe,Cr)_{23}C_6$. Normally, the initial gettering of carbon above 870 °C eliminates sensitization by Cr-carbide formation that normally occurs over the range from 425 to 815 °C in austenitic stainless steels.

Unfortunately this process can be thwarted in the case of knife-line attack. Essentially, NbC and TiC formed during annealing are redissolved when a narrow portion of the weld HAZ just next to the weld metal (i.e. the knife line) exceeds a temperature of about 1150 °C. Rapid cooling during such an initial weld pass prevents subsequent Cr-carbide precipitation. However, the knife line then lacks beneficial niobium or titanium carbides and allows formation of $(Fe,Cr)_{23}C_6$ if slow cooling through the range of 480 to 760 °C occurs during a subsequent weld pass or reheating. Cr-depletion regions are, thereby, created in the knife-line region that are susceptible to IGC. This form of attack differs from normal HAZ sensitization occurring in nonstabilized austenitic stainless steels. Here, the TTT details of $(Fe,Cr)_{23}C_6$ formation can produce a zone of material (heat-affected zone) that can be sensitized upon welding in a single heat excursion as discussed above.

Sensitization may also occur in annealed austenitic stainless steels by nonequilibrium segregation of phosphorus and silicon to grain boundaries [62]. Such segregation can be produced thermally and by irradiation in nuclear reactions. The sensitized material is then rendered susceptible to IGC in highly oxidizing environments such as nitric acid containing high-valence metal ions [69]. Regarding electrochemical mechanisms, this type of IGC is often observed at high oxidizing potentials near those associated with transpassive dissolution. Hence, the transpassive dissolution rate is faster in the grain boundary region.

4.3.3.2 Sensitization and Intergranular Corrosion in Ni-Cr-Fe and Fe-Cr-Ni-Mo Alloys

The metallurgical conditions promoting IGC in Ni-Cr-Fe and Fe-Cr-Ni-Mo alloys containing considerable nickel differs from stainless steels [62]. Carbon

solubility decreases as nickel content rises in austenite [70]. Secondly, Cr diffusion is faster in Ni-base austenitic alloys compared to austenitic Fe-base alloys [61]. These metallurgical factors dictate that the TTT behavior associated with carbide formation and, hence, sensitization is shifted to higher temperatures compared to austenitic stainless steels. In addition, other types of carbides are formed in addition to, or instead of $M_{23}C_6$, (e.g. M_3C_7, M_6C) [70]. Moreover, faster Cr diffusion and more rapid carbide precipitation kinetics in these alloys lead to leveling of Cr concentrations in the bulk and Cr-depletion profiles are not observed. Thus, IGC is not as unambiguously associated with Cr depletion as in the case of stainless steels. Significant heat-to-heat variations in the levels of Cr depletion are observed in alloy 600. Semicontinuous carbides have even been observed to be beneficial towards IGSCC and not detrimental to IGC. Alloy 690 (60% Ni-30% Cr-10% Ni) containing 0.02% C is not readily sensitized and will not exhibit IGA in the severe Huey test [71]. Other phases have been postulated to cause IGC in this class of alloys such as Sigma and Laves phases. Several reviews discuss the IGC behavior of high Ni alloys [72, 73].

4.3.3.3 Intergranular Corrosion in Al-base Alloys

Severe IGC is not observed in high purity Al, or Alclad products that do not form second-phase precipitates at grain boundaries [74]. It is also not observed in alloys that form coarse constituents possessing similar electrochemical properties as the matrix. However, small levels of impurities can induce mild IGC. The mechanisms responsible for IGC is high-purity alloys are complex. They range from the segregation of elements that disrupt passivity to elements that replate preferentially along boundaries and then enhance local cathodic reactions.

IGC is observed in heat-treatable, precipitation age-hardened Al alloys, particularly after slow cooling of thick sections or after certain isothermal heat treatments. In fact, quench rate over the temperature range from 400 to 315 °C is a very strong factor determining both IGC and IGSCC susceptibility in Al-Cu and Al-Cu-Mg alloys that are, subsequently, naturally aged [75].

The metallurgical cause for susceptibility to IGC varies with alloy composition and microstructure. Exfoliation refers to a highly directional form of IGC in rolled or wrought product with unrecrystallized grains elongated in one direction, typically parallel to the rolling or extrusion direction. Cross-sectional metallography may reveal flaking or peeling back of elongated grains due the force exerted by corrosion product wedging. This produces a layered, flaked appearance in the direction parallel to the rolling or extrusion direction. IGC refers to intergranular corrosion in equaixed grains typical of recrystallized microstructures. In general, IGC results from the segregation of a corrosion stimulating element, the depletion of a beneficial alloying element in a zone adjacent to the boundary during precipitation of a second phase, and the formation of precipitates that are detrimental to corrosion resistance. All of these can render a zone along the grain boundary susceptible to corrosion while grain interiors remain passive. However, the electrochemical framework describing susceptibility differs from stainless steels in which the susceptible grain boundary zone exhibits an active-passive transition in E-log(i) behavior as shown in Fig. 4(a). In the case of Al-base alloys, the grain boundary region is proposed

to either have a more negative open circuit potential resulting in microgalvanic coupling between the boundary and matrix and/or is more susceptible to pitting [76]. The Cu-depleted grain boundary zone exhibits a more negative critical pitting potential compared to grain interiors when the composition of the grain boundary zone is reproduced in large surface area test coupons and evaluated for pitting susceptibility [77]. This is consistent with the notion that the critical pitting potentials of Al-Cu solid solution alloys are a strong function of Cu content [78]. Hence, the proposed criterion for selective grain boundary pitting is $E_{\text{crit-gb}} < E_{\text{app}} < E_{\text{crit-grain}}$. Thus, a line of pits along the grain boundary is proposed to cause IGC at certain potentials in which the grain interior remains below their pitting potentials as shown in the electrochemical framework of Fig. 4(b). This is consistent with some experimental observations that support this electrochemical framework for IGC [77]. However, such theories are complicated by many factors including evidence of a transition to IGC within large pits formed across many grains in some Al alloys. Although this observation is consistent with the notion of a specific chemistry for IGC susceptibility in addition to a specific metallurgical condition, it is inconsistent with the notion that IGC occurs over a potential range at which grain interiors do not pit in comparison to the grain boundary regions. Other complications with the preferential pitting theory exist as well such as the problem that pitting potentials are often dependent on specimen surface area, scan rate, oxide properties, and so on. Thus, further refinements in these theories are probably required. It suffices to say that the electrochemical properties of grain boundaries differ from those of grain interiors.

4.3.3.3.1 **Intergranular Corrosion in Al-Cu, Al-Cu-Mg, and Al-Cu-Li Alloys** A prominent factor in the IGC susceptibility of Al-Cu, Al-Cu-Mg, and Al-Cu-Li alloys is grain boundary Cu depletion as a result of heterogeneous nucleation of Cu-containing grain boundary phases. According to the electrochemical framework discussed above, this leads to differences in localized corrosion susceptibility between grain boundaries and interiors. This is the often cited mechanism proposed to explain IGC and IGSCC susceptibility in these alloys after slow cooling or isothermal age-hardening heat treatment over the 400 to 150 °C range at which such grain boundary phases may develop [75–79]. Figures 21 and 22 show the predicted windows of IGC susceptibility in terms of critical potentials for localized corrosion [80, 81]. Figure 22(a) shows a schematic of the microstructure that could produce such behavior according to the Cu-depletion mechanism. Figure 23 shows the resulting corresponding region of IGC/IGSCC susceptibility in terms of aging time. Note the agreement with Fig. 22(b). Prolonged isothermal heat treatment can lead to Cu depletion from the grain interiors of these alloys such that an electrochemical framework that bases IGC susceptibility on differences in critical potentials between the grain boundary depleted zone and grain interiors is eliminated. IGSCC resistance is thus restored at long aging times as shown in Fig. 23. Other mechanisms have been proposed on the basis of the presence of anodic precipitate phases at grain boundaries. The Al_2Cu phase is cathodic to the Al-Cu_{ss} as well as regions adjacent to grain boundaries and, therefore, cannot account for an anodic electrochemical path that enables IGC in Al-Cu alloys [77]. In contrast with more noble Al_2Cu, the Al_2CuMg and Al_2CuLi

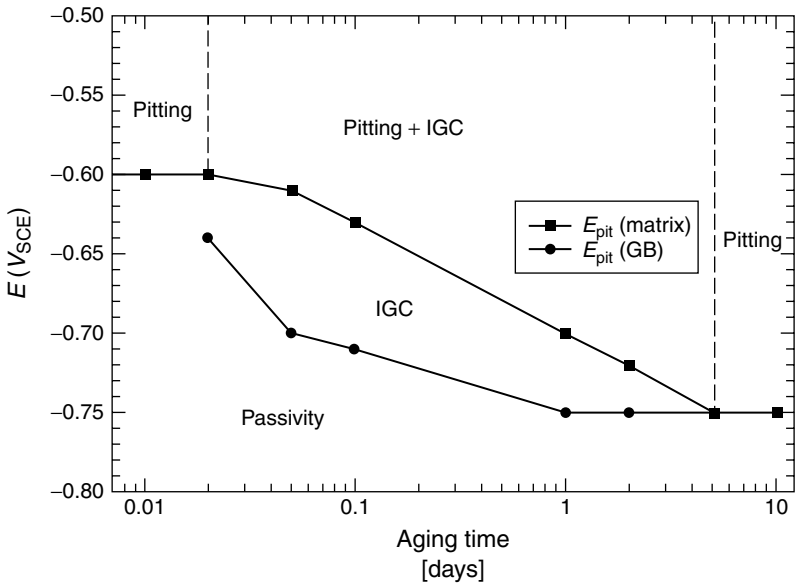


Fig. 21 Pitting potentials as a function of heat-treatment time for grain matrix and solute-depleted zone associated with grain boundary in Al-4 wt. % Cu alloy. The region of IGC (and also IGSCC) susceptibility is indicated. (After Ref. [80].)

phases are known to actively dissolve in most solutions [80–82]. Therefore, these phases could account for IGC when such anodic precipitates form along boundaries. However, it has been rationalized and suggested from the potential dependency of IGC and IGSCC in Al-Cu, Al-Cu-Mg, and Al-Cu-Mg-Ag alloys that Cu depletion at grain boundaries is a main factor promoting IGC susceptibility [81, 83, 84]. Similar arguments have been made in the case of Al-Cu-Li alloys [85]. IG growth kinetics are often observed to follow a t^n penetration law with respect to time such as

$$D = Kt^n \tag{9}$$

Where D is the depth of penetration, K is a constant, and n is a faction often found to be between 0 and 1. Experiments conducted on IGA of Al-4% Cu using the foil penetration technique have indicated such a penetration law [86]. In these experiments, little effect of stress was seen 80% [86]. This method has been used more recently to study AA 2024-T3 [87]. A $t^{1/2}$ penetration dependency was observed. IG growth kinetics were affected by stress and specimen orientation. Faster penetration was observed in the rolling direction. Applied stress had a tendency to increase the value of K and slightly decrease n.

4.3.3.3.2 **Intergranular Corrosion in Al-Mg Alloys** These alloys are not heat-treatable and derive strength from solid solution, strain hardening, and dispersion strengthening [88]. Nevertheless, thermal exposure may occur in service. The main factor promoting the IGC susceptibility of Al-Mg alloys is thought to be the Mg_2Al_3 phase that is anodic to Al-Mg solid solution in grain interiors. A limit of 3 wt. % Mg is often proposed to minimize IGC of wrought Al-Mg alloys on the basis of the premise that

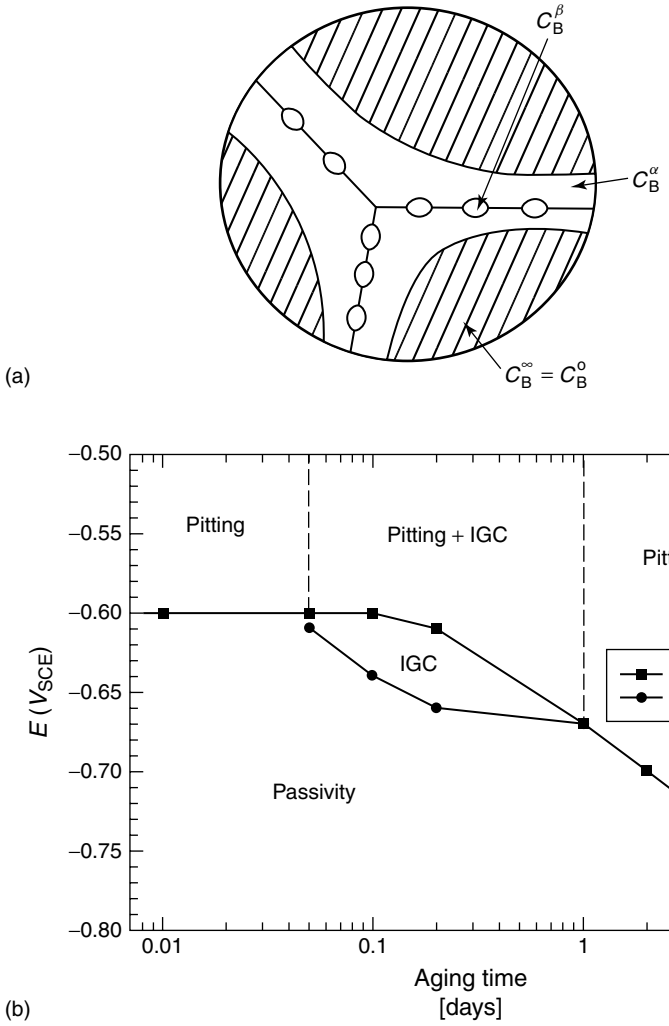


Fig. 22 (a) Schematic of heterogeneous grain boundary precipitates formed along a grain boundary. The white zone indicated a solute-depleted zone. The matrix is supersaturated in solute B above the equilibrium concentration. C_B^∞ is the supersaturated matrix composition far from the precipitate taken to equal the overall composition C_B^o. C_B^α is the alloy composition in equilibrium with the β phase precipitate. (b) Pitting potentials as a function of heat-treatment time for grain matrix and solute-depleted zone associated with grain boundary in Al-4% Cu-1.47% Mg alloy (wt. %). The region of IGC (and also IGSCC) susceptibility is indicated. (After Ref. [81].)

the decreased rate of Mg_2Al_3 phase precipitation and lack of a continuous network of this phase on grain boundaries would impart IGC resistance. However, some evidence suggests that Mg segregation may play a role in IGC susceptibility [89] and that such segregation may precede precipitation of Mg_2Al_3. Moreover, the

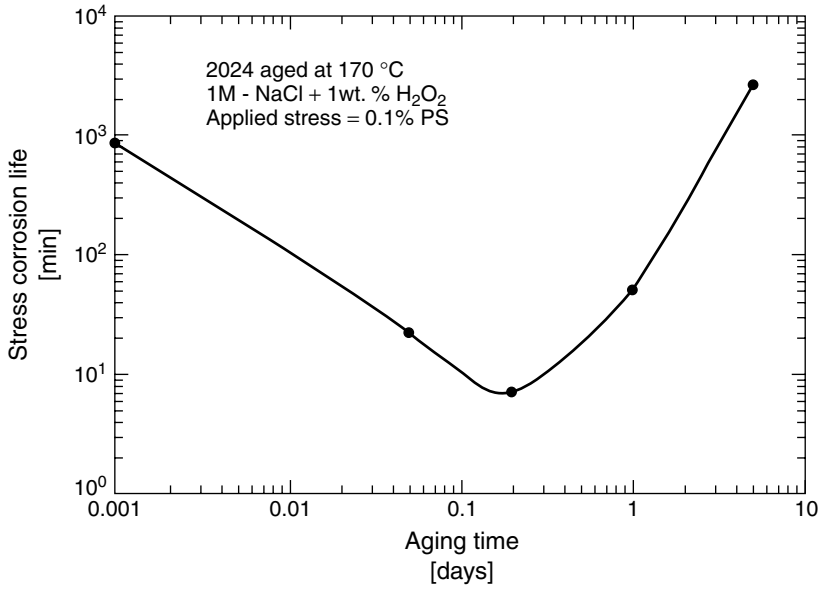


Fig. 23 Time-to-failure as a function of isothermal aging time for Al-Cu-Mg alloy. The region of rapid time-to-failure coincides with the electrochemical framework illustrating the expected region for IGC susceptibility based on critical potentials. (After Ref. [81].)

exact Mg compositional limit depends critically on strain hardening, grain structure, and time–temperature history as well as on Mg content [88]. Certain Al-Mg alloys and tempers are very susceptible to exfoliation corrosion. In general, heat treatments that promote more homogeneous precipitation improve IGC resistance.

4.3.3.3.3 **Intergranular Corrosion in Al-Zn-Mg and Al-Zn-Mg-Cu Alloys** IGC in the Al-Zn-Mg class of heat-treatable alloys has been attributed to Mg and Zn segregation, as well as formation of Mg- or Zn-containing grain boundary phases such as the $MgZn_2$ phase [90]. In Al-Zn-Mg-Cu alloys, Cu depletion is also cited as a metallurgical condition leading to IGC [74, 91]. Slow quenching and certain isothermal heat treatments can lead to susceptibility by creating these conditions. The electrochemical framework advanced for all of these cases involves differences in critical pitting potentials between Cu-depleted grain boundary regions, active grain boundary phases, and the solid solution in grain interiors. Al-Zn-Mg-(Cu) alloy plate and sheet can be very susceptible to exfoliation especially in peak-aged tempers when galvanically coupled to other metals such as steel rivets. T73 and T76 tempers reduce such susceptibility but the exact mechanism by which improvement is imparted remains uncertain [74].

4.3.3.3.4 **Intergranular Corrosion in Al-Mg-Si Alloys** This class of heat-treatable alloys can be made resistant to IGC when an ideal combination of magnesium and silicon are alloyed to result in an Mg_2Si

constituent phase. However, an excess of Si can lead to IGC, which is attributed to the cathodic nature of the insoluble silicon. IGC is more prevalent in the peak strength tempers when exposed to a harsh environment. Cathodic additions or impurities can increase susceptibility [92].

4.3.3.4 Grain Boundary Segregation and Intergranular Corrosion in Ferrous and Nickel-base Alloys

Grain boundary enrichment of impurities can contribute to IGC and IGSCC susceptibility in ferrous and nickel-base alloys. Enrichment of impurities is another mechanism by which these alloys can be rendered susceptible to IGC and IGSCC besides Cr depletion upon carbide formation. Susceptibility depends on electrolyte composition, temperature, and level of impurity segregation. Enrichment ratios, β_b, as high as 10^5 are possible [93]. Therefore, a minor impurity with a low overall concentration can be enriched at grain boundaries to concentrations greater than 10 to 20 at. %. Hence, the electrochemical properties of the boundary can be altered from grain interiors. Electrochemical frameworks for susceptibility in these materials are based on the existence of an active-passive region in E-log(i) behavior (Fig. 4a) over a potential range at which the grain matrix is passive [62]. Alternatively, transpassive dissolution occurs more readily than in grain interiors when exposure to oxidizing solutions occurs.

Ferritic stainless steels exhibit IGSCC in hot nitrate, caustic, carbonate, and other environments. The phenomenon is potential dependent as discussed above. Susceptibility has been attributed to carbon and phosphorus segregation [94, 95]. Levels as low as 2 to 3 at. % can alter the passivity of iron in hot nitrate solutions. Iron corrodes intergranularly at +800 mV versus SCE in nitrate solutions with 10 ppm carbon [96]. Grain boundary impurity segregants including phosphorus, silicon, sulfur, and nitrogen have been reported for austenitic stainless steels [97]. Phosphorus is proposed to induce IGC in highly oxidizing solutions. Phosphorus is the primary segregant cited in the case of alloy 600 [98]. However, IGC and IGSCC have not been unambiguously linked to phosphorus content in this alloy. Phosphorus has also been shown to cause IGSCC in nickel at oxidizing potentials in sulfuric acid [99]. Sulfur is an effective promoter of IGC in these materials at both oxidizing potentials and those associated with active dissolution [99]. However, stress was still required to produce IGC even though an active grain boundary dissolution mechanism could be traced to grain boundary susceptibility [99].

4.3.4 Modern Concepts

4.3.4.1 Understanding Dissolution Path Connectivity Using Bond Percolation Theory

A critical question is whether a continuous IGC path made up of a connected cluster of highly susceptible boundaries can grow in a polycrystalline material and whether there exists a critical threshold percentage of *active* boundaries (i.e. *active* bonds) that enables intergranular cracking. Theories on fracture in disordered media have long considered the idea of a critical connected cluster of defects and statistical distributions of clustered defects [100]. In bond percolation theory, the probability of forming an infinite cluster of connected bonds rapidly approaches one at a critical percentage of active bonds [101]. This critical percentage is called the percolation threshold [102]. In two dimensions, uniformly

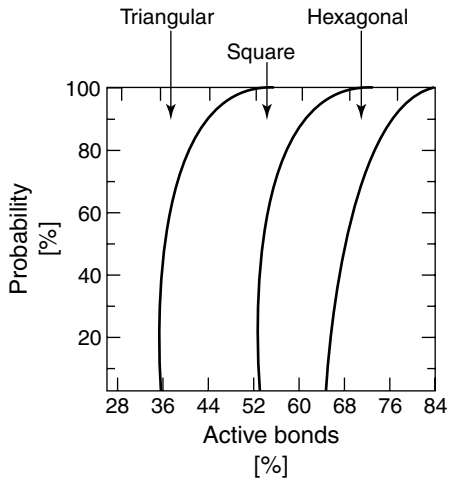


Fig. 24 Bond percolation thresholds predicted for two-dimensional arrays of space-filling boundaries consisting of various geometries [101].

sized grains can be modeled by arrays of hexagons at which each of the six sides forming the boundaries is a bond. The bond percolation threshold for a hexagonal array of bonds is 0.65, that is, 65% of the bonds are defective [101] as seen in Fig. 24. A three-dimensional array of grain boundaries can be represented as a collection of two-dimensional planar interfaces, each representing a grain boundary facet (called bonds) that represents the interface between two grains [103]. An array of such grain boundaries has been represented by a Kelvin tetrakaidecahedron consisting of eight hexagonal facets and six square facets [104]. In a binary approach in which bonds are described as either active or inactive, each of the grain boundaries (bonds) can be *active* (e.g. sensitized, in the case of IGSCC of stainless steel) or *inactive* (e.g. not sensitized). Monte Carlo computer simulations have revealed the fraction of active bonds required for percolation in this three-dimensional structure [104]. The simulations were performed on arrays of 5,4,000 tetrakaidecahedral-shaped grains, and 10 simulations were performed at each percentage of *active* bonds to produce statistically valid results [104]. The critical percentage of *active* grain boundary facets required to form a large cluster of connected grain boundary facets, each touching one another along a common edge of the Kelvin's tetrakaidecahedron, was found to be 23% as shown in Fig. 25. The meaning of such a percolation threshold, once exceeded, is that a high probability exists of obtaining an infinite cluster of connected, *active* grain facets. Another percolation threshold at 89% *active* bonds was found for a two-dimensional array of connected *active* grain facets that form a ''rumpled'' sheet within the three-dimensional array of grains [104]. In the context of environment-assisted intergranular corrosion or cracking, the resulting premise is that a material possessing greater that 23, 65, or 89% of easily embrittled or easily corroded *active* grain boundaries will undergo corrosion with a significant degree of IGA. Moreover, any material with a percentage of *active* grain boundaries less than 23% will not exhibit widespread IGC since a large continuous connected path of *active* grain boundaries cannot exist. The 23% threshold has unambiguously been associated with an abrupt increase in IGC

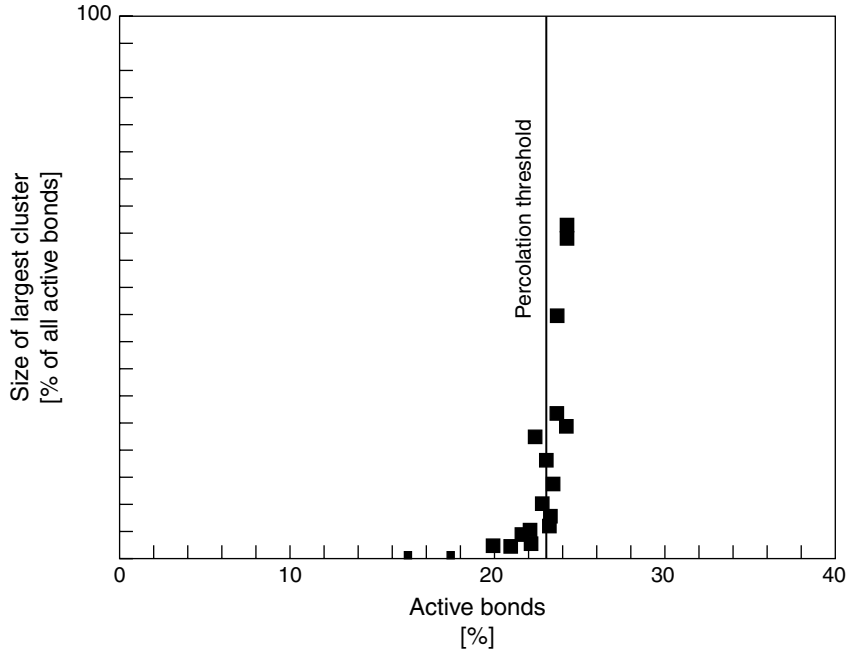


Fig. 25 Size of largest connected grain boundary cluster expressed as a percentage of all boundaries versus % active grain boundaries for an array of space-filling, tetrakaidecahedral-shaped grains. The connected cluster size increases abruptly at the 23% percolation threshold. (After Ref. [104].)

and IGSCC susceptibility in sensitized stainless steels [104, 105].

4.3.5 Mitigation of Intergranular Corrosion by Metallurgical Alteration

4.3.5.1 Quench Rate Sensitivity

The effects of quench rate on IGC for Al-Cu, Al-Cu-Mg, and Al-Cu-Mg-Mn alloys as well as for austenitic stainless steels is considered to be well-understood [43, 74, 75, 106]. Integration of the effects of precipitation and solute depletion at each temperature during a quench (i.e., quench factor analysis) can be compared to isothermal time–temperature-sensitization diagrams in order to predict the quench rate required to avoid IGC [43, 74]. Alloys such as 2024-T3 require quench rates faster than $500\,^{\circ}\mathrm{C\ sec^{-1}}$. [75] For Al-Zn-Mg and Al-Zn-Mg-Cu alloys, the situation regarding quench rate is a little less clear [107]. For such alloys, the required quench rate is believed to depend upon the Cu content of the alloy. Slow quench rates are considered to be better for Cu-lean alloys. The benefits of slow quench rates are believed to be associated with promotion of the formation of incoherent precipitates that favor homogeneous plastic deformation. Fast quench rates are required for Cu-bearing alloys with greater than 1% Cu. This requirement can be interpreted within the context of the Cu-depletion mechanism as one that minimizes grain boundary precipitation and formation of Cu-depletion profiles.

4.3.5.2 Alloy Additions to Countersensitization and IGC in Stainless Steels: Stabilized Grades

Several measures can be taken to improve the IGC resistance of austenitic stainless steels. One approach is to minimize carbon content. Another is to add alloying elements that form carbides that are more stable than those of Cr. Lowering the carbon content below 0.03% will prevent sensitization and IGC during most welding and thermal treatments [70]. Stabilized grade austenitic stainless steels contain Ti and Nb. These elements form stable carbides that remove carbon from solid solution, thereby minimizing chromium carbide formation and associated Cr depletion. The % Ti required is often estimated as five times the sum of the carbon and nitrogen contents (C + N %) [70]. Nitrogen must be considered because TiN is very stable and could form preferentially, leaving carbon available for sensitization. The Nb content required to suppress IGC susceptibility is often estimated to be eight times the % C [70]. Stabilized stainless steels are often heated at 900 °C to form stabilizing carbides.

The clearest approach to avoiding sensitization in ferritic stainless steels is to minimize the interstitial C and N contents. However, the exact levels allowed depend on exact alloy composition. The greater the Cr and Mo contents are in the alloy, the more resistant the alloy will remain for higher interstitial levels [70]. For 18Cr-2Mo steels, the C + N level must be as low as 60 to 80 ppm. Ti and/or Nb can also be added to ferritic steels. For 26Cr-1Mo steels, the minimum stabilizer content required is given by [108]:

$$\mathrm{Ti} + \mathrm{Nb} = 0.2 + 4(\mathrm{C} + \mathrm{N}) \qquad (10)$$

4.3.5.3 Retrogression and Re-age of Al Precipitation Age-hardened Alloys

Heat-treatable Al-base alloys are often overaged using a duplex heat treatment to improve IGC, IGSCC, and/or exfoliation resistance. However, the loss in peak strength makes this practice undesirable. In contrast, retrogression (e.g. reversion) and re-age (RRA) of Al-Zn-Mg-Cu alloys make it possible to optimize resistance to IGSCC and IGC by rendering it equivalent to the resistant overaged condition [107]. Peak-aged strength levels are obtained as well. The concept of RRA of Al-Zn-Mg-(Cu) alloys involves the reheating of peak-aged material in the temperature range from 180 to 280 °C followed by re-aging at lower temperatures to achieve peak strength. The RRA practice is thought to alter either the grain boundary precipitates, grain boundary segregation or grain boundary solute distributions but current understanding is uncertain. Alteration of any of these metallurgical factors could conceivably alter IGC and IGSCC susceptibility.

Preaged Al-Li, Al-Li-Cu, and Al-Li-Cu-Mg alloys have been heat-treated in a way such that δ' precipitates in the matrix can be redissolved (e.g. reverted and re-aged) while grain boundary phases such as δ in Al-Li binary alloys and T_1 (Al_2CuLi) and T_2 (Al_6Li_3Cu) formed during preage in Al-Li-Cu alloys remain undissolved [109–111]. This heat treatment was mainly applied to address poor short transverse direction fracture toughness properties of these alloys [112]. The double age has been found to affect both fracture toughness [109–112] and IGSCC behavior [113]. Changes in fracture toughness have been attributed to desegregation, solute redistribution in PFZs, changes in deformation mode, and precipitation of other phases. Currently, complete understandings of the effect of the double age on IGC are lacking.

4.3.5.4 Healing and Leveling of Solute-depletion Profiles

Leveling of solute-depletion profiles such that the concentration of beneficial solute in the matrix is equal to the equilibrium concentration at all positions is one way of eliminating a zone of preferential corrosion attack along grain boundaries. Schematically, this is illustrated by Fig. 26. Figure 26(a) illustrates overlap of solute-depletion profiles between adjacent precipitates. Figure 26(b) illustrates solute consumption to the extent that solute-depletion profiles are eliminated. In the case of Al-Cu alloys, leveling of the copper concentration in substitutional solid solution eliminates the potential difference between grain boundary and matrix as shown in Figures 21 and 22(b).

A slightly more complicated situation can exist during sensitization of austenitic stainless steels discussed above. Here, carbon activity is assumed to be at equilibrium because of fast diffusion of interstitial carbon at all relevant temperatures. Moreover, the bulk carbon content is negligibly altered during early stages of the carbide formation reaction since one carbon atom consumes almost four Cr atoms to form the carbide: $23Cr + 6C = Cr_{23}C_6$. This is in contrast to the situation regarding Cr content. At high temperatures (e.g. $>825\,^{\circ}C$ in austenitic stainless steels), fast Cr diffusion minimizes Cr depletion and sensitization is minimized. However, at lower temperatures, Cr diffuses more slowly and cannot be assumed to be at equilibrium except at the carbide interface when precipitation and growth is diffusion controlled. However, prolonged sensitizing heat treatment and extensive carbide formation can eventually deplete carbon from the alloy matrix such that its concentration falls below the initial content. When this happens, the Cr content in equilibrium with the carbides formed begins to increase. This can be rationalized using the equilibrium solid-state reaction shown in Eq. (8). Under equilibrium conditions, assuming unity carbide activity and a fixed equilibrium constant, a decrease in equilibrium interstitial carbon

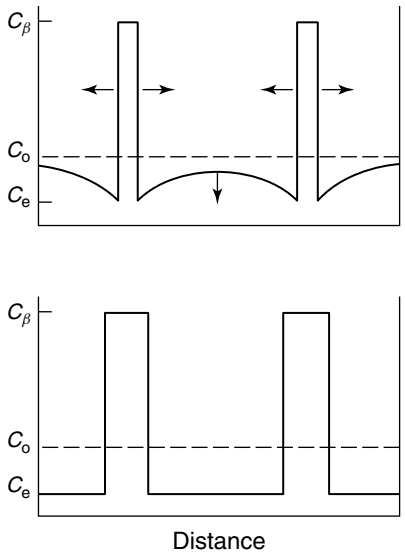


Fig. 26 Schematic of overlapping solute-depletion profiles illustrating (a) solute depletion between nearby precipitates, (b) attainment of equilibrium solute concentration uniformly across the grain between precipitates. C_o is overall alloy composition, C_e is the concentration in equilibrium with the β phase. (Ref. [25], from Physical Metallurgy Principles, 3rd edition by Reed-Hill/Abbaschian, © 1992. Reprinted with permission of Brooks/Cole, a division of Thomson Learning: www.thomsonrights.com, Fax 800 730-2215.)

activity results in a corresponding increase in equilibrium Cr activity. This is the Cr content in the matrix around the carbide assumed to be in equilibrium with the carbide. Hence, the phenomenon of healing during isothermal heat treatment is one in which the equilibrium Cr content adjacent to a carbide at first decreases as short times when carbon content is preserved but then increases during prolonged sensitization heat treatment due to carbon depletion. The ''healed'' microstructure has improved IGC resistance because the zone of metal adjacent to boundary carbides possesses a greater Cr content than the initial equilibrium Cr concentration before carbon depletion. Healing is more likely during intermediate temperature heat treatments in which diffusion control carbide growth is fast [114, 115].

4.3.5.5 Minimization of Metalloid Impurities (i.e., Alloy Cleanliness) and Grain Boundary Engineering

Use of high purity grade alloying elements can improve resistance to IGC and IGSCC. This practice is notable in Ni and Fe-base alloys in which metalloid impurities such as sulfur and phosphorus promote IGC. Therefore, a cleaner, low-sulfur alloy would possess greater resistance to IGC. Another approach would be to add alloying elements that getter detrimental metalloids. A third approach would be to purposely add alloying elements that preferentially segregate to grain boundaries but that do not by themselves exacerbate corrosion. Another approach applies to nonequilibrium segregation. Alloying elements can be added to alter the binding energy of detrimental solute to vacancies so as to minimize segregation by nonequilibrium processes whereby vacancies drag solute to vacancy sinks. Finally, concepts of grain boundary engineering have been employed to produce a network of unsusceptible, low angle or CSL boundaries that resist IGC [21–23, 116].

References

1. Standard Tech. Relating to Corrosion Testing, Standard G-15, ASTM, Philadelphia, Pa., 1999, *03.02*, pp. 65–69.
2. K. Osozawa, H. J. Engell, *Corros. Sci.* **1966**, *6*, 389.
3. R. P. Frankenthal, H. W. Pickering, *J. Electrochem. Soc.* **1973**, *120*, 23.
4. T. M. Devine, *Acta Metall. Mater.* **1988**, *36*, 1491.
5. H. J. Rocha, G. Lennartz, *Arch. Eisenhuettenwesen* **1955**, *26*, 117.
6. R. C. Newman, K. Sieradzki, *Corros. Sci.* **1983**, *23*, 363.
7. K. T. Aust, O. Iwao, Segregation and corrosion at grain boundaries in *Localized Corrosion*, NACE 3, (Eds.: R. W. Staehle, B. F. Brown, J. Kruger, A. Agarwal), NACE, Houston, Tex., 1973.
8. M. G. Fontana, *Met. Trans.* **1970**, *1*, 3251.
9. J. M. Howe, *Interfaces in Materials*, John Wiley & Sons, New York, 1997.
10. W. T. Read, W. Shockley, *Phys. Rev.* **1950**, *78*, 275.
11. D. Wolf, K. R. Merkle in *Material Interfaces: Atomic Level Structure and Properties* (Eds.: D. Wolf, S. Yip), Chapman & Hall, London, 1992, pp. 87–150.
12. E. D. Hondros, D. McLean, *Philos. Mag. A* **1974**, *29*, 771.
13. T. Wantanabe, P. W. Davies, *Philos. Mag. A* **1978**, *37*, 649.
14. J. Don, S. Majumdar, *Acta Metall. Mater.* **1986**, *34*, 961.
15. T. Wantanabe, M. Yamada, S. Shima et al., *Philos. Mag. A* **1979**, *40*, 667.
16. J. A. Kargol, D. L. Albright, *Metall. Trans. A* **1977**, *8*, 27.
17. O. P. Arora, M. Metzger, *Trans. Metall. Soc. AIME* **1966**, *236*, 1205.
18. G. Hasson, J.-Y. Boos, I. Herbeuval et al., *Surf. Sci.* **1972**, *31*, 115.
19. M. Yamashita, T. Mikaki, S. Hashimoto et al., *Philos. Mag. A* **1991**, *63*, 695–705.
20. M. Yamashita, T. Mikaki, S. Hashimoto et al., *Philos. Mag. A* **1991**, *63*, 707–726.
21. G. Palumbo, K. T. Aust, *Acta Metall. Mater.*, **1990**, *38*, 2343.

22. D. C. Crawford, G. S. Was, *Metall. Trans. A* **1992**, *23A*, 1195.
23. T. A. Mason, B. L. Adams, *J. Mater.* **1994**, *October 1994*, 43–45.
24. M. L. Kronberg, F. H. Wilson, *Trans. AIME* **1949**, *85*, 501.
25. R. E. Reed-Hill, R. Abbaschian, *Physical Metallurgy Principles*, 3rd ed., PWS Publi., Boston, Mass., 1994, pp. 194–201, 501–506, 698–706.
26. H. Kaesche, *Metallic Corrosion, Principles of Physical Chemistry and Current Problems*, NACE, Houston, Tex., 1985.
27. W. Frank, L. Graf, *Z. Metallkd.* **1975**, *66*, 555.
28. L. Graf, *Acta Metall. Mater.* **1958**, *6*, 116.
29. R. G. Kelly, R. C. Newman, *Metall. Trans. A* **1991**, *22A*, 531–541.
30. E. D. Hondros, M. P. Seah, *Int. Metals Rev.* **1977**, *222*(22), 262.
31. E. D. Hondros, *Precipitation Processes in Solids*, The Metallurgical Society of AIME, Warrendale, Pa., 1978, pp. 8–20.
32. E. D. Hondros, M. P. Seah in *Physical Metallurgy* (Eds.: R. W. Cahn, P. Haasen), Elsevier, Amsterdam, 1993, p. 888.
33. M. P. Seah, *J. Catal.* **1979**, *57*, 450.
34. A. R. Miedema, P. F. de Chatel, F. R. de Boer, *Physica* **1980**, *B100*, 1.
35. M. P. Seah, E. D. Hondros, *Proc. R. Soc. London* **1973**, *A335*, 191.
36. C. P. Flynn, *Philos. Mag.* **1964**, *10*, 909–915.
37. R. P. Johnson, *Phys. Rev.* **1939**, *56*, 814.
38. T. R. Anthony, *Acta Metall. Mater.* **1969**, *17*, 603.
39. P. Marcus, J. Oudar, *Mater. Sci. Eng.* **1980**, *42*, 191–197.
40. P. Marcus, Sulfur assisted corrosion mechanisms and the role of alloyed elements in *Corrosion Mechanisms in Theory and Practice* (Eds.: P. Marcus, J. Oudar), Marcel Dekker, New York, 1995.
41. C. Zener, *J. Appl. Phys.* **1949**, *20*, 950.
42. W. L. Fink, L. A. Willey, *Trans. AIME* **1948**, *175*, 414–427.
43. J. E. Hatch, *Aluminum, Properties and Physical Metallurgy*, ASM, Metals Park, Ohio, 1984, pp. 158–160.
44. H. B. Aaron, H. I. Aronson, *Acta Metall. Mater.* **1968**, *16*, 789.
45. E. C. Bain, R. H. Aborn, J. J. B. Rutherford, *Trans. Am. Steel Treating Soc.* **1933**, *21*, 481.
46. S. M. Bruemmer, B. W. Arey, L. A. Charlot, *Corrosion* **1992**, *48*, 42.
47. S. M. Bruemmer, L. A. Charlot, *Scr. Metall.* **1986**, *20*, 1019.
48. *Grain Boundary Structure and Kinetics*, ASM, Metals Park, Ohio, 1980, p. 322.
49. ASTM Standard A 262, Practices for Detecting Susceptibility to Intergranular Attack in Austenitic Stainless Steels, Annual Book of ASTM Standards, 1999, *01.03*.
50. ASTM Standard G 28, Standard Test Methods of Detecting Susceptibility to Intergranular Corrosion in Wrought, Nickel Rich, Chromium-Bearing Alloys, Annual Book of ASTM, 1999, *03.02*.
51. M. A. Streicher, Intergranular corrosion in *Corrosion Tests and Standards: Application and Interpretation* (Ed.: R. Baboian), ASTM Manual 20, ASTM, Philadelphia, Pa., 1995.
52. ASTM Standard G 67, Standard Test Method for Determining the Susceptibility to Intergranular Corrosion of 5XXX Series Aluminum Alloys by Mass Loss After Exposure to Nitric Acid, Annual Book of ASTM, 1999, *03.02*.
53. ASTM Standard G 110, Standard Practice for Evaluating Intergranular Corrosion Resistance of Heat Treatable Aluminum Alloys by Immersion in Sodium Chloride + H_2O_2 Solutions, Annual Book of ASTM, 1999, *03.02*.
54. B. J. Connolly, J. R. Scully, *Corrosion/2000*, Paper No. 00367 NACE International, Houston, Tex., 2000.
55. B. J. Connolly, J. R. Scully, *Corrosion/2002*, Paper No. 02434, NACE International, Houston, Tex., 2002.
56. A. Rota, H. Bohni, *Mater. Sci. Forum* **1989**, *44–45*, 177–190.
57. H. W. Pickering, F. H. Beck, M. G. Fontana, *Corros. J.* **1962**, *18*, 230.
58. M. J. Robinson, *Corros. Sci.* **1983**, *23*, 887–899.
59. M. J. Robinson, *Corros. Sci.* **1982**, *22*, 775–790.
60. E. C. Bain, R. H. Aborn, J. J. B. Rutherford, *Trans. Am. Steel Treating Soc.* **1933**, *21*, 481.
61. A. John Sedriks, *Corrosion of Stainless Steels*, ECS Monogram Series, 2nd ed., John Wiley & Sons, New York, 1996, p. 231.
62. R. H. Jones, ASM Metals Handbook, 9th ed., ASM-International, Metals Park, Ohio, 1987, p. 55, Vol. 13.
63. E. L. Hall, C. L. Briant, *Metall. Trans.* **1984**, *15A*, 793–811.

64. R. L. Cowan, C. S. Tedmon, *Advances in Corrosion Science and Technology*, Plenum Press, New York, 1973, Vol. 3, p. 293.
65. R. M. Davidson, T. BeBold, M. J. Johnson, *Corrosion*, 9th ed., Metals Handbook, ASM, Metals Park, Ohio, 1987, Vol. 13, p. 547.
66. V. Cihal, *Protect. Metals* **1968**, *4*(6), 563.
67. M. A. Streicher, *Intergranular Corrosion of Stainless Steels*, ASTM STP 656, ASTM, Philadelphia, Pa., 1978, p. 3.
68. H. L. Holzworth, F. H. Beck, M. G. Fontana, *Corrosion* **1951**, *7*, 441.
69. J. S. Armijo, *Corrosion* **1968**, *24*, 24.
70. R. Steigerwald, *ASM Metals Handbook*, 9th ed., ASM-International, Metals Park, Ohio, 1987, p. 128, Vol. 13.
71. A. J. Sedriks, J. W. Schultz, M. A. Cordovi, *Boshoku Gijutsu (Corros. Eng.)* **1979**, *28*, 82.
72. M. H. Brown, *Corrosion* **1969**, *25*, 438.
73. M. H. Brown, R. W. Kirchner, *Corrosion* **1973**, *29*, 470–474.
74. J. R. Davis, (Ed.), *Corrosion of Aluminum and Aluminum Alloys*, ASM-International, Metals Park, Ohio, 1999, p. 67.
75. D. O. Brown, R. H. Brown in *Stress Corrosion Mechanisms for Aluminum Alloys, Fundamental Aspects of Stress Corrosion Cracking* (Eds.: R. W. Staehle, A. J. Forty, D. Van Rooyen), NACE, Houston, Tex., 1969, pp. 466–506.
76. H. Kaesche, Pitting and intergranular corrosion of Al alloys in *Localized Corrosion* (Eds.: B. F. Brown, J. Kruger, R. W. Staehle), NACE, Houston, Tex., 1975, p. 516.
77. J. R. Galvele, S. M. de Micheli, *Corros. Sci.* **1970**, *10*, 795.
78. I. L. Muller, J. R. Galvele, *Corros. Sci.* **1977**, *17*, 179–193.
79. C. Kumai, J. Kusinski, G. Thomas et al., *Corrosion* **1989**, *45*(4), 294–302.
80. K. Sugimoto, H. Hoshino, M. Kageyama et al., *Corros. Sci.* **1975**, *15*, 709–720.
81. K. Urushino, K. Sugimoto, *Corros. Sci.* **1979**, *19*, 225–236.
82. R. G. Buchheit, J. P. Moran, G. E. Stoner, *Corrosion* **1994**, *50*(2), 120–130.
83. A. Garner, D. Tromans, *Corrosion* **1979**, *35*, 55–60.
84. D. A. Little, J. R. Scully, An electrochemical framework to explain IGSCC in an Al-5.4% Cu-0.5% Mg-0.5% Ag alloy in *Chemistry and Electrochemistry of Stress Corrosion Cracking: A Symposium* Honoring R. W. Staehle (Eds.: R. W. Staehle, R. H. Jones), TMS, 2001, pp. 555–572.
85. F. D. Wall, G. E. Stoner, *Corros. Sci.* **1997**, *39*(5), 835–853.
86. A. Rota, H. Bohni, *Werkst. Korros.* **1989**, *40*, 219–228, 295–303.
87. X. Liu, W. Zhang, G. S. Frankel, Effect of stress on penetration of IGC in Al alloys: transition of IGC to IGSCC in *Chemistry and Electrochemistry of Stress Corrosion Cracking: A Symposium* Honoring R. W. Staehle (Eds.: R. W. Staehle, R. H. Jones), TMS, 2001, pp. 543–553.
88. E. H. Hollingsworth, *ASM Metals Handbook*, 9th ed., ASM, Metals Park, Ohio, 1987, p. 589, Vol. 13.
89. N. J. H. Holroyd, G. M. Scammans, *Scr. Metall.* **1985**, *19*, 919.
90. S. Maitra, G. C. English, *Metall. Trans.* **1981**, *12A*, 535.
91. P. Doig, P. E. J. Flewitt, J. W. Edington, *Corrosion* **1977**, *33*(6), 217–221.
92. J. Zahavi, J. Yahalom, *J. Electrochem. Soc.* **1982**, *129*, 1181.
93. E. D. Hondros, M. P. Seah, *Int. Metals Rev.* **1977**, *22*, 262–301.
94. L. Long, H. Uhlig, *J. Electrochem. Soc.* **1965**, *112*(10), 964–967.
95. J. Kuppa, E. Erhart, H. Grabke, *Corros. Sci.* **1981**, *21*, 227.
96. G. Tauber, H. J. Grabke, *Corros. Sci.* **1979**, *19*(11), 793.
97. A. Joshi, D. J. Stein, *Corrosion* **1972**, *28*(9), 321.
98. M. Guttman, P. Dumoulin, N. T. Tai et al., *Corrosion* **1981**, *37*, 416.
99. R. H. Jones, M. J. Danielson, D. R. Baer, *J. Mater. Energy Syst.* **1986**, *8*, 185.
100. H. J. Herrmann, S. Roux, *Statistical Models for the Fracture of Disordered Media*, North Holland, New York, 1990.
101. V. K. S. Shante, S. Kirkpatrick, *Adv. Phys.* **1991**, *20*, 325.
102. D. Stauffer, *Introduction to Percolation Theory*, Taylor & Francis, London, 1985.
103. D. McLean, *Grain Boundaries in Metals*, Clarendon Press, Oxford, UK, 1957.
104. D. B. Wells, J. Stewart, A. W. Herbert et al., *Corrosion* **1989**, *45*, 649–660.
105. M. A. Gaudett, J. R. Scully, *Metall. Trans. A.* **1994**, *25A*, 775–787.
106. J. T. Staley, *Aluminum Technology* (Ed.: T. Sheppard), Institute of Metals, London, 1986, p. 396.

107. N. J. H. Holroyd, Environment-induced cracking of high strength aluminum alloys in *Environment-Induced Cracking of Metals* NACE 10, (Eds.: R. P. Gangloff, M. B. Ives), NACE, Houston, Tex., 1990, pp. 311–345.
108. H. J. Dundas, A. P. Bond in *Intergranular Corrosion of Stainless Alloys*, (Ed.: R. F. Steigerwald), STP 656, ASTM, Philadelphia, Pa., 1978, pp. 154–178.
109. A. K. Vasudevan, E. A. Ludwiczak, S. F. Bauman et al., *Mater. Sci. Technol.* **1986**, *2*, 1205–1209.
110. A. K. Vasudevan, R. D. Doherty, *Acta Metall. Mater.* **1987**, *35*, 1193–1219.
111. C. P. Blankenship, E. A. Starke Jr., *Metall. Trans. A* **1993**, *24A*, 833–841.
112. C. J. Peel, S. P. Lynch, Auxiliary Heat Treatment for Al-Li Alloys, US Patent No. US 5258081, 1993.
113. R. E. Ricker, J. L. Fink, A. K. Vasudevan, *Metall. Trans. A* **1991**, *22A*, 264–267.
114. K. Osozawa, K. Bohnenekamp, H. J. Engell, *Corros. Sci.* **1966**, *6*, 421–433.
115. D. L. Reichert, G. E. Stoner, *J. Electrochem. Soc.* **1990**, *137*, 411–413.
116. G. Palumbo, K. T. Aust, *Acta Metall. Mater.* **1990**, *38*, 2343–2352.

5.1 Anodic and Cathodic Protection

U. Kamachi Mudali, H. S. Khatak, and Baldev Raj
Indira Gandhi Centre for Atomic Research, Kalpakkam, India

5.1.1 Introduction to Anodic and Cathodic Protection

Both cathodic and anodic protection methods involve modification of a metal's potential. In these methods, the potential of the metal to be protected is shifted, either by the application of a direct current from a power supply or by galvanic action from the connection of dissimilar metals. The potential can be decreased or shifted into a region of passivity for the metal. Shifting the potential of the metal to a lower value is referred to as *cathodic protection* (CP). Shifting the metal to more oxidizing conditions or more positive potentials within a region of passivity is referred to as *anodic protection*.

5.1.1.1 Anodic Protection

5.1.1.1.1 **Definition** Anodic protection (AP) is a method by which corrosion protection is achieved for active–passive metals and alloys by maintaining their electrode potential in the passive region using a potentiostat [1]. Anodic protection, one of the recently developed corrosion control methods, was first used in the field in the late 1950s. Anodic protection did not become commercially successful until the early 1970s, and it is currently used on a smaller scale than other corrosion control techniques.

5.1.1.1.2 **Electrochemical Fundamentals** Anodic protection was developed using the principles of electrode kinetics and is difficult to understand without introducing advanced concepts of electrochemical theory. Briefly, anodic protection is controlled by the formation of protective passive film on metals and alloys using an externally applied potential. Anodic protection is used to a lesser degree because of the limitations on metal-environment systems for which anodic protection is viable. In addition, it is possible to accelerate corrosion if proper controls are not implemented during anodic protection.

The concept of anodic protection can be understood through a potential-pH diagram and the electrochemical polarization curve for an active–passive metal (Fig. 1a, b). In the potential-pH diagram, the starting condition for the steel/electrolyte combination is indicated by the X in the active

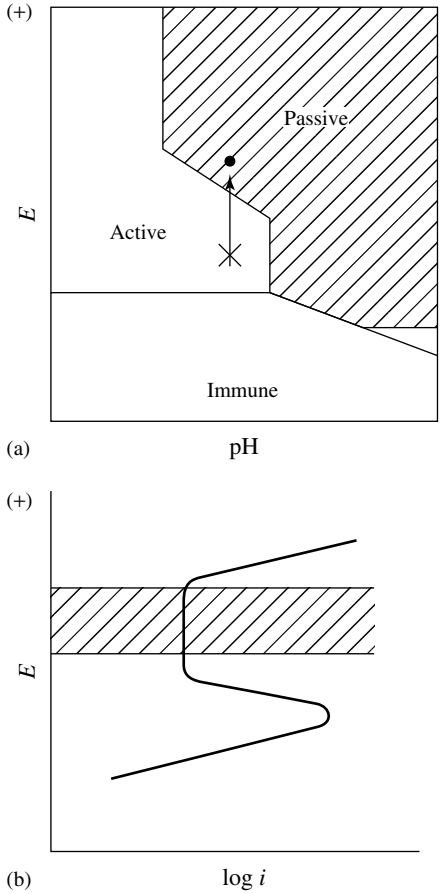


Fig. 1 The concept of anodic protection related to: (a) a potential-pH diagram and (b) electrochemical polarization curves [1].

region. Through the application of AP, the potential of steel is raised from the active region into the passive region as shown by the arrow in the diagram. The corrosion rate of the steel is significantly reduced through the onset of passivity. Anodic protection with respect to the electrochemical polarization curve is shown in Fig. 1(b). The potential is increased to more oxidizing conditions and maintained in the region designated by the crosshatched area in the figure. Within this potential range, the corrosion rate of the steel is quite low, as indicated by the passive current within this range.

Anodic protection is effective only for metal/environment combinations in which passivity is achievable and maintainable. If, for any reason, the passive film is damaged and breaks down, the application of anodic protection can result in greater damage than would be observed with no protection at all. This situation is shown schematically in Fig. 2 for a metal exhibiting active–passive behavior. The application of anodic protection is good if the passive film is developed, and a low current is achieved. If a sustained breakdown of the passive film occurs, however, then no decrease in the current is observed, and the corrosion current follows the dashed path indicated on the diagram. In this latter case, the increase of potential for oxidizing values will accelerate the corrosion as indicated by the X marked ''bad''.

5.1.1.2 **Cathodic Protection**

5.1.1.2.1 **Definition** Cathodic protection (CP) is defined as the reduction or elimination of corrosion by making the metal a cathode using an impressed current or attachment to a sacrificial (galvanic) anode. It is a process that reduces the anodic corrosion reaction by creating an electric field at the surface of the metal so that the net flow of current is into the metal.

5.1.1.2.2 **Electrochemical Fundamentals** For simplicity, in a buried pipe under freely corroding conditions, an area on the steel surface can be considered as an anode while another area becomes a cathode (Fig. 3). The potential difference

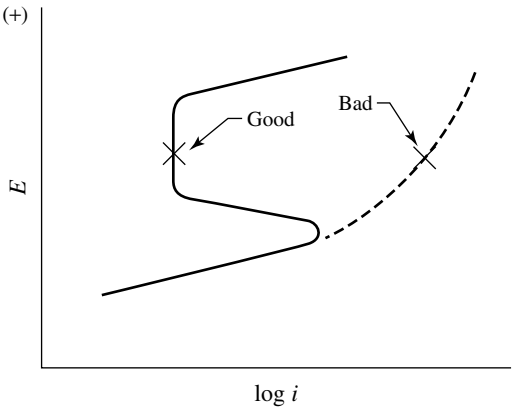


Fig. 2 Danger of anodic polarization when a protective (passive) film is not realized.

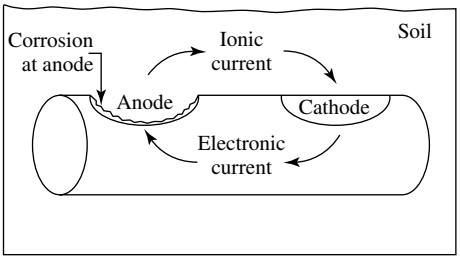


Fig. 3 Schematic of a corrosion cell operating on a steel pipe buried in the soil.

between the anode and the cathode gives rise to a corrosion current flowing from the anode into the soil. The corrosion current enters the steel structure from the soil at the cathode, and the circuit is completed by current flow through the steel by electronic conductivity from the cathode to the anode. The result of this operating corrosion cell is metal loss at the anodic area [2]. However, for general corrosion to occur at the free corrosion potential, separate anode and cathode areas are not mandatory as both anodic and cathodic reactions are polarized to their respective equilibrium potentials at a single mixed potential. Thus, under homogeneous conditions there are no separate anodic and cathodic regions where respective oxidation and reduction reactions occur.

The concept of CP can be understood through potential-pH (Pourbaix) diagrams and electrochemical polarization curves as shown in Fig. 4(a, b). Under freely corroding conditions, the metal in the electrolyte has a potential and pH combination in the active region as indicated by the X in the diagram. In this region, soluble corrosion products are the stable species, and the prediction of the potential-pH diagram is that the metal will corrode [1]. The concept of CP is to shift the potential from the active region to more reducing (negative) values, and this is very effective when the potential is shifted to the immune region. Corrosion is thus prevented or reduced depending on the extent of shift of potential to the more reducing (negative) values. An electrochemical polarization curve for an active/passive metal is shown in Fig. 4(b). The freely corroding metal is at a potential in the active range, and corrosion is observed. The application of CP shifts the

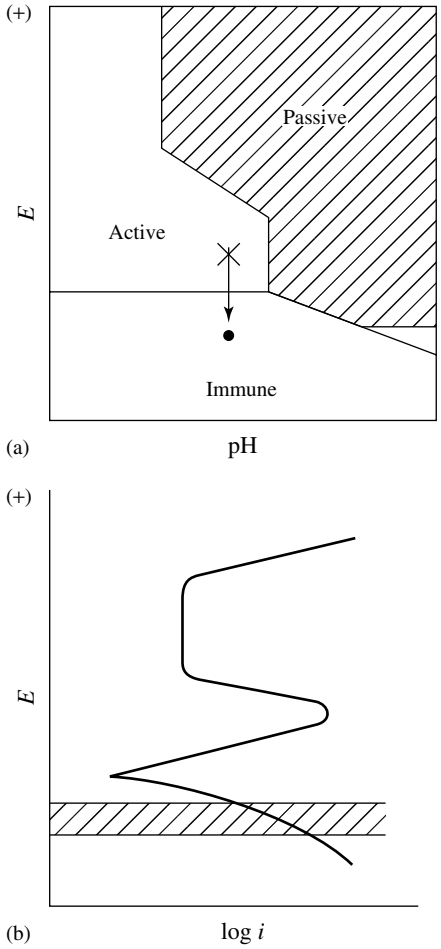


Fig. 4 The concept of cathodic protection related to (a) a potential-pH diagram and (b) electrochemical polarization curves [1].

potential below the original corrosion potential into the region designated by the crosshatched area. This indicates the magnitude of CP current required for maintaining the metal at the desired protection potential. The location of the immune region on the potential-pH diagram and the shape and magnitude of currents on the polarization curve are a function of the metal/electrolyte combination.

Under corrosion at open circuit, all the electrons released in the anodic reaction are consumed by the cathodic reaction. However, if electrons are supplied to the metal from an external power source, the electron consumption (cathodic) reaction will speed up and the electron release (anodic) reaction will slow down. Consequently, the rate of cathodic reaction will increase, the rate of metal dissolution will slow down, and the electrode potential will fall. Thus, by supplying electrons to the metal from an external source, we can slow down its dissolution. This is the principle of cathodic protection.

Figure 5 [3] shows the kinetics of the anodic and cathodic reactions as a function of electrode potential, assuming that the cathodic reaction is hydrogen evolution, in the case of a steel vessel used for storing acid. Since these reactions either release or produce electrons, the rates may be expressed conveniently as an electrical current density (i). As a convention, electron release is shown as a positive current and electron consumption as a negative current. At the reversible potential E_H, the net rate of the hydrogen evolution reaction is shown in the diagram as being vanishingly small; in fact the net rate is zero. The value of E_H depends on the pH of the environment and can be calculated using the Nernst Equation. Above E_H the hydrogen evolution reaction cannot occur. Similarly, at the reversible potential for the iron dissolution reaction E_{Fe}, the net rate of the anodic reaction is zero. The value of E_{Fe} depends on the ferrous ion concentration and can also be calculated. Below E_{Fe} the anodic dissolution of iron cannot occur. E_{Fe} therefore represents the threshold for iron dissolution. At E_{corr} the anodic and cathodic reaction rates are equal in

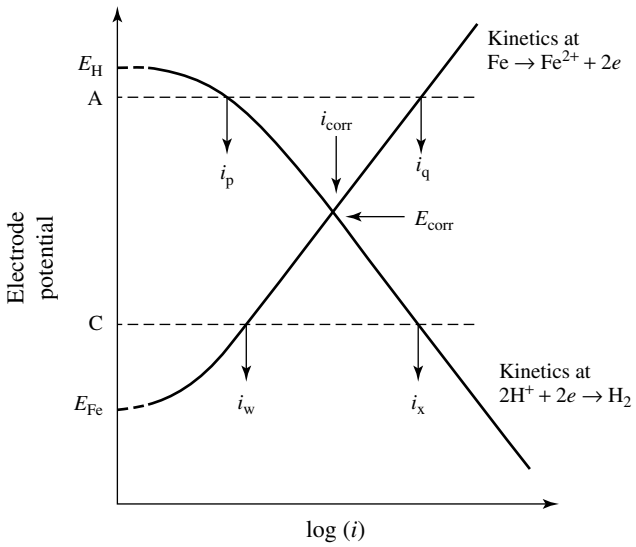


Fig. 5 Anodic and cathodic kinetics for Fe/HCl redrawn to demonstrate the location of E_{corr}.

magnitude and opposite in sign, that is, all the electrons released in the anodic reaction are consumed in the cathodic reaction. If the potential is raised from E_{corr} to A, the rate of dissolution of iron is increased (from i_{corr} to i_p). Conversely, if the potential is lowered to C, the rate of iron dissolution is lowered (from i_{corr} to i_w) and the rate of hydrogen evolution is increased (from i_{corr} to i_x). However, neither potential A nor potential C can be reached spontaneously, because in the former case there is an excess of electron release (given by $i_q - i_p$) and in the latter case an excess of electrons consumption (given by $i_x - i_w$). To raise the potential above E_{corr}, electrons must be withdrawn from the metal and, to lower the potential below E_{corr}, electrons must be supplied to it.

In Fig. 5, the relationship between potential and current is shown as semilogarithmic over a wide range of electrode potential. When the CP of steel is considered, something approximating to this relationship for the anodic reaction kinetics will usually prevail. If the cathodic reaction is hydrogen evolution, then the cathodic kinetics will also approximate to this behavior. In Fig. 5, the logarithm of the rate of iron dissolution is plotted as a function of electrode potential. At E_{Fe} the dissolution rate is zero, and further lowering of the potential has no beneficial effect. The amount of the cathodic current that must be supplied to the iron to achieve a particular potential is the difference between the cathodic and anodic current at any fixed potential. At E_{corr} the current to be supplied is zero because that potential is reached spontaneously. Apart from the first few millivolts, at more negative potentials the current increases in a logarithmic fashion. The following is found:

1. Iron can be protected fully by shifting its potential to E_{Fe} and that this requires a cathodic current equal to i_{prot};

2. A lower level of protection can be achieved by shifting the potential to a value between E_{corr} and E_{Fe} and this can be achieved with the application of a lower current;
3. Shifting the potential to a value more negative than E_{Fe} provides no further benefit as far as preventing corrosion is concerned, but a greater expenditure of current than i_{prot} is required to do it;
4. The first increment of potential fall is more effective in preventing dissolution than the next increment as there is logarithmic relationship between dissolution rate and potential. Further, each successive increment of potential fall requires an order of magnitude increase in current.

In short, it is possible to protect partially, to protect fully, or to overprotect (i.e. to waste current without additional benefit) through cathodic protection. Further, the application of more current follows the law of diminishing returns as far as corrosion control is concerned. If oxygen reduction is the cathodic process, the cathodic reaction rate does not continue to increase in a logarithmic manner as the potential is lowered but tends initially to a limiting value. The specific conclusions drawn above will not then apply, but the general conclusions are quite correct. In the case of oxygen reduction, the hydroxyl ions generated near the cathodic surface can produce high-pH conditions. This causes the precipitation of calcium and magnesium carbonates as well as that of magnesium hydroxide as their solubilities decrease with increasing pH. The calcareous layer can be beneficial as it acts as a barrier to oxygen, and helps to retard any corrosion reaction if the protection system becomes ineffective. The high resistance of this layer also helps to extend the cathodic protection to areas further from the current source, lengthens the life of the sacrificial anodes, and reduces the current density requirements of the impressed current systems. It should also be borne in mind that the increase in pH also shifts the equilibrium potential in the negative direction and makes it difficult to get into the immunity region. In the case of a buried pipe line, the chemistry of the soil, the diffusion of ionic species like chlorides, and the stability of salts like carbonates/bicarbonates and so on also affects the environmental polarization. The increase in pH of the surface of buried pipelines could also be due to the interaction of carbon dioxide present in the soil. In this case, the steel undergoes high-pH stress corrosion cracking (SCC). The other parameters affecting the high-pH SCC are a narrow CP potential between −600 to −750 mV ($Cu/CuSO_4$); a narrow pH range of about 9; and, high temperatures. It mainly occurs on pipelines that have coal tar or asphalt coating, and the failure occurs at locations where there is disbondment or cracking.

The scope of application of CP is enormous and continuously increasing. It is possible to protect vessels and ships, docks, berths, pipelines, deep wells, tanks, chemical apparatus, underground and underwater municipal and industrial infrastructure, reinforced concrete structures exposed to the atmosphere, as well as underground parts, tunnels, and other metal equipments using cathodic protection. Apart from reduction of general corrosion, cathodic protection reduces SCC, pitting corrosion, corrosion fatigue, and erosion–corrosion of metallic materials.

5.1.1.2.3 **Comparison between Cathodic and Anodic Protection [1, 3]**

	Cathodic protection	***Anodic protection***
Applicability	All metals and alloys	Active–passive metals and alloys only
Solution corrosivity	Weak to moderate for practical systems	Moderate to aggressive
Comparative cost		
Installation	Lower	High
Maintenance	Lower	High
Operation	Higher	Very low
Throwing power	Low	Very low
Rectifiers	Constant current or controlled potential	Controlled potential
Applied current	Higher depends on the cathodic reduction current. Is not an exact measure of corrosion rate but increases with corrosion rate	Very low often a direct measure of corrosion rate during protection
Operation conditions	Usually, determined by empirical testing or exercise	Can be accurately determined by electrochemical measurements.

5.1.2 Anodic Protection

Anodic protection has been effectively used to control corrosion by sulfuric acid for many years [4]. It has been used effectively to protect carbon steel against 10 to 45% solutions of sodium hydroxide at 25 to 60 °C. When sodium chlorate, chloride, and sulfate were added to the solution, protection was not adversely affected [5]. The technique has also been used with success in ammonia-ammonium nitrate and nitrogen fertilizer solutions, among others [6]. Anodic protection of heat exchangers also permits better heat transfer by allowing greater velocities and reduces initial costs by making it possible to use smaller exchangers and related components. Anodic protection can also be used in hot and cold alkaline solutions [7–9], such as caustics, for protection against hydroxylamine sulfate [10], nitrate, and chloride solutions, and as a standby to protect titanium-palladium heat-exchanger tubes exposed to residues from zinc reduction [11]. This latter application is particularly important because process upsets could cause catastrophic failure of equipment without standby protection. Anodic potentials protect titanium from chlorides up to 170 °C, but not from bromides or iodides [12]. Other experimental evidence indicates that Nichrome and Inconel 600 [13] can be protected against corrosion attack by molten sodium sulfate. Tanks containing hydroxylamine solutions contaminated with sulfate and sulfur dioxide have been protected. Protection has also been provided against attack by chloride solutions containing nitrates.

5.1.2.1 Anodic Protection – Methods and Materials

A typical anodic protection system for a vessel used for storing sulfuric acid is shown in Fig. 6. The main parts of the system include a cathode, reference electrode, potential controller and a power supply. The cathode is connected to the negative pole of the power supply, and the vessel wall is connected with the positive pole as an anode, while the reference electrode

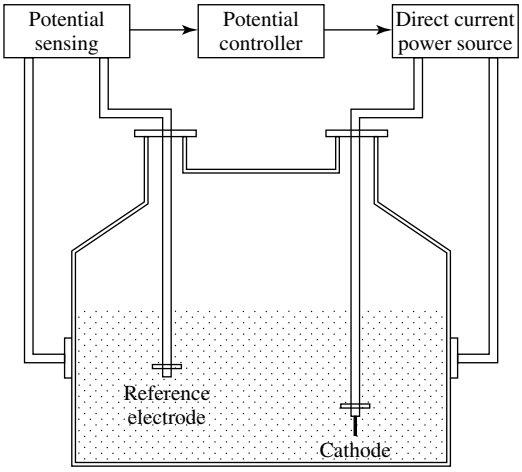


Fig. 6 Schematic of an anodic protection system.

completes the circuit. The potential between the reference electrode and the tank wall is adjusted using the potential controller such that the potential of the system remains in the predetermined point in the passive region. Several such vessels can be protected with a single potential controller and power supply by using switching modes. The optimum potential for anodic protection is selected in the passive region of the polarization curve that is established in the laboratory experiments. It is often the potential at which the current is less in the passive region. These current values are highly time-dependent and in general, are lower in the actual field installations than those values established in the laboratory. Also, the current values required for passivation steadily decrease with time for systems showing low corrosion rates. The cathodes should be chemically inert to the environment and should not undergo any change in their dimension during service by the reactions occurring at the surface due to the impressed current. The various cathode materials employed for anodic protection of different systems are shown in Table 1. Care should be taken while selecting the reference electrodes for showing electrochemical stability for changing time and temperature during service. Several reference electrodes based on $Hg/HgCl_2$, Ag/AgCl, $Hg/HgSO_4$ and Pt/PtO are used for field applications in anodic protection systems.

Tab. 1 Various cathode materials employed for anodic protection

S.no.	*Cathode material*	*Environment*
1.	Pt-clad brass	H_2SO_4 -miscellaneous concentrations
2.	Cr-Ni steel	H_2SO_4
3.	Si-cast iron	H_2SO_4
4.	Steel pipe	Kraft pulping liquor
5.	Steel cable	Kraft pulping liquor
6.	1Kh18N10T	Nitrogen fertilizer solution, ammonium hydroxide
7.	Hastelloy C	H_2SO_4, fertilizer solution
8.	Air electrode	H_2SO_4
9.	AISI 304 SS	H_2SO_4
10.	Ni-plated	Electroless nickel plating bath

5.1.2.2 Anodic Protection for Materials

5.1.2.2.1 **Steels and Stainless Steels** The reactive tendency for passivation is strongly

dependent on the interaction between a metal and its environment. Among the various series of stainless steels, 300 series alloys are widely used in acid storage applications rather than 400 series, even though their cost is more.

Carbon steels and stainless steels are the most common construction materials for equipment used in the manufacture, storage, and transportation of sulfuric acid. Anodic protection was successfully used to control the corrosion of the various equipments made of these materials in this acid over a wide range of temperatures. While the corrosion rates of carbon steels in sulfuric acid are mainly functions of temperature, velocity, and acid concentration and purity, particularly the iron content, these rates are greatly affected by minor alloying elements in steel, particularly copper. The corrosion rates of steel in 77 to 100% concentrations are in the range of 20 to 40-mils per year (mpy) at 24 °C [14].

Austenitic stainless steels show low corrosion rates in sulfuric acid. In many cases, rates of less than 1 mpy have been listed for AISI 300 series steels. However, if the steels are in the active state, the rate can be as high as 100 mpy. Stainless steels that are not resistant to 50% H_2SO_4 can be protected anodically and thereby the corrosion rate can be reduced to a thousand fold. However, a catastrophic rupture of a 3000 ton tank containing 93% sulfuric acid resulted in the failure due to wall thinning of an inlet nozzle from which acid splashed during filling [15]. Blistering is also a common problem in sulfuric acid storage vessels. As is well known, these blisters are caused by the accumulation of hydrogen in laminations, inclusions, or minute voids within a metal plate. The accumulation of hydrogen is often the result of diffusion of atomic hydrogen generated by corrosion. The hydrogen atoms penetrate the metal matrix until they reach a discontinuity, where they combine to form molecular hydrogen gas.

Many attempts to control corrosion in sulfuric acid vessels are made to preserve product purity. As an example, electrolytic-grade sulfuric acid must not have over 50 ppm of iron. It is almost impossible to store acid for any reasonable time in a bare or unprotected steel tank and maintain this level. Iron pick-up in a storage vessel containing 94% sulfuric acid increased from 110 to 280 ppm during 28 days storage [16]. It can be said that the iron content may increase at rates of 5 to 20 ppm day^{-1} of unprotected storage tanks. In order to maintain a low iron content in acid, it is necessary to use some sort of corrosion control in storage vessels.

The most common use of anodic protection has been to control corrosion of sulfuric acid storage tanks made of carbon steel, with a particular emphasis to reduce iron pick-up. Table 2 shows that anodic protection drastically decreased the amount of iron pick-up, as compared to that in the unprotected tank [17]. In addition to the iron content, the corrosion rate of anodically protected steel in 94% acid with a mean temperature of 10 °C was 10.5 times lower than that of unprotected steel. These data (Table 3) [17] indicate that anodic protection is an efficient means of controlling the corrosion of steel storage

Tab. 2 Average iron contents during anodic protection of storage tanks, 100% sulfuric acid [5]

Location	*Iron content, ppm*	
	Before	*After*
Discharge	145	35
Feed	31	26
Iron pick-up	114	9

Tab. 3 Results of test on anodically protected and unprotected coupons exposed for 50 days in 100% sulfuric acid storage tanks [6]

Distance of coupon from tank bottom		*Corrosion rate*			
		Unprotected		*Protected*	
Feet	*Cm*	*mpy*	*μm yr*$^{-1}$	*mpy*	*μm yr*$^{-1}$
0	0.00	35.3	896.6	3.6	91.44
1.0	30.48	34.1	866.1	3.4	86.36
2.0	60.96	31.2	729.5	3.1	78.74
3.0	91.44	2.0	50.8	3.2	81.26
4.0	121.92	29.9	759.5	3.5	88.90
5.0	152.40	22.1	561.3	5.8	147.3
6.0	182.88	4.3	109.2	5.4	137.2
7.0	213.36	6.3	160.0	5.3	134.6
8.0	243.84	3.8	96.5	4.1	104.11
9.0	274.32	2.2	55.9	1.4	35.66
10.0	304.80	0.8	20.3	0.9	22.88
11.0	335.28	0.8	20.3	0.8	20.33

tanks in sulfuric acid service. This has been confirmed by the successful use of anodic protection for as long as 25 years on many vessels in the sulfuric acid industry.

5.1.2.2.2 **Valve Metals** Titanium is extensively used in the chemical process industry owing to its excellent corrosion resistance. However, anodic protection of titanium is required for certain environments. For example, anodic protection has been recommended widely for application of titanium in sulfuric acid applications. Experiments indicated that anodic protection considerably increased the corrosion resistance of titanium. In sulfuric acid up to 65% concentration at 65 °C, the corrosion rate of anodically protected titanium was found to be 0.025 mm yr^{-1}. Even at a higher temperature of 90 °C, for sulfuric acid concentration of 57%, the corrosion rate under anodic protection was found to be only 0.13 mm yr^{-1} [18, 19]. A welded titanium tank heated up to 60 °C was connected to two titanium tubes each 2.5 m long and to a centrifugal pump made of titanium. A tantalum cathode was used and the anodic protection was maintained using a storage battery. There was no need for accurate maintenance of the potential as titanium showed extended passivity up to 30 V. The current applied was 25 mA and the total power required was 0.03 W m^{-2}. The corrosion rate after a period of six weeks was found to be 0.005 mm yr^{-1}. Examination of the equipment did not show any pitting or crevice corrosion and a blue or purple colored film was found developed throughout the surface. Even when the power was disconnected or a scratch was made on the surface nine hours after the current disconnection, there was no significant change in the corrosion potential. Only after 30 h, the film dissolved and the equipment corroded rapidly, but the corrosion

could be completely stopped within 7 s by applying a current of 55 mA. This indicated the superiority of anodic protection in improving the corrosion resistance of equipments made of titanium in sulfuric acid. Anodic protection was also successfully applied for protecting equipment made of titanium in hydrochloric acid, and phosphoric acid.

5.1.2.3 Application and Limitations of Anodic Protection

The primary advantage of anodic protection is its applicability for extremely corrosive environments. It is most extensively applied to protect equipment used to produce, store, and handle sulfuric acid. It is also used in chemical and nuclear industries, during the production of fertilizers, and for the protection of heat exchangers and tankers with hot concentrated acids; sulfuric, nitric, phosphoric, ammonium nitrate, and so on, involving components usually made of carbon steels, alloy steels, stainless steels, titanium, nickel and its alloys, and so on.

Other advantages of AP are as follows:

- Significant extension of the life of metal structures made of expensive materials (e.g. high alloy steels, titanium),
- The possibility of replacement of expensive materials with less expensive ones (e.g. alloy steels with carbon steels),
- Retardation of some types of local corrosion (intergranular, selective, stress),
- High throwing power due to which protection of apparatus of complicated shapes is possible (pumps, coolers),
- A decrease of the impurity content (corrosion products) in chemical media, which is of great importance in the production of artificial fibers, and in the pharmaceutical and food industries, and
- Relatively low operating cost due to the application of low currents maintaining the passive state.

The disadvantages and limitation of AP are as follows:

- can only be used in metal-electrolyte systems that exhibit an active–passive transition, high initial installation cost,
- difficulties with failure-free operation of control regulation systems,
- high initial polarizing current, and
- design difficulties.

Among the advantages of anodic protection, notable is its ability to protect surfaces at a distance from the cathode including surfaces inside crevices that cannot be protected by other techniques. An extremely narrow crevice (0.023 cm) in a chromium-nickel casting steel (CF-8 or UNS 92600) cannot be protected in sulfuric acid at 25 °C, whereas a crevice present in AISI 304 stainless steel can be protected. The reason for this difference is that the current required to passivate CF-8 is several orders of magnitude greater than that required for AISI 304 stainless steel. Thus, the successful application of anodic protection requires a precise match among environment, materials, and protective currents. The requirement of high anodic initial current required for establishing the passivation process is another difficulty. The potential control must be designed such that sufficient current for the initial passivation process is available which then can be automatically reduced to maintain the equipment in the stable passive state. The difficulty in anodically protecting long pipelines could be overcome by the use of wire cathodes inside the pipe such that the entire length of the pipe length can be protected. The materials

undergoing localized corrosion due to instability of the passive films would be very difficult to be protected anodically because of dangers in exceeding the breakdown potential.

Equipment to be anodically protected should be designed with a minimum of irregularities because incomplete passivation can have catastrophic consequences. In some environments, specifically in reducing environments, titanium may be alloyed with 0.1% palladium, which effectively protects crevices. While the TiPd alloy is effective in preventing crevice attack, it will dissolve at a rate four times faster than commercial grade titanium when both are anodically protected. In contrast to cathodic protection, in which historically a substantial amount of trial and error is involved, the limitations of anodic protection can be determined in laboratory tests in advance of the actual installation. Results of these tests usually establish the exact conditions that must be maintained for effective protection. Similarly, laboratory tests can be used to determine in advance what effects process variables will have on protection. Expert surveillance is desirable in many cases because minor changes in system parameters that are not anticipated in design can result in a shift of potentials into an active region with a resulting acceleration of attack. Furthermore, it is obvious that there should be an uninterrupted supply of electricity to the system. Interruption of the protective current does not invariably result in immediate corrosive attack, however, because in some systems, passivation may persist for extended times. Loss of passivity may require application of massive currents to reestablish it. Laboratory tests can determine, with respect to given combination of corrosives and materials, whether or not such persistence can be expected and if so, for what interval.

5.1.3 Cathodic Protection

The first application of cathodic protection and statement of the principles of the technique were made by Sir Humphrey Davy in 1824 [20–22]. Using small buttons of zinc, or iron nails, attached to the protective copper sheathing installed on the hulls of wooden warships, Davy was able to arrest ''the rapid decay of the copper''. Unfortunately, the suppression of toxic, biocide, and copper ions allowed the growth of marine organisms, which impaired the sailing speed. Since the latter was regarded as more undesirable than the corrosion, cathodic protection was discontinued. Cathodic protection was first used extensively in the 1920s for buried steel pipelines transporting petroleum products in the Gulf coastal oil fields belonging to the United States. Cathodic protection of steel-hulled ships became prevalent in the 1950s to supplement corrosion- and fouling-resistant coatings. Cathodic protection finds its greatest use for coated carbon steels in many applications of intermediate corrosion rate. Thus, it extends the service life of thousands of miles of buried steel pipelines, oil and gas well casings, offshore oil-drilling structures, seagoing ship hulls, marine pilings, water tanks, and some chemical equipment [23].

5.1.3.1 Criteria for Cathodic Protection

The minimum potential values for CP of metal and alloys obtained in typical corrosion environments are given in Table 4. In the case of steel structures with cathodic protection, the maximum

Tab. 4 Recommended criteria for cathodic protection [24]

Criterion	*Notes*
1. A negative (cathodic) potential of a least 850 mV with the cathodic protection applied. This potential is measured with respect to a saturated copper/copper sulfate reference electrode contacting the electrolyte. Voltage drops other than those across the structure-to-electrolyte boundary must be considered for valid interpretation of this voltage measurement. 2. A negative polarized potential of at least 850 mV relative to a saturated copper/copper sulfate reference electrode. 3. Special conditions: 1. On bare or ineffectively coated pipelines where long-line corrosion activity is of primary concern, the measurement of a net protective current at predetermined current discharge points from the electrolyte to the pipe surface, as measured by an earth current technique, may be sufficient. 2. In some conditions, such as the presence of sulfides, bacteria, elevated temperatures, acid environments, and dissimilar metals, the above criteria may not be sufficient. 3. When a pipeline is encased in concrete or buried in dry or aerated high – resistivity soil, values less negative than the criteria listed above may be sufficient.	Consideration is understood to mean the application of sound engineering practice in determining the significance of voltage drops by methods such as • measuring or calculating the voltage drop(s), • reviewing past performance of the cathodic protection system • evaluating the physical and electrical characteristics of the pipe and its environment, and • determining whether or not there is physical evidence of corrosion

potential should not be more than −1.1 V versus CSE (copper sulfate electrode). Exceeding this value requires appropriate investigations and justification.

A critical paper on these potential criteria was published by Gummow [25], who described the effect of placement of a reference electrode during measurement on the IR ohmic voltage drop, the importance of the resistivity of the soil, the presence of bacteria, and the temperature. He has also warned against overprotection of the structure and recommended maintaining the CP potential of steel in the range −0.85 V to −1.1 V versus SCE.

An important aspect of cathodic protection is the means to monitor the effectiveness and the criteria for protection. Criteria recommended by NACE (RP0169-96) for the CP of steel and cast iron piping are given in Table 4 [24]. Although several criteria are described for CP of steel structures, the most commonly used criterion is that the steel structure to be protected should be maintained at a potential more negative than −0.85 V versus $Cu/CuSO_4$ reference electrode. The primary disadvantages of this criterion are no connection of the potential of the steel to the corrosion rate, and a large difference in protective

potential values depending on the environmental conditions. For metals other than steel, the general criterion for protection is based on a minimum level of potential shift in the negative direction from the freely corroding potential. In addition, test coupons can be connected to the structure to be protected and removed periodically to determine the level of protection and effectiveness of the CP system.

The criteria for cathodic protection are not free from criticism. It is believed that all the listed criteria are deficient to some extent and therefore qualitative in practical application. However, one should be optimistic that any level of cathodic polarization is beneficial, and a broad range of cathodically applied potentials will yield adequate protection. As a result, the use of any criterion listed in Table 4 [24] will produce adequate cathodic protection if applied judiciously. The amount of cathodic protection should be sufficient to reduce the corrosion rate to an acceptable range. Caution should be exercised to avoid overprotection. Overprotection results in the premature consumption of sacrificial anodes or excessive amounts of impressed current demands. Moreover, the application of too much cathodic protection can result in damage to the structure to be protected as a result of hydrogen embrittlement.

5.1.3.1.1 **Electrochemical Basis for Cathodic Protection Criteria** The corrosion rate of a steel structure tends to zero when it is polarized to the equilibrium potential because the rate of forward and reverse reactions becomes equal at this potential. For a neutral electrolyte, the calculated potential for the reaction of Fe is −0.59 V (versus saturated hydrogen electrode, SHE), which corresponds to −0.90 V (versus Cu-saturated $CuSO_4$ electrode), not much varied from −0.85 V recommended by NACE. However, the effect of environmental polarization needs to be considered in reality at the field.

It would be preferable to implement CP criteria based on the actual corrosion rate of the protected metal – that is, by lowering the corrosion rate using the anodic Tafel constant to some value that is adequate. However, this may be impractical because, in practice, the actual corrosion rate of the structure may not be available. A workable alternative would be to specify the potential change necessary to reduce corrosion by a given percentage. The anodic Tafel constant provides a reasonable guide or criterion for cathodic protection and enables a better understanding of how and why the cathodic protection is effective. However, determination of an accurate anodic Tafel constant for the protected structure is not an easy task.

5.1.3.2 **Types of Cathodic Protection**

There are two types of CP systems. Sacrificial CP uses galvanic action through a corroding anode to provide the current to the structure to be protected. An impressed current CP system uses a power supply to provide the current to the structure to be protected using a dimensionally stable anode (Fig. 7). Design and installation of both types of systems should be conducted by companies that specialize in cathodic corrosion control. Sacrificial (galvanic) protection is often used in preference to impressed current techniques when the current requirements are low and the electrolyte has relatively low resistivity (less than about 10 000 ohm.cm). Clearly, it has an advantage when there is no source of electrical power and when a completely unmanned system is desired, such as for an underground or undersea installation. Capital investment will generally be lower, particularly for smaller installations, and it

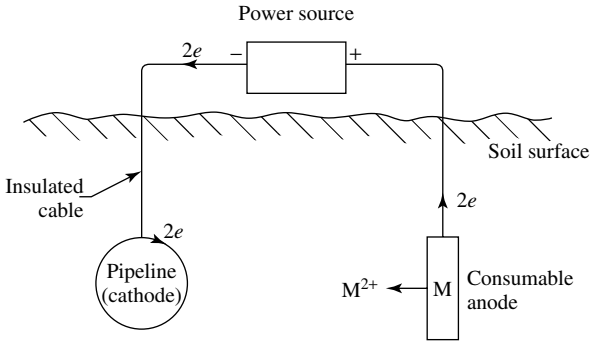


Fig. 7 Cathodic protection for underground pipe-impressed current anode [1].

is often the most economical method for short-life protection. Routine replacement of anodes must also be considered in this case.

The most common source of electricity for impressed current systems is a local power utility. Power normally involves the DC rectifier arrangement. Remote locations can use solar cells, thermoelectric current sources, special fuel-driven electric generators, or even windmills. Impressed current systems are preferred when current requirements and electrolyte resistivity are high. These systems require an inexpensive source of electrical power, are well suited to long-time operation and large structures, and can be automatically controlled. Automatic control reduces maintenance and operating costs.

5.1.3.2.1 **Impressed Current Techniques** In this technique, the electrical current is delivered to the structure to be protected from a direct current (dc) power source through an auxiliary electrode. The structure acts as a cathode and the auxiliary electrode becomes the anode in the cell [26, 27]. Figure 8 shows an impressed current system used to protect a pipeline. Both the buried anode(s) and the pipeline are connected to an electrical rectifier, which supplies direct current to the buried

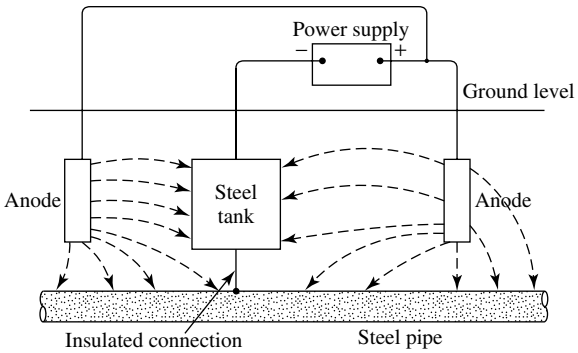


Fig. 8 Circuit and typical reactions for impressed current protection for steel pipeline buried in soil.

electrodes (anodes and protected cathode) of the system.

The use of consumable electrodes, for example scrap iron, is cheap but consumable electrodes must be replaced at regular intervals [28]. Furthermore, these electrodes cannot sustain high current densities and must therefore be rather bulky. Moreover, the dissolution products from these electrodes tend to contaminate the environment. These disadvantages can be avoided with the use of nonconsumable electrodes such as, silicon-iron [29], lead-antimony-silver [30], platinum-titanium [31, 32] or platinum-tantalum [33, 34]. However, they are expensive.

Impressed current anodes need not be naturally anodic to steel and, in fact, most impressed current anodes are made from nonconsumable electrode materials that are naturally cathodic to steel. These electrodes would cause accelerated corrosion of the structure if they were directly connected to the structure. The dc source reverses the natural polarity and allows the materials to act as anodes.

In anaerobic aqueous environment, the hydrogen evolution reaction will be dominant reaction at the cathode, or protected electrode. If the solution is aerated, the reduction of oxygen becomes possible and may occur in place of, or together with, the hydrogen evolution reaction depending on the potential to which the structure is depressed. If the auxiliary electrode is a base metal, then the anodic reaction will be

$$M \longrightarrow M^{z+} + ze^{-}$$

and the electrode will be steadily consumed. By contrast, if the electrode is a noble metal and electrochemically inert, oxidation of the environment will occur in preference. Thus, in water the reaction will be

$$2H_2O \longrightarrow O_2 + 4H^{+} + 4e^{-}$$

or in brine it will possibly be

$$2Cl^{-} \longrightarrow Cl_2 + 2e^{-}$$

In either case, the electrode will not be normally consumed.

The magnitude of the driving voltage required from the DC source depends on a number of factors including

1. the electrolytic conductivity of the environment,
2. the area of structure to be protected,
3. the nature of the electrode reaction at the auxiliary electrode, and
4. the resistance of the auxiliary electrode.

In most cases the electrolytic conductivity is the controlling factor, and the electrode reaction is of least importance. Clearly, if the environment does not have reasonable electrolytic conductivity, large IR (or voltage) drops will occur within it creating the need for a high driving voltage.

The most common power source for impressed current protection is the transformer rectifier. This unit, commonly called simply a rectifier, reduces incoming ac voltage and rectifies it to dc. There are also solid-state switch mode rectifiers that perform similar functions without the use of transformers. Rectifiers can be provided with constant voltage, constant current or structure-to-electrolyte potential control. In areas where electrical power is not readily available, solar power and wind driven generators coupled with storage batteries are used. There is also some use of thermoelectric cells, in-line turbine generators (in gas or oil pipelines), and internal combustion engine driven generators.

A variety of materials is used for impressed current anodes. Among the oldest

are high silicon, chromium bearing cast iron, graphite and junk steel. Magnetite and lead-silver anodes are also used, with lead-silver being confined to use in seawater. Among newer materials are ''dimensionally stable anodes'', so-called because the anode itself consists of a deposit on an inert substrate. Included in this category are platinized niobium or titanium and mixed metal–metal oxide/titanium anodes.

5.1.3.2.2 **Sacrificial Anodes** In contrast to the impressed current technique, the use of sacrificial anodes does not depend on the creation of driven electrochemical cell. Rather, a galvanic cell is formed between the structure and the sacrificial anode in which electrons pass spontaneously from the latter to the former (Fig. 9). Thus, the source of the electrons (the sacrificial anode) must have a more negative electrode potential than the structure. It was for this reason that Humphrey Davy chose zinc or iron to protect copper, and it also explains why magnesium, aluminum and zinc alloys are used to protect steel today.

The sacrificial CP technique involves the use of a more active metal than that used in the structure to be protected to supply the current needed to control corrosion. The more active metal is called a sacrificial anode [35]. Coupling two dissimilar metals in the same environment can lead to accelerated corrosion of the more active metal and protection of the less active (nobler) one. In a galvanic couple between dissimilar metals, the galvanic current cathodically protects the more noble metal and preferentially dissolves the more active metal. Although galvanic corrosion is generally considered a nuisance, it can be used here constructively as a corrosion control method. Electrons flow from the active sacrificial anode to the noble cathode structure. The anodic reaction at the cathode structure, for example,

$$\mathrm{Fe} \longrightarrow \mathrm{Fe}^{2+} + 2e^{-}$$

can be reduced by the surplus of electrons provided by the sacrificial anode. At the same time, the reduction of dissolved oxygen or the evolution of hydrogen is accelerated. The cathode structure is cathodically protected, and the same electrochemical reactions are present at the cathode as when polarization is provided by impressed current.

It should be noted that in contrast to the impressed current system in which a driving voltage of up to 100 V may be made available, in the sacrificial anode system the maximum driving voltage is controlled by the open circuit potential difference between the anode and the structure with the result that it cannot exceed about 1.0 V.

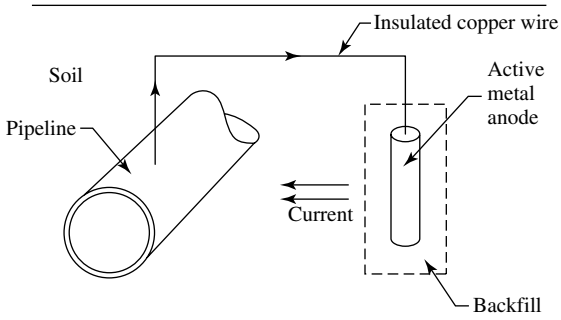


Fig. 9 Cathodic protection for underground pipe – sacrificial or galvanic anode.

Capital investment for sacrificial (galvanic) protection will generally be lower, particularly for smaller installations, and it is often the most economical method for short-life protection, although this is not its only application. Routine replacement of anodes must also be considered. Therefore, maximum anode life requires only minimum current for adequate protection. Only zinc, aluminum, and magnesium alloys have been consistently applied as sacrificial anodes [36]. Magnesium and zinc are the most common galvanic anodes for underground use. In salt water, zinc anodes and aluminum alloy anodes are commonly used. In freshwater, magnesium is frequently used. For underground use, magnesium and zinc anodes are packaged in a backfill consisting of 75% gypsum, 20% bentonite, and 5% sodium sulfate. The purpose of the backfill is to absorb products of corrosion and to absorb water from the soil to keep the anodes active. Magnesium and zinc are also available in ribbons and extruded rods.

5.1.3.2.3 **Comparison of Sacrificial Anodes and Impressed Current Techniques** It is evident from the above that both impressed current CP technique and sacrificial anode CP technique have their own merits and demerits.

The advantages of using sacrificial anode CP technique include

- easy operation without an independent supply of electrical power;
- easy installation and provision for introducing additional anodes even after commissioning;
- the possibility of improper electrical connection to the structure is eliminated;
- there is no control function to be exercised; and
- it is difficult to overprotect, and moderately easy to obtain a uniform electrode potential across the structure.

The advantages of the impressed current CP technique include

- protection of large and even complicated structures in high-resistivity environments can be achieved since it is possible to apply a large driving voltage;
- performance of the system can be increased by proper tuning of the voltage; and,
- the requirement for anodes is relatively lower.

The most severe limitation of the sacrificial anode CP technique is the small driving force, which restricts its use to conductive environments, short current throws and, marine use apart from, well-coated structures. The need for a reliable dc power supply, the danger of overprotection, the difficulty of achieving a satisfactory potential profile over a complex shape and the possibility of improper connection causing corrosion of the structure intended to be protected are the major disadvantages of the impressed current CP technique.

5.1.3.3 **Reference Electrodes for Cathodic Protection**

The criterion for the cathodic protection of most metals is expressed as a potential of the metal relative to a reference device. A constant potential device is required which should possess the following properties:

1. Its potential should be constant irrespective of the electrolyte in which it is used and it should not vary greatly with changes in electrolyte temperature or other parameters;
2. Any changes should be predictable and should have no hysteresis effect;

3. The device should not polarize at small cathodic or anodic currents, and it should have a low internal resistance.

All these properties should be constant with time or the device should have a definable life. For use in most electrolytes, the device should not be bulky so as to have an effect upon the current paths in the electrolyte and the point of measurements should be small so that precise positional determinations of potential can be made.

The half-cell generally used for cathodic protection in the field is the copper sulfate electrode. This consists of an electrode of electrolytic copper in a saturated solution of copper sulfate. The electrode can easily be made to have a large current capacity and will carry current better when it is acting as an anode than as a cathode. In the field, the cell is easily recharged and commercially pure copper sulfate solutions give potentials consistent to within 5 mV.

The most universal cells are of the silver chloride type. These consist of silver wire coated with silver chloride so that both the silver and silver chloride are in contact with a chloride ion electrolyte. The potential of the half-cell will depend upon chloride ion concentration or more exactly upon the logarithm of chloride ion activity.

5.1.3.4 Elimination of IR Drops during Potential Measurements

Potential measurements of protected structure, especially in soil, are comprised with an error resulting from the voltage drop between the structure and the reference electrode. This error depends on the resistance of layers of corrosion products and insulation, and the resistance of the electrolytic environment. Equation (1) shows the amount of ohmic potential drop in the measurement of the potential of a structure with CP,

$$E_{CP} = E_{CORR} + \Delta E + IR \qquad (1)$$

where ΔE is the true polarization and IR is the ohmic potential drop. The IR drop can be eliminated by measuring the instant-off potential. The IR drop vanishes immediately upon interruption of the current, whereas the true polarization takes time to decay owing to the capacitance of the component and the time required for any changes in the environment to decay. However, instant-off measurements require synchronized interruption of all of the current sources, which can be difficult to achieve in the field. The current-off (instant-off) measurements indicate whether the -0.85 V criterion has been met or the starting point for the polarization decay measurement of -100 mV period. If the -0.85 V current-off criterion is not met, then voltage readings of the polarization decay should also be conducted and recorded, unless native potential readings are available. SCC is a potential dependant phenomenon, and so a potential more negative than 1.1 volts would be detrimental for SCC to occur. A highly negative potential can also produce hydrogen-induced cracking under some soil conditions. This high negative potential would also increase the possibility of cathodic delamination damage to the protective coatings.

The application of new insulation materials and technologies has led to a decrease in the required protective currents. The unit insulation resistance is a significant parameter determining the usefulness of structural insulation in cathodic protection. It characterizes the CP current transfer resistance from the ground to the pipeline. The interaction range of cathodic protection and the protective current density change depend on its value.

The value of unit insulation resistance R_i is determined from the formula

$$R_i = \frac{E_{ON} - E_{OFF}}{j}$$

where R_i is the unit insulation resistance ($\Omega.cm^2$), E_{ON} the pipeline potential measure when the CP current is on (V), E_{OFF} the pipeline potential measured when CP current is off (V) and J, the mean cathodic protection current density ($A.m^{-2}$).

The detrimental value of the unit insulation resistance in real conditions depends not only on the resistance parameter of the insulation material, but also on the resistance of the environment and the electrolyte resistance in insulation defects. Mostly, the unit insulation resistance changes exponentially as a function of the operating time. The process of insulation ageing can thus be observed and forecast on the basis of unit insulation resistance measurements.

5.1.3.5 Development of Sacrificial Anodes for Cathodic Protection

Different requirements for sacrificial anodes lead to the use of widely different materials for these applications. The following are requirements for the selection of sacrificial anodes:

- The anode must be a metal that is more active than the metal to be protected. Commercial sacrificial anodes for the protection of steel include magnesium, zinc, and aluminum.
- The potential difference between the freely corroding potential of the structure to be protected and the sacrificial anode must be large enough to provide the necessary CP current.
- The sacrificial anodes must be of sufficient size and have sufficient efficiency to provide the necessary useable life.

Magnesium anodes are the only sacrificial anodes that are routinely specified for use in buried soil applications. Most magnesium anodes are supplied with a prepackaged bentonite clay backfill in a permeable cloth sack. This backfill ensures that the anode will have a conductive environment and will corrode reliably. Some magnesium anodes have been used offshore in recent years in an attempt to polarize the structures to a protected potential faster than would occur if zinc or aluminum alloy anodes were used. Magnesium tends to corrode quite readily in salt water, and most designers avoid the use of magnesium for permanent long-term marine CP applications.

Zinc is used for cathodic protection in freshwater and marine water. Zinc is especially well suited for cathodic protection on ships that move between salt water and harbors in brackish rivers or estuaries. Zinc anodes also are used to protect ballast tanks, heat exchanger, and many mechanical components on ships, coastal power plants, and similar structures.

Aluminum and aluminum-zinc alloy anodes have become the preferred sacrificial anodes for the cathodic protection of offshore platforms. This preference is because aluminum anodes demonstrate reliable long-term performance when compared with magnesium, which might be consumed before the platform has served its useful life. Aluminum also has better current/weight characteristics than zinc. Weight can be a major consideration for large offshore platforms. The major disadvantage of aluminum for some applications, for example, the protection of painted ship hulls, is that aluminum is too corrosion resistant in many environments. Aluminum alloys will not corrode reliably onshore or in freshwater [37]. In marine

environments, the chloride content of seawater depassivates some aluminum alloys and allows them to perform reliably as anode materials. Unfortunately, it is necessary to add mercury, antimony, indium, tin, or similar metals to the aluminum alloy to ensure that this depassivation occurs. Heavy metal pollution concerns have led to bans on the use of mercury alloys in some locations.

5.1.3.6 Development of Impressed Current Anodes for Cathodic Protection

Impressed current anodes must be corrosion resistant and otherwise durable in the environment in which they are used. They must have low consumption rates when connected to a CP source. All materials used for impressed current anodes are cathodic (more noble) than steel. High silicon cast iron (Fe-0.95C-0.75Mn-14.5Si-4.5Cr) is used for onshore CP applications and in other locations where abrasion resistance and other mechanical damage considerations are important [1]. Graphite anodes are extensively used for onshore pipeline CP applications in which they can be buried in multiple-anode ground beds. However, graphite must be stored and handled carefully because of its brittle nature.

Polymeric anodes are used to mitigate the corrosion of reinforcing steel in salt-contaminated concrete. The system consists of a mesh type of anodes with a conductive polymer film coating on copper conductors.

Precious metals are used for impressed current anodes because they are highly efficient electrodes and can handle much higher currents than anodes fabricated from other materials. Precious metal anodes are actually platinized titanium or niobium anodes; the platinum is either clad or electroplated on the substrate. Platinized anodes are used in marine work on ships, hulls, and for applications involving the interior parts of structures such as condenser water boxes, internal parts of pumps, certain pipeline interiors.

Lead alloy anodes, containing 2% silver, or 1% silver and 5% antimony, are used for CP systems in seawater. Lead alloy anode should not be buried in the sea bottom or used in freshwater applications.

Oxide-metal composite anodes consist of a mixed ruthenium dioxide and titanium oxide coating sintered onto a commercially pure titanium substrate. These expanded-mesh anodes also are used for protecting reinforcing steel in concrete [37].

5.1.3.7 Problems with Cathodic Protection

Cathodic protection has many problems and limitations apart from huge capital investment and maintenance costs. One of the more serious problems associated with cathodic protection is the possible effects of stray currents on the corrosion of adjacent metal structures. For example, a CP system that is efficiently protecting pipeline ''A'' might increase the corrosion of neighboring pipeline ''B'' (Fig. 10a). This increase can lead to unexpected corrosion problems/failure, as well as undesirable legal ramifications. Although it is possible to eliminate stray current corrosion (Fig. 10b) with the help of proper design features, the solution is not simple. The best solution to stray current problems is electrical bonding of nearby structures, as shown in Fig. 11. Installation of additional anodes and possibly additional rectifier results in protection of both structures [38].

The use of deeply buried anodes can solve the problem when stray currents affect structures just below ground level. The problems due to stray current corrosion warrant a survey of all other metal

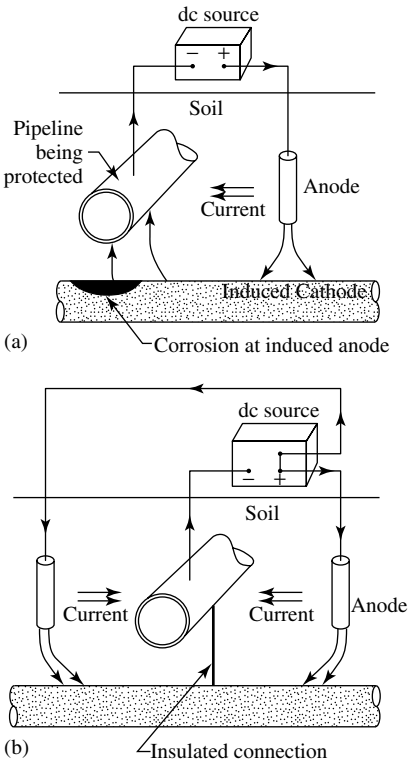


Fig. 10 Stray current effects in underground pipelines: (a) stray currents cause corrosion in neighboring pipelines (b) redesign minimize stray current effects [39].

structures in the area, which is essential before installing cathodic protection. Such inspection also might reveal a source of protection from a neighboring system.

Other problems associated with cathodic protection are related to the chemical reactions occurring at the surface of the protected structure because it is the cathode in the circuit. It is considered to be a major drawback when the cathodic reaction is hydrogen evolution. Figure 5 makes evident that the greater the protection required, the greater the external current that must be delivered and faster the rate of hydrogen evolution. Hydrogen generated at steel surfaces is undesirable because of the danger of hydrogen entry into the metal causing embrittlement. This is a particular cause for concern in the protection of high strength steels. The cathodic reaction can also create problems because of the resultant buildup of hydroxyl ions (increased alkalinity). This increased alkalinity can be harmful to an amphoteric metal such as aluminum. The alkaline environment breaks down the protective film on aluminum and can result in severe corrosion.

Although coatings and cathodic protection are mutually supportive of each other, it is important to recognize the potential dangers when they are used together. When the structure is acting as a cathode in aqueous solutions, it will sustain either

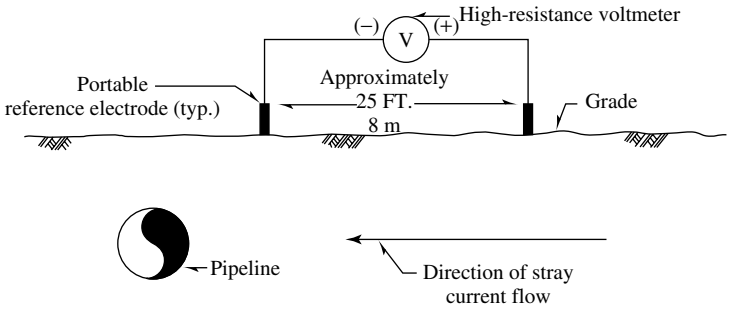


Fig. 11 Prevention of stray current corrosion by proper design [39].

hydrogen evolution or oxygen reduction. Both reactions consume hydrogen ions or release hydroxyl ions, thus causing an increase in pH adjacent to the structure. Hence it is important that the coatings applied to the structure must possess the ability to resist the chemical attack by the hydroxyl ions. Oil-based and oleoresinous paints are softened and tend to blister with alkali and are therefore unsuitable for use with cathodic protection. Bituminous paints, epoxy resins, chlorinated rubbers, and especially coal tar epoxy paints are resistant and suitable for alkali environments. Another problem with the combined use of coatings and cathodic protection is the disbonding of coatings due to the generation of hydrogen at the metal-coating interface where there is excessive protection current. If the amount of current applied is excessive, hydrogen can be generated on the surface of the structure being protected, which can cause disbondment and premature failure of the coatings used.

Many other issues are involved in the application of cathodic protection. For example, consider the case of cathodic protection of underground structures in which the corrosivity of soil is likely to play a major role, as does the degree of aeration and the resistivity. Bacterial effects also can change the corrosion potential. All these factors influence the corrosion process so that along a pipeline there can be varying cathodic control requirements that have to be estimated from potential measurements, experience, and so forth.

Achieving full protection through cathodic means depends on the potential maintained during the period. The only proper indication of the protection is the electrode potential of the different parts of the structure being protected.

Tab. 5 Full protection ranges of potential and the current required to protect steel and other metals

Metals to be protected	*E vs $Cu/CuSO_4$ [V]*
Iron and steel	
(a) aerobic environment	−0.85
(b) anaerobic environment	−0.95
Lead	−0.6
Copper-based alloys	−0.5 to −0.65
Aluminum	
Positive *E* limit	−0.95
Negative *E* limit	−1.2
Environment	Current density Am^{-2}
Steel	
H_2SO_4 (Hot, Static)	350–500
Soils	0.01–0.5
Fast-flowing seawater	0.3 decaying to 0.15
Air-saturated hot water	0.1–0.15
Flowing freshwater	0.05–0.1

Figure 12 shows the relationship between the electrode potential of the steel and the assurance of protection offered in the potential ranges. Table 5 shows the full protection ranges of potential and the current densities required to protect steel and other metals in various environments.

5.1.4 Advanced Aspects of Cathodic Protection

5.1.4.1 Stray Current Effects in Cathodic Protection

The causes and common means of detecting and mitigating stray current interference effects that result from direct current sources are reviewed in this Sect. [1, 40–44]. Alternating current, while creating a potential safety hazard, may contribute to corrosion of ferrous structure [42]. Extensive research is in progress in this regard.

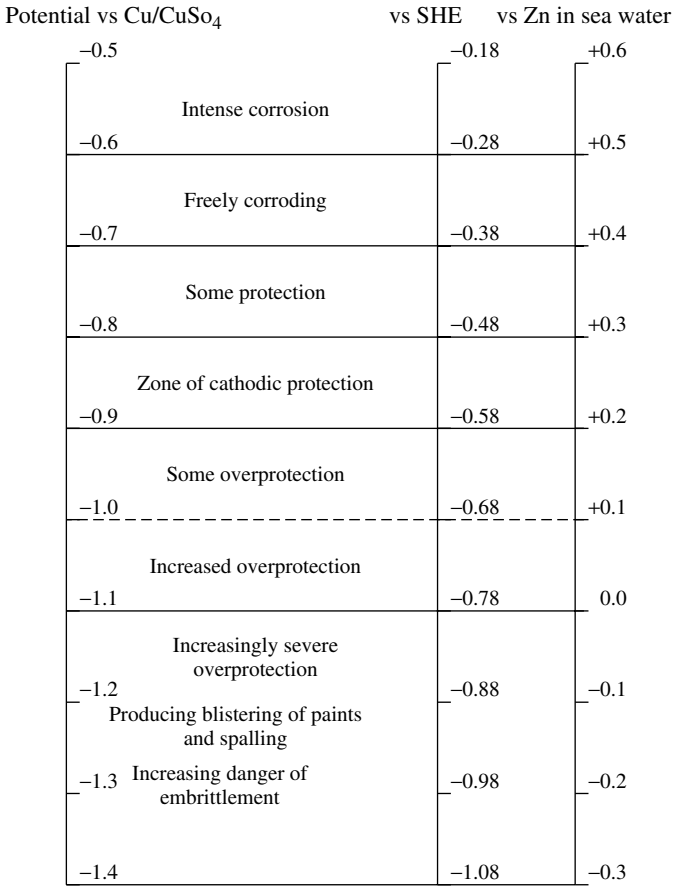


Fig. 12 The relationship between potential and the possibility of corrosion and cathodic protection of steel [3].

Stray currents are defined as electrical currents flowing through electrical paths other than the intended path [43]. Stray currents, or interference currents, can be classified as being either static or dynamic.

Static interference currents are those that maintain constant amplitude and constant paths. Example of typical sources are railroad signal batteries, high voltage direct current (HVDC), ground electrodes, and CP system rectifiers. Dynamic interference currents on the other hand, are those that are continually varying in amplitude and/or continually changing their electrolytic paths. These currents can be manmade (e.g. dc welding equipment, dc railway systems [44], chloride plants, and aluminum plants or caused by natural phenomena. Natural sources of dynamic stray currents, called tellurics, are caused by disturbances in the earth's magnetic field resulting from sun spot activity. Telluric effects may contribute to corrosion [45] and in, addition, can create measurement difficulties and interfere

with the ability to assess CP system performance.

The effects of stray currents are more severe when the resistivity of the soil is very low. If there is a current flowing in the earth and a potential difference exists between points where a metallic conductor, such as pipeline or cable, is located, then the conductor will readily acquire a part of the current that is flowing. Thus, metallic pipelines and cables can become conductors of stray currents in the earth movement.

5.1.4.1.1 **Detection of Stray Currents** Static stray currents of a pipeline can be detected by analyzing pipe-to-soil potentials. The graph in Fig. 13 shows a pipeline with no interference. Figure 14 shows a potential plot for a coated pipeline with stray current interference. Interference may be

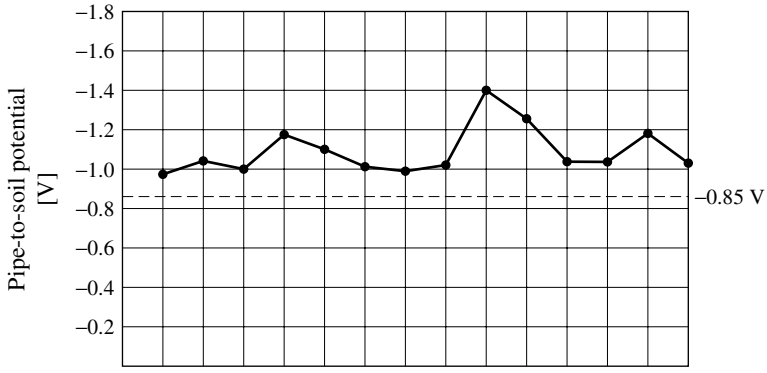


Fig. 13 Potential versus distance plot.

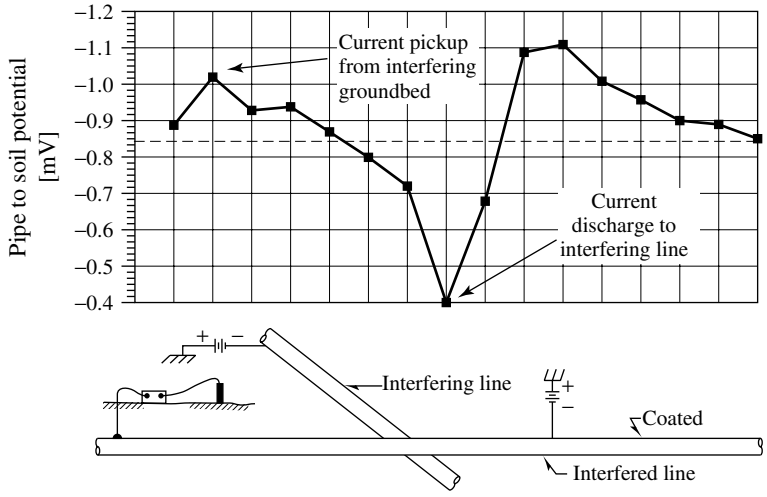


Fig. 14 Potential plot with interference; coated pipeline [39].

suspected if the voltage curve profile shows abnormal variation from previous survey graphs. High negative values are noted remote from any CP system on the surveyed line.

Dynamic stray currents are more easily detected than static ones. Dynamic stray currents are present if the structure-to-soil potential is continually fluctuating, while the reference electrode is kept in a stationary position in contact with the soil. These potential changes result from current changes at the source of the interference.

5.1.4.1.2 **Locating the Source of Static Interference** The path of current flow in the earth can be tracked to its source by measuring the currents in the earth, using two identical portable reference electrodes and a high-resistance voltmeter. By measuring the potential difference between the two electrodes spaced about 8 m (25 ft) apart, the direction of current flow can be determined and its path traced.

If there are test facilities for measuring current flow along the pipeline, a line current survey can be conducted to determine the areas of current pick-up and discharge. This information can also be used to track stray currents toward their source.

To confirm the cause of abnormal pipe-to-soil potential readings, the effect of interrupting the suspected current source on potential survey along the protected pipeline or structure should be assessed. If there is no effect on the potential readings of the interfered structure, the search for the current source must continue until the actual interfering current source is located.

5.1.4.1.3 **Locating the Source of Dynamic Interference** After identifying possible sources, such as dc electrical railway system, mines, or industrial plants, such as aluminum and chlorine, the current flow should be traced along the interfered structure to its source. One method is to observe the current flow at intervals along the structure using millivolt drop test station lead wires to determine the direction of current flow.

Assume that a situation exists in which a single source is causing interference problems. A voltmeter connection, to be used for pipe-to-soil potential measurements, is made between the pipeline (interfered structure) and a reference electrode within earth current pattern of the source and its load. Observing the fluctuation of potential readings at this point alone would not enable one to determine if the readings are being taken at a point where the pipeline is picking up or discharging current. If measurements were being taken at a point of current pick-up, a negative potential swing would be indicated. A positive swing would indicate a decrease of current flow and a condition of the pipe returning to its steady state condition. Readings observed at a discharge point swinging in the positive direction would indicate an increase in current leaving the line and a negative swing would indicate a decrease in current discharge.

Test location can be identified as pick-up or discharge points by correlating the pipe circuit voltage between the interfered pipeline and the stay current source, and the pipe-to-soil potential of the pipeline. A plot of these data is called a beta plot. Figure 15 illustrates the typical experimental setup to obtain a beta plot. Typical beta plots for a current pick-up area and for a current discharge area are presented in Fig. 16(a, b), respectively.

As the connection shown in Fig. 15 indicates, a positive value of E_1 occurs

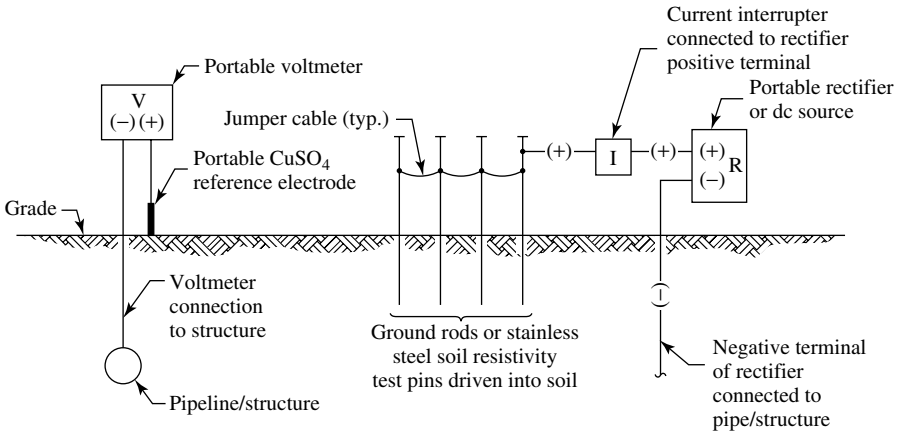


Fig. 15 Typical setup used to locate point of maximum exposure [39].

when current flows from the stray current source to the pipeline. Conversely, a negative value of E_1 indicates a current flow from the pipeline to the stray current source. The slope of straight line through the data points is the value of beta $= \Delta E_1/\Delta V_g$. This type of testing requires that pipe-to-soil potential, V_g, be measured at two or more locations. Many readings should be taken at these locations simultaneously and the meters used must be identical, or comparison of the sets of readings will be difficult. In most cases, a dual channel recorder, such as X-Y plotter, or multichannel data logging is used.

If the points plotted form a vertical line, a neutral curve, there is no influence on V_g by the output fluctuation of the current source. The point of maximum exposure to stray current can be determined from a plot of slopes of beta curves versus distance along the pipeline. The location of minimum discharge area slope is the location of maximum exposure.

5.1.4.1.4 **Potential Measurements in the Presence of Stray currents** Stray currents flow in the electrolyte from external sources, not directly associated with the CP system. Stray currents tend to enter the buried structure at one place and leave it in another. It is where the current leaves the structure that severe corrosion can be expected.

Stray current problems and the general appraisal of a CP system often require knowledge of the potential variations in the electrolyte. To do this, either the potential between the two half-cells placed in the electrolyte is measured or the potential of the structure is measured relative to the same half-cell placed in the electrolyte. When measurements are made between half-cells, the meter must have a high resistance. Alternatively, a bridge system can be used, particularly in liquid electrolytes, in which the half-cell is placed in contact with two different areas of structure.

5.1.4.2 Mitigation of Stray Current Corrosion

5.1.4.2.1 **Controlling Stray Currents at the Source** Groundbed site selection can be used to eliminate or greatly reduce

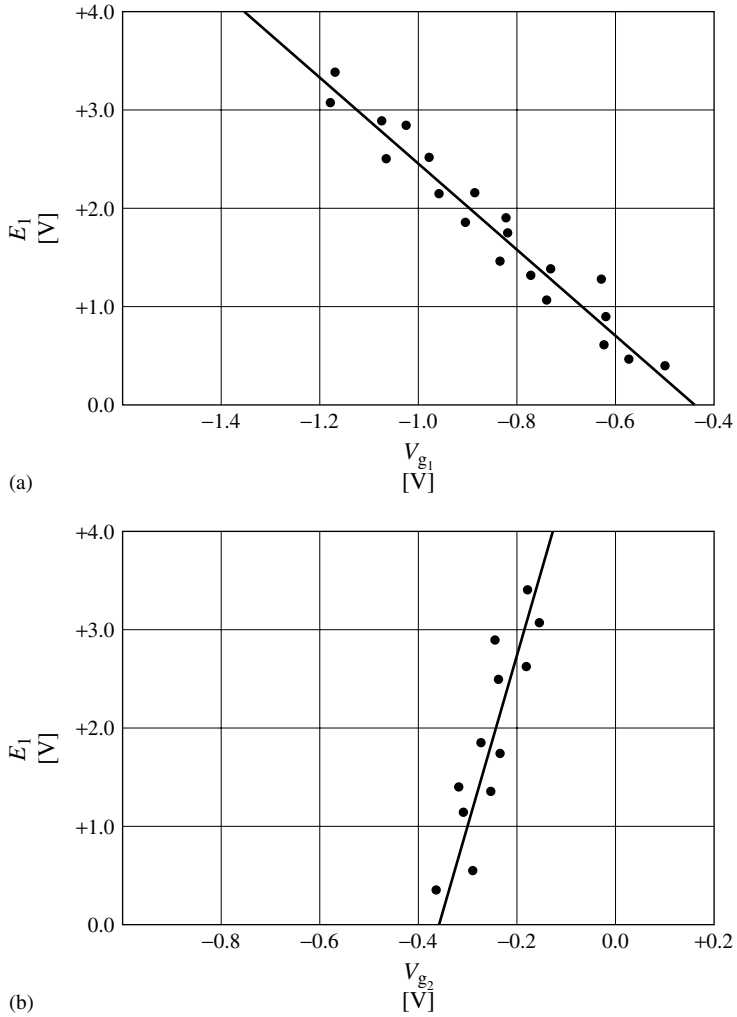


Fig. 16 (a) Typical beta curve- pick-up area, (b) typical beta curve – discharge area [39].

stray currents and the potential gradients that accompany them. Ideally, groundbed should be installed as far as possible from any foreign structure in the area, in order to minimize the effects of the electric field from the groundbed.

In transit systems and any of the other systems involving rail returns, the rails should be installed on well-ballasted roadbeds or on insulated ties or padding. Similarly, when dealing with equipment, if isolated positive and negative circuits can be employed, stray current problems will be minimized because of the high resistance to earth [40, 41]. During welding, care should be taken to ensure that the ground connection and the welding electrode are relatively close together and

that the electrical path between them is of negligible resistance.

5.1.4.2.2 **Static Stray Currents** Mitigation bonds are used to mitigate the effects of stray current corrosion on a structure. The purpose of the mitigation bond is to eliminate current flow from a metallic structure into the earth by providing metallic return path for the current. This drainage bond allows the stray current flowing from a groundbed to the interfered structure to flow through the structure and back to the protected structure through the bond. The typical current flows form the metal surface into the earth.

In order to size the mitigation bond, the point of maximum current flow between the two affected structures must be located. Typically, this point is situated near the point of pipeline crossing, where the circuit resistances are the lowest, but it can be situated some distance away, particularly with well-coated pipelines at areas of coating failure or damage.

A ''trial-and-error'' method can be used to determine the correct bond resistance and current for a solution to static stray current problem. A reference cell is placed at the point of maximum stray current exchange to monitor the potential-to-soil of the interfered structure. With the current source operating, a series of bonds are placed between the two pipelines. When the potential-to-soil with the current source operating and the bond installed equals the potential-to-soil with the current source deactivated (with the bond disconnected), the correct bond resistance is determined. The current flow through the bond and the resistance of the bond can be measured.

The required bond resistance can also be calculated mathematically, using the following equation:

$$R_b = \frac{E_0}{I_b} + \frac{\Delta E}{I_{SC}} - R_I$$

Where, R_b = Resistance of the mitigation bond
R_I = Resistance between the structures
E_0 = Open circuit potential without the stray current source operating
ΔE = Change in open circuit potential caused by stray current source
I_{SC} = Current flow from stray current source
I_b = Current in the mitigation bond

5.1.4.2.3 **Dynamic Stray Currents** Once the location of maximum exposure is determined and its slope or beta curve plotted, the size of the resistance bond can be determined. The required size of the resistance bond is such that its installation will cause the beta curve at the point of maximum exposure to assume a neutral or pick-up slope. Figure 17 shows a beta curve at a point of maximum exposure as well as the required mitigation curve.

In sizing the mitigation bond, a trial-and-error solution may be possible in relatively simple cases in which a single source of stray current is involved. The size of the resistance bond can be determined by installing temporary variable resistances and by determining when stray current corrosion has been mitigated. The procedure is similar to that described for static stray currents, except that a mitigation curve, such as is shown in Fig. 17 must be obtained.

Where a more complex interference problem exists, which precludes the use of the trial-and-error method, a mathematical

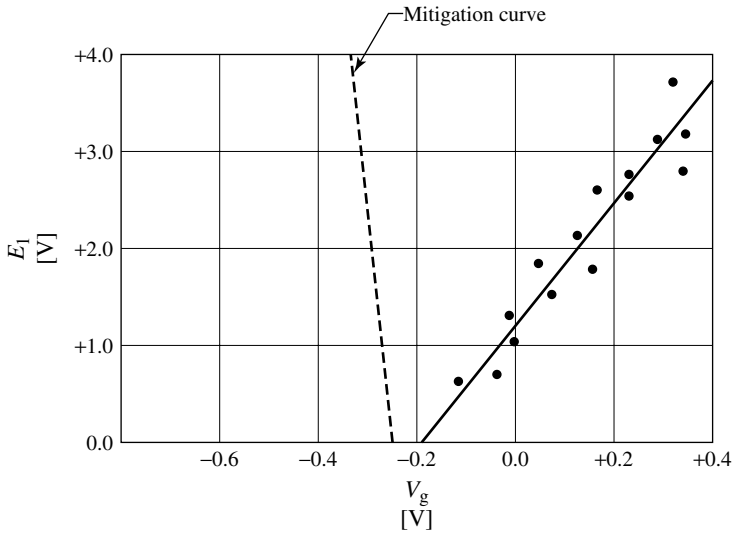


Fig. 17 Beta curve – discharge area (mitigation current) [39].

method can be used. In this method, the following equation is used to obtain the required resistance of the mitigation bond

$$R_b = \frac{\Delta V_g / I_b}{\beta} - R_I$$

where, R_b = Resistance of the mitigation bond
R_I = Resistance between the structures
β = Beta slope
ΔV_g = change in pipe-to-soil potential resulting from application of the bond current, I_b.

5.1.4.3 Design Aspects of Sacrificial Cathodic Protection System

Galvanic anode systems are typically used where protective current requirements are relatively low, usually in the range of several hundred milliamperes to perhaps 4 or 5 A. Offshore structures, having current requirements of many hundreds of amperes can also be protected by large galvanic anodes weighing anywhere from 135 kg to 635 kg. Common places to use galvanic anode protection include well-coated, electrically isolated structures, offshore structures, ship hulls, hot spot pipeline protection, heat-exchanger water boxes, and in environments of resistivity below ~10 000 Ω cm, although they can be used in much higher resistivities, especially if isolation conditions are favorable.

5.1.4.3.1 **Design Parameters** The electrolyte resistivity, the protective current requirement, the desired life of the anodes, whether or not the structure is electrically isolated, whether or not there are any stray current concerns, and the physical configuration design for the anodes are important design parameters.

5.1.4.3.2 **Current Requirements** There are two ways of establishing current requirements. In this procedure, a test current is applied to the structure and the

resultant change in structure-to-electrolyte potential is measured. From, the data, the current-requirement can be calculated. Details on current requirement testing are given by Peabody in Refs. [46] and [47].

In new construction, the current requirement is often calculated from estimates such as those in Table 6. The amount of bare steel depends on the assumed quality of the coating, both to begin with and after several years of operation. A coating efficiency, for example, of 95% equals 5% bare metal. The current requirement is then the total area of the pipe, times the percent bare (as a decimal) times the current per square meter, or

$$I_{\text{req}} = A \times \%\,\text{bare} \times \text{mA m}^{-2}$$

where I_{req} is the total current requirement in milliamperes (mA) and A is the total area of the structure is square meters (m^2).

5.1.4.3.3 **Anode Selection** Table 7 lists the characteristics of several types of galvanic anodes. There are two types of magnesium anode alloys, standard (H-1) alloy and high-potential alloy. Generally, speaking high-potential anodes are desirable if the electrolyte resistivity exceeds 8000 Ω cm. There are two grades of zinc anodes, one for seawater use and one for groundwater use. There are also two grades of aluminum alloy anodes for salt water use.

If zinc anodes are chosen, it is important that they meet the purity required by ASTM B-418, Type I (Mil Spec A-18001) for seawater use and ASTM B-418 Type II for underground use. Lower purity anodes will not function properly. Zinc anodes are generally limited to environments of resistivity below 1500 Ω cm because of their low driving voltage. Zinc anodes are used successfully in higher resistivity soils, however, on some very well coated, electrically isolated facilities such as underground storage tanks.

Tab. 6 Typical current requirements for cathodic protection for bare steel

Environment	*[mA cm^{-2}]*
Neutral soil	4.5–156.0
Well-aerated neutral soil	21.5–32.0
Highly acid soil	32.0–160.0
Soil supporting surface reducing bacteria	65.0–450.0
Heated soil	32.0–270.0
Stationery freshwater	11.0–65.0
Moving, oxygenated freshwater	54.0–160.0
Seawater	32.0–110.0

Tab. 7 Galvanic anode characteristics

Material	*Theoretical output [A-h kg^{-1}]*	*Actual output [A-h k^{-1}]*	*Efficiency*	*Consumption*	
				Rate [Kg A-yr^{-1}]	*Potential to CSE*
Zinc type I	860	781	90%	11	1.06
Type II magnesium	816	739	90%	12	1.10
H-1 alloy	2205	551–1279	25–58%	6.8–16	1.40–1.60
Magnesium high potential	2205	992–1191	45–54%	7.3–8.6	1.70–1.80
Al/Zn/Hg	2977	2822	95%	3.1	1.06
Al/Zn/In	2977	2591	87%	3.3	1.11

5.1.4.3.4 **Cathodic Protection Circuit Resistance** The resistance of a vertical anode to ground can be calculated from the following equation based on the dimensions of the anode package [48]

$$R_V = \frac{\rho}{2\pi L}\left(\ln\frac{8L}{d} - 1\right)$$

Where R_V is the resistance to earth in ohms (Ω), ρ is the soil resistivity in ohm centimeters (Ω cm), L is the anode length in centimeters (cm), and d is the anode diameter in centimeters.

5.1.4.3.5 **Anode Output** The anode output depends on the anode circuit resistance and the potential difference between the anode and the structure (the driving potential). The potential difference between the anode and the structure, ΔV_g (V) is the difference between the open circuit potential of the anode, or

$$\Delta V_g = V_{ga} - V_{gs}$$

the current output, I in milliamperes, is then calculated from Ohm's Law

$$I = \frac{\Delta V_g}{R_t} \times 1000$$

5.1.4.3.6 **Number of Anodes Required** The number of anodes required is calculated from the current requirement divided by the individual anode output,

$$anodes\ required = \frac{current\ requirement}{anode\ output}$$

Anodes are usually spaced evenly along or around the structure. It is also good practice to place anodes near isolating fittings, building walls, or other locations where an inadvertent, although likely high resistance, contact to another structure might occur.

5.1.4.3.7 **Anode Life** Anode life can be calculated from [49]

$$L = \frac{Th \times W \times E \times UF}{h \times I}$$

where L is life in years, Th is the theoretical A-h kg^{-1} output (Table 7), W is the anode weight in kilograms, E is the current efficiency (Table 7), UF is the utilization factor, h is the hour per year (8766), and I is the anode output in amperes. The utilization factor is usually chosen as 0.85 (85%); this means that once the anode is 85% consumes, its resistance to earth begins to increase to the point that its output is reduced significantly.

If the calculated life is insufficient, then the designer needs to choose a heavier anode or perhaps use more anodes than the design calculation require. Total required anode weight for a given life could be solved from the above equation. The total weight can then be divided by the individual anode weight to obtain the required number of anodes.

5.1.4.4 Design of Impressed Current Cathodic Protection System

Impressed current cathodic protection has wide application. It is especially applicable when current requirements are large, in some cases as high as 500A or more. Then too, a small impressed current system, putting out less than an ampere might be used to replace a dissipated galvanic anode system. Common uses of impressed current include long transmission pipelines, complex underground structures, piling, marine structures and ship hulls, replacements for dissipated galvanic systems, large condenser water boxes, reinforcing steel in concrete, bare or poorly coated structures, unisolated structures, and water storage tank interiors.

5.1.4.4.1 **Design Process** The following steps describe the design process based on an underground pipeline [47]: establish the electrolyte resistivity, the protective current required, the desired life of the groundbed (anodes), whether or not the structure is electrically isolated, and the physical state on impressed current design.

5.1.4.4.2 **Current Requirements** The current requirement can be determined by testing, if the structure is in place as described by Peabody [46] which is similar to the sacrificial CP system discussed in Sect. 5.1.4.3.2.

5.1.4.4.3 **Anode Selection** High silicon, chromium bearing cast iron and graphite have similar characteristics. Dissipation rate varies with the environment, but 0.5 kg A-yr^{-1} is typical; steel dissipates at 9.1 kg A-yr^{-1}.

In determining the number of anodes required for an impressed current groundbed, it is best to start with the calculation of anode life. While the dissipation rate of high SiCrFe and graphite anodes is actually ~0.5 kg A-yr^{-1} or less, it is common practice to use 1.0 kg A-yr^{-1} to allow for a safety factor (similar to the utilization factor used in galvanic anode design). For other anode materials, the designer should follow the dissipation information given by the manufacturer. The total anode weight (W_t) for the desired life, then is

$$W_t = D_r \times I_{req} \times L$$

where W_t is the total weight required in kilograms, D_r is the dissipation rate in kg A-yr^{-1}, I_{req} is the current requirement in amperes, and L is the life in years. The number of anodes required is simply the total weight required divided by the individual anode weight.

5.1.4.4.4 **Cable and Total Circuit Resistance** Figure 18 shows a typical surface point groundbed layout. There are three types of cable resistances to consider: negative cable to the pipeline, positive cable to the groundbed and positive cable in the anode groundbed. Since the current flow through the anode portion of the groundbed cable drops as each anode is encountered, the effective resistance of the groundbed cable is usually taken as one half of its length. Thus, the total effective cable resistance in ohms becomes:

$$R_c = R_{(-)} + R_{(+)} + R_{gb}$$

where R_c is the total cable resistance, $R(-)$ is the negative cable resistance, $R(+)$ is the positive cable resistance, and R_{gb} is one half of the resistance of the total length of the anode portion of the groundbed.

The total circuit resistance in ohms (R_t) is the sum of the anode to ground (R_a), cable (R_c) and structure to ground (R_s) resistances, or

$$R_t = R_a + R_c + R_s$$

5.1.4.4.5 **Rectifier Selection** The required driving voltage (E) is determined by Ohms law:

$$E = \frac{I_{req}}{R_t}$$

The designer should allow for some increase in current requirement over the years; 25% is a reasonable figure, but the designer should also rely on experience. It is prudent to also allow for some circuit resistance in the future, so the required rectifier voltage is usually multiplied by 1.5.

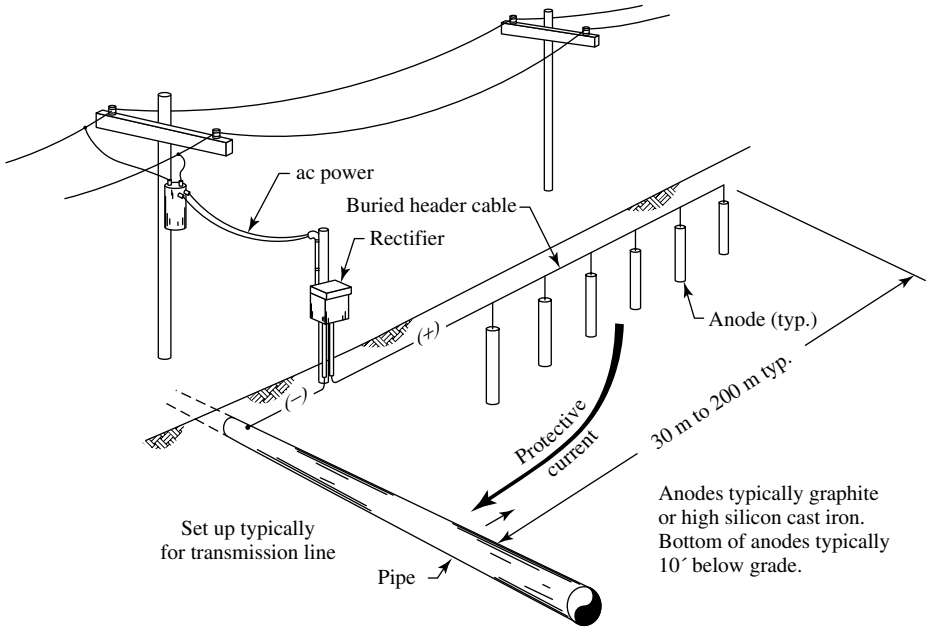


Fig. 18 Impressed current cathodic protection using surface point groundbed [39].

5.1.4.5 Other Design Concerns

5.1.4.5.1 **Electrical Continuity** In almost all cases, the structure to be protected must be electrically continuous. This is particularly true for piping, reinforcing steel, bulkheads, foundation piles, and the like. Where electrical continuity does not exist, such as in piping with mechanical joints, or among many structures in a complex network, joint bonds consisting of insulated copper cable are necessary to insure that all of the structures to be protected are electrically continuous.

There are times where electrical continuity is not required. One example is the installation of galvanic modes on existing ductile iron pipe where anodes can be installed on individual lengths of pipe.

5.1.4.5.2 **Shielding** In complex situations such as tank farms, industrial plants, and other large underground and underwater structures, it is important to lay out the anodes so that all structures receive protection. This may require a distributed anodes system or several small installations to insure that all areas are protected.

5.1.4.5.3 **Cathodic Interference** This term refers to the stray current effect that a cathodic protection installation may have on other structures. Interference is seldom a problem with galvanic anode protection because of its inherent small current output and driving voltage. With impressed current, however, stray current effects may occur on adjacent structures. This needs to be taken into consideration in the design of the protection [50].

5.1.4.5.4 **Attenuation** For long pipelines many kilometers in length, the attenuation,

or reduction of protection with distance must be considered. This becomes increasingly important as the pipeline to electrolyte resistance decreases or as the linear resistance of the pipeline increases. [51, 52].

5.1.4.6 Applications of Cathodic Protection

Although cathodic protection can be applied to any bare metal surface, the current density required is often so large as to render the process uneconomical. Metals may equally be protected from corrosion by the application of coatings that separate the metal, to a greater or lesser extent, from the environment. Unfortunately, such coatings will often contain flaws and further defects will develop over a period of time in service. The conjoint use of coatings and cathodic protection takes advantage of the two attractive features of each method of corrosion control. Thus, the bulk of the protection is provided by the coating and the CP system ''throws'' protection into the areas where the flaws in the coating exist. Further, as the coating degrades the CP system takes over to control the deficiencies of the coating. Undoubtedly, cathodic protection with protective coatings is a very powerful combination in corrosion control.

Cathodic protection has been traditionally used for a long time to protect structures in seawater. Zinc ''bracelet'' anodes are installed on pipelines immersed in seawater to provide sacrificial CP to the outer surfaces of the steel pipe. Offshore structures for gas and oil exploration, drilling, and production are commonly protected by the use of aluminum anodes on the steel structures. Cathodic protection is employed by several power plants located near coastal sites for protecting steel structures submerged in seawater.

The use of cathodic protection for the protection of the internal surfaces of process equipment in the chemical process and in the pulp and paper industries, the protection of water boxes and condenser tube sheets in the electric power industry [53], and the protection of steel reinforcing bars in concrete in highway bridges and parking garages, clearly reveal that this technique is used in a broad variety of applications.

5.1.4.7 Freshwater and Seawater

In general, the rate of corrosion is very low for most of the materials in freshwater owing to high resistivity and scale formation [54]. But the situation is different in the presence of contamination and extraneous ions. Freshwater is stored in a variety of materials including steel, cast iron, wrought iron, copper, galvanized steel and aluminum. When freshwater is contaminated with ions of copper either from piping or from other parts like pumps and so forth, they are deposited over the tank and this causes severe galvanic corrosion. A deep pit will penetrate the tank wall leading to severe damage. In general, hot-water tanks are severely corroded in comparison with cold-water tanks. Corrosion can even be generated with scales, debris, deposits, and sediments, and so forth, present in the tank by creating differential aeration cells and temperature fluctuations.

In reality, a variety of shapes and sizes of tanks, piping and so forth are used, with and without coatings and inhibitors for corrosion-control purposes. Thus the area, size and shape of the anodes needed for cathodic protection also vary depending on the size and shape of the tanks. A current density of 1 mA sq.ft^{-1} is required to bring the potential to -1.1 V against a copper–copper

sulfate half-cell for protecting domestic galvanized steel tanks. The freshwater tanks generally coated with paints are protected with current densities of lower magnitude. Zinc anodes of smaller size can be used, or larger magnesium anodes can be used if the current densities are higher. Platinized titanium anodes are used for cathodically protecting larger tanks by impressed current methods. Protecting corners and other inaccessible regions pose a big problem. However, painted and coated tanks have no such problems.

Seawater is a naturally available corrosive medium containing chlorides, carbonates, several minerals such as sodium, calcium, magnesium and potassium, and dissolved oxygen of 8 parts per million. The corrosion rate of bare steel immersed in seawater is uniform at 5 mils per year, and the ferrous ions released during corrosion further oxidize into ferric ions to form a rust layer over the surface. The presence of mill scale, weld zones, rivets and so forth cause severe galvanic attack on steel resulting in deep pitting and localized attack. Microbiologically influenced corrosion and fouling are other major problems in the use of steel structures in seawater. Barnacles, mussels, sulfate reducing bacteria, algae and so forth seriously damage the structures by providing site for corrosion to initiate and also taking part in the corrosion processes.

In general, cathodic protection in seawater is classified into (1) inshore purposes for pipelines, tanks and structures, (2) structures and ships immersed and active in seawater, and (3) those that are inactive or stationary in seawater. A variety of static structures including floating docks, chains, light ships, nets and so forth in various shapes and sizes are protected by (1) anodes directly and closely mounted on them, (2) anodes remotely placed away from the structure and (3) impressed current method. Mostly sacrificial anodes are employed for small structures and impressed current methods for large structures. If anodes required are large in number and expensive, the impressed current method is also employed for such conditions. With respect to the cathodic protection of the ships' hulls, the movement of the ship relative to the seawater decides the current density required to protect the structure. As the velocity of the ship underway increases, the current density increases significantly. There are two purposes for which cathodic protection is employed, (1) to stop the corrosion of hull plates and welds from uniform and pitting attack, and (2) to maintain the smoothness of the hull surface which is necessary for avoiding the frictional drag and to enhance the fuel efficiency of the ship. The design of a CP system for having a smooth surface with minimum corrosion and highly integral paint surface is a commendable achievement required for maintaining a ship with minimum problems. Anticorrosion and fouling paints of self-polishing in nature and a highly reliable CP would solve this problem.

Jetties are individual or multiple piles interconnected together to form a structure in the seabed and support a deck. The piles of a jetty usually have half of their length in the seabed and the rest in the high tide and splash zones up to the jetty deck. They are often concrete structures reinforced with steel. Cathodic protection using sacrificial zinc or aluminum anodes is installed after the completion of the jetty. With a deep-water jetty the suspension of more than a single anode or placing of alternate anodes at different levels is necessary. A few and larger anodes are necessary while impressed current method is employed. An

array of anodes suspended and mounted on the piles is sufficient to supply the demanded current for cathodic protection. In order to have efficient cathodic protection, the structure of the whole jetty must be connected effectively so that good electrical contact exists.

5.1.4.8 Marine Structures

Design of cathodic protection for marine structures in both fresh and salt water require special techniques. Galvanic systems usually employ zinc or aluminum alloy anodes. Impressed current systems frequently use high silicon, chromium bearing iron, platinized niobium, or mixed-metal oxide/titanium anodes. The structure being protected affects the design. Stationary facilities such as bulkheads and support piles require different techniques from ship hulls [55].

Sacrificial anodes are usually applied for the protection of vessels up to 10 000 tons. Impressed cathodic protection is used for larger objects. Electrochemical protection should assist existing coating protection systems. Appropriate sets of organic coatings resistant to alkalis are used as coating protection. Cathodic protection station usually work in automatic mode with continuous control of the hull potential, which results from the variable operating conditions. Continuous change in the draught of hulls dependent on the load, waves, temperature changes, and salinity of the water have a large effect on the CP parameters, especially the current requirement. Modern insoluble anodes are most frequently made from platinized titanium [56]. Zinc sacrificial anodes are used for the protection of tankers. Magnesium and aluminum anodes cannot be used because of the possibility of sparking and causing explosions.

Ship hulls Painting cannot always protect hostile marine conditions, in ships and, areas above keel blocks. Stern and rudder areas suffer erosion and corrosion due to the high turbulence caused by the propeller coupled with the galvanic effects of the noble bronze propeller. Effective cathodic protection of ship hulls and similar marine structures in seawater against corrosion can be applied using either aluminum or zinc alloy sacrificial anodes. Twenty percent of the anodes required for full hull protection are required for stern protection only.

5.1.4.9 Offshore Technology

The anticorrosion protection of offshore platforms subjected to aggressive operation conditions is an especially difficult task. Apart from the continuous strongly corrosive effects of seawater, periodical phenomena are also encountered, such as storms, earthquakes, hurricanes, pressure of ice floats, and other phenomena, thereby increasing the corrosion hazard. These interactions cause stress and fatigue corrosion and other forms of corrosion attack. In such conditions, special protective coating systems are applied to protect the objects, coupled with cathodic protection realized by the use of sacrificial anodes or an external power supply. The spud cans or mat of jack-up drilling rigs in the submerged and buried steel structures of the jacket of an offshore platform are usually left uncoated and cathodic protection is applied to protect these areas. For the protection of columns and spud cans of a jack-up rig, the anodes are flush mounted to reduce resistance during transit. Sacrificial anodes for the platforms are generally cast with tubular steel cores, which are welded to the structure [57–59].

Submarine pipelines used for the transportation of oil, gas or other fluids are

generally coated with concrete, besides the corrosion resistance coatings. Cathodic protection supplemented by coatings of these pipelines is achieved by means of either aluminum or zinc alloy anodes in bracelet form installed at regular intervals of the pipelines.

5.1.4.10 Soil and Biological Environments

Most of the clays and waterlogged soils create an anaerobic condition in which the bacteria and biological species can thrive. Corrosion is very severe under such conditions, though the main oxidizing agent oxygen, that is required for corrosion to occur is not available. The main reason for such accelerated corrosion is the presence of sulfate-reducing bacteria that thrive under anaerobic conditions in the soil environment. These bacteria are reduced to sulfides, and this reaction consumes the electrons that allow the corrosion to occur. The corroding surface is entirely covered with a black slime of iron sulfide and this can be easily recognized by its characteristic smell. Under aerobic conditions, that is, in the presence of oxygen in soil or water, anaerobic bacteria are not active but can become active once anaerobic conditions are established. Cathodic protection of iron and steel structures are possible in the presence of such bacteria [60]. Aerobic bacteria are also active under some aerobic conditions and this should be considered carefully, particularly if such bacteria produce acids. In general, a large current density is warranted particularly in the initial stages. As the open circuit potential of surfaces covered with microbiological species are anodic, shifting them from such positive potential to more negative points for cathodic protection is necessary.

In comparison with seawater, soils, clays and rocks present a heterogeneous structure with very high resistances ranging up to 1 000 000 ohm cm. The resistivity of a soil varies greatly with the water content. Apart from water, moisture content, salt content and temperatures of the environment around, the soil dictates the resistivity of the soil and clays. Most of the structures that are buried in the earth face the problem of resistivity of the soil and groundbed in determining the potential and current density required for cathodic protection. If the resistivity of the adjacent layers of soil present near the pipes is different, then the voltage gradients in the soil will be increased beyond those expected for a homogeneous medium like seawater. As the variations of a hundred to one in the resistivity of the topsoil to rocks are expected, large differences in the behavior of the cathodic protection installations are experienced in reality. The soil potentials of a pipeline can be changed considerably by adopting different methods of pipe-laying techniques. Nowadays, coatings of very high resistance are applied over the pipelines such that the coating resistance controls the protection parameters [61]. For example, if the product of current required per foot multiplied by the soil resistivity for large pipes is less than 1 A.ohm.cm per foot, then the coating resistance controls the cathodic protection parameters.

5.1.4.11 Chemical Environments

Cathodic protection is commonly employed in many chemical plants depending on the compatibility of the process medium with the CP system. Sacrificial anodes may produce unwanted corrosion products or permanent anodes may generate chlorine and other gases and thus affect the quality of the medium stored or transported in the vessels, piping and so forth. Cathodic protection of the most

commonly used steel components in the chemical industry is associated with the corrosion of welded regions [62], SCC in chloride and acidic environments [63], and caustic cracking in alkaline environments. Cathodic protection was successfully employed to prevent caustic corrosion cracking of vessels used in the refining of alumina. Aluminum storage vessels used for storing aqueous liquor were cathodically protected by using zinc anodes, which was acceptable. In the pulp and paper industry, cathodic protection along with anodic protection is successfully employed for effluent treatment clarifiers, buried fuel storage tanks and so forth.

Cargo/Ballast tanks In conjunction with approved coatings, cathodic protection of cargo/ballast tanks is by means of long slender tank anodes using either zinc or aluminum alloy anodes with a system life of not less than four years. Use of magnesium and magnesium alloy anodes is not permitted in oil cargo tanks or tanks adjacent to them because of the possibility of spark hazard that may be caused by metal parts falling on the anodes fixed.

5.1.4.12 Steels in Concrete Structures

The alkaline nature of the environment surrounding the reinforcement steel rods embedded in the concrete matrix passivates the steel; however, corrosion attack takes place when chloride ions penetrate into them from the seawater and other surroundings [64, 65]. The other ions like sulfate and carbonate ions also enhance the possibility of corrosion of the steel rods. Cathodic protection of such steel rods can be classified into two categories: the surrounding of the steel rod is the only concrete environment; and the other is any medium encountered by the structure, for example soil, seawater or a storage tank containing water. Hence, the concrete itself is considered as a medium or any other medium in contact with the concrete is considered as a medium for CP purposes. The current densities required for protecting the steel depends on the age of the concrete or mostly on the alkalinity as it affects the polarization and initial current of cathodic protection. Most of the times it is difficult to establish the potentials due to large IR drops in the soil. The use of zinc and epoxy-coated reinforcing steel rods require lesser current for cathodic protection. It is very important to place sacrificial anodes closer to the rod area and also to maintain a conducting path between the anodes kept at different distances. Platinized titanium wires are used for impressed current CP purposes that can be placed along the reinforcing rods in a conducting backfill [66]. Use of many individual anodes of smaller sizes distributed throughout the structure is preferable even though it is expensive. Accelerated corrosion occurs when reinforced concrete is buried in the ground as the rods act as cathodes to the buried steel. This has caused a large number of failures, particularly for the pipelines where the pipe is connected to the rebar in a concrete pit structure. Cathodic protection of the rebar is easier and conventional techniques can be applied if the rebars are continuous. When a structure lies partly in the ground and extends out of it, then the cathodic protection applied within the ground does not spread through the concrete to outside regions for any appreciable height.

Cathodic protection can be used to effectively arrest the detrimental corrosion of steel in chloride-containing concrete [67, 68]. A schematic diagram of a CP system for steel and concrete is shown in Fig. 19. A DC power supply provides the

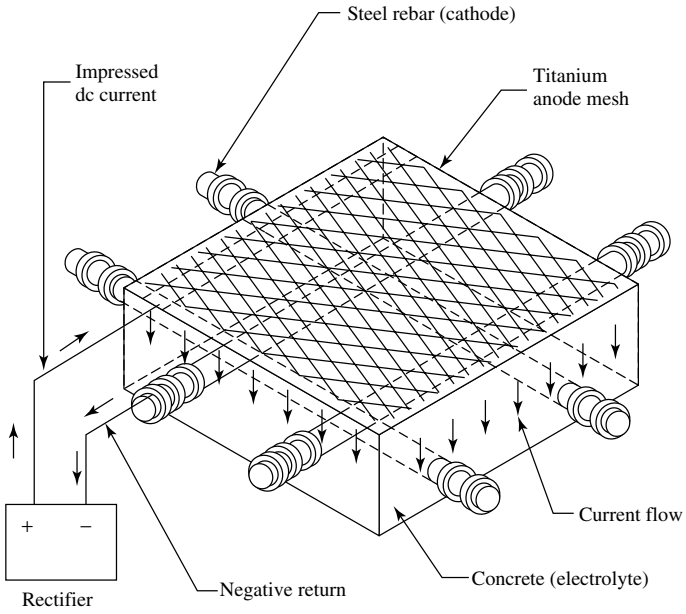


Fig. 19 Schematic of the cathodic protection of steel reinforcing bars in concrete [1].

protective CP current to an anode on the surface of the concrete. The protective current then moves through the concrete to the steel structure to be protected. For effective protection, the steel piece to be protected must be in electrical contact and a return current path must be provided to the power supply. The anode for these systems can be either oxide-coated titanium, conductive polymer cables, or conductive polymeric paint systems. Installations of oxide-coated, expanded titanium mesh anodes on a sidewalk and a bridge substructure is very common [69, 70]. The expanded titanium metal anodes are coated with a grouting material after application to the concrete structure. Polymer mesh anodes are used to protect reinforcing steel in bridge decks, parking garages, and other large structures. The anode mesh is placed on the surface of the reinforced concrete structure, covered with an overlay of portland cement or polymer-modified concrete, and then connected to a low-voltage dc power source.

Bridge decks, parking structures, and other reinforced concrete structures lend themselves to cathodic protection, particularly when the concrete is contaminated with cathodic chlorides from deicing salts or a marine environment. Special techniques are required as described by Rog and Swait [71] NACE [72, 73] and Morgan [74].

Prestressed concrete pipelines occasionally require cathodic protection. Protection must be done carefully to avoid damage to the prestressing wire from hydrogen embrittlement or SCC [75].

Acknowledgments

The authors gratefully acknowledge the help of Shri N. Bhuvaneswaran of University of Madras and Dr. T. Sankara

Narayanan of National Metallurgical Laboratory, Madras for technical discussions during the preparation of the manuscript.

References

1. C. E. Locke, Corrosion: cathodic and anodic protection, *Encyclopedia of Chemical Processing and Design*, Marcel Dekker, New York, 1981, pp. 13–59, Vol. 12.
2. *Cathodic Protection Criteria – A Literature Survey*, NACE International, Houston, Tex., 1989.
3. V. Ashworth, *Cathodic Protection, Theory and Practice* (Eds.: V. Ashworth, C. Googan), Ellis Horwood, New York, London, 1993.
4. R. Juchniewicz, *Corros. Sci.* **1966**, *6*, 69.
5. O. L. Riggs Jr., C. E. Locke, *Anodic Protection, Theory and Practice in the Prevention of Corrosion*, Plenum Press, New York, 1981.
6. A. J. Sprott, *Corros. Australasia* **1984**, *9*, 10.
7. A. I. Tsinman, L. A. Danielyan, *Zash. Met.* **1976**, *12*, 450–452.
8. G. Herbsleb, W. Schwenk, Potential dependence of intercrystalline stress corrosion of unalloyed and low alloys, *Steels in Hot Alkaline Solution*, Stahl Eisen 1970, p. 903, Vol. 90.
9. H. Grafen, D. Kuron, *Arch. Eisenhuttenvesen* 36.
10. V. S. Kuzub, A. L. Anokhin, *Zash. Met.* **1976**, *12*, 282–284.
11. V. S. Kuzub, V. S. Noavasiti, *Zash. Met.* **1975**, *15*, 560–562.
12. J. B. Cotton, A perspective view of localized corrosion of titanium in *Localized Corrosion* (Eds.: R. W. Staehle, B. F. Brown, J. Kruger et al.), NACE International, Katy, Tex., 1969, 676–679.
13. J. B. Berkowitz, W. D. Lee, *Investigation of the Possibilities for Electrochemical Control or Hot Corrosion*, Final Report ADL-75526-FR, NNTIS, Cambridge, Mass., 1972–1973.
14. M. G. Fontana, *Ind. Eng. Chem.* **1951**, *43*, 652.
15. D. Fyfe, R. Vanderland, J. Rodda, *Chem. Eng. Prog.* **1977**, *73*, 65–68.
16. Ya. M. Kolotyrkin et al., *Zasch. Met.* **1971**, *7*, 722.
17. O. L. Riggs Jr., C. E. Locke, *Anodic Protection: Theory and Practice in the Prevention of Corrosion*, Plenum Press, New York, 1981.
18. C. E. Locke, *Corrosion*, Metals Handbook in (Eds.: J. Korb, D. L. Olson), 9th ed., ASM International, Metals Park, Ohio, 1987, pp. 463–466, Vol. 13.
19. V. Kuzub, V. Novitskijv, *Proc. 9th Intl. Congress on Metallic Corrosion*, NRCC, Toronto, Ottawa, 1984, pp. 307–310, Vol. 1.
20. H. Davy, *Philos. Trans. R. Soc.* **1824**, *114*, 197.
21. H. Davy, *Philos. Trans. R. Soc.* **1824**, *114*, 242.
22. H. Davy, *Philos. Trans. R. Soc.* **1825**, *115*, 328.
23. *Cathodic Protection of Vessels and Flow lines in Oil and Gas Production*, NACE International, Houston, Tex., 1997.
24. Control of External Corrosion on Underground or Submerged Metallic Piping Systems, NACE Standard RP-01-69-96, NACE International, Houston, Tex., 1996.
25. R. A. Gummow, *Corrosion/86*, Preprint 343, NACE International, Houston, Tex., 1986.
26. G. Burgmann, H. Hildebrand, *Werkst. Korros.* **1970**, *22*, 1012.
27. V. A. Prituala, *Cathodic Protection of Pipelines and Storage Tanks*, Department of Scientific and International Research, London, 1953.
28. J. H. Morgan, *Cathodic Protection*, 2nd ed., NACE International, Houston, Tex., 1987, pp. 145–184.
29. R. J. Emerson, *Corrosion* **1960**, *16*, 65t, NACE Publ. 60-3, T-2B, Rep.
30. J. A. Lehmann, *Mater. Protect.* **1964**, *3*(2), 36.
31. K. G. C. Berkely, *Corros. Prev. Control* **1976**, *23*(1), 6.
32. J. F. Tatum, *Mater. Perform.* **1979**, *18*(7), 30.
33. B. Crondwell, Ch. Forn, *Anti Corros. Methods Mater.* **1979**, *26*, 13.
34. L. L. Shrier, Corrosion, *Corrosion Control*, Part ii, 2nd ed., Verlag Newnes-Butterworth, London, Boston, 1976.
35. R. L. Benedict, (Ed.), *Classic Papers and Reviews on Anode Resistance Fundamentals and Applications*, NACE International, Houston, Tex., 1986.
36. R. H. Heidersbach, *Corrosion, Metals Handbook*, 9th ed., ASM International, Metals Park, Ohio, 1987, pp. 466–477, Vol. 13.
37. J. H. Morgon, *Cathodic Process*, 2nd ed., NACE International, Houston, Tex., 1987.
38. M. G. Fontana, *Corrosion Engineering*, McGraw-Hill, New York, 1987, pp. 294–304.
39. R. W. Revive, (Ed.), Engineering of cathodic protection systems, *Uhlig's Corrosion Handbook*, Electrochemical Society Series, 2nd ed., John Wiley & Sons, New York, USA, 2000.
40. P. Pignatelli, *Mater. Perform.* **1985**, *24*, 30.
41. W. M. Rivers, D. R. Price, *Mater. Perform* **1989**, *28*, 17.

42. Stray current analysis, *Appalachian Underground Corrosion, Short Advanced Course Text*, West Virginia University, Morgantown, WVa, 1993.
43. Wyer, Samuel, Digest of Publications of Bureau of Standards on Electrolysis of Underground Structures caused by the Disintegrating Action of Stray Electric Current from Electric Railways, National Bureau of Standards, Washington, DC, 1918.
44. Szeliga, Michael, (Ed.), *Stray-Current Corrosion: The Past, Present and Future of Rail Transist Systems*, NACE International, Houston, Tex., 1994.
45. D. H. Boteler, W. H. Seager, *Corrosion* **1988**, *54*, 751.
46. A. W. Peabody, *Control of Pipeline Corrosion*, NACE International, Houston, Tex., 1978, pp. 38–50.
47. *Appalachian Underground Corrosion, Short Advanced Course Text*, West Virginia University, Morgantown, WV, 1993, Chapter 5.
48. A. W. Peabody, *Control of Pipeline Corrosion*, NACE International, Houston, Tex., pp. 94–108.
49. *Appalachian Underground Corrosion, Short Advanced Course Text*, West Virginia University, Morgantown, WV, 1993, Chapter 6.
50. *Appalachian Underground Corrosion, Intermediate Course Text*, West Virginia University, Morgantown, WV, 1993, Chapter 5.
51. R. Pope, Application of cathodic protection in *Corrosion Handbook* (Ed.: H. H. Uhlig), Wiley, New York, 1963, p. 942ff.
52. J. H. Morgan, *Cathodic Protection of Buried Structures (Chapter 6), Cathodic Protection*, 2nd ed., NACE, Houston, Texas, USA, 1993, p. 201.
53. B. C. Syreft, *Mater. Perform.* **1992**, *31*, 52.
54. C. Deslouis, D. Festy, O. Gil et al., *Electrochim. Acta* **1998**, *43*, 1891.
55. J. H. Morgan, Chap. 7, *Cathodic Protection*, 2nd ed., NACE International, Houston, Tex., 1993,
56. C. Leius, *Mater. Sci. Eng., A* **1999**, *263*, 112.
57. O. T. de Rincon, M. F. De Romero, A. R. de Carruyo et al., *Mater. Struct.* **1997**, *30*, 556.
58. S. C. Krane, A. A. Sagues, F. J. Presuel-Moreno, Corrosion-97, Paper No. 231, NACE International, Houston, Tex., 1997.
59. A. A. Sagues, S. C. Krane, F. J. Presuel-Moreno, Advanced computational model for sacrificial cathodic protection of partially submerged reinforced concrete marine footers in *Repair and Rehabilitation of Reinforced Concrete Structures: The State of the Art* (Eds.: W. F. Silva-Araya, O. T. De Rincon, L. P. O'neil), American Society of Civil Engineering, Reston, 1997.
60. H. A. Videla, *Int. Biodeterior. Biodegrad.* **2002**, *49*, 259.
61. I. C. P. Margarit, O. R. Mattos, *Electrochim. Acta* **1998**, *44*, 363.
62. C. Lindey, W. J. Rudd, *Mar. Struct.* **2001**, *14*, 397.
63. Z. Li, F. Gan, X. Mao, *Corros. Sci.* **2002**, *44*, 689.
64. C. L. Page, *Nature* **1975**, *258*, 514.
65. T. Yonezawa, V. Ashworth, R. P. M. Procter, *Corrosion* **1988**, *44*, 489.
66. R. Myrdal, Embeddable Reference Electrodes for Concrete – A State of the art Report, European Federation of Corrosion, WP 11 Corrosion in Concrete, Task Group 5, Draft 3, August, 2000.
67. P. Pedeferri, Cathodic protection of new concrete constructions in *Proceedings of the International Conference on Structural Improvement through Corrosion Protection of Reinforced Concrete*, Institute of Corrosion, London, 1992.
68. L. Bertolini, F. Bolozoni, L. Lazzari et al., *J. Appl. Electrochem.* **1998**, *28*, 1321.
69. A. Tvarusko, 12th Intl. Corrosion Congress, ICC, Paper No. 547, NACE International, Houston, Tex., 1993,
70. P. C. S. Hayfield, *Platinum Met. Rev.* **1998**, *42*, 116.
71. J. W. Rog, W. J. Swait Guidelines for selection of cathodic protection systems for reinforces concrete, Corrosion 87, San Francisco, NACE International, Houston, Tex., 1990.
72. V. Chaker, (Ed.), *Corrosion Forms and Control for Infrastructure*, NACE International, Houston, Tex., 1992.
73. Impressed Current Cathodic Protection of Reinforcing Steel in Atmospherically Exposed Concrete Structures, NACE International Recommended Practice RP02-90-90, NACE International, Houston, Tex., 1990.
74. J. H. Morgan, *Cathodic Protection of Buried Structures (Chapter 6), Cathodic Protection*, 2nd ed., NACE, Houston, Texas, USA, 1993, p. 242.
75. M. Szeliga, (Ed.), *Corrosion in Prestressed Concrete: Pipes, Piles, and Decks*, NACE International, Houston, Tex., 1995.

5.2
Corrosion Protection by Inhibition

Olaf M. Magnussen
Institut für experimentelle und angewandte Physik, Universität Kiel, Olshausenstr. 40, 24161 Kiel, Germany

5.2.1
Phenomenological Aspects

5.2.1.1 Fundamentals

A corrosion inhibitor is generally defined as a substance that, when added at small concentrations to a corrosive environment, effectively reduces the corrosion rate of a metal exposed to that environment. Corrosion protection by inhibiting additives is of considerable practical importance, with an annual market of several million tons of inhibiting substances, and is the subject of significant research activities [1–3]. For the classification of a substance as an inhibitor as well as for a discussion of the underlying inhibition mechanisms, both the metal and the environment have to be defined. Usually, inhibition results from the formation of an adsorption layer or protective film, which influences the electrochemical reactions involved in the corrosion process (also termed *interface* and *interphase* inhibition, respectively [4]). In other cases, the inhibitor promotes the passivation of the metal or modifies the solution chemistry, for example, by scavenging aggressive species. Inhibitors are mainly used for the control of homogeneous corrosion; their application to localized corrosion is less developed.

The overall corrosion rate of a freely corroding metal is determined by the anodic and cathodic partial reactions (see Chapter 1, this volume), both of which can be affected by the inhibitor. It is therefore common to distinguish anodic, cathodic, and mixed inhibitors, dependent on the type of electrochemical reactions that are inhibited (see Sect. 5.2.1.2). In all three cases, the inhibitor can either lower the rate of the rate-determining step of the corresponding reaction(s) or introduce a new rate-determining step. The efficiency by which the corrosion process is reduced usually depends strongly on the inhibitor concentration as well as characteristic system parameters, such as the solution pH, the concentration of aggressive species in the solution, the nature and the state of the metal surface, and the hydrodynamic conditions (see Sect. 5.2.1.3).

In practice, inhibitors are employed predominantly for corrosion control in closed systems, as a cost-efficient alternative to the use of high corrosion-resistant materials. Practical criteria for the selection of corrosion inhibitors from the great variety of inorganic and organic substances with inhibiting properties are not only their inhibition efficiency but also safety of use, economic constraints, compatibility with other chemicals in the system, and environmental concerns. For example, chromates and zinc salts, highly efficient inorganic inhibitors, are used increasingly less due to their toxicity and are nowadays largely replaced by organic inhibitors. Examples of commonly used inhibitors as well as their classification and predominant inhibition mechanisms are given in Table 1.

5.2.1.2 Classification

A common classification of inhibitors is based on their effects on the electrochemical reactions involved in the corrosion process. In the framework of mixed potential theory (see Chapter 1.3, this volume), these effects are most conveniently visualized by $E - \log|j|$ diagrams, such as shown in Fig. 1. For a freely corroding metal, the corrosion potential E_c and the corrosion

Tab. 1 Examples of substances used as corrosion inhibitors.

Species	*Type*	*Mechanism*
Orthophosphates	Anodic	Nonoxidizing passivator
Polyphosphates	Cathodic	Film-forming
Phosphonates	Mixed	Film-forming
Tannins and lignins	Cathodic	Film-forming
Benzoates	anodic	Nonoxidizing passivator
Silicates	Mixed	Film-forming
Chromates	Anodic	Oxidizing passivator
Nitrites and nitrates	Anodic	Oxidizing passivator
Molybdates	Anodic	Nonoxidizing passivator
Zinc salts	Cathodic	Film-forming
Aromatic azoles	Mixed	Adsorption, film-forming
Amines and amides	Mixed	Adsorption
Acetylenic alcohols	Mixed	Adsorption
Sulfur-containing compounds	Mixed	Adsorption
Hydrazine	Oxygen scavenger	
Sulfites	Oxygen scavenger	

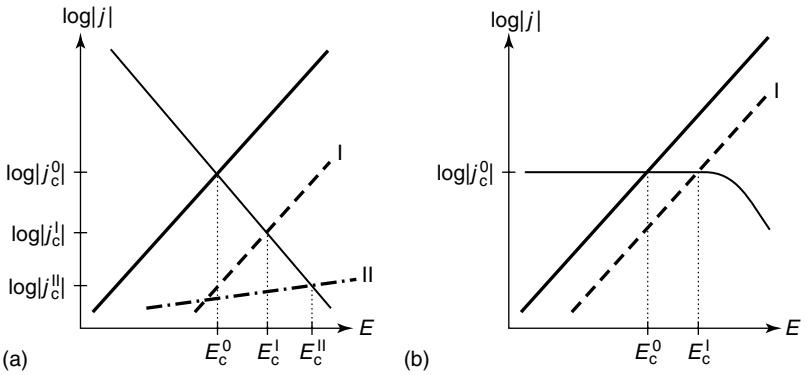


Fig. 1 $E-\log|j|$ diagrams showing the effect of an anodic inhibitor on the corrosion potential E_c and the corrosion current density j_c (visualized by thin dotted lines) for (a) a reaction-controlled and (b) a diffusion-controlled cathodic process. Here and in the following figures, the solid lines denote the anodic (bold) and cathodic (thin) partial reactions in inhibitor-free solution, whereas the corresponding reactions in the presence of inhibitors are shown as dashed and dashed-dotted lines.

current density j_c are defined by the condition that anodic and cathodic current densities are equal, that is, the anodic (bold lines) and cathodic (thin lines) curves in these diagrams intersect. $E-\log|j|$ diagrams can be interpreted in two slightly different ways: On the one hand, they may describe corrosion of a perfectly homogeneous surface, a situation usually realized only in model systems, in which case they depict the true microscopic current densities on this surface. On the other hand, they may be used to discuss the more realistic case of a heterogeneous (e.g. partly

passivated) metal surface, in which anodic and cathodic reactions are located at different, coexisting surface areas (with the size of the cathodic areas usually exceeding by far that of the anodic ones). In this case the $E-\log|j|$ diagrams show the macroscopic current densities, which are given by the local, microscopic current densities, multiplied by the surface fraction occupied by the anodic or cathodic areas, respectively.

5.2.1.2.1 **Anodic Inhibitors** Inhibitors that directly affect the anodic reaction, that is, the metal dissolution process, are termed *anodic inhibitors*. Addition of an anodic inhibitor to the corrosion system (dashed and dashed-dotted lines in Fig. 1) can either lower the rate (i.e. the exchange current density) of the anodic process (I) or influence the reaction mechanism (II), resulting in a change in the Tafel slope $\partial(\log|j|)/\partial E$, as compared to that in inhibitor-free solution. In the case that both the anodic and the cathodic process are determined by the activation-controlled reaction rates (Fig. 1a), this causes an anodic shift of the corrosion potential E_c^0 of the inhibitor-free system to E_c^{I} (or E_c^{II}) in inhibitor-containing solutions and a decrease in the corrosion current density from j_c^0 to j_c^{I} (or j_c^{II}).

To achieve inhibition, it is necessary that the reaction affected by the inhibitor actually determines the corrosion rate. This point is illustrated by the important case that the cathodic reaction is limited by the diffusion of the reacting species (Fig. 1b), a common situation for corrosion in neutral, oxygen-containing solutions. Obviously, E_c^0 is shifted also here anodically to E_c^{I} in the presence of an anodic inhibitor. The corrosion current density, however, does not change in this system as long as E_c remains within the range in which the cathodic process is diffusion-limited. This demonstrates that measurements of the corrosion potential alone are of rather limited use in monitoring the efficiency of an inhibitor.

5.2.1.2.2 **Cathodic Inhibitors** In a similar way, an inhibitor can interfere with the cathodic partial reaction, as shown schematically in the $E-\log|j|$ diagram in Fig. 2(a). In this case, E_c is shifted to more negative potentials, resulting in a reduced corrosion current density j_c. Again, the inhibitor can affect both

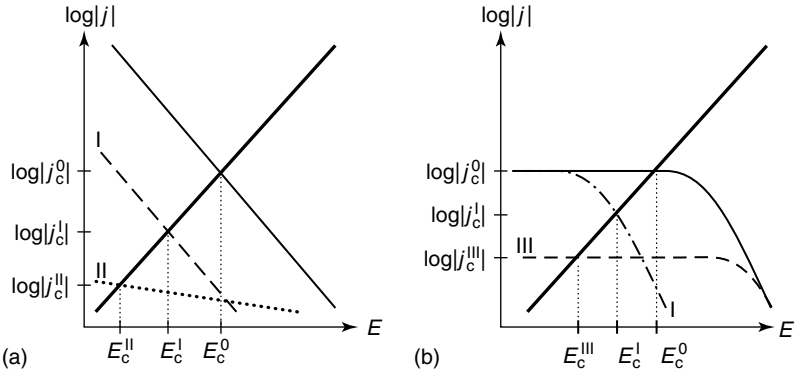


Fig. 2 $E-\log|j|$ diagrams for a cathodic inhibitor in the case of (a) a reaction-controlled and (b) a diffusion-controlled cathodic process.

the rate (I) and the mechanism (II) of the cathodic process. Cathodic inhibitors may also be effective under diffusion-controlled cathodic reaction conditions (Fig. 2b), either by inducing a crossover to reaction-controlled conditions (I) or by reducing the surface concentration of species involved in this reaction (III), for example, by the formation of surface films that block their transport to the surface.

5.2.1.2.3 **Passivating Inhibitors** Some of the most effective inhibitors stifle corrosion by promoting passivation of the metal surface, that is, by shifting the corrosion potential into the range positive of the critical passivation potential E_p (see Chapter 3.2, this volume). To induce passivation of an active surface, the corrosion current density j_c has to exceed the critical current density for passivation j_{crit}. This can be achieved either by increasing j_c via enhancing the rate of the cathodic reaction (Fig. 3a, curve II) or by decreasing the critical current density j_{crit} (Fig. 3b). The first case usually refers to inhibitors that are easily reduced on the metal surface, resulting in an increasing cathodic current density. Since these inhibitors are oxidizing in their action on the metal, they are often termed *oxidizing inhibitors*, in contrast to *nonoxidizing inhibitors*, which require the presence of oxygen in solution to achieve inhibition in near-neutral solution. Most passivating (and usually even *oxidizing*) inhibitors, however, rely predominantly on the second mechanism, in which the anodic process is inhibited [5]. This effect may be caused even by pure inhibition of active metal dissolution (as described in Sect. 5.2.1.2.1), provided j_{crit} is reduced sufficiently to shift the corrosion potential anodic of E_p (i.e. in the potential range of passive oxide growth). More frequently, however, the inhibitor is more directly involved, resulting in passive films that differ strongly from those formed in inhibitor-free solution and contain the inhibitor or reaction products formed by interaction of the inhibitor with the corroding surface (see Sect. 5.2.3).

As shown in Fig. 3(a), the efficiency of passivating inhibitors depends strongly on their presence at a sufficient (critical) concentration. Below this critical concentration (curve I) a bistable situation may arise, in which the corrosion potential can either sit in the passive (E_c^{I}) or active ($E_c^{I'}$) region, resulting generally in pitting. Because of this problem, which can even cause an increase in the corrosion

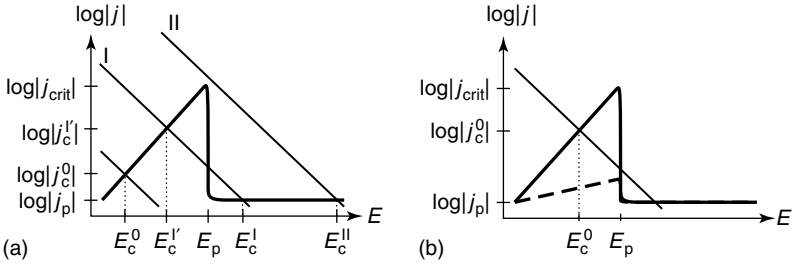


Fig. 3 $E-\log|j|$ diagrams for a passivating inhibitor for the case of a reaction-controlled cathodic process. Passivation is achieved (a) by increasing the cathodic current density and (b) by decreasing the critical current density for passivation.

current ($j_c^{I'}$), passivating inhibitors are often termed as *dangerous*. Finally, passivating inhibitors not only induce the formation of passive films on active metals but also help to maintain passivity on already passivated metal surfaces, a property that is of key importance for practical applications. This can be rationalized by the same mechanisms as described above, with the inhibitor promoting repassivation of small active sites. In this case, even inhibitor coverages far below one monolayer may lead to effective inhibition.

5.2.1.2.4 **Mixed and Ohmic Inhibitors**
Some substances inhibit corrosion by reducing simultaneously the rate of the anodic and cathodic reactions involved in the corrosion process and are therefore called *mixed inhibitors*. Mixed inhibition not only requires that both of the electrochemical reactions are influenced by the inhibitor, which indeed is often the case, but also that the corrosion rate is actually limited by anodic as well as cathodic reactions. As an example, again a diffusion-limited cathodic reaction may be considered, in which inhibition may rely solely on the reduction of the cathodic reaction rate (see Fig. 2b, curve III), even if the anodic reaction is also affected by the inhibitor (see Fig. 1b). In this case, the inhibitor effectively is cathodic in its action. Furthermore, it is noted that a substance may also inhibit one partial reaction, but accelerate the other.

Finally, inhibition may also be (partially) caused by the presence of ohmic potential drops (e.g. because of the formation of poorly conducting films) between anodic and cathodic surface areas. Here the rates of the partial reactions are additionally reduced due to the opposite negative and positive potential shifts in the anodic and cathodic areas, respectively, resulting in a further decrease in j_c.

5.2.1.3 Inhibition Efficiency

5.2.1.3.1 **Definition and Measurement**
The efficiency S of a corrosion inhibitor is commonly defined as the relative reduction in corrosion rate:

$$S = 100\% \left(\frac{1 - k_c^i}{k_c^0} \right) \qquad (1)$$

with k_c^0 and k_c^i corresponding to the corrosion rates in inhibitor-free and inhibitor-containing solutions, respectively. The values for k_c are determined from measurements of weight loss, corrosion current densities j_c, metal content in solution, pit depth, or time to failure under mechanical loads, depending on the type of corrosion to be inhibited and the practical application. In addition, the effectiveness of inhibitors is often judged from microscopic studies or direct visual perception of the corrosion attack. The latter is also indispensable due to the fact that an inhibitor may highly effectively inhibit a certain type of corrosion (e.g. homogeneous corrosion) but be ineffective or may even promote another type (e.g. pitting or hydrogen embrittlement).

Apart from a few exceptions, notably chromate, the protection ability of inhibitors depends strongly on the nature and composition of the metal or alloy and even small differences may cause substantial changes in the inhibition efficiency. A well-known example is sodium benzoate, which in neutral solution is an anodic inhibitor for mild steel but not for cast iron, although the anodic corrosion reaction is the same for both materials [5]. Similarly, the state of the surface, in particular the presence and nature of passive films and

corrosion products, can obviously have a pronounced influence on the efficiency of the inhibitor. Other important parameters, which will be discussed in the following sections, are the inhibitor concentration and environmental parameters, such as pH, aggressiveness of the solution, and the hydrodynamic conditions.

5.2.1.3.2 **Influence of Inhibitor Concentration** Efficient corrosion inhibition requires that the inhibitor concentration in the solution exceeds a critical limit, which depends on the environmental conditions. This is illustrated in Fig. 4 for several anodic inhibitors [6]. Below this critical concentration the protection is only partial or, as in the case of carbonate, phosphate, silicate, or tungstenate, the corrosion is even enhanced (see Sect. 5.2.1.2.3). It should be noted that not only underdosing but also overdosing of the inhibitor may in some cases have adverse effects on the inhibition efficiency, for example, due to a complexing action of the inhibitor (e.g. inhibition of steel by polyphosphates) [7]. The concentration dependence is usually controlled by the adsorption energies and film-forming properties of a substance (see Sects. 5.2.2 and 5.2.3) and can only in rare cases (e.g. for oxygen scavengers) be calculated from thermodynamic data. Hence, experimental determination of the optimum inhibitor concentration as a function of the other environmental parameters is of key importance in the development of practical formulations.

In addition, the inhibition efficiency also depends on the geometry of the system, which controls the availability of the inhibitor. Especially for a large ratio of metal surface area to electrolyte volume, the latter rather than the concentration may determine the degree of protection. Practical inhibitor testing should hence be performed in systems with dimensions that are comparable to the application. A related problem is to maintain permanent protection in systems in which after

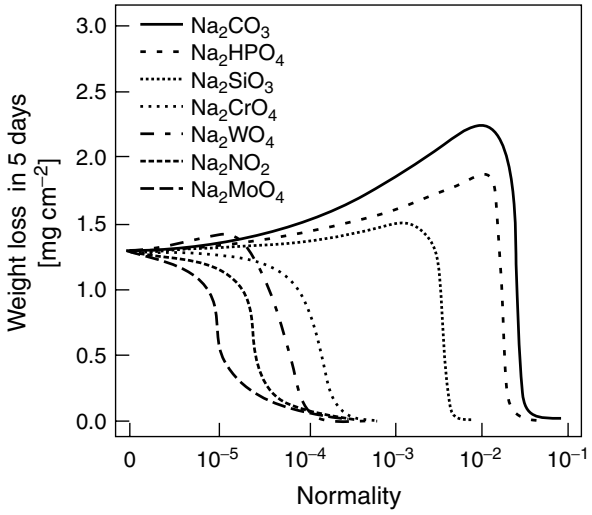


Fig. 4 The effect of concentration of different inhibitors on the corrosion rate of iron in air-containing water. (Adopted from Ref. [6].)

the initial application the solution is inhibitor-free (''once-through systems'').

5.2.1.3.3 **Influence of Solution pH and Aggressive Ions** In view of the pronounced differences in the mechanisms of metal corrosion in acidic and in neutral/alkaline solutions, it is not surprising that the types of substances used as inhibitors in the two environments and the corresponding mechanisms of inhibition also differ strongly. Whereas inhibitors of acid corrosion are mostly organic molecules that adsorb strongly on the bare metal surface, most inhibitors for neutral/alkaline environments are film-forming. Furthermore, small variations in pH may influence the efficiency of the inhibitor for the following reasons: First, the inhibiting species often exhibits a pH-dependent solubility (in particular the oxides/hydroxides formed by inorganic inhibitors). In addition, the film structure and morphology may also depend on pH. Second, for both adsorbing and film-forming organic inhibitors, deprotonation reactions are frequently involved in the formation of the inhibiting species, resulting in comparable pH effects. Third, inhibition may require displacement of adsorbed OH^- ions by the inhibitor, which will be determined by the (potential- and pH-dependent) adsorption behavior of the two competing species.

In a similar way, the concentration of aggressive anions, such as chloride, sulfate, or nitrate, affects the adsorption or film-forming properties of the inhibitor. It is emphasized that the pH as well as inhibitor and anion concentrations at the corroding metal surface rather than in the bulk of the solution are relevant for the inhibition efficiency, which is especially important in the case of localized corrosion. For example, a linear relationship between the logarithms of the inhibitor concentration log c_i and of the anion concentration log c_a is found in a number of systems, which can be explained by the combined effects of (1) active dissolution within small anodic pits above a critical ratio c_a/c_i and (2) electromigration of ions under a potential gradient in the pits [5]. A more detailed discussion of the pH and anion effects described above will be given in Sects. 5.2.2 and 5.2.3.

5.2.1.3.4 **Synergistic Effects** In practical formulations, it is common to use several different inhibitor species, frequently a combination of anodic and cathodic inhibitors. The simultaneous use of two or more different inhibitor species often results in a more efficient inhibition than the sum of the individual effects of the inhibitors. For example, the inhibition of mild steel in chloride-containing solution by polyphosphate is only effective upon the addition of Ca^{2+} traces [8]. Synergistic effects often depend sensitively on the ratio of the different inhibitor species. This is illustrated in Fig. 5, in which the data of Felhösi and coworkers on the effect of Zn^{2+} ions on the corrosion inhibition of steel by 1-hydroxyethane-1, 1-diphosphonic acid (HEDP) are shown [9]. In this case, optimum protection is obtained at a Zn^{2+}/HEDP ratio of 3 : 1, resulting in an inhibition efficiency of 98% (as compared to 52% for solution containing HEDP alone). Such positive synergistic effects indicate chemical interactions between the different inhibitors, such as cooperative adsorption (see Sect. 5.2.2.1.1) or bulk chemical reactions between the species, leading to the formation of protective layers (see Sect. 5.2.3). For Zn^{2+}/HEDP the improved efficiency was

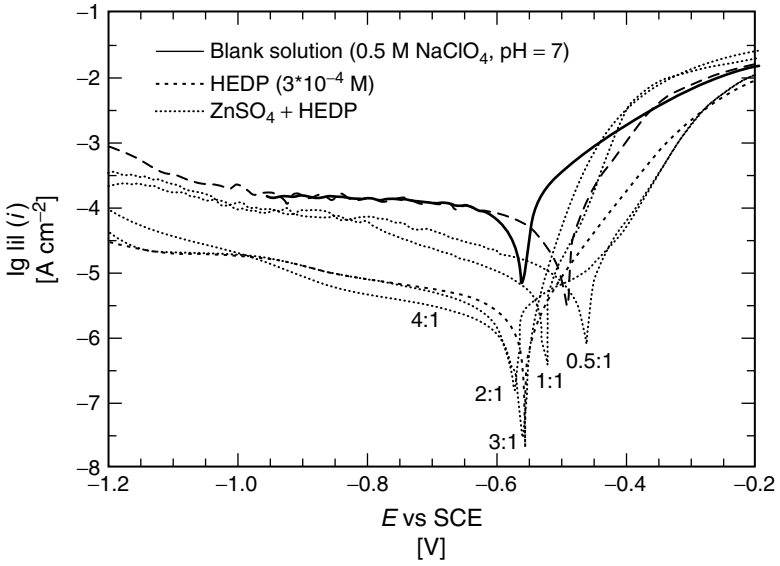


Fig. 5 Polarization curves of carbon steel at different molar ratios of Zn^{2+}/HEDP. (From Ref. [9] with permission.)

related to the formation of complex species between HEDP and the cation additive [9].

5.2.1.3.5 **Influence of Hydrodynamic Conditions** Inhibitors are often applied under conditions of liquid flow (e.g. in cooling systems or pipelines) and, consequently, the effect of the flow rate on their performance also has to be considered. First, the hydrodynamic conditions determine the transport of all dissolved species in the solution (inhibitor, H^+, OH^-, anions, corrosion products) and hence their concentration at the surface of the corroding metal. Since both inhibiting and corrosion-accelerating species are affected, the effect of transport on the inhibition efficiency is not easy to estimate and will depend strongly on the inhibition mechanism. Second, the liquid flow may exert mechanical forces on the metal surface, which may promote corrosion and counteract inhibition. Examples for such tribological effects are erosion due to hydrodynamic shear forces or cavitation effects, both of which can disrupt inhibiting films. This problem affects, in particular, the rather thick, weakly adhesive films formed by many cathodic inhibitors.

5.2.2 Inhibition by Adsorbed Layers

5.2.2.1 Adsorption on Metals in Solution

In most cases, inhibition relies on the interaction of inhibiting species with the corroding metal surface, of which adsorption is the first and often decisive step. A detailed treatment of adsorption at electrochemical interfaces and the resulting structure of the electrochemical double layer is given in Chapter 5 of Volume 1. In the following sections, the most important aspects will be briefly reviewed, with particular emphasis on systems relevant for corrosion inhibition.

5.2.2.1.1 **Adsorption on Bare Metal Surfaces** The adsorption of ions or neutral molecules on bare metal surfaces immersed in solution is determined by the mutual interactions of all species present at the phase boundary. These include electrostatic and chemical interactions of the adsorbate with the surface, adsorbate–adsorbate, and adsorbate–solvent interactions. Inhibitors are usually specifically adsorbed species that adsorb directly on the metal surface in a process involving (partial) desolvation of the adsorbate species and replacement of solvent molecules from the electrode surface. Consequently, the interaction of the adsorbate with the surface has to exceed that of the solvent. Commonly, one distinguishes chemisorption, in which the adsorbate chemically interacts with the surface, and physisorption, caused by much weaker van der Waals or (hydrophobic) adsorbate–solvent interactions.

The dependence of the adsorbate surface coverage θ on the concentration of the adsorbate species in the solution c_A is described by the adsorption isotherm. In the simplest case, that is, adsorption of a species with a single adsorption state on a structurally well-defined surface (e.g. a liquid or single-crystalline electrode), the adsorption can be usually described by the phenomenological Frumkin isotherm

$$\frac{\theta}{1-\theta} = c_A \beta \exp(-g\theta)$$
$$\beta \equiv \exp\left(-\frac{\Delta G^0_{ad}}{RT}\right) \qquad (2)$$

where a single (potential-dependent) Gibbs free energy of adsorption ΔG^0_{ads} and a coverage-dependent contribution (described by the empirical parameter g) due to lateral adsorbate–adsorbate interactions are assumed. Many chemisorbed species, however, exhibit a more complex adsorption behavior, involving the formation of several adlayer phases with a different lateral order and/or adsorption geometry (see also Chapter 5.3 of Volume 1). Furthermore, the adsorption isotherm and the Gibbs energy of adsorption often depend strongly on the crystallographic orientation of the electrode surface (see below). For these reasons, adsorption on highly defective polycrystalline surfaces, a more realistic scenario for inhibitor systems, is often better described by the empiric Temkin or Freundlich isotherms

$$\theta_{Temkin} \propto \ln(c_A \beta) \qquad (3)$$

$$\theta_{Freundlich} \propto c_A^{1/\beta} \qquad (4)$$

where a continuous distribution of energetically different adsorption sites is assumed and the energetically most favored sites are covered first.

The adsorption process is influenced by

1. the electrode potential E,
2. the nature and surface structure of the metal,
3. the molecular structure of the adsorbate, and
4. the presence of other species in the electrolyte.

The potential determines the electronic charge on the metal surface, σ_e, and hence the electrostatic interactions. More precisely, for a given system, σ_e depends on the position of the potential relative to the potential of zero charge (*pzc*), where $\sigma_e = 0$. For $E > E_{pzc}$ the metal is positively polarized and the adsorption of anions is preferred [10]. Correspondingly, cation adsorption is favored for $E < E_{pzc}$. Neutral molecules adsorb preferentially in a potential range around the *pzc* and

are displaced from the surface at higher anodic or cathodic potentials by ions and (strongly polarized) water molecules [11]. Often chemisorption involves significant charge transfer from the adsorbate to the metal, resulting in a shift in the *pzc*. The metal surface charge not only determines the type of adsorbing species but can also affect the adsorption geometry, in particular for molecular species with significant dipole moments. For example, on low-index Au, single-crystal electrodes pyridine and pyrazine are adsorbed at negative potentials in a flat geometry with the π-system parallel to the surface, but change to a vertical, N-bonded orientation at potentials above the *pzc* [12]. The position of the *pzc* can be correlated with the metal work function [13] and consequently depends on the metal species and surface structure. For reactive metals, such as Fe or Cu, the *pzc* seems to be located at potentials several hundred mV below SHE [13], which is significantly more negative than typical corrosion potentials. It is therefore not surprising that anodic adsorption inhibitors are primarily anionic or neutral molecules. The *pzc* of high-index surfaces (i.e. surfaces with a high density of steps and kinks) can be significantly more negative than that of close-packed metal surfaces (see Chapter 3.5 in Volume 1). This is shown explicitly in Fig. 6 for pyridine on Au, where chronocoulometric measurements of the potential-dependent pyridine surface concentration by Lipkowski and coworkers are reproduced [12, 14]. In this case, the pyridine saturation coverage is obtained on the high-index Au(210) surface at 0.8 V more negative potentials than on Au(111); the curve for polycrystalline gold apparently contains contributions of low-index as well as high-index facets. Consequently, the surface coverage is strongly inhomogeneous on defective polycrystalline electrodes. In

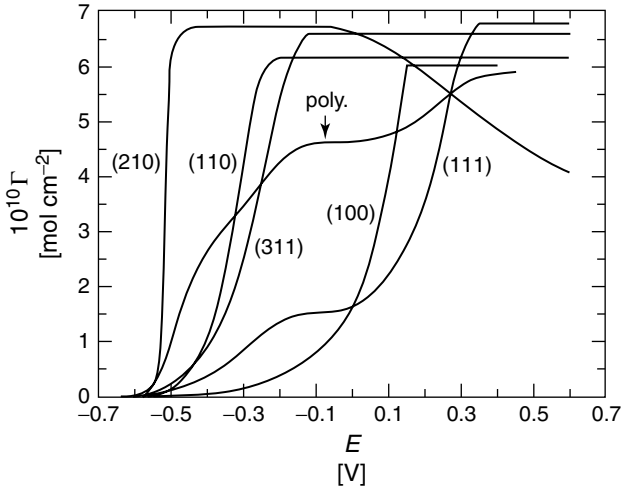


Fig. 6 Potential-dependent pyridine surface concentration (measured versus SCE) for various single-crystal gold surfaces and polycrystalline gold. The pyridine bulk concentration is 10^{-4} M; the supporting electrolyte is 0.1 M $HClO_4$. (From Ref. [14] with permission.)

particular, at low concentrations c_A or negative potentials (assuming an anionic or neutral species), the adsorbate will tend to segregate to atomic-scale defects and/or low-index facets. Beside these electrostatic contributions, the chemical interactions obviously also depend strongly on the nature and (local) surface structure of the metal, in particular on the mixing of the adsorbate orbitals with the electronic states of the metal. The latter is determined by the position of the highest occupied and lowest unoccupied molecular orbitals relative to the metal bands, as well as by symmetry considerations [11].

Particular emphasis has been placed on the relationship between the structure of organic molecules and the adsorption behavior (or the inhibition efficiency) [2, 15, 16]. Typically, organic inhibitors are chemisorbing substances with at least one functional group (e.g. groups containing O, N, or S heteroatoms), which is considered as the reaction center for adsorption. As shown by systematic studies of homologous series, the adsorption strength and the resulting metal protection considerably varies with the type and position of the substituent, which can be related to variations in the polarizability of the functional group and in the electron density on the heteroatom [2, 16–18]. Qualitatively, the role of the functional group has been often explained by the HSAB principle, which states that hard acids prefer to react with hard bases, whereas soft acids preferably react with soft bases [17–19]. Hard acids or bases have low polarizability and acceptor atoms with low electronegativity or donor atoms with high electronegativity, respectively (i.e. are hard to reduce or oxidize); soft acids and bases exhibit the opposite properties. Since bare metals can be classified as soft acids, the general tendency of the adsorption energy to increase with the functional group in the order O < N < S can be associated with the corresponding increase in polarizability. The structure of the rest of the molecule can affect the adsorption energy via influencing the electron density on the heteroatom. A quantitative measure of the ability of substituents to provide or withdraw electrons is the Hammett constant, which has been introduced to acid corrosion inhibition by Donahue and Nobe [15] and subsequently employed by a number of authors to the description of substitution effects (see Sect. 5.2.2.2.1). Generally, the electron density of the functional group and the inhibition efficiency increase upon replacement of a hydrogen atom by electron-donating substituents. In addition, strongly polar substituents increase the dipole moment of the molecule, resulting in a stronger adsorption.

The molecular structure not only determines the adsorbate–substrate interactions but also the lateral interactions between the adsorbed molecules. Attractive adsorbate–adsorbate interactions, for example, due to van der Waals forces between molecules with long hydrocarbon chains, result in the formation of condensed, often ordered adlayer phases (“self-assembled monolayers,” see Chapter 2.1 in Volume 10), in which the strength of adsorption is increased. Reciprocally, repulsive interactions (e.g. dipole–dipole interactions) weaken the adsorption.

Furthermore, the interactions with other species in the solution can also stabilize or destabilize the molecular adsorption at solid–liquid interfaces. This includes the interaction of water with hydrophilic and hydrophobic groups of the molecules, which may promote the aggregation of hydrophobic groups at the interface via formation of adlayers or

hemimicelles (''hydrophobic effect'') [20], an effect which is particularly important for physisorbed species. Dissolved species, such as anions or cations, may coadsorb with the inhibitor species, resulting in a stronger adsorption (''cooperative adsorption''), or compete with the inhibitor species (''competitive adsorption'') and displace them (at least partially) from the metal surface. An example of cooperative adsorption is the adsorption of quaternary ammonium cations, which coadsorb with halides on several metal surfaces [21].

The adsorption of inhibiting species on reactive metals is predominantly estimated from macroscopic corrosion data, in which the inhibitor coverage often is simply equated with the reduction in corrosion rate. In view of the complex relationship between inhibitor coverage and corrosion rate (see Sect. 5.2.2.2), the insight that can be gained by this empirical approach is limited and has to be supplemented by fundamental studies based on microscopic measurements, which are currently emerging (see also Chapter 3 of Volume 3). As an example of the latter, in situ scanning tunneling microscopy (STM) images by Vogt and coworkers of Benzotriazole (BTAH) on copper, one of the best studied inhibitor systems, are shown in Fig. 7 [22–25]. As visible in Fig. 7(a), chains of molecules with defined orientation are formed on Cu(100) at low surface concentrations. At higher coverages these form islands of a densely packed, commensurate superstructure (Fig. 7b). From the STM [22–25] and spectroscopic [26] data, a stacking-type of adsorption geometry was concluded, in which the molecules are adsorbed with the molecular plane perpendicular or slightly tilted to the surface and the π-systems of the molecules in each stack are parallel to each other (Fig. 7c). These phases are stable in pure sulfuric acid solution, in which they retard the step-flow dissolution of the Cu substrate, but are completely replaced from the surface by chemisorbed chloride adlayers, in accordance with the well-known reduction of the BTAH inhibition efficiency in the presence of chloride [22–25].

5.2.2.1.2 **Adsorption on Oxide/Hydroxide Surfaces** Since the metal species at oxide or hydroxide surfaces are present in form of isolated cations (i.e. nonzerovalent species), separated from each other by O^{2-} or OH^{-} anions, they resemble the metal centers of mononuclear metal complexes in solution more than metal atoms in a bare metal surface. Consequently, concepts from coordination chemistry of the corresponding solute complexes can be applied more readily in this case. The exposed cations and anions on oxide surfaces can be regarded as hard acids and bases, respectively. Studies of oxide single crystals under ultrahigh vacuum (UHV) conditions identified three key concepts to describe the surface chemistry of metal oxides [27]:

1. the coordination environment of surface atoms,
2. the redox properties of the oxide, and
3. the oxidation state of the surface.

All three effects strongly depend on the oxide surface structure, in particular on the type and density of surface defects. Data on the structural and chemical properties of oxide–liquid interfaces are considerably less detailed and usually are obtained on oxides without defined surface structure. In aqueous solutions, the oxide surface is usually terminated by hydroxyl groups

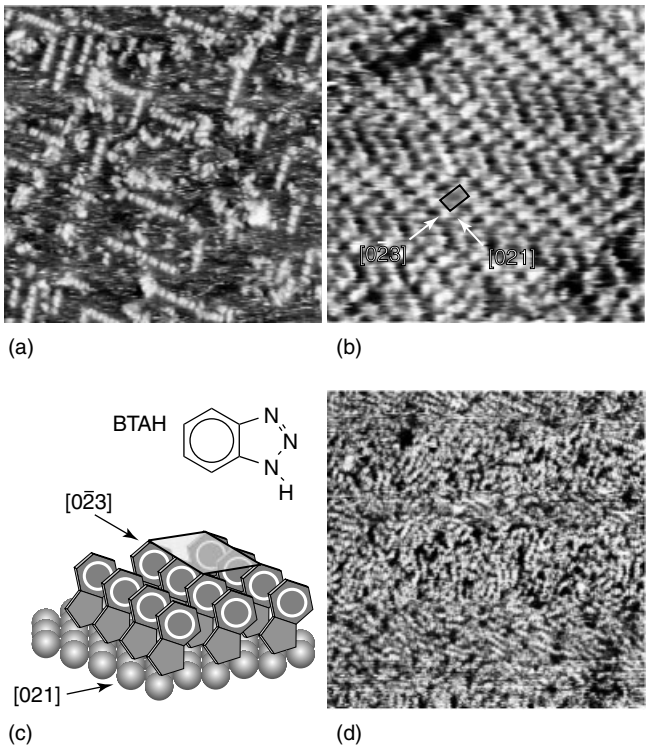


Fig. 7 High-resolution in situ STM images showing the structure of inhibiting BTAH films on Cu(100) at different BTAH coverages. (a) Chainlike structures at submonolayer coverages (350 Å × 350 Å); (b) close-packed arrangement in the completed chemisorbed BTAH monolayer (100 Å × 100 Å); (c) model of the BTAH adsorption geometry in the close-packed monolayer phase [rectangles in (d) and (c) indicate the surface unit cell of the BTAH adlayer]; and (d) disordered polymeric chains in the Cu(I)BTA multilayer phase (300 Å × 300 Å) [22, 24, 25].

and exhibits a pH-dependent charge, which determines the potential drop across the oxide–solution interface and becomes zero at a critical solution pH (pH_{zpc}, "pH of zero proton condition") [28]. When the solution pH is less than the pH_{zpc} of the oxide, the oxide surface is positively charged due to predominant adsorption of H^+; for $pH > pH_{zpc}$ the surface is effectively deficient of H^+ and therefore negatively charged. Various models have been suggested to describe the specific adsorption of ions and organic molecules at this interface [28], which equally well describe the experimental data (usually determined by titration experiments employing colloidal oxides/hydroxides). In addition to acid base reactions, adsorption on hydroxylated oxide surfaces has been interpreted in terms of ligand exchange reactions, in which the metal ion replaces its OH^- ligand by another ligand (e.g. an anion or a weak acid) [29].

Only a few direct measurements of ionic or molecular adsorption on the surface of a passivated metal exist. As an example, in situ radiotracer studies

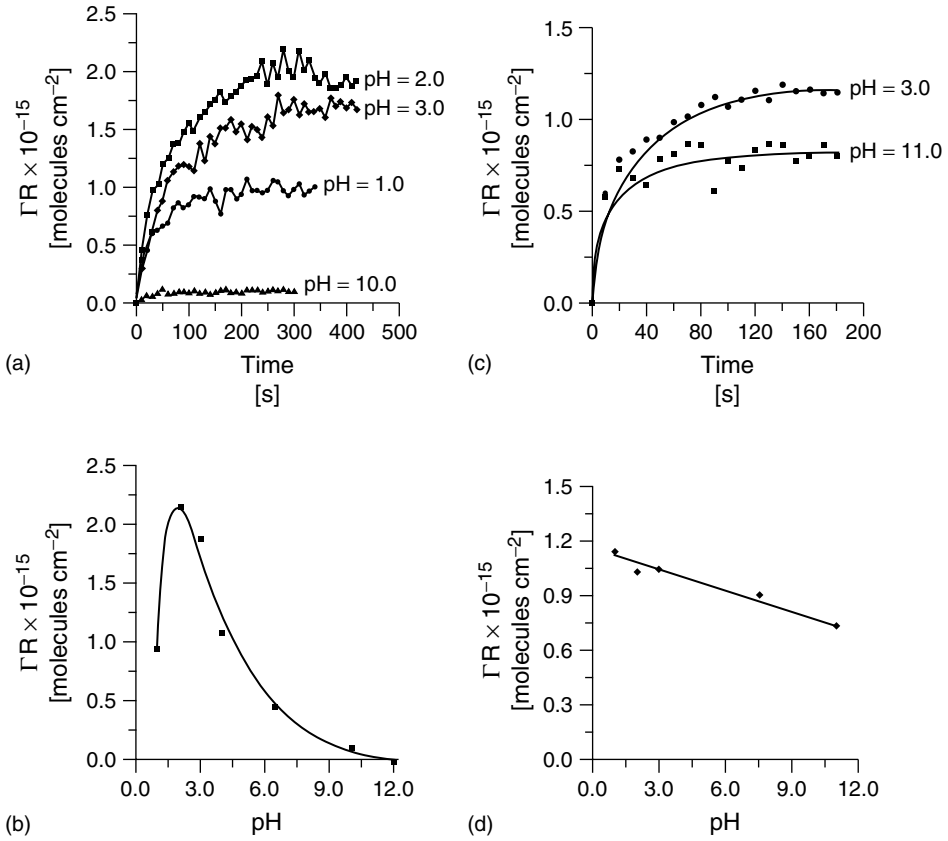


Fig. 8 Adsorption of (a, b) sulfate and (c, d) chloride on the passive film of aluminum in 0.1 M $NaClO_4$ solution at different pH and open circuit potential. (a) Sulfate and (c) chloride surface concentration versus time at different pH values (sulfate and chloride bulk concentrations are 10^{-4} M and 10^{-3} M, respectively). pH dependence of (b) sulfate and (d) chloride saturation surface concentrations. (From Ref. [30] with permission.)

of sulfate and chloride adsorption on aluminum by Kolics and coworkers are shown in Fig. 8 [30]. The adsorption transients (Fig. 8a, c) indicate a diffusion-limited adsorption in the submonolayer to monolayer regime, which occurs over a broad potential regime and depends on pH, albeit to a different degree for the two anion species (Fig. 8b, d). About 20% of the sulfate and 40% of the chloride surface species were found to be irreversibly adsorbed due to partial incorporation of the anions into the oxide. The (reversible) adsorption of the hard base sulfate on the passive film surface is stronger and exhibits a more pronounced dependence on pH than that of the more polarizable chloride anions. This was attributed to the pH-dependent charge state of surface hydroxyl groups and chemical binding of sulfate via a ligand exchange process on Al-OH_2^+ sites (the rapid decrease for pH < 2 was related to Al/Al oxide dissolution) [30]. In contrast, chloride adsorption is more

electrostatic in character and (partly) suppressed by the competing adsorption of the perchlorate anions of the base electrolyte. The anion surface concentrations only slightly increase with increasing potential in the regime in which the metal is passivated. This is in agreement with previous models, according to which adsorption at oxide surfaces is mainly controlled by pH (see above). Similar data were obtained for sulfate and thiosulfate adsorption on stainless steel [31, 32], demonstrating the validity of this approach for the more complex (passive) surfaces of technologically important metals.

According to these studies, molecular adsorption on passivated metal surface areas differs strongly from that on active metal surfaces. Following the HSAB principle, adsorption of hard acids or bases should be favored on oxides/hydroxides, whereas molecules with strongly polarizable groups, which interact strongly with bare metal surfaces, should adsorb more weakly, as indeed observed for sulfate and chloride adsorption on aluminum (see above). On the one hand, this is often a desirable property in corrosion inhibition since it may allow the selective adsorption of anodic inhibitors at small active surface areas, but not on the surrounding passivated metal, thus decreasing the total inhibitor concentration required for efficient inhibition (i.e. increasing the inhibitor reserve). On the other hand, adsorbates that bind to oxide/hydroxide surfaces may help to chemically stabilize passive films, resulting in a lower probability for depassivation (i.e. the initiation of local etch pits), or may promote the adhesion of cathodic inhibitor films. In addition, specific applications may explicitly require protection of oxide surfaces (see Sect. 5.2.4.4).

5.2.2.2 Mechanisms of Corrosion in the Presence of Adsorbed Layers

5.2.2.2.1 Influence of Adsorbed Layers on Metal Dissolution Reactions The active dissolution of a metal surface in electrochemical environment is a complex process, which strongly depends on the surface (defect) structure (see Chapters 4.1 and 4.5 in Volume 2). In the simplest case, the dissolution of a single-crystalline surface of a pure, elemental metal, the metal atoms are dissolved preferentially at kinks in steps on the crystal surface. The type and density of these active sites depends on the crystallographic orientation and can be strongly influenced by the presence of adsorbates [23]. On real metal surfaces different crystallographic orientations as well as inhomogeneities, such as emergence points of dislocations, grain boundaries, and inclusions, exist, resulting in a highly heterogeneous surface with a variety of active sites. Adsorbate layers can inhibit the dissolution process via

1. geometric blocking of the surface by high adsorbate coverages (i.e. via formation of a physical barrier),
2. deactivation of active sites (e.g. kinks) owing to selective adsorption at those sites,
3. changing the type or density of active sites (e.g. by stabilizing certain crystallographic orientations or step directions),
4. altering the adsorption of aggressive species by shifting the *pzc*, or
5. introducing new (rate-determining) steps into the dissolution reaction (usually involving direct participation of the adsorbate).

If the inhibitor simply blocks surface sites, only the dissolution rate is reduced, whereas adsorbates that intervene

with the dissolution process can change the reaction mechanism and hence the Tafel slope. An example of the latter is the effect of various organic inhibitors on active Fe dissolution, where it is assumed that instead of intermediate $(FeOH)_{ad}$, stable chelate surface complexes $[(FeOH)\cdot(Inh)_n]_{ad}$ are formed [33].

The ability of adsorbates to inhibit surface reactions depends on the strength of the bond to the metal (i.e. the adsorption energy) and on the hydrophobicity of the molecules. Systematic studies of acid corrosion inhibition by homologous rows of organic substances found correlations between the inhibitor efficiencies and the electron-donating properties of the substituent, as expressed by the Hammett constant σ, for both blocking and direct involvement in the dissolution mechanism [2, 15, 16]. According to this approach, $\log(k_c^H/k_c^R)$ is proportional to σ, where k_c^H and k_c^R are the corrosion rates in the presence of the inhibitor without and with substituent R, respectively (for a detailed discussion see Refs. [2, 16]). Recently, first attempts to correlate the inhibitive properties of organic inhibitors with ab initio calculations of the molecular species emerged, which support these trends. For example, the inhibition efficiency was found to clearly increase with decreasing molecular ionization potential in a study of thiourea and its derivatives [34]. Finally, not only strong adsorption but also a very low solubility of the corresponding metal–adsorbate complexes is necessary for effective inhibition (otherwise the adsorbate may even promote dissolution).

5.2.2.2.2 **Influence of Adsorbed Layers on Cathodic Reactions** In a similar way, adsorbates may retard the cathodic reactions on bare or passivated metal surfaces. It should be noted, however, that the active sites for anodic and cathodic partial reactions are not necessarily identical and consequently may be affected differently by the inhibitor. In acidic environments, the predominant cathodic reaction is hydrogen evolution, which involves H adsorption and subsequent recombination to H_2. Some inhibitors block the second but not the first step of this reaction and thus promote hydrogen penetration into the metal, resulting in embrittlement. Stable inhibitors, such as quaternary ammonium ions, amines, and aldehydes, are capable of inhibiting both metal dissolution and hydrogen penetration.

5.2.3 Inhibition by Protection Layers

5.2.3.1 Structure of Protection Layers Formed by Inhibitors

The vast majority of corrosion inhibitors in neutral environment as well as a number of acid corrosion inhibitors form protective 3D films on the metal surface (“interphase” inhibition [4]). These films may consist of adsorbate multilayers, oxide/hydroxides, salts, or reaction products formed by interaction of the inhibitor with solution species on or near the corroding metal surface (e.g. dissolved metal ions). The type, structure, and thickness of the inhibiting films are strongly influenced by the environmental conditions. The interphase films act as a physical barrier that blocks or retards transport processes and the kinetics of the corrosion reactions at the metal surface. The inhibitive properties could, in some cases, be correlated with the chemical stability of the corresponding insoluble complexes as well as with the solubility, adsorbability, and hydrophobicity of the inhibitor molecules [35]. Often, other ions from the electrolyte, such as

anions, OH^-, or H^+, are also incorporated, although their role in stabilizing or destabilizing the protection layers is largely unclear. Good adhesion and low porosity of the film are other important factors. A detailed microscopic understanding of the corrosion resistance provided by these films is currently missing. However, it is likely that, as in the case of native passive films, the degree of protection depends strongly on the defect structure of the film. Film-forming inhibitors are of particular importance for inhibition in near-neutral solution (pH 5–10), in which they are commonly classified as cathodic and anodic inhibitors, although they often may influence both partial reactions (see also Sect. 5.2.1.2).

5.2.3.1.1 **Film-forming Cathodic Inhibitors**
Cathodic inhibitors in near-neutral solutions interfere with the oxygen reduction reaction by restricting the diffusion of dissolved oxygen to the electrode surface. These substances usually form thick surface layers with poor electronic conductivity (the latter is an important prerequisite to avoid oxygen reduction on the film surface). Examples are phosphates, polyphosphates, silicates, borates, and inorganic inhibitors, such as Zn^{2+}, which precipitate as Zn hydroxide, and Ca^{2+}, which forms calcium carbonate films in the presence of CO_3^{2-} [3]. These inhibitors are effective on a variety of metals.

5.2.3.1.2 **Film-forming Anodic Inhibitors**
Anodic inhibitors are, in most cases, species that can form insoluble salts with the ions of the corroding metal, thus rendering the surface passive. Therefore, their effectiveness usually depends on the metal. As an example, again the protection of copper by benzotriazole (BTAH) is considered, which is largely based on the formation of a polymeric Cu(I)BTA salt film [36–38]. STM images of this phase (Fig. 7d) show similar chains of parallel oriented molecules as for the chemisorbed BTAH monolayer (Fig. 7b, c), but with a random orientation, demonstrating the close structural relationship of both inhibiting layers on the molecular level [22–25]. Other examples are surface-active chelating agents that form insoluble surface films (e.g. 2-mercaptocarboxylic acids for steel). An important and extensively studied class of film-forming inhibitors are substances that promote passive film growth (''passivators''), such as nitrites, chromates, molybdates, or tungstates. In some of these cases (e.g. nitrite [39]), the resulting passive film seems to be identical in structure and composition to that formed in inhibitor-free solution. More often, however, the inhibitor is incorporated. In particular, for the inhibition of Fe corrosion by chromates, a mixed Cr and Fe hydrous oxide similar to that found on FeCr alloys in acidic solution is formed [40]. In general, the predominant role of anodic inhibitors in neutral solution seems to be the maintenance of passivity by stabilization of the existing passive oxide and plugging of pores in the passive film. Finally, it is emphasized that many anodic inhibitors also affect the cathodic partial reaction and/or provide an increased ohmic resistance across the interface.

5.2.3.2 **Mechanisms of Protection Layer Formation**
Only a limited knowledge of the kinetics and mechanisms of the formation of protective layers has been obtained up to now. Similar to passive films (see Chapter 3.2, this volume), the inhibitor films may form via precipitation from

solution or via chemisorption, followed by a 3D growth on the metal surface.

5.2.3.2.1 **Precipitation from Solution** Thick corrosion inhibiting layers are usually assumed to form on the metal surface via precipitation of insoluble products from solution. Possible processes are

1. the precipitation of oxide/hydroxides of the inhibiting species (e.g. Zn^{2+}),
2. the reaction of the inhibitor with metal ions in solution (e.g. Cu(I)BTA film formation on Cu), and
3. the reduction or decomposition of the inhibitor at the metal surface, followed by precipitation.

Examples of the latter are chromates, which are reduced to Cr(III) hydroxide or oxyhydroxide on the metal surface, or polyphosphates, in which decomposition and subsequent precipitation of Ca phosphate has been suggested [8]. The precipitation reactions will depend on the local solution composition (pH, metal ion concentration) in the near-surface region of the corroding metal, which may pronouncedly deviate from that in the bulk. For instance, the production of OH^- in the cathodic partial reaction will raise the surface pH and thus promote the precipitation of compounds, such as Zn hydroxides, even in noticeable acidic solution. In a similar way, the pore-plugging ability of anodic inhibitors may be enhanced by reactions with local metal ion accumulations in the vicinity of active pores in a passive film.

5.2.3.2.2 **Direct Film Growth** Protective films may also be formed directly at the metal–solution interface via a 3D growth mechanism. The first step of this process is the monolayer adsorption of the inhibiting species (see Sect. 5.2.2.1.1). Subsequently, a thicker film may form either by multilayer adsorption (e.g. due to hydrophobic interactions) or, more commonly, by a reactive growth process, in which ions of the protected metal are incorporated into the film. The former is less desirable in practice since it leads to rapid depletion of the inhibitor in the system. In the second case the film growth requires the transport of metal ion and/or inhibitor species through the film, for example, via a high-field mechanism (see Chapter 3.2, this volume). The 3D growth occurs on a much slower time scale than the initial adsorption and usually saturates at a certain film thickness that depends on the environmental parameters and growth conditions. This was illustrated in a kinetic study of 3-amino-5-heptyl-1,2,4-triazole (AHT) on Cu by Beier and Schultze [41]. Figure 9 shows the current decay and the time-depended capacity in this system, obtained by potentiostatic pulse measurements. Starting from the bare (active) Cu surface (I), first slow adsorption of an AHT monolayer (II) up to a saturation coverage (III) was observed, followed by a much slower film growth (IV) until a stable film had been formed (V), which changed only slightly due to aging effects. On the basis of these measurements, a high-field growth mechanism was suggested.

Finally, several film-formation mechanism can be active in parallel for a given inhibitor/metal system. As an example, radiotracer experiments by Gáncs and coworkers on the accumulation of phosphate on aluminum are reproduced in Fig. 10 [42, 43]. After a first rapid increase in phosphate surface concentration, which was assigned to phosphate adsorption and (partial) incorporation into the passive film, a slower accumulation is observed, which can continue up to several days and which was explained by precipitation

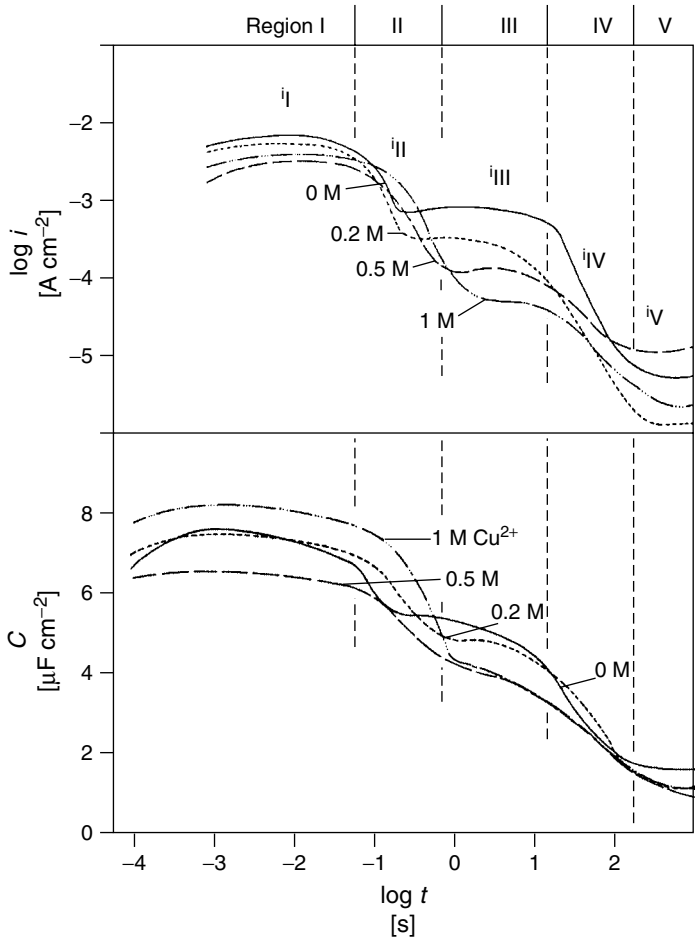


Fig. 9 Double logarithmic plot of current and capacity transients for AHT/Cu. The data were obtained in aerated 0.5 M H_2SO_4, containing $2{\cdot}10^{-3}$ M AHT and various Cu^{2+} concentrations, at 0.35 V_{SHE} and a rotation rate of 30 Hz. (From Ref. [41] with permission.)

of aluminum phosphates (Fig. 10a). The pH dependence of the precipitation rate and the resulting phosphate accumulation (Fig. 10b) exhibits a peak at pH 4.7, reflecting the solubility minimum of these aluminum phosphates. Furthermore, a strong effect of anions on the precipitation process was found, which was attributed to the enhancement or suppression of aluminum ion release from the metal [44].

5.2.4 Special Cases

5.2.4.1 Control of Solution Composition ("scavengers")

In addition to improving the corrosion resistance of the metal, the aggressiveness of the environment may be reduced by the addition of substances that lower the concentration of corrosive agents. This

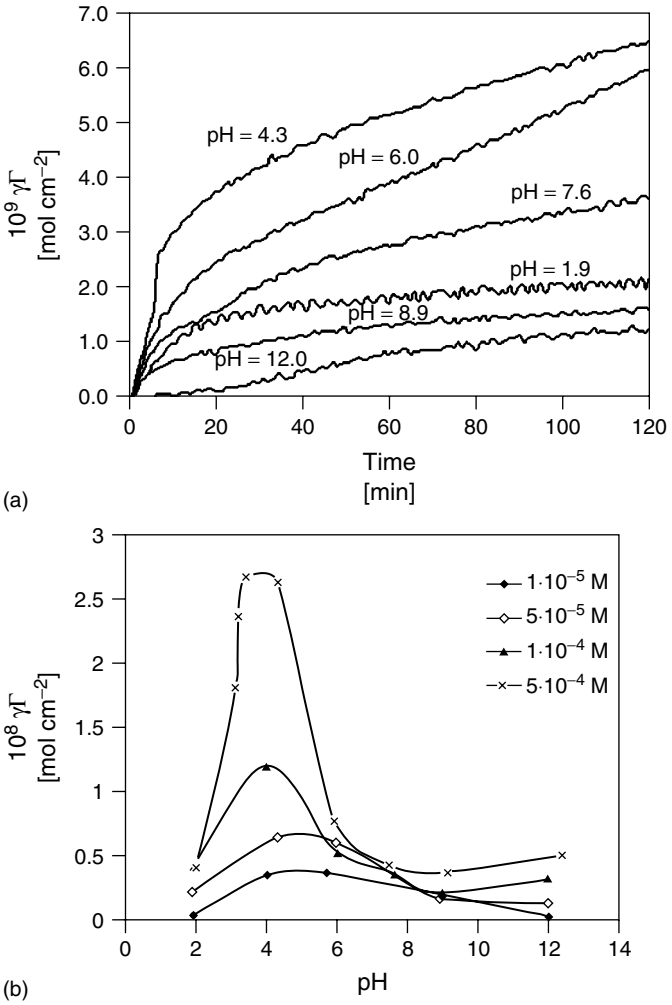


Fig. 10 Phosphate accumulation on aluminum in 0.1 M NaCl solution. (a) Phosphate surface concentration versus time at different pH values (bulk phosphate concentration is 5×10^{-5} M). (b) pH dependence of accumulated phosphate surface concentration at different phosphate bulk concentrations after 120 min. (From Ref. [42] with permission.)

includes chemicals that remove oxygen ("oxygen scavengers"), adjust the pH ("buffer"), or change the water hardness or scale forming properties. In these cases the required concentrations can be calculated on the basis of the corresponding chemical equilibria. In particular, oxygen scavengers, such as Na_2O_3 and hydrazine, are commonly used in the oil industry and in steam generation. The latter inhibitor, however, also acts as a passivator, which at least partly accounts for its effectiveness. Furthermore, the control of corrosion-inducing microorganisms by

biocides may be considered as a special (but technologically important) case of substances that reduce the aggressiveness of the solution.

5.2.4.2 Inhibition of Localized Corrosion

In localized corrosion, aggressive anions induce a breakdown of the passive film at small, localized areas of the metal, resulting in the rapid growth of etch pits (see Chapter 4.2, this volume). Ideally, effective inhibitors of localized corrosion should inhibit both the nucleation and the growth of these pits. Because of the extremely aggressive environment within growing pits (low pH, high concentration of anions), however, the inhibition of pit growth is difficult and inhibition of pit nucleation or of the early stages of pit formation seems more promising. The nucleation of pits can be inhibited by promoting passive film growth (Sect. 5.2.3.1.2), reducing the defect density in the film, or stabilizing the passive film via protective adsorbates (usually organic species), which compete with the anions, thus reducing anion adsorption at the passive film surface. Localized corrosion occurs only above a critical potential (''pitting potential''), which is found to shift proportional to the logarithm of the ratio of anion to inhibitor concentration, $\log c_a/c_i$ [45].

5.2.4.3 Inhibition of Stress-corrosion Cracking

The simultaneous effect of corrosion and tensile stress causes stress-corrosion cracking above a certain threshold stress (Chapter 4.4, this volume). Stress-corrosion cracking is a highly localized form of corrosion and confined to a rather narrow potential range. The inhibition of stress corrosion is not well understood but may be due to the following mechanisms:

1. a shift of the corrosion potential out of the cracking range,
2. a modification of the chemistry of the local cell,
3. a disturbance of the critical balance between active and passive areas usually associated with cracking, and
4. an inhibition of hydrogen penetration and embrittlement [3].

5.2.4.4 Inhibition of Chemical Corrosion Processes

In modern technology an increasing number of nonmetallic materials, such as semiconductors, oxides, ionic crystals, and polymers, is employed, which corrode or degrade via chemical rather than electrochemical mechanisms. Corrosion protection of these materials by inhibitors is currently only marginally studied and will be an important future challenge for inhibitor science. For the important case of oxides, similar concepts as employed for the stabilization of passive films in the inhibition of localized corrosion should be applicable.

5.2.4.5 Inhibition of Atmospheric Corrosion

Metals exposed to humid atmosphere corrode by an electrochemical mechanism due to the formation of a thin electrolyte layer on the metal surface (Chapter 3.1, this volume). This type of corrosion can be controlled by Vapor-phase Corrosion Inhibitors (VCIs), that is, volatile inhibiting substances that allow vapor-phase transport to the corroding surface (examples are amines, benzoates, imidazoles, or triazoles [3]). The vapor pressure should be sufficiently high to ensure a protective surface concentration of the inhibitor, but low enough to prevent premature depletion of

the inhibitor. VCIs have been classified as interface and electrolyte-layer inhibitors, depending on whether they influence processes at the metal–electrolyte interface or alter the chemistry of the thin electrolyte layer. In practice, VCIs are oil- or water-soluble and applied in form of powders, sprays, foams, or impregnated papers. Applications are widespread and range from the protection of engines and machine parts to the preservation of antiques.

An alternative method to inhibit atmospheric corrosion, in particular in outdoor applications, is to add corrosion inhibitors to surface coatings, especially paint films. Here the inhibitor reduces corrosion reactions, resulting from the residual permeability of the polymer film (see Chapter 5.4, this volume).

5.2.5 Practical Applications

5.2.5.1 Overview

Because of the complexity of real systems, inhibitor selection is by far not straightforward and requires testing by laboratory and field studies. Commercial formulations usually contain a combination of several active inhibitors, blended with a specific surfactant/solvent package, which controls the release of the inhibitors into the environment (i.e. the available inhibitor concentration). The protection of multimetal systems requires particular care, since efficient inhibitors for one metal may be ineffective or even corrosion-accelerating for another metal. In general, the performance of formulations depends on the system parameters and has to be evaluated by field tests to ensure protection.

By far, the most important applications for inhibitors are water treatment (Sect. 5.2.5.2) and oil production, refinement, and transportation (described in detail in Chapter 6.6, this volume). In addition, inhibitors are used as additives to antifreeze formulations, lubricants, and acid solutions for industrial usage (Sect. 5.2.5.3). A field of increasing importance is the inhibition of atmospheric corrosion (see also Sect. 5.2.5.4).

5.2.5.2 Water Treatment

The control of corrosion in cooling and heating systems by inhibitors is an established technology [3]. In these systems, corrosion occurs under near-neutral conditions, with the reduction of oxygen as the cathodic reaction. In addition, corrosion may be promoted by

1. the presence of corrosive agents, such as acidic impurities, chloride, and sulfate;
2. local galvanic elements in multimetal systems;
3. sediments, resulting in crevice corrosion;
4. erosion due to water flow;
5. microbiological activity; and
6. stray electric currents.

The resulting corrosion processes not only lead to leakage but also may induce failure of system components owing to clogging with corrosion products (e.g. scales and precipitates). Corrosion inhibitors for water treatment should be effective at variable water composition, temperature, and flow conditions for a wide range of inhibitor concentrations. They should protect all exposed metals and should not be aggressive to other materials in the system (e.g. solder, rubber, and plastics). Furthermore, they should not stimulate the buildup of scales, thermally isolating

films, and nonadhering precipitates and be nonvolatile, nontoxic, and compatible with other additives. Finally, they have to be cost-effective and ideally should possess a sufficient reserve so that monitoring and precise additions are not necessary.

Formulations usually contain a combination of different anodic and cathodic inhibitors. Commonly used are ortho- and polyphosphates, phosphonates, tannins, lignins, benzoates, silicates, chromates, molybdates, nitrites, nitrates, zinc salts, aromatic azoles, carboxylic acids, amides, amines, soluble oils, and oxygen scavengers, such as hydrazine and sulfites [3, 46]. Some of these substances (e.g. silicates) are employed predominantly in synergy with other inhibitors, whereas in other cases the combination of inhibitors may have adverse effects (e.g. nitrites and organic amines or amides may form carcinogenic nitrosamines at elevated temperatures).

5.2.5.3 Acid Systems

In industrial applications of acids, such as acid-pickling and descaling, inhibitors are usually added to minimize the corrosive attack of metallic materials. These inhibitors have to be able to effectively inhibit metal dissolution at high acid concentration, high content of dissolved metal salts, and elevated temperatures, without delaying the removal of scales, that is, they should not inhibit the dissolution of metal oxide/hydroxide species. In addition, they should inhibit the entry of hydrogen into the metal. Typically, adsorption inhibitors are used, in particular mixtures of nitrogen- and sulfur-containing organic compounds and acetylenic alcohols. These active components are blended with wetting and foaming agents, detergents, and solvents in formulated inhibitor packages [3, 46].

5.2.5.4 Corrosion Inhibition in Electronic Devices

The worldwide spreading of electronic and information technology imposes new challenges for corrosion protection. Electronic components employ a wide variety of different materials (metallic and nonmetallic) that are usually not primarily selected on the basis of their corrosion properties and may involve adverse material combinations (e.g. between metal and solder). Furthermore, substantial voltage differences are present during device operation, often over small distances (<0.5 mm for surface-mounted device components) and strongly varying with time. Consequently, severe corrosion problems can arise, in particular since already small defects may lead to device failure. The predominant type of attack is atmospheric corrosion, especially in heavily polluted urban areas and outdoor devices (e.g. in communication technology). Here, corrosion inhibitors are applied in the form of vapor-phase inhibitors and inhibiting additives in organic coatings, for example, in the protection of printed circuit boards. Furthermore, inhibitors are used in components with intrinsic electrochemical systems, such as electrolytic capacitors and batteries. The ongoing miniaturization, the emergence of new micromechanical devices, and the increasing use of electronics in countries with adverse climatic conditions (e.g. high humidity) will require continuous efforts in the development of effective inhibitors.

References

1. *Proceedings of the 1st, 2nd, 3rd, 4th, 5th, 6th, 7th, and 8th European Symposium on Corrosion Inhibitors*, University of Ferrara,

Ferrara, Italy, 1960, 1965, 1970, 1975, 1980, 1985, 1990, 1995.
2. Yu. I. Kuznetsov, *Organic Inhibitors of Corrosion of Metals*, Plenum Press, New York, 1996.
3. V. S. Sastri, *Corrosion Inhibitors. Principles and Applications*, Wiley-VCH, Weinheim, Germany, 1998.
4. W. J. Lorenz, F. Mansfeld in *Corrosion Inhibition* (Ed.: R. H. Hausler), *International* Corrosion *Conference Series*, National Association of Corrosion Engineers, Houston, Tex., 1988, pp. 7–13.
5. S. Turgoose in *Chemical Inhibitors for Corrosion Control* (Ed.: B. G. Clubley), The Royal Society of Chemistry, Cambridge, UK, 1990, pp. 72–88.
6. M. J. Pryor, H. Cohen, *J. Electrochem. Soc.* **1953**, *100*, 203–215.
7. M. Cohen, *Corrosion*, Newnes, London, 1963, p. 18.
8. G. Butler, *Proceedings of the 3rd European Symposium on Corrosion Inhibitors*, University of Ferrara, Ferrara, Italy, 1970, pp. 15–21.
9. I. Felhösi, Zs. Keresztes, F. H. Kármán et al., *J. Electrochem. Soc.* **1999**, *146*, 961–969.
10. J. O'M. Bockris, B. E. Conway, E. Yeager, R. E. White, (Eds.), *Comprehensive Treatise of Electrochemistry*, Plenum Press, New York, 1980, Vol. 1.
11. J. Lipkowski, P. N. Ross, (Eds.), *Adsorption of Molecules at Metal Electrodes*, Wiley-VCH, Weinheim, Germany, 1992.
12. J. Lipkowski, L. Stolberg in *Adsorption of Molecules at Metal Electrodes* (Eds.: J. Lipkowski, P. N. Ross), Wiley-VCH, Weinheim, Germany, 1992, pp. 171–238, Chap. 4.
13. S. Trasatti in *Trends in Interfacial Electrochemistry* (Ed.: A. F. Silva), D. Reidel Publishing, Dordrecht, 1986, pp. 25–48.
14. D.-F. Yang, L. Stolberg, J. Lipkowski et al., *J. Electroanal. Chem.* **1992**, *329*, 259–278.
15. F. M. Donahue, K. Nobe, *J. Electrochem. Soc.* **1965**, *112*, 886.
16. Yu. I. Kuznetsov in *Review on Corrosion Inhibitor Sciences and Technology* (Ed.: A. Raman), National Association of Corrosion Engineers, Houston, Tex., 1993, pp. 3-1–3-41, Chap. I-3.
17. K. Aramaki, *Proceedings of the 5th European Symposium on Corrosion Inhibitors*, University of Ferrara, Ferrara, Italy, 1980, p. 267.
18. K. Aramaki; H. Nishihara, *Proceedings of the 6th European Symposium on Corrosion Inhibitors*, University of Ferrara, Ferrara, Italy, 1985, p. 67.
19. R. G. Pearson, *J. Chem. Educ.* **1968**, *45*, 581.
20. G. Schmitt, *Proceedings of the 6th European Symposium on Corrosion Inhibitors*, University of Ferrara, Ferrara, Italy, 1985, pp. 1600–1614.
21. I. L. Rosenfeld, *Corrosion Inhibitors*, McGraw-Hill, New York, 1981, pp. 109–119.
22. M. R. Vogt, W. Polewska, O. M. Magnussen et al., *J. Electrochem. Soc.* **1997**, *144*, L113–L116.
23. O. M. Magnussen, R. J. Behm, *Mater. Res. Bull.* **1999**, *24*, 16–23.
24. M. R. Vogt, R. J. Nichols, O. M. Magnussen et al., *J. Phys. Chem. B* **1998**, *102*, 5859–5865.
25. M. R. Vogt, O. M. Magnussen, R. J. Behm, *Proc. Electrochem. Soc.* **1999**, *17–98*, 591–618.
26. J.-O. Nilsson, C. Törnkvist, B. Liedberg, *Appl. Surf. Sci.* **1989**, *37*, 306–326.
27. M. A. Barteau, *Chem. Rev.* **1996**, *96*, 1413–1430.
28. J. Westall, H. Hohl, *Adv. Colloid Interface Sci.* **1980**, *12*, 265–294.
29. W. Stumm, R. Kummert, L. Sigg, *Croat. Chem. Acta* **1980**, *53*, 291–312.
30. A. Kolics, J. C. Polkinghorne, A. Wieckowski, *Electrochim. Acta* **1998**, *43*, 2605–2618.
31. A. E. Thomas, A. Kolics, A. Wieckowski, *J. Electrochem. Soc.* **1997**, *144*, 586–594.
32. A. Wieckowski, A. Kolics, J. C. Polkinghorne et al., *Corrosion* **1998**, *54*, 800.
33. F. M. Donahue, K. Nobe, *J. Electrochem. Soc.* **1967**, *114*, 1012.
34. A. E. Stoyanova, S. D. Peyerimhoff, *Electrochim. Acta* **2002**, *47*, 1365–1371.
35. K. Wippermann, J. W. Schultze, R. Kessel et al., *Corros. Sci.* **1997**, *32*, 205–230.
36. J. B. Cotton, I. R. Scholes, *Br. Corros. J.* **1967**, *2*, 1–5.
37. G. W. Poling, *Corros. Sci.* **1970**, *10*, 359–370.
38. F. Mansfeld, T. Smith, E. P. Parry, *Corrosion* **1971**, *27*, 289–294.
39. J. B. Lumsden, Z. Szklarska-Smialowska, *Corrosion* **1978**, *34*, 169.
40. E. McCafferty, M. K. Bernett, J. S. Murday, *Corros. Sci.* **1988**, *28*, 559.
41. M. Beier, J. W. Schultze, *Electrochim. Acta* **1992**, *37*, 2299–2307.

42. L. Gáncs, Z. Németh, A. Kolics et al., *Proceedings of European Corrosion Congress 1999* (CD-Rom), Dechema, Frankfurt, 1999.
43. Z. Németh, L. Gángs, G. Gémes et al., *Corros. Sci.* **1998**, *40*, 2023–2027.
44. A. Kolics, P. Waszczuk, L. Gáncs et al., *Electrochem. Solid State Lett.* **2000**, *3*, 369–372.
45. K. J. Vetter, H.-H. Strehblow, *Localized Corrosion*, National Association of Corrosion Engineers, Houston, Tex., 1977.
46. B. G. Clubley, (Ed.), *Chemical Inhibitors for Corrosion Control*, The Royal Society of Chemistry, Cambridge, UK, 1990.

5.3 Conversion Coatings

Kevin Ogle
Irsid, Arcelor Research, Maizieres-les-Metz, France

Rudolph G. Buchheit
The Ohio State University, Columbus, Ohio, USA

Conversion coatings are thin inorganic layers formed on metal and alloy surfaces by the reaction of the metal with solutions of specific chemical composition. Coatings form spontaneously by contact of a metallic surface with the coating solution, and no externally imposed potential or current is required. Conversion coatings are usually applied as a pretreatment to facilitate further coating and painting. Two primary classes of coatings are in common use today: phosphate- and chromate-based conversion coatings. Phosphate conversion is widely used on ferrous alloys and is important in the pretreatment of painted steel products used in automotive applications. Chromate conversion is used primarily on light metals, such as aluminum, and is important in the pretreatment of aerospace products for painting. Chromate conversion coatings (CCCs) are also used as stand-alone corrosion-resistant coatings for aluminum housings and chassis for electronic instrumentation and appliances subject to benign atmospheric exposure. Key elements of the science and technology of these coatings processes are presented in this chapter.

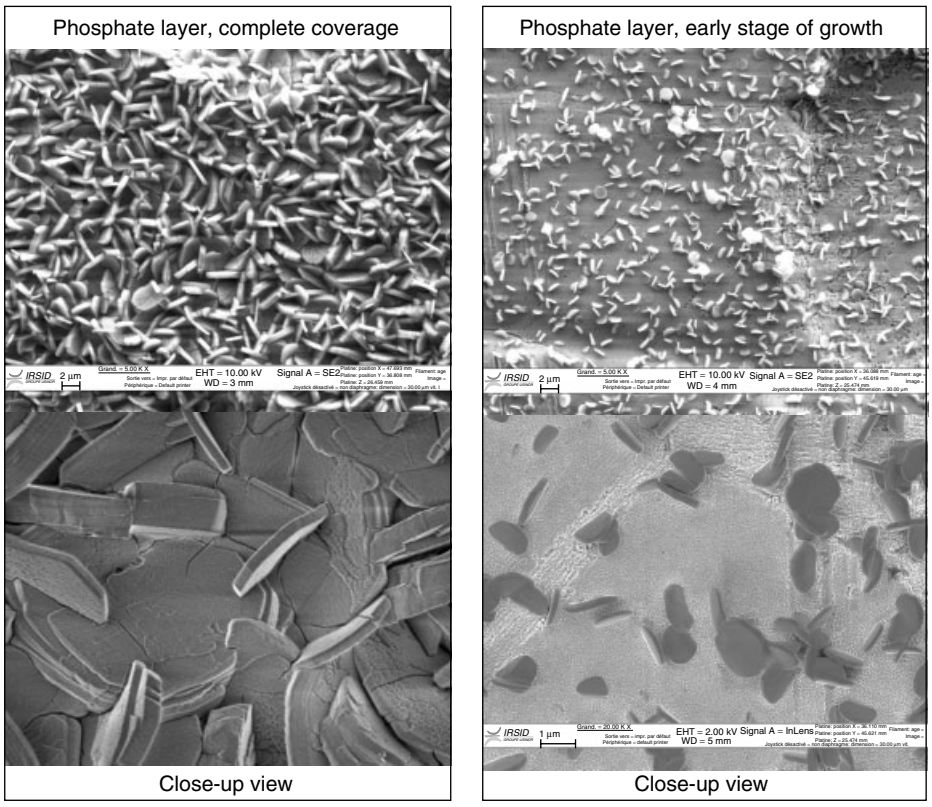
5.3.1 Phosphate Conversion Coatings

5.3.1.1 Overview

Phosphate conversion coatings are widely used throughout the metalworking industry for substrates such as iron, steel, galvanized steel, aluminum, copper, and magnesium and its alloys. Two major applications include its use as a lubrifying film for cold extrusion, and as a pretreatment before painting. Other applications include temporary corrosion resistance for unpainted metal and electrical resistance. As this chapter focuses on the electrochemical properties of the phosphated metal surface, discussion will be limited to the phosphate film as a pretreatment for painting. For this application, the electrochemical properties are paramount, while other applications such as cold extrusion rely more on the mechanical properties of the layer. Extensive reviews of phosphating technology may be found in Refs. [1–3].

Phosphating involves the formation of inorganic tertiary metal phosphates, $M_3(PO_4)_2 \cdot x H_2O$, on the surface of the treated metal. Phosphate layers are generally classified as either crystalline or amorphous [1]. The crystalline phosphate layer consists of discrete crystals rather than a continuous film. This is seen in the field emission microscopic images of the phosphate crystals on galvanized steel shown in Fig. 1. Figure 1(a) shows the completed phosphate crystals after they have converged to form a practical phosphate layer, and Fig. 1(b) shows the initial stages of crystal growth where large bare patches of the substrate material can be observed. The composition and crystal structure of the phosphate crystals will depend on the substrate material and the phosphatation bath. The crystal structure of two of the more common zinc phosphate species is shown in Fig. 2, hopeite ($Zn_3(PO_4)_2 \cdot 4H_2O$) and phosphophyllite ($Zn_2Fe(PO_4)_2 \cdot 4H_2O$).

The major use of crystalline phosphating today is as a pretreatment before cataphoretic painting for the automotive industry. The metal is formed and assembled



(a) (b)

Fig. 1 Morphology of the phosphate layer: field emission microscopy images of a trication phosphated galvanized steel surface; (a) after complete formation of the phosphate layer; and (b) early stages of phosphating (several seconds in the bath). Original results, Irsid. Upper photo shows a survey over a large surface area, and the lower photo shows a close-up view of the crystals. Original data, Irsid.

prior to the surface treatment, and the phosphating bath is applied either as an immersion or spray process. In the steel fabrication mills, phosphating may be performed either as a pretreatment for coil coating (although chromatation is more popular for this application) or for the production of ''prephosphated'' steel. In the steel mill, either a spray process similar to that used in the automotive industry, or a special ''no rinse'' phosphatation bath may be used. The later is applied by a roller directly to the steel band.

Crystalline phosphate layers of natural origin are rare. Vivianite ($Fe_2(PO_4)_2{\cdot}4H_2O$) layers have been observed on steel artifacts dating from around the third century AD, and not withstanding speculation that the Romans had discovered the process, it is probable that the vivianite films were of natural origin [2]. Recently, the formation of protective vivianite films on low-alloyed steel by bacteria cultures [4, 5] has been demonstrated under very mild conditions (neutral buffered solution and 25 C).

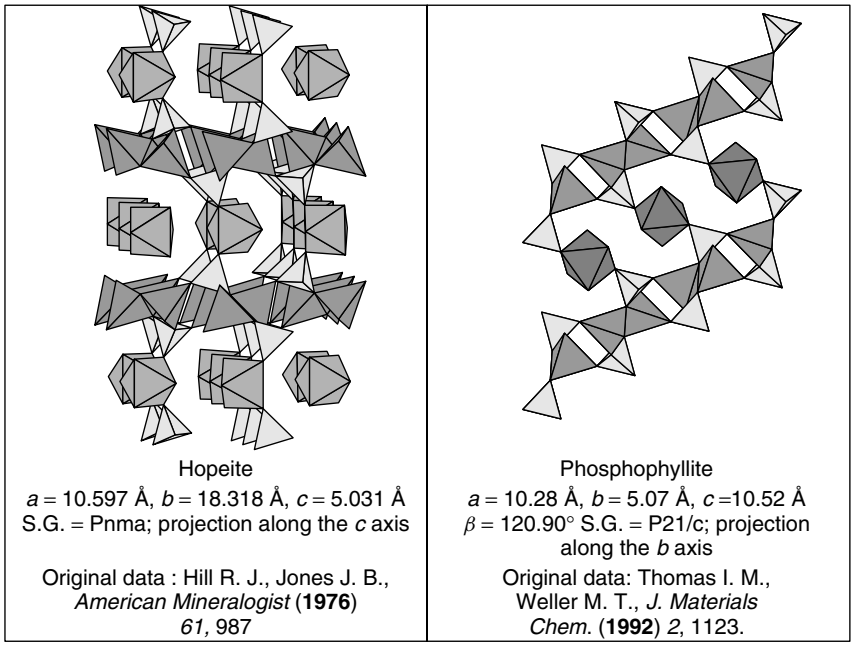


Fig. 2 Crystallography of the phosphate layer: crystal structures of hopeite and phosphophyllite showing tetrahedral and octahedral metal ion sites within the crystal lattice. (Courtesy Jean Steinmetz, University Henri Poincaré, Nancy I.)

Amorphous phosphate films are formed during the process of ''alkali phosphating'' [1]. This type of film is generally used on iron and steel and may be used for temporary corrosion protection or as a low-cost pretreatment for painting. The phosphate layers are a mixture of iron phosphate ($Fe_3(PO_4)_2 \cdot 8H_2O$), iron oxides, and hydroxides. The treatment baths consist of phosphoric acid solutions of pH 3–5 with minimal or no divalent cations present. Nitrate or other additives are used as accelerators.

5.3.1.1.1 **Historical Perspectives** A British patent [2, 3] of 1869 to improve the corrosion resistance of steel by treatment in boiling phosphoric acid was proposed by W. A. Ross [3]. A number of similar patents appeared in the following years, but the process was largely ignored until a patent of T. W. Coslett appeared in 1906 [2, 3]. Coslett added Fe filings to the phosphoric acid bath with the idea of reducing the violence of the reaction. Coslett's original formulation consisted of an aqueous solution of phosphoric acid, saturated with ferrous phosphate. The solution was used at near boiling temperature and the treatment could take as long as three to four hours. Coslett recognized that the phosphated metal showed a markedly improved retention of oil. He introduced the final chromic acid rinse to improve the corrosion resistance and the process became known as ''Coslettizing''. In 1909, he improved the bath by the addition of zinc dihydrogen phosphate as an additive to the phosphoric acid. A bit later, in 1911, a patent appeared

by Richards of Coventry describing the use of solutions containing manganese dihydrogen phosphate.

On the basis of these previous works, Clark and Wyman Parker developed the Parkerizing process, which was an improvement of ''Coslettizing'' in that Zn and Mn were added to the formulation. In 1917, Parker opened the first factory at Detroit, and by 1931, 20 million square meters of steel were treated in the US. Around the same time, the American Chemical Paint Company promoted the phosphatation process as a pretreatment before painting. At that time the treatment required on the order of 10 min.

During the years that followed, new types of accelerators were developed in order to decrease the treatment time and temperature. Around 1930, copper and nickel additions were introduced to speed up the reaction and to permit the use of lower temperatures. The rate of the phosphatation reaction was dramatically increased by the introduction of the activation step with Ti colloids by Jernstedt [6] in 1940. The development of spray application methods greatly improved the speed of phosphatation lines, and the phosphatation time has decreased from hours to minutes, and even reduced down to below 10 s for phosphatation on coil coating lines.

Today environmental issues represent the major driving force for the evolution of phosphate technology, for example, by the elimination of the heavy metal Ni^{2+} and the suspected carcinogen, nitrite. The chromate final rinse has been abandoned by many users as a result of the suspected carcinogenic properties of Cr(VI). The second driving force for technological development is the necessity to treat different metals with the same bath. In the early years, applications were limited essentially to steel and later to galvanized steel. Today, galvanized steel is often assembled with light alloys such as Al and Mg, and therefore, the phosphatation bath must work equally well on all these surfaces.

5.3.1.2 Overview of Process and Reaction Mechanisms

Details of the industrial process and the particular problems that may occur are beyond the scope of this work (see Refs. [1–3]). In this section, we will limit ourselves to a discussion of the chemical mechanisms that are observed. There are four chemically important steps in the phosphatation process as it is generally used: (1) Degreasing in an alkaline cleaner; (2) ''activation'' with a treatment involving titanium colloids; (3) phosphating, + water rinse; and (4) optional passivation rinse. Phosphating is sometimes performed by induction: the activation and phosphating are applied sequentially, and the phosphatation bath is dried directly on the surface.

5.3.1.2.1 Degreasing Degreasing is typically performed using an alkaline solution at elevated temperature. As the name indicates, the primary role of the degreasing step is to remove oil from the metal product. Such oil is often added to the steel as a lubricant during forming and for temporary corrosion protection during the period between fabrication of the metal and the painting of the metal. For zinc and aluminum alloys, the alkaline solution ''pickles'' the surface, removing aluminum oxides and increasing the surface pH of the remaining oxides. The dissolution of zinc increases the surface roughness as well. Alkaline cleaners are composed of inorganic compounds such as alkali, phosphates, silicates, and/or borates and

nonionic surfactants. Complexing agents such as ethylene diamine tetra-acetic acid (EDTA) are used to stabilize metal ions from the pickling reaction. High alkaline solutions are useful for steel, but zinc and aluminum are normally degreased with a mild alkaline cleaner to reduce pickling. For steel, the chemical effect of the degreasing is less evident, but it is thought that the alkaline oxidation of the surface is important for the initiation of the phosphating reaction [7].

5.3.1.2.2 **Activation** During this step, the surface is exposed to a slightly alkaline solution of Ti colloids consisting of $Na_4TiO(PO_4)_2 \cdot 0\text{–}7H_2O$. The colloidal solution is prepared at ambient temperature and the particle size dispersion is defined by having 70% of its population between 60 and 130 nm. During the immersion of the surface in the activation bath, the colloidal particles are adsorbed on the surface. These particles are thought to serve as the nucleation centers for the phosphate crystal in the subsequent phosphating step. Therefore, the activation step determines the number (and thus, the size) of the crystals.

Direct measurement of the adsorbed particles has proven difficult because of their weak binding to the surface. Nevertheless, the adsorbed colloidal particles have been detected by ion microprobe analysis [8], atomic force microscopy (AFM) [9, 10] and time-of-flight secondary ion mass spectroscopy (ToF-SIMS) [10]. AFM results of Van Roy and coworkers [10] are shown in Fig. 3, along with their proposed nucleation and growth mechanism on the aluminum surface. These results demonstrate that under the conditions of these experiments, the adsorbed particles are flat with 7 to 8 nm thickness and 100 to 300 nm in diameter. According to Tegehall [11], the Ti colloid undergoes cationic exchange reactions between Na^+ and bivalent cations such as Zn^{2+}, Mn^{2+}, Mg^{2+}, and Ba^{2+}. The bivalent Ti phosphate species are less soluble than the sodium titanium phosphate. Nucleation of phosphate crystals occurs during the first milliseconds of immersion in the phosphating bath, followed by bulk precipitation of the crystal. According to the model in Fig. 3, the form and distribution of the nucleation center determines the morphology of the phosphate crystals. According to these authors, the crystals grow epitaxially away from the nucleation center.

5.3.1.2.3 **Phosphating** The phosphating bath consists of a phosphoric acid solution containing various heavy metal ions. They are classified as monocation (metal ion = Zn^{2+} or Fe^{2+} in older formulations), bication (Zn^{2+} and either Mn^{2+} or Ni^{2+}), and trication (Zn^{2+}, Mn^{2+}, and Ni^{2+}). Typical concentration ranges for a trication bath are given in Table 1. Ni^{2+} is sometimes replaced by Cu^{2+} for environmental reasons. Although copper is considered to have nearly the same toxicity as nickel, it can be used in much lower concentration in the phosphating bath. In comparison to nickel, the relations lie between 1 : 50 and 1 : 100. Oxidizing agents such as nitrite are added as accelerators, and fluoride ions are added to dissolve aluminum oxides if necessary.

Following the pioneering work of Machu [12, 13], it is well known that the phosphating reaction is a mixed potential process. The schematic diagram of Fig. 4 outlines some of the major chemical phenomena occurring during phosphating in a simplified form. The anodic reaction is the oxidation of the substrate metal while the cathodic reaction is

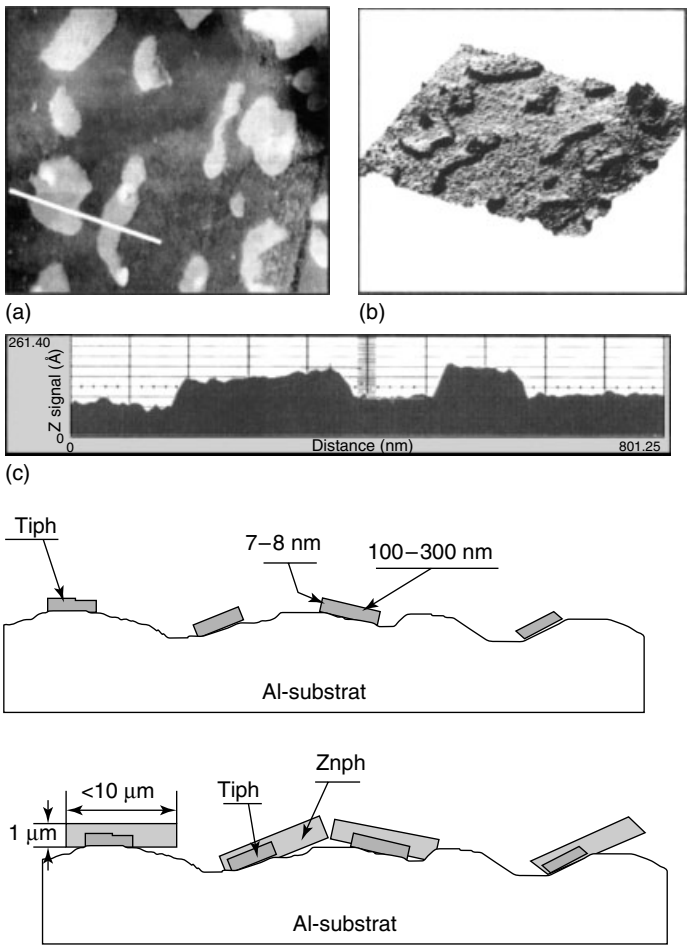


Fig. 3 Germination of phosphate crystals: AFM results showing adsorbed colloidal particles on aluminum after treatment in an activation bath; these particles are believed to be the nucleation sites for crystal growth, as shown in the schematic diagram. (After [10].)

Tab. 1 Typical trication phosphate bath composition range used for galvanized steel in the automotive industry. Courtesy Michael Wolpers (Voest Alpine)

Free acid[a]	***Total acid***	***Concentration (g L^{-1})***					
		Zn^{2+}	Mn^{2+}	Ni^{2+}	NO_3^-	PO_4^{3-}	F^-
1–2	20–35	1–2	0.8–2	0.5–2	2–25	13–20	0–2

[a] Free and total acid are defined as the number of milliliters of 0.1 M NaOH needed to reach the first and second endpoint, respectively.

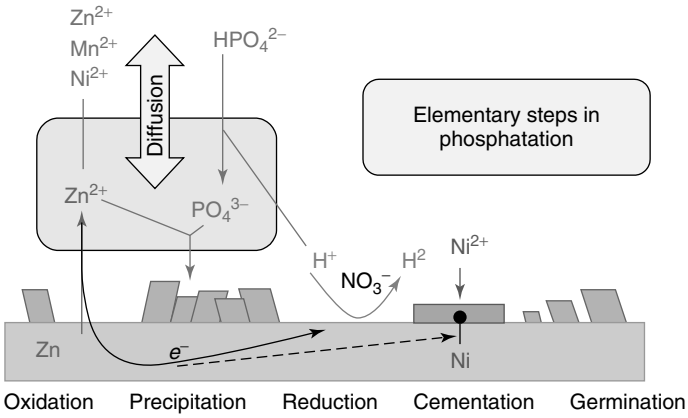


Fig. 4 Phosphatation as a mixed potential process: schematic diagram illustrating a simplified view of different chemical phenomena occurring during the growth of the phosphate film on an Fe surface in a trication phosphating bath.

the reduction of hydrogen ions or other oxidizing agents in the electrolyte. The operating conditions of the phosphatation bath require that the bath be very close to saturation in metal phosphate in a pH range of 2.8 to 3.0. Under these conditions, both the anodic and cathodic reaction result in a local decrease in the solubility of the metal phosphate: the anodic reaction by increasing the concentration of metal ions in anodic zones, and the cathodic reaction by increasing the pH and thus the concentration of PO_4^{3-}. It is important to note that the pH of the bath is just below the first endpoint in the titration curve of phosphoric acid, so that the introduction of even a small amount of hydroxide ion from the cathodic reaction can produce significant local pH changes. The pH increase at the metal/electrolyte interface has been experimentally demonstrated using micro pH electrodes [14].

The anodic reaction plays an important role if the treated metal is not present in the phosphating bath. This occurs when a zinc phosphate bath reacts with steel. The Fe^{2+} formed by the anodic reaction is incorporated into the phosphate crystal structure. This improves the corrosion resistance properties of the zinc phosphate crystals. Figure 5 shows the simultaneous measurement of the coating weight increase coupled with the pickling rate of cold rolled steel in a commercial trication phosphating bath.

Phosphating is an autopassivation process. The reaction of the substrate metal with the phosphating bath leads to the formation of the phosphate crystals, which in turn block the surface, lowering the reaction rate. When the reaction rate is sufficiently slowed so that precipitation can no longer be maintained, crystal growth will stop. Therefore, a period of redissolution and reorganization of the crystal layer may follow the initial period of crystal growth. The steady state surface structure will correspond to a minimum crystal porosity necessary to maintain the precipitated layer at the surface. An inverse relation between crystal size and crystal number is observed, since a small number

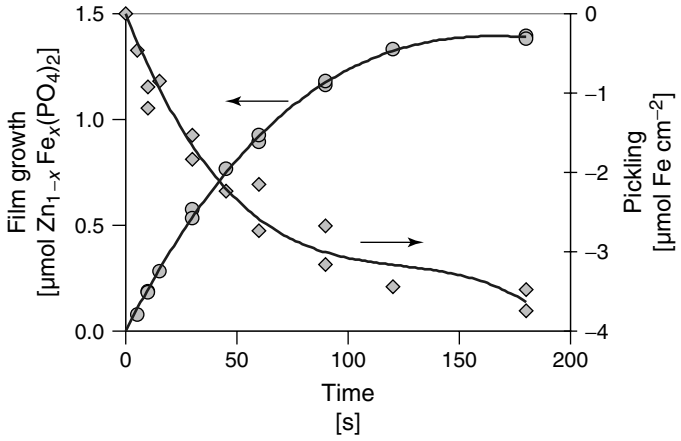


Fig. 5 Phosphating as a mixed potential process: gravimetric measurement of the film growth and metal dissolution reaction during the phosphating of steel in a trication phosphating bath. Original data Irsid.

of large crystals is necessary to give the same relative coverage as a large number of small crystals.

These relationships are illustrated in Fig. 6 in which the variation of coating weight, crystal size, the relative surface coverage, and the rate of substrate dissolution were measured as a function of time for the phosphatation of steel in a laboratory trication phosphatation bath. The partial free metal surface $(1-\theta)$ decreases as the average crystal size (d_z) and coating mass increase. The dissolution rate of the metal r_{diss} (here defined as a negative value) drops toward zero at the end of the reaction.

Accelerators The exact function of accelerators is not well understood [16]. Some, such as hydrogen peroxide or borates, are known to be powerful oxidants and it is thought that these species increase the total cathodic current and area at the surface. However, other species, such as the most common nitrate and nitrite, are not strong oxidants at a pH typical of a phosphatation bath, and other mechanisms must be invoked. It has been suggested [3, 16] that these species increase the number of hydrogen ions consumed per electron transferred, while reducing the amount of hydrogen gas produced, which would otherwise block areas of the surface and create defects in the conversion layer. The accelerator may also contribute to the passivation of the surface between the crystals of phosphate.

Because of the potential toxicity of the nitrate/nitrite system a number of alternatives have been proposed including organic acids with a nitrate substitution such as nitrobenzoic acid, nitrosulfuric acid, nitroguanidine, and so forth. Oxidants such as chlorates and hydrogen peroxide have also been proposed. The use of chlorate results in the formation of free Cl^- that in the case of zinc alloys can lead to the localization of the anodic reaction into a pitting mechanism, with a resulting defect in the phosphate layer, known as "white spotting". Hydrogen peroxide has been intensely studied

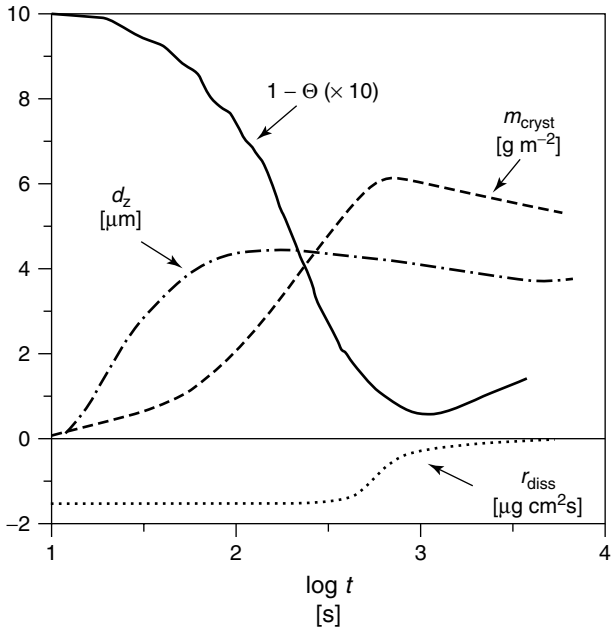


Fig. 6 Phosphating as an autopassivation process: variation of partial free surface ($1-\theta$), metal dissolution rate (r_{diss}), crystal size (d_z), and coating mass (m_{cryst}) with time during the phosphating of mild steel in a trication phosphate bath. (From Ref. [15].)

because of the fact that only water is formed during its reduction, making it an ideal solution from an environmental perspective. Unfortunately, solutions of hydrogen peroxide are not very stable, and for most applications, it is not considered a practical accelerator. Reductants such as hyposulfite, phosphite, and hydroxylamine, have also proven interesting. The search for new environmentally friendly accelerators is a major axis for innovation in phosphating today.

Heavy metal ions A phosphating bath usually contains several metal ions that can incorporate into the crystal structure improving the physical and chemical properties of the phosphate layer. At least one component, often nickel, is nobler than the base metal. During the phosphating treatment, Ni^{2+} and Cu^{2+} will deposit as nickel and copper metal on the surface [17, 18]. This gives rise to a large potential jump at the end of the phosphating reaction, as shown in Fig. 9. By increasing and homogenizing the cathodic area, the deposited metallic nickel may insure that the phosphate crystals are well distributed on the surface. At the end of the reaction, the cementation of nickel insures that metal surface exposed between the crystals is in fact a surface of nickel rather than the base metal.

Ni^{2+} is also known to reduce the crystal size [19]. This suggests that in addition to its effect on the electrochemistry, Ni^{2+} may play an important role in the nucleation process, probably through the

ion exchange mechanism proposed by Tegehall [11].

Other additives Other species may be added to increase the stability of the bath, to enhance wetting or spraying properties, and so forth. HF is frequently added to remove aluminum oxide layers when phosphating aluminum or zinc–aluminum alloys. The F^- ions form a complex with Al^{3+} in solution and can also precipitate in the form of Na_3AlF_6 (cryolite) or, in the presence of K^+, NaK_2AlF_6 (elpasolith). BF_4^- and SiF_6^{2-} may be used as fluoride source. It has been suggested that silicate additions might help seal the phosphate layer, increasing its resistance to environmental attack. Tartaric acid has also been suggested as a stabilizer for the Ni cementation.

The substrate metal The aptitude of a particular material for phosphating depends largely upon its reactivity in the phosphating bath. Passive materials such as aluminum are more difficult to phosphate because the passive film must be overcome, which for aluminum requires the addition of HF to the phosphating bath. Magnesium is another extreme because the dissolution is so rapid that it inhibits nucleation.

Low alloy steel is readily phosphatable as long as the percentage of Cr is low (below 3% according to Rausch [2]). Carbon seems to inhibit nucleation leading to larger crystal sizes [20, 21] probably by inhibiting the adsorption of the activating colloids. The surface oxide composition of steel can be controlled by the annealing conditions and considerable effort has been made to determine the optimum oxide composition for phosphating [22–25]. Segregated oxides produced during annealing steps may influence the reactivity in either a positive or negative way. Insoluble oxides such as silicates block the surface and lead to poor results. By contrast, manganese oxides seem to have a positive effect on phosphating probably because they are soluble in the phosphate bath and therefore destabilize the iron oxides.

5.3.1.2.4 **Posttreatment** The phosphated surface is often treated with a chromate postrinse although the trend in Europe is to either skip this step altogether or use chromium-free posttreatments based on ZrF_6^{2-}, TiF_6^{2-}, Cu^{2+}, and/or polymer compounds, in particular acrylic polymers. This final rinse is thought to passivate the surface of the metal between the crystals and to alter the surface of the crystal so as to render them more resistant to elevated pH. These phenomena will be treated in more detail in subsequent sections.

5.3.1.3 The Nature of the Phosphate Layer

The basic function of the phosphate layer before painting is to promote the adherence of paint and increase the corrosion resistance of the painted product. Each of the different structural features of the phosphate layer plays an important role in achieving this goal. The phosphate layer must offer sufficient surface roughness to anchor the organic coating, and sufficient porosity (exposed metal between the crystals) to allow the passage of current during cationic painting. Nevertheless, the electrochemical activity of the metal surface exposed between the phosphate crystals should be reduced so as to prevent corrosion. The phosphate crystals themselves must be stable with respect to the chemical and thermal environments that they will encounter during usage. In the automotive

industry, phosphating is usually applied to the assembled piece, and therefore, the mechanical properties of the phosphate layer during forming are not critical. Mechanical properties are important for prephosphated or coil coated steel.

5.3.1.3.1 Morphology

General considerations One of the more striking differences between a phosphate conversion layer and other conversion layers, such as those formed during chromatation and alkaline oxidation, is the thickness and morphology of the layer. The phosphate layer consists of an array of crystals in the form of needles, flakes, or tiles (Fig. 1). They are usually around 1 to 10 μm in diameter, with a coating weight on the order of 1 to 6 g m^{-2}, although crystal size and coating weight can be highly variable with the process conditions.

The Phosphate/paint interface The irregular structure of the phosphate film is important for the anchoring of the paint layer [15]. The metal surface of the substrate is always exposed in between the crystals so that sufficient cathodic current can be passed across the phosphate layer to drive the cationic deposition process. The paint is thus deposited at the base of phosphate crystals and then, extends out toward the exterior. By this mechanism, the paint is very well anchored in a lock and key manner into the conversion coating.

The Phosphate/metal interface The crystals are anchored into the roughness of the surface. Even if the metal is initially polished, the acid attack will increase the surface roughness simultaneously with the formation of the phosphate layer. The primary crystals grow epitaxially with the initial surface, while secondary crystals nucleate on the surface of other crystals [26]. The secondary crystals are notably weaker than the primary crystals. Ong and coworkers [27] have measured a shear strength of 850 kN m^{-2} for the primary layer versus 450 kN m^{-2} for the secondary crystals.

5.3.1.3.2 Chemical and Surface Composition

Mono- and bication phosphatation For monocation Zn phosphate layers, the major phases (Fig. 2) are hopeite (H), $Zn_3(PO_4)_2{\cdot}4H_2O$, which is an orthorhombic structure, and phosphophyllite (P), $Zn_2Fe(PO_4)_2{\cdot}4H_2O$, which is monoclinic. In general, the presence of phosphophyllite is associated with a better corrosion resistance than hopeite, probably due to its enhanced chemical stability relative to alkaline electrolytes [28, 29]. The ratio of hopeite to phosphophyllite intensity in the diffraction pattern has been proposed as a measure of the quality of the phosphate layer [30] for steel. The Fe in the phosphophyllite phase comes from the dissolution of the steel surface. Therefore, the P/(H + P) ratio will depend on the kinetics of steel pickling in the phosphating bath [31]. Further, the Fe content of the phosphate layer will be increased near the metal phosphate interface, in which the Fe concentration is presumably higher [13, 21]. Secondary crystals that grow further away from the metal substrate will more closely reflect the composition of the bath.

Trication phosphating The addition of Mn^{2+} and Ni^{2+} in the bi- and trication phosphating baths leads to the formation of ''pseudo–phosphophyllite'', $Zn_{(3-x-y-z)}Fe_xMn_yNi_z(PO_4)_2{\cdot}4H_2O$. The Mn^{2+} replaces Zn^{2+} in both the

octahedral and tetrahedral sites of the hopeite crystal lattice while Ni^{2+} replaces Zn^{2+} only in the octahedral sites (see Fig. 2). The presence of Mn^{2+} in the layer leads to a partial amorphization of the zinc phosphate layer and the P/(H + P) ratio is no longer meaningful, nor has a similar diagnostic been defined. The ratio of Mn to Ni is higher in the phosphate layer than in the bath composition.

Crystal surface modification The surface of the crystals may also be modified by the final passivation rinse. When a final rinse containing chromate or Cr(III) is used, a thin film of either $ZnCrO_4$, $CrPO_4$ [32], or CrOOH [33] is formed on the surface. Likewise, when steel is used as the substrate material, and in the presence of passivating additives such as nitrite, a thin layer of $FePO_4$ may be formed on the surface of the crystals. Further modification of the phosphate surface may be induced if the crystals come into contact with an alkaline environment, as described below.

Metal surface modification The reactivity of the metal surface exposed between the crystals is an important factor in underpaint corrosion resistance. Simply reducing the electrochemically active metal surface by the presence of nonconducting crystals will go a long way toward preventing the underpaint corrosion. However, it is known that the surface exposed between the crystals is modified by the phosphating treatment. The nature of the metal may differ significantly from that of the original surface, since Ni or Cu may also be deposited by cementation from the bath. This is reflected in potential changes during the phosphatation reactions. Further, amorphous phosphate films are thought to form during the phosphating treatment, in particular in conjunction with oxidizing agents such as nitrate or nitrite. The passivating effect may be further reinforced by a final rinse with chromate solution.

5.3.1.3.3 Thermal and Chemical Properties

Dehydration Drying temperatures for cataphoretic paint are on the order of 150 to 200 °C. The dehydration of hopeite occurs in two steps [34]: two water molecules are lost in the temperature range of 80 to 120 °C, and the two final water molecules are lost around 250 °C. The first dehydration step is reversible and in the presence of humidity, the tetrahydrate is reformed, but the crystals are finer and the orientations are different [35]. Van Ooij and Sabata [36] have proposed that the rehydration of the dihydrate is an important mechanism in the adherence failure of phosphate coatings. The presence of Mn and Ni substitutions in the hopeite phase increases the temperature of dehydration [37, 38]. In contrast to hopeite, the phosphophyllite phase is transformed into an amorphous phase, and the dehydration is irreversible.

Alkaline resistance An important chemical property of the phosphate layers is their ability to resist attack by hydroxide ion when exposed to alkaline electrolytes [36, 39]. Such an exposure may occur during: (1) the cationic deposition of paint (by imposition of a cathodic current); (2) during subsequent alkaline degreasing operations (in particular for prephosphated steel products); and (3) under the paint layer during cathodic delamination. The destruction of the phosphate layer by the alkaline

environment under the paint during active corrosion has been proposed as an important step in the mechanism of cathodic delamination from a scratch type defect [32].

The reaction of the phosphate layer with an alkaline medium occurs by solid-state ion exchange between the phosphate and the hydroxide, leaving behind an oxide/hydroxide phase rich in the less soluble heavy metals. If allowed to continue, all phosphate will be removed from the crystals. The presence of substitution elements such as Fe, Mn, or Ni lowers the solubility of the $Zn(OH)_2$ layer. On the steel surface, the process occurs with very little change in the morphology of the crystals as seen through the electron microscope, although the diffraction pattern disappears [39].

5.3.1.4 Electrochemical Properties and Characterization Methods

5.3.1.4.1 Porosity and Coverage Measurements As cited above, the paint–metal adherence mechanism involves mechanical locking of the paint into the voids between the crystals, thus it is not surprising that extensive studies have been conducted into the characterization of the so-called *porosity* of the layer, especially for the steel surface. The simplest methods involve treating the phosphated solution with a chemical reagent such that a specific reaction may occur on the metal surface. The detection of the reaction products may be visual as with Turnbull's blue reaction [40]. This consists of treatment with a ferrocynanide indicator solution that detects the amount of Fe^{2+} on the surface. Another popular technique is the cementation of copper [41] onto the active surface. This permits the visualization of the porosity by scanning electron microscopy (SEM). These methods are useful for quality control of phosphate coatings.

Electrochemical methods of estimating the coverage of the phosphate layer have been extensively developed in recent years. The phosphate crystals are electronic insulators. Therefore, the electrochemical response of the phosphated metal may be attributed to the metallic surface exposed between the crystals. The basic idea of most electrochemical methods is to obtain a measurement that is proportional to the free surface. By comparing the variable magnitude obtained with a phosphated surface with the response of the unphosphated surface, a coverage fraction can be defined. A number of different measurements have been investigated including the diffusion-limited currents for the reduction of oxygen, the anodic charging curves corresponding to the oxidation of the surface metal, the polarization or charge-transfer resistance of the metal, the electrode admittance, and the double-layer capacitance. Each of these measurements has specific advantages and disadvantages. Detailed studies and comparisons of the different techniques have been given by Schultze and coworkers [42, 43].

Diffusion-limited reduction of oxygen This method involves polarizing the phosphated surface to a potential at which the reduction of oxygen occurs at a diffusion-limited rate [44]. The flux of oxygen to the surface, and thus the limiting current, will depend upon the area of the surface exposed. A difficulty is that the limiting current may depend upon the specific pore volume and geometry as well as the exposed surface [42]. This may also be an advantage – the surface coverage being a poorly defined parameter in any case, at least this measurement simulates the process of cationic painting. Another problem

is that the reduction of oxygen on the free surface may lead to an alkalization of the electrolyte in the confined volume between the crystals, which could lead to an alteration or dissolution of the phosphate crystals. Coverage area can also be measured by impedance spectroscopy under diffusion-limited conditions [45]. In principle, surface alteration is less of a problem than with DC techniques, as impedance measurements require only modest polarization of the electrode.

Oxidation of the exposed metal The idea of coulometrically measuring the surface area by the integration of the metal oxidation peaks during linear scan voltammetry in an appropriate buffer solution was first proposed by Machu and coworkers [46] in the 1940s, and has been thoroughly developed in recent publications [43, 47]. The method has been extended to zinc-coated steel by Klusmann and coworkers [18]. The advantage of this method is that only the exposed metal contributes to the oxidation peaks. Thus, the measurement should be independent of pore geometry and volume, and should give a fairly quantitative analysis of the number of metal atoms exposed per unit area of surface. The drawback is that the electrochemical properties of the metal exposed between the crystals may not be representative of the initial surface, and in addition, may not be uniform on the phosphated surface. The cementation of heavy metal ions or the formation of amorphous phosphate and chromate layers could affect the electrochemical response. Likewise, localized surface contamination by carbon or segregated oxides may adversely affect phosphate crystal growth and therefore, such zones might show up preferentially in the metal exposed between the crystals.

Polarization resistance Polarization resistance measurements can be measured for phosphated samples in the DC mode [48, 49] or using electrochemical impedance [42, 50]. The idea is that the polarization resistance is related to the corrosion rate by the Stern–Geary equation. Therefore, if the corrosion rate is uniform on the exposed metal, the corrosion rate will be proportional to the exposed area. The advantage of this method is that the measurement is made by imposing a small perturbation around the open-circuit potential, and relatively speaking, should be less damaging than either an anodic or cathodic sweep. The interpretation is more problematic, however, as the corrosion rate may vary across the surface and may depend upon pore geometry. Finally, if the anode and cathode are spatially separated, the polarization resistance will be proportional only to the surface, which controls the rate. For example, if the rate is controlled by oxygen reduction on carbon particles, as has been proposed by Nazarov and Thierry [51], $1/R_p$ will be proportional only to the cathodic surface, and not the free metal surface.

Double-layer capacitance The double-layer capacitance has also been used as a measure of the free surface area [42]. The advantage of this method is that the measurement can be obtained rapidly by admittance measurements at a single frequency. In principle, the relationship between the coverage and the capacitance is

$$\theta = \frac{C(\theta) - C(\theta = 0)}{C(\theta = 1) - C(\theta = 0)} \qquad (1)$$

One major difficulty is that the capacitance of the totally blocked electrode, $C(\theta = 1)$, is necessary for the calculation and yet cannot be measured even in principle as

a phosphate layer with a coverage of 1 is not obtainable. Other difficulties include the dispersion of capacitance values across the surface.

Figure 7 gives the oxide charge, admittance, and corrosion current as a function of phosphatation time for a steel surface in a trication phosphatation bath. The different parameters give quite different results, especially at long times. The authors attribute the long time changes to the alteration of the surface between the crystals as shown in the schematic diagram.

Copper electrodeposition into the pore volume The lock and key mechanisms of paint adherence will also depend upon the specific pore geometry and volume, which are not really assessed by the electrochemical methods described above. A very clever method of investigation has been proposed by Losch and Schultze [15]. In this method, copper is electrodeposited

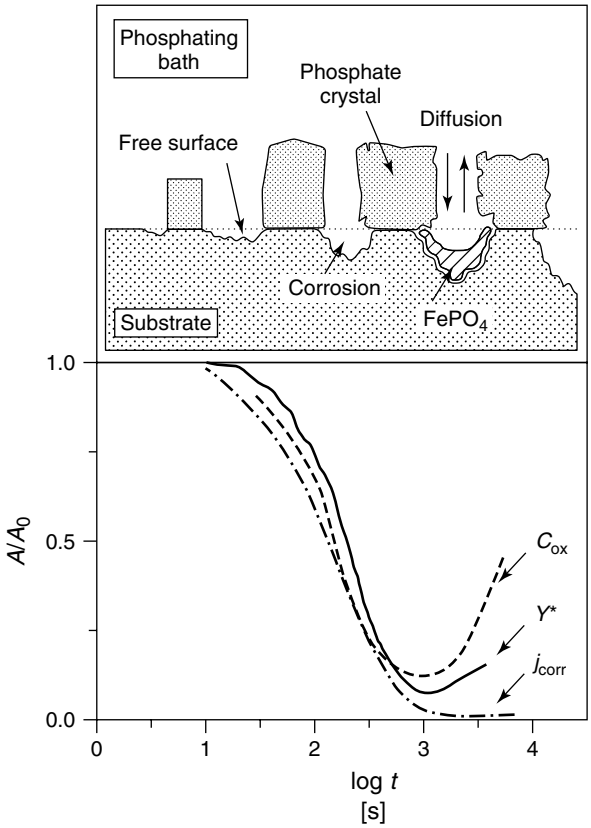


Fig. 7 Comparison of different electrochemical methods of estimating the partial free surface: ex situ oxide capacitance, in situ electrochemical admittance, and corrosion current (determined from R_p). Differences between these values may be accounted for by the variation of surface morphology as shown in the schematic diagram. (From Ref. [42].)

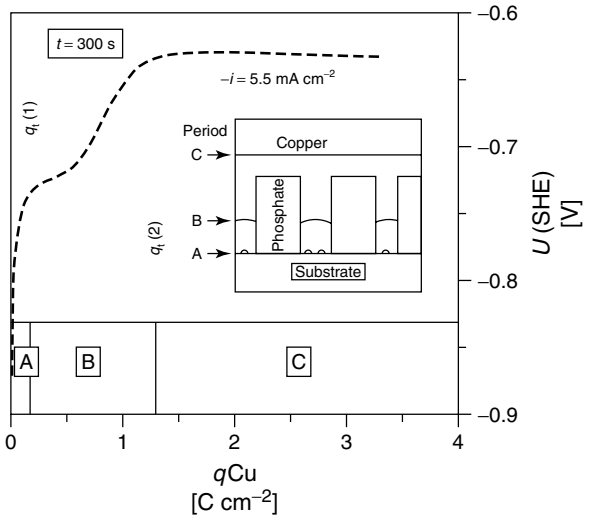


Fig. 8 Determination of free surface and pore volume from galvanostatic copper deposition: typical potential–time transients and a schematic diagram of the surface pore structure during the different phases of the experiment. (From Ref. [15].)

at constant current onto the phosphated surface and the potential transient is recorded. An example is shown in Fig. 8 along with a schematic diagram of the interpretation. The first transition corresponds to the time necessary to deposit copper on the electrochemically active surface in the porosity; the time between the first and second transition gives the amount of copper necessary to fill the pore volume. In this way, information on the electrochemically active surface, the pore volume, and the crystal volume are obtained in the same experiment. In addition, the quantitative nature of the deposition reaction is clearly defined in coulometric terms, and the experiment directly simulates the cationic painting process.

5.3.1.5 In Situ Monitoring of the Phosphating Reaction

Phosphating is a spontaneous reaction between the metal surface and the phosphating bath. It is an open-circuit process and thus current transient techniques cannot be used to follow the kinetics of nucleation and growth. The majority of work has involved the measurement of the open-circuit potential as a function of time, beginning with the work of Machu [12, 13] and Ghali and coworkers [52], and more recently, the work of Schultze [18]. The interpretation of the potential changes may not be straightforward, especially when cementation reactions occur simultaneously with the phosphate crystal growth. Further, the potential changes may be very minor for zinc surfaces in the absence of Ni^{2+} in the bath.

Impedance spectroscopy is a particularly promising technique for in situ measurements. Impedance spectroscopy is performed by applying a small perturbation to the open-circuit potential, and is considered to be nonintrusive. Work along these lines has been performed by

Charbonnier and coworkers [53] and by Schultze and coworkers [42] on the basis of admittance measurements. These methods are interesting as a complement to the open-circuit potential, but nevertheless are only qualitatively related to the extent of the phosphating reaction.

The quartz crystal microbalance has been applied to phosphating of zinc [17, 54]. This technique complements other electrochemical techniques as ideally, it gives the mass as a function of time. A typical example is shown in Fig. 9 in which the variations of the open-circuit potential and the quartz resonance frequency (assumed to be proportional to the negative of the mass change as indicated) are monitored as a function of time. Nevertheless, this technique presents a number of difficulties. First of all, even if they are properly measured, mass changes alone are ambiguous as phosphating involves precipitation and metal dissolution. Therefore, it is of interest to couple the microbalance method with another technique such as inductive coupled plasma (ICP) emission spectroscopy [55]. Second, the microbalance is subject to artifacts

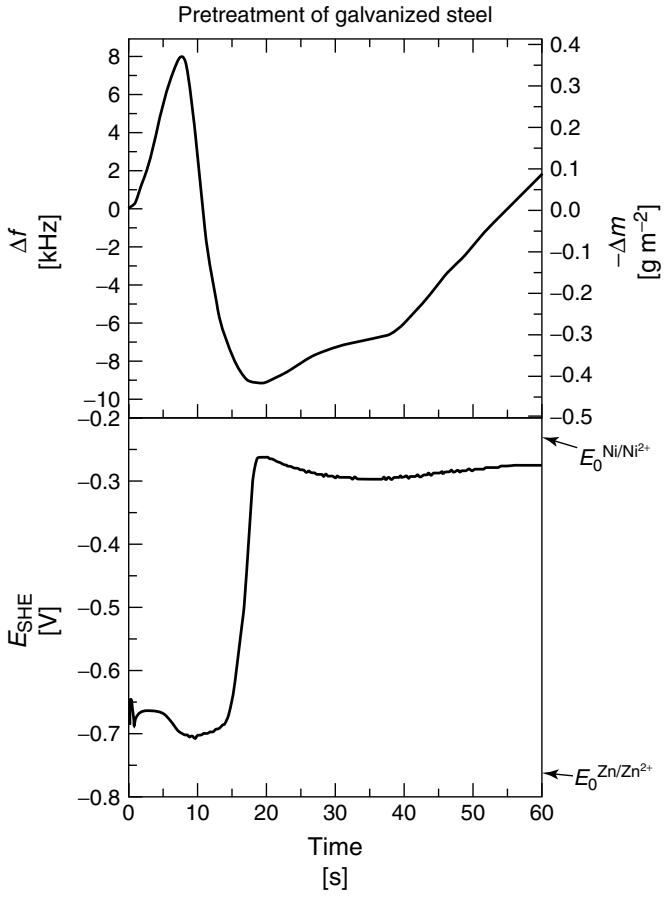


Fig. 9 In situ monitoring of phosphating reactions: quartz crystal microbalance and corrosion potential measurements. (From Ref. [17].)

caused by the changes in surface roughness as the phosphate layer is formed. Finally, the technique is limited to surfaces that can be deposited onto the quartz crystal and therefore, at present, cannot be readily applied to technical samples.

5.3.1.6 Corrosion Resistance Measurements

Many factors contribute to the corrosion resistance of a modern painted steel or aluminum product including the nature of organic coating, the metal substrate and/or metal coating, and the conversion layer. It is impossible to speak of the corrosion resistance afforded by the conversion layer without reference to the total product. In this section, we will briefly describe some phenomena unique to the conversion layer, which do contribute to the corrosion resistance. A detailed description of corrosion mechanisms under paint is given in Chapter 5.4.

Figure 10 gives an indication of the results of a standard accelerated corrosion test (salt spray test) for painted panels of phosphated steel, as a function of the porosity of the phosphate layer as determined by diffusion-limited oxygen reduction currents [44]. The first point corresponds to bare steel, which obviously corrodes very rapidly under the severe conditions of the salt spray test. The subsequent points show the important role played by the conversion layer in corrosion resistance. However, a relationship between porosity and time to failure is only observed for the very poor samples, >3% porosity and time to failure >400 h. For the better samples, with a failure time between 400 and 1000 h, other factors must account for the dispersion of the results.

The enhanced corrosion resistance of phosphated steel can be attributed to two phenomena: the increased paint adherence and the chemical passivation of the metal surface by an insulating barrier film of phosphates. A difference between phosphate and chromate conversion coatings is that the later are thought to function as

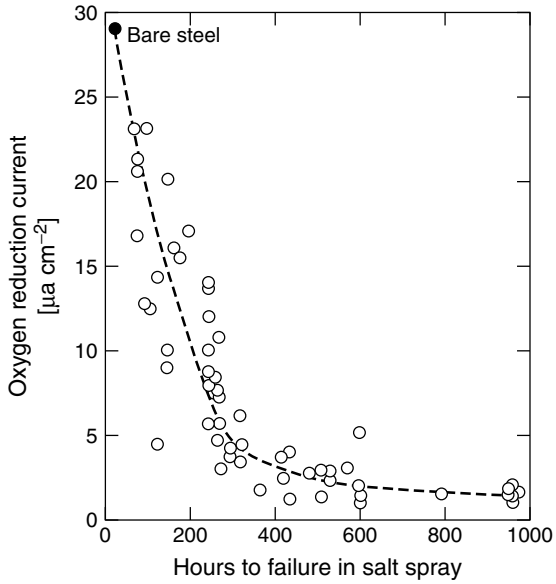


Fig. 10 Relationship between accelerated test results for painted, phosphated steel panels, and the magnitude of the diffusion-limited oxygen current (proportional to the "porosity"). (From Ref. [44].)

reservoirs of water soluble Cr(VI), which is a strong corrosion inhibitor. No similar leaching/inhibition mechanism has been identified for phosphate layers in the absence of chromate post-treatment, even though other similar phenomena such as the capacity of the phosphate crystals to buffer the pH under the paint might also be taken into consideration.

The passivating effect of a phosphate layer is clearly illustrated by the data shown in Fig. 11. Here, the z component of the electrolytic current was measured using a scanning vibrating electrode (SVET) near a scratch defect on the surface of phosphated galvanized steel in 30 mM NaCl solution without paint. Although the measurement is obtained at a height of about 100 µm above the surface, the value of the current faithfully reflects the current distribution on the surface [56, 57]. A positive value is obtained in regions of anodic activity, while a negative value is obtained in cathodic regions. On a galvanized steel surface, the

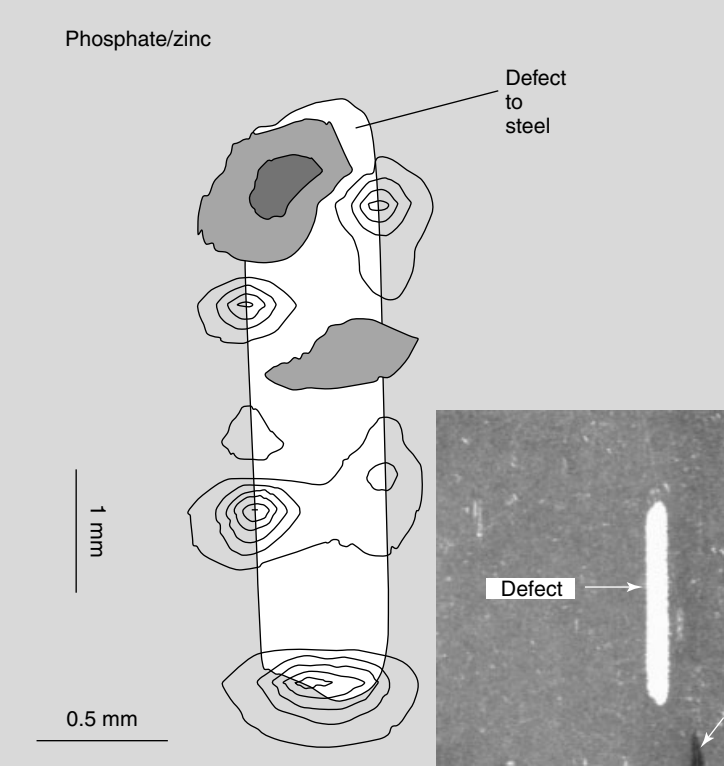


Fig. 11 Passivating effect of a phosphate layer. Distribution of vertical component of current over a scratched phosphated galvanized steel surface measured by the SVET method. The scratch penetrates down to the steel surface. Cathodic zones (current < 0) are indicated by the filled areas, while anodic zones (current > 0) are transparent. Because of the passivating properties of the phosphate layer, the anodic reaction remains localized in the vicinity of the scratch defect. Each isocurrent line represents 10 µA cm^{-2}. Original data: Irsid.

zinc should become anodic to the steel exposed in the defect. In the absence of a phosphate layer, the anodic reaction would be distributed over the zinc surface, and if the surface were painted, the anodic reaction would move under the paint layer in a mechanism of anodic delamination. In this case, we see that the phosphate layer confines the anodic reaction to the proximity of the scratch.

For nongalvanized steel, cosmetic corrosion generally involves a cathodic delamination mechanism: the surface under the paint becomes cathodic and the surface exposed in the hole becomes anodic. To slow down or prevent atmospheric corrosion, it is therefore important that the surface treatment be a good cathodic inhibitor in the finished product. The phosphate layer increases corrosion resistance by limiting the available free surface for the cathodic reaction. In general, the activity of the free surface is further reduced by passivating posttreatments or by the deposition of amorphous phosphate films between the crystals.

The effect of the phosphate layer as a cathodic inhibitor under atmospheric conditions is illustrated in Fig. 12. In this experiment, the Volta potential of a galvanized steel surface is measured as a function of time during a transition from air to Ar atmosphere, as indicated [51]. The measurement is performed with a Kelvin probe, and the Volta potential of the corroding surface is directly proportional to the corrosion potential with appropriate calibration [58]. The potential jump induced by the presence of air is a measure of the sensitivity of the surface to the oxygen reduction reaction. Here, we see that the galvanized steel surface shows a very large potential jump, on the order of 200 mV. However, the phosphated surface shows only a small potential jump indicating significantly less sensitivity to oxygen reduction. The third curve shows a similar experiment obtained with a phosphated surface contaminated with carbon deposits. The conclusion of these experiments was that the carbon deposits served as cathodic sites on the phosphated galvanized steel surfaces.

5.3.2 Chromate Conversion Coatings

5.3.2.1 Overview

5.3.2.1.1 Chromate Conversion Coatings: Definition and Applications Chromate conversion coatings (CCCs) are thin (0.01–3 μm) amorphous inorganic films that form by contacting a metallic surface with a solution whose main film-forming agent is a soluble chromate species. Coatings consist of a mixture of oxides and hydroxides derived from chemical oxidation of the substrate, and reduction, hydrolysis, precipitation, and condensation of chemical species present in solution. Coating thickness, color, corrosion resistance, and so forth, depend on contact times, temperatures, solution chemistry, application method, and substrate composition. CCCs are applied most commonly to Al-, Zn-, Mg-, Fe-, Cd-, and Sn-based alloys. Chromate solutions are also used to seal coatings formed by anodizing or hydrothermal treatment. CCCs are primarily used to improve adherence of subsequently applied organic coatings, or to impart corrosion resistance under atmospheric exposure conditions. Certain types of CCCs contain labile hexavalent chromium (Cr(VI)), which can be leached from the coating when it is contacted by an attacking solution. This Cr(VI) can be transported

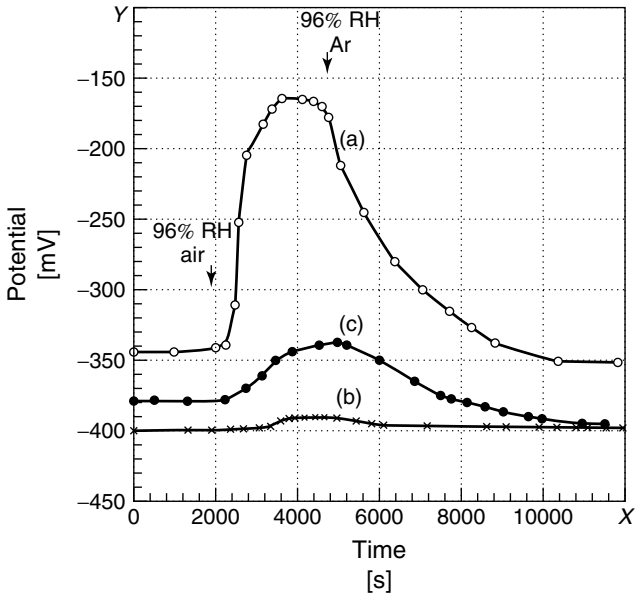


Fig. 12 The phosphate coating as a cathodic inhibitor under atmospheric conditions. Volta potential transients of a phosphated galvanized steel surface during a transition from Ar to humid air and back to Ar. The sensitivity of the surface to oxygen reduction is indicated by the magnitude of the potential jump: (a) Galvanized steel without phosphate; (b) with phosphate; (c) phosphate layer with carbon impurities. (From Ref. [51].)

through solution to coating defects where it may act to stifle further corrosion. In this sense, some CCCs are regarded as being "self-healing".

5.3.2.1.2 **Historical Perspectives** The use of inorganic chromate surface treatments can be traced at least to the early 20th century [59, 60]. Alkaline carbonate–chromate solutions were devised for Duralumin alloys in the 1920s [61, 62]. Chromium–phosphate coatings evolved prior to and during World War II [63]. Certain formulations of this type continue to be used today, especially for Zn substrates. Chromium–chromate coatings, with excellent corrosion resistance were developed in the 1950s [64, 65]. These types of coatings were among the first to be widely recognized as being self-healing [66]. Accelerated chromium–chromate conversion coating formulations were introduced around 1970 [67]. Today, the predominant CCC types are accelerated chromium–chromate coatings, which are used as Al alloys for stand-alone corrosion protection or as a paint-base, and chromium–phosphate coatings, which are used to suppress white rust on Zn and Zn–Al metallic coatings applied to steels.

The primary film-forming agent in CCC baths is Cr(VI). This compound is a potent human toxin and known cancer-causing agent [68–74]. Since the 1980s, there has been significant research and development

effort aimed at identifying chromate-free coatings that match the ease of applicability, and excellent performance of CCCs. While chromate replacement has occurred in certain applications [75], widespread replacement requires simplifying chromate-free coating processing and improving coating performance.

5.3.2.2 Substrates

5.3.2.2.1 **Aluminum** On aluminum alloys, accelerated chromium–chromate coatings are typically used as a foundation layer in coating systems (conversion coating–primer–topcoat), a sealant on anodized layers, and as a stand-alone corrosion-resistant coating. CCCs can be formed all alloy grades, but CCC characteristics and performance vary from alloy to alloy. In particular, the corrosion resistance of conversion coated surfaces scales with the intrinsic corrosion resistance of the alloy substrate. Normally, the greater the alloying element content, the lower the corrosion resistance. Alloys containing high concentrations of Cu or Si are regarded as being the most difficult to conversion coat effectively. In nonaerospace applications, chromium–phosphate coatings are commonly used to provide temporary corrosion protection and enhance paintability, especially for architectural products.

5.3.2.2.2 **Zinc** Zn or Zn–Al coatings are widely used for sacrificial corrosion protection of steel [76]. Zn and Zn–Al are readily susceptible to formation of white rust during humid-air exposure. Chromium–phosphate and to a lesser extent chromium–chromate formulations are used to suppress white rust formation. CCCs on Zn are believed to be mixtures of Cr(III) and Zn(II) oxides [77]. On Al–Zn alloys, the CCC outer layer contains Cr(VI), while an intermediate layer contains Cr(III) and Al(III) and Zn(II) oxides and hydroxides. The innermost layer of the coating consists of Cr(0) [78]. Lower oxidation state forms of Cr, especially Cr(0) have also been attributed to photoreduction or ion etching that occurs during surface characterization [79, 80].

5.3.2.2.3 **Magnesium** CCCs are usually formed in acidic solutions in which Mg surfaces are easily activated. Nitric acid- and chromic acid-based mixtures are common. Because of the high corrosion susceptibility of Mg alloys, CCCs are more often used as a surface pretreatment for paint than as stand-alone corrosion-resistant coatings.

5.3.2.2.4 **Cadmium** Cadmium plating is used to increase the corrosion resistance of steel fasteners and electrical connectors. However, the Cd plate is itself subject to oxidation and tarnishing in humid and tropical environments to such an extent that electrical and mechanical functionality may be adversely affected. CCCs may are applied to Cd to resist oxidation, or to increase paintability [81]. Cd plating can be successfully conversion coated using chemistries applicable to other metals.

5.3.2.2.5 **Steel** Strip and coiled steel sheet is often chromated after descaling, or ''pickling'', to enhance resistance to staining corrosion that occurs because of entrapment of moisture during storage and shipping of sheet product. In these applications, the CCC is used only to provide temporary corrosion protection.

5.3.2.2.6 **Stainless Steels** Most grades of stainless steel are ''passivated'' by immersion in oxidizing acid solutions [82]. The main function of passivating solutions is to remove residual iron from machining, grinding or forming, to dissolve sulfide and oxide inclusions, and to etch away Cr-depleted surfaces that result from Cr-rich oxide scale formation during elevated temperature treatment. Semistainless martensitic and precipitation hardened steels (Cr < 12–13%) are usually passivated in a chromic acid–nitric acid mixture to ensure the formation of a Cr-rich surface film that will aid in resisting pitting and crevice corrosion [83].

5.3.2.3 Chromate Conversion Coating Types

5.3.2.3.1 **Alkaline Chromate and Dichromate Formulations** In these processes, coatings are formed by immersion in a hot (90–95 °C) potassium carbonate–potassium (di)chromate solution [60–62] and then further sealed by immersion in a dichromate solution [84–86]. Contact times range from tens of minutes to 4 h. The primary film-forming reaction is hydrothermal Al oxide film growth, and the contribution of chromate to film formation is secondary. Polycrystalline coatings up to 6 μm in thickness can be formed. Little information on corrosion resistance has been reported for these types of coatings. Processing time of alkaline carbonate–chromate formulations can be shortened to 3–5 min by controlling the carbonate/chromate ratio in solution [87]. Postcoating sealants are still required to increase corrosion resistance on Al–Cu alloys [88]. The use of small additions (millimolar) of phosphate, and inhibiting transition metal oxoanions (permanganate) in the alkaline carbonate–chromate solutions are also used [89]. In some of these formulations, chromate is absent [90]. These coatings are reported to perform well as a base for paint, and provide good protection for high-Cu aluminum alloys.

5.3.2.3.2 **Acidic Chromium–phosphate** These chemistries are distinguished by their acidic chemistry [60] (<pH 1.8). Thin amorphous coatings with excellent corrosion resistance are produced. Coatings consist of predominantly amorphous $CrPO_4 \cdot 4H_2O$ with a small amount of hydrated Cr_2O_3. As such, they are distinct from polycrystalline phosphate coatings in structure, chemistry, and performance. These coatings have been used primarily as a base for painting. Boric acid additions limit film formation to improve appearance, weldability, and corrosion resistance.

5.3.2.3.3 **Acidic Chromium–chromate** A range of bath chemistries falls in this classification. Bath formulations for these coatings consist of 30 to 70 mM chromic acid, and 10 to 30 mM dichromate, though Cr(VI) speciation in solution is determined by concentration and pH and not by the form of Cr(VI) added. These types of baths also typically contain 10 to 20 mM fluoride [63, 91]. Solution pH values range from 1.2 to 1.8, and contact times range from 2 to 5 min at 30 to 35 °C. These chemistries are intended for use primarily on Al alloys, and produce yellow to brown coatings. Coatings as thick as one micrometer or more can be produced. Corrosion resistance on Al alloys is high, though not as high as with sealed anodized coatings. There is virtually no dimensional change associated with coating formation, and coatings can be applied to machined parts.

5.3.2.3.4 **Accelerated Chromium–chromate** Accelerants are used to increase coating weight and shorten coating time. Many different accelerants can be used including a variety of organic and transition metal compounds [60, 91]. The predominant accelerant in commercial formulations is ferricyanide, $Fe(CN)_6^{3-}$, which is added to acid chromate–fluoride formulations in concentrations ranging from 2 to 5 mM [92, 93]. The two primary theories for the action of $Fe(CN)_6^{3-}$ are (1) formation of mixed metal cyanide compounds [91, 94, 95]; and (2) acceleration of the film-forming Cr(VI) to Cr(III) reduction reaction by $Fe(CN)_6^{3-/4-}$ redox mediation [96]. These types of CCCs are discussed in more detail below.

5.3.2.4 Chromate Conversion Coating Formation

5.3.2.4.1 **Chromium–chromate Coatings** Chromate present in solution in very minute quantities either has no effect or a slight accelerating effect on corrosion of ferrous [97], and a slight inhibiting effect aluminum alloys in millimolar chloride solutions [98]. At concentrations greater than about 10^{-3} M over a fairly broad range of pH, chromate stimulates film formation, which is the basis for conversion coating. Modern coating chemistries typically consist of 50 mM CrO_3, 30 to 40 mM mixture of fluoride and fluoro salts, and 2 to 5 mM potassium ferricyanide. Commercial formulations often include other minor ingredients and may have alternate activators and accelerators. These reagents are added to a basis solution consisting of nitric acid whose pH is usually very close to 1.6.

In the case of Al alloys and probably Zn and Mg as well, coating formation proceeds in two stages. The first stage is characterized by intense electrochemical activity, which lasts for several tens of seconds as illustrated in Fig. 13. Figure 13 shows the net current density on a 0.5-mm diameter Al wire, which was a single electrode contained in a regularly spaced 5-by-5 electrode array [98]. During coating formation, current flowed among all elements in the array, and the current on each element was monitored by separate zero resistance ammeter. The electrochemical activity indicated in Fig. 13 arises primarily from reduction of Cr^{6+} to Cr^{3+} and oxidation of Al to a hydrated oxide resulting in the formation of a mixed Al^{3+}/Cr^{3+} hydrated oxide. Hydrogen and oxygen reduction may also occur at coating formation potentials though gas evolution is not usually observed. These reactions may serve to increase the near-surface pH, which aids in the precipitation of a mixed Al–Cr hydrated oxide [99]. The overall formation reaction for a chromium–chromate coating on aluminum has been given as [100]:

$$Cr_2O_7^{2-} + 2Al + 2H^+ + H_2O \longrightarrow 2CrOOH_{(s)} + 2AlOOH_{(s)} \quad (2)$$

In "accelerated" formulations, this reaction is mediated by ferricyanide, and accelerated by fluoride as is discussed below. First stage coating growth results in round nanometer-sized nodules that nucleate quickly cover the surface [101]. Preferential nucleation and growth on local cathodic sites defined by local impurity element enrichment, and second-phase particle inclusions has also been reported [102, 103]. Coatings formed in just several seconds do confer useful levels of corrosion resistance, but are not as corrosion resistant as coatings formed by longer immersion times.

The reaction scheme indicated by Eq. (2) is conceptually useful because it illustrates

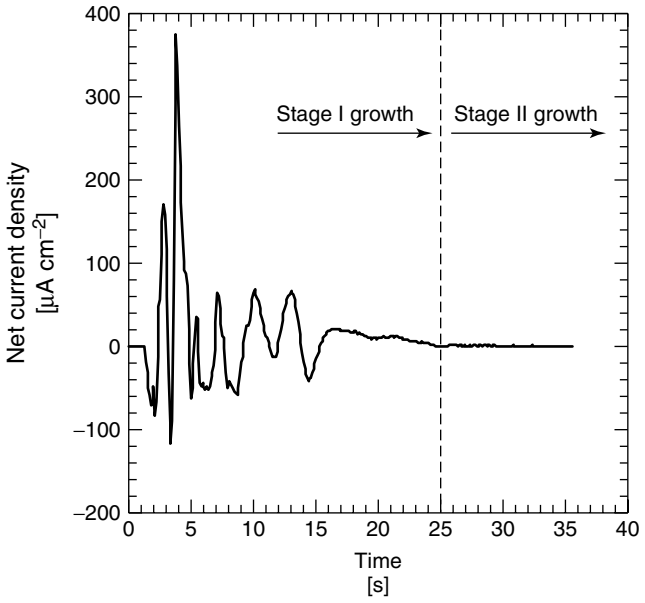


Fig. 13 Net electrochemical current during CCC formation on 99.999% Al illustrating the two stages of coating growth. Stage I growth is characterized by intense electrochemical activity. In stage II growth, there is little detectable electrochemical activity though the coating continues to thicken. In this experiment, the CCC solution consists of 50 mM K_2CrO_7, 50 mM NaF, and 3 mM $K_3Fe(CN)_6$ dissolved in a pH 1.6 HNO_3 solution. (From Ref. [98].)

coupling of Al oxidation and chromate reduction, followed by formation Cr(III) or mixed Cr/Al hydroxide. However, CCCs are usually far more Cr-rich than the stoichiometry of the reaction in Eq. (2) suggests [104, 105], and coatings continue to thicken with increased exposure time.

A second stage of coating growth occurs at longer contact times. This stage is characterized by continued coating thickening and a comparative absence of detectable electrochemical activity. Coatings grown through this second stage exhibit an increase in the Cr : Al and Cr(VI) : Cr(III) ratios [105]. In this stage of coating formation, condensation polymerization of a $Cr(OH)_3$ inorganic polymer "backbone" is an important component of film growth as shown in Fig. 14. The labile Cr(VI) reservoir also builds up in the coating by a condensation reaction. Condensation involves nucleophilic attack by dichromate of hydroxyl ligands on the Cr(III) or mixed Cr(III)/Al(III) hydroxide backbone deposited in stage I growth (Fig. 14) [106]. This results in the formation of Cr(III)–O–Cr(VI) linkages [107]. These linkages are characteristic of CCCs and are readily detectable by Raman spectroscopy [107]. This stage of CCC formation is in some ways like sol–gel coating formation [108], and results in an easily removed, gelatinous film, which subsequently hardens upon drying. Other components of film growth operate during this stage resulting in the incorporation

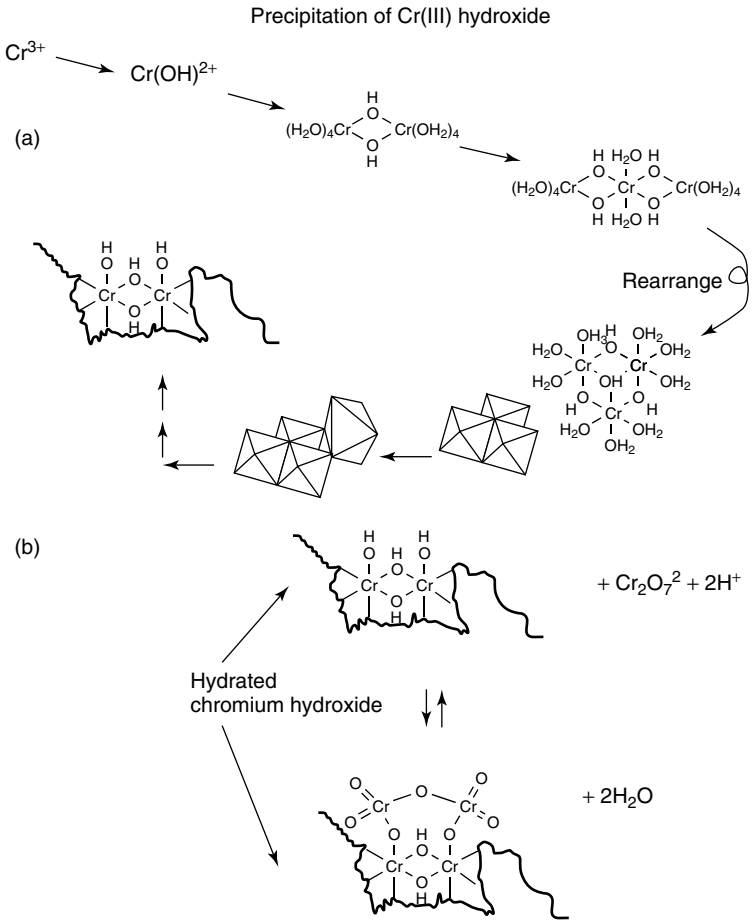


Fig. 14 (a) Schematic representation of the hydrolysis–polymerization–precipitation mechanism for $Cr(OH)_3$ "backbone" formation; (b) condensation of Cr(VI) on the Cr(III) backbone by nucleophilic attack of hydroxyl ligands in the backbone. (Adapted from Ref. [107].)

of minor coating bath ingredients such as ferricyanide and insoluble fluorides; however, these incorporation mechanisms are not yet well described. Additionally, a small electrochemical component of film growth probably occurs in stage II. Electrochemical film growth in stage II, while a minor component of overall coating rate, may be significant, because it continues to build the $Cr(OH)_3$ backbone and may act to form the coating preferentially at strong defect sites that were resistant to CCC formation earlier.

After removal from solution, CCCs are gelatinous and easily damaged by mechanical or chemical action. Immediately after CCC formation, it is possible to wipe the deposit off of a metal surface with a sponge. If a CCC is to be used for stand-alone corrosion protection, it is usually allowed to harden for at least 24 h before any further handling [109]. However, as CCCs

harden, they become decreasingly receptive to organic overcoats. Therefore, it is common for conversion-coated surfaces to be painted within the first 24 h after coating application [110].

5.3.2.4.2 **Chromium–phosphate Coatings** Chromium–phosphate conversion coatings (CPCCs) are widely used in aluminum coil coating operations for the good corrosion resistance and paint adhesion properties conferred by short contact time spray application. CPCCs are formed by contact with acidic solutions containing CrO_3, H_3PO_4, and NaF as the primary ingredients. Fluoride serves to dissolve the air formed oxide and activate the surface, while $CrPO_4$ and H_3PO_4 are the primary film-forming agents. Coating formation occurs by reduction of Cr(VI) to Cr(III) and precipitation of hydrated $CrPO_4$, Cr(III) and Al(III) hydroxides [111]. Depending on the bath formulation, substrate type, contact time, and temperature, CPCCs can be either amorphous [112], or crystalline [113]. Chromium–phosphate is often the predominant compound in the coating comprising up to 80% of freshly formed films [94, 114–116]. Most or all of the Cr in CPCCs is present in an insoluble Cr(III) form. Little or no Cr(VI) is present in the coating. As such, these coatings do not possess the self-healing characteristics of CCCs and provide corrosion resistance by barrier protection only.

5.3.2.4.3 **Cr(VI) and Cr(VI) Speciation** Cr(VI) speciation in coating baths is an important variable in CCC formation. Cr(VI) in solution can rapidly speciate via hydrolysis and condensation reactions to chromate, CrO_4^{2-}, dichromate, $Cr_2O_7^{2-}$, or bichromate $HCrO_4^-$ [117]. The predominant species depends on Cr(VI) concentration and pH as shown in Fig. 15, and not on the form of the salt or

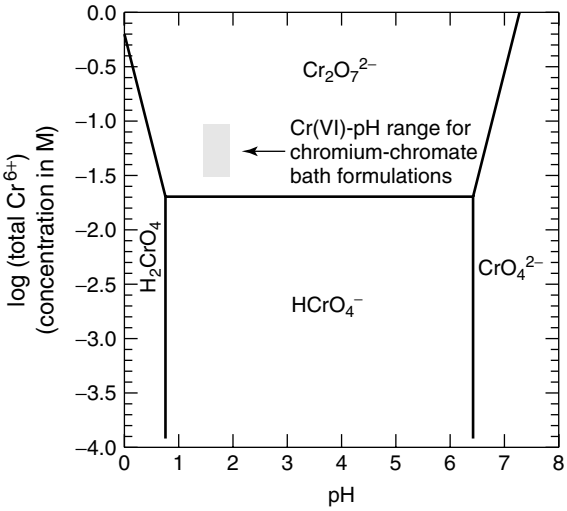


Fig. 15 Speciation of soluble Cr(VI) as a function of pH and concentration. Many commercial CCC bath formulations have Cr(VI) concentrations that fall in the shaded box so that the film-forming species is dichromate (equilibrium constants used in diagram construction from Baes and Mesmer [113]).

acid added to solution. Corrosion-resistant films can be formed over a wide range of pH suggesting that all three of these species are film formers to some extent. However, modern chromium–chromate and chromium–phosphate processes are operated at chromate concentrations and pH values at which dichromate is the predominant soluble species. Solution concentrations of 50 mM Cr(VI) and a pH of 1.6 are typical. Under these conditions, the total chromate concentration may vary by a factor of two or more without a significant impact on the film formation rate [118]. Some processes based on the use of trivalent Cr have also been developed [119]. Self-healing can be imparted to trivalent Cr coatings by contacting them with a solution that oxidizes some of the Cr(III) in the coating to Cr(VI) without otherwise damaging it.

5.3.2.4.4 **Activators and Accelerators** CCC formation is greatly aided by "activating" species such as fluoride, sulfate, nitrate, formate, acetate, and others [60]. Fluoride is particularly effective in promoting film growth and is often added to both chromium–chromate and chromium–phosphate bath formulations. Fluoride is typically added as NaF and mixed metal fluoride salts whose total concentration is in the 30 to 40 mM range. Fluoride attacks existing surface films, particularly on aluminum. It readily complexes Al^{3+} in solution and has the effect of lowering the Al content in CCCs. Consequently, CCCs are found to be enriched in Cr and of greater thickness when F^- is added to the bath [120].

The use of "accelerators" in chromium–chromate coating formulations dates to about 1970 [121]. Accelerators used in commercial CCC formulations include: ferricyanides, acetates, formates, and chlorides, among others [118]. Of these, potassium ferricyanide, $K_3Fe(CN)_6$, has been most widely studied and described in the literature. Potassium ferricyanide is added to CCC formulations in 2 to 5 mM concentrations to increase coating weight. The active component in this compound is the ferricyanide anion, which increases chromate reduction reaction kinetics that are normally slow on oxide covered surfaces [96]. On aluminum, ferricyanide, $Fe(CN)_6^{3-}$, is readily reduced to ferrocyanide, $Fe(CN)_6^{4-}$. Ferrocyanide is oxidized by chromate, which is subsequently reduced to its trivalent form contributing to film formation. Coupling substrate oxidation to chromate reduction through this ferri/ferrocyanide mediation mechanism increases the film formation rate, which results in a more corrosion-resistant coating. Ferricyanide is also incorporated into the CCC [61], with Fe : Cr ratios of 1 : 10 reported in at least two studies [91, 96]. Ferricyanide has been proposed to exist as mixed metal cyanide in CCCs [94, 122, 123], but any *direct* effect of these compounds on coating corrosion resistance or paint adhesion has not been clearly established.

5.3.2.4.5 **Coating Formation on Metallurgical and Structural Defects** CCC bath chemistries tend to be optimized for coating formation on the basis metal of an alloy, for example, Al, Zn, or Fe. Alloying element additions, particularly when segregated into second-phase particles, alter CCC formation locally. Some of these alterations have been characterized, but none are well understood. In Al alloys, for example, CCC formation from accelerated bath formulations has been reported to be both enhanced [103, 124, 125], and inhibited [91, 100, 126] at impurity-enriched

grain and cell boundaries and intermetallic particles such as Al_2Cu, Al_2CuMg, Al_3Fe, Al_7Cu_2Fe, and $Al_{12}Si(Fe,Mn)$ [91, 100, 103, 124, 125]. This response has been attributed to facile electron transfer at these sites, which permits reduction and precipitation of chromate. However, in the case of Cu-rich intermetallic particles, such as Al_2Cu and Al_2CuMg, the coating that forms is a thin chemisorbed cyano-rich film that prevents proper CCC formation locally [126, 127]. This results in a thinner, chromium-deficient coating at these locations for short coating times. For longer immersion times, coating defects of this type have been reported to persist [128], or to be diminished [91].

5.3.2.4.6 **CCC Morphology, Structure, and Composition** Thin chromium–chromate coatings consist of a mass of small nanometer-sized particles that nucleate and cover the entire alloy surface [101]. This nodular morphology is recognizable in thicker coatings, but these coatings tend to develop shrinkage cracks as the coating dries and hardens [123, 129] (Fig. 16). Both thin and thick coatings are conformal, and coatings readily form in pits and scratches on the alloy surface left over from deoxidation and surface machining. Both thin and thick coatings are amorphous [129, 130]. All coatings are three-dimensional with distinct horizontal layers and compositional variations that can be observed in ultramicrotomed coating cross sections [103, 124, 125, 131, 132] (Fig. 16).

Thin coatings are mixtures of hydrated Cr and Al oxides with a small amount of Cr (VI) present in the outer regions of the coating [105, 134, 135]. In thicker coatings, the Cr : Al and Cr(VI) : Cr(III) ratios increase substantially. Estimates of the Cr(VI) to total Cr ratio vary from 20 to 40% [105, 135], and composition–depth profiles indicate that most of the Cr(VI) resides in the outer portions of the coating consistent with the two-stage coating growth mechanism.

Coating compositions depend strongly on alloy substrate, bath formulation details of the processing parameters and coating age. There is general agreement that CCCs consist of a mixture of complex chromium compounds, other bath ingredients, and elements from the substrate, but opinions differ on the specific types of compounds and their relative abundance in the coating. Compounds proposed to exist within accelerated chromium–chromate coatings include: Cr_2O_3, $Cr_2O_3{\cdot}nH_2O$, $Cr(OH)_3$, CrOOH, $Cr(OH){\cdot}CrO_4$, $Cr_x(CrO_4)_y$, CrF_3, $CrFe(CN)_6$, AlOOH, Al_2O_3, and AlF_3 [94, 95, 120, 122, 130]. The coating model shown in Fig. 17 portrays a structural model that has evolved over the past several decades on the basis of X-ray photoelectron spectroscopy (XPS), Auger electron spectroscopy (AES), X-ray absorption near edge spectroscopy (XANES), transmission electron microscopy (TEM), SEM, and electron diffraction Spectroscopy (EDS) analyses [100]. Figure 17 also provides supporting composition depth profile data. In this model, the external surface of the coating consists of hydrated chromium oxides and fluorides, ferricyanide, and chromate. The bulk of the coating is a complex mixture of Cr oxides and hydroxides, oxyhydroxides fluorides, and chromium ferricyanide. The coating nearest the substrate contains hydrated aluminum oxides, metallic and oxidized forms of copper on Cu-bearing Al alloys, and chromium and aluminum oxyfluorides. Characterization of CCCs by Raman spectroscopy has shown that a significant component

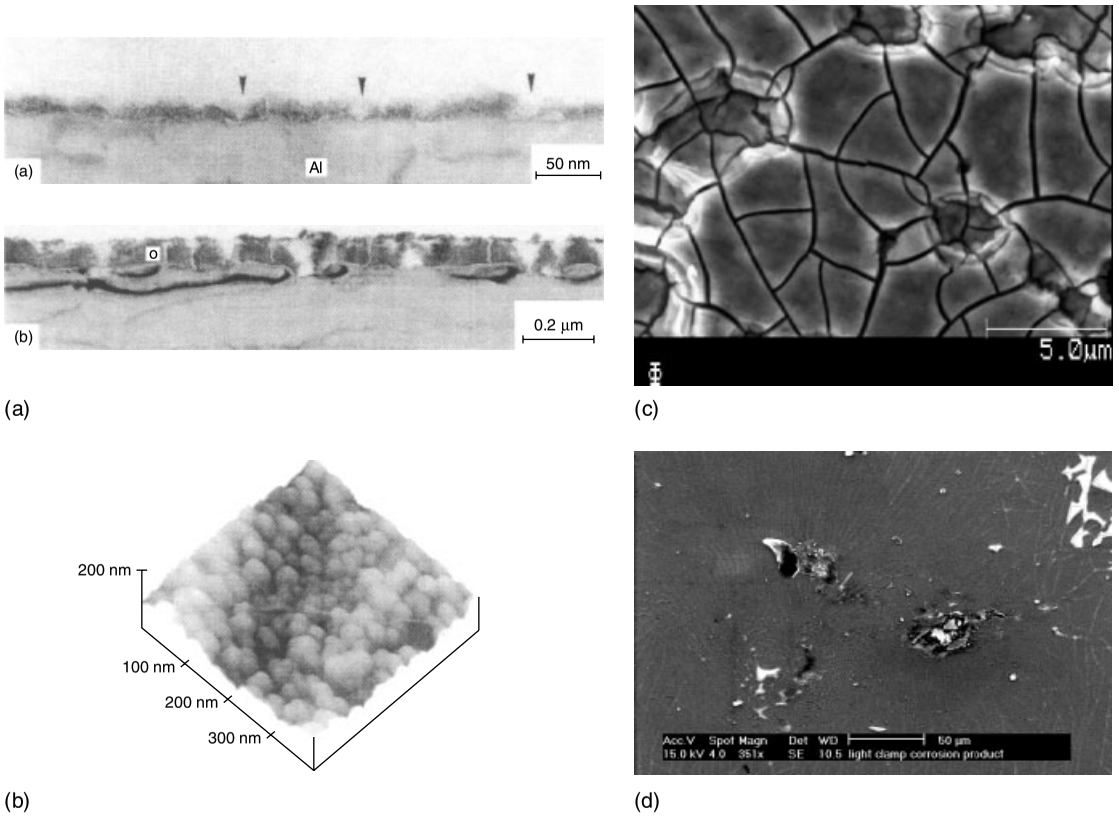


Fig. 16 (a) Ultramicrotomed cross sections of CCC formed by 5- (upper) and 30-s (lower) immersions in the coating bath. (From Ref. [102].) (b) AFM image of a 1-s CCC on the matrix phase of 2024-T3. (From Ref. [103].) (c) A scanning electron micrograph of an accelerated chromium–chromate coating applied by immersion for 180 s to 2024-T3 (Al–4.4Cu–1.5Mg–0.6Mn). (From Ref. [133].) (d) A scanning electron micrograph of a chromium–phosphate coating on a Zn–Al-plated steel surface. There is evidence of CCC cracking, and spalling in the upper right corner of the image (bright region). (Reproduced from R. G. Buchheit, Report to Holophane Lighting, Inc., 1999.)

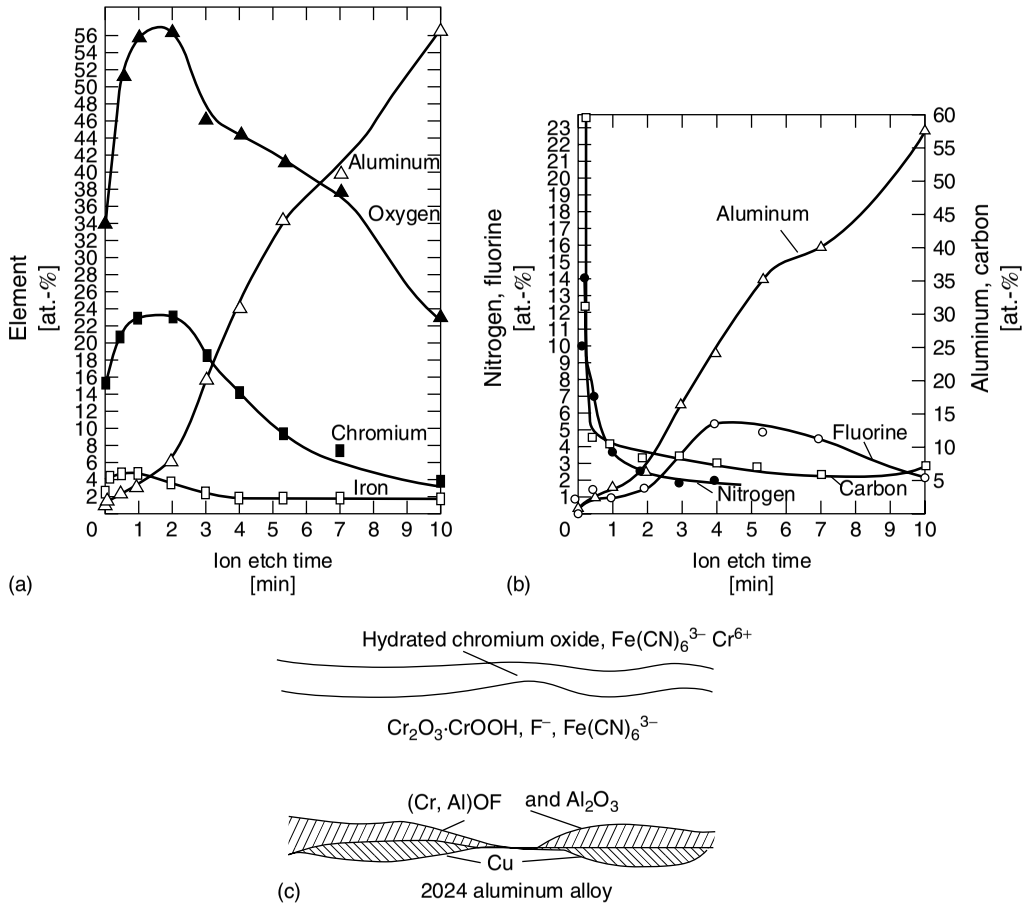


Fig. 17 (a, b) Composition–depth profiles for the major elements found in chromium–chromate CCCs. (From Ref. [94].) (c) A CCC structural model illustrating the distributions of compounds through the thickness of a CCC. (From Ref. [100].)

of the coating consist of a $Cr(OH)_3$ polymer to which chromate or dichromate is reversibly bound [107].

The accurate determination of the Cr(VI) content of CCCs is an issue that has attracted special attention. Measurement of Cr(VI) in CCCs is complicated by the fact that the species can be inadvertently reduced by photoreduction or ultrahigh vacuum exposure [79, 104, 136]. This complicates analysis and interpretation of CCC chemistry by XPS and AES. Other techniques such as XANES and X-ray absorption fine-structure (EXAFS) measurements can be carried out at under ambient environmental conditions and have been used to study CCC chemistry and structure without risk of inadvertent Cr(VI) reduction [137]. X-ray absorption spectra for Cr are distinctive in that there is a discrete absorption peak associated with Cr(VI) that occurs at energies just below the main Cr K_α absorption edge (Fig. 18). This greatly facilitates Cr(VI) analysis and has been exploited to show that range of Cr(VI) in CCCs typically ranges from 20 to 40%. XANES has also been used to study chromate leaching, the effects of aging, and the effects of different processing chemistries and procedures [105, 138–141].

EXAFS phenomena arise from the effect of short-range molecular structure on the details of the absorption spectrum [137]. EXAFS probes an environment within a 6-Å range around an absorbing atom. This technique has been used to study the coordination environment around Cr

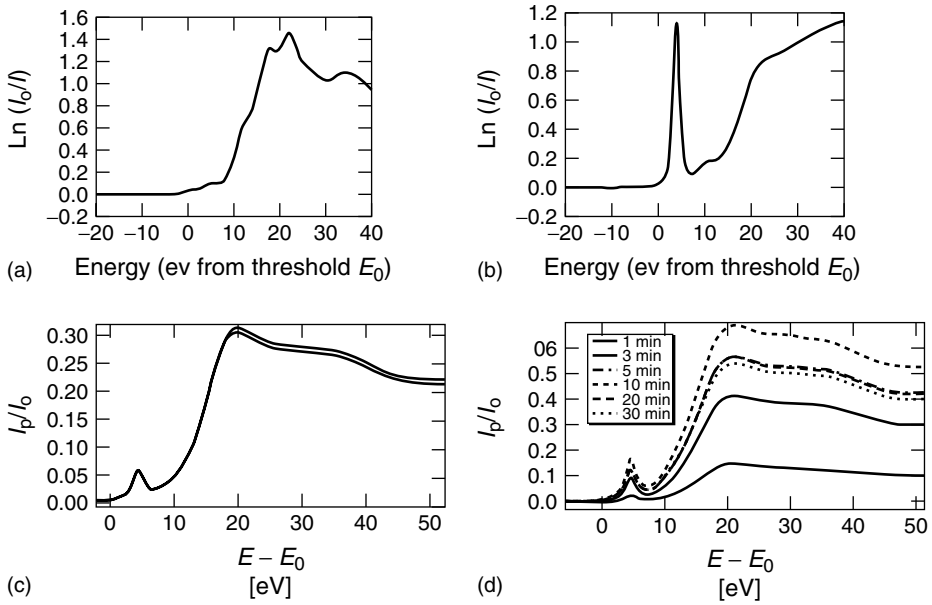


Fig. 18 X-ray absorption spectra for (a) Cr_2O_3, and (b) K_2CrO_4 standards. (From Ref. [138].) (c) Replicate absorption spectra from CCCs on an Al–Mn alloy exhibit a preabsorption edge peak that indicated the presence of Cr(VI); (d) absorption spectra collected as a function of immersion time in a chromate conversion coating bath illustrating the changes in Cr(VI) and total Cr in the coating. (Reproduced from M. W. Kendig, A. J. Davenport, H. S. Isaacs, *Corrosion Sci.* (**1993**) *34*, 41.)

in CCCs and has shown that Cr(VI) is tetrahedrally coordinated, and Cr(III) is octahedrally coordinated with surrounding oxygen atoms. Cr(VI)–O bond lengths have been measured at 1.71 ± 0.03 Å; Cr(III)–O bond lengths are measured to be 1.99 ± 0.01 Å [122].

Chromium–phosphate coatings can be either amorphous or crystalline. Crystalline coatings consist of $CrPO_4$, which is the predominant compound, and a lesser amount of a mixture of compounds. Minor compounds reported in CPCCs include Cr_2O_3, $AlPO_4$, CrF_3, $Cr(OH)_3$, and $Al(OH)_3$. Cr(VI) is not a component of CPCCs and these coatings do not self-heal in the manner that CCCs do.

5.3.2.5 Corrosion Protection

5.3.2.5.1 Corrosion Protection Mechanisms A large component of CCC corrosion protection is due to the barrier properties associated with the insoluble components of the coating. This barrier prevents contact of the attacking environment with the underlying metal and slows oxygen and hydrogen reduction reactions that support metal dissolution. In cases in which aging and heating immobilize the leachable Cr(VI), some large measure of corrosion protection may be retained because of barrier properties [142]. CCC corrosion protection has also been evaluated in the context of the bipolar membrane model for passivity of ferrous metals [143, 144]. The structure and chemistry of CCCs is consistent with that required to enable this mechanism. In the CCC, the outer layer of the coating is negatively charged and cation selective, while the inner layer of the coating is positively charged and is anion selective. Ion transfer through the coating is therefore constrained, resulting in reduced surface reactivity.

Perhaps the most widely known component of corrosion protection is "self-healing". Self-healing refers to the distinctive ability of a chromate conversion coating to heal small chemical or mechanical defects that expose unprotected underlying metal. The classic manifestation of self-healing is the absence of corrosion in scribe marks made through CCCs on samples exposed to salt spray. The self-healing process involves: (1) liberation of Cr(VI), latent in the coating, into an attacking aqueous environment; (2) migration of the Cr(VI) to an incipient defect; and (3) reduction to insoluble Cr(III) hydroxide or interaction with the corrosion product to stifle further corrosion. The key attribute of CCCs in this regard is their ability to store and release Cr(VI) into an attacking solution. The Cr(VI) reservoir in CCCs is a function of coating weight or thickness, and has be estimated to be on the order of 10^{-7} mol Cr(VI) cm^{-2} of CCC [145]. Release of dichromate occurs by hydrolysis of Cr(III)–O–Cr(VI) bonds in the porous $Cr(OH)_3$ network in the CCC according to the following equilibrium reaction [145]:

$$\mathrm{Cr(III)–OH_{(s)} + Cr(VI)O_{4(aq)}^{2-} + H_{(aq)}^{+} \longleftrightarrow Cr(III)–O–Cr(VI)O_{3(s)}^{-} + H_2O} \quad (3)$$

Equilibrium between the Cr(III)/Cr(VI) mixed oxide of the CCC and dichromate in solution, hence the extent of dichromate release, is proposed to be governed by Langmuir-like adsorption behavior that depends on solution ionic strength, pH, and the ratio of CCC surface area to solution volume. Therefore, the extent of Cr(VI) release is not simply governed by solubility of dichromate in solution, or total amount of Cr(VI) in the mixed oxide, as is more closely the case for $SrCrO_4$ pigments in primer coatings. Kinetically,

the rate of chromate release appears to be well described by a diffusion control of Cr(VI) in the CCC [146].

Equation (3) also shows that the Cr(III)/Cr(VI) equilibrium is pH-dependent in a manner that favors Cr(VI) uptake during coating formation, and Cr(VI) release during service. Dichromate adsorption is favored at low pH – typical of coating baths. Dichromate release is favored under higher pH conditions; more typical of service conditions in which release and self-healing are necessary.

Opinions vary on how important a component CCC self-healing is to overall corrosion resistance in coating systems since the soluble chromate reservoir in a CCC is small compared to that in $SrCrO_4$-bearing primer coatings. However, recent experiments using an exposure cell that duplicates important aspects of a scratch demonstrate the self-healing effect is potent for CCCs [147]. In these experiments, a conversion-coated Al alloy surface and a bare alloy surface (the simulated scratch) are placed a few millimeters apart facing one another. Solution is then introduced into the gap. After several hours, Cr(VI) leached from the coating can be detected in the solution. Hydrated chromium-containing deposits are observed on the bare originally bare surface, and its corrosion resistance is observed to increase by several orders of magnitude as measured by polarization resistance methods.

5.3.2.5.2 **Aging and Heating** After removal from the coating bath, CCCs dehydrate and harden. The film transforms from a fragile gel to a robust, damage tolerant coating in a matter of a few hours. Aging effects appear to be due to consolidation in the Cr(III) backbone, which can be detected by EXAFS measurements [133, 148, 149]. How this consolidation occurs is still a matter of speculation, but the structural rearrangement appears to be closely linked to coating dehydration [148]. Shrinkage cracking also appears to be a consequence of backbone consolidation (Fig. 16). Backbone rearrangement over the time-frame of days to months produces profound changes in coating properties. Losses in corrosion resistance begin to be detected in times as short as 20 days after coating formation. In an extreme case, after 100-day exposure to ambient laboratory air, there was no evidence of corrosion protection in an impedance spectroscopy-based test conducted on a 1-min CCC on 2024-T3 exposed chloride solution [148]. Chromate leaching also diminishes with time even though the Cr(VI) content of the coating remains the same. This indicates that backbone consolidation traps Cr(VI) in the coating [133]. Ultimately, over tens of years, the Cr(VI) content of CCCs diminishes. No Cr(VI) was detected by XANES measurements on 20-year-old CCCs on 7475-T73 exposed to the ambient environment. However, CCCs on the same component that were covered by a paint layer appears to retain an amount of Cr(VI) that is commonly observed in freshly formed coatings [150]. This result clearly implicates dehydration in long-term coating aging.

CCCs are not heat-tolerant [151, 152]. Exposure to elevated temperature accelerates dehydration, consolidation of the Cr(III) backbone, and losses in properties described above. Losses in CCC corrosion protection, Cr(VI) leaching, and increases in shrinkage cracking are profound when coatings are subject to temperatures in excess of 60 °C. Corrosion resistance in salt spray exposure testing and electrochemical testing can be completely lost when CCCs are heated for more than 15 min at temperatures in excess of 60 °C [133].

5.3.2.6 Macroscopic Characteristics of Chromate Conversion Coatings

5.3.2.6.1 CCC Weight, Thickness, and Color

In the metal finishing trade, CCC thickness is generally referred to in terms of coating weight [153], which is easily measured by chemical stripping methods. Coating weights range from less than 1.0 mg dm^{-2} for the thinnest coatings to greater than 10 mg dm^{-2}. This range translates to thicknesses of 10 nm to 3 µm. The color of CCCs ranges from clear to dark brown depending on coating weight, chemistry, and alloy substrate type. In general, coatings with weights less than about 1 mg dm^{-2} are clear to light yellow, 1.1 to 3.8 mg dm^{-2} coatings are iridescent to yellow, and 3.2 to 11 mg dm^{-2} coatings will range from deep yellow to brown. Green coloration in coatings is due to the presence of trivalent chromium, which is common in CPCCs.

5.3.2.6.2 Chemical and Corrosion Resistance

The corrosion resistance of CCCs depends on thickness and coating age. Corrosion resistance has been observed to scale with total chromium content [153]. Some studies have found that corrosion resistance does scale with Cr(VI) content [154], while others have found no such correlation [155]. Corrosion resistance is evaluated by continuous or cyclic accelerated exposure testing and electrochemical methods. On aluminum alloys, heavy CCCs will resist pitting for as long as 400 to 1000 h [156]. CCC-coated surfaces will exhibit total impedances of 1 to 2 MΩ cm^{-2} after exposure to aerated 0.5 M NaCl solution for 24 h. Such coatings can be expected to withstand 168 h of salt spray exposure without serious pitting [157]. CCCs usually perform well in mild neutral environments, but do not fare as well under more acidic conditions such as those containing SO_2 [158]. As described above, corrosion resistance will diminish with age in a matter of days due primarily to coating dehydration, which causes shrinkage cracking and immobilization of leachable hexavalent chromium.

5.3.2.6.3 Mechanical and Thermal Stability

Freshly formed coatings are gelatinous and can be wiped off easily. As the coating dries, it hardens considerably. CCCs dried for at least 24 h are mechanically robust. Coating weight determinations by chemical stripping of the CCC are nearly impossible to carry out after this time. Coatings will withstand some mechanical damage, but are not nearly as abrasion resistant as anodized coatings. CCCs rapidly lose their corrosion resistance if exposed to temperatures in excess of about 60 °C. Corrosion resistance on Al alloys can be completely lost by exposure times as short as 15 min at 150 °C. This occurs as a result of coating dehydration, which, like aging, causes shrinkage cracking and immobilization of leachable hexavalent chromium.

5.3.2.6.4 Paint Adhesion

Typical aircraft coating systems consist of a CCC foundation layer, a primer coating, and a topcoat [159]. In these systems, the primary function of the CCC is to promote initial and long-term adhesion of the organic coating on the metal substrate. Organic coating adhesion is promoted by surface topography, surface cleanliness, and possibly coating acidity [123, 160]. Long-term interfacial adhesion is fostered by the high corrosion resistance provided by the inhibiting effects of Cr(VI) leached from the primer and the CCC [59].

5.3.2.6.5 **Electrical Contact Resistance** Chromated metal surfaces exhibit low electrical contact resistance as measured with a flat metal electrode applied with a small impinging load. Since CCCs are thin and brittle, they are easily breached allowing metal-to-metal contact. In service, mechanical breaches can sometimes be tolerated without risk of corrosion because of the self-healing nature of the coating. In some instances, mechanical damage is too severe and galvanically assisted atmospheric corrosion will increase the contact resistance to such an extent that rework of the electrical contact is required [161]. Low electrical contact resistance also makes conversion-coated surfaces amenable to various types of spot welding and arc welding procedures.

Electrical contact resistance is distinct from the intrinsic coating resistivity, which is quite high. Al oxide films thickened by contact with chromate solutions [162], and CCCs themselves [160], demonstrate high electrical resistance. DC resistances of CCCs measured with a small (4×10^{-3} cm^2) Hg droplet range from 10^{10} to $10^{12}\Omega$ [163].

5.3.2.7 **Chromate-free Coatings** Many different chromate-free coating chemistries and application methods have been devised in response to the desire to reduce or eliminate the use of Cr(VI) in the workplace and the environment. Several classes of Cr-free coatings are briefly described below. More information on these and other types of Cr-free coatings can be found in recent reviews on the subject [159, 164–166].

5.3.2.7.1 **Sol–gel Coatings** Sol–gel coatings, usually less than 1-μm thick, are formed by hydrolysis, condensation, and polymerization of metal alkoxides from alcohols, or metal aquo-ions or hydroxides from aqueous solutions [167]. Sol–gel systems are chemically diverse and coatings have been devised on the basis of a range of metal oxide systems including: Si, Al, Ti, B, Zr, Nb, Y, Ge, Sn, Zn, Hf, and Ta. Of these, SiO_2, ZrO, SiO_2/TiO_2, and SiO_2/Al_2O_3 have been widely studied. This chemical diversity makes it possible to tailor coatings for specific properties. Sol–gel coatings form metal oxygen covalent bonds to the metal interface and covalent bonds with organic molecules at the sol–gel surface. This gradation in bonding makes sol–gel coatings excellent adhesion promoters for organic coatings. The intrinsic corrosion resistance of sol–gel coatings can be high if the coating forms as a barrier layer, but there is no evidence that the are self-healing.

5.3.2.7.2 **Hydrothermal Coatings from Alkaline Solutions** Aluminum oxide will thicken during exposure to hot water. This stimulates the formation of hydrated aluminum oxide that is amorphous at short contact times, but becomes crystalline at longer times. Thickening is accelerated under oxidizing and alkaline conditions. Hydrothermal coatings are formed using practices that are similar to older alkaline chromate, and chromate–phosphate coating methods, but the chemistries have been modified to be more environmentally benign. Chemistries based on the used of lithium [168–171], and permanganate solutions [75, 172, 173] been reported. Normally, these coatings must be sealed to achieve high levels of corrosion resistance on the most susceptible alloys.

5.3.2.7.3 **Rare Earth Metal Coatings** Research and development conversion coatings for ferrous and aluminum alloys based on the use of rare earth metal salts (REMs) has been extensive over the past 20 years. This work has been extensively reviewed in a recent publication [174]. Rare earth metal coatings, notably those based on the use of Ce, form by precipitation under the alkaline conditions promoted by cathodic activity on a metal surface. Precipitation can be local as in the case of precipitation at Cu-rich intermetallic particles in Al alloys, or general as promoted by cathodic polarization. Cerium is the chief REM used in these types of coatings, but inhibition has been demonstrated by La, Pr, Y, and others. REM treatments are sometimes used in conjunction with hydrothermal film thickening, or are used to seal porous anodized coatings.

References

1. K. Ogle, M. Wolpers, Phosphate conversion coatings in *ASM Handbook Vol. 13A: Corrosion: Fundamentals and Protection*, ASM International, Ohio in press.
2. W. Rausch, *The Phosphating of Metals*, Finishing Publications, Teddington, UK, 1990.
3. G. Lorin, *La Phosphatation des Métaux*, Editions Eyrolles, Paris, 1973.
4. H. P. Volkland, H. Harms, B. Müller et al., *Appl. Environ. Micorbiol.* **2000**, *66*, 4389.
5. H.-P. Volkland, H. Harms, K. Kaufmann et al., *Corros. Sci.* **2001**, *43*, 2135–2146.
6. G. W. Jernstedt, *Trans. Electrochem. Soc.* **1943**, *83*, 361.
7. CRM, Surface reactivity of compressed steel sheets in the course of a double alkaline degreasing and phosphatation treatment, European Community Report, EUR11213, 1988.
8. S. Maeda, *Prog. Org. Coat.* **1983**, *11*, 1.
9. M. Wolpers, J. Angeli, *Appl. Surf. Sci.* **2001**, *179*, p. 281–291.
10. I. Van Roy, H. Terryn, G. Goemine, *Colloids Surf.* **1998**, *136*, 89.
11. P.-E. Tegehall, *Colloids Surf.* **1990**, *49*, 373.
12. W. Machu, *Korros. Metall.* **1941**, *17*, 157.
13. W. Machu in *Interface Conversion for Polymer Coatings* (Eds.: P. Weiss, G. D. Cheever), American Elsevier Publishing Company, New York, 1968, pp. 128–149.
14. J. W. Schultze, N. Müller, U. König, R. Krumm, *Proceedings of the Symposium on Critical Factors in Localized Corrosion III*, PV 98-17, The Electrochemical Society, N. J., Boston, MA, pp. 31–41.
15. A. Losch, E. Klusmann, J. W. Schultze, *Electrochim. Acta* **1994**, *39*, 1183.
16. P. Xin, *Finishing* **1989**, *13*, 24.
17. K. H. Stellnberger, M. Wolpers, T. Fili et al., *Faraday Discuss.* **1997**, *107*, 307.
18. E. Klusmann, U. König, J. W. Schultze, *Mater. Corros.* **1995**, *46*, 83.
19. R. W. Miller, M. Petschel Jr., R. G. Hart, *Met. Finish.* **1994**, *92*, 13.
20. S. Maeda, T. Asai, S. Arai et al., *Trans. ISIJ* **1982**, *22B*, 390.
21. S. Maeda, *J. Coat. Technol.* **1983**, *55*(707), 43.
22. P.-E. Augustsson, I. Olefjord, Y. Olefjord, *Werkst. Korros.* **1983**, *34*, 563.
23. J. A. Slane, S. P. Clough, J. Riker–Nappier, *Metall. Trans. A* **1978**, *9A*, 1840.
24. S. Wakano, N. Usuki, M. Nishihara et al., *Tetsu to Hegané* **1980**, *66*, 945.
25. T. Fukuzuka, K. Kajiwara, K. Miki et al., *Tetsu to Hegané* **1980**, *66*, 935.
26. A. Neuhaus, M. Gebhardt in *Interface Conversion for Polymer Coatings* (Eds.: P. Weiss, G. D. Cheever), American Elsevier Publishing Company, New York, 1968, pp. 91–120.
27. H. W. K. Ong, L. M. Gan, T. L. Tan, *J. Adhes.* **1985**, *18*, 227.
28. W. J. van Ooij, *Surf. Interface Anal.* **1986**, *9*, 367.
29. W. J. van Ooij, T. H. Visser, *Spectrochim. Acta* **1984**, *39B*, 1541.
30. M. Richardson, D. R. Gabe, *Trans. Inst. Met. Finish.* **1990**, *68*, 99.
31. T. Kanamaru, T. Kawakami, S. Tanaka et al., *Tetsu to Hagané* **1991**, *77*, 192.
32. W. J. van Ooij, *Proc. ACS Div. Pol. Mat. Sci. Eng.* **1985**, *53*, 698.
33. S. Maeda, M. Yamamoto, *Prog. Org. Coat.* **1998**, *33*, 83.
34. Y. Arnaud, E. Sahakian, M. Romand et al., *Appl. Surf. Sci.* **1988**, *32*, 281.
35. T. Sugana, L. Kucacka, N. Carciello et al., *J. Mater. Sci.* **1991**, *26*, 1045.
36. W. J. van Ooij, A. Sabata, *J. Coat. Technol.* **1989**, *61*, 51.

37. Y. Arnaud, E. Sahakian, J. Lenoir et al., *Appl. Surf. Sci.* **1988**, *32*, 296.
38. N. Satoh, *Surf. Coat. Technol.* **1987**, *30*, 171.
39. S. Maeda, T. Asai, H. Okada, *Corros. Eng. (Boshoku Gijutsu)* **1982**, *31*, 268.
40. G. D. Cheever, *J. Paint Technol.* **1969**, *41*, 259.
41. M. Khaleghi, D. R. Gabe, M. O. W. Richardson, *Wear* **1979**, *55*, 277.
42. A. Losch, J. W. Schultze, *J. Electroanal. Chem.* **1993**, *359*, 39.
43. A. Losch, J. W. Schultze, H.-D. Speckmann, *Appl. Surf. Sci.* **1991**, *52*, 29.
44. R. W. Zurilla, V. Hospadaruk, SAE Technical Paper No 780187, 1978.
45. L. Mészaros, G. Lendvay-Györik, B. Lengyel, *Mater. Chem. Phys.* **1989**, *23*, 267.
46. W. Machu, *Korros. Metall.* **1944**, *20*, 6–16.
47. K. Kiss, M. Coll-Palagos, *Corrosion* **1987**, *43*, 8.
48. N. Satoh, T. Minami, *Surf. Coat. Technol.* **1988**, *34*, 331.
49. W. Machu, *Korros. Metall.* **1941**, *17*, 157.
50. A. Jardy, R. Rosset, R. Wiart, *J. Appl. Electrochem.* **1984**, *14*, 537.
51. A. Nazarov, D. Thierry, *J. Electrochem. Soc.* **1998**, *145*, L39.
52. E. L. Ghali, R. J. A. Potvin, *Corros. Sci.* **1972**, *12*, 583.
53. E. Sahakian, A. Roche, J. Lenoir et al., *J. Chim. Phys.* **1987**, *84*, 269.
54. K. Ogle, C. Gabrielli, M. Keddam et al., *J. Electrochem. Soc.* **1994**, *141*, 2655.
55. K. Ogle, S. Weber, *J. Electrochem. Soc.* **2000**, *147*, 1770.
56. H. Issacs, *J. Electrochem. Soc.* **1991**, *138*, 722.
57. K. Ogle, V. Baudu, L. Garrigues, X. Phillips, *J. Electrochem. Soc.* **2000**, *147*, 3654.
58. M. Stratmann, H. Streckel, *Werkst. Korros.* **1992**, *43*, 316.
59. T. Biestek, J. Weber, *Electrolytic and Chemical Conversion Coatings*, Porticullis Press Limited-Redhill, Surrey, UK, 1976.
60. S. Wernick, R. Pinner, P. G. Sheasby, Chemical conversion coatings, *The Surface Treatment and Finishing of Aluminum and its Alloys*, 5th ed., ASM International, Metals Park, Ohio, 1987, pp. 220–284, Vol. 1.
61. O. Bauer, O. Vogel, German Patent Specification 226 776, 1923.
62. O. Bauer, O. Vogel, German Patent Specification 423 758, 1923.
63. J. Spruance, U. S. Patent 2 438 887, 1945.
64. W. Marchand, *Electroplat. Met. Finish.* **1961**, *14*, 439.
65. S. Spring, K. Woods, *Met. Finish.* **1981**, *79*, 49.
66. G. W. Ostrander, *Plating* **1951**, *38*, 1033.
67. N. J. Newhard, *Met. Finish.* **1981**, *68*, 69.
68. P. O. O'Brien, A. Kortenkamp, *Trans. Met. Chem.* **1995**, *20*, 636.
69. IARC, Monograph on the Evaluation of the Carcinogenic Risk of Chemicals to Humans, Chromium, Nickel and Welding, International Agency for the Research on Cancer, Lyon, 1990, Vol. 49.
70. Y. Suzuki, K. Fukuda, *Arch. Toxicol.* **1990**, *64*, 169.
71. Y. Suzuki, *Ind. Health* **1990**, *28*, 9.
72. D. Stearns, K. Wetterhahn, *Chem. Res. Toxicol.* **1994**, *7*, 219.
73. P. Lay, A. Levina, *J. Am. Chem Soc.* **1998**, *120*, 6704.
74. M. Krumploc, J. Rocek, *J. Am. Chem Soc.* **1979**, *101*, 3206.
75. J. W. Bibber, *Met. Finish.* **1993**, *91*, 46.
76. D. E. Tonini, Hot dip galvanized coatings, *Metals Handbook*, 9th ed., ASM International, Metals Park, Ohio, 1987, pp. 321–422, Vol. 5.
77. R. H. Abu Zahara, A. M. Shams El Din, *Corros. Sci.* **1965**, *5*, 517.
78. H. E. Townsend, R. G. Hart, *J. Electrochem. Soc.* **1984**, *131*, 1345.
79. G. P. Halada, C. R. Clayton, *J. Electrochem. Soc.* **1991**, *138*, 2921.
80. K. Asami, M. S. DeSa, V. Ashworth, *Corros. Sci.* **1986**, *26*, 15.
81. R. E. Marce, Cadmium plating, *Metals Handbook*, 9th ed., ASM International, Metals Park, Ohio, 1987, pp. 256–269, Vol. 5.
82. R. M. Hudson, Pickling of iron and steel, *Metals Handbook*, 9th ed., ASM International, Materials Park, Ohio, 1987, pp. 68–82, Vol. 5.
83. A. J. Sedricks, *Corrosion of Stainless Steels*, 2nd ed., John Wiley & Sons, New York, 1996, p. 163–175.
84. J. D. Edwards, U. S. Patent No. 1 946 151, 1934.
85. J. D. Edwards, U. S. Patent No. 1 946 152, 1934.
86. J. D. Edwards, U. S. Patent No. 1 946 153, 1934.
87. T. Biestek, J. Weber, *Electrolytic and Chemical Conversion Coatings*, Portcullis

Press Limited-Redhill, Surrey, UK, 1976, pp. 319–320.
88. R. P. Marshall, *Met. Ind.* **1947**, *71*, 93.
89. Pyrene Co. Ltd., UK Patent 441 088, 1936.
90. Continentale Parker, French Patent 698 699, 1931.
91. P. L. Hagans, C. M. Haas, *Surf. Interface Anal.* **1994**, *21*, 65.
92. Henkel Corporation, International Patent Application, PCT/US92/04962, 1993.
93. L. J. Bailin, Kostinko, U. S. Patent 5 123 978, 1992.
94. J. A. Treverton, N. C. Davies, *Met. Technol.* **1977**, *4*, 480.
95. J. A. Treverton, N. C. Davies, *Surf. Interface Anal.* **1981**, *3*, 194.
96. L. Xia, R. L. McCreery, *J. Electrochem. Soc.* **1999**, *146*, 3696.
97. H. H. Uhlig, A. Geary, *J. Electrochim. Soc.* **1954**, *101*, 215.
98. W. Zhang, B. Hurley, R. G. Buchheit, *J. Electrochem. Soc.* **2002**, *149*, B357.
99. P. L. Hagans, C. M. Haas, Chromate conversion coatings, *Metals Handbook*, Surface Engineering, ASM International, Metals Park, Ohio, 1987, pp. 389–411, Vol. 5.
100. E. Hughes, R. J. Taylor, B. W. R. Hinton, *Surf. Interface Anal.* **1997**, *25*, 223.
101. D. J. Arrowsmith, J. K. Dennis, P. Sliwinski, *Trans. Inst. Met. Finish.* **1984**, *62*, 117.
102. G. M. Brown, K. Shimuzu, K. Kobyashi et al., *Corros. Sci.* **1993**, *34*, 1045.
103. J. R. Waldrop, M. W. Kendig, *J. Electrochem. Soc.* **1998**, *145*, L11.
104. K. Asami, M. Oki, G. E. Thompson et al., *Electrochim. Acta* **1987**, *32*, 337.
105. M. W. Kendig, A. J. Davenport, H. S. Isaacs, *Corros. Sci.* **1993**, *43*, 41.
106. M. Henry, J. P. Jolivet, L. Livage, Aqueous chemistry of metal cations: hydrolysis, condensation, and complexation, *Structure and Bonding*, Springer-Verlag, Berlin, Germany, 1992, pp. 155–206, Vol. 77.
107. L. Xia, R. L. McCreery, *J. Electrochem. Soc.* **1998**, *145*, 3083.
108. J. C. Brinker, G. W. Scherrer, *Sol-Gel Science: The Physics and Chemistry of Sol-Gel Processing*, Harcourt, Brace, Jovanovich, Boston, Mass., 1990.
109. Department of Energy Specification 9904151, Coating, Chromate on Aluminum, 1989.
110. MIL-C-5541E, Chemical Conversion Coatings on Aluminum and Aluminum Alloys, NAEC, Lakehurst, N. J., November, 1990.
111. R. A. Haaksma, J. R. Weir, Proceedings of the 27th International SAMPE Technical Conference, SAMPE, October, 1995, p. 1074.
112. J. A. Treverton, A. Bosland, J. M. Brown, *Corros. Sci.* **1990**, *30*, 1159.
113. L. Fedrizzi, F. Marchetti, *J. Mater. Sci.* **1991**, *26*, 1931.
114. N. J. Newhard Jr., *Met. Finish.* **1972**, *70*, 49.
115. N. J. Newhard Jr., *Met. Finish.* **1972**, *70*, 66.
116. L. A. Nimon, G. K. Korpi, *Plating* **1972**, *59*, 421.
117. C. F. Baes Jr., R. E. Mesmer, *Hydrolysis of Cations*, Wiley & Sons, New York, 1976.
118. F. W. Eppensteiner, M. R. Jenkins, Chromate conversion Coatings, *Metal Finishing, Guidebook and Directory Issue*, Hackensack, N.J.: Metals and Plastics Publications, 1999, pp. 494–507.
119. F. Pearlstein, V. S. Agarwala, *Plat. Surf. Finish.* **1994**, *81*, 50.
120. A. Katzman, G. Malouf, R. Bauer et al., *Appl. Surf. Sci.* **1979**, *2*, 416.
121. N. J. Newhard Jr., *Met. Finish.* **1972**, *70*, 69.
122. F. W. Lytle, R. B. Greegor, G. L. Bibbins et al. *Corros. Sci.* **1995**, *37*, 349.
123. J. A. Treverton, M. P. Amor, *Trans. Inst. Met. Finish.* **1982**, *60*, 92.
124. G. M. Brown, K. Shimuzu, K. Kobayashi et al., *Corros. Sci.* **1992**, *33*, 1371.
125. G. M. Brown, K. Shimuzu, K. Kobayashi et al., *Corros. Sci.* **1993**, *35*, 253.
126. W. R. McGovern, P. Schmutz, R. G. Buchheit et al., *J. Electrochem. Soc.* **2000**, *147*, 4494.
127. G. P. Halada, C. R. Clayton, M. J. Vasquez et al., *Critical Factors in Localized Corrosion III*, The Electrochemical Society, Pennington, N. J., PV 98-17, 1998, pp. 300–310.
128. M. J. Vasquez, G. P. Halada, C. R. Clayton et al., *Corrosion and Corrosion Prevention in Light Metals*, The Electrochemical Society, Pennington, N. J., PV 00–23, 2001, pp. 57–68.
129. L. Kintrup, L. de Riese-Meyer, *Inst. Phys. Conf. Ser.* **1991**, *119*, 257.
130. Z. Yu, H. Ni, G. Zhang et al., *Appl. Surf. Sci.* **1992**, *62*, 217.
131. R. C. Furneaux, G. E. Thompson, G. C. Wood, *Corros. Sci.* **1979**, *19*, 63.

132. G. M. Brown, K. Shimizu, K. Kobayashi et al., *Corros. Sci.* **1993**, *34*, 1853.
133. V. Laget, H. S. Isaacs, C. S. Jeffcoate et al., *ATB Metall.* **2000**, *40–41*, 295.
134. J. Wan, G. E. Thompson, K. Lu et al., *Physica, B* **1995**, *208* & *209*, 511.
135. J. A. Treverton, M. P. Amor, *J. Mater. Sci.* **1988**, *23*, 3706.
136. A. G. Schrott, G. S. Frankel, A. J. Davenport et al., *Surf. Sci.* **1991**, *250*, 139.
137. D. C. Koningsberger, R. Prins, (Eds.), *X-ray Absorption Principles, Applications, Techniques of EXAFS, SEXAFS and XANES*, John Wiley & Sons, New York, 1988.
138. J. K. Hawkins, H. S. Isaacs, S. M. Heald et al., *Corros. Sci.* **1987**, *27*, 391.
139. J. K. Hawkins, H. S. Isaacs, S. M. Heald et al., *Proc. Electrochem. Soc.* **1986**, *86-11*, 345.
140. J. S. Wainright, O. J. Murphy, M. R. Antonio, *Corros. Sci.* **1992**, *33*, 281.
141. S. W. M. Chung, J. Robinson, G. E. Thompson et al. *Philos. Mag. B* **1991**, *63*, 557.
142. W. E. Pocock, *Met. Finish.* **1954**, *52*, 48.
143. N. Sato, *Corrosion* **1989**, *45*, 354.
144. N. Sato, *Corros. Sci.* **1990**, *31*, 1.
145. L. Xia, E. Akiyama, G. Frankel et al., *J. Electrochem. Soc.* **2000**, *147*, 2556.
146. E. Akiyama, A. S. Markworth, G. S. Frankel, *J. Electrochem. Soc.* **2001**, in press.
147. J. Zhao, G. S. Frankel, R. L. McCreery, *J. Electrochem. Soc.* **1998**, *145*, 228.
148. V. Laget, H. Isaacs, C. S. Jeffcoate et al., *Proc. Electrochem. Soc.* **2000**, *99-26*, 173.
149. F. Pearlstein, M. R. D'Ambrosio, *Plating* **1968**, *55*, 345.
150. L. P. Montes, V. N. Laget, 2000; personal communication.
151. A. Gallacio, F. Pearlstein, M. R. D'Ambrosio, *Met. Finish.* **1966**, *64*, 50.
152. A. L. Glass, *Mat. Protect.* **1968**, *7*, 26.
153. I. Suzuki, *Corrosion Resistant Coatings Technology*, Marcel Dekker, New York, 1989.
154. Report NAEC-AML 2065, Effect of Hexavalent Chromium Content on Performance of Chromate Films, Aeronautical Materials Lab, Naval Engineering Center, Philadelphia, Pa., 1964.
155. L. F. G. Williams, *Surf. Tech.* **1978**, *7*, 113.
156. ''Alternatives to Chromium for Metal Finishing'' (Ed.: P. D. Chalmer), Final Report 0273RE95, National Center for Manufacturing Sciences, Ann Arbor, MI, (1995).
157. R. G. Buchheit, M. Cunningham, H. Jensen et al., *Corrosion* **1998**, *54*, 61.
158. V. S. Argawala, *ACS Symp. Ser.* **1986**, 211–219.
159. R. L. Twite, G. P. Bierwagen, *Prog. Org. Coat.* **1998**, *33*, 91.
160. D. Wick, (Ed.), *Tool and Manufacturing Engineers Handbook*, Society of Manufacturing Engineers, Dearborn, Mich, 1983, Vol. III, Chap. 19, pp. 19-1–19-33.
161. A. Wehr, H. C. Hardee, N. R. Auckland et al., *Proceedings of the 48th Electronic Components and Technology Conference*, IEEE, New York, 1998, pp. 14–20.
162. M. A. Heine, M. J. Pryor, *J. Electrochem. Soc.* **1967**, *114*, 1001.
163. G. E. Pike, Electrical Properties of Alodine 1200, Internal Memorandum, Sandia National Laboratories, Albuquerque, N. M., 1981.
164. W. R. Hinton, *Met. Finish.* Sept., 55 (**1991**) *and* Oct., 15 (**1991**) *89*.
165. M. W. Kendig, R. G. Buchheit, Surface conversion for aluminum and ferrous alloys for corrosion resistance, Proceedings of the Research Topical Symposium, NACE/2000, NACE, Houston, Tex., 2000, p. 1.
166. S. M. Cohen, *Corrosion* **1995**, *51*, 71.
167. M. Guglienlmi, *J. Sol.-Gel Sci. Technol.* **1997**, *8*, 442.
168. R. G. Buchheit, G. E. Stoner, U. S. Patent 5 266 356, 1993.
169. R. G. Buchheit, M. D. Bode, G. E. Stoner, *Corrosion* **1994**, *50*, 205.
170. C. A. Drewien, M. O. Eatough, D. R. Tallant et al., *J. Mater. Res.* **1996**, *11*, 1507.
171. R. G. Buchheit, M. A. Martinez, *Proceedings of Advances in Coating Technologies for Corrosion and Wear Resistant Coatings*, TMS, Warrendale, Pa., 1995, pp. 173–182.
172. J. W. Bibber, *Met. Finish.* **1991**, *89*, 51.
173. J. W. Bibber, *Met. Finish.* **1998**, *96*, 28.
174. R. G. Buchheit, M. R. Jaworoski, P. D. Chalmer, Surface conversion of aluminum and ferrous alloys for corrosion resistance, Research Topical Symposium, CORROSION/2000, NACE International, Houston, Tex., 2000.

5.4 Corrosion Protection by Organic Coatings

Guido Grundmeier
Max-Planck-Institut für Eisenforschung, Düsseldorf, Germany

Alda Simões
Universidade Técnica de Lisboa, Lisbon, Portugal

5.4.1 Introduction

Organic coatings and adhesives are commonly used to coat and join reactive metals for use in corrosive environments. Organic coatings not only serve as a barrier layer to protect the metal surface but also are responsible for the aesthetic properties of the metal surface. The degradation of an organically coated metal usually occurs along the metal–polymer interface starting from local defects in the coating. Mainly electrochemical processes such as the reduction of water and oxygen or the anodic dissolution of the metal substrate are responsible for the corrosive attack.

The application of electrochemical methods to study this kind of corrosion in which small defects lead to localized corrosion and undermining of the organic coating is by no way trivial because the high impedance of the organic coating hinders the measurement of electrochemical processes that occur at the interface in the delaminated area. Only recently modern electrochemical techniques such as electrochemical impedance spectroscopy (EIS) or the Scanning Kelvin Probe (SKP) provide better insights into the corrosion behavior of organic coatings.

A lot of excellent reviews already report on the corrosion protection by organic coatings. In this review, the authors focus on the relevance of electrochemical methods for the characterization of the protective properties of organic coatings and on fundamental mechanisms of corrosion. It is far beyond the scope of this chapter to review the recent developments in the formulation of corrosion protecting paints. A good introduction to the chemistry of coatings can be found in Ref. [1].

After a short introduction to fundamental aspects of organic coatings such as composition, adhesion and transport in organic coatings, an overview is given on the application of modern electrochemical techniques to organic coatings. The corrosion mechanisms of polymer-coated iron, zinc, and aluminum are discussed in detail. Finally a short overview is given on the influence of interfacial layers and pigments in organic coatings on the kinetics of the corrosion process.

The authors hope that the chapter provides the reader with an electrochemical understanding of corrosion processes of organically coated metals that can be applied to the variety of corrosion problems in this field.

5.4.1.1 The Composition of Corrosion Protecting Organic Coatings

A complete coating system, recommended for highly demanding situations, consists of several layers – the primer, the intermediate coats and the topcoat. The primer is an essential component for corrosion protection, because it is responsible for the adhesion of the coating to the substrate and also it provides most of the anticorrosive properties, through the use of inhibitors. Its requirements are a good adhesion to the substrate and to the intermediate coat, flexibility and cohesion and good chemical resistance.

The intermediate coats are used mainly for increasing the final thickness, and consequently hinder the moisture permeation

and increase the electrical resistance of the coating. The most evident property of the topcoat is related with its aesthetic function, since it is responsible for the color and the gloss that give the coating system its final appearance. But the topcoat also provides an important barrier effect against the environment. It must therefore have a good resistance to water, aggressive chemicals, and to weathering.

These various layers, although with different functions and purposes, have basically the same ingredients, which are common to organic coatings. In general, an organic coating consists of four basic constituents:

- binder
- pigments
- additives and fillers
- solvent.

Further to these basic constituents, inhibitors are frequently added to the formulation, for enhanced corrosion protection.

The main properties and functions of the various components will be briefly introduced in the following subparagraphs. For further information on the subject, the reader is advised to consult more specific literature [2–9].

5.4.1.1.1 **Binder** The binder constitutes the matrix of the coating, that is, the continuous polymeric phase in which the other components are incorporated. It provides cohesive forces that hold the film together, and also adhesive forces between the film and the substrate. It is mainly responsible for the physical barrier provided by the coating against aggressive agents. Its density and composition are determinant for properties such as permeability, UV resistance, and chemical resistance of the coating.

Coatings are usually classified according to the resin binder. Thus, names such as acrylic, alkyd, epoxy, or chlorinated rubber are commonly used to identify coatings with those classes of binders. Other classes of coatings, as the fluoropolymers [10, 11] have also become of common application e.g. in coil-coated steel.

The formation of a continuous dry film from a liquid coating after application is achieved by physical drying or by curing (chemical drying). In physical drying, film formation occurs as a result of the evaporation of the volatile components, that is, solvents and diluents. The cohesive forces that hold the film together are in this case weak, and the bonds can usually be broken again by solvents. The curing, or chemical drying, involves a chemical reaction between the molecules of the binder. These reactions can occur either at ambient temperature or by baking at elevated temperature (usually above 70 °C). Frequently, these reactions occur between two components mixed prior to the application, and the coating is known as a two-component coating or a reaction coating. Another form of drying is the oxidative drying, which starts with oxygen uptake from the air. The oxygenated molecules of the binder then react between them. Although slow, the process can be accelerated by the use of additives, called dryers, which are in fact catalysts for the reactions taking place. Moreover, curing by means of electron beams and ultraviolet light, both leading to a network formation via radicals is possible.

5.4.1.1.2 **Pigments** Pigments are powdered materials that confer the desired color to the coating. They also provide opacity, and are partially responsible for properties such as hardness, resistance to abrasion and resistance to weathering. The

barrier effect of the coating can also be increased by the use of lamellar pigments that align parallel to the surface, increasing the tortuosity of the path followed by the penetrating aggressive agents, therefore decreasing the diffusivity of those agents in the coating [4] (Fig. 1).

Pigments can be either organic or inorganic. Organic pigments tend to act only as coloring agents, whereas inorganic pigments frequently have anticorrosive properties. Among the inorganic pigments, several types can be distinguished [9]:

1. earth pigments – obtained from naturally occurring rocks, for example, ochre;
2. mineral pigments – obtained from minerals, for example, barytes, calcium sulfate, and dolomites;
3. synthetic inorganic pigments, for example, titanium dioxide, zinc oxide, chrome yellow;
4. metallic pigments, for example, aluminum powder, zinc dust.

The choice of a pigment must be made carefully, to ensure that it is compatible with the binder and resistant to the environment. Pigments can be chemically inert, in which case they provide only barrier protection against corrosion, or they can actively protect the substrate, either by a sacrificial effect or by inhibiting properties. Because of the relevance of these effects, they will be treated separately. An important parameter in the comparison of the performance of pigments is the pigment volume concentration (PVC), defined as the volume ratio of pigment to the total nonvolatile components in a coating. Each pigment has a certain PVC range at which it will have an optimum performance [6]. The critical pigment volume concentration (CPVC) is the concentration of pigment in a dry coating at which the binder is the minimum necessary to fill the spaces between the pigment particles, corresponding to a compromise between the main properties of the dry film [4].

5.4.1.1.3 **Anticorrosive Pigments** Anticorrosive pigments can be divided in two categories: those that have an inhibiting effect on the corrosion reaction by minimizing

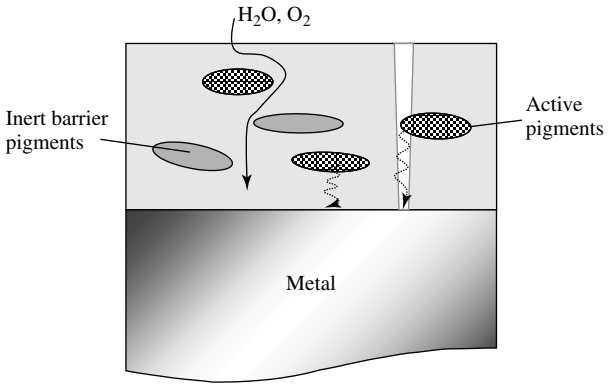


Fig. 1 Effect of pigments on the path of the aggressive agents and the active properties of pigments with regard to the interfacial reactions and passivation of pores in the organic coating.

the rates of the partial reactions, and those that become anodic relative to the substrate, providing sacrificial protection.

Inhibitive inorganic pigments are substances capable of minimizing the corrosion rate by retarding the cathodic or the anodic reaction or by limiting the ionic current between the anodic and the cathodic regions. Some pigments react with the hydroxyl ions formed in neutral solutions at the cathode, forming an insoluble deposit that increases the resistance polarization. Others, as in the case of lead, work as indirect inhibitors, since they react with the resin, producing the inhibiting substances [6]. Inhibitors such as zinc chromate, phosphate, silicate, and borate, are anodic inhibitors [12]. Molybdate pigments can passivate the surface by the formation of a layer of ferric molybdate. Many inhibitors also act by neutralizing acid species, and by rendering the medium more alkaline, facilitating the precipitation of salts. A reasonably large number of compounds used as inhibitors can be found in the literature [6, 12]. They include borates, chromates, leads, molybdates, phosphates, phosphites, and silicates, of various metals such as zinc, calcium, aluminum, barium, or strontium. However, strict limitations to the use of leads and chromates have been imposed by legislation, due to the toxicity of those compounds [12, 13]. Nowadays, zinc phosphate is probably the most important pigment in anticorrosive paints [14]. Figure 1 illustrates the effect of active pigments as sources for species that inhibit corrosion at the polymer–metal interface or in small pores in the coating.

The sacrificial protection is typically used for protection of ferrous substrates. It is attained by adding to the paint actual particles or flakes of zinc, which act as anodes with respect to the ferrous substrate [15], providing cathodic protection to the substrate. In order to ensure electrical conduction, necessary for the protection, these coatings require a high content of metallic zinc – typically a minimum of 80% [9].

5.4.1.1.4 **Fillers and Additives** Fillers, or extenders, are powdered materials used with the aim of increasing the nonvolatile content of the dry coating, but also to improve mechanical properties, reduce the gloss and also reduce the price. Common fillers are talc, mica, and barium sulfate [4]. Additives are typically added in small quantities, and address a large number of specific purposes [16, 17]. For example, they can improve the stability of the mixture before application, prevent sedimentation of pigments and fillers, accelerate drying, act as fire-retardant agents, UV-absorbers for better weathering resistance or to prevent growth of fungi.

5.4.1.1.5 **Solvents** Solvents and diluents are both volatile liquids added to the coating formulation. However, there is a difference between them. The solvent is necessary for the homogeneous mixing of the other components before application, whereas a diluent is a liquid that is not capable of dissolving the binder by itself but which, added to the binder solution, helps to achieve a viscosity adequate for the application of the coating. Together, solvent and diluents are responsible for the viscosity and the evaporation rate, which in their turn influence the adhesion and the internal stresses inside the dry film. For many years, organic liquids were intensively used as solvents and diluents in the coatings industry. However, the ecological concerns about volatile organic compounds (VOCs) have resulted in an enormous shift towards water-based

coatings [18–24]. These are convertible coatings, that is, they undergo chemical changes during drying, usually involving crosslinking of the polymeric chains of the binder [8, 23], which is essential to ensure that they resist the contact with water after curing.

Finally, some coatings do not require the use of a solvent. Examples are solvent-free coatings, or powder coatings. The latter are applied as a powder that, upon heating, undergoes sintering and forms a continuous film [25]. They can be classified as thermosetting or thermoplastic [26]. Examples are epoxy coatings, which require the mixing of two components just before application, or powder coatings, such as polyvinyl chloride.

5.4.1.2 Transport Phenomena in Organic Coatings

The durability of organic-coated systems greatly depends on the protective properties of the coating. Organic coatings usually act at several levels: they can act on the corrosion reactions, by limiting their rate, but they usually constitute a barrier to the penetration of external aggressive agents. Corrosion reactions can only proceed if in the vicinity of the metal surface, there are a reactant for the cathodic reaction (usually oxygen), and a conductive medium (normally water). Further, it is known that corrosion reactions are greatly accelerated under the effect of aggressive ions. In this way, the resistance to permeation of gases, vapors, liquids, and ions is thus a matter of concern in such systems. The situations considered below correspond only to corrosion in contact with an aqueous medium, either with the coated system immersed in a solution or in contact with atmospheric humidity.

5.4.1.2.1 Transport of Oxygen

In aerated solutions of neutral pH, the cathodic reaction in the corrosion process is usually the reduction of oxygen:

$$\tfrac{1}{2}O_2 + H_2O + 2e^- \longrightarrow 2OH^- \qquad (1)$$

Since this reaction occurs at the surface of the metal, the permeation of oxygen is therefore crucial in the initiation and progression of corrosion. The subject of gas permeation has been addressed in other areas, as for example in the development of packaging plastic films or of separation membranes in chemical engineering [27]. In the case of corrosion underneath organic coatings, the interest on the subject arises from the question if the oxygen transport across the coating may be the rate-determining step for the corrosion process. Guruviah [28] determined the oxygen permeability of films of epoxy, alkyd, and chlorinated rubber pigmented with iron oxide. Baumann [29] also determined oxygen permeability in several paint films. The values he obtained were in the range $1 \times 10^{-8} - 4 \times 10^{-6}\,\mathrm{l\,cm^{-2}\,day^{-1}}$. On the basis of a consumption of oxygen of $6 \times 10^{-6} - 1.06 \times 10^{-4}\,\mathrm{l\,cm^{-2}\,day^{-1}}$ determined for corrosion on bare carbon steel [29], he concluded that the oxygen permeability could, in certain conditions, be the rate-controlling factor for corrosion underneath a coating. This conclusion contradicted earlier results of Mayne [30], who determined higher oxygen permeation rates and consequently reasoned that oxygen permeation could not be the rate-controlling factor in the corrosion process. Potentiostatic measurements made across an alkyd resin coating allowed Feser and Stratmann [31] to estimate the diffusivity of molecular oxygen as $1.7 \times 10^{-8}\,\mathrm{cm^2\,s^{-1}}$.

As in any other mass transport process, the permeability can be expected to depend

on the composition of the coating and also to decrease with increasing thickness, provided the composition and structure are not affected by the thickness. The subject of oxygen transport in polymeric films has been addressed by other authors [32, 33], but some doubts still remain on the importance of oxygen permeation kinetics for the corrosion process. A review on the subject of oxygen transport in organic coatings has been made by Walter [34].

5.4.1.2.2 **Transport of Water and Ions**

Water can be contained inside an organic coating in two states: either bound to the matrix or in microscopic water-filled cavities, known as *clusters*. Temperature, and particularly the glass transition temperature, T_g, greatly influence the solubility of water in the coating. The formation of clusters seems to be enhanced by a loss of solubility resulting from a decrease in temperature across T_g [35].

Water penetration not only promotes corrosion, but it also induces internal stresses in the coating. It extracts soluble components from the coating, inducing contractive internal stresses. On the other hand, water penetration causes swelling, and therefore an expansive internal stress [36]. As a result of these stresses, water can lower the value of T_g [35].

Under natural exposure, an organic coating can be in contact with water in different forms, such as rain, dew, or humidity. Some coatings are more permeable to water vapor than to liquid water, whereas with others liquid water permeates faster [37]. The permeability is also different depending on the film being applied on a substrate or as a freestanding film [38].

In the description of water permeation, several parameters are considered. The diffusivity D ($m^2\ s^{-1}$) is defined as the ratio between the flux j of a species and the concentration gradient, according to Fick's law for steady state transport:

$$j_z = -D\frac{\partial C(z)}{\partial z} \tag{2}$$

where C is the concentration of water and z, the direction of the flux. The solubility S corresponds to the water content at saturation, and is dimensionless:

$$S = \frac{\text{volume of water at saturation}}{\text{volume of the coating}} \tag{3}$$

The permeability P may be defined as the product of diffusivity and solubility:

$$P = D \cdot S \tag{4}$$

Diffusion of water in a semipermeable membrane is caused by a concentration gradient. In the simplest case, and for one-dimensional diffusion, the process is governed by Fick's law for transient transport:

$$\frac{\partial C(z,t)}{\partial t} = D\frac{\partial^2 C(z,t)}{\partial z^2} \tag{5}$$

For water in organic coatings, D is typically in the range 10^{-12}–10^{-15} $m^2\ s^{-1}$ [39–42].

For a coating of thickness L submerged in the dry state at an instant $t = 0$, the initial and boundary conditions are

$$C = 0 \text{ at } t = 0 \tag{6}$$

$$C = C_\infty \text{ at } z = 0 \tag{6'}$$

$$\frac{\partial C}{\partial z} = 0 \text{ at } z = L \tag{6''}$$

where C_∞ corresponds to the water concentration at saturation. The solution to this equation can be expressed either as a distribution of concentration [43] or as a saturation function, ϕ, which corresponds to the ratio between the mass of water

contained in the coating at an instant t and at saturation, M_t/M_∞. In this last form, the complete solution is given by a summation [44–47]:

$$\phi = 1 - \frac{8}{\pi^2} \sum_{n=0}^{\infty} \frac{1}{(2n+1)^2} \times \exp\left(\frac{-(2n+1)^2 \pi^2 t D}{4L^2}\right) \quad (7)$$

For short times, the summation can be replaced by an integration, giving [44]:

$$\phi \cong \frac{2}{\sqrt{\pi}} \sqrt{\frac{tD}{L^2}} \quad (8)$$

Therefore, for short exposure times, the water content is proportional to the square root of time. For long times, it is a good approximation to retain only the first term of the summation ($n = 0$), which gives [44]:

$$\phi \cong 1 - \frac{8}{\pi^2} \exp\left(\frac{-\pi^2 t D}{4L^2}\right) \quad (9)$$

The dimensionless variable tD/L^2, which appears in the solution, is the Fourier number for mass transport and provides a convenient way of presenting the results of mass transport. This treatment assumes a homogeneous coating, with uniform properties. A theoretical analysis for the case of multilayered coatings can also be found in the literature [48].

The principles presented here are concerned with the permeation of water in intact coatings, that is, in the absence of defects such as scratches or blisters. After the initiation of corrosion, however, the ionic concentration at the coating–metal interface increases, causing transport of water by an osmotic process [49–52] and causing further deformation of the film.

Since water is essential at the metal–coating interface for the initiation of corrosion, it is thus important to decrease the permeability of the coating. This can be achieved either by increasing the coating thickness, by using a coating of low porosity, by the use of multilayer coatings and by using lamellar pigments or fillers in the formulation. The use of several layers has the advantage that the pores from the different layers do not match geometrically (Fig. 2), hindering water penetration. The use of lamellar pigments [4] increases the effective length of the path that water has to travel before it reaches the metal–coating interface – see Sect. 5.4.1.1.2. The consequence is a decrease of the effective diffusivity in Fick's law.

Measuring techniques The most direct way to determine the water content in a coating is by weight measurements [38, 38, 53, 54], either as weight gain during absorption or as weight loss during drying. It can be used on either freestanding

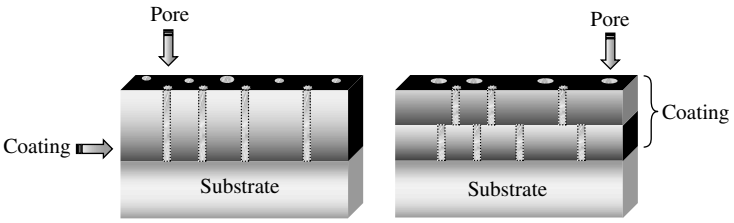


Fig. 2 Effect of having one or more layers on the geometry of the pores and the barrier properties of the coating.

or applied films. Although a reliable technique, it is not free of limitations, that is, due to the leaching of soluble components [54]. For freestanding films, the permeation of water vapor can also be assessed by the Payne cup, in which the water permeated is determined from the weight gain of a desiccant material contained in the cup. Differential scanning calorimetry (DSC) is another possibility, although it has the limitation of detecting only the clustered water [35].

The easiest method for the study of water permeation is in situ capacitance determination by electrochemical impedance. The principle is based on the fact that the presence of water increases the capacitance of the coating. The most used equation for estimating the water content in a coating is the Brasher–Kingsbury equation [55], as described in Sect. 5.4.2.2.3. The subject has been treated in the literature by several researchers, who have determined either the water content ϕ [40, 53–56] or the diffusivity of water [41, 57] in the coating.

A nonelectrochemical method also sensitive to the presence of water is infrared spectroscopy with multiple internal reflection, applied by Nguyen and coworkers to study the swelling of an organic coating at the metal–polymer interface in situ [58]. The integration of the stretching vibration of water was used as a measure of the water uptake at the interface. Stratmann and coworkers measured the increase of the water concentration at the Fe–alkyd-polymer interface by means of single attenuated total infrared reflection spectroscopy (ATIRS) [59]. An ultrathin Fe film was evaporated onto a ZnSe crystal and coated with an alkyd primer. The authors concluded that no separate water film is formed at the interface between iron and the alkyd primer.

Transport of ions According to Mayne [60], in the absence of inhibitive pigments, organic coatings retard corrosion primarily by acting as a barrier to the flow of ions. It is known that the permeation of ions is much slower than the permeation of liquid water and of water vapor [61]. Moreover, most polymer films are permselective to cations [62], and therefore greatly retard the permeation of inorganic anions like Cl^- or SO_4^{2-} [63, 64]. This permselectivity (or Donnan exclusion) can be lost if the activities of ions become high compared to that of the fixed ion in the membrane [65], but it can play an important role at small concentrations.

Kittleberger and Elm [33] measured the rate of diffusion of sodium chloride through several paint films, and found a linear relationship between the rate of diffusion and the reciprocal of the film resistance. This behavior, however, is probably insufficient to describe the diffusion through coatings. In a study made by Mayne and coworkers [30, 66], a number of cast varnish films were used to determine the resistance of the film in contact with potassium chloride. Two opposite behaviors were observed: either the conductivity increased with increasing electrolyte concentration – direct or D conduction – or the conductivity decreased when the solution became more conductive – inverse or I conduction. The interpretation for the I behavior was associated with the entry of water into the film. It was also concluded that the D films have a heterogeneous structure, with I and D areas, arising from differences in crosslinking density within the film. As observed by Mills and Mayne [67], films from noncrosslinking systems yield films with reasonably

uniform resistance, whereas crosslinked polymer films contain small areas with significantly lower ionic resistance than the rest of the film.

Techniques such as the Hittorf method for the diffusivity of ions or radiotracer counting for the ionic capacity have been applied to the study of the transport of ions in organic coatings [43].

5.4.1.3 Adhesion of Organic Coatings

The adhesion of a paint to the substrate is a presupposition for the performance of the coating as a corrosion protecting layer. Adhesion is based on the physical and chemical behavior of the underside of the paint and the surface of the metal substrate. The formed interfacial zone should be called an interphase rather than a sharp interface because it is three dimensional in nature.

Different theories have been developed to explain the origin of adhesion including [68]

- the electrostatic theory, based on a charge transfer between the substrate and the coating;
- the diffusion theory, based on the interdiffusion of polymer chains at the interface;
- mechanical interlocking, based on the spreading of liquid paint into cavities of the surface leading to an anchoring of the paint after solidification; and
- the adsorption theory, based on covalent, polar, and disperse interactions as well as acid–base interactions between the substrate surface and the paint.

It has been argued that the formation of acid–base interactions between the polymer and the substrate may represent a major type of intrinsic adhesion force [69]. The acid may be an electron acceptor in the Lewis sense, or a proton donor in the Bronsted sense. The base may be an electron donor, in the Lewis sense, or a proton acceptor in the Bronsted sense. The acid-base theory has found widespread acceptance and an increasing number of papers deal with the understanding and application of these forces at the interface [70].

While the adsorption theory is the most accepted one, mechanical interlocking comes into play in case of substrates with a special kind of roughness such as galvannealed steel where the liquid can spread into cavities and thereby interlock with the substrate. The diffusion theory does not play an important role for polymer–metal interfaces. The contribution of the electrostatic theory is not easy to estimate. However, the electrical component of the adhesive force between the planar surfaces of solids becomes important if the charge exchange density corresponds to 10^{17} electronic charges, meaning about 1% of the surface atoms [71].

Wetting of the surface is crucial for the formation of the interphase and is determined by the surface energy of the substrate and that of the liquid paint [72]. The basic step in the liquid coating process is the replacement of the substrate–air interface with the substrate–liquid and liquid–air interface. The wetting condition for static conditions can be described by the Young equation. Young expressed the conditions for equilibrium at a solid–liquid interface like that in Fig. 3 as

$$\gamma_{sv} - \gamma_{sl} = \gamma_{lv} \cos \Theta \qquad (10)$$

where γ_{sv} and γ_{lv} are, respectively, the surface energies of the solid and liquid in equilibrium with the saturated vapor of the liquid.

The so-called spreading coefficient S is given by the difference in surface energy

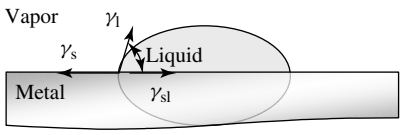


Fig. 3 Schematic illustrating the Young equation.

between the uncovered and the covered surface according to

$$S = \gamma_{sv} - (\gamma_{sl} + \gamma_{lv}) \qquad (11)$$

where γ_{sv} and γ_{sl} are the solid–air and solid–liquid interfacial energies, respectively, while γ_{lv} is the surface tension of the liquid [71]. For complete wetting to occur, S must be positive. The greater the value of S, the more rapidly the liquid will rush to cover the substrate.

The adhesion strength of an interface between two materials α and β can be defined by the work of adhesion. This is the work required to separate reversibly the interface to infinity per unit area

$$W_a = \gamma_\alpha + \gamma_\beta - \gamma_{\alpha\beta} \qquad (12)$$

where W_a is the work of adhesion, γ_α and γ_β the surface tensions of α and β phases, respectively, while $\gamma_{\alpha\beta}$ is the interfacial tension between α and β.

While the above mathematical treatment is true for equilibrium conditions, the real coating process is highly dynamic. Solvents and thinners strongly influence the wetting process and immediately after the paint application evaporation of solvents, orientation of macromolecules at the interface and crosslinking of oligomer chains start leading to non–steady state conditions [72]. During solvent evaporation, adhesion-promoting groups can adsorb at the inorganic surface. Examples of these adhesion-promoting groups are hydroxyls, carboxyls, amides, isocyanates, and epoxies.

When water molecules reach the interface between the coating and the inorganic surface of the substrate, they may interfere with the adhesion between the polymer and the substrate. Eventually, in combination with intrinsic stresses in the coating this might lead to a loss of adhesion. The water molecules compete with and substitute the polar groups of the polymer at the metal surface. Moreover, accumulation of water at the interface caused by residual solvents or ions can lead to high osmotic pressures and subsequently to a hydrostatic disbonding. The degree to which permeated water may change the adhesion properties of a paint–metal composite is referred to as wet adhesion [36, 73]. An excellent review on the durability of adherents has been written by Kinloch [74].

5.4.1.4 Introduction to the Mechanisms of Protection and Degradation

5.4.1.4.1 Mechanisms of Protection The thermodynamic tendency for a metal to corrode in aqueous medium depends on its thermodynamic stability in that medium, as described by its Pourbaix diagram [75]. If it is not stable in the metallic form, or in the presence of oxidizing species in solution, the metal will undergo oxidation that shall lead either to ions in solution or to solid corrosion products. If these products are not passivating, then the process will lead to active corrosion of the metal. For the case of iron in contact with dissolved oxygen, the reactions involved will be

$$Fe \longrightarrow Fe^{2+} + 2e^- \quad \text{anodic reaction} \qquad (13)$$

$$\tfrac{1}{2}O_2 + 2e^- + H_2O \longrightarrow 2OH^- \text{ cathodic reaction} \quad (14)$$

The anodic reaction is therefore the anodic dissolution of iron. The free electrons resulting from this reaction are consumed at the cathodic sites, in the reaction of oxygen reduction, with formation of hydroxyl ions. The overall reaction will then be

$$Fe + \tfrac{1}{2}O_2 + H_2O \longrightarrow Fe(OH)_2 \quad (15)$$

Ferrous hydroxide is soluble in water, but in the presence of oxygen it may be converted into ferric oxide [5]:

$$2Fe(OH)_2 + \tfrac{1}{2}O_2 \longrightarrow Fe_2O_3 \cdot H_2O + H_2O \quad (16)$$

This species is less soluble than ferrous hydroxide, and precipitates on the surface.

In the absence of oxygen, the cathodic reaction can also be

$$H_3O + e^- \longrightarrow \tfrac{1}{2}H_2 + H_2O \quad (17)$$

Under conditions of oxygen or electrolyte concentration gradients, or due to heterogeneities of the metallic substrate, the cathodic and anodic sites may be separated. For each of the two electrodes, the equilibrium potential for their actual conditions can be determined by the Nernst equation. The electromotive force (EMF) for the corrosion process to occur is the difference between the two equilibrium potentials. When the cathode and the anode are short-circuited, a mixed potential results, known as corrosion potential, E_{corr}. The value of E_{corr} lies between the two separate electrode potentials, although shifted towards the equilibrium potential of the faster reaction. This situation can be easily visualized with the help of the Evans ($E - \log i$) diagrams, described in Chapter 1.

It can thus be concluded that for corrosion to initiate at the metallic substrate at neutral pH, the presence of both water and oxygen is required. Organic coatings retard both the initiation of corrosion and its rate of development, in two ways: by a barrier mechanism and by an inhibiting mechanism.

Barrier properties An organic coating is a physical barrier separating the metal substrate from the aqueous corrosive environment. This barrier is blocking the flow of electrons, an important function in order to avoid the shift of the cathodic reaction from the metal to the outer surface of the coating [30]. Further, it hinders the penetration of chemical species from the environment, although in practice every organic coating has some permeability to water, oxygen and even ions. Figure 4 schematically shows the influence of an organic coating on the electrode potential and the size of the double layer in front of the metal surface. Fast metal dissolution due to the large electric field (10^7 V cm^{-1}) leads to a negative electrode potential with respect to the polymer-coated area where metal dissolution is strongly inhibited and a diffuse double layer is found. It has been found that under normal, outdoor conditions, the content of water in a coating is close to saturation. Also, the diffusion of oxygen though the coating may be sufficient to support unlimited corrosion, as discussed in Sect. 5.4.1.2.1.

These observations suggest that other properties beyond the physical barrier properties may be determinant for the protective action of coatings.

Another component of the barrier effect is the resistance inhibition, which consists of the ionic current flow between those

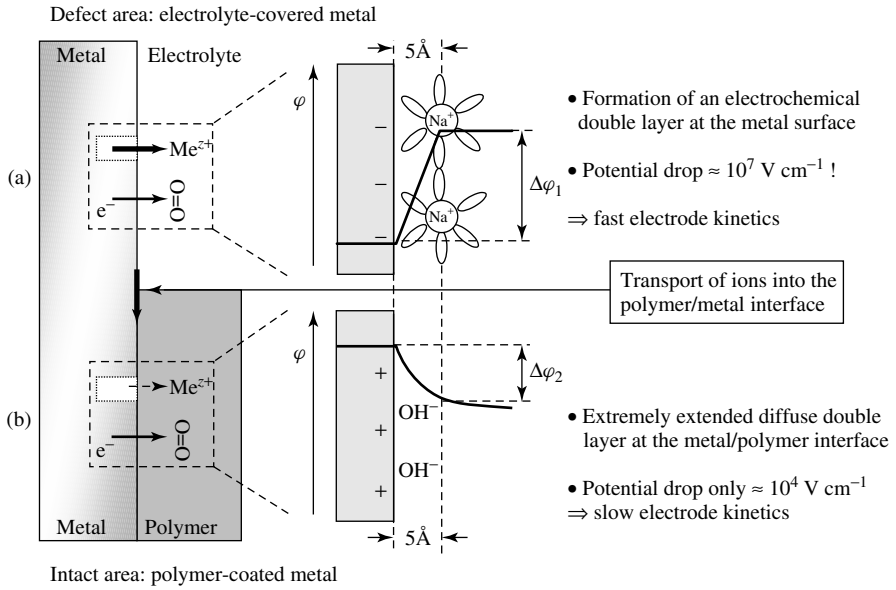


Fig. 4 Schematic of the double layer for electrolyte-covered metal (a) and polymer-coated metal (b) (after Ref. [76]). (Reprinted with permission.)

areas. The more difficult the ionic flow, the slower the corrosion process. Naturally, this effect is intimately connected to the adhesion of the coating to the substrate. When adhesion is lost, pathways for ionic conduction are formed, facilitating the corrosion process. The barrier protection is made essentially by the topcoat because it has a large thickness and a high content of pigment and fillers.

Inhibiting properties Because the barrier properties are often insufficient for corrosion protection, corrosion inhibitors are often used. Inhibitors can act by limiting the cathodic or the anodic reaction, or both. They are typically added to the primer, where they are close to the metal surface. This subject was treated in Chapter 5.2.

5.4.1.4.2 **Blistering** Blister formation is frequently the first sign that the protection provided by the organic coating is insufficient. The phenomenon can have several origins, described in the literature by the following mechanisms [63, 77, 78]:

Blistering by volume expansion due to swelling: Organic coatings for corrosion protection typically absorb water up to 3 or 4%; if this absorption occurs locally, blisters may form because of accumulation of water. This mechanism is however unimportant when compared with other mechanisms.

Blistering due to gas formation or gas inclusion: Volatile components leading to blister formation can become incorporated in the coating during application, or they can result from inclusions of solvents from phase separation. They can also be generated because of cathodic protection or even to a corrosion process if it generates H_2.

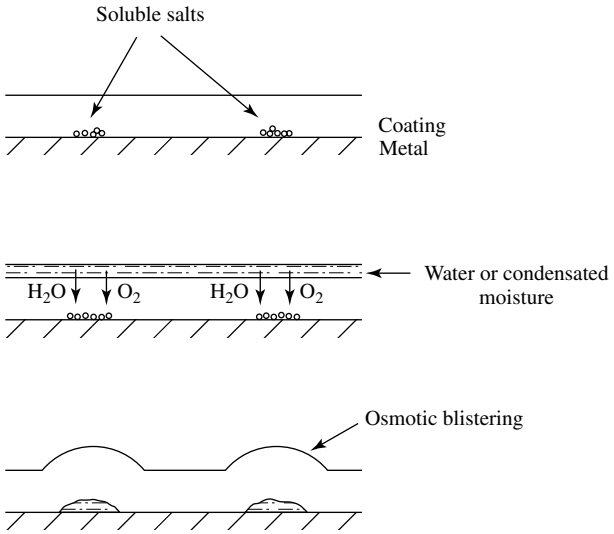


Fig. 5 Mechanism of osmotic blistering due to soluble impurities (adapted from Ref. [79]). (Reprinted with permission.)

Electroosmotic blistering: Electro-osmosis involves water transport though a membrane or a capillary system under the influence of a potential gradient. It is relatively unimportant because with increasing salt concentration the conductivity increases, decreasing the water transport by this mechanism.

Blistering due to phase separation during film formation: This phenomenon may occur when there are two volatile components of different evaporation rates. Water may diffuse into the voids left by one of the solvents, generating blisters. This is therefore an early blistering, since it occurs during film formation [77].

Blistering by osmotic processes, due to soluble impurities at the film–substrate interface: When a coating is applied on a surface contaminated with soluble salts, osmotic blistering takes place. If water is in contact with the painted surface, water will permeate, promoted by the osmotic pressure generated by the difference in the concentrations of the solutions on the two sides of the film (Fig. 5). The process will continue until the concentrations become equal. A review on the subject was made by Morcillo [79].

Osmotic blistering can also occur because of the formation of corrosion products at the metal–coating interface. Once water reaches that interface and metal ions from the substrate are produced, a difference in the ionic force on either side of the coating is also capable of generating a flow of water across the coating. This is a key mechanism in the blistering associated with corrosion. According to the literature [79], the osmotic pressure inside a blister can reach 2500–3000 kPa, which is enormous, compared to the yield strength of an organic coating, of the order of 6–40 kPa. The viscoelastic behavior of organic coatings determines the way in which the blisters develop. It is believed that they grow by steps, releasing the pressure as they become deformed [63].

5.4.1.4.3 **Corrosion Initiation** Defects in coatings are always preferential sites for corrosion initiation. Apart from the cases mentioned above – soluble salts inclusions, volatile components – the accidental formation of defects during its service life is common, that is, in the form of pinholes or scratches. The electrochemical description of a defect next to an intact coating area is shown in Fig. 4. When a small defect is exposed to a corrosive environment – which may be either a bulk liquid phase or only a thin film of condensed water – the part of the substrate that is directly exposed will start to corrode, forming metal oxides and hydroxides that block the defect. These corrosion products are permeable to water but impermeable to oxygen. Therefore, a separation between the cathodic and the anodic areas occurs. Underneath the oxides, that is, at the center of the defect, the anodic reaction takes place, whereas the cathodic reaction occurs further away from the defect [80] (Fig. 6).

Although organically-coated systems are particularly vulnerable to corrosion at defects, such as pinholes, scratches, or cut edges, the truth is that even apparently uniform coatings are prone to corrosion. During exposure of a coating to liquid water or to water vapor, water and oxygen are capable of diffusing into the film and of reaching the coating-substrate interface. After a certain time, a few monolayers of water accumulate, possibly at points of poor adhesion. In contact with water, the metal substrate (typically iron, zinc, or aluminum) is thermodynamically unstable in its metallic form, and with the presence of oxygen the conditions are fulfilled for corrosion to initiate. At this stage, the cathodic and anodic reactions take place at sites randomly dispersed on the metal surface. The metal ions resulting from the anodic process increase the ionic force underneath the coating, giving rise to an osmotic phenomenon, with the formation of a blister.

After the initiation step, blisters can grow by different mechanisms, known as cathodic delamination, anodic undermining or filiform corrosion (FFC). The first two shall be briefly described, whereas FFC, due to its specific characteristics, will be left for Sect. 5.4.3.3.

5.4.1.4.4 **Cathodic Delamination** The growth of blisters along the surface often occurs via a mechanism that is schematically presented in Fig. 7, for the case of

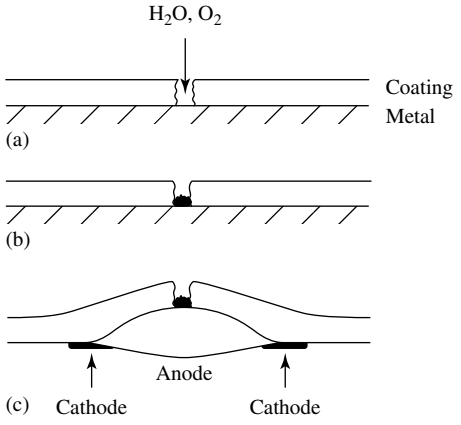


Fig. 6 Formation of a blister underneath a defective coating: (a) corrosion initiation; (b) blocking of a pore by corrosion products; and (c) osmotic blistering with anode–cathode separation.

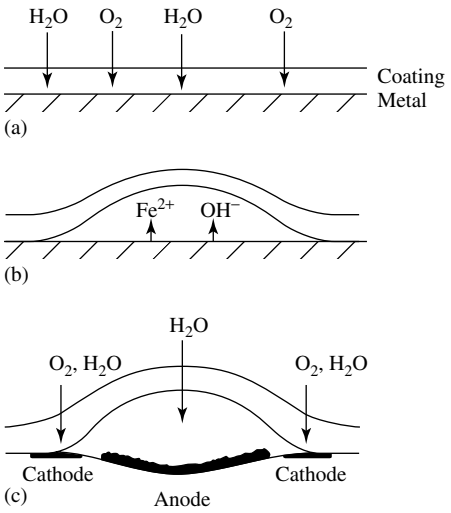


Fig. 7 Cathodic delamination of coated iron: (a) permeation of water and oxygen; (b) corrosion initiation; and (c) separation of cathode and anode, with osmotic growth of the blister.

iron. After the initiation steps, the Fe^{2+} and OH^- resulting from the anodic and cathodic reactions, respectively, together with some oxygen coming from across the coating, can precipitate in the form of a mixture of iron oxides and hydroxides. This layer is considered to be semipermeable, allowing only the permeation of water but impeding the transport of oxygen to the metal. In the region under the oxide, therefore, only the anodic reaction can occur, whereas the cathodic reaction becomes shifted to the edges of the blister, where oxygen can still diffuse across the organic coating. Under these conditions, the cathodic area will therefore be much smaller than the anodic area. The result of this is that the current density in the cathodic area is high, and large quantities of OH^- are formed in a confined volume, producing very high local pH values. These conditions will then lead to a loss of adhesion, possibly due to chemical disintegration of the polymer of the coating at the interface. This mechanism was proposed by Leidheiser and Kendig [81] in the following steps:

1. Penetration of water, ions, and oxygen.
2. Development of a low-resistance pathway between the bulk electrolyte and the substrate.
3. Anodic reaction (metal oxidation) taking place on the steel surface.
4. Cathodic reaction (oxygen reduction) also taking place also on the steel surface, and leading to some delamination.
5. As a consequence of the cathodic and anodic reactions proceeding in a confined volume, the ion concentration at the base of the low-resistance pathway increases, and corrosion products precipitate on the metal surface.
6. Precipitation of the corrosion products causes a drop of pH at the corrosion site.
7. A difference in acidity develops between the cathodic and the anodic areas, the pH being higher at the cathodic areas.

The rise of alkalinity below the coating has been verified experimentally [82], and pH values of 10 have been detected [83]. The effect of the pH on the loss of adhesion is supported by the existence of

carboxylated species [84] at the interface, suggesting chemical attack to the polymer.

One major question is the rate-controlling factor for delamination. It is clear that the oxygen reduction reaction produces an excess of anions, that needs to be compensated either by the counterdiffusion of cations to the cathode or by the diffusion of anions from the cathode to the area of the defect. Leidheiser and Wang [80] verified that the delamination rate was smaller in thicker coatings, and suggested that the rate-limiting step might be the diffusion of alkali metal cations through the coating. It has been observed that in the presence of chloride ion, the rate of delamination decreases with decreasing mobility of the cation, that is, CsCl > KCl > NaCl > LiCl [80, 83]. For coatings with an artificial scribe, Leng and coworkers [85] concluded that for a simple, nonpigmented polymer applied on steel, the delaminated area increased with the square root of time, and that there was hardly any influence of the anion on that rate. He also concluded that the reaction rate of the oxygen reduction reaction was determined by the ohmic potential drop between the exposed area and the delamination front [85], and suggested that the transport of ions was made along the delaminated area, underneath the coating. For a zinc substrate, Fürbeth [86] detected preferential migration of sodium cations towards the delamination front, which could control the rate of the process. On galvanized steel, he also studied the influence of carbon dioxide and concluded that the effect depends upon its concentration. Below 1 vol% of CO_2 the rate of delamination becomes reduced without effect on the mechanism, whereas between 1 and 2 vol%, the delamination rate becomes controlled by charge transfer of the oxygen reduction reaction [86].

Although mostly it is accepted that the corrosion reaction requires the existence of the oxygen reduction reaction, Hoffmann has concluded that, in the absence of oxygen, dissolution can be compensated by reduction of iron oxyhydroxides [87].

5.4.1.4.5 **Anodic Undermining** Anodic undermining corresponds to a situation in which the loss of adhesion is caused by the anodic dissolution of the substrate. The metal at the edge of the blister is therefore anodic. The process is usually initiated at preferential sites, such as a particle of contaminant from the cleaning procedure or a scratch on the surface. The initiation step is identical to the one described for cathodic delamination. The corrosive deadhesion of the coating is mainly caused by the dissolution of the metallic substrate. The mechanism of progression can be described by a process similar to crevice corrosion, the crevice being formed between the substrate and the organic coating. This crevice is very sharp, because only a very thin layer of metal is dissolved [88]. The cathodic areas may be either close to the scratch, where oxygen access is easy, or at small cathodic blisters in the vicinity of the anodic blister. As an example, Fig. 8 shows the corrosion of coil-coated galvanized steel starting from a scratch down to steel. The zinc coating dissolves close to the scratch underneath the coating thereby protecting the bare iron in the scratch. Anodic blisters are formed along the scratch. However, small blisters with cathodic activity are observed around the large anodic blisters.

Aluminum substrates are particularly prone to anodic undermining, whereas on steel this form of corrosion usually occurs under an applied potential [88]. Under conditions of free corrosion potential,

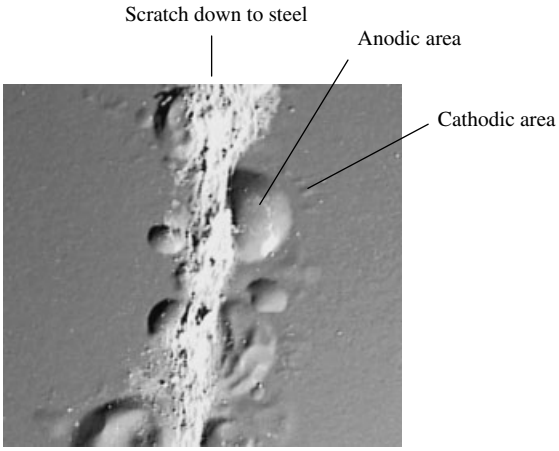


Fig. 8 Microscopic image of the corrosion of galvanized steel starting from a scratch down to steel.

coated steel substrates fail predominantly by cathodic delamination [78].

5.4.2 Application of Electrochemical Methods for the Characterization of the Protective Properties of Organic Coatings on Metals

5.4.2.1 Monitoring of the Open Circuit Potential

The open circuit potential (or rest potential) is the potential spontaneously assumed by an electrode in contact with an electrolyte. When different anodic and cathodic reactions occur on the surface, the spontaneous potential is called a mixed potential and it results from a compromise between the cathodic and anodic reactions occurring at the surface. Its value can therefore provide information on the state of activity of the surface.

Among the electrochemical techniques available for the study of corrosion of metals, potential monitoring is the most simple and inexpensive of all. Its non-destructive character is also an advantage. The measurements are made using only a reference electrode and a high impedance voltmeter (Fig. 9). The readings correspond to the open circuit

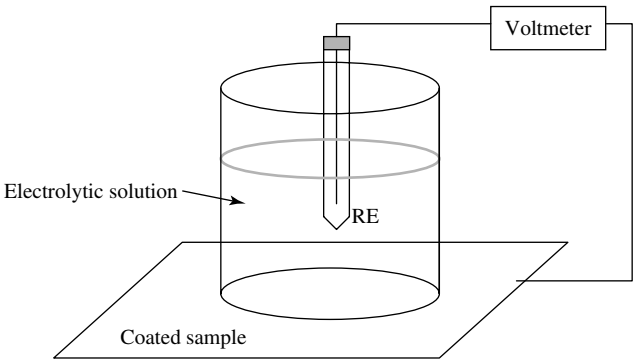


Fig. 9 Experimental arrangement for open circuit potential measurements. RE: reference electrode.

potential (or half-cell potential) of the system under study, versus the reference electrode. The interpretation is usually based on the principle that a shift towards more negative potentials is a sign of development of active corrosion, whereas more positive (more noble) potentials indicate formation of a film, or passivation, and thus the absence of active corrosion. This criterion, although valid in many systems, is subject to exceptions. In fact, a positive potential shift within a region of active corrosion may reveal cathodic depolarization, with inherent increase of corrosion rate. On the other hand, at a pH in the passive region of the potential–pH diagram, a positive shift in the potential may correspond to a decrease in the corrosion rate, since the anodic reaction becomes hindered by passivation. For reliability of the potential readings, the input impedance of the voltmeter needs to be at least two orders of magnitude above the DC resistance of the coating system, otherwise a meaningless value of 0 V may be read [89].

Reviews and discussions of the technique have been made by Murray [89], Wolstenholme [90], and Walter [91]. The technique was first applied by Burns and Haring [92] to interpret the action of pigments and primers, and later by Haring and Gibney [93] to compare with the results from outdoor exposure on a set of 50 different paints. For painted steel immersed in artificial seawater, Wormwell and Brasher [94] observed three sections in the potential–time curve (Fig. 10): an initial drop in potential, followed by a rise and finally a gradual decline. The time required to reach the potential peak was considered as the period of useful life of the paint, since the mass loss increased significantly after that instant.

Although the technique is simple and effective in the study of pretreatments, one major difficulty lies in the fact that, for highly resistive coatings, the potential is not easily measurable prior to the failure of the coating, and therefore no information is usually obtained during that stage [91].

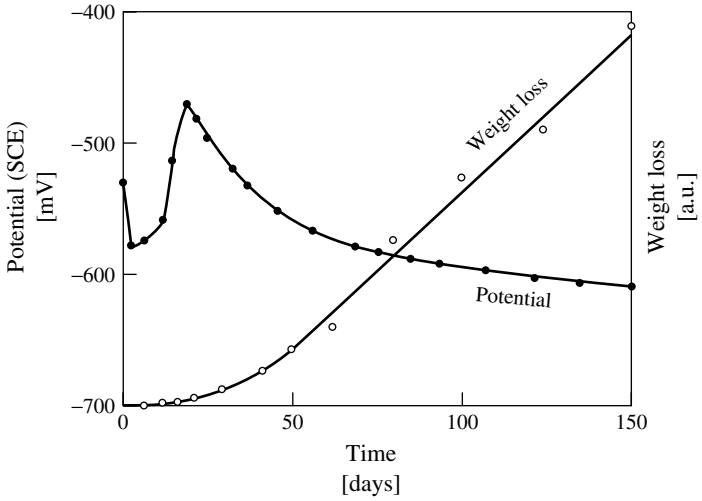


Fig. 10 Potential–time and weight loss curves for painted steel (adapted from Wormwell and Brasher [94]). (Reprinted with permission.)

This limitation also makes the method a nonaccelerated one.

In the past decade, with the development of more refined and more informative techniques, potential measurements found only very limited application.

5.4.2.2 Electrochemical Impedance Spectroscopy

Electrochemical impedance spectroscopy (EIS) is a convenient and effective method of assessing the properties and performance of organic-coated metal systems. The AC impedance of an electrochemical cell can be determined by applying a sine wave of potential (V) of a certain frequency (ω) and measuring the corresponding current (I) flowing across the cell. The ratio of potential and current is the impedance of the cell (Z) at the chosen frequency, according to Ohm's law:

$$Z = \frac{V}{I} = \frac{V_0 \sin \omega t}{I_0 \sin(\omega t - \varphi)} \qquad (18)$$

The phase angle φ accounts for the shift of the current with respect to the potential, whereas V_0 and I_0 are the moduli of potential and current, respectively.

The impedance is given by a complex number, with a real (Z') and an imaginary component (Z''):

$$Z = Z' - jZ'' \qquad (19)$$

where $j = \sqrt{-1}$. A spectrum can be obtained by varying the frequency of the applied signal, in which case the technique is called EIS. The fundamentals of the technique are given in Chapter 7. This subsection shall deal essentially with the characteristics of the technique that are specific to polymer-coated systems. The possibilities of the technique have been reviewed by Mansfeld [95].

When compared to other techniques for corrosion evaluation, EIS has several advantages:

- It gives kinetic information on the corrosion processes. The use of AC signals allows the separation between the resistances of charge transfer resistance, of the coating itself and of the solution. With polarization curves only the polarization resistance is measured, which is the sum of all the resistances in the system. The possibility of separation of each of those components is of great importance, particularly in highly resistive systems, such as organic coatings.
- It gives mechanistic information. This is based upon the use of "equivalent circuits", which are electronic circuits whose response is identical to that of the cell under study.
- It provides information on the properties of the coating itself, namely its resistance and capacitance. The changes in these properties have been associated with the loss of protective properties.
- The technique is nondestructive, in contrast with DC polarization curves, and it provides immediate information on the systems, in contrast to exposure of samples in natural environments or even in climatic chambers.

The greater disadvantages are the difficulty of interpreting the spectra in an unknown system, and also the need to control the area under measurement, since all the values determined are affected by the extension of the surface.

5.4.2.2.1 Basic Analysis

The easiest way of using impedance data is to make visual examination of the shape of the spectrum and of its evolution with time. In a coated system of high protection, the Nyquist plot

comes as an arc of very large diameter that cannot be totally defined because of experimental limitations.

If water penetrates into the coating, the impedance of the system decreases. In this phase, the resistance of the coating decreases, whereas its capacitance increases with time. Upon prolonged immersion, the initial arc tends to close, approaching the real axis, and a second semicircle develops, corresponding to a corrosion reaction underneath the coating. The smaller the semicircles, the lower the resistance of the corresponding component, revealing a higher permeability of the coating, a higher corrosion rate, or the combination of both. An example of this evolution is presented in Fig. 11.

5.4.2.2.2 **Equivalent Circuits** For a more detailed analysis of spectra, the theory of electronic AC circuits is required. In this approach, numerical fitting of an equivalent circuit is made, using appropriate software. There are a number of equivalent circuits proposed in the literature for organic-coated metals [96, 97]. From these, only the most relevant will be presented.

Figure 12 describes a simple electrochemical cell with a bare metal, in which the corrosion process is controlled by charge transfer. In this circuit, R_Ω is the ohmic resistance, corresponding to the solution in the cell plus the cables and connections. R_{ct} is the charge transfer resistance and C_{dl} the capacitance of the double layer at the solution–metal interface. The Nyquist and Bode plots for this circuit are also presented.

For an electrode with a highly protective film of organic coating, the circuit in Fig. 13 is usually applied. In this circuit, C_c

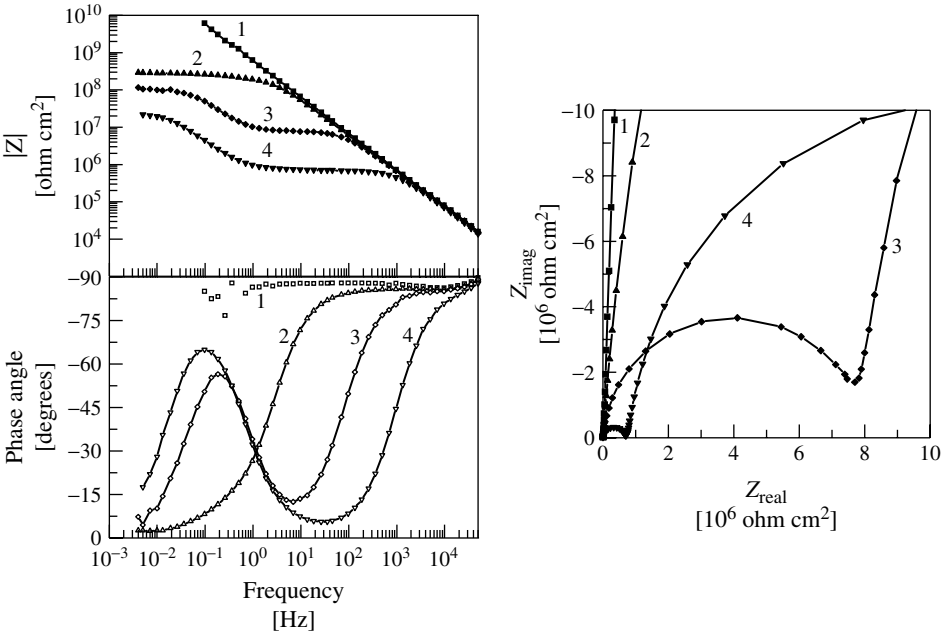


Fig. 11 Evolution of the impedance spectrum of organic-coated zinc during immersion in NaCl solution, after: (1) 6 h; (2) 2 days; (3) 7 days; and (4) 32 days.

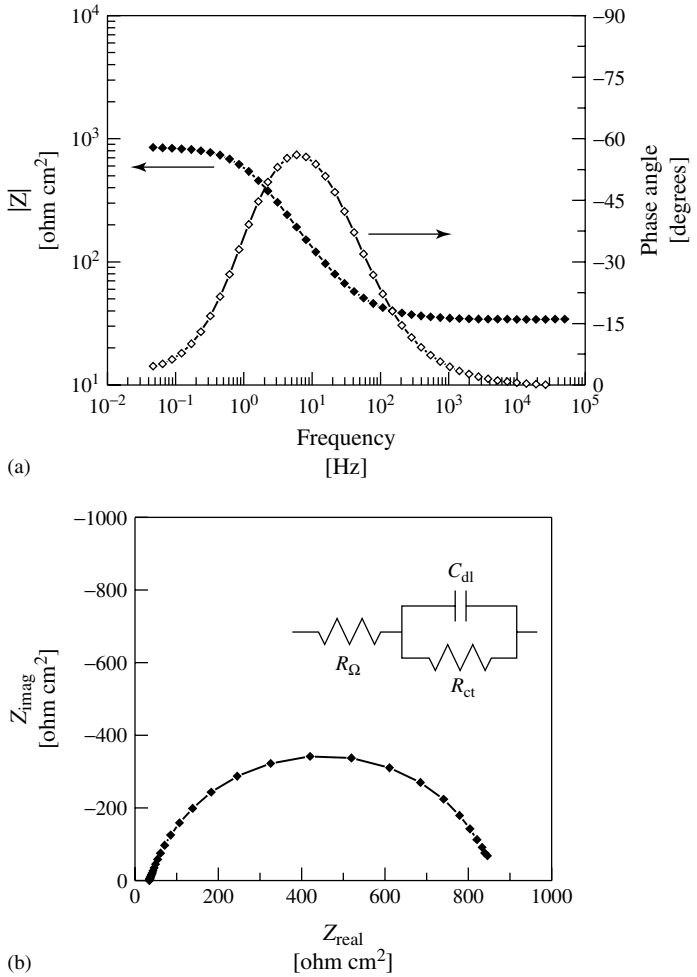


Fig. 12 Impedance spectrum and equivalent circuit for a metallic electrode undergoing a corrosion process ((a) Bode plot, (b) Nyquist plot).

is the capacitance of the coating and R_c the resistance of the film to ionic conduction. If the coating is considered as a dielectric, then its capacitance is given by:

$$C_c = \frac{\varepsilon \cdot \varepsilon_0 \cdot A}{d} \qquad (20)$$

where ε_0 is the permittivity of free space ($\varepsilon_0 = 8.85 \times 10^{-14}$ F cm^{-1}), ε the dielectric constant of the polymer, d the coating thickness, and A the exposed area of the electrode under test. The coating resistance, R_c, accounts for the ionic conduction along preferential paths across the coating. In new coatings, this resistance often exceeds the capabilities of the measuring equipment. The solution resistance R_Ω cannot usually be measured, since it becomes masked by the coating capacitance in the working range of frequencies.

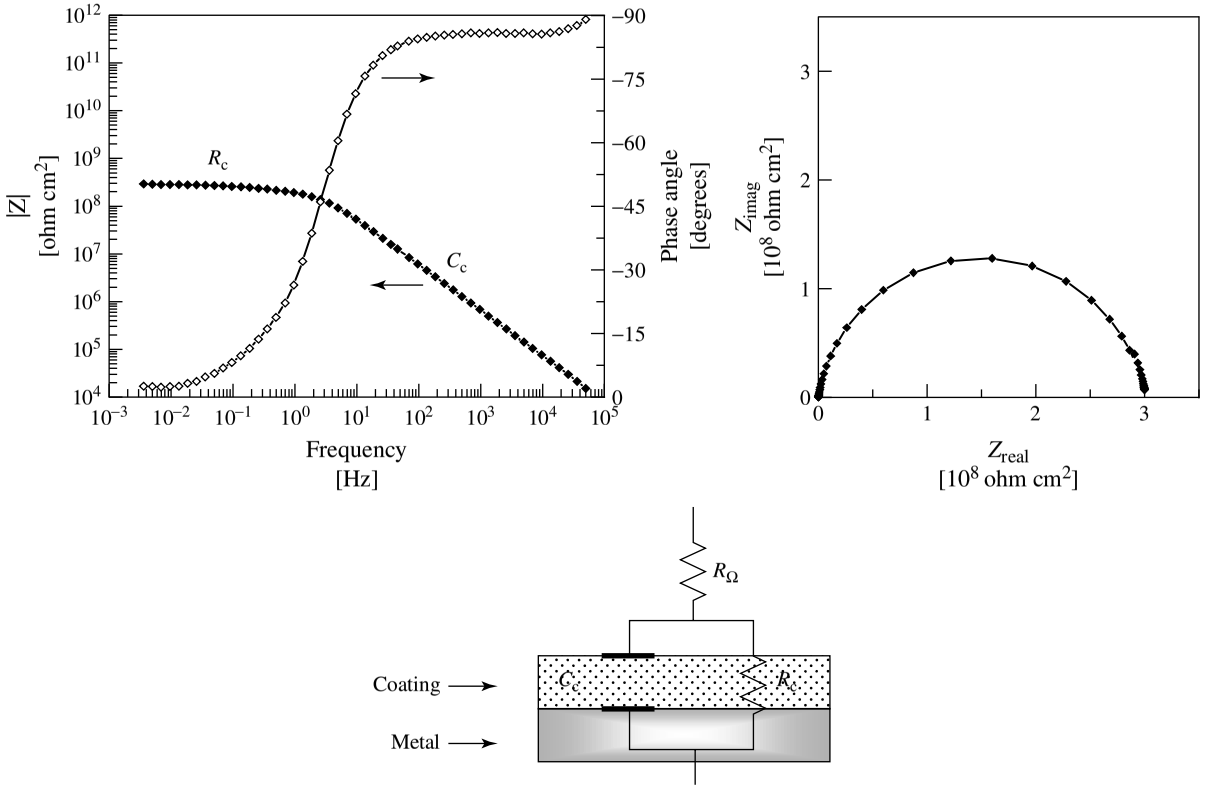


Fig. 13 Impedance spectrum and equivalent circuit for organic-coated metal without apparent degradation. Notice the high impedance of the coating.

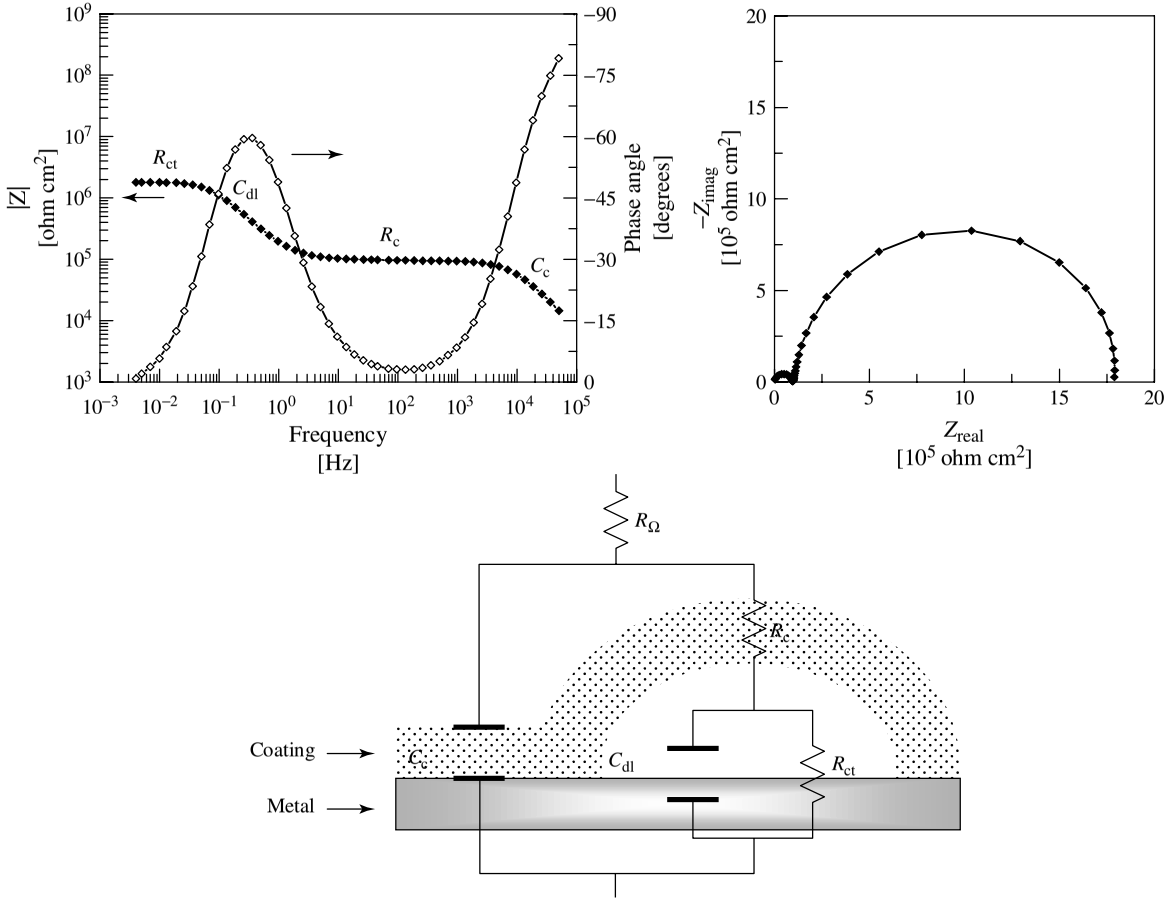


Fig. 14 Impedance spectrum and equivalent circuit for organic-coated metal, with corrosion occurring under the blisters.

In the case of corrosion underneath the coating, at disbonded or blistered areas, both the coating and the corrosion processes underneath can be detected. The circuit usually applied and the corresponding spectra are presented in Fig. 14. It is interesting to note that the resistance R_Ω is usually not detected in the range of frequencies tested, since it is masked by the coating capacitance. The coating capacitance has very low values, usually in the range 10^{-10}–10^{-9} F cm^{-2}, whereas a double layer capacitance can be taken as 20–60 μF cm^{-2}. A more complicated circuit was proposed by Hirayama and Haruyama [98], to account for large pores or defects in the coating (Fig. 15). In this circuit, corrosion processes are considered in two areas in parallel: underneath the blisters and at the defects. The defects are described by a charge transfer resistance R_{ctp} and a double layer capacitance C_{dlp}, at the bottom of the defect, and a resistance for ionic migration through the defects, R_p. If there are several defects – or several large pores – the model describes them as one single defect having the total area of the defects. The spectrum is characterized by having the time constant related with the coating at the high frequencies, followed by the responses of the two separated corrosion areas. Since the high frequency limit of the measuring equipment usually does not exceed 10^5 Hz, part of the spectrum may be out of the working frequency window. The positioning of the various processes may also be shifted in the spectrum, resulting in some overlapping of the time constants. A numerical simulation of this circuit is presented in Fig. 16.

The equivalent circuits described above are capable of describing most painted systems. Nevertheless, interpretation may sometimes be difficult, particularly after long exposure periods, when large quantities of corrosion products accumulate on the surface. Another difficulty for the technique is associated with the existence of blisters under intact coatings. In fact, for highly dielectric coatings, free of pores, the very high impedance of the coating masks the electrochemical processes underneath. To circumvent the problem of the high impedance of the coating between the reference electrode and the metal polymer interface, Scantlebury made measurements using an artificial blister [82], whereas Feser and Stratmann developed a setup in which the reference electrode was directly placed at the interface [31]. This experimental setup consisted of one reference

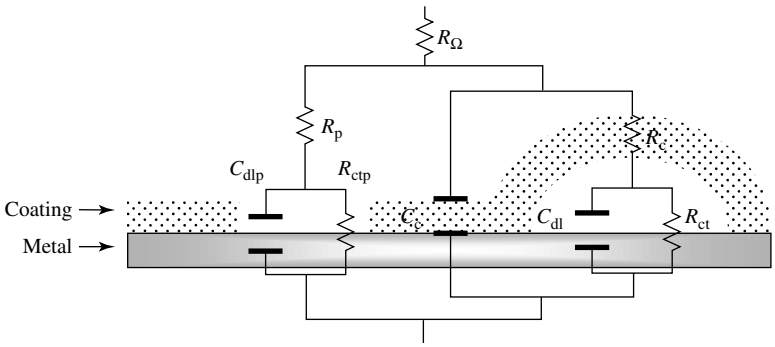


Fig. 15 Equivalent circuit for a coated metal with corrosion at defects on the surface and also underneath blisters.

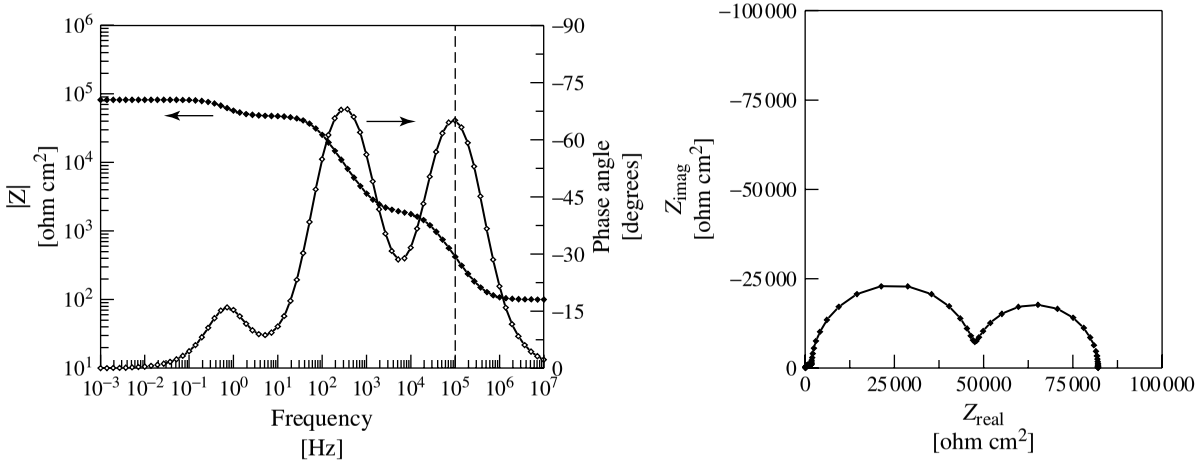


Fig. 16 Simulated spectrum using the circuit in Fig. 15. Values used in the simulation: $R_\Omega = 100\ \Omega\ cm^2$; $C_c = 4 \times 10^{-9}$ F cm^{-2}; $R_c = 1 \times 10^5\ \Omega\ cm^2$; $C_{dl} = 2 \times 10^{-6}$ F cm^{-2}; $R_{ct} = 6.5 \times 10^5\ \Omega\ cm^2$; $R_p = 2 \times 10^3\ \Omega\ cm^2$; $C_{dlp} = 5 \times 10^{-8}$ F cm^{-2}; $R_{ctp} = 9 \times 10^4$ F cm^{-2}. The dashed vertical line corresponds to a typical high frequency limit of the measurements.

electrode located at the metal–polymer interface and a second one positioned in front of the coating. Although this setup is interesting for fundamental studies, it is too sophisticated for the evaluation of technical systems.

5.4.2.2.3 **Relevant Parameters** In addition to the mechanistic information, relevant parameters can be obtained, related with the corrosion and/or loss of protective properties of the coating.

The coating capacitance C_c is sensitive to water absorption. The dielectric constant of polymer coatings is usually in the range 4–7, whereas for water at 20 °C it is approximately 80. Consequently, water uptake results in an increase of the coating capacitance, according to Eq. (20). Bellucci and Nicodemo [45] have made a theoretical approach of the subject. A review of several models proposed for the determination of water absorption as well as experimental comparison was made by Lindqvist [53], who observed that for a large number of coatings and for the conditions under test, the best agreement with gravimetric results was obtained with the Brasher–Kingsbury equation [55]:

$$\phi = \frac{\log[C_c(t)/C_c(0)]}{\log(80)} \qquad (21)$$

in which ϕ is the volume fraction of water in the coating and $C_c(t)$ and $C_c(0)$ are the coating capacitance at an instant t and of the dry coating, respectively. This last parameter is obtained from extrapolation to $t = 0$. From the double layer capacitance, C_{dl}, the fraction of the surface with loss of adhesion, D, can also be determined [99]:

$$D = \frac{C_{dl}}{C_{dl}^0} \qquad (22)$$

In this, C_{dl}^0 is the double layer capacitance of a totally delaminated surface.

Apart from these, a few other items concerning organic coatings have also been addressed in the literature. In a series of publications, de Wit and coworkers [40, 56, 100] have addressed the subjects of curing of coatings and protective mechanisms of pigments, water uptake, and loss of adhesion.

The properties of freestanding films, particularly the water permeation, have also been addressed and compared with the behavior of supported films [38, 54].

Apart from water and ions, other factors contribute to the degradation of organic coatings. Ultraviolet radiation, often combined with oxygen exposure, lead to modifications in the polymeric chains, decreasing the barrier properties of the coatings. Bonora and coworkers [101] have observed a rise of water permeability as a consequence of coating irradiation.

Other problems have been investigated in recent years, such as the effect of mechanical strain on the loss of protective properties [102, 103], or the delamination starting from cut edges [104].

5.4.2.3 **Electrochemical Noise**

Generally speaking, the term "noise" describes the random fluctuations of a property around a mean value. Noise can be of various kinds, from acoustic to meteorological, or even associated with the rotation speed of planets.

The first studies on electrical noise in physical systems were due to Einstein [105]. In the 1960s, Hagyard and Williams [106] were the first to report electrochemical noise, observed as fluctuations of the potential of aluminum immersed in a potassium chloride solution.

Iverson reported the first observation of potential noise associated with metallic corrosion [107]. He also observed that the noise could be decreased by the addition of a corrosion inhibitor.

The fluctuations of potential – potential noise – and of current – current noise – can be made independently or together. The current measurements are made between two identical electrodes coupled by means of a zero resistance ammeter (ZRA), which keeps them at the same potential. If potential and current are followed simultaneously, then the potential measurements are made between the coupled electrodes and a third electrode (Fig. 17). This third electrode can be either a reference electrode, such as the saturated calomel electrode (SCE), or even identical to those of the pair connected to the ZRA. When only the potential measurements are taken, it is sufficient to measure the potential between two identical electrodes or between the electrode under test and a reference. By taking discrete measurements during a certain period of time, a "time record" of potential or of current is obtained.

The first step in the analysis of the data consists in removing the DC trend, leaving only the fluctuations [108] (Fig. 18). Because of the nature of the measurements, the influence of instrumental noise is of major importance, and it is therefore essential either to minimize the spurious noise by adjusting the setup [109] or to remove the instrumental noise from the "noise signal" of the electrochemical system. This subject has been discussed earlier by Epelboin

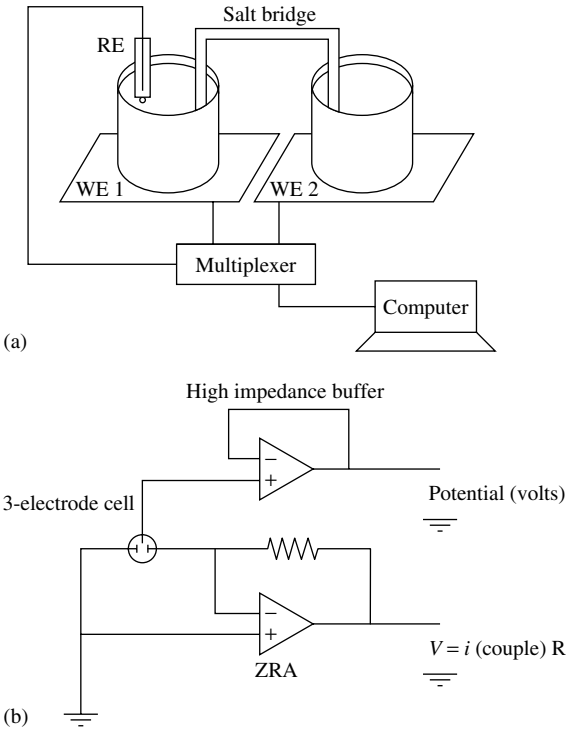


Fig. 17 Arrangement for simultaneous potential and current noise measurements: (a) experimental setup and (b) electronic configuration.

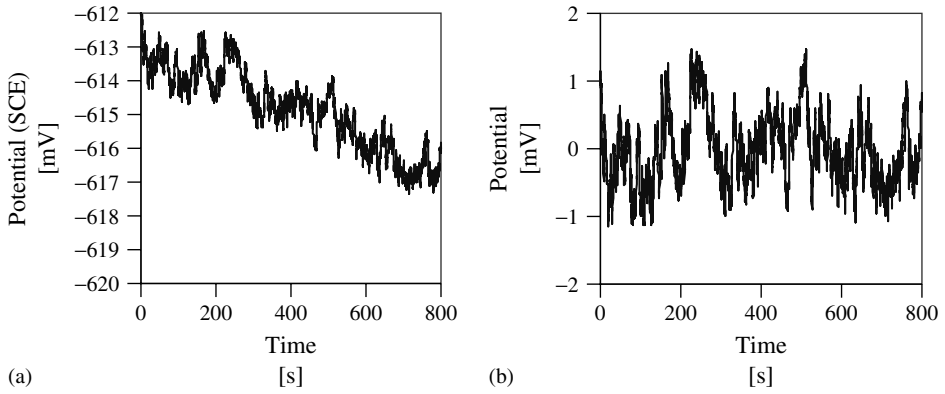


Fig. 18 Potential–time record: (a) as obtained and (b) after DC trend removal.

and coworkers [110], and more recently by Bertocci and Huet [111].

The most simple attempts to quantify noise and correlate it with corrosion rates were based on the standard deviation either of the potential – $\sigma(V)$ – or of the current – $\sigma(I)$ [112–114]. Those values were then compared with the corrosion rate, determined by some other method.

In a different approach, the time record of potential or current is converted into a power spectral density (PSD), which is the distribution of the power in the frequency domain. This transformation is usually made by means of the fast Fourier transform (FFT) algorithm [115]. Alternatively, the maximum entropy method (MEM) can also be used [116], although with some limitations [117]. In corrosion systems, both the potential noise and current noise are of the $1/f$ type, that is, the maximum occurs at low frequencies.

The range of frequencies depends on the sampling interval Δt (typically $\Delta t = 0.5$ s) and on the number of readings M of a time record (usually 1024). The maximum and minimum frequencies that can be analyzed are:

$$f_{\max} = \frac{1}{2\Delta t} \tag{23}$$

and

$$f_{\min} = \frac{1}{M\Delta t} \tag{24}$$

In practice, spectral noise plots can be obtained only in a frequency range that is more limited than in EIS. On the high-frequency side, the limit is imposed by the instrumental noise, whereas in the low-frequency region, the time of acquisition becomes very long [118].

The noise signal has been studied in a variety of situations, and it has been associated with localized rupture in passivating oxides [119–121] and with hydrogen bubbling on a corroding electrode [115]. Reviews of the applications of the technique have been made by Dawson [122] and by Eden [123].

The technique was first applied to organic coatings by Skerry and Eden [124], who proposed the concept of noise resistance R_n as the ratio between the standard deviations of the potential and current

noise, in an analogy with Ohm's law:

$$R_n = \frac{\sigma(V)}{\sigma(I)} \tag{25}$$

The noise resistance has given consistent trends when compared with the coating resistance from impedance measurements [125]. Some authors also suggest that R_n corresponds to the polarization resistance, which encompasses the coating, the charge transfer and also the diffusion processes [124].

Provided the potential and current data are acquired simultaneously, it is possible to obtain spectral noise plots for each of them, and another resistance, R_{sn}, can also be defined [126, 127]:

$$R_{sn}(f) = \left| \frac{V_n(f)}{I_n(f)} \right| \tag{26}$$

$V_n(f)$ and $I_n(f)$ are the power spectral distributions of potential and current, respectively, obtained by the FFT or the MEM method. The spectral noise resistance, R^0_{sn}, is determined [128] as the DC limit of the plot of $R_{sn}(f)$:

$$R^0_{sn} = \lim_{f \to 0} R_{sn}(f) \tag{27}$$

From the plot of $\log - R_{sn}$ versus $\log f$, the slope m can be determined. Changes in this slope have also been related with coating degradation [129].

From the studies of several authors [130, 131], it can be concluded that a decrease of R_n and R_{sn} is associated with the onset of corrosion. However, if two identical electrodes are used, this decrease may only be observed when both electrodes are affected by corrosion. This was explained by the circumstance that the electrodes are placed in series, and therefore the electrode with the higher impedance controls the response of the pair [118].

Comparison between noise and impedance measurements has shown a reasonable agreement between the spectral noise plots and the impedance plots. Mansfeld and Lee [132] also concluded that although for very protective polymer coatings, R_n did not have a relationship to a particular coating property, for degraded coatings the noise resistance was identical to the polarization resistance. This, however, was limited to the cases in which the PSD plots of potential and current had the same slopes.

Mills and Mabbutt have pointed out that accurate determination of R_n requires that the statistical distribution of the intensity of the fluctuations should have a Gaussian distribution about the mean intensity [130]. These authors observed that in situations of competition between passivity and inhibition, a non-Gaussian, bimodal distribution could occur, and suggested that a second parameter in addition to R_n might be appropriate.

The technique was successfully applied to monitoring at remote test sites, under computer control and data transmission to the laboratory via modem [133]. Another interesting application is the ranking of organic coatings, based on the principle that a high R_n corresponds to a good performance [134, 135].

A recent approach to electrochemical noise, based upon fractal analysis, was proposed by Greisiger and Schauer [136]. Although the principles of electrochemical noise are reasonably well understood, there is still some controversy regarding the information that can be extracted from the results. The technique may possibly work as an alternative to EIS for high impedance coatings [134], when the impedance of the coating exceeds the capabilities of the measuring equipment. On the other hand, the equipment required

is cheaper than for EIS, which is another advantage. From an experimental standpoint, the technique is also quite attractive. It is nondestructive, data acquisition is easy, and, provided a simple analysis is made, reasonable information can be obtained with relatively small expertise. Up to present, however, the questions that still arise on the interpretation of results justify the fact that it is mostly used as a complement to other techniques.

5.4.2.4 Scanning Reference Electrode Techniques

Defects in organic coatings may originate from the production process (e.g. cut edges, forming induced defects) or from mechanical impact (e.g. stone chipping). However, coatings may possess ionic conductive pathways or ionic residuals, which are located at the interface so that corrosion starts at not visibly damaged sites of the coating. Since EIS is, a priori, an integral method it can detect the existence of such defects but it cannot assign it to certain points on the examined surface. The idea of a local measurement is to examine areas separately that differ in their local activity.

Measuring local electrode potentials by means of scanning reference electrodes has a long history in electrochemistry. Recently, the development of the scanning vibrating electrode technique (SVET) led to the utilization of localized current density maps to detect local defects in an organic coating after forming or to measure the activity of cut edges in corrosive environments [137–140]. The local measurement of currents cannot overcome the inherent difficulty to measure through insulating layers but helps to understand the origin of defects and the influence of inhibitors and pigments on the activity of these defects. The fundamentals of the scanning electrode techniques are given in Chapter 7. The local mapping of currents thus provides insight into the existence and distribution of defects and galvanic currents at cut edges. Moreover, it is an interesting tool to study the effect of active corrosion pigments in organic coatings as shown recently [139–141].

The following schematic representation in Fig. 19 shows the application of the SVET for two types of defects in a polymer coating on galvanized steel.

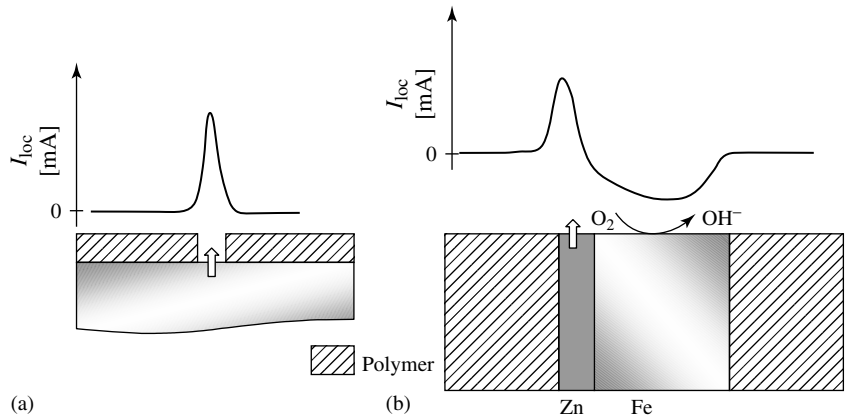


Fig. 19 Schematic current distributions for polymer-coated steel above a scratch (a) and a cut edge and (b) of galvanized steel.

In Fig. 19(a), a defect in a polymer coating on a metal substrate is shown. The anodic dissolution in the defect leads to a positive current peak. The intact polymer-coated area shows zero current. A second important situation, a cut edge of coil-coated galvanized steel, is shown in Fig. 19(b). The zinc dissolution leads to a positive peak while the area of oxygen reduction on the cathodically protected steel surface is characterized by a broad negative current peak. The activation, distribution, and passivation of these local anodes and cathodes can now be studied by the SVET as a function of coating compositions.

Isaacs and coworkers measured the distribution of current density on scribed, painted zinc-coated steel during early stages of exposure in sodium chloride and sodium sulfate solution [142]. Samples were electroplated steel and steel with hot-dipped 55% Al −1.6% Si – balance Zn alloy. Different kinds of defects such as shallow scratches to the coating, deep scratches to the underlying steel, and those after mechanical deformation of the coated surface were prepared. The current distributions in the defect area were dependent on the kind of scratch that was produced and the change with the time of exposure in the NaCl solution.

Worsley and coworkers utilized an SVET to investigate the corrosion at cut edges of coil-coated steel [143]. Samples were hot-dip galvanized steel, chromate treated and coated on both sides by a 5-μm epoxy-based polymer. A 140-μm PVC laminate coating was applied to one or both sides of the sheet to produce asymmetrically and symmetrically coated samples. Measurements were done in 0.86 M NaCl solution. Interestingly, the measurements of line scans across the cut edge of asymmetrically coated samples showed a marked displacement of cathodic activity to the side were the organic coating is thinner. The authors moreover observed that the anodic current is increased on the side with the thicker coating compared to both symmetrically coated samples. The separation of anodic area and cathodic area stayed almost constant in the asymmetric case whereas both symmetrically coated samples showed a current profile that seemed to diminish with time, especially for the thicker coating. The authors argue with an establishment of a differential aeration cell in the asymmetric case to explain the distinct behavior of this coating system. The observed faster delamination of the thinner coating in the asymmetric case is explained by a predominant oxygen reduction where the coating is thinner.

Localized electrochemical impedance spectroscopy (LEIS) technique has been applied to study the local ac solution current density above a polymer-coated specimen surface [144, 145]. Carbon steel samples were polished, cleaned and than contaminated by dropping a small amount of NaCl solution in the center of the specimen. After drying, the sample was coated with an epoxy resin. Impedance measurements were done in a dilute NaCl solution. The authors revealed that even above a visible blister underneath the coating an impedance spectrum almost equal to that of the intact area is measured by LEIS as long as the coating itself is intact. The reason is the high impedance of the coating in series with the low impedance of the interface in the contaminated region. A smaller change observed directly above the blister was assigned to a local change in the capacitance of the coating.

5.4.2.5 The Application of the Scanning Kelvin Probe

As reported in Chapter 7, the SKP allows one to overcome the difficulty of conventional reference electrode techniques, which require a conducting path between the reference electrode and the working electrode. In principle, the Kelvin probe measures the work function of a sample using the vibrating condenser method. Under certain circumstances, the work function is determined by the electrode potential, and therefore the Kelvin probe is able to measure local electrode or corrosion potentials. The major advantage of the Kelvin probe in comparison to conventional reference electrodes is the fact, that it measures electrode potentials without touching the surface under investigation across a dielectric medium of infinite resistance. In the case of organic coatings, this means that the SKP measures the electrochemical potentials at the polymer–metal interface with high spatial resolution.

A relation between the Volta potential difference $\Delta\Psi^{\mathrm{Ref}}_{\mathrm{sample}}$ and the corrosion potential of the corroding interface exists, which must be derived for different interfaces of interest. For polymer-coated materials, the Kelvin probe provides information on the potential distribution at the inner buried interface [59, 85, 146–149]. In Fig. 20(a and b), the potential distributions across a metal–polymer composite are schematically shown for different corrosion situations [147].

5.4.2.5.1 System Metal–Polymer–Humid Air

For nonhighly oriented polymers with rather small dipole potential, the following result is obtained for the correlation of the corrosion potential E_{corr} and the measured Volta potential difference $\Delta\Psi$ [150]:

$$E_{\mathrm{Corr}} = \left\{ \frac{W_{\mathrm{Ref}}}{F} - \chi_{\mathrm{Pol}} - \varepsilon^{\mathrm{Ref}}_{1/2} \right\} + \Delta\Psi^{\mathrm{Ref}}_{\mathrm{Pol}} \tag{28}$$

where W_{Ref} is the work function of the reference metal, χ_{Pol} is the surface dipole potential of the polymer, and $\varepsilon^{\mathrm{Ref}}_{1/2}$ is the half-cell potential of the reference metal.

Similar to an electrolyte-covered metal surface, an electrode potential of the inner interface would be measured. However, the physical meaning of this electrode potential is not as obvious, as it cannot be interpreted by conventional electrochemical kinetics. The electrode potential could in the absence of any faradaic currents be determined by dipole orientation of segments of the polymer chain. If, however,

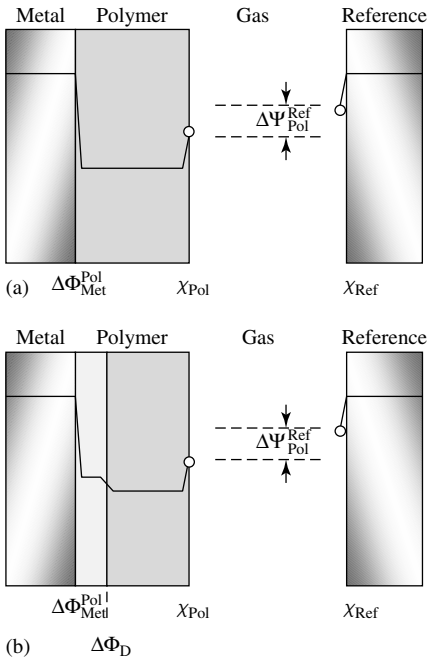


Fig. 20 Diagram of the Galvani potential between the polymer-coated substrate and the reference electrode for: (a) a polymer-coated metal and (b) a delaminated polymer.

faradaic currents like the reduction of oxygen are possible at the inner interface then the interface will be polarized until the rate of the oxygen reduction is negligible. This is true, for example, for polymer-coated gold surfaces.

5.4.2.5.2 **System Metal–Oxide–Polymer–Humid Air** Usually, at atmospheric conditions reactive metals are covered with a thin native metal oxide. Consequently, the real polymer–metal interface consists of an interfacial inorganic nonmetallic layer, which influences the reactivity of the composite system. In this case, the Volta potential difference is given by Ref. [150]

$$\Delta\Psi_{\mathrm{Pol}}^{\mathrm{Ref}} = \Delta\Phi_{\mathrm{Ox}}^{\mathrm{Me}} + \Delta\Phi_{\mathrm{Ox}} + \Delta\Phi_{\mathrm{Pol}}^{\mathrm{Ox}} - \frac{1}{F}\mu_{\mathrm{e}}^{\mathrm{Me}} - \frac{W_{\mathrm{Ref}}}{F} + \chi_{\mathrm{Pol}} \quad (29)$$

where $\Delta\Phi$ is the respective Galvani potential difference and μ_{e} is the chemical potential of the electron.

If the Volta potential drop across the oxide layer is substituted by the corresponding change in chemical composition, for example, for oxide-covered iron, then for an iron substrate $\Delta\Psi_{\mathrm{pol}}^{\mathrm{ref}}$ is:

$$\Delta\Psi_{\mathrm{Pol}}^{\mathrm{Ref}} = -\frac{\Delta\mu^{0}_{\mathrm{Fe^{3+}/Fe^{3+}}}}{F} + \Delta\Phi_{\mathrm{Pol}}^{\mathrm{Ox}} - \frac{W_{\mathrm{Ref}}}{F} + \chi_{\mathrm{Pol}} + \frac{RT}{F}\ln\frac{[\mathrm{Fe^{3+}}]}{[\mathrm{Fe^{2+}}]} \quad (30)$$

Thus, the Volta potential difference represents the oxidation level within the oxide scale at the metal–polymer interface [151].

5.4.2.5.3 **System Metal–Metal Oxide–Electrolyte–Polymer–Humid Air** The system metal–metal oxide–electrolyte–polymer–humid air is valid for a delaminated interface where an electrolyte layer is formed between the substrate and the polymer. $\Delta\Phi_{\mathrm{D}}$ is called the membrane or Donnan potential, and is directly associated with the preferential incorporation of ions into the polymeric matrix [149, 152, 153]. The following correlation exists between the Volta potential difference and the corrosion potential [150]:

$$E_{\mathrm{Corr}} = \frac{W_{\mathrm{Ref}}}{F} - \chi_{\mathrm{Pol}} - \varepsilon_{1/2}^{\mathrm{Ref}} + \Delta\Phi_{\mathrm{D}} + \Delta\Psi_{\mathrm{Pol}}^{\mathrm{Ref}} \quad (31)$$

Therefore, the Volta potential difference $\Delta\Psi_{\mathrm{Pol}}^{\mathrm{Ref}}$ allows one to measure the corrosion potential at the inner metal–electrolyte interface buried below the polymeric coating only if the Donnan potential is known or small. Usually, the Donnan potential is significant for polymers with a high density of fixed charges (ion exchange membranes), as polymers with fixed cationic functional groups will exchange exclusively anions and vice versa [153, 154]. Lacquers used for corrosion protection may have some fixed ionic groups; however, their concentration is orders of magnitudes lower than that of typical ion exchange membranes.

5.4.2.5.4 **Sample Preparation for SKP Measurements** Presuppositions for Kelvin probe measurements on polymer-coated metals are that:

- no electric surface charge exists on the polymer coating,
- no electrolyte covers the coating surface that is in contact with the metal substrate,
- an electronic equilibrium exists between the coatings surface and the metal substrate.

Thus, the polymer surface has to be clean and often it has to be in its swollen state. Careful sample preparation is thus needed to avoid misinterpretation of data.

5.4.3 Corrosion Mechanisms of Polymer-coated Metals

Electrochemical reactions that lead to a degradation of the metal–polymer interface are influenced by the following properties: the electron transfer properties at the interface, the redox properties of the oxide between the metal and the polymer and the chemical stability of the interface with respect to those species, which are formed during the electron transfer reaction.

- The rate of electron transfer reactions (ETRs) is strongly influenced by the surface composition of the metal. As most materials are covered by oxides, their electronic properties will determine the rate of ETR. Therefore, metals that are covered by electron conducting or semiconducting oxides such as iron or zinc will show a higher ETR rate at the substrate–polymer interface in comparison to materials that form highly insulating oxides such as aluminum.
- Certain oxides are characterized by a fixed ratio of anions and cations (e.g. Al_2O_3), whereas others have a strongly potential dependent composition such as iron oxides due to the flipping of valence states (Fe^{2+}, Fe^{3+}) in the cation sublattice. Any change of the electrode potential is reflected in a change of the valence states and this will change the semiconducting properties, as, for example, Fe^{2+}-states can be regarded as donors of the n-type semiconductor [155, 156]. Furthermore, during reduction of the oxide, the base material will be oxidized and this may limit the adhesion of the coating.
- During the electron transfer, very reactive intermediates and reaction products are formed that will chemically react with the interfacial layer. It is shown below that major reaction products such as OH^- ions, which are generated during the reduction of molecular oxygen, are of significance for the delamination process. Certain materials such as iron are very stable under those alkaline conditions, whereas others such as aluminum or zinc are covered with oxides that are unstable in alkaline electrolytes [75].

Accordingly, it must be expected that steel, zinc-coated steel, aluminum and magnesium will behave rather differently according to their respective electronic, redox, and chemical surface properties.

5.4.3.1 Corrosion of Polymer-coated Iron

5.4.3.1.1 Introduction While currently a steadily increasing amount of steel sheet is coated by a zinc or zinc alloy coating prior to the application of an organic coating (see Chapter 5.5), for steel structures there is no alternative to using painted low alloy steel. Moreover, painted steel structures such as bridges, piers, and pipelines are exposed to extremely hostile environments such as salt spray, rain, high humidity, UV radiation, and extremes of temperature.

Under atmospheric conditions, iron is covered by an ultrathin n-semiconducting oxide (see Chapter 3.2). This thin oxide can be directly coated with an organic coating or the oxide sometimes is first replaced by a conversion coating (see Chapter 5.3). The

conversion coating increases the corrosion stability of the organically coated iron surface significantly.

Polymer-coated mild steel can exhibit two fundamental corrosion processes:

- cathodic delamination and
- filiform corrosion,

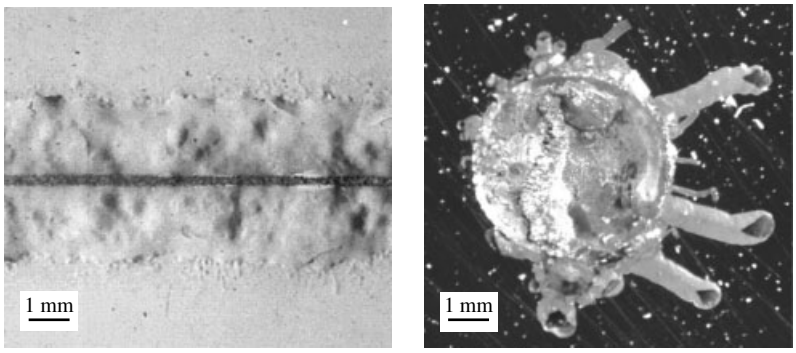
depending on the corrosive conditions. While cathodic delamination is the process that is most often found under atmospheric conditions, certain situations may lead to anodic undermining. Typical pictures of these two corrosion forms are shown in Fig. 21.

The cathodic delamination mechanism is discussed in detail in Sect. 5.4.3.1.2 while the FFC on iron is discussed together with FFC on aluminum in Sect. 5.4.3.3 because of the similar mechanisms.

5.4.3.1.2 **Cathodic Delamination on Polymer-coated Iron** Certain areas at the metal–polymer interface may become sufficiently cathodic to promote a cathodic reaction underneath the coating. This cathodic polarization might be the result of a purposely induced polarization, for example, cathodic protection of pipelines or it is induced by the separation of the anodic and cathodic reaction sites. The cathodic reaction underneath the organic coating leads to a deterioration of the interfacial zone and thereby leads to a deadhesion of the organic coating from the iron substrate.

An overview of the mechanism for cathodic delamination was published by Leidheiser and coworkers [157]. The authors described in detail the influence of various parameters such as oxygen concentration, water permeability of the coating, and the diffusion coefficient of cations on the delamination kinetics. At the beginning of the 1990s, Stratmann and coworkers used the SKP to measure locally the corrosion potentials underneath an organic coating on iron. These measurements proved the mechanism presented by Leidheiser and coworkers and, moreover, provided additional information on the reactivity of the metal surface underneath the coating and the spatial distribution of anodes and cathodes.

In Fig. 22, a potential map of the SKP shows a typical situation during the cathodic undermining of polymer-coated iron. In the presence of oxygen, the electrode potential of the metal–polymer



(a) (b)

Fig. 21 Microscopic pictures of: (a) cathodic delamination and (b) FFC on polymer-coated iron.

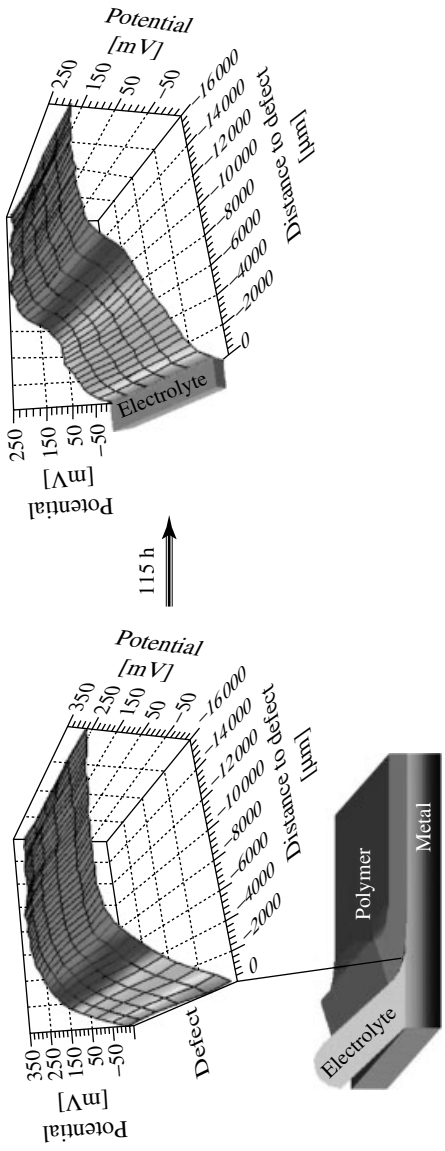


Fig. 22 Typical potential maps above a delaminating organic coating on iron as measured with SKP as a function of time in humid air. The defect (filled with 0.5 M KCl) is located on the left. The mapping covers the area from the defect border to the intact area.

interface changes in a well-defined manner with increasing distance from the defect: close to the defect the potential is negative, whereas far away from the defect rather anodic potentials are observed (Fig. 22). For most coatings, the steep increase of the electrode potential also marks the delamination front, and the region of rather anodic potentials represents the intact interface. The physical origin of the sudden change of the electrode potential is, however, given by the migration of ions from the defect into the interface that results in the polarization of the highly polarizable interface to the potential of the nonpolarizable defect [147]. This was shown by Leng and Stratmann who measured potential profiles underneath the organic coating in the absence of oxygen by means of a SKP. The missing galvanic current led to an equipotential area underneath the organic coating [147]. When the partial pressure of oxygen was suddenly increased, again the potential in the zone where ions were incorporated in the interface was shifted back to rather positive values.

The three regions clearly seen in Fig. 22 shall be discussed separately. The intact interface is characterized by an anodic potential plateau. This plateau results from the high electronic conductivity of the oxide-covered iron surface, which allows ETR but no ion transfer reactions. Therefore, oxygen will be reduced at this interface and this reaction is balanced by the anodic oxidation of the oxide. As the electrode potential of the oxide is given by the activity of Fe^{2+} and Fe^{3+} states, any oxidation results in an anodic potential shift accompanied by a steady decrease of the donor density and therefore by a decreasing rate of the ETR. Above a certain anodic potential, the rate of the oxygen reduction is extremely small and no further anodic potential shift is observed. This is the actual potential as measured by the Kelvin probe. This transient of the anodic potential shift therefore is determined by the capability of the surface for ETR. It has been shown that an appropriate surface treatment decreases the rate of this anodic potential shift dramatically up to a point where no further anodic shift is observed because of a completely blocked interface (Fig. 38).

The sudden potential step at the delamination front marks the most interesting position, as here reactions will occur that are responsible for the loss of adhesion. As discussed before, the potential step is caused by the ingress of ions into the interface and the galvanic coupling of the interface to the defect. The cathodic potential step also marks the partial reduction of the iron oxide and the increase in its donor density. Obviously, this must result in an increase in the rate of the electron transfer. Surface analysis reveals no anodic activity in this area, as no thick oxide layers are found in the delaminated area [85]. The anodic counterreaction of the oxygen reduction therefore must be the dissolution of the base material within the defect. Indeed, a galvanic current has been measured between both sites [148] and oxygen is reduced within the zone marked by the potential increase. Between the defect and the steep potential increase, a steady potential increase to more anodic values is observed. Experiments have proven that the steady potential increase is linked to the galvanic current between defect and the frontier of incorporation of ions, and is measured only if oxygen will be reduced within the latter zone [85, 147, 148].

In order to compensate the charge, soluble cations have to migrate to the zone of oxygen reduction. On the other hand, negative ions such as chlorides are

repelled from the delamination zone. This is confirmed by spatially resolved X-ray photoelectron spectroscopy (XPS) measurements, which reveal the distribution of chlorides and sodium ions underneath the coating after the separation of the latter from the iron substrate (Fig. 23). The electrochemical situation is summarized in Fig. 24.

5.4.3.1.3 **Degradation of the Interface by the Oxygen Reduction Process** During oxygen reduction, a strongly alkaline electrolyte is formed that stabilizes the oxide on the metal. Therefore, anodic metal dissolution is never observed within the zones described above. As the galvanic element obviously does not destroy the metallic substrate, the delamination of the organic coating is only caused by bond breaking within the organic zone. It has indeed been proven that intermediate radicals such as HO_2^-, OH, and O_2^- form during oxygen reduction [158] and may contribute to the oxidation of the organic layer [84, 159].

The mechanism of oxidative degradation of the polymer was postulated by Wroblowa [158] who proposed as an initial step of the reaction

$$O_2^- + R - H \longrightarrow R^\bullet + HO_2^- \qquad (32)$$

and as a subsequent reaction mechanism

$$R^\bullet + O_2 \longrightarrow ROO^\bullet \qquad (33)$$

$$ROO^\bullet + R - H \longrightarrow ROOH + R^\bullet \qquad (34)$$

Besides the chemical attack of oxygen reduction products on the organic layer, it has been discussed by several authors that a change in the oxide thickness due to the high pH of about 12–14 is also possible, and contributes to the delamination process [160, 161]. However, in situ XPS measurements showed that, even in alkaline media, a significant iron oxide reduction is possible only at potentials more negative than $-0.8\ V_{SHE}$ [162].

5.4.3.2 Corrosion of Polymer-coated Zinc and Galvanized Steel

5.4.3.2.1 **Cathodic Delamination on Polymer-coated Zinc** The situation described for polymer-coated iron and steel is also

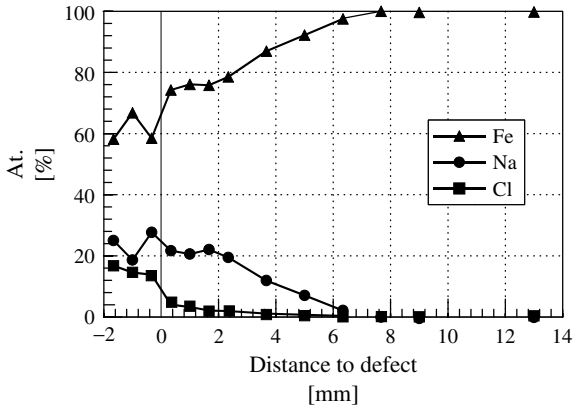


Fig. 23 Distribution of ions from the defect to the delamination front as measured by means of small spot XPS after the removal of the organic coating [76]. (Reprinted with permission.)

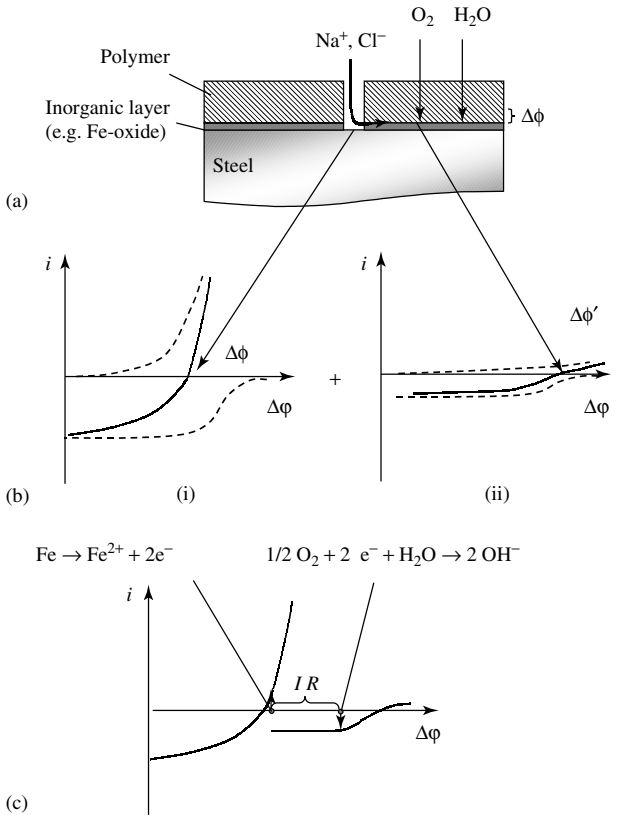


Fig. 24 Principal corrosion model explaining the formation of a galvanic element in case of cathodic delamination on polymer-coated iron. (a) Cross section through a metal–polymer interface with a defect in the polymer coating; (b) overview of the polarization curves at the defect (i), the intact interface (ii); and the situation after galvanic coupling of the parts (c).

typical for a zinc–polymer interface. Like iron, zinc is covered by n-semiconducting oxides and therefore oxygen reduction is possible at the oxide surface. Polymer-coated galvanized steel is of considerably higher technological interest than coated zinc. However, as long as the defect will only penetrate the coating and zinc is still present at the defect the situation is identical to the one of pure zinc, which can be used as a model substrate.

For the intact polymer–zinc interface, the anodic partial reaction is suppressed and therefore, the oxygen reduction will result in an oxidation of the zinc oxide layer until the electronic properties are such that no further electron transfer is possible. If, however, the atmosphere is changed to an oxygen-free one, then a rapid increase of the electrode potential is observed even for the intact interface (Fig. 25), whereas for iron the potential is stable for rather long times.

The potential transient underneath the organic coating proves that oxygen reduction is possible underneath the

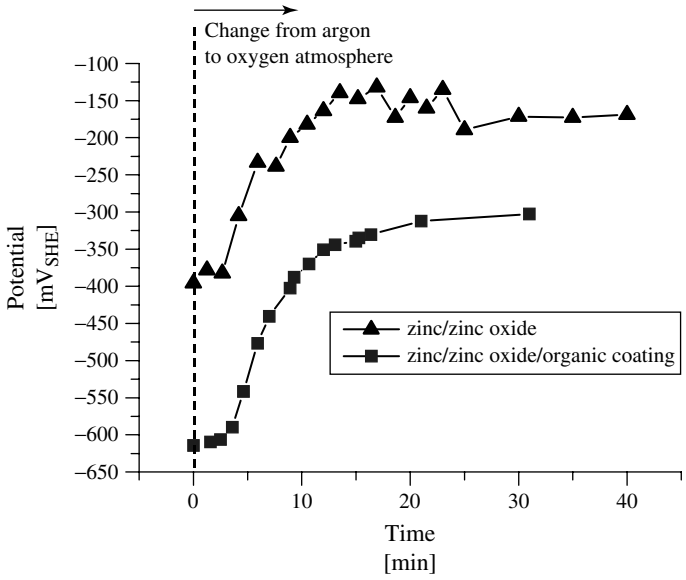


Fig. 25 Change of the electrode potential of oxide-covered zinc and polymer-coated oxide-covered zinc (UV-cured organic clear coat) after a change of the atmosphere from humid argon to humid air (at $t = 0$).

organic coating. It can be assumed that the following reactions take place within the zinc oxide

$$Zn \longrightarrow Zn_{oxide}{}^{+} + e_{oxide}{}^{-} \quad (35)$$

$$Zn_{oxide}{}^{2+} + e_{oxide}{}^{-} \longrightarrow Zn_{oxide}{}^{+} \quad (36)$$

The concentration of ionized zinc interstitials in the zinc oxide crystal lattice thereby reflect the polarization by the oxygen reduction.

As soon as ions are incorporated into the interface, a galvanic element is set up between the defect and the adjacent polymer–metal interface. The potential of the interface is polarized to more negative values and oxygen will be reduced.

Figure 26 shows three typical two-dimensional potential distributions underneath a clear coat as measured with an SKP as a function of time in vicinity of an artificial defect [83].

Obviously, a large potential difference between the active metal surface in the defect (ca. $-0.8\ V_{SHE}$) and the intact zinc–polymer interface is observed. Between these areas, a steep potential increase marks the location of the delamination front. The potential maps indicate that, as for polymer-coated iron, a cathodic reaction leads to the delamination of the coating. Fürbeth and Stratmann proved the cathodic mechanism by small spot XPS analysis of the delaminated surface [83]. While no chloride was detected in the delaminated region, the amount of sodium decreased from a high value near the defect to a small value at the front of the delamination. The distribution of sodium ions was in total agreement with the potential maps.

However, in contrast to iron oxides, zinc oxides are less stable within the induced alkaline environment. Auger electron

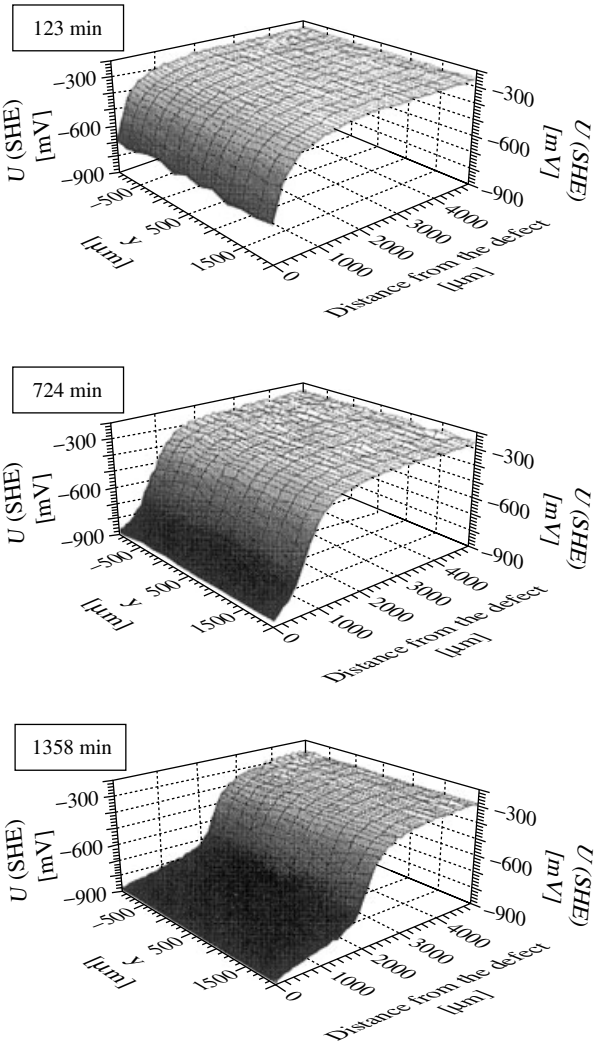


Fig. 26 Typical two-dimensional potential profiles on a polymer-covered zinc substrate as measured with the SKP in air (95% relative humidity) for different corrosion times (as indicated) with 0.5 M NaCl at the defect [83]. (Reprinted with permission.)

spectroscopy (AES) sputter profiles measured within the delaminated zone prove the significant growth of the oxide scale, which indicates anodic reactions [83]. This behavior is also reflected in potential profiles measured with the Kelvin probe after a change to an oxygen-free atmosphere (Fig. 27). Zinc potential profiles show a strong cathodic potential shift within the zone, which had been assigned to the area of oxygen reduction before. The potential shift even inverts the potential difference

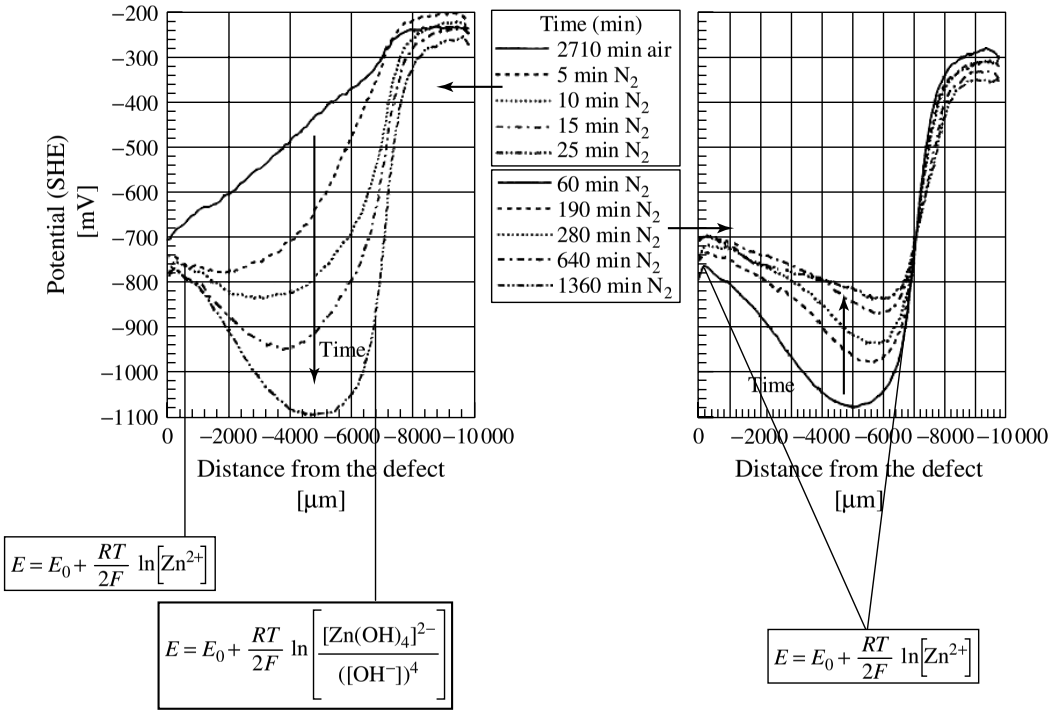


Fig. 27 Potential profiles as measured with SKP on partly delaminated polymer-coated zinc sample after a change of the atmosphere from air to pure nitrogen; corrosion time before the change: 2710 min; corrosion times since change as indicated [83]. The Nernst equations explain the local potentials in the absence of oxygen. (Reprinted with permission.)

between the defect and the frontier of ion incorporation: now the potential in the latter position is 400 mV more negative than the potential within the defect. This observation is not caused by an inversion of the galvanic element as in the absence of oxygen no galvanic current flows between the defect and the interface. The electrode potentials are only defined by the thermodynamic equilibrium potential. Within the defect the equilibrium is given by the Zn/Zn^{2+} couple, whereas at the metal–polymer interface the couple $Zn/Zn(OH)_4{}^{2-}$ will prevail. Thus, the observed potential inversion is explained on a thermodynamic basis [75]. In the absence of oxygen, the Kelvin probe is therefore a tool to hint at a local pH at the buried interface and the observed time dependence of the potential profiles are dominated by the diffusion of OH^- along the interface. Interestingly, zinc–polymer interfaces may therefore also be destroyed by an anodic metal dissolution triggered by the cathodic oxygen reduction, but the combination of both reactions will buffer the pH and therefore limit any destruction of the interface due to extremely high OH^- concentrations.

The mechanism of the cathodic delamination on zinc is illustrated by the schematic current–potential curves in Fig. 28 [83]. After the galvanic coupling of the defect with the delamination front, the potential in the delaminated region is shifted to more negative values. Besides the oxygen reduction zinc oxidation, leading to a thickening of the oxide, takes place underneath the coating.

5.4.3.2.2 **Cathodic Protection in the Case of Polymer-coated Galvanized Steel** In most cases, Zn or Zn-alloy coatings are used to protect steel sheets because of the barrier properties of zinc and its sacrificial function leading to a cathodic protection of steel. For applications in the automotive, household and building industries, the metal coating is additionally covered by organic coatings leading to a so-called *duplex system* [4]. Scratches might lead to defects down to zinc or even iron. Both situations are schematically presented in Fig. 29(a and b).

In case the metallic coating is penetrated and iron is exposed to the electrolyte, a galvanic element between zinc and iron is established. Zinc then acts as an anode while cathodically protecting iron according to the following reactions (see Chapter 5.5):

$$Zn \longrightarrow Zn^{2+} + 2e^- \quad (37)$$

$$\tfrac{1}{2}O_2 + 2e^- + H_2O \longrightarrow 2OH^- \quad (38)$$

The oxygen reduction is located on the steel surfaces as well as on the corroding zinc surface. Now, two mechanisms of delamination have to be considered. Depending on the coating system and the corrosive environment cathodic and anodic undermining have been observed (Ref. [185] and references therein). Either the oxygen reduction on zinc leads to a destruction of the interface between the organic coating and zinc, or the oxygen reduction is hindered and the anodic dissolution of zinc leads to the undermining. For rather weak interfaces, Fürbeth and Stratmann showed that a cathodic delamination precedes the anodic dissolution of zinc [86]. On the other hand for technical organic coatings it is observed that in case of a defect down to steel the delamination of a purely alkaline cleaned galvanized steel surface is not significantly faster than that of a phosphated surface for corrosion tests including wet–dry cycles (Fig. 39 in Sect. 5.4.3.4.1). Such a behavior can be explained by an anodic mechanism. If the corrosion

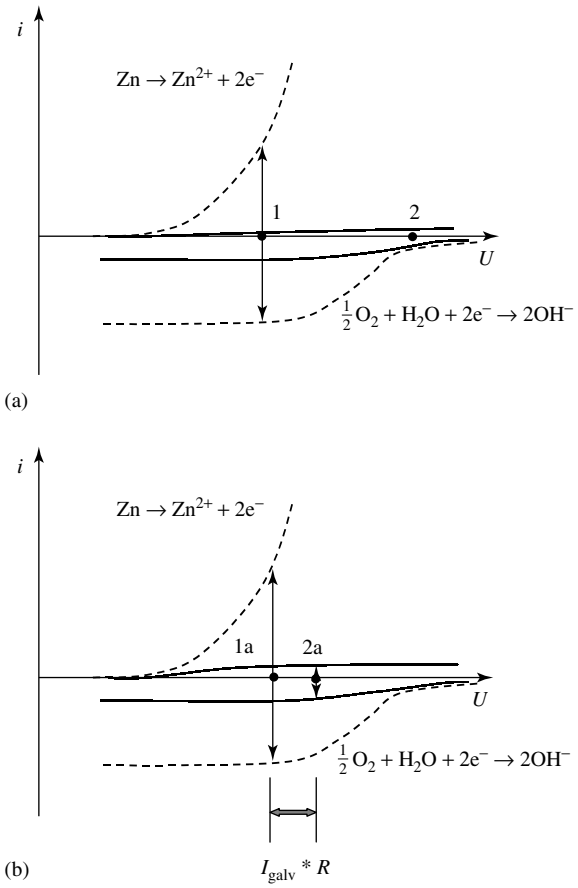


Fig. 28 (a, b) Electrochemical model for the delamination from a defect with an intact zinc layer in terms of schematic current–voltage curves for the defect 7(a) and the delaminated area 7(b) [83]. (Reprinted with permission.)

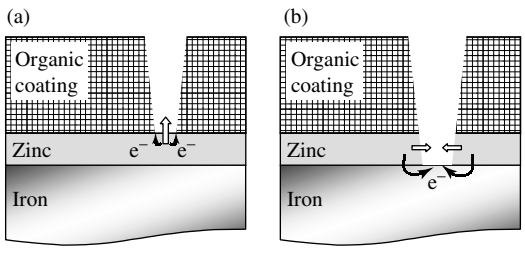


Fig. 29 Schematic cross sections for scribes down to zinc (a) and iron (b) on polymer-coated galvanized steel.

conditions are such that the formation of a cathode is kinetically hindered in front of the anode, then just the kinetics of zinc dissolution determine the degradation of the polymer–metal composite.

The size of the cathodic region preceding the anodic dissolution front depends on the structure of the interface and the coating composition itself. The more hindered the oxygen reduction, the smaller is the cathodic region in front of the anodic region.

Figure 30 shows some typical two-dimensional potential distributions underneath a clear coat as measured with an SKP as a function of time [86].

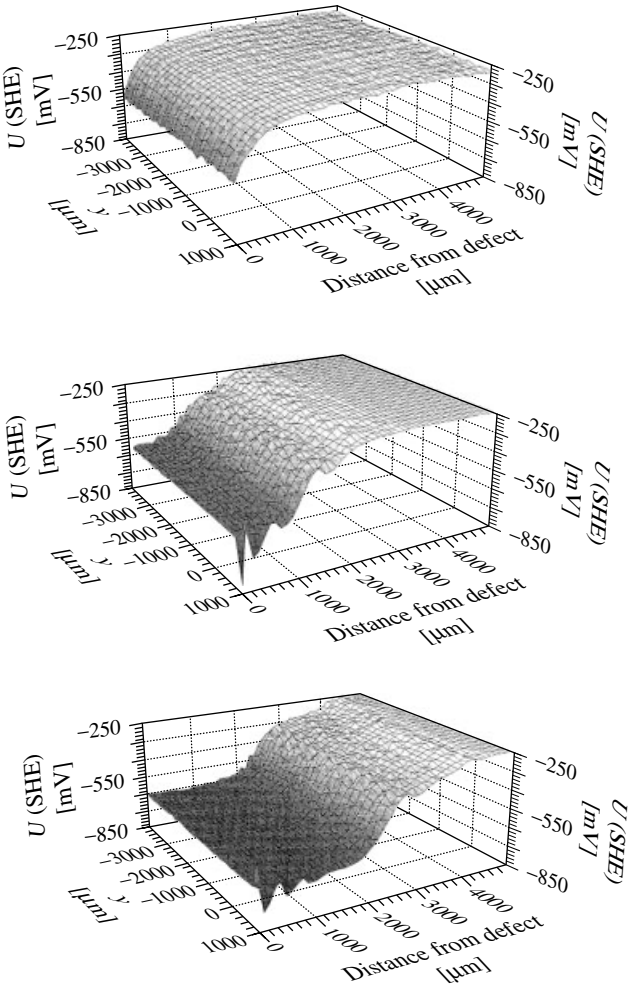


Fig. 30 Typical potential profiles as measured with the SKP during the delamination of polymer-coated galvanized steel with a defect down to iron (defect, 0.5 M NaCl; atmosphere, humid air; times as indicated) [86]. (Reprinted with permission.)

In the advanced state of delamination, two zones of different activity can be located underneath the organic coating. The shift of the corrosion potential close to the rather anodic potential of the intact interface marks the front of the advancing cathode. Behind this cathodic area the steep slope marks the front of anodic undermining. Fürbeth and Stratmann proved this interpretation of the SKP data with cross-sectional and surface analysis of the delaminated area [86].

An overall schematic illustration of anodic and cathodic undermining for the case when a cathode is located in front of the anode is shown in Fig. 31.

Oxygen reduction takes place in the defect with a rate that is controlled by the transport of oxygen through the electrolyte layer (a, i). Thus, a galvanic current is established between the anodic site (zinc within the delaminated zone) and the defect (cathode). In the area between the two potential steps (b, ii), no equilibrium potential surface is observed but the potential rises continuously from the borderline of the local anode to the potential jump, which indicates the intact metal–polymer interface. It can be assumed that the closer the zinc to the cathodic delamination front the smaller is the local anodic current while the

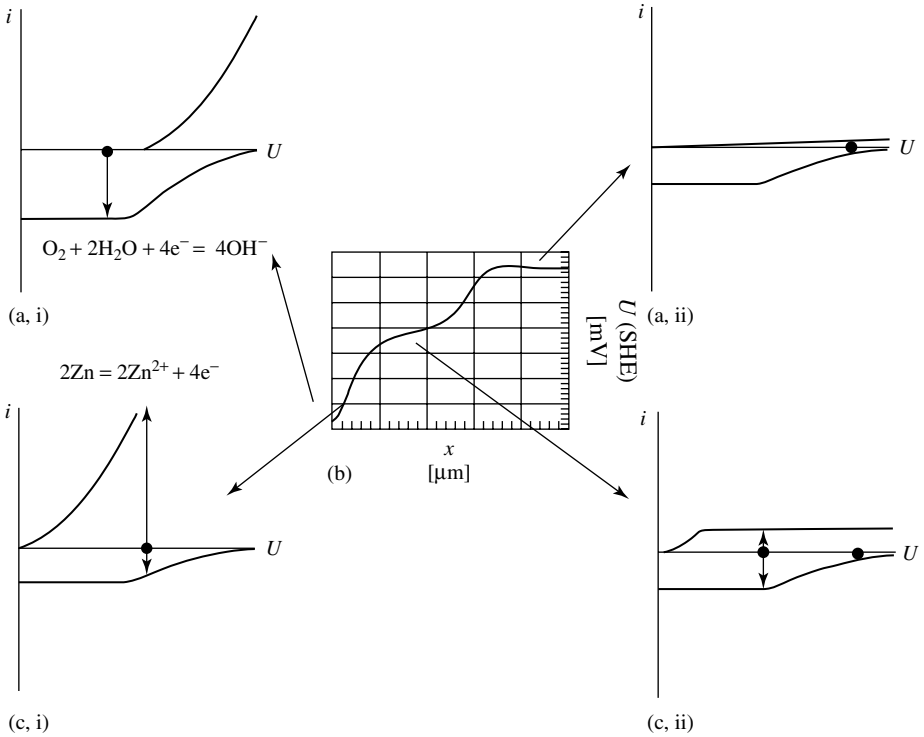


Fig. 31 Electrochemical model for the delamination of an organic coating from galvanized steel with a defect down to iron in terms of the current–voltage curves for the defect (a, i), the anodically delaminated area (c, i), the cathodically delaminated area (c, ii), and the intact area (a, ii); relative electrode potential distribution as shown in the (b) [86]. (Reprinted with permission.)

cathodic current stays rather constant in this area.

5.4.3.3 FFC on Polymer-coated Iron, Aluminum, and Magnesium

5.4.3.3.1 **Introduction to FFC** FFC is characterized by growing threadlike filaments [163–166]. FFC occurs in wet environments and usually arises from surface defects in the protective film in the presence of soluble ionic species. Various metals such as Al, Fe, and Mg show this kind of corrosion underneath a (polymer) coating. However, zinc-coated steel, and even electroplated silver plate and gold plate can also be affected by FFC [167]. An extended literature review of FFC investigations on aluminum is given by Bautista [168], earlier reviews have been presented by Hahin [169], Hoch [167] and Ruggeri and Beck [170]. Some recent results of FFC on aluminum alloys can be found in Refs. [171–174].

Figures 32(a and b) show typical microscopic pictures of FFC on polymer-coated iron, and aluminum. FFC develops in the presence of pores, mechanical defects, unprotected cut edges, or residual salt crystals underneath the organic coating. The corrosion filaments start growing perpendicular from a defect into the polymer-coated area. FFC occurs only at moderate humidity (60–95%) and therefore, not under full immersion conditions. FFC has been found to be triggered by anions such as chloride, bromide, and sulfate. The filament growth rate increases with temperature. Like for cathodic delamination on iron and zinc the corrosion kinetics depend strongly on the surface pretreatment and coating composition.

It is commonly accepted that the basic driving force underlying the FFC process is a differential aeration cell. Filaments are normally quite thin and shallow but can reach a length of several hundred millimeters. Two different regions of the progressing filaments can be observed: the liquid filled ''active head'' and a tail of corrosion products. In their active head, filaments carry an acidic solution of the metal cations and the initiating anions [170].

The following characteristics and differences are apparent for the three different metals such as Fe, Al, and Mg:

- At too low or too high relative humidity filaments dry up or turn into blisters, respectively [167].

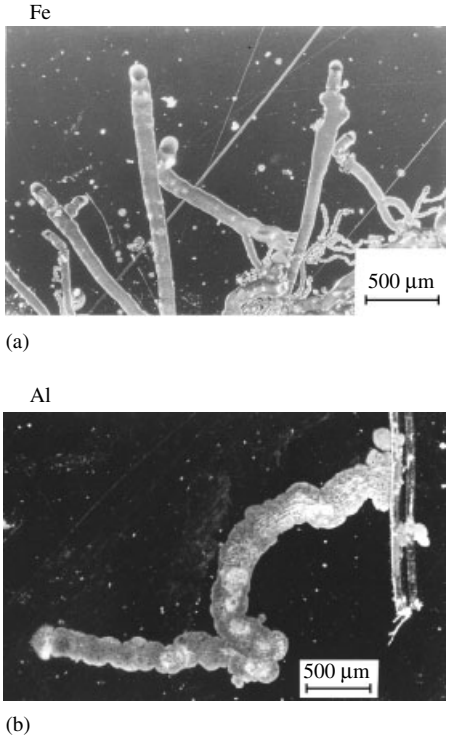


Fig. 32 Photographs of FFC attack on: (a) epoxy-coated iron and (b) aluminum alloy AA2024-T3. Filaments start growing from the artificial defect.

- The average width of the filaments is smaller for steel (0.2 mm) than for aluminum (0.5–1.0 mm) [169].
- For aluminum and magnesium, FFC and blistering are the predominant coating failure mechanisms. For iron, FFC is observed only under special conditions and cathodic delamination is the primary failure mechanism; see Ref. [168] and references therein.
- An interesting aspect of FFC on iron is that filaments do not cross each other. As one filament approaches another, it is reflected or stops growing. On the other hand, corrosion filaments on aluminum have been reported to cross each other, branch, reinitiate, or even tunnel [167].
- FFC is enhanced when aluminum is alloyed; especially Cu and Fe have a detrimental effect on FFC resistance due to the existing intermetallic particles (IMPs); see Ref. [168] and references therein.
- Iron exhibits a brown colored, and often V-shaped membrane between the front (anode) and the back (cathode) of the head. While the head front is blue, greenish blue or gray, the back is rust colored [175].

5.4.3.3.2 **Initiation of FFC** FFC is initiated by local metal dissolution in a salt containing droplet and the subsequent formation of a differential aeration cell.

If a differential aeration cell develops, oxygen is mainly reduced at the outer region of the droplet and then delamination can occur via the cathodic process of oxygen or proton reduction. However, if this cathodic process is hindered underneath the coating due to

- an insulating oxide layer,
- a lacquer with small permeation rate for water and oxygen, or
- an insufficient formation of an ultrathin conductive electrolyte layer between the polymer and the metal, which is necessary for the acceleration of oxygen reduction,

then no cathodic delamination occurs.

This might lead to a differential aeration cell where the metal is mainly dissolved next to the organic coating. In this case, a galvanic element can stabilize itself, which leads to a directional growth of a filament at the polymer–metal interface. The front of the filament is then the anode. During the formation of the differential aeration cell, the halide anions are moved to the

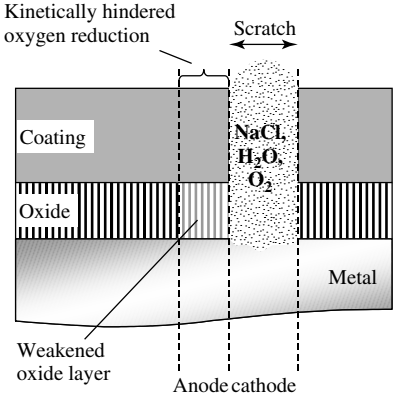


Fig. 33 Schematic cross section for an initiation of FFC in the case of a local defect in an organic coating.

front of the head and hydroxide anions are produced at the back of the head. The initiation situation for a polymer-coated metal with a scratch is shown in Fig. 33.

5.4.3.3.3 **Propagation of Filaments** In accordance with the differential aeration cell, the propagation of the filament is most likely anodic in nature [165, 170]. Only few authors claim that a cathodic area in front of the head promotes the growth of the filament [176, 177].

In the following discussion, the anodic mechanism is described in detail. Figures 34(a and b) schematically illustrate the galvanic element with respect to the current potential curves for anodic metal dissolution in the head and oxygen reduction at the back of the head. SKP measurements clearly show that the head of the filiform exhibits a more negative potential than the tail (Fig. 35).

With regard to the fact that the anodic metal dissolution leads to corrosive undermining, the mechanism of this process is of importance. The mechanisms of chloride induced corrosion of iron and aluminum are discussed elsewhere (see Chapter 4.2). The special conditions of an occluded cell are considered here only for iron, aluminum, and magnesium.

Chloride ions attack oxide layers on iron, aluminum, and magnesium. Subsequently, the metal is electrochemically dissolved. The hydration of Fe^{2+}, Al^{3+}, or Mg^{2+} releases protons and thereby leads to an acidification of the tip of the filament. At the cathodic site, the primary cathodic reaction, the reduction of oxygen to hydroxyl ions takes place. In between the anode and the cathode a potential gradient is established, which forces anions to migrate to the front and cations to the back. As the distance from the anode increases, the pH also increases on the basis of the dilution of hydronium ions and the migration of hydroxyl ions from the cathodic site. When favorable conditions are reached, the corresponding hydroxides of the cations are formed as gels. As the head advances, these hydrated corrosion products lose their water and convert to the dry corrosion products that fill the tail; see Ref. [168] and references therein.

An occluded cell is formed when dissolution of the metal occurs in the crevice between the coating and the substrate. In this case, corrosion products block the entry of the crevice so that the anode and cathode are separated.

Although similar in nature, the corrosion processes in the head differ between the respective metals and are described presently below for iron and aluminum.

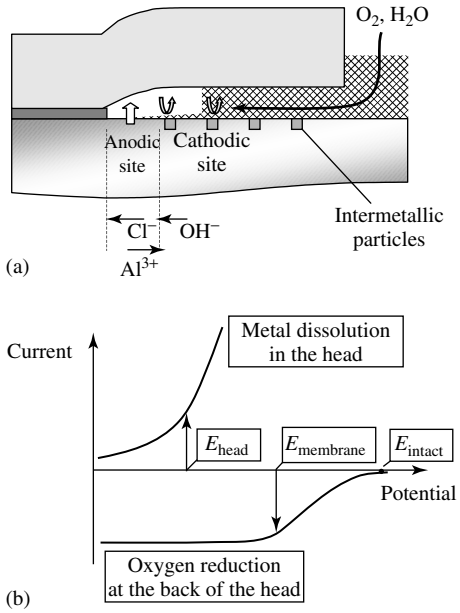


Fig. 34 Schematic illustration of the mechanism of FFC for polymer-coated aluminum: (a) cross section and (b) schematic current–voltage curves.

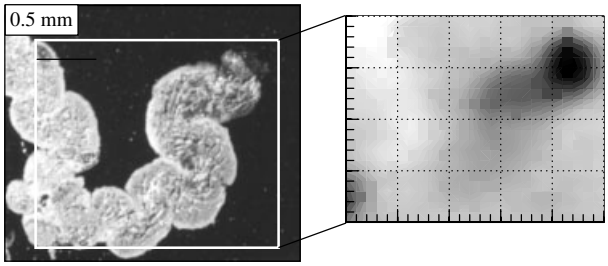


Fig. 35 (a) Photograph and (b) corrosion potential distribution of an FFC sample (AA2024-T3). The potential scale is 300 mV from black (low potential) to white (high potential) [178]. (Reprinted with permission.)

1. *Iron*: For iron, Fe^{2+} is formed at the very tip. Fe^{2+} then migrates to the back of the head where it is oxidized to Fe^{3+}. The boundary between the regions containing the ferrous and ferric ions is the variably colored interface observed in filament heads.

The green color of the anolyte can be explained by the existence of a slightly hydrolyzed $FeCl_2$ solution [175].

head:

$$Fe \longrightarrow Fe^{2+} + 2e^- \quad (39)$$

tail next to membrane:

$$\tfrac{1}{2}O_2 + 2e^- + H_2O \longrightarrow 2OH^- \quad (40)$$

membrane:

$$Fe^{2+} + 2OH^- \longrightarrow Fe(OH)_2$$
$$2Fe(OH)_2 + \tfrac{1}{2}O_2 \longrightarrow 2FeOOH + H_2O \quad (41, 42)$$

tail:

$$2FeOOH \longrightarrow \gamma - Fe_2O_3 + H_2O \quad (43)$$

$$\tfrac{1}{2}O_2 + 2e^- + H_2O \longrightarrow 2OH^- \quad (44)$$

2. *Aluminum and Magnesium*: The electrochemical reactions in FFC of aluminum and magnesium are slightly different from those for iron since the former two elements have only a single oxidation state. Moreover, in the case of aluminum or magnesium small hydrogen bubbles are observed at the head of the filament.

For aluminum, the outer surface of the oxide layer in humid environments is considered to be a mixture of aluminum oxide and aluminum hydroxide. After the adsorption of chloride ions, an ion exchange can occur leading to the substitution of hydroxyl ions by chloride ions [179, 180]. After the chemical attack of the oxide, aluminum is electrochemically dissolved. The chloride ions are regenerated after the dissolution of the transitory hydroxychloride compounds. Thus, a relatively small amount of chloride ions can result in a progressive attack of the protective layer. Within the head of the filiform filament, the anodic dissolution of aluminum leads to a local acidification of the anolyte due to the hydration of aluminum ions. It has been observed that a secondary cathodic reaction, the reduction of hydrogen ions, can occur. Hydrogen evolution has been observed within the head [166].

– *Aluminum*

head:

$$Al \longrightarrow Al^{3+} + 3e^- \quad (45)$$

$$H_3O^+ + e^- \longrightarrow \tfrac{1}{2}H_2 + H_2O \quad (46)$$

tail:

$$\tfrac{1}{2}O_2 + 2e^- + H_2O \longrightarrow 2OH^- \quad (47)$$

membrane:

$$Al^{3+} + 3OH^- \longrightarrow Al(OH)_3 \quad (48)$$

– *Magnesium*

head:

$$Mg \longrightarrow Mg^{2+} + 2e^- \quad (49)$$

$$H_3O^+ + e^- \longrightarrow \tfrac{1}{2}H_2 + H_2O \quad (50)$$

tail:

$$\tfrac{1}{2}O_2 + 2e^- + H_2O \longrightarrow 2OH^- \quad (51)$$

membrane:

$$Mg^{2+} + 2OH^- \longrightarrow Mg(OH)_2 \quad (52)$$

One model to explain the deadhesion of the organic coating and the very tip of the filament is the osmotic pressure of the highly concentrated electrolyte within the filiform head. For iron, a dense membrane of iron oxides is formed between the head and the tail of the filament [175]. This pressure causes a mechanical disbonding of the interface as was proposed by van der Berg and coworkers [175] for iron FFC. Therefore, the electrochemical reaction front can jump from one reactive site to the next one without the need of any electrochemical activity in between. Scheck reported a correlation between the extent of FFC and the glass transition temperature (T_g) of the polymer coating [181]. He observed a sharp rise in the extent of FFC attack if the storage temperature exceeded T_g, which provides further evidence for a purely mechanical deadhesion mechanism.

Pietschmann and Pfeiffer explained the directional growth of filaments on aluminum with the fact that the metal dissolution rate is highest were the oxygen concentration is lowest [173]. With the advancing anode a new membrane is formed at the back of the head and the old membrane dehydrates. Oxygen can then diffuse along the tail, which is filled with the dry corrosion products. The authors state that if the humidity is too high, the corrosion products remain moist. This would lead to a much slower diffusion of oxygen to the head of the filament. In this case, the separation of the occluded cell would be abolished and the FFC would turn into blistering. Indeed, blistering is observed at relative humidities higher than 95%. Thus, the dehydration of the corrosion products formed at the back of the head determines the direction of growth.

5.4.3.3.4 **Transport of Oxygen** To reveal the transport phenomena of oxygen, Ruggeri and Beck [170] performed a series of mathematical computations comparing the order of magnitude of oxygen diffusion through a paint film with oxygen diffusion through a porous oxide. They concluded that diffusion through the oxide was most likely and verified this experimentally. In this experiment, the defect where the filament had initiated was sealed which led to the end of the growth of the filiform filament. Further, Morita and Yoshida found that sealing the portion of the tail emerging on the surface immediately halted the process [182]. This mechanism is supported by the fact that FFC has been found not only for organic coatings but also under metals and oxygen-impermeable coatings.

On the other hand, different authors found an influence of the coating properties on FFC [171, 173] and claimed that transport occurs via the paint film. However, since the coating structure influences not only the permeation rate but also such important phenomena as adhesion and

intrinsic stress, it is not easy to distinguish between these effects. It might well be that, in case of a small degree of crosslinking, the diffusion through the organic coating might contribute to the overall transport of oxygen. However, since FFC is found also for impermeable coatings and can be halted by sealing the tail, transport via the tail is likely to be the most important mechanism.

5.4.3.3.5 **Electrochemical and Auxiliary Measurements of FFC** Slabaugh and coworkers [166] attempted to measure the corrosion potentials of different parts of the FFC track to detect anodic and cathodic areas. They did this by cutting the polymer along the FFC track, lifting the organic coating off the surface, and immediately measuring the electrode potentials by inserting microreference electrodes. This method, however, involves a major disturbance to the fragile FFC system.

By using the SKP (see Sect. 5.4.2.5), it was possible to measure the local potentials underneath an organic coating in situ without the deterioration of the corroding system [178]. The mechanism of FFC consisting of an anodic reaction at the corrosion front is reflected in rather different electrode potentials around the filament's head. Whereas, for cathodic undermining, the delamination front is positively polarized with respect to the already delaminated zone and the head of the filiform filament shows a negative potential with respect to the tail (Fig. 35) [178]. Therefore, the tip can be identified as the local anode and the local cathode is situated behind the anode within the tail.

Scanning electron microscopy (SEM) analysis of FFC tracks on coated Al alloys shows the exposure of IMPs. These IMPs of technical alloys, which are covered by electric conducting oxides, act as local cathodes for the oxygen reduction process in the tail (Fig. 36a–c).

This aspect of the corrosion mechanisms was considered by Nisancioglu and coworkers [172] who studied the role of the IMPs as local cathodes during FFC of Al alloys. Recently, Nisancioglu and coworkers showed that a number of commercial aluminum coil materials that contain appreciable amounts of Mn, Mg, and Fe, either as alloying elements or impurity content, became susceptible to FFC as a result of annealing. The latter being a part of the fabrication process [183, 184]. Removal of at least 1 μm of the surface layer by etching or pretreatment was sufficient to render the surfaces resistant to FFC. Susceptibility to FFC was correlated to the higher activity of the surface layer compared to the bulk in mildly acidic chloride solution.

The activity of the substrates was determined by means of corrosion potential measurements and potentiostatic data. The presence of the surface layer was related to the FFC susceptibility of the painted surface [183]. Analysis of cross-sectional foils by means of transmission electron microscopy revealed grain refined surface layers with a thickness of about 1 μm, consisting of subgrains in the size range 20–200 nm. However, it was shown that the grain refined surface layers alone were not responsible for the surface activity, since etched-and-rolled substrates without subsequent annealing displayed a grain refined surface layer without enhanced surface reactivity. The anodic behavior of the reactive surface layer might be explained by enrichment of magnesium on grain boundaries during annealing.

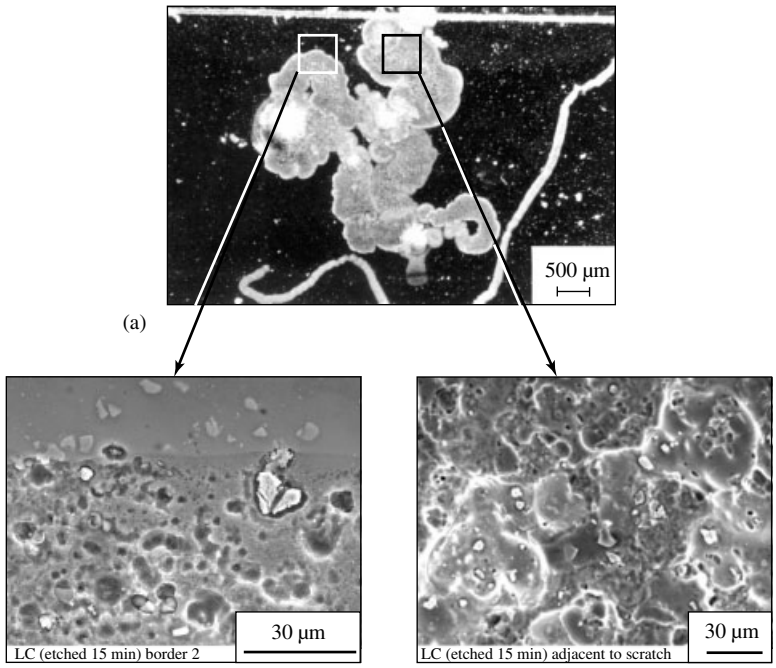


Fig. 36 (a–c): Optical microscopic and SEM pictures of the filiform tail on aluminum (AA2024-T3) after removal of the organic coating.

5.4.3.4 Influence of Surface Treatments and Compositions of Organic Coatings on the Corrosion Kinetics

For enhanced performance of corrosion protecting organic coatings on metal substrates, the composition and the interface between the coating and the metal have to be optimized. A special pigmentation of the paint is responsible for the barrier properties of the paint as well as for the storage of corrosion inhibiting species near the interface. To enhance adhesion and decrease the rate of corrosive undermining at the interface, a so-called conversion layer is often formed on the metal prior to paint application (see Chapter 5.3).

The mechanisms of corrosion stress the importance of the interface between the metal and the organic coating. Indeed, the pretreatment of the metal prior to the coating application is, aside from the composition of the coating and its state of curing, the most important for the performance as a corrosion protection layer. In the case of galvanized steel, the type of zinc alloy additionally influences the corrosion process by its specific galvanic action and the nature of the corrosion products formed underneath the organic coating (Ref. [185] and references therein).

In the automotive industry, a cathodic electrocoat (electrodeposited or ED paint) with a thickness of about 20 µm is deposited on top of the phosphate coating as a corrosion-resistant primer [185]. Coil coating as a second very important process,

is a widespread technology that applies paints onto metal sheets by roll coating [4]. Metal sheets can be continuously coated at speeds of up to 120 m min^{-1}. Products are organically precoated galvanized steel or aluminum sheets which are used for household applications, the building industry and most recently the automotive industry. Such a system normally consists of a primer and a topcoat. The pretreatment is often an alkaline passivation with additional Cr(VI) passivation or Cr-free thin layers (Ref. [4] and references therein). While the ED-paint is applied on already formed and cut metal sheet, coil-coated metal sheets are formed and cut after the paint application leading to microdefects and free cut edges respectively. The ED-paint and coil-coating systems are schematically shown in Fig. 37 for galvanized steel.

In a recent review article written by and Amirudin and Thierry, different models of delamination on zinc-coated steel are discussed that range from purely cathodic to purely anodic [185]. Obviously, the mechanism depends strongly on the zinc alloy, and the exposure conditions.

Other parameters that have a strong influence on the corrosion mechanism are the metal pretreatments and coating composition. For example, conversion coatings such as phosphate or chromate layers significantly impede the oxygen reduction reaction at the intact metal–polymer interface. In this case, the size of the cathodic region becomes rather small or might even diminish. Moreover, pigmentation and the curing state of the organic coating as well as the testing conditions have a significant influence on the mechanism of undermining [185].

5.4.3.4.1 **Conversion Coatings** Conversion layers have been described in detail in chapter 5.3. In this section, the effects of the pretreatment on the kinetics of the coating delamination are discussed with focus on the electrochemical principles. For conversion layers the substrate metal provides ions, which become part of the protective coating after the electrochemical

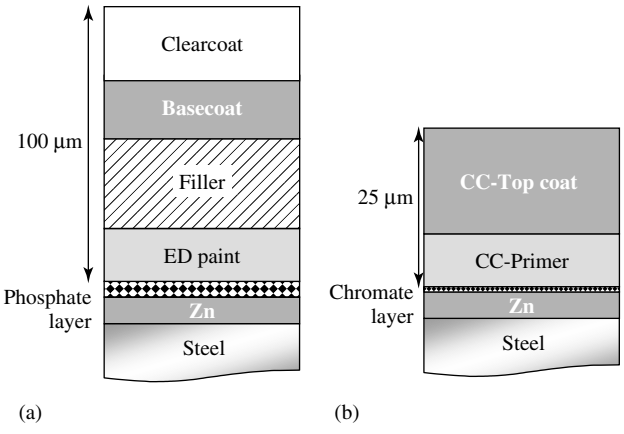


Fig. 37 Schematic cross section of typical paint systems for steel and galvanized steel: (a) automotive coating system including an ED-paint and (b) a coil-coating system for the building industry including a roll-coated paint as corrosion-resistant primer.

reaction of the substrate with the reactive medium. The most prominent conversion layers are phosphate layers on steel and zinc, chromate layers on zinc and aluminum, and anodized layers on aluminum (see chapter 5.3).

Conversion layers lead to an increased adhesion strength of organic coatings on metals under dry and wet conditions. In addition, the kinetics of ion and electron transfer processes at the metal–polymer interface are slowed down. In case of iron and zinc, especially the oxygen reduction rate, which strongly influences the delamination kinetics of the coating, is reduced.

Galvanized steel For galvanized steel, the most prominent conversion layers are phosphate layers for automotive and chromate layers for coil-coating applications [4, 185].

The effect of the pretreatment on the kinetics of oxygen reduction can be quantitatively illustrated by the electrode potential in humid air as measured by the SKP. Figure 38 compares the potentials for bare steel, phosphated, phosphated and Cr(VI) rinsed, and an ED-painted phosphated steel sample [76]. Obviously, the phosphatation and Cr(VI) passivation lead to a blocking of the surface. Especially in combination with an ED paint, the potential is rather negative. This can be explained by the reduction of the inner oxide layer during the ED process and the effective blocking of the interface versus reoxidation.

In Fig. 39, the delaminated area of an organic coating on alkaline cleaned galvanized steel and the same coating on phosphated and Cr(VI) passivated galvanized steel are compared. Defects were prepared down to steel and down to zinc. The ten weeks corrosion test

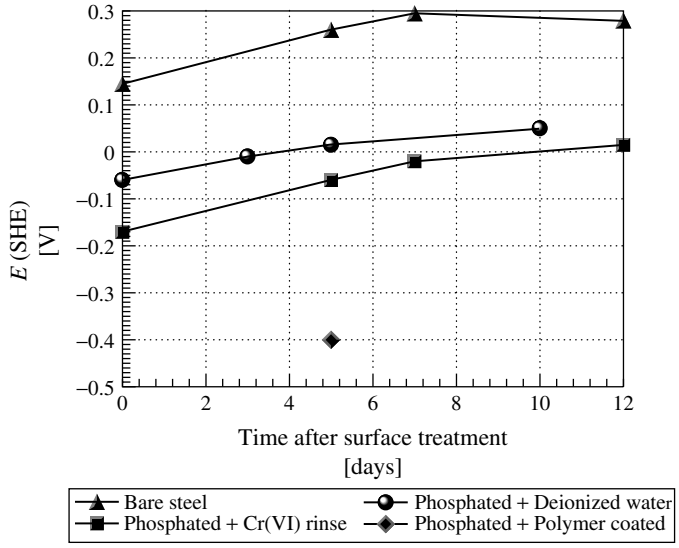


Fig. 38 Transient of the potential relaxation in air after cathodic polarization at 1 V SHE in borate buffer as measured by means of an SKP. Surface treatment of the steel substrate as indicated [76]. (Reprinted with permission.)

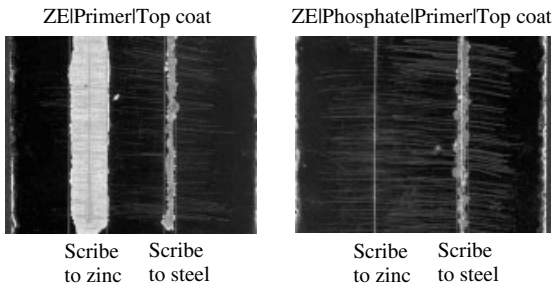


Fig. 39 Corrosion results after 10 cycles of a cyclic corrosion test for the same organic coating system (two-layer coil-coating system) on just alkaline cleaned and on prephosphated and chromate rinsed galvanized steel. Scribes had been prepared down to iron and zinc, respectively. For the evaluation of the undermined region, the deadhered organic coating was removed.

consisted of a combination of an exposure to salt spray, pure humid environment and a period of drying.

It is obvious that in case of a defect down to steel, which leads to the enhanced anodic dissolution of zinc, the delamination of the purely alkaline cleaned galvanized steel surface is not faster than that of a phosphated surface. Such a behavior can be explained by an anodic delamination process. If the corrosion conditions are such that no formation of a cathode is possible in front of the anode, then just the kinetics of zinc dissolution determine the degradation of the polymer–metal composite.

The situation changes when the defect is prepared just down to zinc and the kinetics of zinc dissolution are rather slow. In this case, the cathodic delamination determines the kinetics of undermining. The delaminated area of the phosphated sample is now smaller than for the defect down to steel, whereas the just alkaline cleaned sample shows delamination that is much faster than in the case of the defect down to steel. This example shows how complex the corrosion mechanisms are and that no generally accepted mechanism can be found in the literature.

A similar coating system (two-coat coil-coating system on phosphated and chromate passivated galvanized steel) was exposed to a pure salt spray test (360 h). The cross-sectional analysis of delaminated technical samples shows two different situations. The cross section in Fig. 40(a) shows a deadhesion of the organic coating from the intact zinc coating followed by an area where zinc has been dissolved. Thus, a cathode is preceding the anodic dissolution.

In Fig. 40(b), a more complex situation is illustrated by the cross-sectional analysis that is representative of a later state of delamination in which the electrolytic resistance between the front of the undermined region and the defect is very high because of the corrosion products. The products were formed underneath the organic coating and hinder the transport of ions along the interface. In this case, the defect is not galvanically coupled to the delamination front anymore, and galvanic coupling occurs between local anodes and cathodes underneath the organic coating.

Aluminum Several authors have compared the efficiency of various pretreatments for aluminum and its alloys [173, 186–189]. Typical pretreatments for aluminum prior to paint application are chromating and anodization (Ref. [168] and references therein).

A deoxidizing step is usually incorporated in standard pretreatment procedures as a first step. It has been observed that the FFC susceptibility of aluminum decreases

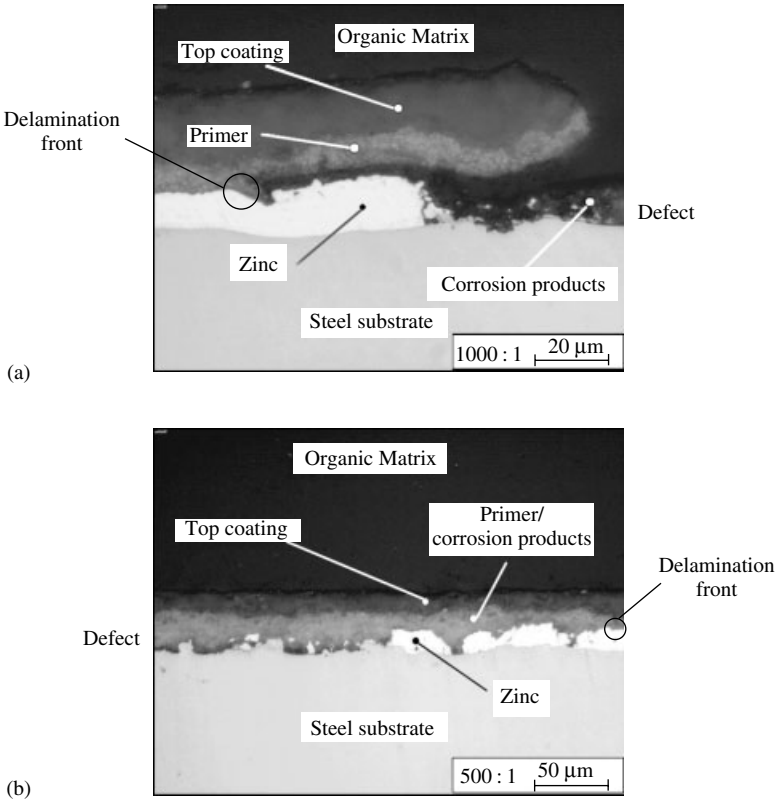


Fig. 40 (a, b) Cross-sectional analysis of the undermined region after 240 h of salt spray testing for a two-layer coil-coating system on prephosphated and chromate rinsed galvanized steel. Scribes had been prepared down to iron. In Fig. 40(a), the scribe is on the right side, while in Fig. 40(b) it is on the left side.

with the removal of the outer surface layer thereby exposing the less electrochemically active underlying bulk material to the corrosive environment [183, 184].

Anodization leads to a thickening of the oxide layer with the typical hexagonal pores that can lead to a mechanical interlocking of the paint. Moreover, both the anodic dissolution and the oxygen reduction are significantly hindered after the anodization [190]. The authors showed that a minimum barrier layer is necessary in order to prevent FFC.

The most widely used pretreatment is chromating. For aluminum substrates, the chromate baths always contain a source of fluoride ions beside a source of hexavalent chromium and an acid to produce a low pH. Fluoride ions effectively attack the aluminum oxide layer and prevent the precipitation of aluminum ions. During the reaction, hexavalent chromium is partially reduced to trivalent chromium according to

$$6H^+ + H_2Cr_2O_7 + 6e^- \longrightarrow 2Cr(OH)_3 + H_2O \qquad (53)$$

The formation of these Cr^{3+}- and Cr^{6+}-containing layers preferentially takes place

at surface heterogeneities and IMPs [191]. To date, the exact mechanism of the corrosion protection of chromates for aluminum alloys has not been clarified. However, the toxicity of and potential carcinogenic nature of chromium have fostered a search for alternative inorganic layers [189, 191].

5.4.3.4.2 **Adhesion Promoters and Interfacial Thin Films** Besides the above-mentioned inorganic conversion coatings, thin films can act as corrosion-resistant interfacial layers. Their thicknesses normally range from the length of a self-assembling molecule (approximately 2 nm) to about 100 nm. Various surface technologies have been developed so far and could be partly introduced into technical processes.

- Self assembly monolayers such as organophosphonates, organosilanes and thiols for iron, copper, and aluminum [192]. These kinds of molecules chemically bind to the metal or metal oxide surface with the surface-active group (e.g. phosphate, sulfur, or silanol) while they orientate themselves almost vertically to the surface and thereby form a dense structure. The other end of the molecule acts as an anchoring group for the subsequently applied organic coating (Fig. 41a).
- Thin adhesion-promoting layers based on bifunctional organosilanes for iron, zinc, and aluminum with a thickness of about 50–100 nm (Fig. 41b). Especially, van Ooij and coworkers developed various adhesion-promoting systems based on this technology [193–195]. In this case, the organosilanes not only bind to the surface, but also crosslink with each other, which leads to a polysiloxane network with free functional groups such as amines, epoxies, or acrylates.
- Plasma polymers that are deposited from a cold electric discharge onto various metal substrates such as iron,

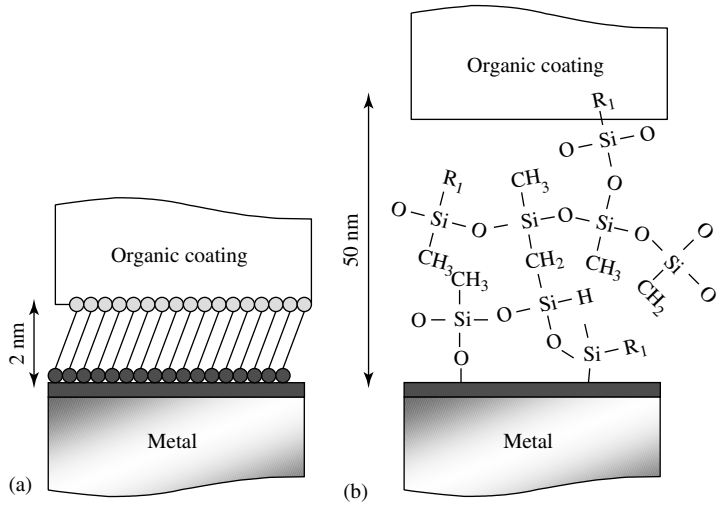


Fig. 41 Schematic illustration of the monomolecular (a) thin film and (b) adhesion-promoting system based on organic monomers.

zinc, aluminum, and copper [196–201]. This vacuum based plasma enhanced chemical vapor deposition leads to highly crosslinked thin films that show an excellent coverage of the surface even at a film thickness of a few nanometers [199].

All three techniques lead to a dense organic film directly adjacent to the metal oxide surface. They can act in the following ways:

- adhesion promotion,
- block adsorption sites for oxygen,
- barrier layer for ions and water directly in front of the metal oxide so that the kinetics of the electron transfer reactions are slowed down.

The positive effect on the adhesion force between a paint and the metal when using thin organosilane primers has been shown by several authors [202, 203]. The reduction of the area where oxygen can be reduced is difficult to measure directly since unavoidable defects in the ultrathin films lead to an array of microelectrodes so that the measurable oxygen reduction current is not significantly lower for thin film coated surfaces. For model systems, coverage of a Au surface by self assembly films of thiols was electrochemically measured by Rohwerder and coworkers, who also characterized the ordering of the films by means of scanning tunneling microscopy (STM) [204]. For aluminum, phosphonates led to a extremely corrosion-resistant metal–paint interface [205].

For plasma polymers, Grundmeier and Stratmann experimentally showed that the ion diffusion along the paint–metal interface is significantly slowed down in the presence of an ultra-thin plasma polymer [199]. The ion incorporation was measured by means of an SKP. This result correlates with the high corrosion resistance of the interfacial plasma polymer. In Fig. 42, the delamination of a paint on zinc-coated steel that was half side plasma polymer coated prior to painting shows a significant delay of the cathodic delamination process by plasma polymers whose thickness is less than 20 nm.

5.4.3.4.3 Influence of Pigments in Paints

As mentioned in the Introduction, the pigments can be divided into two classes:

- barrier-effect pigments and
- electrochemically active pigments.

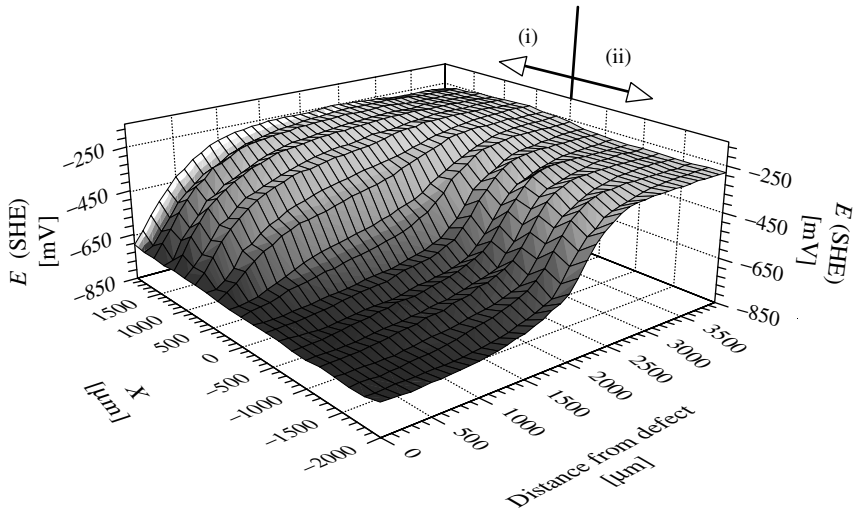
While barrier-effect pigments solely increase the diffusion path of corrosive species and the coating practical adhesion of the coating, active pigments such as chromates additionally inhibit electrochemical reactions at the metal–polymer interface as well in defects of organic coatings.

Because cut edges are crucial areas of coil-coated material and can be used to study the effect of pigments in organic coatings on the corrosion in defects, they have been extensively studied by means of different electrochemical techniques such as electrochemical impedance and scanning vibrating electrodes [102, 139, 140].

The effect of pigments especially chromates can be divided into two modes of actions:

1. inhibition of reactions at the metal–polymer interface and
2. inhibition of corrosion reactions within a defect.

A chromate passivation usually used in coil-coating lines prior to the application of the organic coating leading to ultrathin



(i) Zn | ZnO | 10 nm plasma polymer | paint

(ii) Zn | ZnO | paint

Fig. 42 Potential distribution measured with an SKP of a half side plasma modified zinc surface, which was subsequently painted with a clear coat and exposed to a corrosive environment. The low potential indicates the delaminated area starting from a scratch.

$Cr^{VI/III}$ films on the surface likely acts mainly at the interface while the existence of chromate pigments in a primer can act in both ways because of the process of leaching.

The action of pigments is often evaluated by measuring the change in the electrode kinetics in solutions of the pigments. It could be shown that chromates act as cathodic inhibitors on zinc surfaces thereby increasing the corrosion resistance of the system. This is proven by the Nyquist plots of uncoated galvanized steel after 3 h in artificial acid rain solution [141]. The resulting values for the corrosion potentials and the charge transfer resistance R_t are given in Table 1.

The inhibition of corrosion in defects of organic coatings could be shown by means of scanning reference electrode techniques [139, 140]. Recently, Zou and

Tab. 1 The values of R_t for galvanized steel in acid rain solutions with and without strontium chromate (100 ppm) [141]

Acid rain solution	E_{corr} *[mV$_{SCE}$]*	R_t *[Ω]*		
		At anodic E, +60 mV	At cathodic E, −60 mV	At E_{corr}
With chromate	−820	2430	41 840	11 440
Without chromate	−940	1660	9315	2960

coworkers [139, 140] investigated the degradation of coil-coated galvanized steel at the cut edge. The authors focused on the influence of the chromate content in the coating on the active zinc dissolution at the cut edge. Chromate clearly leads to a rapid diminishing of anodic activity of the exposed zinc. The chrome-free primer (phosphate based) did not lead to the equivalent inhibition of the zinc dissolution. The SVET measurements were combined with the salt spray and the prohesion test (French standard NFX 41002). Not surprisingly, the inhibition of the Zn dissolution measured with the SVET was in accordance with a high corrosion resistance of the chromate containing primer.

5.4.3.4.4 Intrinsically Conducting Polymers

Intrinsically conducting polymers (ICPs) have been proposed as protective coatings against corrosion of steel [206]. The application of these polymers is hindered by their insolubility in common solvents. Several approaches have been done to overcome this problem. ICPs can be chemically synthesized and the resulting powder is then dispersed in an organic solvent or directly in an organic primer. ICPs can also be deposited by electropolymerization on chemically inert materials such as Au or Pt. However, nonnoble metals such as iron undergo strong anodic dissolution before the oxidation potential of the monomer is reached.

Applied ICPs are mainly polythiophene, polyaniline, and polypyrrole. The potential corrosion protection properties of ICPs is still controversially discussed in the literature. It is far beyond the scope of this section to review these contradictory results. In a recent paper by Rammelt and coworkers, the authors provide a helpful overview on the current state of the discussion and present new results on the corrosion protection of polymethylthiophene films on specially pretreated mild steel [207].

Two principle mechanisms that are discussed as possible corrosion protection mechanisms on mild steel are discussed in short. ICPs may induce the formation of a passive oxide [206]. The ICP will be reduced as a consequence of passivation and will be reoxidized by oxygen reduction. Consequently, the ICP may promote the cathodic oxygen reduction on the polymer surface rather than at the metal–polymer interface. On the basis of the good corrosion results gained by the combination of a molecular adhesion promoter and the subsequent electrodeposition of the polymethylthiophene film Rammelt and coworkers [207] concluded that the essential aspect of the corrosion protection by ICPs could be the local separation of iron oxidation and oxygen reduction. This would eliminate the local pH increase at the metal surface and subsequent cathodic disbondment.

5.4.4 Overall Conclusions

The corrosion protection of reactive metals by modern organic coatings has undergone significant optimization during the last decade. Electrochemical techniques have helped to understand the processes of transport through organic coatings and the localized corrosion starting from defects in the coatings. The organically coated metal substrate is the most complex system with regard to the fundamental understanding of the corrosion mechanism. The system consists of a metal

substrate sometimes a metal coating, a conversion coating and then one to four layers of polymer. Each of the components affects the corrosion process. Moreover, organic coatings themselves are complex systems containing inorganic pigments in an organic matrix. The reviewed literature shows that the most detrimental processes that lead to the failure of organic coatings are induced by a localized defect in the coating which provides electrolyte–metal contact. Principle mechanisms of corrosion then occur which depend mainly on the metal substrate.

Integral electrochemical methods such as EIS provide information on the ingress of corrosive medium into the organic coating and indicate the formation of pores. Recently developed electrochemical methods such as the SVET or the SKP enable to study the corrosion locally. The Kelvin probe is the only electrochemical technique that has proven to measure electrochemical reactions underneath organic coatings with spatial resolution and has helped to significantly improve the understanding of the corrosion protection of organic coatings.

However, in the future new techniques have to be developed that lead to a more molecular understanding of the corrosive deadhesion of organic coatings. The problem will always be that molecular information has to be revealed from a buried interface. This, inevitably, leads to the study of model systems such as self-assembling films with nanoscopic techniques such as the STM or the SKP force microscopy.

Parallel to these fundamental studies, electrochemical techniques will be further improved with regard to the early detection of failure of organically coated metals and the characterization of macroscopic parameters such as barrier or passivating properties.

Organic coating themselves have to be modified in the future with regard to the environmental requirements and it can be foreseen that the complexity of organic coating will still increase when multifunctional pigments such as chromates have to be replaced by a multitude of surrogates. The importance of electrochemistry as a method to understand corrosion properties of coatings and the improvement of organic coatings will thus, further increase in the future.

References

1. R. Lambourne, (Ed.), *Paint and Surface Coatings*, Ellis Horwood, Chichester, UK, 1987.
2. P. R. Roberge, *Handbook of Corrosion Engineering*, McGraw-Hill, New York, 2000.
3. D. A. Jones, *Principles and Prevention of Corrosion*, 2nd ed., Prentice Hall, Norwell, Mass., 1996.
4. J. F. H. van Eijnsbergen, *Duplex Systems*, Elsevier, Amsterdam, 1994.
5. L. L. Shreir, R. A. Jarman, G. T. Burstein, *Corrosion Vol. 2- Corrosion Control*, 3rd ed., Butterworth-Heinemann, Woburn, Mass., 1994.
6. *Surface Coatings*, Chapman & Hall, New York, 1993, Vol. 1.
7. G. Wranglén, *An Introduction to Corrosion and Protection of Metals*, Institut för Metallskydd, Stockholm, 1972.
8. Oil & Colour Chemists' Association, *Paint Technology Manuals – Part Three: Convertible Coatings*, 2nd ed., Chapman & Hall, New York, 1972.
9. P. Nylen, E. Sunderland, *Modern Surface Coatings*, Interscience Publishers, John Wiley & Sons, New York, 1965.
10. R. A. Iezzi, Fluoropolymer coatings for architectural applications in *Modern Fluoropolymers*(Ed.: J. Schreir), John Wiley & Sons, Chichester, UK, 1997.
11. S. Munekata, *Prog. Org. Coat.* **1988**, *16*, 113.

12. M. J. Austin, Inorganic anti-corrosive pigments in *ASTM Manual Paint and Coating Testing Manual*, American Society for Testing and Materials, Philadelphia, Pa., 1995, pp. 238–251, Chap. 27.
13. R. L. Twhite, G. P. Bierwagen, *Prog. Org. Coat.* **1998**, *33*, 91.
14. A. Amirudin, C. Barreau, R. Hellouin et al., *Prog. Org. Coat.* **1995**, *25*, 339–355.
15. T. K. Ross, J. Wolstenholme, *Corros. Sci.* **1977**, *17*, 341.
16. V. Verkholantsev, *Eur. Coat. J.* **1997**, *September*, 818.
17. V. Verkholantsev, *Eur. Coat. J.* **1999**, *January/ February*, 54.
18. J. Krüger, *Protect. Coat. Eur.* **2000**, *5*, 30.
19. Y. Nakayama, *Prog. Org. Coat.* **1998**, *33*, 108.
20. N. S. Allen, C. J. Regan, R. McIntyre et al., *Prog. Org. Coat.* **1997**, *32*, 9.
21. W. Funke, *Prog. Org. Coat.* **1997**, *31*, 5.
22. B. Müller, I. Förster, W. Kläger, *Prog. Org. Coat.* **1997**, *31*, 229.
23. M. Ooka, H. Ozawa, *Prog. Org. Coat.* **1994**, *23*, 325.
24. A. D. Broek, *Prog. Org. Coat.* **1993**, *22*, 55.
25. T. A. Misev, *Powder Coatings – Chemistry and Technology*, Wiley, New York.
26. Z. W. Wicks, F. N. Jones, S. P. Pappas, *J. Coat. Tech.* **1999**, *71*, 41, 47, 52, 67.
27. G. S. Park, Transport principles – solution, diffusion and permeation in polymer membranes in *Synthetic Membranes: Science, Engineering and Applications* (Eds.: P. M. Bungay, H. K. Lonsdale, M. N. Pinho), NATO ASI Series, D. Reidel Publishing, Dordrecht, Holland, 1986, pp.
28. S. Guruviah, *J. Oil Col. Chem. Assoc.* **1970**, *53*, 669.
29. K. Baumann, *Plaste Kautsch* **1972**, *19*, 694, 455.
30. J. O. Mayne in *The Mechanism of the Protective Action of Paints in Corrosion* (Ed.: L. L. Shreir), 2nd ed., Newnes-Butterworths, London, 1976, Vol. II.
31. R. Feser, M. Stratmann, *Steel Res.* **1990**, *61*(10), 482.
32. H. Haagen, W. Funke, *J. Oil Col. Chem. Assoc.* **1975**, *58*, 359.
33. W. W. Kittleberger, A. C. Elm, *Ind. Eng. Chem.* **1952**, *44*, 326.
34. G. W. Walter, *Corros. Sci.* **1986**, *26*, 27.
35. G. E. Johnson, H. E. Blair, E. W. Anderson in *Corrosion Control by Organic Coatings* (Ed.: H. Leidheiser Jr.), NACE International, Houston, Tex., 1981.
36. O. Negele, W. Funke, *Prog. Org. Coat.* **1996**, *28*, 285.
37. J. Boxall, J. A. Franhofer, S. C. Warren, *J. Oil Col. Chem. Assoc.* **1972**, *55*, 24.
38. G. W. Walter, *Corros. Sci.* **1991**, *32*, 1059, 1085.
39. V. B. Miskovic-Stankovic, D. M. Drazic, M. J. Teodorovic, *Corros. Sci.* **1995**, *37*, 241.
40. E. P. M. Westing, G. M. Ferrari, J. H. W. de Wit, *Corros. Sci.* **1993**, *34*, 1511.
41. B. N. Popov, M. A. Alwohaibi, R. E. White, *J. Electrochem. Soc.* **1993**, *140*, 947.
42. R. T. Ruggeri, T. R. Beck in *Corrosion Control by Organic Coatings* (Ed.: H. Leidheiser Jr.), NACE International, Houston, Tex., 1981.
43. J. Crank, G. S. Park, *Diffusion in Polymers*, Academic Press, London, 1968.
44. M. M. Wind, H. J. W. Lenderink; *Prog. Org. Coat.* **1996**, *28*, 239.
45. F. Bellucci, L. Nicodemo, *Corrosion* **1993**, *49*, 235.
46. C. Perez, A. Collazo, M. Izquierdo et al., *Prog. Org. Coat.* **1999**, *36*, 102.
47. E. M. Rosen, D. C. Silverman, *Corrosion* **1990**, *46*, 945.
48. L. De Rosa, T. Monetta, D. B. Mitton et al., *J. Electrochem. Soc.* **1998**, *145*, 3830.
49. W. Funke, *Prog. Org. Coat.* **1981**, *9*, 29.
50. L. A. van der Meer-Lerk, P. M. Heertjes, *J. Oil Col. Chem. Assoc.* **1975**, *58*, 79.
51. J. L. Prosser, T. R. Bullet, *J. Oil Col. Chem. Assoc.* **1962**, *45*, 836.
52. D. M. James, *J. Oil Col. Chem. Assoc.* **1960**, *43*, 391.
53. S. A. Lindqvist, *Corrosion* **1985**, *41*, 69.
54. A. S. L. Castela, A. M. Simões, M. G. S. Ferreira, *Prog. Org. Coat.* **2000**, *38*, 1.
55. D. M. Brasher, A. H. Kingsbury, *J. Appl. Chem.* **1954**, *4*, 62.
56. E. P. M. Westing, G. M. Ferrari, J. H. W. de Wit, *Corros. Sci.* **1994**, *36*, 957, 979, 1323.
57. Z. Kolek, *Prog. Org. Coat.* **1997**, *30*, 287.
58. T. Nguyen, E. Byrd, D. Bentz et al., *Prog. Org. Coat.* **1996**, *27*, 181.
59. M. Stratmann, R. Feser, A. Leng, *Electrochim. Acta* **1994**, *39*(8–9), 1207.
60. J. E. O. Mayne, *J. Oil Col. Chem. Assoc.* **1949**, *32*, 481.
61. M. Yaseen in *Corrosion Control by Organic Coatings* (Ed.: H. Leidheiser Jr.), NACE International, Houston, Tex., 1981.

62. C. A. Kumins, *Off. Digest* **1962**, *34*, 843.
63. W. Funke, *Prog. Org. Coat.* **1981**, *9*, 29.
64. M. Svoboda, J. Mleziva, *Prog. Org. Coat.* **1974**, *2*, 207.
65. P. Meares, Transport in ion exchange membranes in *Synthetic Membranes: Science, Engineering and Applications* (Eds.: P. M. Bungay, H. K. Lonsdale, M. N. Pinho), NATO ASI Series, D. Reidel Publishing, Dordrecht, Holland, 1986.
66. B. W. Cherry, J. E. O. Mayne, *First International Congress on Metallic Corrosion*, Butterworths, London, 1962, p. 539.
67. D. J. Mills, J. E. O. Mayne in *Corrosion Control by Organic Coatings* (Ed.: H. Leidheiser Jr.), NACE International, Houston, Tex., 1981.
68. L.-H. Lee in *Fundamentals of Adhesion* (Ed.: L.-H. Lee), Plenum Press, New York, 1991, pp. 1–75.
69. F. M. Fowkes, C.-Y. Sun, S. T. Joslin in *Corrosion Control by Organic Coatings* (Ed.: H. Leidheiser Jr.), NACE International, Houston, Tex., 1981, pp. 1–3.
70. K. L. Mittal, *Acid-Base Interactions: Relevance to Adhesion Science and Technology*, VSP, Zeist, The Netherlands, 2000.
71. D. A. Hays in *Fundamentals of Adhesion* (Ed.: L.-H. Lee), Plenum Press, New York, 1991, pp. 249–278.
72. J. L. Prosser, *Adhesion of Coatings. Theory and Practice*, Paint Research Station, Teddington, UK, 1993.
73. H. Leidheiser, W. Funke, *JOCCA 121* **1987**.
74. A. J. Kinloch, *Adhesion and Adhesives*, Chapman & Hall, London, 1987.
75. M. Pourbaix, *Atlas of Electrochemical Equilibria in Aqueous Solutions*, NACE International, Houston, Tex., 1974.
76. G. Grundmeier, W. Schmidt, M. Stratmann, *Electrochim. Acta* **2000**, *45*, 2515–2533.
77. W. Funke in *Corrosion Control by Organic Coatings* (Ed.: H. Leidheiser Jr.), NACE International, Houston, Tex., 1981. p. 97–102.
78. H. Leidheiser Jr., *Corrosion* **1982**, *38*, 374.
79. M. Morcillo, *Prog. Org. Coat.* **1999**, *36*, 137.
80. H. Leidheiser Jr., W. Wang in *Corrosion Control by Organic Coatings* (Ed.: H. Leidheiser Jr.), NACE International, Houston, Tex., 1981, p. 70–77.
81. H. Leidheiser Jr., M. W. Kendig, *Corrosion* **1976**, *32*, 69.
82. J. D. Scantlebury, A. Guiseppi-Elie, D. A. Eden et al., *Corrosion* **1983**, *39*, 108.
83. W. Fürbeth, M. Stratmann, *Corrros. Sci.* **2001**, *43*, 207.
84. J. S. Hammond, J. W. Holubka, R. A. Dickie, *J. Coat. Technol.* **1979**, *51*, 45.
85. A. Leng, H. Streckel, K. Hofmann et al., *Corros. Sci.* **1999**, *41*, 579.
86. W. Fürbeth, M. Stratmann, *Corrros. Sci.* **2001**, *43*, 229, 243.
87. K. Hoffmann, M. Stratmann, *Corros. Sci.* **1993**, *34*, 1625.
88. E. L. Koehler in *Corrosion Control by Organic Coatings* (Ed.: H. Leidheiser Jr.), NACE International, Houston, Tex., 1981, p. 87–96.
89. J. N. Murray, *Prog. Org. Coat.* **1997**, *31*, 225.
90. J. Wolstenholme, *Corros. Sci.* **1973**, *13*, 521.
91. G. W. Walter, *Corros. Sci.* **1986**, *26*, 39.
92. R. M. Burns, H. E. Haring, *Trans. Electrochem. Soc.* **1936**, *69*, 169.
93. H. E. Haring, R. B. Gibney, *Trans. Electrochem. Soc.* **1939**, *76*, 287.
94. F. Wormwell, D. M. Brasher, *J. Iron Steel Inst.* **1949**, *162*, 129.
95. F. Mansfeld, *J. Appl. Electrochem.* **1995**, *25*, 187.
96. L. Beaunier, I. Epelboin, J. C. Lestrade et al., *Surf. Technol.* **1976**, *4*, 237.
97. D. H. Weijde, E. P. M. Westing, J. H. Wit, *Corros. Sci.* **1994**, *36*, 643.
98. R. Hirayama, S. Haruyama, *Corrosion* **1991**, *47*, 952.
99. J. Titz, G. H. Wagner, H. Spaehn et al., *Corrosion* **1990**, *46*, 221.
100. E. P. Westing, G. M. Ferrari, J. H. de Wit, *Corros. Sci.* **1994**, *36*, 957, 979, 1323.
101. F. Deflorian, L. Fedrizzi, P. L. Bonora, *Corros. Sci.* **1996**, *38*, 1697.
102. A. S. Castela, A. M. Simões, M. G. Ferreira in *Electrochemical Methods in Corrosion Research VI* (Eds.: P. L. Bonora, F. Deflorian), Trans Tech Publications, Switzerland, 1997, p. 247.
103. F. Deflorian, L. Fedrizzi, S. Rossi, *Corros. Sci.* **2000**, *42*, 1283.
104. I. Dehri, R. L. Howard, S. B. Lyon, *Corros. Sci.* **1999**, *41*, 141–154.
105. A. Einstein, *Ann. der Phys.* **1906**, *19*, 371.
106. T. Hagyard, J. R. Williams, *Trans. Faraday Soc.* **1961**, *57*, 2288.
107. W. P. Iverson, *J. Electrochem. Soc.* **1968**, *115*, 617.
108. Y. J. Tan, S. Bailey, B. Kinsela, *Corros. Sci.* **1996**, *38*, 1681.

109. C. Gabrielli, M. Keddam, *Corrosion* **1992**, *48*, 794.
110. I. Epelboin, C. Gabrielli, M. Keddam et al., *J. Electroanal. Chem.* **1978**, *93*, 155.
111. U. Bertocci, F. Huet, *J. Electrochem. Soc.* **1997**, *144*, 2786.
112. K. Hladky, J. L. Dawson, *Corros. Sci.* **1981**, *21*, 317.
113. K. Hladky, J. L. Dawson, *Corros. Sci.* **1982**, *22*, 231.
114. P. C. Searson, J. L. Dawson, *J. Electrochem. Soc.* **1988**, *127*, 1931.
115. C. Gabrielli, F. Huet, M. Keddam, *J. Appl. Electrochem.* **1985**, *15*, 503.
116. J. C. Uruchurtu, J. L. Dawson, *Corrosion* **1987**, *43*, 19.
117. U. Bertocci, J. Frydman, C. Gabrielli et al., *J. Electrochem. Soc.* **1998**, *145*, 2780.
118. F. Mansfeld, C. Chen, C. C. Lee et al., *Corros. Sci.* **1996**, *38*, 497.
119. M. Keddam, M. Krarti, C. Pallotta, *Corros. Sci.* **1987**, *43*, 454.
120. K. Nachstedt, Heusler, *Electrochim. Acta* **1988**, *33*, 311.
121. U. Bertocci, Y. Yang-Xiang, *J. Electrochem. Soc.* **1984**, *131*, 1011.
122. J. L. Dawson in *Electrochemical Noise Measurements for Corrosion Applications* (Eds.: J. R. Scully, P. R. Roberge, D. L. Reichert et al.), STP1277, ASTM International, West Conshohocken, Pa., 1996, pp. 3–35.
123. D. A. Eden, Paper presented at CORROSION'98, NACE, Houston, Tex., 1998.
124. B. S. Skerry, D. A. Eden, *Prog. Org. Coat.* **1987**, *15*, 269–285.
125. C.-T. Chen, B. S. Skerry, *Corrosion* **1991**, *47*, 598.
126. U. Bertocci, C. Gabrielli, F. Huet et al., *J. Electrochem. Soc.* **1997**, *144*, 31.
127. U. Bertocci, C. Gabrielli, F. Huet et al., *J. Electrochem. Soc.* **1997**, *144*, 37.
128. F. Mansfeld, L. T. Han, C. C. Lee et al., *Corros. Sci.* **1997**, *39*, 255.
129. F. Mansfeld, L. T. Han, C. C. Lee, *J. Electrochem. Soc.* **1996**, *143*, 286.
130. D. J. Mills, S. Mabbutt, *Prog. Org. Coat.* **2000**, *39*, 41.
131. H. Marchebois, S. Touzain, C. Savall et al., EMCR2000, Paper 189, Budapest, Hungary, 2000.
132. F. Mansfeld, C. C. Lee, *J. Electrochem. Soc.* **1997**, *144*, 2068.
133. H. Xiao, L. T. Han, C. C. Lee et al., *Corrosion* **1997**, *53*, 412.
134. G. P. Bierwagen, C. S. Jeffcoate, J. Li et al., *Prog. Org. Coat.* **1996**, *29*, 21.
135. J. Li, C. S. Jeffcoate, G. P. Bierwagen et al., *Corrosion* **1998**, *54*, 763.
136. H. Greisiger, T. Schauer, *Prog. Org. Coat.* **2000**, *39*, 31.
137. H. S. Isaacs, *Corros. Sci.* **1988**, *28*(6), 547.
138. H. S. Isaacs, *J. Electrochem. Soc.* **1991**, *138*(3), 723.
139. F. Zou, C. Barreau, R. Hellouin et al., *Mater. Sci. Forum* **1998**, *289*, 83.
140. F. Zou, C. Barreau, R. Hellouin et al., *Mater. Sci. Forum* **1998**, *292*, 92.
141. I. M. Zin, R. L. Howard, S. J. Badger et al., *Prog. Org. Coat.* **1998**, *33*, 203–210.
142. H. S. Isaacs, A. J. Aldykiewicz Jr., D. Thierry et al., *Corrosion* **1996**, *52*(3), 163–168.
143. D. A. Worsley, H. N. McMurray, A. Belghazi, *Chem. Commun.* **1997**, *24*, 2369, 2370.
144. F. Zou, D. Thierry, *Electrochim. Acta* **1997**, *42*(20–22), 3293, 3301.
145. F. Zou, D. Thierry, H. S. Isaacs, *J. Electrochem. Soc.* **1997**, *144*(6), 1957–1965.
146. M. Stratmann, H. Streckel, *Corros. Sci.* **1990**, *30*, 681.
147. A. Leng, H. Streckel, M. Stratmann, *Corros. Sci.* **1999**, *41*, 547.
148. A. Leng, H. Streckel, M. Stratmann, *Corros. Sci.* **1999**, *4*, 599.
149. M. Cappadonia, K. Doblhofer, M. Jauch, *Ber. Bunsen-Ges. Phys. Chem.* **1988**, *92*, 903.
150. G. Grundmeier, K. Jüttner, M. Stratmann, Novel electrochemical techniques in corrosion research in *Corrosion and Environmental Degradation*(Ed.: M. Schütze), Wiley-VCH, Weinheim, Germany, 2000, pp. 285–381.
151. G. Grundmeier, M. Stratmann, *J. Appl. Surf. Sci.* **1999**, *141*, 43.
152. K. Doblhofer, R. D. Armstrong, *Electrochim. Acta* **1988**, *33*, 453.
153. M. Stratmann, H. Streckel, *Corros. Sci.* **1990**, *30*, 681.
154. K. Doblhofer, *Bull. Electrochem.* **1992**, *8*, 96.
155. U. Stimming, J. W. Schultze, *Ber. Bunsen-Ges. Phys. Chem.* **1976**, *80*, 1297.
156. U. Stimming, J. W. Schultze, *Electrochim. Acta* **1979**, *24*, 859.
157. H. Leidheiser Jr., W. Wang, G. Igetoft, *Prog. Org. Coat.* **1983**, *11*(1), 19–40.
158. H. S. Wroblowa, *J. Electroanal. Chem.* **1992**, *339*, 231.

159. G. Grundmeier, C. Reinartz, M. Rohwerder et al., *Electrochim. Acta* **1998**, *43*, 1, 2, 165–174.
160. H. Leidheiser Jr., *Corrosion* **1983**, *39*, 189.
161. J. J. Ritter, J. Kruger in *Corrosion Control by Organic Coatings* (Ed.: H. Leidheiser Jr.), NACE International, Houston, Tex., 1981, Vol. 1.
162. M. W. Kendig, J. B. Lumsden, P. P. Stocker in *Surface and Interface Characterization in Corrosion* (Ed.: S. Shah), NACE International, Houston, Tex., 1994.
163. C. F. Sharman, *Nature* **1944**, *153*, 621.
164. M. Van Loo, D. D. Laiderman, R. R. Bruhn, *Corrosion* **1953**, *9*, 277.
165. H. Kaesche, *Werkst. Korros.* **1959**, *11*, 668.
166. W. H. Slabaugh, W. Dejager, S. E. Hoover et al., *J. Paint Technol.* **1972**, *44*, 76.
167. G. M. Hoch in *Localized Corrosion* (Eds.: R. W. Staehle, B. F. Brown, J. Kruger et al.), NACE International, Houston, Tex., 1974, pp. 134.
168. A. Bautista, *Prog. Org. Coat.* **1996**, *28*(1), 49–58.
169. C. Hahin in *Metals Handbook* (Eds.: L. J. Korb, D. L. Olson, J. R. Davis), 9th ed., ASM International, Metals Park, Ohio, 1987, pp. 104–, Vol. 13.
170. R. T. Ruggeri, T. R. Beck, *Corrosion* **1983**, *39*, 452.
171. H. Hagen, K.-H. Rihm, *Farbe Lack* **1990**, *96*, 509.
172. H. Leth-Olsen, J. H. Nordlien, K. Nisancioglu, *J. Electrochem. Soc.* **1997**, *144*, L196.
173. J. E. Pietschmann, H. Pfeifer, *Aluminium* **1993**, *69*, 1019, 1081.
174. A. Rudolf, W.-D. Kaiser, *Aluminium* **1996**, *72*, 726, 832.
175. W. van der Berg, J. A. W. van Laar, J. Suurmond, *Proc. 3rd Int. Conf. Org. Coat. Sci. Technol.* **1979**, *1*, 18.
176. W. Funke, *Ind. Eng. Chem. Prod. Res. Dev.* **1985**, *24*, 343–347.
177. H. J. Lenderink, Ph.D. thesis, Technical University Delft, Delft, The Netherlands, 1995.
178. W. Schmidt, M. Stratmann, *Corros. Sci.* **1998**, *40*, 1441–1443.
179. R. T. Foley, *Corrosion* **1986**, *42*, 277.
180. R. Li, M. G. Ferreira, *Mater. Sci. Forum* **1995**, *237*, 192–194.
181. K. Scheck, Ph. D. thesis, Institut für Technische Chemie der Universität, Stuttgart, Germany, 1991.
182. J. Morita, M. Yoshida, *Corrosion* **1994**, *50*, 11.
183. H. Leth-Olsen, K. Nisancioglu, *Corros. Sci.* **1998**, *40*, 1179, 1195.
184. H. Leth-Olsen, J. H. Nordlien, K. Nisancioglu, *Corros. Sci.* **1998**, *40*(12), 2051.
185. A. Amirudin, D. Thierry, *Prog. Org. Coat.* **1996**, *28*, 59–76.
186. J. P. Rique, *Surfaces* **1978**, *17*, 55.
187. J. E. Pietschmann, H. Pfeifer, *Aluminium* **1994**, *70*, 82.
188. V. T. Talim, *Finishing* **1989**, *13*(11), 31.
189. F. Mansfeld, Y. Wang, *Br. Corros. J.* **1994**, *29*(3), 194.
190. M. B. Spoelstra, T. Zuidwijk, D. H. van der Wijde et al., Eurocorr'97, Trondheim, 1997, Vol. II.
191. J. H. de Wit, Inorganic and organic coating in *Corrosion Mechanisms in Theory and Practice* (Eds.: P. Marcus, J. Oudar), Marcel Dekker, New York, 1995, pp. 581–628.
192. M. Rohwerder, G. Grundmeier, M. Stratmann in *Corrosion Mechanisms in Theory and Practice* (Eds.: P. Marcus, J. Oudar), Marcel Dekker, New York, 2002, pp. 479–528.
193. W. J. van Ooij, T. Child, *CHEMTECH* **1998**, *2*, 26–35.
194. A. Sabata, W. J. van Ooij, R. J. Koch, *J. Adhes. Sci. Technol.* **1993**, *7*, 1153.
195. V. Subramanian, W. J. van Ooij, *Corrosion* **1998**, *54*(3), 204–215.
196. K. D. Conners, W. J. van Ooij, S. J. Clarson et al., *J. Appl. Polym. Sci.* **1994**, *54*, 167–184.
197. W. J. van Ooij, D. Surmann, H. K. Yasuda, *Prog. Org. Coat.* **1995**, *25*, 319–337.
198. T. F. Wang, T. J. Lin, D. J. Yang et al., *Prog. Org. Coat.* **1996**, *28*, 291–297.
199. G. Grundmeier, M. Stratmann, Interfacial and corrosion studies of plasma polymer coated steel and galvanised steel in *Silanes and Other Coupling Agents* (Ed.: K. L. Mittal), VSP, Zeist, The Netherlands, 2000, Vol. 2.
200. H. K. Yasuda, T. F. Wang, D. L. Cho et al., *Prog. Org. Coat.* **1997**, *30*, 31–38.
201. Y. Lin, H. Yasuda, *J. Appl. Polym. Sci.* **1996**, *60*, 543–555.
202. P. Walker, *Surf. Interface Anal.* **1991**, *17*(7), 465–470.
203. S.-E. Hörnstrom, J. Karlsson, J. W. J. van Ooij et al., *J. Adhes. Sci. Technol.* **1996**, *10*(9), 883–904.

204. M. Rohwerder, K. de Weldige, M. Stratmann, *J. Solid State Electrochem.* **1998**, *2*, 88–93.
205. I. Maege, E. Jaehne, A. Henke et al., *Macromol. Symp.* **1997**, *126*, 7–24.
206. B. Wessling, J. Posdorfer, *Electrochim. Acta* **1999**, *44*, 2139.
207. U. Rammelt, P. T. Nguyen, W. Plieth, *Electrochim. Acta* **2001**, *46*, 4251–4257.

5.5
Corrosion Protection by Metallic Coatings

Waldfried Plieth and Andreas Bund
Technische Universitaet Dresden, Germany

5.5.1
Introduction

Metallic coatings are one of the most widely used methods to change the surface properties of construction elements. While the coatings change a great variety of surface properties such as hardness, wearability, solderability, brightness, and so forth, a second effect is connected with most of these coatings, that is, the protection or improved protection against corrosion. Several procedures are used to prepare a metallic coating. Dipping into a metallic melt is one of the oldest procedures that is widely used for zinc coatings. Thin metallic films such as gold or copper filaments are mechanically prepared and then transferred to the surface of another material, for example, wood, stone, or another metal. The latest developments are chemical vapor deposition (CVD) and plasma vapor deposition (PVD). Unfortunately, the metal coatings prepared with these processes are not very well suited for corrosion protection, because of their crystallographic structure and surface properties.

The most commonly used process is electroplating, either by electrochemical or by electroless deposition. For nearly all conditions, these methods provide a corrosion-protective solution, either consisting of the deposition of a one layer or a multilayer process. Because electroplating also provides the most economical solution for metallic coatings, we will concentrate on this method in this article. The main advantage of an electrochemically prepared metallic coating is the mechanism of growth of the film; because this growth occurs in an electrical field, the film becomes very compact and very dense. These properties are prerequisites for a good chemical resistance.

5.5.1.1 Principles of Electrochemical Metal Deposition

The deposition process of a metal is a special case of electrochemical kinetics. Details can be found in a recently published monography [1]. It is connected with the stepwise transfer of a cation from the electrolyte into the metal layer with its specific crystalline structure (cf. Fig. 1). The metal cation in the plating electrolyte exists as a complex MeL_x with ligands, either molecules of the solvent (e.g. H_2O) or special complexing agents such as ammonia (NH_3) or cyanide (CN^-). After transport of this complex by diffusion or migration to the electrode (Step 1), it is adsorbed on the electrode surface accompanied by a partial loss of the ligand molecules and a partial reduction (Step 2, Eq. 1)

$$[MeL_x]^{z+} + \lambda e^- = [MeL_{x-y}]_{ad}^{(z-\lambda)+} + yL \tag{1}$$

The adsorbed metal ion is called an *ad-atom*. From the ad-atom position, the cation is transported by surface diffusion to a position at which it is already part of the growing metal structure (Step 3, Eq. 2). This position is called the *kink site position* (Halbkristallage $Me_{1/2}$). Step 3 is accompanied by transfer of $(z - \lambda)$ electrons.

$$[MeL_{x-y}]_{ad}^{(z-\lambda)+} + (z - \lambda)e^- \longrightarrow Me_{1/2} + (x - y)L \tag{2}$$

Various intermediate steps are possible between Steps (2 and 3).

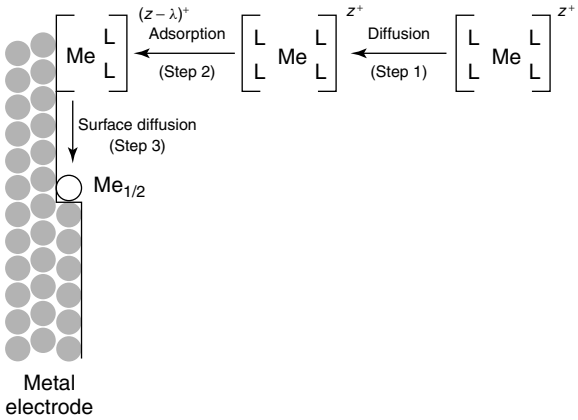


Fig. 1 Schematic representation of the primary processes of electrochemical metal deposition.

As can be seen from this schematic description, electrocrystallization is a consecutive charge-transfer process with at least two separate primary charge-transfer steps [2]. The preliminary for this mechanism is the permanent availability of kink site positions, which are only available on an imperfect crystal or as long as a crystalline structure has not yet been terminated. After such a termination, a nucleation process is necessary similar as in the beginning of the deposition. The formation of a stable nucleus demands a certain oversaturation or, for electrochemical deposition, a certain overvoltage. The critical size of the nucleus (i.e. the transition between redissolution or stable growth) is obtained from a plot of the free enthalpy ΔG necessary to form a nucleus of N atoms versus N (cf. Fig. 2). The N value of the maximum, N_{crit}, is considered to be the critical size. While old theories were based on a homogeneous cluster model, new calculations take into account the stepwise growth of the cluster but come, in principal, to similar conclusions. With the continuous formation of new nuclei, the growth of the nuclei, and the final termination of the growth at some predetermined size, the mechanism of electrodeposition would be completely described. The mechanism is also the basis for understanding the film properties. The morphology, the optical properties (brightness), and the mechanical properties (ductility, hardness) are all related to the grain structure.

Unfortunately, many of the factors controlling these processes are still unknown. One knows, for instance, how to control the size of the nuclei by the addition of small amounts of organic additives (see Sect. 5.5.1.3). Additives are adsorbed on energetically favorable positions, thus causing termination of growth and producing a finer grain structure. We also know how to stimulate deposition by high currents and high concentrations causing a fractal surface topography. But the development of a fundamental mechanism, which takes into account the interplay of all parameters, is still far away.

5.5.1.2 Principles of Alloy Deposition

The simple model described in Sect. 5.5.1.1 is valid only for the deposition

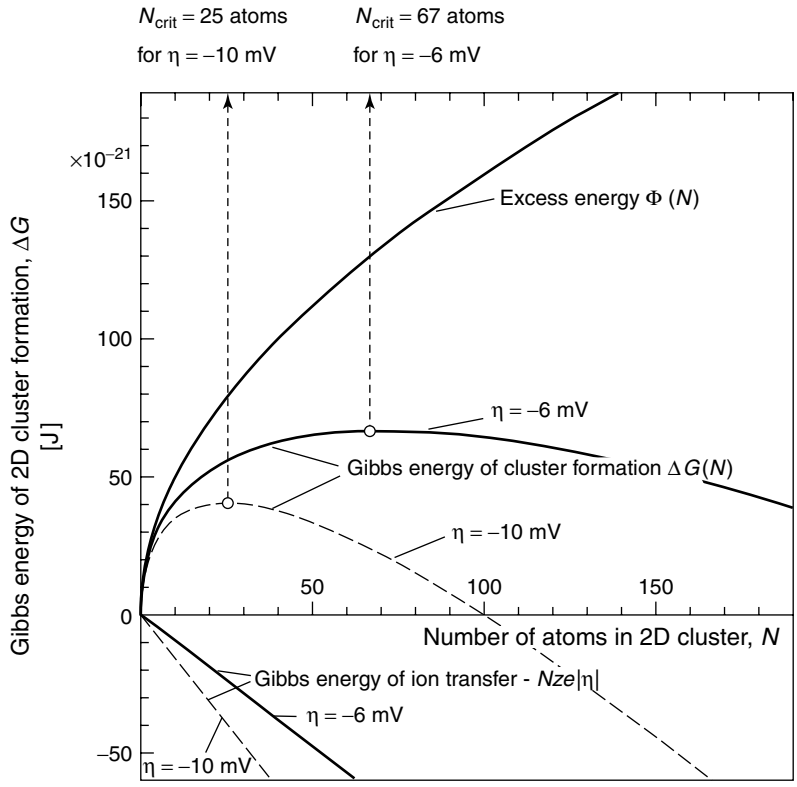


Fig. 2 Gibbs energy of 2D cluster formation as a function of size *N*. (From Ref. [1].)

of a pure metal. Since the beginning of electrochemical deposition, plating of alloys has played an important role. The first alloys of practical importance for corrosion protection were Zn-Cu (brass) and Sn-Cu (bronze) alloys. In the last years, electrolytes for plating Zn-Co (see Sect. 5.5.4.6.1), Zn-Fe (see Sect. 5.5.4.6.2), and Zn-Ni (see Sect. 5.5.4.6.3) alloys have been developed for improved corrosion protection of Zn layers.

Alloy deposition is possible if the rate of deposition is controlled in such a manner that the different electrochemical natures of the alloy components (noble or nonnoble) are compensated. This can be achieved by complexing, shifting the deposition potentials of the more noble metal to more negative values until similar deposition rates are obtained (thermodynamic approach). A second possibility to control the alloy composition is by limiting the diffusion rate of the two components by concentration regulation (kinetic approach). In principle, one expects the more noble metal to be deposited preferentially. In contrast to this so-called normal codeposition [3], an anomalous codeposition is observed in which the less noble metal is deposited preferentially (e.g. Fe-Ni). In some cases (Ni-W, Ni-Mo, etc. [4–6]), the codeposition of a metal is obtained, which cannot be deposited alone from aqueous electrolytes (induced codeposition).

Models were developed to explain such a behavior, for example, assuming special catalytic surface effects and/or adsorption of special complexes [4–10].

Very little is known about the mechanism of corrosion protection by alloys. For some alloys, the depletion of the passive layer of the alloy by the less stable metal can be assumed, producing a thin surface film of improved corrosion protection (e.g. Fe-Cr-Ni). Recently, it was proposed that the corrosion protection of Zn-Ni alloys might be connected with the formation of an intermetallic phase [11].

5.5.1.3 **Role of Additives**

The electroplating of metals for corrosion-protection applications often involves the use of so-called additives (mostly organic compounds) in the plating electrolyte. These additives are used to yield special properties of the deposited metal layer, such as brightness, good levelling, and throwing power. The use of additives in plating baths must be distinguished from the application of corrosion-inhibiting additives (e.g. benzotriazole in the case of copper), which are treated in Chapter 5.2 of this volume. The choice of additives has been (and still is to a certain degree) performed on a highly empirical basis. Substances with undefined chemical composition such as animal glue or gelatin are still used in electroplating processes. Recently, there have been increasing research efforts to clarify the role of additives in electroplating processes. From the vast amount of literature, we will report only some important aspects. For reviews, see for example Refs. [12, 13].

Adsorption of the additive (physi- or chemisorption) plays a key role in the mechanism of action of additives. One general scheme classifies additives as inhibitors and as a reactivators [13]. It is the balance between inhibition and reactivation, which controls the final form (brightness, structure, etc.) of the deposit. As an example, for the complex interplay between additives, we shortly summarize the results of an investigation of copper deposition from a sulfuric acid copper bath, containing chloride, dithiadecyl disodiumsulphonate (DDS), and a surfactant (polyethylene glycol) [13]. DDS alone shows an inhibiting effect in the electrodeposition process by blocking the growth centers (kink sites, cf. Fig. 1) of the developing Cu film. When the surfactant alone is added to the bath, almost no Cu deposition is observed. Only a combination of DDS, surfactant, and chloride will yield finely grained bright copper deposits. This result can be explained by a model (cf. Fig. 3) that assumes blocking of the surface by the surfactant (inhibition) and local perforation of the adsorbed film by DDS molecules to produce pathways for the cupric ions (reactivation).

The main mechanisms of bright deposition are diffusion-controlled leveling,

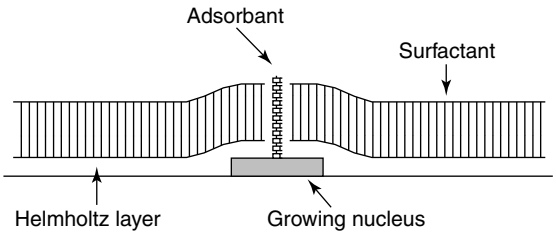


Fig. 3 The model of "local perforation" to explain the synergistic action of brightener and surfactant in the case of Cu plating. (From Ref. [13].)

grain refining, and orientation of crystal growth [14]. Grain refining occurs when the additive inhibits growth processes and thus increases the relative rate of nucleation processes. Crystallite sizes below the wavelength of visible light (<400 nm) are prerequisites for bright deposits. Furthermore, the orientation of reflecting crystal planes parallel to the surface is important. These conditions are fulfilled, if the additive produces high surface coverages in combination with high rates for the adsorption and desorption reaction (fast dynamic equilibria).

Leveling describes the reduction of surface roughness during deposition. The leveling of scratches and other unwanted surface features is an important aspect in metal finishing. Geometric and true leveling are distinguished [12]. To obtain geometric leveling, the thickness of the deposit must be larger than the depth of the grooves to be filled (for details see Ref. [14]). True leveling, which occurs under the influence of additives, is achieved at much smaller plating thicknesses. Field-dependent adsorption of a reactivating additive molecule (cf. Fig. 4) is one possible mechanism for true leveling. It will lead to increased deposition rates in concave surface features and therefore a fast leveling of the rough surface.

The consumption of additives by incorporation in the deposit, removal with the plated object, or electrochemical reaction during the electroplating process requires careful monitoring and correction.

5.5.2 Mechanisms of Corrosion Protection by Metallic Coatings

Corrosion protection by metallic coatings comprises application of a coating metal onto a substrate consisting either of a nonmetallic substrate or of a base metal. In the following, we will concentrate on a base metal as a substrate.

Important for the metal dissolution process are the hydrogen evolution, and the oxygen-reduction reaction as cathodic processes of the anodic corrosion reaction. We distinguish acid corrosion and oxygen corrosion (for details see Chapter 1). The potential of these processes provides the driving force for the metal oxidation. A metal coating can inhibit or catalyze these reactions. Depending on the Nernst potential of the coating metal, the base metal will act as an anode or cathode. If a more noble metal is coated with a less noble metal (e.g. Fe with Zn), the latter will act as a sacrificial anode driving the potential of the underlying metal into

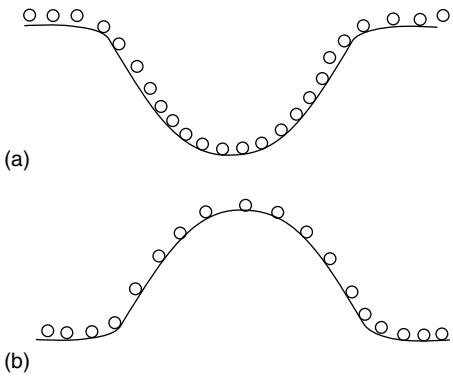


Fig. 4 Field-induced increase and decrease of surface concentration of adsorbates at (a) concave and (b) convex surface areas. (From Ref. [13].)

the cathodic region with no net corrosion current (cathodic protection). Pores and cracks in the coating can be tolerated to a certain degree as the base metal acts as the cathode.

If the coating metal is more noble than the base metal (e.g. Cr, Ni, or Sn on Fe), effective corrosion protection is only possible with coatings that are free of pores, cracks, and so on. Otherwise, the large ratio of the cathode (coating) to the anode (base metal) area will give rise to pitting corrosion (see Chapter 4.2). The effective corrosion rate will depend on the kinetic parameters such as overvoltage, exchange current density, electrolyte, and so on.

If complexing agents are involved, the ranking between the metals can be altered because the concentration of the free metal ions in the solution can go to a very low level. This is, for example, the case with citrus fruits in tin-coated iron cans. To prevent dissolution of the tin countered by hydrogen evolution, an additional polymer or lacquer coating (see Chapter 5.4) can be applied.

5.5.3 Pretreatment of the Base Metal

5.5.3.1 Mechanical Pretreatment

The fundamental procedure during the mechanical pretreatment is the removal of surface films, impurities, and so on by the grinding or the polishing material. The hardness of the grinding material should be 2.5 to 3 times higher than that of the material to be ground. Therefore, hard metals must be pretreated with diamond (hardness 8000 HV) suspensions whereas, for softer metals, SiC (2500 HV) or Al_2O_3 (2000 HV) can be used. For flat surfaces, commercial grinding machines with grinding discs can be used. For complex geometries (e.g. some automotive parts), grinding and polishing is a time-consuming task and must be performed by hand. The mechanical pretreatment usually comprises the following steps:

1. Plain grinding (PG): to achieve high grinding rates, the particles of the grinding material should be relatively large and should be fixed to the surface of the grinding disk (e.g. grinding paper).
2. Fine grinding (FG): particle sizes between 6 and 15 µm are used. As an alternative to grinding paper, grinding tissues, which are continuously soaked with diamond suspension, can be applied.
3. Polishing (DP): the necessary low grinding rates are achieved with particle sizes between 1 and 3 µm. Because of their good leveling power, modern electrolytes will level smaller scratches and pores in the surface of the base metal and DP (and even FG) may not be necessary.

For more details on mechanical polishing and a lot of examples, the interested reader is referred to Ref. [15].

5.5.3.2 Chemical Pretreatment

After the grinding/polishing, the base metal must be degreased. The cleaners usually applied can be subdivided as follows:

1. Alkaline cleaners: contain hydroxides, carbonates, silicates, phosphates of the alkali metals, tensides.
2. Organic cleaners: mostly chlorinated hydrocarbons.
3. Emulsion cleaners: combination of alkaline, organic cleaners, and emulsifiers.

Ultrasound may be used to enhance the performance of the cleaner.

The last chemical pretreatment step is the electrolytic or fine degreasing, in which the chemical cleaning power of an alkaline cleaner is enhanced by an electric current. The underlying mechanisms have not been fully clarified. Saponification of the esters of fatty acids may play a role. Furthermore, the evolving gas bubbles will tear off the last traces of contaminants from the surface.

Electrolytic degreasing can be performed cathodically or anodically. In the cathodic case, twice the amount of gas is produced and the cleaning is more effective. Problems may arise from hydride formation and hydrogen embrittlement (e.g. with steel as base metal) or deposition of positively charged contaminants (e.g. metal ions). Sometimes changing between cathodic and anodic degreasing will give good results.

It should be noted that the optimization of the electrolytic degreasing procedure is a special and challenging task for each system.

Depending on the base metal and the procedure used for fine degreasing, an acid or cyanide pickling may be necessary to remove oxides from the surface of the base metal.

5.5.4 Examples

The following sections give some typical examples of metallic coatings for corrosion protection. More details can be found in Refs. [16–19].

5.5.4.1 Zinc/Cadmium

Zinc and cadmium coatings are mainly used for corrosion protection of iron and steel, where they show cathodic protection, good corrosion stability, and excellent adherence. As cadmium is toxic and more expensive than zinc, it is used only in some special applications in which its particular properties are demanded: higher electric conductivity and ductility than zinc, better solderability, lower coefficient of friction, and higher throwing power of the electrolytes. In sea or tropical environments, cadmium shows better corrosion protection than zinc, whereas zinc is superior in industrial atmospheres. Futhermore, zinc has better long-range protecting properties (corrosion protection is still effective if small areas of the base metal are exposed).

5.5.4.1.1 **Zinc** Zinc layers can be prepared by dipping a metal into a zinc melt (hot dipping or galvanizing) or by an electroplating process. Compared to nickel or chromium (see Sects. 5.5.4.2 and 5.5.4.3, respectively), zinc coatings offer the most economic corrosion protection on steel. Under corrosive conditions (industrial air, salt spray test), the protective properties are proportional to the thickness of the layer. The stability of zinc is based on the formation of a uniform, well-adhering, layer of zinc hydroxide and carbonate (with a small amount of chloride or sulfate). If large amounts of sulfur dioxide are present, water-soluble zinc sulfate is formed, giving rise to increased corrosion. The relation between the corrosion rate and the runoff rate (i.e. the amount of metal being released from the corrosion product layer) and the ecotoxicity of zinc have been investigated recently [20]. Application of a chromate conversion (see Sect. 5.5.5.2) treatment improves the long-term stability of the corrosion protection and yields colored coatings (depending on thickness and chromium content of the conversion layer). Zinc protects iron and steel sacrificially (cathodic protection, see

Sect. 5.5.2) and can be plated mechanically (i.e. hot dipping, metal spraying, etc.) and electrochemically. Mechanical plating is the preferred method for layers with thickness >25 µm [21] and in which hydrogen embrittlement represents a problem [22]. With modern processes, electroplating rates up to 700 m min^{-1} can be achieved [23]. During the last few years, zinc alloys (see Sect. 5.5.4.6) with cobalt (0.8%), nickel (10–14%), iron, and tin have found increased interest due to their improved corrosion stability (e.g. automotive applications).

For the electroplating of pure zinc layers, there are mainly three types of zinc electrolytes: alkaline cyanide, alkaline noncyanide, and acid. The acid electrolytes, which exhibit current efficiencies >95% (cf. Fig. 5), can be subdivided into weak acid–containing ammonium, weak acid ammonium free, and moderate acid (see Table 1). They contain zinc as chloride and/or sulfate. For high plating rates (current densities up to 88 A dm^{-2}), fluoroborate electrolytes can be used [16]. Besides the inorganic ingredients listed in Table 1, the baths usually contain organic additives acting as brighteners, levelers, and so on (see Sect. 5.5.1.3). Because of their lower current efficiency (cf. Fig. 5) and higher concentration polarization, the alkaline baths exhibit better throwing power [21]. This makes them preferable for plating irregularly shaped parts with a coating of uniform thickness. The current efficiency and other operating conditions of alkaline cyanide electrolytes mainly depend on the ratio of total cyanide to zinc, which should lie between 2 and 3 [16]. The acid baths yield brighter deposits [21]. As an alternative, an acetate bath has been proposed, which yields adherent and smooth zinc coatings under the following conditions: 50 g l^{-1} $Zn(CH_3COO)_2 \cdot 2H_2O$, 10 ml l^{-1} CH_3COOH, 2.66 A dm^{-2}, 25 °C [24].

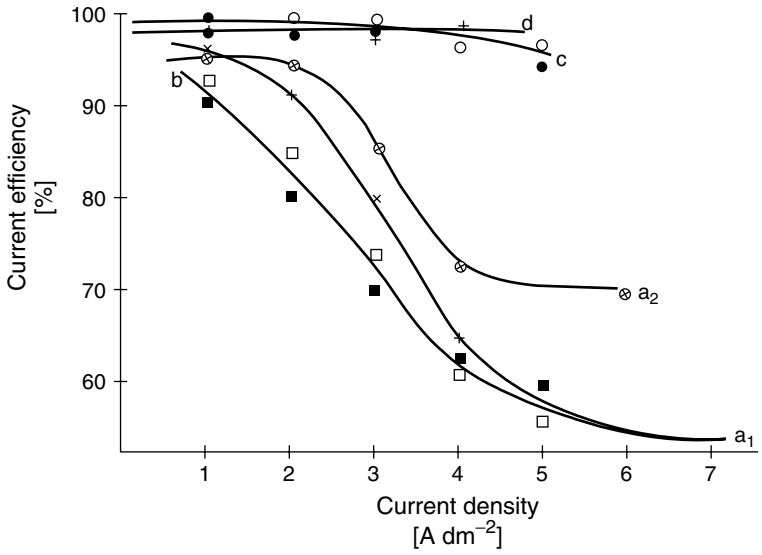


Fig. 5 Current efficiencies in different zinc electrolytes: (from Ref. [21])
(a) alkaline cyanide × ⊗; (b) cyanide-free alkaline □ ■; (c) weakly acid ○ ●;
(d) weakly acid Zn-Co +.

Tab. 1 Anorganic composition of typical zinc electrolytes in g l^{-1} (from Ref. [21])

	Alkaline cyanide	*Alkaline noncyanide*	*Weak acid–containing ammonium*	*Weak acid ammonium free*	*Moderately acid*
Zn^{2+}	7–40	5–15	20–50	20–50	100–150
NaCN	7–130	–	–	–	–
NaOH	70–100	80–150	–	–	–
NH_4^+	–	–	10–60	–	5–10
Cl^-	–	–	100–120	100–125	–
H_3BO_3	–	–	10–30	10–30	–
SO_4^{2-}	–	–	–	–	200–250

A typical zinc electroplating process comprises the following steps: (1) cleaning, (2) electrocleaning (see Sect. 5.5.3.2), (3) rinsing, (4) acid pickle, (5) rinsing, (6) electroplating of zinc, (7) rinse, (8) chromate conversion (see Sect. 5.5.5.2), (9) rinse, and (10) drying [21].

Table 2 compares the physical properties of zinc coatings plated from different electrolytes.

5.5.4.1.2 **Cadmium** Cadmium has a long tradition as a corrosion-protective coating. Because of its high ductility, the film acts as a lubricant. Table 3 lists some typical cadmium baths and their operating conditions. There is nearly no hydrogen evolution with the fluoroborate electrolyte.

With the use of cadmium coatings, a variety of environmental protection measures must be connected. A removal of the cadmium layers at the end of the lifetime of the coated part should be guaranteed.

5.5.4.2 Copper/Nickel

Copper alone is rarely used as a corrosion-protection coating. It mainly serves as an undercoat (5–10 μm) for nickel layers.

5.5.4.2.1 **Copper** Copper is mostly plated from acid, fluoroborate, or cyanide baths (see Table 4). Among these, the cyanide electrolyte reveals the best throwing power but needs intensive convection.

To obtain well-adhering coatings on steel parts, a pretreatment by a commercial

Tab. 2 Physical properties of zinc electrodeposits (from Ref. [21])

	Acid	*Alkaline noncyanide*	*Cyanide*
Lattice structure	Hcp	Hcp	Hcp
Type of crystallization	Nonoriented dispersion type	Field-oriented dispersion type	Field-oriented dispersion type
Crystallite size (nm)	70 ± 30	90 ± 40	130 ± 50
Micro strain (N mm^{-2})	80	120	150
Macro strain (N mm^{-2})	−40	80	40
Micro vickers hardness	100 ± 30	130 ± 30	140 ± 40
Ductility (%)	0.5–7.5	1–5.5	0.2–3.2

Tab. 3 Composition and operating conditions of some typical cadmium plating baths

	Cyanide bath	*Sulfate bath*	*Fluoroborate bath*
Cadmium	20–30 g l^{-1} CdO	50–60 g l^{-1} $CdSO_4$	100 g l^{-1} CdO
Sodium cyanide ($g\ l^{-1}$)	120	–	–
Sodium hydroxide ($g\ l^{-1}$)	10–130	–	–
Nickel sulfate ($g\ l^{-1}$)	0.1–0.2	–	–
Ammonium sulfate ($g\ l^{-1}$)	–	100–250	–
Fluoroboric acid (46%) ($g\ l^{-1}$)	–	–	400
Additives, etc.	0.1 g l^{-1} (e.g. turkey red oil)	10–20 g l^{-1} (gelatine, urotropine, wetting agent)	50 g l^{-1} dextrine 30 g l^{-1} dioxyphenylsulfone
Current density ($A\ dm^{-2}$)	2.5–5	0.5–1.5	3
Temperature (°C)	20–35	20–30	25
pH		5	2.5–3

pickling bath should be applied before the plating itself.

5.5.4.2.2 **Nickel** In not too corrosive environments (electronic devices, houseware, etc.), nickel coatings are often used on metals and alloys to prevent tarnishing or corrosion. The lifetime of the layer is proportional to its thickness. The main base metals protected by nickel are iron, zinc, aluminum (and its alloys), and copper. In combination with iron, zinc, and aluminum, nickel usually is cathodic. Therefore, to provide corrosion protection on these metals, the nickel layer must be dense and free of pores.

Bright surfaces can be obtained by polishing or by using bright nickel electrolytes. However, in industrial atmospheres, tarnishing will occur. Therefore, in many cases, a thin chromium layer is plated above the nickel coating with thickness between 0.25 and 1.5 µm (see Sect. 5.5.4.3). The presence of the chromium layer, which is passivated by a layer of chromium(III)oxides, further improves the corrosion protection. The underlying mechanism has been investigated in great detail (see Sect. 5.5.4.4). The best corrosion protection of iron and zinc is obtained with a combination of dull or semibright nickel covered by a layer of bright nickel [25]. The thickness ratio should be 4 : 1 for iron and 3 : 1 for zinc. The texture of the nickel layers is very important, the semibright nickel should be columnar, the bright nickel lamellar.

Most modern nickel electrolytes are based on the composition proposed by Watts [26], which contains boric acid besides nickel chloride and sulfate. The chloride facilitates the dissolution of the anodes, but also increases the internal tensile stresses of the deposit. Boric acid serves as a buffering agent. The throwing power can be improved by adding inorganic salts. Recently, it

Tab. 4 Composition and working conditions of different copper plating baths

	Acid bath	*Fluoroborate bath*	*Cyanide bath*
Copper	250 g l^{-1} $CuSO_4 \cdot 5H_2O$	200–500 g l^{-1} $Cu(BF_4)_2$	270 g l^{-1} $K[Cu(CN)_2]$
Sulfuric acid 96% (g l^{-1})	75	–	–
Chloride (g l^{-1})	0.02–0.2	–	–
NaCN (g l^{-1})	–	–	10
KCNS (g l^{-1})	–	–	10
Na_2SO_4 (g l^{-1})	–	–	5
NaOH (g l^{-1})	–	–	5
Additives, etc.	Various organic additives, wetting agents	Small amounts of copper sulfate, various organic additives, wetting agents	Organic brighteners, wetting agents
Current density (A dm^{-2})	Up to 20 with effective convection	5–50	1.5–8
pH		0.5–2	
Temp. (°C)	20–40	25–50	70

has been found that the addition of sodium hypophosphite strongly enhances the throwing power [27]. Besides the Watts electrolyte, sulfamate and fluoroborate electrolytes are used. The sulfamate electrolyte yields deposits with the lowest internal stresses, which can be completely eliminated by additives or even be transformed to compressional stresses. Therefore, it is also used for electroforming applications. The fluoroborate electrolyte is strongly buffered and can be operated at relatively high-current densities. Table 5 summarizes the composition and working conditions of the various nickel electrolytes.

Because of the concurrent hydrogen evolution, the current efficiency is always less than 100% [28]. Pore formation as a consequence of hydrogen bubbles sticking to the electrode can be avoided by the addition of hydrogen peroxide or wetting agents.

Bright nickel deposits are obtained from one of the above electrolytes with additives. Because of its low costs, the Watts electrolyte is the most often used base

Tab. 5 Composition and working conditions of various nickel electrolytes (from Ref. [16])

	Watts	*Fluoroborate*	*Sulfamate*
Nickel	240–450 g l^{-1} $NiSO_4 \cdot 6H_2O$ + 45–90 g l^{-1} $NiCl_2 \cdot 6H_2O$	300 g l^{-1} $Ni(BF_4)_2$	300 g l^{-1} $Ni(NH_2SO_3)_2$ + 30 g l^{-1} $NiCl_2 \cdot 6H_2O$
Boric acid (g l^{-1})	30–50	30	30
pH	1.5–4.5	2.7–3.5	3.5–4.5
Temperature (°C)	40–70	37–76	25–70
Current density (A dm^{-2})	2–10	2–20	2–14

electrolyte. The additives can be divided into the following classes:

1. *Brighteners*: The group of brighteners is further subclassed into first-class brighteners and second-class brighteners. Nickel electrolytes with first-class brighteners will only yield semibright deposits. First-class brighteners will render the electrolyte less sensitive towards second-class brighteners and metallic contaminations. According to Saubestre [29], the molecule of a first-class brightener must contain the functionality =C−S=O with the sulfur atom in a hexavalent state. Brighteners of the second class will improve the brightness of the deposit considerably even in low concentrations. They increase the cathodic polarization and cause brittleness and tensile stresses. Therefore, they are always combined with first-class brighteners. Soluble salts of metals with high hydrogen overvoltages can act as second-class brighteners (Zn, Cd, Hg, Tl, Pb) as well as organic compounds with double and triple bonds (coumarin, thiourea, etc.). All brightener systems contain sulfur. As a consequence, bright nickel deposits will always contain some sulfur, which lowers the corrosion resistance of the layer. Studies on the mechanisms by which additives influence the deposit morphology can be found in Refs. [30–32].

2. *Wetting agents (surfactants)*: The role of these additives is to lower the surface tension and thus to facilitate the release of hydrogen bubbles adhering to the electrode surface, which would otherwise lead to pores in the deposit. Hydrocarbons with chain lengths between 8 and 18 carbon atoms and a sulfate or sulfonate group are used.

3. *Internal stress reducers*: Brighteners of the first class usually lower the internal tensile stresses and thus improve the ductility of the deposits.

4. *Leveling additives*: These substances increase the cathodic polarization. Possible candidates are coumarin, thiourea, 2-butyne-1,4-diol, propargylalcohol, pyridines, and others.

As with all high-performance electrolytes, continuous monitoring of the composition is necessary, which can be performed by spectroscopic or chromatographic methods. In addition, cyclic voltammetry [33] and electrochemical impedance spectroscopy [34] have been proposed for the screening of nickel electrolytes and the deposits obtained from them.

5.5.4.2.3 **Nickel-phosphorus** Excellent corrosion protection is observed if the nickel layer contains phosphorus. This was first observed with electroless NiP layers (see Sect. 5.5.4.2.4). During the last years, electrochemical plating processes for nickel phosphorus have been developed. In these processes, a phosphorus source has to be added to the electrolyte; either sodium phosphite or sodium hypophosphite are used. The other components of the electrolyte are similar to a Watts bath (see Sect. 5.5.4.2). Table 6 lists a typical composition.

Tab. 6 Composition of a nickel–phosphorus plating bath

$NiSO_4 \cdot 6H_2O$ (g l^{-1})	150
$NiCl_2 \cdot 6H_2O$ (g l^{-1})	45
$NiCO_3$ (g l^{-1})	30
H_3PO_4 (g l^{-1})	58
NaH_2PO_2 (g l^{-1})	30
pH	0–1
Temperature (°C)	50–70

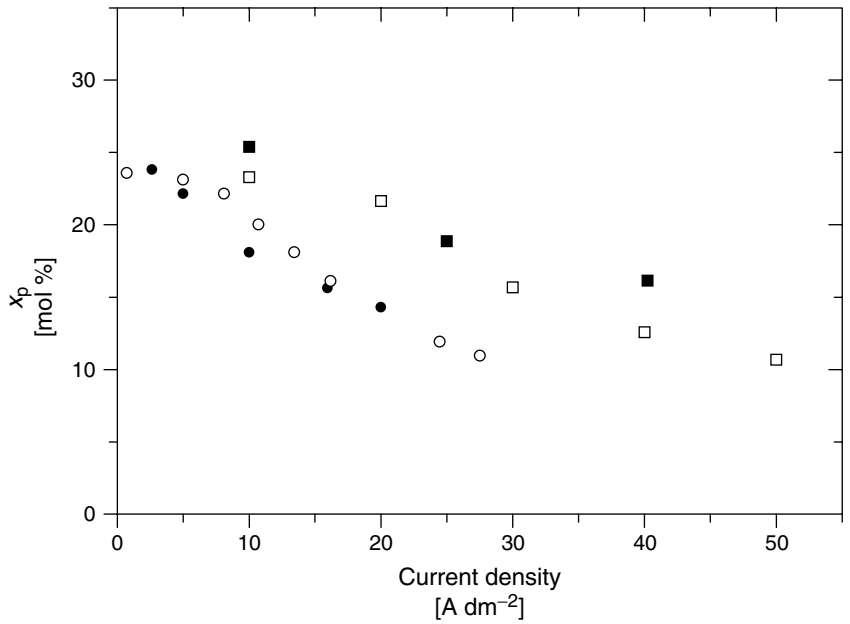


Fig. 6 Content of phosphorus in nickel–phosphorus layers as function of the current density. (From Ref. [35].)

The phosphorus content of the nickel layer increases with increasing the pH of the electrolyte. Another important parameter is the current density. The phosphorus content decreases with increasing current density [35, 36] (cf. Fig. 6). Finally, the phosphorus content depends on the concentration of hypophosphite.

5.5.4.2.4 **Electroless Copper and Nickel**
The electroless deposition of a metal is based on the electrochemical reduction of the metal cation by a reducing agent. The reduction takes place only on a catalyst so that the electrolyte is stable if no catalyst is in the bath. For further improvement of the stability, stabilizers are added to the electrolyte.

The catalyst can be small metal particles. To start the reduction process, palladium catalysts are prepared on the substrate. Later, the nuclei of the deposited metal take over the catalyst function.

In the case of copper, formaldehyde is used mostly for the reduction. A typical electrolyte composition is given in Table 7.

To decrease the pH of the bath, hypophosphite was tried as reducer [37]. Because the oxidation of hypophosphite only occurs on nickel particles, nickel had to be added to the bath resulting in coatings with a small

Tab. 7 Electrolyte composition and working conditions for electroless copper plating

$CuSO_4 \cdot 5H_2O$ (g l^{-1})	15
Potassium sodium tartrate (g l^{-1})	40
Formaldehyde, 37% (ml l^{-1})	6
Stabilizer, e.g. V_2O_5 (mg l^{-1})	1–3
pH	10–13
Temperature (°C)	70–75
Typical deposition rate (µm h^{-1})	1–5

nickel content. This is one reason this bath was not accepted by the plating industry.

In the case of nickel reduction, hypophosphite dominates the market [38]. Two types of electrolytes are used: a weakly acid bath with a pH between 2 to 5, which generates nickel deposits with a higher P content in the film that are better for corrosion protection, and an alkaline bath ($8 < pH < 13$), which can be used at lower temperatures.

The compositions and working conditions of the baths are summarized in Table 8.

There are also electrolytes on the market using sodium borohydride, methyl- or ethylamino borane, or hydrazine [39]. Rather pure nickel layers are deposited from these electrolytes.

The autocatalytic nickel deposition can also be used for alloy deposition (Ni-Co, Ni-Fe) and for the deposition of nickel dispersion coatings (Ni/SiC). The nickel film can be heat-treated, below or well above 280 °C, the transition temperature amorphous/crystalline. The hardness increases up to 400 °C (1000–1200 HV) and then decreases again. Especially the corrosion protection is improved if the layer is heated to 650 °C.

5.5.4.3 Hard and Decorative Chromium Coatings

Chromium coatings are mostly applied onto copper/nickel subcoatings (see Sect. 5.5.4.2). Reference [40] gives a short historic overview of chromium/nickel plating with special regard to the automotive industry.

The plating baths contain chromium in a hexavalent state. Furthermore, sulfuric acid and/or fluoric acid must be present to act as a catalyst for the chromic acid reduction. The typical ratio of chromic acid/catalyst should be varied only in a small tolerance regime. The surface area ratio between anode and cathode is also important because the chromate is reduced partially to chromium(III). A small content is necessary for the process, but, to control the concentration of chromium(III), some part must be reoxidized on the anode. A surface area ratio anode/cathode of 1 : 1.5 down to 1 : 3 is used. Table 9 lists some typical electrolytes for chromium plating.

The mixed electrolyte was introduced as a self-regulating high-speed chromium

Tab. 8 Electrolyte composition and working conditions for electroless nickel plating

	Weakly acid	***Alkaline***	***Borane***
Nickel	25 g l^{-1} $NiCl_2 \cdot 6H_2O$+ 25 g l^{-1} $Ni_2SO_4 \cdot 6H_2O$	30–40 g l^{-1} $NiCl_2 \cdot 6H_2O$ or 30 g l^{-1} $Ni_2SO_4 \cdot 6H_2O$	93 g l^{-1} $NiCl_2 \cdot 6H_2O$
Reducing agent	25 g l^{-1} NaH_2PO_2	10–30 g l^{-1} NaH_2PO_2	37 g l^{-1} dimethyl-amino borane
Lactic acid (g l^{-1})	27	–	25
Sodium citrate (g l^{-1})	–	100	–
NH_4Cl (g l^{-1})	–	50	–
Stabilizers, etc.	1–3 mg l^{-1} Pb,Sb or 0.1–0.2 g l^{-1} thiourea	–	1 g l^{-1} thiodi-glycolic acid
Temperature (°C)	85–95	60	30
pH			4–4.5

Tab. 9 Composition and working conditions of some chromium-plating baths

	Sulfuric acid bath	*Fluoric acid bath*	*Mixed catalyst bath*	*Nonfluoride bath*
CrO_3 (g l^{-1})	250–400	300	300 15 g l^{-1} $K_2Cr_2O_7$	
Catalyst	2.5–4 g l^{-1} H_2SO_4	1.5 g l^{-1} HF	2.5 g l^{-1} $SrSO_4$ 3.6 g l^{-1} K_2SiF_6	
Typical ratio chromic acid/catalyst	100 : 0.9–100 : 1.2	150 : 1–200 : 1		
Temperature (°C)	50–60		55	35–55
Current density (A dm^{-2})	20–40		Up to 60	5–100 (depending on temperature)

bath. Strontium sulfate and potassium fluorosilicate are added in access as precipitates, thus self-controlling the concentrations.

5.5.4.3.1 Corrosion Protection of Copper/Nickel/Chromium Layers

The system of a copper layer, a nickel layer (see Sect. 5.5.4.2), and an additional chromium coating (see Sect. 5.5.4.3) is one of the classical layer combinations for an effective corrosion protection. The nobility of each successive layer in the stack decreases. With possible variations in layer thickness, layer properties such as sulfur content (in the case of nickel layers), heat treatment, and so on, any protection can be obtained, either in a reductive (cities, industrial complexes), or in an oxidative atmosphere (land and sea atmosphere).

While the copper film acts primarily as a primer coating, which improves the stability of the following nickel layer or layers by its more noble character as well as the adhesion, the nickel film has direct protective properties. For this purpose, it must be deposited pore free, which demands a thicker film (>10 μm), or a double layer. In this case, optimal corrosion protection is achieved if the second nickel layer is less noble than the first. A typical combination is a semibright nickel layer, free of sulfur, followed by a bright nickel layer. The protective properties are controlled by measuring the potential difference between the two layers. A difference $\Delta E > 50$ mV is necessary, the outer layer having the more negative potential.

The corrosion protection is increased if a crack-free chromium layer or a chromium layer with microcracks is added to the copper/nickel or to the nickel or double nickel layer. A crack-free chromium film is possible if special additives are added to the chromium-plating electrolyte. Manganese salts, selenic acid, and indium sulfate are mentioned in the literature. The film also has to be sufficiently thick (>22 μm). The stability of the film is not very high because crack formation is a permanent process in these films.

More effective are films with microcracks or micropores as obtained with modern chromium-plating electrolytes. Furthermore, double layer or multilayer chromium films provide very stable corrosion protection.

5.5.4.4 **Tin** Tin itself is relatively resistant to corrosion and tarnishing. Plated on iron and copper alloys, it provides good ductility and corrosion protection under mild conditions (e.g. in-house applications). For outside applications, zinc coatings (see Sect. 5.5) should be used. Tin is mainly used in the food (e.g. canning of food) and electronics industry, because of its nontoxic and solderable behavior, respectively. Because of its standard potential (−0.14 V), tin generally acts as a cathode when in contact with iron (anodic corrosion protection, see Sect. 5.5.2). Electroplated thicknesses lie between 1 µm (pretreatment for painting, lacquering) and 50 µm (corrosion protection). Tin is problematic for low-temperature applications (e.g. parts of refrigerators) because of the allotropic phase change at 13.2 °C (tin pest) from the metallic β-phase to the semimetallic powdery α-tin. Even for pure tin, the conversion proceeds slowly, and it can be almost completely suppressed by alloy deposition (e.g. Bi or Zn, see Sect. 5.5.4.6).

Tin is plated from alkaline baths, containing Sn(IV) as stannates, or from acid Sn(II) electrolytes (sulfate, chloride, fluoroborate). As electrolytes containing both two and four valent tin yield no useable electrodeposits, special care must be taken during the plating process. In the stannate electrolytes, the anodes must be filmed (preoxidized at high-current densities to form tin suboxides) before each plating process in order to prevent the formation of Sn(II). The acid electrolytes contain several additives to prevent the oxidation of Sn(II) to Sn(IV) and to produce smooth deposits. Because of the higher polarization during deposition, the stannate electrolytes exhibit higher throwing power. They can be used without additives but must be operated at temperatures between 80 and 90 °C.

Electroplated tin, which in contrast to hot dipped tin, mostly looks matte or semilustrous, but can be brightened by reflowing, that is heating for a short time (some seconds up to a minute) above the melting point of tin (232 °C). Table 10 summarizes the composition and working parameters of the commonly used tin electrolytes.

5.5.4.5 **Noble Metals**

The typical metals in this category are silver, gold, and the platinum metals rhodium, palladium, platinum, and ruthenium. The demands for corrosion protection by noble metal coatings are a pore- and crack-free deposit and a layer thickness that is able to protect the substrate for the expected lifetime of the plated parts.

5.5.4.5.1 **Silver** Silver is one of the oldest metal deposits used for corrosion protection of less noble metals. Because of the very high deposition rate, compact and bright deposits can only be obtained if the free silver ion concentration is controlled by complexing agents. The most widely used bath is a cyanide bath. Cyanide-free electrolytes have also been developed. A typical cyanide bath for bright silver deposits is given in Table 11.

The pH of the electrolyte is reduced by absorption of carbon dioxide from the air. Therefore, carbonate has to be removed regularly.

To obtain a good adhesion of the silver layer on steel substrates, usually a thin silver layer is predeposited using a low silver content (0.5–2 g l^{-1}) and a high-current density. Applying this procedure, the formation of a cementation layer of

Tab. 10 Composition and operating conditions of some tin electrolytes (from Refs. [16, 41])

	Sulfate	*Fluoroborate*	*Na stannate*	*K stannate*
Tin (g l^{-1})	30–40	40–80	30–50	40–160
Sulfuric acid (g l^{-1})	40–70	–	–	–
Fluoroboric acid (g l^{-1})	–	40–200	–	–
Boric acid (g l^{-1})	–	10–30	–	–
Free hydroxide (g l^{-1})	–	–	12–15 (NaOH)	15–22 (KOH)
Temperature (°C)	20–30	20–40	70–80	65–88
Cathode current density (A dm^{-2})	0.1–2.7	0.1–32	0.5–2.2	0.1–11
Anode current density (A dm^{-2})	<2.7	<2.7	1.6–2.7	1–4.3
Additives	Phenol- or cresol-sulfonic acid, β-naphtol, resocinol	Peptone, gelatine, β-naphtol, catechol, hydroqinone		

Tab. 11 Composition and working conditions of a silver plating electrolyte

$KAg(CN)_2$ (g l^{-1})	55
KCN (g l^{-1})	120
KOH (g l^{-1})	5
Sodium benzenedisulfonic acid (g l^{-1})	25
Turkey red oil (g l^{-1})	60
Brighteners (g l^{-1})	1
Selenic acid (g l^{-1})	0.1
Temperature (°C)	50
pH	12
Current density (A dm^{-2})	1–2

silver on the steel is prevented, which would be formed if the parts were brought into the higher concentrated electrolyte.

To prevent the formation of the typical dark brown film on the silver layer, a thin protection layer of rhodium is deposited.

5.5.4.5.2 **Gold** Society's admiration for gold has stimulated early developments of plating solutions for gold deposition. Table 12 summarizes the commonly used electrolytes. Reference [42] reviews recent topics in electrolytic and electroless gold plating.

By adding copper and/or cadmium salts to the neutral electrolyte, gold-copper-cadmium alloys can be plated.

5.5.4.5.3 **Platinum Metals** These metals are used for deposits only in special conditions in which extreme chemical stability is demanded. Examples are protective coatings on vanadium, tantalum, niobium, or conditions in which the extreme corrosion stability of these materials is the important property. We refer to the literature (e.g. Ref. [19]).

5.5.4.6 **Alloys**

In the automotive industry, coatings of pure zinc have been more and more replaced by zinc alloy coatings [43, 44]. The latter offer better corrosion resistance at lower coating thickness. They are also used as replacements for

Tab. 12 Composition and working conditions of some typical gold electrolytes

	Alkaline cyanide	*Neutral*	*Weakly acid*	*Sulfite*
Gold	2–20 g l^{-1} $KAu(CN)_2$	7 g l^{-1} $KAu(CN)_2$	7 g l^{-1} $KAu(CN)_2$	10 g l^{-1} $K_3Au(SO_3)_2$
KCN (g l^{-1})	5–30	–	–	–
Na_2HPO_4 (g l^{-1})	0–20	28	0–100	–
Na_2CO_3 (g l^{-1})	0–20	–	–	–
Na_2SO_3 (g l^{-1})	–	–	–	70
Additives, etc.	–		0.25 g l^{-1} Co 100 g l^{-1} citric acid	
Temperature (°C)	45–70	70	35	55
pH	11–13	7	3–6	9–10
Current density (A dm^{-2})	0.6	1	1	0.5

electrodeposited cadmium coatings. The effect of anomalous codeposition is often observed in these systems, that is, the less noble metal is deposited preferentially. See Sect. 5.5.1.2 and Refs. [3, 17, 45] for a discussion of the fundamentals of alloy electrodeposition.

5.5.4.6.1 **Zinc-cobalt** Zn-Co with Co contents from 0.2 to 7 wt% (solid solution of Co in Zn) can be deposited from sulfate (see Table 13). Furthermore, there are mildly acid chloride and alkaline cyanide–free baths. The acid baths show high-current efficiencies (i.e. plating rates) but poor throwing power. With increasing Co content, the corrosion rate decreases significantly (up to a factor of 5–7 compared to pure Zn), but the coatings seem to become more sensitive to cracking. Phosphatability for alloys with 0.5 to 1.7 wt% Co has been shown.

This system shows the effect of anomalous codeposition (see Sect. 5.5.1.2). The deposits have a light-gray appearance.

5.5.4.6.2 **Zinc-iron** Zinc-iron can be electroplated from weak acid chloride or sulfate baths or from alkaline baths. The typical Fe content is 0.3 to 0.6% (see Table 14 for an alkaline electrolyte). The alkaline baths contain complexing agents to prevent precipitation of nickel and iron hydroxides. Special conversion electrolytes have to be used for efficient corrosion protection. After chromating (see Sect. 5.5.5.2), the coating offers similar improvement of corrosion protection as Zn-Co. Without chromating, the corrosion resistance is comparable to pure zinc. It has been found that Fe diffuses into the chromate film, in which it reacts with the components of the conversion layer to form a very corrosion-resistant film [43].

Tab. 13 Electrolyte composition and process parameters for electrodeposition of Zn-Co alloys (from Ref. [46])

$ZnSO_4 \cdot 7H_2O$ (g l^{-1})	625
$CoSO_4 \cdot 7H_2O$ (g l^{-1})	125
Na_2SO_4 (g l^{-1})	75
pH	2–4
Current density (A dm^{-2})	53–133
Electrolyte flow rate (m s^{-1})	1.5–4.3
Temperature (°C)	55
Current efficiency (%)	88–95

Tab. 14 Composition and working conditions of a Zn-Fe electrolyte

Zn (g l^{-1})	20
Fe (g l^{-1})	0.3–0.35
NaOH (g l^{-1})	100
Complexing agents	Aliphatic amines
Temperature (°C)	20
Current density (A dm^{-2})	1–3

5.5.4.6.3 **Zinc-nickel** Zn-Ni alloys with 5 to 15 wt% Ni offer excellent corrosion resistance and are mainly used in the automotive, aerospace, and electronics industries. Above 15% Ni, the alloy coating becomes more noble than steel, and the corrosion-protection mechanism changes from a sacrificial to a pure physical one (comparable to pure Ni coatings, see Sect. 5.5.4.2.2). They can be electrodeposited from acid or alkaline baths. The acid baths are usually based on sulfate, chloride, sulfate-chloride, pyrophosphate, or acetate (Table 15). The system shows anomalous codeposition (see Sect. 5.5.1.2), which has been explained by a hydroxide suppression mechanism [47]. As in the case of Ni-Fe, the alkaline baths must contain complexing agents (see Sect. 5.5.4.6.2). The alloys electroplated from acid baths contain approximately 10 to 14% Ni, whereas the alkaline Zn-Ni alloys contain 5 to 10% Ni. Because the alloys with high Ni content are difficult to chromate, special conversion coatings have been developed for the acid Zn-Ni coatings.

5.5.4.6.4 **Zinc-manganese** This alloy received attention when an US Air Force report was published [50]. In contact with metals more negative in the list of standard potentials than zinc, such as aluminum or magnesium, a better corrosion behavior is expected. Although the system found new interest in recent years [51, 52], a commercial electrolyte seems not to be available at the moment. The good corrosion resistance has been explained with the formation of a dense γ-Mn_2O_3 layer on the surface of the alloy [43]. On the other hand, an intermetallic phase (ε phase) has been found [52], which could also be responsible for the high corrosion resistance (see Sect. 5.5.1.2). Table 16 lists a possible bath formulation, from which bright deposits are obtained. So far these coatings showed only limited corrosion-protection properties.

5.5.4.6.5 **Tin-zinc** Tin-zinc alloys offer good corrosion resistance, even after heavy mechanical stressing (bending, crimping)

Tab. 15 Electrolyte composition and process parameters for the electrodeposition of Zn-Ni alloys

	Alkaline [48]	***Weak acid [48]***	***Acetate [49]***
Zn (g l^{-1})	7.0	32	6.5–16.3
Ni (g l^{-1})	1.0	25	5.9–14.7
NaOH (g l^{-1})	125	–	–
NH_4Cl (g l^{-1})	–	105	–
CH_3COOH (g l^{-1})	–	–	6–15
Complexing agents	Aliphatic amines	–	–
Current density (A dm^{-2})	0.5–4.0	0.5–3.0	0.7–1.3
pH	>14	5.9	4–5
Temperature (°C)	32	40	20–60

Tab. 16 Composition and working conditions of a possible Zn-Mn plating bath from Ref. [52]

Manganese sulfonate (mol l^{-1})	0.75
Zinc sulfonate (mol l^{-1})	0.25
NH_4Cl (g l^{-1})	105
Sodium acetate (g l^{-1})	30
Wetting agent Ralufon NAPE 14/90 (g l^{-1})	15
Brightener benzalacetone (g l^{-1})	0.2
pH	3
Temperature (°C)	25
Current density (A dm^{-2})	7.5

and have been proposed as an alternative to cadmium coatings. Their good solderability and low electrical resistance makes them attractive candidates for electronic contacts [53]. Furthermore, the problem of tin pest (see Sect. 5.5.4.4) does not arise. Tin-zinc can be plated from acid, neutral, alkaline cyanide, and alkaline noncyanide baths (see Table 17). The proprietary acid bath operates at pH 1 and yields deposits with a zinc content <1%, which makes the application of chromate conversion coatings difficult. The alloys plated from neutral and alkaline baths can be easily treated with chromate conversion coatings (see Sect. 5.5.5.2) to improve corrosion resistance, where the adhesion is even better than on pure zinc (anchor function of tin). During the chromate conversion, the tin content at the surface increases as only zinc is dissolved.

5.5.4.6.6 **Nickel-iron** Because of their Fe content of up to 35 wt%, Ni-Fe alloys are less expensive than bright nickel coatings. They show good corrosion resistance, leveling, ductility and brightness, and readily accept chromium coatings (see Sect. 5.5.4.3). The Fe-Ni system shows anomalous codeposition. Table 18 lists the composition and process parameters of a Fe-Ni alloy plating bath.

5.5.4.7 Intrinsically Conducting Polymers (ICP's, "Synthetic Metals")

Twenty years ago, a new class of organic polymer materials was discovered with the new property of electronic conductivity comparable to metallic conductors [55]. The first representative was the polyacetylene followed in the subsequent years by several other polymers, such as polyaniline, polypyrrole, and polythiophene (see Fig. 7). The neutral structure is shown in Fig. 7. This structure has properties comparable to a semiconductor. The metal like conductance is obtained by chemical or electrochemical oxidation (shown for polypyrrole in Fig. 8). In this example, up to 30% of the pyrrole rings can be oxidized. The positive charge of the heterocyclic ring

Tab. 17 Tin-zinc plating baths (from Ref. [53])

	Neutral	*Alkaline cyanide*	*Alkaline noncyanide (Stanzec process)*
Tin (g l^{-1})	10–30	18	1–1.6
Zinc (g l^{-1})	3–15	14	40–60
Cyanide (g l^{-1})	–	34	–
Hydroxide (g l^{-1})	–	10 (KOH)	16–26 (free OH^-)
pH	5.5–7		12.5–13
Temperature (°C)	15–30		60–70
Tin content of the layer (wt%)	70–80	70–80	70–80

Tab. 18 Composition and working conditions of a Fe-Ni plating bath (from Ref. [54])

Nickel	131 g l^{-1} $NiSO_4 \cdot 6H_2O$ or 118 g l^{-1} $NiCl_2 \cdot 6H_2O$
Iron	2.8 g l^{-1} $FeSO_4 \cdot 7H_2O$ or 2.0 g l^{-1} $FeCl_2 \cdot 4H_2O$
H_3BO_3	25 g l^{-1}
Citric acid	9.6 g l^{-1}
L-ascorbic acid	3.5 g l^{-1}
pH	2–3
Temperature	25 °C
Current density	0.5–2 A dm^{-2}

is compensated by incorporated anions. Typical conductance values of conducting polymers in their reduced and oxidized states are summarized in Table 19.

Another characteristic value of the conducting polymers is their oxidation potential E_{redox} (see Table 19). It is not a thermodynamically well defined value, but depends on the structure of the polymer as chain lengths, branching, and so on. With an increasing degree of polymerization (increasing chain length), E_{redox} shifts to more cathodic values. The reported

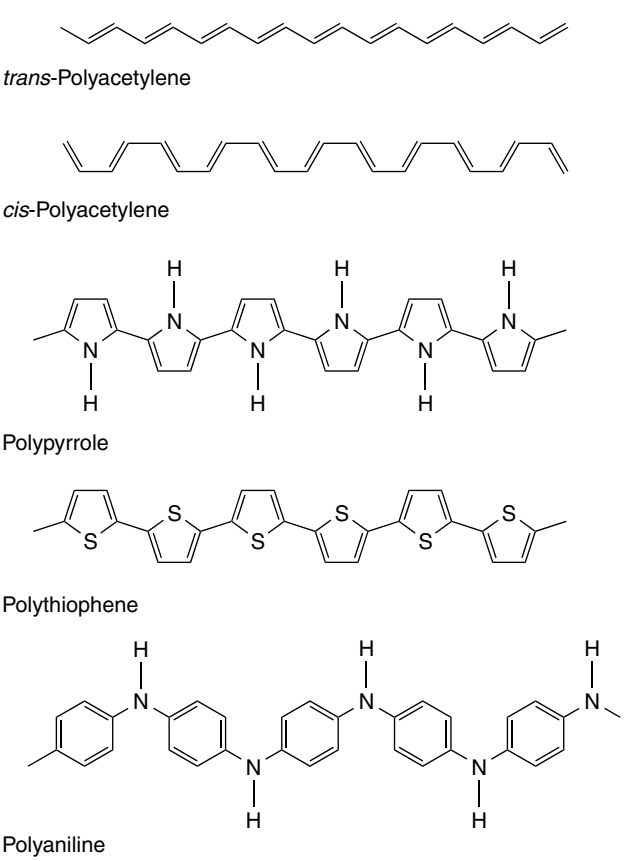


Fig. 7 Examples of the chemical structure of intrinsically conducting polymers. The structure shown is nonconducting. The metal like conductivity is obtained by chemical or electrochemical oxidation. This is shown for polypyrrole as an example in Fig. 8

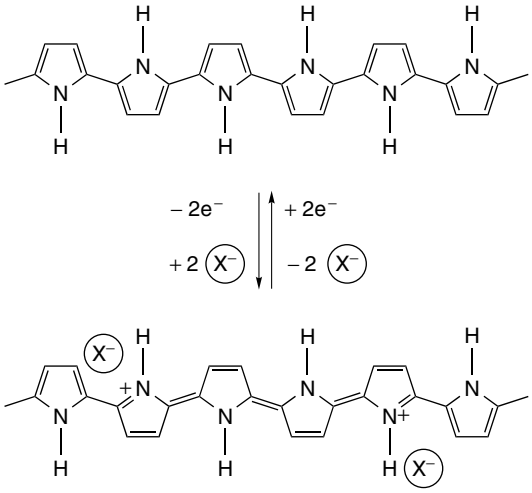


Fig. 8 Neutral and oxidized structure of polypyrrole.

Tab. 19 Properties of typical representatives of intrinsically conducting polymers

	κ at 25 °C (S cm^{-1})		E_{redox} (V vs SHE)
	Reduced	*Oxidized*	
Polyacetylene	10^{-5}	10^{3}	0.8
Polypyrrole	10^{-8}	10^{2}	0.1
Polythiophene	10^{-8}	50	1.2
Polyaniline	10^{-10}	10^{-2}	0.4

values represent a saturated situation with approximately constant chain length obtained after cycling the polymer film in a solution of its monomer. The most widely investigated ICP for corrosion protection is polyaniline [56–59]. In the last years, polypyrrole [60–62] and polythiophene [63–65] have been investigated.

There is still an intensive discussion about the real corrosion-protective properties of ICPs. While some groups are enthusiastic, there is also a very critical attitude towards the use of these materials. In any case, a film of an ICP cannot act as a protective film itself. It must be considered as a new type of primer, which has to be covered by another polymer or paint coating. Also, particles of the ICPs in the submicrometer range were added to the paint.

The reason for the unclear situation concerning the degree of protection may be seen in the different types of applications to the metal surface and its combination with a secondary, protective paint film (see Sect. 5.5.4.7.1).

5.5.4.7.1 **Application of Intrinsically Conducting Polymers to a Metal Surface** For the application of ICPs to a metal surface, different procedures are described in the literature.

One application brings the conducting polymer as a dispersion coating to the surface [66]. A powder of polyaniline (with a particle size in the range of some tens of nanometers) is dispersed in a conventional paint, and this is painted onto the metal surface. The authors use a very low powder concentration of 4% and explain the corrosion-protection properties with a percolation model.

In a second procedure, a polymer film is prepared on the metal surface (by

chemical or electrochemical oxidation), after a pretreatment of the metal surface. Different procedures of the pretreatment are described. Beck and Michaelis describe a treatment with manganese oxide/oxalic acid [60]; a treatment with nitric acid is reported by Ferreira and coworkers [61].

In a third procedure, an adhesion promoter of a 3-(ethyl-phosphonic-acid)thiophene was applied to the metal surface followed by an electrochemical film preparation [65]. The following procedure was used in this case: Mild steel was mechanically polished, then the specimen were treated for 60 minutes in a solution of 3-(ethyl-phosphonic-acid)thiophene. Afterwards, a layer of poly(3-methylthiophene) was formed by electropolymerization in an electrolyte consisting of 0.1 mol l^{-1} 3-methylthiophene, 0.1 mol l^{-1} tetrabutylammonium-hexafluorophosphate $(N(Bu)_4 PF_6)$ in dichloromethane (CH_2Cl_2).

In all examples, a secondary protecting coating had to be applied to achieve corrosion protection.

5.5.4.7.2 Mechanism of Corrosion Protection by Intrinsically Conducting Polymers

The first explanation of the corrosion protection of conducting polymers was based on the idea that the typical noble character of the conducting polymers (compare the redox potentials given in Table 19) simply transforms the coated metal into a noble one. This of course requires compact films, free of pores, which is not observed in practice. Also, the stability of the polymer film against the atmospheric degradation is not sufficient.

Another mechanism of the interaction of conducting polymers with metal surfaces is based on the idea that the conducting polymer passivates the metal that is to be protected [56]. The polymer is reduced to the neutral form. As a compensating reaction, the metal (iron) is dissolved as Fe^{2+} and oxidized to Fe^{3+}. Then the passivating oxide is formed. The process depends on the positive redox potentials of the conducting polymers. The theory assumes that the oxidized state is constantly renewed by a permanent reoxidation of the neutral form of the polymer by oxygen.

A third mechanism considers the local separation of the different processes connected with the metal corrosion inhibiting the delamination of a coating by a corrosion product [58, 65, 67].

5.5.4.8 Aluminum

The deposition of aluminum is not possible from aqueous solution. Several nonaqueous processes were developed, for example, one based on tetraalkylammonium complexes dissolved in toluene [68] or similar procedures by other groups [69, 70]. The process has been continuously improved [71] but so far a breakthrough in the application of electroplated aluminum is still pending. The problem is the price, compared to zinc coatings. Electroplated aluminum is more expensive than zinc by a factor of 3 to 5. Therefore, electroplated aluminum is restricted to some high-tech applications, for example, special optical surfaces. As a corrosion-protective coating, the material is not yet an alternative to the established systems.

5.5.5 Posttreatment

The corrosion-protection metal layers, deposited on a substrate as described in the previous sections, are often subjected to some posttreatment. The following describes the most widely used procedures: the formation of an additional organic film, or the formation of a conversion layer.

5.5.5.1 Wax, Lacquer, Paint

Protective organic films are described in detail in Chapter 5.4.

Only a few general remarks: The organic film can be a thicker film of paint or a very thin film not distorting the geometry of the parts. In the latter case, a thin wax film (10–100 nm) is applied to the surface. The film is hydrophobic and keeps moisture away from the surface. The film can also prevent direct contact of the metal deposited with the human skin. This is important with toxic or problematic metals like chromium and nickel.

5.5.5.2 Conversion Coatings

The most important treatment is the conversion coating (see Chapter 5.3 of the same volume). This type of treatment is typically used for zinc or cadmium layers or on bulk metals like aluminum or magnesium. The classical conversion coating is chromating, the formation of a metal oxide/chromium oxide film. We will discuss the process for the example of zinc layers.

1. *Blue chromating*: Two typical bath compositions are given in Table 20.

The layers have a more or less blue color depending on the thickness of the film. The thickness of the layer should be 50 to 90 nm, however exact control of the layer thickness is difficult. The corrosion protection of a blue chromating film is very limited.

2. *Yellow chromating*: The bath contains 2 to 20 g l^{-1} chromium as chromic acid or dichromate, 1 to 5 g l^{-1} sulfuric acid, and 0.1 to 1 g l^{-1} sulfate, chloride or nitrate as a catalyst for the chromate reduction. The film has a yellowish color and a thickness of up to 1 µm. This film is very efficient in corrosion protection, and a time of 500 h in a salt spray testing without any corrosion spots is achieved. Moreover, the film has the property of self-healing of mechanical defects, which makes this procedure so superior to alternatives. But the film contains up to 200 mg m^{-2} chromate and this will probably soon lead to an end of this very cheap and effective protection process.

3. *Formation of chromium films containing only chromium(III)*: A first example was the blue chromating films without chromium(VI). But these films are too thin and reveal only limited corrosion protection.

Recent publications report on chromium films containing only chromium(III)oxides and with thicknesses similar to the yellow chromating films [72, 73]. The thicker film is formed if a bath contains a more efficient catalyst like silicofluoro anions at elevated temperatures (80–90 °C). The film is not self-healing. The process is called *chromiting*. The high process temperature and the lack of self-healing properties of the film demand further

Tab. 20 Typical bath for blue chromating (concentrations in g l^{-1})

	With Cr(VI)	*Without Cr(VI)*
Chromic acid (CrO_3)	0.5	–
Chromium potassium sulfate ($CrK(SO_4)_2 \cdot 12H_2O$)	–	3
Ammonium fluoride (NH_4F)	0.6	1.5
Fluoric acid	0.2	0.5
Nitric acid	4	4

research efforts towards substituting the yellow chromating process.

4. *Olive chromating*: These films are thicker than the yellow chromated films and contain even more chromium(VI). They do not show much better corrosion-protective properties than the yellow film. They are used for military applications and where the special color is demanded.

A typical bath contains 30 g l^{-1} chromic acid (CrO_3), 3 g l^{-1} sulfuric acid (H_2SO_4), and acetic acid/sodium acetate mixture of 100 to 200 g l^{-1}.

5.5.6 Conclusion

Electrochemical metal deposition and electroless metal deposition are the most reliable processes if a corrosion protection by metal coatings is demanded. The available systems can be adapted to most of the requirements of the design engineers. The technology has achieved a high standard offering either clean separated solutions or production-integrated processes. But the classical plating process is developing continuously. This concerns more complex systems such as special alloys, or dispersion coatings. Nonaqueous processes might also be applied in the future. It also concerns high-speed electrolytes for more production-integrated processes. The latest development might be the simulation of metallization for the deposition of tailored materials. Corrosion protection will benefit from these developments.

References

1. E. B. Budevski, G. T. Staikov, W. J. Lorenz, *Electrochemical Phase Formation and Growth: An Introduction to the Initial Stages of Metal Deposition*, Wiley-VCH, Weinheim, Germany, 1996.
2. K. J. Vetter, *Electrochemical Kinetics – Theoretical and Experimental Aspects*, Academic Press, New York, 1967.
3. A. Brenner, *Electrodeposition of Alloys*, Academic Press, New York, 1963.
4. E. J. Podlaha, D. Landolt, *J. Electrochem. Soc.* **1996**, *143*, 885–892.
5. E. J. Podlaha, D. Landolt, *J. Electrochem. Soc.* **1996**, *143*, 893–898.
6. E. J. Podlaha, D. Landolt, *J. Electrochem. Soc.* **1997**, *144*, 1672–1679.
7. B. C. Baker, A. C. West, *J. Electrochem. Soc.* **1997**, *144*, 164–168.
8. B. C. Baker, A. C. West, *J. Electrochem. Soc.* **1997**, *144*, 169–174.
9. D. Landolt, *Electrochim. Acta* **1994**, *39*, 1075–1090.
10. S. Hessami, C. W. Tobias, *J. Electrochem. Soc.* **1989**, *136*, 3611–3615.
11. A. M. Zaky, F. H. Assaf, K. G. Weil et al., *AESF SUR/FIN '99 Proceedings*, Cincinatti, Ohio, June 1999, pp. 311–317.
12. L. Oniciu, L. Muresan, *J. Appl. Electrochem.* **1991**, *21*, 565–574.
13. W. Plieth, *Electrochim. Acta* **1992**, *37*, 2115–2121.
14. M. Paunovic, M. Schlesinger, *Fundamentals of Electrochemical Deposition*, John Wiley & Sons, New York, 1998.
15. L. E. Samuels, *Metallographic Polishing by Mechanical Methods*, 3rd ed., American Society for Metals (ASM), Metals Park, Ohio, USA, 1982.
16. H. W. Dettner, J. Elze, *Handbuch der Galvanotechnik*, Carl Hanser Verlag, München, Germany, 1963.
17. F. A. Lowenheim, *Electroplating*, Technical Reference Publications, Bristol, 1995.
18. F. A. Lowenheim, (Ed.), *Modern Electroplating*, 3rd ed., John Wiley & Sons, New York, 1974.
19. T. W. Jelinek, (Ed.), *Praktische Galvanotechnik*, Eugen G. Leutze Verlag, Saulgau, 1997, pp. 325–335.
20. I. Odnevall Wallinder, C. Leygraf, C. Karlen et al., *Corros. Sci.* **2001**, *43*, 809–816.
21. W. Paatsch, *Galvanotechnik* **1992**, *83*, 2633–2638.
22. S. Schneider, *Plat. Surf. Finish.* **1999**, *86*, 70, 71.
23. A. Choms, *Plat. Surf. Finish.* **1993**, *80*, 72, 73.
24. S. S. Abd El Rehim, S. M. Abd El Wahaab, E. E. Fouad et al., *J. Appl. Electrochem.* **1994**, *24*, 350–354.

25. D. L. Snyder, *Met. Finish.* **1997**, *95*, 29–32.
26. O. P. Watts, *Trans. Am. Electrochem. Soc.* **1916**, *29*, 395.
27. Z. Abdel-Hamid, *Mater. Sci. Commun.* **1998**, *53*, 235–238.
28. F. Lantelme, A. Seghiouer, A. Derja, *J. Appl. Electrochem.* **1998**, *28*, 907–913.
29. E. B. Saubestre, *Plating* **1958**, *45*, 479–485.
30. O. Devos, A. Olivier, J. P. Chopart et al., *J. Electrochem. Soc.* **1998**, *145*, 401–405.
31. O. Devos, O. Aaboubi, J. P. Chopart et al., *J. Electrochem. Soc.* **1998**, *145*, 4135–4139.
32. D. Mockute, G. Bernotiene, *Surf. Coat. Technol.* **2000**, *135*, 42–47.
33. W. Dahms, R. Schumacher, *Galvanotechnik* **1996**, *87*, 3962–3972.
34. M. Holm, T. J. O'Keefe, *J. Appl. Electrochem.* **2000**, *30*, 1125–1132.
35. S. Ripper, Ph. D. Thesis, Technische Universitaet Darmstadt, Darmstadt, Germany, 1987.
36. C.-C. Hu, A. Bai, *Surf. Coat. Technol.* **2001**, *137*, 181–187.
37. W. Kronenberg, *Galvanotechnik* **1990**, *81*, 236.
38. W. Riedel, *Funktionelle Chemische Vernickelung*, Eugen G. Leutze Verlag, Saulgau, 1989.
39. H. Niederprüm, H. G. Klein, *Metalloberfläche* **1970**, *24*, 468.
40. D. L. Snyder, *Met. Finish.* **1997**, *95*, 29–33.
41. S. Hirsch, *Met. Finish.* **1995**, *93*, 298–313.
42. Y. Okinaka, M. Hoshino, *Gold Bull.* **1998**, *31*, 3–13.
43. G. W. Loar, K. R. Romer, T. J. Aoe, *Plat. Surf. Finish.* **1991**, *78*, 74–79.
44. G. D. Wilcox, D. R. Gabe, *Corros. Sci.* **1993**, *35*, 1251–1258.
45. M. Paunovic, M. Schlesinger, *Fundamentals of Electrochemical Deposition*, John Wiley & Sons, New York, 1998.
46. J. Mahieu, K. De Wit, A. De Boeck et al., *J. Mat. Eng. Perf.* **1999**, *8*, 561–570.
47. D. E. Hall, *Plat. Surf. Finish.* **1983**, *70*, 59–65.
48. R. Pfiz, G. Stube, *Jahrb. Oberflaechtechn.* **1997**, *53*, 47–58.
49. S. S. Abd El Rehim, E. E. Fouad, S. M. Abd El Wahab et al., *Electrochim. Acta* **1996**, *41*, 1413–1418.
50. G. Faust, A. Tripler, C. Konecny, Air Force Technical Report, No. 5682, Wright Air Development Center, Cincinatti, Ohio, 1952.
51. N. Boschkov, K. Petrov, S. Nikolova, *Metalloberfläche* **1998**, *52*, 514–519.
52. C. C. Fels, Ph. D. Thesis, Technische Universitaet Dresden, Dresden, Germany, 2000.
53. E. Budman, M. McCoy, *Met. Finish.* **1995**, *93*, 10–15.
54. V. C. Kieling, *Surf. Coat. Technol.* **1997**, *96*, 135–139.
55. T. A. Skotheim, R. L. Elsenbaumer, J. R. Reynolds (Eds.), *Handbook of conducting polymers*, 2nd ed., M. Dekker, New York, 1997.
56. B. Wessling in *Handbook of organic conductive molecules and polymers: Vol. 3. Conductive polymers: Spectroscopy and Physical Properties* (Ed.: H. S. Nalwa), Chap. 11, John Wiley & Sons, New York, 1997.
57. B. Wessling, J. Posdorfer, *Electrochim. Acta* **1999**, *44*, 2139–2147.
58. P. J. Kinlen, D. C. Silverman, C. R. Jeffreys, *Synth. Met.* **1997**, *85*, 1327–1382.
59. J. L. Camalat, J. C. Lacroix, S. Aeiyach et al., *J. Electroanal. Chem.* **1998**, *445*, 117–124.
60. F. Beck, R. Michaelis, F. Schloten et al., *Electrohim. Acta* **1994**, *39*, 229–234.
61. C. A. Ferreira, A. Aeiyach, J. J. Aaron et al., *Electrochim. Acta* **1996**, *41*, 1801–1809.
62. S. Wencheng, J. O. Iroh, *Electrochim. Acta* **2000**, *46*, 1–8.
63. U. Barsch, F. Beck, *Synth. Met.* **1993**, *55–57*, 1638–1643.
64. S. Aeiyach, E. A. Bazzaoui, P. C. Lacaze, *J. Electroanal. Chem.* **1997**, *434*, 153–162.
65. U. Rammelt, T. Nguyen, W. Plieth, *Electrochim. Acta* **2001**, *46*, 4251–4257.
66. B. Wessling, *J. Phys. II (France)* **1996**, *6*, 395–404.
67. J. C. Lacroix, J. L. Camalat, S. Aeiyach et al., *J. Electroanal. Chem.* **2000**, *481*, 76–81.
68. R. Dötzer, *Chem.-Ing.-Tech.* **1973**, *45*, 653.
69. J. F. M. van den Berg, T. E. G. Daenen, G. Kriji et al., *Metalloberfläche* **1981**, *35*, 218–221.
70. J. Eckert, K. Gneupel, German Patent DD 244 573 A1, Galvanisches Bad zum Abscheiden von Aluminium-Magnesium Legierungen.
71. H. de Vries, European Patent EP 0 948 670, Elektrolyt zur galvanischen Abscheidung von Aluminium; (see *Galvanotechnik* **2000**, *91*, 438, 439).
72. R. Jansen, P. Preikschat, *Metalloberflaeche* **1998**, *52*, 183–185.
73. P. Hülser, R. Jansen, A. Möller et al., *Metalloberflaeche* **1996**, *50*, 794–797.

6.1
Molten Salt-induced Corrosion of Metals (Hot Corrosion)

Michael Spiegel
Max Planck Institut für Iron Research, Düsseldorf, Germany

6.1.1
Introduction

Hot corrosion is designated as the accelerated attack of metals and ceramics in oxidizing environments by the presence of a thin molten salt film, for example, a fused sulfate, carbonate, chloride, or nitrate. In many high-temperature processes, molten salts are present either in partially molten ashes, as deposits on boiler tubes from conventionally fired plants such as waste fired boilers (chlorides, sulfates), as a single salt deposits on gas turbines (Na_2SO_4), or as the electrolytes in molten carbonate fuel cells [$(Li,K)_2CO_3$].

Corrosion reactions beneath molten salts are generally complicated, because the number of possible corrosion products is much higher than in the case of gas phase corrosion, and a variety of chemical and electrochemical reactions are possible.

Many different steps are involved in Hot Corrosion and not all of them are understood in detail at this time. First of all, the metal is separated from the gas phase by the melt film and transport of oxidizing species from the gas phase to the metal/melt interface has to occur. Hence, the solubility of gases in the salt is one important factor in Hot Corrosion. In some systems, counterdiffusion of the oxidized and reduced ionic solutes of a transition metal solute, Fe^{3+} and Fe^{2+}, can support transport of the reduced species to the salt/gas interface. Subsequent to diffusional transport of the dissolved gas species through the molten salt, interfacial reactions take place at the metal/melt interface and corrosion products are formed. As the corrosion products are partially soluble in the salt, their solutes are transported toward lower concentrations by diffusion in the salt film. Most of the generally passivating oxides such as Cr_2O_3 are soluble in salt melts; thus the formation and maintenance of a passivating layer on the metal surface is made difficult.

As the molten salt is electrolytic, Hot Corrosion processes involve electrochemical reactions like oxidation of the metal and reduction of melt components and dissolved gases. Hence, many of investigations of Hot Corrosion have been done by electrochemical techniques, mostly combined with conventional corrosion

experiments such as thermogravimetry and exposure tests.

In this article, some fundamental aspects of Hot Corrosion are explained. For practical reasons, most of the investigations were done on sulfate and carbonate melts, and the article will focus on these two types of melts. For sulfate melt–induced Hot Corrosion, the excellent review article by Rapp [1] is recommended for further reading.

6.1.2 Chemistry of Deep Salt Melts

6.1.2.1 Sulfates

The early model of Flux [2] and Flood and Forland and Motzfeld [3] describes the sulfate melt as a melt with oxyanions. According to this model, the SO_4^{2-}-anion dissociates, giving SO_3 and O^{2-}-ions (Eq. 1):

$$SO_4^{2-} = SO_3 + O^{2-} \qquad (1)$$

For further considerations, it has to be mentioned that the activity of ionic species is a difficult and ambiguous concept and provides a valid definition of a standard state. Hence, under consideration of cations (for example, Na^+), being present in the melt, the equilibrium (1) can be written as

$$Na_2SO_4 = Na_2O + SO_3 \qquad (2)$$

The *basicity* of the melt is then defined by $\log a(Na_2O)$ and the acidity is defined by $\log p(SO_3)$. This is analogous to the definition of pH value in aqueous corrosion.

It is important to note that the basicity of the melt can be changed by gas phase composition. From Eq. (2) [setting $a(Na_2SO_4) = 1$], it can be seen that

$$a(Na_2O) = Kp(SO_3)^{-1} \qquad (3)$$

Hence, by decreasing $p(SO_3)$ in the gas phase $a(Na_2O)$, the basicity of the melt is

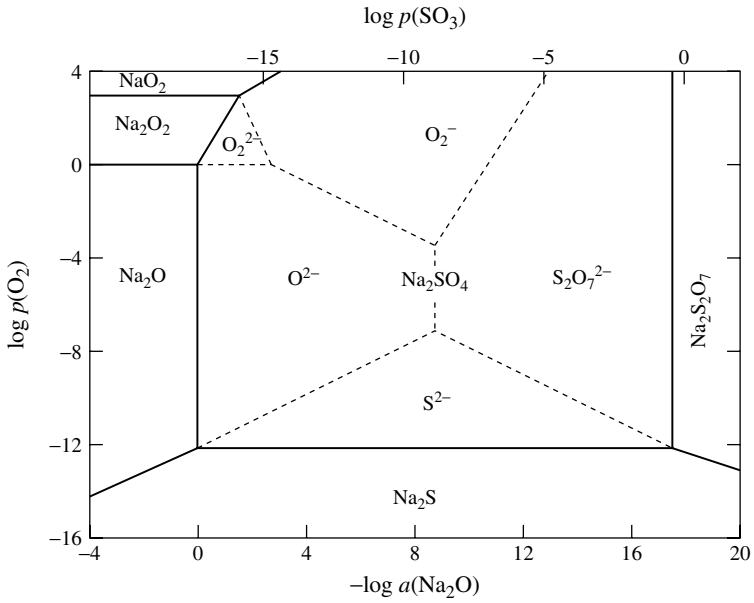


Fig. 1 Na-S-O phase stability diagram for 900 °C, indicating the solutes O^{2-}, O_2^{2-}, $S_2O_7^{2-}$, and S^{2-}.

increased. According to the construction of Pourbaix Diagrams in aqueous corrosion, Eq. (2) can be plotted as a Na-S-O stability diagram [4], showing the stable species as a function of melt basicity. Figure 1 shows the Na-S-O phase stability diagram for 900 °C, indicating the solutes O^{2-}, $O_2{}^{2-}$, $S_2O_7{}^{2-}$, and S^{2-}.

6.1.2.1.1 **Solubility of Gases** The possible change in the melt character by variation of the gas phase in contact with the molten salt strongly depends on the solubility of gas species. The solubility of gases also affects the corrosive nature of the melt by changing its redox potential and oxidizing character.

The solubilities of O_2 and SO_2 in molten Na_2SO_4 were measured by Andresen [5], who used a manometric method measuring the pressure drop in a closed vessel for a constant amount of molten salt in contact with the gas phase under investigation. For O_2 and SO_2, low solubilities were observed, following Henry's law. For the temperature range of 1175 to 1350 K, the Henrian constant (K_H) for O_2 and SO_2, respectively, are defined by the Eqs. (4 and 5):

$$\ln K_H(O_2) = -9.425 - \frac{7.111 \times 10^3}{T} \times [\text{mole cm}^{-3}\ \text{bar}^{-1}] \quad (4)$$

$$\ln K_H(SO_2) = -1.003 - \frac{14.91 \times 10^3}{T} \times [\text{mole cm}^{-3}\ \text{bar}^{-1}] \quad (5)$$

Flood and Forland [6] published an equation for the solubility of SO_3:

$$\ln K_H(SO_3) = -22.84 + \frac{18.26 \times 10^3}{T} \times [\text{mole cm}^{-3}\ \text{bar}^{-1}] \quad (6)$$

This equation is only valid at low concentration of physically dissolved SO_3. At higher concentrations, deviation from Henry's law was observed according to a reactive solubility of SO_3 with the sulfate ion (Eq. 9):

$$SO_4{}^{2-} + SO_3 = S_2O_7{}^{2-} \quad (7)$$

From Eqs. (4 to 6), it is clear that the solubilities of O_2 and SO_2 in Na_2SO_4 are negligibly low, whereas the solubility of SO_3 is significantly higher.

6.1.2.1.2 **Anodic and Cathodic Reactions** Upon cathodic and anodic polarization with noble metal electrodes, disregarding dissolved gas species from the atmosphere, the following reduction and oxidation reactions in a pure Na_2SO_4 melt are possible:
cathodic reactions (increasing overpotential):

$$SO_4{}^{2-} + 2e^- = SO_3{}^{2-} + O^{2-} \quad (8)$$

$$SO_4{}^{2-} + 6e^- = S + 4O^{2-} \quad (9)$$

$$SO_4{}^{2-} + 8e^- = S^{2-} + 4O^{2-} \quad (10)$$

anodic reactions:

$$SO_4{}^{2-} = SO_3 + \tfrac{1}{2}O_2 + 2e^- \quad (11)$$

Furthermore, the reduction of SO_3 and O_2 produced by equilibrium (1) is also possible according to

$$SO_3 + 2e^- = SO_2 + O^{2-} \quad (12)$$

$$\tfrac{1}{2}O_2 + 2e^- = O^{2-} \quad (13)$$

The decomposition of the sulfate only occurs in highly basic melts under reducing conditions or at high cathodic or anodic overpotentials. In principle, this is possible in deep melts or if the melt is trapped in pores within the oxide scale.

Dissolved gas species and, therefore, the gas phase composition in contact with the

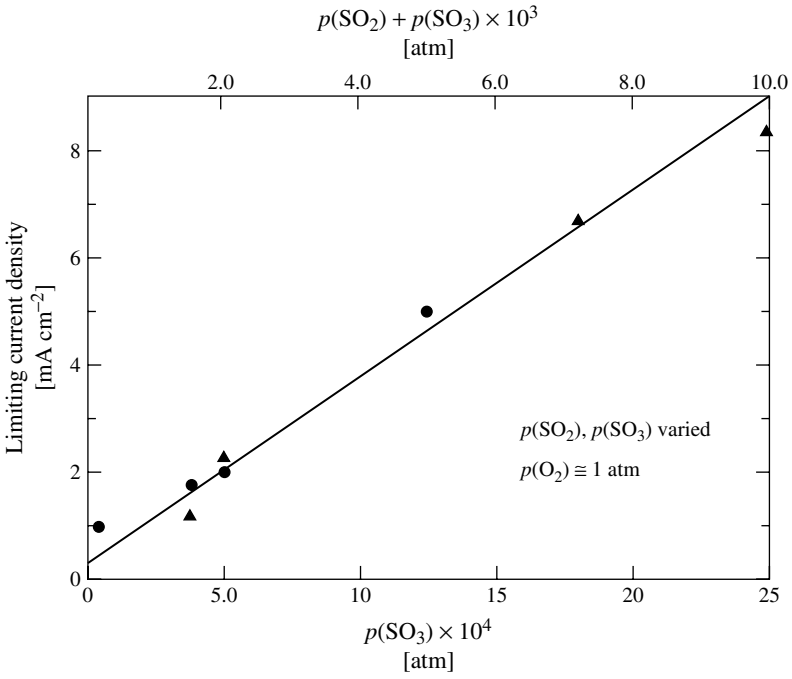


Fig. 2 Limiting diffusion current density at Pt electrodes beneath a thin Na_2SO_4 melt as a function of $p(SO_3)$ at constant $p(O_2)$ at 896 °C.

melt changes the major reduction reactions. In a thin Na_2SO_4 film, experiments at 896 °C in an O_2-($SO_3 + SO_2$) gas mixture have shown that the limiting diffusion current (see Electrochemical Techniques in Corrosion Engineering and research, Vol 4, Chapter 7) increases with increasing $p(SO_3)$ at constant $p(O_2)$ (Fig. 2) and also increases with increasing $p(SO_3)$ at constant $p(SO_2)$ (Fig. 3) [7]. This shows quite clearly that SO_3 is dissolved in the salt as the major electrochemically active species. From the experiments, the diffusion coefficient of $S_2O_7^{2-}$ was determined to be 2.1×10^{-4} cm^2 sec^{-1}. As SO_3 is dissolved as $S_2O_7^{2-}$ in the melt, the major oxidizing species in a thin Na_2SO_4 melt film in the presence of SO_3 is $S_2O_7^{2-}$.

The major reactions involved in the reduction of $S_2O_7^{2-}$ were investigated with the use of chronopotentiometric measurements in a relatively deep Na_2SO_4 melt at 900 °C in an $O_2 + 1\%$ ($SO_2 + SO_3$) atmosphere [8]. Two cathodic steps (transition times) were observed (Fig. 4) and attributed to the following reduction steps:

$$S_2O_7^{2-} + e^- = SO_4^{2-} + SO_3^- \quad (14)$$

$$SO_3^- + e^- = SO_3^{2-} = SO_2 + O^{2-} \quad (15)$$

In addition to the reduction of $S_2O_7^{2-}$, the reduction of O_2 is also possible in an O_2- and SO_3-containing atmosphere, however, to a much smaller extent because of the low solubility of O_2 in the sulfate melt.

If the melt is highly basic and no SO_2/SO_3 is present in the gas atmosphere, the reduction of oxygen ions also occurs, as

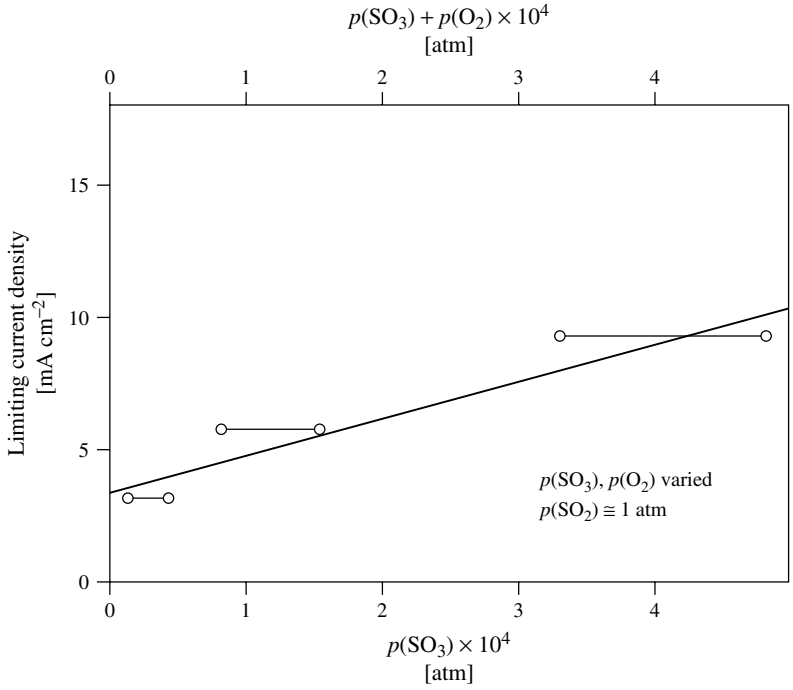


Fig. 3 Limiting diffusion current density at Pt electrodes beneath a thin Na_2SO_4 melt as a function of $p(SO_3)$ at constant $p(SO_2)$ at 896 °C.

shown in chronopotentiometric measurement in an Na_2SO_4 melt with addition of 5 mole% Na_2O_2 in air at 900 °C [8]. Two major reactions were identified:

$$O_2^- + 3e^- = 2O^{2-} \quad (16)$$

$$2O^{2-} + 4e^- = 2O_2^- + O_2^{2-} \quad (17)$$

In corrosion studies, the supply of electrons for the reduction reactions is the oxidation of the metal in contact with the sulfate melt.

6.1.2.2 Molten Carbonates

Like sulfates, molten carbonates are also oxyanion melts, containing O^{2-} ions, stemming from the dissociation of the carbonate ion:

$$CO_3^{2-} = CO_2 + O^{2-} \quad (18)$$

In accordance with the definition of the acid/base character of sulfate melts, the basicity of carbonate melts is also defined by Eq. (19):

$$Na_2CO_3 = Na_2O + CO_2 \quad (19)$$

and

$$a(Na_2O) = Kp(CO_2)^{-1} \quad (20)$$

6.1.2.2.1 **Solubility of Gases** The solubility of oxygen in carbonate melts takes place by a chemical reaction between the O_2 molecules and the basic component of the melt (Na_2O); hence, it does not obey Henry's Law. On the basis of impedance measurements in a $(Li,K)_2CO_3$ melt at 615 to 800 °C, the following reduction steps for oxygen species take place

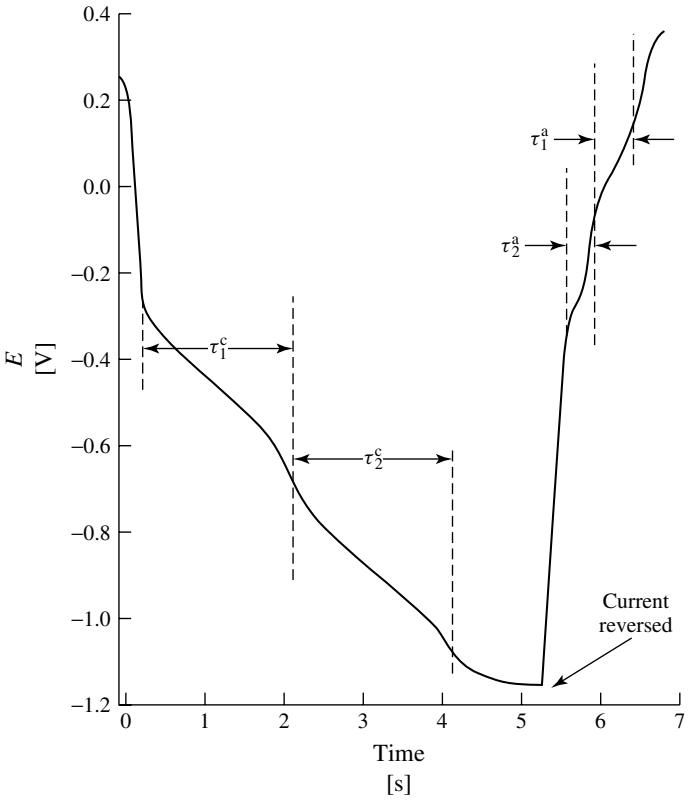


Fig. 4 Chronopotentiometric curve on Pt electrodes in a deep melt of Na_2SO_4 in $O_2 + 1\%$ ($SO_2 + SO_3$) at 900 °C.

by dissolution in the carbonate melt (see also Sect. 6.1.2.2.2) [9]:

1. Peroxide formation:

$$2CO_3^{2-} + O_2 = 2CO_2 + 2O_2^{2-} \quad (21)$$

Peroxide ions are mainly present in K-rich melts.

2. Superoxide formation:

$$2CO_3^{2-} + 3O_2 = 2CO_2 + 4O_2^{-} \quad (22)$$

Superoxide formation does not take place in pure Li_2CO_3 melts; therefore, superoxide ions are not present in predominately Li-rich melts.

Another possibility for oxygen dissolution is peroxycarbonate formation:

$$2CO_3^{2-} + O_2 = 2CO_4^{2-} \quad (23)$$

However, no clear experimental evidence for the peroxycarbonate mechanism exists up to now.

According to experiments by Cleas and coworkers [10], in a molten Na_2CO_3–K_2CO_3 melt at 800 °C, the solubility of CO_2 in carbonate melts is rather high. The results of cyclovoltametric experiments indicate a very weak anodic reduction peak for CO_2 to CO, but a significant solubility of CO_2 in the carbonate melt. Hence the solubility of

CO_2 occurs by chemical reaction of CO_2 with the carbonate ion according to

$$CO_2 + {CO_3}^{2-} = {C_2O_5}^{2-} \qquad (24)$$

6.1.2.2.2 **Anodic and Cathodic Reactions**
Anodic polarization of a carbonate melt with inert Au electrodes is limited by the oxidation of the carbonate ion according to reaction Eq. (18). The cathodic process is generally the deposition of alkali metal according to

$$Me^{n+} + ne^- = Me \qquad (25)$$

There is also evidence that in contact with O_2 and CO_2-containing gas, some contributions to the cathodic current are caused by the following reduction reactions:

$$CO_2 + \tfrac{1}{2}O_2 + 2e^- = {CO_3}^{2-} \qquad (26)$$

$$\tfrac{1}{2}O_2 + 2e^- = O^{2-} \qquad (27)$$

$$CO_2 + 2e^- = CO + O^{2-} \qquad (28)$$

Special interest has to be paid to the electrochemical behavior of oxygen species stemming from the reactive dissolution of oxygen in the carbonate [9]. The following reduction steps of oxygen species take place after reactive dissolution by the peroxide and superoxide mechanisms in a $(Li,K)_2CO_3$ melt at 615 to 800 °C:

1. Peroxide formation:

$$2{CO_3}^{2-} + O_2 = 2CO_2 + 2{O_2}^{2-} \qquad (29)$$

peroxide reduction steps:

$${O_2}^{2-} + 2e^- = 2O^{2-} \qquad (30)$$

$$O^{2-} + CO_2 = {CO_3}^{2-} \qquad (31)$$

2. Superoxide formation:

$$2{CO_3}^{2-} + 3O_2 = 2CO_2 + 4{O_2}^- \qquad (32)$$

superoxide reduction steps:

$${O_2}^- + e^- = {O_2}^{2-} \qquad (33)$$

$${O_2}^{2-} + 2e^- = 2O^{2-} \qquad (34)$$

Hence, in corrosion studies in an oxygen-containing environment, the reduction of oxygen species is the relevant reduction reaction.

6.1.3 Solubility of Oxides

Alloys, used at high temperatures, obtain their protection from a dense and adherent oxide layer formed on the metal surface. The corrosive attack of metals and alloys in molten salts is due to the solubility of oxide scales by basic and acidic dissolution. This breakdown of the passive film gives rise to accelerated metal consumption by enhanced oxidation (Hot Corrosion). The phenomenon is closely related to pitting corrosion of metals and alloys in aqueous solutions.

6.1.3.1 **Solubility of Oxides in Sulfate Melts**
In general, the solubility of oxides is a function of melt basicity and depends on the chemical composition of the passive layer. Hence, the corrosion process of alloys in molten salts is quite complicated as a result of the heterogeneous composition of the oxide scales formed on alloys.

By combination of thermodynamic stability diagrams of the salt phase to be investigated and the oxide phase under consideration, phase stability diagrams can be constructed to predict the behavior of any oxide in any molten salt. Figure 5 shows the Na-Fe-S-O-phase diagram [11, 12] for prediction of corrosion of iron in a Na_2SO_4 melt at 1200 K. This diagram is constructed from

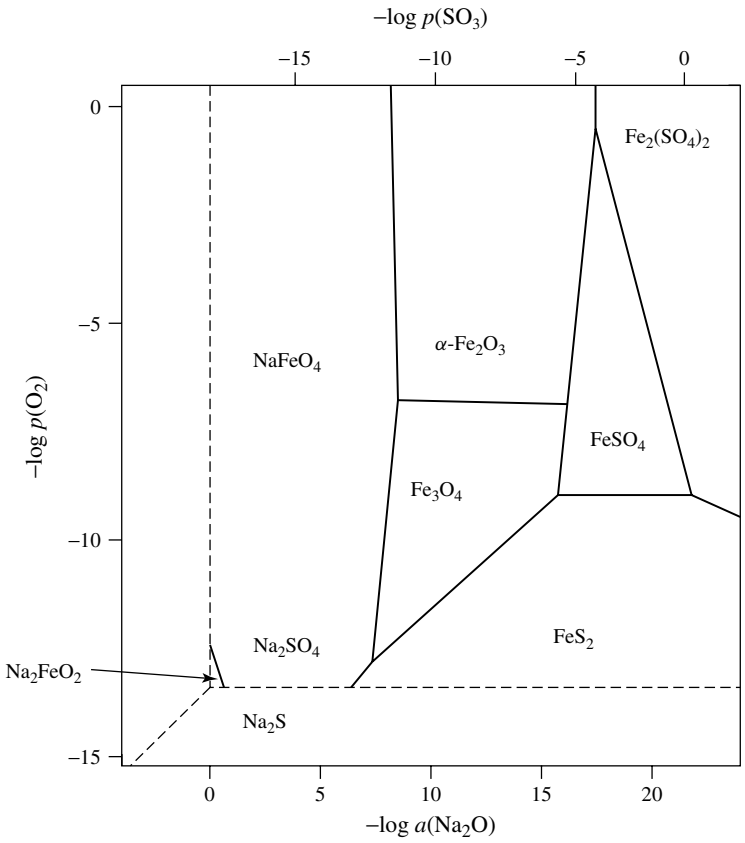


Fig. 5 Na-Fe-S-O-phase diagram for prediction of corrosion of iron in a Na_2SO_4 melt at 1200 K.

superposition of the Na-S-O- and Fe-S-O-stability plots. The diagram shows clearly the basic corrosion products $NaFeO_2$ at high $a(Na_2O)$ and the acidic corrosion products $FeSO_4$ and $Fe_2(SO_4)_3$ at low $a(Na_2O)$.

6.1.3.1.1 **Solubility Plots** To investigate solubilities of oxides in molten salts as a function of melt basicity, experiments were carried out by Rapp and coworkers in molten Na_2SO_4 at 1200 K [13]. The melt basicity was fixed by variation of the gas atmosphere containing $p(SO_2)$ and $p(O_2)$ and by addition of Na_2O_2 to the molten salt. Control of the basic conditions was done electrochemically by a combination of a Ag/Ag_2SO_4 reference electrode (RE) with a Na^+-conducting closed-end mullite membrane (Fig. 6) measuring differences in the activity of Na and a closed-end and internally platinized yttria-stabilized zirconia oxygen sensor (Fig. 7) measuring differences in the oxygen activity. The sum of the EMFs of the combination two electrodes gives a measure for the Na_2O activity at 1173 K:

$$E = -1.466 - 0.116 \log a(Na_2O) \quad (35)$$

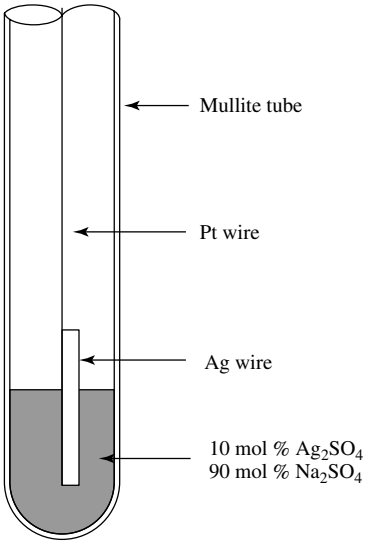


Fig. 6 $Ag/AgSO_4$ RE with a Na^+-conducting closed-end mullite membrane for measuring differences in the activity of Na^+-ions.

Figure 8 shows solubility plots of various oxides in molten Na_2SO_4 at 1200 K as a function of melt basicity $-\log a(Na_2O)$. The characteristic shape of the plots represents the amphoteric dissolution behavior of oxides in molten sulfates. Basic solubility occurs at high $a(Na_2O)$ (left-hand side of each curve), acidic solubility occurs at low $a(Na_2O)$ (right-hand side of each curve). A characteristic minimum is reached at which the dominant dissolution mechanism changes from basic to acidic.

6.1.3.1.2 **Basic Dissolution** By the oxidation of the bare metal surface by Na_2SO_4 in a basic melt, metal oxide, sulfide, and additional basic Na_2O are formed according to:

$$3Me + Na_2SO_4 = 3MeO + Na_2O + MeS \quad (36)$$

Hence, the Na_2O resp. O^{2-} concentration on top of the metal oxide is higher than in the entire melt and dissolution of oxide takes place according to:

$$MeO + Na_2O = 2Na^+ + MeO_2{}^{2-} \quad (37)$$

In the case of basic dissolution, the metal oxide is dissolved as a complex oxide ion.

Dissolution reactions were investigated by Rapp and coworkers for several oxides in a Na_2SO_4 melt at 1200 K, such as Al_2O_3 [14], Fe_2O_3 [11], NiO, and Co_3O_4 [15] and by Zhang for Cr_2O_3 [16]. The most important basic dissolution reactions are

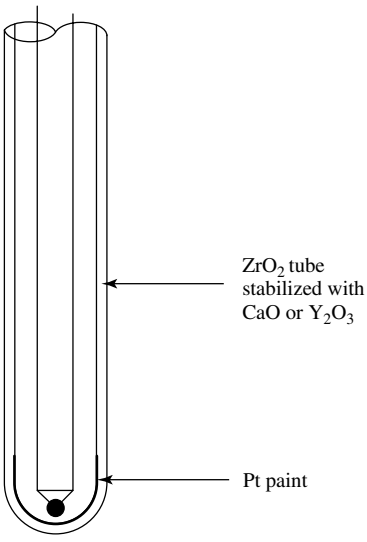


Fig. 7 Internally platinized yttria-stabilized zirconia oxygen sensor measuring differences in the oxygen activity.

Al_2O_3:

$$Al_2O_3 + O^{2-} = 2AlO_2{}^- \quad (38)$$

Fe_2O_3:

$$Fe_2O_3 + O^{2-} = 2FeO_2{}^- \quad (39)$$

The dissolution of *chromia* depends on the oxygen partial pressure of the gas atmospheres at $p(O_2)$ smaller than 1 bar

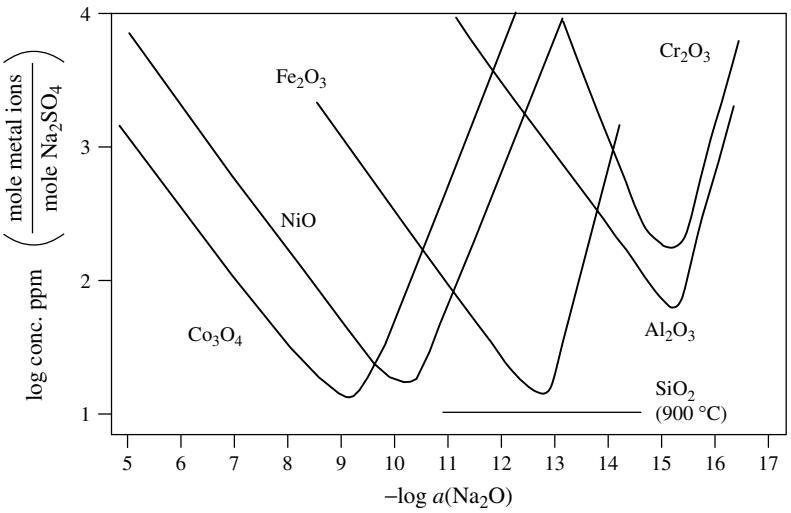


Fig. 8 Solubility plots of various oxides in molten Na_2SO_4 at 1200 K as a function of melt basicity $a(Na_2O)$.

(10^{-7} Pa), and T = 1200 K dissolution of chromia occurs as chromite:

$$Cr_2O_3 + O^{2-} = 2CrO_2^- \qquad (40)$$

At higher $p(O_2)$, chromate is formed:

$$Cr_2O_3 + 2O^{2-} + \frac{3}{2}O_2 = 2CrO_4^{2-} \qquad (41)$$

NiO:

$$2NiO + O^{2-} + \frac{1}{2}O_2 = 2NiO_2^- \qquad (42)$$

Co_3O_4:

$$2Co_3O_4 + 3O^{2-} + \frac{1}{2}O_2 = 6CoO_2^- \qquad (43)$$

As discussed in detail in Sect. 6.1.4, the dissolved species are transported from the melt/scale interface toward the melt/gas interface and precipitation of oxides takes place.

6.1.3.1.3 **Acidic Dissolution** Acidic dissolution occurs by interaction with SO_3, which is dissolved in the molten sulfate as $S_2O_7^{2-}$. In principle, the following reaction takes place:

$$MeO + SO_3 = Me^{2+} + SO_4^{2-} \qquad (44)$$

The oxides are dissolved as metal ions in the sulfate melt and metal sulfates are formed. Acidic dissolution reactions are

Al_2O_3:

$$Al_2O_3 = 2Al^{3+} + 3O^{2-} \qquad (45)$$

Fe_2O_3:

$$Fe_2O_3 = 2Fe^{3+} + 3O^{2-} \qquad (46)$$

At low $p(O_2)$, magnetite Fe_3O_4 can also be dissolved as a sulfide FeS:

$$Fe_3O_4 + 3SO_4^{2-} = 3FeS + 3O^{2-} + \frac{13}{2}O_2 \qquad (47)$$

The acidic solubility of iron oxides slightly increases with decreasing $p(O_2)$.

Cr_2O_3:

At high $p(O_2)$, chromia is dissolved as a sulfate according to

$$Cr_2O_3 = 2Cr^{3+} + 3O^{2-} \qquad (48)$$

At lower $p(O_2)$, sulfide is more stable:

$$Cr_2O_3 + 2SO_4{}^{2-} = 2CrS + 2O^{2-} + \frac{9}{2}O_2 \quad (49)$$

NiO:

$$NiO = Ni^{2+} + O^{2-} \quad (50)$$

Co_3O_4:

$$2Co_3O_4 = 6Co^{2+} + 6O^{2-} + O_2 \quad (51)$$

6.1.3.1.4 **Synergistic Solubility** Hwang and Rapp [17] have shown that the dissolution kinetics of different oxides are not independent and a synergistic effect is observed. An accelerated dissolution of both oxides with respect to the single oxide phase occurs.

At 1200 K, Fe_2O_3 and Cr_2O_3 powders were dissolved in a Na_2SO_4 melt with a certain basicity given by an atmosphere of oxygen containing 1 vol.% SO_2. In Fig. 8, this condition is placed between the solubility minima of Cr_2O_3 and Fe_2O_3.

Hence, Cr_2O_3 is dissolved by basic fluxing:

$$Cr_2O_3 + \frac{3}{2}O_2 + 4Na_2SO_4 = 2Na_2CrO_4 + 2Na_2S_2O_7 \quad (52)$$

The $Na_2S_2O_7$ leads to acidic fluxing of the Fe_2O_3, according to

$$Fe_2O_3 + 3Na_2S_2O_7 = Fe_2(SO_4)_3 + 3Na_2SO_4 \quad (53)$$

The accelerated dissolution is due to the short diffusion distance of the SO_3 in the melt.

6.1.3.2 Solubility of Oxides in Carbonate Melts

As in the case of sulfates, the solubilities of oxides in carbonate melts depends on the partial pressure of CO_2 in the gas

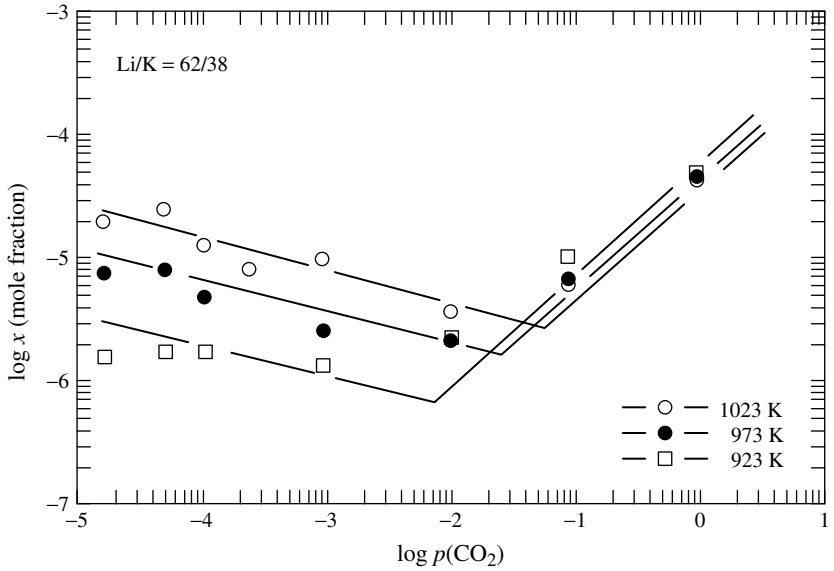


Fig. 9 Solubility plot of NiO in a $(Li_{0.62}K_{0.38})_2CO_3$ mixture as a function of $p(CO_2)$ in the gas phase at temperatures of 923 to 023 K.

phase and therefore on the basicity of the melt. As NiO is the cathode material in molten carbonate fuel cells, its solubility is of major interest and has been investigated in detail. Figure 9 shows the solubility plot of NiO in a $(Li_{0.62}K_{0.38})_2CO_3$ mixture as a function of $p(CO_2)$ in the gas phase at temperatures of 923 to 1023 K [18]. Two different solubility regimes are observed, showing a negative slope [low $p(CO_2)$] and a positive slope [high $p(CO_2)$]. These two regimes correspond to the basic [low $p(CO_2)$] and acidic dissolution [high $p(CO_2)$] of NiO in the carbonate melt according to basic dissolution:

$$NiO + {CO_3}^{2-} = {NiO_2}^{2-} + CO_2 \quad (54)$$

acidic dissolution:

$$NiO + CO_2 = Ni^{2+} + {CO_3}^{2-} \quad (55)$$

Further investigations on the basic dissolution of NiO in other carbonates have shown that the solubility also depends the nature of the carbonate. Figure 10 shows that the solubility of NiO at 910 °C in an CO_2-O_2-Ar atmosphere is highest for Rb_2CO_3 and lowest for Na_2CO_3, especially in the acidic

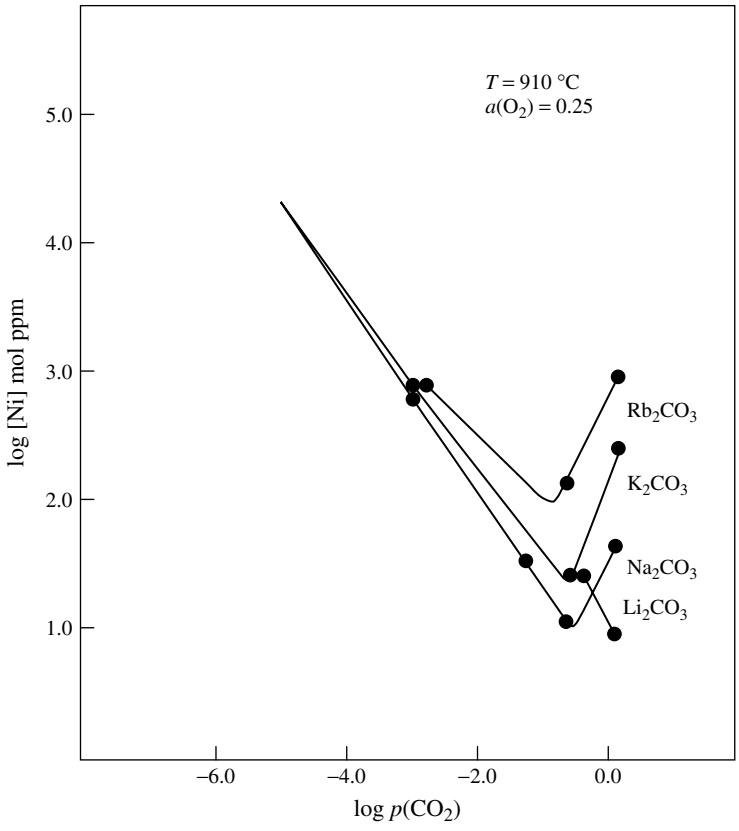


Fig. 10 Solubility of NiO at 910 °C in molten Li_2CO_3, Na_2CO_3, K_2CO_3, and Rb_2CO_3 in an CO_2-O_2-Ar atmosphere. The solubility is highest for Rb_2CO_3 and lowest for Na_2CO_3.

regime [19]. Evidence is given to the fact that the basic solubility of NiO in K_2CO_3 at constant $p(CO_2)$ slightly depends on $p(O_2)$ in the gas phase. This dependence is due to the following basic dissolution reaction:

$$K_2O + 2NiO + \tfrac{1}{2}O_2 = 2KNiO_2 \qquad (56)$$

6.1.4 Corrosion Mechanisms in Sulfate Melts

Corrosion mechanisms in molten sulfates consist of a sequence of chemical reactions and transport processes including oxide dissolution, transport of dissolved species through the salt film, and subsequent precipitation of oxide within the salt film in contact with the gas atmosphere.

6.1.4.1 Oxide Fluxing/Precipitation: The Rapp–Goto Model

From the electrochemical point of view, the oxidation of the bare metal Me requires the reduction of dissolved gas species such as SO_3 and O_2, or under highly basic conditions and very deep melts, of the SO_4^{2-} ion itself.

By oxidation of the metal beneath a highly basic molten sulfate film, O^{2-} ions are generated at the oxide/melt interface by reduction of O_2 or of the sulfate ion:

$$Me = Me^{2+} + 2e^- \qquad (57)$$

$$O_2 + 2e^- = O^{2-} \qquad (58)$$

and

$$Me + SO_4^{2-} = MeO + O^{2-} + SO_2 \qquad (59)$$

Furthermore, metal-sulfide formation is also possible at the metal/oxide interface, as observed in many corrosion products on metal samples, formed by basic fluxing. Hence, the region close to the oxide surface is much more basic than the entire salt film and basic dissolution of the oxide occurs, as described in detail for several oxides in Sect. 6.1.3.1.2. In the ideal case, the dissolved species form a separate layer, comparable to a Nernst concentration interface. From these interfaces, transport of the dissolved oxide species and also oxidant gas occurs by Fick diffusion within its concentration gradient in the melt film toward the melt/gas or the gas/oxide interface. According to Fick's law, transport of any dissolved species, including oxidant gas, through the melt film is given by

$$j_i = -D_i \frac{C_i^{g} - C_i^{s}}{\delta} \qquad (60)$$

j_i = flux of species i
D_i = diffusion coefficient of i
C_i^{g}, C_i^{s} = concentration of species i at the melt/gas and melt/scale interface
δ = melt film thickness.

As a consequence of the concentration gradient in the melt film, a basicity gradient also exists from regions of high $p(O^{2-})$ at the melt/oxide interface to regions of low $p(O^{2-})$ at the melt/gas interface. By reaching regions with low $p(O^{2-})$, the solute experiences a lower solubility and precipitation of solid oxide occurs by the reversal of the dissolution reactions:

$$MeO_2^{2-} = MeO + O^{2-} \qquad (61)$$

This precipitation creates a permanent sink for the solute, promoting the continuous flux of the dissolved oxide in the melt film. On the other hand, the consumption of oxidant gas O_2 by the formation of O^{2-} and subsequent dissolution reaction at the melt/oxide interface creates the gradient for oxidant diffusion. Figure 11 shows a schematic plot of the gradients and transport processes within the melt film.

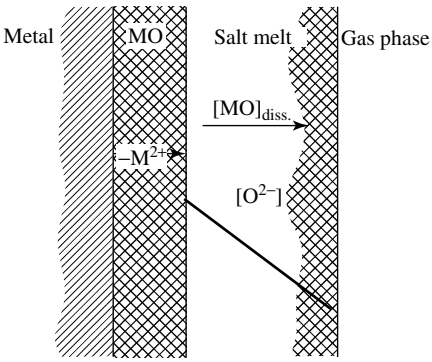


Fig. 11 Schematic plot of the solubility gradient and transport processes within the melt film. At the melt/gas interface, the oxide precipitates.

Rapp and Goto [20] analyzed the general fluxing conditions and developed a criterion (negative solubility gradient) for the continuous fluxing of oxide scales:

$$\left(\frac{d_{(\mathrm{sol})}}{\mathrm{d}x}\right)_{x=0} < 0 \qquad (62)$$

As long as the negative solubility gradient is valid, as defined by Eq. (62) (Rapp–Goto criterion), fluxing proceeds and the corrosion process is enhanced. A detailed analysis of the Rapp–Goto criterion is given by Shores [21]. He emphasized the role of the thickness of the melt film on the basic and acidic fluxing conditions. In thin films, the chemistry of the melt is governed by the composition of the gas phase, whereas in deep melts, local equilibria at the melt/oxide and melt/gas interface will control the corrosion mechanism. As a consequence, NiO may not be dissolved by basic dissolution beneath a thin salt film in an atmosphere containing SO_3, because the solubility minimum of NiO occurs at more basic conditions than given by the gas phase.

As response to this question and as a proof for the Rapp–Goto fluxing model, Otsuka and Rapp [22] performed a potentiometric measurement on preoxidized Ni at 1173 K in O_2-0.1% SO_2 gas, covered with a thin film of molten Na_2SO_4. Control of the basic conditions was done by a combination of a $Ag/AgSO_4$ RE with a Na^+-conducting closed-end mullite membrane and a closed-end and internally platinized yttria-stabilized zirconia oxygen sensor, as already reported in Sect. 6.1.3.1.1. With this equipment, the authors continuously recorded the basicity and oxygen activity of the melt as a function of time. Figure 12 shows the result of the experiments plotted in the Ni-Na-S-O diagram. The dashed line in Fig. 12 indicates the $p(O_2)$-dependent solubility minimum of NiO. At the beginning of the corrosion reaction, the melt was found to be more basic than expected to be in equilibrium with the gas atmosphere. With time, the conditions in the melt pass the stability field of NiS by becoming more and more basic with time. In conclusion, the local chemistry of the melt film is different from that expected by equilibrium with the gas phase. The formation of NiS leads to a significant increase in the basicity of the melt film and results in basic fluxing of the Ni.

The Rapp–Goto model was supported and Shores was refuted by Otsuka and Rapp. In most cases, the diffusion of gas species is the rate-controlling step in hot corrosion, as shown in various electrochemical experiments (see also Sect. 6.1.6).

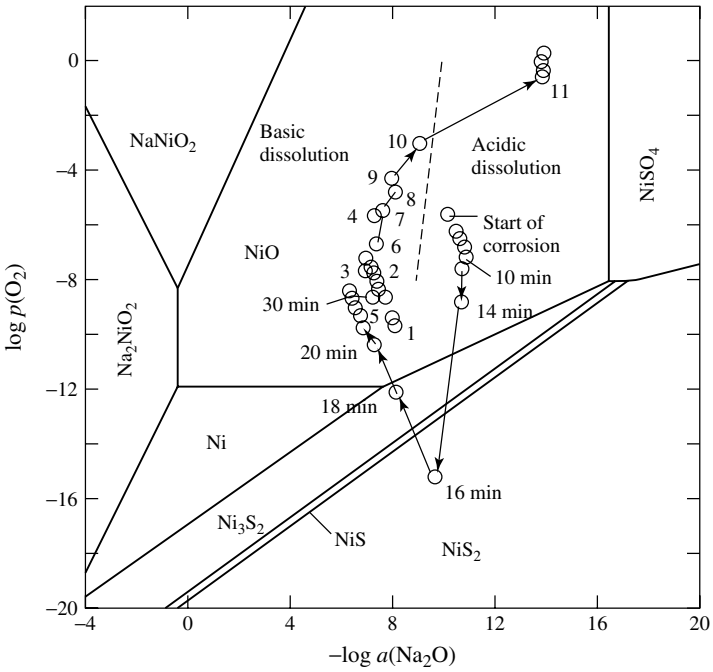


Fig. 12 Basicity and oxygen activity measures during corrosion of preoxidized Ni beneath a Na_2SO_4 film at 1173 K in O_2-SO_2, plotted in the Ni-Na-S-O-stability diagram.

6.1.4.2 **Acidic Fluxing**

Acidic fluxing occurs by dissolution of the oxide in the melt, as already described in Sect. 6.1.3.1.3. This acidic fluxing requires a higher $p(SO_3)$ in the gas phase and/or some alloying elements such as Co and Ni, from which molten eutectic mixtures are able to form with the sulfate deposit (alloy-induced acidic fluxing). The main feature of acidic fluxing is the dissolution of certain metal sulfates formed by reaction of the alloying elements and SO_3 from the gas phase within the salt deposit. Generally, no sulfide formation occurs by acidic fluxing.

6.1.5 Corrosion Mechanisms in Carbonate Melts

The corrosion mechanisms of metals and alloys in carbonate melts are quite different from the corrosion mechanisms observed in molten sulfates. As already described in Sect. 6.1.3.2, NiO suffers basic and acidic fluxing within a molten carbonate. As further analyzed by Lee and Shores in Thermogravimetric (TG) experiments [23], the hot corrosion of nickel in a eutectic $(Li_{0.62}K_{0.48})_2CO_3$ melt in an O_2-CO_2 atmosphere at 650 °C can be described by a fluxing mechanism, most probably according to the Rapp–Goto model. The authors suggested the following reactions:

Li-rich melt:

$$Ni + O_2^{2-} = Ni^{2+} + 2O^{2-} \text{ acidic} \quad (63)$$

$$Ni + O_2^{2-} = NiO_2^{2-} \text{ basic} \quad (64)$$

$$Ni + O_2^{2-} = NiO + O^{2-} \text{ saturated} \quad (65)$$

K-rich melt:

$$Ni + 2O_2^- = Ni^{2+} + 2O^{2-} + O_2 \text{ acidic} \quad (66)$$

$$Ni + 2O_2^- = NiO_2^{2-} + O_2 \text{ basic} \quad (67)$$

The reaction Eqs. (63 and 65) are producing oxide ions at the melt/scale interface, whereas at the melt/gas interface, oxide ions (in form of CO_3^{2-}) are consumed by the dissolution reactions involving O_2 in the melt. This gives rise to a gradient in O^{2-} concentration toward the melt film and a solubility gradient, as described in Sect. 6.1.4.1.

Regarding alloys as construction materials for molten carbonate fuel cells, the corrosion mechanisms are characterized by the formation of solid oxides on top of the metal surface, rather than by the fluxing mechanism. These oxides are formed by chemical reactions of the native oxide scale formed on the metal surface and the Li_2O compound of the molten salt. For example, iron oxide Fe_2O_3 reacts with a eutectic $(Li_{0.62}K_{0.48})_2CO_3$ melt at 650 °C in synthetic air containing 15 vol.% CO_2 to form $LiFeO_2$ according to

$$Fe_2O_3 + Li_2CO_3 = 2LiFeO_2(s) + CO_2 \quad (68)$$

If chromia is present on the metal surface, soluble K_2CrO_4 is formed:

$$Cr_2O_3 + 2K_2CO_3 + \frac{1}{2}O_2 = 2K_2CrO_4(l) + CO_2 \quad (69)$$

If the alloy contains elements such as Mn or Co, solid compounds like Li_2MnO_3 and $LiCoO_2$ are also formed [24].

6.1.6 Methods of Investigation

This chapter is closely related to the chapter titled "Electrochemical Techniques in Corrosion Engineering and Research, Vol 4, Chapter 7". Hence, no detailed description of the techniques will be given here; however, examples are provided for use of electrochemical techniques for molten salt corrosion studies.

A typical setup of a high-temperature electrochemical cell is shown in Fig. 13. The melt is placed in an alumina crucible

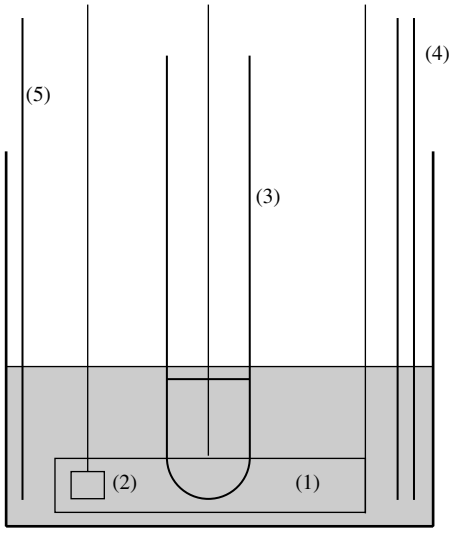


Fig. 13 Typical setup of the inner crucible of a HT-electrochemical cell with counterelectrode (CE) (1), the working electrode (WE) (2), the reference electrode (RE) (3), the gas-inlet tube (4), and the thermocouple (5).

situated in a vertical, closed-end furnace. To avoid electronic disturbances from the furnace heating wires, a cylindrical vessel made of stainless steel is placed between the alumina crucible and the furnace. The vessel is electrically grounded to avoid electrical charges on the surface. The alumina crucible is closed by a heat-resistant pyrex-glass-flange with breaches for the electrodes, the thermocouple, and the gas-inlet tube. The electrode wires and the thermocouple are shielded with small diameter alumina tubes. The alumina tubes are fixed with cayon fittings in the glass flange.

6.1.6.1 Polarization Studies

For polarization studies, a three-electrode setup is necessary, consisting of a WE, a CE, and a RE. As the WE, the metal to be investigated is chosen, or for studies of the polarization behavior of the melt itself Au or Pt are appropriate, as well as for the CE.

The main difference to aqueous corrosion studies is the design of reference electrodes. The most useful types are closed-end tubes of either internally platinized Y_2O_3-stabilized ZrO_2, mullite (see Sect. 6.1.3.1.1.), or glass membranes, depending on the composition of the melt and temperature. Glass membranes, especially Pyrex®, Supremax®, and Duran 50®, are Na^+- and K^+-conducting membranes and also useful for studies in molten salts, especially at temperatures up to 700 °C. Similar to the mullite RE, a silver wire is dipped into the molten chloride or sulfate to be investigated, additionally containing $AgCl_2$ or Ag_2SO_4 in concentrations of 1 to 10 mol.% [25].

As for aqueous corrosion, polarization studies provide mainly information about the potential-dependent behavior of a piece of metal in the melt regarding active dissolution, passive range, and breakthrough potentials. A lot of work

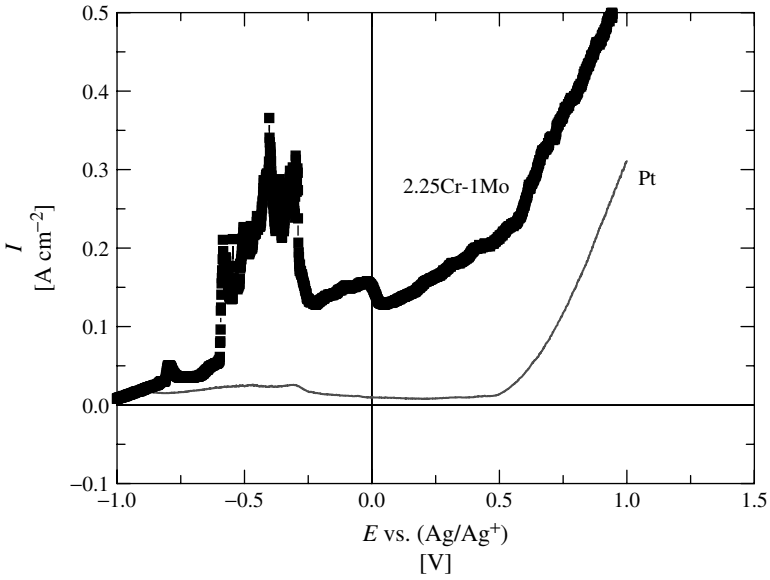


Fig. 14 Polarization curve of 2.25Cr-1Mo-steel in a eutectic (Ca-K-Na)-sulfate mixture at 850 °C in an N_2-5 vol.% O_2 gas mixture in comparison with Pt.

on this topic was carried out by Jäkel and Schwenk [26] in a eutectic (Li-K-Na-)-sulfate melt at 700 °C, using a Duran 50® $Ag/AgSO_4$ RE.

Figure 14 shows a polarization curve for 2.25Cr-1Mo-steel in a eutectic (Ca-K-Na)-sulfate mixture at 850 °C in an N_2-5 vol.% O_2 gas mixture, using a mullite $Ag/AgSO_4$ RE. After an active region, the material becomes passive in the potential range of approximately −0.25 to 0.25 V, followed by an increasing current with increasing potential. Investigation of the sample within the passive region shows the formation of a porous Fe_2O_3 scale on the metal surface [27].

To detect electrochemical reactions of an active metal in a given melt as a function of metal potential, cyclic voltammograms are useful. Figure 15 shows a cyclic voltammogram of pure iron in a eutectic 62 wt.% Li_2CO_3-38 wt.% K_2CO_3 melt at 650 °C in synthetic air, containing 25 vol.% CO_2. The details regarding RE and setup are described elsewhere [28]. Upon anodic polarization, the voltammogram shows three different anodic peaks (A,B,C) and two cathodic peaks (D,E). According to detailed investigation by Scanning Electron Microscopy (SEM) and X-ray diffraction (XRD) on samples held at the different anodic potentials, the following reactions were identified:

$$\text{A: } Fe + {CO_3}^{2-} = FeO + CO_2 + 2e^- \quad (70)$$

$$\text{B: } Fe + 4FeO + 4{CO_3}^{2-} + 5Li^+ = Li_5Fe_5O_8 + 4CO_2 + 3e^- \quad (71)$$

$$\text{C: } Li_5Fe_5O_8 + 2{CO_3}^{2-} = LiFe_5O_8 + 2Li_2CO_3 + 4e^- \quad (72)$$

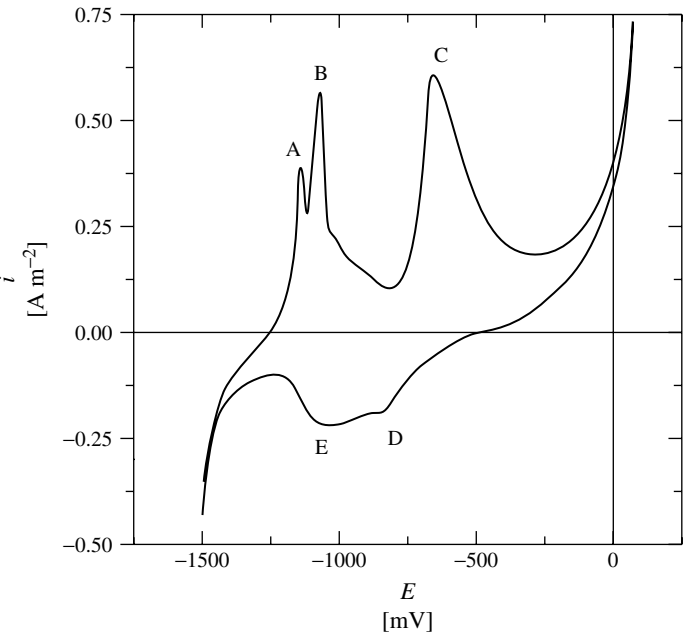


Fig. 15 Cyclic voltammogram of pure iron in a eutectic 62 wt.% Li_2CO_3-38 wt.% K_2CO_3 melt at 650 °C in synthetic air, containing 25 vol.% CO_2.

6.1.6.2 Impedance Spectroscopy

Impedance spectroscopic measurements are randomly used in molten salt corrosion studies. In general, most of the impedance spectra emphasize diffusion-controlled kinetics for the active corrosion of metals in molten salts. This behavior is expected, as the activation energy for charge-transfer reactions is easily reached at higher temperatures.

One example is the hot corrosion of a preoxidized nickel specimen by a thin Na_2SO_4 melt film in a 0.1 wt. % SO_2-O_2 gas mixture at 1200 K [29]. By variation of the oxide scale thickness and the purity of the material, different regimes of corrosion were investigated: passive state, pseudopassive state, and active state. The passive state of 99.9975% of pure nickel, preoxidized in pure O_2 for 2 h at 1200 K is controlled by diffusion of $S_2O_7^{2-}$ in the salt melt. The corresponding Nyquist plot of impedance data shows linear behavior in the low-frequency range with a slope of 45° (Fig. 16). The semicircle at higher frequencies was attributed to the resistance of the NiO layer itself. The active state was established on less pure nickel and following short preoxidation time, resulting in an ultrathin, nonprotective oxide scale on the nickel surface. After 670 min of reaction, diffusion-controlled behavior was again observed, as shown in the Nyquist plot in Fig. 17.

In addition to experimental work, the most recent paper by Zheng and coworkers [30] gives some theoretical impedance models for hot corrosion of metals in molten salts. In general, the authors propose large semicircles in the Nyquist plot for nonactive metals, resulting from rate-limiting charge-transfer reaction. For active metals, the total impedance may result from the scaling of the metals, and the Nyquist plot should show two capacitance loops, and the rate-limiting step is the charge-transfer reaction. For porous scales on the surface, a line should be shown in the low-frequency range, related to a diffusion-controlled process. The authors proved these assumptions by an impedance measurement of FeAl in molten $(Li,K)_2CO_3$ at 650 °C after 48 h of corrosion, showing a diffusion-controlled behavior in the low-frequency range (Fig. 18).

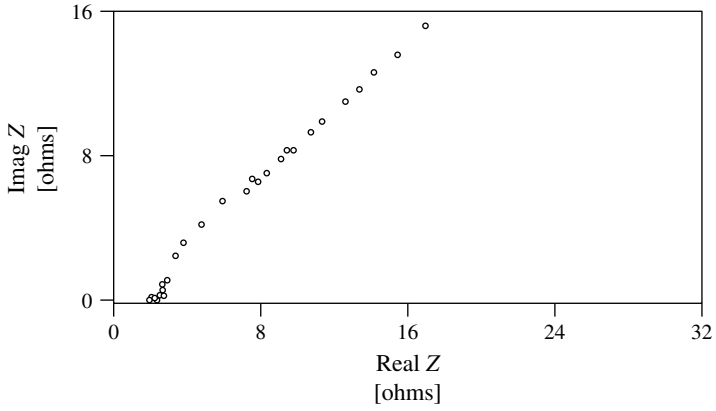


Fig. 16 Nyquist plot of impedance data of the passive state of 99.9975% pure nickel in a Na_2SO_4 melt in an 0.1 wt. % SO_2-O_2 gas mixture at 1200 K, showing linear behavior in the low-frequency range with a slope of 45°.

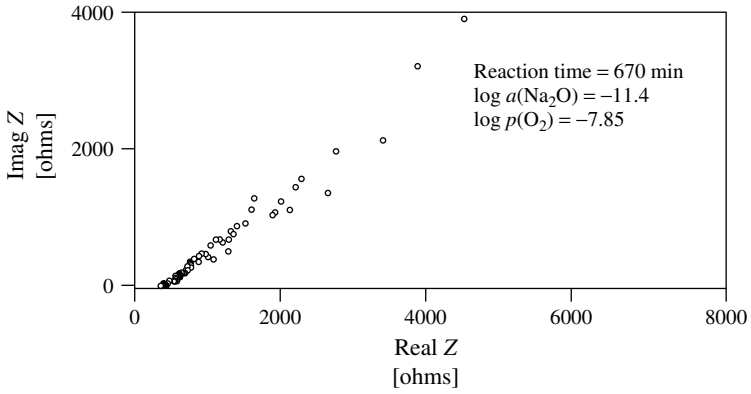


Fig. 17 Nyquist plot of the active state of Ni after 670 min of reaction in a Na_2SO_4 melt in an 0.1 wt. % SO_2-O_2 gas mixture at 1200 K. Also, diffusion-controlled behavior was observed.

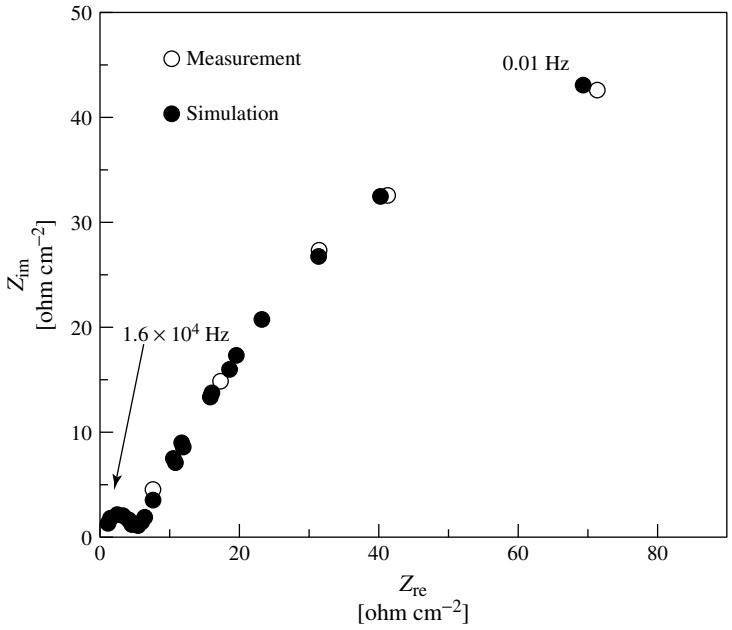


Fig. 18 Nyquist plot of impedance data from FeAl in molten $(Li,K)_2CO_3$ at 650 °C after 48 h of corrosion, showing a diffusion-controlled behavior in the low-frequency range.

6.1.6.3 Other Methods

6.1.6.3.1 Exposure Tests Exposure tests are conducted to give an overview on the long-term corrosion kinetics. The main advantage of these tests is the possibility of exposure of many samples at the same time. The furnace for the tests will be connected to a gas flow device, as described elsewhere [31]. There are

several methods of applying the salt for investigation:

- evaporation of the salt in a hot zone of the furnace and condensation on the cooler sample surface (Dean test);
- full immersion of the sample in the salt (crucible test, thick salt film);
- top surface coverage of the sample (thin salt film);
- applied as a slurry or an aqueous solution (thin salt film).

In general, thick salt films are used to simulate the situation of corrosion beneath partially molten ashes such as waste or coal ash. Thin salt films mainly exist on turbine blades (Na_2SO_4) or on current collectors in molten carbonate fuel cells $(Li,K)_2CO_3$ (see also Sect. 6.1.7). In general, corrosion beneath a thin salt film is much faster than beneath a thick film because the kinetics of oxidant gas supply from the gas atmosphere through the thin film is much faster. For long-term exposures, the redeposition of salt is necessary, simulating the continuous supply of salt during the process to be investigated. From this point of view, the Dean test is more appropriate than the other methods.

Determination on the extent of corrosion can be done by measurements of the scale or remaining metal thickness or by determination of total weight loss after removal of corrosion products. The last method is especially favored, if a high amount of oxide is dispersed in the solidified salt.

For kinetic studies and according to the guidelines developed in the TESTCORR project [32], the extent of corrosion has to be determined on a logarithmic timescale after 1, 3, 10, 30, 100, 300, 1000 h of exposure and redeposition has to occur after every 20 h.

6.1.6.3.2 **Thermogravimetric Experiments**
In contrast with exposure tests, thermogravimetric experiments are useful to study short-term kinetics regarding possible incubation times or the influence of gas phase composition. Evidence must show that the overall mass change is not influenced by reactions of the salt itself, by significant evaporation, or by reaction with the gas phase.

The most appropriate method of sample coating for TG studies is the deposition from a slurry or an aqueous solution and suspending the sample subsequently by glass hooks directly in the flowing gas stream. By this method, gas supply to the sample surface is nearly equal over the entire sample geometry. Using the crucible test does not allow homogeneous gas diffusion to the sample surface and gives rise to misinterpretation of the kinetic results.

6.1.7 Applications

6.1.7.1 Gas Turbines

Nickel-based alloys, used in gas turbines such as aircraft engines, often show accelerated attack compared to exposure in oxygen or air. It has been established that deposition of Na_2SO_4, formed by salt from the air and sulfur from the fuel, is responsible for these kinds of attack, especially work by Goebel and Pettit [33] as well as by Bornstein and DeCrescente [34, 35] recognized that the formation of sulfides on the metallic engine parts results from the presence of a thin salt film on the metal surface. Extensive research was performed on alloys, coated with Na_2SO_4 and reacted in air, oxygen, and SO_3-containing gases. Not all of the work done can be described here in detail but some principles on the

reaction mechanisms will be given in the following. In general, two types of hot corrosion regimes are distinguished and designated as type I and type II.

Type I Hot Corrosion occurs when the metal surface temperature is higher than the melting point of Na_2SO_4 ($T > 884\,^{\circ}C$). When Ni with Na_2SO_4 deposits is reacted above 900 °C in SO_3-containing oxygen, the Na_2SO_4 is molten from the very start of the reaction (m.p. of Na_2SO_4 is 884 °C) and accelerated corrosion occurs.

Type II Hot Corrosion takes place at temperatures below the melting point of Na_2SO_4. As the reaction proceeds, dissolution of corrosion products occurs and a melt is formed. In the case of Ni, $NiSO_4$ and/or a solid solution of $Na_2SO_4 + NiSO_4$ is gradually formed through the reaction of $NiO + SO_3$:

$$NiO + SO_3 + Na_2SO_4 = Na_2SO_4 - NiSO_4(s) \quad (73)$$

With further reaction, the $NiSO_4$ content in the $Na_2SO_4 - NiSO_4$ solid solution increases and for a critical concentration of $Na_2SO_4 - NiSO_4$, the sulfate mixture melts. Under these conditions, the more rapid hot corrosion is initiated. With increasing $p(SO_3)$, the melting point of the $NiSO_4 - Na_2SO_4$ solid solution decreases and a $NiSO_4 - Na_2SO_4$ liquid solution with $T_m < 884\,^{\circ}C$ forms [36, 37].

In aircraft turbines, especially nickel- and cobalt-based alloys suffer from salt-induced corrosion. On these alloys, type II corrosion mechanisms were observed, depending on the surface temperature of the turbine blades. Studies were performed on Co-Cr, Co-Al, Ni-Cr, Ni-Cr-Al, and Co-Cr-Al-Y alloys [38, 39]. It was shown that on Co-Cr and Co-Cr-Al pits were formed on the alloy, filled with corrosion products. On Co-Cr and Co-Cr-Al, the morphology of the corrosion products depends on the temperature and $p(SO_3)$. At 750 °C, an outer layer is formed, consisting of Co_3O_4 and $CoSO_4$, whereas Cr_2O_3 and $CoCr_2O_4$ were detected as an inner scale in pits underneath the original metal surface. At lower temperatures (600, 650 °C), an outer scale of porous Cr_2O_3 was formed and no pits were detected. On Co-Al, no pits were formed and a uniform corrosive attack was observed by the formation of Co_3O_4 and $CoSO_4$. In addition, also aluminum sulfides were detected at the metal/scale interface. A detailed corrosion mechanism of Co-based alloys in O_2- and SO_3-containing gases was also provided by Luthra [38]. In this model, in only SO_3-containing gases, the SO_3 is dissolved in the melt and transported via SO_4^{2-} ions from the melt/gas to the melt/oxide interface at which $CoSO_4$ is formed. In only O^{2-}-containing gases, Co^{2+} is dissolved from the oxide and transported to the melt/gas interface at which it is oxidized by O_2 to Co^{3+} and Co_3O_4 is formed. Some Co^{3+} also diffuses to the melt/oxide interface at which it is reduced to Co^{2+} again. If $p(SO_3)$ is quite low and O_2 is present in the gas, $CoSO_4$ is also formed at the melt/gas interface.

Alloying elements like Mo, W, and also V as a fuel impurity form acidic oxides MoO_3, WO_3, and V_2O_5. The effect of $NaVO_3$ on the acidic fluxing of CeO_2, HfO_2, and Y_2O_3 was studied in detail by Zhang and Rapp [40] and it was shown that fluxing was accelerated by the presence of acidic solutes in the melt. This behavior results from complexing reactions between the solute VO_3^- and oxide ions, provided by acidic dissolution of ceria:

$$3CeO_2 + 4NaVO_3 = 2Na_2O + Ce_3(VO_4)_4 \quad (74)$$

This reaction principle is also valid for any other oxide.

6.1.7.2 Waste Incineration

Corrosion of superheaters and water walls in waste fired boilers results from the deposition of fly ash on the metal surface. This produces a characteristic failure situation in which the covered part of the tube is significantly damaged (Fig. 19). In these ashes, molten phases are formed, mainly chlorides KCl, NaCl, $ZnCl_2$, and $PbCl_2$ on cooler parts such as water walls (300 to 400 °C) and sulfates $CaSO_4$, K_2SO_4, Na_2SO_4, $PbSO_4$, and $ZnSO_4$ on hotter parts such as superheaters (450 to 550 °C) [41]. Because of the significant amount of heavy metals, these salt mixtures form low melting eutectics down to 250 °C.

A typical sulfate melt–induced attack of superheater ($T \approx 550$ °C) from a waste fired boiler is shown in Fig. 20. The morphology of the scale is typical for a molten salt attack, a thick and dense chromium-rich oxide scales in contact

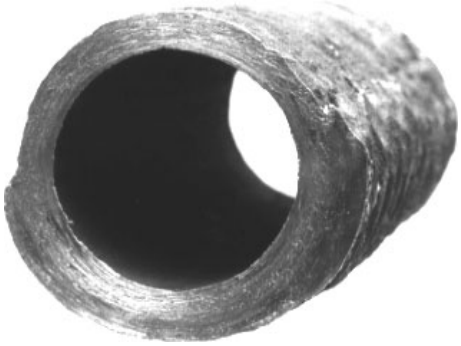


Fig. 19 Characteristic failure situation of a superheater from a waste fired boiler. The ash covered part of the tube is significantly damaged.

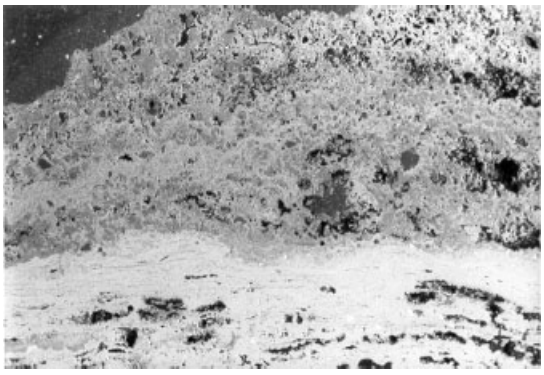


Fig. 20 Typical sulfate melt–induced attack of superheater ($T \approx 550$ °C) from a waste fired boiler. The morphology of the scale is typical for a molten salt attack, a thick and dense chromium-rich oxide scales in contact with the metal and iron oxide precipitate and nickel oxide precipitate in the molten salt.

with the metal and iron oxide precipitate and nickel oxide precipitate in the molten salt. Systematic investigations on the corrosion mechanism of steels and nickel-based alloys beneath molten sulfates under waste incineration conditions were carried out by Spiegel [42]. The corrosion mechanism is closely related to hot corrosion, as described by the Rapp–Goto model.

Regarding molten chlorides, mainly KCl-$ZnCl_2$ mixtures are present in the ashes and fast corrosion occurs at relatively low temperatures. Figure 21 presents results of a thermogravimetric measurement on 2.25Cr-1Mo-steel beneath a molten 50 wt.% KCl-50 wt.% $ZnCl_2$ mixture at different temperatures in He-5 vol.% O_2 gas mixture. At 350 °C, significant corrosion occurs by the molten salt. The main corrosion mechanism is the dissolution of metal in the molten salt as soluble metal chlorides.

6.1.7.3 Molten Carbonate Fuel Cells

Molten carbonate fuel cells operate at 650 °C with a molten 62 wt.% Li_2CO_3-38 wt.% K_2CO_3-eutectic mixture as the electrolyte, CO_2 and O_2 as oxidant gases, and H_2 as the fuel. The relevant reactions are:

cathode:

$$CO_2 + \tfrac{1}{2}O_2 + 2e^- = {CO_3}^{2-} \qquad (75)$$

anode:

$$H_2 + {CO_3}^{2-} = H_2O + CO + 2e^- \qquad (76)$$

Figure 22 shows the principal setup of such a fuel cell. In practice, the stack technology is applied by combining many modules into a bigger device. The main

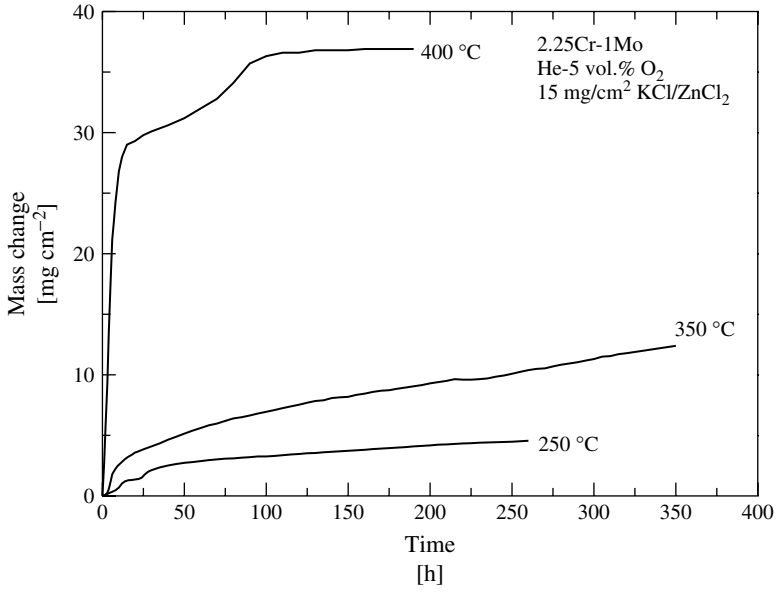


Fig. 21 Results of a thermogravimetric measurement on 2.25Cr-1Mo-steel beneath a molten 50 wt.% KCl-50 wt.% $ZnCl_2$ mixture at different temperatures in He-5 vol.% O_2 gas mixture.

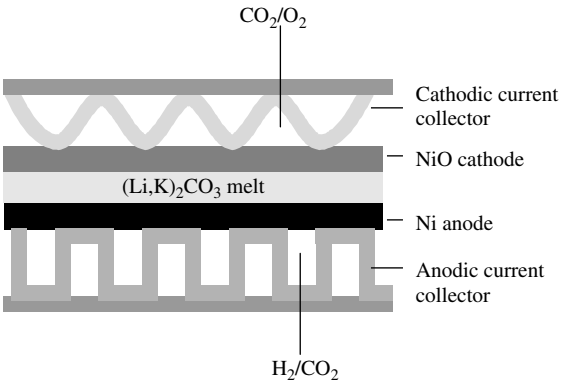


Fig. 22 Principle setup of a molten carbonate fuel cell.

corrosion problems occur at the cathodic side at which NiO is used as the cathode material and stainless steel as the current collector. Both parts contact the gas phase (O_2, CO_2) and the molten carbonate, leading to hot corrosion attack. NiO as the cathode materials starts to dissolve in the melt and reprecipitates in the electrolyte, leading to a short circuit and breakdown of the cell voltage. Furthermore, corrosion of the cathodic current collector by the molten carbonate occurs and the cell voltage decreases because of the growth of poorly conducting oxide phases such as $LiCrO_2$. Laboratory research is continuing to find metallic materials with good corrosion resistance, forming corrosion products with reasonable electric conductivity such as spinels, doped with Co and Mn.

References

1. R. A. Rapp, *Metall. Mater. Trans. A* **2000**, *31A*, 2105.
2. H. Lux, *Z. Elektrochem. Angew. Phys. Chem.* **1939**, *45*, 303.
3. H. Flood, T. Forland, K. Motzfeld, *Acta chem. Scand.* **1952**, *6*, 257.
4. C. O. Park, R. A. Rapp, *J. Electrochem. Soc.* **1986**, *133*, 1636.
5. R. E. Andresen, *J. Electrochem. Soc.* **1979**, *126*, 328.
6. H. Flood, T. Forland, *Acta chem. Scand.* **1947**, *1*, 781.
7. D. A. Shores, W. C. Fang, *J. Electrochem. Soc.* **1981**, *128*, 346.
8. W. C. Fang, R. A. Rapp, *J. Electrochem. Soc.* **1983**, *130*, 2335.
9. T. Nishina, I. Uchida, J. R. Selman, *J. Electrochem. Soc.* **1994**, *141*, 1191.
10. P. Claes, B. Thirjon, J. Gilbert, *Electrochim. Acta* **1996**, *41*, 141.
11. Y. S. Zhang, R. A. Rapp, *J. Electrochem. Soc.* **1985**, *132*, 734.
12. Y. S. Zhang, R. A. Rapp, *J. Electrochem. Soc.* **1986**, *133*, 2498.
13. R. A. Rapp, *Corrosion* **1986**, *42*, 568.
14. P. D. Jose, D. K. Gupta, R. A. Rapp, *J. Electrochem. Soc.* **1985**, *132*, 735.
15. D. K. Gupta, R. A. Rapp, *J. Electrochem. Soc.* **1980**, *127*, 2194, 2656.
16. Y. S. Zhang, *J. Electrochem. Soc.* **1986**, *133*, 655.
17. Y.-S. Hwang, R. A. Rapp, *J. Electrochem. Soc.* **1990**, *137*, 1276.
18. K. Ota, S. Mitsushima, K. Kato et al., *Proceedings of the Second Symposium in MCFC-Technology*, The Electrochemical Society, Princeton, N.J., 1990, Vol. 90-16, p. 318.
19. M. L. Orfield, D. A. Shores, *J. Electrochem. Soc.* **1988**, *135*, 1662.
20. R. A. Rapp, K. Goto in *Proceedings of the Fused Salt Symposium 2* (Eds.: J. Braunstein, R. Selman), The Electrochemical Society, Princeton, N.J., 1979.
21. D. A. Shores in *High Temperature Corrosion* (Ed.: R. A. Rapp), NACE International, Houston, Tex., 1983, p. 493.
22. N. Otsuka, R. A. Rapp, *J. Electrochem. Soc.* **1990**, *137*, 46.

23. K. N. Lee, D. A. Shores, *J. Electrochem. Soc.* **1990**, *137*, 859.
24. P. Biedenkopf, M. Spiegel, H. J. Grabke, *Mater. Corros.* **1997**, *48*, 731.
25. A. Rahmel, *Werkst. Korros.* **1968**, *19*(9), 750.
26. U. Jäkel, W. Schwenk, *Werkst. Korros.* **1975**, *26*(7), 521.
27. M. Spiegel, Electrochemical investigations on the corrosion of metals in a (Ca, Na, K)-Sulfate Melt. ''Proceedings EUROCORR'00, London, (2000).
28. P. Biedenkopf, M. Spiegel, H. J. Grabke, *Electrochim. Acta* **1998**, *44*, 683.
29. Y. M. Wu, R. A. Rapp, *J. Electrochem. Soc.* **1991**, *138*, 2683.
30. C. L. Zheng, W. Eang, W. T. Wu, *Corros. Sci.* **2001**, *43*, 787.
31. M. Spiegel, H. J. Grabke, *Mater. Corros.* **1996**, *47*, 179.
32. A. B. Tomkins et al., TESTCORR, Code of Practise, ERA Report 2000–0546, 2001, unpublished.
33. J. A. Goebel, F. S. Pettit, *Metall. Trans.* **1970**, *4*, 1943.
34. N. S. Bornstein, M. A. DeCrescente, *Trans. Met. Soc. AIME* **1969**, *245*, 1947.
35. N. S. Bornstein, M. A. DeCrescente, *Metall. Trans.* **1971**, *2*, 2875.
36. K. L. Luthra, D. A. Shores, *J. Electrochem. Soc.* **1980**, *127*, 2202.
37. K. P. Lillerud, P. Kofstad, *Oxid. Met.* **1984**, *21*, 233.
38. K. L. Luthra, *Metall. Trans. A* **1982**, *13A*, 1647, 1843, 1853.
39. K. L. Luthra, *J. Electrochem. Soc.* **1985**, *132*, 1293.
40. Y. S. Zhang, R. A. Rapp, *Corrosion* **1987**, *43*, 348.
41. M. Spiegel, *Mater. Corros.* **1999**, *50*, 373.
42. M. Spiegel, *Mater. Corros.* **2000**, *51*, 303.

6.2
High-temperature Corrosion of Metals by Gases

Hans Jürgen Grabke
Max-Planck-Institut für Eisenforschung
Düsseldorf, Germany

Günther Holzäpfel
Lehrstuhl für Physikalische Chemie I,
Universität Dortmund, Germany

6.2.1
Introduction

High-temperature corrosion is a practical problem in most applications of metals and alloys at elevated temperatures in corrosive environments. In power plants, chemical and petrochemical process industries, for aircraft engines, heat treatment and other metallurgical processes, and new technologies such as waste-incineration plants, high-temperature fuel cells, and so on, the metallic materials must be carefully selected, to allow sufficient lifetime and avoid premature failure. Sometimes processes are not possible since the materials would not withstand the process conditions that must be adapted to the available materials.

The corrosion by atmospheres generally is by oxidation but also carburization, nitridation, chloridation, and sulfidation are possible, in the flue gases, process gases. Oxidation and formation of a slowly growing oxide scale can be considered as positive and helpful to suppress the ingress and attack by C, N, S, Cl, and so on. All high-temperature alloys are tailored so that they can withstand high-temperature corrosion by the formation of a scale that is protective: Fe_3O_4 and Fe_2O_3 on low-alloy steels up to about 550 °C, Cr_2O_3 and spinels on high-alloy Cr-steels up to about 900 °C, and Al_2O_3 or SiO_2 on materials used at very high temperatures. These alloys certainly must also have sufficient mechanical strength at high temperature to be creep resistant. The high-temperature corrosion behavior of these engineering alloys by all possible kinds of attack has been described in a book by Lai [1], which gives extensive information on the mechanisms and kinetics of corrosion and the necessary background for the material's selection in the industry. More emphasis on the fundamental aspects of high-temperature corrosion and especially oxidation of metals was put by Kofstad in his textbook [2].

This chapter now concentrates on the electrochemical aspects of oxide growth, which have been studied mainly in earlier years for fundamental interest. These studies concerned the more rapidly growing oxides, for which the system metal/scale/gas can indeed be compared to an electrochemical cell – the so-called protective oxides Cr_2O_3, Al_2O_3, and SiO_2 are more complex cases, but will be discussed also. Considering the vast amount of literature on oxidation of engineering alloys, this discussion is only short and concentrates on the electrochemical aspects. Some rare studies have been done on the electrochemical processes in sulfidation and chloridation, and these will be reported. But carburization and nitridation are not considered since these reactions are not electrochemical in any way.

In principle, most metals (except some noble ones) are unstable at high temperatures in gaseous environments. They should react to oxides, sulfides, chlorides, and so on depending on the kind of environment. Generally, the Gibbs free energies of oxidation are most negative, so that oxides are most stable and their formation pressures very low. For an oxidation reaction

$$\frac{2x}{y}\,M + O_2 = \frac{2}{y}\,M_x\,O_y \qquad (1)$$

the formation pressure results from

$$pO_2 = \exp\left(\frac{\Delta G^\circ}{RT}\right) \qquad (2)$$

where ΔG° is the Gibbs free energy under standard conditions. Thus, data on ΔG° are important to find out the most stable reaction products (Fig. 1), and an electrochemical method has been put forward by Wagner for its determination [3]. This method is based on the use of a solid electrolyte, doped ZrO_2, and its use for determination of thermodynamic data [4] is described in Sect. 6.2.1.2.

In the oxidation, sulfidation, and so on of metals and alloys, solid reaction products are growing as film, scale, crystals, or in other morphologies, on the metal phase. A frequent case is the formation of a dense scale, separating the metal and gas phase. In this case, generally, a parabolic rate law is observed for the increase of film thickness x

$$x^2 = 2k\,t \text{ which results from } \frac{dx}{dt} = \frac{k}{x} \qquad (3)$$

indicating diffusion-controlled growth. The parabolic law was first observed by Tammann [5] in 1920 for growth of AgI on silver and later (1923) by Pilling and Bedworth [6] for the oxidation of iron.

In the following years, knowledge about disorder and defects in oxides and other solid compounds was gained (see Sect. 6.2.2.1). On the basis of this knowledge, Wagner could develop his theory on the growth of scales by diffusion of ions [7–9] (Fig. 2). In fact, the model proposed corresponds to an electrochemical cell, with anodic and cathodic reaction, diffusion of cations and/or anions, and charge transport by electrons. Wagner's theory correlates the scale growth and the parabolic rate constant with ionic conductivities and transference numbers or with the ionic self-diffusivities [7–9].

However, in oxidation, sulfidation, and so on, not only diffusion in the solid reaction product, but also phase boundary reactions play a role:

- the surface reaction in which O, S, and so on are transferred from the oxidants O_2, CO_2, H_2O or S_2, SO_2, H_2S ... to the scale surface and
- the transfer of the metal atoms through the oxide/metal-, sulfide/metal-, and so on interface.

Wagner was well aware that these processes also may affect or even control the kinetics of oxidation, sulfidation, and so on, and he initiated research on the phase boundary reaction kinetics [10–18]. Some cases of surface reaction control are described in Sect. 6.2.3.2. The surface reactions generally have no electrochemical character, but as shown, electron transfer steps are involved [10–12]. Least is known about the reactions at the inner interface, but studies on sulfidation [13–18] have proven its role.

So, Wagner and his followers have covered not only the diffusion-controlled kinetics, by the generally so-called Wagner's theory, but also the other fundamental aspects of scaling kinetics. This kind of fundamental research on mechanisms and kinetics of scale growth, also on the electrochemical reactions in high-temperature oxidation, sulfidation, and so on was flourishing till the 1960s.

Since for protection against high-temperature corrosion, slow-growing, dense, well-adherent oxide scales are of greatest importance, later on the research concentrated on the growth and adherence of such scales, that is, mainly Cr_2O_3 and

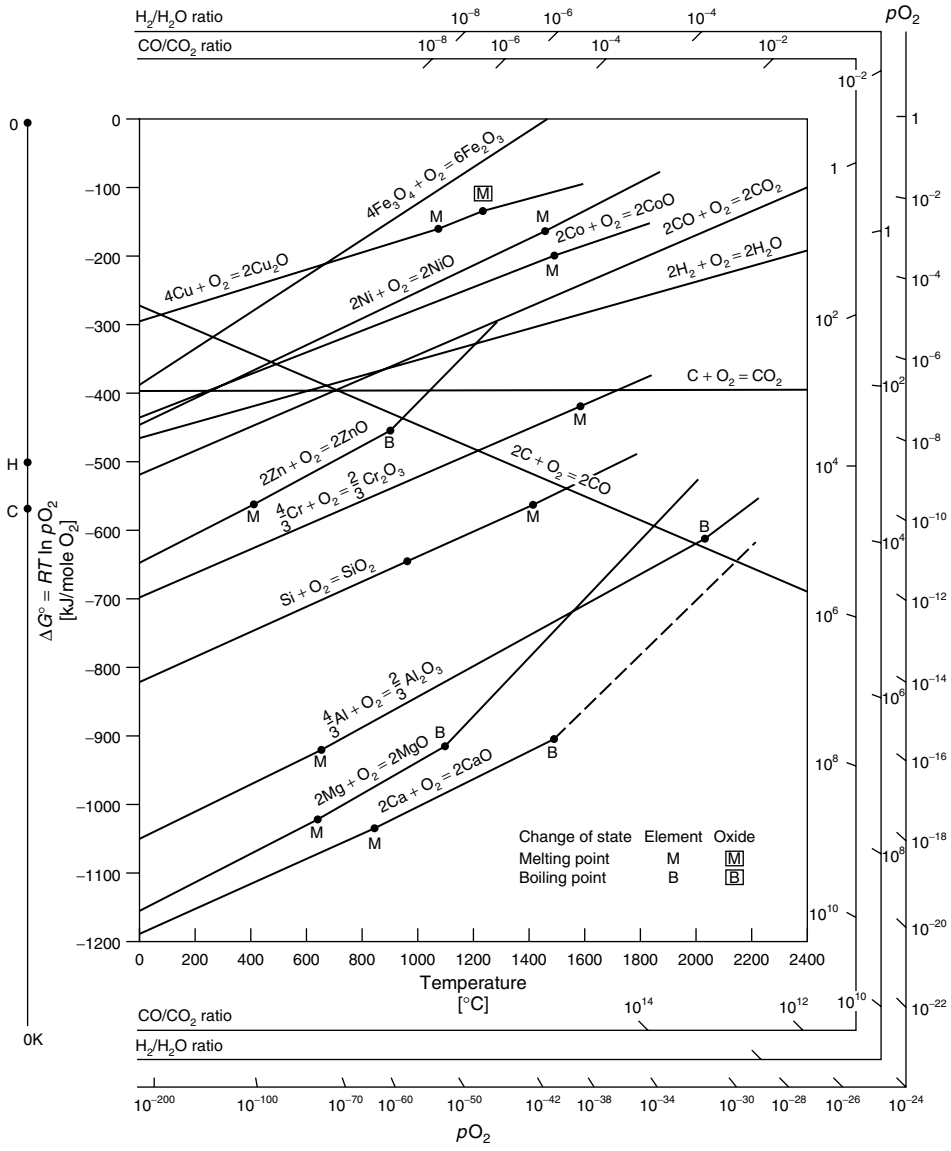


Fig. 1 Plot of Gibbs energy of formation per mole O_2 versus temperature, for some important oxides (Ellingham–Richardson diagram). Lines of constant pO_2, pH_2O/pH_2, and pCO_2/pCO are drawn by connecting the point at 0 K with the mark at the auxiliary scale.

Al_2O_3. In these oxides, the transport of ions is mainly along grain boundaries and the electronic conductivity is low so that transport of electrons may play a role (see Sect. 6.2.2.1.3). Furthermore, the attack by mixed oxidants is of great practical interest, and the phenomena involved in attacks by oxidation, sulfidation, carburization,

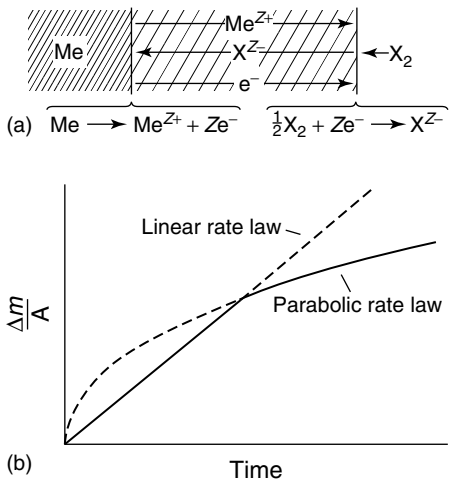


Fig. 2 (a) Schematics of the reactions and transport processes in a growing scale, during the corrosion of a metal in a gas phase with $X_2 = O_2$, S_2, Cl_2 or else; (b) curves for growth of thickness or mass gain per area $\Delta m/A$ according to linear and parabolic kinetics.

nitridation, and/or chloridation rarely can be discussed as electrochemical processes.

6.2.1.1 Determination of Thermodynamic Data

6.2.1.1.1 Measurements of Gibbs Energies

The electrochemical measurement of standard Gibbs energies ΔG^o for the formation of metal oxides and other compounds is briefly described here, since it is a generally very elegant and precise method. Its limitation is to have available a solid electrolyte with prevailing ionic conductivity, that is, the transference number for ions $t_{ion} \cong 1$, this has been discussed in detail [19–24]. In a wide range of temperatures and oxygen pressures, doped ZrO_2 can be used, in the galvanic cell

$$Pt|Me, Me_xO_y|$$

$$ZrO_2 + CaO(\text{or } Y_2O_3)|Pt, O_2(g)$$

for determination of ΔG^o of the general oxidation reaction (1) where the oxygen pressure pO_2 at the right-hand side, maybe $pO_2 = 1$ bar, or $pO_2 = 0.21$ bar (in air) or given by the oxygen pressure of a suitable two phase mixture, for example, Fe + FeO, FeO + Fe_3O_4, and so on, whose equilibrium pressure is well-known. The Gibbs standard energy of reaction (1) then results from

$$\Delta G_1^o = -E_1 F + \tfrac{1}{2} RT \ln pO_2 \qquad (4)$$

where E_1 is the open-circuit voltage in equilibrium, F is Faraday's constant, and R the gas constant. From measurements at different temperatures, one can derive the standard entropy change ΔS_1^o and the enthalpy ΔH_1^o

$$\Delta S_1^o = \frac{-\mathrm{d}\Delta G_1^o}{\mathrm{d}T} \quad \Delta H_1^o = \Delta G_1^o + T\Delta S_1^o \qquad (5)$$

As mentioned, cells can be constructed involving two condensed-phase coexistence electrodes, for example,

$$Fe, FeO|ZrO_2 + CaO|Ni, NiO$$

$$\Delta G^o = -2FE = \Delta G^o(FeO) - \Delta G^o(NiO)$$

The virtual cell reaction is a displacement reaction

$$NiO + Fe = FeO + Ni \qquad (6)$$

and the Gibbs energy obtained is the difference of the Gibbs energies of FeO and NiO formation. So if the value of ΔG^o for one of the coexistence electrodes is well-known, the other one can be determined. In high-temperature oxidation, the formation of mixed oxides and spinels is also of interest, and was studied for many systems [25–27] using solid electrolyte cells, for example,

$$\mathrm{Pt|Ni, NiAl_2O_4, Al_2O_3|ZrO_2 + Y_2O_3|}$$
$$\mathrm{Ni, NiO|Pt}$$

for the virtual cell reaction

$$\mathrm{NiO + Al_2O_3 = NiAl_2O_4} \qquad (7)$$

Corresponding cell values of ΔG^o for the formation of many ternary compounds have been obtained. Besides doped zirconia, also some iodides, AgI, CuI have been used as cation conductors in electrochemical cells for thermodynamic and kinetic studies. The Gibbs energy of a sulfide formation can be determined [21], for example, by the cell

$$\mathrm{Pt, Ag|AgI|Ag_2S, S, Pt}$$

The transfer of Ag^+ ions to the right side of the cell and their reaction with molten sulfur corresponds to the virtual reaction

$$\mathrm{2\,Ag + S = Ag_2S} \qquad (8)$$

6.2.1.1.2 Measurement and Control of Partial Pressures and Activities

Oxygen pressure For measurement or control of oxygen pressures, the following cell is used:

$$\mathrm{Pt, O_2(g)'|ZrO_2 + Y_2O_3|O_2(g)'', Pt}$$

In the case of an oxygen sensor with the reference electrode in air (0.21 bar O_2), the oxygen partial pressure pO_2'' results in the cell voltage

$$E = \frac{RT}{4F} \ln\left(\frac{0.21}{pO_2''}\right) \qquad (9)$$

Such cells can be used, not only for measuring pO_2 in gas mixtures containing O_2, but also in CO_2-CO or H_2O-H_2 mixtures [28], and, in addition, for controlling pO_2 by getting oxygen from or pumping oxygen into gas streams. Oxygen pressures and therefore activities can also be measured or established in solid metals and alloys or in liquid metal baths [4].

It may be noted that initial states of oxidation, that is, the formation of oxygen adsorption structures on Ni and on Fe, could be studied using an electrochemical cell (Fig. 3) for establishing defined oxygen activities in and on a metal sample [29]. The electrochemical cell was mounted in an ultrahigh vacuum (UHV) system and could be heated so that adsorption isotherms and surface structures could be determined by Auger electron spectroscopy (AES) and low-energy electron diffraction (LEED). In another study [30], the surface composition of wustite FeO was measured as a function of E and ln pO_2 at high temperatures 720–900 °C.

Sulfur pressure The following cell is suitable to control the chemical potentials and activities of silver and sulfur in Ag_2S [31]:

$$\mathrm{Pt|Ag|AgI|Ag_2S|Pt}$$

Through AgI as cationic conductor, Ag^+ ions can be transferred to and from the sulfide Ag_2S,

$$\mathrm{Ag = Ag^+(in\ Ag_2S) + e^-} \qquad (10)$$

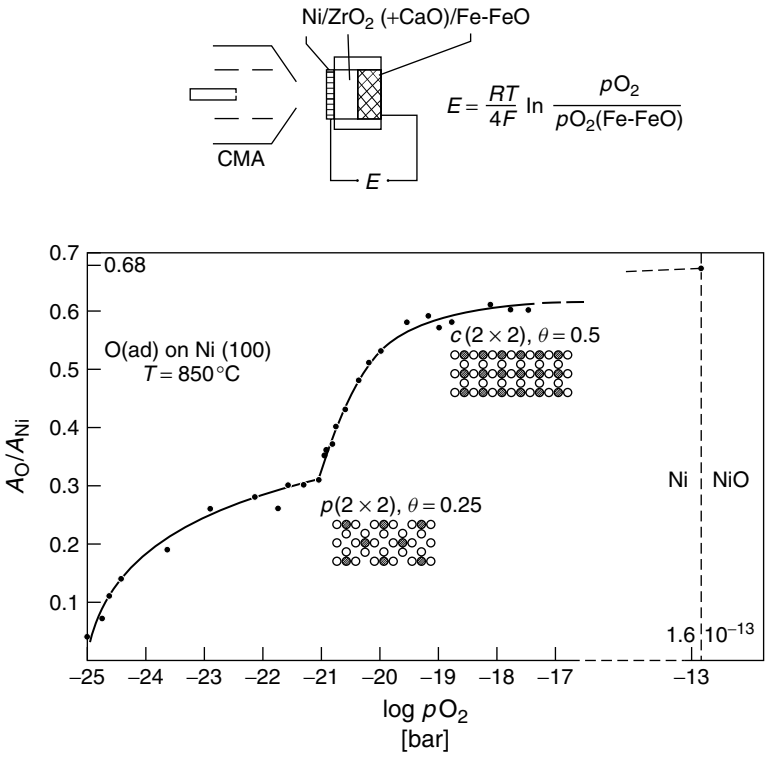


Fig. 3 Use of a solid electrolyte cell $Ni/ZrO_2(+CaO)/Fe\text{-}FeO$ to measure the oxygen adsorption isotherm on a Ni single crystal at 850 °C by AES (adsorption structures obtained from LEED), step isotherm approaching the coverages 0.25 and 0.5 at free energies −260 kJ mol^{-1} O and −220 kJ mol^{-1} O [29, 30].

the Gibbs energy of this reaction is given by

$$\Delta G = \mu_{Ag}(Ag_2S) - \mu^{o}_{Ag} = -EF \quad (11)$$

and the silver activity in Ag_2S can be derived from

$$a_{Ag} = \exp\left(\frac{-EF}{RT}\right) \quad (12)$$

Since the chemical potentials of Ag and S are coupled by the Gibbs–Duhem equation, one can derive that

$$a_S = -\exp\frac{2(E - E^{o})F}{RT} \quad (13)$$

where E^{o} is the electromotive force (emf) of the cell corresponding to equilibrium with liquid sulfur.

6.2.2 Nonstoichiometry and Defect Structure of Oxides and Other Corrosion Products

After formation of a dense film, separating gas phase and metal, transport processes must be possible in the film for continued growth. In a rigid ordered lattice, transport of particles would be impossible and scale growth would not be possible. In all solid compounds, however, there is a certain disorder caused by interstitials

and vacancies in the lattice, which enable solid-state diffusion. The defect structures and diffusion will be summarized in the following for ionic crystals since oxidation, sulfidation, and chloridation, and so on mostly form ionic crystals. For denotations of the defects, somewhat modified symbols according to Kröger are used.

6.2.2.1 Cation-deficient Oxides

The oxidation products of the base metals of most alloys are cation-deficient oxides: for example, NiO, FeO, CoO, and Cu_2O. These will be discussed in turn.

6.2.2.1.1 **NiO** Studies of nonstoichiometry, electrical conductivity, and thermoelectric power [32–35] have shown that NiO is a metal deficient, p-type semiconductor, that is, vacancies exist in the cation sublattice and are compensated by positive holes h^+, corresponding to Ni^{3+} ions. The electric conductivity is proportional to the concentration of positive holes $[h^+]$; NiO is accordingly a p-conductor. The reaction for the incorporation of excess oxygen into the lattice is

$$\tfrac{1}{2}O_2(g) = O_O^x + {V_{Ni}}^{2-} + 2h^+ \qquad (14)$$

where O_O^x is a normal oxygen ion on an oxygen site, and ${V_{Ni}}^{2-}$ is a vacancy on a nickel site, which carries a 2− charge in relation to the normal lattice. The law of mass action can be applied to this dilute solution, with the activity of normal oxygen ions equal to unity

$$K = \frac{[{V_{Ni}}^{2-}][h^+]^2}{(pO_2)^{1/2}}$$

$$\text{and with } [h^+] = 2[{V_{Ni}}^{2-}]$$

$$\text{results } [h^+] \approx (pO_2)^{1/6} \qquad (15)$$

Accordingly, the conductivity of pure NiO was found to be proportional to $(pO_2)^{1/6}$ at temperatures >850 °C [34] (Fig. 4a).

The electrical properties of NiO, doped with monovalent ions (Li^+) and trivalent ions (Ga^{3+}, Cr^{3+}) have been studied quite extensively. The study of Cr-doped NiO is of particular interest for understanding the oxidation behavior of Ni−Cr alloys. When trivalent Cr ions are introduced into a NiO crystal, the electrical compensation could occur by formation of doubly ionized nickel vacancies, according to

$$Cr_2O_3 = 2{Cr_{Ni}}^{+} + 3O_O^x + {V_{Ni}}^{2-} \qquad (16)$$

where ${Cr_{Ni}}^{+}$ represents a Cr ion on a Ni site with a +1 charge relative to the normal site occupation. Since $[{Cr_{Ni}}^{+}] = 2[{V_{Ni}}^{2-}]$:

$$[h^+] \approx \frac{(pO_2)^{1/4}}{[{Cr_{Ni}}^{+}]^{1/2}} \qquad (17)$$

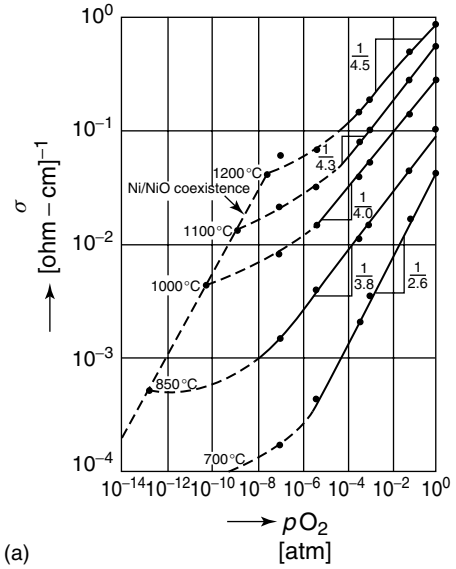
In fact, the conductivity of NiO doped with Cr is proportional to $(pO_2)^{1/4}$ at temperatures >850 °C and decreases with the Cr content, if the $NiCr_2O_4$ solubility is not exceeded [34].

Upon doping NiO with an oxide of a monovalent metal, for example, Li_2O, the lithium cation occupies sites in the cation lattice and this defect has a negative charge relative to the normal lattice. Doping with Li_2O may increase the number of electron holes, or decrease the concentration of ${V_{Ni}}^{2-}$:

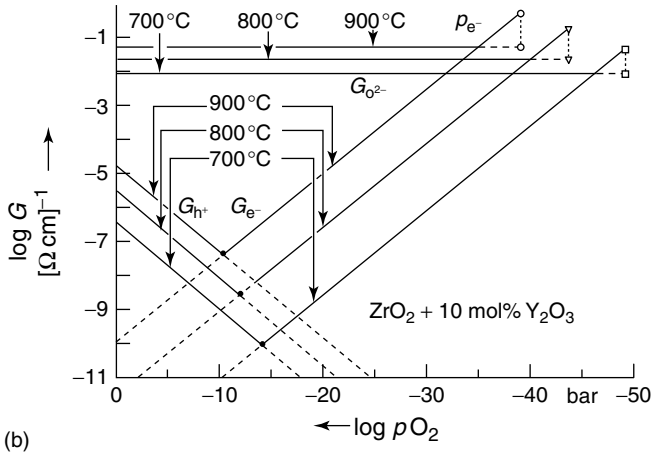
$$Li_2O = 2{Li_{Ni}}^{-} + O_O^x + 2h^+ \qquad (18a)$$

$$Li_2O + {V_{Ni}}^{2-} = 2{Li_{Ni}}^{-} + O_O^x \qquad (18b)$$

Accordingly Li doping enhances the conductivity of Ni, but decreases the cation diffusivity since cation vacancies are annihilated. Correspondingly, Cr doping



(a)



(b)

Fig. 4 Conductivities of semiconducting oxides in dependence on the oxygen pressure: (a) of a pure NiO single crystal, σ increasing with pO_2, approximately $\sim (pO_2)^{1/4}$, at low oxygen pressure contribution by excess electrons [34]; (b) of ZrO_2 + 10 mol Y_2O_3, at low oxygen pressure increasing electronic conductivity by electrons σ_{e^-} and at high oxygen pressure, contribution of electronic conductivity by defect electrons σ_{h^+}; through the doping with Y_2O_3 ionic conductivity prevails – but without doping a very low-conductivity results at intermediate oxygen pressures!

enhances the cation diffusivity, and these doping effects on diffusivity should affect the growth rate of oxide scales by cation diffusion. These ''Wagner–Hauffe'' doping effects have been studied and confirmed for $NiO + Cr_2O_3$ and $NiO + Ag_2O$ [36].

6.2.2.1.2 **CoO** Measurements of the electrical conductivity of CoO as a function of oxygen partial pressure [37, 38] show that the same vacancy model applies as for NiO up to $pO_2 \sim 10^{-5}$ bar. For higher oxygen pressures, it was found $\sigma \sim (pO_2)^{1/4}$, which indicates formation of singly charged vacancies

$$\tfrac{1}{2}O_2 = O_O^x + V_{Co}{}^- + h^+ \qquad (19)$$

Corresponding results were obtained in a recent study [39] using a very pure CoO single crystal. Measurements at 1000–1300 °C temperature and pO_2 led to a model in which free electron holes are considered and electron holes trapped by cation vacancies. The latter configuration corresponds to the singly charged vacancy; its lifetime could be estimated to be twenty times larger than the residence time of an electron hole on a cation site.

Oxidation studies [40] showed that, in CoO, singly charged and neutral vacancies are the prevailing species. The latter cannot be detected by conductivity measurements, but affect the cation diffusivity, according to

$$\tfrac{1}{2}O_2 = O_O^x + V_{Co}$$
$$D_{Co} \approx [V_{Co}] \approx p(O_2)^{1/2} \qquad (20)$$

6.2.2.1.3 **FeO** As a measure of nonstoichiometry, the value of y in $Ni_{1-y}O$ is rather small: 2.75×10^{-4} at 1200 °C and 0.21 bar O_2 [35]. The corresponding values for $Co_{1-y}O$ are considerably higher: about 0.01 at 1150 °C and 1 bar O_2, up to 0.14 for wustite $Fe_{1-y}O$ at 1300 °C [41]. The phase field of wustite could be studied using a solid-state electrochemical cell [42].

$$Pt/Fe,\ Fe_{1-y_1}O/ZrO_2 + CaO/Fe_{1-y}O/Pt$$

varying the composition of $Fe_{1-y}O$ by coulometric titration and measurements of the equilibrium cell voltage. The defects in wustite correspond to those in NiO and CoO, that is, cation vacancies and electron holes. However, because of the high-defect concentration, occurrence of complexes, for example, of two cation vacancies and one Fe^{3+} interstitial, have been assumed, and existence of three wustite regions has been proposed, separated by order-disorder transitions [42]. The most important consequence of the high-vacancy concentration is the high-iron self-diffusivity [43], resulting in high-oxide growth rates.

An electrochemical method could be applied to measure chemical diffusion in wustite [44], using the solid electrolyte cell:

$$pO_2, Pt/ZrO_2 + Y_2O_3/Fe_{1-y}O/Pt, N_2$$

At first, the relation of the emf E of this cell and the stoichiometric composition of the wustite sample was measured by coulometric titration. Then galvanostatic or potentiostatic measurements of the relaxation curves for oxidation or reduction of the wustite samples were obtained and the chemical diffusivities determined. The values are consistent with those obtained from tracer diffusion measurements, considering thermodynamic and correlation factors. As already mentioned, surface compositions of wustite were also measured by AES, using an electrochemical cell to establish the oxygen activities [28] (see section on Oxygen Pressure).

6.2.2.1.4 **Cu_2O** For Cu_2O, the conductivity is proportional to about $p(O_2)^{1/7}$ in the temperature range 800–1000 °C [45]. Thus, Cu_2O is a p-conductor and oxygen can be inserted in the lattice according to

$$\tfrac{1}{2}O_2 = O_O^x + 2V_{Cu}{}^- + 2h^+ \qquad (21)$$

which leads to

$$K = \frac{[V_{Cu}{}^-]^2[h^+]^2}{p(O_2)^{1/2}} \quad [h^+] = [V_{Cu}{}^-] \qquad (22)$$

and $\sigma \approx [h^+] \approx p(O_2)^{1/8}$ for this oxide, in approximate agreement with the experimental result [45]. *Transference numbers* have also been determined by a simple experiment [45]: a Cu-foil was contacted at its ends with Pt-wires and the foil was oxidized at high temperature to Cu_2O. After that, a high dc-current was passed through the oxide for a long time and then the foil was fractured in its middle and the two parts weighed. In this experiment, Cu^+-ions are transferred into the cathode part of the sample causing a mass increase, which can be used for calculation of the cation transference number: $t_{Cu^+} = 5.2 \times 10^{-4}$ at 1000 °C. Thus, only a little part of the current is transported by cations, the electron conductivity (by defect electrons) is prevailing: $t_{e^-} \cong 1$. In fact, the electrical properties σ and t_i of oxides, important for the oxidation behavior of metals, have been determined only in rare cases. Mostly diffusivities were studied.

6.2.2.2 Cation-excess Oxides

6.2.2.2.1 **ZnO** Zinc oxide can lose oxygen at high temperatures [46] according to

$$ZnO = \tfrac{1}{2}O_2 + Zn_i{}^+ + e^- \qquad (23a)$$

or

$$ZnO = \tfrac{1}{2}O_2 + Zn_i{}^{2+} + 2e^- \qquad (23b)$$

In these reactions, a zinc cation enters an interstitial site either with one or with two positive charges. Writing the mass action law for reaction (23a)

$$K = (pO_2)^{1/2}[Zn_i{}^+][e^-]$$

$$\text{where} \quad [Zn_i{}^+] = [e^-] \qquad (24)$$

one obtains for the oxygen pressure dependence of the conductivity, which is proportional to the concentration of free electrons

$$\sigma \approx [e^-] \approx (pO_2)^{-1/4} \qquad (25)$$

In the case of reaction (23b), the oxygen pressure dependence should be given by

$$\sigma \approx [e^-] \approx (pO_2)^{-1/6} \qquad (26)$$

In fact, conductivity measurements [46] gave exponents between $-1/4.5$ and $-1/5$ in dependence on temperature and pO_2, so that both defect equilibria (a) and (b) are valid.

The addition of a lower valent oxide to ZnO

$$Li_2O + 2e^- + \tfrac{1}{2}O_2 = 2Li_{Zn}{}^- + 2ZnO \qquad (27a)$$

or

$$Li_2O = 2Li_{Zn}{}^- + 2Zn_i{}^+ + \tfrac{1}{2}O_2 \qquad (27b)$$

decreases the concentration of free electrons and increases that of interstitial zinc ions. The addition of a higher valent oxide

$$Zn_i{}^+ + Al_2O_3 = 2Al_{Zn}{}^+ + e^- + ZnO \qquad (28a)$$

or

$$Al_2O_3 = 2Al_{Zn}{}^+ + 2e^- + 2ZnO + \tfrac{1}{2}O_2 \qquad (28b)$$

increases the concentration of free electrons and decreases that of interstitial zinc ions [46].

6.2.2.2.2 **TiO_2 and ZrO_2** Interstitial cations most probably are also the prevailing

defects in rutile TiO_2, the defect equilibrium being described by

$$\text{Zero} = {Ti_i}^{4+} + 4e^- + O_2(g) \qquad (29)$$

where zero represents the perfect stoichiometric crystal TiO_2.

Mass action law and electroneutrality condition lead to

$$K = [{Ti_i}^{4+}][e^-]^4(pO_2) \quad 4[{Ti_i}^{4+}] = [e^-] \qquad (30)$$

thus, the electrical conductivity should be

$$\sigma \sim [e^-] \sim (pO_2)^{-1/5} \qquad (31)$$

and conductivity measurements [47] between 944 and 1205 °C yielded for the exponent: $-1/4.24\ldots\ -1/4.7$ indicating that also trivalent Ti-ions are present in the interstitial sites. That the defects are interstitial cations was confirmed by transference studies by the Tubandt method [47]. Three sintered TiO_2 tablets were pressed together and a dc-current between 100 and 400 mA was passed for 10–12 h at 3.4×10^{-13} bar O_2. After this experiment, the tablets were separated and weighed. The mass of the tablet at the cathode increased and the mass of the anodic tablet decreased. The transference numbers in the temperature range 842–982 °C were determined to be about $1–3 \times 10^{-4}$ for the interstitial Ti^{4+} and Ti^{3+} ions. At high temperatures, >977 °C and low pO_2 gravimetric studies indicate the existence of oxygen vacancies in TiO_2 with a concentration proportional to $(pO_2)^{-1/6}$, which corresponds to the defect equilibrium

$$\text{Zero} = {V_O}^{2+} + 2e^- + \tfrac{1}{2}O_2(g) \qquad (32)$$

with the mass action law

$$K = [{V_O}^{2+}][e^-]^2(pO_2)^{1/2} \quad 2[{V_O}^{2+}] = [e^-] \qquad (33)$$

leading to $\sigma \sim e^- \sim (pO_2)^{-1/6}$.

A corresponding defect reaction occurs for ZrO_2 at low (pO_2) and high temperatures, whereas ZrO_2 becomes a p-conductor at high (pO_2) (Fig. 4b). A most important ceramic is ZrO_2 doped with CaO, MgO, or Y_2O_3. The doping oxides suppress the temperature-dependent transformations of ZrO_2 and stabilize the cubic high-temperature modification. In addition, the lower valent cations introduced by doping cause a fixed concentration of oxygen vacancies, according to

$$CaO + Zr_{Zr}^{x} + O_O^{x} = {Ca_{Zr}}^{2-} + {V_O}^{2+} + ZrO_2 \qquad (34)$$

These oxygen vacancies confer an ionic conductivity to $ZrO_2 + CaO$, which is used in many applications, especially for measurement and control of oxygen pressures (see Sect. 6.2.1.2.2). For this purpose, solid electrolyte cells are used for which the voltage results from Nernst's law

$$E = \left(\frac{RT}{4F}\right) \ln\left[\frac{p'(O_2)}{p''(O_2)}\right] \qquad (35)$$

where R is the gas constant, F Faraday's constant and $p'(O_2)$ the oxygen pressure to be measured, and $p''(O_2)$ a reference oxygen pressure. Air is often used as reference and sometimes metal/metal oxide mixture, so here $p''(O_2)$ is given by the formation pressure of the oxide.

6.2.2.3 Chromia and Alumina

The stable modifications α-Cr_2O_3 and α-Al_2O_3 both have the corundum structure and are closely stoichiometric; deviations from stoichiometry as a function of pO_2 could not be observed. Many steels and high-temperature alloys rely on the formation of slow-growing Cr_2O_3 or Al_2O_3 as a major component of the oxide scale [1, 2].

6.2.2.3.1 **Cr_2O_3** Cr_2O_3 is a semiconductor with an ionic conductivity as calculated from self-diffusion that is 10^{-3}–10^{-5} times the electronic conductivity [48]. Two regions are distinguished [49]: (1) a low-temperature range at which conductivity depends on doping and pO_2, and (2) a high-temperature range at which conductivity is independent of pO_2. The high-temperature conductivity at $>1250\,^{\circ}C$ is intrinsic, due to excitation of carriers across the forbidden gap or caused by self-defect semiconductivity (Eigenstörstellen–Halbleitung) that can be written:

$$Cr_{Cr}^{x} = V_{Cr}{}^{3-} + Cr_i{}^{2+} + h^{+} \qquad (36)$$

This or similar processes lead to an electronic conductivity at high T, which is independent of pO_2, as observed. Doping with acceptors such as Mg, Cu, Ni, or Li increases the hole conductivity according to, for example,

$$Cu_2O + O_2 = 2Cu_{Cr}{}^{2-} + 4h^{+} + 3O_O^{x} \qquad (37)$$

Doping with donors such as W, Ti, Nb, or V leads to n-type conductivity at low pO_2, but p-type behavior after annealing in air.

Self-diffusion and rates of oxidation [49] creep and sintering are dependent on the presence of ionic defects in Cr_2O_3. The self-diffusion of oxygen is much slower than that of chromium. However, recent data [50, 51] are 4–7 orders of magnitude lower than previously published data, which were dominated by dislocation and grain boundary effects. The new data, obtained for single crystals, show a dependence on pO_2 corresponding to the reaction

$$\tfrac{3}{2}O_2 = 3O_O^{x} + 2V_{Cr}{}^{3-} + 6h^{+} \qquad (38)$$

At $1100\,^{\circ}C$, and at low pO_2, the diffusion data suggest diffusion of Cr interstitials formed according to

$$Cr_2O_3 = \tfrac{3}{2}O_2 + 2Cr_i{}^{3+} + 6e^{-} \qquad (39)$$

from which $D_{Cr}^{*} \approx (pO_2)^{-3/16}$ is expected. This defect equilibrium had been assumed to be predominant by Kofstad [2, 52] and he had calculated k_p from Wagner's theory using the earlier D_{Cr}^{*} data. The calculation rendered values in the experimentally observed range of k_p. However, this agreement appears to be fortuitous, considering the more recent diffusion studies. Most probably, both in the oxidation studies, and in the diffusion studies, the same fast diffusion paths, grain boundaries, and dislocations determine the processes. The rate of oxidation is limited by the fastest moving ion with an activation energy of about 245 kJ mol^{-1}, close to that of Cr tracer diffusion in hot pressed oxide. In the $Cr_i{}^{3+}$ model, oxidation is governed by diffusion between the interface Cr/Cr_2O_3 where $[Cr_i{}^{3+}]$ is large and the surface Cr_2O_3/O_2 where it is small at any pO_2. Therefore, the rate should be independent of pO_2, yet a dependence proportional to $(pO_2)^{3/16}$ has been found [2, 52] corresponding to a defect equilibrium

$$\tfrac{3}{4}O_2 = \tfrac{3}{2}O_O^{x} + V_{Cr}{}^{3-} + 3h^{+} \qquad (40)$$

Oxidation of Cr leads to scales of different morphologies. Thin flat films grow by volume diffusion only. Thicker polycrystalline films are wrinkled, as a result of compressive stresses, attributed to growth at grain boundaries, by volume diffusion of Cr and grain boundary diffusion of oxygen.

6.2.2.3.2 **Al_2O_3** Al_2O_3 has a band gap of about 9.9 eV and is an insulator at room temperature [49]. Concentrations of defects formed by electronic or ionic disorder are extremely small, conductivities and diffusivities in most studies on Al_2O_3

have been governed by impurities. Acceptors are Mg, Fe, Co, Ni, and V, donors are Ti, Si, H, and Y. Ionic and electronic transference numbers have been obtained from measurements of emf in an oxygen concentration cell [53]

$$\mathrm{Pt, O_2|Al_2O_3|Pt, O_2}$$

Combination with the conductivity data gives partial ionic and electronic conductivities as $f(p\mathrm{O_2})$. The conductivities usually show a minimum at about 10^{-4} bar O_2. In acceptor-dominated material, the conductivity is electronic (by holes) at high $p\mathrm{O_2}$ and ionic at low $p\mathrm{O_2}$. In donor-dominated material, the conductivity is electronic at low $p\mathrm{O_2}$ and ionic at high $p\mathrm{O_2}$. Oxidation-reduction of Al_2O_3 with Fe as impurity is described by:

$$\tfrac{1}{2}\mathrm{O_2} + 2\mathrm{Fe_{Al}}^{-} + \mathrm{V_O}^{2+} = \mathrm{O_O^x} + 2\mathrm{Fe_{Al}^x} \tag{41}$$

Oxidation–reduction of Al_2O_3 containing Ti is described by:

$$\tfrac{3}{4}\mathrm{O_2} + 3\mathrm{Ti_{Al}^x} = 3\mathrm{Ti_{Al}}^{+} + \mathrm{V_{Al}}^{3-} + \tfrac{3}{2}\mathrm{O_O^x} \tag{42}$$

Calculations of defect formation energies [49] suggest that Schottky disorder

$$0 = 2\mathrm{V_{Al}}^{3-} + 3\mathrm{V_O}^{2+} \tag{43}$$

is the dominant ionic disorder process. However, in Al_2O_3, oxygen diffuses slower than aluminum [49, 54, 55] suggesting that $[\mathrm{V_O}^{2+}] < [\mathrm{Al_i}^{3+}]$ and prevailing Frenkel disorder, if not the mobility of $\mathrm{Al_i}^{3+}$ is much higher than that of oxygen vacancies. In any case, the ionic defects are the major defects, electronic defects being the minority species.

Self-diffusion experiments show that grain boundary diffusion of oxygen is faster than bulk diffusion [54, 55], whereas for Al, these processes are about equally fast. Measurements of dc conductivity as a function of grain size show that there is no preferential ionic conductivity at the grain boundaries [56]. Therefore, the rapid oxygen grain boundary diffusion that has been observed must involve neutral species. According to oxygen pressure dependence of oxidation–reduction processes, neutral, atomic $\mathrm{O_i^x}$ is the species diffusing at grain boundaries.

6.2.2.4 Sulfides

There are great differences in the electrical properties and disorder for the sulfides of interest, as typical examples manganous sulfide MnS, silver sulfide Ag_2S, iron sulfide FeS, and nickel sulfide NiS are described here. In this sequence, the degeneracy of electrons increases, corresponding to a transition to metallic conductivity.

6.2.2.4.1 Manganous Sulfide

Nonstoichiometry and defect concentrations are very low in $\mathrm{Mn_{1-y}S}$; of the order of that in nickel oxide. The predominant defect equilibrium is

$$\tfrac{1}{2}\mathrm{S_2} = \mathrm{V_{Mn}}^{2-} + 2\mathrm{h}^{+} + \mathrm{S_S^x} \tag{44}$$

Thus, it is a metal-deficit, p-type semiconductor in a wide range of sulfur activities. Only at very low $p\mathrm{S_2}$ near the Mn/MnS equilibrium it is a metal-excess, n-type semiconductor with doubly ionized interstitial cations and quasi-free electrons [57, 58]. The growth of MnS proceeds by outward diffusion of cations, being the rate-determining step of manganese sulfidation. The low nonstoichiometry is the reason the MnS growth is several orders of magnitude slower than that of other transition metal sulfides [59, 60].

In a recent paper, sulfidation kinetics of Mn–Li and Mn–Cr alloys have been studied [61], and the doping effects have

been found as to be expected: Li decreasing the rate since the concentration of V_{Mn}^{2-} is decreased and Cr increasing the rate since the cation vacancy concentration is increased in the mixed sulfides formed.

6.2.2.4.2 **Ag_2S** Silver sulfide can attain a small metal excess, $y \sim 0.0025$ at 300 °C. The relatively small Ag^+ ions are distributed statistically on many sites in the rigid S^{2-} lattice, and are very mobile. Therefore the activity and chemical potential of the Ag^+ ions is virtually constant at varied chemical potential of Ag. The variation of μ_{Ag} can be conducted in an electrochemical cell:

$$Ag/AgI/Ag_2S$$

by electrochemical titration [31] since AgI is a ionic conductor for Ag^+ ions. Little changes of stoichiometry are correlated to strong changes of $\mu_{Ag} = \mu_{Ag}^{\circ} - EF$ where E is the cell voltage measured and μ_{Ag}° corresponds to $a_{Ag} = 1$, that is, equilibrium Ag/Ag_2S [31]. The conclusion is that the strong change of the chemical potential of μ_{Ag} is caused by its electronic part:

$$\mu_{Ag} = \mu_{Ag^+} + \mu_{e^-} \qquad (45)$$

that is, the thermodynamics of Ag_2S is determined by the concentration of free electrons, which could be determined by measuring the electronic conductivity [13, 31].

The electronic conductivity σ_e increases proportional to the deviation from stoichiometry y, but for high values of y and σ_e, there is a deviation caused by the beginning of electron degeneracy, that is, transition from Boltzmann- to Fermi–Dirac-statistics. The ion conductivity in Ag_2S is much smaller than σ_e, so it could be measured by using AgI/Ag-probes [13]. Because of the disorder and mobility of the Ag^+ ions, σ_{Ag^+} is independent of stoichiometry and chemical potential of Ag.

6.2.2.4.3 **FeS and NiS** The high-temperature modification of ferrous sulfide $Fe_{1-y}S$ has a wide composition range up to $y \approx 0.11$, similar to wustite $Fe_{1-y}O$. Equilibration in H_2S-H_2 mixtures leads to continuous isotherms $y \sim (pS_2)^{1/n}$ where n varies between 2 and 8. This result cannot be explained by a simple defect structure [62, 63]. In addition, the conductivity has metallic character, according to its magnitude and its decrease with increasing temperature. Overlapping 3d and 4s bands are responsible for the metallic conductivity, which shows a minor increase with sulfur activity, linear with the deviation y from stoichiometry [64].

The equation for the defect equilibrium

$$\tfrac{1}{2}S_2 + 2e^- = V_{Fe}^{2-} + S_S^x \qquad (46)$$

would lead to $[V_{Fe}^{2-}] \approx (pS_2)^{1/2}$ if the activity of electrons is assumed to be constant. This relation is valid only in the range $10^{-2} < y < 10^{-1}$, and the enhancing increase of pS_2 with y can be considered as being caused by repulsive interactions between the cation vacancies [64]. Similar considerations are valid for the high-temperature modification of nickel sulfide [65, 66].

6.2.3 Mechanisms and Kinetics of High-temperature Scale Formation

6.2.3.1 Surface Reaction Control (Linear Rate Law)

After a continuous dense layer has formed in the oxidation of metals or alloys, the oxidant (O, S, Cl, etc.) must be transferred

by some surface reaction to the surface of the layer. Oxygen is transferred mainly by three reactions

$$CO_2(gas) = CO\ (gas) + O\ (in\ the\ oxide) \quad (47)$$

$$H_2O\ (gas) = H_2(gas) + O\ (in\ the\ oxide) \quad (48)$$

$$O_2(gas) = 2O\ (in\ the\ oxide) \quad (49)$$

6.2.3.1.1 **Linear Oxidation in CO_2–CO Mixtures** The first of these reactions is relatively slow and can be rate determining for long periods of time and considerable thicknesses of the oxide layer, for example, in the oxidation of iron to wustite [11, 69–73], which will be described in more detail.

The following reaction steps describe the mechanism:

$$CO_2(gas) = CO_2(ads) \quad (50a)$$

$$CO_2(ads) + 2e^- = {CO_2}^{2-}(ads) + 2h^+ \quad (50b)$$

$${CO_2}^{2-}(ads) = O^{2-}(in\ the\ oxide) + CO(gas) \quad (50c)$$

In the second step, negatively charged CO_2(ads) is formed by electron transfer from the solid [12, 30], its decomposition is the rate-determining step. A rate equation was proven:

$$\frac{dn_O}{A dt} = k_1 {a_O}^{-m} pCO_2 - k_1' {a_O}^{1-m} pCO \quad (51)$$

$$j = k_1 {a_O}^{-m} pCO_2 \left(1 - \frac{k_1' a_O}{\frac{k_1 pCO_2}{pCO}}\right) \quad (52)$$

The rate of oxygen transfer per unit area is described by terms for the forward and the backward reaction, including the rate constants and dependencies on the oxygen activity a_O present on the surface, which in equilibrium with the given CO_2–CO mixture would be

$$(a_O)_{eq} = \frac{k_1}{k_1'} \frac{pCO_2}{pCO} = K_1 \frac{pCO_2}{pCO} \quad (53)$$

A general rate equation for oxidation and reduction results

$$j = k_1 {a_O}^{-m} pCO_2 \left(1 - \frac{a_O}{(a_O)_{eq}}\right) \quad (54)$$

Oxidation occurs if the oxygen activity on the surface is lower than in the gas phase, reduction takes place in the reverse case [69–71]. This rate equation is composed of two terms: an exchange velocity comprising the dependencies on temperature, partial pressures, and activities

$$j^o = k f(p_i) f(a_O) \quad (55)$$

and a term describing the distance from equilibrium. The "exchange velocity" of the oxygen transfer from CO_2 could be measured in equilibrium CO_2–CO–FeO, using an isotope-exchange reaction [12, 70], the result (Fig. 5)

$$j_O^o = k_1 {a_O}^{-2/3} pCO_2 \quad (56)$$

(at >900 °C) indicates participation of two electrons from the solid oxide in this reaction as formulated in the reaction mechanism, given above. At lower temperatures, increasing values of the exponent m are caused by increasing coverage with O(ads), as confirmed by AES-studies in which the oxygen activity of the FeO was varied by using a solid electrolyte cell [30].

The "linear" oxidation of metals, determined by the surface reaction that delivers oxygen from the gas phase and rate Eq. (54), can be applied to describe the

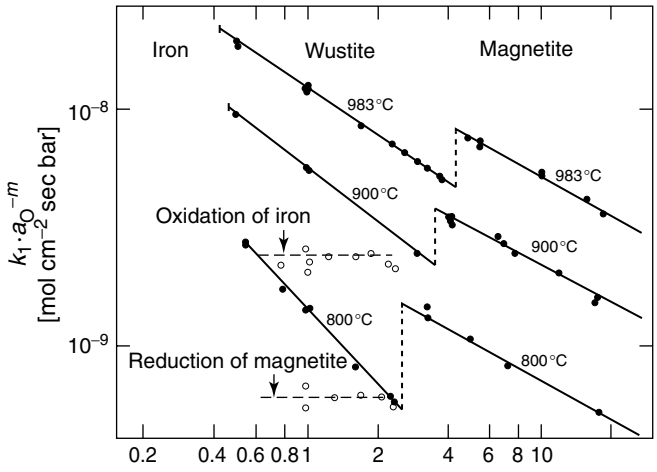


Fig. 5 Oxygen exchange rate coefficients $k(a_O) = k_1 a_O^{-m}$ measured by isotope-exchange method [12, 69–72] at surfaces of wustite and magnetite in gas–solid equilibrium, and during the oxidation of iron to wustite, or during the reduction of magnetite to wustite.

oxidation of iron to wustite in CO_2-CO mixtures. For a long time and considerable thickness of the oxide film (~100 μm), the wustite surface is in near-equilibrium with iron, since the diffusion processes in wustite are so fast (see Sect. 6.2.2.1.3) that is, $a_O \cong a_O(\text{Fe, FeO})$ and the rate coefficient $k_1 a_O^{-m}$ is practically constant. Accordingly, the isotope exchange measurement yielded constant values during the oxidation of iron to wustite; and also during the reduction of magnetite, the rate coefficient was constant corresponding to equilibrium wustite/magnetite (Fig. 5).

The situation during the oxidation was illustrated also by measuring the emf during the oxidation of an Fe-foil, fixed on a plate of $ZrO_2 + CaO$, versus a reference electrode [73] (Fig. 6). The iron foil is held at first in a nonoxidizing CO_2-CO mixture, then at $t = 0$, it is changed to an oxidizing CO_2/CO ratio. After adsorption of O(ad) and nucleation of FeO, the emf is constant at the value for equilibrium Fe–FeO, until at t_B the thin foil (5 μm) is oxidized thoroughly. Then the oxygen activity of the wustite rises and the emf decreases. From t_B the rate constant could be calculated [73], which corresponded well to results of the isotope exchange studies [12]. In the oxidation of thicker iron samples, the equilibrium metal-oxide cannot be maintained and the oxygen activity on the surface slowly decreases. This causes the slow decrease of oxidation rate, observed in several studies of oxidation in CO_2-CO [10–12, 74–77].

In principle, the rate equations for surface reaction kinetics are "linear" and describe a linearly time-dependent growth of the corrosion layer. However, during this growth the oxygen activity on the surface increases and gradually approaches the value for equilibrium of gas phase and oxide surface. Because of the dependence on a_O with a negative exponent, the rate gradually decreases, and several authors have misinterpreted this kinetics as "parabolic kinetics" (see Sect. 6.2.3.2).

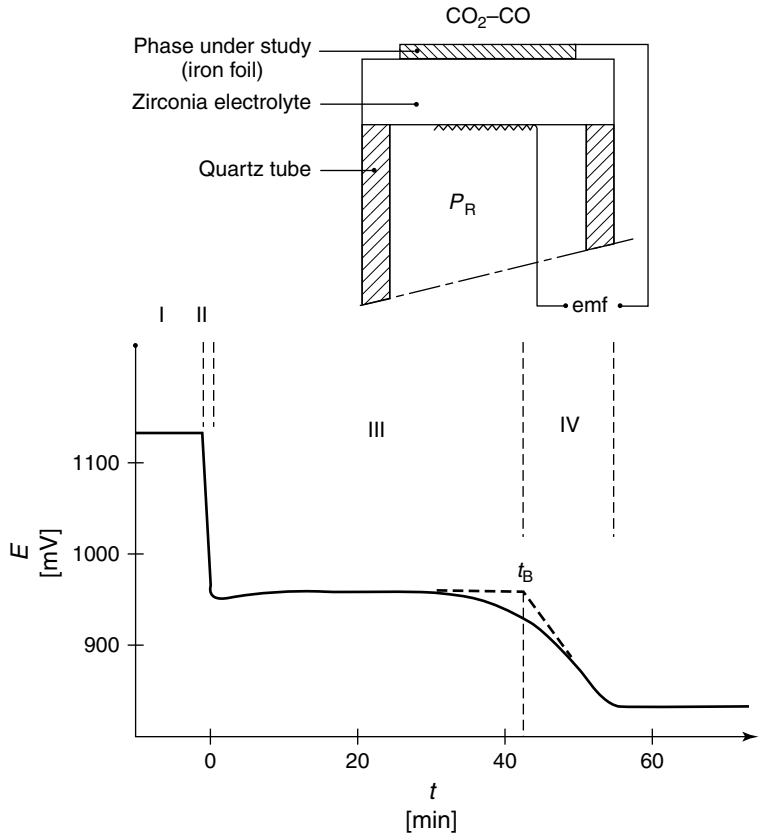


Fig. 6 Use of a solid electrolyte cell for measurement of oxygen transfer reactions [78]: (a) schematic setup and (b) emf versus time curve for the oxidation of an iron foil (5 µm) in CO_2-CO at 960 °C, periods: I Fe in reducing gas, II nucleation of Fe, III oxidation Fe → Fe till consumption of Fe, IV equilibration of FeO.

6.2.3.1.2 **Linear Oxidation in H_2O-H_2 Mixtures** In the reaction sequence of the oxygen transfer from H_2O, reaction (48), either the dissociation of H_2O(ads) or of OH(ads), is rate determining and its exchange velocity is given by

$$j^o = k_2 a_O{}^{-n_1} p H_2O$$

or by

$$j^o = \frac{k_2' a_O{}^{-n_2} p H_2O}{(p H_2)^{1/2}} \qquad (57)$$

These velocities are higher by a factor of about 10^2 than the values for oxygen transfer in reaction (47), thus oxidation by H_2O and reduction by H_2 are much faster than these reactions in CO_2-CO [69, 71].

6.2.3.1.3 **Linear Oxidation in O_2** The oxygen transfer by dissociation of O_2, reaction (49) appears to be even faster than oxygen transfer from H_2O. To measure the rate of oxygen transfer from molecular O_2 to and into oxide surfaces. Wagner initiated relaxation measurements on Cu_2O and NiO [79]. Another possibility

are isotope-exchange studies using $^{16}O_2$ and $^{18}O_2$ [80], and here an electrochemical method should be mentioned [81] in which a test electrode covered with oxide was brought in single point contact with a $ZrO_2 + Y_2O_3$ electrolyte (Fig. 7a). Current-potential measurements were made in air at 1000 °C. The test electrode materials markedly affect the shape and the hysteresis of the polarization curves and the electrochemical reactions of oxygen are differently catalyzed by the electrode materials (Fig. 7b). Also impedance measurements had been conducted, but no clear conclusions were drawn on the oxygen reactions.

6.2.3.1.4 **Linear Sulfidation in H_2S-H_2** Owing to the high disorder and diffusivities in many sulfides, sulfidation is often controlled by phase boundary reactions. The surface reactions of oxidation in H_2S and reduction in H_2 have been studied on Ag_2S [82] at 300 °C using the electrochemical cell Ag|AgI|Ag_2S|Pt. As described in Sect. 6.2.2.3.2, the chemical potential of Ag in Ag_2S is given by

$$\mu_{Ag} = \mu^{\circ}_{Ag} - EF \qquad (58)$$

and can be fixed by applying a constant voltage E. Removal of S by reduction is accompanied by transfer of Ag^+ through the AgI to Ag, and the current measured corresponds to the rule of reduction. Upon sulfidation at constant E, the current for supply of Ag into Ag_2S is measured. It can be concluded [82] that electrons take part in the reaction:

$$H_2S(g) + 2e^-(\text{in } Ag_2S) = H_2S(g) + S^{2-}(ad) \qquad (59)$$

since the forward reaction rate is strongly dependent on the applied potential. It will be shown that the Ag_2S growth can be affected also by the reaction at the inner phase boundary, that is, by the transfer of Ag^+ ions from Ag to the sulfide [15].

The surface reaction is rate controlling also for the sulfidation of iron in H_2S-H_2 mixtures. Up to large thicknesses of the $Fe_{1-y}S$ formed the rate equation was found [83]:

$$\frac{dn_S}{A dt} = k\frac{pH_2S}{a_S} - k' pH_2 \qquad (60)$$

The forward reaction is retarded with increasing sulfur activity, probably due to adsorbed sulfur, since the electrons in $Fe_{1-y}S$ are highly degenerated and a_{e^-} is independent of a_S.

6.2.3.2 Bulk Diffusion Control–Parabolic Kinetics

6.2.3.2.1 **Transition from Linear to Parabolic Kinetics** When thermodynamic equilibrium is nearly established at the surface and also at the oxide/metal interface, oxidation is virtually controlled by diffusion in the solid oxide. For oxides such as FeO, NiO, CoO, Cu_2O, and so on with cation vacancies V_M as the prevailing defects, the growth occurs by outward flux of cations and inward flux of vacancies, both fluxes are equal and given by

$$j_M = -j_V = D_V\frac{c''_V - c'_V}{x} = \frac{k'}{x} \qquad (61)$$

where x is the oxide thickness, D_V the diffusion coefficient of cation vacancies, and c''_V and c'_V are the vacancy concentrations at the gas/oxide and oxide/metal interfaces, respectively.

Equation (61) can be rewritten and integrated

$$V_{Oxide}\frac{dx}{dt} = \frac{k'}{x} \qquad x^2 = 2kt \qquad (62)$$

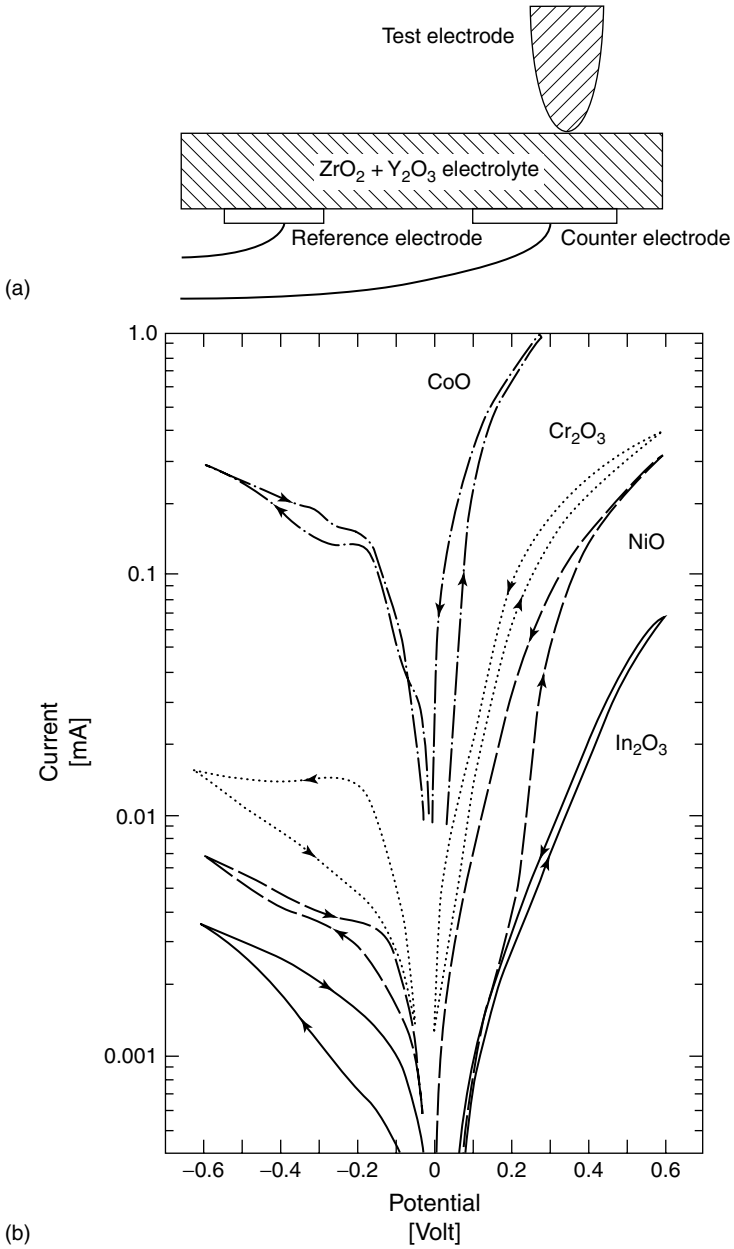


Fig. 7 Oxides as catalysts for oxygen reactions on zirconia electrolyte: [81] (a) schematic of the polarization cell, (b) polarization behavior of single contact electrodes.

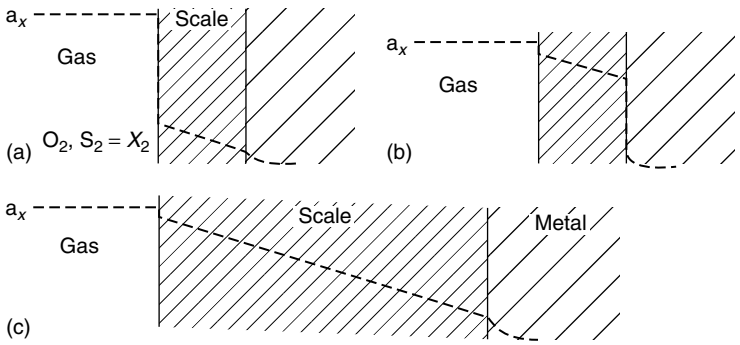


Fig. 8 (a) Schematics of the development of the activity steps and gradients of nonmetal activity in a growing scale; (b) initial states when either a surface reaction or an interfacial reaction is rate controlling (''linear'' kinetics); and (c) state after continued corrosion, near-equilibrium established at the phase boundaries (parabolic kinetics).

which leads to the well-known parabolic rate law.

It has been shown before that the cation vacancy concentration in equilibrium with the atmosphere for the oxides discussed is given by $c_V = \text{const.}\ (pO_2)^{1/n}$. Accordingly, the variation of the parabolic rate constant with the oxygen partial pressure results:

$$k \infty [(pO_2'')^{1/n} - (pO_2')^{1/n}] \tag{63}$$

where the latter pO_2' generally is constant.

The transition between linear surface reaction controlled kinetics and parabolic bulk diffusion-controlled kinetics certainly must be gradual. This transition could be observed very well for the case of the oxidation of iron in CO_2-CO mixtures to wustite [10, 11] and was described by Wagner. For this special case, the mathematical description was derived from the fact that the flux of oxygen transfer to the FeO surface must be always equal to the flux of Fe transported to the surface by diffusion needed for the formation of the nonstoichiometric $Fe_{1-y}O$:

$$j_O = \frac{j_{Fe}}{(1-\delta)} \tag{64}$$

$$k_1 {a_O}^{-2/3} pCO_2 \left(1 - \frac{a_O}{\left(\frac{K_1 pCO_2}{pCO}\right)}\right) = (c_V'' - c_V') \frac{D_V}{x} \tag{65}$$

With increasing thickness x of the oxide layer, the difference $(c_V'' - c_V')$ increases, that is, the driving force in the process is needed for the diffusion in the oxide. On the other hand, the oxygen activity on the wustite surface approaches equilibrium with the atmosphere $a_O \rightarrow K_1(pCO_2/pCO)$, that is, the oxygen transfer needs only a lessening part of the thermodynamic driving force (Fig. 8).

Equation (65) demonstrates that decreasing rates are to be expected in the transition from linear to parabolic kinetics. Therefore, the kinetics of oxidation, sulfidation, and so on cannot be exactly linear, even in the start of reaction, but the rate must decrease. This decreasing ''linear'' rate often has been misinterpreted, for example, in

the oxidation of Mn in CO_2-CO [74] and in the sulfidation of Fe in H_2S-H_2 [84].

6.2.3.2.2 **Wagner's Theory of Oxidation**

A more general approach was given by Wagner [7–9, 67, 68] relating the parabolic rate constant to the ionic conductivities, σ_i, and diffusivities of cations and anions in the scale. In the growing scale, a force is acting on an ion or electron with the charge z_i, which results from the chemical potential gradient $d\mu_i/dx$ and the electric potential gradient $d\phi/dx$, and causes movement at a constant drift velocity.

The drift velocity u_i in cm s^{-1} of particles of the type i in the direction of the x-axis is given by

$$u_i = -B_i \left(\frac{1}{N_A} \frac{d\mu_i}{dx} + z_i e \frac{d\Phi}{dx} \right) \qquad (66)$$

Here, B_i is the mobility, that is, the steady state velocity under unit force per particle, corresponding to a change of chemical potential per particle by unit energy for a displacement of unit length. Further N_A is Avogadro's number, e is the electronic charge, and z_i the electrical valence of a particle of type i. It follows that the flux in moles migrating per unit cross-section A per unit time equals:

$$\frac{dn_i}{A dt} = c_i u_i = -B_i c_i \left(\frac{1}{N_A} \frac{d\mu_i}{dx} + z_i e \frac{d\phi}{dx} \right) \qquad (67)$$

where c_i is the concentration in moles per unit volume. The mobility B_i is related to ionic conductivity σ_i and to the self-diffusion coefficient of particles D_i.

$$\sigma_i = z_i^2 F^2 c_i B_i \qquad (68)$$

$$D_i = B_i RT \qquad (69)$$

Using the relation to transport number and conductivity, Wagner derived the equation for the rate of formation of an oxidation product oxide, sulfide, or halide:

$$\frac{dn}{A dt} = \frac{1}{\Delta x} \frac{1}{z_2 F^2} \int_{\mu_x'}^{\mu_x''} \frac{(\sigma_1 + \sigma_2)\sigma_3}{\sigma_1 + \sigma_2 + \sigma_3} d\mu_x \qquad (70)$$

$$\frac{dn}{A dt} = \frac{1}{\Delta x} \frac{1}{z_2 F^2} \int_{\mu_x'}^{\mu_x''} (t_1 + t_2) t_3 \sigma \, d\mu_x = \frac{k_r}{\Delta x} \qquad (71)$$

where, $dn/A dt$ is the rate of both outward migrating cations and inward migrating anions (moles s^{-1}), Δx is the instantaneous thickness of the reaction product (cm), z_2 is the charge number of the anions, μ_x is the chemical potential of the oxidizing nonmetal, μ_x'' and μ_x' are its chemical potentials at the outer surface and the inner interface of the scale, σ is the electrical conductivity of the scale, σ_1, σ_2, and σ_3 the cationic, anionic, and electronic conductivities, and t_1, t_2, and t_3 the transference numbers of these species, respectively. According to these equations, the "rational rate constant" k_r can be calculated from data for the ionic and electronic conductivities in solids, which, however, are not easily determined (see Sect. 6.2.2).

In the case of oxidation, the parabolic rate constant can be expressed in terms of electrical parameters in the following form:

$$k_p = \frac{RT}{4F^2 c_2} \int_{pO_2'}^{pO_2''} (t_1 + t_2) t_3 \sigma \, d\ln pO_2 \qquad (72)$$

The limits of integration are the activities of O_2 at the metal/oxide interface pO_2' and the oxide gas interface pO_2''. In most oxides of interest, the ionic conductivity is very much less than the electronic conductivity

$$(t_1 + t_2) \ll t_3 = 1 \qquad (73)$$

and it is more convenient to cast Eq. (66) in a form that includes the most readily accessible parameters, that is, the tracer self-diffusion coefficients of the cations D^*_M and of the anions D^*_O

$$k_p = \int_{pO_2'}^{pO_2''} \left(\frac{z_1}{z_2} \frac{D^*_M}{f_M} + \frac{D^*_O}{f_O} \right) d \ln pO_2 \tag{74}$$

In this equation, f_M and f_O are the correlation factors for the cation and oxygen ion self-diffusion mechanisms, respectively, and are of the order of unity. Evaluation of k_p from Eq. (74) merely requires that data exist for the self-diffusion coefficients D^* as function of pO_2.

The electric field that develops during oxidation is an important feature of the process. It is the difference in electrostatic potential across the film,

$$\phi'' - \phi' = \frac{RT}{4F} \int_{'}^{''} t_{ion} \, d \ln pO_2 + \frac{1}{F}(\mu_e'' - \mu_e') \tag{75}$$

where μ_e is the chemical potential of an electron. The measurement with electronically conducting electrodes (Pt) yields the difference in the electrochemical potential of the electrons between electrodes ''and'', that is,

$$V_e = \frac{RT}{4F} \int_{pO_2'}^{pO_2''} t_{ion} \, d \ln pO_2 \tag{76}$$

If t_{ion} is independent of oxygen pressure, this equation can be integrated to give

$$V_e = -\frac{\Delta G(MO_\nu)}{2F\nu} t_{ion} \tag{77}$$

where $\Delta G(MO_\gamma)$ is the free energy of formation of the oxide MO_ν.

The potential measured using electrodes that conduct ions is given by

$$V_{ion} = \frac{\Delta G(MO_\nu)}{4F\nu} t_e \tag{78}$$

The electrostatic potential difference $\phi'' - \phi'$ is thus of the order $\Delta G(MO_\nu)/F$ and typically a few volts.

6.2.3.2.3 **Diffusion-controlled Growth of Some Oxides** The growth of some specific oxides is described in this section. The oxides have been selected either because they can be considered as model oxides (CoO, NiO) or because they are important in the corrosion of low-alloy steels (Fe_3O_4, Fe_2O_3) or as slow-growing oxides (Cr_2O_3, Al_2O_3) attributing corrosion resistance to high-temperature alloys [1, 2].

SiO_2 is another slow-growing oxide, which attributes corrosion resistance to high-temperature materials such as SiC, Si_3N_4, and $MoSi_2$. At lower temperatures, the growth of insulating SiO_2 films is of great importance for electronic devices. However, up to very high temperatures, the growth of SiO_2 is prevailingly by interstitial diffusion of neutral molecules, O_2 or H_2O in the amorphous scale [85], so SiO_2 growth is not an electrochemical process and not a topic for this encyclopedia. There are results [86, 87] indicating that going to very high temperatures, $>1400\,^\circ C$, the ionic conductivity and contribution in transport during SiO_2 growth increases, but these processes are not fully understood as yet [88].

CoO CoO is a p-type electronic conductor and is metal deficient (see Sect. 6.2.2.1.2). The cation vacancy concentration increases with the oxygen pressure.

The Co diffusivity is several orders of magnitude greater than that of oxygen.

Cobalt diffusion measurements of different workers [89, 90] are in good agreement and show that at 1200 °C, diffusion is by singly charged vacancies at high oxygen activity and doubly charged vacancies at low oxygen activity. Most oxidation studies have been conducted at high temperatures and for thick films, so that Wagner's theory should be valid. The tracer diffusion studies have shown that $D^*_{Co} \approx (pO_2)^{1/4}$. Equation (74) can be integrated to give $k_p = 5.1\ D^*_{Co}$, where the diffusion coefficient is that at the oxide/gas interface ($f = 0.78$ for a vacancy mechanism). The agreement with the most recent data for k_p [91] is excellent at the high temperatures (5 %), somewhat less at the lower temperatures (Fig. 9). The dependence of k_p on pO_2 is in agreement with the tracer diffusion studies. As the temperature is lowered, the oxygen pressure dependence of k_p changes from $\sim p(O_2)^{1/4}$ to $\sim p(O_2)^{1/3.3}$ at 950 °C. This is consistent with a contribution from uncharged cation vacancies at the lower temperature. The growth of CoO on Co at temperatures 950–1300 °C is the best example for the validity of Wagner's theory.

NiO In the case of nickel oxidation, integration of Eq. (74) gives $k_p = 6.4\ D^*_{Ni}$ where the diffusion coefficient is that at the oxygen activity of the oxide/gas interface. The reported values for k_p are in agreement with the diffusivity data only above ~1200 °C. At lower temperatures, they show great scatter and are generally higher than expected for bulk diffusion control. The scatter has been explained by effects of metal impurities (doping the oxide), surface conditions, and crystal orientation. At high temperatures,

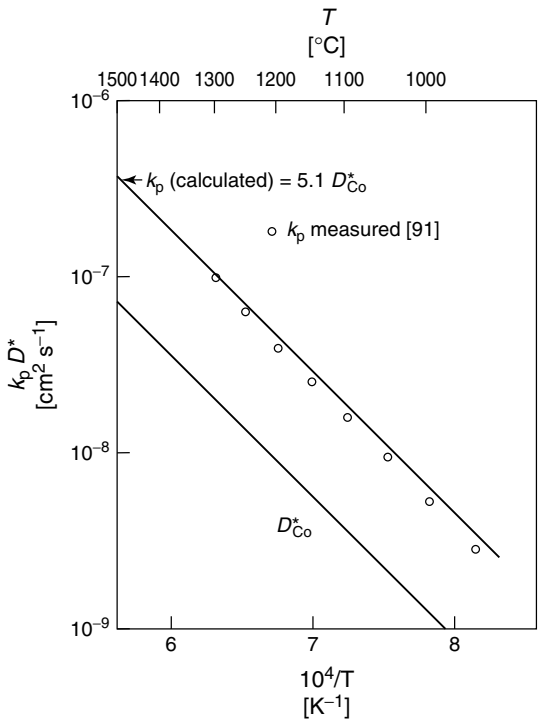


Fig. 9 Arrhenius-plot of the parabolic rate constant measured for the growth of CoO on Co in air [91] compared with that calculated from Wagners' theory and the tracer diffusion coefficient D^*_{Co} for Co in CoO [89, 90].

>1200 °C, the values for k_p measured [92] and calculated from D^*_{Ni} are in reasonable agreement and $k_p \sim (pO_2)^{1/n}$ with $3.5 < n < 6$ [92]. The higher values of k_p in the lower-temperature range are caused by fast diffusion at oxide grain boundaries [93–95]. Data for diffusion along grain boundaries and along dislocations have been determined, which could be used to predict k_p when grain boundary diffusion prevails:

$$k_p = 6.4\left(D^*_{Ni} + \frac{z(D'\delta)^*}{g}\right) \qquad (79)$$

where D' is the grain boundary diffusion coefficient, δ the effective width of the grain boundary (~1 nm) and g is the grain size in the oxide film (determined by transmission electron microscopy). Measurements and calculations of k_p with Eq. (79) for the temperature range 500–800 °C, oxide films of 0.3–30-μm thickness and grain sizes 0.15–1.4 μm were in excellent agreement. The grain growth during oxidation leads to a deviation from parabolic kinetics, that is, a time dependence with $n < 0.5$. The oxidation kinetics of Ni thus can be explained by the Wagner theory when modified to include grain boundary diffusion.

ZrO_2, TiO_2, Ta_2O_5, and so on For the growth of CoO and NiO, it could be assumed that the same defects prevail in the whole scale between surface and oxide/metal interface. This assumption cannot be true for the more stable oxides, where the oxygen activity varies from about 1 bar to about 10^{-40} bar O_2, for example, in the case of ZrO_2 at 1000 °C. At the surface at high pO_2, ZrO_2 will be a p-type conductor $\sigma_{h^+} \approx (pO_2)^{1/4}$. At the oxide/metal interface, ZrO_2 will be an n-type conductor $\sigma_{e^-} \approx (pO_2)^{-1/4}$. Both electronic conductivities decrease to the inner part of the scale. Throughout the whole scale a low ionic conductivity is given by O^{2-} diffusion via anion vacancies. However, the very low electronic conductivity in the center of the scale limits the oxidation rate. This consequence was clearly shown by an experiment [96] in which the surface of the ZrO_2 scale was short-circuited to the underlying Zr-metal with a Pt wire. The oxidation rate is markedly increased by this short-circuit (Fig. 10). The kinetics change from a cubic rate law, $\Delta m \approx t^{1/3}$, to the normal parabolic kinetics and the parabolic constant is given by

$$k_p = \frac{-\Delta G^o}{2F^2}\sigma_{ion} \qquad (80)$$

Inserting the oxygen ion conductivity and ΔG^o of ZrO_2 formation results in a value that is in good agreement with the measured one.

Similar situations can be expected for other oxidation reactions, for example, in the oxidation of Ti, Nb, Ta, and so on, even more complex situations, since mostly multilayers of different oxides should be formed. The growth of oxides involving zones with different disorder and insufficient electronic conduction, however, has not been studied and discussed satisfactorily as yet [2]. One reason may be that most of these oxides do not form dense compact oxides, but tend to crack and spall, due to growth by inward oxygen diffusion and a high ratio of the molar volumes of the oxide and metal (Pilling–Bedworth ratio).

Cr_2O_3 In the oxidation of high-alloy steels and other high-temperature alloys, Cr_2O_3 is the most important constituent of protective oxide films. Its formation is

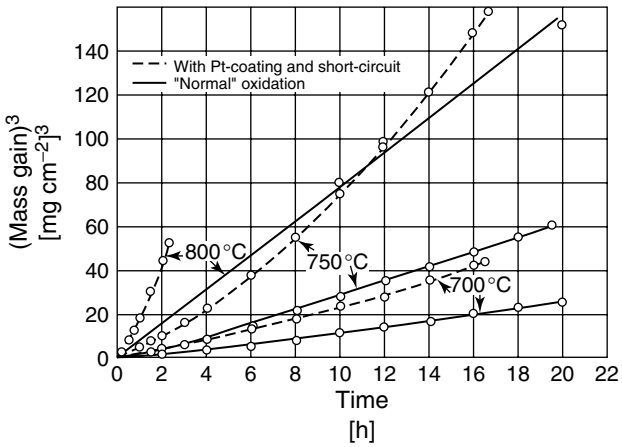


Fig. 10 Kinetics of Zr oxidation in oxygen (1 bar) at different temperatures, with short-circuit the kinetics are accelerated and the rate low changes from a cubic to the parabolic law [96].

affected by many complications such as the volatilization of CrO_3 and $CrO_2(OH)_2$ at high temperatures and high pO_2, loss of contact between metal and oxide and cracking and blistering of the film. Thus the k_p values for oxidation of Cr show a wide scatter [2] and dependence on the way in which the metal surface was prepared. Cr_2O_3 is a p-type conductor at high pO_2 and low temperatures but is an intrinsic conductor at above ~1200 °C (see Sect. 6.2.2.3.1). Diffusion of Cr in Cr_2O_3 is mainly at grain boundaries and dislocations for polycrystalline oxide.

There have been many studies on lattice diffusion and grain boundary diffusion in single crystal and polycrystalline Cr_2O_3. However, for discussion of Cr_2O_3 growth on Cr and Cr-alloys, these data proved to be too small to account for the oxidation rate [97]. Accordingly, the diffusivities in grown Cr_2O_3 layers must be higher, and some studies were conducted on diffusion of cations and oxygen in such scales [98–100]. At 900 °C values for the lattice diffusion coefficients, D_{Cr}, D_{Fe}, D_{Ni}, and D_O resulted in a range 10^{-15}–10^{-14} cm^2 s^{-1} and grain boundary diffusivities in the range 10^{-12}–10^{-9} cm^2 s^{-1}, whereas lattice diffusivities extrapolated from studies on massive single crystals are $D_{Cr} \approx 2 \times 10^{-21}$ cm^2 s^{-1} and $D_O \approx 1 \times 10^{-19}$ cm^2 s^{-1} and the grain boundary diffusivities are not higher: $\sim 1 \times 10^{-21}$ cm^2 s^{-1}. With the data for grown scales, k_p values were calculated using Eq. (74) for the cases of scale growth by lattice, grain boundary diffusion, and both mechanisms [101] and the result indicates that chromia scale growth is occurring by countercurrent diffusion of chromium and oxygen in lattice and grain boundaries, the latter transport is prevailing. So in fact, Wagner's theory is applicable if the actual lattice and grain boundary diffusivities measured for the growing scale are inserted Eq. (74) results in the measured k_p value. It may be noted that the diffusivity of Mn in chromia scales is clearly faster than that of other cations [100]. As a consequence, an outer layer of $MnCr_2O_4$ is found on the chromia scale of most steels.

Al_2O_3 The growth of Al_2O_3 has been studied on alloys only, since Al metal melts at 660 °C, but its kinetics is of great interest since α-Al_2O_3 is the most protective oxide. At temperatures <1000 °C at first metastable aluminas are formed, but at high temperatures and under the influence of reactive element additions (Y, Ce, La, Ti, etc.), the stable α-Al_2O_3 grows. This oxide has low concentrations and mobilities of intrinsic ionic and electronic defects, so that conductivity and diffusivities are dominated by solute ions, impurities, or dopants.

The electrical properties of growing Al_2O_3 scales have been measured by putting a platinum electrode in contact with the upper side of an oxide layer grown on an alloy. At 1100 °C, the potential difference, V_o, between the two interfaces of the scale were measured at $i = 0$ and the potential–current curve was recorded. Outer oxygen partial pressures in the range 1×10^{-14} bar were applied by using mixtures of O_2, Ar, CO_2, and CO. The oxygen partial pressure in the experimental setup was measured using a zirconia solid electrolyte cell [102–104].

Evaluation according to Eq. (76) leads to $t_{ion} = 0.4$ at low oxygen pressures and $t_{ion} = 0.1$ at higher pressures. Accordingly the scale consists of two parts, an inner zone with considerable ionic transport and an outer zone with high electronic conduction. This leads to an oxygen pressure at the oxide/alloy interface of 2.2×10^{-27} bar O_2, near the expected equilibrium pressure.

Calculation of the rate constant from the electrical data yields a value that is close to the experimental value. This indicates that mainly charged species sustain the α-Al_2O_3 growth.

In an earlier investigation [105] of aluminum scales formed on a Pt–Al alloy, the oxide was shown to behave as a mixed conductor ($t_{ion} \sim 0.5$) down to 10^{-15} bar O_2 and as a majority electronic conductor for lower pressures. The open-circuit voltage was found to decrease from ~1 to ~0.2 V over the first 300 h. If the oxide were an ionic conductor, the open-circuit voltage should have been 2.12 V. Thus, after extended oxidation time, $t_{ion} \sim 0.1$ indicating that the film becomes predominantly an electronic conductor. These data show that a detailed application of Wagner's theory to Al_2O_3 growth is fruitless because of the uncertainties concerning the defect and transport properties of the film. However, values of the "parabolic rate constant" for the growth of Al_2O_3 have been compiled and show a relatively small scatter [106]. Lattice diffusion studies have been conducted (using Cr or Fe for determination of cationic diffusivities), and one can conclude from the data that D^*_{Al} is always greater than D^*_O in the Al_2O_3 and that D^*_{Al} is too small by at least two orders of magnitude to explain the values of k_p measured at high temperature. Grain boundary diffusion of oxygen inward is the most likely transport process controlling the growth of Al_2O_3 films at high temperatures, as can be concluded from $^{16}O_2/^{18}O_2$ tracer experiments and measurements of ^{18}O diffusion in grain boundaries in polycrystalline Al_2O_3 [106] (see Fig. 11 [51]).

Iron oxide scale Oxidation of iron or low-alloy steels at temperatures >570 °C (wustite stable) leads to a scale composed of an inner thick layer of wustite, $Fe_{1-y}O$, and two outer thinner layers of magnetite Fe_3O_4 and hematite Fe_2O_3. The disorder of $Fe_{1-y}O$ has been described in Sect. 6.2.2.1.3, its very high-iron vacancy concentration being the reason for fast outward cation diffusion and rapid growth.

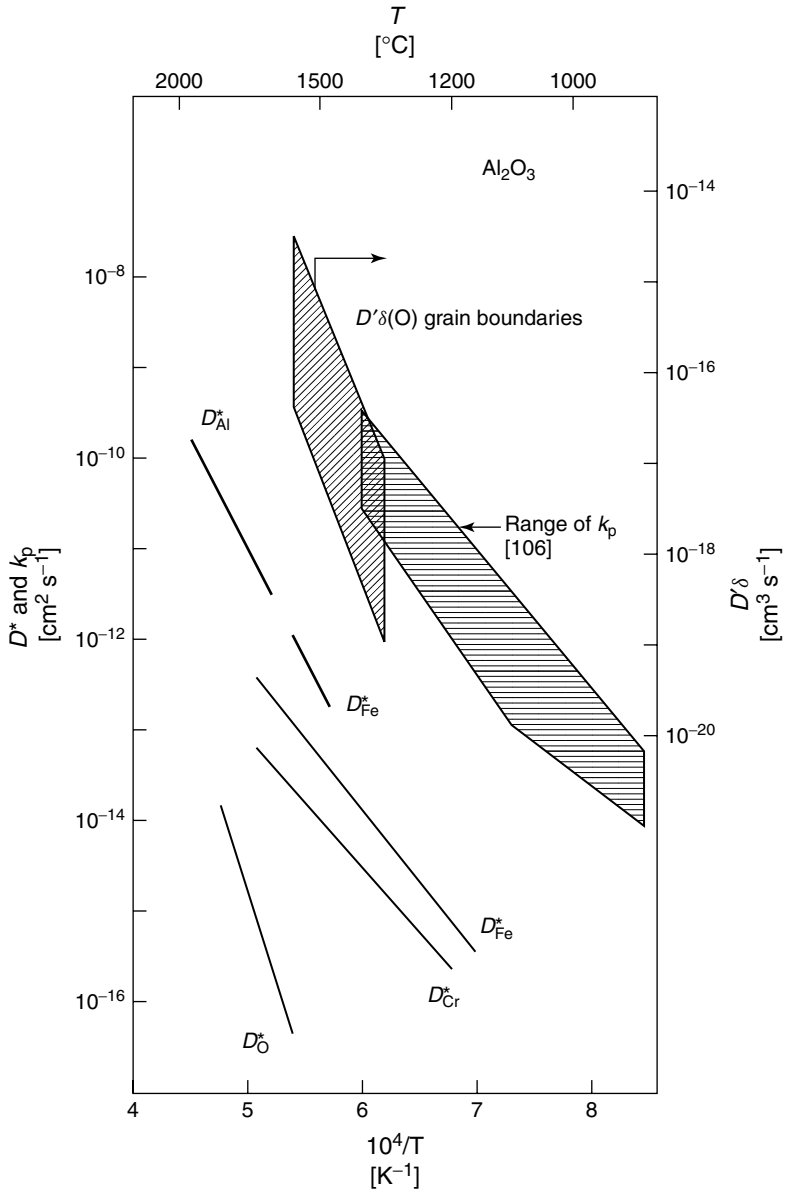


Fig. 11 Arrhenius-plot relating the parabolic rate constant for the growth of Al_2O_3 scales and data for diffusion in Al_2O_3, (the scale for the grain boundary diffusion data at the right has been adjusted, so that if $\delta = 1$ nm, the grain boundary diffusion coefficient corresponds to the bulk diffusion scale) [51].

The gradient of the vacancy concentration, that is, of the deviation from stoichiometry y, proved to be linear. This was shown by controlled electrochemical dissolution of the layer [107–109] at a potential in which only the Fe^{2+} ions are dissolved, an external current supplied electrons e^- for the reduction of the Fe^{3+} ions and thus a measure for y, since $2[V_{Fe}{}^{2-}] = [h^+]$.

The growth of Fe_3O_4 is also by outward diffusion of cations, Fe^{2+} and Fe^{3+}, which can move via free interstitial sites and vacancies in the cationic lattice [110]. The disorder in Fe_2O_3 is very low similar to the case of Cr_2O_3 and Al_2O_3. Outward diffusion of Fe^{3+} and inward diffusion of oxygen are possible, but so slow that the growth of the inner layers could not be sustained. Therefore it is most probable that most of the oxygen needed is transported through the Fe_2O_3 layer by atomic or molecular diffusion through cracks, fissures, and grain boundaries (Fig. 12). Surprisingly, there has been only little recent research on this important system, so that the role of Fe_2O_3 growth is not well understood. Owing to prevailing outward cation diffusion in the scale of iron oxides, a separation of metal phase and wustite can occur. The formation of a gap at the interface can cause the oxidation process to stop. If not, oxygen is transported via this gap by reduction/oxidation reactions that are possible in the presence of CO_2-CO and/or H_2O-H_2 [110, 111].

6.2.3.2.4 Validity Range of Wagner's Theory

Wagner's theory is valid only for the growth of relatively thick films. The Nernst–Einstein relationship and the equation for transport by gradients of chemical and electrical potential (66) are valid only for small electric fields, whereas according to Eqs. (77 and 78) the voltage between the two interfaces of a film can be high. Thus, high electric fields may arise for thin films. Furthermore, in Wagner's theory, one precondition is electrical charge neutrality at every point in the film, whereas space charges will exist near the outer surface due to chemisorption of the oxidizing species and also at the oxide/metal interface [112].

The extent of this space charge is of the order of the Debye–Hückel screening length [113]

$$l_{DH} = \left(\frac{\varepsilon\varepsilon_O kT}{e^2 c_e}\right)^{1/2} \qquad (81)$$

where c_e is the concentration of elementary charges of electronic and ionic defects. For most oxides with typical values of c_e, the space charge regions will extend to less than 1 μm at $>500\,^\circ C$.

One can conclude that for most oxides Wagner's theory is valid for film thicknesses greater than ~1 μm at temperatures $>500\,^\circ C$. In oxides with large concentrations of charged defects, Wagner's theory is valid for films greater than 20 nm in thickness, only for thinner films the electric field is too high.

6.2.4 Theory of Thin Film Growth

Theories of thin film growth must consider jumps in the presence of large electric fields and the possibility of large space charges. Several approaches have been put forward to describe thin film growth, and numerous expressions have been proposed for kinetic laws: logarithmic, inverse logarithmic, cubic, parabolic, and so forth.

6.2.4.1 Theory of Cabrera and Mott

The theory of Cabrera and Mott [114] is widely accepted as a fundamental base

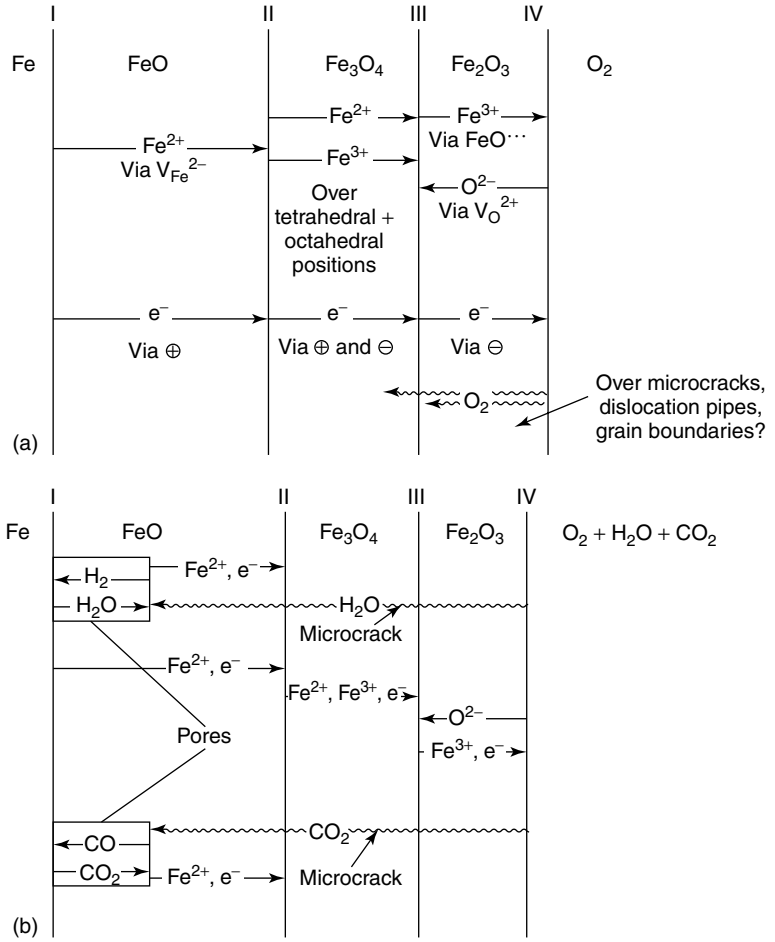


Fig. 12 Schematics of the diffusion processes and phase boundary reactions during the oxidation of iron [110, 111]: (a) in oxygen and (b) in CO_2 and H_2O containing atmospheres.

for discussing thin film growth. Here, it is assumed that electrons can freely pass from the metal to ionize adsorbed oxygen at the oxide surface. A uniform field is created in the film by the negative charge from the excess oxygen ions (O^{2-}) on the oxide/gas interface and the positive surface charge on the metal surface. In the Cabrera–Mott mechanism, it is this field that drives the slow ionic transport across the film and causes its growth.

The free passage of electrons through the film is possible at thicknesses <5 nm by tunneling. For higher thicknesses, it is assumed that the electrons surmount any charge barrier by their thermal energy, corresponding to thermoionic emission.

6.2.4.2 Field Caused by Chemisorption

Grimley [115] has derived an approach to calculate charges and voltages for the case of oxygen chemisorption according to

$$\tfrac{1}{2}O_2(\text{gas}) + 2e^-(\text{metal}) = O^{2-}(\text{surface}) \quad (82)$$

For chemisorption, equilibrium results

$$\frac{a(O^{2-})}{p(O_2)^{1/2}a(e^-)^2} = \exp\left(\frac{-\Delta G^o}{kT}\right) \quad (83)$$

with $a(e^-) = \exp(-e\Delta\phi/kT)$ the activity of electrons. At low surface coverage, the number of excess oxygen anions is given by

$$n(O^{2-}) = N_S p(O_2)^{1/2} \times \exp\left(\frac{-(\Delta G^o + 2e\Delta\phi)}{kT}\right) \quad (84)$$

Regarding surface charge and film as a simple capacitor, one obtains

$$n(O^{2-}) = \frac{\varepsilon\varepsilon_O\Delta\phi}{2ex} \quad (85)$$

and for the electrical potential difference results a dependence

$$\Delta\phi = -\frac{\Delta G^o}{2e} + \frac{kT}{2e} \times \ln\left(\frac{4e^2 N_S p(O_2)^{1/2}x}{kT\varepsilon\varepsilon_O}\right) \quad (86)$$

that is, it mainly depends on the free energy change for the chemisorption (82) but is also dependent on T, $p(O_2)$, and x. The surface excess of oxygen anions calculated from this equation, widely corresponds only to a small fraction of a monolayer.

6.2.4.3 Field Effect on the Reactions at the Metal/Oxide and Gas/Oxide Interfaces

In Wagner's theory, near-equilibrium is assumed at the metal/oxide interface, that is, the frequency of jumps through the interface is about equal in both directions. The presence of the field, however, decreases the activation energy W for the jump of a metal atom into the oxide lattice by an amount $qa\Delta\phi/2x$ (Fig. 13). According to Cabrera and Mott, the interface is far from equilibrium if the field is large enough, and the jumps into the oxide are favored strongly. The condition for the reverse jumps to be negligible is $1/2\ qaE > kT$, which is likely to be true for films less than 20 nm in thickness. Since the interface jump has the highest activation energy, the rate of these jumps determines the film growth rate:

$$\frac{dx}{dt} = a\nu\exp\left(\frac{-W}{kT}\right)\exp\left(\frac{qa\Delta\phi}{2kTx}\right) = \left(\frac{D_i}{a}\right)\exp\left(\frac{x_l}{x}\right) \quad (87)$$

where ν is the vibrational frequency of atoms at the interface, $x_l = qa\Delta\Phi/kT$ and $D_i = a^2\nu\exp(-W/kT)$, having the dimension of a diffusion coefficient.

The rate Eq. (87) describes an oxidation rate that exponentially decreases with film thickness. Integration gives the inverse logarithmic law:

$$\frac{x_l}{x} = -\ln\left(\frac{D_i x_l t}{a x_L^2}\right) \quad (88)$$

where x_L is a limiting thickness at which the growth rate falls below an arbitrary negligible value, according to Cabrera and Mott: 10^{-15} m s^{-1}. The inverse logarithmic rate equation can be rewritten in a simplified version:

$$\frac{1}{x} = A - k_{il}\log t \quad (89)$$

Also, the transfer of defects, metal vacancies, or interstitial oxygen from the surface into an oxide is affected by an electric field. There are some differences in the mechanism, which leads to different constants in the law, but in principle the inverse logarithmic law applies also in this case.

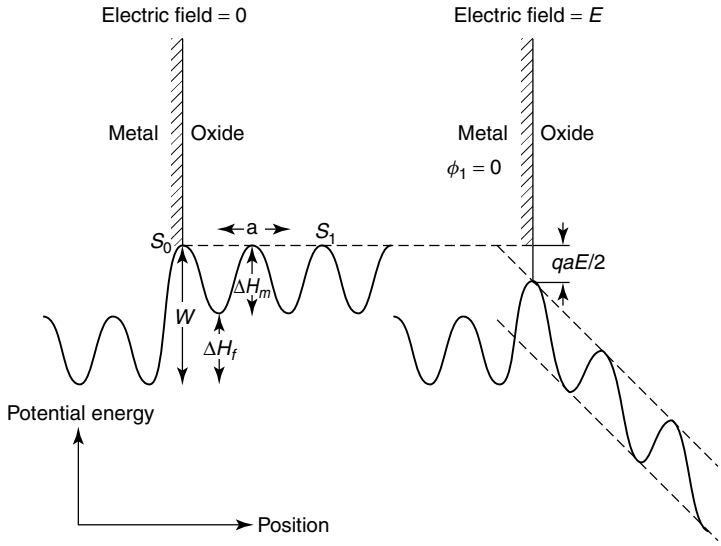


Fig. 13 Schematic diagrams [114], showing the potential energy of a metal ion as a function of position near the metal/oxide interface during thin film growth. The electric field generated by the transfer of electrons to adsorbed oxygen lowers the energy barriers for ions moving away from the metal/oxide interface.

6.2.4.4 Interfacial Reactions During Scale Growth

As pointed out before, the equations derived by Wagner are applicable for bulk diffusion control in the scale, that is, if the reactions at the surface gas/scale and the interface scale metal are approximately in equilibrium. The role of the surface reactions in the growth of FeO on iron, upon oxidation in CO_2-CO or H_2O-H_2 has been pointed out already. However, also the interfacial reactions may play a role.

In the case of prevailing cation diffusion as in the formation of FeO, CoO, NiO, Cu_2O, metal vacancies arrive at the internal interface and are occupied by a metal atom $\underline{M}_M$ from the metal phase, which is ionized when jumping into the oxide lattice:

$$V_M{}^{z-} + z h^+ + \underline{M}_M = M_M^x \qquad (90)$$

In this reaction, the cation vacancies are annihilated at the scale-metal interface. Sometimes, the reaction at the interface is described as vacancy injection, that is, a transfer of cation vacancies to persist as metal vacancies $\underline{V}_M$ in the metal lattice

$$V_M{}^{z+} + z h^+ + \underline{M}_M = M_M^x + \underline{V}_M \qquad (91)$$

In the latter reaction, additional lattice sites are created, so that the vacancies must be annihilated at vacancy sinks, or voids and cavities are created. In the case of prevailing anion diffusion, growth of oxide lattice and consumption of metal lattice occur at the interface

$$\underline{M}^x = \frac{z}{2} V_O{}^{z-} + M_M^x + z e^- \qquad (92)$$

In this reaction, a new unit of oxide results from a direct displacement of the interface and does not involve a jump of metal atoms. But a jump of metal atoms may

take place also, perhaps following some diffusion in the interface,

$$\underline{M}^x = \frac{z}{2}\mathrm{V_O}^{2-} + M_\mathrm{M}^x + z\mathrm{e}^- + \underline{\mathrm{V}}_\mathrm{M} \quad (93)$$

and metal vacancies are created, which must be annihilated. Thus, in both cases reactions occur at the interfaces, which may involve jumps of atoms and annihilation of vacancies. Such processes are possible only by the operations of structural defects, such as disorientation and misfit dislocations. Such defects are generally present at the interface, and their role in enabling vacancy annihilation and progress of oxidation has been emphasized by Pieraggi and Rapp [116, 117]. A general analysis of the scale growth kinetics, considering the steps: (1) surface reaction, (2) diffusion, and (3) internal interfacial reaction has been given [116, 117]. The growth kinetics for the series combination of surface and interfacial steps and of the diffusion step is described by

$$\frac{\mathrm{d}m}{A\mathrm{d}t} = \left(\frac{1}{k_\mathrm{l}} + \frac{2m}{k_\mathrm{p}}\right)^{-1} \quad (94)$$

where the linear constant k_l involves both steps, the surface reaction and the interfacial reaction. Integration leads to

$$t = \frac{\Delta m^2}{k_\mathrm{p}} + \frac{\Delta m}{k_\mathrm{l}} \quad (95)$$

Different initial conditions have to be considered, for example, in the case of transient oxidation of alloys, see

$$t - t_\mathrm{o} = \frac{(m - m_\mathrm{o})^2}{k_\mathrm{p}} + \frac{m - m_\mathrm{o}}{k_\mathrm{l}} \quad (96)$$

and $t - t_\mathrm{o}$ must be introduced instead of t, and $\Delta m - \Delta m_\mathrm{o}$ instead of Δm. Furthermore, considering that anionic and cationic interfacial and diffusion steps occur in parallel during scale growth, the overall growth rate is expressed by

$$\frac{\mathrm{d}m}{A\mathrm{d}t} = \left(\frac{\mathrm{d}m}{A\mathrm{d}t}\right)_a + \left(\frac{\mathrm{d}m}{A\mathrm{d}t}\right)_c = \left(\frac{1}{k_{\mathrm{l}a}} + \frac{zm}{k_{\mathrm{p}a}}\right)^{-1} + \left(\frac{1}{k_{\mathrm{l}c}} + \frac{2m}{k_{\mathrm{p}c}}\right)^{-1} \quad (97)$$

where the indices a and c refer to anionic and cationic growth control, respectively. One can see from Eqs. (94 and 97) that, if one of the interfacial steps is blocked with increasing reaction time, the rate of the overall reaction may decrease due to a decrease in k_l, and the mechanism of oxidation may change between cationic and anionic control. The authors [116, 117] apply plots of $t/(\Delta m/A)$ versus $\Delta m/A$ for evaluation of oxidation studies on Cr and Cr implanted with Y, on Ni−30Cr implanted with different doses of Ce and of Fe−25Cr alloys with deposits of sputtered ceria of different thickness. In all cases, doping leads to decreasing values of k_l and k_p, which was explained by blocking of the cationic interfacial reaction and diffusion. This is one possible explanation of the well-known reactive element effect. According to this "poisoned interface model" (PIM), the scaling of pure metals Fe, Ni, Co, and Cu should also be affected by deposited alkaline earth metals: Ca, Sr, or Ba. In fact, strong retardations of oxidation were observed, indicating that the alkaline earth cations may accumulate at the interface oxide/metal and block the cation transfer.

6.2.4.5 Evidence on the Reactions at the Scale/Metal Interface

Conclusive studies on the role of the transfer reactions at the inner phase boundary are rare. The ΔG necessary for the sulfidation of Ag and Cu could be measured [15, 21]. In the sulfidation of

Ag, the chemical potential of Ag can be measured bringing AgI/Ag-electrodes in contact with the Ag_2S and the Ag (see Sect. 6.2.2.4.2). A current was led through the sequence Pt|Ag|Ag_2S|AgI|Ag|Pt (Fig. 14a). Through this setup, only Ag^+ ions can pass, since AgI is an ion conductor but not an electronic conductor. The difference of electrochemical potential of Ag^+ is measured at the interface Ag|Ag_2S, using the AgI/Ag-probes and, with increasing ion current increasing potential differences were observed (Fig. 14b). The transfer of only electrons, which can be monitored with Pt-electrodes, causes no potential differences and the potential difference caused by simultaneous transfer of Ag^+ ions and electrons is corresponding to the case of only Ag^+ ions. In the transfer of Ag into Ag_2S, the Ag^+ ions occupy interstitial sites in the sulfide:

$$\mathrm{Ag(in\ the\ metal)} = \mathrm{Ag_i^+ + e^- + V_{Ag}} \quad \mathrm{(in\ the\ metal)} \quad (98)$$

A vacancy is created in the metal phase, which can be annihilated by operations of structural defects, disorientation, and misfit dislocations [116, 117]. Prolonged sulfidation also can cause void nucleation and cavity growth at the interface. In the case of sulfidation by liquid sulfur, the separation of sulfide and metal by cavities could be avoided by applying a pressure on the growing sulfide [13–18].

The formation of cavities and of a gap between scale and metal phase was already mentioned for the case of oxide growth by inward migrating vacancies, for example, FeO, where the interfacial reaction is

$$\mathrm{Fe\ (from\ the\ metal)} + \mathrm{V_{Fe}^{2-}} + 2\mathrm{h^+} = \mathrm{Fe_{Fe}^x} + \mathrm{V_{Fe}\ (in\ the\ metal)} \quad (99)$$

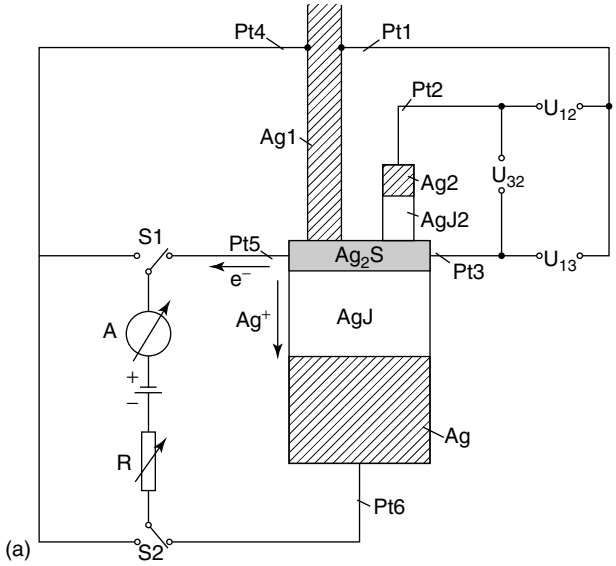
After separation of scale and metal, the scale is converted to the higher oxides Fe_3O_4 and Fe_2O_3 and the oxidation may be completely stopped, if not continued by oxygen transfer through redox reactions of the gases H_2O-H_2 and/or CO_2-CO. The transfer reactions such as reaction (99) will be hindered when impurities accumulate or segregate at the interface; this has been studied for the oxidation of steels [108–110].

In connection with the role of interfacial ledges, and interfacial misfit and misorientation dislocations (see Sect. 6.2.4.4), it was proposed that the ledges and dislocations may be pinned by impurity and doping elements in the metal phase, especially the ''reactive elements'' such as the rare earth elements Ce, Y, La, and so on and Ti, Zr, Hf, and others that generally have a retarding effect on scale growth. This pinning effect would affect the transfer reactions. A new explanation results for the ''reactive element effect'', which is beneficial concerning growth rate and adherence of protective oxide scales. However, it is difficult to prove this effect – and it may be noted that more explanations of the reactive element effect, more or less well proven, were put forward in the oxidation literature.

One may conclude this chapter with the statement that not much is known in fact on the reactions at the interface metal/oxide and new experimental approaches are necessary.

6.2.5
Local Cell Action in High-temperature Corrosion

Mostly, in high-temperature oxidation processes, diffusion of ions or electrons in the solid reaction product are rate determining. Both cases are possible: rate-limiting



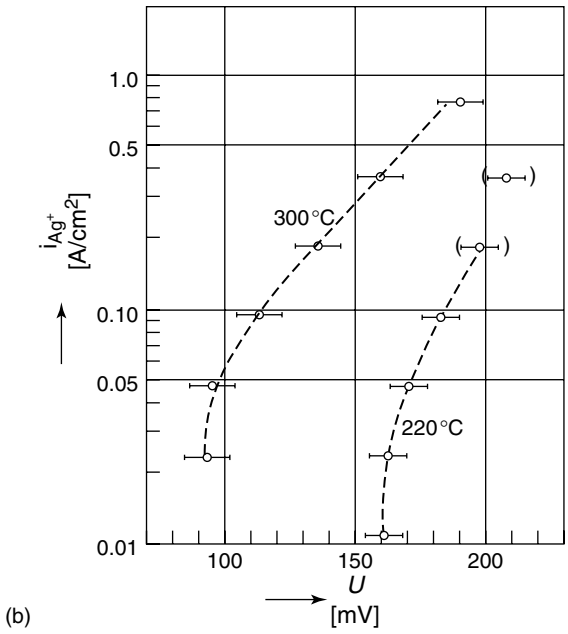


Fig. 14 Measurement of the current density-potential curves for the interfacial reaction $Ag \rightarrow Ag^+$ (in Ag_2S) $+ e^-$ at the phase boundary Ag/Ag_2S. (a) Experimental setup and (b) curves measured at 300 and 220 °C [15].

ion diffusion or rate-controlling electron transport. Corrosion can be enhanced by local cell action if two phases are present, one phase with high ionic conductivity, the other phase with high electronic conductivity. Wagner [118] had put forward examples of local cell action during the scaling of metals.

As an example, for the case that the main product has a high ionic but a low electronic conductivity, and another phase providing easy flow of electrons is present, the following reaction was studied:

$$\mathrm{Ag(s)} + \tfrac{1}{2}\mathrm{I_2(gas)} = \mathrm{AgI(s)} \qquad (100)$$

where solid AgI is mainly a ionic conductor with a high Ag^+ mobility. For the experiment, Ta wires were covered with Ag by immersing their ends in an Ag-melt; these wires were enclosed with iodine in ampoules and heated at 174 °C.

An AgI layer grows not only on the Ag surface, but also spreads along the Ta wire (Fig. 15a) due to diffusion of Ag^+ in the AgI layer and migration of electrons in the Ta wire. The length x of the AgI layer increases proportional to $t^{1/2}$. The flux of Ag^+ ions results mainly from the electrical field, since their chemical potential is virtually constant, due to the high degree of cationic disorder in AgI [119–121], thus

$$j_{\mathrm{Ag^+}} = u_{\mathrm{Ag^+}} c_{\mathrm{Ag^+}} \left(\frac{\partial \Phi}{\partial x}\right) \qquad (101)$$

Wagners' derivation leads to an expression for x

$$x = \left(\frac{4}{\pi}\right)(u_{\mathrm{Ag^+}} E t)^{1/2} \qquad (102)$$

where $u_{\mathrm{Ag^+}}$ is the mobility of Ag^+ ions and $E = -\Delta G^{\circ}/F$ results from the free energy of the formation of AgI. The values measured for x are in excellent agreement with the data calculated from the ionic conductivity and thermodynamic data for AgI.

Similar processes, sidewise growth of chlorides or bromide, are expected also when a wire is partly covered with Ag and exposed to chlorine or bromine gas. But in view of the lower ionic conductivity, that is, lower Ag^+ mobility in AgCl and AgBr, the phenomenon will be less spectacular.

Very high oxidation rates can be expected when an alloy yields a scale consisting of a melt providing fast flow of ions and a solid phase providing easy flow of electrons. A model experiment for such a case was also proposed by Wagner [122]. When Ni is covered by a borate melt, oxidation can take place only by dissolution and diffusion of oxygen in the melt to the metal surface. Low oxygen solubility and therefore slow transport rate result in a very low rate of oxidation, as confirmed, corroding a Ni spiral inserted in $Na_2B_4O_7{\cdot}K_2B_4O_7$ at 780 °C. But when the Ni spiral was connected to a Pt gauze, only partly covered with melt, the mass loss of the Ni by oxidation was about two orders of magnitude higher (Fig. 15b). Obviously, a cathodic reaction occurs at the three-phase boundary air/gauze/melt and oxygen is reduced

$$\mathrm{O_2(g)} + 4\mathrm{e^-} = 2\mathrm{O^{2-}} \qquad (103)$$

The electrons are easily transported to the Ni in the metal gauze, and the oxygen anions are diffusing in the melt to the Ni, where formation of NiO occurs. It was shown also that in a Ni-Pt couple the current is mainly controlled by cathodic polarization.

These results are of great importance considering the oxidation or "hot corrosion" of alloys where the scale consists of electronic conducting oxides and a melt.

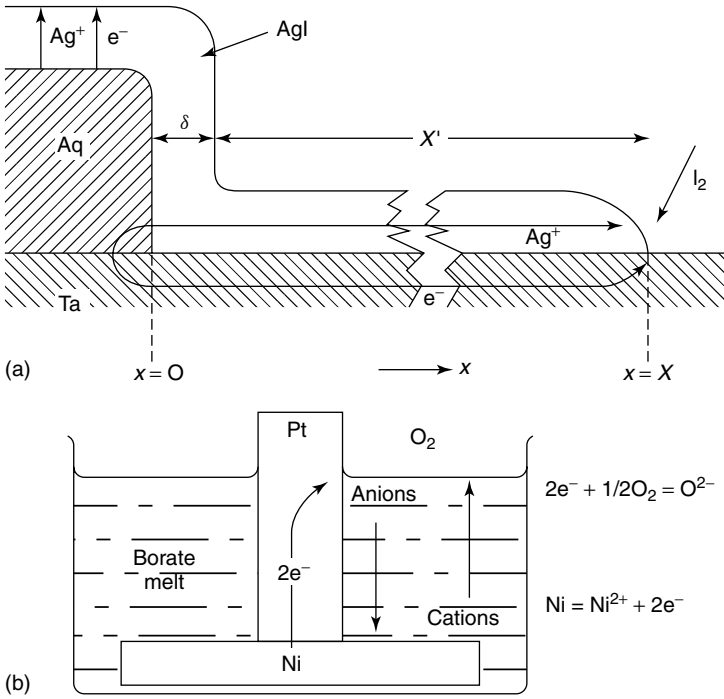


Fig. 15 Local cell action in high-temperature corrosion [118, 122]. (a) Growth of AgI on an Ag—Ta couple in I_2 (gas). (b) Corrosion of Ni in a borate melt, reactions on a Ni—Pt couple.

Local cell action can lead to high oxidation rates, when by close contact of oxides and melt a large area is presented for the cathodic reaction. The oxides provide the fast transport of electrons and the melt the fast transport of ions. Transport of electrons is possible also by cations that are oxidized at the surface of a melt and reduced at the interface melt/alloy, for example, Fe^{2+}–Fe^{3+}, V^{4+}–V^{5+}, and so forth.

These experiments demonstrate again the analogies between the process of electrochemical corrosion and that of gaseous high-temperature oxidation, in both processes ions and electrons must be transported. The transport of both can take place in a scale but also by independent paths, and these processes can be separated similarly as in an electrochemical cell.

References

1. G. Y. Lai, *High-Temperature Corrosion of Engineering Alloys* ASM International, Materials Park OH, 1990.
2. P. Kofstad, *High Temperature Corrosion* Elsevier Applied Science, London, 1988.
3. K. Kiukkola, C. Wagner, *J. Electrochem. Soc.* **1957**, *104*, 308, 379.
4. R. A. Rapp, D. A. Shores, Solid electrolyte cells in *Techniques of Metals Research* (Ed.: R. F. Bunshah), Interscience Publishers, New York, 1970, pp. 123–192.
5. G. Tammann, *Z. Anorg. Chem.* **1920**, *111*, 78.
6. N. B. Pilling, R. E. Bedworth, *J. Inst. Metals* **1923**, *29*, 529.
7. C. Wagner, *Z. Phys. Chem.* **1933**, *21*, 25.

8. C. Wagner, H. Hammen, *Z. Phys. Chem.* **1938**, *40*, 197.
9. C. Wagner, *Z. Phys. Chem.* **1936**, *B32*, 447.
10. F. S. Pettit, R. Yinger, J. B. Wagner Jr., *Acta Metals* **1960**, *8*, 617.
11. F. S. Pettit, J. B. Wagner Jr., *Acta Metals* **1964**, *12*, 35.
12. H. J. Grabke, *Ber. Bunsen-Ges. Phys. Chem.* **1965**, *69*, 48.
13. H. Rickert, *Z. Phys. Chem. N.F.* **1960**, *23*, 355.
14. H. Rickert, C. Wagner, *Z. Phys. Chem. N.F.* **1962**, *31*, 32.
15. H. Rickert, C. D. O'Briain, *Z. Phys. Chem. N.F.* **1962**, *31*, 71.
16. S. Mrowec, H. Rickert, *Z. Phys. Chem. N.F.* **1961**, *28*, 422.
17. S. Mrowec, H. Rickert, *Z. Phys. Chem. N.F.* **1962**, *32*, 212.
18. S. Mrowec, H. Rickert, *Z. Phys. Chem. N.F.* **1963**, *36*, 22.
19. H. Schmalzried, *Z. Elektrochem.* **1962**, *66*, 572.
20. J. W. Patterson, E. C. Bogren, R. A. Rapp, *J. Electrochem. Soc.* **1967**, *114*, 752.
21. H. Rickert, *Werkst. Korros.* **1968**, *19*, 864.
22. G. Holzäpfel, H. Rickert, *Ber. Bunsen-Ges. Phys. Chem.* **1975**, *79*, 1140.
23. H. Rickert, *Electrochemistry of Solids*, Springer, Berlin, 1982.
24. H. Schmalzried, *Z. Phys. Chem. N.F.* **1963**, *38*, 87.
25. R. Taylor, H. Schmalzried, *J. Phys. Chem.* **1964**, *68*, 2444.
26. Y. D. Tretyakov, H. Schmalzried, *Ber. Bunsen-Ges. Phys. Chem.* **1965**, *69*, 396.
27. Y. D. Tretyakov, H. Schmalzried, *Ber. Bunsen-Ges. Phys. Chem.* **1966**, *70*, 180.
28. T. H. Etsell, S. N. Flengas, *Met. Trans.* **1972**, *3*, 27.
29. H. J. Grabke, H. Viefhaus, *Surf. Sci.* **1981**, *112*, 779.
30. H. J. Grabke, H. Viefhaus, *Ber. Bunsen-Ges. Phys. Chem.* **1980**, *84*, 152.
31. C. Wagner, *Z. Chem. Phys.* **1953**, *21*, **1819**.
32. S. Pizzini, R. Morlotti, *J. Electrochem. Soc.* **1967**, *114*, 1179.
33. J. G. Aiken, A. G. Jordan, *J. Phys. Chem. Solids* **1968**, *29*, 2153.
34. G. H. Meier, R. A. Rapp, *Z. Phys. Chem. N.F.* **1971**, *74*, 168.
35. H. G. Sockel, B. Ilschner, *Z. Phys. Chem. N.F.* **1971**, *74*, 284.
36. H. Pfeiffer, K. Hauffe, *Z. Metallkd.* **1952**, *43*, 364.
37. C. Wagner, E. Koch, *Z. Phys. Chem.* **1936**, *B 32*, 439.
38. B. Fisher, D. S. Tannhauser, *J. Chem. Phys.* **1966**, *44*, 1663.
39. F. Lange, M. Martin, *Ber. Bunsen-Ges. Phys. Chem.* **1997**, *101*, 176.
40. S. Mrowec, K. Przybylski, *Oxidat. Metals* **1977**, *11*, 365, 383.
41. D. S. Darken, R. W. Gurry, *J. Am. Chem. Soc.* **1945**, *67*, 1398.
42. B. E. F. Fender, F. D. Riley, *J. Phys. Chem. Solids* **1969**, *30*, 793.
43. L. Himmel, R. F. Mehl, C. E. Birchenall, *Trans AIME, J. Metals* **1953**, 827.
44. H. Rickert, W. Weppner, *Z. Naturforschg.* **1974**, *29a*, 1849.
45. C. Wagner, K. Grünwald, *Z. Phys. Chem.* **1938**, *40*, 445.
46. H. H. von Baumbach, C. Wagner, *Z. Phys. Chem.* **1933**, *B22*, 199.
47. L. Singheiser, W. Auer, *Ber. Bunsen-Ges. Phys. Chem.* **1977**, *81*, 1167.
48. W. C. Hagel, A. U. Seybolt, *J. Electrochem. Soc.* **1961**, *108*, 1146.
49. F. A. Kröger in *High Temperature Corrosion* (Ed.: R. A. Rapp), NACE International, Houston, Tex., 1983, p. 89.
50. K. Hoshino, N. L. Peterson, *J. Am. Chem. Soc.* **1983**, *66*, C–202.
51. A. Atkinson, Transport Processes During the Growth of Oxide Films at Elevated Temperatures, Report AERE-R 11293, Harwell, June, 1984.
52. P. Kofstad, K. P. Lillerud, *J. Electrochem. Soc.* **1980**, *127*, 2410.
53. J. Yee, F. A. Kröger, *J. Am. Ceram. Soc.* **1973**, *56*, 189.
54. Y. Oishi, W. D. Kingery, *J. Chem. Phys.* **1960**, *33*, 480.
55. A. E. Paladino, W. D. Kingery, *J. Chem. Phys.* **1965**, *37*, 957.
56. H. A. Wang, F. A. Kröger, *J. Am. Chem. Soc.* **1980**, *63*, 613.
57. H. Rau, *J. Phys. Chem. Solids* **1978**, *39*, 339.
58. S. Mrowec, H. J. Grabke, M. Danielewski, *J. Mater. Sci.* **1990**, *25*, 537.
59. S. Mrowec, K. Przybylski, *High Temp. Mater. Processes* **1984**, *6*, 1.
60. S. Mrowec, K. Przybylski, *Oxidat. Metals* **1985**, *23*, 107.
61. S. Mrowec, Z. Grzesik, *J. Phys. Chem. Solids* **2000**, *61*, 809.

62. W. Burgmann, G. Urbain, M. G. Frohberg, *Mém. Sci. Rév. Mét.* **1968**, *65*, 567.
63. H. Rau, *J. Phys. Chem. Solids* **1976**, *37*, 425.
64. W. Burgmann, H. J. Grabke, unpublished.
65. H. Rau, *J. Phys. Chem. Solids* **1975**, *36*, 1199.
66. H. Rau, *J. Phys. Chem. Solids* **1976**, *37*, 929.
67. C. Wagner, K. Grünewald, *Z. Phys. Chem.* **1938**, *40*, 445.
68. C. Wagner, *Atom Movements*, ASM International, Cleveland, Ohio, 1951, p. 153.
69. H. J. Grabke, A. Gala, K. J. Best, *Werkst. Korros.* **1970**, *21*, 911.
70. H. J. Grabke, *Ann. N.Y. Acad. Sci.* **1973**, *213*, 110.
71. H. J. Engell, H. J. Grabke, W. Pluschkell, *Die Naturwissenschaften* **1972**, *59*, 263.
72. H. J. Grabke, H. Viefhaus, *Ber. Bunsen-Ges. Phys. Chem.* **1980**, *84*, 152.
73. V. B. Tare, H. Schmalzried, *Trans. Metallurg. Soc. AIME* **1966**, *236*, 444.
74. P. Kofstad, *Oxidat. Metals* **1983**, *19*, 129.
75. R. Bredesen, P. Kofstad, *Oxidat. Metals* **1990**, *34*, 361.
76. R. Bredesen, P. Kofstad, *Oxidat. Metals* **1991**, *35*, 107.
77. R. Bredesen, P. Kofstad, *Oxidat. Metals* **1991**, *36*, 27.
78. P. Roy, H. Schmalzried, *Ber. Bunsen-Ges. Phys. Chem.* **1967**, *71*, 200.
79. S. Stotz, *Ber. Bunsen-Ges. Phys. Chem.* **1966**, *70*, 769.
80. G. K. Boreskov, V. S. Muzykantov, *Ann. N.Y. Acad. Sci.* **1973**, *213*, 137.
81. H. S. Isaacs, L. J. Olmer, *J. Electrochem. Soc.* **1982**, *129*, 436.
82. H. Kobayashi, C. Wagner, *J. Chem. Phys.* **1957**, *26*, 1609.
83. S. Wegge, H. J. Grabke, *Werkst. Korros.* **1992**, *43*, 437.
84. J. P. Orchard, D. J. Young, *J. Electrochem. Soc.* **1986**, *133*, 1734.
85. B. E. Deal, A. S. Grove, *J. Appl. Phys.* **1965**, *36*, 3770.
86. P. J. Jorgenson, *J. Chem. Phys.* **1962**, *37*, 874.
87. P. J. Jorgenson, *J. Electrochem. Soc.* **1967**, *114*, 820.
88. J. D. Cawley in *Corrosion of Advanced Ceramics* (Ed.: K. G. Nickel), Kluwer Academic Publishers, Dordrecht, Netherlands, pp. 35–46.
89. R. Dieckmann, *Z. Phys. Chem. N.F.* **1977**, *107*, 189.
90. N. L. Peterson, W. K. Chen, *J. de Phys. Colloq.* **1980**, *C-6*, 319.
91. S. Mrowec, K. Przybylski, *Oxidat. Metals* **1977**, *11*, 365.
92. K. Fueki, J. B. Wagner Jr., *J. Electrochem. Soc.* **1965**, *112*, 384.
93. A. Atkinson, R. I. Taylor, *Philos. Mag.* **1979**, *A39*, 581.
94. A. Atkinson, R. I. Taylor, A. E. Hughes, *Philos. Mag.* **1982**, *A45*, 823.
95. A. Atkinson, R. I. Taylor, *Philos. Mag.* **1981**, *A43*, 979.
96. J. H. Eriksen, K. Hauffe, *Z. Phys. Chem. N.F.* **1968**, *59*, 332.
97. K. P. Lillerud, P. Kofstad, *J. Electrochem. Soc.* **1980**, *127*, 2397.
98. A. C. S. Sabioni, A. M. Huntz, J. Philibert, B. Lesage, C. Monty et al., *J. Mater. Sci.* **1992**, *27*, 4782.
99. M. J. Graham, J. I. Eldridge, D. F. Mitchell, R. J. Hussey et al., *Mater. Sci. Forum* **1989**, *43*, 207.
100. R. E. Lobnig, H. P. Schmidt, K. Hennesen, H. J. Grabke et al., *Oxidat. Metals* **1992**, *37*, 81.
101. A. M. Huntz, S. C. Tsai, *J. Mater. Sci. Lett.* **1994**, *13*, 821.
102. J. Balmain, A. M. Huntz, *Oxidat. Metals* **1996**, *45*, 183.
103. J. Balmain, M. K. Loudjani, A. M. Huntz, *Mater. Sci. Eng.* **1997**, *A224*, 87.
104. J. Balmain, A. M. Huntz, *Oxidat. Metals* **1996**, *46*, 213.
105. J. S. Sheasby, D. B. Jory, *Oxidat. Metals* **1978**, *12*, 527.
106. H. Hindam, D. P. Whittle, *Oxidat. Metals* **1983**, *18*, 245.
107. H. J. Engell, *Z. Elektrochem.* **1956**, *60*, 905.
108. H. J. Engell, *Arch. Eisenhüttenwes.* **1957**, *28*, 109.
109. H. J. Engell, *Acta Metals* **1958**, *6*, 439.
110. A. Rahmel, *Werkst. Korros.* **1965**, *16*, 837.
111. A. Rahmel, J. Tobolski, *Werkst. Korros.* **1965**, *5*, 33.
112. W. Schottky, *Z. Phys.* **1939**, *113*, 367.
113. K. L. Kliewer, J. S. Koehler, *Phys. Rev.* **1965**, *140*, A1226.
114. N. Cabrera, N. F. Mott, *Rep. Prog. Phys.* **1949**, *12*, 163.
115. T. B. Grimley, *Chemistry of the Solid State*, Butterworths, London, 1956, pp. 336–366.
116. B. Pieraggi, R. A. Rapp, J. P. Hirth, *Oxidat Metals* **1995**, *44*, 63.
117. R. A. Rapp, *Mater. Sci. Forum* **1994**, *154*, 119.

118. Ch. Ilschner Gensch, C. Wagner, *J. Electrochem. Soc.* **1958**, *105*, 198.
119. H. Reinhold, H. Seidel, *Z. Elektrochem.* **1935**, *41*, 499.
120. W. Jost, K. Weiss, *Z. Phys. Chem. N.F.* **1954**, *2*, 112.
121. C. Tubandt, *Z. Anorg. Allg. Chem.* **1921**, *115*, 105.
122. Ch. Ilschner Gensch, *J. Electrochem. Soc.* **1958**, *105*, 635.

6.3 Microbiologically Influenced Corrosion

Brenda J. Little
Stennis Space Center, Mississippi

Florian B. Mansfeld
University of Southern California, Los Angeles, California

Peggy J. Arps and James C. Earthman
University of California, Irvine, California

Microorganisms growing on metal surfaces influence the fate of those materials in the environment, with results ranging from severe localized corrosion to significant reductions in corrosion rate [1]. Corrosion resulting from the presence and activities of microbes on metals and metal alloys is generally referred to as microbiologically influenced corrosion (MIC). The terms microbially induced corrosion or biocorrosion are also used interchangeably with MIC. Microbiologically mediated reactions can alter both the rates and types of electrochemical reactions, resulting in several forms of localized corrosion, including pitting, crevice corrosion, differential aeration cells, metal concentration cells, selective dealloying, enhanced erosion, and enhanced galvanic corrosion. Most MIC studies have focused on bacterial involvement; however, other single-celled organisms (fungi, yeast, algae, etc.) can also influence corrosion processes. Numerous test kits are available for culturing microorganisms known to influence corrosion. However, accurate diagnosis of MIC requires a combination of microbiological, surface analytical, and electrochemical techniques. Since microorganisms are ubiquitous and can be attracted to both anodic [2] and cathodic [3] sites, spatial relationships between microorganisms and corrosion products cannot be independently interpreted as MIC. The following sections describe biofilm formation/structure, microbial processes influencing corrosion, and corrosion inhibition.

6.3.1 Biofilm Formation

Liquid water is needed for all forms of life and availability of water influences both the distribution and growth of microorganisms. Water availability can be expressed as water activity (a_w) with values ranging from 0 to 1.0. Microbial growth has been documented over a range of water activities from 0.60 to 0.998. Fungi are the most desiccant-resistant microorganisms and can remain active down to $a_w = 0.60$, whereas few bacteria remain active at a_w values below 0.9 [4]. The temperature range in which living organisms can grow is that in which liquid water can exist, approximately 273 to 373 °K. Life is possible over concentrations of H^+ ions varying by several orders of magnitude, and some individual microorganisms can grow over a range of 10 pH units or more. Many microorganisms can withstand hundredfold or greater variations in pressure. For example, pressure in the depths of the sea is only mildly inhibitory to growth of many microorganisms. Heavy metal concentrations as low as 10^{-8} M can inhibit growth of some microorganisms, while others may be resistant to concentrations of a millionfold greater. Microbial species show thousandfold differences in susceptibility to irradiation [5].

In addition to water, all organisms require carbon, nitrogen, phosphorus, sulfur and other trace elements for growth. Microorganisms can use many organic and inorganic materials as sources of nutrients and energy. Many microorganisms can grow on trace nutrients found in

laboratory-distilled water. MIC has been documented for metals exposed to seawater, freshwater, distilled/demineralized water, crude and distillate hydrocarbon fuels, process chemicals, food stuffs, soils, human plasma and sewage [6].

In aqueous environments, cells attach to solid surfaces and produce biofilms consisting of polymeric substances and multilayered assemblages of cells in microcolonies (Fig. 1) [5]. Biofilm formation consists of a sequence of steps that begins with adsorption of macromolecules (proteins, polysaccharides, and humic acids) and smaller molecules (fatty acids, lipids) at solid surfaces. Adsorbed molecules form conditioning films that alter the physicochemical characteristics of the water–surface interface, including hydrophobicity and electrical charge.

Transport of microorganisms to an interface and subsequent attachment are

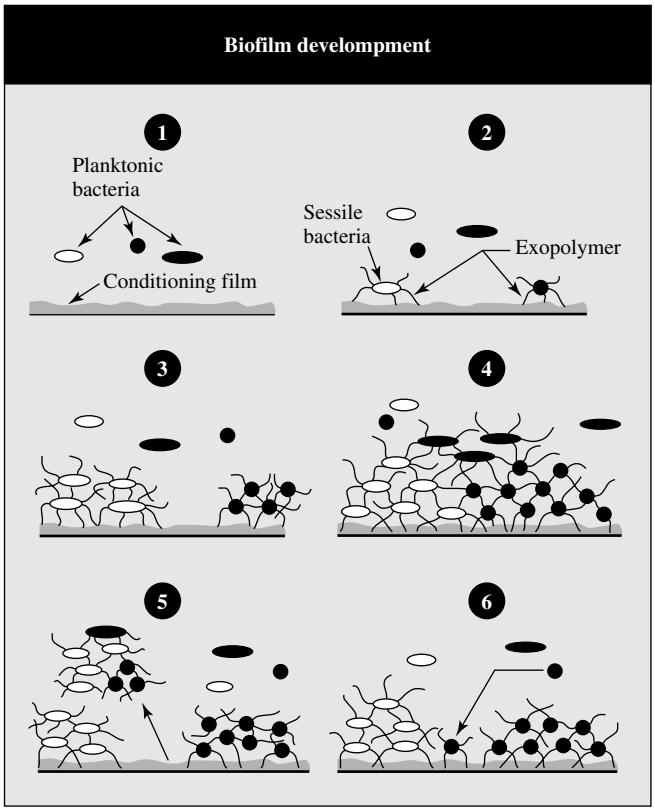


Fig. 1 Biofilm development and regeneration illustrated in six steps. **Step 1**: initial attachment to substratum; **Step 2**: synthesis of EPS to establish more secure association with substratum; **Step 3**: bacterial replication on the substratum and microcolony formation; **Step 4**: formation of mature biofilm; **Step 5**: sloughing and detachment of portions of biofilm; **Step 6**: recolonization of areas of substratum exposed by sloughing events [5].

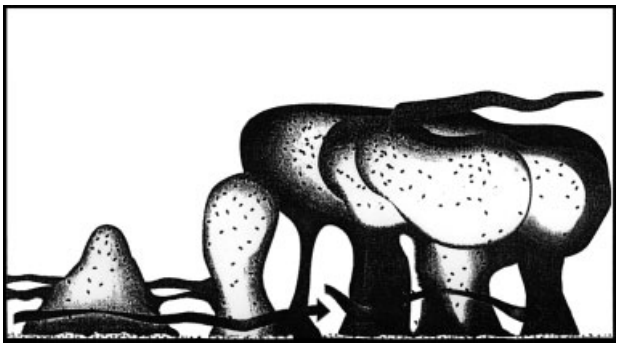


Fig. 2 Conceptual illustration of heterogenous biofilm structure [11].

mediated by diffusive transport due to Brownian motion, convective transport due to liquid flow, and active movement of motile bacteria near the interface. The influence of convective transport exceeds the other two mechanisms by several orders of magnitude. Once a microbial cell is in contact with a surface it may or may not adhere. The ratio of adhering cells to the total number of cells transported to an interface depends on substratum properties (including charge density), physiological state of the microbes, hydrodynamics, and nutritional signals from the environment. For many bacteria, attachment requires cell-surface appendages (flagella, fimbriae, pili) or adhesive substances [7].

After attachment, microorganisms produce adhesive substances, collectively known as extracellular polymeric substances (EPS), which provide the matrix that holds bacteria together and allows formation of microcolonies and ultimately a mature biofilm. EPS also bridge microbial cells with the substratum and permit negatively charged bacteria to adhere to both negatively and positively charged surfaces.

Biofilm formation is dynamic and can be viewed as a developmental cycle [8], beginning with microbial attachment, followed by division of cells and recruitment of planktonic cells to form a complicated architectural structure, and ending with detachment of individual cells and aggregates [9, 10]. Biofilms are typically composed of pillar- and mushroom-shaped cell clusters separated by water channels that allow nutrients in and waste products out (Fig. 2) [11]. Biofilm accumulation at surfaces is a self-perpetuating and continuous process. Initial colonization increases surface irregularity and promotes recruitment of free-swimming cells, promoting further surface irregularity. These changes can influence particle transport and attachment rate by (1) increasing convective mass transport near the surface, (2) providing shelter from shear forces, and (3) increasing surface area for attachment. Growth is due to microbial replication. Each species in the biofilm has its own growth parameters and there appear to be spatial distributions of growth [12]. Detachment includes two processes: sloughing and erosion. Sloughing is the process in which large pieces of biofilm are removed, exposing the underlying surface. Reasons for biofilm sloughing are not well understood. Biofilm erosion is the continuous removal

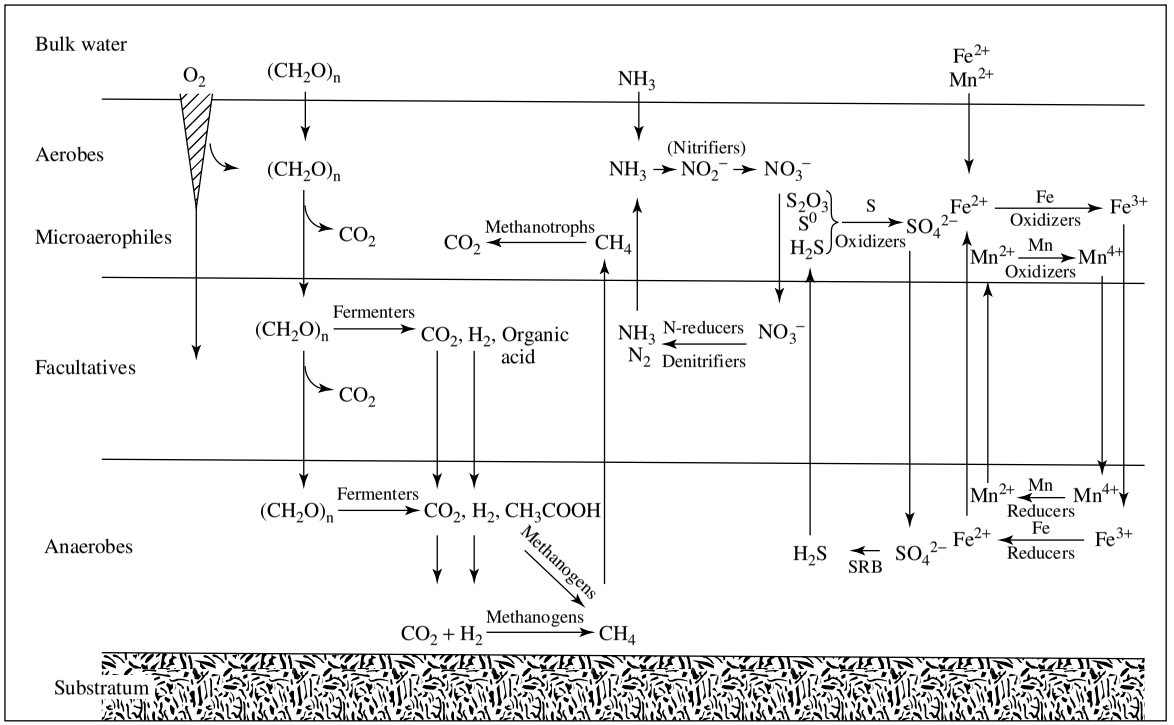


Fig. 3 Possible reactions that can occur in a biofilm.

of single cells or small groups of cells from the biofilm and is driven by shear stress at the biofilm–fluid interface. An increase in shear stress increases erosion rate and decreases biofilm accumulation rate. Empirical observations indicate that erosion rate is related to flow velocity, biofilm thickness, density, and tertiary structure [13].

Biofilms are capable of maintaining environments at biofilm/surface interfaces that are radically different from the bulk fluid in terms of pH, dissolved oxygen, and other organic and inorganic species (Fig. 3). In some cases, these interfacial conditions could not be maintained in the bulk medium at room temperature near atmospheric pressure. The consequence is that microorganisms within biofilms facilitate reactions that are not predicted by thermodynamic arguments based on the chemistry of the bulk medium.

6.3.2 Corrosion Promoting Mechanisms

The most serious MIC takes place in the presence of microbial consortia where many types of microorganisms are present within the structure of the biofilm. These include sulfate-reducing bacteria (SRB), sulfur oxidizing bacteria, metal-reducing and metal-oxidizing bacteria, acid-producing and slime-producing bacteria, in addition to other aerobic and anaerobic microbes.

6.3.2.1 Sulfur, Sulfate and Thiosulfate Reduction

Reduction of elemental sulfur or thiosulfate results in production of hydrogen sulfide (H_2S), which acidifies a corrosive medium and catalyses the penetration of hydrogen into steels, a process known as H_2S-induced cracking or sulfide stress cracking. Crolet and Magot [14] described a group of bacteria isolated from an oilfield production facility capable of reducing thiosulfate ($S_2O_3^{-2}$), not sulfate, to sulfide. The non-SRB fermentative strains produced H_2S and organic acids from $S_2O_3^{-2}$ and peptides. Corrosion penetration rates of carbon steel in the presence of these organisms were in excess of 1 cm yr^{-1}.

SRB are the organisms most closely identified with MIC. SRB are a phylogenetically diverse group of anaerobic bacteria found in natural and industrial environments. SRB use sulfate as the terminal electron acceptor during respiration and produce H_2S. When the aerobic respiration rate within a biofilm is greater than the oxygen diffusion rate, the metal/biofilm interface can become anaerobic and provide a niche for SRB (Fig. 4) [15]. The critical biofilm thickness required to produce anaerobic conditions depends on availability of oxygen and the respiration rates of organisms in the biofilm. The metabolic activity of SRB causes accumulation of sulfide near metal surfaces.

McNeil and Odom [16] developed a thermodynamic model to predict metal susceptibility to MIC by SRB. If the reaction to produce the sulfide from the oxide has a negative Gibbs free energy, the reaction will take place. If the value is positive, the metal is immune to derivation by sulfides and will not be vulnerable to corrosion by SRB. The model is limited to thermodynamic predictions as to whether a reaction will take place and does not consider metal toxicity to the organisms, tenacity of the resulting sulfide or others factors that influence corrosion rate. The following is a summary of mineralogical products

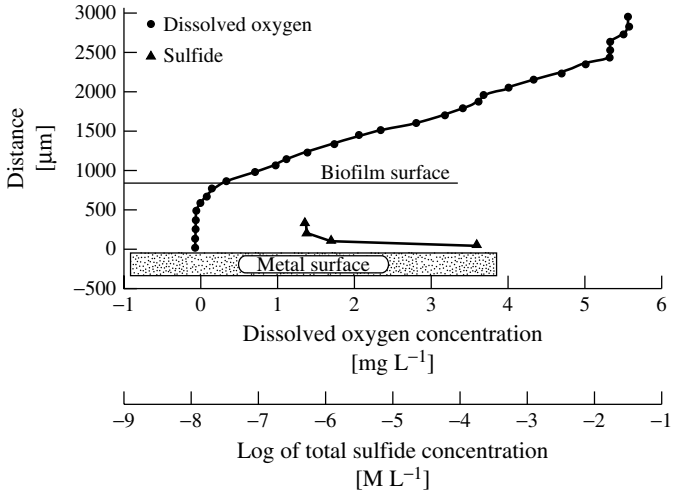


Fig. 4 Concentration profiles of sulfide and oxygen in a biofilm on mild steel [15]. (Reproduced with permission of Taylor and Francis Ltd, http://www.tandf.co.uk/journals.)

formed during SRB-influenced corrosion reactions [16].

- *Ag*: acanthite (Ag_2S).
- *Ag-Cu alloys*: acanthite, argentite [the high temperature polymorph of Ag_2S or jalpaite (Ag_3CuS_2)].
- *Cu*: complex suites of sulfide minerals: the most common product is chalcocite (Cu_2S). Final product in many cases is blue-remaining covellite (CuS_{1+x}).
- *Cu-Ni alloys*: sulfide corrosion products similar to those of Cu but with significant djurleite ($Cu_{31}S_{16}$). No Ni minerals observed.
- *Cu-Sn alloys*: corrosion products similar to those found with in Cu.
- *Fe (carbon steel)*: final product is pyrite (FeS_2) with numerous intermediates.
- *Fe (stainless alloys)*: product formation rates are slower than for pure Fe or carbon steel. No Ni minerals have been detected. Stainless steels with 6% or more Mo appear to be very resistant.
- *Ni*: millerite (NiS).
- *Pb*: galena (PbS).

6.3.2.2 Practical Aspects

The corrosion rate of iron in the presence of H_2S is accelerated by the formation of iron sulfide minerals [17] that stimulate the cathodic reaction. Once electrical contact is established, mild steel behaves as an anode and electron transfer occurs through the iron sulfide. At low ferrous ion concentrations (0–10 mg L^{-1}), adherent and temporarily protective films of iron sulfides form on the steel surface with a consequent reduction in anodic and cathodic currents. High-corrosion current densities associated with SRB-induced corrosion of mild steel are maintained only in high concentrations of ferrous ion [18].

MIC failures due to SRB have been reported for mild steel piping and equipment in marine and soil environments, as well as to waters in oil refining, process industries, and fossil fuel and nuclear power plants. Volumes edited by Dexter [19], Kobrin [20] and Stoecker [21] provide numerous case histories.

Sanders and Hamilton [22] analyzed microbial corrosion in North Sea oil

exploration and defined two distinct forms of SRB-mediated corrosion: pitting caused by SRB growing in the biofilm on metal surfaces, and sulfide-induced stress corrosion cracking, hydrogen induced cracking or blistering caused by hydrogen permeation of the metal alloy in high dissolved sulfide conditions.

Bibb [23] presented three case histories of pipe failures in South African power plants including failure of mild steel pipework handling raw water, an epoxy-lined seawater cooling pipe and galvanized hot water pipework. The presence of the organism *Desulfovibrio desulfuricans* was confirmed in all failures. Honneysett et al. [24] documented MIC of carbon steel caused by SRB in a cooling system for a casting machine. The onset of the problem coincided with the use of reclaimed sewage water.

The impact of oxygen on SRB was examined by Hardy and Bown [25] using mild steel specimens and weight loss measurements. Successive aeration–deaeration shifts caused variation in the corrosion rate. The highest corrosion rates (129 mg dm^{-2} d^{-1} $\cong$ 5 cm yr^{-1}) were observed during periods of aeration. Lee and coworkers [15, 26] determined that corrosion of mild steel could not be initiated by SRB in the absence of ferrous ion. King and coworkers [27] demonstrated that weight loss of steel was proportional to the concentration of ferrous sulfide and depended on the stoichiometry of the particular ferrous sulfide minerals.

The impact of biogenic sulfides on the corrosion of copper alloys has received a considerable amount of attention. The general phenomenology of SRB-influenced corrosion of copper can be understood by considering the following scenario. Microbial consortia that include SRB produce anoxic, sulfide-rich environments in which the conversion of copper to copper sulfides is thermodynamically favored at a concentration of 10^{-2} M total sulfur. The first sulfur-poor compounds are converted to sulfur-rich compounds. Little and coworkers [28–30] published several reports documenting localized corrosion of copper alloys by SRB in estuarine environments. Others [31, 32] reported the failure of copper alloys due to pitting and stress corrosion cracking in polluted seawater containing waterborne sulfides. CDA 706 (90 : 10, Cu : Ni) suffered accelerated corrosion attack in seawater containing 0.01 ppm sulfide after a 1-day exposure.

It has been argued that if the copper sulfide layer were djurelite, the sulfide layer would be protective [33]. Even if such a sulfide film were technically passivating, the mechanical stability is so poor that sulfide films on copper surfaces are useless for corrosion protection. In the presence of turbulence, the loosely adherent sulfide film is removed, exposing a fresh copper surface to react with sulfide ions. For these reasons, turbulence-induced corrosion and sulfide attack of copper alloys cannot easily be decoupled. In the presence of oxygen, the possible corrosion reactions in a copper sulfide system are extremely complex because of the large number of stable copper sulfides [34], their differing electrical conductivities, and catalytic effects. Transformations among sulfides, or conversions of sulfides to oxides, result in changes in volume that weaken the attachment scale and oxide subscale leading to spalling (Fig. 5) [35].

MIC has also been documented for copper and copper alloys used in potable water applications. Alanis and coworkers [36] described a case of localized corrosion in underground brass pipes of low zinc content (8.22%) used for drinking water distribution. Perforation was due to SRB

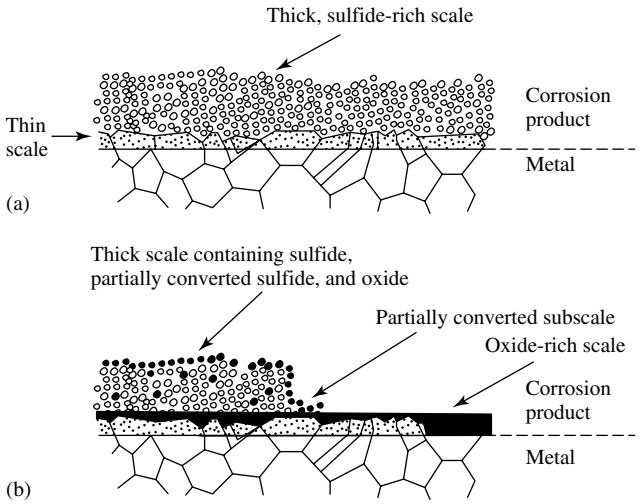


Fig. 5 Schematic of (a) thick sulfide-rich scale on copper alloy and (b) disruption of sulfide film [35].

and aggressive anions such as chlorides in the soil.

Monel 400, a nickel alloy containing 66.5% nickel, 31.5% copper and 1.25% iron, has a marked tendency for the initiation of pitting in chloride-containing environments where the passive film can be disturbed. Under stagnant conditions chlorides penetrate the passive film at weak points and cause pitting attack. Sulfides can cause either a modification of the oxide layer, as described for copper, or breakdown of the oxide film of nickel alloys. Pit initiation and propagation depend on depth of exposure, temperature and presence of surface deposits. Little and coworkers [30] reported selective dealloying of nickel in Monel 400 in the presence of SRB from an estuarine environment.

Pope [37] reported a case study from a nuclear power plant in which Monel heat exchanger tubes were found to have many discrete deposits under which severe pitting corrosion was observed. Deposits, formed by iron-and manganese-depositing bacteria in association with SRB, contained large amounts of iron and copper in addition to significant amounts of manganese and silicon and reduced amounts of nickel.

Two attempts have been made to develop a diagnostic for SRB corrosion of copper alloys: mineralogical fingerprints and sulfur isotope fractionation. Many sulfides under near-surface conditions can only be produced by microbiological action on specific precursor materials such as metals. If a corrosion process can be shown to have taken place in a pH-Eh range typical of near-surface conditions and no compelling kinetic arguments can be reached, then mineralogical and geochemical data indicate that the presence of these minerals as corrosion products implies SRB activity. McNeil and coworkers [38] demonstrated that djurleite, spionkopite and the high temperature polymorph of chalcocite appear to be mineralogical fingerprints for the SRB corrosion of copper-nickel alloys. The stable isotopes of sulfur (^{32}S and ^{34}S), naturally present in a sulfate source, are selectively metabolized during

sulfate reduction by SRB and the resulting sulfide is enriched in ^{32}S [39]. The ^{34}S isotope accumulates in the starting sulfate as the ^{32}S is removed and concentrated in the sulfide. Little and coworkers [40] demonstrated sulfur isotope fractionation by SRB in sulfide corrosion products on a copper alloy.

Several investigators have demonstrated that there is no direct correlation between numbers of SRB and the likelihood that corrosion has occurred or will occur. Jack and coworkers [41] prepared a review of 30 months of electrochemical measurements, weight-loss data, water chemistry and microbiological data for an oilfield waterflood operation in which produced brine was injected to displace oil from the reservoir. They concluded that SRB numbers could be used as an index of biocide performance in these field systems. No other correlations between corrosion measurements and microbial numbers were found. In a two-year study of MIC in natural gas pipeline facilities Pope and coworkers [42] failed to establish a relationship between numbers of SRB and MIC for carbon steel.

6.3.2.3 Sulfur/Sulfide Oxidation

Elemental sulfur, thiosulfates, metal sulfides, H_2S, and tetrathionates can be oxidized to sulfuric acid by microorganisms generically referred to as thiobacilli. Corrosion in sewers and other concrete structures is often due to oxidation of sulfides generated by the activities of SRB and may occur in many steps. Concrete is a moderately porous mixture of alkaline inorganic precipitates and mineral aggregates. Anaerobic conditions in sewage support SRB that convert sulfate to H_2S, which volatilizes to the sewer atmosphere and redissolves in condensate on the sewer crown [43] (Fig. 6). A second community of microorganisms at the

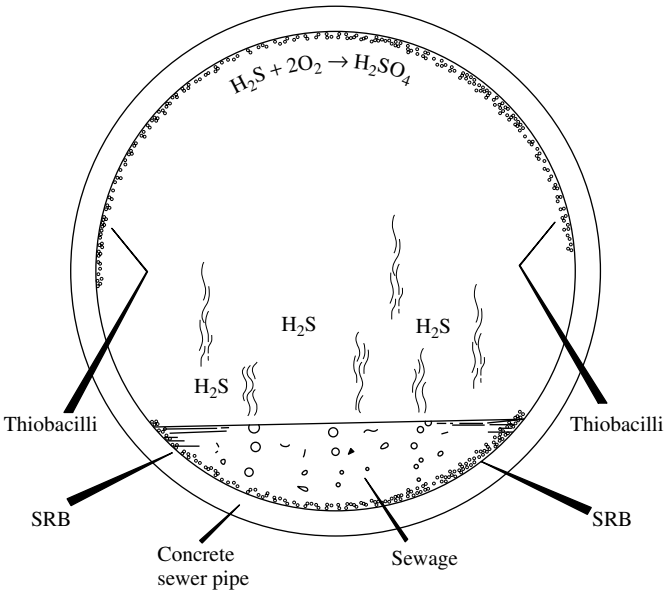


Fig. 6 Diagram of sulfur cycling by microorganisms in a sewer.

crown oxidizes the sulfide to corrosive sulfuric acid.

Mansfeld and coworkers [44] used linear polarization to determine polarization resistance, R_p, for mild steel sensors embedded in concrete exposed to a sewer environment. One concrete sample was periodically flushed with sewage to remove sulfuric acid produced by sulfur-oxidizing bacteria. Another sample was used as a control. A data logging system collected R_p at 10-min intervals simultaneously for the two corrosion sensors and two additional pH electrodes placed at the concrete surface. Figure 7 [44] shows cumulative corrosion loss, Σ INT obtained by integration of the $1/R_p$- time curves as

$$\sum \text{INT} = \int \frac{dt}{R_p} \qquad (1)$$

Corrosion losses remained low during the first two months followed by a large increase for both the flushed sample and control. Increased corrosion rates of embedded steel electrodes occurred when surface pH reached values of 1 or less due to accumulation of sulfuric acid (H_2SO_4).

Mittleman and Danko [45] determined that sulfur cycling, that is, sulfate reduction and sulfide oxidation, by microorganisms

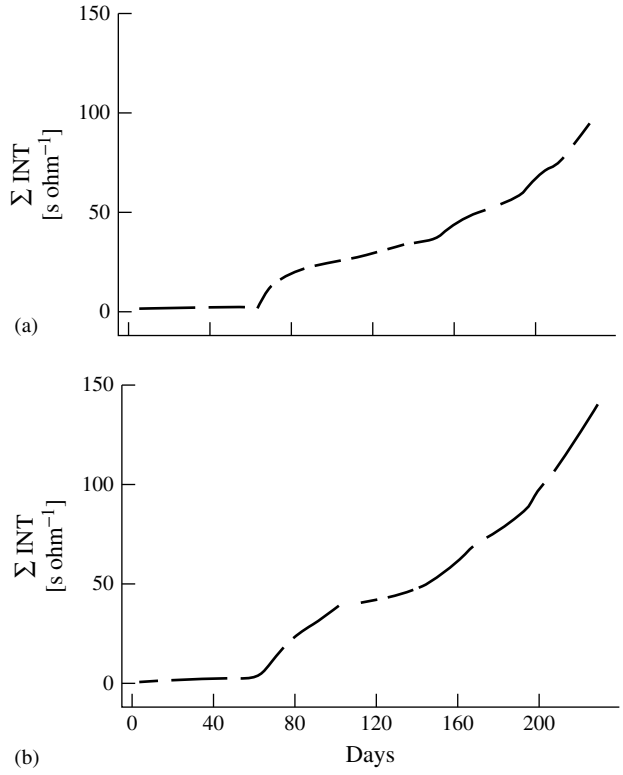


Fig. 7 Cumulative corrosion loss Σ INT for mild steel sensors embedded in concrete and exposed in a sewer bypass; (a) control sample and (b) flushed sample [44]. (© NACE International 1991.)

was responsible for concrete and carbon steel deterioration in a dam in South America. Cleland [46] demonstrated the coexistence of elemental sulfur and sulfate in the presence of iron sulfide corrosion products in ship ballast tanks, indicating microbial oxidation.

Sulfide oxidation reactions are important to the formation of sulfuric acid in coal, gold, and copper mines, and in other sulfur-containing deposits. All coals consist of organic material containing carbon, hydrogen and oxygen, and smaller amounts of sulfur (principally as sulfide and organic sulfur). Variation of coal types is related to the biological starting materials and variations in conditions during coal diagenesis through geological time. Inorganic and organic compounds are present in coal. Inorganic sulfur occurs predominantly as ferrous sulfide (FeS_2) in its mineral forms, pyrite and marcasite, whereas organic sulfur compounds are part of the molecular configuration of the coal. If FeS_2-containing coals are exposed to moisture and oxygen, spontaneous FeS_2 oxidation starts, resulting in production of ferric iron and sulfuric acid, as given below.

$$4FeS_2 + 15O_2 + 2H_2O \longrightarrow 2Fe_2(SO_4)_3 + 2H_2SO_4 \quad (2)$$

The pH of the water phase will drop during the oxidation process. Because rates of spontaneous pyrite oxidation decrease as pH falls, the process will stop at pH 4. Acidophilic pyrite-oxidizing bacteria, indigenous to coals, thrive at low pH and continue the oxidation to pH values lower than 2.

The South African Rail Company, a carrier for large quantities of low-grade coal, reported accelerated corrosion of steel due to the presence and activities of *Acidithiobacillus ferrooxidans* (formerly *Thiobacillus ferrooxidans*) and the fungus, *Hormoconis resinae*. The individual organisms caused an approximate doubling of the corrosion rate compared to sterile conditions. The corrosion pattern included scaling, pitting, and stress-cracking [47]. Similar situations are found where pipelines are buried in soils that contain coal ash, industrial wastes, landfills or railway right-of-ways through coal outcroppings and rivers in the coal mining regions.

Formation of elemental sulfur during microbial oxidation of reduced sulfur compounds has been reported [48, 49]. Case histories of corrosion in the presence of elemental sulfur can be attributed to either direct oxidation to H_2SO_4, or electron transport from the metal through a metal sulfide to elemental sulfur.

The disproportionation of elemental sulfur in water at elevated temperatures yields H_2S and sulfuric acid, which acidify the corrodant, activate metal dissolution, inhibit repassivation and favor crevice corrosion and stress corrosion cracking. Elemental sulfur is a powerful oxidant for organic and inorganic materials. Metals and metal oxides react with either dissolved or undissolved sulfur at ambient or higher temperatures, regardless of the presence of oxygen, to form sulfides that act as catalysts for the cathodic reduction of elemental sulfur. The availability of sulfur in soils limits the activities of the sulfur-oxidizing bacteria. Where sulfur is present, corrosive activities and rates can be dramatic. Railroad tracks through the sulfur producing areas of the Gulf Coast of Texas have high corrosion rates due to the activities of thiobacilli [50]. Steel troughs and drainage pipes failed after 15 to 30 days and 1.5 to 3 months, respectively, when used in Russian coal mines with

acid-producing bacteria [51]. The predicted lifetime of the materials when operated with waters at neutral pH is 1 to 2 years. Chromium-nickel and chromium-molybdenum steels are sensitive to attack by thiobacilli-contaminated environments containing elemental sulfur.

Schmitt [52] reviewed the effect of elemental sulfur on corrosion of construction materials (carbon steels, ferric steels, austenitic steels, ferritic-austenitic steels (duplex steels), nickel and cobalt-based alloys and titanium. Wet elemental sulfur in contact with iron is aggressive and can result in the formation of iron sulfides or in stress corrosion cracking. Iron sulfides containing elemental sulfur initiate corrosion only when the elemental sulfur is in direct contact with the sulfide-covered metal. Iron sulfides are highly electron conductive and serve to transport electrons from the metal to the elemental sulfur. The coexistence of hydrogen sulfide and elemental sulfur in aqueous systems, that is, sour gases and oils, causes crevice corrosion rates of 3 mm yr^{-1} and stress-oriented hydrogen induced cracking of iron-containing alloys. The corrosion rate is enhanced in the presence of chlorides. Corrosion-resistant alloys experience lower corrosion rates than carbon steels, with the exception of the duplex steels that are corroded at the same rate as carbon steels. The resistance to sulfur increases with the content of nickel, chromium and molybdenum in the alloy. High-alloy stainless steels are susceptible to stress corrosion cracking at temperatures above 150 °C. Grade 2 titanium suffers sulfur-induced crevice corrosion above 130 °C, however, the Beta-C alloy retains passivity in sulfur-containing brines up to 300 °C.

Dowling [53] proposed a mechanism for corrosion of structural steel exposed to wet solid elemental sulfur (Fig. 8). Freestanding moisture and steel/sulfur contact are requisites for corrosion of structural steel by solid elemental sulfur. The principal form of attack in S/H_2O media is not due to secondary acid generation resulting from hydrolysis of the sulfur. Instead, the author demonstrated that steel oxidation was coupled to sulfur reduction through an electron conductive iron sulfide layer. Evidence is also presented for the direct electrochemical reduction of solid elemental sulfur in the presence of FeS, supporting the role of this process as the partial cathodic step in the mechanism of the sulfur corrosion reaction.

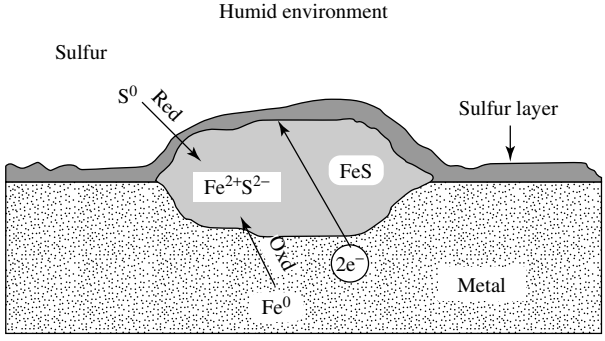


Fig. 8 Mechanistic view of relationship between elemental sulfur and metal sulfide during corrosion of mild steel.

6.3.2.4 Metal-oxidizing Bacteria

Biomineralization of iron and manganese oxides occurs widely in natural waters, and is a dominant control in the geochemical cycling of these elements. Mineralization can be carried out by a variety of organisms including bacteria, yeast, and fungi, but is particularly associated with genera of the so-called iron- and manganese-oxidizing bacteria, including *Siderocapsa, Gallionella, Leptothrix, Sphaerotilus, Crenothrix,* and *Clonothrix*.

Manganese oxidation is coupled to bacterial cell growth and metabolism. While Mn^{2+} is soluble, the oxidized forms (Mn_2O_3, MnOOH, Mn_3O_4, MnO_2) are insoluble. Microbially deposited manganese oxides have an amorphous structure as MnO_2 (vernadite) and sometimes form a black precipitate of MnO_2 (birnessite), found with *Leptothrix* and spores of *Bacillus* spp. (Fig. 9) [54]. As a result of microbial action, manganese oxide deposits are formed on submerged materials including metal, stone, glass, and plastic and can occur in natural waters with manganese levels as low as 10–20 ppb. Deposition rates of 1 mcoul cm^{-2} day^{-1} on stainless steel have been observed [55].

Results by Linhardt [56] and Lewandowski [57] demonstrate ennoblement (an increase of E_{corr} from −150 mV to +350 mV vs. SCE) of stainless steels in river waters involving formation of MnO_2. Linhardt found large amounts of manganese minerals (mainly MnOOH and MnO_2) on severely pitted turbine runner blades in a hydroelectric plant and suggested that pitting was due to biomineralized Mn oxides. Renner reported severe pitting around welds in type SS 316 pipes used to pump cooling water from the Rhine River [58]. He suggested that the failure mechanism involved iron- and manganese-oxidizing bacteria causing ennoblement and pitting. Linhardt [56] concluded that ennoblement was due to the formation of MnO_2 according to the reaction:

$$Mn^{+2} + 2H_2O \longrightarrow MnO_2 + 4H^+ + 2e^- \quad (3)$$

Pitting occurred as a result of galvanic interaction between areas covered by manganese oxides acting as cathodes and bare stainless steel surfaces serving as anodes. The extent to which the elevated current density can be maintained is controlled by the electrical capacity of the mineral,

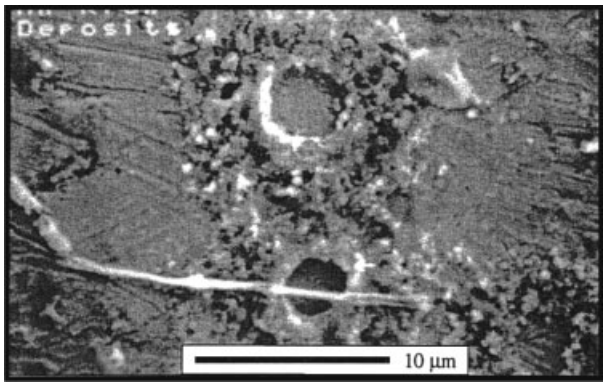


Fig. 9 Manganese deposits on stainless steel after 13 days of exposure to fresh water [54]. (Reproduced with permission of Taylor and Francis Ltd, http://www.tandf.co.uk/journals.)

reflecting both total accumulation and conductivity of the mineral-biopolymer assemblage (only material in electrical contact with the metal will be cathodically active). Oxide accumulation is controlled by the biomineralization rate and the corrosion current, in that high corrosion currents will discharge the oxide as rapidly as it is formed.

Iron-oxidizing bacteria produce orange-red tubercles of iron oxides and hydroxides by oxidizing ferrous ions from the bulk medium or the substratum (Fig. 10). Deposits of cells and metal ions create oxygen concentration cells (Fig. 11) [59] that effectively exclude oxygen from the area immediately under the deposit and initiate a series of events that are individually

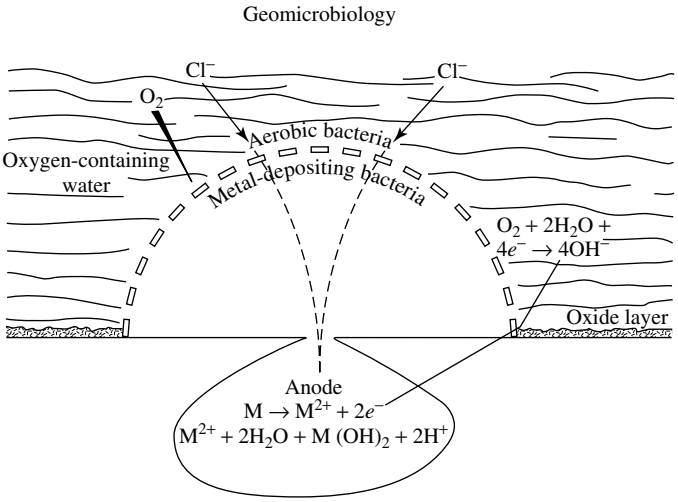


Fig. 10 Reactions under metal-depositing bacteria.

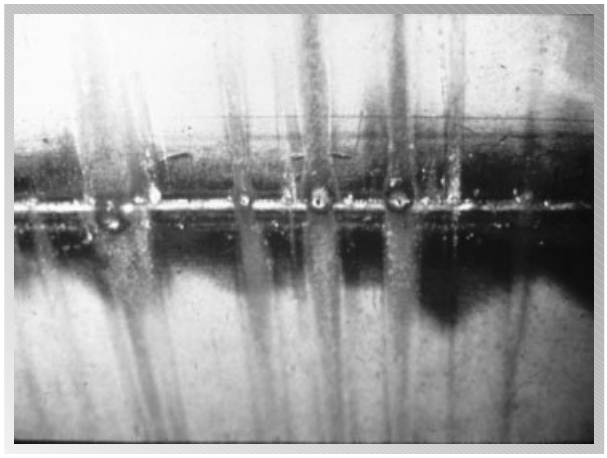


Fig. 11 Tubercle formation, resulting from the activities of iron-oxidizing bacteria [59]. (© NACE International 1976.)

or collectively very corrosive. In an oxygenated environment, the area immediately under individual deposits becomes deprived of oxygen. That area becomes a relatively small anode compared to the large surrounding oxygenated cathode. Cathodic reduction of oxygen may result in an increase in pH of the solution in the vicinity of the metal. The metal will form metal cations at anodic sites. If the metal hydroxide is the thermodynamically stable phase in the solution, the metal ions will be hydrolyzed by water with the formation of H^+ ions. If cathodic and anodic sites are separated from one another, the pH at the anode will decrease and that at the cathode will increase. In addition, Cl^- ions from the electrolyte will migrate to the anode to neutralize any buildup of charge, forming heavy metal chlorides that are extremely corrosive. Under these circumstances, pitting involves the conventional features of differential aeration, a large cathode to anode surface area ratio, and the development of acidity and metallic chlorides. Stainless steels containing 6% or more molybdenum are not vulnerable to this type of attack.

6.3.2.5 Metal-reducing Bacteria

Other microorganisms promote corrosion of iron and its alloys through dissimilatory iron reduction reactions that lead to the dissolution of protective iron oxide/hydroxide films on the metal surface. Passive layers are either lost or replaced by less stable films that allow further corrosion. Obuekwe and coworkers [60] evaluated corrosion of mild steel under conditions of simultaneous production of ferrous and sulfide ions by an iron-reducing bacterium. They reported extensive pitting when both processes were active. When only sulfide was produced, initial corrosion rates increased but later declined due to formation of an iron sulfide (FeS) film. High amounts of soluble iron prevent formation of protective sulfide layers on ferrous metals.

6.3.2.6 Acid-producing Organisms

Most heterotrophic bacteria secrete organic acids during fermentation of organic substrates. The kinds and amounts of acids depend on the type of microorganisms and the available substrate molecules. Organic acids may force a shift in the tendency for corrosion to occur. The impact of acidic metabolites is intensified when they are trapped at the biofilm/metal interface. The organic acids of the Krebs cycle can promote electrochemical oxidation of a variety of metals by removing or preventing the formation of an oxide film. Burnes and coworkers [61] showed that under aerobic conditions solutions of citric, fumaric, ketoglutaric, glutaric, maleic, malic, itaconic, pyruvic, and succinic acids formed metallic salts when incubated with copper, tin or zinc. Acetic, ketoglutaric, succinic, and lactic acids were isolated from an anaerobic culture of *Escherichia coli* in which enhanced corrosion of carbon steel had been documented. Little and coworkers [62] demonstrated that isobutyric and isovaleric acids accelerate the corrosion of nickel. Gerchakov and Udey [63] suggested that amino and dicarboxylic acids were also aggressive.

The pH under algal fouling varies with photosynthesis and respiration. Daily pH changes of up to 2 units have been recorded under algal biofilms, with pH values above 10 during photosynthesis. [64] Decaying algae contribute to a type of corrosion known as ligament cutting during which pH values as low as 1.8 have been recorded under decaying algal filaments.

Fungi are ubiquitous in atmospheric and aquatic environments where they assimilate organic material and produce organic acids including oxalic, lactic, formic, acetic and citric. Most fungi are aerobes and are only found in aerobic habitats. Fungi are nonphotosynthetic organisms that have vegetative structures known as hyphae, the outgrowth of a single microscopic reproductive cell or spore. A mass of threadlike hyphae make up a mycelium. Mycelia are capable of almost indefinite growth in the presence of adequate moisture and nutrients, allowing fungi to often reach macroscopic dimensions. Spores, the nonvegetative dormant stage, can survive long periods of unfavorable growth conditions, e.g., drought and starvation. When conditions are favorable for growth, spores germinate and produce hyphae, completing the cycle.

Fungal contamination and decomposition of hydrocarbons are well-documented phenomena [65–79]. The major limiting factor for microbial activity in fuels is availability of water [65]. The volume of water required for microbial growth in hydrocarbon fuels is extremely small. Since water is a product of the microbial mineralization of organic substrates, it is possible for microbial mineralization of fuel to generate a water phase for further proliferation. For example, *Cladosporium resinae*, the kerosene fungus, grew in 80 mg water per liter of kerosene and after four weeks incubation, the concentration of water increased more than tenfold [65].

Fungal influenced corrosion has been reported for carbon steel and aluminum alloys exposed to hydrocarbon fuels during transport or storage. The following mechanisms for MIC in fuel/water systems were elucidated by Videla et al. [69]: (1) a local increase in proton concentration derived from organic acidic metabolites, (2) an increase of the oxidizing characteristics of the medium favoring pitting attack, (3) production of metabolites that decrease the surface energy of the passive film/electrolyte interface, (4) microbial adhesion enhancing metal dissolution, and (5) microbial uptake of fuel additives, including corrosion inhibitors. Rosales [77] demonstrated metal ion binding by fungal mycelia, resulting in metal ion concentration cells on aluminum surfaces. Differential aeration caused by the adherence of fungal mats can cause crevice corrosion [71]. De Mele and coworkers [72] reported that corrosivity increased with contact time due to accumulation of metabolites under microbial colonies attached to metal surfaces. De Meybaum and de Schiapparelli [73] demonstrated that the metabolic products enhanced aqueous phase aggressiveness even after the life cycle of the *Cladosporium* sp. was completed.

Numerous reports document fungal degradation of coatings and, in some cases, corrosion of the underlying metal [80–82]. Stranger–Johannessen [83] reported that ship cargo holds coated with chlorinated rubber and carrying dry cereals and woods were severely corroded within months. Heavy pitting and reduced thickness of the steel plate were observed. Corrosion products were populated with viable fungi. Stranger–Johannessen [83] demonstrated that fungi derived nutrients from degradation of the protective coating in addition to the cargo. Corrosion resulted from acidic metabolic byproducts. Stranger–Johannessen [84] reported deterioration of an epoxy resin coating in ship holds filled with molasses, fatty oils and other fluid cargoes. She also confirmed fungal degradation of polyurethane cable sheathing in the marine environment [85].

6.3.2.7 Slime-producing Bacteria

As previously indicated, many microorganisms produce EPS or slime, and several researchers have investigated the role of EPS in corrosion [86–88]. EPS consist of polysaccharides and proteins, plus significant amounts of nucleic acids, (phospho) lipids and humic substances [89–91]. The final composition of the EPS matrix results from a combination of the following: active secretion, shedding of cell surface material, cell lysis, and/or adsorption of substances from the environment. EPS are usually acidic and contain functional groups, such as carboxylic and amino acids that, as mentioned earlier, readily bind metal ions. EPS can bind metal ions from the substratum or from a liquid medium and control interfacial chemistry at a metal/biofilm interface. EPS are also implicated in increased resistance of biofilm cells to biocides and other antimicrobial compounds [9].

A unique type of corrosion referred to as copper by-product release, cuprosolvency, or 'blue water' occurs in potable water systems constructed of copper tubing, and has been reported worldwide [92–95]. The problem is most often attributed to EPS induced metal concentration cells. The condition is characterized by the release of copper as fine particles in plumbing systems distributing soft water in the neutral or neutral-alkaline pH range. Water may contain between 5 to 300 ppm copper (as Cu^{2+}) as finely suspended precipitates. A bacterial biofilm and associated acidic EPS bind copper ions at the metal surface and alter the porosity of the oxide film [96]. Geesey and coworkers [97] characterized binding of an acidic polysaccharide to thin copper films and suggested a cupric ion interaction with carboxyl groups on EPS. These interactions promoted ionization of metallic copper [98]. Beech and coworkers [99, 100] found that a large polysaccharide-protein complex (>200 kDa) produced by a marine SRB in the genus *Desulfovibrio*, is capable of accelerating the deterioration of mild steel. They suggested that the high affinity of the EPS complex for Fe ions accounted for its corrosive nature.

Heavy metals, such as chromium, that are toxic to certain microbes may increase production of EPS. Fang and colleagues [101] found an increase in the EPS of an SRB-enriched marine culture when chromium (50–100 ppm) was added to seawater. Exposure of mild steel samples to this solution for 20 d under anaerobic conditions resulted in corrosion. A subsequent study by Chan and coworkers [102] suggested that corrosion of mild steel, immersed in synthetic seawater containing extracted and purified EPS (from the same SRB-enriched culture as above) and incubated under anaerobic conditions as before, was aided by oxidation reactions provided by EPS. The electrochemical reductions of EPS were coupled to iron oxidation. Polysaccharides in EPS were electrochemically reduced and converted to hydrocarbons, as shown by changes in the X-ray photoelectron spectra.

6.3.2.8 Corrosion Inhibiting Mechanisms

Inhibition of general corrosion by biofilms has been reported for mild steel, copper, aluminum and stainless steels, and brass. The mechanisms most frequently cited for the inhibition are formation of a diffusion barrier to corrosion products that stifles metal dissolution, consumption of oxygen by respiring aerobic microorganisms within the biofilm causing a diminution of that reactant at the metal surface, production of metabolic products that act as corrosion inhibitors (e.g., siderophores) or specific antibiotics that prevent proliferation

of corrosion-causing organisms (e.g. SRB), and formation of passive layers that are unique to the presence of microorganisms.

One apparent contradiction that has not been resolved is that some microorganisms in biofilms can cause localized corrosion and others inhibit generalized corrosion. To further complicate matters, the same organisms and mechanisms to which MIC has been attributed can also reportedly inhibit corrosion. For example, strains of *Pseudomonas* and *Serratia* are reported to increase the corrosion rate of iron and nickel compared to sterile conditions [103], but can have a protective effect on some metals under certain circumstances [104, 105]. Videla and Guiamet [106] found a protective action of *S. marcescens* on aluminum. Metal-binding by extracellular polymers has been reported as a mechanism for both MIC [107] and for corrosion inhibition [86].

Under laboratory conditions using electrochemical techniques, Hernandez and coworkers [108] observed increased corrosion resistance when mild steel was exposed to complex nutrient-rich media containing a *Pseudomonas* sp. or *Serratia marcescens*. They determined the following:

1. Inhibition required bacterial adhesion.
2. The inhibition effect disappeared when *in situ* cells were fixed in glutaraldehyde.
3. When cell-covered surfaces were transferred to nutrient-deficient synthetic seawater, the inhibition continued despite the predicted diminished respiration.
4. After exposure to natural seawater the inhibitive effect disappeared and *Pseudomonas* could not be located in the biofilm.

Hernandez and coworkers [108] speculated that corrosion inhibition might have been due to the formation of a protective layer containing bacteria, exopolymers and other metabolic products. In addition, since *Pseudomonas* sp. is an aerobe and *Serratia marcescens* is a facultative organism that can also consume oxygen, the authors concluded that corrosion inhibition could be related to O_2 consumption. Dissolved O_2 concentrations were similar in bulk solutions with and without bacteria. Bacterial concentrations at the metal surface decreased the number of O_2 molecules that were reduced at the surface. The authors hypothesized that at low O_2 partial pressure under the biofilm a passive film of magnetite formed that would not have formed without the microorganisms. The proposed explanations are not completely satisfactory since corrosion inhibition was not observed with killed cells but was observed when respiration was reduced in stressed cells. The absence of *Pseudomonas* after a six-week exposure in natural seawater may indicate competition from other microorganisms once the controlled corrosion-inhibiting biofilms are introduced into natural environments.

Jayaraman and coworkers [109–111] demonstrated that corrosion inhibition is a very general phenomenon among aerobic bacteria and the extent of corrosion varied with areal coverage and proportion of variable cells. Bacterial by-products in the medium did not account for their observations since fermentations in the absence of oxygen had nearly identical corrosion rates as sterile anaerobic systems [112]. The authors concluded that only a thin layer of actively respiring cells consuming oxygen was required to inhibit corrosion. When cells were killed with addition of an antibiotic to the medium, an immediate increase in the corrosion rate was noted, as measured by electrochemical impedance spectroscopy (EIS). Lower corrosion rates

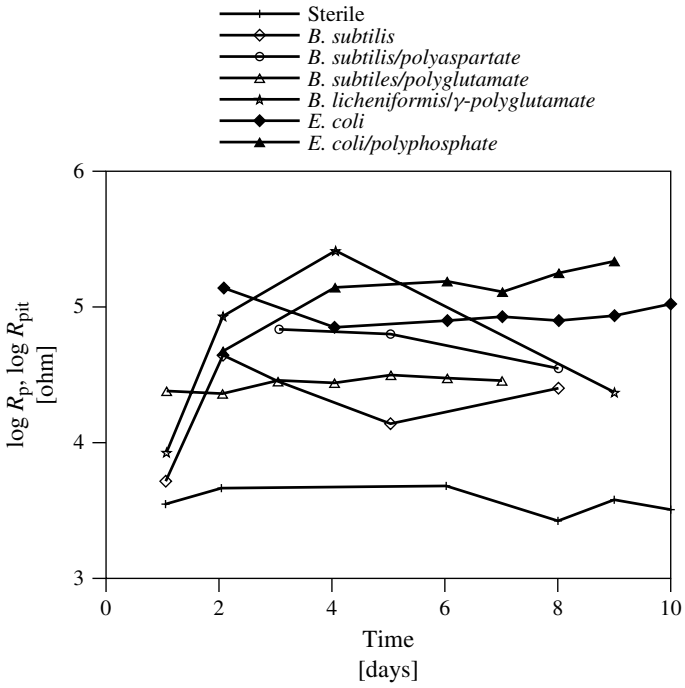


Fig. 12 Time dependence of R_{pit} and R_p for Al 2024 exposed to synthetic medium with and without *B. licheniformis* or *E. coli*.

were accompanied by increases in the corrosion potential (E_{corr}), ennoblement. The authors suggested that this increase might be due to the presence of corrosion inhibiting compounds. This group also discovered that aerobic biofilms protect copper, aluminum, and brass [113] in a laboratory setting, indicating that aerobic biofilms may be beneficial on a wide range of metals.

The concept of corrosion control using regenerative biofilms using both naturally occurring strains and genetically engineered bacteria has been investigated [114–127]. Electrochemical measurements of aluminum (Al 2024-T3) samples exposed to artificial seawater or synthetic growth medium in the presence of each of three strains of bacteria showed a significant reduction of active pit growth rates (Fig. 12) produced and ennoblement (Fig. 13) in both media [118–121]. A significant reduction of relative corrosion rates and ennoblement of E_{corr} were also observed for cartridge brass (C26000) in both media in the presence of the same bacterial biofilms [116–118].

Regenerative biofilms have been tested under industrial conditions in the chill water system at the University of California, Irvine (UCI) and at Three Mile Island Nuclear Power Station (TMI) using EIS [123, 124]. Reciprocal polarization resistance ($1/R_p$), considered to be directly proportional to the corrosion rate, was compared as a function of time for preexposed mild steel samples tested in unaltered (standard) service water and samples tested in service water inoculated with protective bacteria. Substantial differences in

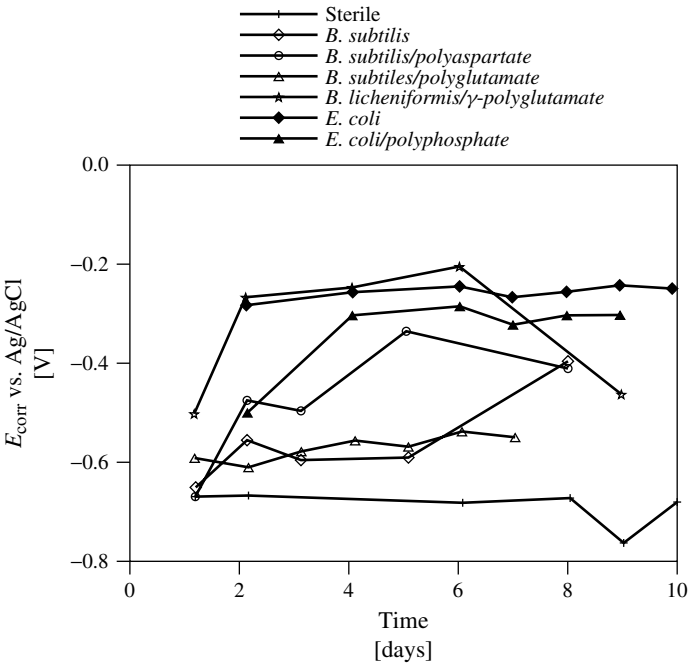


Fig. 13 Time dependence of E_{corr} for Al 2024 exposed to synthetic medium with and without *B. licheniformis* or *E. coli*.

relative corrosion rate were observed when a *Bacillus* strain was added to a system in which coupons have been exposed to service water. E_{corr} versus time, for the same samples, demonstrate ennoblement that accompanied corrosion control. A reduction of dissolved oxygen normally results in a more negative corrosion potential in sterile solution. This result strongly suggests that in this case bacteria do more than metabolize oxygen while reducing the corrosion rate of mild steel.

References

1. H. A. Videla, *Manual of Biocorrosion*, CRC Press, Boca Raton, Fla., 1996.
2. M. J. Franklin, D. C. White, B. J. Little et al., *Biofouling* **1999**, *15*(1–3), 13–23.
3. B. J. Little, A. Wagner, The interrelationship between marine biofouling, cathodic protection and microbiologically influenced corrosion, *Materials Science Forum*, Part 1 (Electrochemical Methods in Corrosion Research V. 5th International Symposium, Sesimbra, Portugal, 5–8 Sept. 1994.), Trans Tech Publications, Switzerland, 1995, pp. 433–446, Vol. 192–194.
4. J. E. Smith, D. R. Berry, *An Introduction to Biochemistry of Fungal Development*, Academic Press, New York, 1974, pp. 1–326.
5. G. Geesey, *A Review of the Potential for Microbially Influenced Corrosion of High-Level Nuclear Waste Containers*, Nuclear Regulatory Commission, San Antonio, Tex., 1993.
6. B. Little, P. Wagner, F. Mansfeld, *Int. Mater. Rev.* **1991**, *36*(6), 253–272.
7. J. W. Costerton, Z. Lewandowski, D. E. Calwell et al., *Annu. Rev. Microbiol.* **1995**, *49*, 711–745.
8. R. Kolter, R. Losick, *Science* **1998**, *280*, 226, 227.
9. J. R. Lawrence, D. R. Korber, B. D. Hoyle et al., *J. Bacteriol.* **1991**, *173*, 6558–6567.
10. D. DeBeer, P. Stoodley, Z. Lewandowski, *Biotechnol. Bioeng.* **1994**, *44*, 636–641.

11. Z. Lewandowski, P. Stoodley, S. Altobelli, *Water Sci. Technol.* **1995**, *3*, 153–162.
12. E. J. Wentland, P. S. Stewart, C.-T. Huang et al., *Biotechnol. Prog.* **1996**, *12*, 316–321.
13. A. Ohashi, T. Koyama, K. Syutsubo et al., *Water Sci. Technol.* **1999**, *39*(7), 261–268.
14. J.-L. Crolet, M. F. Magot, *Mater. Perform.* **1996**, *35*(3), 60–64.
15. W. Lee, Z. Lewandwoski, S. Okabe et al., *Biofouling* **1993a**, *7*, 197–216.
16. M. B. McNeil, A. L. Odom, Thermodynamic prediction of microbiologically influenced corrosion by sulfate reducing bacteria in *Microbiologically Influenced Corrosion Testing* (Eds.: B. J. Little, J. R. Kearnes), ASTM, West Conshohocken, 1994, pp. 173–179, STP 1232.
17. A. G. Wikjord, T. E. Rummery, F. E. Doern et al., *Corros. Sci.* **1980**, *20*, 651–671.
18. W. Lee, W. G. Characklis, *Corrosion* **1993**, *49*(3), 186–198.
19. S. C. Dexter, (Ed.), *Biologically Induced Corrosion*, NACE International, Houston, Tex., 1986, pp. 1–363.
20. G. Kobrin, (Ed.), *A Practical Manual on Microbiologically Influenced Corrosion*, NACE International, Houston, Tex., 1993, pp. 1–232.
21. J. Stoecker, (Ed.), *A Practical Manual on Microbiologically Influenced Corrosion*, NACE International, Houston, Tex., 2001.
22. P. F. Sanders, W. A. Hamilton, Biological and corrosive activities of sulfate-reducing bacteria in industrial process plant, *Biologically Induced Corrosion*, No. 47, NACE International, Houston, Tex., 1986.
23. M. Bibb, Bacterial corrosion in the South Africa power industry, *Biologically Induced Corrosion '86*, NACE International, Houston, Tex., 1986.
24. D. G. Honneysett, W. D. Van Den Burgh, P. F. O'Brien, *Mater. Perform.* **1985**, *24*(10), 34.
25. J. A. Hardy, J. L. Bown, *Corrosion* **1984**, *40*, 650–654.
26. W. Lee, Z. Lewandowski, P. H. Nielsen et al., *Biofouling* **1993b**, *7*, 217–239.
27. R. A. King, B. S. Skerry, D. C. A. Moore et al., Corrosion behavior of ductile and grey iron pipes in environments containing sulphate-reducing bacteria, *Biologically Induced Corrosion*, No. 83, NACE International, Houston, Tex., 1986, pp. 83–95.
28. B. J. Little, P. A. Wagner, O. J. Jacobus, *Mater. Perform.* **1988**, *27*(8), 51–56.
29. B. J. Little, P. A. Wagner, O. J. Jacobus et al., *Estuaries* **1989**, *12*(3), 138–141.
30. B. J. Little, P. A. Wagner, R. I. Ray et al., *J. Marine Tech. Soc.* **1990**, *243*(3), 10–17.
31. J. C. Rowlands, *J. Appl. Chem.* **1965**, *15*, 57–63.
32. J. P. Gudas, H. P. Hack, *Corrosion* **1979**, *35*, 67–73.
33. N. A. North, I. D. Macleod, Corrosion of metals in *Conservation of Archaeological Objects* (Ed.: C. Pearson), Butterworths, London, 1986, pp. 69–98.
34. C. W. Keevil, Detection of biofilms associated with pitting corrosion of copper pipework in Scottish hospitals in *Biocorrosion* (Eds.: C. C. Gaylord, H. G. Morton), Biodeterioration Society, Kew, UK, 1989, pp. 48–62.
35. B. C. Syrett, *Corros. Sci.* **1981**, *21*, 187–209.
36. I. Alanis, L. Berardo, N. De Cristofaro et al., A case of localized corrosion in underground brass pipes in *Biologically Induced Corrosion* (Ed.: S. C. Dexter), NACE International, Houston, Tex., 1986, pp. 102–108.
37. D. H. Pope, D. J. Duquette, P. C. Wayner et al., *Microbiologically Influenced Corrosion: A State of the Art Review*, Materials Technology Institute of the Chemical Process Industries, Columbus, Ohio, 1984.
38. M. B. McNeil, J. Jones, B. J. Little, Mineralogical fingerprints for corrosion processes induced by sulfate-reducing bacteria, *Proc. [21] Corros. 91*, No. 580, NACE International, Houston, Tex., 1991.
39. L. A. Chambers, P. A. Trudinger, *Geomicrobiol. J.* **1979**, *1*, 249–293.
40. B. Little, P. Wagner, J. Jones-Meehan, *Biofouling* **1993**, *6*, 279–288.
41. J. R. Jack, B. Rogoz, B. Bramhill et al., ASTMSTP 1232, The Characterization of Sulfate-Reducing Bacteria in Heavy Oil Water Flood.
42. D. H. Pope, T. P. Zintel, A. K. Kuruvilla et al., Organic acid corrosion of carbon steel: a mechanism of microbiologically influenced corrosion, *Proc. Corrosion '88*, No. 79, NACE International, Houston, Tex., 1988.
43. R. I. Islander, J. S. Devinny, F. Mansfeld et al., *J. Environ. Eng.* **1991**, *117*(6), 751–770.
44. F. Mansfeld, H. Shih, A. Postyn et al., *Corrosion* **1991**, *47*, 369–376.

45. N. W. Mittleman, J. C. Danko, Corrosion of a concrete dam structure: evidence of microbially influenced corrosion activity, *1995 International Conference on Microbially Influenced Corrosion*, Welding Society and NACE International, Houston, Tex., 1995, pp. 15-1–15-7.
46. J. H. Cleland, *Eng. Failure Anal.* **1995**, *2*(1), 79–84.
47. V. S. Brozal, A. Hall, R. deBruin, Effect of microbial flora in low grade coal on the corrosion of 3Cu12 steel, *Biodeterioration and Biodegradation 9th International Symposium*, 1997, pp. 494–499.
48. M. Beyer, H. G. Eber, H. Assenmacher et al., *Fuel* **1987**, *66*, 551–555.
49. W. Hazeu, W. H. Batenburg-van der Vegte, P. Bos et al. *Arch. Microbial.* **1988**, *150*, 574–579.
50. J. O. Harris, The role of soil microorganisms in corrosion in *Proceedings of the 7th Annual Appalachian Underground Corrosion Short Course* (Ed.: R. E. Hannah Jr), West Virginia University, West Virginia, 1962.
51. S. M. Beloglazov, A. N. Charoshavin, Corrosion behavior of steel in coal mining waters in the presence of thiobacillus thiooxidans and thiobacillus ferroxidans, *Proceedings of the 3rd International EFC Workshop*, The European Federation of Corrosion by the Institute of Material, 1995, pp. 398–404.
52. G. Schmitt, *Corrosion* **1991**, *47*(4), 285–308.
53. N. I. Dowling, Corrosion of materials used in storage and handling of solid elemental sulphur, *Materials Performance Sulphur and Energy*, Canadian Institute of Mining, Quebec, Canada, 1992, pp. 104–115.
54. W. H. Dickinson, Z. Lewandowski, *Biofouling* **1996**, *10*, 79–93.
55. W. H. Dickinson, F. Caccavo Jr, Z. Lewandowski, *Corros. Sci.* **1996**, *38*, 1407–1422.
56. P. Linhardt in *Microbially Influenced Corrosion of Materials* (Eds.: E. Heitz, H.-C. Fleming, W. Sand), Springer-Verlag, Berlin, Germany, 1996, pp. 221–230.
57. Z. Lewandowski, Corrosion/2000, Paper No. 400, NACE, 2000.
58. M. H. W. Renner, *Dechema Monogr.* **1996**, *133*, 59.
59. G. Kobrin, *Materials Performance* **1976**, *15*(7), 38–43.
60. C. O. Obuekwe, D. W. S. Westlake, J. A. Plambeck et al., *Corrosion* **1981**, *37*(8), 461–467.
61. J. M. Burnes, E. E. Staffeld, O. H. Calderon, *Dev. Ind. Microbiol.* **1969**, *8*, 327.
62. B. Little, P. Wagner, S. M. Gerchakov et al., *Corrosion* **1986**, *42*(9), *533*.
63. S. M. Gerckakov, L. L. Udey, *Marine Biodeterioration: An Interdisciplinary Study*, Naval Institute Press, Annapolis, Md., 1984, pp. 82–87.
64. L. A. Terry, R. G. J. Endyvean, *Algal Biofouling*, Elsevier, New York, 1986, pp. 211–229.
65. K. Bosecker, *Microbially Influenced Corrosion of Materials*, Springer-Verlag, Berlin, Germany, 1996, pp. 439–446.
66. H. A. Videla, P. S. Guiamet, S. DoValle et al., *A Practical Manual on Microbiologically Influenced Corrosion*, NACE International, Houston, Tex., 1993, pp. 125–139.
67. J. D. Walker, H. F. Austin, R. R. Colwell, *J. Gen. Appl. Microbiol.* **1975**, *21*, 27.
68. R. J. Watkinson, *Microbial Problems and Corrosion in Oil and Oil Products Storage*, The Institute of Petroleum, London, 1984, pp. 50–56.
69. H. A. Videla, P. S. Guiamet, S. DoValle et al., Proceedings Corrosion '88, Paper No. 91, NACE International, Houston, Tex., 1988.
70. B. M. Rosales, Proceedings of the Argentine-USA Workshop on Biodeterioration, CONICET-NSF, La Plata, Argentina, 1985, pp. 135–143.
71. E. R. De Schiapparelli, B. R. De Meybaum, *Mater. Perform.* **1980**, *19*(14), 47–50.
72. M. F. L. De Mele, R. C. Salvarezza, H. A. Videla, *Int. Biodeterior. Bull.* **1979**, *15*, 39.
73. B. R. De Meybaum, E. R. De Schiapparelli, *Mater. Perform.* **1980**, *19*(8), 41–44.
74. R. A. King, J. F. Stott, *Microbial Problems and Corrosion in Oil and Oil Products Storage*, The Institute of Petroleum, London, 1984, pp. 93–105.
75. P. McKenzie, A. S. Akbar, J. D. Miller, Microbial corrosion affecting the petroleum industry, Institute of Petroleum, Microbiological Group Symposium IP 77-001, pp. 37–50.
76. H. A. Videla, *Biologically Induced Corrosion*, NACE International, Houston, Tex., 1977, pp. 215–222.
77. B. M. Rosales, A. Puebla, D. Cabral, *Proceedings of 12th International Corrosion Congress*, NACE International, Houston Tex., 1993, pp. 3773–3785.

78. R. C. Salvarezza, H. A. Vadela, *Acta Cientifica Venezolana* **1984**, *35*, 244.
79. J. D. Walker, L. Cofone Jr, J. J. Cooney, *Proceedings of Joint Conference on Prevention and Control of Oil Spills*, American Petroleum Institute, Washington, D.C., 1973, pp. 821–825.
80. W. J. Cook, J. A. Cameron, J. P. Bell et al., *J. Polym. Sci., Polym. Lett. Ed.* **1981**, *19*, 159.
81. D. R. Houghton, R. N. Smith, H. O. Eggins, Eds., Mechanistic aspects of polyurethane biodeterioration, *Biodeterioration 7*, Elsevier Applied Science, London, 1988, pp. 351–358.
82. R. A. Zabel, F. Terracina, *Dev. Ind. Microbiol.* **1980**, *21*, 179.
83. M. Stranger-Johannessen, 6th International Biodeterioration Symposium, Washington, D.C., 1984.
84. M. Stranger-Johannessen, *Microbial Problems in the Offshore Oil Industry*, John Wiley & Sons, New York, 1987, pp. 57–71.
85. S. Barry, D. R. Houghton, Eds., *Biodeterioration 6*, C.A.B. International Mycological Institute, The Biodeterioration Society, pp. 218–223.
86. T. Ford, J. Maki, R. Mitchell, Biodeterioration 7, Paper No. 70, The Biodeterioration Society, Cambridge, UK, 1988.
87. G. G. Geesey, M. W. Mittelman, T. Iwaoka et al., Corrosion/85, Paper No. 297, NACE International, Houston, Tex., 1985.
88. P. J. Bremer, G. G. Geesey, *Appl. Environ. Microbiol.* **1991**, *57*, 1956.
89. B. Frølund, R. Palmgren, K. Keiing et al., *Water Res.* **1996**, *30*, 1749–1758.
90. T. R. Neu, *Microbiol. Rev.* **1996**, *60*, 151–166.
91. P. H. Nielsen, A. Jahn, R. Palmgren, *Water Sci. Technol.* **1997**, *36*, 11–19.
92. G. G. Page, *Mater. Perform.* **1972**, *11*, 53.
93. D. B. Wells, B. J. Webster, P. T. Wilson et al., Australasian Corrosion Assoc. Inc. Conference, Corrosion and Prevention, Adelaide, November 27–30, 1994.
94. New England Water Works Association, National Conference on Integrating Corrosion Control and Other Water Quality Goals, Cambridge, Mass., May 19–21, 1996.
95. Japan Copper Development Association, Final Report No. TPT-0478, 1994.
96. B. J. Webster, S. E. Werner, D. B. Wells et al., *Corrosion* **2000**, *56*, 942.
97. G. G. Geesey, T. Iwaoka, P. R. Griffiths, *J. Coll. Interface Sci.* **1987**, *120*, 370–375.
98. G. G. Geesey, L. Jang, J. G. Jolley et al., *Water Sci. Technol.* **1988**, *20*, 161–165.
99. I. B. Beech, V. Zinkevich, R. C. Tapper et al., *Geomicrobiol. J.* **1998**, *15*, 119–134.
100. I. B. Beech, V. Zinkevich, R. C. Tapper et al., *J. Microbiol. Methods* **1999**, *36*, 3–10.
101. H. H. P. Fang, L. C. Xu, K. Y. Chan, *Biotechnol. Lett.* **2000**, *22*, 801–805.
102. K. Y. Chan, L. C. Xu, H. H. P. Fang, *Environ. Sci. Technol.* **2002**, *36*(8), 1720–1727.
103. A. Pedersen, S. Kjelleberg, M. Hermansson, *J. Microbiol. Methods* **1988**, *8*, 191.
104. A. Pedersen, M. Hermansson, *Biofouling* **1989**, *1*, 313.
105. A. Pedersen, M. Hermansson, *Biofouling* **1991** *3*, 1.
106. H. A. Videla, P. Guiamet in *Biodeterioration Research 1* (Eds.: G. Llewellyn, C. O'Rear), New York, Plenum Press, 1987, pp. 275–281.
107. G. Geesey, L. Jang, Binding of metal ions by extracellular polymer in *Metals, Ions and Bacteria* (Eds.: T. Beveridge, R. Doyle), John Wiley & Sons, New York, 1988, pp. 325–327.
108. G. Hernandez, V. Kucera, D. Thierry et al., *Corrosion* **1994**, *50*(8), 603.
109. A. Jayaraman, J. C. Earthman, T. K. Wood, *Appl. Microbiol. Biotechnol.* **1997**, *47*, 62–68.
110. A. Jayaraman, E. T. Cheng, J. C. Earthman et al., *J. Ind. Microbiol.* **1997**, *18*, 396–401.
111. A. Jayaraman, A. K. Sun, T. K. Wood, *J. Appl. Microbiol.* **1998**, *84*, 485–492.
112. A. Jayaraman, E. T. Cheng, J. C. Earthman et al., *Appl. Microbiol. Biotechnol.* **1997**, *48*, 11–17.
113. A. Jayaraman, D. Ornek, D. A. Duarte et al., *Appl. Microbiol. Biotechnol.* **1999**, *52*, 787–790.
114. A. Jayaraman, P. J. Hallock, R. M. Carson et al., *Appl. Microbiol. Biotechnol.* **1999**, *52*, 267–275.
115. A. Jayaraman, F. B. Mansfeld, T. K. Wood, *J. Ind. Microbiol. Biotechnol.* **1999**, *22*, 167–175.
116. B. C. Syrett, P. J. Arps, J. C. Earthman et al., *La Metallurgia Italiana* **2001**, *93*, 39–44.
117. B. C. Syrett, P. J. Arps, J. C. Earthman et al., Biofilms that prevent corrosion in Proc. Symp. ''Microbiologically Influenced Corrosion'', *CORROSION/2002* (Ed.: B. Little), NACE International, Houston, Tex., 2002, pp. 145–154.

118. F. Mansfeld, C. H. Hsu, D. Ornek et al., Corrosion control using regenerative biofilms (CCURB) on aluminum 2024 and brass in different media, *Proc. Symp. "New Trends in Electrochemical Impedance Spectroscopy (EIS) and Electrochemical Noise Analysis (ENA)"*, PV 2000–2024, The Electrochemical Society, Pennington, NJ, 2001, pp. 99–118.
119. D. Ornek, A. Jayaraman, T. K. Wood et al., *Corros. Sci.* **2001**, *43*, 2121–2133.
120. A. Nagiub, F. Mansfeld, *Mater. Corros.* **2001**, *52*, 817–826.
121. A. Nagiub, F. Mansfeld, *Corros. Sci.* **2001**, *43*, 2001–2009.
122. F. Mansfeld, Z. Sun, C. H. Hsu, *Electrochim. Acta* **2001**, *46*, 3651–3664.
123. K. Trandem, P. J. Arps, J. C. Earthman, Closed-loop sidestream systems for investigating corrosion control using regenerative biofilms (CCURB) in service water, CORROSION/2000, Paper No. 648, Houston, Tex., 2001.
124. K. Trandem, Z. S. Farhangrazi, T. K. Wood et al., Field sidestream investigations of corrosion control using regenerative biofilms (CCURB), CORROSION/2001, Paper No. 1271, Houston, Tex., 2001.
125. Kh. M. Ismail, T. Gehrig, A. Jayaraman et al., *Corrosion* **2002**, *58*(5), 417–423.
126. F. Mansfeld, Z. Sun, C. H. Hsu et al., *Corrosion* **2002**, *58*, 187–191.
127. M. Dubiel, C. H. Hsu, C. C. Chien et al., *Appl. Environ. Microbiol.* **2002**, *68*(3), 1440–1445.

7
Electrochemical Techniques for Corrosion

Gerald S. Frankel
Ohio State University, Columbus, Ohio

Michael Rohwerder
Max Planck Institute, Duesseldorf, Germany

7.1 Goals of Testing 689

7.2 Experimental Design Considerations 691
7.2.1 Sample Selection 691
7.2.2 Surface Preparation 691
7.2.3 Sample Masking 692
7.2.4 Choice of Electrolyte 694
7.2.5 Cell Design 694
7.2.6 Choice of Technique 696

7.3 Electrochemical Techniques for Determination of Corrosion Rate . . 696
7.3.1 Potentiodynamic Polarization 697
7.3.1.1 Corrosion Rate Measurement by Tafel Extrapolation 697
7.3.1.2 Corrosion Rate Measurement by Fitting Polarization Curve to Wagner–Traud Equation 700
7.3.1.3 Corrosion Rate Measurement by Linear Polarization 700
7.3.2 Electrochemical Impedance Spectroscopy 702
7.3.3 Corrosion Rate Determination by Electrochemical Noise Analysis (ENA) 707
7.3.4 Comparison of the Techniques for Assessment of Corrosion Rate . . 708

7.4 Techniques for Studying Passivity 709

7.5 Techniques for Evaluating Localized Corrosion 710

7.6 Exposure Testing 716

7.7 Quartz Crystal Microbalance 716

7.8 Scanning Kelvin Probe 717

7.9 Scanning Probe Microscopy 719
References 720

The understanding of the electrochemical phenomena underlying corrosion processes provides a basis for experimental techniques that allow simple and accurate measures of corrosion rates. The electrochemical fundamentals are discussed in Sects. 1.2–1.4 of this volume and in other volumes of this series. This chapter will discuss a wide range of experimental techniques commonly used in the field of corrosion and issues associated with their use. Electrochemical techniques will be the focus, but some nonelectrochemical techniques will also be discussed. Electrochemical techniques take advantage of our ability, with modern instrumentation, to utilize feedback control and measure very small currents. These techniques allow highly sensitive measurements that far exceed the capabilities of most nonelectrochemical techniques based on, for instance, weight loss or appearance. On the other hand, some nonelectrochemical techniques are also extremely sensitive to small amounts of material loss. An example is the quartz crystal microbalance (QCM), which provides submonolayer sensitivity as will be described in the following sections.

7.1 Goals of Testing

Before beginning a series of experiments to measure corrosion rates or to study some other aspect of corrosion, it is important to determine clearly what the goal of the work is. Usually, such studies require the use of an accelerated test method to provide answers to problems quickly. Exposure testing in the service environment is an important tool in corrosion engineering, but the time frame for exposure tests is often too long for timely decisions on design.

Corrosion testing is frequently used to address questions and solve problems regarding the stability of a material in a given environment. Corrosion-related failures take several forms. A general loss of material to corrosion usually leads to mechanical failure as a result of thinning of the cross section of the part, and an increase in the stress for a given load. Localized corrosion can lead to failure by perforation of a tube or vessel. Localized corrosion can also initiate a crack that could propagate as a result of mechanical loading, or from synergistic interactions

of environment and stress. Breaching of a coating might define the failure of a coated structure. This cosmetic failure associated with a coating can lead to accelerated attack under the coating and subsequent failure by another mechanism. Failure of electronic devices is often associated with an open or a short in thin-film wiring or loss of optical, magnetic, or some other property.

The first question that might be of interest is to determine if the material passivates or undergoes uniform active corrosion in the relevant environment. If the form of corrosion is active corrosion, then the corrosion rate needs to be measured, and a determination can be made if there is sufficient material to survive the lifetime requirements. Corrosion rate, r (units of thickness loss per unit time), is related to a corrosion current density, i_{corr} (A cm^{-2}), which is the outcome of most electrochemical tests, by way of Faraday's law:

$$r = C\left(\frac{M}{\rho n F}\right) i_{corr} \qquad (1)$$

where M is the molecular weight of the corroding metal (g mol^{-1}), ρ is the density of metal (g cm^{-3}), n is the charge number (dimensionless), F is the Faraday constant (96 485 C mol^{-1}), and C is a constant to alter units of thickness and time.

The rate of corrosion is commonly a function of time because of changes in the sample surface or in the environment. However, most electrochemical techniques provide an instantaneous corrosion rate. Long-term exposure tests do not provide the time-dependent corrosion rate, but rather an average rate over the exposure time. If a reasonable estimate of the time dependence of corrosion rate is not available, it is commonly assumed that the rate is constant. The total loss of material over a period of time, X, is given by the integral of the rate:

$$X = \int r \, dt \qquad (2)$$

If i_{corr} is constant, X for a given time t is simply $C(M/\rho n F)t \; i_{corr}$. The lifetime of the component would be the time for the development of a critical material loss, which might be associated with a reaching a critical stress leading to ductile failure.

If a material is found to be passive in the service environment, then it is often of interest to know if it is susceptible to localized corrosion. Material loss by uniform passive dissolution is typically small enough to be ignored when predicting lifetimes. For a system that exhibits localized corrosion, prediction of lifetime is difficult. The main problem is the determination of the time for initiation of a localized attack. Once localized corrosion initiates, the time to perforate a structure can be determined if the propagation rate of localized corrosion is known. Localized corrosion propagation rates typically are not constant with time; they tend to decrease with time, following a $t^{-1/2}$ dependency [1]. Techniques are available to determine this rate, as described in the following text. The penetration distance is obtained from the integral of the rate, as in Eq. (2), and typically follows a $t^{1/2}$ dependency [1]. So, if the propagation rate is known as a function of time and some initiation time is assumed, failure times by penetration can be determined.

Testing of real components can provide information regarding the susceptibility of the component to crevice corrosion. The propagation of crevice corrosion is often similar to that of other forms of localized corrosion, so failure prediction

has the same requirements. Initiation of crevice corrosion is also not well understood.

Other questions can be answered by electrochemical testing. By measuring the behavior of the different materials in a complex structure, it is possible to determine if the corrosion rate of certain components of a structure will be enhanced by galvanic interactions. The basis for making this assessment was given in Sect. 1.3 of this volume.

Often, it is of interest to know if reductions in corrosion rate can be achieved by certain means, such as changing the material or alloy, using protective surface films, altering the environment, or modifying the design. Electrochemical testing can generate useful input to these questions by providing comparative results. For instance, the influence of detrimental or beneficial agents in solution can be determined by a series of experiments in solutions of varying concentration.

A final question that might be addressed by experiments is the susceptibility to environmental cracking. Such experiments, of course, would require the application of a stress in some form.

7.2 Experimental Design Considerations

When designing an electrochemical experiment, there are several factors that need to be decided. It is common that the design of the experiment and the preparation of samples comprise the hardest and most time-consuming part of electrochemical experimentation. Decisions need to be made regarding sample selection, surface preparation, masking to expose a certain area, specifics of the experimental cell, selection of the appropriate test environment, and choice of the best technique. These factors will be addressed in turn.

7.2.1 Sample Selection

The microstructure of a metal often plays a critical role in the corrosion process. Therefore, it is critical to choose the material stock for testing carefully. Microstructure can change depending on the form of the material, that is, plate, rod, sheet, or thin film. End grains of a worked structure are often more susceptible to attack. Temper can play a very important role in the corrosion of Al alloys. Ideally, the material used in experiments should be identical to that used in the real application. If the form of the material is unknown, it might be of interest to investigate the role of processing and microstructure on the corrosion process.

7.2.2 Surface Preparation

Details of the surface preparation can exert a dominant influence on the corrosion rate and mechanism. Mill scales can be protective or act as sites for aggressive attack. As a minimum, as-received surfaces are typically cleaned with organic solvents and water prior to testing. Because of inherent variability of as-received surfaces, it is common to generate a fresh and reproducible metal surface by abrading and polishing. Abrading a surface to a 600-grit finish is sufficient to prepare a reproducible surface. However, the roughness of a freshly prepared surface can affect the corrosion rate. Samples polished to a mirror finish typically exhibit lower corrosion rates than those that are only abraded. Abrading and

polishing are typically performed under water, and the conditions generated during such surface preparation can be aggressive to some materials. High-strength Al alloys should be polished in a nonaqueous slurry, such as alcohol or kerosene, to minimize corrosion during polishing. If polished in water, the reactive intermetallic particles in these alloys will be attacked.

7.2.3 Sample Masking

Since corrosion rate must be normalized to the exposed area, it is critical to know and control the area of exposure. Furthermore, for electrochemical tests, an electrical connection must be made to the sample, and this connection should be protected so that it does not contact the solution.

It is possible to simply immerse a sample partially in a beaker of solution, making electrical contact above the water line. Inherent in this approach, however, is the existence of a sample/solution/gas interface, which can influence the corrosion rate. Oxygen from the gas phase would have greater access to the meniscus at this interface, and attack can be accelerated there as a result of an oxygen concentration cell. If the solution is agitated by stirring or bubbling, the position of the interface would not be constant, which can also affect the measurement. It is common, for samples that are immersed through the water line, to use a flag electrode (Fig. 1a)

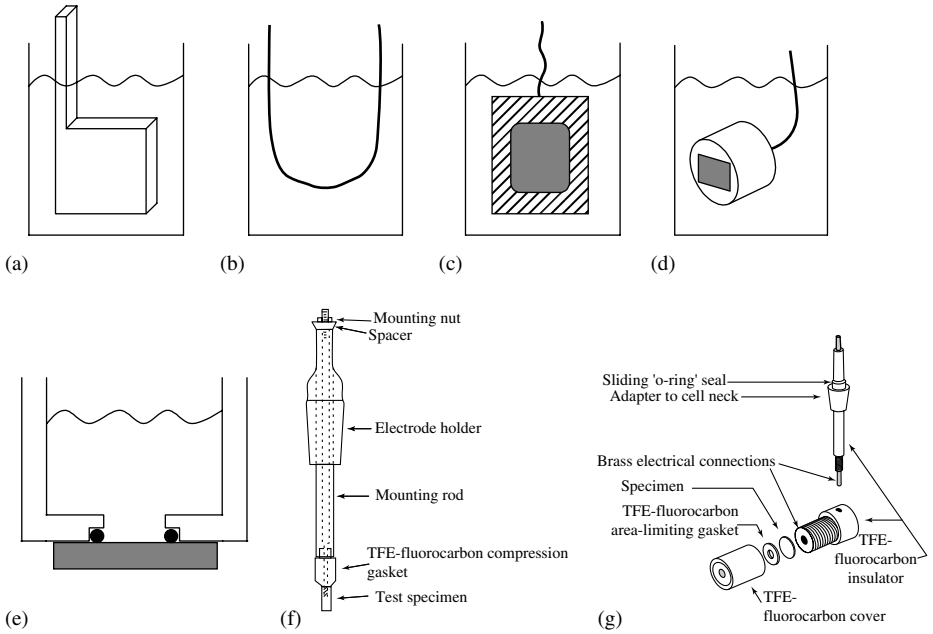


Fig. 1 Schematic representations of various masking techniques and sample configurations. (a) Flag electrode; (b) wire loop electrode; (c) sample painted with protective coating; (d) sample mounted in epoxy or other metallographic mount. The wires for electrical connection in (c) and (d) must be coated to prevent exposure to the electrolyte. (e) Sample pressed against an o-ring; (f) rod with Teflon compression gasket, from ASTM G5-94; and (g) Teflon seal from ASTM G61–86.

that minimizes the interface length. Wire loop electrodes achieve the same goal for wire samples (Fig. 1b).

Protective coatings are often used to mask off an area of a sample (Fig. 1c). This approach generates an interface at the edge of the coating and the exposed area, which is a region that is often the site of crevice corrosion for systems that are susceptible to crevice attack. A slight delamination or poor adhesion at this edge is sufficient to create an occluded region at which attack is enhanced. The crevice corrosion at such an artifact can dominate the signal from the sample. A commonly used organic coating for masking samples is red Microstop lacquer. It is resistant to many solutions, easily applied, and it dries quickly. However, it is not extremely adherent and is susceptible to crevice attack. Marine epoxy paint is another masking material that is more resistant to crevicing. Apiezon W black wax is very resistant because, for a period of about two days, it is extremely adherent. Prior to application, it is dissolved into an organic solvent, such as trichloroethylene, and must dry for several hours before use. After two days, as drying continues, it becomes very hard and can form a crevice.

Corrosion samples can be mounted in epoxy or some other mounting medium as is commonly done for the preparation of a metallographic sample, Fig. 1(d). Samples mounted into a round puck are easily handled during polishing. An electrical connection can be made to the back of the sample with a shielded wire attached by a setscrew, spot-welding or conductive epoxy. Such a sample can be simply immersed into a cell. However, the sample/mounting edge of a polished surface is very susceptible to crevice attack in crevicing environments, and those interfaces should be covered with another layer of protective coating material, such as described earlier.

The masking of a sample is often related to the form of the sample and the choice of the cell. One approach is to use a cell with an opening in one of the walls. The sample can be pressed against the opening using an o-ring or gasket as a seal, Fig. 1(e). This approach can only be used on flat samples, and such cells are often called ''flat cells''. Standard rubber o-rings can also generate occluded regions that result in crevice corrosion when pressed against a metallic sample. Special Teflon o-rings with a knife-edge reduce this effect because of the compressibility of Teflon. These Teflon o-rings can be easily damaged, and so should really only be used once. However, they are often used repeatedly in practice owing to the cost of such special o-rings. Standard rubber o-rings can be used in conjunction with another protective coating. The o-ring is pressed against the coating in this approach, with the masking and crevice prevention accomplished by the coating.

Figure 1(f, g) show electrode configurations from two ASTM standards. The first uses a Teflon compression gasket to seal a cylindrical sample. The standard, ASTM G5 [2], is for testing stainless steel in sulfuric acid, so crevice corrosion is not a concern. The electrode assembly in Fig. 1(g) is from ASTM G61 [3], which is for testing localized corrosion resistance of stainless steels and similar alloys in a chloride solution. The seal is made by a Teflon gasket that is pressed against the sample by a cover. Electrical connection is made through a rod pressed against the back of the sample.

ASTM G150 is a new standard for the determination of critical pitting temperature (CPT) [4]. That standard describes a flushed port cell, in which the sample is pressed against an o-ring attached to a cell.

The o-ring is set back from the opening to form an intentional crevice. The crevice region contains a showerhead type manifold through which deionized water is forced. This water flushes the crevice to prevent accumulation of aggressive species. Such a masking design can be very effective at preventing crevice corrosion, but it is critical to ensure that the deionized water is delivered uniformly to the whole crevice region to prevent crevice corrosion.

7.2.4 Choice of Electrolyte

The choice of electrolyte is sometimes, but not always, a simple matter. If the service environment is well known and controlled, then it should be used for the test environment. However, the service environment is not always known or can be quite varied, as in the case of an airplane that travels from place to place. The choice of environment is less restricted in such cases. To characterize the corrosion behavior of a material, a range of pH values is often studied, and the effects of chlorides in solution are usually of interest. The solution should have sufficient conductivity to avoid problems associated with ohmic potential drops. *IR* compensation techniques should be used in those situations. Some studies attempt to assess the corrosion susceptibility of a range of alloys, or the efficacy of different coatings or inhibitors. It is critical to find solutions of the right aggressiveness when making such comparisons. If an overly corrosive environment is used, then all of the samples will exhibit poor corrosion resistance. Conversely, if a too-benign environment is used, then all of the samples will look good, with no differentiation achieved. The correct level of corrosivity will change from case to case, and must be determined empirically.

A decision must also be made regarding the concentration of dissolved oxygen in the electrolyte. Again, if the service conditions are known, then the test conditions should match them. Sometimes it is of interest to deaerate the electrolyte, which is typically performed by sealing the cell and bubbling Ar or N_2 gas through the electrolyte. Deaeration will often reduce the open circuit potential (OCP) by eliminating the oxygen reduction reaction. This allows observation of the oxidative behavior of a sample in a region that would not otherwise be accessible because of the dominating current associated with oxygen reduction.

7.2.5 Cell Design

A wide range of cells can be used for corrosion experiments. As mentioned, the selection of the cell is connected to the form of the sample and the masking scheme. It is often possible to simply immerse a sample into a beaker, Fig. 1. The water line can be managed with a flag electrode, or by masking the sample to expose only a submerged area.

A round-bottomed multinecked flask is a common approach when a sealed cell is required, Fig. 2(a). The multiple ports allow for insertion of tubes for deaeration, thermometers, and the various electrodes. As mentioned above, cells that press the sample against a window are called flat cells. Flat cells are easily sealed and convenient to use, Fig. 2(b). A clamp-on cell is a type of flat cell commonly used for coated samples, Fig. 2(c). Large areas are typically needed for clamp-on cells, and crevice corrosion is not a problem. The clamp-on cell uses a common glassware

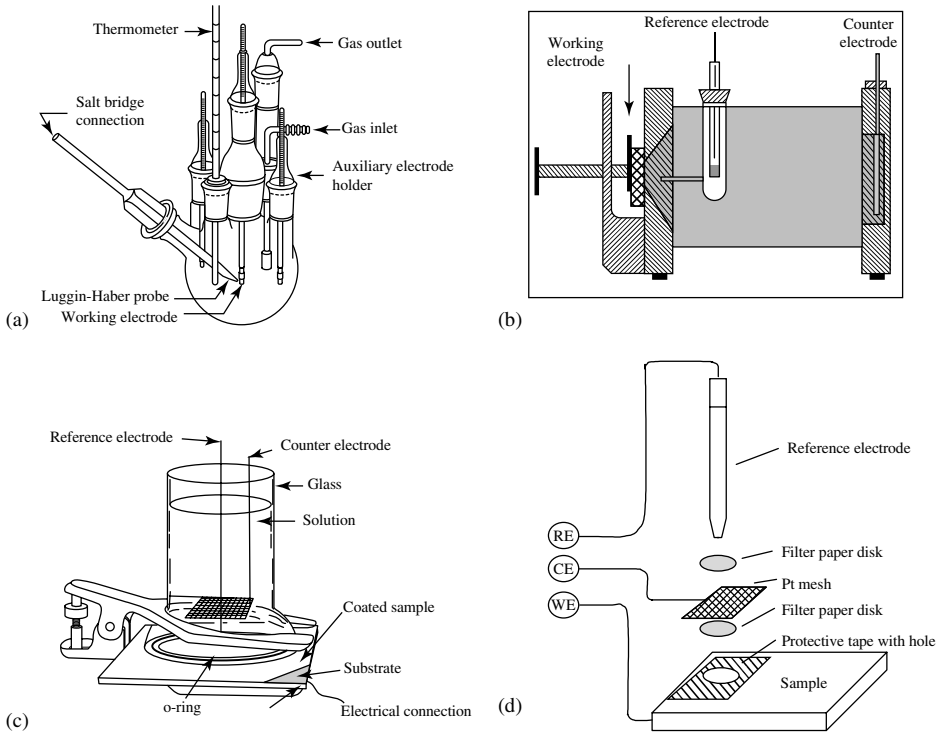


Fig. 2 Various types of cells for corrosion experiments. (a) Greene cell; (b) flat cell, can also be configured for sample on bottom; (c) clamp-on cell to expose large area of a coated sample; and (d) droplet cell, which can be used with pure water to simulate atmospheric corrosion.

fitting with a large opening and an o-ring seal.

There are several issues related to the reference and counterelectrodes. Reliable reference electrodes are commercially available. The saturated calomel electrode (SCE) is extremely robust and is commonly used for studies in chloride solutions. For studies in which chloride is to be avoided, the mercurous sulfate electrode (MSE) is suitable. The location of the reference electrode is critical in cells in which large ohmic potential drops exist. In these cases, a Luggin capillary should be used to bring the sensing location of the reference electrode close to the working electrode surface and minimize the ohmic potential drop. The tip of the capillary should be no closer to the working electrode surface than a distance equal to twice the capillary diameter to prevent shielding effects. If the inner diameter of the Luggin capillary gets too small, the resistance in the electrometer circuit can lead to oscillations in the potentiostat control circuit. Stability issues can be surmounted by using a Pt wire that is connected to the reference electrode lead through a small capacitator (several microfarads).

Counterelectrodes should be made from an inert material such as Pt or graphite, and should have a large enough area to

prevent current limitations. If products that form at the counterelectrode are a concern, it can be isolated from the rest of the solution by a semipermeable membrane or a glass frit. In resistive electrolytes, the counterelectrode should be as parallel as possible to the working electrode. Nonuniform current distribution can lead to spurious results. For perfectly uniform current distribution, the working electrode should comprise one complete wall of the cell and the counterelectrode should comprise the complete opposite wall.

The droplet cell, Fig. 2(d), has uniform current distribution and shrunken dimensions that allow resistive electrolytes to be used [5]. This approach was developed for the use of pure water as an electrolyte as a means to mimic atmospheric corrosion, but it can be used with any electrolyte. An area of a flat sample is exposed through a hole in a piece of protective tape. Electroplater's tape is a very resistant tape with good adhesion that is useful for this and other masking applications in corrosion. If the hole in the tape is made with a round punch, the same punch can be used to make circular dots from pieces of filter paper. One such dot is placed securely into the exposed hole. A small (typically 10–20 μl) droplet of solution is placed on the filter paper using a calibrated pipette. This wet filter paper acts as the electrolyte. A piece of woven Pt mesh is placed on top of the wet filter paper, and a reference electrode is held against the back of the Pt counterelectrode. As mentioned, the small dimensions allow the use of even very pure water. This simulates atmospheric corrosion, in which a thin water layer forms on the surface. As in atmospheric corrosion, soluble species on the sample surface and pollutant gases in the air are dissolved into the water droplet, which provides some conductivity. This technique has been used to assess the effects of various cleaning steps after reactive ion etching on the corrosion of thin-film Al samples [6].

7.2.6 Choice of Technique

Many different electrochemical and nonelectrochemical techniques exist for the study of corrosion and many factors should be considered when selecting a technique. Corrosion rate can be determined by Tafel extrapolation from a potentiodynamic polarization curve. Corrosion rate can also be determined using the Stern–Geary equation from the polarization resistance derived from a linear polarization or an electrochemical impedance spectroscopy (EIS) experiment. Techniques have recently been developed to use electrochemical noise for the determination of corrosion rate. Susceptibility to localized corrosion is often assessed by the determination of a breakdown potential. Other techniques exist for the determination of localized corrosion propagation rates. The various electrochemical techniques will be addressed in the next section, followed by a discussion of some nonelectrochemical techniques.

7.3 Electrochemical Techniques for Determination of Corrosion Rate

This section will discuss a number of different electrochemical techniques used for determination of corrosion resistance or corrosion rate. It will be assumed that a modern, computer-controlled, potentiostat is available for use. Such instruments are now relatively inexpensive. The menu-driven software for experiment control and data collection, as well as powerful

programs for data analysis, make modern systems very easy to use.

A number of good sources of information exist on the topic of electrochemical and nonelectrochemical test methods for corrosion. This chapter refers to many ASTM standards, most of which are in Volume 3.02 of the ASTM Annual Book of Standards entitled ''Wear and Erosion; Metal Corrosion''. Books [7–9] and review articles [10–12] on corrosion testing provide more detail than can be given here.

Data will be presented below from different techniques applied to Fe in 0.5 M H_2SO_4. Figures 3, 4, 6, and 7 represent experiments performed sequentially on a single sample in the same electrolyte to facilitate comparison of the different techniques. The experiments were performed in the following sequence (which is different from the order of presentation): linear polarization, EIS, potentiodynamic polarization over a wide potential range. The noise analysis was performed on different Fe electrodes taken from the same stock.

7.3.1 Potentiodynamic Polarization

The relationship between current and potential at an electrode/electrolyte interface can be probed by either controlling the potential and measuring the current, or by controlling the current and measuring the potential. In order to investigate the relationship over a range of values, the controlled parameter is either stepped or scanned. The most common approach for determining the current/potential relationship is potentiodynamic scanning. The potential is scanned at a fixed rate between two set values and the current is measured at periodic intervals. By automatically switching between measuring resistors with a range of values, potentiostats can accurately determine currents over many orders of magnitude.

ASTM G5 describes a procedure for a potentiodynamic polarization test on type 430 stainless steel in sulfuric acid that is intended to be a means to check experimental technique and instrumentation [2]. It indicates that the multinecked flask shown in Fig. 2(a) and the electrode configuration shown in Fig. 1(f) are suitable for the cell and working electrode configuration, respectively. A scan rate of 0.167 mV s^{-1} is specified.

7.3.1.1 Corrosion Rate Measurement by Tafel Extrapolation

As described in Chapter 1.3 the understanding of mixed potential theory through the use of Evans diagrams provides the basis for the determination of corrosion rate by Tafel extrapolation. For systems under activation control, Tafel-type behavior (a linear relationship between potential and the log of the current density) is exhibited when the potential is sufficiently far from the OCP (>50–70 mV) that the current associated with the reaction of the opposite polarity is insignificant. A potentiodynamic polarization experiment for Tafel extrapolation typically starts at a potential about 250 mV negative to the OCP, and scans upward through the potential of zero current (which might be different than the original OCP) to a value that is about 250 mV positive to the original OCP. The zero-current potential is an instantaneous open circuit or corrosion potential, and is often referred to as such. However, the zero-current potential measured during a polarization experiment might be different than the OCP measured before or after the experiment owing to reactions that occur during the scan, such as oxide reduction, dissolution, and passivation. One

can avoid this type of artifact by combining the results of two separate scans that each start at the OCP, one proceeding in the anodic direction and one in the cathodic direction.

The ±250-mV range of potential is sufficient to allow the observation of a Tafel region if it exists. Less polarization is required if the Tafel slope is low. The line describing the behavior in the Tafel region can be extrapolated to the corrosion potential to determine the corrosion rate, as described in Chapter 1.3. A Tafel region extending for at least one order of magnitude of current is needed for accurate extrapolation. The rate of polarization in a potentiodynamic scan is typically between 0.1 and 1 mV s^{-1}. The intent of such tests is to determine steady state behavior, so, given practical limitations, slower scanning is preferred. Furthermore, at high potential scan rates, non-faradaic current associated with charging of the capacitance associated with the interface double layer or a surface oxide film ($I = C\,dE/dt$) will add to the current associated with faradaic, or electrochemical reactions.

An example of a potentiodynamic polarization scan is given in Fig. 3 for Fe in 1 N H_2SO_4. In this experiment, the potential scan began at a value 250 mV below the OCP, and continued upwards to very high values. The full polarization curve is given in Fig. 3(a). The portion of the curve near the OCP is expanded in Fig. 3(b). The potential at which the current switched polarity, the zero-current potential, is where the curve points downwards. The currents are negative at lower potentials, and positive at higher potentials. For Fe in 1 N H_2SO_4, the cathodic portion of the curve exhibits clear Tafel behavior over a wide range of potential. It is a simple matter to extrapolate this region to the zero current or corrosion potential to obtain the corrosion current density. As shown in the figure, a value of 1.8×10^{-4} A cm^{-2} is obtained. The cathodic Tafel slope can be determined to be 114 mV $decade^{-1}$.

Unlike the cathodic portion of the polarization curve, the anodic portion of the curve in Fig. 3(b) does not exhibit clear Tafel-type behavior. The mechanism for Fe dissolution in acids is quite complex. A line can be drawn in the region just above the corrosion potential, giving a Tafel slope of 34 mV $decade^{-1}$. Extrapolation of this line intersects the zero-current potential at 7×10^{-5} A cm^{-2}, a considerably different value than the extrapolation of the cathodic portion of the curve. This is not uncommon in practice. When this happens, it is usually considered that the anodic portion of the curve is affected by changes on the electrode surface, that is, surface roughening or film formation. The corrosion rate is typically determined from the extrapolated cathodic Tafel region.

Potentiodynamic polarization over a wide range of potential, such as is seen in Fig. 3(a), provides more information about the system than just the corrosion rate. The behavior of the electrode over a range of potential is often of interest. The various regions of electrode behavior are labeled in Fig. 3(a). The cathodic and active dissolution regions are used for the determination of corrosion rate by Tafel extrapolation to the corrosion potential. Extrapolation of these regions to the reversible potentials of the oxidation and reduction reactions provides a measure of the exchange current density of the reactions. As the potential is increased further, the curve bends away from the linear Tafel-like behavior. The 0.5 M H_2SO_4 solution is quite conductive. Nonetheless, ohmic potential drops become significant at large currents as described in Chapter 1.3.14. The curves were

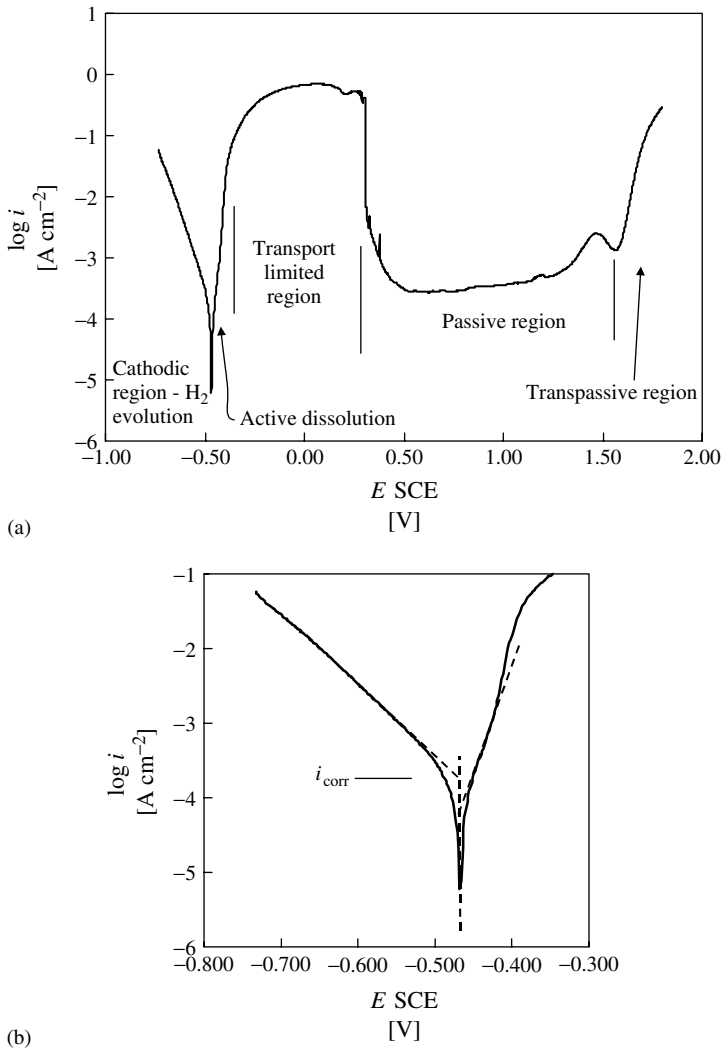


Fig. 3 Potentiodynamic polarization curve for Fe in 0.5 M H_2SO_4: (a) full polarization curve and (b) portion of curve near zero-current potential.

measured without the use of *IR* correction by current interruption, which was available on the equipment used, because the current interruption would lead to an instability in the active/passive transition region at higher potentials. For an accurate measurement of only the active dissolution region, *IR* compensation should have been applied.

As the applied potential increased further, a region of limiting current was observed. The reaction is limited in this region by mass transport of the dissolution product away from the surface, as described in Chapter 1.4. The surface was covered by a $FeSO_4$ salt film, and the solution in contact with the salt film was saturated with $FeSO_4$. Further increases

in potential, above +250 mV SCE, resulted in a precipitous decrease in current density by about three orders of magnitude as a result of the formation of a thin, protective passive film. The passive region then ensued for over 1 V of polarization, during which the passive current density changed little. At very high potentials, in the transpassive region, the current increased again. This increase is associated with the evolution of oxygen on the electrode surface.

7.3.1.2 Corrosion Rate Measurement by Fitting Polarization Curve to Wagner–Traud Equation

For a situation in which the anodic and cathodic reactions are both under pure activation control, the net current measured as a function of potential is the difference between two exponential expressions, as given by the Wagner–Traud equation [13]:

$$i_{\text{net}} = i_{\text{corr}}\left[\exp\left(\frac{2.3(E-E_{\text{corr}})}{b_{\text{a}}}\right) - \exp\left(-\frac{2.3(E-E_{\text{corr}})}{|b_{\text{c}}|}\right)\right] \quad (3)$$

This expression was derived in Chapter 1.3. An experimental polarization curve, such as that shown in Fig. 3(b), can be fitted by nonlinear least squares fitting to this expression. Such a fit will yield values for the corrosion rate, corrosion potential, and anodic and cathodic Tafel slopes. Most modern software packages for analysis of corrosion data have this capability.

In this approach, the behavior is assumed to be perfect activation polarization for both reactions, so that the extrapolated Tafel regions intersect the corrosion potential at the same value of current density. As was seen for Fe in H_2SO_4, this is often not the case. The fit usually provides a corrosion rate that is between the values determined by extrapolation of the anodic and cathodic regions. The fitted values can depend strongly on the limits of the curve chosen for the fit, and these limits must be chosen carefully. If limits are chosen such that non-Tafel-type behavior is included in the fitted region, then nonsensical results could be generated.

The corrosion rate determined by the fit for the polarization curve shown in Fig. 3(b) is 1.4×10^{-4} A cm^{-2}, and the fitted anodic and cathodic Tafel slopes are 47 and 98 mV decade^{-1}, respectively. The corrosion rate is between the values determined by extrapolation of the anodic and cathodic Tafel regions, and the Tafel slopes are different than those determined manually.

7.3.1.3 Corrosion Rate Measurement by Linear Polarization

As mentioned in Chapter 1.3, the slope, dE/di, at the zero-current potential is a measure of the polarization resistance, R_{P}. The corrosion can be determined from the polarization resistance using the Stern–Geary equation, if the Tafel slopes are known:

$$i_{\text{corr}} = \frac{b_{\text{a}}b_{\text{c}}}{(b_{\text{a}}+b_{\text{c}})2.3R_{\text{P}}} \quad (4)$$

Recall that both Tafel slopes are positive in this form of the equation. The Stern–Geary equation is the basis for the linear polarization method in which the polarization resistance is determined typically by scanning the potential from a value slightly below the corrosion potential to one slightly above the corrosion potential. It is an extremely easy technique that has been put to considerable use in corrosion monitoring. The polarization resistance can be determined by a simple two-point measurement at values above

and below the OCP. Or even simpler, a single measurement can be made at a value either above or below the OCP and the slope dE/di can be determined using the (net current, potential) point of (0, OCP) since the $i-E$ curve must go through this point. These simplified analyses assume that the polarization response is perfectly linear, and an error will result if there is any deviation from linearity.

ASTM G59 describes a method for conducting potentiodynamic polarization resistance measurements [14]. It describes a setup for type 430 stainless steel in sulfuric acid, as for ASTM G5 described earlier, and the same apparatus is specified. According to this standard, the potential should be scanned from 30 mV negative of the corrosion potential to 30 mV positive of the corrosion potential at a rate of 0.167 mV s^{-1}.

Figure 4 shows the results of a linear polarization experiment for Fe in 1 N H_2SO_4 in which the potential was scanned from −20 to +20 mV relative to the OCP. A relatively linear response is observed in this potential range. From Fig. 4, the polarization resistance can be found to be 80 Ω cm^2. Using the Tafel slopes for this system determined from the potentiodynamic polarization curve given in Fig. 3 and the polarization resistance taken from Fig. 4, the corrosion rate is found to be 1.4×10^{-4} A cm^{-2}, which is close to the value determined by the Tafel extrapolation technique.

It is possible to use the data from a standard potentiodynamic polarization curve to determine polarization resistance. So, even though the scan was performed over a wide potential range, the data near the zero-current potential can be analyzed. The Tafel slopes are determined from the potentials further away from the zero-current potential, and the corrosion rate is determined from

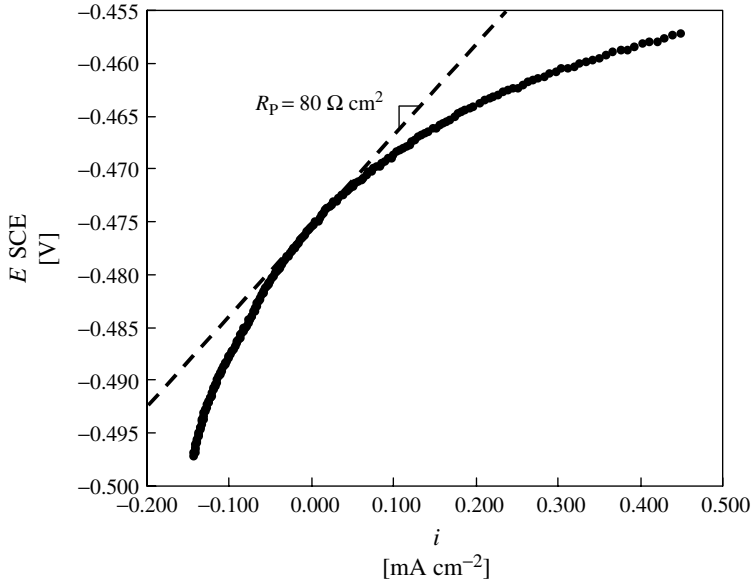


Fig. 4 Linear polarization experiment for Fe in 0.5 M H_2SO_4. Tangent is drawn at point where $i = 0$.

the Stern–Geary equation. This then is a second measure of the corrosion rate, along with Tafel extrapolation, that can be obtained from a potentiodynamic polarization curve.

The linear polarization technique is considered to be ''nondestructive'' relative to potential scanning over a wide range because the electrode is barely disturbed from the open circuit condition. Larger polarization in either the anodic or cathodic direction can affect the electrode surface, and therefore might be ''destructive''. Certainly, for field monitoring, large polarizations are undesirable. However, Tafel slopes are needed to get a value of corrosion rate from Eq. (4), and large potential scans are needed to get those values. Values for Tafel slopes can sometimes be found in the literature. Alternatively, as mentioned in Chapter 1.3, it is possible to determine a value of corrosion rate in the absence of knowledge of the Tafel slopes by arbitrarily assuming that the slopes were both 100 mV decade^{-1}. The corrosion rate is then given by $0.022/R_P$, which is 2.75×10^{-4} A cm^{-2} for the data shown in Fig. 4. This value is not too different than that obtained using the actual Tafel slopes, and is still close to the value determined by Tafel extrapolation.

Mansfeld has described a method to determine Tafel slopes from the nonlinearity found in small magnitude linear polarization measurements [15]. The approach is similar to the fitting method described earlier for fitting potentiodynamic polarization curves to the Wagner–Traud equation, Eq. (3). Mansfeld showed that the fit can be made with only two parameters, the Tafel slopes, instead of four. The values of E_{corr} and R_P can be determined, and i_{corr} can be eliminated from Eq. (3) by insertion of Eq. (4) to get:

$$i_{net} = \frac{b_a b_c}{(b_a + b_c)2.3R_P} \times \left[\exp\left(\frac{2.3(E - E_{corr})}{b_a}\right) - \exp\left(-\frac{2.3(E - E_{corr})}{b_c}\right)\right] \quad (5)$$

Experimental data for net current as a function of potential over a small range near the corrosion potential can therefore be fitted to this equation to extract the Tafel slopes, and the corrosion rate can then be determined from the Stern–Geary equation.

It should be noted that the Stern–Geary equation is dominated by the smaller of the Tafel slopes. Often in corrosion, the cathodic reaction is diffusion limited oxygen reduction, so $b_c = \infty$. In that case, the corrosion rate is given by:

$$i_{corr} = \frac{b_a}{2.3R_P} \quad (6)$$

7.3.2 Electrochemical Impedance Spectroscopy

The electrochemical techniques described in the preceding text measure the response of the system to a voltage perturbation. Tafel extrapolation requires a large perturbation from the steady state condition to be applied. The polarization resistance can be measured by the application of a smaller perturbation. By applying a small varying perturbation over a range of frequency, it is possible to probe the full response of the system, and not just the resistive components. In the EIS technique, a small AC signal (typically a sine wave of amplitude ±10 mV) is applied over a wide range of frequency (typically from 10^5 to 10^{-2} or 10^{-3} Hz) at a

number of discrete frequencies (typically 5–10 frequencies per decade), and the current response is measured at each frequency, ω. The impedance is determined by $Z(\omega) = V(\omega)/i(\omega)$. The low magnitude of the applied voltage signal means that EIS, like the linear polarization technique, does not polarize a system far from its steady state condition and it may be considered to be a nondestructive technique.

ASTM G106 describes a method to check the equipment and technique for collecting and presenting EIS data [16]. Type 430 stainless steel is to be tested in 0.005 M H_2SO_4 + 0.495 M Na_2SO_4. A 10-mV amplitude signal is applied at the corrosion potential at 8–10 steps per decade from 10 000 to 0.1 Hz. The results of round-robin testing are provided.

For a linear system, the current response will be a sine wave of the same frequency as the excitation signal, but shifted in phase. Since the impedance is the ratio of two sine waves, it is a complex number that can be represented by an amplitude and a phase shift or as the sum of real and imaginary components, $Z(\omega) = Z'(\omega) + jZ''(\omega)$.

Complete commercial systems including both hardware and software allow EIS measurements and data analysis to be made rather easily. However, some care should be taken when using this approach, since the generation of artifacts and the misinterpretation of data are possible. A number of good references on EIS describe the technique and its application to corrosion [7–9, 12, 17–23].

As described in Chapter 1.1.2.3, the discontinuity generated by an electrode surface in an electrolyte results in separation of charge to create parallel planes of charge as is found in a capacitor. However, the electrode–electrolyte interface does not behave as a perfect capacitor. If it did, the current would cease flowing when the capacitor became fully charged. The interface behaves instead like a leaky capacitor, or like a circuit composed of a capacitor and resistor in parallel. Figure 5 shows a circuit that represents well the behavior of many electrochemical interfaces. The resistor in parallel with the capacitor is labeled as R_P, the polarization resistance. For a simple electrochemical reaction under activation control, the polarization resistance can be considered to be a charge transfer resistance, and is sometimes labeled as R_{CT}. The capacitor is labeled in Fig. 5 as C_{DL}, the double layer capacitance, which is associated with the separation of charge at the electrode/electrolyte interface. Many corroding interfaces have a surface film (e.g. a surface oxide) and still exhibit behavior that is represented well by the circuit shown in Fig. 5. The capacitance in that case can be associated with the capacitance of the film. The parallel resistor and capacitor are in series with another resistor

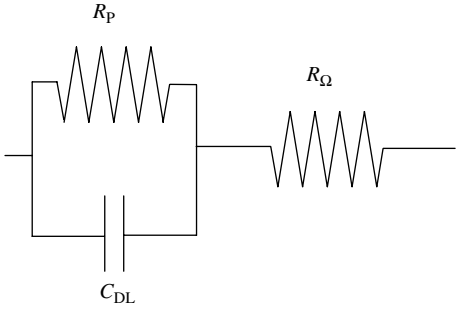


Fig. 5 Circuit describing the behavior of a simple electrochemical interface.

that represents the ohmic resistance in solution between the sample and the reference electrode. For an applied signal with a very low frequency (as in DC techniques such as linear polarization), the capacitor exhibits high impedance and the measured response is the series combination of the two resistors. At very high applied frequencies, the capacitor acts as a short, and the system again behaves as a resistor. However, only the ohmic resistance is sensed since the polarization resistance is shorted by the capacitance. At intermediate frequencies, the capacitor affects the response of the overall circuit.

In the field of corrosion, impedance data are usually reported in one of two formats. Figure 6 shows the impedance spectrum for the case of Fe in 0.5 M H_2SO_4 presented in the format of a Bode plot. Both the log of the impedance magnitude and the phase angle are plotted as a function of the log of the frequency of the excitation signal in this format. The behavior of the Fe/H_2SO_4 system is very close to that of a perfect RC circuit. Modern EIS analysis software allows fitting of the data to the behavior expected for a given equivalent circuit, such as the RC circuit shown in Fig. 5. Such fitting provides best values for all of the circuit components. By fitting the data to the behavior expected for the circuit shown in Fig. 5, the polarization resistance and double layer capacitance were found to be 90 Ω cm^2 and 84 μF cm^{-2}, respectively.

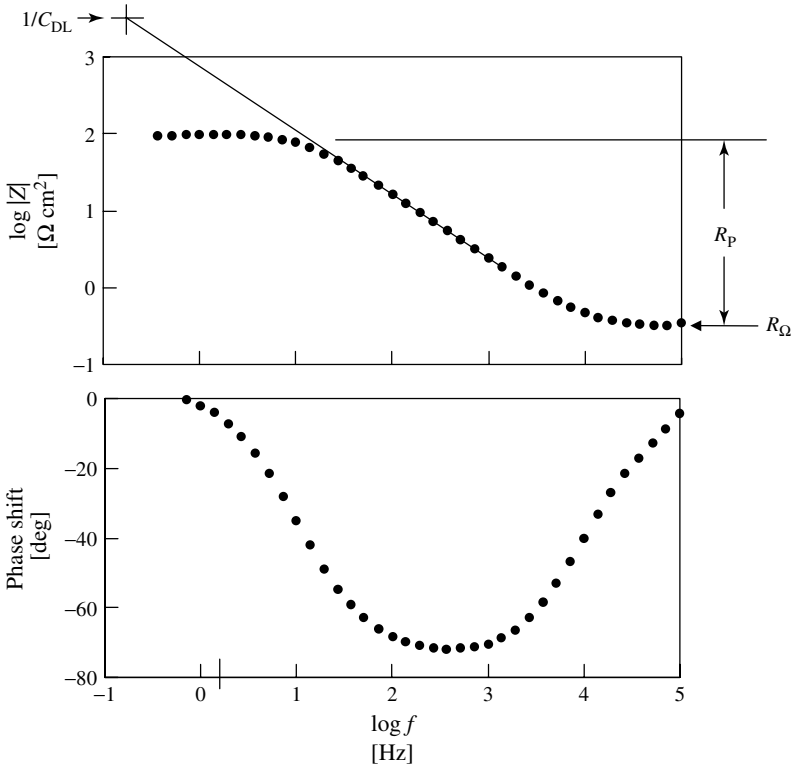


Fig. 6 Bode plot of EIS data for Fe in 0.5 M H_2SO_4.

It is possible sometimes to determine the values of the equivalent circuit elements without the use of a computer. Understanding how this is done is important for evaluating the fits provided by the computer and for determining initial values required for the fitting routines. As mentioned, the impedance for the RC circuit in Fig. 5 at high frequency is given by the ohmic resistance, and the impedance at low frequency is given by the sum of the ohmic resistance and the polarization resistance. R_P is therefore the difference between the high- and low-frequency impedance, as is easily seen in the Bode plot. The phase shift at low- and high-frequency approaches 0, which is expected for resistive behavior. At intermediate frequencies, the impedance has an out-of-phase component, and is influenced by the capacitance of the interface. The phase angle approaches $-90°$, which is the value found for a pure capacitor. The slope of the log impedance magnitude versus log frequency plot should be -1. The capacitance can be determined by extrapolating the capacitive region at intermediate frequencies to a value of $f = 0.16$ Hz ($\omega = 2\pi f = 1$), and determining the inverse of the impedance at that frequency.

For the data in Fig. 6, the ohmic and polarization resistances can be determined to be about 0.3 and just under 100 $\Omega\ cm^2$, respectively. The value of R_P is slightly higher than that determined by linear polarization (Fig. 4) in a measurement that just preceded the EIS experiment on the same electrode. The double layer capacitance is seen to be $1/3000\ \Omega\ cm^2 = 333\ \mu F\ cm^{-2}$. The polarization resistance determined by EIS can be used to determine the corrosion rate with the Stern–Geary equation, just as was described above for polarization resistance determined by linear polarization. EIS data provide no estimation of the Tafel slopes, which are required in the Stern–Geary equation.

The other common plot for impedance data in corrosion is the complex plane plot or Nyquist plot, in which the imaginary component is plotted as a function of the real component at each frequency. The data from Fig. 6 are plotted in Fig. 7 in

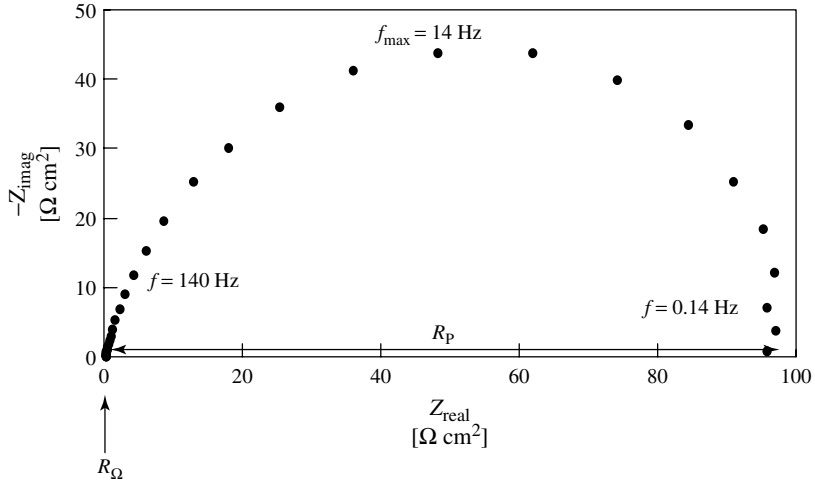


Fig. 7 Nyquist plot of EIS data for Fe in 0.5 M H_2SO_4.

the Nyquist format. The frequency for each point is not explicitly given in this format. A perfect RC circuit such as is given in Fig. 5 will form a semicircle in the complex plane, which intercepts the real axis twice. The high-frequency intercept is the ohmic resistance, and the low-frequency intercept is the sum of the ohmic and polarization resistances. The data for the Fe/H_2SO_4 system is close to being a perfect semicircle. Since this plot is on linear axes, the low ohmic resistance is difficult to resolve in Fig. 7. As mentioned, most data are analyzed nowadays by computer fitting. However, the double layer capacitance also can be determined for a system exhibiting behavior similar to a perfect RC circuit from the polarization resistance and f_{max}, the frequency for the point at which the imaginary component has a maximum value:

$$C_{DL} = \frac{1}{2\pi f_{max} R_P} \tag{7}$$

Analysis of the data in Fig. 7 shows that, for the Fe/H_2SO_4 system, R_P is about 98 $\Omega\ cm^2$, and $C_{DL} = 1/\{(2\pi)(14\ Hz)(98\ \Omega\ cm^2)\} = 116\ \mu F\ cm^{-2}$. The R_P value is similar to that determined by analysis of the Bode plot and by the computer fitting. However, the C_{DL} value is about a third of that determined from the Bode plot. The discrepancy is caused by the fact that the behavior of the interface is not exactly that of a perfect Randles circuit. The slope of the Bode magnitude plot is about -0.8 rather than -1, and the Nyquist plot is not a perfect semicircle, as the maximum imaginary impedance is less than twice the polarization resistance. So it is inappropriate to treat the data as if they were generated by a perfect RC circuit.

There is no reason, of course, that an electrochemical interface must behave as a collection of perfect electrical components. In particular, as shown above, the capacitance is often nonideal. Nonideal capacitors can be represented by constant phase elements with an impedance given by:

$$Z = A(j\omega)^{-\alpha} \tag{8}$$

where A is a constant and the exponent α is less than or equal to 1. When $\alpha = 1$, this expression represents the impedance of a perfect capacitor. When $\alpha = 0$, the impedance is a constant, independent of frequency, which is the behavior of a resistor. Electrochemical interfaces often exhibit behavior that can be modeled by a constant phase element as shown in Eq. (7), with α less than 1.

The transfer function or impedance is valid only if the following conditions are met [18]:

Causality: The response of the system must be determined entirely by the perturbation.

Linearity: The perturbation/response must be described by a series of linear differential equations, the impedance must not depend on the voltage amplitude.

Stability: The system must return to its original state when the perturbation is removed.

Continuity and Finiteness: The impedance must be continuous and finite over complete frequency range: $0 < \omega < \infty$. This condition is not met by EIS experiments, since the full range of frequencies is not accessible.

The validity of EIS data can be checked using the Kramers–Kronig transformations, which calculate the imaginary component of the impedance from the real component, and vice versa [17, 18].

The EIS technique is particularly powerful for certain applications. The use of DC techniques is problematic in highly

resistive electrolytes, whereas the ohmic potential component is clearly identified in EIS. EIS allows for identification of components in complex equivalent circuits, such as is exhibited by electrodes coated by an organic layer. EIS measurements have provided early evidence for failure of painted metals.

The standard methods for EIS determine an average impedance for the whole exposed area of a sample. Many samples, in particular coated samples or those undergoing localized corrosion, have spatial variations in behavior. A local EIS method has been developed to measure these variations [24–26]. The local AC solution current density is mapped across a surface using a two-electrode microprobe. The ratio of the applied AC voltage (using distant reference and counterelectrodes) to the local current density gives the local impedance. It is possible to obtain a full EIS spectrum at each location, or to map the impedance at a fixed frequency. This method provides information on the location of the attack, and can detect failure prior to visual observation.

7.3.3 Corrosion Rate Determination by Electrochemical Noise Analysis (ENA)

The electrochemical techniques described in Sects. 7.3.1 and 7.3.2 measure the response of the system to an externally applied perturbation. It is possible to use the inherent noise in the system as a stimulus and measure the system response [27–36]. The fundamental basis to use noise analysis as a determination of corrosion rate is not as strong as that for the other techniques. However, the advantage of noise analysis is that there is no need to apply any external signal, and the system is not polarized at all away from its natural condition. This makes it particularly suited for corrosion rate monitoring in the field.

A variety of techniques based on noise exists, but the most common uses two identical working electrodes and a noise-free reference electrode situated between the two working electrodes. The current flowing between the two working electrodes is measured by a zero-resistance ammeter, and their potential is monitored versus the reference electrode.

The noise resistance has been defined as the ratio of the potential/current standard deviations, σ:

$$R_{\mathrm{n}} = \frac{\sigma_V}{\sigma_I} \tag{9}$$

Therefore, if a small amount of potential noise drives a high-current noise between the two electrodes, the noise resistance is low. Noise resistance has been found to correlate with polarization resistance determined by EIS for certain systems [30].

Another approach for ENA is to transform the recorded potential and current fluctuations into the frequency domain using the Fast Fourier Transform (FFT) method [37]. The spectral noise resistance, R_{sn}, is given by the ratio of the voltage and current FFTs at each frequency and the limiting value, R^0_{sn}, can be used as a measure of corrosion resistance:

$$R_{\mathrm{sn}}(f) = \frac{V_{\mathrm{FFT}}(f)}{I_{\mathrm{FFT}}(f)} \tag{10}$$

$$R^0_{\mathrm{sn}} = \lim_{f \to 0}[R_{\mathrm{sn}}(f)] \tag{11}$$

For steel with polymer coatings exposed to 0.5 M NaCl for 130 days, the values of R_{n} and R^0_{sn} were found to be very close to each other but different in magnitude than the EIS parameters [37].

The spectral noise response can be determined in a different fashion, that is, from the power spectral densities

(PSDs), which are calculated from the FFT or using the maximum entropy method (MEM) [31]. The spectral noise resistance is determined from the PSDs by:

$$R_{sn}(f) = \left(\frac{V_{PSD}(f)}{I_{PSD}(f)}\right)^{1/2} \qquad (12)$$

The values of R_{sn} calculated by Eqs. (11 and 12) are identical if a single potential and current data set is used [31]. It was shown that:

$$R_n = R_{sn}(0) = |Z(0)| = R_P \qquad (13)$$

if the impedance of the two test electrodes are identical and much higher than the resistance of the solution between them [31]. Experiments validated this relationship for several systems [32]. Nonetheless, there is no agreement on the fundamental basis for the relation between noise resistance and corrosion rate.

A commercial software package [38] was used to perform a noise experiment on two Fe electrodes in 0.5 M H_2SO_4 and to analyze the data. Data were collected for several minutes at a rate of 100 Hz. The ratio of the potential and current standard deviations resulted in a noise resistance of 20–40 Ω cm^2, which is the same order of magnitude as found by linear polarization or EIS.

7.3.4 Comparison of the Techniques for Assessment of Corrosion Rate

Several electrochemical techniques for the assessment of corrosion rate have been presented in this chapter. It is of use to summarize and compare the different techniques. Table 1 provides a summary of the data generated by the different techniques for Fe in 0.5 M H_2SO_4, and the corrosion current densities determined from those data.

Potentiodynamic polarization over a relatively wide range of potential provides information of the behavior of the sample at potentials different than the

Tab. 1 Values determined by different techniques applied to Fe in 0.5 M H_2SO_4

Tafel extrapolation	$b_a = 34$ mV decade^{-1}
	$b_c = 114$ mV decade^{-1}
	i_{corr}(cathodic extrapolation) $= 1.8 \times 10^{-4}$ A cm^{-2}
	i_{corr}(anodic extrapolation) $= 7 \times 10^{-5}$ A cm^{-2}
Fitting to Wagner–Traud equation	$b_a = 47$ mV decade^{-1}
	$b_c = 98$ mV decade^{-1}
	$i_{corr} = 1.4 \times 10^{-4}$ A cm^{-2}
Linear polarization	$R_P = 80\ \Omega$ cm^2
	$i_{corr}(b = 100$ mV decade$^{-1}) = 2.75 \times 10^{-4}$ A cm^{-2}
	i_{corr} (real b values) $= 1.4 \times 10^{-4}$ A cm^{-2}
EIS	C_{DL} (manual Bode) $= 333\ \mu$F cm^{-2}
	C_{DL} (manual Nyquist) $= 116\ \mu$F cm^{-2}
	C_{DL}(fit) $= 84\ \mu$F cm^{-2}
	$R_\Omega = 0.3\ \Omega$ cm^2
	$R_P = 98\ \Omega$ cm^2
	i_{corr} ($b = 0.1$ V decade$^{-1}) = 2.2 \times 10^{-4}$ A cm^{-2}
	i_{corr} (real b values) $= 1.1 \times 10^{-4}$ A cm^{-2}
Electrochemical noise	$R_n = 20$–$40\ \Omega$ cm^2

corrosion potential. The Tafel slopes can be measured, and the corrosion current density is determined by the Tafel extrapolation method. Alternatively, the data can be fitted to the Wagner–Traud equation using a computer. The technique is not suited for corrosion monitoring owing to the large polarization required.

Linear polarization is simple, easy, and fast. The sample is not polarized far from the corrosion potential, so it is suitable for in situ monitoring. The polarization resistance is measured, but the Tafel slopes are needed to determine corrosion rate. Under certain conditions, Tafel slopes can be extracted from the data.

EIS requires more sophisticated equipment and analysis, but provides more information on the behavior of the interface than DC techniques. Tafel slopes are needed to determine corrosion rate. Using a scanning probe to map the local current, local EIS measurements can be made.

ENA is a promising technique for corrosion monitoring. However, the fundamental basis for determining corrosion rate from noise is not as developed as for other techniques.

All of these techniques monitor the response of the electrode to stimulation by a potential change. The magnitude of the potential stimulation and current response decreases in the order potentiodynamic polarization, linear polarization, EIS, ENA. Each of the methods provides information, and there are trade-offs involved in the decision of which is the best to use.

7.4 Techniques for Studying Passivity

As described in the chapter on passivity (see Chapter 3.2, ''Passive Metals'') passive films play a critical role in the field of corrosion. Experimental techniques specific to the study of passive films typically determine the current transient associated with passive film formation or reformation. For an oxide that can be removed by cathodic reduction, the experiment is a simple one. Following a cathodic treatment, the potential is stepped into the passive region and the anodic current is monitored as a function of time. The current will decay approximately exponentially [39–45], so, to obtain data over a wide range of current and time, it is necessary to have a high-resolution analog-to-digital converter or a series of data collection devices operating at different current and timescales [42–44]. In the latter case, it is necessary to piece together the different time segments, which is not easy. With a wide dynamic range of data, it is possible to plot log current density versus log time to determine the kinetics of the passivation process. If the sample area and peak current are large, a limiting value and subsequent small shoulder in the decay can be observed. This has been attributed to ohmic potential drop associated with the high initial current [46]. The ohmic potential drop decreases as the current decreases, so the potential at the electrode surface is not constant with time in that situation. Therefore, it is desirable to minimize ohmic potential drop by using a conductive electrolyte and an electrode configuration that minimizes the area of the exposed metal.

Many different techniques have been used to depassivate or bare small areas of metal to follow the repassivation kinetics, including, scratching, breaking, guillotining, impinging particles, and incident laser irradiation. Burstein and coworkers have developed and extensively used the scratching and guillotining approaches [42–44, 46]. Scratching is easily accomplished

using a hardness indentation stylus and a rotating disk electrode. The stylus is pulsed against the surface to cut a groove into the sample. A simpler approach is to manually scratch the surface with a sharp scribe. In this case, the scratch can be more reproducible if the sample has a short dimension, such as is achieved by mounting a thin foil on edge into an epoxy mount. The manual scratching across the thin sample can then be accomplished relatively quickly and reproducibly [47].

To study the earliest stages of repassivation where the current densities are the highest, it is necessary to create the fresh area as quickly as possible. A very small area of fresh metal can be created extremely quickly (on the order of microseconds) by the thin-film-breaking experiment [48]. In this approach, a thin film deposited onto a brittle substrate such as glass or Si is suspended into the solution. Breaking of the thin-film electrode results in the creation of a fresh metal area of size equal to the cross-section of the thin film. Current densities on the order of 1000 A cm^{-2} were measured using this technique on Al thin films [48].

7.5 Techniques for Evaluating Localized Corrosion

As described in Chapter 4.2 on localized corrosion, alloys that are protected by a thin passive film tend to be susceptible to localized corrosion resulting from a breakdown of that film and aggressive dissolution at the breakdown sites. The tendency for breakdown increases as the potential increases. The electrochemical techniques described in Sect. 7.3 can be used to address localized corrosion. Other techniques specific to localized corrosion have been developed. This section will summarize the various approaches that are commonly used.

The most common electrochemical approach for the evaluation of susceptibility of a material to localized corrosion is potentiodynamic polarization, typically starting at the corrosion potential and scanning upward until breakdown is observed. In a cyclic polarization test, the scan direction is reversed after some amount of localized corrosion, and the potential for repassivation of the localized corrosion is determined. Figure 8 shows a schematic polarization curve for a material that exhibits localized corrosion in the test environment. In this schematic, the corrosion potential is below the pitting potential and the material is spontaneously passive at the corrosion potential, as no active region is indicated as the potential is scanned upward. It is not uncommon for the current signal to become noisy as the potential approaches the pitting or breakdown potential. The current transients observed are associated with metastable pitting events, or pits that initiate, grow for a period, and then repassivate [49]. At some point, one or more stable pits form so that the current continues to increase rather than returning to the passive current density. The potential for the formation of a stable pit has been given several names: pitting potential, E_p, breakdown potential, E_b, or pit nucleation potential, E_{np} [50]. This critical potential will be referred to here as E_p, but it is not clear from an electrochemical experiment alone if the breakdown is associated with a pit, crevice, or other form of localized corrosion, such as intergranular corrosion. The surface must be examined after an experiment to determine the form of attack.

If the potential scan direction is reversed after some period of localized corrosion growth, a hysteresis is observed. Once

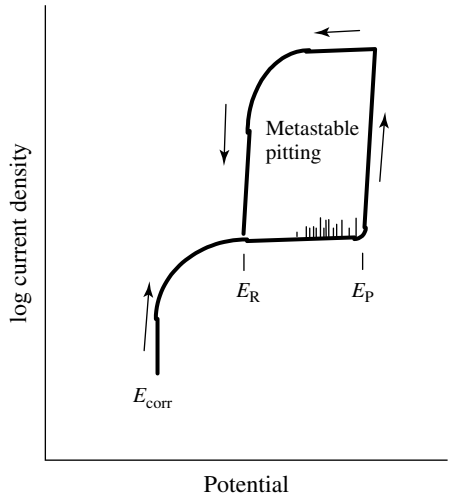


Fig. 8 Schematic cyclic polarization curve for a system exhibiting localized corrosion.

initiated, localized corrosion will tend to grow at lower potentials, in the potential region at which stable growth would not initiate. Eventually, as the potential is decreased further, the localized corrosion will repassivate and the current will decrease back to a value near the passive current density. The potential at which this happens is called the repassivation potential, E_r, or protection potential, E_{prot}.

A correlation has been between pitting potential and pitting in the field: the tendency to form pits naturally at open circuit increases as the experimentally determined pitting potential decreases [51]. The difference between E_p and E_r, which is related to the extent of hysteresis in a cyclic potentiodynamic polarization curve, has also been considered to be a measure of the susceptibility to localized corrosion [3, 52]. Issues associated with this interpretation have been reviewed [53].

Cyclic polarization measurements to determine E_p and E_r are simple to perform. However, care must be taken to avoid artifacts or misinterpretation. The biggest problem is the possibility for crevice corrosion, which is large for most systems that exhibit localized attack. If one is interested in determining E_p, the formation of crevices associated with the masking scheme comprises an artifact that masks E_p because crevices will form at lower potentials than pits.

ASTM G61 describes a method for cyclic potentiodynamic polarization measurements and presents data from round-robin testing at five different laboratories on Type 304 stainless steel in 3.5% NaCl [3]. The scatter band for the pitting potential is large, from 0 to 350 mV SCE. The masking and sample holder used for these tests are shown in Fig. 1(g); a Teflon gasket was used to make the seal. Numerous replications of this experiment in classroom laboratory exercises at The Ohio State University have shown that the system is very susceptible to crevice corrosion. The breakdown potential exhibited for experiments that generate a crevice is in the range of values reported in the ASTM standard, 0 to 400 mV SCE. For samples in which only pits form with no evidence of crevices, the breakdown potential is higher; in the range of 400–650 mV SCE. It is possible that the 304 stainless steel material used in the

round-robin testing was more susceptible to attack than that used for the more recent testing. However, it is also possible that the round-robin tests were all compromised by crevice corrosion. This example highlights the care that must be taken to avoid crevice corrosion when attempting to measure E_p. On the other hand, the standard actually only refers to "localized corrosion susceptibility" and not to pitting susceptibility, and crevice corrosion is certainly a form of localized corrosion. To test the susceptibility to crevice corrosion, however, it is best to use a device that forms a reproducible crevice, such as is described in ASTM G48 [54].

If the oxidizing power of an electrolyte is high enough, or the pitting potential low enough, pitting will occur at open circuit. In this case, the OCP is pinned to a value that is close to the pitting potential because of the relative nonpolarizability of the pit dissolution reaction. ASTM G69 describes a method for testing of Al alloys in 1 M NaCl and 30% hydrogen peroxide [55]. The corrosion potential in this case will be close to the pitting potential because the extra cathodic reaction provided by the peroxide polarizes the alloy to E_p.

Temperature can also be used as an acceleration factor in a fashion similar to potential. Many materials will not pit at a temperature below a critical value that is often extremely sharp and reproducible [56–62]. At low temperatures, extremely high breakdown potentials are observed, corresponding to transpassive dissolution, not localized corrosion. Just above the critical pitting temperature (CPT), pitting corrosion occurs at a potential that is far below the transpassive breakdown potential. This value of CPT is independent of environmental parameters and applied potential over a wide range, and is a measure of the resistance to stable pit propagation [61]. CPTs for many stainless steels are in the range of 10–100 °C [61]. The CPT can be used, like pitting potential, as a means for ranking susceptibility to pitting corrosion – the higher the CPT, the more resistant the alloy to pitting [61].

The CPT can be determined by performing a series of potentiodynamic polarization curves over a range of temperatures that are held constant for each experiment. Alternatively, the CPT can be measured in a single experiment by holding the potential at a high value (but below the potential for transpassive dissolution) and slowly increasing the temperature of the solution. The latter approach, which requires a programmable temperature controller, is described in ASTM G150 [4]. According to the standard, the temperature is to be increased at a rate of 1 °C min^{-1}. The artifact of crevice corrosion is a real concern during CPT testing since crevice corrosion becomes increasingly prevalent and difficult to prevent at high temperatures. CPT can also be determined by immersion in $FeCl_3$ solutions of varying temperature for a period of time and inspecting the surface for the presence of pits.

The scratching technique described earlier can be used to test the susceptibility for the formation of stable pits [63]. By purposely removing the passive film, the initiation stage of pitting is eliminated and the repassivation potential is directly measured. A sample can be scratched during potentiostatic polarization at various potentials or periodically during potentiodynamic polarization. At potentials below the repassivation potential, the current will quickly decay to the passive current level following scratching. When the sample is scratched at a potential above the repassivation potential, the current will increase continuously. This approach

for determination of the repassivation potential avoids the complication associated with the dependency of repassivation potential determined in a cyclic polarization curve on the apex current or the depth of the pit [52]. An electrochemical equivalent to the mechanical scratching experiment involves stepping the potential for a short period to a high potential, E_1, to initiate pits, and then stepping down to a low potential, E_2 [64]. If the pits repassivate and the current decays at E_2, then the cycle is repeated, but the value of E_2 is increased during each step until the pits formed at E_1 no longer repassivate. The highest value of E_2 at which the pits repassivate is then the repassivation potential.

EIS is a method that is not very well suited for the study of pitting corrosion because, as described earlier, it should be applied to electrodes at steady state, and pitting is a non–steady state condition. Nonetheless, EIS can be used to assess the low-frequency impedance at open circuit, which provides a measure of corrosion rate without the need to polarize away from open circuit. It is therefore possible to use EIS to determine if pitting is occurring at open circuit.

The study of metastable pitting has provided unique opportunities for understanding pitting corrosion since metastable pits involve initiation, growth, and repassivation in short, discrete and plentiful events. It is easier to address the stochastics of pitting with the numerous metastable pits generated in a few experiments than by performing many experiments that generate stable pits. The signal associated with each metastable pitting event can be analyzed to determine pit current density, which allows determination of the electrochemical kinetics of dissolution in pits and assessment of the rate-controlling steps. Observation of metastable pitting current transients requires low background current because the current associated with metastable pits is small. The smaller the background signal, the smaller the events that can be resolved. It is critical to avoid artifacts associated with crevice corrosion, which will swamp the metastable pitting signal. In order to get a low background current, it is necessary to use electrodes with small surface areas. Data collection must be at a high enough rate to distinguish the individual events.

Studies of pit growth are complicated by problems associated with accurate measurement of the pit current density. The current measured from a sample held at a fixed potential may come from several pits with unknown active pit surface area. For this situation, it is possible to count the pits, assume that the current is evenly divided between the pits, and assume that the pits have a certain shape, such as a hemisphere. This, however, can result in considerable error. Furthermore, if pits are not all initiated at the same time, then current is coming from pits of varying size, which confounds the determination of current per pit. Another problem in accurate determination of the $i-E$ relationship for a pit is that a considerable amount of hydrogen evolution can occur within pits, especially for Al and Al alloys. It has been found that about 15% of the total anodic dissolution current is consumed locally by hydrogen evolution in Al pits and crevices [65, 66]. This means that the current measured at an applied potential is only a fraction of the true anodic dissolution current. Finally, the determination of pit growth kinetics at open circuit is a challenge, because by definition, no net current is passed at open circuit.

A variety of experimental approaches address the problems listed in the preceding

text in different ways. In general, they involve either the formation of a single pit, or nonelectrochemical means for determination of the growth kinetics. One of the reasons that metastable pits are so interesting is that metastable pit current transients represent individual pitting events. Other techniques for forming a single pit include the exposure of a small area, laser irradiation of a small spot, implantation of an activating species at a small spot, or the use of artificial or single pit electrodes. Other than the artificial pit electrode technique, in which the whole exposed area is active, the other techniques listed still require an assumption regarding the geometry of the active pit surface in order to determine the pit area and thus a pit current density.

Artificial pit electrodes are formed by imbedding a wire in an insulator such as epoxy [67–69]. The local environment within an artificial pit electrode crevice should be identical to that formed in real pits. The whole exposed area is active so the measured current can be easily converted to pit current density. Furthermore, artificial pit electrodes have an ideal one-dimensional geometry allowing for easy modeling of transport. Artificial pit electrodes have been used extensively to study Fe and stainless steel behavior. Polarization curves for artificial pit electrodes of FeCrNi alloys with and without 2.7% Mo in a 1 M Cl^- bulk solution showed that anodic polarization curve in the pit environment for the Mo-containing alloy was shifted to higher potentials [70]. The change in the corrosion potential was approximately equal to the change in pitting potential measured on a standard electrode by potentiodynamic polarization [70]. This indicates that the effect of Mo on the pitting potential can be explained solely by its influence on the pit dissolution kinetics.

Nonelectrochemical techniques are useful for the study of localized corrosion growth because they eliminate several problems: the need to determine the current from a single site, assumptions regarding active surface area, and complications associated with hydrogen evolution within the pits or intergranular regions, which can consume a reasonable fraction of the anodic pit current density in the case of Al [65, 66]. The foil penetration method is a nonelectrochemical method that measures the time for localized corrosion to perforate foils of varying thickness as a means to determine the growth rate of the fastest growing localized corrosion site [1, 71, 72]. The penetration time is determined by exposing one side of a foil sample to an aqueous environment. A piece of filter paper and then a Cu foil are pressed against the back of the sample. Penetration of localized corrosion on the other side is sensed by a decrease in resistance between the sample and Cu foil resulting from wetting of the filter paper by the localized corrosion environment. This technique has been successfully applied to the study of pitting, crevice corrosion, and intergranular corrosion in stainless steel, Al and Al alloys [1, 71, 72].

Another nonelectrochemical approach to pitting involves the study of two-dimensional pits in thin-film samples [1, 66, 73–75]. Pits in thin metallic films with thickness on the order of 10–1000 nm rapidly penetrate the metal, reach the inert substrate, and proceed to grow outward in a two-dimensional fashion with perpendicular sidewalls. The measurement of pit wall velocity from the analysis of magnified images of the growing two-dimensional pits provides a simple and direct means for determination of pit current density via Faraday's law, with no need for assumptions. Since the pit depth

is limited by the metal film thickness, pits in thin films grow at steady state with no increase in ohmic path or diffusion length with time as is the case described earlier for pits in bulk samples. As a result, two-dimensional pits in thin films exhibit a pit current density that is constant with time at a given applied potential. This steady state aspect of pitting in thin-film samples allows unambiguous determination of the current-density/potential relationship. The typical form for the polarization curve of a thin-film pit includes a region at low potentials at which the current density is almost linearly dependent on applied potential followed by a region at high potential at which the pit current density reaches a limiting value, and pitting is mass-transport limited. Another consequence of the constant pit depth is the finding that the repassivation potential and the lowest pit current density at which a pit can grow are extremely reproducible. It is therefore possible with pits in thin films to accurately assess the critical conditions for pit stability. One final advantage of working with thin films produced by physical vapor deposition is that the full range of compositional variety can be achieved with a single-phase structure (typically nanocrystalline or amorphous) because of the nonequilibrium nature of the as-deposited microstructure.

Several ASTM standards address the susceptibility of alloys to intergranular corrosion. Stainless steels are tested for sensitization by immersion in different boiling acids according to ASTM A262 [76]. Similar tests are described in ASTM G28 for Ni-rich Cr-bearing alloys [77]. ASTM A262 also describes an electrolytic etch test in oxalic acid, which can be used to screen prior to the more lengthy immersion tests.

Testing for intergranular and exfoliation corrosion in Al alloys is described in ASTM G34, G66, G110, and G112 [78–81]. These are immersion tests, with visual observation of the results. No electrochemical tests for exfoliation resistance exist.

The single loop electrochemical potentiokinetic reactivation (EPR) test is an electrochemical test for the sensitization of stainless steels that is described by ASTM G108 [77]. Type 304 or 304 L stainless steel with a 1 μm polished surface is tested in a 0.5 M H_2SO_4 + 0.01 M KSCN solution at 30 °C (±1 °C). The potential is first held at +200 mV SCE for 2 min to passivate the sample, and scanned back to E_{corr} at a constant rate of 6 V h^{-1}. This downward sweep in potential leads to reactivation of the specimen. Reactivation is the result of the preferential breakdown of the passive film covering the Cr-depleted regions of the alloy near the grain boundaries, and results in a large peak in the potential versus current curve for sensitized material only. Nonsensitized stainless steel will remain passive during the downward scan and exhibit little or no peak. The normalized size of the reactivation peak during downward scanning, P_a, is therefore a measure of sensitization. P_a has units of C cm^{-2} and is determined by

$$P_a = \frac{Q}{X} \tag{14}$$

where Q is the charge under the peak and X is the normalization factor for both specimen and grain size:

$$X = A_s[5.1 \times 10^{-3} e^{0.347G}] \tag{15}$$

A_s is the specimen area in units of cm^2 and G is the grain size as determined by ASTM E 112.

P_a correlates to data measured from immersion tests such as ASTM A262. It is more sensitive to the degree of sensitization than immersion tests only

if the degree of sensitization is low. P_a does not distinguish well various degrees of high sensitization.

The need to polish the sample and determine grain size is avoided by a modification of the single loop EPR test described above. In the so-called double loop EPR test, the sample is tested in the same environment [82]. In this test, the potential is scanned from the corrosion potential, through the active/passive transition, to a value of 300 mV SCE, and then the scan direction is reversed, scanning downward to the original corrosion potential. The peak current during the downward reactivation scan, I_r, normalized to the peak current during the upward scan, I_a, is a measure of sensitization. I_a is relatively independent of sensitization. However, reactivation is observed in the downward scan if the sample is sensitized. Like the single loop EPR, the double loop EPR test is most sensitive to small degrees of sensitization. A value of I_r/I_a greater than 0.001 is considered to be an indication of the onset of sensitization.

7.6 Exposure Testing

This encyclopedia and this chapter are focused on electrochemistry. However, a few words about nonelectrochemical techniques are in order for completeness. Exposure testing of samples to service or accelerated environments is widely used, and there are several ASTM standards describing appropriate methods. Several immersion tests for intergranular and exfoliation corrosion were mentioned in the last section. ASTM G31 describes methods for immersion testing of metals [83]. This standard practice contains mostly common sense, but also has information that will help experimentalists avoid common pitfalls. A cell is described, in which samples are simultaneously exposed in three conditions: fully immersed, partially immersed, and exposed to the vapor phase.

One of the most common accelerated exposure tests is the salt spray or salt fog test described in ASTM B117 [84]. In this test, samples are exposed to a spray or fog of 5% NaCl solution at 30 °C. Several US military specifications require salt fog testing, and many corrosion engineers have considerable experience with this test. It is therefore of use as a qualification procedure to evaluate materials. However, the results of salt spray testing do not always correlate with other types of exposure, and considerable variability in test results is not uncommon.

ASTM G85 describes modified versions of salt spray testing in which the spray solution is acidified with acetic acid, SO_2 is added, or the test conditions are cycled. These modifications result in a more corrosive environment than the standard salt spray test.

7.7 Quartz Crystal Microbalance

The most common nonelectrochemical approach for the study of corrosion is weight loss measurements. Such measurements are limited by the resolution of the gravimetric device, and, for aqueous corrosion, are usually applied in aggressive environments such as the boiling acids used to evaluate sensitization of stainless steels in ASTM A262 [76]. The Quartz Crystal Microbalance (QCM) is a gravimetric instrument capable of submonolayer sensitivity that has been increasingly applied over recent years in the area of corrosion [85, 86].

The QCM takes advantage of the fact that quartz crystals have a well-defined

resonant frequency that depends on their thickness or mass. The deposition of a thin, uniform film onto the quartz will affect the frequency by an amount equal to that caused by a layer of quartz of the same mass [85, 86]. Any subsequent change in mass of the deposited layer will alter the resonant frequency according to the Sauerbrey equation [87]:

$$\Delta f = -K\Delta m \tag{16}$$

$$K = \frac{2f}{A\sqrt{\mu_q \rho_q}} \tag{17}$$

where f is the resonant frequency prior to the mass change, A is the area, and μ_q and ρ_q are the quartz shear modulus and density, respectively. For a 6-MHz crystal, the mass sensitivity is 1.2×10^{-8} g cm^{-2} Hz^{-1}, or [86]:

$$\Delta m = -1.2 \times 10^{-8} A \Delta f \tag{18}$$

This equation holds for small mass loadings, that is, those that result in about less than 2% change in frequency. Such thin deposited films do not experience shear deformation since they are located at the antinode of the standing wave [86]. As a result, the properties of the film do not affect mass sensitivity factor K. Thicker films will experience shear deformation during the measurement, and so the properties of the film will influence the relationship between Δm and Δf, and alter the relationship shown in Eq. (18). Therefore, QCMs are typically only applied in the linear region, which limits their use to thin films. Nonetheless, thin films can be used to model bulk materials as long as the environment is not extremely aggressive. Furthermore, thin films are used extensively in electronics and magnetic storage, and the corrosion behavior of thin films themselves is of great interest. QCMs have been applied to the study of atmospheric corrosion [88, 89], passivation [90], and inhibition [91]. Recently, QCM in the nonlinear region has been implemented, allowing the use of bulk metal samples cut as thin disks from single- or polycrystalline materials and glued to the quartz crystal [92]. Thus, mass change studies can now be performed not only on evaporated or electrodeposited thin films but also on all kinds of materials.

7.8 Scanning Kelvin Probe

The Kelvin probe is a noncontact, nondestructive, vibrating capacitor technique for measuring work functions, or more precisely the difference between the work function of sample and probe. It was first used by Thomson, later Lord Kelvin, in 1862 [93]. This method has been further improved throughout the following decades [94] and is now a well-established method for measuring work functions, or, from a more electrochemical point of view, Volta potentials. Whereas in traditional Kelvin probes, the probe is a small gold plate or mesh of several square millimeters or centimeters, in Scanning Kelvin Probes (SKP), the probe is a small metal tip with a diameter of typically several tens of micrometers, which can be scanned across the surface of the sample.

Under certain circumstances, the electrode potential of a surface determines its Volta potential, and thus SKP microscopy allows measurement of local electrode or corrosion potentials. Conventional scanning electrochemical reference electrode techniques require a finite electrolytic resistance between sample and reference electrode, whereas the Kelvin Probe operates across a dielectric medium of infinite

resistance. This dielectric layer could be air or an electrically insulating film covering the sample. However, experience shows that usually the Volta potential of the surface at the outermost layer is measured, that is, most films are conductive enough to act as the active surface of the sample in the vibrating capacitor. In the case of electrolyte or polymer covered metal, a suitable calibration allows the electrode potential at the buried metal/electrolyte or metal/polymer interface to be obtained. This opens a plethora of different applications for SKP microscopy, such as:

- Outdoor corrosion of metals such as steel, weather resistant steel, galvanized steel, copper, and so on. SKP can be used to study the effects of the ultrathin electrolyte layers formed during daily wet/dry cycles, which are of ultimate importance for the average corrosion rate, but cannot be analyzed by conventional electrochemical techniques [95–97].
- Indoor corrosion of electronic materials such as aluminum or copper. Usually, electrolyte layers of only some monolayers are formed, which still results in slow corrosion of the metal. SKP has successfully been applied for the investigation of the corrosion behavior of such materials [98].
- Delamination of polymer coated materials in the vicinity of defects. In particular, corrosion potential maps have been measured close to defects, which provide direct information on the progress of the delamination front [99–102].
- Investigation of the stability of modified metal surfaces, the modification layer being as thin as one monolayer [103].

If a metal is brought in contact with another metal with different Fermi energy level, which will act as a reference, reciprocal charging shifts both levels to a common level causing a potential difference $\Delta\Psi^{\mathrm{ref}}_{\mathrm{sample}} = \Psi^{\mathrm{ref}} - \Psi^{\mathrm{sample}}$ [104, 105], the so-called contact bias potential [106]. The reference metal is often in the form of a tip, and the tip and the sample area below the tip form a capacitor. If the tip is subject to periodic mechanical vibration, periodic changes of the capacitance, C, and thus the charge $Q = C \cdot \Delta\Psi^{\mathrm{ref}}_{\mathrm{sample}}$ result. This causes an AC electric current $i_{\mathrm{AC}} = \Delta\Psi^{\mathrm{ref}}_{\mathrm{sample}} \cdot \mathrm{d}C/\mathrm{d}T \propto 1/d^2$ to flow, where d is the distance between tip and surface. $\Delta\Psi^{\mathrm{ref}}_{\mathrm{sample}}$ could be determined from this current if d and C were known, but more reliable is the method of electronic compensation of i_{AC} [107–109]. Electronic compensation of this current requires the application of an external bias $U = -\Delta\Psi^{\mathrm{ref}}_{\mathrm{sample}}$, that is, the vibrating tip is scanned over the surface while the current is being electronically compensated, thus obtaining a Volta-potential map of the surface [95–97]. Kelvin probe measurements with submicron resolution can be obtained with the Scanning Kelvin Probe Force Microscope (SKPFM, see following text).

It is possible to measure the work function of metal, electrolyte, or polymer surfaces; only sufficient conductivity for currents in the order of 10^{-12} A is required. Furthermore, as already mentioned, the work function at the surface of a thin layer of electrolyte or polymeric coating and the electrode potential at the metal/electrolyte or metal/polymer interface beneath it are linearly related [99]. Once the calibration curves are known, it is possible to ''measure through the coating'' and obtain information about the electrochemical conditions at the interface without destroying it. For more details, see other references [110].

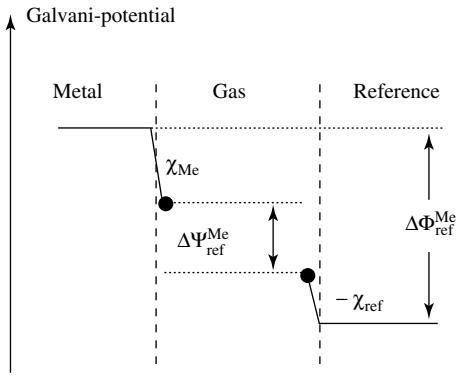


Fig. 9 Galvani potential distribution across the metal interface.

In the simplest system, the sample is exposed to ultrahigh vacuum (UHV). If the metal is free of any oxide film (Au, Pt, etc.) the Kelvin Probe will measure the work function of the metal (see Fig. 9):

$$\Delta\Psi^{ref}_{Me} = \left(-\frac{W_{ref}}{F}\right) - \left(-\frac{W_{Me}}{F}\right) = \left\{-\frac{W_{ref}}{F}\right\} - \left\{\frac{1}{F}\mu_{Me} - \chi_{Me}\right\} \quad (19)$$

where W is the work function, μ is the chemical potential, and χ is the surface potential.

If the metal surface is covered by a bulk electrolyte layer, then the Volta-potential difference is directly linked to the absolute electrode potential $\varepsilon_{1/2}$ [112, 113] of the metal/electrolyte interface as well for an oxide free as for an oxidized surface (Fig. 10):

$$\Delta\Psi^{ref}_{El} = \Delta\Phi^{Me}_{El} - \frac{\mu^{Me}_e}{F} + \chi_{El} + \left(-\frac{W_{ref}}{F}\right) = \varepsilon_{1/2} + \chi_{El} + \left(-\frac{W_{ref}}{F}\right) \quad (20)$$

where $\Delta\Phi^{Me}_{El}$ is the Galvani potential difference between the metal and electrolyte. This simple linear relation between the Volta-potential difference and the electrode potential has been proven to be valid experimentally [96, 114].

7.9 Scanning Probe Microscopy

Many types of microscopy have been used in corrosion experiments. The ability to visualize the electrode during or after corrosion experiments is extremely illuminating. Scanning probe microscopy (SPM) techniques are particularly powerful for corrosion because they have the ability to generate quantitative and high-magnification images of the surface in situ. SPM techniques utilize some interaction between a tip and a surface that is extremely sensitive to their separation distance. For scanning tunneling microscopy (STM), the interaction is electron tunneling, and for atomic force microscopy (AFM), it is electrostatic forces. SPMs also use very sensitive piezoelectric scanners to accurately control the $x-y$ position of the tip and, through a feedback loop on the interaction phenomenon, its separation from the surface.

Both STM and AFM have been used in corrosion studies. STM requires a

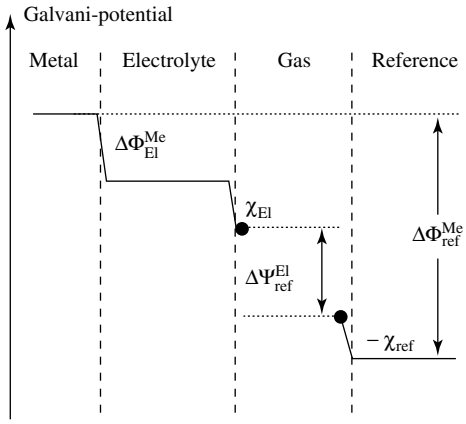


Fig. 10 $\Delta\Phi_{El}^{Me}$ is directly correlated to the absolute electrode potential, so in the case that both dipole potentials χ remain constant, the measurement of $\Delta\Psi_{ref}^{El}$ allows to obtain the electrode potential ε.

flat and conducting surface, but has been used in the study of the early stages of passivity [114–116], as well as dealloying [117, 118]. AFM does not have as good a spatial resolution as STM, but the range of 100 nm –100 μm is of interest for many corrosion applications, such as localized corrosion [119, 120].

One approach to using the AFM to study localized corrosion is to press hard with the tip or "scratch" the surface to stimulate passive film breakdown. Scratching with large tips has been used with success to study the repassivation process [120, 121]. By scratching in a controlled fashion over a small area with an AFM tip, it is possible to study the conditions under which the freshly bared surface will repassivate or propagate into localized corrosion [120, 121]. The effects of potential and environment, including inhibitors can be probed.

It is also possible to combine AFM with SKP to achieve the capability to map Volta potentials with submicron resolution [90, 120, 121]. The Scanning Kelvin Probe Force Microscope (SKPFM) operates by scanning the topography across a line and then, during a rescan of that line at a fixed distance from the surface, applying an AC voltage between the metal-coated tip and sample, which will cause the tip to oscillate. On a point-by-point basis during the rescan, a DC voltage ramp is added to the AC signal until the first harmonic of the oscillations is nulled. The DC voltage required is equal to and opposite of the local Volta potential, thereby providing a map of the Volta potential across the surface. The SKPFM has been used to study the effects of the intermetallic particles in high strength Al alloys, which generate local heterogeneities that control the corrosion process. These micron-sized particles can be clearly observed by the SKPFM signal because of the sharp contrast in the local Volta potential associated with the difference in composition [90, 120, 121]. The ability to visualize the particles is an extremely powerful tool for understanding how they behave in the localized corrosion process.

References

1. F. Hunkeler, H. Bohni, *Corrosion* **1981**, *37*, 645.
2. G5-94, Standard reference test method for making potentiostatic and potentiodynamic anodic polarization measurements,

Annual Book of ASTM Standards, ASTM International, Philadelphia, Pa., 2000, p. 57, Vol. 3.02.
3. G61-86, Conducting cyclic potentiodynamic polarization measurements for localized corrosion susceptibility of iron-, nickel-, or cobalt-based alloys, *Annual Book of ASTM Standards*, ASTM International, Philadelphia, Pa., 2000, p. 240, Vol. 3.02.
4. G150-99, Standard test method for electrochemical critical pitting temperature of stainless steel, *Annual Book of ASTM Standards*, ASTM International, Philadelphia, Pa., 2000, p. 638, Vol. 3.02.
5. V. Brusic, M. Russak, R. Schad et al., *J. Electrochem. Soc.* **1989**, *136*, 42.
6. V. A. Brusic, G. S. Frankel, C.-K. Hu et al., *Corrosion* **1991**, *47*, 35.
7. NACE, *Electrochemical Techniques*, NACE International, Houston, Tex., 1986.
8. ASTM, *Corrosion Tests and Standards*, ASTM International, Philadelphia, Pa., 1995.
9. W. S. Tait, *An Introduction to Electrochemical Testing for Practicing Engineers and Scientists*, PairODocs Publications, Racine, Wis., 1994.
10. F. Mansfeld, The polarization resistance technique for measuring corrosion currents in *Advances in Corrosion Science and Technology* (Eds.: M. G. Fontana, R. W. Staehle), Plenum Press, New York, 1976, p. 163. Vol. 6.
11. J. R. Scully, *Corrosion* **2000**, *56*, 199.
12. J. R. Scully, Electrochemical methods for laboratory corrosion testing in *Corrosion Testing and Evaluation: Silver Anniversary Volume* (Eds.: R. Baboian, S. W. Dean), ASTM International, Philadelphia, Pa., 1990, p. 351, *ASTM STP 1000*.
13. C. Wagner, W. Traud, *Z. Elektrochem.* **1938**, *44*, 391.
14. G59-97, Standard practice for conducting potentiodynamic polarization resistance measurements, *Annual Book of ASTM Standards*, ASTM International, Philadelphia, Pa., 2000, p. 233, Vol. 3.02.
15. F. Mansfeld, *J. Electrochem. Soc.* **1973**, *120*, 515.
16. G106-89, Standard practice for verification of algorithm and equipment for electrochemical impedance measurements, *Annual Book of ASTM Standards*, ASTM International, Philadelphia, Pa., 2000, p. 450, Vol. 3.02.
17. M. Kendig, F. Mansfeld, *Corrosion* **1983**, *39*, 466.
18. D. D. Macdonald, M. Urquidi-Macdonald, *J. Electrochem. Soc.* **1985**, *132*, 2316.
19. J. R. Macdonald, *Impedance Spectroscopy*, edited by John Wiley & Sons, New York, 1987.
20. M. Urquidi-Macdonald, S. Real, D. D. Macdonald, *J. Electrochem. Soc.* **1986**, *133*, 2018.
21. I. Epelboin, M. Keddam, *J. Electrochem. Soc.* **1970**, *117*, 1052.
22. I. Epelboin, M. Keddam, H. Takenouti, *J. Appl. Electrochem.* **1972**, *2*, 71.
23. W. J. Lorenz, F. Mansfeld, *Corros. Sci.* **1981**, *21*, 647.
24. R. S. Lillard, P. J. Moran, H. S. Isaacs, *J. Electrochem. Soc.* **1992**, *139*, 1007.
25. R. S. Lillard, J. Kruger, W. S. Tait et al., *Corrosion* **1995**, *51*, 251.
26. M. W. Wittmann, R. B. Leggat, S. R. Taylor, *J. Electrochem. Soc.* **1999**, *146*, 4071.
27. K. Hladky, J. L. Dawson, *Corros. Sci.* **1981**, *21*, 317.
28. K. Hladky, J. L. Dawson, *Corros. Sci.* **1982**, *22*, 231.
29. P. C. Searson, J. L. Dawson, *J. Electrochem. Soc.* **1988**, *135*, 1908.
30. F. Mansfeld, H. Xiao, *J. Electrochem. Soc.* **1993**, *140*, 2205.
31. U. Bertocci, C. Gabrielli, F. Huete et al., *J. Electrochem. Soc.* **1997**, *144*, 31.
32. U. Bertocci, C. Gabrielli, F. Huete et al., *J. Electrochem. Soc.* **1997**, *177*, 37.
33. U. Bertocci, F. Huet, *J. Electrochem. Soc.* **1997**, *144*, 2786.
34. U. Bertocci, J. Frydman, C. Gabrielli et al., *J. Electrochem. Soc.* **1998**, *145*, 2780.
35. R. A. Cottis, *Corrosion* **2001**, *57*, 265.
36. F. Huet, *Interface* **2001**, *10*, 40.
37. H. Xiao, F. Mansfeld, *J. Electrochem. Soc.* **1994**, *141*, 2332.
38. ESA400, Ver. 1.11, Gamry Instruments, Warminster, Pa., 2001.
39. J. Kruger, J. P. Calvert, *J. Electrochem. Soc.* **1967**, *114*, 43.
40. B. MacDougall, M. Cohen, *J. Electrochem. Soc.* **1976**, *123*, 191.
41. N. Sato, M. Cohen, *J. Electrochem. Soc.* **1964**, *111*, 513.
42. G. T. Burstein, P. I. Marshall, *Corros. Sci.* **1983**, *23*, 125.
43. G. T. Burstein, R. C. Newman, *Electrochim. Acta* **1980**, *25*, 1009.

44. G. T. Burstein, D. H. Davies, *Corros. Sci.* **1980**, *20*, p. 989.
45. J. A. Bardwell, B. MacDougall, M. J. Graham, *J. Electrochem. Soc.* **1988**, *135*, 413.
46. G. T. Burstein, A. J. Davenport, *J. Electrochem. Soc.* **1989**, *136*, 936.
47. R. G. Kelly, R. C. Newman, *J. Electrochem. Soc.* **1990**, *137*, 357.
48. G. S. Frankel, C. V. Jahnes, V. Brusic et al., *J. Electrochem. Soc.* **1995**, *142*, 2290.
49. G. S. Frankel, L. Stockert, F. Hunkeler et al., *Corrosion* **1987**, *43*, 429.
50. Z. Szklarska-Smialowska, *Pitting Corrosion of Metals*, NACE International, Houston, Tex., 1986.
51. H. P. Leckie, H. H. Uhlig, *J. Electrochem. Soc.* **1966**, *113*, 1262.
52. B. E. Wilde, E. Williams, *Electrochim. Acta* **1971**, *16*, 1971.
53. G. S. Frankel, *J. Electrochem. Soc.* **1998**, *145*, 2186.
54. G48-99a, Pitting and crevice corrosion resistance of stainless steels and related alloys by use of ferric chloride solution, *Annual Book of ASTM Standards*, ASTM International, Philadelphia, Pa., 2000, p. 188, Vol. 3.02.
55. G69-97, Standard practice for measurement of corrosion potentials of aluminum alloys, *Annual Book of ASTM Standards*, ASTM International, Philadelphia, Pa., 2000, p. 268, Vol. 3.02.
56. R. Qvarfort, *Corros. Sci.* **1989**, *29*, 987.
57. R. Qvarfort, *Corros. Sci.* **1988**, *28*, 135.
58. R. J. Brigham, E. W. Tozer, *Corrosion* **1974**, *30*, 161.
59. R. J. Brigham, E. W. Tozer, *Corrosion* **1973**, *29*, 33.
60. P. E. Arnvig, R. M. Davison, *Proceedings of 12th International Corrosion Congress*, Paper No. 209, NACE, Houston, Tex., 1993, p. 1477.
61. P. E. Arnvig, A. D. Bisgard, *Corrosion 96*, Paper No. 437, NACE International, Houston, Tex., 1996.
62. N. J. Laycock, M. H. Moayed, R. C. Newman, Prediction of pitting potentials and critical pitting temperatures in *Critical Factors in Localized Corrosion II* (Eds.: P. M. Natishan, R. J. Kelly,G. S. Frankel et al.), ECS, Pennington, N. J., 1995, p. 68. Vol. PV 95–15.
63. N. Pessall, C. Liu, *Electrochim. Acta* **1971**, *16*, 1987.
64. F746-87, Standard test method for pitting or crevice corrosion of metallic surgical implant materials, *Annual Book of ASTM Standards*, ASTM International, Philadelphia, Pa., 2000, p. 203, Vol. 13.01.
65. E. Akiyama, G. S. Frankel, *J. Electrochem. Soc.* **1999**, *146*, 4095.
66. G. S. Frankel, *Corros. Sci.* **1990**, *30*, 1203.
67. J. W. Tester, H. S. Isaacs, *J. Electrochem. Soc.* **1975**, *122*, 1438.
68. G. T. Gaudet, W. T. Mo, T. A. Hatton et al., *AIChE J.* **1986**, *32*, 949.
69. H. S. Isaacs, R. C. Newman, Dissolution kinetics during localized corrosion in *Corrosion and Corrosion Protection* (Eds.: R. P. Frankenthal, F. Mansfeld), ECS, Pennington, N. J., 1981, p. 120, Vol. PV 81–8.
70. R. C. Newman, *Corros. Sci.* **1985**, *25*, 331, 341.
71. W. Zhang, G. S. Frankel, *Electrochem. Solid State Lett.* **2000**, *3*, 268.
72. A. Sehgal, G. S. Frankel, B. Zoofan et al., *J. Electrochem. Soc.* **2000**, *147*, 140.
73. G. S. Frankel, J. R. Scully, C. V. Jahnes, *J. Electrochem. Soc.* **1996**, *143*, 1834.
74. G. S. Frankel, J. O. Dukovic, B. M. Rush et al., *J. Electrochem. Soc.* **1992**, *139*, 2196.
75. A. Sehgal, D. Lu, G. S. Frankel, *J. Electrochem. Soc.* **1998**, *145*, 2834.
76. A262-93a, Standard practices for detecting susceptibility to intergranular attack in austenitic stainless steels, *Annual Book of ASTM Standards*, ASTM International, Philadelphia, Pa., 1994, p. 42, Vol. 1.03.
77. G108-94, Standard test method for electrochemical reactivation EPR for detecting sensitization of AISI Type 304 and 304L stainless steels, *Annual Book of ASTM Standards*, ASTM International, Philadelphia, Pa., 2000, p. 467, Vol. 3.02.
78. G112-92, Standard guide for conducting exfoliation corrosion tests in aluminum alloys, *Annual Book of ASTM Standards*, ASTM International, Philadelphia, Pa., 2000, p. 489, Vol. 3.02.
79. G34-99, Standard test method for exfoliation corrosion susceptibility in 2XXX and 7XXX series aluminum alloys EXCO test, *Annual Book of ASTM Standards*, ASTM International, Philadelphia, Pa., 2000, p. 124, Vol. 3.02.
80. G66-99, Standard test method for visual assessment of exfoliation corrosion susceptibility of 5XXX series aluminum alloys

ASSET test, *Annual Book of ASTM Standards*, ASTM International, Philadelphia, Pa., 2000, p. 261, Vol. 3.02.
81. G110-92, Standard practice for evaluating intergranular corrosion resistance of heat treatable aluminum alloys by immersion in sodium chloride + hydrogen peroxide solution, *Annual Book of ASTM Standards*, ASTM International, Philadelphia, Pa., 2000, p. 481, Vol. 3.02.
82. A. J. Sedriks, *Corrosion of Stainless Steels*, John Wiley & Sons, New York, 1996.
83. G31-72, Standard practice for laboratory immersion corrosion testing of metals, *Annual Book of ASTM Standards*, ASTM International, Philadelphia, Pa., 2000, p. 99, Vol. 3.02.
84. B117-97, Standard practice for operating salt spray fog testing apparatus, *Annual Book of ASTM Standards*, ASTM International, Philadelphia, Pa., 2000, p. 1, Vol. 3.02.
85. D. A. Buttry, The quartz crystal microbalance as an in situ tool in electrochemistry in *Electrochemical Interfaces* (Ed.: H. D. Abruna), VCH Publishers, New York, 1991.
86. W. H. Smyrl, K. Naoi, New monitoring techniques in corrosion: microbalances and surface acoustic wave SAW devices in *Perspectives on Corrosion* (Eds.: G. Prentice, W. H. Smyrl), AIChE, New York, 1990, p. 71, Vol. 278–286.
87. G. Sauerbrey, *Z. Phys.* **1959**, *155*, 206.
88. W.-Y. Lee, H. C. Seigmann, J. M. Eldridge, *J. Electrochem. Soc.* **1977**, *124*, 1744.
89. D. W. Rice, P. B. P. Phipps, R. Tremoureux, *J. Electrochem. Soc.* **1979**, *126*, 1459.
90. P. Schmutz, D. Landolt, *Corros. Sci.* **1999**, *41*, 2143.
91. E. Szocs, G. Vastag, A. Shaban et al., *J. Appl. Electrochem.* **1999**, *29*, 1339.
92. H. Ehahoun, C. Gabrielli, M. Keddam et al., *J. Electrochem. Soc.* **2001**, *148*, B333.
93. L. Kelvin, *Philos. Mag.* **1862**, *46*, 82.
94. W. A. Zisman, *Rev. Sci. Instrum.* **1932**, *3*, 367.
95. M. Stratmann, H. Streckel, *Corros. Sci.* **1990**, *30*, 681, 697.
96. M. Stratmann, H. Streckel, K. T. Kim et al., *Corros. Sci.* **1990**, *90*, 715.
97. M. Stratmann, *Berichte Bunsengesellschaft Physikalische Chemie* **1990**, *94*, 626.
98. R. E. Lobnig, D. J. Siconolfi, L. Psota et al., *J. Electrochem. Soc.* **1996**, *143*, 1539.
99. A. Leng, H. Streckel, M. Stratmann, *Corros. Sci.* **1999**, *41*, 547, 579.
100. A. Leng, H. Streckel, K. Hofmann et al., *Corros. Sci.* **1999**, *41*, 599.
101. W. Fürbeth, M. Stratmann, *Corros. Sci.* **2001**, *43*, 207, 229.
102. M. Rohwerder, M. Stratmann, *MRS Bull.* **1999**, *24*, 43.
103. M. Wolpers, M. Stratmann, H. Viefhaus et al., *Thin Solid Films* **1992**, *210/211*, 592.
104. E. Lange, H. Göhr, *Thermodynamische Elektrochemie*, Hüthig, Heidelberg, Germany, 1962.
105. R. Gomer, G. Tryson, *J. Chem. Phys.* **1987**, *66*, 4413.
106. A. W. Adamson, *Physical Chemistry of Surfaces*, John Wiley & Sons, New York, 1990.
107. F. Kohlrausch, *Praktische Physik*, Teubner, Stuttgart, Germany, 1968, Vol. 2.
108. M. Stratmann, *Die Korrosion von Metalloberflächen unter dünnen Elektrolytfilmen*, VDI-Verlag, Düsseldorf, Germany, 1994.
109. H. D. Liess, R. Maeckel, J. Ren, *Surf. Int. Anal.* **1997**, *25*, 855.
110. G. Grundmeier, K. Jüttner, M. Stratmann, Novel electrochemical techniques in corrosion research in *Corrosion and Environmental Degradation* (Ed.: M. Schütze), Wiley-VCH, Weinheim, Germany, 2000, p. 285, Vol. 1.
111. S. Trasatti, *Electroanal. Chem. Interfacial Electrochem.* **1974**, *52*, 313.
112. S. Trasatti in *Comprehensive Treatise of Electrochemistry* (Eds.: J. O. M. Bockris, B. Conway, E. Yeager), Plenum Press, New York, 1984, p. 45, Vol. 1.
113. S. Yee, M. Stratmann, R. A. Oriani, *J. Electrochem. Soc.* **1991**, *138*, 55.
114. V. Maurice, W. P. Yang, P. Marcus, *J. Electrochem. Soc.* **1994**, *141*, 3016.
115. V. Maurice, W. P. Yang, P. Marcus, *J. Electrochem. Soc.* **1996**, *143*, 1182.
116. A. Miyasaka, H. Ogawa, *Corros. Sci.* **1990**, *31*, 99.
117. I. C. Oppenheim, D. J. Trevor, C. E. D. Chidsey et al., *Science* **1991**, *254*, 687.
118. T. P. Moffat, F.-R. F. Fan, A. J. Bard, *J. Electrochem. Soc.* **1991**, *138*, 3224.
119. K. Kowal, J. DeLuccia, J. Y. Josefowicz et al., *J. Electrochem. Soc.* **1996**, *143*, 2471.
120. P. Schmutz, G. S. Frankel, *J. Electrochem. Soc.* **1998**, *145*, 2285, 2298.
121. P. Schmutz, G. S. Frankel, *J. Electrochem. Soc.* **1999**, *146*, 4461.